ADRIAN GOLDSTEIN | ANDREAS KRELL
ZEEV BURSHTEIN

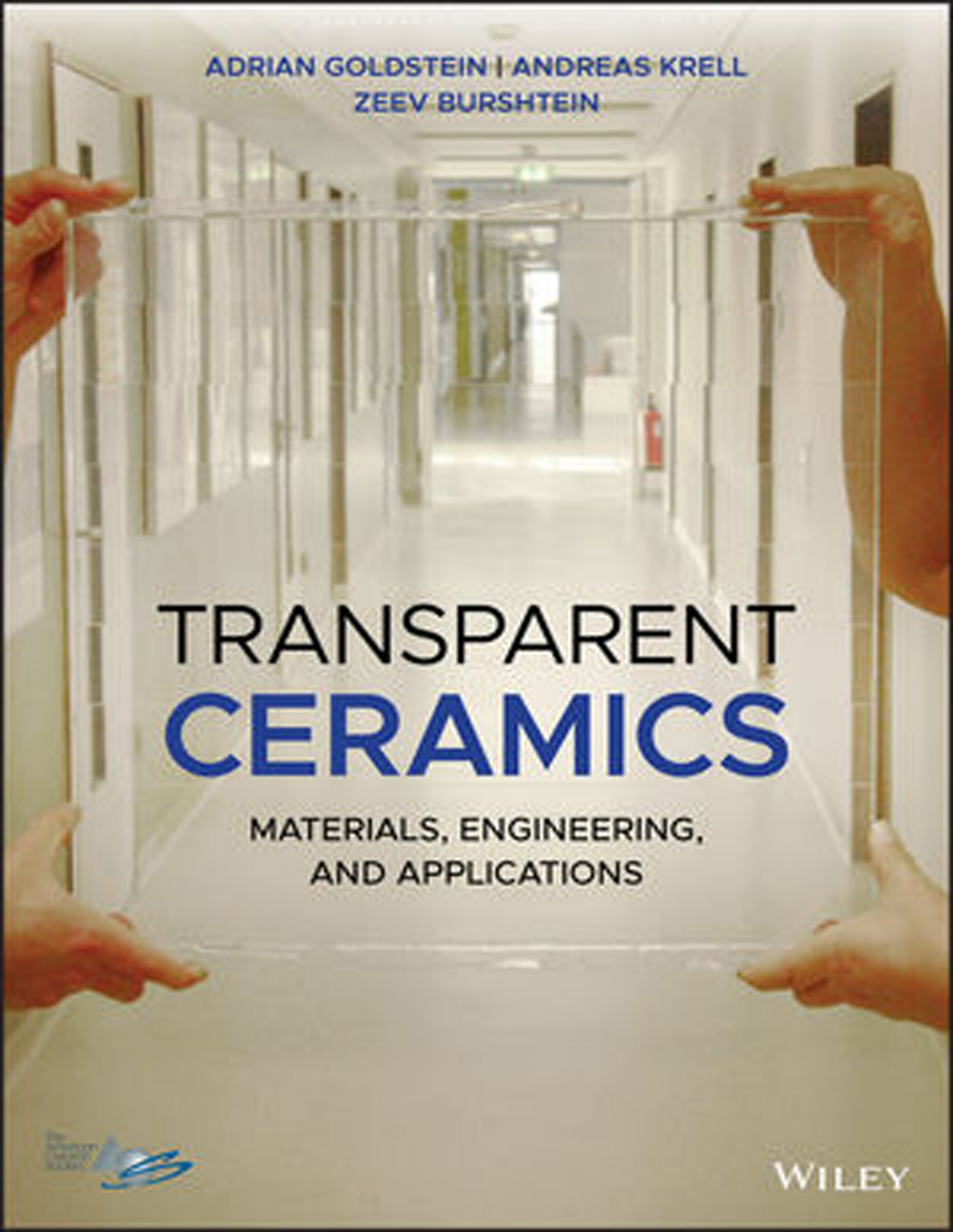

TRANSPARENT CERAMICS

MATERIALS, ENGINEERING, AND APPLICATIONS

WILEY

Transparent Ceramics

Transparent Ceramics

Materials, Engineering, and Applications

Adrian Goldstein, Andreas Krell, and Zeev Burshtein

WILEY

The American Ceramic Society

Published by John Wiley & Sons, Inc., Hoboken, New Jersey.
Published simultaneously in Canada.

Registered Office
John Wiley & Sons, Inc., 111 River Street, Hoboken, NJ 07030, USA

Editorial Office
111 River Street, Hoboken, NJ 07030, USA

For details of our global editorial offices, customer services, and more information about Wiley products visit us at www.wiley.com.

Wiley also publishes its books in a variety of electronic formats and by print-on-demand. Some content that appears in standard print versions of this book may not be available in other formats.

Library of Congress Cataloging-in-Publication Data

Names: Goldstein, Adrian, 1951- author. | Krell, Andreas, author. | Burshtein, Zeev, author.
Title: Transparent ceramics : materials, engineering, and applications / Adrian Goldstein, Andreas Krell, Zeev Burshtein.
Description: First edition. | Hoboken, New Jersey : John Wiley & Sons, Inc., 2020.
Identifiers: LCCN 2019035288 (print) | LCCN 2019035289 (ebook) | ISBN 9781119429494 (hardback) | ISBN 9781119429487 (adobe pdf) | ISBN 9781119429555 (epub)
Subjects: LCSH: Transparent ceramics. | Ceramic materials.
Classification: LCC QC378.5 .G65 2010 (print) | LCC QC378.5 (ebook) | DDC 620.1/404295—dc23
LC record available at https://lccn.loc.gov/2019035288
LC ebook record available at https://lccn.loc.gov/2019035289

Cover Design: Wiley
Cover Image: Corporations/Companies – Used with permission Fraunhofer IKTS

Set in 10/12pt WarnockPro by SPi Global, Chennai, India

Printed in the United States of America

10 9 8 7 6 5 4 3 2 1

I dedicate this book to my mother Sia and my wife Piticul

- Adrian Goldstein

Contents

Foreword

Who had imagined in 1964 that the first solid-state laser of Nd^{3+}-doped $Y_3Al_5O_{12}$ (YAG) single crystals might be replaced by Nd^{3+}-doped YAG transparent laser ceramics? Requests to fabricate such transparent ceramics are at the frontier of materials science and everyone considered at this time that transparent ceramic materials could not be used for laser or optical materials. However, dreams came true in 1995 and now garnet transparent laser ceramics are commercialized and have been extended also to Ce^{3+}-doped YAG as phosphors associated with blue LED for high power white lighting. Recently, the list of application of transparent ceramics, for which some of them are highly sophisticated, for laser media, phosphors, scintillators, armor windows, infrared domes, and electro-optical components have widely increase in all domains and have impacted our daily life.

This book addresses precise topics on available transparent ceramics (TCs) materials, how they are processed, their applications, and aspects of the progress made in their engineering as well as our scientific understanding. Adrian Goldstein, Andreas Krell, and Zeev Burshtein, well-known authorities in the international community of the ceramics, animated during all their scientific lives by the passion of the field and the desire to communicate it, were able to pause and review carefully the accomplishments of this period, the remaining challenges, and future prospects.

Clearly, the data presented are well explained, in correlation with the theoretical science and engineering background. This book answers well with the evolution of the transparent ceramics so that it will successfully help students and researchers for any developments still in a laboratory stage. As an example, data help to understand relationships between microstructures (porosity and size distribution of pores) and optical properties, and also processing strategies of densification and transparency. Their upgrading in the near future has to be relevant for industrial operations and will likely lead to significantly strengthen the economic relevance of the transparent ceramics.

Students, scientists, and engineers working with ceramics should get this book providing extensive references to contemporary works and being a basis for studying the field. It covers applications through detailed case studies and therefore a comprehensive guide to the current status of transparent ceramics, well suited to readers who wish to use it, either to understand these materials or to solve specific problems.

UCB Lyon 1, France

Georges Boulon
Emeritus Professor

Acknowledgments

We would like to thank some of the people who, in one way or other, had helped us in bringing this book to life: Prof. Julius Menessy, Dr. Michael Katz, Prof. Georges Boulon, Smadar Karpas, Prof. Ken-ichi Ueda, and Prof. Lisa Klein.

Dr. Zeev Burshtein has authored Sections: 2.1–2.5 (with minor contributions from A. Krell and A. Goldstein) and Sections 5.2.9.1.1–5.2.9.1.3 (included).

General Abbreviations

The "[]" contains units for parameter or molar concentration.

A	absorptance
A_{BET}	powder specific surface area [m^2/g], determined by the same calculation model applied to experimental gas adsorption data
AR	anti-reflective
ArS	sintering under 1 atm. of argon
AS	sintering under 1 atm. of air
a-SiO_2 (or other chemical compound)	amorphous silica
Vol%, atm.% or mol %	volume, atomic or molar percentage
wt.%	weight percentage
B	magnetic induction (or magnetic flux density) [T (=10^4 G (the gauss (G) is used in (cgs system)))]
BD	bulk density (g/cm^3 or % of TD)
BD_f	fired state density
BD_g	green-body density
BET	Brunauer–Emmett–Teller
c	cubic lattice
CAD	computer-assisted design
CAM	computer-assisted machining
CCT	correlated color temperature
CF	crystal field
CFT	crystal field theory (used for electronic spectra interpretation)
CIE	commission int. de l'èclairage
CRI	color rendition index
CVD	chemical vapor deposition
CW	continuous wave laser
D_0	ionic diffusion coefficient at standard temperature [cm^2 or m^2/s]
D_{50}	median particles size in a distribution
D_{BET}	equivalent particle diameter [nm] as calculated by BET method
DTA	derivatographic thermal analysis
E	Young modulus [GPa]
EDS (EDX)	energy dispersive X-ray spectroscopy (for elemental chemical analysis)
EFG	edge defined film fed growth (technique for crystals growth)
EMPA	electron microscope probe elemental analysis
EMR	electromagnetic radiation
EO	electro-optic
EPR	electron paramagnetic resonance
ESR	electron spin resonance
FEA	finite element analysis
FIR	far infrared subdomain (15–1000 μm)
FOG (or FOX)	fluoro-oxide glass
GB	grain boundaries
GS	grain size
GSM	maximal GS
GSm	minimal GS
H	magnetic field strength [A/m; Oe (in cgs system)]
h	Planck's constant
HAADF	high angle annular dark field imaging
HIP	hot isostatic pressing
HK	hardness measured with the Knoop indenter
HP	hot pressing
HR-SEM	high resolution SEM
HR-TEM	high resolution TEM

HV	hardness measured with the Vickers indenter
IR	infrared domain of the spectrum
k or k_B	Boltzmann's constant
k	wave vector (magnitude is the wave number)
K_{Ic}	[MPa $m^{0.5}$]
LCD	liquid crystal display
LED	light-emitting diode
LF	ligand field
LFT	crystal field theory improved by consideration of covalency
m	monoclinic
M_b	grain-boundaries migration rate in pore-free matrix
MIR	middle domain of IR (2.5–15 μm)
MW	microwaves (EMR of wavelength 1 mm to ~3 dm)
N_C	critical coordination number, in particles, of pores
NIR	near infrared subdomain of the IR (0.75–2.5 μm)
NUV	near ultraviolet subdomain (300–380 nm)
OLED	organic light emitting diode
op	open porosity (%)
OPA	optical parameter amplifier
OPA–CPA	amplifier based on chirped pulse amplification
PCA	polycrystalline (ceramic) alumina
PECS	pulsed electric current sintering (alternative to SPS)
PL	photo luminescence
PLE	photo luminescent emission
PLED	power LED
PLZT	La containing PZT
PMN	plumb magnesium niobate
Po	porosity [vol%]
P_oSD	pore size distribution
PS	pressureless (viz., at around 1 atm. of gas pressure) sintering
PSD	particle size distribution
PT	ceramic with composition located in the PbO–TiO_2 system
PVDF	polyvinylidene fluoride
PW	power [W]
PZT	ceramic with composition located in the PbO–ZrO_2–TiO_2 system; main source of piezoceramics
R	gas constant
R	reflectance
RE^+	rare-Earth cation
RIT	real in-line transmission
RT	room temperature
RTP	ready-to-press powder
S	scattered fraction of incident EMR beam intensity
SEM	scanning electron microscope
SIMS	secondary ions mass spectroscopy
SOX	solid oxides
SPS	spark-plasma sintering
STEM	scanning TEM
t	tetragonal
$t_a{}^0$	post-sintering annealing (mostly in air) temperature
t_f	melting (fusion) temperature
t_g	glass transition temperature
t_l	liquidus temperature (phase diagrams)
$t_s{}^0$	sintering temperature
T	transmittance (T% transmission percentage)
T%	transmission (in %) as a function of wavelength
TC	transparent ceramic
TD or ρ	theoretical density [g/cm^3]
TEM	transmission mode electron microscope
TEOS	tetra-ethyl-ortho-silicate
TFT	total forward transmission
TGC	transparent glass-ceramic
TGG	Terbium, Gadolinium garnet
TM^+	transition element cation
TRS	transversal rupture strength
T-YAG (or other transparent ceramic compound)	transparent YAG
TZP	tetragonal zirconia polycrystals
UV	ultraviolet domain of the spectrum (10 to ~380 nm)
VIS	segment of the electromagnetic radiation spectrum to which the human eye is sensitive (~0.38 to ~0.75 μm)

VS	sintering under vacuum	$\mathbf{\Delta}$	small variation
WLED	white light emitting LED	ε	extinction coeff. [l/(mol cm)]
X	powder particle size	λ	wavelength [nm, µm]
XRD	X-ray diffraction	λ_{th}	thermal conductivity [W/Km]
YAG	Yttrium, Aluminum garnet	ν	frequency [Hz]
YSAG	scandium containing	$\bar{\nu}$	wave number [cm^{-1}]
[K^{-1}]	thermal expansion coefficient [$^{\circ}$C/K]	τ	time
		ϕ	phase of wave
γ	surface tension [N/m]		

1

Introduction

1.1 Importance of Transparent Ceramics: The Book's Rationale Topic and Aims

Ceramics constitute a relatively new family of optical materials belonging to a larger class of transparent solids; other members of this class are glasses, single crystals, and some organic polymers [G21].

Overall performance of certain transparent components of many high-tech optical devices may be improved if manufactured using ceramics rather than alternative transparent solids. This is because transparent ceramics offer improved performance and/or robustness. Potentially they may also provide cost benefits to manufacturers. These claims can be exemplified with the case of the first commercially used transparent ceramic, which was translucent alumina Al_2O_3 (see details in Section 1.5.2). The material has provided its developer (General Electric of the United States) more than half a billion dollars in revenue during the final decades of the last century [B67]. It has been mostly used in the manufacturing of envelopes for high vapor pressure sodium Na streetlamps. Such feat has yet not been replicated. However a number of later developed optical components like armor, sand-blasting installations or chemical reactor windows, infrared (IR) sensor protective domes, solid-state lighting systems, $Nd^{3+}:Y_3Al_5O_{12}$ (Nd:YAG, yttrium–aluminum garnet) light gain media, scintillators, dental prosthetics, lenses, and various decorative objects are also commercialized (small scale) or in the upscaling to industrial manufacturing phase. Quite probably, transparent ceramics fabrication costs will be reduced (a lot of effort and financial resources are invested in this task worldwide), thanks to current research and development efforts, allowing enhanced commercialization of that important technology.

Transparent ceramics study is also relevant for advancing the general ceramics science, as some basic requirements like densification and purity are more stringent. Achievement of such targets requires innovative thinking and new technological approaches, based on deep and comprehensive understanding of underlying physical and chemical processes involved in ceramics engineering.

The above suggests that transparent ceramics may represent a topic of interest for many ceramists and also for people outside this community, like laser, lighting, or military optical systems developers. That potential interest is the rationale for the writing of this book. It intends to summarize the most interesting information accumulated during the 60-year-long history of the transparent ceramics domain: relevant materials, engineering specifics, properties, and applications. The information presented emanates mostly from published literature, but to some extent also from research performed by this book's authors. Emphasis is made on providing critique comparison between certain ceramics performance and their competitor materials per their targeted applications.

Most of the text was written at an introductory level, the main goal being to offer a **one-stop broad scope presentation** of the topic. To a certain extent, in-depth discussion was sacrificed for practical brevity. Exhaustive presentation, simultaneous with a wide range of considered issues, is obviously a feat difficult to achieve. Some quite modest background of general physics, chemistry, and ceramics science and engineering is sufficient for reasonable comprehension of most of the discussed issues. For a few, seemingly "arcane" yet basic topics, the book provides its own background. Thus, Chapter 2 in its entirety carries such support information. It is devoted to various aspects of electromagnetic radiation interaction with matter; its most important part is the section dealing with the interpretation of electronic spectra produced by transition element cation (TM^+) and RE^+ dopants. Chapter 3 deals with engineering and

Transparent Ceramics: Materials, Engineering, and Applications, First Edition. Adrian Goldstein, Andreas Krell, and Zeev Burshtein.

characterization of transparent ceramics. The general procedures encountered when dealing with advanced ceramics are also applicable to transparent ceramics. Certain aspects like severity of the demands related to some characteristics, however, are unique to transparent ceramics. Chapter 3 also focuses on these specifics without offering a detailed presentation of operational procedures. These can be found in dedicated excellent textbooks [G12, R5]. Chapter 4 presents the main transparent ceramic materials currently investigated. For each material, the main addressed issues are their structure and specific processing conditions and approaches, allowing fabrication of transparent samples. Those are discussed because the overall benefit of a transparent ceramic is also determined by its other-than-optical properties. Technological applications are treated in Chapter 5. In the chapter, for some of the more complex applications, like laser gain media, a review of the basics of laser physics and engineering is provided; a brief presentation of the projectiles/armor interaction is also preceding the discussion of transparent ceramics armor. For solid-state light sources, the background presents an extended gamut of historic lighting sources. Chapter 6 discusses briefly the further prospects of the domain. The book ends with conclusions related to the previous chapters.

To the best of our knowledge, only a single previous publication exists [K36] that addresses a similar broad scope of transparent ceramics. For a narrower but important domain of transparent ceramics relevant for laser applications, a useful source book authored by A. Ikesue et al. [I3] is available. It is our pleasure to express our appreciation of these previous efforts.

Note for facilitating reading: The text includes a number of abbreviations. The most ubiquitous are defined in a special section located the opening of the book; others, relevant only for specific sections are defined "locally". For often used parameters, their label is provided in the list of general abbreviations. However in certain places, a different notation had to be used for a parameter; in such cases the "locally" relevant label is indicated. Conversely a given letter may designate different parameters, in different sections; the local correct parameter letter correspondence is always indicated.

1.2 Factors Determining the Overall Worth of Transparent Ceramics

People are interested in transparent ceramics mostly owing to practical applications of various such products. Some of them exhibit a "large" volume, like lamp envelopes used in public road illumination, phosphors for solid-state lighting sources, or artificial gems. Others are remarkable, owing to their destined high-tech applications, like in outer space-stationed lasers for solar energy harvesting, gain media for laser wake-field charged particle accelerators [B34] or sparkless car engine igniters [T3]. Yet others are impressing owing to the sophisticated technology required for their fabrication, like in the case of the anisotropic derived ceramics gain media (particle orientation under strong magnetic fields [S11]), transparent polycrystalline c-boron nitride and diamond (GPa-range hot pressing [I13, T20]), or solid-state transformation of polycrystalline material into single crystals [I3].

In this section we will briefly discuss the main factors (technical and economical) that determine the worth of transparent ceramics.

1.2.1 Technical Characteristics

The fundamental useful characteristic of a transparent ceramic is obviously its electromagnetic transmission capability, especially in the optical region and its general optical properties [K56, K59]. The spectral transmission window width and/or its level are the most important features. Transmission level is not exactly identical with the transparency concept. The transparency (see Section 1.4) is assessed by the fraction between the total forward transmission (TFT) and the so called real in-line transmission (RIT). For most applications, transparency is the important feature, but in some cases, like streetlamp envelopes, the TFT is the relevant parameter. However it has to be emphasized that transparency alone is rarely sufficient to make a transparent ceramic-based product interesting. The optical transmission property has to be accompanied by other favorable functional properties. The nature of these properties depends on the specific application. For instance, hardness and stiffness are critical properties for use as armored windows; ferroelectric properties count the most for antiglare goggles; a high refractive index coupled with a low optical dispersion are important for lenses. For all transparent ceramics, high resistance to ambient chemical aggressive agents is a fundamental requirement. A transparent ceramic suitability to a destined application is expressed using figures of merit, which take into account a weighted assessment of all relevant properties.

In many cases besides performance, the practical value of a transparent ceramic is strongly affected by the availability of suitable geometric dimensions and/or shapes. For instance, for armor applications, fabrication technology is fully developed for plates, 30–100 cm wide (sometimes exhibiting some curvature). For missile IR sensors, dome or cone-shaped protective noses are needed. Certain laser applications require a thin chip, or fiber geometry.

1.2.2 Fabrication and Characterization Costs

Designed transparent ceramic samples are always in competition with other transparent materials, like glasses or single crystals. A transparent ceramic may become commercially relevant only if **in addition** to technical performance, it also makes sense economically, namely, it can be manufactured at a competitive cost. For example, spinel $MgAl_2O_4$-based transparent armor strike-faces of large size can now be fabricated, exhibiting excellent performance; however, their price is still prohibitive, leaving most of the market to all-glass or glass + glass-ceramic offers. Processing costs are usually the determinant factor, but in some cases characterization costs also need consideration. The relative weight of these two aspects varies among different applications and may also change over time.

1.2.3 Overview of Worth

Transparent ceramics may thus exhibit benefit in two ways. One relates to cases where they provide improved functional abilities. Second relates to (still very few) cases where they provide lower manufacturing cost compared to manufacturing of other competing transparent solids. A best situation is of course when both advantages exist simultaneously. In our view, some transparent ceramics **have the potential** to achieve this desired goal. In this context, we venture to point out items like phosphors and scintillators, laser gain media, armor (heavy-duty industrial equipment) and IR windows.

1.3 Spectral Domain for Ceramics High Transmission Targeted in This Book

1.3.1 High Transmission Spectral Domain

Many natural or human-caused physical processes are accompanied by emission or absorption of electromagnetic waves, carrying different amounts of energy and particularly exhibiting different wavelengths or frequencies. The said wavelength range is named **electromagnetic radiation spectrum**.

Let us recall that the energy E_{ph} of an electromagnetic wave quantum (photon) is proportional to its frequency ν or to the inverse of its free-space wavelength λ:

$$E_{ph} = h\nu = hc/\lambda \tag{1.1}$$

where $c = \lambda\nu$ is the free space speed of light constant and h is Planck constant. The latter are universal constants: $c = 2.9979 \times 10^8$ m/s and $h = 6.626 \times 10^{-34}$ J s. The wavelength reciprocal $\overline{\nu} \equiv 1/\lambda$ is called wave-number. The quantic nature of the electromagnetic field expresses itself particularly during absorption and emission by matter. The electromagnetic wavelength spectrum is virtually infinite and quite broad even in practice (Figure 1.1). In practice means as measured or used by us humans. Even then, it covers about 15 orders of magnitude!

Gamma ray wavelengths range between approximately 1 and 10 Å, while, say, radio waves, may reach and exceed 10^3 m. Here we cite several examples. A natural process emitting gamma (γ) rays is the decay of excited atomic nuclei and deceleration of charged particles during impacting other particles. X-rays appear, for example, when energetic electrons bombard atoms (this process involves initial ejection of bound electrons, then filling the remaining empty atomic state by an external electron). Particles collision may also involve X-ray emission. Solar activity is a daily source of electromagnetic radiation emission, with frequencies ranging in the ultraviolet (UV), VIS, and IR. Fuel combustion (namely, fast, mainly carbon oxidation) generates mostly near-infrared (NIR) radiation. Electrical currents, based mostly on negative charge movement inside electrical conductors, are used in devices like radio broadcasting or telecommunication systems, which generate electromagnetic radiation in the range of so-called radio waves. Part of the electromagnetic radiation (EMR) generated by the sources described above and others travels around us. A lot of devices need various amounts and spectral segments of this radiation. The transparent ceramics' mission is to select the spectral segment and intensity of the EMR entering some of these devices; they can do this for different spectral segments; the one of interest in this book will be specified below.

When an incident electromagnetic wave (light) hits the surface of a macroscopic solid, it may undergo several processes, classified as reflection, absorption, scattering, and **transmission** (a part of absorbed light may be re-emitted). The ratios among the said process intensities depend on the physical characteristics of the solid.

Various technological applications require the use of solids that are transmissive to electromagnetic radiation over different segments of the spectrum. For instance, X-ray windows favor low atomic number Z solids; carbon, in the form of a graphite plate, is a reasonable solution. Ceramics often transmit variable fractions of incident electromagnetic radiation in different spectral sections; in other sections they may absorb massively. For instance, beryllium oxide BeO is highly transmissive in the microwave region; thus BeO-based ceramic samples are used for windows there.

This book will not consider all spectral ranges where ceramics exhibit transparency. It focuses on the 0.1

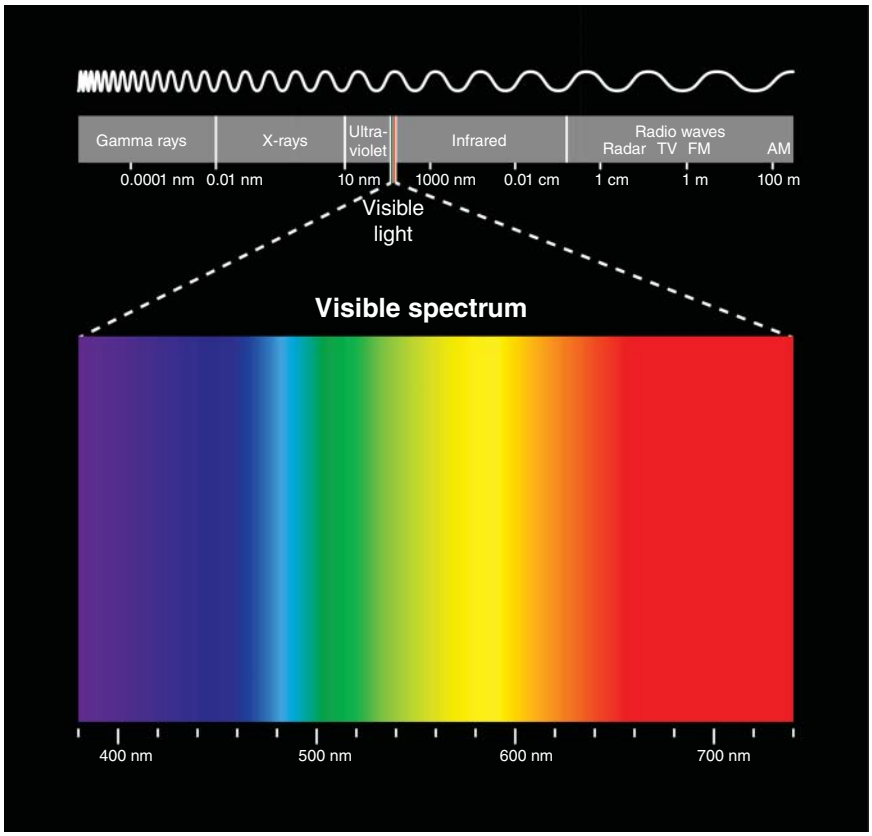

Figure 1.1 Overall wavelength range of the spectrum of EMR (domain to which human eye is sensitive, the VIS, is enlarged in the lower part of the figure). Source: Reproduced from Shutterstock Images with purchased permission.

to ~25 µm range, namely, **from the near-ultraviolet (NUV) to the mid-infrared (MIR)**, that is often addressed as **optical region**. Electromagnetic radiation in that range is simply addressed as **light**. The frequency/wavelength range in which a specific material is actually transmissive is termed **transparency/transmission window**. This means that only ceramics exhibiting significant transmissivity in portions of the range defined above will be considered. Figure 1.2 illustrates transmission windows offered by several already commercially available ceramics; for comparison, the transmission spectra of two popular oxide glasses is also shown (wider transparency glass windows also do exist).

The earth atmosphere is transparent [H15] (luckily for us) only to certain ranges of the overall EMR spectrum. It contains various molecules that significantly absorb electromagnetic radiation at various frequencies of the range of interest here. The most important ones are water H_2O, carbon dioxide CO_2, and to a certain extent also ozone O_3. Eventually, the atmosphere is transparent in the VIS and up to about 2.7 µm, with two narrow opaque ranges above about 1 µm. Best transparency in the IR is found in a so-called midwave window, ranging between 3 and 5 µm, and a second, long wavelength window, between 8 and 14 µm. Evidently, transparent ceramics exhibiting transparency overlapping the same regions as the atmosphere would be useful for a host of technological applications.

1.3.2 Electromagnetic Radiation/Solid Interaction in the Vicinity of the Transparency Domain

As seen in Figure 1.2, the relevant inorganic solids (ceramics and certain glass-ceramics) exhibit a broad optical transmission window ending quite abruptly at short and long wavelengths (high and low frequencies, respectively) termed **cutoff edges**. The short wavelength edge is often called UV edge, while the long wavelength edge is correspondingly called the IR edge, or MIR edge. Strong absorptions occur off the two cutoff edges, however involving different physical mechanisms, briefly discussed in Section 2.4.1 and 2.4.2.

1.4 Definition of Transparency Levels

Besides the **transparency** term describing the nature of light crossing through a ceramic material, an associated **translucency** term is often used. Both terms describe the same physical process, indicating difference only in

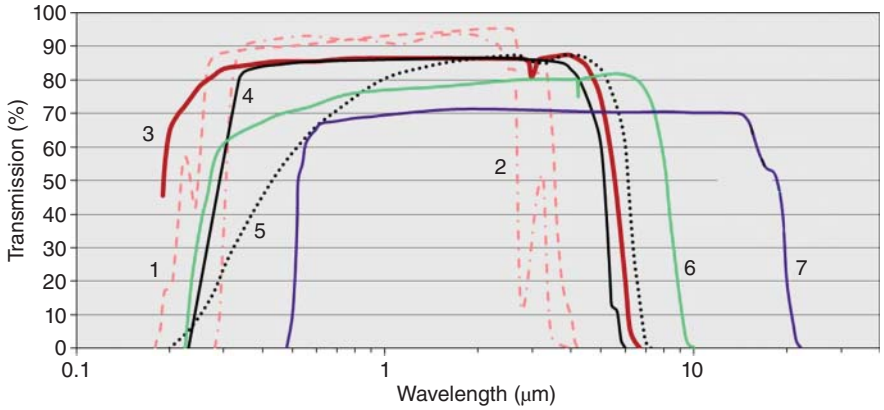

Figure 1.2 Transmission range of a few transparent ceramics and glasses shown by the aid of optical spectral curves. 1, Fused silica glass; 2, borosilicate glass; 3, $MgAl_2O_4$ ceramic; 4, AlON ceramic; 5, submicron alpha alumina ceramic; 6, yttria ceramic; and 7, ZnSe single crystal/ceramic.

the degree by which an incident light beam preserves its ordered properties upon interaction with a transmissive solid.

Any light beam incident on a highly polished ceramic plate undergoes reflection at the plate surfaces, possibly in bulk scattering and absorption and what remains is transmitted. Each process may be described by a parameter defined as the ratio of its intensity relative to the incident beam intensity.

Transparency: A solid is defined here as **transparent** if it allows the formation of a **clear and undistorted image** on a screen (practically a human eye retina) by light emanating from an object and passing through the solid. Transparency requires that a considerable fraction of light emanating from an object point crosses undistorted through the solid. Any light crossing the solid classifies into RIT and "diffusely forward transmitted." Together with the RIT, they form the total transmitted light (TLT). If scattering occurs, then scattered light is divided between forward- and back-scattered. Only the RIT fraction contributes to formation of a clear image, namely, transparency. Transparency experimental characterization requires discriminating the in-line forward transmitted intensity from the diffuse one. Technically, this means that spectral measurements using sensors of less than 0.5° angular resolution need to be used for the RIT measurements. The main factors determining ceramics optical transmission are the chemical constituent material and crystalline structure. Second in importance is light scattering owed to the presence of second phases and/or birefringence in the constituent material. Lower scattering improves transmission. Absorption is also a deleterious factor, but in most cases, optical absorption may be kept sufficiently low to make its effect negligible.

Translucency: The term **translucency** is a qualitative term, with the connotation of low to moderate transparency. It implies the existence of a considerable diffuse component in the transmitted light intensity; the total transmission is then usually also quite low (but not in all cases). It is impossible to unequivocally distinguish between translucency and transparency merely by the experimentally measured transmission. It was proposed to label a material "transparent," over a certain spectral range, when its in-line forward transmission (RIT) is larger than about 65% for a 2 mm thick plate [K56]. It is quantified as only **translucent**, if the in-line forward transmission is smaller than about 65%, but larger than about 15%. However such limits while practically useful are arbitrary; translucent is a qualitative term. At even lower transmission levels (say, a transmittance of less than 15%), the material is called **opaque**. A translucent material usually exhibits a relatively low transmission, since the existence of a forward diffuse transmission also entails considerable backward scattering. While the former may exceed the latter, the ratio cannot be too high. Simplified, rather quick laboratory practices are common for gross assessment of ceramic transparency/translucency. The studied ceramic is machined as an optically polished plate, several millimeters thick. One then looks by the unaided eye through the plate onto a printed, well-illuminated text, with the sample positioned about 2 cm above. Such visual inspection is quite useful, in practice, to discriminate between translucent and transparent samples (Section 3.2.3): thin translucent and transparent plates may look similar if the sample position is intimately close to the text, but it blurs with distance for a translucent plate. Visual inspection of specimen thickness variation on the printed letters resolution is also a good approach to compare transparency levels. For highly transparent samples, thickness produces only a minor effect; it leads to gross distortions and clarity loss, if the sample is only translucent.

1.5 Evolution of Transmissive Ability Along the Ceramics Development History

There are three varieties of transmissive polycrystalline ceramics, which differ markedly as to the mechanism conferring them that optical property. The first family (dominant phases are crystalline), representatives of which were already fabricated more than 1000 years ago (porcelains as an example), owe their transparency, low or moderate, **to a certain content of glassy phase(s)**. The second family contains materials that include **glassy and crystalline phases, which are both transmissive**; most of glass-ceramics belong to this family. The third family, of **all-crystalline materials**, owe its transparency to the fact that the specific crystalline phases are transparent. Members of this family usually contain less than 1% of non-crystalline residues (see Section 1.3.1; paragraph preceding Figure 1.2).

This book's major topic is the realm of all-crystalline ceramics. Glass-ceramics are also considered, but not discussed in detail. In our view, their phase assemblage makes them a topic that deserves an independent comprehensive treatment; their discussion is mandatory for both books concerned with glass and with ceramics.

1.5.1 Ceramics with Transparency Conferred by Glassy Phases

The word "ceramic" originates from the Greek word "κεραμοξ" that describes clay-made (burnt earth) wares. The root of the word is an older Sanskrit word meaning "to burn" [O1]. For a long time, ceramics were objects derived mainly from various types of clay. Other important ingredients were sand and flux like feldspars. Shaping utilized the plasticity of wet clays. Strength and other mechanical properties were achieved by heating at various temperatures, mostly between 900 and 1450 °C. Later on, sintering of nonmetallic powder compacts – formed by pressing or slip casting – was included as a common ceramic fabrication method.

Ceramic objects are being manufactured by humans for a long time [H7]. The first clay-based objects related to the worship of various deities. A notable discovery was the "Venus" at Dolni Vestonice (Czech Republic), dated as some 27 000 years old in the Paleolithic era [V3]. They are among the first art objects produced by man, dating from the same period with the "Lion-man" made of ivory [H7]; in this period man was still a gatherer and hunter (agricultural revolution started around 15 000 years later).

For much of their history, said ceramic samples were opaque. Some 5000 years ago, glass making started across the Middle East (Egypt through Mesopotamia) [M2]. Glass objects manufactured in the early days of the Roman Empire achieved a very high level of transparency [M2]. Especially tableware were either ceramic or transparent glass made. People then started to explore materials that would combine some superior functional properties of the opaque ceramics with the esthetically enticing transparency and gloss of glass. Particularly since ceramics and standard glasses contain combinations of similar oxides, silica SiO_2, sodium oxide Na_2O, potassium oxide K_2O, and alumina Al_2O_3. Obviously, the manufacturing processes are fundamentally different.

A glass is formed by fast cooling of melts; it is a mono-phased solid, based on a disordered lattice, which is isotropic at the optical wavelength scale. It can be produced as large blocks devoid of any internal interfaces on the microlevel. When well processed, "large" (over several millimeters sized) pieces lack any regions that might produce light scattering; non-optimally processed glasses may still contain air bubbles causing light scattering. The absorption bandgap of usual silicate glasses is in the UV, and absorption by transition element cations is very low. Consequently, conditions are well met for allowing VIS light transmission. A silicate-based glass window can be highly transparent.

In contrast to glass, earthen ware like a pot, the earliest ceramic form, are polycrystalline, including phases like quartz and aluminosilicates. Most crystallites making up these bodies are optically anisotropic, exhibiting different refractive indices at different light propagation orientations and/or polarizations, and they are randomly oriented. Moreover, large amounts of variable size pores are present. Such samples are thus opaque to VIS light (see Section 2.1).

When sufficiently thin, the first ceramic showing faint translucency was the porcelain (English name adopted from the French, itself converted from the Italian "porcellana," a translucent marine shell variety). Invented in China, it is often called chinaware. It was perfected in the Jingdezhen region of southeast China, sometime under the Tang dynasty (seventh till tenth century). This ceramic, while also including anisotropic quartz SiO_2 or mullite $2Al_2O_3 \cdot SiO_2$ crystallites, had almost all its intercrystallite regions filled with a feldspathic glass. It exhibited only less than ~0.5% open porosity, and the refractive indices difference among the various phases was relatively low. Owing to the large amount of glass (>60%), thin samples of this material achieved some translucency. In fact, this ceramic comprises a dispersion of crystalline grains in a glassy matrix. The so-called soft porcelains, containing more glass, are more transparent. Still their translucency level can be characterized as moderate. A more significant level of optical transmission was achieved with the advent of bone-china. This kind of soft porcelain was developed in England at

(a) (b)

Figure 1.3 Evolution of transparency during ceramic history (a) clay pitcher (around 1000 current era), opaque. Source: Reproduced with permission from Hecht Museum, Haifa University, Israel. (b) Bone China saucer, translucent.

the end of the eighteenth century. It consists of anorthite feldspar $CaAl_2Si_2O_8$, β-tricalcium phosphate $Ca_3(PO_4)_2$, and a few quartz SiO_2 crystals, all dispersed in a large volume of a heterogeneous silicate glass including calcium oxide CaO and alumina Al_2O_3, with minimal amounts of phosphorus oxide P_2O_5. The high mechanical strength of this porcelain allows fabrication of very thin section wares. Figure 1.3 provides photographs of an opaque ceramic and a bone-china dish.

The glass-ceramic class of materials was discovered during the forties of the twentieth century [S47–S49]. As finished products, these materials were initially entirely crystalline, or comprising a small volume fraction of glass and various crystalline phases. While having many useful mechanical properties, these glass-ceramics were opaque. The glass-ceramics are derived from a "mother glass" by **controlled** partial or close to full crystallization. They typically contain at least 20 vol%, up to over 98 vol% polycrystalline phase(s). Further work [B21–B23, P10, P30] in the 1950s and early 1960s resulted in the development of transparent glass-ceramics. In these materials, transparency appears either because the crystallites, which may be even micrometers sized, exhibit only slight anisotropy. For example, stuffed beta-quartz β-SiO_2-like solid solutions (including lithium Li^+, aluminum Al^{3+}, magnesium Mg^{2+}, and/or other positive ions) have a refractive index matched to that of the substantial fraction of residual glass phase or are based on nanosized crystals (grain-sized GS < 50 nm) that produce relatively little light scattering. Most of the early transparent glass-ceramics included at least 20–30 vol% glass, which was as important as the transmissive ability of the crystalline phases to their transparency. Recently, controlled crystallization also became a method for "fully" crystalline transparent sample production [R30] (glass content being less than 0.5 vol%; see Section 3.1.4).

In the late 1950s, the first real transparent ceramic objects, exhibiting a fair level of light transmission, comprising only polycrystalline phases, was developed [B66]. A brief presentation of that development is the subject of the next section.

1.5.2 The First Fully Crystalline Transparent Ceramic

General Electric's research department has developed a fully dense polycrystalline alpha-alumina α-Al_2O_3 product named **Lucalox** (acronym for trans**luc**ent **al**uminum **ox**ide), exhibiting a high (mostly diffusive) TFT, together with a significant in-line transmittance, for less than approximately 1.5 mm thickness. This development demonstrates a good example of synergy between ceramic and engineering sciences [B66, C2, C39]. The latter contributed a highly pure, only slightly agglomerated submicron raw material. As opposed to most alumina powders of that time, it was based on quite isometric particles. It has also been observed that very small additions of magnesium oxide MgO could promote sintering densification and eliminate or reduce the fraction of excessively large grains in the sintered product. Regarding ceramic science, the Lucalox development occurred in a period when modern understanding of sintering made a huge leap forward. Some of the luminaries of sintering theory, first and foremost R. L. Coble, were directly involved in the Lucalox saga. Combining experimental observations (some made by chance) with suggested sintering models, the developers concluded that (i) intra-grain occlusion massively stabilized pores; (ii) occlusion is favored by grain growth, especially its "abnormal" variety; (iii) abnormal grain growth may be reduced by suitable dopants (that control, probably selectively, grain boundary mobility); and (iv) magnesium oxide MgO was the most efficient such additive. Work started around 1956 and by 1959 led to the eventual achievement of a pore-free, highly translucent alumina, such as that shown in Figure 1.4.

Compared to fused silica, the Lucalox product at that time combined a very reasonable transmittance with excellent refractoriness, reasonable resistance to thermal shock, and enhanced resistance to chemical attack by high pressured sodium Na vapor at ~1200 °C. The Lucalox allowed the design of streetlamps, based on the fluorescence of high pressure sodium oxide NaO vapor. The high pressure and temperature – allowed by alumina but not the silica containers – conferred to the lamps exceptional luminosity, up to about 100 Lm/W. This device (Figure 1.5), the first to include transparent ceramic as a key component, was marketed in 1966 and achieved great commercial success. By 1990, some US$500 million worth of such lamps were sold.

The advent of the Lucalox, and then its commercial success, immediately triggered great interest in

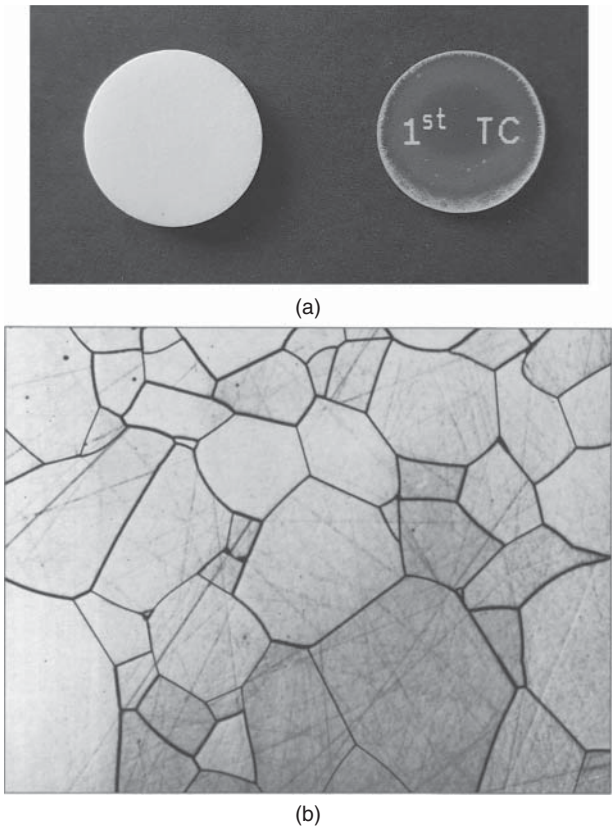

Figure 1.4 First translucent, all-crystalline ceramic: imaging and microstructure (a) White opaque regular alumina ceramic (left) translucent "Lucalox" (GE) ceramic alumina (right) and (b) microstructure (center grain = 95 micron) of translucent part shown above.

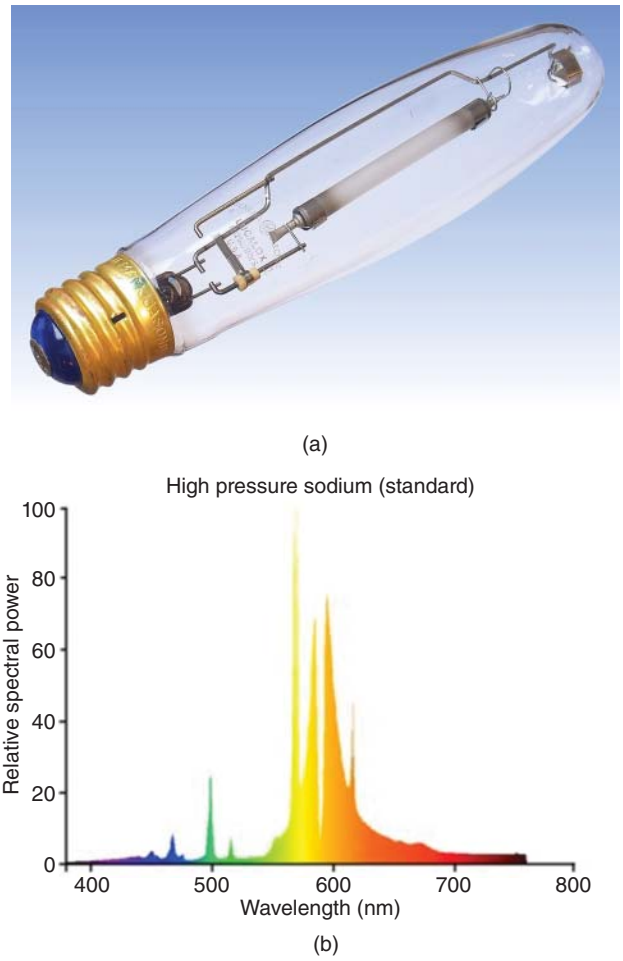

Figure 1.5 Lamp (high pressure Na vapor) including vapors, envelope made of translucent Lucalox alumina. From GE advertising material. (a) Product image and (b) spectral composition of light emitted by lamp of panel (a).

transparent ceramics. New materials and processing approaches, along with considerable basic knowledge, resulted in efforts to develop new transparent ceramics.

1.5.3 A Brief Progress History of All-Crystalline Transparent Ceramics

The Lucalox alumina described in Section 1.5.2 was the first transparent ceramic devoid of any glassy phases. It has been manufactured by the powder compacts sintering method. One may rightfully define the date of that development completion, roughly in 1960, as the start of transparent ceramics research and development era.

Progress in this domain involved development of new materials and introduction of new processing and characterization methods. Some contributions were of a basic nature, being relevant for the general ceramics science and engineering.

One may cite magnesium oxide MgO and magnesium fluoride MgF_2 (1962), perovskite lead zirconate titanate (PLZT, $PbZr_xTi_{1-x}O_3$) (1967), and magnesium spinel $MgAl_2O_4$ (1969) among the first transparent ceramics developed (lab scale) after Lucalox. Unlike alumina, the lattice of these materials is cubic, thus allowing high transmission levels, quite close to that of glass. Various other passive transparent ceramics, like aluminum oxynitride (ALON, $(AlN)_x(Al_2O_3)_{1-x}$), or diamond C, were achieved in later years (eighties through nineties). Transparent ceramic Neodymium-doped yttrium–aluminum garnet $Nd:Y_3Al_5O_{12}$ (Nd:YAG abbreviated) [I6] (Figure 1.6) was developed in the early 1990s; transparent zirconia ZrO_2 (allowing special lenses fabrication) was produced more recently. The progress in the 1960s was accomplished mostly by the efforts of some American private companies (indeed under governmental financial backing) like General Electric, Avco, Raytheon, Eastman-Kodak, Alpha, and Motorola, or by national research organizations like Sandia, North Carolina State University, and Missouri-Rolla University (PLZT). As of the 1980s,

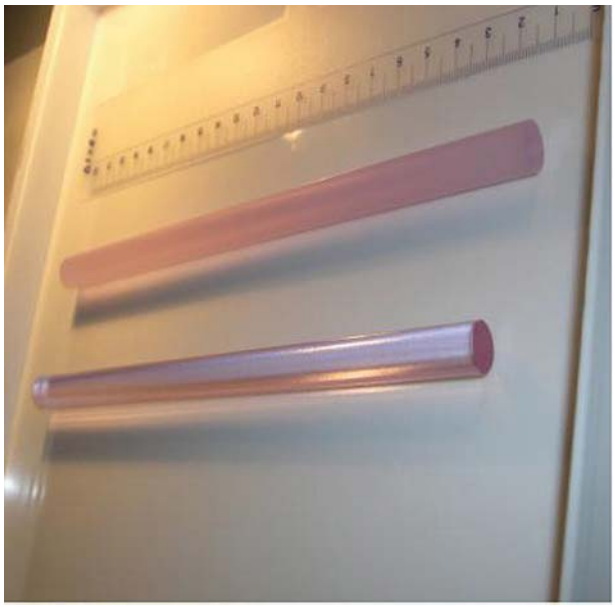

Figure 1.6 Nd:YAG rod-shaped ceramic gain media for solid-state lasers. Top: rod etched surface and bottom: rod polished after etching. Source: Reproduced with permission from R. Feldman et al., Israel [F4].

transparent ceramics development spread throughout the world. Most remarkable results have been achieved in Japan, Germany, France, Russia, Italy, Poland, China, Singapore, and Israel. Each material has also been characterized by its specific structure and non-spectral properties, allowing widening the applications range for which the transparent ceramics became useful. In some cases, it became more attractive than the competing glasses or single crystals. For example, magnesium spinel $MgAl_2O_4$ was found preferable for fabrication of armor windows strike-faces and IR sensor-protective covers; PLZT ($PbZr_xTi_{1-x}O_3$) allowed the production of goggles protective against atomic explosion flash. Materials like calcium fluoride CaF_2, YAG ($Y_3Al_5O_{12}$) and yttria Y_2O_3 were able to accommodate rare-earth (RE)-type cations in crystallographic sites of suitable symmetry and size. It allowed fabrication of laser light gain media, phosphors, scintillators, and artificial jewelry. Zinc sulfide ZnS functions as a good window for light sensors operating in the 8–14 μm range, which is even resilient as dome covers for forward looking IR cameras of aircrafts, flying at moderate speed. A more detailed list of transparent ceramic materials is given in Chapter 4. Applications are further discussed in Chapter 5.

Processing progress (Chapter 3) was achieved by a number of sometimes interacting ways. One way was multiplication of basic fabrication methods. Some methods exhibited a broad scope of usability; others were developed specifically for transparent ceramics. The general pulsed electric current sintering (PECS) method allowed reduction of sintering temperatures. For instance, spinel $MgAl_2O_4$ could be densified at around 1200 °C under a pressure of 400 MPa, or even more so, under 1000 °C and hot pressing at ultrahigh pressure (2–8 GPa). At such high pressures, spinel densification could be obtained at as low as 550 °C. Consequently, remnant pores size was of only a few micrometers, providing optical transparency to samples that still had some 2 vol% porosity (usually, transparency is lost for over ~200 ppm porosity if pores size is in the submicrometer or larger range). Direct conversion of graphite to transparent diamond became feasible at 20 GPa. These methods are improved variants of the powder sintering approach, the one used exclusively in early production of transparent ceramics. Over time, other approaches, like bulk chemical vapor deposition (CVD) and bulk sol–gel reaction, allowed fabrication of exotic components, such as polycrystalline diamond domes and transparent cubic alumina γ-Al_2O_3. More recently, fully controlled crystallization made possible the transformation of initially glassy samples into transparent ceramics; for example, barium oxy-aluminate $Ba_2Al_4O_7$. A large step toward extension of the usable materials from cubic to those of lower symmetry has been accomplished by the development of particles orientation by "slip"-casting under a magnetic field. Scattering owed to birefringence in non-cubic dense ceramics could be massively reduced by fabrication of nanograined ceramics and glass-ceramics. Solid-state conversion of polycrystalline ceramics into single crystals allowed fabrication of laser gain media with improved optical characteristics. For that purpose, preparation of ultrapure spheroidal particles by flame spray pyrolysis, or via laser vaporization, deserve a special mention. An important step toward full densification of sintered powders was the realization that shaping of the green bodies is crucial. To achieve that goal, new powder synthesis and processing methods were introduced. One may also cite attrition and jet-milling, supercritical conditions fluid expansion, or sprayed-suspension freeze drying. Pressure slip casting, gel-casting magnetic-pulsed uniaxial pressing, or centrifugal deposition was used in order to shape and consolidate powders into compact green bodies exhibiting low average pore size at even distribution. Progress was made also regarding the material characterization during various stages of the fabrication processes (Chapter 3).

2

Electromagnetic Radiation: Interaction with Matter

To facilitate understanding of the issues debated in Chapters 3–5, this chapter discusses certain aspects of electromagnetic radiation interaction with matter in general, and with solid matter in particular, with emphasis on the relevant spectral range. The focus is on processes that lead to disruption of the light beams impacting solid objects: intensity loss, polarization change, and others. A quite large fraction of space is devoted to theoretical background necessary for interpretation of optical and magnetic electronic spectra. The intention is to provide, for that topic, a relatively easy-to-read text for the interested ceramicists. Original sources for acquiring this knowledge, while excellent, require extensive and in-depth knowledge of some aspects of physics and mathematics, often not part of the background ceramicists have acquired during their studies and from experience. Emphasis is put on theoretical spectroscopy because it is well presented in some books devoted to glass technology [B18, P14] while otherwise in books on ceramics engineering.

2.1 Electromagnetic Radiation: Phenomenology and Characterizing Parameters

An accelerated charged particle generates electromagnetic radiation, roughly classified as "near field" and "far field."

Near field occurs in the light source vicinity and diminishes at distances of only several wavelengths away. The field radiation intensity decreases proportionately to the third power of distance. For example, loops of electrical currents (electron hordes in movement) produce a static magnetic field (magnetic dipole type), rapidly diminishing away from the source current. Moving charges, particularly antennas, which generate an alternating electric field (namely, an alternating electrical dipole), produce an alternating electromagnetic field propagating in space. It also quickly attenuates with growing distance.

Far field relates to electromagnetic radiation propagation at long distances compared to its wavelength. It is not affecting, nor being affected, by the source. In free space, these electromagnetic fields exhibit mutually perpendicular, transversely oscillating electric field $\mathcal{E}$ and magnetic field $\mathcal{H}$. The wave-front propagation direction, called **wave-vector,** symbolized as $\underline{k}$, is given the value $2\pi/\lambda$, where λ is the radiation wavelength. Waves forming a planar wave-front over a considerable region in space are called plane waves. The three vectors, $\mathcal{E}$, $\mathcal{H}$, and $\underline{k}$, form a right-handed system.[1] A schematic illustration of a spatial slice representing the relations among the said vectors is provided in Figure 2.1.

The fundamental characteristics of electromagnetic waves are the electric and magnetic field amplitudes; their wavelength λ, which is the distance between adjacent peaks; and its corresponding frequency ν. The inverse frequency, $T = 1/\nu$, is the oscillation time period (the time duration required for a full oscillation cycle). Electromagnetic propagation speed in free space, $c = 2.9979 \times 10^{10}$ cm/s (speed-of-light constant), satisfies the relation $\lambda\nu = c$. The wave propagation velocity c appears always constant to the observer, independent of the source relative velocity. Medium wave propagation speed like sound waves are characteristic constants of the medium.

Electromagnetic waves require no medium for their propagation. Still, they carry energy, as well as linear and angular momentums, away from their source. The field

1 The meticulous reader is advised that inside matter, the wave-front propagation direction is rather perpendicular to the dielectric displacement D and magnetic induction $\mathcal{B}$ vectors. The propagation direction indicated in Figure 2.1 is that of the energy flow. In anisotropic materials there is a slight yet noticeable difference between the two, termed **walk-off angle**.

Transparent Ceramics: Materials, Engineering, and Applications, First Edition. Adrian Goldstein, Andreas Krell, and Zeev Burshtein.

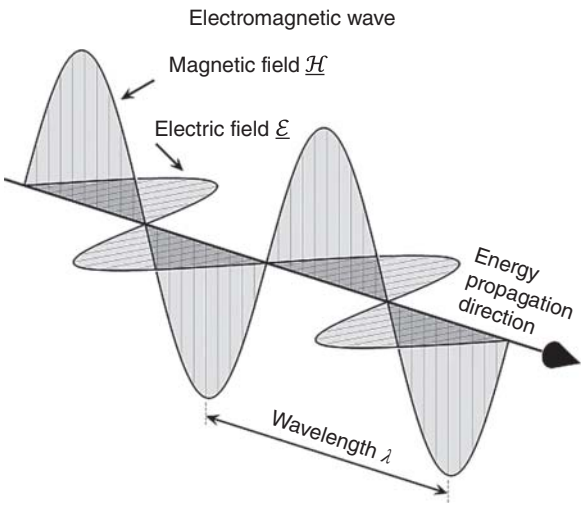

Figure 2.1 Schematic illustration of a spatial slice (temporal snapshot image) representing the relations among the electric and magnetic fields of a coherent electromagnetic radiation, the wave energy propagation direction, and definition of the radiation wavelength λ.

energy is conserved within any imaginary spherical boundary drawn around the source. The area of such sphere is proportional to the squared distance from the source. Thus, if evenly distributed and undisturbed, the local power density is inversely proportional to the square of that distance. Unless specifically otherwise indicated, when speaking of electromagnetic radiation, one usually refers to radiation conforming to the far field behavior.

Electrically charged moving particles, or particle systems, are capable of generating electromagnetic radiation, for example, positive or negative atomic or molecular ions, electrons, protons, positrons, α-particles (helium He nuclei), and charged particles' currents. Bound electron transitions from higher to lower states are a common source for electromagnetic radiation. Variation of electromagnetic radiation with frequency (or wavelength) is called **spectrum** (Figure 1.1).

The electromagnetic radiation wavelengths range, experienced in human everyday practice and science, is very broad. It extends between $\sim 10^{-10}$ cm (γ-rays, generated by internuclear decay transitions) and $\sim 10^{5}$ cm for long radio waves (generated by oscillating currents in antennas). Various physical phenomena are known to involve the emission of electromagnetic radiation. For example, solids or atoms bombarded by energetic electrons generate X-rays in the order of $\sim 10^{-8}$ cm wavelength, so do certain interparticle collisions. Solar-type celestial bodies typically emit a broad spectrum of electromagnetic radiation, spanning wavelengths from $\sim 10^{-6}$ cm (ultraviolet, UV) through $\sim 0.5 \times 10^{-4}$ cm (visible, VIS) till $\sim 10^{-3}$ cm (infrared, IR). The term **light** is used in all these ranges – both by layman and many scientists, synonymously with "electromagnetic radiation." Various man-made devices, like light bulbs, flying vehicle's exhausts, munition explosion, or furnaces, also constitute sources of light. **All these are of interest in this book**. Some people prefer to restrict the spectral domain coverable by the term "light" to where the human eye is sensitive, between 380 and 780 nm.

The quantum energy of electromagnetic radiation is called **photon**. Photons have no rest mass, yet they interact with gravity and other fields and matter. A photon energy E_{ph} is given by Eq. (1.1).

Due to the basic nature of Eq. (1.1), and its common use in a variety of physical and technological disciplines, some modified forms are well established; particularly

$$E_{ph} = \hbar\omega \tag{2.1}$$

where $\hbar \equiv (h/2\pi) = 1.0546 \times 10^{-27}$ erg s is the *reduced* Planck constant and $\omega \equiv 2\pi\nu$ is the angular frequency expressed in "rad/s" units. In view of the simple proportionality between the photon energy and its inverse vacuum (free space) wavelength $(1/\lambda)$, the spectroscopic community most often use the latter as a legitimate measure of the photon energy, expressing it in reciprocal centimeter units "cm^{-1}." Solid-state research community often uses the electron volt $\mathrm{eV} \equiv 1.6022 \times 10^{-12}$ erg as an energy unit.

Electromagnetic radiation usually preserves its frequency upon crossing between different materials, meaning that it changes its propagation velocity. For example, on crossing from vacuum into any homogeneous material, its propagation speed υ lowers. Correspondingly, the wavelength λ shortens by the same factor. The ratio $n = c/\upsilon$ is termed "refractive index." The name stems from the fact that its occurrence is the origin for changes in light beam propagation direction upon crossing between material media of different refractive indices. This issue will be discussed later. Air at standard conditions has a refractive index of $n_{air} \cong 1.0003$. Refractive indices of transparent ceramics in the near-visible range between 1.4 and 3.5. The refractive index frequency dependence $n = n(\nu)$ (or equivalently $n = n(\lambda)$) is called **dispersion**. Except for special, limited near-visible regions, the refractive index reduces with increasing wavelength. Empiric dispersion expressions of a refractive index are termed **Sellmeier relations**. They often exhibit the form

$$n^2 - 1 = \sum_i \frac{A_i \lambda^2}{\lambda^2 - {\lambda_i}^2} \tag{2.2}$$

where all A_i and λ_i are positive, experimentally adjustable parameters.

2.2 Interference and Polarization

Hereby we list two important features and effects related to electromagnetic radiation: interference and polarization. Both may be subject to manipulation, for exploiting of technical advantages.

Interference: When two light beams overlap over a certain region in space, their field amplitudes add up. Depending on their relative phases, the resultant field sometimes increases or decreases. Figure 2.2 provides a demonstration of two extreme cases. In one case, the two beams of equal intensity and frequency are both in phase, the result being a higher intensity beam; in the other case the two beams exhibit a π phase shift, causing a null-intensity resultant beam. The field addition principle (and its effects) is termed **interference**. The above two extreme effects demonstrated in Figure 2.2 are correspondingly described as "constructive" and "destructive."

Polarization: Light polarization state refers to the orientation behavior of its *electric field* and necessarily its associated magnetic field as well. Light wave whose electric field oscillates at random in more than one plane over only several oscillation periods is classified as **unpolarized**. Light wave whose electric field oscillates persistently at only one plane is classified as **linearly polarized**. If the electric field vector tip describes a circular contour over an oscillation period on any perpendicular plane along its propagation line, the light is classified as **circularly polarized**. If the electric field vector tip describes an elliptic contour under same conditions, the light is classified as **elliptically polarized**. In circularly and elliptically polarized cases, the electric field vector tip displays a propagating left- or right-handed screw along the propagating direction at any single moment.

All above polarization states may be resolved to components on perpendicular planes crossing the $\underline{k}$ wave-vector. For example, if the two electric field components describe equal amplitude waves of same phase, the resultant beam is a linearly polarized beam on a plane forming 45° angle between the component planes. If the electric field components exhibit a phase lag $\mathbf{\Delta}\varphi$ of exactly $\pm\pi/2$, the resultant field is (either left- or right-handed) circularly polarized. For phase differences other than $\mathbf{\Delta}\varphi = 0$ or $\mathbf{\Delta}\varphi = \pm\pi/2$, the resultant field is (either left- or right-handed) elliptically polarized. Manipulation of light beam polarization states may be achieved, for example, by use of **retardation plates** based on anisotropic transparent single crystals, which exhibit different refractive indices for different electric field orientations.

The first two situations are demonstrated in Figure 2.3. It provides temporal snapshots of the electric field characteristics in space. The left side of each part [(a) or (b)] shows the field resolution into its components. The center planes perpendicular to the propagation directions provide the edge-field contours. The right sides provide the resultant field images.

2.3 Main Processes which Disturb Electromagnetic Radiation After Incidence on a Solid

The above formal definition of high transparency implies that light incident on a ceramic sample could propagate through the solid with its impacts undisturbed. However, any material body exhibits quite a number of mechanisms interrupting the free light propagation. They include partial **reflection**, **refraction**, **absorption**, and **scattering**. Comprehensive and rigorous description of

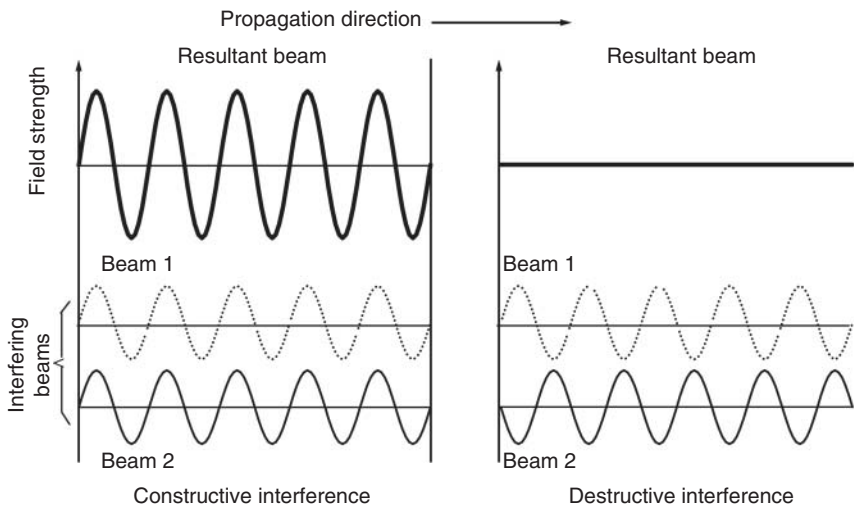

Figure 2.2 Demonstration of constructive and destructive interference cases of overlapping two coherent propagating waves. For clarity, the interfering and resultant waves are plotted along shifted lines, although interference occurs only at spatial overlap.

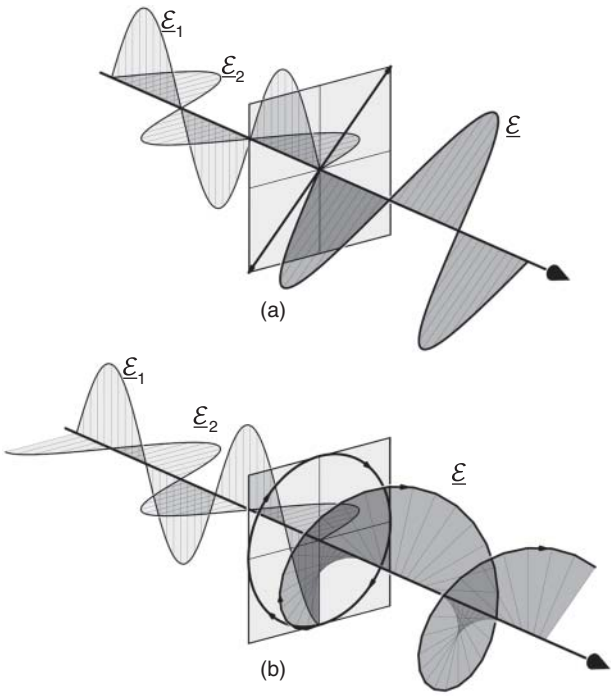

Figure 2.3 Various light polarization forms: (a) linearly polarized and (b) circularly left-hand polarized.

the phenomena requires consultation with specialized textbooks. Here we provide only a brief survey of most apparent phenomena and the parameters used for their characterization. The first three loss-producing phenomena are treated within the framework of the **geometrical optics** scheme, valid precisely only when the light beam cross section is very large compared to its wavelength λ; scattering needs a treatment focusing on the molecular level.

We now consider an electromagnetic radiation beam, impacting the surface of a solid, formed as a perfectly polished rectangular plate. We assume the air-placed plate to be devoid of any adsorbed chemical species, free of bulk bubbles or other second phases, and containing only a very small amount of, say, transition metal (TM) cations. The incident beam power P_0 is given in W/cm^2 units. Part of the beam is reflected at the surface; the rest, P_1 enters the solid. The bulk residing cations usually absorb an additional fraction of P_1. The P_2 power surviving at the second solid/air interface is lower than P_1. At that interface, a part of P_2 reflects again, and the exiting radiation has a further reduced P_3 power. The actual P_3 is not trivially calculated since the initially second interface back-reflected fraction of P_2 echoes between the two surfaces, losing power on each crossing and surface reflection. Neglecting the second interface reflection, the attenuated P_2 power is given by

$$P_2/P_1 = \mathbf{exp}(-\alpha L) \tag{2.3}$$

where L is the plate thickness and α, usually expressed in cm^{-1} units, is the bulk **absorption coefficient**.

The absorption coefficient is an indicator of the radiation absorbing ability of the solid. The P_2/P_1 ratio is called **internal transmittance**, while the $T \equiv P_3/P_0$ ratio is called **external transmittance** or simply **transmittance**. The $A \equiv (P_2 - P_1)/P_0$ ratio is called **absorbance**. Overlooking contributions by multiple reflection/transmission events inside the solid, the P_2/P_1 ratio represents the **reflectance** R. Scattering occurs in most real transmissive solids. It causes transmission power loss by a similar exponential behavior like absorption. Its contribution is expressed by defining an effective attenuation (absorption) coefficient α_{eff}, which is a sum of one addend describing absorption and a second one describing scattering. Denoting the scattered power by S, one has

$$R + A + S + T = 1 \tag{2.4}$$

In a few text paragraphs below, we introduce some details of the solid refraction process. Then, we will elaborate on the quantities denoted by R, S, and A, the ones causing the attenuation of electromagnetic radiation incident on a solid sample, that eventually determine the value of R.

2.3.1 Refraction

Above it was already explained that a change in light propagation velocity – when it transfers from one medium to another – occurs. The phenomenon is called refraction and the parameter describing the ratio between the light speed in vacuum and a medium is the refraction index.

Macroscopically, the refraction effect is observed as a "bending" of a light ray passing, say, from air into a transparent solid (or more generally between two media with different dielectric properties). In Figure 2.4 it can be seen that the refracted ray angle θ_t differs from the incidence ray angle θ_i, while the reflected ray angle θ_r is equal to that of the incident light ray (note that it propagates in the same medium as the incident light). This effect is due to dependence of the light wave velocity on the medium dielectric properties. Transition between two dielectric media affects also other light wave characteristics, like the polarization state, that may also change upon transition and reflection. The light wave velocity is expressed by a parameter called **refractive index**. It is the ratio between the light phase velocity c in free space (vacuum) to the light phase velocity υ inside the solid: $n \equiv c/\upsilon$.

Obviously, in vacuum $n = 1$. For example, the speed of light propagating through a silica glass window whose refractive index is $n_s = 1.5$ is reduced to $1/1.5 = 67\%$ of the speed in vacuum. The light frequency ν, however,

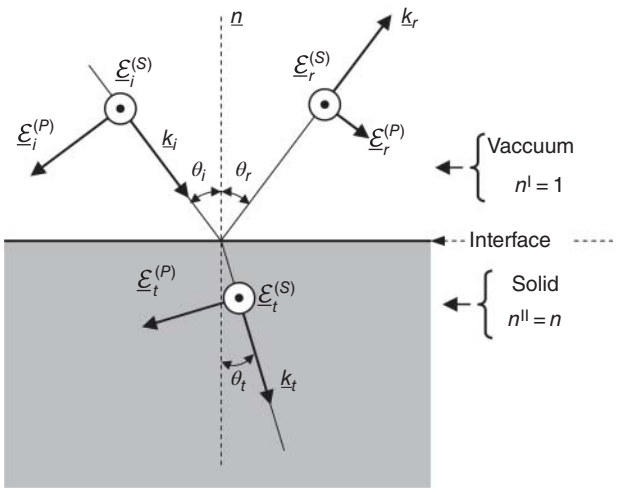

Figure 2.4 Graphic representation of the refraction process.

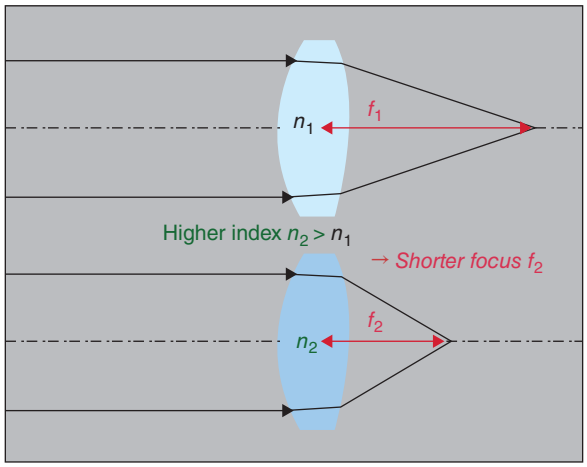

Figure 2.5 Dependence of optical lens focal length on the value of refraction index.

remains unchanged! Therefore, the light wavelength λ shortens by the same 67% factor, satisfying the relation $\lambda\nu = \upsilon = c/n$.

Among other things, the refractive index also determines the amount of reflected light. It can be shown that for normal incidence, where $\theta_i = \theta_t = 0$, the expression for the primary reflectance, called **Fresnel reflectance** reduces to

$$R = \left(\frac{n^I - n^{II}}{n^I + n^{II}}\right)^2 \tag{2.5}$$

where n^I and n^{II} are the refractive indices of the two involved media (Figure 2.4). The Figure 2.5 shows the effect of increasing the value of n^{II} on the focal distance of a lens (Figure 2.5) - with the final consequence of "chromatic aberration" when light with a *spectrum of different* wavelengths passes through an optically homogeneous lens with one given index (Figure 2.8); the reason is dispersion, the change of the index with the wavelength from color to color (Figure 2.6). The expression for R gives higher values if $(n^I - n^{II})$ increases. This behavior indicates that transparent ceramics of higher refractive indices are providing less transmission. The refractive indices of certain materials, for example, cubic zirconia ZrO_2, lutetia Lu_2O_3, and to a certain extent also yttria Y_2O_3, exhibit higher refractive indices than yttrium aluminum garnet $Y_3Al_5O_{12}$ (YAG), spinel $MgAl_2O_4$, or calcium fluoride CaF_2. Therefore plates made of the former materials display more reflectance ("brilliance") than plates made of the latter ones (see Chapter 4). As will be seen below, the refractive index affects other loss mechanisms and directly influences certain transparent ceramics applications. For example, some controlled variation of a material refractive index helps in the control of lenses' focal distance; see Figure 2.5. Obviously, refractive index is not the sole parameter considered for designing best-suited optical quality; other quantities will be discussed later.

Accuracy required for measuring the refractive index depends on the intended application. Three figures past the decimal point are common for most applications. For special applications, especially for accurate optical lens design, knowledge of n up to six figures after the decimal point is required.

Dispersion: The refractive index n depends on several physical quantities like wavelength, temperature, and ambient pressure. The wavelength dependence is called **dispersion**. It obviously affects optical lens performance for manipulating a broad spectrum of wavelengths. Some issues regarding this parameter are discussed below. Usually, the refractive index reduces with wavelength (**normal dispersion**) except for limited regions near absorption lines, where it is called **anomalous dispersion**.

A graph showing the refractive index as a function of wavelength (Figure 2.6) provides the most complete characterization of the spectral dispersion. A shorter single parameter, useful for assessing suitability for lens performance, is provided by the Abbé number, defined as

$$\nu_d \equiv (n_d - 1)/(n_F - n_C) \tag{2.6}$$

where n_d, n_F, and n_C are the refractive indices at characteristic, well-defined visible light emission wavelengths of helium (587.56 nm), hydrogen H_β (486.13 nm), and hydrogen H_α (656.28 nm). Analogous combinations of other well defined (Fraunhofer) atomic spectral lines are possible for defining an adjusted Abbé parameter; however, the above (Eq. (2.6)) is the most accepted in the lens production industry for the visible region. Wavelength dispersion is inherent to lens performance, since the focal position varies with wavelength, hence causing image blurring (called **chromatic aberration**).

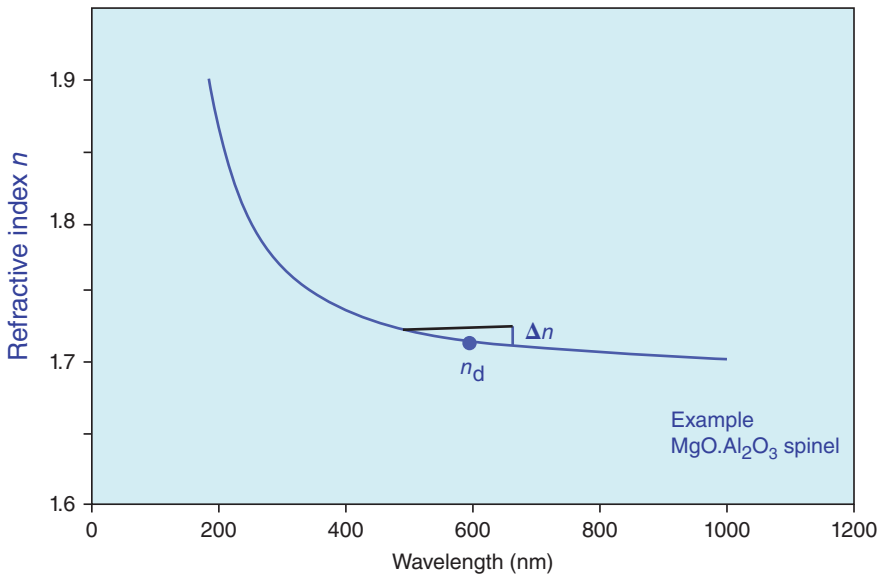

Figure 2.6 Wavelength dependence ("dispersion") of the refractive index $n(\lambda)$ for spinel. Note the strong increase of the index toward the bandgap absorption edge; for Mg spinel at 160 nm.

For reduced blurring, smaller dispersion, namely, larger Abbé number materials, is thus favorable. Opticians often use specialized combinations of lenses to reduce chromatic aberrations, sometimes designed for special regions of the spectrum. For the latter assessment, knowing the refractive indices to the fifth or even sixth digit after the decimal point is required. As will de detailed in Section 5.2.5, certain ceramics may offer better combinations of index and Abbé number than traditional glass materials in lens fabrication. For that purpose, the ceramist must be very cautious in characterizing its product, since differently graded materials may exhibit non-negligibly different refractive indices.

The experimental relationship between the refractive index and the dispersion describing the ν_d Abbé parameter is shown in Figure 2.7, which also depicts the relationship for the case of newly developed transparent ceramics.

In Figure 2.8 the deleterious effect of chromatic aberration, on the images produced by a lens, is illustrated.

In Figure 2.9 the dependence of an important partial dispersion on "n" is given.

Chromatic aberration can be corrected or diminished by achromatic compound lenses, in which materials with differing dispersions are assembled.

For certain optical systems building related operations, like the lens assembling for aberrations reduction, lens materials have to meet special requirements, concerning their partial dispersion ratio θ. The θ values characterize, as distinguished from the Abbé number, the amount of dispersion in "partial" segments of the spectrum; partial dispersion values vary for different ranges of the spectrum.

Examples of segments, considered for their relevance to applications, are given below:

- In the blue range (G-line = 435.83 nm → F-line = 486.13 nm)

$$\theta_{g,F} = (n_g - n_F)/(n_F - n_C)$$

- In the orange/red range (D-line = 587.56 nm → C-line = 656.28 nm)

$$\theta_{d,C} = (n_d - n_C)/(n_F - n_C)$$

When such a partial dispersion ratio is plotted over the refractive index, we see that glasses behave in a manner different from that of the crystalline transparent solids; the latter have higher index values (Figure 2.9). Plotting, however, the same parameter over Abbé numbers produces in a diagram where the "normal" (by definition) linear dependence exhibited by most glasses appears also for most crystalline substances (Figure 2.10). However, some of the latter exhibit larger positive (Y-Al garnet "YAG") or negative (perovskite, ZrO_2) deviations from the line of normal dispersion ("anomalous dispersion" $\mathbf{\Delta}\theta$).

In Figure 2.10, examples of positive and negative anomalous dispersion $\mathbf{\Delta}\theta$ are marked by red arrows. Note that the address of "normal" or "anomalous dispersion *materials*" (cp. e.g. [K20]) in the generalized plot of Figure 2.10 is not identical with the physical terms of normal and anomalous *dispersion* given above.

Figures 2.9 and 2.10 must not be misunderstood as indicating a *generally positive* anomalous dispersion of, e.g. YAG and yttria (Y_2O_3) with *negative* $\mathbf{\Delta}\theta$ values of cubic zirconias (c-ZrO_2). The position of materials data in Figure 2.10 depends on the fourth and even the fifth digit of the index, which means different grades of YAG, yttria, or other ceramics may exhibit slightly different indices, even at nominally fixed compositions and will then occupy very different positions in the Figures 2.9

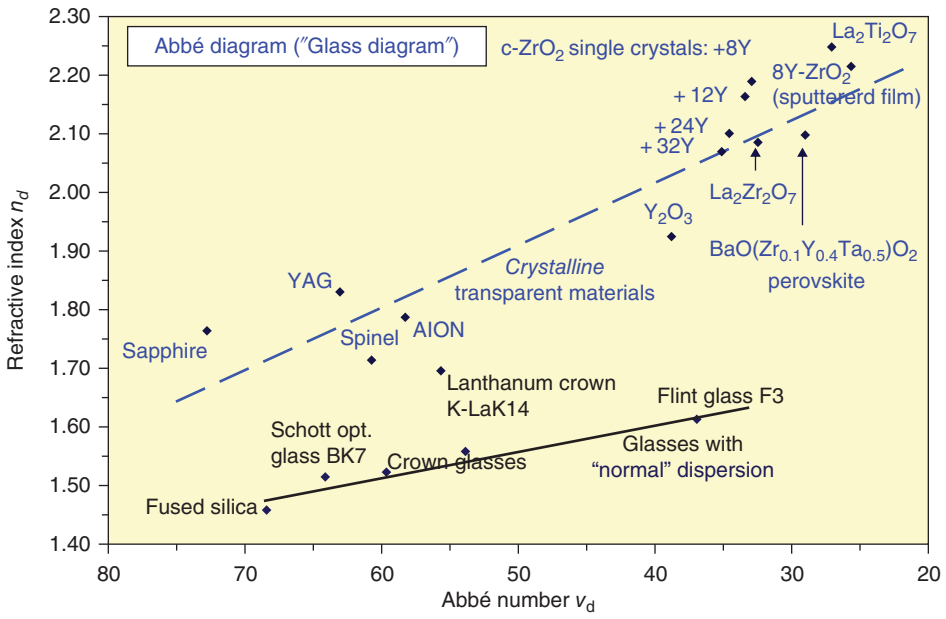

Figure 2.7 Relationship between refraction index and dispersion for optical glasses (Abbe diagram); points corresponding to new ceramic lens materials are also indicated.

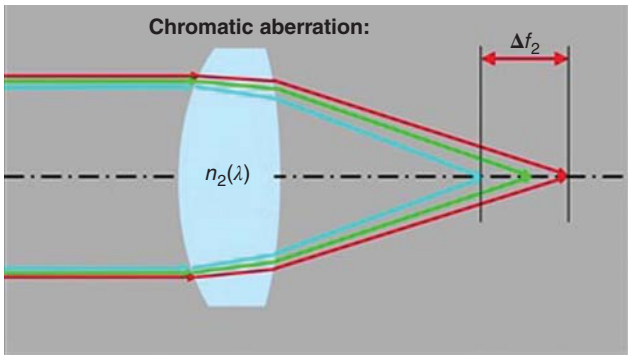

Figure 2.8 Deleterious effect of chromatic aberration.

and 2.10; differences may be induced by variation in the concentration of oxygen vacancies or other defects. Also, such plots of partial dispersion ratios over Abbé numbers look very different for different parts of the spectrum. For instance, comparing anomalous dispersion in the blue ($\theta_{g,F}$) and in the orange/red ($\theta_{d,C}$) parts of the spectrum, a study [K59] had shown that $\boldsymbol{\Delta\theta}$ of YAG is always positive, while yttria (Y_2O_3) and sapphire (Al_2O_3) switch from positive (in the blue range) to negative anomalous dispersion at longer wave lengths; in contrast, cubic zirconia grades with different amounts of yttria stabilization and *negative* $\boldsymbol{\Delta\theta}_{g,F}$ in the *blue* range (Figure 2.10) turned to *positive* anomalous dispersion at red wave length.

2.3.2 Reflection

The refraction is always accompanied by reflection [H20, H23]. Reflection on a fully flat smooth surface is called **Fresnel reflection**. Rigorously speaking not only refraction but also reflection implies changes in propagation velocity and polarization state. Figure 2.4 summarizes the relevant wave parameters under consideration for transition between vacuum and a dielectric medium. The *i*, *r*, and *t* subscripts relate to incident, reflected, and transmitted quantities. The dot-centered circles indicate a vector orientation perpendicular to the page. The surface-normal vector $\underline{\boldsymbol{n}}$ and the incident, reflected, and transmitted wave-vectors $\underline{k}_i$, $\underline{k}_r$, $\underline{k}_t$, respectively, all belong to the *same plane* called **incidence plane** (the page plane in the figure). The incident and reflected beam angles θ_i and θ_r, respectively, are equal, namely, $\theta_r = \theta_i$ (**specular reflection**). The transmitted beam angle θ_t, however, is different and follows **Snell's law**

$$\mathbf{sin}\theta_i/\mathbf{sin}\theta_t = n \tag{2.7}$$

If the incidence light medium is other than just vacuum, the relevant refractive index in Eqs. (2.4)–(2.7) is the ratio $n \equiv n^{II}/n^{I}$. The electric field components parallel or perpendicular to the incidence plane are granted (*P*) and (*S*) superscripts, respectively.

The expressions for the reflectance *R* and transmission *T* intensity ratios of these different components are

$$\begin{cases} R_S = \dfrac{\mathbf{sin}^2(\theta_i - \theta_t)}{\mathbf{sin}^2(\theta_i + \theta_t)}; & T_S = 1 - R_S; \\ R_P = \dfrac{\mathbf{tan}^2(\theta_i - \theta_t)}{\mathbf{tan}^2(\theta_i + \theta_t)}; & T_P = 1 - R_P \end{cases} \tag{2.8}$$

A special important case occurs when $\theta_i + \theta_t = 90°$. R_P then diminishes, and simultaneously $T_P = 100\%$. Namely, the reflected beam remains purely *S*-polarized,

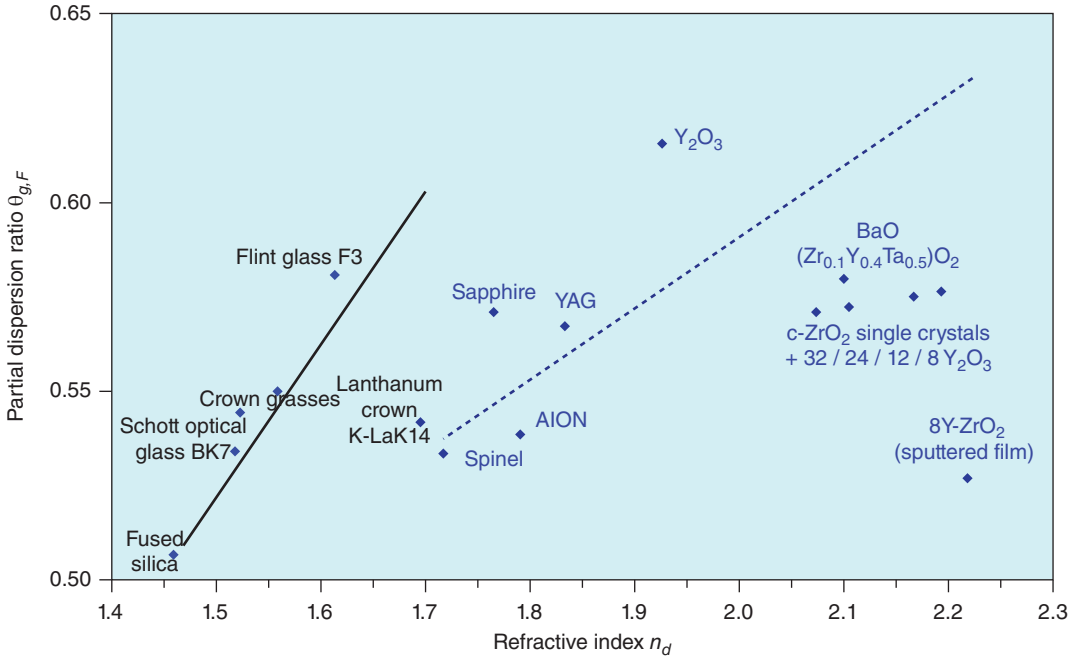

Figure 2.9 Plot of the partial dispersion ratio $\theta_{g,F}$ against refractive index n_d.

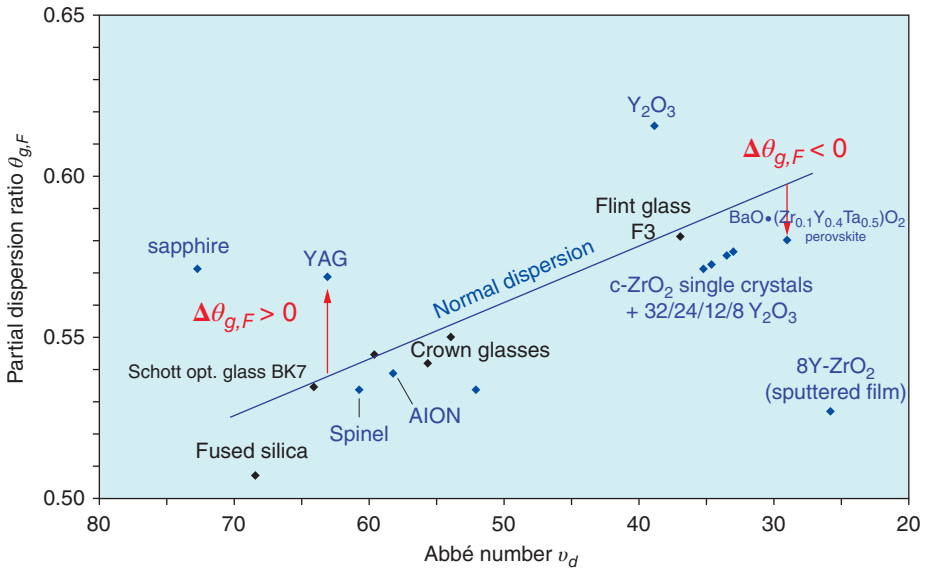

Figure 2.10 Plot of partial dispersion against Abbé number υ_d. Two examples of ceramics with positive and negative anomalous dispersion $\Delta\theta$ are marked by arrows.

and the *P*-component is fully transmitted. The specific incidence angle θ_B for that situation is called **Brewster's angle**, satisfying

$$\theta_B = \textbf{arctan}\, n \tag{2.9}$$

The Brewster configuration is often used for cropping by reflection of a linearly polarized component off a light beam of any other polarization state. As an example, Figure 2.11 shows the variation of the Fresnel reflection from a dielectric medium surface as a function of the incidence beam angle for $n = 1.5$.

Notably, near normal incidence ($\theta_i \lesssim 10°$), the *S* and *P* reflections are equal, given by

$$R = R_S = R_P = \frac{(n-1)^2}{(n+1)^2} \tag{2.10}$$

Toward the grazing incidence limit ($\theta_i \to 90°$), the two polarization reflections join again, approaching a full reflectance state ($R \to 100\%$).

Material media also exhibit absorption. Light entering one material side and reaching the other side over a distance L reduces its intensity due to absorption and

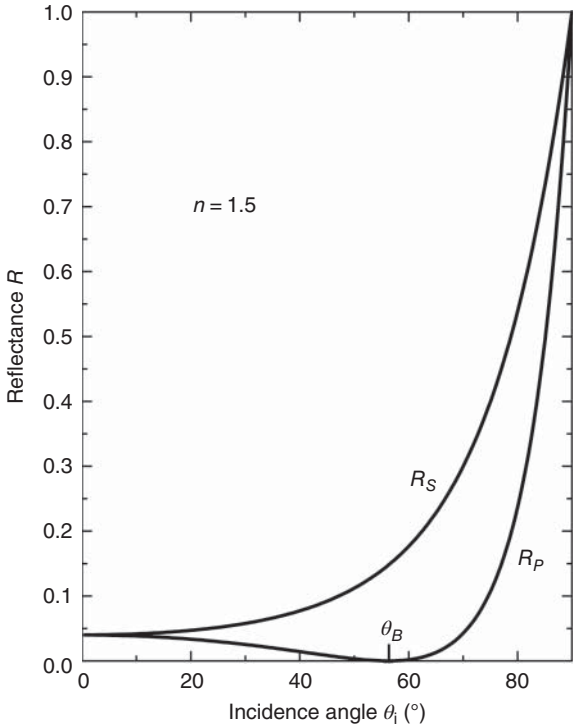

Figure 2.11 Light reflectance vs. incidence angle of its *S* and *P* polarization components, for a material possessing a refraction index of 1.5.

scattering. In a homogeneous material, the light at distance L is given by the **Beer–Lambert** expression

$$I(L) = I(0)\mathbf{exp}(-\alpha L) \tag{2.11}$$

where $I(0)$ and $I(L)$ are the inner material light intensities near the front and exit planes, respectively, in W/cm^2 units, and α is the **attenuation or extinction coefficient** (absorption + scattering) in cm^{-1} units.

Intrinsic and extrinsic (in the sense that they are caused by impurities introduced from external sources into the pure material) material absorption processes have some effect on the material refractive index. If no scattering exists, an **extinction coefficient** $\kappa \equiv c\alpha/4\pi\nu = (\lambda/4\pi)\alpha$ is defined to account especially for aspects related to light phase changes upon reflection and transmission. Correspondingly, a mathematical **complex refractive index** $\widetilde{n}$ is defined as $\widetilde{n} = n + i\kappa$. The near-normal reflectance for both *S* and *P* polarizations is given by

$$R_S = R_P = \frac{|\widetilde{n}-1|^2}{|\widetilde{n}+1|^2} = \frac{(n-1)^2+\kappa^2}{(n+1)^2+\kappa^2} \tag{2.12}$$

Ceramic light absorption, in the visible range, is dominated by the extrinsic presence of atomic and molecular impurities, exhibiting absorption coefficients that, however rarely, exceed about $30\,cm^{-1}$. A representative wavelength is 5×10^{-5} cm (green). The resultant extinction coefficient $\kappa \cong 1.2\times10^{-4}$ is very small compared to both $n-1$ and $n+1$. Therefore, the extinction coefficient effect on Fresnel reflection may be entirely neglected in such cases. On the other hand, in regions belonging to the infrared (IR) and far infrared (FIR), all material atoms, not only impurity ones, involve in absorption. There, the extinction coefficient κ plays a dominant role in Fresnel reflections.

Fresnel reflection requires smooth optical surface polishing. If not "optically polished," some light is backscattered over surface irregularities, a component called **diffuse reflection**, in contrast to Fresnel's **specular reflection**. Obviously, a similar, generally larger proportion of light is also forward-scattered. The above optical reflection and transition processes involve a single interface. A material plate, however, has *two* surfaces. Thus, the initially in-line transmitted light across the "front" surface bounces back and forth between the two surfaces, partially transmitting upon incidence at each surface. In the case of normal incidence of an incoherent light beam, the total transmission is given by

$$T = \frac{(1-R_1)(1-R_2)\mathbf{exp}(-\alpha L)}{1-R_1R_2\mathbf{exp}(-2\alpha L)} \tag{2.13}$$

where R_1 and R_2 are the *individual* front and back surfaces reflectance, respectively; α, the **attenuation coefficient**, (or **attenuation constant**) is the summed bulk absorption and scattering coefficients; and L is the ceramic plate thickness. Note that front and back surface reflections may differ if they couple to media of different refractive indices.

In a simplified case, where the bulk medium exhibits no absorption nor scattering ($\alpha = 0$), and the two surfaces are coupled to identical media ($R \equiv R_1 = R_2$), the expressions for the in-line transmission T and the *summed* Fresnel two-surface reflections R_{sum} reduce to

$$T = \frac{2n}{n^2+1}; \quad R_{sum} \equiv 1 - T = \frac{(n-1)^2}{n^2+1} \tag{2.14}$$

The most practical method for assessing the bulk attenuation coefficient α is by direct measurement of the in-line transition T at normal (or near-normal) incidence in an optically polished parallel plate of thickness L and the same *individual* (Fresnel) reflectance R of each surface; then solving Eq. (2.13) for α, the expression obtained is

$$\alpha = -\frac{1}{L}\mathbf{ln}\left\{\frac{1}{2R^2T}\left[\sqrt{(1-R)^4+4R^2T^2}-(1-R)^2\right]\right\} \tag{2.15}$$

The normal (Fresnel) *individual* surface reflectance R is either directly measured or calculated for cases where the material refractive index n is known.

An interesting, technically quite useful effect occurs in the case of light propagating in a high refractive index material n^I toward an interface with a lower refractive index material n^{II}. The effective refractive index $n = n^{II}/n^I$ is then smaller than a unity. By Snell's law (Eq. (2.4)), the transmitted beam angle θ_t is then larger than the incidence angle θ_i. Such condition is realizable as long as $\theta_t \leq 90°$. For incidence angles θ_i that are larger than a critical angle $\theta_c \equiv \textbf{arcsin}\, n$ (for which $\theta_t = 90°$), no solution exists to Snell's equation (Eq. (2.7)). Only specular reflection is then possible, and the incident beam exhibits 100% reflection for both P and S components, an effect termed **total internal reflection**. For example, the critical angle for light crossing from inside a glass of $n^I = 1.5$ into vacuum of $n^{II} \equiv 1.0$ is $\theta_c \equiv \textbf{arcsin}\,(1/1.5) = 41.8°$.

The total internal reflection effect is technologically utilized in a variety of optical configurations. An important example is fiber technology, used for achieving uninterrupted transmission of light over long distances and bent paths. Figure 2.12 demonstrates the general fiber configuration and its operation principles. A thin cylindrical transparent fiber, typically of sub-millimeter diameter, is used as a **core** for the light transmission. It is intimately wrapped with a thin layer of another transparent material, yet of a lower refractive index, called **cladding**. Importantly, the cladding thickness needs to be large compared to the light wavelength λ. Final wrapping with a protective soft material (jacket), not necessarily transparent, is often administered. Light properly fed into the core front end produces core-cladding incidence angles smaller than their joint critical angle. It is then efficiently reflected back and forth from the cladding into the core, till exiting the fiber at the other end. The range of light-feeding angles fulfilling the inner fiber total internal reflection condition is limited, defining a geometric **acceptance cone**.

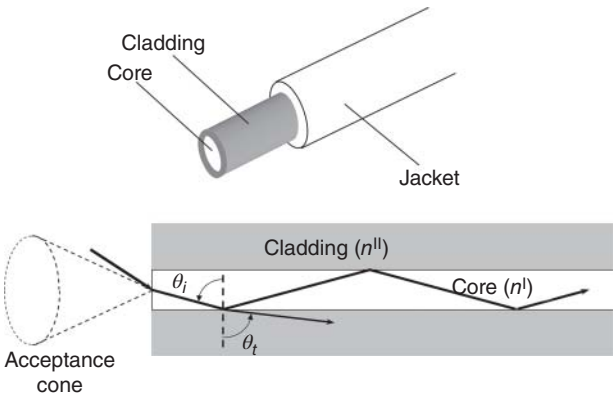

Figure 2.12 Use of total reflection, at the core/cladding interface, for keeping light beam inside optical fiber.

Being very thin, the fiber may be bent without breaking, and still functioning, as long as the inner total internal reflection condition is properly maintained.

2.3.3 Birefringence

An important source for light scattering in polycrystalline ceramics relates to **birefringence** in the constituent crystallites [K2]. This effect occurs in all anisotropic single crystals, namely, those belonging to all crystallographic families except the cubic ones. It does not occur in the case of glasses, which although highly anisotropic on molecular scales are highly isotropic on larger scales. In an anisotropic material, the refractive index differs for different light polarizations. Mathematically, the squared refractive index is a 3×3 symmetric tensor (n^2). It can thus always be described by a diagonal matrix related to its three principal X, Y, and Z axes, which of course depend on the crystal symmetry. For optical considerations, the relevant quantities are the squared refractive indices n_i^2, where n_i is the refractive index of the light polarization component along the i-th principal axis (X, Y, or Z). In other words, anisotropic crystals are basically characterized by three different refractive indices, n_x, n_y, and n_z.

In the following we describe a geometric recipe that allows finding the refractive index for light propagating in any $\hat{\underline{k}}$ direction in a single-crystal medium, where $\hat{\underline{k}} \equiv \underline{k}/|\underline{k}|$ is a unity length vector in the wave-vector $\underline{k}$ direction. One describes a spatial ellipsoid by the expression

$$\frac{x^2}{{n_x}^2} + \frac{y^2}{{n_y}^2} + \frac{z^2}{{n_z}^2} = 1 \tag{2.16}$$

where (x, y, z) are Cartesian coordinates, along the (X, Y, Z) principal axes of the **index ellipsoid** (n^2) (**indicatrix** tensor), respectively. Its crossings with the coordinates are (n_x, n_y, n_z). A plane perpendicular to $\hat{\underline{k}}$ is attached at the vector origin. That plane crossing with the index ellipsoid portrays an ellipse. The long and short axes indicate the beam normal polarization orientations when the beam is propagating in the $\hat{\underline{k}}$ direction.[2] Each axis length is, respectively, twice the refractive index of the beam belonging to its polarization: $2n_a$ and $2n_b$, respectively.

A special, still important case of anisotropy occurs for crystals belonging to the tetragonal, trigonal, and hexagonal families, for which two of the indices are equal, namely, $n_x = n_y \neq n_z$. These crystals are called **uniaxial** (in contrast to the triclinic, monoclinic, and orthorhombic cases, where all indices are different and

2 The said polarization orientation is actually that of the electric displacement D vector rather than the electric field $\mathcal{E}$ vector. In an anisotropic material, there is some slight difference between the two.

called **biaxial**). The following notation and naming are used: $n_o \equiv n_x = n_y$ is named **ordinary** refractive index; $n_e \equiv n_z$ is named **extraordinary** refractive index. The Z axis is named **optic axis**. The reason for the latter naming is the fact that the refractive index for light propagating in the Z direction is identical for all polarization states ($=n_o$). If $n_e > n_o$, the crystal is termed **positive uniaxial**. If $n_e < n_o$, the crystal is termed **negative uniaxial**. The difference $\Delta n \equiv n_e - n_o$ is called **refractive index anisotropy**.

The index ellipsoid of uniaxial crystals forms as a rotation ellipsoid around the Z axis (see Figure 2.13). The set of mutually perpendicular X and Y axes may then be chosen arbitrarily in the plane perpendicular to Z. For presentation convenience, the Y axis is chosen in the plane formed by the Z axis and light propagation direction $\hat{\underline{k}}$ vector, as described in Figure 2.14 for a positive uniaxial case. θ marks the angle between $\hat{\underline{k}}$ and Z. The long axis length of the ellipse, portrayed by the plane perpendicular to $\hat{\underline{k}}$ and crossing the origin O, is $2n_e(\theta)$; the quantity $n_e(\theta)$ is marked in Figure 2.14. The short axis length of that ellipse is $2n_o$, and it is perpendicular to the $(\hat{\underline{k}},\ Z)$ plane at the origin O (actually the X orientation). Thus, a beam propagating in the $\hat{\underline{k}}$ direction exhibits two normal polarization states: one perpendicular to Z, of n_o refractive index (**ordinary polarization**), and one in the (y, z) plane, of $n_e(\theta)$ refractive index (**extraordinary polarization**). The $n_e(\theta)$ extraordinary refractive index depends on θ and changes from n_o for $\theta = 0$ to n_e for $\theta = 90°$. The specific dependence is given by

$$\frac{1}{n_e^2(\theta)} = \frac{\mathbf{cos}^2\theta}{n_o^2} + \frac{\mathbf{sin}^2\theta}{n_e^2} \tag{2.17}$$

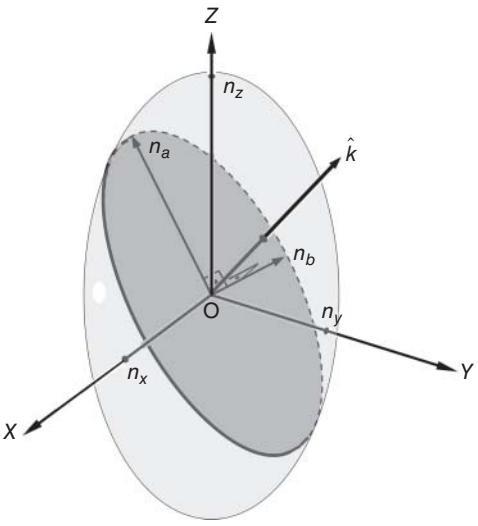

Figure 2.13 The refraction index ellipsoid and graphic determination of the normal polarization states with their "n" values.

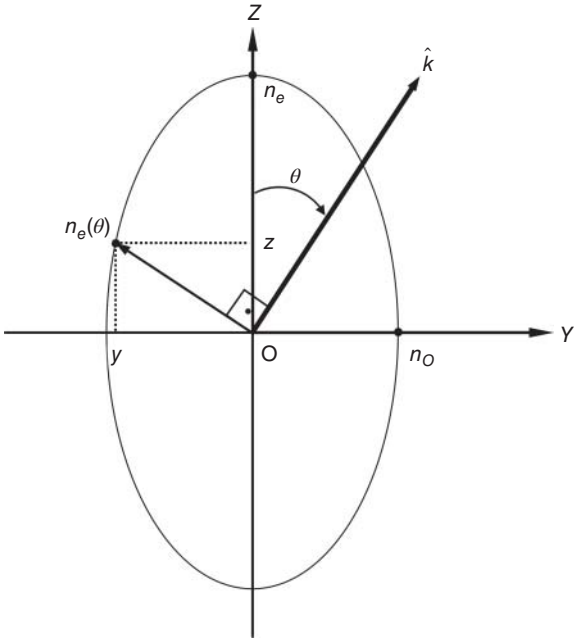

Figure 2.14 Cross section of the refractive index ellipsoid of a uniaxial crystal in the (z, y) plane. $n_e(\theta)$ is the refractive index for the extraordinarily polarized component of a planar wave propagating in the crystal in the $\hat{\underline{k}}$ direction.

A well-known example is the birefringence in the sapphire single crystal (corundum; Al_2O_3). It exhibits negative birefringence. The optic axis is oriented in the trigonal (rhombohedral) crystal [1, 1, 1] direction (the unique threefold rotation axis). For $\lambda = 589.6$ nm (a sodium Na vapor fluorescence line), the indices are $n_o = 1.768$ and $n_e = 1.760$.

In the context of ceramic transparency and translucency issue, use of constituent birefringent materials may be detrimental to both. The reason is that beams crossing through a birefringent crystalline grain split in two, each of different polarization and propagation direction. Numerous such events, within even a thin slab, cause the transmitted light to exhibit a diffuse nature. Cubic materials are thus the only ones usable for the formation of thick transparent ceramic windows. Still, when the refractive index anisotropy $\mathbf{\Delta}n$ is sufficiently small, thin transparent plates may be usable. A different means to circumvent the birefringence adverse effects is to produce ceramics having, in the finished state, tiny grain dimensions d that are very small compared to the shortest wavelength of interest; specifically, $d \lesssim \lambda/20$ is usually acceptable for that purpose. More precisely, even under such conditions, transmission loss in the near-ultraviolet (NUV) or blue section of the visible (VIS) is not negligible, while for other wavelengths in the visible, the overall transmission may be kept quite high. In that respect, see discussion of birefringence elimination by alignment of

the grains parallel to a given symmetry axis, for example, Section 3.1.2.2.3 (Slip-Casting Under Magnetic Fields). It is a procedure allowing the use of non-cubic materials for the development of new transparent ceramics.

2.3.4 Scattering

Scattering in transparent ceramics is the most difficult to control transparency loss mechanism. It is usually caused by small ($\leq 10\,\lambda$) dispersed zones of various morphologies, exhibiting a different refractive index from the cubic host material [B37, H43]. Such zones could be residual pores (in practice the most problematic second-phase) or solid second-phase grains. For non-cubic matrix forming materials (a growing minority within the transparent ceramics population), neighboring grains of the primary phase themselves may exhibit a different refractive index. Micro-cracks, or zones subject to high remnant stress fields, are also part of the list. In non-cubic materials, the refractive index differences between grains depend on deviations among their crystallographic orientation. Grain boundaries themselves, however, despite their disordered structure and possible presence of second phases, are usually insignificant as scattering agents, owing to their nanometric dimensions. Only in rare cases (mostly for thick specimens) may their contribution to transparency reduction become noticeable. It occurs when their particular orientation with respect to the incident beams makes the latter travel longer paths within the grain boundary.

The behavior of light encountering a scattering zone cannot be treated simplistically by geometrical optics, as the latter applies only to "very large" objects, namely, of dimensions large compared to the wavelength λ. On contact with a scattering zone, the light electric field interacts with the zone's electrical dipoles and multipoles. Then some of the beam energy is diffusively radiated (scattered), as graphically sketched in Figure 2.15 [A23].

The vast majority of scattered light exhibit the same wavelength as the incident one. The left unidirectional light beam then interferes with co-directional scattered light, resulting in some irregular intensity patches in the transferred beam cross section. A fundamental analytical approach for light scattering was provided by Mie [M30]. It addresses the scattering of an electromagnetic plane wave by a homogeneous metal sphere. The solution takes the form of an infinite series of spherical multipole partial waves. Due to its complicated form, researchers most often resort to use of more simple models for describing specific experimental cases.

In the total attenuation coefficient α_{att}, the contribution of scattering is represented by the α_s term ($\alpha = \alpha_{abs} + \alpha_s$) where α_{abs} and α_s are the impurity

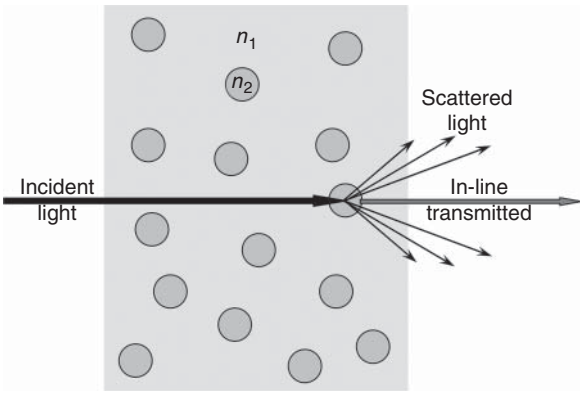

Figure 2.15 Schematic demonstration of light scattering by randomly dispersed identical spherical zones (darker gray circles) in a homogeneous ceramic matrix. The matrix refractive index is n_1 and that of the scattering zones is n_2. Only one sphere performing in-line transmission and scattering is sketched.

electronic absorption and scattering contributions, respectively.

2.3.4.1 Scattering by Pores

In transparent ceramics, the most widespread (and difficult to fully eliminate) scattering zones are, as already noted above, residual pores. A simplified (compared to the reality) yet practical modeling of pore existence is of equal-sized spheres of a refractive index only slightly different from the matrix and to a random distribution. For such an approximation, the effective pores contribution to the attenuation is given by the coefficient α_p:

$$\alpha_p = \frac{P_o}{(4/3)\pi {r_p}^3} C_s \tag{2.18}$$

where P_o is the bulk porosity fraction (ratio between the volumes of all pores and of the sample), r_p is the average pore radius, and C_s is the average pore scattering cross section (in cm^2 units). Intuitively, C_s may be assumed to be proportional to the pore geometric cross section $\sigma = \pi {r_p}^2$ (also in cm^2), namely, $C_s = Q_{eff}\sigma$. The proportionality factor Q_{eff} is an adjustable empiric parameter termed **scattering efficiency factor**; as its name suggests, it reflects the scattering ability of the pores. A useful way of treating the porosity is the employment of Mie's theory (applicable also to pores). Based on it, for small pore radii $r_p \ll \pi\lambda/n_p\,\Delta n$ [B1, H1], the geometric cross section is replaced by

$$\sigma = \frac{8\pi^3 r_p^4}{\lambda^2}(\Delta n)^2 \quad \text{for } r_p \ll \pi\lambda/n_p\ \Delta n \tag{2.19}$$

where $\Delta n \equiv |n_p - n_1|$ is the absolute difference between the refractive indices of the pore n_p and matrix n_1. The expression for the pore caused light attenuation constant

then reduces to

$$\alpha_p = Q_{eff}\frac{6\pi^2 P_o r_p}{\lambda^2}(\mathbf{\Delta}n)^2 \tag{2.20}$$

Notably, α_p increases linearly with the pore radius and is inversely proportional to the squared light wavelength. In the case of vacuum, or of air-filled pores, $\mathbf{\Delta}n = n_1 - 1$. The Mie treatment has the serious advantage of being applicable also to the situations where the pore size is similar to that of the incident wavelength.

Another theoretical approach for the treatment of light scattering by an inhomogeneous material (it may be pores in a ceramic matrix) is via Rayleigh–Gans–Debye theory [H1, R10]; as opposed to the Mie treatment, it works well only when the pore size is significantly smaller than the wavelength of the scattered light, and the scatterer units are not too close [A11]. The theory addresses directly the angular distribution of the scattered light and is valid only if, in addition to a small scatterer size, the difference between its refraction index and that of the matrix is small. In this theory the single pore contribution to the scattered intensity at a distance L large compared to both the incident beam geometric cross section and the sample thickness d is given by [B1]

$$I(\theta) = I(0)\frac{32n^4\pi {r_p}^6}{9\lambda^4 L^2}\left(\frac{\mathbf{\Delta}n}{n}\right)^2(1+\mathbf{cos}^2\theta)P(u)$$
$$\text{for}\ \ \Delta n \ll n \tag{2.21}$$

where $I(0)$ is the incident light intensity and $I(\theta)$ as the scattered light intensity at angle θ between the incident and scattered light; the function $P(u)$, termed **form factor**, is given by

$$P(u) \equiv \frac{9}{u^6}(\sin\, u - u\, \cos\, u)^2$$
$$\text{for}\ \ u \equiv \frac{4\pi n r_p}{\lambda}\sin(\theta/2) \tag{2.22}$$

The total scattered light intensity for a sample illuminated volume V containing N scattering zones per unit volume is given by

$$I_{total}(\theta) = I(0)(NV)\frac{32n^4\pi {r_p}^6}{9\lambda^4 L^2}\left(\frac{\mathbf{\Delta}n}{n}\right)^2$$
$$\times(1+\cos^2\theta)P(u)\ \ \text{for}\ \ \mathbf{\Delta}n \ll n \tag{2.23}$$

There are three notable issues related to Eq. (2.23). First, it is independent of the azimuth scattering angle φ. Second is that the scattered light intensity reduces as the fourth power of the incident light wavelength λ. Third is the role of the **form factor** $P(u)$. Figure 2.16 provides the variation of $P(u)$ as function of u. $P(u)$ reduces from a unity at $u = 0$ to practically zero above approximately $u \cong 4$. In the limit of $|u| \to 0$, as obtains for *all* θ values when $r_p \ll \lambda$, the form factor $P(u) \to 1$. Then, both forward- and back-scattered light

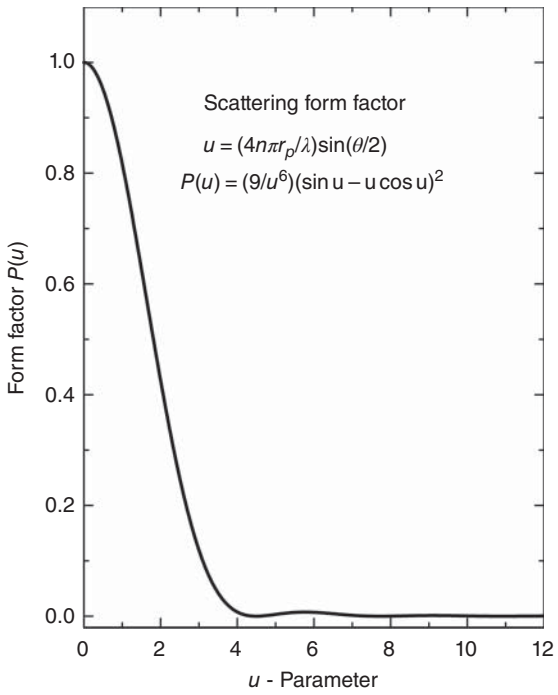

Figure 2.16 Scattering form factor as function of the dimensionless u scattering zone parameter.

($\theta \to 0$ and $\theta \to 180°$, respectively) exhibit identical intensity. To appreciate the $P(u)$ role in the general case, consider the scattered light intensity as a function of θ. The u parameter varies continuously from zero at forward direction ($\theta = 0$) to $u_{\max} = 4\pi n r_p/\lambda$ at backward direction ($\theta = 180°$). For example, for $u_{\max} = 2$, the scattered light changes between maximal value in the forward direction, to only its 42% fraction in the backward direction (Figure 2.17). If $u_{\max} \gtrsim 4$, the scattered light is maximal in the forward direction and is practically zero in the backward direction. In relatively small $u_{\max}$ values, the scattered light intensity as a function of scattering angle exhibits a minimum near perpendicularity to the incident beam orientation ($\theta \cong 90°$). Particularly, comparing between back-scattered and forward-scattered intensities provides a direct measurement of $u_{\max}$, hence of the effective scattering zones radius r_p.

Both the above theoretical models (Eqs. (2.19) and (2.23)) predict enhanced scattering for increased scattering zone dimensions. As zone dimensions grow, larger portions of their inside volume cease to scatter and behave rather like a continuous material. Furthermore, their number density decreases inside the sample.

These effects express themselves in the decrease of optical attenuation or equivalently in the increase of optical in-line transmission through same-thickness samples.

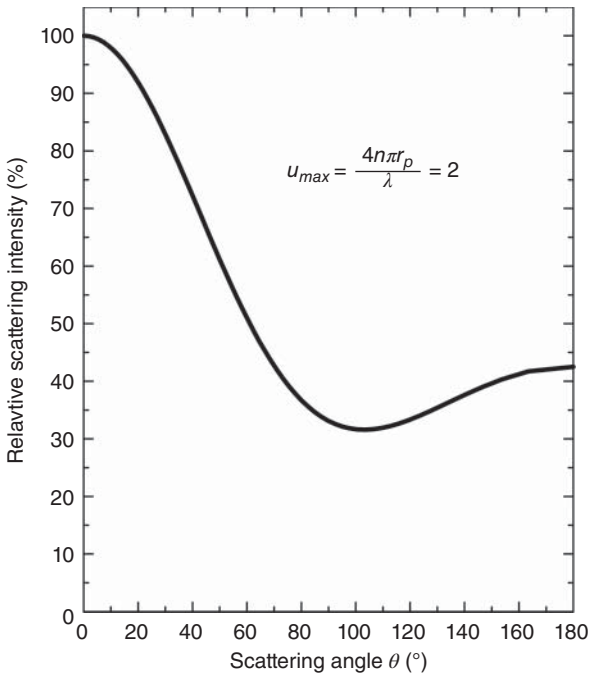

Figure 2.17 Relative scattering intensity as function of scattering angle in the special $u_{max} = 2$ case.

While the Rayleigh-type models are more amenable to calculations, the Mie approach is more useful because of its ability (noted above) to treat situations where the pores size is in the range of the wavelength. Let us illustrate this with an example. Figure 2.18a provides theoretical Mie calculations [K61] of optical transmission through 0.01% porous polycrystalline spinel ($MgAl_2O_4$) windows of different thickness (1 and 5 mm) as a function of pore dimensions at 200, 600, and 2500 nm wavelengths. All curves exhibit high transmission as long as pore dimensions are small. All show a progressive reduction in transmission as pore dimensions grow. However, the decrease reaches a minimum followed by a transmission rise upon further increase in pore dimensions. The minima positions depend directly on the light wavelength: for the $d = 1$ mm, cases (a), (b) and (c) in Figure 2.18A [K61], it resides at ~140 nm for $\lambda = 200$ nm (ultraviolet (UV)), at ~430 nm for $\lambda = 600$ nm (visible, VIS), and at ~2000 nm for $\lambda = 2500$ nm (mid-infrared, mid-IR). The transmission minima turn larger (namely, scattering turns smaller) with increased wavelength: ~13%, ~55%, and ~90%, respectively. For an increased sample thickness $d = 5$ mm, the transmission minimum position appears at smaller pore dimensions (compare curves (d) and (c)): at ~450 nm in curve (d), instead of ~2000 nm in curve (c), both belonging to the same $\lambda = 2500$ nm wavelength. Furthermore, the transmission minimum is much smaller: ~5% compared to ~90%, respectively.

The position of the minima is affected also by the value of "*n*," as illustrated in Figure 2.18B. In Figure 2.19 [K59] the effect of loss, produced by scattering on pores, is illustrated for the case of sinter/hot isostatic press (HIP) spinel; both calculated and measured values are given.

More elaborate modeling considers a variety of scattering conditions and mechanisms, such as distribution in pore shapes and dimensions, spatial distribution, multiple scattering, broadness of wavelength spectrum, and phase lags of light while crossing the pore volume. This book will not be addressing these models.

It is possible, for specific cases, to make calculations on systems where both scatterers are present together with particles that absorb light. As an example, Figure 2.20 [B30] presents the real in-line transmission (RIT) of a spinel specimen, which includes both residual porosity and light-absorbing graphite particles of 20 μm dimension.

2.3.4.2 Scattering Owed to Birefringence

This subsection concerns ideally densified ceramics, viz. lacking porosity, which are of less than cubic symmetry. Each grain is a crystalline fragment, and in most cases, the grains are randomly oriented. In such specimens, variation of refractive indices occurs at the boundaries and induces light scattering. Optical transmission thus drops quickly with increasing specimen thickness *d*. Even if the refractive index variation is small, as for example in alumina Al_2O_3, optical transmission levels exceeding about 50% may be expected only for specimen thickness smaller than about 2 mm.

For this kind of ceramics, experiment showed an unexpected fact, namely, that grain boundary scattering contribution (owed to refraction index difference of neighboring grains) reduces with decreasing grain size. This behavior is demonstrated in Figure 2.21 [H17].

Apetz and van Bruggen [A23] endeavored to rationalize this observation. They showed that regarding scattering, such a birefringent dense ceramic may be approximated by the model depicted in Figure 2.15, for porous specimens, to which a Rayleigh-type treatment can be applied. Thus the RIT is given by Eq. (2.24):

$$RIT = (1 - R_S)\exp\left(-\frac{3\pi^2\Delta n^2 d}{{\lambda_0}^2}\right) \tag{2.24}$$

In the equation the λ_0 is the wavelength in vacuum and "*d*" the sample thickness. The relationship assumes absence of multiple scattering, which, for alumina and similar ceramics, is reasonable for plates thickness of around 1 mm even if $GS < 1$ μm. In such conditions and when the birefringence is low (the case of alumina where the average $\Delta n = 0.08$), the Rayleigh approximations used in the model are valid. The pores of the model are equivalent (not real) ones; the model implies that they

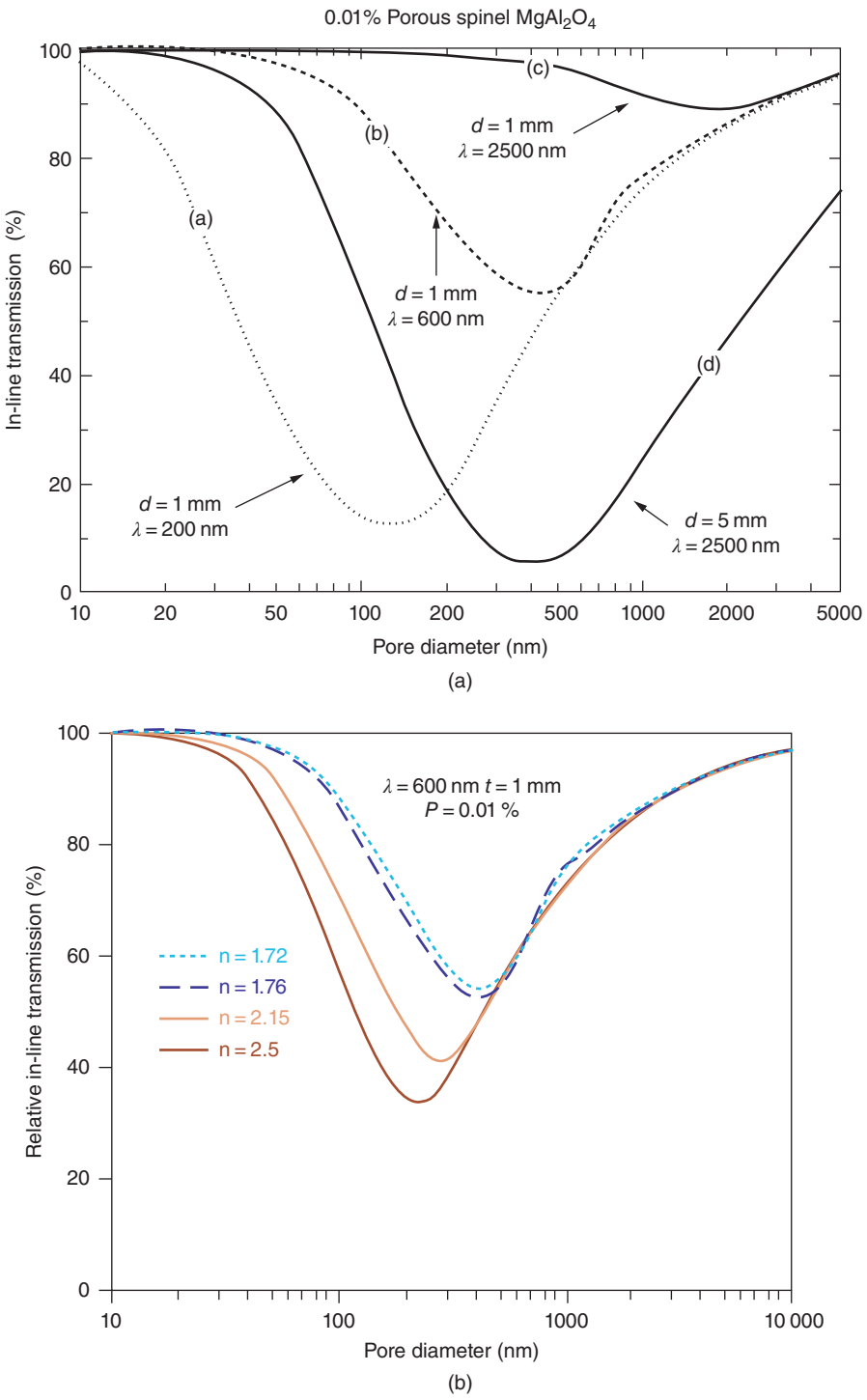

Figure 2.18 Effect of pore size/λ ratio on scattering intensity. (a) Theoretical Mie plot [M30] of in-line optical transmission through 0.01% porous polycrystalline spinel ($MgAl_2O_4$) as function of the pore diameter for different wavelengths λ and sample thickness d, as marked in the figure frame. (b) The variation of the pore size and scattering intensity, for which a minimal RIT appears when a 600 nm wave transits through a $t = 1$ mm thick TC, as a function of the ceramic's refraction index. Source: Reproduced from (a) [K61] with permission from SPIE Optical Proc. Press, (b) [K59] with permission from Elsevier.

would produce a scattering similar to that generated by the birefringence of the ceramic.

The counterintuitive results reported by Hayashi could be thus explained by the Apetz and van Bruggen model [A23]. They have shown that the transmittance of polycrystalline ceramic alumina (PCA) is, as opposed to that of cubic materials, strongly dependent on the grain size (GS) and that it is increasing with a decreasing grain size. Such an effect starts to be felt for grains of about 10 µm and becomes significant under 2 µm. As we said above, in such a case, adjacent grains represent crystallites usually with different orientation, and light is refracted (refraction is low but not zero) on arriving at the GB. They had to consider also the variable grain size. This was done by

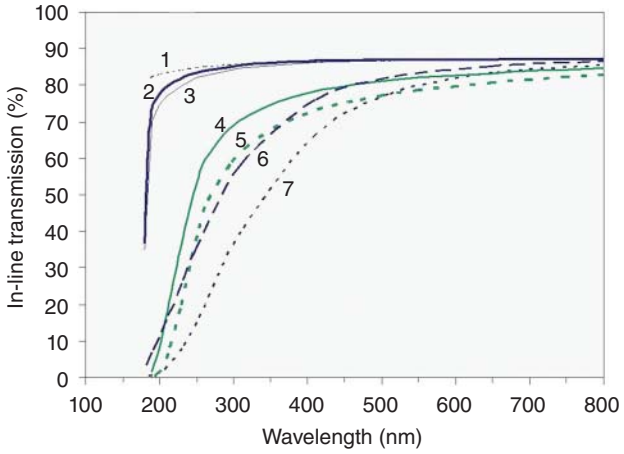

Figure 2.19 Measured in-line transmission of single and polycrystalline Mg–Al-spinel (bold curves) compared with calculated ones which combine the influences (dotted/fine lines) of (i) bandgap absorption and (ii) scattering losses (caused by residual porosity). 1 – theoretical level. 2 – single crystal ($t = 5$ mm). 3 – single crystal ($P = 1$ ppm, 40 nm pores , $t = 5$ mm). 4 – sintered spinel for $t = 3$ mm. 5 – sintered spinel for $t = 5$ mm. 6 – single crystal ($P = 0.005\%$, 40 nm pores, $t = 5$ mm). 7 – single crystal ($P = 0.01\%$, 40 nm pores , $t = 5$ mm). Source: Krell et al. 2009 [K59]. Reproduced with permission from Elsevier.

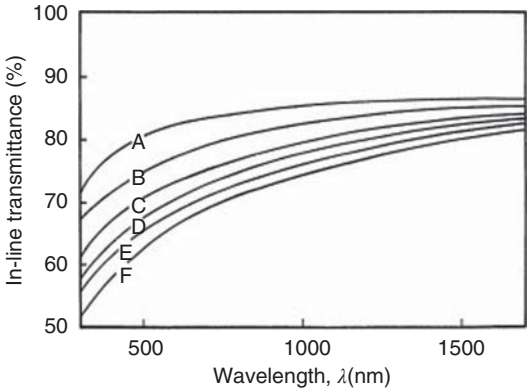

Figure 2.21 Changes of transmission, for high density, variable grain size, translucent, alumina specimens (t = 0.5 mm) sintered, in air, for various times (from A = two hours to F = 96 hours) at 1280 °C; HIPing under Ar at the same temperature (two hours,100 MPa). Reproduced from [H17] with permission from Jap. Inst. Met.

introducing a polydispersity factor, which transformed the form factor $P(u)$ (see Eq. (2.22)) into a summation in which a given "i" represents a certain "pore" size. Thus the final form of Eq. (2.23) becomes (2.25):

$$I_{tot}(\beta) = I_0 \frac{32\pi^4}{9\lambda_m l^2}\left(\frac{\Delta n}{n}\right)^2 (1 + \cos^2\beta) \sum_V r_i^6 P_i(u_i) \tag{2.25}$$

The parameter β, in (2.25), is the scattering angle.

Figure 2.22b [A23] shows that the RIT of a fully dense 0.8 mm alumina plate at 645 nm, drops from ~70% for grain size $GS = 0.7$ µm to approximately zero at $GS = 8$ µm. Figure 2.22a shows the grain-size (GS) effect in terms of scattering angle width. The scattering angle width is seen to be lower for fine-grained specimens. Obviously, larger scattering angle width reduces the RIT.

Notably, while total forward transmission (TFT) might be large, the RIT, being only a part of it, could be quite small. The two kinds of transparent ceramics are often usable, yet for different applications. The high TFT one for applications such as the LUCALOX alumina and the high RIT one for applications such as lenses and laser amplifying media components.

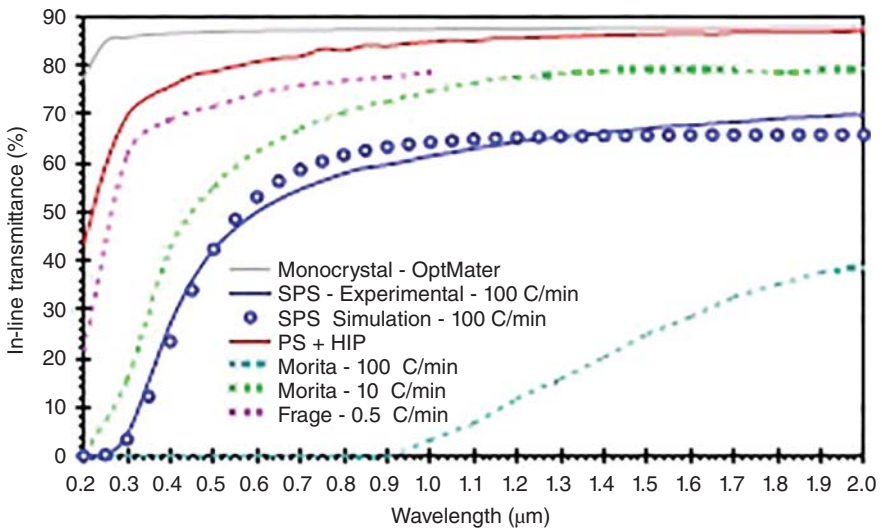

Figure 2.20 In-line transmittance as a function of wavelength for polycrystalline spinel sintered by SPS (100 °C/min). Previous results from the literature are compared with data obtained for the single crystal (calculated with Optimar software), with results from a sample prepared by PS + HIP, and with the calculated curve taking into account residual pores and graphite particles. 1 – single crystal (calculated). 2 – pressureless sintering + HIP. 3 – Frage 8.5 °C/min. 4 – Morita 10 °C/min. 5 – SPS 100 °C/min. calculated. 6 – SPS Experiment 100 °C/min. Source: Bernard-Granger et al. 2009 [B30]. Reproduced with permission from Elsevier.

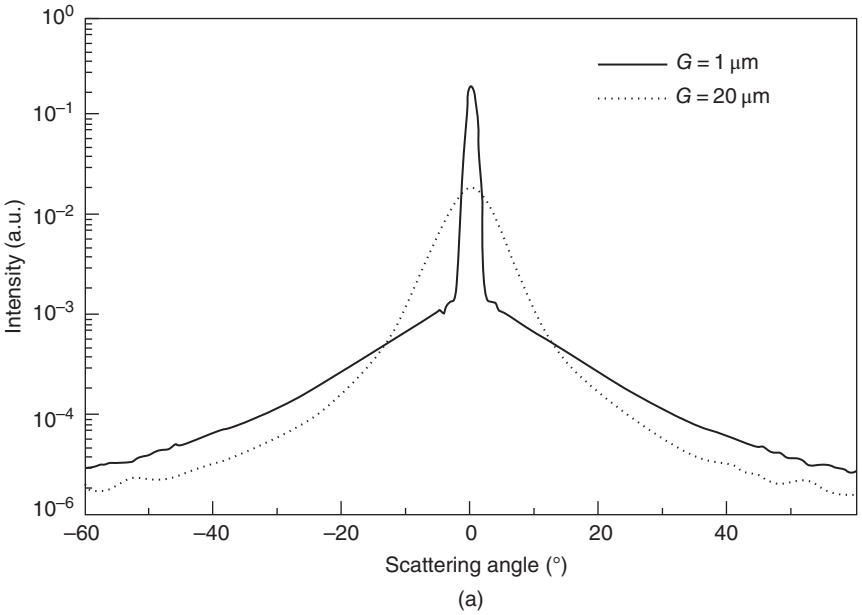

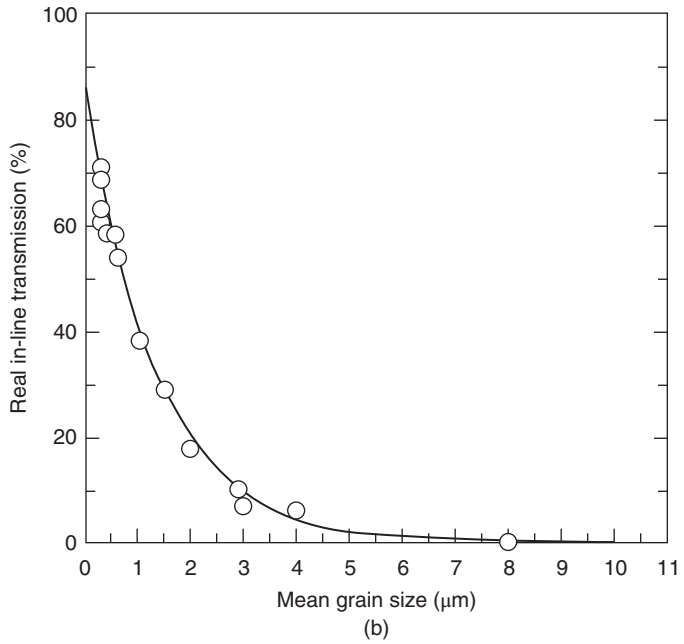

Figure 2.22 Scattering parameters dependence on grain size. (a) Scattering intensity angular profiles of fine-grained and large-grained PCA. Both samples were polished on both sides and were 0.8 mm thick. Intensity is on a logarithmic scale. (b) RIT at 645 nm as a function of the mean grain size ((*E*) experimental data points). All samples were virtually pore-free, polished on both sides, and had a thickness of 0.8 mm. Sample thickness is 0.8 mm, wavelength is 645 nm, and refractive index difference used for the theoretical curve (—) is 0.005. Source: Apetz and van Bruggen 2003 [A23]. Reproduced with permission from John Wiley & Sons.

2.3.5 Absorption

2.3.5.1 Transition Metal and Rare-Earth Cations in Transparent Ceramic Hosts

In their pure (ideal) state, transparent solids of our interest (**transparent ceramics**) absorb visible (VIS) and ultraviolet (UV) light, prominently by exciting electrons from their valence into the conduction band. The low-frequency edge of that strong absorption is usually still in the ultraviolet (UV); it represents the high-frequency start of the transparency region (going from high to lower frequencies). The transmissivity ends at frequencies, in the near, mid or FIR where, depending on their chemistry and structure, the various transparent ceramic materials become absorptive again; the incident electromagnetic radiation leads, at such frequencies, to excitation of a broad range of lattice vibrations. Thus, most transparent ceramics are optically transparent throughout the entire VIS range, down to a wavelength situated more or less deep into the infrared. In this book, this spectral region is often referred to as the material **optical transparency window** (see Section 1.3), or just **window**.

After synthesis and powder processing, real materials contain low amounts of various transition metal and rare-earth elemental cations (sometimes only few parts per million, but never zero). They are addressed as "impurities." Depending on the specific applications, the impurities may be useful, harmless, or deleterious. For many applications, such cations are added on purpose, to exploit their optical emission or absorption properties. In such cases, the same cations are addressed here as "dopants." These cations substitute the host's "native" cations, establishing strong bonding with the surrounding anions. The strongly bonded units often exhibit properties that are similar to the transition metal complex molecules encountered in wet chemistry. The oxidation states and the maximal amount of dopant elements a given transparent ceramic lattice can accommodate ("dissolve") depend on the relationship between the dopants and the lattice characteristics. One critical aspect is the difference between the ionic dopant radius at each oxidation state and the radiuses of the native lattice cations [S28]. It is considered that up to a 15% difference, between the dopant and lattice cation radii, exchange is easy. As we will see in more detail in other chapters, that means that large radius RE^+-type dopants would need large site hosts, like YAG, Y_2O_3, etc. However small amounts of RE^+ cations – high enough, however, to confer fluorescence abilities to the host – could be introduced in small size sites only TCs, like spinel [B46]. The possible role of the added cation to donate or accept electrons is another. By some, the capability of being a donor in its hosting ligand is called **basicity**, a label used in this book as well [D21]. Symmetry of the lattice sites accommodating the dopant and their ligand field stabilization energy [B19] are important factors. Preexisting impurities and point defects that may interact with the dopants also need to be considered. Processing temperatures and ambient atmospheres also play important roles. These issues are treated in various publications especially papers published by Duffy and collaborators and [B19, G29].

A structural aspect that also influences on dopants spectral features is the actual topology of the dopant ions entering an oxide host. In many cases, the dopant concentration is larger on the grain boundaries than inside the grains (see Section 3.2.4) [B48, B49]. In extreme cases, practically all dopant ions may reside on grain boundaries. Dopant ligand symmetries inside a grain and on its boundaries are not necessarily identical. Dopant spectral characteristics are sensitive to these factors.

The mechanism(s) determining an impurity entrance into a particular host lattice site is a complicated issue. Its results obviously determine the spectral profile. Discussion of this issue is not within the scope of the present section; it will be given in a companion second volume of this book. The vast majority of transparent ceramics are oxides. Therefore, the general constitution of dopant/impurity sites may be schematically presented as $TM^+(RE^+)\,O_X^{\delta-}$, where TM^+ represents a transition metal cation, RE^+ represents a rare-earth cation, $\delta-$ is the real (as opposed to the formal 2) negative charge on the anion (usually $|\delta| \leq 2$), and X marks the number of anions surrounding the central cation (the ligand-forming members). Such entities possess their own *local set* of characteristic electronic states, lying within the energy gap between the top valence and bottom conduction bands. Electromagnetic radiation absorption and emission belongs to transitions involving these local electronic states. The transition bands are relatively narrow, spanning optical regions from the near ultraviolet (near-UV) to the near infrared (near-IR); most are located in the visible region. Embedded transition metal and rare-earth cations also affect their hosts, like modifying their point defects population and producing ionic diffusion and electrical conductivity. In this chapter, however, we are interested only in the spectroscopic effects, mostly optical, also of electron spin (paramagnetic) resonance (**ESR** or **EPR**, respectively), belonging to radio frequencies in the GHz region.

2.3.5.2 Absorption Spectra of Metal and Rare-Earth Cations Located in TC Hosts

As noted above, transition metal and rare-earth-type extrinsic cations hosted by a transparent ceramic produce specific profile absorption spectra. They constitute localized electronic systems, which are able to absorb discrete frequency photons of energy equal to the gaps between the ground- and excited-states of these systems. Actually, the transitions are broadened due to the host vibrations; therefore, each electrical transition is addressed as a "band." Practically, one wishes to be able to predict, or at least explain, the observed shape of electromagnetic spectra produced by transition metal and rare-earth cations embedded in ceramic hosts. Particularly, aspects like the number of absorption bands, their location on the frequency scale, and their maximal intensity and shape are of interest. With that knowledge, it would be possible to mitigate, by suitable processing, some negative impurities' effects and control the desired effects of purposely added dopants. As will be addressed below, ligand field theory (**LFT**), in its different variants, may be used quite efficiently for that purpose when the absorbers are of the transition metal cation type. The theoretical base for interpretation of spectra generated by rare-earth cation-type absorbers (considerably different from the transition metal cation-type absorbers) is also given.

The spectral characteristics are basically determined by the oxidation states assumed by the transition metal and rare-earth atoms entering the transparent ceramic host, their concentration, the strength of the spin/orbital coupling, and the symmetry of the ligand polyhedron formed by the lattice anions surrounding the active cation. The central cation plus the surrounding lattice anions are often considered as forming a "complex."

Interpretation of the absorption spectra by identifying the dopant element(s) and the oxidation state(s) can be achieved by the aid of the given theoretical background. The theory also allows determining the ligand polyhedron symmetry and in some cases even determines the covalency of the different complex bonds.

2.3.5.2.1 Transition Metal and Rare-Earth Cations' Electronic Spectra: Theoretical Basis

Quantum and wave mechanics offer the best basis for interpretation of the complex phenomenology occurring on the atomic and particle scale. Phenomena relevant to electronic spectroscopy are no exception. The discussion below uses this framework. A rigorous treatment of the issues is given in [B9, B33, C40, F8, H24, I10, J16, J17, L42, O3, T9, V4]. For the objectives important here, however, a simplified semiquantitative approach is still able to provide much of the needed information. A number of books dedicated to glass science and technology include such simplified presentations of spectroscopic theory [B19, P14]. It obviates the need for consulting the primary texts, cited above, the reading of which requires in-depth knowledge of quantum and wave mechanics and relatively complicated mathematics. The reason for including the present section is the lack of a similar approach in basic books destined for ceramists.

Familiarity of the reader with some basic concepts of quantum mechanics, such as wave equations, wave-functions, eigen-functions, eigen-values, quantum numbers, photons, and phonons, is still assumed.

2.3.5.2.1.1 Electronic States of a Cation in Free Space

Most transition metal and rare-earth cations do indeed generate optical spectra in the present frequency region of interest. They always exhibit incomplete d^q or f^q electronic configurations. The simplest ionic case is that of a single electron under the influence of the central attractive electric field of the nucleus. Schrödinger's equation, i.e. the mathematical expression describing the system in quantum-wave mechanics, is of the form

$$-\frac{\hbar^2}{2m}\nabla^2\psi - \frac{Ze^2}{r}\psi = E\psi \tag{2.26}$$

where $\hbar = 1.0546\times10^{-27}$ erg s is the reduced Planck constant, $m = 9.1096\times10^{-28}$ g is the electronic mass, $\nabla \equiv (\partial/\partial x,\ \partial/\partial y,\ \partial/\partial z)$ is the spatial gradient operator, Z is the number of protons occupying the nucleus, $e = 4.8032\times10^{-10}$ esu is the absolute value of the electronic charge, r is the electron distance from the nucleus, E is the total electronic energy, and ψ is the time-independent wave function. The first addend on the equation's left-hand side accounts for the electronic kinetic energy, while the second, $V = -Ze^2/r$, accounts for its Coulomb attractive potential energy.

For poly-electronic ions, the wave equation would be

$$-\frac{\hbar^2}{2m}\left(\sum_i \nabla_i{}^2\right)\psi - \left(\sum_i \frac{Ze^2}{r_i}\right)\psi + \left(\sum_{i,j}\frac{e^2}{r_{i,j}}\right)\psi = E_{total}\psi \tag{2.27}$$

where the i and j subscripts run over all electrons, $r_{i,j}$ is the distance between the i and j electrons, ψ is a spatial wave function of all electronic positions, and E_{total} is the total state energy. The first addend on the equation's left-hand side accounts for the sum of all electronic kinetic energies; the second one accounts for the sum of all electronic potential energies due to attraction by the positive nucleus; the third one accounts for the sum of all inter-electronic repulsion potential energies.

While the solution of Eq. (2.26) is already quite complicated, a direct analytic solution of Eq. (2.27) is hopeless, due to the large number of variables. For that reason, the approach is converted into a modified "independent electrons" model. In the model's zero-order approximation, each electron is assumed to follow the same wave equation, which is quite similar to Eq. (2.27) under an effective non-Coulomb yet central, attractive potential. This assumed potential visualizes all other electrons as forming a partial, distance-dependent screening of the nuclear positive electric charge. Owing to the central symmetry of the said effective potential, the angular part of the solution remains identical with that of the single electron problem of Eq. (2.27). This approach provides an identical set of possible states for each independent electron. The states are classified by the quantum numbers $|n, \ell, m_\ell, s, m_s\rangle$, where n is the principal quantum number, with possible 1, 2, 3, … numbers, ℓ is the orbital angular momentum quantum number with possible 0, 1, 2, …, $n-1$ values, and m_ℓ is the magnetic (or projection) quantum number with possible ℓ, $\ell-1$, …, 0, …, $-\ell$ values. $s = 1/2$ is the spin quantum number, and m_s is the spin projection quantum number, with possible $+1/2$, $-1/2$, values. The non-Coulomb nature of the effective potential removes the energy degeneracy among different ℓ states belonging to the same n.

In the next-order correction, the electrons, subject to **Pauli's exclusion principle**, are assumed to gradually fill the allowed states according to their energetic order. There are $2\ell+1$ different m_ℓ values for a particular

ℓ, and each may exhibit two different values of the spin projection: $m_s = \pm 1/2$. Therefore, each $|n, \ell\rangle$ set of levels may accommodate up to $2(2\ell + 1)$ electrons. The accommodation direction is from a low to a higher n number. Energies of a set of electrons belonging to the same n-number are close to each other but exhibit large separation from electrons belonging to other n's. They are thus classified as forming a **shell**. A full shell is called a **closed shell**. Shells belonging to $n = 1, 2, 3, 4, \ldots$ are symbolized by the capital letters K, L, M, N, …, respectively. Electrons belonging to the same shell, and of the same ℓ, form a **sub-shell**, of more tightly close energies. Sub-shells belonging to $\ell = 0, 1, 2, 3, \ldots$ are symbolized by the lowercase letters s, p, d, f, …, respectively. In all shells, the *s* electrons form the deepest sub-shell; among the other sub-shells, *deeper* in energy are those of *larger* ℓ.

A set of independent electrons forming an electronic atomic or ionic state is called **electronic configuration**. It is symbolized by Configuration $= \cdots n\ell^q \cdots$, where q is the number of electrons belonging to the principal quantum number n and orbital quantum number ℓ. For example, $[1s^2]\,[2s^2 2p^6]\,[3s^2 3p^6]3d^5 4s$ is the electronic configuration of the chromium Cr atom. The first configuration enclosed in square brackets, $[1s^2]$, is identical with the closed shell of the noble helium He gas atoms. The first two $[1s^2]\,[2s^2 2p^6]$ are identical with the two closed shells of the noble neon Ne gas atoms. The first three $[1s^2]\,[2s^2 2p^6]\,[3s^2 3p^6]$ are identical with the three closed shells of the noble argon Ar gas atoms. To save space, the chromium configuration is then written as $[Ar]3d^5 4s$.

A further refined approximate correction obtains by considering interaction among shell electrons or among sub-shell electrons, based on their total angular and total spin momentums; specifically between $\boldsymbol{L} = \sum_i \boldsymbol{\ell}_i$ and $\boldsymbol{S} = \sum_i \boldsymbol{s}_i$ vector sums, of L and S quantum numbers, respectively. Both L and S are considered "good quantum numbers," characterizing their state properties. This consideration is called the **Russell–Saunders** approach. There are a number of possible combinations to sum the component vectors. Particularly for the spin summing, Pauli exclusion principle, stating that only a single independent electron may accommodate any possible electronic state, is considered. Closed shells and sub-shells exhibit a zero total angular momentum $L = 0$ and a zero total spin $S = 0$. For most near-visible spectroscopic issues, only electrons belonging to partially filled sub-shells need to be considered. A spectroscopic state symbols reflecting the L and S values is called **Term**, and written as ${}^{2S+1}L$.

The following Tables 2.1 and 2.2 summarize the different Terms [N8] obtained for every d^q configuration of electrons residing in a d sub-shell ($\ell = 2$) and Terms obtained for several f^q configurations of electrons residing in an f sub-shell ($\ell = 3$). A filled d sub-shell contains 10 electrons; a filled f sub-shell contains 14 electrons. A Term generated by a partially occupied shell is identical with that of a partially unoccupied shell. Most dopant transition metal or rare-earth cations relevant for optical usage of transparent ceramics belong to the d and f sub-shells, respectively.

Table 2.1 Terms derived from d^q electronic configurations.

Configurations	Term
d or d^9	^{2}D
d^2 or d^8	^{1}S, ^{1}D, ^{1}G, ^{3}P, ^{3}F
d^3 or d^7	^{2}P, ^{2}D, ^{2}F, ^{2}G, ^{2}H, ^{4}P, ^{4}F
d^4 or d^6	^{1}S, ^{1}D, ^{1}F, ^{1}G, ^{1}I, ^{3}P, ^{3}D, ^{3}F, ^{3}G, ^{3}H, ^{5}D
d^5	^{2}S, ^{2}P, ^{2}D, ^{2}F, ^{2}G, ^{2}H, ^{2}I, ^{4}P, ^{4}F, ^{4}D, ^{4}G
d^{10}	^{1}S (filled subshell)

Table 2.2 Terms derived from f^q electronic configurations.

Configurations	Term
f or f^{13}	^{2}F
f^2 or f^{12}	^{1}S, ^{3}P, ^{1}D, ^{3}F, ^{1}G, ^{3}H, ^{1}I
f^3 or f^{11}	^{4}S, ^{2}P, ^{2}D, ^{4}D, ^{2}F, ^{4}F, ^{2}G, ^{4}G, ^{2}H, ^{2}I, ^{4}I, ^{2}K, ^{2}L
f^{14}	^{1}S (filled subshell)

Energy splitting among different Terms of same configuration emanates from different electrostatic and exchange interactions between all pairs of their constituting electrons. An analysis by Racah [R3] showed that any Term energy in a d^q sub-shell may be expressed by three constants, *A*, *B*, and *C*; any Term energy in an f^q sub-shell may be expressed by four constants, *A*, *B*, *C*, and *D*. They are all addressed as **Racah Constants**. The constants are in fact combinations of Coulomb and exchange interaction integrals between independent sub-shell electron pairs. The following Table 2.3 summarizes Racah's expressions for all d^q and several relevant f^q configurations.

The Racah *A* constant is unimportant in determining the energy separations among Terms in any specific d^q or f^q configuration. Theoretical estimates of Racah Constants for each free ion are reasonably close to experimental ones yet not identical. Empiric estimates are quite successful in predicting especially the energy order among the Terms, as well as the actual separation,

Table 2.3 Racah's energies for all d^q and a few relevant f^q configurations.

Configurations	Term	Energy
nd^2 and nd^8	^1S	$A+14B+7C$
	^3P	$A+7B$
	^1D	$A-3B+2C$
	^3F	$A-8B$
	^1G	$A+4B+2C$

Configurations	Term	Energy
nd^3 and nd^7	^2P	$3A-6B+3C$
	^4P	$3A$
	^2D	$3A+5B+5C\pm(193B^2+8BC+4C^2)^{1/2}$
	^2F	$3A+9B+3C$
	^4F	$3A-15B$
	^2G	$3A-11B+3C$
	^2H	$3A-6B+3C$

Configurations	Term	Energy
nd^4 and nd^6	^1S	$6A+10B+10C\pm2(193B^2+8BC+4C^2)^{1/2}$
	^3P	$6A-5B+(11/2)C\pm\frac{1}{2}(912B^2-24BC+9C^2)^{1/2}$
	^1D	$6A+9B+(15/2)C\pm\frac{3}{2}(144B^2+8BC+C^2)^{1/2}$
	^3D	$6A-5B+4C$
	^5D	$6A-21B$
	^1F	$6A+6C$
	^3F	$6A-5B+(11/2)C\pm\frac{3}{2}(68B^2+4BC+C^2)^{1/2}$
	^1G	$6A-5B+(15/2)C\pm\frac{1}{2}(708B^2-12BC+9C^2)^{1/2}$
	^3G	$6A-12B+4C$
	^3H	$6A-17B+4C$
	^1I	$6A-15B+6C$

Configuration	Term	Energy	Term	Energy
nd^5	^2S	$10A-3B+8C$	$^2F'$	$10A-25B+10C$
	^6S	$10A-35B$	^4F	$10A-13B+7C$
	^2P	$10A+20B+10C$	^2G	$10A-13B+8C$
	^4P	$10A-28B+7C$	$^2G'$	$10A+3B+10C$
	^2D	$10A-3B+11C\pm3(57B^2+2BC+C^2)^{1/2}$	^4G	$10A-25B+5C$
	$^2D'$	$10A-4B+10C$	^2H	$10A-22B+10C$
	^4D	$10A-18B+5C$	^2I	$10A-24B+8C$
	^2F	$10A-9B+8C$		

Table 2.3 (Continued)

Configurations	Term	Energy
$nf^2$and nf^{12}	^1S	$A+60B+105C+9D$
	^3P	$A+45B$
	^1D	$A+19B-72C+2D$
	^3F	$A-10B$
	^1G	$A-30B+110C+2D$
	^3H	$A-25B$
	^1I	$A+25B+2D$

Configurations	Term	Energy
nf^3 and nf^{11}	^4S	$3A-30B$
	^2P	$3A-25B+35C+3D$
	^2D	$3A-7B+(57/2)C+3D\pm\frac{1}{2}(2176B^2-18096BC+74529C^2)^{1/2}$
	^4D	$3A+25B$
	^2F	$3A+55B+(75/2)C+6D\pm\frac{1}{2}[9700B^2-180B(45C+2D)+9(45C+2D)^2]^{1/2}$
	^4F	$3A-30B$
	^2G	$3A+7B+(113/2)C+3D\pm\frac{1}{2}(12676B^2-31676BC+36169C^2)^{1/2}$
	^4G	$3A-10B$
	^2H	$3A-23B+(63/2)C+3D\pm\frac{1}{2}(5056B^2-18816BC+29169C^2)^{1/2}$
	^2I	$3A-5B+45C+3D$
	^4I	$3A-65B$
	^2K	$3A-40B+80C+3D$
	^2L	$3A+3D$

Note: The nd^3 configuration generates two energy states for the ^2D Term. The nd^4 configuration generates two energy states for each of the ^1S, ^3P, ^1D, ^3F, and ^1G Terms. The nd^5 configuration generates three energy states of a ^2D Term, and two energy states for each of the ^2F and ^2G Terms.
Note: The nf^3 and nf^{11} configurations generate two energy states for each of the ^2D, ^2F, ^2G, and ^2H Terms.

usually with only small deviations. In the d^q configurations, all constants increase in magnitude with the ionic degree. The C/B ratio, however, remains nearly constant, 4.6 on the average, with approximately 10% mean deviation. Some empiric Racah Constants for different free ions are listed in Tables 2.4 and 2.5 [C11, O3]. Constants for other ions may as well be calculated on the basis of level lists compiled in Ref. [N7].

As an example of fits and deviations related to Racah Constants, we consider the valence electronic states of the free chromium ion Cr^{4+}, which belongs to the $3d^2$ configuration. Its empiric Racah A Constant was estimated as $-7350\,cm^{-1}$. The B and C constants are listed

Table 2.4 Empiric *B* and *C* Constants for different representative $3d^q$ configurations subshell.

Ion	Configurations	B (cm^{-1})	C (cm^{-1})	Ion	Configurations	B (cm^{-1})	C (cm^{-1})
Ti^{2+}	$3d^2$	695	2910	Cr^{4+}	$3d^2$	1000	5250
V^{2+}	$3d^3$	755	3257	V^{3+}	$3d^2$	862	3815
Cr^{2+}	$3d^4$	810	3565	Cr^{3+}	$3d^3$	918	4133
Mn^{2+}	$3d^5$	860	3850	Mn^{3+}	$3d^4$	965	4450
Fe^{2+}	$3d^6$	917	4040	Fe^{3+}	$3d^5$	1015	4800
Co^{2+}	$3d^7$	971	4497	Co^{3+}	$3d^6$	1065	5120
Ni^{2+}	$3d^8$	1030	4850	Ni^{3+}	$3d^7$	1115	5450

Table 2.5 Empiric *B*, *C*, and *D* Racah Constants for different representative free ions belonging to the $4f^q$ subshell.

Ion	Configurations	B (cm^{-1})	C (cm^{-1})	D (cm^{-1})
Ce^{2+}	$4f^2$	205	45	2809
Pr^{2+}	$4f^3$	242	13.25	7768
Nd^{3+}	$4f^3$	295	2.9	3273

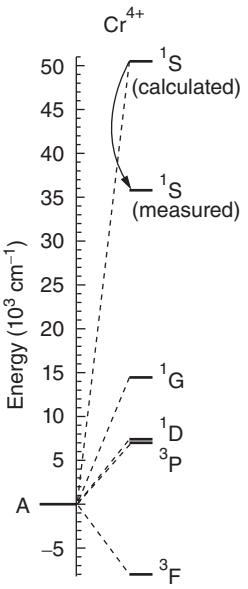

Figure 2.23 Energy scheme of a Cr^{4+} ion calculated par Racah constants of Table 2.4.

in Table 2.4. An accordingly calculated energy scheme is provided in Figure 2.23.

Excellent fit with experiment is demonstrated for the lower energy Terms ^3F, ^3P, ^1D, and ^1G, but a considerable deviation for the higher energy ^1S Term. A similar behavior is apparent in virtually all cases of atomic and ionic states.

A higher-order correction to the state energies is obtained by considering the spin–orbit coupling. The resultant $\boldsymbol{L}$ and $\boldsymbol{S}$ angular momentums are coupled to form their vector sum $\boldsymbol{J} = \boldsymbol{L} + \boldsymbol{S}$, which assumes the quantum number J; it is the best quantum number characterizing the state's angular momentum. The possible J values are $|L-S|, |L-S|+1, \ldots, (L+S)$. States belonging to the different possible combinations of the same L and S values are called **multiplet**. The multiplet individual states are characterized by different J values and symbolized as $^{2S+1}L_J$. In that respect, the left superscript $2S+1$ value in the Term symbol is called **multiplicity**. For $S \leq L$, the multiplicity provides the number of possible different J values belonging to the particular ^{2S+1}L Term. For $S > L$, however, the number of possible different J values is given by $2L+1$.

The Term energy splitting due to different J's is given by

$$\Gamma_{SLJ} = \tfrac{1}{2}\xi_{SL}[J(J+1) - L(L+1) - S(S+1)] \tag{2.28}$$

where ξ_{SL} is the **spin–orbit coupling constant**. Its empiric absolute value in different situations ranges between 50 and 1000 cm^{-1}.

Observation of empiric behavior of state energies is summarized as **Hund's laws** as follows:

[1] For Terms of equal L values, the energy is a decreasing function of the multiplicity $2S+1$.
[2] For Terms of equal multiplicities, the energy is a decreasing function of L.
[3] In each multiplet, the energy of an individual state-member is an *increasing function* of J for a less-than-half-filled sub-shell (namely, $\xi_{SL} > 0$ in Eq. (2.28)) and is a *decreasing function* of J for a more-than-half-filled sub-shell (namely, $\xi_{SL} < 0$ in Eq. (2.28).

In Figure 2.24 we consider an energy level scheme of the Ni^{2+} ion's ^3F ground-state splitting by the spin–orbit interaction. The Ni^{2+} ion belongs to the d^8 sub-shell

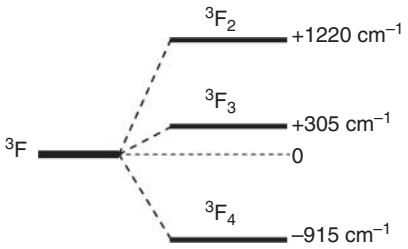

Figure 2.24 Ni^{2+} cation's ^3F ground-state level splitting by the spin/orbital interaction.

and is thus more than half filled. The spin–orbit coupling constant is correspondingly negative, specifically $\xi_{SL} = -305\,\mathrm{cm}^{-1}$. According to Eq. (2.28), the ^3F Term splits into $^3F_4$, $^3F_3$, and $^3F_2$ levels.

In free atoms and ions up to about $Z \cong 30$, the above schemes provide quite a satisfactory description of state energies, especially the energy order among the states. For $Z > 30$, however, angular momentum interactions become relatively more important. With growing Z, deviations from Hund's empiric laws become more frequently apparent. Transition metal ions usually belong to the $Z < 30$ region; rare-earth ions belong to the $Z > 30$ region.

Optical absorption or emission spectra result from transitions between electronic states. Only transitions that involve a change in an electric or a magnetic multipole moment can occur. Strongest transitions relate to electric dipole changes, second in strength are electric quadrupole changes, and third are magnetic dipole ones. So-called **selection rules** distinguish between relatively strong transitions, termed **allowed**, and extremely weak transitions, termed **forbidden**. Allowed optical electric dipole moment transitions obey the following selection rules:

$$\mathbf{\Delta}L = \pm 1;\quad \mathbf{\Delta}S = 0;\quad \mathbf{\Delta}J = 0, \pm 1;\quad \mathbf{\Delta}M_J = 0 \pm 1 \tag{2.29}$$

except for $J = 0 \rightarrow J' = 0$, and except for $\mathbf{\Delta}M_J = 0$, when $\mathbf{\Delta}J = 0$ where M_J is the state's total angular momentum projection quantum number and $\mathbf{\Delta}L \equiv L' - L$, $\mathbf{\Delta}S \equiv S' - S$, $\mathbf{\Delta}L \equiv J' - J$, and $\mathbf{\Delta}M_J \equiv M_{J'} - M_J$ are the changes between the L, S, J, and M_J quantum numbers of the initial and final states, respectively.

2.3.5.2.1.1.1 Electronic Structure of Transition Metal Cations in a Crystalline Site; Crystal Field Approach Cations with $Z < 30$

When an ion resides in a crystalline site, gross changes of state energies and selection rules occur. They classify as emanating from five different effects:

{1} The first effect is some reduction in energy separations among states. It is attributed to the host matrix influence as a "dielectric medium," which effectively reduces the attractive forces between each electron and the nucleus, as well as the repulsive forces among all electrons. For practical purposes, these changes require empirical adjustment (usually reduction) of the Racah and spin–orbit coupling Constants.

{2} The second effect is splitting of the state energies due to the reduced symmetry experienced by the atom or ion while residing in the hosting site, as compared to the full rotational symmetry experienced in free space. The effect is usually addressed as **crystal field splitting**, or sometimes as **Stark splitting**. (The latter naming should not be misinterpreted! The *classical Stark effect* employs a static external electric field that is *constant across atomic dimensions*. The **crystal field**, although static, involves *huge electric field gradients across atomic dimensions*; particularly, it vanishes at the site center.) The symbols assigned to the individual split states (and their wave functions) replace the angular momentum letter symbol by a different letter. It represents the wave-function spatial angular symmetry in the frame of the hosting site point group symmetry. Group theoretical notation of symmetry operations use **Schoenflies notation** as follows:

(i) The capital letter E symbolizes the identity operation.
(ii) C_p symbolizes a rotation by $2\pi/p$ (called ***p*-fold rotation**, or **rotation of order *p***).
(iii) S_p symbolizes a p-fold rotation followed by a perpendicular mirror reflection.
(iv) $\boldsymbol{i}$ symbolizes an inversion operation about the site center.
(v) σ_v symbolizes a mirror reflection in a plane that contains the highest-order C_p axis.
(vi) σ_h symbolizes a mirror reflection in a plane perpendicular to the highest-order C_p axis.
(vii) σ_d symbolizes a σ_v plane bisecting the angle between two C_2 axes.

All rotational axes and reflection mirrors contain the site mass center point. Mathematical groups generated by the operations are thus called **point groups**. E and all C_p's are called **proper rotations**; $\boldsymbol{i}$, all S_p's, and all σ ones, are called **improper rotations**.

Each quantum state exhibits the symmetry properties of an **irreducible representation** belonging to the site symmetry group (often called **symmetry species**, or just **species**). In group theory, a general species (or a sum of ones) is marked by the letter Γ. Following Mulliken, description and notation of specific species (and their corresponding states!) are as follows:

[i] States (species) are addressed as symmetric or anti-symmetric with respect to a site symmetry

operation if the state wave function preserves or reverses sign, respectively, as a result of the operation.

[ii] The capital letter A or B symbolizes non-degenerate states that are either symmetric or anti-symmetric, respectively, to rotations about the principal (highest order) C_p.

[iii] The capital letter E also symbolizes doubly degenerate states.

[iv] The capital letter T symbolizes triply degenerate states.

[v] The numerals "1," "2," or "3" may attach as subscripts to all capital letter symbols for numbering, also to indicate symmetry or anti-symmetry in relation to other symmetry operations. Particularly in the case of A and B symbols, the "1" or "2" subscripts are used to indicate symmetry or anti-symmetry, respectively, to rotation about C_2 axis that is perpendicular to the principal rotational axis. If no such axes exist, these subscripts indicate symmetry or anti-symmetry, respectively, in relation to a mirror reflection in a σ_v plane.

[vi] The subscript letters "g" or "u" may attach to all capital letter symbols to indicate symmetry or anti-symmetry, respectively, in relation to inversion about the site's symmetry center (if such exists).

[vii] A prime "′" or a double prime "″" may attach as superscripts to all capital letter symbols, to indicate symmetry or anti-symmetry, respectively, in relation to a mirror reflection in a σ_h plane.

Table 2.6 below details the wave-function splitting obtained for atomic and ionic states belonging to the total orbital angular momentums $L = 0, 1, 2, 3, 4, 5, 6, 7$, namely, to S, P, D, F, G, H, I, J states, respectively, when the atom or ion that resided in free space (exhibiting full spatial rotation/inversion symmetry forming the $O[3]$ group) is placed in sites exhibiting the full octahedral symmetry (O_h), or in sites exhibiting the full dodecahedral symmetry (D_{6h}).

There are 32 possible crystal site symmetries. If a crystal site exhibits a symmetry lower than either O_h or D_{6h}, different symmetry species result, often involving further splitting. Thus, each of the new species correlates to the former according to a correlation table that relates the species of any group to those of its subgroups. Such tables are handy in books invoking group theory [W26, W36] and in specialized scientific papers [K38, R33]. An example of a partial correlation table is provided below in Table 2.7.

Table 2.6 Correlation table among atomic and ionic states' wave functions in $O[3]$, O_h, and D_{6h} site symmetries.

$O[3]$	O_h	D_{6h}
S(1)	A_{1g}	A_{1g}
P(3)	T_{1u}	$A_{2u} \oplus E_{1u}$
D(5)	$E_g \oplus T_{2g}$	$A_{1g} \oplus E_{1g} \oplus E_{2g}$
F(7)	$A_{2u} \oplus T_{1u} \oplus T_{2u}$	$A_{2u} \oplus B_{1u} \oplus B_{2u} \oplus E_{1u} \oplus E_{2u}$
G(9)	$A_{1g} \oplus E_g \oplus T_{1g} \oplus T_{2g}$	$A_{1g} \oplus B_{1g} \oplus B_{2g} \oplus E_{1g} \oplus 2E_{2g}$
H(11)	$E_u \oplus 2T_{1u} \oplus T_{2u}$	$A_{2u} \oplus B_{1u} \oplus B_{2u} \oplus 2E_{1u} \oplus 2E_{2u}$
I(13)	$A_{1g} \oplus A_{2g} \oplus E_g \oplus T_{1g} \oplus 2T_{2g}$	$2A_{1g} \oplus A_{2g} \oplus B_{1g} \oplus B_{2g} \oplus 2E_{1g} \oplus 2E_{2g}$
J(15)	$A_{2u} \oplus E_u \oplus 2T_{1u} \oplus 2T_{2u}$	$A_{1u} \oplus 2A_{2u} \oplus B_{1u} \oplus B_{2u} \oplus 3E_{1u} \oplus 2E_{2u}$

The $O[3]$ orbital degeneracy, given by $2L + 1$, is specified in parentheses.

Table 2.7 Correlation table among atomic and ionic states' wave-function species in O_h, D_{3d}, D_{4h}, T_h, O, T_d, and D_2, and among D_{6h}, D_{3h}, and D_6 site symmetries.

O_h	D_{3d}	D_{4h}	T_h	O	T_d	D_2	D_{6h}	D_{3h}	D_6
A_{1g}	A_{1g}	A_{1g}	A_g	A_1	A_1	A	A_{1g}	A_1'	A_1
A_{1u}	A_{1u}	A_{1u}	A_u	A_1	A_2	A	A_{1u}	A_{11}''	A_1
A_{2g}	A_{2g}	B_{1g}	A_g	A_2	A_2	A	A_{2g}	A_2'	A_2
A_{2u}	A_{2u}	B_{1u}	A_u	A_2	A_1	A	A_{2u}	A_{22}''	A_2
E_g	E_g	$A_{1g} \oplus B_{1g}$	E_g	E	E	2A	B_{1g}	A_1''	B_1
E_u	E_u	$A_{1u} \oplus B_{1u}$	E_u	E	E	2A	B_{1u}	A_1'	B_1
T_{1g}	$A_{2g} \oplus E_g$	$A_{2g} \oplus E_g$	T_g	T_1	T_1	$B_1 \oplus B_2 \oplus B_3$	B_{2g}	A_2''	B_2
T_{1u}	$A_{2u} \oplus E_u$	$A_{2u} \oplus E_u$	T_u	T_1	T_2	$B_1 \oplus B_2 \oplus B_3$	B_{2u}	A_2'	B_2
T_{2g}	$A_{1g} \oplus E_g$	$B_{2g} \oplus E_g$	T_g	T_2	T_2	$B_1 \oplus B_2 \oplus B_3$	E_{1g}	E″	E_1
T_{2u}	$A_{1u} \oplus E_u$	$B_{2u} \oplus E_u$	T_u	T_2	T_1	$B_1 \oplus B_2 \oplus B_3$	E_{1u}	E′	E_1
							E_{2g}	E′	E_2
							E_{2u}	E″	E_2

Often, when a cation's closest neighbors are four, six, or eight identical anions, T_d, O, or D_6 site symmetries are correspondingly approximated, although the actual occupying sites may exhibit lower symmetries. Such approximations are quite successful in describing many of cations states' properties.

To demonstrate the meaning and use of Tables 2.6 and 2.7, we consider the splitting of an orbital F state when placed in a D_2 symmetry site.

Imagine that the ion had initially been placed in an O_h symmetry site. Then, due to a lattice distortion, the site symmetry has reduced to D_2. Initially, the ionic state splits into three $A_{2u} \oplus T_{1u} \oplus T_{2u}$ states. Then, the A_{2u} state transformed into an A state, and each of the T_{1u} and T_{2u} states transformed into three $B_1 \oplus B_2 \oplus B_3$ states. Figure 2.25 provides a **correlation map** describing the said splitting and changes.

Importantly, while the correlation map resembles an energy scheme, it is definitely not so. Particularly, the state positions do not represent neither the energetic order nor the separation among the states. To avoid confusion, correlation maps are sometimes called **Term schemes**. Reliable conversion of correlation maps into energy schemes requires both theoretical calculations and experiments!

In spectroscopy, the symbols attached to each state include, in parentheses, the parent state symbol as a reminder. For example, split states from a ^{3}F parent residing in an O_h symmetry site will be written as $A_{2u}(^3F)$, $T_{1u}(^3F)$, and $T_{2u}(^3F)$. For additional demonstration, Figure 2.26 shows an experimental energy scheme of a Co^{2+} ion residing in the T_d symmetry site of a spinel $MgAl_2O_4$ single crystal, by replacing the lattice original Mg^{2+} one. An important observation is that, in this particular case, the crystal field splitting is larger than the spin–orbit coupling one. Therefore, the ^{4}F Term splits into three well-separated multiplets. The ^4P_J and ^4P_J symbols in parentheses attached to each multiplet component are reminiscent of the original free ion spin–orbit coupling splitting.

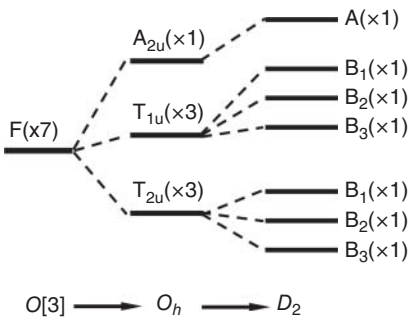

Figure 2.25 Correlation map (Terms scheme) demonstrating changes in the symmetry species of orbital angular momentum species of an atom or ion, which starts as an F-state in free space and ends in a crystalline site of D_2 symmetry. State degeneracy is written in parentheses.

Solid arrows mark optically dipole-allowed transitions between multiplets; a dashed arrow marks a dipole-forbidden transition. To avoid overcrowding, arrow plotting connects only between the lowest states of each multiplet, but they correspond equally to each individual member of the multiplets. The issue on selection rules relevant to the above is discussed in detail in the following section. The spectroscopic transition lines actually broaden due to the host matrix vibrations. This issue is discussed in more detail in the section below.

If, in contrast, the crystal field splitting had not been large compared to the spin–orbit one, a **double group** nomenclature should have been used for the multiplet components. The double group concept will be described in more detail in item {3} below, in relation to the $Z > 30$ cations case.

{3} The third crystal field effect is the introduction of an entirely different set of selection rules. For example, in the free ion, transitions between F and P states are forbidden, as not conforming to the $\mathbf{\Delta}L = \pm 1$ selection rule. The allowed optical transitions provided in Figure 2.26 violate entirely that rule. In principle, specific selection rules may be worked out for each case, by considering the overlap integral between the transition-operated initial state wave function $\boldsymbol{O}\psi_i$ and the final state wave function ψ_f. In other words, the oscillator strength is proportional to the squared integral $|\langle \psi_f \,|\, \boldsymbol{O}\psi_i \rangle|^2$, where $\boldsymbol{O}$ is the **transition operator**; for electric dipole transitions, it is $\boldsymbol{O} \equiv e\boldsymbol{r}$. A transition is allowed if the oscillator strength is positive; it is forbidden, if the oscillator strength diminishes.

Group theory allows obtaining an answer to whether the probability diminishes, or is positive, without actually carrying out the integral. It involves consideration of the involved state symmetry species, together with the symmetry species belonging to the transition operator $\boldsymbol{O}$. The underlying mathematics is detailed as follows:

(i) The integral between two $\Gamma^{(q)}$ and $\Gamma^{(r)}$ species satisfies $\langle \Gamma^{(q)} \,|\, \Gamma^{(r)} \rangle = N_G \delta_{qr}$, where N_G is the number of different symmetry operations forming the G site group. In other words, wave functions belonging to different species are orthogonal.

(ii) If a general (reducible) representation Γ is a sum of several species, namely, $\Gamma = \sum_s \oplus \Gamma^{(s)}$, then $\langle \Gamma^{(q)} \,|\, \Gamma \rangle = \sum_s \langle \Gamma^{(q)} \,|\, \Gamma^{(s)} \rangle$.

(iii) Multiplication between species, written $\Gamma^{(q)} \otimes \Gamma^{(r)}$, follows a special algebra:

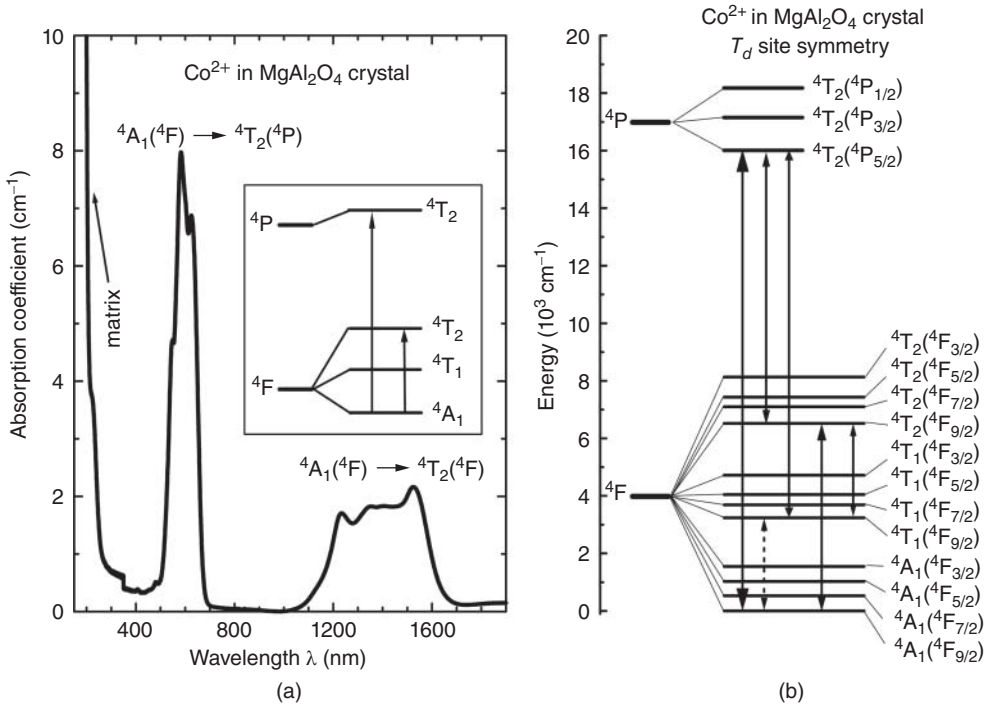

Figure 2.26 Absorption curve and electronic levels scheme (deduced from spectral data) of a Co^{2+} cation residing in a T_d site.

(a) General rules

$$\begin{cases} A \otimes A = A;\ A \otimes B = B;\ A \otimes E = E; \\ A \otimes T = T;\ A \otimes E_1 = E_1;\ A \otimes E_2 = E_2; \\ B \otimes B = A;\ B \otimes E_1 = E_2;\ B \otimes E_2 = E_1; \\ g \otimes g = g;\ g \otimes u = u;\ u \otimes u = g; \\ \text{`} \otimes \text{`='};\ \text{`} \otimes \text{`='};\ \text{`}\otimes\text{'} = \text{'} \end{cases} \tag{2.30}$$

(b) Subscripts for A or B

$$1 \otimes 1 = 1; \quad 1 \otimes 2 = 2; \quad 2 \otimes 2 = 1 \tag{2.31}$$

except for the $D_2 \equiv V$ and $D_{2h} \equiv V_h$ groups, for which $1 \otimes 2 = 3$; $1 \otimes 3 = 2$; $2 \otimes 3 = 1$.

(c) Doubly degenerate species
For the C_3, C_{3h}, C_{3v}, D_3, D_{3h}, D_{3d}, C_6, C_{6h}, C_{6v}, D_6, D_{6h}, S_6, O, O_h, T, T_d, and T_h groups:

$$\begin{cases} E_1 \otimes E_1 = E_2 \otimes E_2 = A_1 \oplus A_2 \oplus E_2; \\ E_1 \otimes E_2 = B_1 \oplus B_2 \oplus E_1 \end{cases} \tag{2.32}$$

For the C_4, C_{4v}, C_{4h}, D_{2d}, D_4, D_{4h}, and S_4 groups:

$$E \otimes E = E_2 \otimes E_2 = A_1 \oplus A_2 \oplus B_1 \oplus B_2 \tag{2.33}$$

For groups appearing in the two above lists that contain A, B, or E species with no attached subscript, A replaces A_1 and/or A_2, and similarly for the B's and E's.

(d) Triply degenerate species
For the T_d, O, and O_h groups:

$$\begin{cases} E \otimes T_1 = E \otimes T_2 = T_1 \oplus T_2; \\ T_1 \otimes T_1 = T_2 \otimes T_2 = A_1 \oplus E \oplus T_1 \oplus T_2; \\ T_1 \otimes T_2 = A_2 \oplus E \oplus T_1 \oplus T_2 \end{cases} \tag{2.34}$$

For the T and T_h groups: the "1" and "2" subscripts deleted in every A or T species.

Symmetry-wise, quantum operation on a wavefunction species is equivalent to *multiplication* between their species. Thus, if the $\boldsymbol{O}$ operator species multiplication with the species belonging to the initial state ψ_i contains the final state species ψ_f as an addend, the $\langle \psi_f | \boldsymbol{O} \psi_i \rangle$ integral is non-zero, and the transition is allowed. If, on the other hand, the multiplication does not contain the final state species as a component, the $\langle \psi_f | \boldsymbol{O} \psi_i \rangle$ integral vanishes, and the transition is forbidden.

The species representing the electric dipole transition operator $\boldsymbol{O} \equiv e\boldsymbol{r}$ in each site symmetry may be readily found in the relevant character table; virtually all textbooks on group theory contain such tables for all

relevant point groups. It is the species belonging to the **translation** symmetry operation components, usually appearing in a right column adjacent to the character table. They read T_z; T_x; T_y; T_x,T_y; (T_x,T_y); or (T). The T_z, T_x, and T_y symbols belong to light polarized in the z, x, or y orientations, respectively. T_x, T_y belongs to light polarized anywhere in the (x, y) plane yet exhibits different responses for the x and y orientations. (T_x, T_y) belongs to light polarized anywhere in the (x, y) plane, with identical responses for any orientation. (T) belongs to any spatial light polarization, with identical response.

As a practical example, Eq. (2.35) provides the character table of the T_d point group in a format used in many books and publications. The topline symbols provide the group symmetry operations, classified by similarity (**similarity classes**). The first column enlists the species. The numbers in-line with each species specifies the **character** belonging to each similarity class; they are the traces (sum of diagonal values) of the matrices forming the mathematical representation of each species. The last two columns point out the species belonging to different operators: **T**, **R**, and $\boldsymbol{\alpha}$, for the electric dipole, magnetic dipole, and electric quadrupole ones, respectively. For our particular example of $Co^{2+}:MgAl_2O_4$ (Figure 2.26), the species belonging to the electric dipole transition operator is T_2. Using the species multiplication algebra, one gets $T_2 \otimes T_1 = A_2 \oplus E \oplus T_1 \oplus T_2$, which contains T_1 and T_2 as addends, but not A_1. Hence, for example, $A_1 \leftrightarrow T_1$ transitions are electric dipole forbidden. On the other hand, $T_2 \otimes T_2 = A_1 \oplus E \oplus T_1 \oplus T_2$ does contain A_1 as an addend. Hence, $A_1 \leftrightarrow T_2$ transitions are electric dipole allowed! Such determined selection rules were used to indicate the allowed and forbidden transitions in the energy level scheme of Figure 2.19. It should be emphasized that these group-theoretical calculations provide only "yes" or "no" answers, namely, "allowed" or "forbidden," respectively; calculation of the actual oscillator strength requires to actually work out the $\langle \psi_f | \boldsymbol{O} \psi_i \rangle$ integral.

T_d	E	$8C_3$	$3C_2$	$6S_4$	$6\sigma_d$		
A_1	1	1	1	1	1		$\alpha_{xx}+\alpha_{yy}+\alpha_{zz}$
A_2	1	1	1	−1	−1		
E	2	−1	2	0	0		$(\alpha_{xx}+\alpha_{yy}-2\alpha_{zz};\sqrt{3}\alpha_{xx}-\sqrt{3}\alpha_{yy})$
T_1	3	0	−1	1	−1	(R)	
T_2	3	0	−1	−1	1	(T)	$(\alpha^z_{xy};\alpha^y_{xz};\alpha^x_{yz})$

(2.35)

In case of a forbidden electric dipole transition, magnetic dipole or electric quadrupole transitions may be considered. The magnetic dipole transition operator relates to the species belonging to the (R) components in the character table; the electric quadrupole transitions operator relates to the species belonging to the (α) tensor components. One may thus similarly determine both magnetic and electric quadrupole allowed and/or forbidden transitions. A further effect that provides some positive probability to forbidden transitions is the lattice vibrations of the host matrix. Normal unit cell (ligand) vibrations must belong to one or more species of the site symmetry. All vibrations except for the "totally symmetric" one, A_1 in the case of the T_d site group (Eq. (2.34)), actually distort the site shape, hence its symmetry. Thus, forbidden electronic states transitions become slightly allowed. This particular effect increases with temperature. Still, the above exceptions to the primary selection rules are extremely weak and may be safely ignored for most practical purposes. Other effects of lattice vibrations are discussed in item {5}.

{4} The fourth crystal field effect is a shifting and crossing among states due to the different influence that the crystal field has on different Terms, and to different "field strengths" in different host materials. The shift depends on a product of two physical quantities: a **D** quantity, which depends on the site potential exerted on the embedded ion, and a **q** quantity, which is a property of the original, undisturbed state of the atom or ion. The product **Dq** has energy units and is called **splitting index**. The actual splitting is different for different states. Tanabe and Sugano [S70, T9] have calculated the splitting characteristics of a large number of rare-earth and transition metal ions as functions of the **Dq** splitting index. Their results are known as **Tanabe–Sugano diagrams**.

Figure 2.27 shows as an example, a Tanabe–Sugano diagram for the triply ionized vanadium ion V^{3+} residing in a cubic O_h symmetry site. This ion belongs to the $3d^2$ configuration. The diagram shows the energy differences between the split ion states and the ground $^3T_{1u}$ state, in Racah's ***B*** Constant units as functions of the **Dq**/***B*** ratio. The latter quantity is called **crystal field perturbation**. The Racah ***B*** Constant for this particular ion is $\boldsymbol{B} = 862\,\mathrm{cm}^{-1}$ (Table 2.4). Level crossings upon increase of crystal field perturbation are clearly apparent. Not shown is the further, smaller splitting of each state by the spin–orbit coupling. The vanadium ion V^{3+} spin–orbit coupling constant for the ^3F free-space

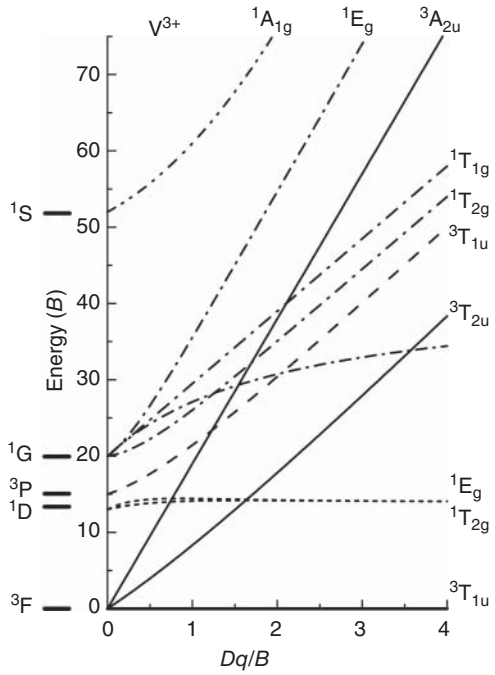

Figure 2.27 A Tanabe–Sugano diagram providing the energy separations between each split state of the triply ionized vanadium ion V^{3+} in an O_h cubic site symmetry and the $^3T_{1u}$ ground state, as functions of the crystal field perturbation $\mathbf{Dq}/\boldsymbol{B}$. The Racah $\boldsymbol{B}$ Constant for this ion is $\boldsymbol{B} = 862\,\mathrm{cm}^{-1}$. Note: the species of the lower split energy of ^1G is $^1A_{1g}$; verify using Table 2.6.

multiplets is approximately $\xi_{SL} \cong 60\,\mathrm{cm}^{-1}$, but is smaller, and different, in different host materials.

For some ions, the ligand field perturbation raises the free-ion ground-state energy while lowering some free-ion higher-state energies. Resulted crossing transforms the higher state to become the ground-state of the site-residing ion. This effect on the higher state is addressed as **ligand field stabilization**.

{5} The fifth effect of the crystalline environment on the dopant atom or ion relates to its interaction with lattice vibrations. Vibrations exist even at the absolute zero temperature limit due to a quantum effect known as **zero-point fluctuations**. The interaction causes broadening of each state, partially due to the crystal acoustic vibrations, and splitting due to optical mode vibrations. Broadening is thus partially temperature dependent, of the order of $k_B T$, where $k_B = 1.3806 \times 10^{-16}$ erg/K is the Boltzmann constant and T is the absolute temperature. At room temperature, it amounts to about $200\,\mathrm{cm}^{-1}$. Optical mode energies typically range between about $100\,\mathrm{cm}^{-1}$ in soft crystals and $1200\,\mathrm{cm}^{-1}$ in hard ones.

For description of optical vibrations, it is useful to imagine the natural atomic basis attached to each lattice point as a complex (or "molecule") comprising the ion-plus-ligand, embedded in the ceramic matrix. Its quasi-isolated motions within the matrix classify as acoustic, vibrational, and librational. Lattice acoustic branches are descendents of the free "molecule" translational motions. Librational motions are descendents of the free "molecule" rotational motions; they stem from a return force moment exerted by the surrounding matrix, which increases proportionately to the "molecular" rotation angle. Vibrational and librational motions are classified as **internal modes** (in free space, only vibrational motions are considered "internal"). Like electronic states, their energy exhibits a quantized spectrum, given approximately by $E_\mathrm{v} = (1/2 + \mathrm{v})\hbar\omega$ for vibrational v quantum numbers $\mathrm{v} = 1, 2, 3, \cdots$, where ω is the mode angular frequency. The $1/2$ addend preceding the v quantum number, expresses the zero-point fluctuation effect.

There is a total of $3N_c - 3$ internal modes for an atomic basis containing N_c atoms/ions. Thus, there are $3N_c - 3$ sets of v numbers. Practically, their frequencies span the entire region, from lowest belonging to the librational motions, to the highest vibrational one, addressed as **cutoff frequency**. The normal coordinate belonging to the highest frequency is termed **configuration coordinate**. Its potential is termed **configuration potential**. For energy scheme and potential graphical presentation, the states are presented in an ascending energy order. Configuration vibrational states are plotted as horizontal lines ending at the classical mechanical oscillator motion edges. Shorter horizontal lines, and accordingly smaller distances, describe lower frequency vibrational modes. To avoid overcrowding, usually only two or three modes are plotted; a schematic example is provided in Figure 2.28. Other energies are listed in tables (if required). Transitions between internal vibrational modes within each electronic state are subject to the $\boldsymbol{\Delta}\mathrm{v}^{(r)} = 0, \pm 1$; $\boldsymbol{\Delta}\mathrm{v}^{(s)} = \pm 1$ selection rule for two different "r" and "s" modes. They are, however, of no direct interest to us, as they belong to the extremely FIR and microwave regions. The electronic transitions spectra of our present interest (visible region and vicinity) are primarily a result of transitions between electronic states. However, such transitions also include transitions between the ligand's internal vibrational modes. In the above selection rules, domination of transitions within each electronic state is no more operative, namely, all vibrational v quantum number changes are allowed for all modes. An absorption spectrum by transitions to a single vibrational state of a higher electronic state is termed v progression. Absorption spectrum due to excitation from a single lower electronic vibrational state to different higher electronic vibrational states is termed v' progression.

Figure 2.29 shows schematically various possible v and v' progressions involving a single vibrational mode for

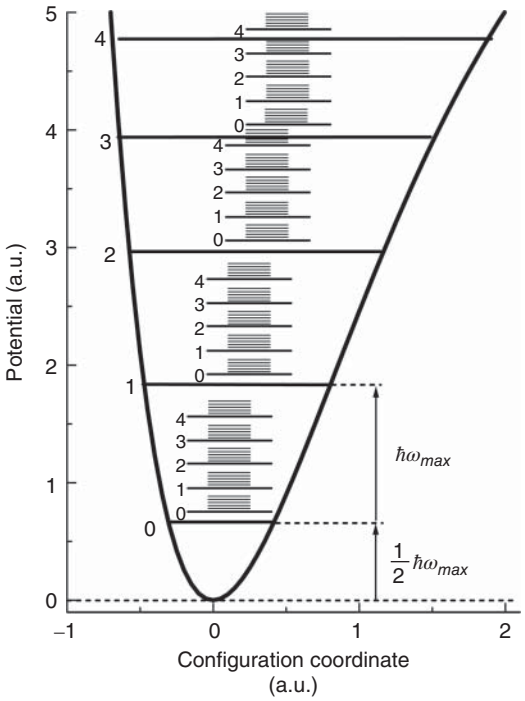

Figure 2.28 Illustrated schematic scheme of the vibrational energy in a multi-atomic ligand, which relates to the configuration potential. To prevent overcrowding, only three modes are presented, belonging to the three highest frequencies. Similar schemes belong to each electronic state.

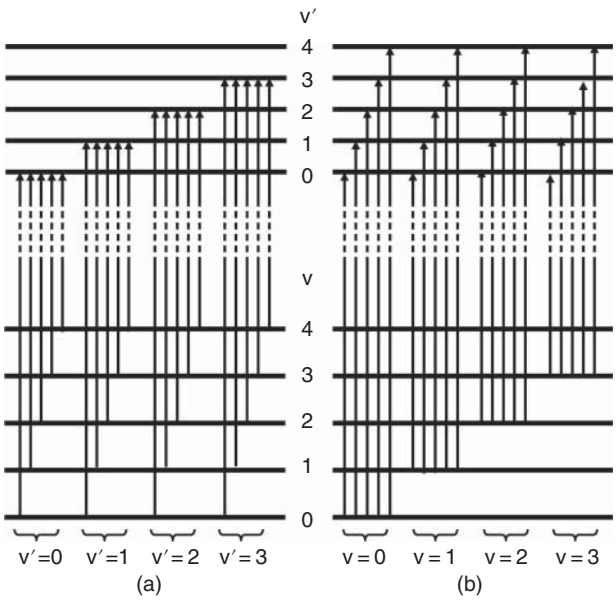

Figure 2.29 Energy scheme of vibrational levels belonging to two different electronic states; the scheme demonstrates different absorption progressions: (b) v-state progressions (a) v′-state progressions. Only five vibrational states are presented per each electronic state.

each electronic state. Symmetrically opposite progressions are seen in emission spectra. The optical absorption and emission spectra are temperature dependent, due to the vibrational state thermal occupation statistics. Quasi-thermal equilibrium establishes very quickly among the vibrational states of both lower and upper electronic states. The most prominent observed progressions are $v = 0 \rightarrow v'$ in absorption and $v' = 0 \rightarrow v$ in emission. Experimental fluorescence spectra thus exhibit longer wavelengths (smaller photon energies) compared to absorption between the same two electronic states, an effect known as **Stokes shift**. A different mechanism of a Stokes shift occurs even between the $v = 0 \rightarrow v' = 0$ and $v' = 0 \rightarrow v = 0$ transitions. It involves the ligand relaxation to a "softer" configuration potential, which takes place at the higher excited state *after* occurrence of an electronic absorption transition.

Oscillator strengths of different transition lines, even within each progression, however, are experimentally not identical. This effect interpretation requires appreciation of the time period differences between electronic and vibrational motions. Time periods of electronic state oscillation are of the order of femtoseconds (10^{-15} seconds), and the same is the order of time during which a transition between electronic states occurs. On the other hand, time periods of vibrational and librational motions are of the order of picoseconds (10^{-12} seconds) or longer. Thus, in the extremely short time elapsed by occurrence of an electronic transition, the positions of the ligand-forming atoms do not exhibit any significant change. In other words, the "molecular" system finds itself in the same constituent atomic and ionic position arrangement in both initial and final electronic states. This statement is called the **Franck–Condon principle**.

Figure 2.30 shows the squared ion + ligand vibrational wave functions for two different electronic states of the central ion. The lower and upper configuration potentials exhibit different equilibrium coordinate positions (different minima). The vibrational energy belonging to the upper electronic state is also smaller than the lower one. Both effects are exaggerated in the figure, to emphasize the argument. The squared wave functions describe the probability density for time spending around the particular position. It is apparent that the probability maxima do not fully overlap. Thus when electronic transitions occur, some will be more likely than others, hence exhibiting different oscillator strengths.

In optical absorption and emission measurements, mostly largest frequency progression structure may be apparent. Finer structure due to lower-frequency vibrational modes appears as broadening of the cutoff frequency progression. Only at extremely low temperatures may some of the fine vibrational structure become apparent.

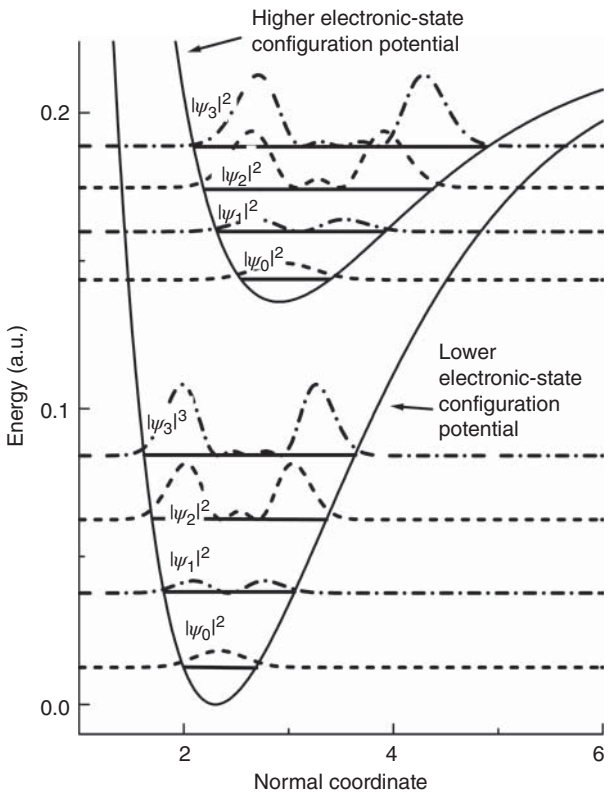

Figure 2.30 Squared vibrational wave functions describing the normal coordinate probability density of a single vibrational mode at each electronic state. Cases symmetric relative to the vibrational center are plotted with dashed lines, while anti-symmetric cases with dash-dotted lines. The vibrational center shift between the two electronic states is exaggerated.

2.3.5.2.1.1.2 Electronic Structure of Rare-Earth Metal Cations (Z > 30) in a Crystalline Site: Crystal Field Approach

Our previous discussion of cation electronic structure provides a very good account and understanding of measured optical spectra for transition metal ions, all belonging to atomic numbers satisfying $Z < 30$. It however requires adjustment for rare-earth ions, all belonging to the $Z > 30$ region. Since the spin–orbit interaction increases with atomic number Z, this effect may no longer be regarded as perturbation to the crystal field splitting. A revised approach is needed, and new spectral effects are seen.

{1} The total spin quantum number S loses its stance as a "good quantum number." Violations of the $\mathbf{\Delta}S = 0$ selection rule for dipole transitions often appear, although the related transitions are relatively faint.

{2} The total angular momentum J strengthens its stance as "the best angular momentum quantum number." In many cases, the spin–orbit coupling splitting is considerably larger than the crystal field one. Analysis of the final states' symmetry species depends on whether J is an integer or a half-odd number. Analysis may still be performed within the Russell–Saunders approach. In its extreme, however, the electronic states should be calculated in a scheme in which each independent electron spin $\boldsymbol{s}_i$ and its orbital angular momentum $\boldsymbol{\ell}_i$ are coupled to a vector sum $\boldsymbol{j}_i$. Then the $\boldsymbol{j}_i$s are coupled to a vector sum over all q participating electrons, namely, $\boldsymbol{J} = \sum_{i=1}^{q} \boldsymbol{J}_i$, of a J quantum number. This approach is known as $\boldsymbol{j}-\boldsymbol{j}$ coupling scheme. We will not address that scheme further.

2.3.5.2.1.1.3 Spin–Orbit > Crystal Field Splitting for an Integer J

The particular case for which J is an integer occurs when an even number of electrons interact to form the state. This is a relatively simple case for analysis, since the total angular momentum J transforms under a symmetry operation "as if it belonged to an L number." In other words, use of Tables 2.6 and 2.7 may be readily taken advantage of.

For demonstration, in Figure 2.31 we provide a Term scheme for the ^{3}H ground Term of the nf^2 electronic configuration (Tables 2.2 and 2.3), when the ion resides in an octahedral, O symmetry site. The spin–orbit coupling splits the Term into a multiplet of $^3H_4$, $^3H_5$, and $^3H_6$ states, in an increasing energy order. Each state then splits by the crystal field according to $^3H_4 \rightarrow {}^3A_1 \oplus {}^3E \oplus {}^3T_1 \oplus {}^3T_2$ (four levels), $^3H_5 \rightarrow {}^3E_1 \oplus {}^3T_1 \oplus {}^3T_1 \oplus {}^3T_2$ (four levels), and $^3H_6 \rightarrow {}^3A_1 \oplus {}^3A_2 \oplus {}^3E \oplus {}^3T_1 \oplus {}^3T_2 \oplus {}^3T_2$ (six levels) per Tables 2.6 and 2.7. The actual energy order among the split states may not necessarily be identical with the plotted ones. Electric dipole selection rules are calculated by performing the multiplication between the species representing the electric dipole transition (T_1 in the O symmetry; consult an O character table in a specialized book) and the species belonging to the initial state. The results per Eq. (2.36) are\textbf{a}

$$\begin{cases} T_1 \otimes T_2 = A_2 \oplus E \oplus T_1 \oplus T_2; \\ T_1 \otimes T_1 = A_1 \oplus E \oplus T_1 \oplus T_2; \\ T_1 \otimes E = T_1 \oplus T_2; \\ T_1 \otimes A_1 = T_1; \\ T_1 \otimes A_2 = T_2 \end{cases} \tag{2.36}$$

Thus, transitions are *allowed* between T_2 and each of A_2, E, T_1, and T_2 states; between T_1 and each of A_1, E, T_1, and T_2 states; between E and each of T_1, and T_2 states; and between A_1 and T_1 states. Transitions are *forbidden* between two A_1 states, between two A_2 states, and between A and E states. Solid arrows in Figure 2.31 show the allowed transitions from the initial lower multiplet states to the final higher ones.

2.3.5.2.1.1.4 Spin–Orbit > Crystal Field Splitting for a Half-Odd J

The particular case for which J is half-odd occurs when an odd number of electrons interact to form the state. For best analysis of the states' symmetry features, their Terms

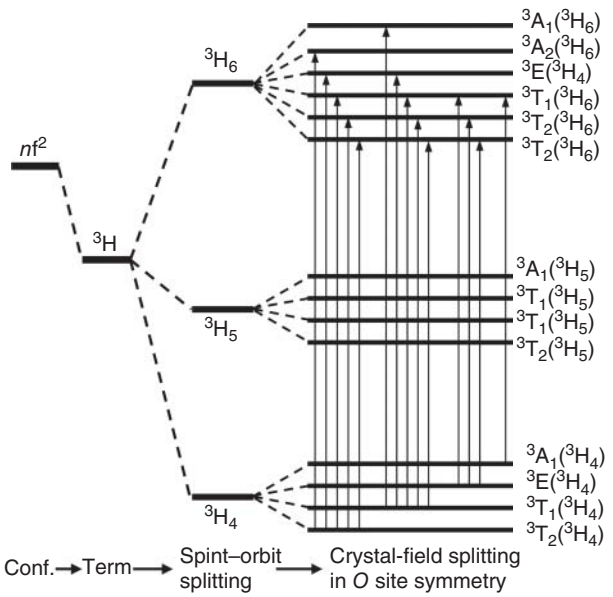

Figure 2.31 Correlation map for the ^3H ground Term of an nf^2 configuration for the situation that the spin/orbital coupling is stronger than the crystal field (ion in an *O* symmetry site).

fourfold degenerate spinor species (when occurring) is symbolized as $\overline{G}$.

As an illustrative and useful example, Eq. (2.37) shows the double group character table related to the D_2 symmetry group, symbolized as $\overline{D}_2$. The triply ionized neodymium cation Nd^{3+} residing in the $Y_3Al_5O_{12}$ single crystal (commonly abbreviated as YAG, acronym for "yttrium aluminum garnet") occupies a site of such symmetry (the Wyckoff *c*-site of the crystallographic O_h^{10} space group [H6]).

Figure 2.32 shows experimentally determined absorption state scheme of that ion. Analysis of the Nd^{3+} situation per Table 2.3 (electronics level scheme in Figure 2.32) indicates that the ground state belongs to the ^4I Term; the closest above is the ^4F Term. By spin–orbit coupling, and since the *f* subshell is less than half-filled, the ^4I Term splits into $^4I_{9/2}$, $^4I_{11/2}$, $^4I_{13/2}$, and $^4I_{15/2}$ states, in an increasing energy order. Note that all resultant *J* values are half-odd; their group theoretical representation is written as $\mathbf{D}^J$. Each of the latter then exhibits further crystal field splitting. In the particular present case of the $\overline{D}_2$ symmetry, only a single two-valued species exists – the double-valued, doubly degenerate $\overline{E}$ (Eq. (2.37). Thus, all split states are $\overline{E}$ species.

$\overline{D}_2$	E	$\hat{E}$	$C_2(z), \hat{C}_2(z)$	$C_2'(y), \hat{C}_2'(y)$	$C_2''(x), \hat{C}_2''(x)$	
A	1	1	1	1	1	
B_2	1	1	−1	1	−1	$T_y; R_y$
B_1	1	1	1	−1	−1	$T_z; R_z$
B_3	1	1	−1	−1	1	$T_x; R_x$
$\overline{E}$	2	−2	0	0	0	

(2.37)

and group theoretical representations should be done using the **double group** species. The underlying concept in formation of a double group is the integration of the angular symmetry of **spinor** wave functions into the relevant ordinary symmetry point group. When viewed in the lab coordinate frame, spinor wave functions exhibit a phase inversion upon a 2π axial rotation; they return to the original phase upon an additional 2π rotation. Accordingly, each ordinary point group is added with new operations, related to the original ones as follows: per each α-angular symmetry rotation, an $\alpha + 2\pi$ symmetry rotation is added. The number of symmetry operations thus doubles, generating *several additional* similarity classes, hence the *same additional* number of irreducible representations, called **spinor species**. They are often also addressed as **double-valued** representations. The new group is symbolized by an added top bar (—). New symmetry operations are symbolized with an added top circumflex (^). The spinor species are also symbolized with an added top bar (—). Particularly, in Mulliken's notation, the entirely new,

The $^4I_{9/2}$ state is 10-fold degenerate; thus $^4I_{9/2} \rightarrow 5\overline{E}$. Indeed 5 states have been experimentally resolved. The $^4I_{11/2}$ state is 12-fold degenerate; thus $^4I_{11/2} \rightarrow 6\overline{E}$. Indeed 6 absorption lines have been experimentally observed. The $^4I_{13/2}$ state is 14-fold degenerate; thus, $^4I_{13/2} \rightarrow 7\overline{E}$. However, only six absorption lines have been experimentally resolved. The $^4I_{15/2}$ state is 16-fold degenerate; thus $^4I_{15/2} \rightarrow 8\overline{E}$. However, only seven absorption lines have been experimentally resolved.

As to the ^4F Term, by spin–orbit coupling, it splits into $^4F_{1/2}$, $^4F_{3/2}$, $^4F_{5/2}$, and $^4F_{7/2}$, in an increasing energy order. Only $^4F_{3/2}$ and $^4F_{5/2}$ were reliably identified by experiment. The $^4F_{3/2}$ state is fourfold degenerate; therefore $^4F_{3/2} \rightarrow 2\overline{E}$. Indeed two absorption lines have been experimentally observed.

Analysis of a general case involves a more complicated two-step group theoretical mathematics. In the first step, the candidate's species representation is calculated in the high-symmetry special orthogonal full rotation double group $\overline{SO}[3]$ for the operations belonging to the end double group. In the second, the representation is

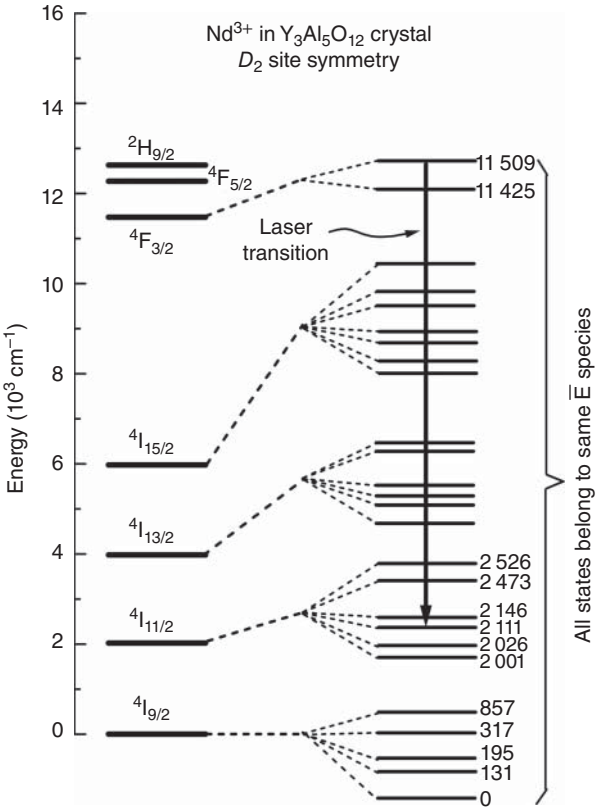

Figure 2.32 Energy scheme of Nd^{3+} ions of $4f^3$ configuration residing in the *c*-site of the $Y_3Al_5O_{12}$ crystal of D_2 symmetry. Numbers adjacent to final split states indicate their energy above the ground state in cm^{-1} units. Transition responsible for the 1064 nm lasing of the Nd:$Y_3Al_5O_{12}$ (Nd:YAG) laser is indicated by a solid arrow. Transitions between shown states are all electric dipole allowed. For details, see text.

reduced to its components. As an example, we demonstrate the mathematical process for the $^4I_{9/2}$ state of Nd^{3+}. The characters $\chi^{(J)}$ for rotation by an angle α, belonging to a half-odd J, are given by

$$\chi^{(J)}(\alpha) = \frac{\sin(J + 1/2)\alpha}{\sin 1/2\alpha}; \quad \chi^{(J)}(\hat{\alpha}) = \chi^{(J)}(\alpha + 2\pi) \tag{2.38}$$

Performing the first step calculations for the $\overline{D}_2$ group yields equation (2.39):

$\overline{SO}[3]$	E $\alpha = 0$	$\hat{E}$ $\hat{\alpha} = 2\pi$	$C_2(z)$ $\alpha = \pi$	$\hat{C}_2$ $\hat{\alpha} = 3\pi$	$C_2'(y)$ $\alpha = \pi$	$\hat{C}_2'(y)$ $\hat{\alpha} = 3\pi$	$C_2''(x)$ $\alpha = \pi$	$\hat{C}_2''(x)$ $\hat{\alpha} = 3\pi$
$D^{9/2}$	10	−10	0		0		0	
$\overline{D}_2$	E	$\hat{E}$	$C_2(z), \hat{C}_2(z)$		$C_2'(y), \hat{C}_2'(y)$		$C_2''(x), \hat{C}_2''(x)$	
A	1	1	1		1		1	
B_2	1	1	−1		1		−1	
B_1	1	1	1		−1		−1	
B_3	1	1	−1		−1		1	
$\overline{E}$	2	−2	0		0		0	

(2.39)

For performing the second step, namely, reducing the $\mathbf{D}^{9/2}$ representation to its component species, the following general reduction formula is used; the number $n^{(i)}$ of each participating end-group species (i), is given by

$$n^{(i)} = \frac{1}{g} \sum_k N_k \chi_k^{(i)*} \cdot \chi_k \tag{2.40}$$

where g is the total number of the end-group operations, N_k is the number of operations belonging to the k-th similarity class, $\chi_k^{(i)*}$ is the complex conjugate of the character residing in the character table box belonging to the i-th species and k-th class, and χ_k is the k-th class character of the representation targeted for reduction.

Calculations are preferably performed by using a partially emptied character table as template:

$\overline{D}_2$	E	$\widehat{E}$	$C_2(z), \widehat{C}_2(z)$	$C_2'(y), \widehat{C}_2'(y)$	$C_2''(x), \widehat{C}_2''(x)$	$g = 8$
A	$1\times1\times10$	$1\times1\times(-10)$	$2\times1\times0$	$2\times1\times0$	$2\times1\times0$	$\frac{1}{8}\times0=0$
B_2	$1\times1\times10$	$1\times1\times(-10)$	$2\times(-1)\times0$	$2\times1\times0$	$2\times(-1)\times0$	$\frac{1}{8}\times0=0$
B_1	$1\times1\times10$	$1\times1\times(-10)$	$2\times1\times0$	$2\times(-1)\times0$	$2\times(-1)\times0$	$\frac{1}{8}\times0=0$
B_3	$1\times1\times10$	$1\times1\times(-10)$	$2\times(-1)\times0$	$2\times(-1)\times0$	$2\times1\times0$	$\frac{1}{8}\times0=0$
$\overline{E}$	$1\times2\times10$	$1\times(-2)\times(-10)$	$2\times0\times0$	$2\times0\times0$	$2\times0\times0$	$\frac{1}{8}\times40=5$

(2.41)

Group theoretically, the result is written as $\mathbf{D}^{9/2} = 0{\cdot}\mathrm{A} \oplus 0{\cdot}\mathrm{B}_2 \oplus 0{\cdot}\mathrm{B}_1 \oplus 0{\cdot}\mathrm{B}_3 \oplus 5\overline{\mathrm{E}} = 5\overline{\mathrm{E}}$, or in spectroscopic language ${}^4\mathrm{I}_{9/2} \rightarrow 5\overline{\mathrm{E}}$, as earlier suggested in relation to Figure 2.31. For further insight, the reader is advised that the above group theoretical methods apply equally to all reduction and correlation processes, for both ordinary and double groups.

The species belonging to electric dipole operator components are B_1, B_2, and B_3. By direct multiplication of their character table lines with that of $\overline{\mathrm{E}}$, it may be verified that $\mathrm{B}_1 \otimes \overline{\mathrm{E}} = \mathrm{B}_2 \otimes \overline{\mathrm{E}} = \mathrm{B}_3 \otimes \overline{\mathrm{E}} = \overline{\mathrm{E}}$. Then all transitions between $\overline{\mathrm{E}}$ states are electric dipole allowed for all electromagnetic radiation polarizations.

2.3.5.2.1.1.5 Spin–orbit ≈ Crystal Field Splitting

Similarity between spin–orbit and crystal field splitting often brings about energy level crossings among states belonging to different species. In other words, energies of two different states may become identical, or very closely so. Such case is called **accidental degeneracy**, in contrast to the **fundamental degeneracy**, occurring for states belonging to the same species. In most cases, noticeable energy splitting appears between two crossing states due to some perturbation interaction. There are various sources of perturbation, especially ligand distortion by crystalline defects, and non-totally symmetric lattice vibrations. The interaction energy is given by the integral $\langle \psi_1 \,|\, V' \psi_2 \rangle$, where ψ_1 and ψ_2 are the wave functions of the two crossing states and V' is the perturbation potential.

This effect diminishes if the perturbation potential belongs to a totally symmetric species. It may not diminish if it belongs to a different species (or a sum of species), such that its multiplication with ψ_2's species contains the ψ_1's species as a component (see details of species multiplication algebra in Eqs. (2.30)–(2.35). The split states belong to the symmetric and anti-symmetric linear combinations $\frac{1}{\sqrt{2}}(\psi_1 + \psi_1)$ and $\frac{1}{\sqrt{2}}(\psi_1 - \psi_1)$, respectively. The split states lose their strict species identity, an effect referred to as **states mixing**. Splitting of accidentally degenerate states is quite noticeable in optical spectroscopy.

Due to the above effects, interpretation of measured optical absorption and emission spectra of rare-earth ions (atomic number $Z > 30$) are never straightforward, and often questionable, especially in cases of energetically close bands.

2.3.5.2.1.1.6 Molecular Orbital Approach

A valid criticism of the crystal field analysis described throughout the above section is that it fails to consider the possibility of any partial covalent bonding between the central cation and its ligand-forming vicinity. This is a rough approximation, which prevents the method to deal with some important spectroscopic issues. For example, there is a class of real complex electronic states in which the ligand electrons have a strong participation. Excitation, from the ground state to such states, is a process implying charge transfer, and the resulting spectral features are called "charge transfer bands"; treatment of such bands requires the use of molecular orbital (MO) based theories. The charge transfer bands are characterized by much larger oscillator strengths ($\boldsymbol{f}$~0.1) than in the $\mathrm{d} \rightarrow \mathrm{d}$ bands. It is the result of the fact that while the ground state includes mostly d-orbitals, the excited ones exhibit admixtures of the non-d ligand orbitals. Thus, transitions involving charge transfer bands are more intense than the $\mathrm{d} \rightarrow \mathrm{d}$ transition bands. The complexes of our interest are mostly located in the NUV advancing sometimes towards the visible (VIS). Another family of bands that may be considered as charge transfer type are those where the ground and excited states correspond to different principal quantum numbers. Figure 2.33 [P14] displays the charge transfer bands generated for example by iron Fe^{3+} cation in a few glass hosts. While less intense, the same bands are located in the same spectral range in oxide ceramics.

There are also finer details of some **electron spin resonance** (ESR) signals (also addressed as **electron paramagnetic resonance**, EPR) that fail to be accounted for within the crystal field approach. For such aspects, the alternative, termed **molecular orbital** (MO) approach, initiated by Mulliken and Hund [O3], appears better suited. In its zero-order approximation, this model considers the central cation plus ligand as an isolated molecule. A serious practical drawback is the fact that

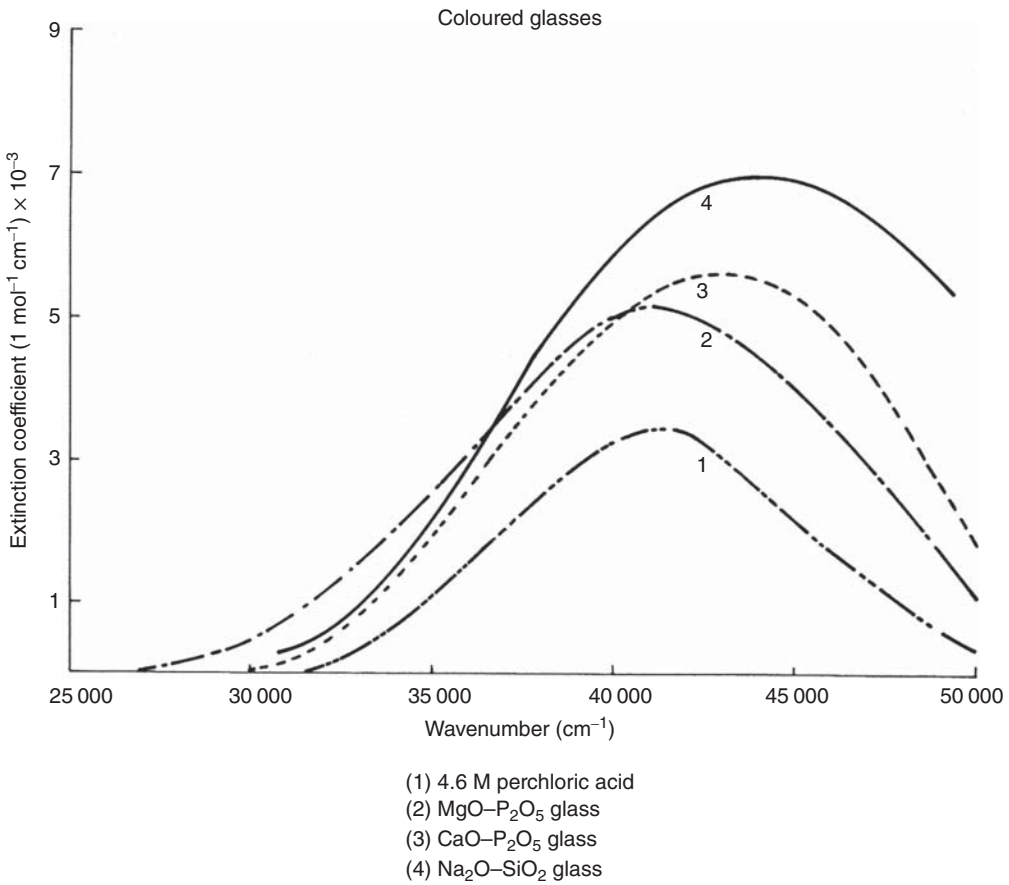

Figure 2.33 Absorption spectrum of Fe^{3+} in disordered hosts (an aqueous solution and various glasses). Source: Paul 1982 [P14]. Reproduced with permission from Springer.

calculation of molecular orbital based states and energies is more difficult to perform.

For the purpose of our present book, the crystal field approach is satisfactory. The interested reader is referred to the numerous books destined to in the basics of electronic spectra theory [B8, B9, H24] and the vast number of specialized publications.

2.3.5.2.1.1.7 Optical Transition Oscillator Strengths, Cross Sections, and Radiative and Non-radiative Lifetimes

Optical absorption or emission spectra allow estimation of the transition oscillator strength between the states involved. Measurement of transmitted light intensity through a plate of thickness L is used for estimating the absorption coefficient $\alpha(\nu) = -(1/L)\ln[I(\nu)/I_0(\nu)]$, where $I(\nu)$ and $I_0(\nu)$ are the transmitted and incident light intensities, respectively, at frequency ν. The oscillator strength $\boldsymbol{f}$ of transition between two isolated, yet broadened states, is given by

$$\boldsymbol{f} = \frac{3mc}{\pi ne^2 N}\int_0^\infty \alpha(\nu)\,d\nu = \frac{3mc}{\pi ne^2}\int_0^\infty \sigma(\nu)\,d\nu \tag{2.42}$$

where m is the electronic mass, $c = 2.998\times10^{10}$ cm/s is the speed of light constant, e is the electronic charge, n is the host matrix refractive index, and N is the dopant ion concentration inside the matrix. The ratio $\sigma(\nu) \equiv \alpha(\nu)/N$ is the ion absorption cross section (of area units). Oscillator strengths never exceed a unity value and almost always $\boldsymbol{f} \ll 1$. Eq. (2.42) expresses the distribution of the transition oscillator strength across the absorption band, resulting from broadening by the lattice vibrations.

In a simplified model of a two-state electronic system, the zero-temperature *radiative* decay rate of the higher (excited; upper) energy state to the lower energy state, is expressed as

$$\tau_{rad}^{-1}(0) = \frac{8\pi n^2 {\nu_0}^2}{c^2}\int_0^\infty \sigma(\nu)d\nu \tag{2.43}$$

where $\tau_{rad}(0)$ is the zero temperature radiative lifetime and ν_0 is the central radiative transition frequency. The radiative lifetime parameter is of prime importance in laser application of optical transitions; it appears in the denominator of the expression for the electromagnetic

radiation gain function $\gamma(\nu)$, namely,

$$\gamma(\nu) = \frac{(N_2 - N_1)c^2}{8\pi n^2 {\nu_0}^2 \tau_{rad}(0)} g(\nu) \tag{2.44}$$

where N_2 and N_1 are respectively the ion population densities at the upper and lower states involved in the transition and $g(\nu)$ is the fluorescence emission shape function normalized to a unity integral. (*The latter obtains as the fluorescence emission spectrum from the upper to the lower state, initially expressed in any units of intensity per unit frequency, then divided by the integrated intensity function over the transition.*) The $\mathbf{\Delta}N \equiv N_2 - N_1$ difference is the **population inversion**; positive gain in the laser resonance cavity obtains by pumping energy into the system, thus generating a positive population inversion. Lasing results only when the gain at a certain frequency ν exceeds the cavity losses.

The actually measured decay rate $\tau_{eff}^{-1}(0)$ is larger than $\tau_{rad}^{-1}(0)$ due to a competing, non-radiative decay that involves the generation of lattice vibrations (phonon/s emission), rather than a photon emission. A transition energy of our interest $E_g = h\nu_0$ (sometimes addressed as **energy gap**) is considerably larger than any phonon energy $\hbar\omega$ of the host matrix. Therefore, a non-radiative transition is practically a multi-phonon one. The non-radiative decay rate $\tau_{nr}^{-1}(0)$ is proportional to the radiative rate [B71]. The effective decay rate $\tau_{eff}^{-1}(0)$ is then given by

$$\tau_{eff}^{-1}(0) = \tau_{rad}^{-1}(0) + \tau_{nr}^{-1}(0) = \tau_{rad}^{-1}(0)[1 + C_{nr}] \tag{2.45}$$

where C_{nr} is a constant, representing the non-radiative contribution to the effective decay transition rate [S32]. This constant depends on the host matrix properties and the transition energy. For sufficiently low energy gaps (infrared region), it is given by

$$C_{nr} \equiv \frac{\hbar c}{e^2} \frac{N_c - 1}{N_c} \cdot \frac{2\pi^2}{n^3} \cdot \frac{[\overline{M}_{at} c^2]\ \hbar\omega_{co}}{E_g^2} \mathbf{B}(\mathrm{v}) \left(\frac{\hbar\omega_{co}}{D} \right)^{\mathrm{v}-1} \tag{2.46}$$

where N_c is the number of atoms/ions constituting the matrix primitive unit cell (the "natural" atomic basis). $\overline{M}_{at} \equiv M_c/N_c$ is the average atomic mass of the lattice atomic basis, where M_c is the primitive unit cell mass; ω_{co} is the cutoff angular frequency of the matrix vibrations, D is the ligand "dissociation energy" parameter of the configuration potential. $\mathrm{v} \equiv E_g/\hbar\omega_{co}$ is the number of cutoff phonons required for the multi-phonon transition. $\mathbf{B}(\mathrm{v})$ is a v-dependent numerical value, given by

$$\mathbf{B}\,(\mathrm{v}) \equiv \frac{(2^{\mathrm{v}} - 1)^2 \mathrm{v}^{\mathrm{v}-2}}{[\Gamma(\mathrm{v} + 1)]^2} \tag{2.47}$$

Importantly, the v parameter need not necessarily be an integer; practically, the lattice vibrational frequencies establish a quasi-continuum up to cutoff. Then, a non-integral number of cutoff phonons is equivalent to an integral number of a somewhat smaller frequency of available phonons forming resonance with E_g. Being inversely proportional to E_g^2, the non-radiative constant C_{nr} reduces strongly with increased energy gap. By definition, $\hbar\omega_{co} \ll D$, thus C_{nr} also reduces much faster with the $D/\hbar\omega_{co}$ ratio. This ratio is in fact a harmonicity measure of the configuration potential: in a perfectly harmonic potential, the $D/\hbar\omega_{co}$ ratio is infinite, and C_{nr} then diminishes. The involvement of non-radiative processes in the electronic decay is a manifestation of a departure from harmonicity of the matrix vibrations.

In the case of a finite temperature, the effective decay rate increases (the effective lifetime shortens) according to

$$\tau_{eff}^{-1}(T) = \tau_{rad}^{-1}(0) \left\{ \left[1 + \frac{1}{\mathbf{exp}(E_g/k_B T) - 1} \right] + C_{nr} \left[1 + \frac{1}{\mathbf{exp}(\hbar\omega_{co}/k_B T) - 1} \right]^{\mathrm{v}} \right\} \tag{2.48}$$

The $[\mathbf{exp}(E_g/k_B T) - 1]^{-1}$ addend inside the first square brackets provides the thermally enhanced population effect of E_g energy *photons* to the stimulated radiative decay mechanism. The $[1 + (\exp(\hbar\omega_{co}/k_B T) - 1)^{-1}]^{\mathrm{v}}$ factor of C_{nr} provides the thermally enhanced population effect of $\hbar\omega_{co}$ energy *phonons* to the stimulated decay mechanism via non-radiative emission of v phonons. For not too far-infrared energies, say, $E_g \gtrsim 2000\ \mathrm{cm}^{-1}$, and not too high temperatures, say, $T \lesssim 900°\mathrm{K}$, the thermal *photon* population effect is negligibly small. Eq. (2.48) then reduces to

$$\tau_{eff}^{-1}(T) \cong \tau_{rad}^{-1}(0) \times \left\{ 1 + C_{nr} \left[1 + \frac{1}{\mathbf{exp}(\hbar\omega_{co}/k_B T) - 1} \right]^{\mathrm{v}} \right\} \tag{2.49}$$

Eq. (2.49) is a valid approximation for our optical region of interest. As an example, Figure 2.34 shows the measured effective fluorescence decay lifetime of the $\mathrm{T}_2(^4\mathrm{F}) \rightarrow \mathrm{T}_1(^4\mathrm{F})$ transition in doubly ionized cobalt Co^{2+} in a silver chloride–bromide $AgCl_{0.5}Br_{0.5}$ crystal, as a function of absolute temperature. The relevant energy scheme belongs to a T_d site symmetry however with crystal field energy splitting somewhat reduced due to the different host material.

For laser technology purposes, shortening of excited-state lifetime at elevated temperatures involves reduction in population inversion, requiring enhanced energy pumping for maintaining the laser operation. Cooling the amplifying medium to a lower temperature is commonly administered to reduce such effects.

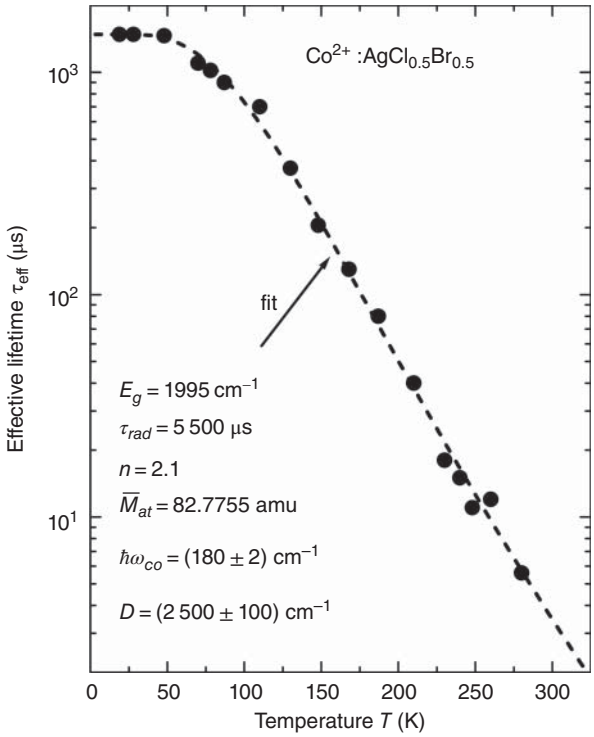

Figure 2.34 Effective fluorescence lifetime of an excited, doubly ionized cobalt, Co^{2+}, in a silver chloride bromide $AgCl_{0.5}Br_{0.5}$ crystal, as a function of the absolute temperature. Full circles are experimental results from Ref. [T32], Figure 2]. Dashed line [S32] is a fit to Eq. (2.49).

2.3.5.2.1.1.8 Electron Spin Resonance (ESR): Fine and Hyperfine Structures

Many transition metal and rare-earth cations acting as dopants in a dielectric ceramic host may exhibit paramagnetic properties on top of the assumed diamagnetic background of their host material. This is due to a non-zero total angular momentum of the guest cations, associated with their orbital and spin magnetic dipole properties. The produced energetic structure is addressed as **fine structure**.

The magnetic moment $\boldsymbol{M}$ of a free-in-space cation relates to its state total angular momentum $\boldsymbol{J}$ by

$$\boldsymbol{M} = -\frac{\mu_B}{\hbar} g_L \boldsymbol{J} \tag{2.50}$$

where $\mu_B \equiv e\,\hbar/2mc$ is the **Bohr magneton** and

$$g_L = \left(1 + \frac{J(J+1) + S(S+1) - L(L+1)}{2J(J+1)}\right) \tag{2.51}$$

is the **Landé factor**, where L, S, and J are the quantum numbers of the orbital, spin, and total state's angular momentums, respectively. The model underlying the above electron Landé factor expression assumed a **gyromagnetic spin factor** $g_e^{(s)} = -2.0024$ and a **gyromagnetic orbital factor** $g_e^{(\ell)} = -1$. The Bohr

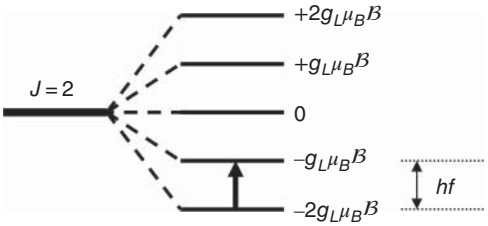

Figure 2.35 Schematic illustration of a $J = 2$ state splitting under a static magnetic induction field $\mathcal{B}$. A solid arrow indicates an allowed absorption transition of f radio frequency radiation at near-zero absolute temperature.

magneton numerical value is $\mu_B = 9.2741 \times 10^{-21}$ erg/G, or in spectroscopic, more useful units, $\mu_B = 4.6686 \times 10^{-5}$ cm^{-1} G^{-1}. Under an external "small" static magnetic induction field $\mathcal{B}$, a $(2J+1)$-fold degenerate state splits into its m_J energy components E_{m_J} according to

$$E_{m_J} = m_J \;\; \mu_B g_L \mathcal{B} \tag{2.52}$$

The $^{2S+1}L_J$ state thus splits into $2J+1$ levels belonging to $m_J = -J,\ -J+1,\ \cdots J-1,\ +J$, with an identical $\boldsymbol{\Delta} = \mu_B g_L \mathcal{B}$ separation between adjacent states. The separation is proportional to the magnetic field strength $\mathcal{B}$. The splitting is known as **Zeeman splitting**.

Selection rules for electromagnetic transitions between two m_J components of the same J state are $\boldsymbol{\Delta} m_J = \pm 1$. Absorption transitions by using electromagnetic radiation of frequency f requires the existence of different populations for different m_J components. The experimentally obtained parameters are the degeneracy and Landé factor values of the states involved. Figure 2.35 shows a schematic splitting of a $J = 2$ state. A solid arrow indicates an allowed absorption transition in the particular case where only the lowest component is occupied under thermal equilibrium conditions. This condition obtains when the system is kept very close to the zero absolute temperature.

When the cation is embedded in a crystalline matrix, there are a number of special issues to be considered, and some expressions to be modified.

{1} *Interaction among the magnetic dipoles*
To minimize effects related to interaction among spatially close magnetic dipoles belonging to the embedded cations, their concentration must be kept sufficiently low. Empirically, a higher limit of 10^{19} cm^{-3} is quite practical for that purpose.

{2} *Crystal vibrations*
Practical laboratory magnetic fields rarely exceed the order of ten thousand gauss, and Landé factors are of the order of unity. Thus, splitting rarely exceeds an order of ~0.5 cm^{-1}. Room temperature spectral broadening of dopant cation states is of the order of

$\sim$200 cm^{-1}; states separation by crystal field splitting is usually of the order of several hundred cm^{-1}. Thus, observation of Zeeman splitting using near-visible absorption and emission spectroscopy would be impractical even at near-zero absolute temperature. On the other hand, utilization of about 10 GHz **radio frequency (RF)**, and a sufficiently low absolute temperature (even below liquid helium temperature of 4.2 K), allows the spectroscopic observation of absorption transitions from lower-lying split m_J states to their adjacent $m_J + 1$ state. The split states involved must then belong to the cation ground state. This type of measurements, which in fact establish a Zeeman splitting studies of the ground-state level, is addressed as either **ESR**, or as **EPR** [L42]. Their temperature dependence, still in the low temperature regime, is also quite informative.

Experimentally, it is more convenient to vary the magnetic field and keep the frequency constant. The radio frequency radiation at frequency f is directed onto the studied sample perpendicularly to the direction of the static magnetic field. The magnetic field strength is increased gradually, and the radiation absorption is simultaneously recorded. Resonance absorption peaks are obtained at a magnetic induction field $\mathcal{B}_p = hf/\mu_B g_L$, where $h = 2\pi\hbar$ is Planck's constant. The absorption peak heights are proportional to the cation concentration inside the matrix. The mostly used work frequencies are of $\sim$10 GHz (called X-band) and $\sim$35 GHz (called Q-band).

{3} *Crystal field site symmetry*

The most apparent crystal field effect on a residing cation is its states splitting, as described in detail in the preceding chapters. This involves also a fundamental change in the angular momentum nature of the state's magnetic properties. In other words, no specific L, S, or J values may be unequivocally assigned to many split states. Accordingly, the $\mathbf{\Delta}m_J = \pm 1$ selection rule, or a reminiscent effective alternative, is no more strictly obeyed. The only invariant property of crystal-field split states is their summed degeneracy. Furthermore, the ground state may not generally be a pure state but may contain admixture of states from the surrounding ions. Accordingly, electrons of the paramagnetic cation may spend some of their time at the surrounding ligand-forming ions. Often, an effective S' quantum number symbol (termed **fictitious spin**) is assigned to the state, to account for its actual degeneracy as $2S' + 1$. For example, a level split in two is assigned an $S' = 1/2$ fictitious spin; a level split in four is assigned an $S' = 3/2$ fictitious spin. Its projection components are granted the simple m symbol.

Figure 2.36 demonstrates the case where a fourfold degenerate crystal-field state undergoes an ESR measurement without strictly obeying the $\mathbf{\Delta}m = \pm 1$ selection rule. The vertical distance as a function of the magnetic field $\mathcal{B}$ provides the energy separation of each m state from the lowest, belonging to $m = -3/2$. Three peak absorption magnetic fields are indicated. The smallest, $\mathcal{B}_1$, belongs to the "fictitious" $(-3/2) \rightarrow (+3/2)$ transition; a larger, $\mathcal{B}_2$, belongs to the $(-3/2) \rightarrow (+1/2)$ fictitious transition; the largest, $\mathcal{B}_3$, belongs to the $(-3/2) \rightarrow (-1/2)$ fictitious transition – the "allowed" one $\mathbf{\Delta}m = 1$. The "forbidden transitions" at $\mathcal{B}_1$ and $\mathcal{B}_2$ often exhibit relatively small absorption peak heights.

In particular cases, results like those presented in Figure 2.37 may be interpreted in terms of crossing between degenerate states. For example, the Cr^{3+} ion belongs to the $3d^3$ configuration (Table 2.4) of a ^4F ground-state Term (Table 2.3). In an octahedral O site symmetry, this Term splits into $A_2 \oplus T_1 \oplus T_2$ at an increasing energy order. Namely, the ground state is A_2. On "ignition" of spin–orbit interaction (assumed small compared to the crystal field one), the state transforms into a fourfold degenerate $\overline{G}$ state under the $\overline{O}$ double group site symmetry. ESR measurements show a *single peak*, related to the $\mathcal{B}_3$ magnetic field of Figure 2.36, including $(-1/2) \rightarrow (+1/2)$ and $(+1/2) \rightarrow (+3/2)$ transitions occurring at the same field when the temperature is larger than zero.

If, on the other hand, the site symmetry is lowered to a uniaxial D_3 one, the $\overline{G}$ state splits according to $\overline{G} \rightarrow \overline{A}_1 \oplus \overline{A}_2 \oplus \overline{E}_2 \equiv \overline{E}_1 \oplus \overline{E}_2$ (calculation for the $\overline{D}_3$ double group symmetry). The "teaming" of the two different $\overline{A}_1$ and $\overline{A}_2$ singlet states into a single, doubly degenerate $\overline{E}_1$ state is because the two are **time-reversal symmetric** and hence belong to the same energy. Mathematically, this physical degeneracy effect expresses itself in the group character table by the characters of the two species being complex conjugates of each other. Such doublets are called **Kramers doublets**.

Under an external magnetic field, both $\overline{E}_1$ and $\overline{E}_2$ split, however, differently: $\overline{E}_1$'s splitting is larger than the $\overline{E}_2$'s. Correspondingly, sometimes alternative symbols are used: $\overline{E}_2 \equiv \overline{E}_{1/2}$ and $\overline{E}_1 \equiv \overline{E}_{3/2}$. (These half-odd subscripts are just labels, emphasizing the species belonging to a "double-valued" representation (spinor species); they do not indicate any specific angular momentum quantity.) An energy scheme would look as shown in Figure 2.37. All marked transitions are allowed, not necessarily conforming to the $\mathbf{\Delta}m_J = \pm 1$ selection rule.

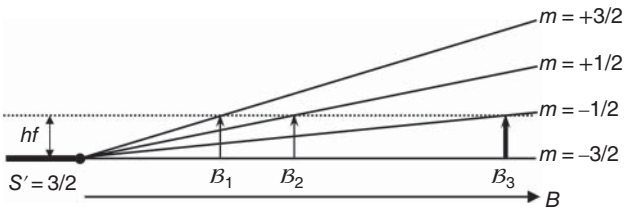

Figure 2.36 Schematic demonstration of possible resonance absorption peaks in an ESR measurement of a fourfold degenerate state, when the $\Delta m_J = \pm 1$ selection rule no more strictly applies.

A somewhat above absolute zero temperature is needed to allow population of the higher-lying initial states. The $\mathbf{B}_p$ resonance positions depend on the initial crystal-field splitting of the $\overline{\mathrm{E}}_1$ and $\overline{\mathrm{E}}_2$ states, and on the Zeeman level splitting strength. In fact, the resonance positions are used as a means for studying the crystal field strength in D_3 symmetry sites of various crystals.

Equations (2.50)–(2.52) and their related, empirically modified expressions may still be very useful. Particularly, Eq. (2.52), often written as $E_m = m\mu_B g_L \mathbf{B}$, is called **spin Hamiltonian**. The Landé factor g_L is considered as a 3×3 tensor, whose principal axes relate to the site symmetry axes. Resonance absorption energies depend on the magnetic field orientation, thus yielding different Landé factors for different field directions. The tensor components are now termed **spectroscopic splitting factors**. Denoting g_x, g_y, and g_z as the spectroscopic splitting factors obtained when the magnetic field was directed along the X, Y, and Z principal axes, the effective g value for an arbitrary magnetic field orientation would be given by

$$g = (\alpha^2 g_x^2 + \beta^2 g_y^2 + \gamma^2 g_z^2)^{1/2} \tag{2.53}$$

where α, β, and γ are the direction cosines of the **B** vector with respect to X, Y, and Z. For example, in the case of the uniaxial D_3 site symmetry (say, in a trigonal crystal), the spectroscopic splitting factor in the threefold axis direction is denoted as $g_\parallel$ and in any perpendicular direction as $g_\perp$.

An often observed peculiarity is that the experimental spectroscopic splitting factors are considerably greater than expected by the effective spin. This is attributed to mixing with higher lying states, which "lend magnetic moment" to the ground state. Theoretical modeling is complicated, but usually provides quite satisfactory account of the experimental results. We will not dwell on this particular aspect in the present book.

{4} *Nuclear magnetic resonance*

While ESR studies relate to the electronic states fine structure, a hyperfine structure also appears, relating partially to the spin and orbital angular momentum magnetic properties of the nucleus and, to a smaller extent, to the nuclear electrical quadrupole moment. We will address only the first effect.

There are a number of basic differences between expressions relating to the electronic and nuclear angular momentums. The **nuclear magneton** (analog of the electronic Bohr magneton) is about 2000 times smaller than the electronic Bohr magneton. It is due to the correspondingly larger rest masses of the nucleons. The expression for the magnetic moment of a nuclear state now involves two types of particles: **protons** of a gyromagnetic spin factor $g_p^{(s)} = +5.5855$ and a gyromagnetic orbital factor $g_p^{(\ell)} = +1$ and **neutrons** of a gyromagnetic spin factor $g_n^{(s)} = -3.8256$ and a gyromagnetic orbital factor $g_n^{(\ell)} = 0$. The **Schmidt factor** g_{Sch}, the nuclear analog of Landé's factor, is then more complex. It exhibits a positive sign if the neutrons contribution dominates (same sign as for electrons) and a negative sign if the protons contribution dominates.

The nuclear total angular momentum is symbolized by the letter I, and it exhibits $2I + 1$ magnetic projection quantum numbers $m_I = I, I-1, \ldots, 0, \ldots, -I$. The nuclear state is already split by an order of approximately $0.1\,\mathrm{cm}^{-1}$ even *before* application of any external magnetic field. Thus, all split states are almost equally populated even at the liquid helium temperature. The splitting is due to a magnetic field of the order of $10^5 - 10^6$ G exerted on the nucleus by the atomic electrons. The external magnetic field

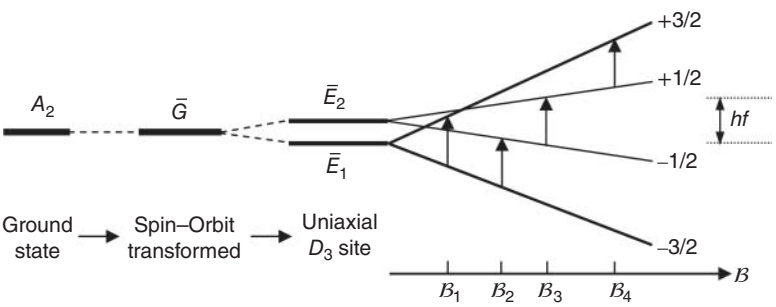

Figure 2.37 Energy levels considering the splitting of the states of a D_3 (uniaxial) site under the action of an external magnetic field.

used for ESR is only of the order of 10^4 G. It thus has only negligible influence on the splitting among the nuclear states. Obviously, it is insufficient to be in resonance with any transition among the m_I components. Thus, effectively, $\mathbf{\Delta}m_I = 0$. Its effect, however, is that the paramagnetic ion population divides into $2I+1$ populations, each belonging to a different m_I.

The interaction between the electronic ground state and the nuclear magnetic moment also affects the electronic state. It expresses itself by affecting the spectroscopic splitting factors (the effective Landé factors) to be slightly different among the different $2I+1$ levels belonging to the different m_I populations. Correspondingly, the spectrum at a fixed radio frequency and variable external magnetic field exhibits $2I+1$ nearly equally spaced lines. They are associated with the case in which the fixed radio frequency quantum hf equals the difference in energy between the electronic levels. This is the electron spin resonance hyperfine structure (**ESR hyperfine structure**).

Figure 2.38 provides an energy scheme illustration of a simple case, where the electronic ground state is a doublet, belonging to $S' = 1/2$, and the nuclear ground state is a quartet, belonging to $I = 3/2$. The nuclear Schmidt factor is taken as negative (protons dominated). Thus the lowest multiplet component belongs to $m_I = 3/2$ and the highest to $m_I = -3/2$. The electronic doublet belonging to each m_I splits in two, linearly with the external magnetic field, yet with slightly differing splitting factors.

In Figure 2.39 we show an idealized schematic hyperfine structure of an electron spin resonance measurement related to the system of Figure 2.38. The figure demonstrates the expected four resonance absorption peaks obtained by the four ion populations related to the different nuclear states. The peak heights increase in the order $m_I = -3/2$, $-1/2$, $+1/2$, and $+3/2$, consistently with the different nuclear state population variation under thermal equilibrium. Notable parameters are the peaks width $\mathbf{\Delta B}$ (full width at half maximum) which are related to the frequency width according to $\mathbf{\Delta}f = (g\mu_B/h)\mathbf{\Delta B}$. This line broadening is the result of the several following effects: *equipment contributions* that are due to noise in the external magnetic field generator and in the absorption power measuring units, *intrinsic heterogeneous contributions* that are due to variations in the ligand dimensions and orientation, and finally *intrinsic homogeneous contributions* that are due to the ligand thermal vibrations, and to

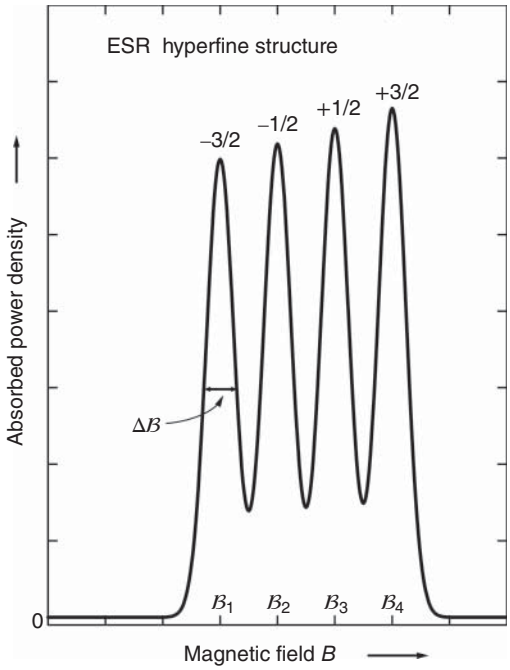

Figure 2.39 Computer-generated spectrum of absorbed radio frequency power density as a function of the external magnetic field, providing an idealized hyperfine structure of an electron spin resonance measurement related to the system of Figure 2.38.

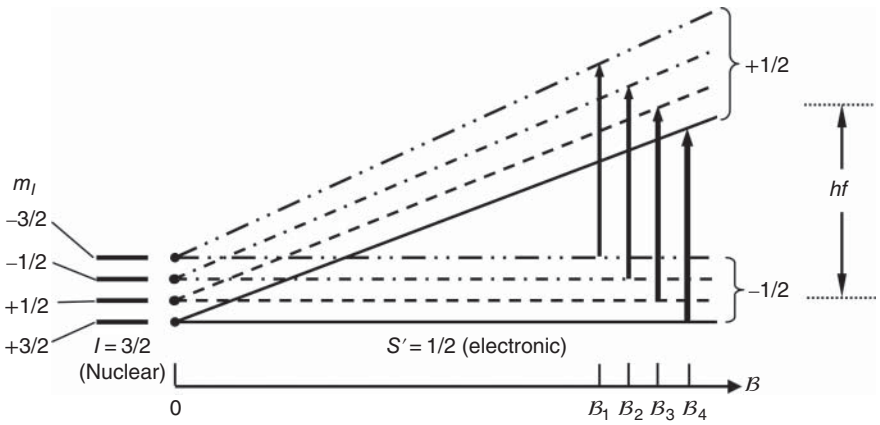

Figure 2.38 Schematic energy level scheme related to an electron spin resonance measurement belonging to a doublet electronic ground state and a quartet nuclear ground state of a negative Schmidt factor. Allowed resonance transitions marked by solid arrows.

radiative and non-radiative transitions between two electronic spin states. The non-radiative transitions are termed **spin–lattice relaxation**. This mechanism is important in understanding of spin-state dynamics, particularly at high magnetic dipole concentrations inside the lattice.

2.3.5.2.2 Absorption Spectra of Transition Metal and Rare-Earth Cations: Examples

The preceding section provided theoretical instruments needed for the interpretation of the absorption spectra produced by transition metal (TM) and rare-earth (RE) dopant cations. A comprehensive description of such spectra for the case of the active ions hosted by transparent ceramics as well as in glasses and single crystals will be provided in a future companion volume to this book. Here only a limited set of spectra will be shown, related to the most used dopants in various applications (Section 5.2.9). Most were recorded during research accomplished by the present authors.

2.3.5.2.2.1 The Considered Solid Hosts

In this section we consider the cations' absorption spectra in both ceramics and glasses. Presentation of the latter is helpful in interpreting the spectra in both types of hosts. The disordered nature of the glass lattice allows simultaneous accommodation of various oxidation and coordination states of a given transition metal; the absorption band intensity is higher and often richer. Among other things, the disorder distorts the cation ligand polyhedron, and the reduced symmetry allows transitions that are forbidden in the higher symmetry. Single-crystal hosts exhibit more similarity to ceramics and are often purer; their crystallographic order also allows studies related to the incident light polarization.

2.3.5.2.2.1.1 3d Subshell Cations

Some of these cations, for example, triply ionized iron Fe^{3+}, are frequently encountered impurities; others are dopants used in quite important applications, for example, triply ionized titanium Ti^{3+} and doubly ionized cobalt Co^{2+}. In free space such cations produce sets of electronic states that can be treated by the Russell–Saunders approximation. The ligand polyhedral features dominantly determine their spectra in a solid host. Their spin–orbit coupling effects are relatively weak and therefore easier to interpret as compared to those belonging to 4d and 5d cations. The crystal field approximation is usually sufficient to explain tall features of such spectra.

2.3.5.2.2.1.2 Ti^{3+}

In the 3d subshell, the first ion series belongs to the $3d^1$ configuration; specific cations are triply ionized titanium Ti^{3+}, fourfold ionized vanadium V^{4+}, and sixfold ionized manganese Mn^{6+}. The V^{4+} ion can be stabilized in certain glass hosts; the glasses usually contain other vanadium ions like V^{5+} and/or V^{3+} [B18]). Manganese sixfold ionized cations Mn^{6+} were detected as forming a $(MnO_4)^{2-}$ complex in green water solutions [G20]. Its presence has also been suggested in some very high basicity glasses [G20], but more recent studies do not verify that suggestion. The Mn^{6+} cations have not been reported as present in crystalline hosts; the required very high oxidation states explains that absence, in spite the expected small cationic radius. The only $3d^1$ ion that can be successfully stabilized in transparent solid hosts is Ti^{3+}, particularly in sapphire Al_2O_3. It has not been found in silicate glasses. It however can be easily stabilized in lower basicity phosphate and borophosphate glasses if melting is done under reducing conditions [G31]. The Ti^{3+} cation imparts blue to violet hues to the glassy hosts. Figure 2.40 shows the Ti^{3+} absorption spectrum when residing in a transparent spinel ceramic (greenish-blue color).

The spectrum shown in Figure 2.40 includes two absorption bands at respectively 16 000 cm^{-1} and 13 000 cm^{-1}. The spectral profile can be accounted

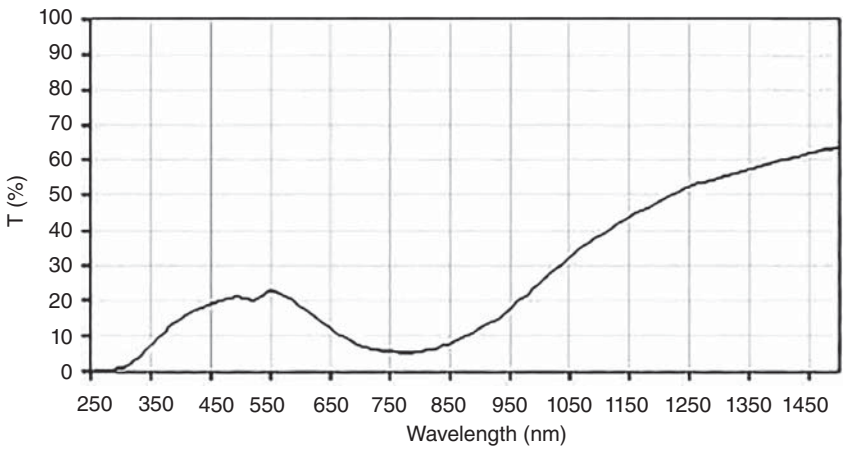

Figure 2.40 Electronic spectrum of a spinel containing 0.1% TiO_2, subjected to oxygen scarce sintering atmosphere (greenish-blue disc obtained by sinter/hot isostatic pressing $t = 2.4$ mm). Source: Goldstein et al. 2007 [G31]. Reproduced with permission from John Wiley & Sons.

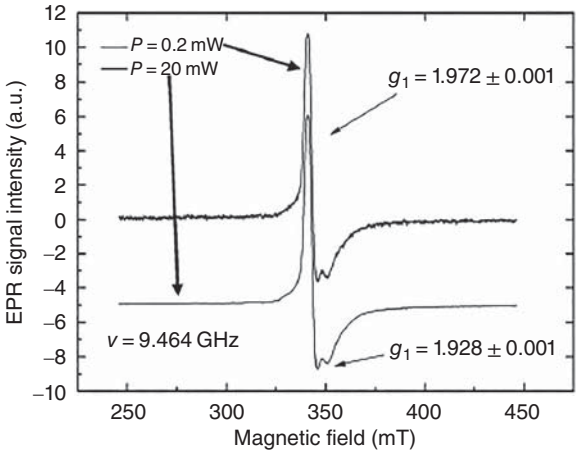

Figure 2.41 Electron paramagnetic resonance signal (RT) of the specimen relevant for Figure 2.40. Source: Goldstein et al. 2007 [G31]. Reproduced with permission from John Wiley & Sons.

for by transitions between bands derived from a distorted octahedral complex in which Ti^{3+} is the central ion and $O^{\delta-}$ anions as its complementing ligand. The distortion is caused by Jahn–Teller effect, being strong since the ground state is a doublet ^2E_g. We showed [G31] that titanium Ti assumes a Ti^{4+} cationic state in spinel $MgAl_2O_4$ transparent ceramic that initially contained 0.06 wt% titanium dioxide TiO_2. It maintained that state during sintering in air, so that white opaque parts resulted. After hot isostatic pressing (HIPing), in an oxygen-deficient atmosphere and high temperature, the specimens become transparent and the dopant was reduced to Ti^{3+}, a process that conferred a bluish-green color to the parts and spectral features similar to that of Figure 2.40. Measured [G31] ESR signal conformed with that expected for a $3d^1$ electron; the signal could be recorded even at room temperature (Figure 2.41).

The experimental results proved that only minute amounts of Ti^{4+} are taken up by the spinel lattice: for 0.1 wt% added TiO_2, a sizable part of oxide separates inside the spinel $MgAl_2O_4$ host matrix, forming opaque spots. These spots remain even after performing HIPing with an oxygen-deficient atmosphere. It is concluded that Ti^{3+} stabilization takes place by formation of oxygen vacancies according to

$$2Ti^{4+} + O \leftrightarrow 2Ti^{3+} + V_O^{\cdot\cdot} + \frac{1}{2}O_2(g) \uparrow \qquad (2.54)$$

The Ti^{3+} cations enter the lattice by substituting for Al^{3+} cations, residing in octahedral voids of the spinel lattice, thus each generating a $Ti_{Al}^{\cdot}$ defect. The original site symmetry (O_h) is distorted, by the Ti^{3+} cation, to a C_{4v} symmetry. Ti^{3+} was stabilized also in single crystal $MgO \cdot 3.5Al_2O_3$ spinel and of course in sapphire Al_2O_3 [G20].

Ti^{3+} inserted in a single crystal or in ceramic hosts like α-Al_2O_3, $Y_3Al_5O_{12}$ (YAG), $MgAl_2O_4$, or $BeAl_2O_4$ may be used, among other things, in laser technology. Particularly, owing to their broad fluorescence spectrum, such lasers can be tuned over a 690 – 870 nm range, and up to ~50 mJ outputs under flash lamps pumping. Such lasers can operate at a continuous wave (CW) mode and ultrashort pulses down to about 10 – 50 fs [M40].

2.3.5.2.2.1.3 Cu

This element is included here because it is capable of assuming three oxidation states: Cu^{2+}, Cu^{+}, and Cu^{0}, sometimes simultaneously in the same host matrix. The first-type cation is capable of forming d ↔ d optical transition bands. The last, when aggregated in colloidal-type metal particles, causes combined absorption and scattering [B10]; this is the source of color in many, so-called "ruby" glasses. Cu^{+} is fluorescent [B10]. A Cu^{3+} cation ($3d^7$) is rarely found in any compound and has not been identified to be present in any transparent solids. In crystalline hosts, copper is accommodated as Cu^{2+} of $3d^8$ configuration. The relatively low oxidation potential, and its considerable ligand field stabilization, makes the formation of this cation energetically favored. Notably, the ligand field stabilization is considered to be augmented by a mild Jahn–Teller splitting of the ground $^3T_{2g}$ state.

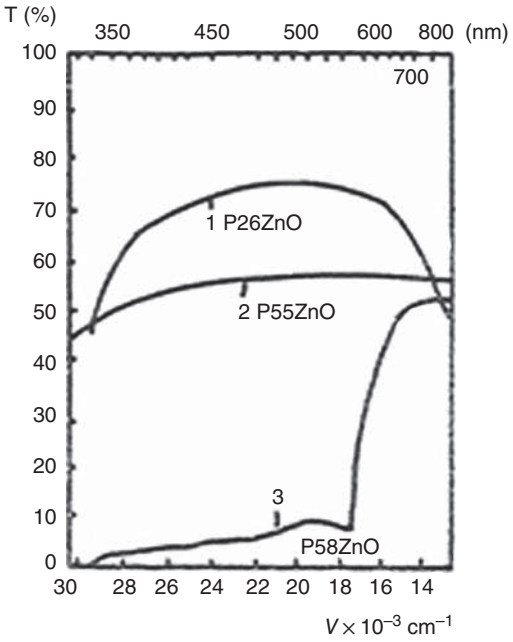

Figure 2.42 The transmission spectra generated by the Cu species present in various Zn-phosphate glass hosts (host compositions are indicated on the curves). Source: Goldstein et al. 2007 [G32]. Reproduced with permission from John Wiley & Sons.

Figure 2.42 presents the optical transmission spectra of a series of three Cu^{2+}-containing glasses with varying compositions of the P_2O_5 – ZnO system [G32]. During melting, these glasses were exposed to a reducing atmosphere. Particularly the 30 mol % ZnO comprising glass exhibits a broad asymmetric absorption band peaked at ~930 nm. It corresponds to a Cu^{2+} cation coordinated by six $O^{\delta-}$ ions located at the corners of an elongated octahedron of D_{4h} symmetry [G20]. The band resolves into two Gaussian profile components peaking at ~930 and ~1300 nm. It is a consequence of a moderate distortion of the ligand octahedron. In such conditions the $^2A_{2g}$ and $^2B_{2g}$ levels are close, and thus only two transitions can be spectrally resolved: $^2B_{1g} \rightarrow {}^2E_g$ and $^2B_{1g} \rightarrow {}^2A_{2g}$; $^2B_{2g}$ [G20].

X-ray photoelectron spectroscopy (XPS) spectrum (Figure 2.43) confirms the presence of the said Cu^{2+} cations, as also does the EPR signal of Figure 2.44.

X-ray photoelectron spectroscopy also reveals the presence of Cu^+ cations ($3d^{10}$ configuration), a species silent in optical absorption spectra. In silicate glasses, the Cu^{2+} band has a similar profile to that in Figure 2.42,

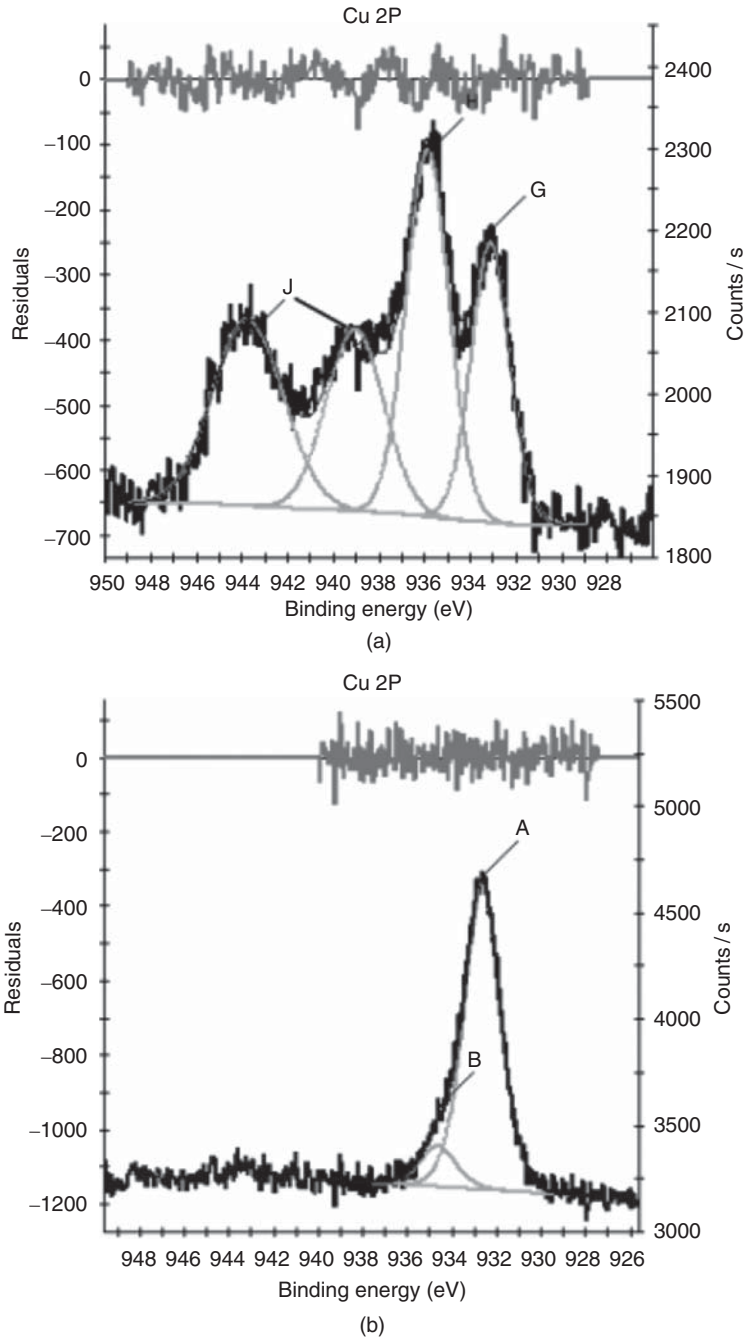

Figure 2.43 Cu 2p X-ray photoelectron spectroscopy signal in Zn-phosphate glasses. (a) P30Zn (peak G = Cu^+, peak H = Cu^{2+}; peaks J = satellites of Cu^{2+} central peak. (b) P50Zn (peak A = Cu^+, peak B = Cu^{2+}). Source: Goldstein et al. 2007 [G32]. Reproduced with permission from John Wiley & Sons.

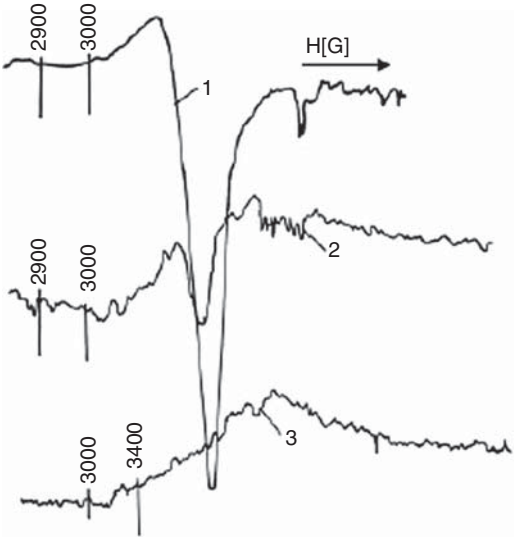

Figure 2.44 EPR signal of Cu^{2+}, located in various Zn-phosphate glasses. 1 – P30ZnO. 2 – P45ZnO. 3 – P56ZnO. Source: Goldstein et al. 2007 [G32]. Reproduced with permission from John Wiley & Sons.

but with a hypsochromic shift of the absorption peak to about 790 nm. It results from a higher ligand field strength caused by the higher basicity of $O^{\delta-}$ ligand forming anions in silicate glasses [G20].

Figure 2.45 shows a copper Cu absorption spectrum when accommodated in a transparent ceramic spinel $MgAl_2O_4$. The obtained green-bluish hue corresponds to a spectral profile different from that obtained for copper Cu in glassy hosts. The ~1490 nm peak position and intensity of the major band in spinel suggests a ligand comprising Cu^{2+} cation inside a slightly distorted $O^{\delta-}$ tetrahedron, the Cu^{2+} substituting a lattice Mg^{2+} cation. The lower intensity band centered around 700 nm could also be assigned to a fourfold coordinated, yet strongly distorted Cu^{2+} tetrahedral site. An alternative interpretation assumes an inverted (for Mg^{2+}) O_h symmetry site. A strong Cu^{2+} charge transfer band appears below ~500 nm.

Figure 2.46 displays an interesting absorption curve of copper Cu-doped transparent $Y_3Al_5O_{12}$ (YAG). Visual observation of such sample reveals a red surface layer simultaneously with a bulk green-bluish region. Figure 2.46 spectral features are easily identified as being generated by colloidal Cu^0 [G18]. It is similar with that seen in zinc phosphate P_2O_5 – ZnO glasses, where the ZnO concentration exceeds 50 mol%. Colloidal Cu^0 particles in such glasses are detectable, as shown in Figure 2.47.

Spectral analysis of dopant/s containing glasses allows verification of correlation dependence between the host basicity and the oxidation state(s) of copper Cu, accommodated by a certain lattice in ceramic or single-crystal forms. The basicity in the P_2O_5 – ZnO glass system decreases with the ZnO concentration. Thus, while Cu^{2+} and Cu^+ are seen at ~30 mol % ZnO content, at higher ZnO content the copper Cu oxidation states equilibrium shifts toward Cu^+ and Cu^0. In crystalline hosts, the less basic $Y_3Al_5O_{12}$ (than spinel) is likely to accommodate

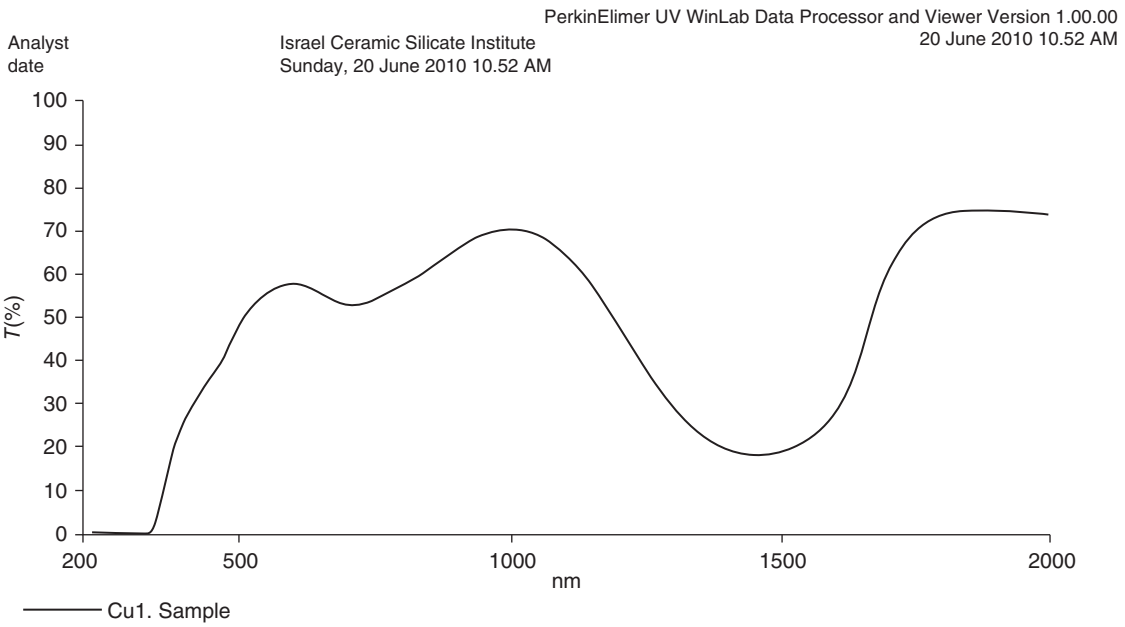

Figure 2.45 Optical spectrum of Cu accommodated (as Cu^{2+} in two coordination patterns) in a transparent spinel ceramic host; specimen fabricated at ICSI, Haifa. Source: ICSI, Haifa.

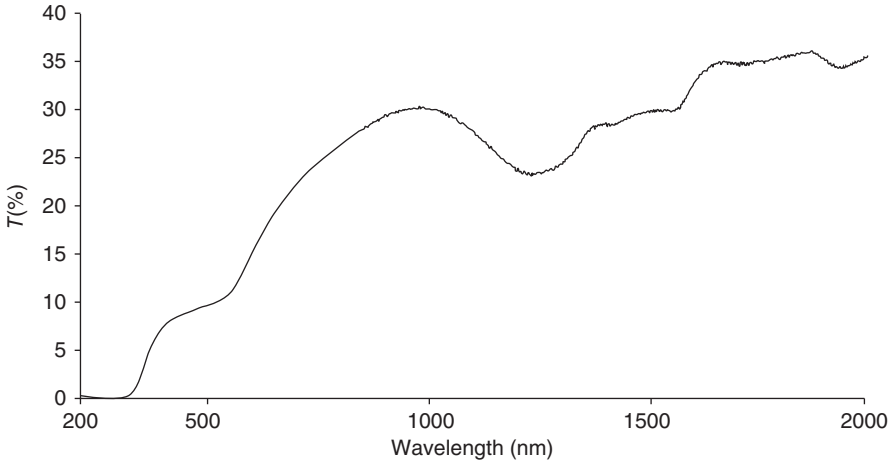

Figure 2.46 Optical spectrum generated by Cu accommodated in a YAG host, which shows Cu^0 band at ~490 nm and Cu^{2+} band in the IR region. Source: ICSI, Haifa.

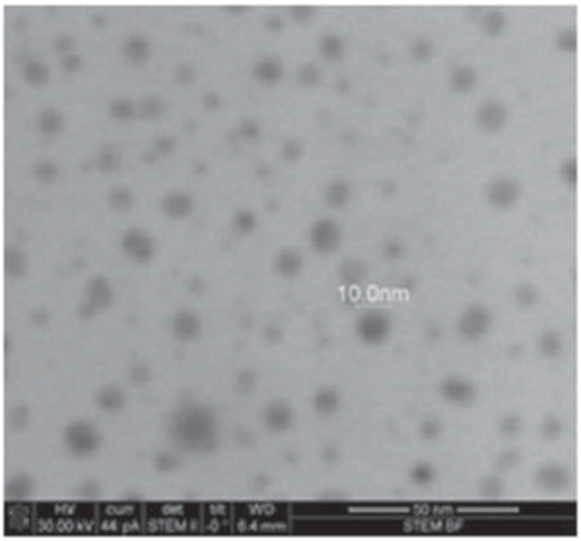

Figure 2.47 Cu^0 nanometric clusters in P-Zn red glass (STEM image). Source: Goldstein et al. 2007 [G32]. Reproduced with permission from John Wiley & Sons.

both Cu^{2+} and Cu^0, while the more basic spinel $MgAl_2O_4$ accommodates only Cu^{2+}.

2.3.5.2.2.1.4 Rare-Earth (RE) Type Cations

Dopant rare-earth-type cations in a ceramic or a single-crystal host have many important applications, mostly related to electromagnetic radiation emission (see Section 5.2.9). The applications include solid substrate lasers, phosphors, scintillators, and artificial gems. Most used dopants belong to the $4f^3$ configuration. Their electronic state structure is significantly different from those produced by transition metal (TM)-type cations due to their spin orbital coupling being much stronger. Thus, energy level splitting due to ligand field perturbation is considerably smaller than the splitting caused by their spin–orbit interaction. Figure 2.48 shows the energy level schemes of triply ionized erbium Er^{3+} ion, while Figure 2.49 that of Yb^{3+} [S55]. The set of Nd^{3+} electronic levels was shown in Figure 2.32. Figure 2.50 shows spectral curves obtained for Yb^{3+} and Er^{3+} hosted by an oxifluoride (FOG) glass-ceramic.

The RE^+-type cations have a radius significantly larger than that of the TM^+. Owing to this in some of the attractive TC hosts like spinel or alumina is difficult or even impossible to introduce such dopants in amount large enough to produce materials usable as laser gain media, phosphors, etc. This is one of the reasons hosts like YAG with larger sites are used in relation to RE^+ active ions. In this context let us note that it would be maybe useful to invest more effort in finding additional hosts, besides YAG and the sesquioxides, to the RE^+s. For instance it was shown that substantial amounts of Er^{3+} can be introduced into translucent tetragonal zirconia [D24]; more such studies would be welcome.

2.4 Physical Processes Controlling Light Absorption in the Optical Window Vicinity

2.4.1 High Photon Energy Window Cutoff: Ultraviolet Light Absorption in Solids

Figure 1.2 shows, among others, the spectral transmission profile of a zinc selenide ZnSe ceramic exhibiting a wide optical transmission window. The transmission window "closes," that is, exhibiting an abrupt reduction in transmission on the high photon energy side, at the NUV. A similar evolution occurs on the low photon energies side, belonging to the mid-infrared (MIR). In the case of ZnSe, the high energy window edge is at ~0.25 μm and that of low energy, around 25 μm. Absorption occurs because photon energies exceeding the short wavelength window edge are high enough to propel

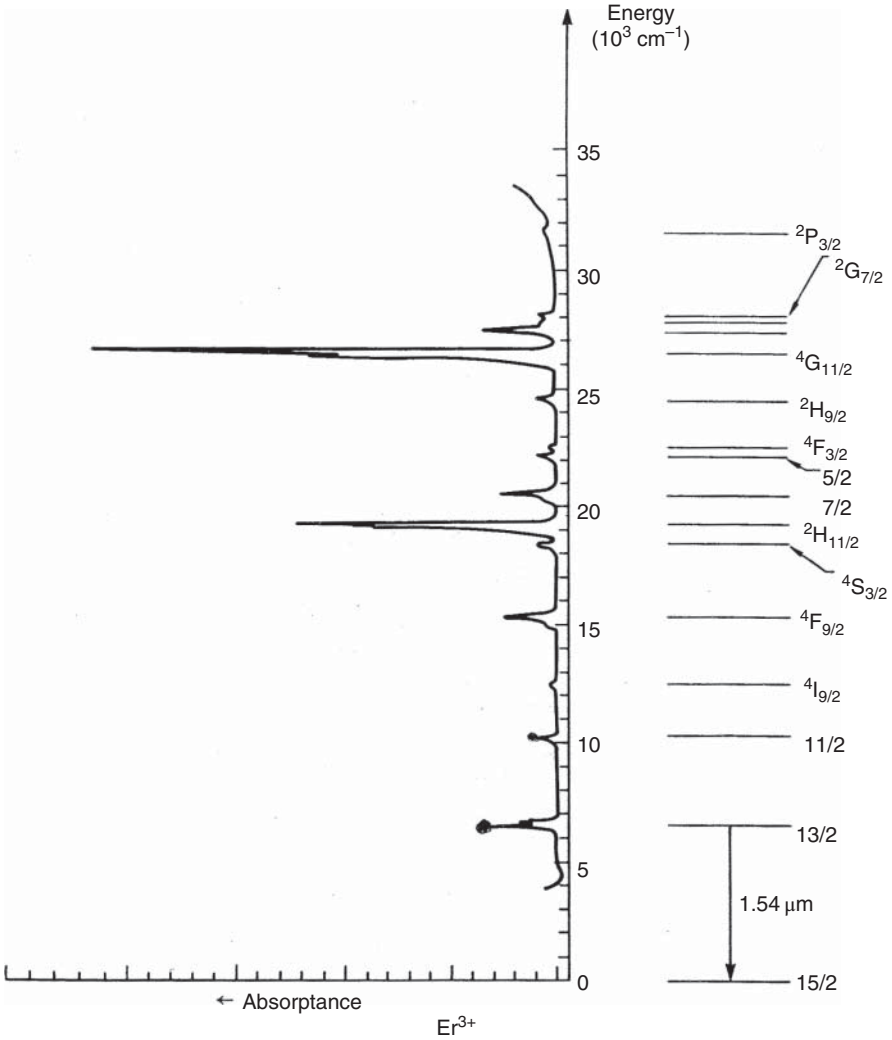

Figure 2.48 Electronic states scheme of Er^{3+} cation. Source: Stokowski 1986 [S55]. Reproduced with permission from CRC Press.

lattice electrons from the valence band to the conduction band. The chemical bonding in solids responsible for forming the energy gap is not a topic discussed in our present book. Only a simplified description is provided right below; particularly, topics like exciton-state formation and similar ones are not presented.

The following description of the nature of electronic transitions in crystalline solids will follow intuitive rather than formal routes. At zero-order approximation, the natural atomic base attached to each lattice point is considered as an independent molecule in free space. The electronic energy states of such molecule are all discrete. When an N_c number of different natural bases coalesce to form a macroscopic solid (not necessarily ordered like in a crystal), each discrete state splits into an N_c number of very close states, forming "allowed state" **bands**. Due to the huge number of states belonging to each band, they are considered to form a quasi-continuum. The inner molecular electronic bands are narrow, due to the only small electronic overlap between the bases. The valence electronic states (ground or excited), on the other hand, exhibit a larger overlap, hence broader bands. In certain cases, some overlap exists among bands of different origin. In many cases, however, gaps between states occur, called **forbidden gaps**. The highest occupied band is addressed as **valence band**. Its top energy is written as E_V. The above (thus empty) closest band is addressed as **conduction band**. Its bottom energy is written as E_C.

When the solid atomic bases organize at a crystalline order, the wave function of each occupying electron $\varphi_{\underline{k}}(\underline{x})$, exhibits a near-free electron structure of the form

$$\varphi_{\underline{k}}(\underline{x}) = u_{\underline{k}}(\underline{x})\, e^{i\underline{k}\cdot\underline{x}} \tag{2.55}$$

where $\underline{x}$ is a position vector in space inside the crystal and $\underline{k}$ is an allowed wave number in the first Brillouin zone. The $u_{\underline{k}}(\underline{x})$ function is periodic in the particular crystal, namely, $u_{\underline{k}}(\underline{x}+\underline{a}) = u_{\underline{k}}(\underline{x})$, where $\underline{a}$ is a lattice vector. Functions of that form are called **Bloch functions**.

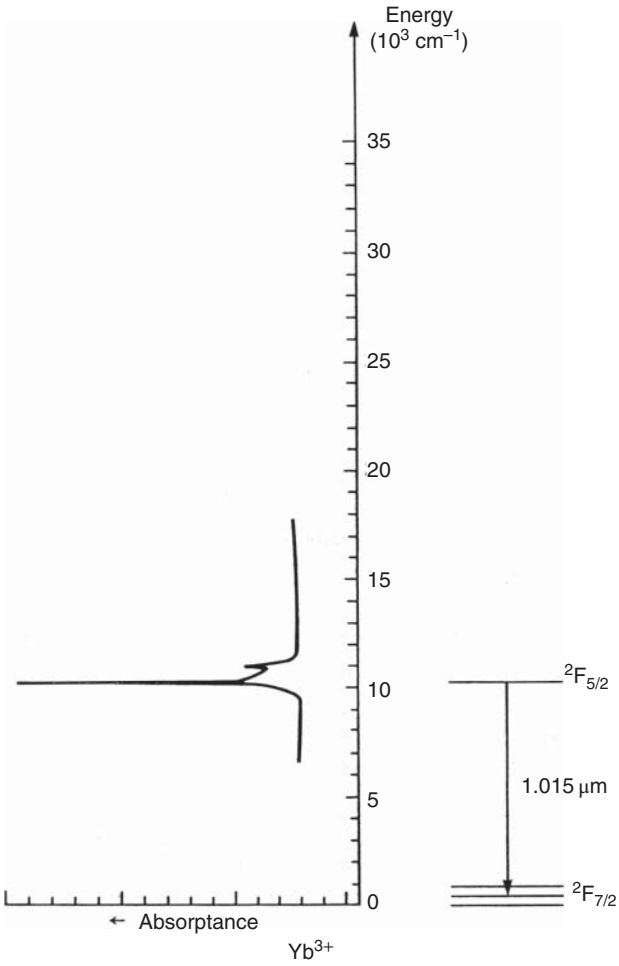

Figure 2.49 Electronic states of Yb^{3+} cation. Source: Stokowski 1986 [S55]. Reproduced with permission from CRC Press.

Each allowed band state may occupy two electrons of opposite spins. Thus simplistically, a valence band that descends from a state of an odd number of valence electrons is only partially filled. A valence band descending from a state of even number of valence electrons is fully occupied. Such bands never contribute to electrical conductivity; application of an external electrical field is unable to change the electrons wave propagation statistics, since all states are equally filled. The result is a null electrical current. Such materials form either semiconductors or insulators, depending on the forbidden gap width E_g between the top valence band and bottom conduction band. Solids are classified by four types per electrical conductivity as follows:

{1} Solids of valence band that are approximately half-filled form **metals** of high electrical conductivity. They are also often addressed as **electrical conductors**. Under thermal equilibrium, the density of electron wave propagation directions in space balance to form a null electrical current. However, application of an external electrical field changes the band occupation statistics toward formerly empty states. Thus, more electrons move according to the field direction than those moving in the opposite direction. It results in a net electrical current. Some trivial examples are aluminum Al, copper Cu, and gold Au.

{2} **Semiconductors** are characterized by energy gaps $E_g \equiv E_C - E_V \widetilde{<} 1.0\,\text{eV}$. Near room temperature, where $k_B T \cong 0.025\,\text{eV}$ (k_B being the Boltzmann constant and T the absolute temperature), thermal excitation is sufficient to bring about excitation of valence electrons into the conduction band.

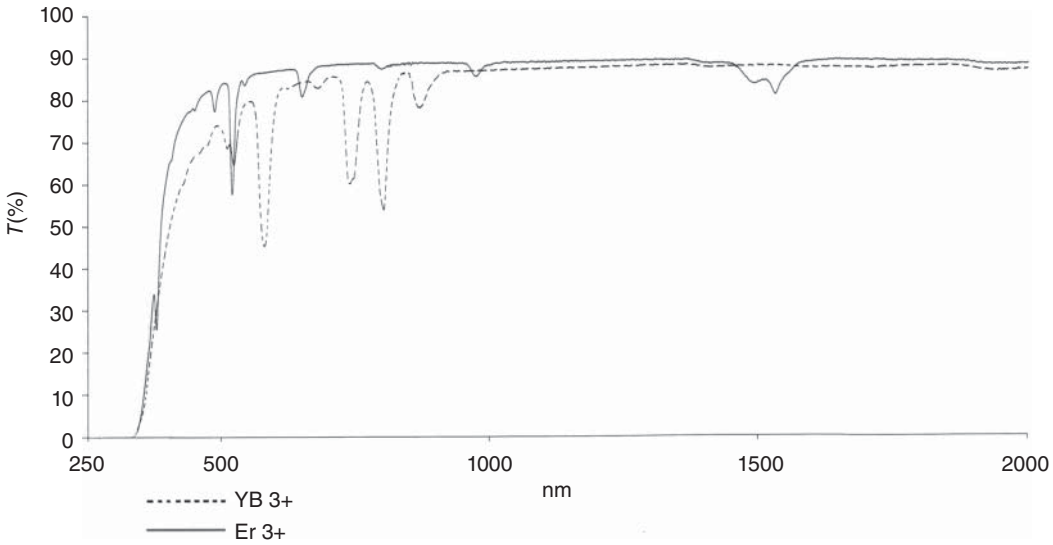

Figure 2.50 Spectra produced by Nd^{3+} and Er^{3+}, respectively, located in FOG-type glass-ceramic hosts.

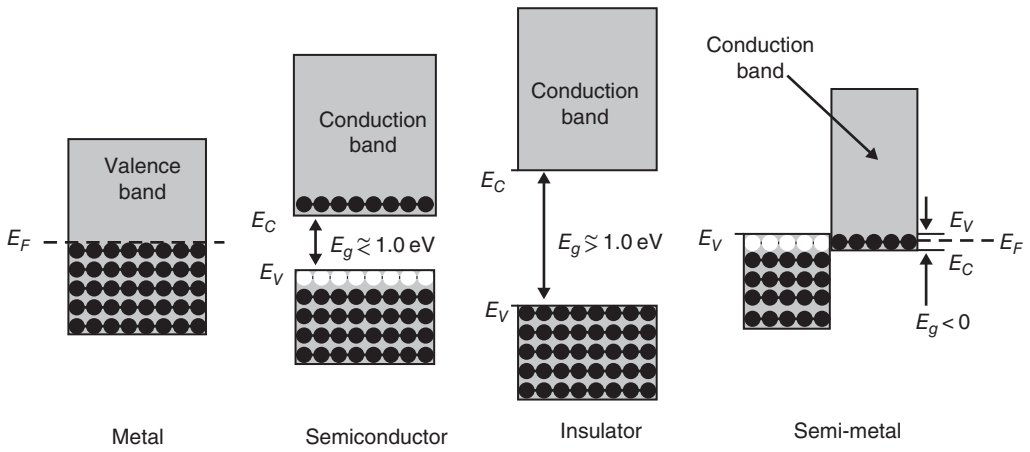

Figure 2.51 Energy schemes describing the classification of solid materials as either metals, semiconductors, insulators, or semimetals. In the latter, the conduction and valance bands are shifted horizontally to avoid confusion.

The empty valence states located at the valence band top, now termed **holes**, behave like free *positive* **charge carriers**, thus contributing to electrical conductivity. The thermally excited electrons located at the conduction band bottom behave like free *negative* **charge carriers**, thus contributing an addition to the electrical conductivity. The summed free **charge carrier** concentration in semiconductors is orders of magnitude smaller than in metals. Therefore, the summed electrical conductivity is also orders of magnitude smaller than of metals. Near the zero absolute temperature $T \cong 0$, the free charge carrier concentrations in semiconductors, hence electrical conductivity, diminish. Some examples are silicon Si, germanium Ge, and gallium arsenide GaAs.

{3} Electrical **insulators** are characterized by energy gaps $E_g \gtrsim 1.0$ eV and exhibit no electrical conductivity near room temperature. Most transparent semiconductors of our interest are oxides, exhibiting energy gaps between approximately 4 and 8 eV. They are thus electrical insulators up to quite high temperatures. Some examples are sapphire Al_2O_3, spinel $MgAl_2O_4$, and YAG $Y_3Al_5O_{12}$.

{4} **Semi-metals** are obtained when the valence and conduction bands exhibit some energetic overlap. In other words, the energy gap E_g is *negative*. Valence electrons now relocate from the valence band top energy region to the bottom conduction band, bringing about a high density of conducting holes at the valence band top, and a high density of conducting electrons at the conduction band bottom. The generated electrical conductivity is now intermediate between metals and semiconductors. Some examples are mercuric telluride HgTe and graphite C.

In Figure 2.51 we provide a set of energy schemes summarizing the above classification. Allowed bands are indicated by a gray background. Occupying electrons are indicated by filled black circles and occupying holes by open ones. A special energy parameter called **Fermi energy** E_F is used, marking a 50% electron occupation probability at the zero absolute temperature $T = 0$ (in chemical terms, the Fermi energy reads **electrochemical potential**). In the $T = 0$ limit, the electron occupation probability for energy $E < E_F$ is 100%; the electron occupation probability for energy $E > E_F$ is zero. Obviously, no occupation is realized unless a state actually exists at E. At higher temperatures the occupation probability below E_F decreases while growing above it according to the Fermi–Dirac distribution function:

$$\mathbf{f}(E) = \frac{1}{1 + \mathbf{exp}\left(\frac{E-E_F}{k_B T}\right)} \tag{2.56}$$

The largest change in the function takes place across a small energy range, approximately $3k_B T$ wide, around the Fermi energy E_F. The function drops in this range from near-unity below E_F to near-zero above it. At room temperature, $k_B T \cong 0.026$ eV, or approximately 200 cm^{-1}. The Fermi–Dirac distribution function is displayed in Figure 2.52.

Temperature rise above zero exhibits only a minor effect on the electrical conductivity of metals, semimetals, and highly insulating materials. It however exhibits very strong effects on semiconductors by causing exponential occupation increase of both holes and electrons.

Our concern in the present book is the optical transmission of different materials. Neither metals nor semi-metals are transparent in our spectral range of interest. The response of the large numbers of free charge carriers to an incident electromagnetic radiation

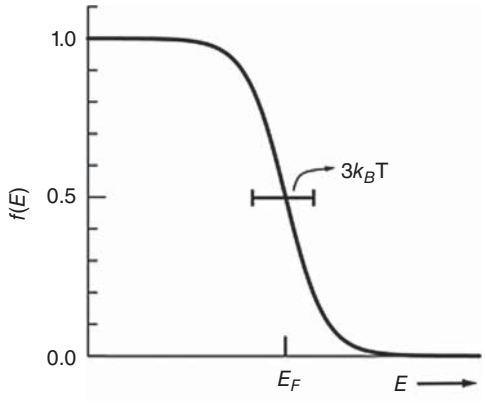

Figure 2.52 Fermi–Dirac distribution function (occupancy of electronic states probability vs. their energy).

causes almost an entire reflection of the light beam, with minimal absorption. Semiconductors and insulators, however, transmit only light of photon energies smaller than the energy band-gap E_g. Light of higher photon energy is absorbed by causing valence electron excitation into the conduction band. This excitation establishes the material *short wavelength* edge of the transparency window. For example, in an insulator of 4 eV energy gap, the short wave transparency range relates to approximately 32 000 cm^{-1}, namely, a 0.3125 μm wavelength, which belongs to the NUV region. If the same material exhibits a cutoff vibrational frequency ω_{co} of approximately 1250 cm^{-1}, its long wave transparency range relates to approximately 8.0 μm wavelength, which belongs to the far-infrared (far-IR) region.

2.4.2 Low Photon Energy Window Cutoff: Infrared Light Absorption in Solids

The optical transparency range of interest in transparent ceramics extends toward the infrared up to approximately 25 μm. The factors limiting transparency, like within the window spectral range, are reflection, absorption, and scattering. This section addresses the issue of infrared "light" absorption mechanisms. The gross contribution arises from the matrix lattice vibrations. For some impure materials, certain polyatomic groups, absorbed or adsorbed, may also contribute to absorption in those cases. Both contributions involve their vibrational modes.

2.4.2.1 Molecular Vibrations

Several atoms, bonded to form a molecule, never actually form a rigid structure; they move and vibrate about their equilibrium positions. The latter are those interatomic distances and inter-bond angles that form a minimum in the total molecular energy. Our reference for consideration is a free molecule in space, as realized in a low-pressured gas.

A molecular motion is called **normal mode** if all participating atoms, while moving, cross their equilibrium positions simultaneously. The different possible modes classify as **translational**, **rotational**, and **vibrational**. In a translational mode, all atoms move in one direction at a common steady velocity, whereby the interatomic distances and inter-bond angles remain unchanged. In a rotational mode, the interatomic posture remains unchanged, while all atoms perform a circular motion about a common axis that passes through their resting mass center, at a common angular velocity. In a vibrational mode, all atoms vibrate about their equilibrium positions at same frequency and phase; namely, they simultaneously pass through their equilibrium positions and simultaneously assume their amplitude edge positions. A general motion describes very accurately a sum of separate motions according to the said classification.

A molecule constituted of N_m atoms exhibits $3N_m$ degrees of freedom, hence the same number of normal modes: three are translational (along three independent directions), three are rotational (about 3 independent principal rotation axes), and $3N_m - 6$ are bound vibrational (only $3N_m - 5$ in a linear molecule). In the "harmonic" binding approximation, each κ-numbered bound normal mode is subject to an independent binding potential of the form $U_\kappa = \frac{1}{2}\omega_\kappa{}^2 q_\kappa{}^2$, with ω_κ being a positive constant. Each q_κ **normal coordinate** is a different linear combination of the atoms square-root-mass-weighted departures from their equilibrium positions. Classically, each mode then executes an independent motion, abiding the equation

$$\ddot{q}_\kappa = -\omega_\kappa{}^2 q_\kappa \quad \text{for } \kappa = 1, 2, \ldots, 3N_m - 6 \qquad (2.57)$$

(only $3N_m - 5$ in a linear molecule). Each equation's solution represents a harmonic oscillation through the equilibrium position, given by

$$q_\kappa(t) = A_\kappa \mathbf{exp}[i(\omega_\kappa t - \varphi_\kappa)] \qquad (2.58)$$

where t is the time, A_κ is the (positive) mode amplitude, ω_κ is the oscillation angular frequency, and φ_κ is the mode (arbitrary) phase lag.

A mode mechanical energy is given by

$$E_\kappa = \frac{1}{2}\omega_\kappa{}^2 A_\kappa{}^2 \qquad (2.59)$$

During vibration, the energy nature changes between fully kinetic when $q_\kappa(t) = 0$ and fully potential when $|q_\kappa(t)| = A_\kappa$. Classically, the amplitude A_κ may attain any arbitrary value, hence also the mode energy. Quantum

mechanically, however, E_κ may exhibit only a **discrete** set of values

$$E_{\kappa,\mathrm{v}} = \left(\frac{1}{2} + \mathrm{v}\right)\hbar\omega_\kappa \quad \text{for } \mathrm{v} = 0, 1, 2, \ldots \tag{2.60}$$

hence obviously also their corresponding amplitudes A_κ. The number v is called **occupation number**. The quantity $\hbar\omega_\kappa$, where $\hbar$ is the reduced Planck constant, is considered a "quasi-particle," called **phonon**. The v-number describes the number of phonons occupying the κ-mode system. The presence of the "half-phonon" energy $E_{\kappa,0} = \frac{1}{2}\hbar\omega_\kappa$ in Eq. (2.60) is a quantum effect, called **zero-point fluctuation**.

In reality, the mode binding potential is never accurately harmonic. An empiric potential quite successful in describing binding potentials and vibrational mode energies is **Morse potential**, given by

$$U_\kappa = D_\kappa(1 - e^{-\beta_\kappa q_\kappa})^2 \quad with \quad \beta_\kappa \equiv \omega_\kappa/(2D_\kappa)^{1/2} \tag{2.61}$$

where D_κ, hence β_κ, are positive constants. While the harmonic potential is symmetric with respect to q_κ's sign, the Morse potential is asymmetric: it saturates at D_κ for $q_\kappa \to +\infty$ but grows to infinity for $q_\kappa \to -\infty$. The ratio $D_\kappa/\hbar\omega_\kappa$ is a measure of Morse potential's inharmonicity; in the limit of a fully harmonic potential, this ratio becomes infinite. The quantized vibrational energies are also different, with the interstate separations gradually reducing with growing energy, according to

$$E_{\kappa,\mathrm{v}} = \left(\frac{1}{2} + \mathrm{v}\right)\hbar\omega_\kappa - \left(\frac{1}{2} + \mathrm{v}\right)^2 \frac{\hbar^2{\omega_\kappa}^2}{4D}$$
$$\text{for } \mathrm{v} = 0, 1, 2, \ldots, \mathbf{int}\left[\frac{2D_\kappa}{\hbar\omega_\kappa} - \frac{1}{2}\right] \tag{2.62}$$

Following Eq. (2.62), the number of bound states is finite, approximately given by $2D_\kappa/\hbar\omega_\kappa$. Recall that electronic states of a free atom, on the other hand, exhibit an infinite number of bound states, with separations gradually diminishing on nearing the ionization energy. An illustration of a Morse potential as function of its vibrational normal coordinate is provided in Figure 2.53. The quantized energy levels are indicated by horizontal bars, resting between the edge locations of a classical oscillator of same energy and angular frequency.

The physical meaning of a D_κ parameter is that the molecule would dissociate in the limit of large positive q_κ's; namely, D_κ is the **dissociation energy**. The energy addition required to cause dissociation is in fact smaller by $\frac{1}{2}\hbar\omega_\kappa$, as marked by D_{exp} in Figure 2.53. Still, different normal modes exhibit different D_κ's. Therefore, the actual dissociation relates to the κ-mode of largest D_κ, which usually also exhibits the *largest* angular frequency.

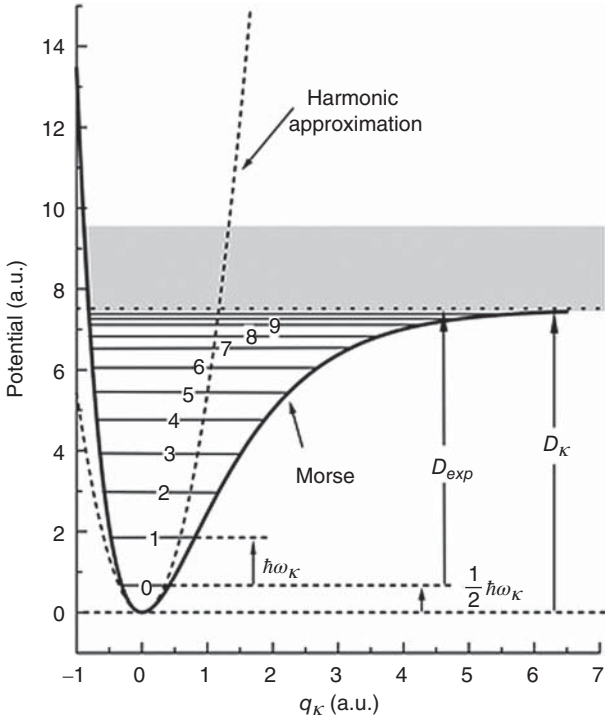

Figure 2.53 Schematic illustration of a Morse potential, and its related harmonic approximations, as a function of the vibrational normal coordinate.

The potential forming that mode is called **configuration potential**, and its characteristic angular frequency ω_{co} is called **cutoff frequency**.

Translational mode energies of a free molecule are continuous, dependent on the molecule's linear velocity. Under thermal equilibrium in a low-pressured molecular gas, the velocity distribution causes some **Doppler** broadening of optical transitions. Practically, the wavelength broadening never exceeds several tenths of an angstrom ($1\ \text{Å} \equiv 10^{-8}$ cm). The rotational motions are rather quantized. However, for molecular structures of our interest, their transitions lie in the very FIR. Still, both translational and rotational modes exhibit some impact in solid-state materials spectroscopy, which will be specifically addressed later on.

2.4.2.2 Solid Vibrations

For dealing with solids, especially with crystalline solids, it will be assumed that the reader is acquainted with some basic concepts like crystal lattice, unit cell, Wigner–Seitz unit cell, reciprocal lattice, and Brillouin zone.

When a number of different atoms coalesce to form a macroscopic solid, the degrees of freedom number of atomic motion increase – many orders of magnitude

larger than for any ordinary molecule. Luckily, most solids tend to form ordered arrangements, namely, crystals (even if sometimes of only several micrometers in dimensions). This order makes it helpful in classifying the various motions. A crystal lattice describes a repeated orderly arrangement of the same group of atoms over a large space, each such group belonging to a lattice point. This group of atoms is addressed as the crystal's **natural atomic basis**. In a zero-order approximation, the atomic basis is assumed to behave much like an isolated molecule, whose motions were described in the previous section. However, due to interaction among the atomic bases, each mode broadens, forming a band of energy states. Regarding translational and rotational motions, the term "isolated molecule" must be updated. The solid environment prevents an atomic basis from performing any undisturbed translation, nor any undisturbed rotation. Return forces transform translations into vibrations about their equilibrium positions. Return force moments transform rotations into limited angular rotations about their equilibrium posture, called **librations**.

Interactions among atomic bases results in vibrational waves propagating through the crystalline volume. The definition of a vibrational mode now needs revision. The requirement that all atoms vibrate about their equilibrium positions at the same frequency and the same *phase* is changed to require same *frequency*, but same *wave-vector* $\underline{k}$ instead of same phase.

The starting point for mathematical treatment is to consider each atomic basis belonging to a lattice point $\underline{x}$ as providing a sum of point-like oscillators; a normal coordinate of an oscillator is $q_{\underline{x}}$ of angular frequency ω_0 (additional use of κ as mode numerator is avoided for brevity). This oscillator is assumed to interact harmonically with any adjacent identical oscillator at lattice point $\underline{s} \neq \underline{x}$ via a spring-like coupling constant $C_{\underline{s}}$. The equation of motion then becomes

$$\ddot{q}_{\underline{x}} = -{\omega_0}^2 q_{\underline{x}} - \sum_{\underline{s}\neq 0} C_{\underline{s}}(q_{\underline{x}} - q_{\underline{x}+\underline{s}}) \tag{2.63}$$

to be rewritten as

$$\ddot{q}_{\underline{x}} = -\left({\omega_0}^2 + \sum_{\underline{s}\neq 0} C_{\underline{s}}\right) q_{\underline{x}} + \sum_{\underline{s}\neq 0} C_{\underline{s}} q_{\underline{x}+\underline{s}} \tag{2.64}$$

The solution of Eq. (2.64) describes a sum of independent propagating plane waves of the form

$$q_{\underline{x}}(t) = \sum_{\underline{k}} A_{\underline{k}} e^{-i(\omega_{\underline{k}} t - \underline{k}\cdot\underline{x})} \tag{2.65}$$

where $\underline{k}$ is the wave vector, $A_{\underline{k}}$ is the wave amplitude, and $\omega_{\underline{k}}$ is the wave angular frequency. A single independent wave component, *defined* as a **crystal normal vibrational mode**, has the form

$$q_{\underline{x}}(t) = A_{\underline{k}} e^{-i(\omega_{\underline{k}} t - \underline{k}\cdot\underline{x})} \tag{2.66}$$

which is realized when all $A_{\underline{k}}$'s diminish, *except* for a particular $\underline{k}$. There are N independent modes ("permitted" modes) in each crystal, where N is the number of atomic bases forming the said crystal. All permitted $\underline{k}$ vectors belong to the **first Brillouin zone**, filling it at an average density of $\mathbf{D} = 1/(2\pi)^3$ per crystal of a unity volume. (Recall that the first Brillouin zone is the Wigner–Seitz unit cell of the crystal **reciprocal lattice**). Each $\underline{k}$ vector orientation is perpendicular to a particular crystal plane family. The angular vibrational frequency dependence on $\underline{k}$ is called a **dispersion function**. Each free base mode frequency ω_0 generates a different dispersion function. The latter issue will be elaborated upon shortly.

To achieve further insight concerning the physical role of the wave-vector $\underline{k}$, recall that $|\underline{k}| = 2\pi/\lambda$, where λ is the wavelength. Also note that in a normal crystal vibration, all $q_{\underline{x}}$'s belonging to a single-crystal plane, which is parallel to the wave front, vibrate at a common phase (Eq. (2.52)). In the $\underline{k} = 0$ limit, the normal coordinates of *all* crystal atomic bases vibrate at the same frequency and same phase. We denote by d the interplanar distance. We further denote by $\underline{d}$ the d-long vector perpendicular to the said crystalline planes. Now assume a particular case where $\lambda = 2d$; then $|\underline{k}| = \pi/d$. If $\underline{k}$'s orientation coincides with that of $\underline{d}$, the normal coordinate of the n-th plane past any selected plane relate to the selected one by the relation $e^{i\underline{k}\cdot n\underline{d}} = e^{in\pi}$ factor. The latter equals $+1$ for an even n and -1 for an odd n. Then, $q_{\underline{x}}$ reverses sign between adjacent planes. We now denote by a the interplane distance in a *major direction* of the first Brillouin zone; it is a direction perpendicular to a Brillouin zone-defining edge plane. Notably, a $|\underline{k}| = \pi/a$ value occurs at a singular point on each edge plane (surface). Other allowed $|k|$'s must be smaller than π/a (hence λ longer than $2a$) to be included inside the first Brillouin zone.

Figure 2.54 demonstrates the relative vibrational interplane phases for three representative $|k|$ values: $k = 0$, $0 < k < \pi/a$, and $k = \pi/a$.

Due to the fact that crystal vibrations may be described as coherent whole-plane vibrations, the interplane interaction constants may be obtained by summing the individual inter-base ones $C_{\underline{s}}$. The resulting constant reads $\overline{C}_p$, where the p subscript is an ordinal distance from an arbitrarily selected plane. The $\overline{C}_p$ constant depends on the $\underline{k}$ wave-vector orientation, but not on its length $k \equiv |\underline{k}|$. The **dispersion function** $\omega(k)$ then satisfies

$$\omega^2(\underline{k}) = {\omega_0}^2 + \sum_{p=1}^{\infty} 2\overline{C}_p(1 - \mathbf{cos}\, pka) \tag{2.67}$$

The vibrational frequency now depends on $\underline{k}$'s both direction and length. Practically, only a limited number

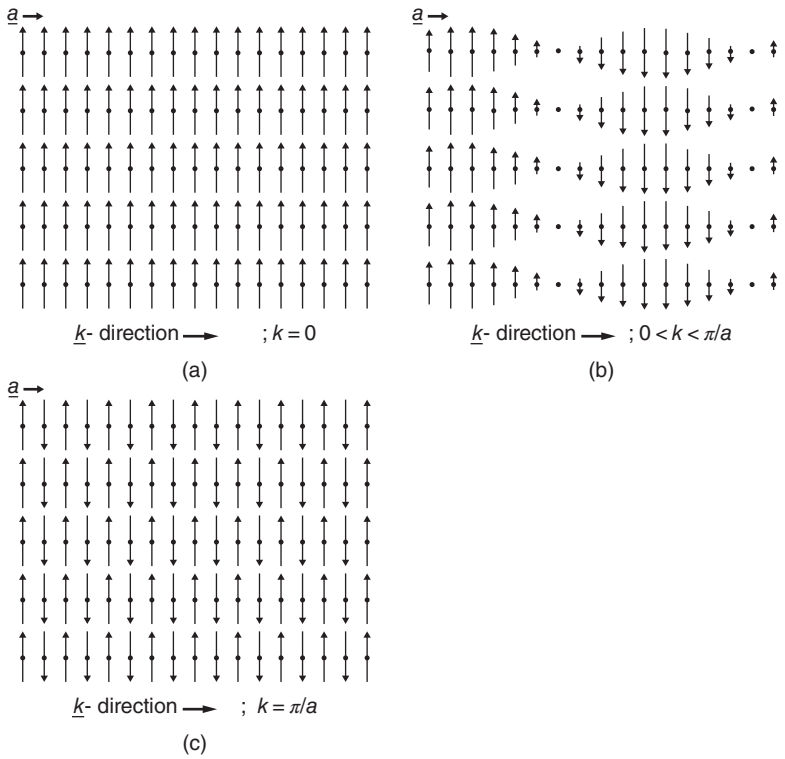

Figure 2.54 Temporal snapshots of the atomic base normal mode states for different crystalline vibrational mode states. Tiny dots indicate crystal lattice points; arrows indicate the vibrational $q_{\underline{x}}$ values.

of addends, those of smallest p's, need to be calculated in the infinite summation of Eq. (2.67), as interaction with far planes diminish. If all $\overline{C}_p$'s are *positive*, $\omega^2(k)$ is a persistently increasing function for small-valued k's. In the particular case where $\underline{k}$ is oriented in a major direction, k varies between zero and π/a on the Brillouin zone edge. The function $\omega(k)$ then varies between a minimum $\omega_{min}(0) = \omega_0$ to a maximum, satisfying ${\omega_{max}}^2 = \omega^2(\pi/a) = {\omega_0}^2 + \sum_{p=1}^{p_{max}} 2\overline{C}_p(1 - \mathbf{cos}\, p\pi)$. Since $\mathbf{cos}\, p\pi = (-1)^p$, one obtains ${\omega_{max}}^2 = {\omega_0}^2 + \sum_{p=1,3,\cdots}^{p_{max}} 4\overline{C}_p$. If, on the other hand, all $\overline{C}_p$'s are negative, $\omega^2(k)$ is a persistently decreasing function of k between zero and π/a, and the "minimum" and "maximum" terms are exchanged.

2.4.2.3 Acoustic Modes

Translational modes of a "free" base, exhibit, like a free molecule, a null vibrational frequency $\omega_0 = 0$. Their crystalline descendents are called **acoustic modes** or **acoustic branches**. Their dispersion functions are of the form

$$\omega^2(k) = \sum_{p=1}^{p_{max}} 2\overline{C}_p(1 - \mathbf{cos}\, pka) \tag{2.68}$$

and correspondingly, ${\omega_{max}}^2 = \sum_{p=1,3,\cdots}^{p_{max}} 4\overline{C}_p$. For analysis of the $\omega(k)$ curve we take the derivative of the two sides of Eq. (2.68). We recall that the slope of the $\omega(k)$ curve $v_g \equiv d\omega/dk$ is also the wave **group velocity** and get

$$v_g = \frac{a}{\omega} \sum_{p=1}^{p_{max}} p\overline{C}_p\, \mathbf{sin}\, pka \tag{2.69}$$

In the $k = \pm\pi/a$ limits of a major direction (Brillouin zone opposite edges), $v_g = 0$. Thus, at these ends the $\omega(k)$ curves flatten to achieve a zero slope. For $|k| \ll \pi/a$, we write

$$\omega^2(k) = 4\sum_{p=1}^{p_{max}} \overline{C}_p\, \mathbf{sin}^2 \frac{1}{2} pka \underset{|k| \ll \pi/a}{\cong} k^2a^2 \sum_{p=1}^{p_{max}} p^2\overline{C}_p \tag{2.70}$$

Thus at these ends, the $\omega(k)$ curves exhibit a constant slope, equally representing the group and phase velocities, v_g and v_φ, respectively:

$$v_g = v_\varphi = \omega/k = a\sqrt{\sum_{p=1}^{p_{max}} p^2\overline{C}_p} \tag{2.71}$$

This constant phase velocity is actually the *sound propagation velocity* in crystalline mediums, which is the reason for the name "acoustic" provided to these branches.

Some special cases of crystal vibrations allow special classifications. Recall that each allowed $\underline{k}$ *orientation* defines a crystal plane family perpendicular to it. When the normal mode coordinates $q_{\underline{x}}$ are simultaneously *parallel* to the said crystal plane family and are equal at

all $\underline{x}$ lattice points belonging to an individual plane, the vibrations are classified as **shear waves**, or **transverse acoustic waves**, abbreviated as TA modes. Each $\underline{k}$ orientation exhibits two basic transverse mode dispersion functions based on the two basic independent orientations in the said family of planes. When the normal mode coordinates $q_{\underline{x}}$ are simultaneously *perpendicular* to the said crystal plane family (i.e. co-oriented with $\underline{k}$), and are equal for all $\underline{x}$ lattice points belonging to an individual plane, the vibrations are classified as **longitudinal acoustic waves**, abbreviated as LA modes. Thus, a longitudinal dispersion function is unique to a $\underline{k}$ orientation. Figure 2.55 provides a demonstration of these two-type acoustic waves; the letter $\xi \equiv q/\sqrt{M}$ stands for the normalized base deviations from their equilibrium positions, where M is the natural atomic base mass. Description of the coupling constants may also be modified to resemble usual spring constants as $K_{\underline{s}} = C_{\underline{s}}/M$. Coupling constants for transverse (shear) waves are usually smaller than for longitudinal waves. Correspondingly, wave frequencies for the same $\underline{k}$ vector are smaller for the formers compared to the latter. Figure 2.56 provides a schematic description of transverse and longitudinal acoustic dispersion functions along a major direction of the first Brillouin zone; the dispersion of the longitudinal and transverse optical waves related to vibration of a same atomic bases is illustrated in Figure 2.57.

2.4.2.4 Optical Modes

Crystalline waves that are vibrational motion descendents of $\omega_0 \neq 0$ are called **optical modes**. The parent modes are vibrational modes of the "free" atomic basis and its crystalline librational ones. Their dispersion functions follow Eq. (2.67), and like the acoustic modes, their slope (group velocity) at the $k = \pi/a$ edge of the Brillouin zone in a major direction is zero. For assessing the slope (group velocity) at $k = 0$, one rewrites Eq. (2.67) in the form

$$\omega^2(\underline{k}) = {\omega_0}^2 + 4\sum_{p=1}^{p_{max}} \overline{C}_p \,\mathbf{sin}^2 \frac{1}{2} pka$$

$$\underset{k \ll 1/p_{max}a}{\cong} {\omega_0}^2 + k^2 a^2 \sum_{p=1}^{p_{max}} p^2 \overline{C}_p \qquad (2.72)$$

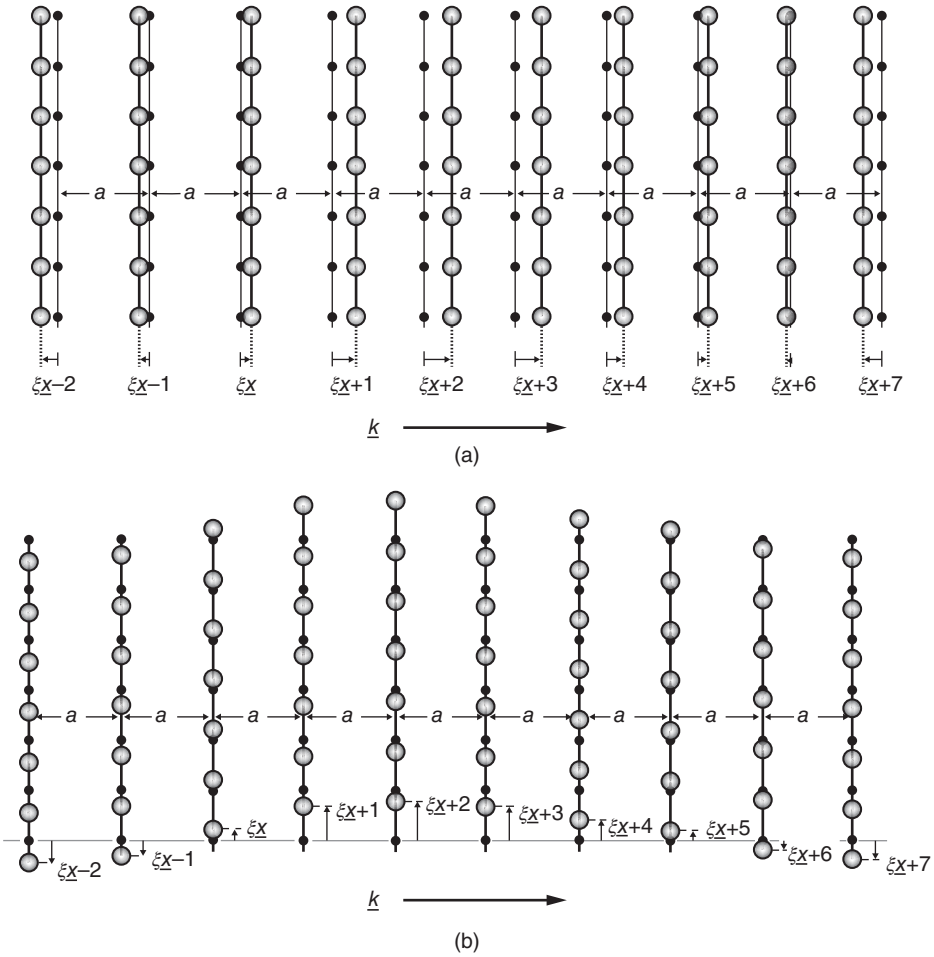

Figure 2.55 Graphic representation of acoustic vibration modes: (b) transversal modes (TA) and (a) longitudinal modes (LA).

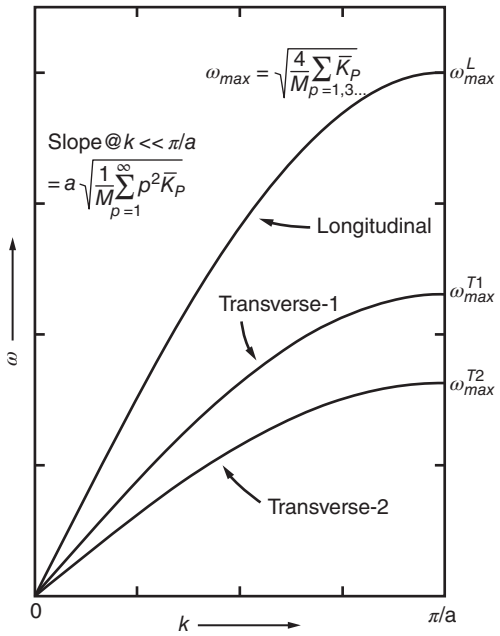

Figure 2.56 Schematic illustration of transverse and longitudinal dispersion functions in a crystal without frequency degeneracy between the modes. The "Transverse-1" and "Transverse-2" labels relate to the transverse shearing of the crystal planes in two independent directions.

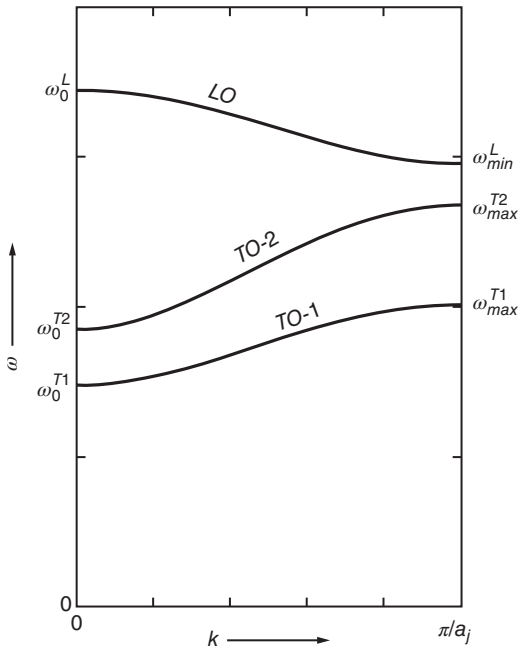

Figure 2.57 Schematic illustration of optical transverse and longitudinal dispersion functions belonging to the same "mechanical" vibration of the atomic basis. The "TO-1" and "TO-2" labels relate to the two non-degenerate transverse optical vibrations. The interplanar distance a_j might also be different for different major j.

Taking the derivatives of both sides yields

$$\frac{d\omega}{dk} \cong k\frac{a^2}{\omega_0}\sum_{p=1}^{p_{max}} p^2\overline{C}_p \Rightarrow \left.\frac{d\omega}{dk}\right]_{k=0} = 0 \qquad (2.73)$$

Thus, the optical mode's dispersion functions flatten at both $k = 0$ and $k = \pi/a$ vicinities, along a major direction of the first Brillouin zone.

Optical modes differ from acoustic ones by lack of movement of their mass center during vibration. On the other hand, most mode vibrations generate electrical dipole moments. Crystal vibrational waves propagating in a dipole direction are called **longitudinal optical modes**, abbreviated as LO modes. Vibrational waves propagating perpendicularly to a dipole direction are called **transverse optical modes**, abbreviated as TO modes. Equation (2.58) suggests that both mode frequencies converge to the common ω_0 value at $k = 0$. The experimental evidence, however, shows that LO modes are always higher than TO ones. This effect is attributed to softening of the TO vibrations due to a collective crystal response of its entailing polarization. The always-positive difference $\omega_0^L - \omega_0^T$ between the LO and TO frequencies at $k = 0$ is called **LO–TO splitting**.

To allow some visualization of the "major directions" concept in a Brillouin zone, in Figure 2.58, we show a three-dimensional image of the first Brillouin zone belonging to a face-centered cubic crystal. Notably, this zone itself is a Wigner–Seitz primitive cell of a mathematical body-centered lattice. The $\hat{\mathbf{i}}$, $\hat{\mathbf{j}}$, and $\hat{\mathbf{k}}$ vectors indicate a right-handed Cartesian unit basis vectors. The zone's polyhedral shape exhibits eight hexagonal faces and six square ones. Thus, there are four symmetry-identical

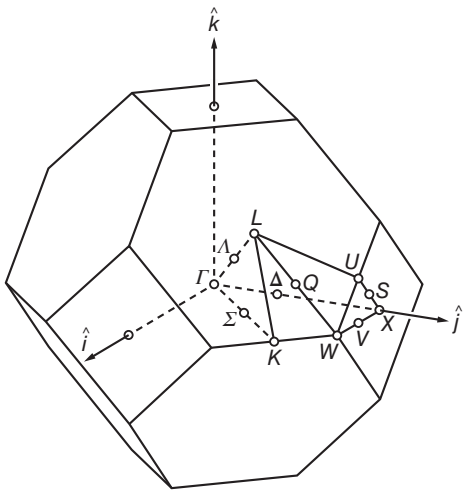

Figure 2.58 First Brillouin zone image of a face-centered cubic crystal (also the Wigner–Seitz primitive unit cell of a mathematical body-centered lattice).

$\Gamma-\Lambda-L$ major directions perpendicularly to the hexagonal faces and three symmetry-identical $\Gamma-\Delta-X$ ones perpendicularly to the square faces. The points marked inside the volume and on the surfaces are of special interest. Particularly, The Γ letter marks the zone center, belonging to the $k=0$ wave-vector. X marks the center point on a square surface. L marks the center point on a hexagonal surface. W marks the crossing point among two adjacent hexagonal faces and their adjacent square surface. Particularly, the $\Gamma-\Lambda-L$ orientation coincides with one of the four cubic crystal (111) directions; the $\Gamma-\boldsymbol{\Delta}-X$ orientation coincides with one of the three (100), (010), or (001) directions. We will not elaborate on the meanings of the other marked special points.

In Figure 2.59 we show crystal vibrational waves dispersion functions for the bi-atomic gallium arsenide GaAs crystal measured using inelastic neutron scattering [S65]. The crystal belongs to the cubic "Zinc Blende" structure: face-centered, #216 space group T_d^2 ($F\bar{4}3m$). Materials exhibiting the same structure are, for example, ZnS, ZnSe, ZnO, and CdTe. The face-centered cubic unit cell contains four formula units; a natural primitive unit cell thus contains just a single formula unit. The Brillouin zone is correspondingly body centered. The figure shows the frequency as function of wave-vector when the latter varies along the Λ points in the ΓL direction and along the $\boldsymbol{\Delta}$ points in the ΓX direction. The waves belonging to these lines may be properly classified as either purely transverse or purely longitudinal. In any other orientation, the wave is always of a mixed nature. The transverse waves, either acoustical or optical, are each doubly degenerate. An interesting frequency inversion between LO and TO modes occurs near both L and X Brillouin zone edges. It is attributed to a considerable covalent nature of the Ga–As bonding. Similar shapes obtain for all Zinc Blende structures, obviously with different frequency scales, and LO–TO frequency inversions. The LO frequency at the Γ point establishes a crystal cutoff vibrational frequency $\omega_{co}=55.23\times10^{12}$ rad/s, equivalent to a phonon energy of 293 cm^{-1}.

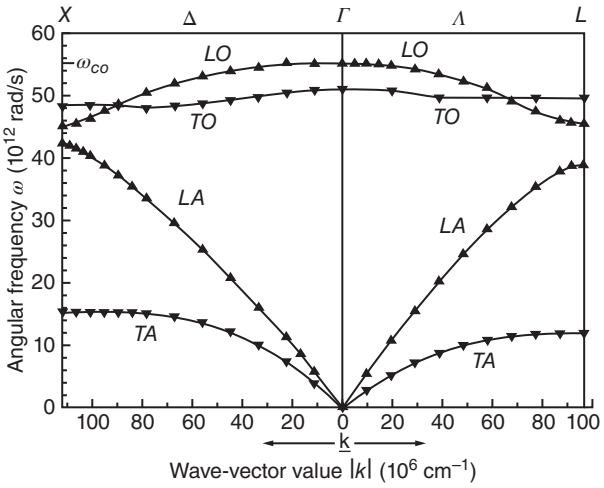

Figure 2.59 Phonon dispersion curves in GaAs along major symmetry directions measured at 12 K.

As demonstrated above, the ω vs. $\underline{k}$ dispersion curves exhibit gaps along the ω axis, called **forbidden gaps**. In ceramics of large number of atoms occupying a primitive unit cell, the number of dispersion curves is correspondingly large. Overlap among curves along different directions occurs often. Thus the number of forbidden gaps turns small, spanning only a small portion on the frequency axis between zero and ω_{co}.

Qualitative considerations allow the assessments of vibrational frequency differences among compounds of similar structure. Recall that a harmonic oscillator composed of two masses M_1 and M_2, which are bonded by a spring of constant K, vibrates at an angular frequency $\omega=\sqrt{K/\mu}$, where $\mu=M_1M_2/(M_2+M_2)$ is the reduced mass. The frequency is thus proportional to the square root of K and inversely proportional to the square root of μ. For different compounds of similar valence components, a similar spring constant K may be assumed. Since for heavier atoms the reduced mass is larger, ω turns smaller. A most simple example is a comparison between the optical bands of silver chloride AgCl and silver bromide AgBr crystals [F15]. In the former, $\omega_0^{TO}=117.5$ cm^{-1} and $\omega_0^{LO}=194.5$ cm^{-1}. In the latter, $\omega_0^{TO}=89.1$ cm^{-1} and $\omega_0^{LO}=139.3$ cm^{-1}. The shift is obviously correlated to the heavier 79.91 amu bromine Br atomic mass, compared to the lighter 35.45 amu chlorine Cl atomic mass. A less obvious comparison relates to different metallic oxides composed of larger number of atoms. For example, the yttria Y_2O_3 lattice includes yttrium atoms, which are heavier (88.9 amu) than, say, the magnesium Mg and aluminum Al atoms (24.31 and 27.0 amu, respectively) in the spinel $MgAl_2O_4$ lattice; therefore the latter exhibits a set of higher vibrational frequencies. Sulfur S atoms are about twice heavier than oxygen O ones (32.06 and 16.0 amu, respectively). Therefore, sulfide crystals exhibit lower frequencies than their analog oxide compound ones.

Generally, cutoff frequencies may be as high as 2000 cm^{-1} in hard crystals (wavelength 5 μm) and as low as 200 cm^{-1} in soft ones (wavelength 50 μm). Ceramic materials are usually oxides, and quite hard, thus exhibit these optical effects in the MIR region. The cutoff frequency establishes the low-frequency (long wavelength) limit of the transparency window.

The involvement of electrical dipoles, especially in the optical vibrational modes, provides a strong interaction with electromagnetic radiation. The interaction expresses itself by bulk absorption, but primarily by

causing strong **surface reflection bands** between vibrational LO and TO mode frequencies at the Γ point. It is accounted for by the **independent oscillator model** through the oscillators' contributions to the dielectric functions by

$$\varepsilon'(\omega) = \varepsilon(\infty) + \sum_j \frac{\varepsilon_j(\omega_{LO,j}^2 - \omega_{TO,j}^2)\,(\omega_{TO,j}^2 - \omega^2)}{(\omega_{TO,j}^2 - \omega^2)^2 + \gamma_j^2\,\omega^2} \tag{2.74}$$

$$\varepsilon''(\omega) = \sum_j \frac{\varepsilon_j(\omega_{LO,j}^2 - \omega_{TO,j}^2)\,\gamma_j\,\omega}{(\omega_{TO,j}^2 - \omega^2)^2 + \gamma_j^2\,\omega^2} \tag{2.75}$$

where $\varepsilon'(\omega)$ and $\varepsilon''(\omega)$ are the real and imaginary parts of the dielectric functions, respectively, at the ω angular frequency. $\omega_{LO,j}$ and $\omega_{TO,j}$ are the LO and TO angular frequencies, respectively, γ_j is the damping parameter, and ε_j is a dielectric constant, all of the j-th oscillator. $\varepsilon(\infty)$ is the dielectric constant (function) at frequencies that are considerably greater than the optical LO cutoff frequency of the lattice vibrations but are considerably smaller than the matrix lowest atomic transition frequency. The related real n and imaginary κ parts of the refractive index are given by

$$n^2 = \frac{1}{2}\sqrt{\varepsilon'^2 + \varepsilon''^2} + \frac{1}{2}\varepsilon' \tag{2.76}$$

$$\kappa^2 = \frac{1}{2}\sqrt{\varepsilon'^2 + \varepsilon''^2} - \frac{1}{2}\varepsilon' \tag{2.77}$$

The surface reflection R is then given by

$$R(\omega) = \frac{|n - 1 + i\kappa|^2}{|n + 1 + i\kappa|^2} \tag{2.78}$$

Figure 2.60 provides a calculated demonstration of an optical front-surface reflection band occurring in a dielectric material involving a single oscillator, between $\omega_{LO} = 1200\,\text{cm}^{-1}$ and $\omega_{TO} = 1000\,\text{cm}^{-1}$. The calculation assumed a matrix high-frequency dielectric constant $\varepsilon(\infty) = 3.5$ and a vibrational frequency width (damping factor) $\gamma = 35\,\text{cm}^{-1}$. In real materials, several oscillators of different LO and TO angular frequency exist, producing several, sometimes partially overlapping reflections.

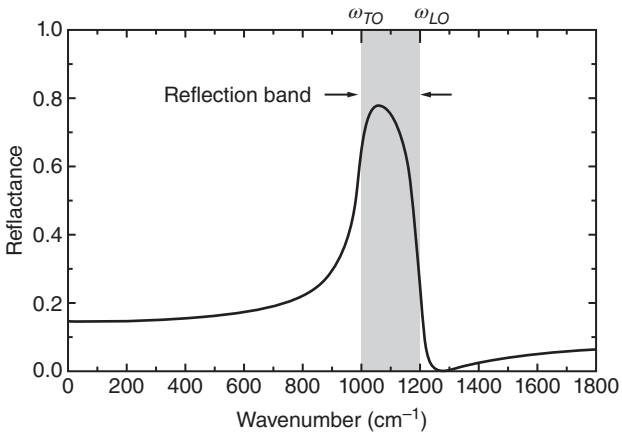

Figure 2.60 Calculated optical front surface reflectance of a dielectric crystal at normal incidence of the electromagnetic radiation.

Notably, in optical transmission measurements through parallel plates, the involvement of both front and back surface reflections may be erroneously interpreted as absorption. Thus, such absorption measurements in the FIR should be complemented with reflection measurements, to be corrected against.

Electromagnetic radiation in the FIR interacts primarily with optical phonons, strongly so when the bonding is at least partially ionic. The interaction involves only near-zero wave-number phonons (Γ-point; $k = 0$). The reason is that resonance between the two-type waves requires not only matching between quanta *energies* (photon and phonon) but also matching of *wavelengths*. Near-visible photon wavelengths are of the order of 1.0 μm, namely, $k_{photon} \approx 2\pi \times 10^4\,\text{cm}^{-1}$. The k_{phonon} values span a range between zero and $\pi/a \approx \pi \times 10^8\,\text{cm}^{-1}$. In that range, interacting phonons are indeed "near-zero" on the wave-vector scale.

Optical selection rules on phonon transitions require that $\Delta v \equiv v_2 - v_1 = \pm 1$ (positive for absorption, negative for emission), where v is the phonon occupation number. Non-harmonic interaction potentials like the Morse one (Eq. (2.61)) provide some fine-tuning of the theory. Several same-phonon excitations, called **vibrational overtones**, while very weak, may often be resolved. Combinations of different phonon energies and modes like longitudinal and transverse, acoustic and optical, are also sometimes resolved. In all such cases, the phonon wave-vectors $\underline{k}$ sum up to match the exciting photon one, namely, to near-zero on the phonon wave-vector scale. Obviously, the absorbed photon energy matches the sum of all generated phonons.

The multi-phonon transitions, overtones, and combinations express themselves as wiggling and small peaking in high-frequency tails of the material absorption spectrum. For demonstration, in Figure 2.61 we show experimental results obtained in the absorption coefficient measurements of a polycrystalline (ceramic) ZnS parallel plate [K26]. The material was produced by **chemical vapor deposition** (CVD) complemented by **HIPing**. The cutoff frequency of $350\,\text{cm}^{-1}$ belongs to the LO mode vibration. The large absorption coefficient at $350\,\text{cm}^{-1}$ extends to lower frequencies; it is actually an artifact, resulting from the surfaces reflection bands below ω_{LO} frequency (Figure 2.61). Structure at higher wave-numbers emanates from vibrational overtones

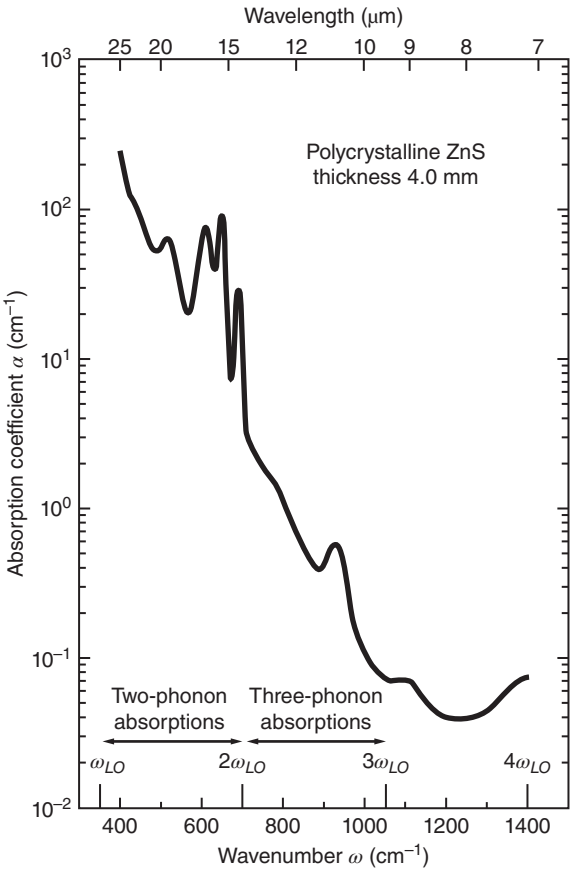

Figure 2.61 Semi-logarithmic plot of room temperature absorption coefficient vs. wave-number of a polycrystalline, 4 mm thick ZnS plate.

and combination absorptions imposed on top of the tail of that "fake" large absorption. They are usually not observable on a linear ordinate scale. Interpretation of the specific modes involved in the structure is quite difficult and often highly speculative [U5].

In Figure 1.2 we showed optical transmission spectra of several different ceramic materials. All exhibit broad optical transmission "windows," for example, in ZnSe between approximately 0.5 and 20 μm and in spinel $MgAl_2O_4$ between approximately 0.2 and 4.0 μm.

2.5 Thermal Emissivity

Due to some even slight light absorption, the temperature of a transparent ceramic correspondingly increases. The ceramic sample must then involve in electromagnetic radiation emission; otherwise its temperature would increase to infinity. An extreme case occurs for a black body that absorbs all incident radiation. A black body typical emission intensity and spectrum depends solely on its temperature and is given by

$$F_{BB}(\lambda, T) = \frac{2\pi hc^2}{\lambda^5} \cdot \frac{1}{\exp\left(\frac{hc}{\lambda k_B T}\right) - 1} \tag{2.79}$$

where $F_{BB}(\lambda, T)$ is the emitted electromagnetic radiation per unit area per unit wavelength. The spectral dependence is demonstrated in Figure 2.62 for several absolute temperatures.

The spectra demonstrate quite different behaviors in the long and short wavelength regions of the spectrum. It may be straightforwardly seen that

$$F_{BB}(\lambda, T) \cong \begin{cases} \frac{2\pi c}{\lambda^4} k_B T & hc/\lambda k_B T \ll 1 \\ \frac{2\pi hc^2}{\lambda^5} \exp(-hc/\lambda k_B T) & hc/\lambda k_B T \gg 1 \end{cases} \tag{2.80}$$

Thus, in the very long wavelength range, the energy density of the black body emission reduces with increasing wavelength. On the other hand, in the very short wavelengths range, the energy density of the black body emission increases with increasing wavelength. This behavior suggests that the energy density exhibits a maximum at some wavelength, to be denoted by λ_{peak}. The energy density increases with temperature for all wavelengths. The peak wavelength decreases with temperature, satisfying what is known as **Wien's displacement law**:

$$\lambda_{peak} \cdot T = Const. = 0.2014 \frac{hc}{k_B} = 0.2898 \text{ cm K} \tag{2.81}$$

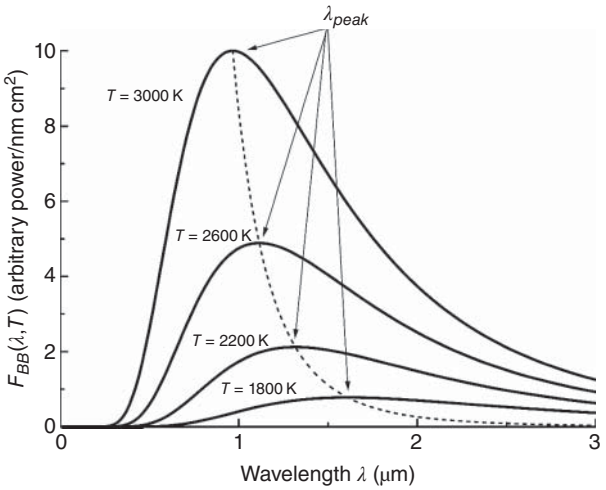

Figure 2.62 Black body radiation spectra at different temperatures. The spectra demonstrate both peak displacements toward shorter wavelengths and increase in total emission with temperature.

The entire emitted power density $\Phi_{BB}(T)$ is proportional to the fourth power of the absolute temperature by an expression known as the **Stefan–Boltzmann law**:

$$\Phi_{BB}(T) = \left[\frac{2\pi^5 {k_B}^4}{15c^2h^3}\right] \cdot T^4 = \sigma_{SB} T^4 \tag{2.82}$$

The proportionality constant; the **Stefan–Boltzmann constant**, is $\sigma_{SB} = 5.67 \times 10^{-5}$ erg/(s cm^2 K^4).

Real bodies, transparent ceramics included, could be considered "black" only approximately and are never ideally black. Thermal emission of a real body is always smaller than of an ideal black body, yet it is quite similar in many respects. It may be often expressed as

$$F(\lambda, T) = \varepsilon(\lambda, T) F_{BB}(\lambda, T) \tag{2.83}$$

The $\varepsilon(\lambda, T)$ quantity is termed **emissivity** and in principle depends on the wavelength and temperature. It is always smaller than a unity, it is a characteristic material parameter, and to a large extent it depends on the material surface conditions. Surface polishing of a solid body always reduces the emissivity, and surface roughening increases the emissivity. Experimental evidence shows that for most solid materials the emissivity spectral and temperature dependences are quite moderate. For many practical needs, it may be safely assumed that the emissivity is constant over a broad range of wavelengths. In a moderately absorbing transparent material that is shaped as a surface-polished parallel plate, it may be approximated as

$$\varepsilon = \frac{(1-R)(1-e^{\alpha L})}{(1-R\,e^{\alpha L})} \tag{2.84}$$

where R is the sample Fresnel surface reflectance, α is the bulk absorption coefficient, and L is the sample thickness. Note that usually $\alpha L \ll 1$ in a transparent material. For an emissivity $\varepsilon \sim 0.1$ at 350 K a thermal emission power of about 8.5 mW/cm^2 may be calculated.

2.6 Color of Solids

2.6.1 Quantitative Specification of Color

Color is an important characteristic for many ceramics including the TCs. In the case of the latter visual color, it is important especially for two different groups of products. One is constituted by colored parts that need to match exact specified absorption characteristics. For example, producers of decorative colored products such as watch cases or others (cf. Section 5.2.4) may wish to achieve not simply some general "red," as known from the different variants of natural ruby, but a definite colors mixture that may become a registered brand, as "Chanel № 5" for ladies perfumes. An opposite target has to be attained in the case of security windows, which need to be sensed as colorless; therefore, for them tolerance ranges are defined in relation to "color" deviations. Qualitative description of color is sufficient in some cases, but there are many instances when a quantitative description is needed (e.g. the watch cases manufacturers). The issue of quantitative description of color is briefly treated in this section.

The measurements used for quantitative specification of color are based on its physical, namely, absorptive, origin. The absorption bands are, in most cases, produced by the TM^+ or RE^+ dopants (or impurities) present in the host added. The spectroscopy of doped TCs and its effect on color was and is the subject of many older and current studies. For example, thin transparent discs of sub-micrometer grained α-Al_2O_3 ceramics doped with Fe, Ni, Cr, and Co, respectively, were investigated by Schuster et al. [S17], while that of Nd:$Y_3Al_5O_{12}$ (Nd:YAG) were examined by Kumar et al. [K65] and Aschauer and Bowen [A27]. Colorimetry (viz. quantitative description), which treats color as the visible consequence of selective absorption, is a separate specialization field. A brief review of its main tenets is given below.

On viewing an object illuminated by white light,[3] the reflected or transmitted beam may be felt, by a viewer, to assume a separate color (for example, yellow) as a function of the absorption pattern used for its production:

{1} The object could contain pigments that absorb all components of the visible spectrum, with exception of the yellow range. Then, the reflected or transmitted radiation will contain only this yellow spectral part, with, however, an intensity massively reduced, compared to that of the incident light. Thus, the result will be a very dark yellow, close to gray, hardly attractive for most products.

{2} Alternatively, coloring additives may be selected such that they absorb only in the wavelength range, which is **complementary** to yellow, in the Helmholtz system (Figure 2.63). Thus, with only blue being absorbed, the mixture of all other components is transmitted but is sensed, by the eye, as yellow, now with a level of the reflected or transmitted intensity significantly higher than in the first case.

Thus, since intentionally produced (or inadvertently occurring) colors are caused by selective absorption of

3 "White" is not actually a color, viz. corresponding to a well-defined wavelength, but a mixture of pure colors being the sum light of the VIS spectral domain. Therefore it is called sometimes an achromatic "color." Further complication to the human visual perception of color is that mixtures of pure colors may appear similar to a "pure" color, as a function of the illuminator's characteristics. Thus a "white" paint appears as such under sunlight illumination but assumes the sense of a pure color when illuminated by a source emitting the pure color.

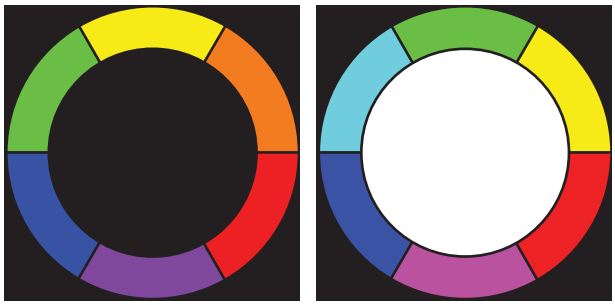

Figure 2.63 Complementary colors at opposing positions of a color wheel (given here in a clockwise spectral sequence of increasing wave lengths from blue to red) for two different color models: (a) Traditional RYB (red-yellow-blue) model based on the *absorption* by pigments in painting colors. (b) The physical (Helmholtz) RGB model based on red, green, and blue *light*.

incoming white light, their formation means associated absorptive losses in certain domains of the VIS transmissive or reflective spectra. In Figure 2.64 the transmission spectra generated by doping thin plates of transparent alumina, and respectively spinel with certain TM^+ type cations is presented; the spectral curves of the undoped hosts are now significantly modified.

Conversion of spectral data to the color they generate (quantitatively specified) is enabled by appropriate software programs, for example, the Color Application Ver. 3.1 of the "Cary WinUV software" applicable to the spectra generated by the Cary 4000 spectrometer (Varian Inc., Mulgrave, Victoria, Australia). Such software provides color quantitative specification based on transmission or reflection data, assuming different standard light sources, and according to different measuring standards (for example, with different observation angles).[4] It is worth recalling, at this juncture, that color is a perception that has two aspects – chromaticity and brightness – and also varies as a function of factors like the angle of viewing. The results of measurements are commonly interpreted based on the Helmholtz red-green-blue (RGB) physical model of color formation, presented as points within the so-called CIE color space (CIE is the acronym of the French "Commission Internationale de l'Eclairage" or the International Commission on Illumination); this space is so defined that a point it contains represents the quantitative specification of a color. The CIE-1931-RGB Color Space and CIE-1931-XYZ Color Space methods were developed by the CIE in 1931 and are still in use; the primary colors chosen reflect the fact that the human eye has three types of sensors, for perception of color in conditions of strong illumination (other sensors work in dim light conditions), each tuned to one of these colors. The basis for that international colorimetry approach are the primary colors red (R) of 700.0 nm, green (G) of 546.1 nm, and blue (B) of 435.8 nm wavelengths, from which most (but not all) other human eye sensed colors can be obtained. Each color is described according to its relative contents of red, green, and blue pure colors. In an improved version the commission replaced the natural RGB colors with a set of virtual primary colors labeled *X*, *Y*, and *Z*; each such color is defined by a specific profile absorption curve, spanning the VIS domain, as shown in Figure 2.57. A given real spectrum is de-convoluted

4 Color perception depends on the observer's field of view. A "CIE 1931 2° Standard Observer" was defined to eliminate this variable. A more recent alternative is the "CIE 1964 10° Standard Observer," which, however, is less frequently used.

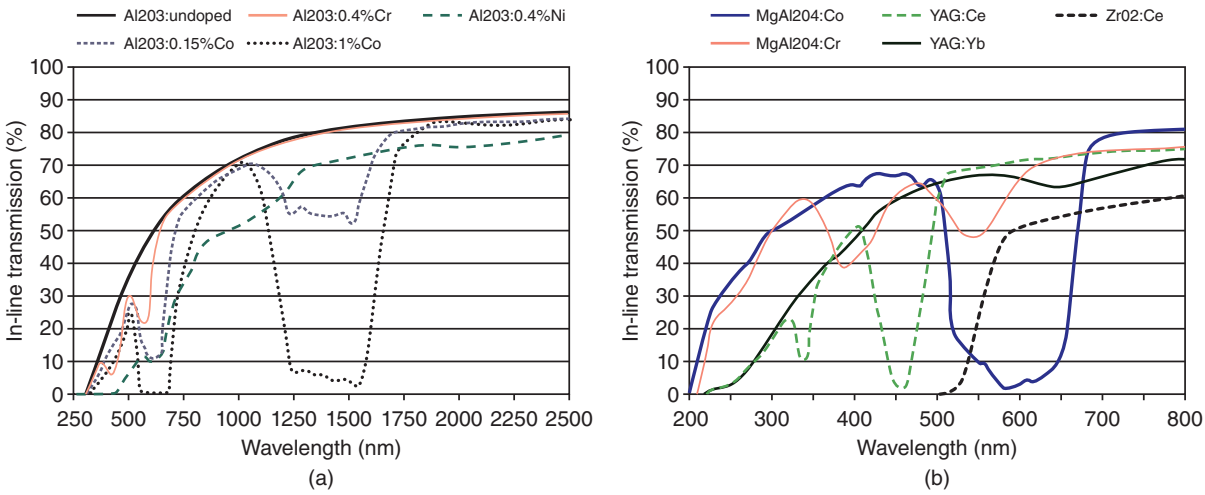

Figure 2.64 Transmission spectra of oxide ceramics with different coloring additives: (a) Sub-µm Al_2O_3. (b) Doped spinel ($MgAl_2O_4$), cubic ZrO_2, and YAG ceramics. Note the substantial loss of total intensity which is associated with coloration.

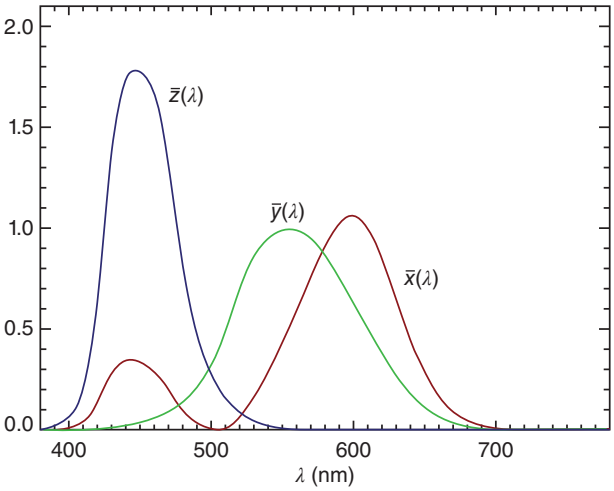

Figure 2.65 CIE 1931 Standard Observer. Virtual color matching functions.

into its virtual X, Y, Z components (Figure 2.65) and the fraction of each component's contribution is calculated.

The tristimulus X, Y, Z values can be converted to a new set of parameters x, y, and z, by normalization to the $X + Y + Z$ sum, viz. x is equal to X divided by the $X + Y + Z$ sum ($x + y + z = 1$). The x, y, and z coordinates define a three-dimensional color space (one of a number of differently defined color spaces now in use) in which, as said above, all colors occupy a point. Thus a convenient and quite rigorous method of quantitatively specifying a color was established. For reasons related to human eyes' cone sensitivity, the Y parameter reflects quite well the brightness of a color (the position in the x,y diagram specifies the chromaticity of the color). In the color space defined right above, a specific combination of red, green, and blue intensities yields per definition a white light of a unity value, and the absence of all colors is by definition black, namely, zero intensity. These features enable one to present the color space in the form of a two-dimensional chromaticity diagram (Figure 2.66), in which the red relative intensity x and green relative intensity y are directly given, and the blue relative intensity z component is simply the difference between the red plus green sum and the unity. The Y quantity is the measure of the color luminance (brightness). Further color spaces were developed in order to respond to the needs of different applications dependent on color. A popular one is that produced by R.S. Hunter called "*L-a-b*." In 1976, the CIE has produced, adapting the original Hunter 1948 color space, a new system abbreviated as "CIE-Lab," as an additional tool, still based on the XYZ-space concept. It provides a more convenient perceptual color characterization. Sometimes, asterisks

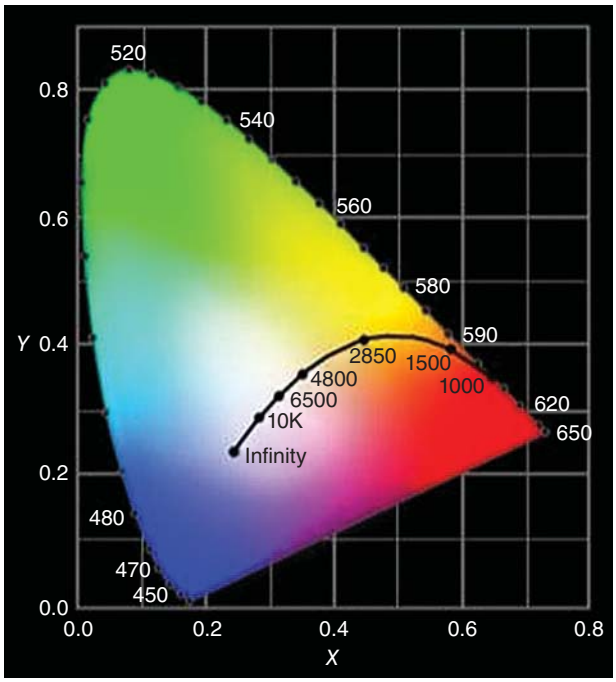

Figure 2.66 CIE 1931 color space chromaticity diagram. The outer curve is the visible spectrum from 380 to 700 nm. The white point (colorless point) is central at $x = y = z = {}^1/_3$. The saturation of colors decreases from the bordering lines toward this white point. The black body curve gives the color temperature of different light sources (e.g. natural daylight: 6774 K at $x = 0.31$, $y = 0.32$; traditional tungsten wire lamp: 2856 K at $x = 0.45$, $y = 0.41$).

are used to distinguish the CIE's L^*, a^*, b^* system from the original Hunter's evaluation, marked LH, aH, and bH. As shown in Figure 2.67, the negative part of the a-axis, in the (a, b) plane, displays the green intensity (expressed between zero and −100).

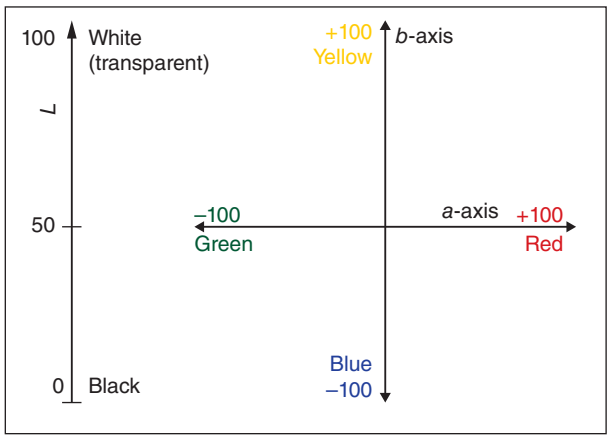

Figure 2.67 *a-b* plane with *L*-scale of the CIE-Lab color space diagram. In three-dimensional presentations, *L* is a third axis positioned at (*a*,*b*) = (0,0); note that *L* = 0 does always mean "black," independent of the actual *a*,*b* values.

The positive branch displays the red component (expressed between zero and +100). Similarly, the *b*-axis negative range displays the blue component intensity, and the positive range displays the yellow component intensity. The *L*-axis, called "lightness" (meaning "brightness"), varies from zero (dark, black) to 100, meaning white, or colorless transparent if, in addition, the chromaticity is $a = b = 0$. The CIE-XYZ and CIE-Lab presentations exhibit a one-to-one correspondence, and each presentation can be readily transformed into the other.

An example, demonstrating the use of these tools for color control of nominally "colorless" transparent spinel $MgAl_2O_4$ ceramics [K30], is offered by the color analysis of transparent spinel fabricated at IKTS-Dresden using undoped, grade S30CR, Baikowski powder. The microstructure, after HIPing, was heterogeneous, including very large grains (result of exaggerated grain growth) dispersed in a fine-grained matrix. It exhibited intragranular, sub-micrometer pores within the largest grains [H46]. Depending on slight variation of the HIPing atmosphere's composition (basically Ar), some of the $MgAl_2O_4$ samples were chemically reduced, showing gray absorption and in some cases an associated slight yellowish taint. Optical transmission spectra, shown in Figure 2.68, clearly document a lower in-line transmission of the darker samples.

Additionally, the different degree and profile of transparency deterioration of the three samples indicates some color variation among those samples. The results of a quantitative color characterization, using the CIE color space (Lab *x,y* diagram), are graphically presented in Figure 2.69, while in Figure 2.70 the colors

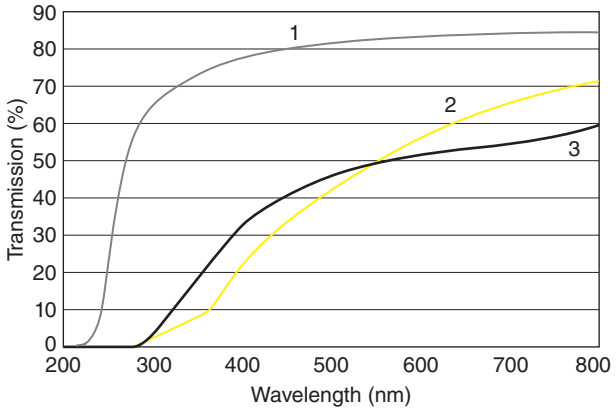

Figure 2.68 In-line transmission spectra of polished $MgAl_2O_4$ spinel discs: The upper curve (1) is the best specimen (thickness $t = 3.7$ mm), whereas the spectrum of a dark-yellow sample (with same thickness of 3.7 mm) is given in yellow (curve 2). The dark curve (3) was obtained from a thinner gray sample ($t = 2.9$ mm; at equal thickness this spectrum would be below that of the yellow specimen).

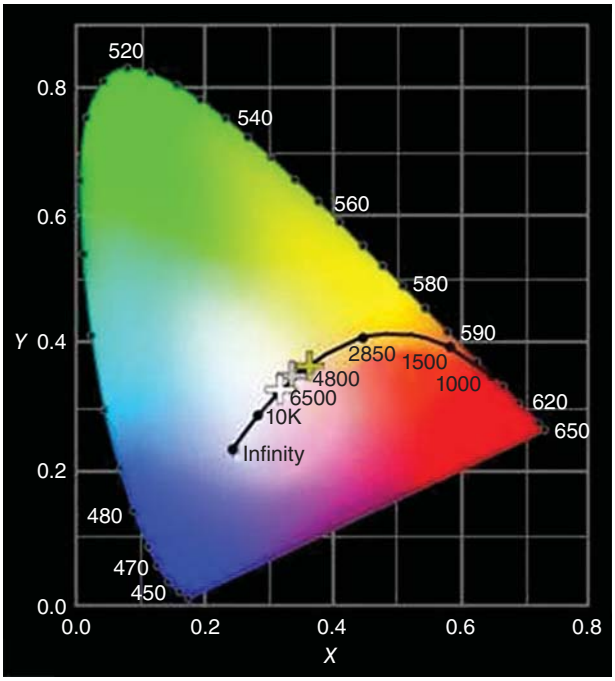

Figure 2.69 Position of color of the transparent spinel discs of Table 2.8 in CIE x,y color space, calculated for standard light D65 and 2° observation angle: The color of the clear reference sample A of Table 2.8 is represented by the white cross (most left) in this figure; it corresponds with spectrum 1 in Figure 2.68. Here, the gray (central) cross represents the specimen B (gray) of Table 2.8 with spectrum 3 of Figure 2.68. Specimen C (dark yellow) of Table 2.8 is represented in this figure by the yellow cross (most right) and by spectrum 2 of Figure 2.68.

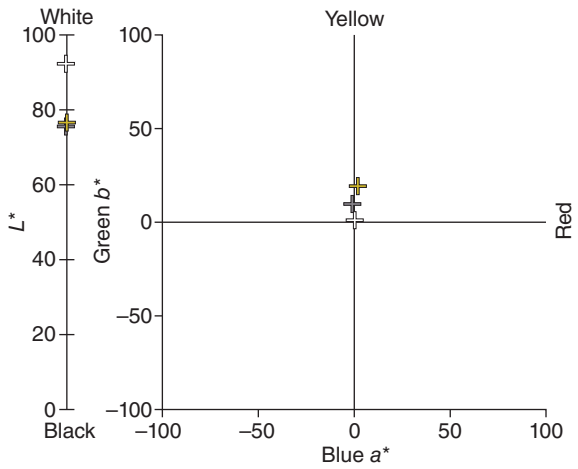

Figure 2.70 Position of transparent spinel samples in CIE-Lab color space for CIE standard light D65 and the 2° observation angle of Table 2.8. On L*-axis, specimen A (standard) occupies the highest and B (gray) the lowest position; C (dark yellow) is just slightly above B. In the 2-dimensional field, specimen A is represented by the white central cross, B (gray) by the dark cross above that of A, and C (dark yellow) by the uppermost cross in this figure.

Table 2.8 Color data of individual spinel samples obtained from transmission spectra (Figure 2.68) for CIE standard light D65 and 2° observation angle.

	A (standard)	*B* (gray)	*C* (dark-yellow)
Tristimulus			
X	77.9287	48.4221	48.1703
Y	82.0163	48.0224	40.0758
Z	88.8432	44.1804	38.7341
Chromaticity			
x	0.3158	0.3327	0.3571
y	0.3323	0.3508	0.3705
z	0.3510	0.3168	0.2723
Hunter Lab			
*L*H	00.5820	69.0445	70.8938
*a*H	−0.0449	−0.2075	1.8517
*b*H	0.9408	4.5300	8.7251
CIE-Lab			
L^*	02.5821	75.4030	76.0544
a^*	−0.0418	−0.2107	1.8830
b^*	1.7217	0.5162	10.4752

are presented on a Hunter format; in numerical form the color coordinates are given in Table 2.8. Compared with Figure 2.69, the plot in Figure 2.70 demonstrates more directly (i) the similar degree of dark haze in *B*- and *C*-noted sample discs and (ii) the presence of some yellow in both; the data of Table 2.8 shows that even the best (looking most clear to the observer) "standard" A-sample does not exactly match the colorless $x = y = 1/3$ point.

Similarly, as in Figure 2.69, the positions shift in the CIE chromaticity diagram, as a function of what was described by Hu et al. for transparent Ce, Gd : $Y_3Al_5O_{12}$ (Ce,Gd:YAG) [H44]. However, whereas CIE characterization has become a common tool in porcelain business [B12] and also widely used for glass-ceramics industry and adopted in dentistry [V10], so far other branches of the ceramic community have taken only little notice of colorimetric tools. For example, over the 10 years of the international "Advances in Ceramic Armor" symposia, CIE characterizations have been addressed first as late as in 2015, still limited to armor glass composites [A5]. That limited interest seems strange, since inadvertent coloration effects are known to occur more often in newly emerging transparent ceramics. Most probably, acceptance of standard CIE characterization is expected to grow rapidly on further optical quality improvement and increased availability of transparent ceramics.

2.6.2 Coloration Mechanisms: Coloration Based on Conductive Colloids

The major part of Section 2.6 dealt with the issue of quantitative color specification. This part of the section is concerned with a listing of coloration mechanisms. The main mechanism is selective light absorption, by transition metal and rare-earth cations (intentional dopants or inadvertent impurities) hosted in a transparent ceramic lattice. This is a complex topic and is discussed in detail fully in Section 2.3.5.2.1. Here we present two other color-generating mechanisms that while more relevant for glass operate, in some cases, also in ceramics (e.g. Cu-doped YAG). Let us note that what is relevant for glass is indirectly relevant for ceramics because, lately, TCs can be fabricated also by full-glass crystallization (see Section 3.1.4). Other coloration mechanisms, for instance, the wavelength dependence of EMR scattering, also do exist; some of them will be discussed where appropriate.

The chromophores discussed here are nanometric particles of electrically conductive materials: metals (of most interest here) or semiconductors. These materials exhibit low solubility in oxides and thus easily separate as second phases; when such particles are nanometric they tend to adopt a spherical shape under the effect of surface tension.

The fact that both light absorption and scattering are involved in the EMR interaction with metal colloids is taken care of, in the calculations, by using a complex refractive index:

$$n(\lambda) = N(\lambda) + i\mathrm{K}(\lambda) \tag{2.85}$$

The real part $N(\lambda)$ quantifies the scattering, and the imaginary part $\mathrm{K}(\lambda)$ quantifies the absorption. Both depend on the incident light wavelength; they are known as the optical constants of the metal. Solving the Maxwell equations for the conditions defined by Mie (his theory allows to calculate scattering produced by conductive small scattering units), one can get expressions linking the optical constants of the metal (N, K) and the refractive index of the matrix (N_g if the matrix is a glass) to "efficiency factors" Q. These factors describe the proportions of incident light scattered(Q_{scat}) and respectively absorbed (Q_{abs}) by the metal particle. The total attenuation (extinction) can be expressed as a sum ($Q_{att} = Q_{scat} + Q_{abs}$) of the formerly defined partial factors because the scattered and absorbed fractions are supposed to be independent. The expressions of the efficiency factors are not discussed here, but using them, one can say that coloration will be seen if the absorption efficiency factor Q_{abs} is significantly larger than the scattering efficiency factor Q_{scat}, if the K is large and the $\mathrm{K}(\lambda)$ function varies sufficiently strongly with

wavelength, in the visible (VIS) region. The K of metals is large, close to 1, but the variation in the VIS region is, for most of them, small. Au, Ag, and Cu constitute an exception and their $K(\lambda)$ varies significantly in the VIS. A large ratio between scattering and absorption intensity exists, however, only when the particles size "a" is smaller than about 50 nm; this because Q_{abs} varies in proportion to $1/a^4$, while Q_{scat} is proportional to a. Thus in the case of the three metals mentioned when they appear as small particles, they produce spectra, the curves of which show band-type features; if particles grow bigger, the scattering process dominates and the bands disappear, leaving an absorption profile corresponding to achromatic gray or black tints. The coloration physical mechanism, leading to the large Q_{abs} , is absorption of light, at the narrow resonance frequency domain of the surface plasma, which exists in the confining environment constituted by a nanometric metal particle.

It is usual in spectroscopy to use the parameter optical density (OD) instead of the internal transmission, which considers only the loss of radiation intensity occurring inside the specimen (owed to absorption and scattering). So the OD, which of course depends on the wavelength, is defined as $OD(\lambda) = -\log_{10} T_i$ where T_i is the internal transmission. Then the effect of the metal colloids can be described, following the Mie calculations, by Eq. (2.86):

$$OD(\lambda) = \frac{3}{4}\frac{Mt}{a\rho}\log\ [Qatt(\lambda)] \tag{2.86}$$

where M is the total metal particles mass per host volume (g/cm^3 units), t is the sample thickness, a is the particles size, and ρ is a particle's density (g/cm^3 units). Au particles of 30 nm or Cu 20 nm particles generate various red hues; Ag colloid leads to yellowish hues.

Another mechanism operates in the case of certain semiconducting nanometric molecule clusters, called **quantum dots.** Quantum dots, as their name suggests, are quantized systems. They are also very small (<10 nm) (therefore they are sometimes called artificial atoms). In such small systems (they contain a number of atoms varying from 100 to 10^5), a quantum confinement process operates and this make the bandgap width dependent on particle size (inversely proportional to the dot's size). Among other factors, the absorbed light (also emission under suitable excitation radiation) energy depends heavily on the quantum dot's bandgap. For certain semiconducting materials and dot's size, the absorbed photons' frequency belongs to the visible (VIS) range. So the macroscopic result is coloration. The transition, responsible for absorption, from the valence band is not to the valence band but to some localized called excitonic states, located under the valence band bottom level, viz. within the gap; the position of these states is related to the bandgap width. Formation of quantum dots has been studied, for example, for the semiconducting cadmium sulfide, selenide and telluride CdS(Se, Te), lead sulfide and selenide PbS(Se), and indium arsenide InAs, dispersed in transparent hosts.

3

Ceramics Engineering: Aspects Specific to Those Transparent

The main issues concerning the ceramics engineer are selection of suitable raw materials and their processing and product characterization during and past the fabrication stages. There are many aspects similar to all types of advanced ceramics, including transparent ones. These general issues are discussed and, in some cases, scientifically explained in a number of authoritative books [G12, K18, R13, R22]. Thus, we did not feel that there is a need to repeat here the general information regarding ceramics processing. The fact that requirements regarding final densification level and purity (both related to presence of second phases and certain atomic scale impurities) are very strict imposes specific demands on the way some of the general procedures, when used in transparent ceramics (TCs) fabrication, can be applied. This chapter discusses only the aspects of the various processing operations, which are affected by those demands. In some cases, in meeting the demands, new ways of processing were introduced; these are described here. As examples, one may cite the polycrystalline to single-crystal state conversion, magnetic particles orientation of powder particles suspended in liquids, full glass crystallization, or bulk chemical vapor deposition (CVD).

Sections 3.1.2–3.1.6 discuss processing procedures, while the Section 3.2 focus on characterization methods.

3.1 Processing

Like for most technical ceramics, the main technological approach used to fabricate transparent ceramics is powder consolidation into porous configurationed green bodies, subsequently densified by sintering. This processing method is described extensively in Section 3.1.2.

3.1.1 List of Main Processing Approaches

Besides powder sintering, other fabrication approaches are used for transparent ceramics. They include polycrystalline parts conversion into single crystals, full glass crystallization, sol–gel method, and CVD, the last two in their variants relevant for bulk parts (as opposed to thin films or coatings) production.

3.1.2 Powder Compacts Sintering

In this approach, as it is known, the raw materials, in powder form, are first processed then formed into a green body (a shaped compact of the powder particles); the significant porosity of the part, in this stage, is eliminated during sintering. Before addressing the topic of this section, let us underline that one of the most important conclusions the present authors drew from their work is that the extreme densification levels, required for transparent ceramic production, can be achieved, during sintering, only if green bodies exhibiting an optimal microstructure are introduced into the furnaces. Errors made in the green forming stage can seldom be corrected in later processing stages. Therefore, we start by pointing out, in the following section, the properties an optimal green body needs to possess.

3.1.2.1 Configuration Requirements for High Green Body Sinterability: Factors of Influence

Forming a green body of a configuration optimal for sintering is in many cases a difficult task. There are a number of conditions its main characteristics must satisfy if one expects to fully densify it during sintering. Defects at different scales need to be considered. Four instance, at the submicron level the way particles arrange themselves one relative to the neighbors may not be compact nor uniform enough. Micro but also larger scale cracks and voids may also form. Regions of too large and random spatial distribution (viz such that their relaxation during heating is accompanied by configuration disruption) stress may be left behind by the forming stage; the existence of this type of defect is difficult to observe. Before discussing the sections topic, let us be reminded that real

Transparent Ceramics: Materials, Engineering, and Applications, First Edition. Adrian Goldstein, Andreas Krell, and Zeev Burshtein.

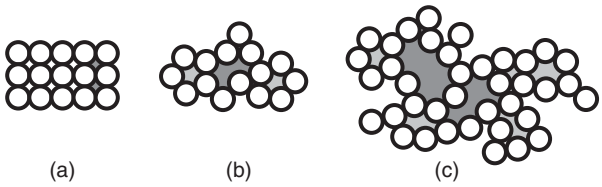

Figure 3.1 Pores average size, size distribution, morphology, and characteristics uniformity as a function of particles agglomeration state and degree of compaction. (a) Spherical basic particles (no agglomerates) in highly compact arrangement (small pores, narrow size distribution, uniform distribution). (b) Pores bordered by low size agglomerates relatively well compacted. (c) Larger agglomerates loosely compacted. Source: Goldstein 2012 [G22]. Reproduced with permission from Elsevier.

powders are seldom collections of basic particles (viz the smallest individual crystallites of the raw material in its as-prepared state). The basic particles are linked in the wet chemistry synthesis product and even more in the calcined material in larger structures called aggregates (or agglomerates), as will be detailed in Section 3.1.2.2.1. The way the powder arranges itself in a green body is a strong function of its agglomeration state; some possible cases are illustrated by Figure 3.1 [G22].

As was noted earlier, the way the powder arranges itself in the green body – viz the part's configuration (not its macroscopic shape but the way its components, the particles, are distributed within the volume) – decisively influences the results of the sintering stage. Some clues regarding the reason this is so are provided by the examination of equations, like (3.1), which describe the volume (V) shrinkage taking place in the first stage of sintering.

$$\frac{\Delta V}{V_0} = 3\left(\frac{20\gamma a^3 D^*}{kT\sqrt{2}}\right)^{2/5} r^{-6/5}\,\tau^{1/5}, \qquad (3.1)$$

where a^3 is the atomic volume of the diffusing vacancy, γ is the interfacial tension coefficient (the solid/air interface), D^* is the self-diffusion coefficient, τ is the sintering time duration, and r is the constituting particles radius.

Inspection of Eq. (3.1) [C32] reveals that pore volume shrinkage depends, among other things, on the radius of the particles, "r," which coordinates the pores.

This is a parameter that needs some further comments. Because, as one sees, the amount of shrinkage is inversely proportional to the "r," it results that it is important to ensure that as small as possible sized particles engage in the sintering process. Let us also clarify that the particles considered by the equation are the basic particles of the powder (un-agglomerated); the equation models the simple case (rare in practice) of a compact constituted from spherical, equal size particles in a compact arrangement. Let us further note that a small particle's size acts by two levers. First, it ensures a strong surface curvature, which promotes fast ionic diffusion. Second it leads, **if the particles are arranged in a compact array**, also to a small size of the pores. The measured shrinkages are seldom equal to those predicted by the equation. This is because it is based on some simplifying assumptions, not always warranted, and it also neglects certain relevant factors. For instance, the above Eq. (3.1) implies that the particles are of identical radius. More important it assumes compact arrangement and absence of aggregation. Real powder compacts seldom exhibit such features. Moreover, the particles morphology is not considered or is known that spherical particles are facilitating diffusion more than faceted ones and that the packing pattern is also influenced by this factor. In any case one of the valuable contributions of the equation is that it suggests the optimal configuration for a sinterable green body: low, monosized, spherical, un-agglomerated particles arranged in a compact fashion. A few powders – exhibiting the required features – have been were prepared, and when they also were formed into compact parts, the resulting green bodies showed excellent sinterability, of the kind needed for the full densification high transparency demands. We illustrate the previous with an example. Reasonably stable suspensions comprising individual (un-aggregated) particles were prepared from certain amorphous alpha-silica α - SiO_2 powders [G30]. Gravitational deposition (Section 3.1.2.2.3) applied to them allowed forming of three-dimensional ordered compacts, like that shown in Figure 3.2 [G30]. Such green bodies exhibit quite a high (~0.65 filled volume fraction) packing density. More important, in such a compact all pores are small, equal sized, and uniformly spaced.

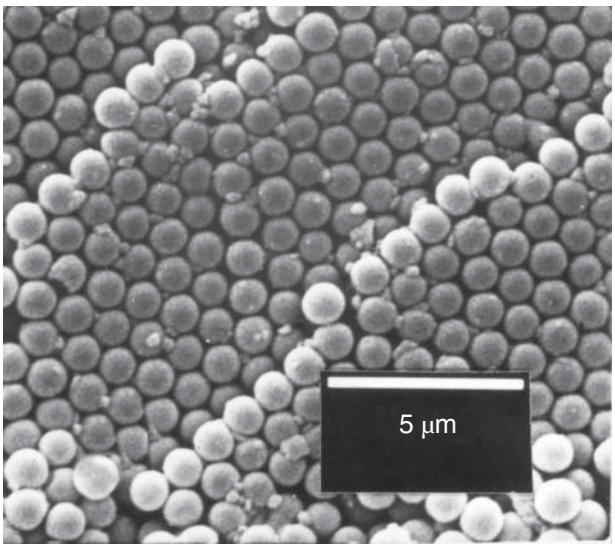

Figure 3.2 Monosized (~1 μm), spherical amorphous silica particles arranged in compact green body (gravitational deposition). Source: Goldstein et al. 1997 [G30]. Reproduced with permission from Springer.

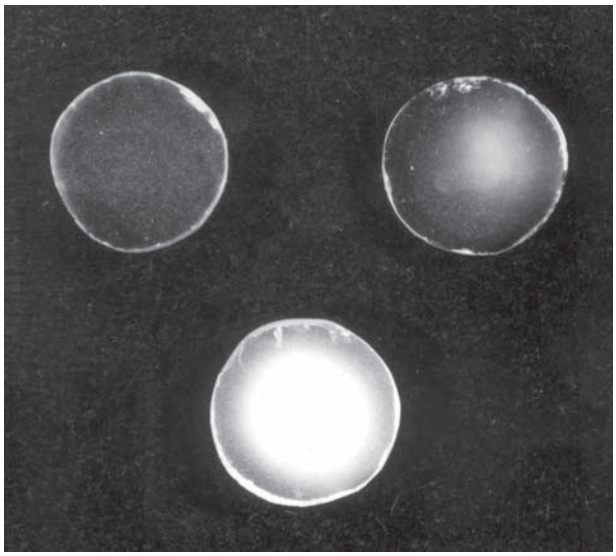

Figure 3.3 Silica glass parts fabricated by fast MW heating of compacts like those in Figure 3.2. Source: Goldstein et al. 1997 [G30]. Reproduced with permission from Springer.

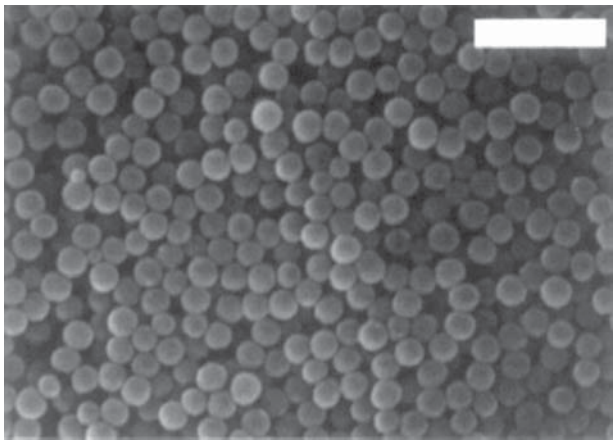

Figure 3.4 Yttria monosized spherical particles synthesized by wet chemistry. Source: Sordelet and Akinc [S44]. Reproduced with permission from John Wiley & Sons.

It has been shown [G30] that such compacts can be fully densified by fast microwave (MW) firing, thus generating transparent pieces, as shown in Figure 3.3.

If the same particles are formed into a compact exhibiting a random loose packing, say, by simple slip-casting, the uniform microstructure shown in Figure 3.2 is not preserved; the green body features a broad pore size distribution. Such a green body cannot be densified to a bulk density (BD) exceeding about 98%; namely, full densification and transparency cannot be achieved. The optimal green-body configuration achieved by gravitational deposition also allowed not only advanced but also fast sintering, such as can be provided by MW heating; formation of cristobalite (a cubic, high temperature, deleterious phase of silica) has thus been avoided.

Monosized spherical powders can be prepared also with yttria Y_2O_3 following the urea ($(NH_2)_2C$) assisted precipitation method developed by M. Sordelet [S44] (see Figure 3.4).

In this case, however, the green-body forming method could not deliver the configuration of Figure 3.2, and, as a consequence, the sintering results were not as good as for silica. Still, improvement of densification compared with that ensured by uncontrolled powders morphology has been achieved [S44]. Also in the case of Lu_2O_3, the monosized, spherical powders, prepared by C. Ma et al., allowed fabrication of highly transparent specimens [M3]. The abilities of sol–gel techniques to prepare monosized spherical fine particles have also been used in the case of materials like zirconia ZrO_2, titania TiO_2, zinc oxide ZnO, and others [B56]. It has to be noted that a rounded form of the basic particles may be helpful even if the particles agglomerate; the rounded form facilitates movement of the agglomerates, composed of such basic particles, under the external forces administered during forming. In Section 4.2.1 we provide an example showing the effect of spherical basic particles morphology in the case of agglomerated powders. It concerns spinel $MgAl_2O_4$ powders and shows that for adequate pressing schedule, round shape of the basic powder helps formation of compact green bodies of high sinterability. Monosphere powder production requires expensive synthesis procedures and forming them into compact, uniform arrays is difficult. Therefore, in practice, even for advanced ceramics such an approach to green-body forming is seldom justified. However, in the case of TCs, which are very high added-value products – and for the fabrication of which alternative technologies are also expensive – the approach may make economic sense, especially in the case of smaller size products.

Turning now to the mainstream pure, advanced ceramic powders let us recall that most of them are made of submicron or even nanometric basic particles, but these are always more or less agglomerated. For this kind of material, fineness of the basic particles, while being a must, represents a factor that does not determine alone resultant pore size; other factors need to be considered. For instance, an important factor is the particles' size distribution (wide size distribution, in most cases, is a consequence of aggregation of the basic particles) and packing pattern; a close to monosized particles distribution is facilitating sintering even if the particles are not spherical. Theoretically a compact packing of spherical, similar size particles exhibits a maximal pore size of about 20% of the particle size. However, in real green bodies, pores of a size similar to that of the powder particles, or even much larger, are often present, together

with the small pores predicted by a compact particles arrangement – as a result of agglomeration and/or poor particles packing; the poor packing is, in many cases, the result of non-adequate forming operations. In this context let us present an example in which the particles size distribution of the as-prepared powder was corrected and, as a result, highly sinterable green bodies, leading to excellent densification, were obtained. W. Li et al. [L36] subjected a suspension of Yb doped SrF_2 to intense centrifugation (11 000 rot./min) and separated, thus, the fine material (collected at the top of the deposit) from the coarse one; materials like those shown in Figure 3.5 (a = coarse fraction; b = fine fraction) were prepared. Hot pressing (HP) the two fractions, produced by the separation, led to specimens of differing transmission (Figure 3.6) – significantly better in the case of the fine fraction. However, also the narrow size distribution material, composed of larger size, particles gave better results than similar powders, having lower average size but wide particles size distribution.

Let us further note that the size and nature (basic particles or agglomerates) of the units that limit the pore influence so significantly the attainable levels of densification, because these aspects control the dynamics of the pores closure process. Pores of a given size may be coordinated by agglomerates of various size and shape, and which, in addition, also include (in most cases) internal porosity. If the small internal pores, of such agglomerates, shrink, the inter-agglomerate pores will increase in size.

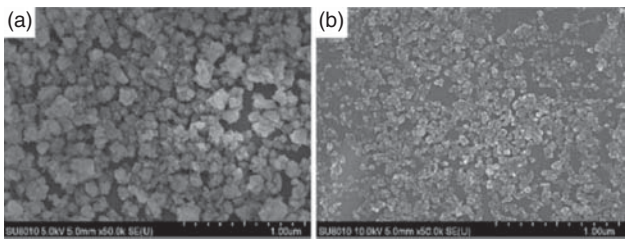

Figure 3.5 Selected, by centrifugation, fraction of Yb:SrF_2 powder. (a) Coarse fraction and (b) fine fraction. Source: Li et al. 2018 [L36]. Reproduced with permission from Elsevier.

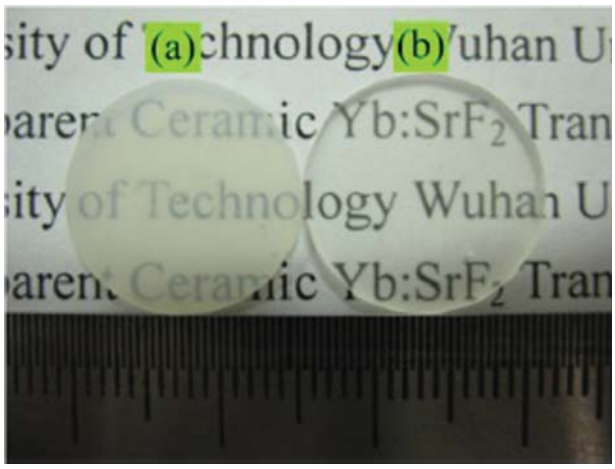

Figure 3.6 Discs resulting from hot pressing of (a) the coarse and (b) the finer powder fractions, mentioned by Figure 3.5. Source: Li et al. 2018 [L36]. Reproduced with permission from Elsevier.

Let us clarify that the aforementioned also means that low average pore size alone is not making a compact sinterable. The size distribution pattern also needs to be suitable: in a graph displaying the pore size percentage vs. pore size, a flat distribution curve running close to the abscissa with a *single* narrow high peak at a low size would be ideal. Multimodal distributions, even if associated with a low average pore size, exhibit low sinterability. For instance, a bimodal size distribution, in which the major mode is at a low size yet accompanies a minor mode located at considerably higher values, is an undesirable profile. In most cases, the small peak represents inter-agglomerate pores that, owing to intra-agglomerate small pores shrinking, further grow in size during the early firing stage. Variable pore size is also deleterious, especially when voids of different size are too close to each other. A gradient in vacancies concentration is one of the consequences of difference in pore size. As a result, vacancies may flow from the small pore region toward the larger pore one causing microstructure coarsening [G12]. A green body that includes larger pores but equally spaced and of uniform size would sinter to a higher density and faster than another body exhibiting lower **average** pore size, but of a non-optimal profile of the size distribution.

A further issue: it is obvious that the volume fraction pertaining to the void space of a powder green compact is desired to be the lowest possible. Still, an important warning has to be presented. In most textbooks on ceramic processing, obtainment of a high green density is indicated as an achievement per se (automatically leading to optimal sintering) without considering how it is achieved. Practice however shows that this is not the case. A high *BD* is significantly helpful **only** if obtained in a manner that simultaneously satisfies the requirements regarding pore size. In fact, it is preferable to have a larger amount of pores (meaning a low green *BD*) of a low average size and a narrow size distribution than a highly compact arrangement of variable size particles (viz a high green density) accompanied by a wide pore size distribution in the green body. Here one includes green bodies that initially exhibit satisfactory pore size distribution, but are bordered by particles that are likely to undergo differential shrinkage; the result is the formation of wide pore size distribution. In this context let us recall that, based on packing efficiency

related factors, use of powder batches that are made up of bimodal mixtures of spheres – which may indeed ensure solid fractional volume as high as 0.87% – or even of variable morphology particles is recommended by some [R5]. While packing efficiency may thus be significantly increased, this benefit is not translated into better sinterability. On the contrary, maximal achievable density is reduced owing to the differential shrinkage of adjacent green-body regions, which lead to inter-region large pores formation. Therefore, a high packing density is a plus only when obtained in the right way. High packing order, however, is always effective as a densification enhancer. In the case of monosized spheres, random dense packing may also generate configurations that are able ensure good sinterability. In principle, non-spherical regular-shaped polyhedral particles can also be packed into arrangements exhibiting low voids size. In practice, however, dense packing of such units is much more difficult, especially when they are of submicron size, owing to particles surface interaction.

The requirements for high sinterability may be satisfied quite well, sometimes, even for the case of aggregated material based on particular agglomerates morphology. For instance, W. Jing et al., [J11] prepared a YAG precursor by the standard coprecipitation technique (NH_4HCO_3·$(NH_4)_2SO_4$), in the reverse strike variant. However, a specific feature was the addition of cation mix solution in microdroplets formed by gas pulses. While the synthesis product is material based on spheroidal basic particles after calcination, low size (narrow size distribution) aggregates of a peculiar (vermicular) morphology, like shown in Figure 3.7, resulted. When the calcines were formed, by gel-casting, into a green body the aggregates arranged themselves into a configuration exhibiting the low, uniform pore sizes conferring sinterability. Excellent densification leading to transmission of ~82% at 400 nm ($t = 4$ mm) was achieved.

Summarizing the section, it can be said that a compact matter arrangement, **simultaneous** with small pore size and narrow size distribution, is a configuration that – if uniformly maintained, throughout the volume of the part – at both the micro- and macroscales, are green body features able to facilitate the very advanced densification TC fabrication requires. The green-body structure is determined by the interaction of factors like the basic particle's size and shape, the powder processing operations applied, the nature of the forming process, and the conditions in which it is accomplished.

In this section the green body's features important for conferring high sinterability were discussed, and also the characteristics of the powders that influence one's ability to form sinterable green bodies were presented. The as-prepared powders exhibit features that rarely respond to the requirements. We address, in the following section,

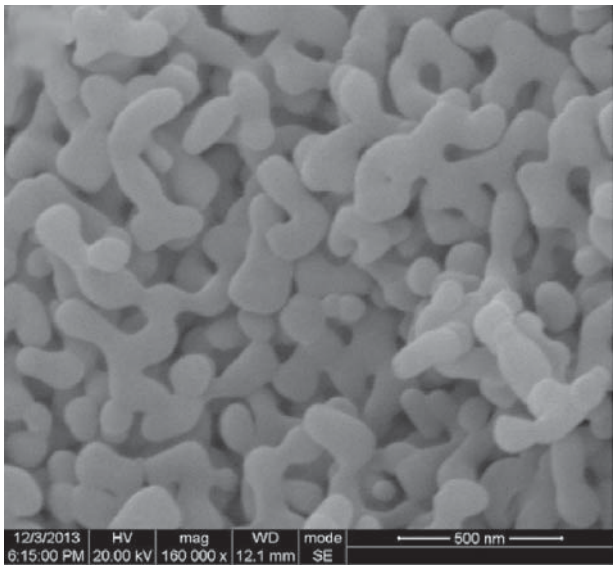

Figure 3.7 Morphology of YAG powder prepared by spray-coprecipitation (state after calcination; vermicular shape; 200–500 nm). Source: Jing et al. 2018 [J11]. Reproduced with permission from Elsevier.

the issue of what can be done – by further processing them, before forming – to correct the faulty characteristics (where needed). To achieve green bodies of high sinterability, one also has to select a forming procedure adequate to the specific characteristics of the processed powder or conversely, when the forming procedure is a given to adapt powder processing to it. The forming methods are also discussed in the following section. The methods discussed are those generally used, in advanced ceramics fabrication, but with an emphasis on the more elaborate mode of applying them requested in the TCs case; some of the forming operations addressed, while in principle usable for any ceramic, make economic sense only in the case of TCs.

3.1.2.2 Powder Processing and Green-Body Forming

Both powder processing and green-body forming have a critical influence on the structure of the shaped and consolidated powder. A main task these operations need to fulfill is agglomerates breaking and preventing re-agglomeration. Therefore, a short summary of agglomerates structure starts the section devoted to green-body related processing.

3.1.2.2.1 Agglomerates

Most of the fine pure powders used for TC fabrication are supplied after being dried and calcined (600 – 1100° C range), and sometimes partially comminuted. While having basic particles of size in the 20 – 300 nm range, the measured particles sizes, of as-prepared powder batches, usually exhibit a broad distribution, with a

cutoff somewhere between 2 and ~15 μm. This is because, in fact, the vast majority of measured particles are **agglomerates formed by aggregation of the basic particles**. Only a minute fraction of the measured particles are basic ones. Recall that initial synthesis products, the basic particles, are tiny particles of nanometer size. Their summed surface area is huge, of the order of $10-1000\ m^2/g$, and these basic particles collections form thermodynamically highly unstable systems. Therefore already during residence in the reactor, calcination, and even during storage, the particles engage in physical processes causing reduction of the initial free surface area. The interaction is determined by summation of the various particles surface forces and those exerted by the medium between the particles. It is important to understand that most agglomerates are multileveled; a few basic particles form clusters, which in turn "glue" among each other to form larger units separated by bigger pores, and so on (see Figure 3.1). Besides its dependence on basic particles size, the agglomerates' structure, shape, and size vary as function of variously originated factors like basic particles geometry, processing history, purity, order degree of the lattice, synthesis chemistry, storage conditions, and maybe more. The size distribution measured before processing differs, in most cases significantly, from that of the powder engaged in the forming operation. Furthermore, use of different measurement methods may also provide different size results. For instance, measurement made on a dry powder sample extracted from a batch used for pressing reflects quite well the powder entering the pressing die when the latter is almost dry. On the other hand, a measurement in which the sample is suspended in a liquid may provide a different result. The latter measurement type would however constitute a good approximation of the actual size distribution in a suspension prepared for slip-casting. Owing to the aforementioned, the data presented in the experimental part of papers may be misleading.

We consider now the main forces acting on the basic particles – during preparation, drying, processing, storage, and forming – leading to their aggregation. In the case of gas phase reactions, or of wet chemistry based synthesis, a part of the particles appear as twinned crystals, and as clusters of crystallites bonded by small area, but very strong contact regions. Many of the latter are formed by ionic diffusion. In the case of gas-phase synthesis, the temperatures are high, facilitating diffusion, but even at the low temperature, existent during wet chemistry operations, the clustering is significant. This incipient particles' bonding takes place, as noted earlier, owing to the minute size (hence huge free surface area) of the precipitated basic particles. The process is facilitated by the fact that the particles get very close to each other in the reactor, during drying, calcination, and storage. It allows strong, yet short ranged surface forces to become important. The fact that such "cold sintering processes" (wet chemistry synthesis or storage stages) occur can be better understood if the consequences on sintering drive of nanometric particles size are considered. For particles with a diameter of the order of 10 nm, the sintering drive created by the enormous free surface and large particles curvature becomes sufficiently high to cause particles bonding even at room temperature. In the initial sintering stage, the driving sintering force F between two contacting spherical particles is given by [L20]

$$F = 2\gamma_s(4 - a/r)\frac{\Omega}{(a/r)^3}\cdot\frac{1}{r^2}, \tag{3.2}$$

where γ_s is the surface tension coefficient, a is half the neck length, r is the particle radius, and Ω is the volume of the slowest diffusing ion. The a/r ratio is dubbed as the "neck-size" parameter. In alumina Al_2O_3, for example, $\gamma_s \approx 1.0\ J/m^2$ and $\Omega = 0.02\ nm^3$. We consider a stage where $a/r = 0.5$. On changing from $r = 500$ to 5 nm, while preserving the same neck-size parameter (a/r ratio), one obtains a 10^4 times increase of F. Thus, particle radius reduction leads to massive enhancement of sintering drive. As a result, the temperatures necessary to start sintering are significantly reduced from 1200°C to the range of those used during synthesis and powders calcination (or even storage). In Figure 3.8 (as prepared powders [K54]) and Figure 3.9 [K1] (processed powder; from a slurry) bonds created by incipient sintering, of basic particles, are visible (cp. details to Figures 3.8 and 3.9 below in Section 3.2.1.1).

These are the strongest bonds acting in an agglomerate and are only partially affected even by the strongest comminution programs, one can bring to bear, without introducing, in the powders, impurities from milling media. It means that even efficiently comminuted powders will generate suspensions having these clusters as its smallest individual solid units (kinetical units = smallest particles able to move independently under the action of forces active in the suspension), rather than the initially synthesized basic particles; the clusters formed by incipient sintering (hereby addressed as "primary agglomerates") usually involve two to four small (<10 nm) basic particles of various shapes.

Besides the aforementioned, it has to be noted that the force, due to the shape fluctuation, in time, of the electronic cloud of an atom – which leads to a transient dipole formation – is also active in aggregates formation. This force, proper to all atoms, operates also on the atoms making up the surface of the powder basic particles. It has a relatively long range. It is relevant here because dipoles of distinct atoms (atoms sitting on close

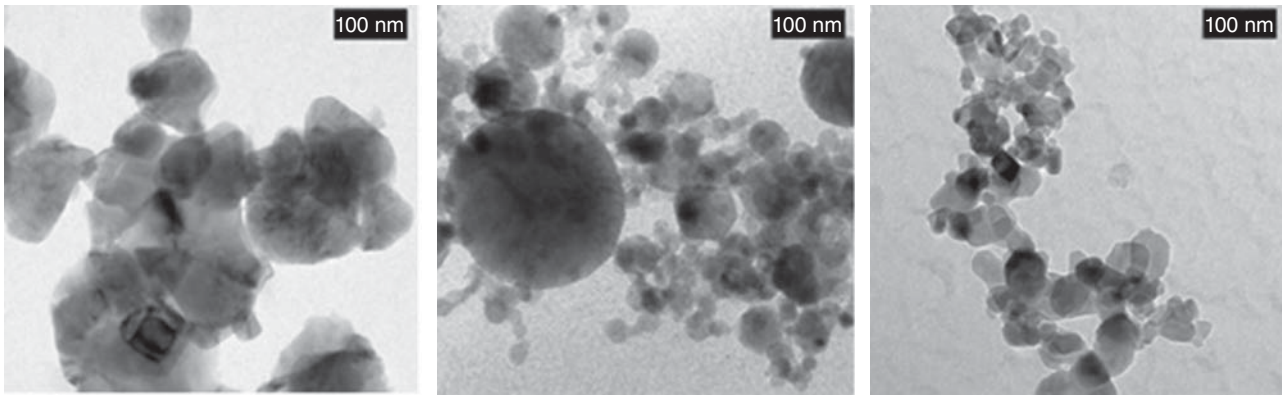

Figure 3.8 Commercial spinel ($MgAl_2O_4$) powders with different particle sizes and shapes for sintering transparent ceramics. The powders were synthesized by (a) thermal decomposition of ammonium carbonates, (b) flame spray pyrolysis, and (c) thermal decomposition of alum salts. A comprehensive analysis of characteristic data of these powders is given in section 3.2.1.1.

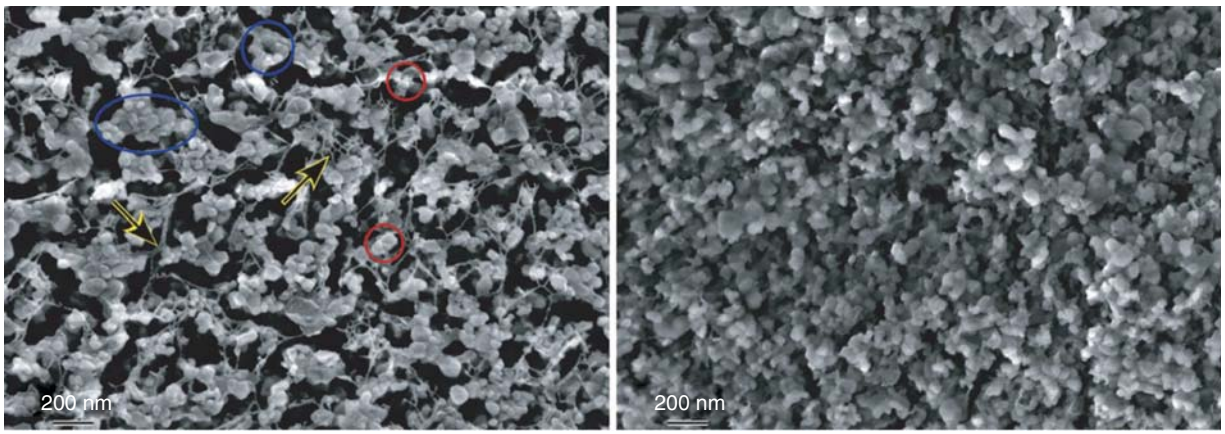

Figure 3.9 Cryo-HRSEM micrographs of an aqueous suspension with 60% solid loading of spinel powder, deflocculated with NH^{4+}-polyacrylate. The suspension is weakly flocculated with flocs indicated by loops (left panel) and fillaments of dispersant pointed to by arrows (left panel = as-prepared suspension and right panel shows suspension aged 0.5 h). Source: Kadosh et al. 2012 [K1]. Reproduced with permission from John Wiley & Sons.

but different particles) interact in a form, which leads to attraction (London dispersion force) [H35]. This is the most important of the so-called van der Waals (dipoles generated) interactions. Macroscopically the strength of the attractive force is dependent on the number of atoms interacting, viz the size of the particles. The dipolar forces always lead to attraction in the case of particles of the solid materials of interest here; in multi-material systems (including separating medium), they may lead also to repulsion, in certain conditions. The other types of van der Waals interaction, owed to permanent dipoles (Keesom and Debye contributions), are not relevant, when the raw materials are pure. When impurities and intentionally added organics are also counted, their contribution, to inter-particle bonding, may become significant or even dominant. The equilibrium distance between the particles is established by the summation of the effects of the van der Waals and repulsive Born forces; the latter are owed to the low size of atoms which leads, when atoms are very close, to electron–electron, nucleus–nucleus repulsive interaction. Electrical charge, when present on the particles surfaces, brings about longer range, electrostatic interaction, which leads to repulsion when the charge is of the same sign, and attraction in the opposite case. When considering also the phases (gas, liquid, solid), which surround the powder particles, in practical systems, additional factors need to be taken into account. For instance, dispersing liquid media, like water or alcohols, lead to formation of inter-particle bridges. In larger amount the water will contribute to bonding by the action of the capillary force. Salts deposits (binding effect) may form in some cases, between the oxide particles, owing to contribution from the raw materials used for synthesis. A dispersing

medium with a large γ_{LS} favors agglomeration. For instance, for many oxides agglomeration in water is facilitated in water if compared with organic solvents like, say, isopropyl alcohol (IPA).

The larger the agglomerate, the higher the probability that more than one type of the forces listed earlier is active within its framework. Because the strength and action range of these forces are significantly different, the morphology of aggregates is variable and they make contact at various angles, there are two important consequences: the agglomerates are porous (variable pore size and morphology) and the degree of cohesion varies throughout their volume. Therefore it is misleading, in most cases, to talk about strong and soft agglomerates; it implies a strength uniformity rarely present in real agglomerates. In each agglomerate – except the primary clusters – various strength bonds are present and the volumetric distribution of the intra-agglomerate strength is not uniform; in general the bonds holding together the components of the higher level of agglomeration are weaker. The primary clusters of basic particles are the strongest – in most agglomerates. So in each agglomerate, regions of higher and lower strength exist.

3.1.2.2.2 Powder Processing

The first and main task of powder processing – irrespective of the forming technique for which it is destined – is breaking of the agglomerates present in the calcined material; the calcines constitute the state in which the material appears at the end of the powder preparation process. Techniques like expansion under supercritical conditions, [T25] and exposure to intense ultrasound waves, are currently examined for comminution purposes; shock compression (under high pressure) was also proposed in this context [C29]. These techniques, however, are expensive, and not easily amenable within industrial systems. In practice, milling of powder suspensions is still the most widely used technique. Regarding milling, it is important to recall that in the transparent ceramics case, the tolerance to second phase type impurities is extremely low. We recall this critical fact here because milling is one of the comminution procedures most likely to introduce such impurities. In this context it is also worth noting that the breaking of agglomerates including strong bonds is facilitated by the application of extreme milling conditions and, as a consequence, manufacturers are tempted to use them. The problem is that more often than not such a strategy leads to introduction of impurities (mostly resulting from wear of the milling media). For instance, it is difficult to totally avoid wear of grinding media when the speed of planetary or attrition mills exceeds certain limits. Thus we determined that after one hour of attrition milling at 1700 rot/min – the time length needed to achieve the desired fineness, of some spinel $MgAl_2O_4$ powders – introduces close to 0.1 wt% zirconia ZrO_2 off the milling balls, despite their top quality. Such a second phase amount is able to reduce the sintered bulk state density, of the spinel, from 99.9% of theoretical density *TD* for pure material, down to less than 95% of theoretical density; specific contamination sources also exist during jet milling.

The need to avoid contamination sets limitations on the force that may be applied for breaking the agglomerates. The powder processing is such an arcane issue because one needs to design methods able, simultaneously, to break strong bonds and preserve the phase purity of the processed material. Many quite ingenious solutions have been found to this problem. Here we cite one example (others will be given in Chapter 4 where processing of the various materials is discussed). For fabrication of fine grained tetragonal zirconia, the precipitated material was subjected (in wet state) to de-agglomeration in a high-speed turbine (at 2000, in the first stage and 7000 rot/min in the second stage); the process does not lead to impurification. As a result green bodies of optimal microstructure could be formed and thus low temperature sintering allowed fabrication of submicron grained well-densified specimens, which exhibited translucency at thickness close to 1 mm [D24]. When applied for long times, mild-condition milling is also an usable strategy that while not very appealing to manufacturers is quite efficient. For instance, applying a ~10 hours ball milling (tetragonal zirconia polycrystalls (TZP) balls), at relatively low rotational speed, to a spinel powder, allowed achievement of sufficient agglomerates breaking without impurifying the materials; in the milling product most particles size ranged between 80 and 200 nm, representing first-, and second-level agglomerates [K1]. The thus processed powder allowed fabrication of excellent transmission, large spinel parts (slip-casting and sintering).

A fact one has not to forget is that even after quite elaborate powder processing, the powder elementary units are still low sized various level agglomerates; in the best case primary clusters of independent basic particles form the majority of particles. Basic particles form only a small fraction of the material (not necessarily desirable). The primary clusters may be fully dense or already include sub nanometric size porosity. In many cases such a state of the comminuted material is acceptable; suitable further use of it may produce high transparency parts. In this context it is, probably, worth noting that an excessively low basic particles size of the as-synthesized material is often associated with a higher average strength of primary agglomerates, which are more difficult to process. Powder producers often advertise the low size of their offer's basic particles because it is considered as beneficial for sintering. As we have seen

low size basic particles are, however, not automatically improving sinterability; when certain limits are exceeded the effect is even opposite to the one desired. Powder sintering ability is a complex function of basic particles size, agglomerates structure, basic particles morphology, and surface chemistry.

Certain aspects of powder processing depend, as opposed to those discussed right above, on the used forming method; when necessary, such aspects will be specifically discussed where the relevant forming technique is addressed. For instance, in the case of forming by pressing, the final stage of powder processing is granulation. In that operation, large agglomerates are purposely reformed from the comminuted calcines. These agglomerates usually have spheroidal shape, and an average size distribution that facilitates material flow inside the pressing die. The bond's strength within these agglomerates is much lower than of those in the calcines; organic additives and residual water ensure it by to some surface forces discussed earlier. The granulation operation will be described further later when forming by pressing is addressed; such a process is not desired at all in other forming methods like, say, slip-casting.

3.1.2.2.3 Forming Techniques

The forming operation transforms the processed powder into a green body exhibiting the desired shape and size for this stage of the fabrication procedure. In many cases, the shape of the green body approximates that of the final product, but in other cases, the item subjected to sintering is a "preform," from which the finished product is generated by post-firing processing. The size of the parts may vary from discs of several millimeters in diameter (for example, to function as laser Q-switches) through more than 1 m large plates (for example, for armor windows) and large cylinders (as lamp envelopes). For certain transparent ceramic applications shapes including curvature are needed. Examples are the missile noses armor windows, lamp envelopes, or certain gain media for high power lasers. The kind of forming method usable for a given product depends on its intended size and shape, and also on the number of fabricated parts. The forming operation has to generate a suitable geometrical configuration uniformly throughout the specimen volume. When selecting a forming procedure, the raw materials features have to suite all the main aspects listed previously. Selection of the right method is, however, only a first step. Success implies determination of suitable conditions, often by tedious trial and error work; theory, in many cases, offers valuable guidelines. Attention to detail is needed. For instance, after pressing, it is important to release pressure sufficiently slow to prevent microstructure disruption caused by too-fast expansion of residual gas.

For transparent ceramic shaping, all the general advanced ceramics fabrication methods are adopted. Pressing, slip-, gel-, and tape-casting, pressure filtration, injection molding, and gravitational or centrifugal deposition have all been used, yet pressing being the most ubiquitous.

3.1.2.2.3.1 Press Forming

Pressing is the fastest and cheapest forming method, hence most popular in advanced ceramics processing, including transparent ceramics. Up to now it has been the only approach usable for mass, cost-competitive production.

As noted earlier (Section 3.1.2.2.2), those aspects of powder processing that are method specific are discussed in the section devoted to a given method. Such an aspect, in the case of pressing, is granulation (or palletization). It is not such a straightforward operation because it means re-agglomeration of the material, after significant effort has been made to comminute, by aggregates breaking, the powder calcines. The reason, for the effectuation of such a counterintuitive action, is the need to ensure material flow-through feeders and within the dies, so as to obtain the most uniform die volume filling compact (without sacrificing powder's chemical homogeneity or causing size segregation). In a comminuted state, before granulation, the contact surface between the particles is so large, that inter particle locking occurs, on a large scale, owing to the van der Waals and other interactions. The variable shape particle clusters, resulting, markedly, hamper powder flow and compact arrangement thus leading to non-uniform and loose space filling. Concretely granulation is aimed at producing large spheroidal units (lowest contact surface and thus minimal friction between the kinetic units), which massively improve powder flow. (Kinetic units mean here the agglomerates that, at a certain moment of the pressing operation, move as independent entities.) Various granulation methods, like spray-drying or freezing, pelletization by the aid of sieves (followed by tumbling), and other methods, are available. Figure 3.10a–c shows examples of the morphology and size of granules prepared by various techniques.

Simultaneously with shaping, the granulation has to provide, to the granules, the adequate size and strength. The size distribution of the granules is preferably narrow. Adequate here means that the strength has to be correlated with the force profile of the pressing step. During the die filling, the granules movement has to ensure the material transport within the die. They are also required to deform and break up into progressively smaller components to allow a compact material's arrangement. Let us clarify that the strength magnitude – of the bonds which hold together the granules components – is much

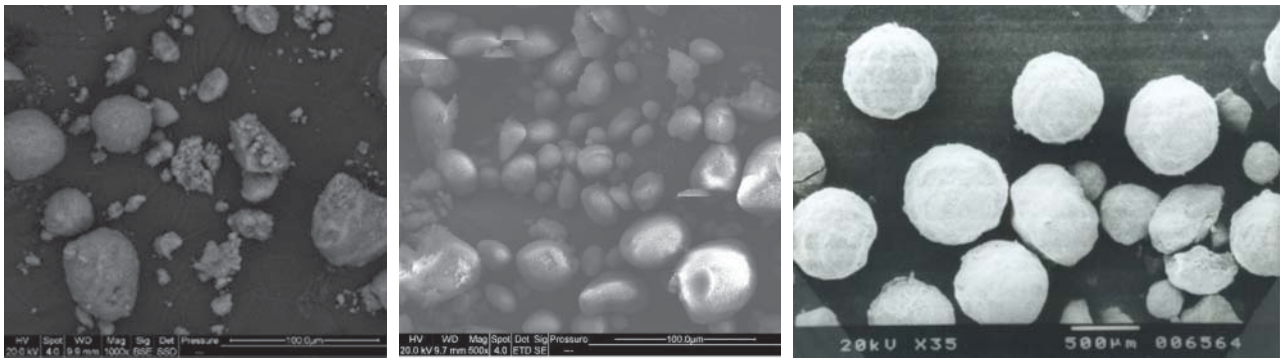

(a) (b) (c)

Figure 3.10 Imaging of granules formed by various procedures (at ICSI, Haifa) from fine ceramic, as-comminuted, powders. (a) Spray freeze-drying (20–60 µm), (b) sieving and tumbling, and (c) spray-drying.

lower than of those existent within the agglomerates destroyed by the calcines milling step. If granules are too weak, they break up too early while if they are too strong they do not disperse fully. Figure 3.11a shows the attainable green BD as a function of compaction pressure for the case of two spray-dried alumina powders. A large BD means a compact material arrangement that occurs only if the granules flow and break in an optimal way. Figure 3.11b shows the granules deformation and spatial arrangement as a function of a rising pressure. It can be seen that a pressing force 170 MPa attained following the pressure raising time profile, chosen by the authors, correlate well with the characteristics of the granules (viz intra-granule strength and shape allowing free flow) so as to lead to a uniform compact green microstructure. This particular 94% alumina powder, when suitably processed and pressed, could be formed into compacts exhibiting a 55% theoretical density (TD) relative green density *TD*. The discussion earlier indicates, among other things, that in practice a study, of the type exemplified by Figure 3.11 [E7], is necessary each time a new material is pressed – in order to harmonize the granules properties with the pressing schedule.

Considering the merits of different granulation methods, let us note that many high performance transparent ceramics have been fabricated by the aid of spray-drying. However, optimization of conditions for this method is much more difficult than in the case of freeze-drying. In the former process, organic additives (part of which are added to the powder to assist in the spray-drying process) migration, during spray-drying, causes reduction of their initial distribution uniformity. Also non-uniform granule shrinkage often occurs, leading to shape loss. Moreover neck strength is raised by the high temperatures (200 – 350° C) attained during the process [S68]. Granules obtained by spray-drying are frequently doughnut-shaped. Owing to the aforementioned, after pressing, the granules produced by spray-drying may leave behind strong irregular shell fragments, which hamper uniform sintering. Freeze granulation, in which the material is granulated by spraying into a freezing liquid (not a simple freeze-drying), is more adapted to transparent ceramics fabrication requirements than spray-drying. The benefits concern powders flowability and uniform granule cross-sectioned microstructure. As to flowability, quantitatively it is assessed by the flow index I_c defined as

$$I_c \equiv 100 - \frac{\rho_t - \rho_b}{\rho_t} 100, \tag{3.3}$$

where ρ_t is the tap density and ρ_b is the BD. Freeze granulation also tends to allow the generation of breakup products, which exhibit narrow size and shape distributions. A flow index $I_c < 10$ is desired; values such as $I_c = 5 - 6$ can be obtained [S68].

It is also important to emphasize that after comminution, during granulation and storage, one has to create conditions preventing reforming of excessively strong inter-particles bonds. This may require introduction, into the package of organic-additives, of components the task of which is just to prevent such bonds reforming. If not properly cared for, the effect of comminution may be partially annihilated in all the stages of powder processing and also during storage. Let us further elaborate a bit on certain aspects of the pressing process. Under the action of the external compressive force, first full granules and then the fragments resulting from their breakup change their relative position, and further breakup. During this stage both inter-particle friction and stable contacts formation may lead to loose packing, a situation highly deleterious for sintering. As already mentioned earlier, in order to generate the required green body configuration, pressing has to be able to ensure compact arrangement of the material (at this stage about 60% of the die volume is void). Related to this the importance of the basic particles morphology is worth noting.

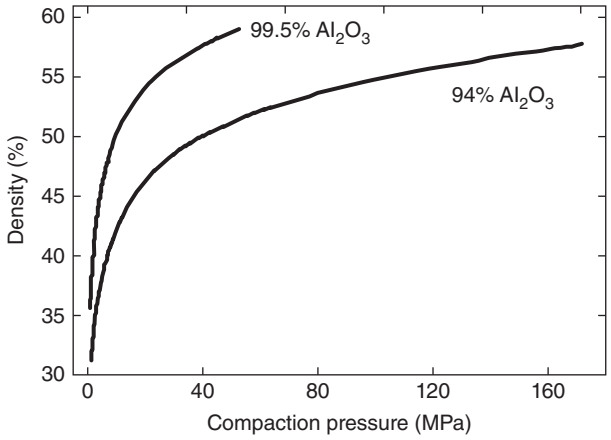

(A)

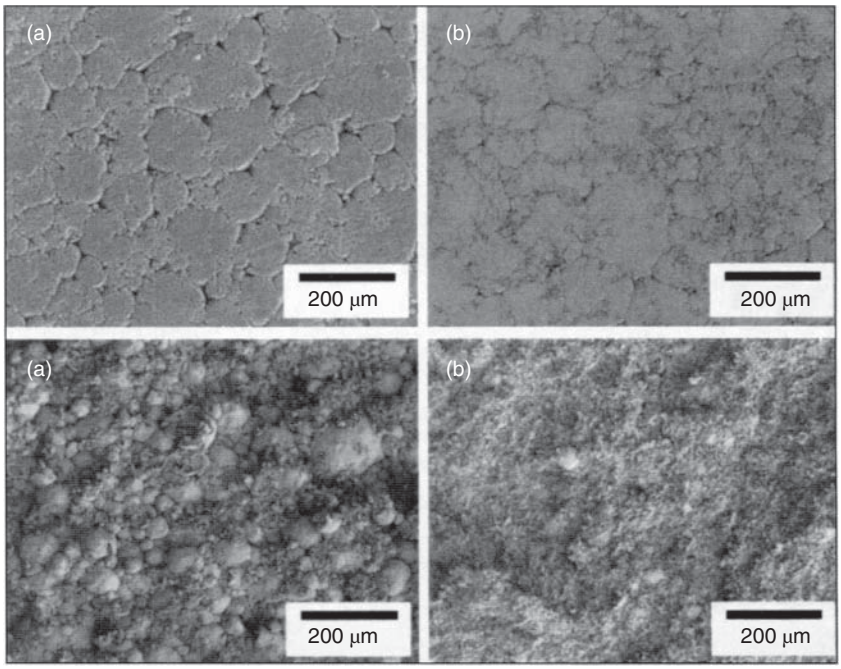

(B)

Figure 3.11 Green density (as a function of compaction pressure) and microstructure of alumina pressed parts. (A) Compaction response curves for spray-dried 94% and 99.5% alumina powders pressed to an in-die density of 60% TD (corrected for springback). (B) Microstructure of surface (top line) and fracture surfaces (bottom line) of 94% alumina powder compacts showing granules deformation and breakdown as a function of pressure. (a) Column = 17 MPa; on compact surface (top panel) and in bulk (cross section) (bottom panel). (b) Column = 138 MPa; panels like in (a). Source: Ewsuk et al. 2003 [E7]. Reproduced with permission from John Wiley & Sons.

While the moving units are agglomerates, friction takes place between the basic particles limiting neighboring agglomerates; the number of bonds established between basic particles that come in contact depends on their morphology; it is minimal for spherical particles. Major help is provided by the use of adequate lubricants. For minimizing inter-particle "locks" during their travel, weak attractive surface forces are desired [G22].

Another aspect that needs consideration is the "spring-back effect"; this effect may cause major disturbance to the green-body configuration. Under the action of the pressing force, the particles also undergo some elastic deformation. Its severity depends on the mechanical properties of the material and the magnitude of the applied force. After pressure release, the stress associated with that straining is relaxed, sometimes gradually, during sintering disrupting the green-body configuration often in a way that leads to the formation of variable shape and size (including large one) new pores. So the high compactness level and small pore size, characterizing the as-pressed part, are lost, in early stages of the sintering process. The sinterability of the parts is thus reduced, sometimes dramatically. For example, working with spinel powders, it was possible to generate green bodies exhibiting a BD_g = 67% TD by pressing under ~1.8 GPa (A. Goldstein, unpublished results). The sintering temperature for attaining a 97% TD fired body density was reduced, but only by some 50° C compared with that necessary for densifying of conventionally pressed green bodies, having BD_g values of only around 50%

TD. Moreover by pressing of uncontrolled morphology heavily agglomerated nano-yttria powder with the same technique, green densities as large as ~80% *TD* could be obtained. After sintering, however, maximal BD_A values achieved failed to exceed 95% *TD*, viz under the level normally pressed powder compacts can deliver. Even when, in another experiment, submicron spherical, weakly agglomerated (i.e. exhibiting suitable features), *n* - Y_2O_3 powder was compacted up to $BD_g \approx 83\%$ *TD* by magnetic pulse pressing at ~1.6 GPa [K10], the green body structure was so severely disrupted by the very strong spring-back effect that firing failed to produce transparent products.

The last but not least issue considered is the package of organic additives: dispersant, binder, lubricant, and sometimes plasticizer. Usually for each of the latter functions, a different type of additive is required. The adsorption mechanisms, stereochemistry in confined liquid volumes, and the mechanisms of molecular interaction in adsorbents, are only partially mastered. All these parameters may vary significantly as functions of influencing factors like the pH, additives concentration, temperature, particle surface structure, and chemistry. Therefore in most cases, tedious Edisonian kind of research, guided by theory, is required for determination of an efficient package of the additives needed for powder processing and green body forming. The additional difficulties, posed by possible additives interaction, are compounded by the fact that a given polymer may act in different ways depending on its molecular mass. For example, the $H-(O-CH_2-CH_2)_n-OH$ polyethylene glycol (PEG – a condensation polymer between ethylene "oxide" and water) is a good dispersant for water-based slurries, as well as other solvents, as long as short macromolecules, of $n < 600$ are used. The same polymer of $n > 1000$ acts as a binder. The $(C_3H_4O_2)_n$ polyacrylic acids (PAAs), even at a given short *n*'s, may act differently as a function of its concentration: dispersant at high concentrations, and as a binder at lower ones. Another example refers to the action of surfactants. It differs markedly as a function of concentration. For instance, if the concentration of such molecules is sufficient to provide a monolayer of adsorbates, it could change a polar surface to a nonpolar one. If the concentration is such as to cause formation of bilayered adsorbates, the decorated surface remains polar (see Figure 3.12 [H35]).

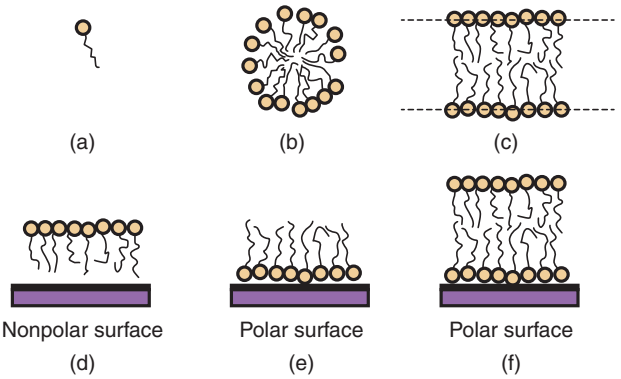

Figure 3.12 Schematic of surfactant molecules contact to particles surface (polar, hydrophilic heads, and nonpolar hydrophobic tales are represented); their adsorption changes polarization state of pristine surface. (a) Surfactant molecule. (b) Molecules in solution tend to aggregate as spherical micelles. (c) Aggregation (prompted by drive to minimize tails contact with polar water) may also take the form of bilayers. (d) Adsorption pattern to a particles having nonpolar surface. (e) Adsorption to particles having polar surface. (f) Pattern of adsorption in case of high surfactant concentration; a second layer forms. Source: Horn 1990 [H35]. Reproduced with permission from John Wiley & Sons.

3.1.2.2.3.2 Liquid-Suspensions Based Forming

As noted earlier, in the case of particulates dried after comminution, their forming, into suitable configuration green bodies, is complicated by re-agglomeration. Therefore, methods based on the use of stable suspensions, produced by dispersing the comminuted powder, present an advantage over pressing (regarding productivity, pressing remains however the most attractive forming technique). In a well peptized suspension, the solid material is dispersed into the smallest particles that comminution can provide. These smallest particles are rarely the basic particles. Usually, most of the solid represents primary aggregates viz clusters (including two to five components) of the basic crystallites, formed by incipient sintering necks (that milling could not break); while these particles are not basic their size is still low, not exceeding a few hundred nanometers (in many cases the size is of 80–150 nm). These units (kinetically independent) are of nonporous, variable shape and exhibit a narrow size distribution; a small fraction of the particles may be basic particles. In an earlier figure (Figure 3.9), the typical shape and size of spinel $MgAl_2O_4$ particulates, present in a suspension that was subjected to strong ball milling, were shown [K1]. The state of the solid particulate achieved there fulfills an important requirement for producing green bodies of optimal configuration: dispersion into sufficiently low size, kinetically independent units. This state of the suspension is a necessary feature, yet by itself not sufficient for efficient forming. The following stage, namely, the liquid separation from the solid, is as critical as the comminution. The way it occurs determines whether the particle system is consolidated into a low pore-sized compact body, or a difficult-to-densify green part. During separation, re-agglomeration of the particles and/or a loose arrangement may occur; avoidance of such mishaps is not a trivial task.

In that context, recall that there are a number of approaches one may use to transform a solid/liquid system into a shaped powder compact: slip-, gel-, or tape-casting, filter pressing, gravitational or centrifugal deposition, and others.

In conventional slip-casting effectuated under atmospheric pressure, the time required for formation of a green body, and its recovery from the mold, is much longer than that prevalent in the case of pressing. Slurry flow (the process that eliminates the liquid) is caused by a weak capillary suction (negative) pressure of no more than 0.1 – 0.2 MPa provided by the mold's porosity; the suspension flow rate is not uniform in space and time. The cast thickness t_c depends (parabolic form) on this pressure p, according to

$$t_c^2 = 2Hp\tau/\eta I \tag{3.4}$$

where η is the liquid viscosity, τ is the time duration, of the casting operation, H is a constant with a value changing for various levels of the solid's volume fraction in the slurry, and $I = V_c/V_s - 1$ (V_c being the volume fraction of solid in the porous cast and V_s the volume fraction of solid in the slurry). The particles arrangement is in most cases less compact than in a green body consolidated by pressing the average pore size is larger and their size distribution wider. Figure 3.13 [R5] shows the hydraulic pressure distribution (across the cast and die) during slip-casting.

Even if well dispersed, high solid load slurries allow the occurrence of quite turbulent flow, and numerous and random particles contact, eventually leading to re-agglomeration during the suspension's cast formation (suction strength over the die surface varies because the non-uniform porosity of the die), appear as a result of liquid flow through the cast. Owing to the variable pore size and volume density in the conventional dies say gypsum ($CaSO_4 \cdot 2H_2O$) made, the suction force acts in a non-uniform manner over the die surface. As a result, solvent passing channels, of variable diameter form. The

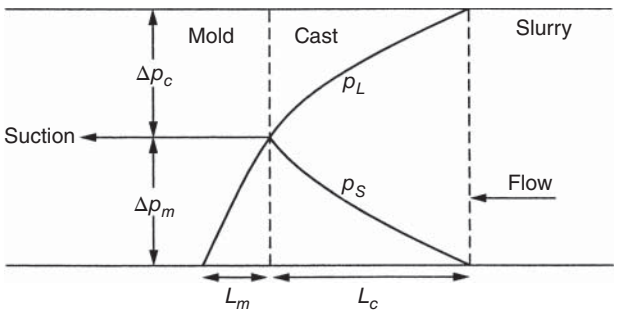

Figure 3.13 Hydraulic pressure distribution across the cast and the mold in slip-casting. Source: Rahaman 2003 [R5]. Reproduced with permission from CRC Press.

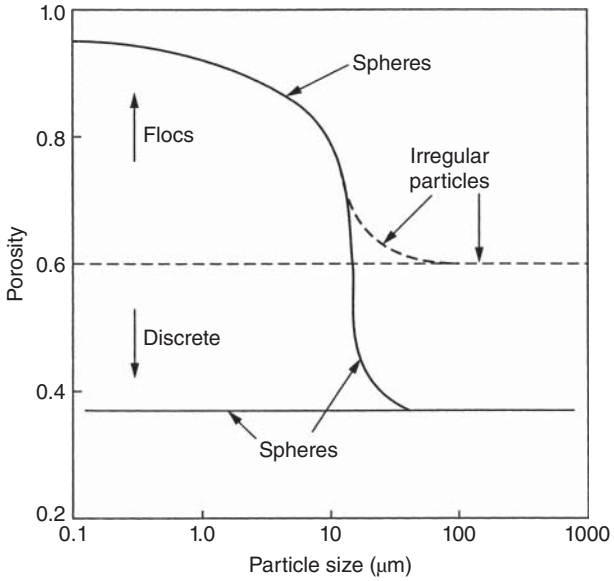

Figure 3.14 Cast porosity level as a function of particles size, shape, and degree of flocculation. Source: Rahaman 2003 [R5]. Reproduced with permission from CRC Press.

amount of porosity and its size distribution in the dry cast vary significantly as a function of slurry characteristics like solid particles size, shape, and flocculation state (those may vary over time until the casting operation has been completed; see Figure 3.14 [R5]).

Macroscopic voids, owed to air bubbles left in the slurry, are rarely fully eliminated, even when good liquid wetting of the particles and proper de-airing are ensured. Same is true for particles segregation by size and shape. Therefore, conventional slip-casting is seldom a recommended forming method for generating green bodies of very high sinterability. In most cases, such parts are less sinterable than those formed by optimized pressing of the same powders. There are, though, exceptions to this consideration. For instance, in the case of $Y_3Al_5O_{12}$ (YAG), fabricated by the reaction-preceded sintering method of an oxides mixture, simple slip-casting yields excellent results (it is not yet clear what merit leads to this specific behavior). Pressure slip-casting is able to overcome, in many cases, the disadvantages of the pressureless variant. If suitable dies (ceramic, polymer, or metal/polymer) instead of conventional gypsum) are available, pressure may be increased up to 3 MPa or more [K37]. Because here liquid flow is ensured by external pressure, one can use dies of very small size; the ceramic and polymer dies available exhibit also a very uniform pore size. Various opinions exist regarding the pressure levels optimal for the formation of highly sinterable casts [R5]. At too high pressure, warpage and cracking owed to strain recovery might occur [L5]. Green BD values in the 60 – 70% TD are achievable by this forming approach,

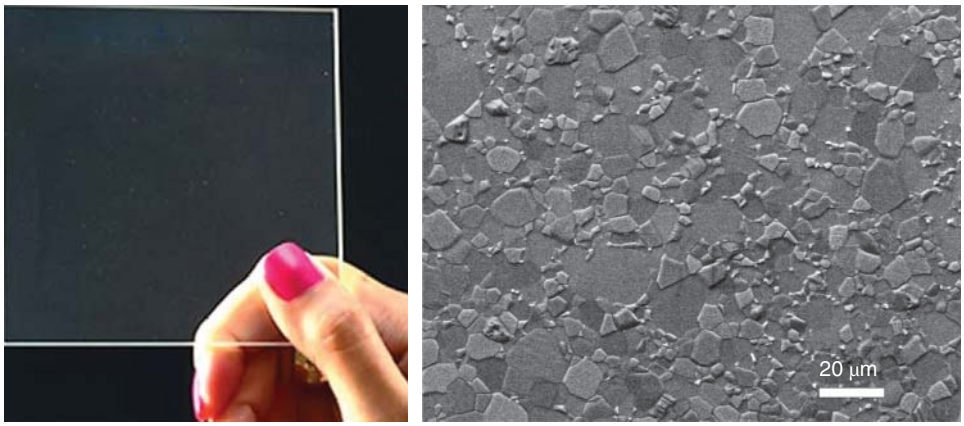

Figure 3.15 Large ($10 \times 10\,cm^2$) plate formed by slip-casting (AS + HIP). (a) Imaging of plate. (b) Microstructure of plate. SEM on polished and etched specimen. Source: Courtesy of A. Shenhar, Israel.

simultaneously with low average pore size and a narrow pore size distribution; residual water content is of only ~15% or lower. For certain oxides, use of suspensions in which a high electrolyte concentration is ensured reduces formation of too early inter-particles "locks." Thus compact casts may be produced even when very low sized particles are present in the suspension [H35]. As a consequence, such green bodies even when formed by pressureless slip-casting exhibit good sinterability.

Figure 3.15 a shows a quite large ($10 \times 10\,cm^2$) 4 mm thick spinel plate, formed by pressure slip-casting. It is devoid of opaque spots, has optical transmission of ~84%, and has excellent ballistic behavior that is similar (if not better) to the best plates formed by cold isostatic pressure (CIP); the microstructure of such parts is illustrated in Figure 3.15b.

3.1.2.2.3.3 Slip-Casting Under Strong Magnetic Fields

A number of reports were published on transparent ceramics slip-casting under the influence of magnetic fields [A4, A27, S75, Y13]. The very important, expected benefit, is a controlled orientation of non-cubic material particles. If that is achieved, a large population of ceramics, till now of limited use for transparent parts fabrication, may be added to the conventional list of cubic materials. For example, alumina Al_2O_3 transparent parts dimensions are limited to under a millimeter thickness. The physical property exploited by this technique is that of magnetic susceptibility anisotropy existing in non-cubic materials. However, most transparent materials exhibit very feeble magnetic susceptibility. Therefore very strong fields, at least of the order of $10 - 12\,T$, need to be used. Experiments with titanium dioxide TiO_2 and alumina Al_2O_3 showed that relatively significant levels of orientation can be achieved. Figure 3.17a,b shows the orientation degree achieved by alumina Al_2O_3 powder

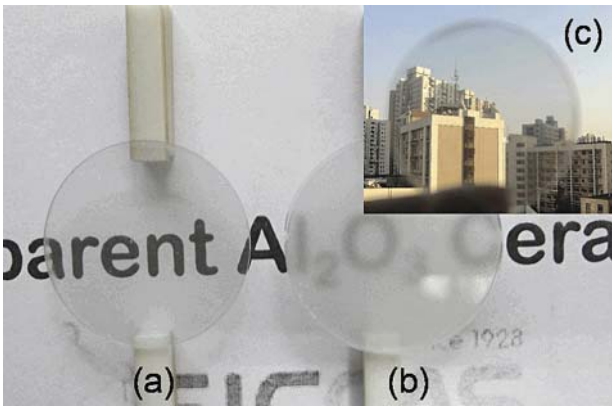

Figure 3.16 Photo of alumina ceramic disc formed by slip-casting under magnetic field. (a) Sintered under optimal conditions. (b) Lower than optimal sintering conditions. Source: Yi et al. 2012 [Y13]. Reproduced with permission from Elsevier.

slip-casting under a strong magnetic field: the visual aspect and transmission spectrum of the sintered specimens are shown in Figures 3.16 and 3.18. For 1 mm thick parts, the transmission of the parts is significant [Y13]. Replacing vacuum sintering by pulsed electric current sintering (PECS) led to further, slight improvement of transmittance [A27].

When materials of somewhat higher magnetic susceptibility, like the rare-earth doped hexagonal fluoroapatite $Ca_5(PO_4)_3F$ (RE^+:FAP) were used, anisotropic ceramic based transparent gain media (a type of product requiring very high optical quality) could be obtained [T2]. Here also, the host offers a weak contribution to the total magnetic susceptibility of the slurry. However, the rare-earth dopant ions increase the magnetic susceptibility to a level that while still low, in absolute terms, allows a practically useful interaction with a moderate strength

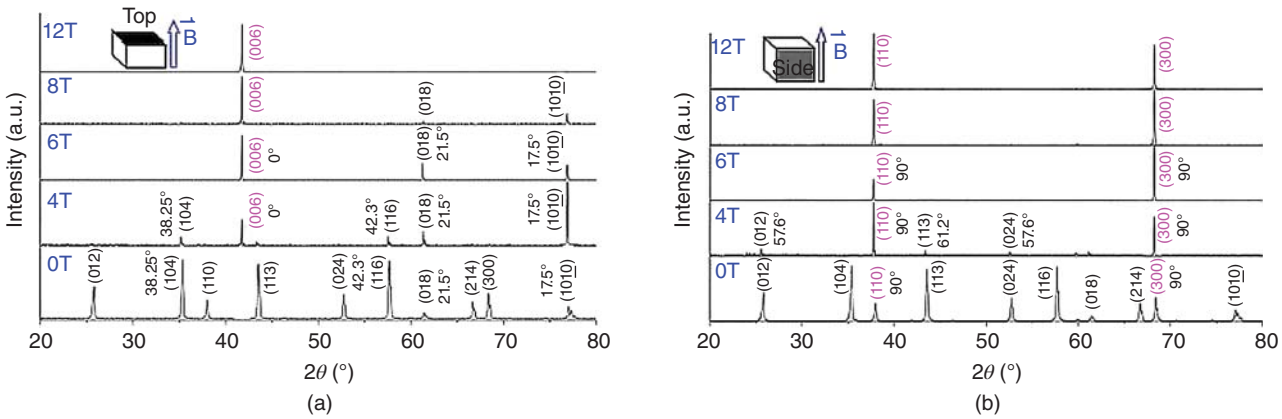

Figure 3.17 Degree of orientation achieved, in the green-specimen from which the disc of Figure 3.16 was derived, shown by the aid of the XRD pattern (magnetic field intensity given in Tesla). (a) X-ray perpendicular on the major surface of specimen. (b) X-ray perpendicular on the side of the specimen. Source: Yi et al. 2012 [Y13]. Reproduced with permission from Elsevier.

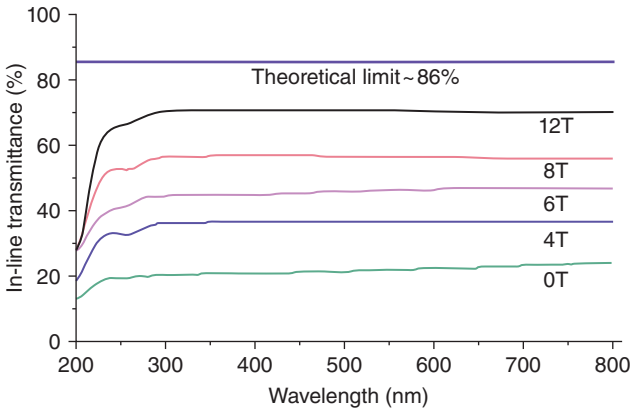

Figure 3.18 Transmission spectra of alumina discs, slip-casted under magnetic field, as a function of magnetic field intensity (sintering in vacuum at 1850°C/5 hours). Source: Yi et al. 2012 [Y13]. Reproduced with permission from Elsevier.

external magnetic field. The susceptibility change $\mathbf{\Delta}\chi$, owed to anisotropy, is equal to

$$\mathbf{\Delta}\chi = \frac{\mu_0 N g_J^{\,2} \mu_B^{\,2}}{VkT}(J_e^{\,2} - J_h^{\,2}), \tag{3.5}$$

where μ_0 is the vacuum magnetic permeability (unitless in cgs, or $4\pi \times 10^{-7}$ V s/A m in MKS units system), μ_B is the Bohr magneton (9.2741×10^{-21} erg/gauss in cgs units), g_J is the Landé factor, J_e is the electronic angular momentum component along the most intense magnetization axis, J_h is the electronic angular momentum component along the least intense magnetization axis, V is the particle volume, and N is the number of rare-earth ions present in a magnetic particle (the particle may be a basic particle or an agglomerate).

Equation (3.5) suggests that triply ionized ytterbium Yb^{3+} ions are more suitable for such experiments than triply ionized neodymium Nd^{3+} ions. The reason relates to the linear dependence of $\mathbf{\Delta}\chi$ on the ions N number: the Nd^{3+} ions exhibit self-quenching, while this effect is much less significant for Yb^{3+} ions. Of course, besides the susceptibility change, the viscosity of the suspending medium is an important limiting factor. Thus, water is a suitable suspending liquid owing to its low viscosity (~200 mPa s at room temperature). Regarding practicalities it is evident that here an optimal material comminution state is that in which a good tradeoff – between the requirements of sinterability and particles ability to rotate, on one hand, and the need for a reasonably large magnetic moment per particle – is realized.

In this context, impressive results were achieved by T. Taira and collaborators [A27, S11]. One of the materials tested was Yb^{3+}-doped fluoroapatite $Ca_5(PO_4)_3F$. As shown in Figure 3.19 [S11], a particle with a $\mathbf{\Delta}\chi$ difference between the axes of hard and weak magnetization is subjected, by the action of an external magnetic field, H, to a torque T_M:

$$T_M = \left(\frac{\mathbf{\Delta}\chi}{2\mu_0}\right) VB^2 \sin 2\theta \tag{3.6}$$

where the symbols have the same meaning like in (3.5), B is the magnetic induction, and the angle θ is defined in Figure 3.19.

In Figure 3.19 the parameters are as follows: μ_0 is the the Bohr elementary magneton; B is the magnetic induction field (magnetic flux density); V is the volume of the FAP particle; Z axis is the direction for orientation control (perpendicular on the strong magnetization direction); θ is the angle between the Z axis and the c-crystallographic axis of the FAP crystal (the c axis is the hard magnetization direction); φ is the angle between the x axis (of the reference coordinates system) and the direction cosine of the c-axis to the magnetic field's rotation plane (x–y); T_M is the alignment torque;

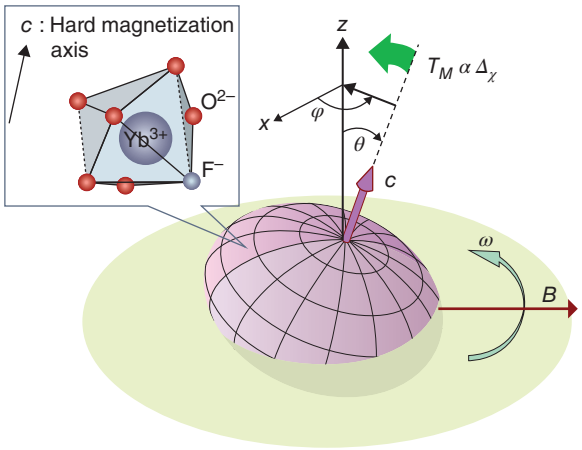

Figure 3.19 Schematic presentation of the mechanism by which an external magnetic field orientates FAP ceramic particles, doped with Yb^{3+}, during slip-casting (parameters description in text). Source: Sato et al. 2014 [S11]. Reproduced with permission from The Optical Society.

$\Delta\chi$ is the magnetic field anisotropy level; ω is the angular velocity of the rotating magnetic field.

In practice the casting mold is the rotating part (17 rpm) of the system. The magnetic axis is perpendicular on the Z axis. x and y are arbitrarily defined. Here x is taken as the direction of the magnetic field at the start of the process.

The schematic of the process is shown in Figure 3.20.

The orientation degree realized in the green body by slip-casting under magnetic field can be checked easily by X-ray diffraction (XRD) measurements. For instance, in the case of the ytterbium doped fluoroapatite $Yb^{3+}:Ca_5(PO_4)_3F$ (Yb:FAP), the (001) peaks, those corresponding to the crystalline planes perpendicular to the crystallographic c-axis, were significantly strengthened. Another parameter used to describe the orientation degree is the Lotgering F factor (defined in [L41]), which assumes values between 0 and 1. As it will be detailed in the Section 3.1.2.3 on sintering, the orientation of particles achieved during the forming stage markedly facilitates full densification and thus transparency achievement.

$Yb^{3+}:Ca_5(PO_4)_3F$ (Yb:FAP) chips have a low optical loss coefficient (≤1%/cm). Transparent layers of the monoclinic potassium-gadolinium-tungstate $KGd(WO_4)_2$, which exhibits a high susceptibility anisotropy, were prepared by electrophoretic deposition under a $2T$ magnetic field.

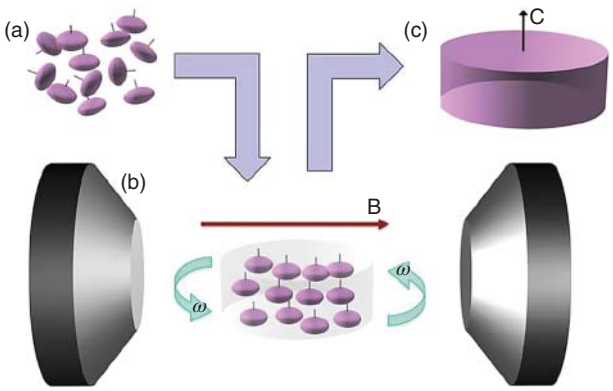

Figure 3.20 Schematic description of the slip-casting under magnetic field. (a) Disordered suspension. (b) Ordering of suspension particles by external magnetic field. (c) Green body including ordered particles. Source: Sato et al. 2014 [S11]. Reproduced with permission from The Optical Society.

3.1.2.2.3.4 Gravitational Deposition, Centrifugal-Casting, and Filter-Pressing

The first procedure – when applied to diluted and well dispersed suspensions, containing particles with moderate segregation tendency (monosphere habitus is ideal [see Section 3.1.2.1]) – allows forming of uniform porosity compact cakes leading to high sinterability [H42]. The method, however, is not convenient for large components, and is time consuming. High-speed (4000 rev/min) centrifugal casting approach is more practical, because it surmounts part of the conventional slip-casting's drawbacks. It can be used for relatively large parts, and even for certain complex shapes [H42]. The casts may attain green densities larger than 65% of the theoretical density TD, and a small size porosity (Figure 3.21 [H42]), finer than that attainable by pressing. The pore size distribution variation across the cast

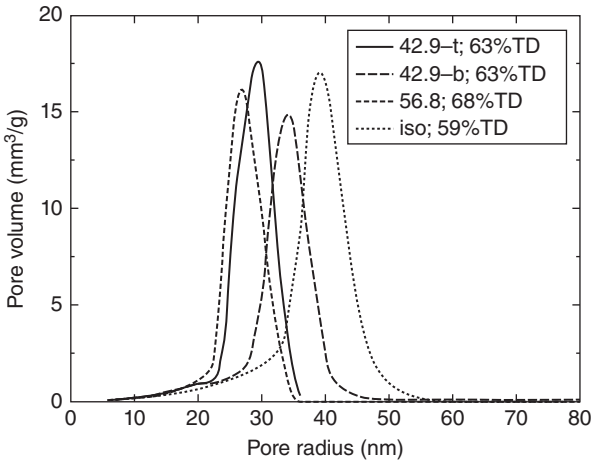

Figure 3.21 Pore size of green cakes formed by centrifugal deposition (initial slurries of 42.9 and 56.8 vol%, respectively, are compared); in case of low solid loading, the pore size of top (t) and bottom (b) layers differs while it shows only small variation when the solid load of casting slurry is higher. Source: Huisman et al. 1995 [H42]. Reproduced with permission from Elsevier.

height is a function of the suspension's solid load as exemplified (alumina powder) in Figure 3.21. As a consequence, required sintering temperatures are reduced compared with those needed for pressed green bodies, and a uniform microstructure can be achieved.

Slip-casting, into poreless dies, followed by gelling (gel-casting) is a procedure introduced, for advanced ceramics during the nineties [O2]. In this method a unifunctional monomer is introduced into a high solid loading slurry (which contains a dispersant) together with another, which is difunctional and a free radicals initiator. The slurry, after being poured into a mold, approximating the shape of the desired part, is brought into conditions allowing polymerization of the monomer. The three-dimensional polymer network thus produced ensures high strength to the green body; it can be machined before sintering. The method was perfected so that monomers that do not represent health hazards can be used and green microstructure of high sinterability can be achieved. Using this forming approach A. Krell et al. and, in other work, H. Shahbazi et al. produced highly transparent spinel parts; the latter showed that isobutylene/maleic anhydride is a monomer very suitable for small pores green bodies. Jiang et al. successfully used the method for transparent YAG fabrication [J8].

Highly compact cakes (green-body density BD_g as high as 70% of theoretical density TD) of quite narrow pore size distributions can be also obtained by pressure filtering (5 – 100 MPa) [L5]; further isostatic pressing can be applied to the cake. Macroscopic cracks formation during recovery of the strain produced during consolidation is, however, difficult to offset. Strengthening with binder polymers alleviates the problem, yet is less effective for larger parts.

3.1.2.3 Sintering

In the case of transparent ceramics, the objective of sintering is the obtainment of practically full porosity closure, namely, **full densification**, while keeping minimal grain growth and energy consumption. Note that in expressing objectives related to other advanced ceramics, the requirements, regarding the level of densification, are less severe.

Since, like for the case of the previous stages of ceramics processing, abundant literature exists on the general ceramics sintering issue [C32, G12, K18, R5, R13], this section focuses on aspects specific to transparent ceramics. However, for the discussion of certain aspects in this section, a number of the suggestive figures and guidelines of [R5] were used.

3.1.2.3.1 Low Relevancy of Average Pore Size

A first specific feature is that in measurements related to transparent ceramics microstructure, one has to focus on *maximal* values rather than average ones. This holds for both grains and pore size and morphology. Even low amounts of too large, especially if occluded, residual pores that are acceptable for other advanced ceramics may prevent the achievement of satisfactory transparency.

3.1.2.3.2 Pore Size Distribution Dynamics During Sintering

Regarding this issue in this section, we discuss a few aspects discovered during studies on TCs.

Except in rare cases like the monosized silica green body shown in Section 3.1.2.1, as-formed powder compacts exhibit various, quite wide pore size distributions. Their morphology and coordination with respect to neighboring particles also vary. The main reason, for the pore size variability, is the fact that the smallest pores existing in the primary basic particle clusters are accompanied by larger inter-cluster pores, and even larger ones separating higher order agglomerates (Figure 3.22 [L6]). Note that the agglomerates shown in the figure don't form a continuous solid; they include voids themselves.

The void fraction of a green body is a tortuous network of individual pores, with a high level of connectivity, in which channels, linking macroscopic surfaces exist, as shown in Figure 3.23a,b [R5].

In the first densification stage, small intra-agglomerate pores shrink first (see Figure 3.23b). As a result, differential shrinkage of the agglomerates which have different internal pore size distributions occurs. The large order

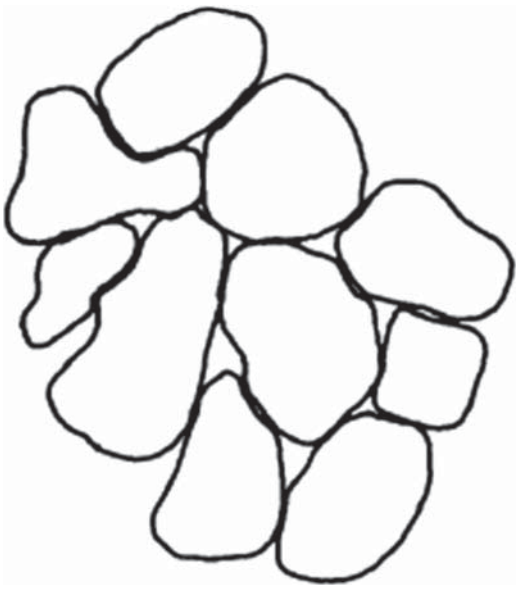

Figure 3.22 Agglomerates of particles, present in the green bodies and the inter-agglomerate pores. The intra-agglomerate pores are not shown. Source: Lange 1984 [L6]. Reproduced with permission from John Wiley & Sons.

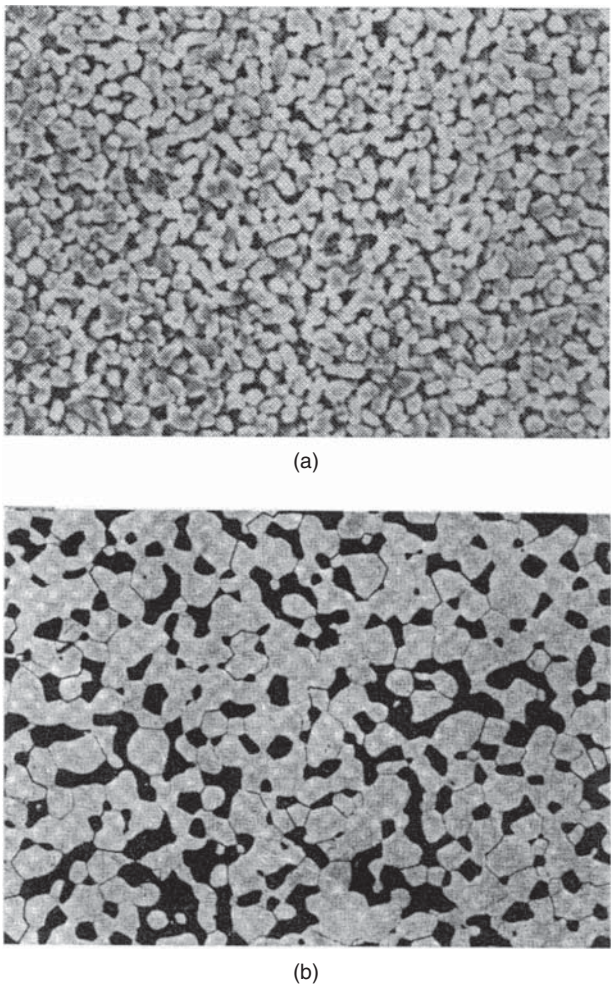

(a)

(b)

Figure 3.23 Voids system pattern and distribution, in the microstructure of a ceramic, during the initial and intermediary stages of sintering; channels pierce the volume of the part. (a) Initial stage and (b) Intermediary stage. Source: Rahaman 2003 [R5]. Reproduced with permission from CRC Press.

agglomerates also differ in size and shape. Therefore, as temperature increases, the inter-agglomerate voids size may increase simultaneously with shrinkage of the small voids present in the lower level agglomerates. After void channels existing during the intermediate stage of sintering breakup and pinch off, discrete pores form, as illustrated in Figure 3.24.

The dominant tendency in that final stage is pore size shrinking. However, under certain conditions, the opposite process, namely, pore size growth, may also occur. One mechanism capable of leading toward such effect is coalescence of smaller pores (Figure 3.25 [R5]).

Pores coalescence is a possible, not ineluctable, side effect of grain growth. However, this mechanism works only as long as pores are sufficiently close, and grain growth is significant. Inter-pore distance grows toward

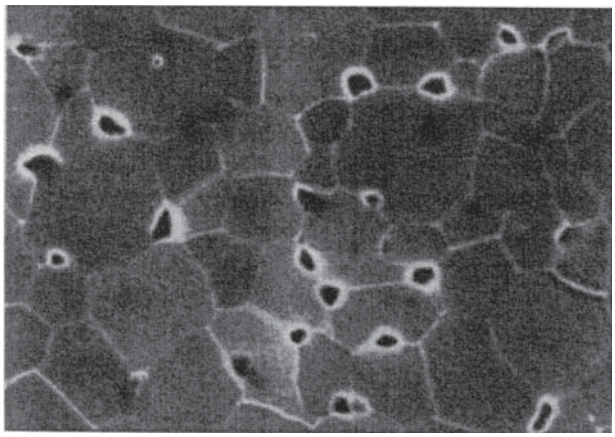

Figure 3.24 The void space distribution, at the start of the last stage of sintering; localized pores, resulting from pinch off from the channels, mostly located at triple points or the grain boundaries (intra-grain pores appear toward the end of this stage). Source: Rahaman 2003 [R5]. Reproduced with permission from CRC Press.

the end of the sintering process. Pores coalescence, when occurring, contributes to microstructure coarsening, but this process is, in fact, quite rarely working in TCs. The coarsening main effect is usually limited to grain growth. It has to be noted that, in many cases where increase of average pore size is observed, it is rather an effect of small pores closing faster than larger ones, and not actually a pore size increase. For instance, R. Boulesteix et al. [B45] observed an increase in the average pore size on $Nd:Y_3Al_5O_{12}$ (Nd:YAG) sintering as the densification and average grain size *GS* increased. The result was explained as caused by faster closure of smaller pores, and not by actual increase in the size (coarsening) of a given pore.

The variability in pore size, shape, and coordination by particles number – within the volume of a given specimen – exists throughout the entire sintering process, not only in the green body. A suggestive illustration of this fact is shown in Figure 3.26 [B45]. This pore size non-uniformity at a given moment of sintering, besides coarsening, is another factor hampering pores closure.

The said variability is one of the reasons that theoretical densification kinetics equations addressing the last sintering stage fail to describe accurately and fully the evolution in real systems; most models assume the existence of equally spaced micron-size pores. Other shortcomings are noted in the following text.

It has been considered, first by W. Kingery and B. Francois [K17], and then discussed in detail by F. Lange and B.I. Davis [L4], that an aspect likely to influence the pores evolution is the coordination number *N* and the coordination pattern assumed by the particles. This pattern is determined by the characteristics of the

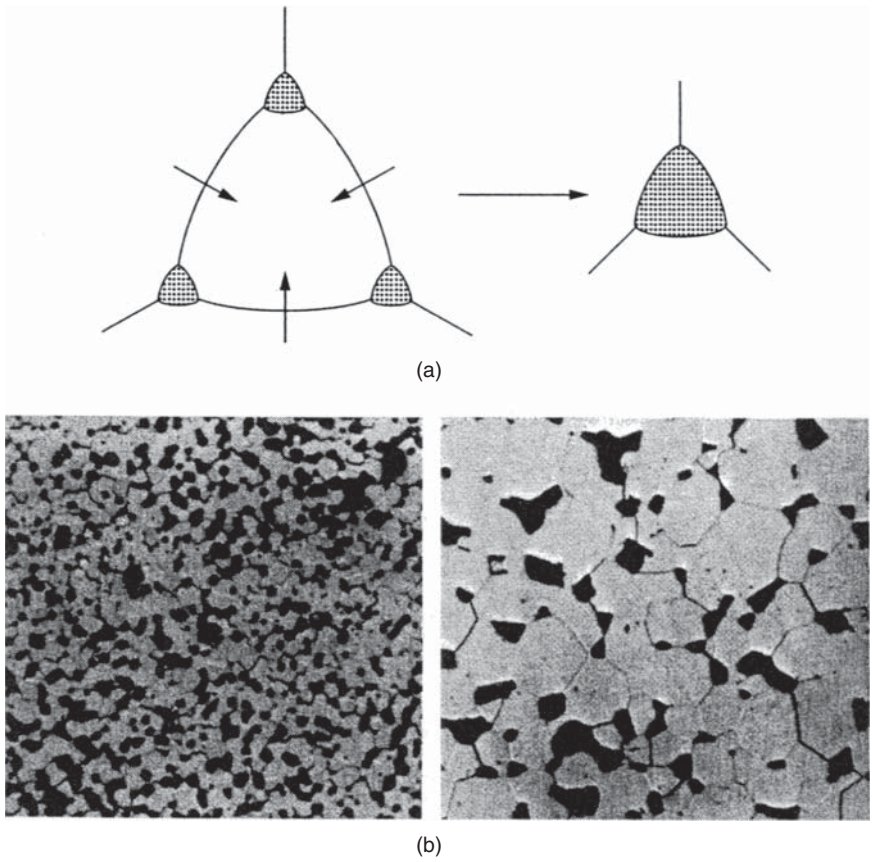

Figure 3.25 The pores coalescence process that may occur, as a result of massive grain growth, and lead to pore size growth. (a) Schematic illustration of the process. (b) Microstructure of UO_2 part, after two minutes at 1600°C (91.5% TD) and five hours (91.9% TD); the process hampers densification. Source: Rahaman 2003 [R5]. Reproduced with permission from CRC Press.

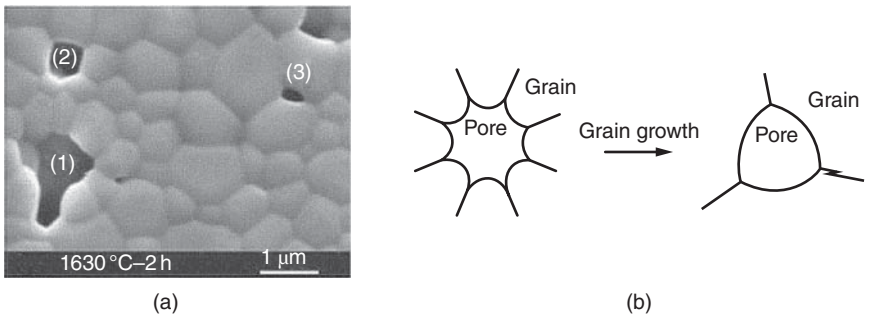

Figure 3.26 Pore coordination (by grains) number (N) in sintering ceramics. (a) Experimental data (vacuum sintering of YAG): pore (1) has $N = 10$, pore (2) has $N = 5$ and pore (3) has $N = 3$. (b) Schematic representation of N variation as a function of grain size. Source: Boulesteix et al. 2013 [B45]. Reproduced with permission from John Wiley & Sons.

initial powder and the applied processing. Kingery and Francois directed attention to the potential influence of the ratio between the grain-size GS and the pores radius r_p on pores state evolution. They argued that pore surface curvature controls the thermodynamic drive toward pore size reduction [K17]. As Figure 3.27 [R5] shows, at equilibrium between the grain boundary energy and the energy generated by the solid/gas interfacial forces, the vector modules have to balance, namely, $2\gamma_{sv}\,\mathbf{cos}\,(\varphi/2) = \gamma_{gb}$, where γ_{gb} is the interfacial energy of the grain boundary, φ is the dihedral angle at the pore/boundary intersection, and γ_{sv} is the solid/vapor interfacial energy.

For, say, an angle $\varphi = 120°$, there are three situations a pore may find itself in, from the point of view of particles coordination pattern. For less than six next neighbors ($N < 6$), the decrease in surface energy brought about by further pore shrinkage is greater than the increase in free energy produced by the new grain-boundary formed zone. It is the other way around for more than six next neighbors ($N > 6$). Thus for $\varphi = 120°$, the sixfold coordination $N = 6 \equiv N_c$ is, in this model, a critical quantity, for which the said two energies balance. For other dihedral φ angles, the critical coordination number is given by $N_c = 360° / (180° - \varphi)$, where φ is expressed in degree units.

Kingery and Francois have analyzed the situation also in three dimensions. The GS/r_p ratio then comes into play because the pore surface curvature depends on the coordination number N, and in turn, N depends

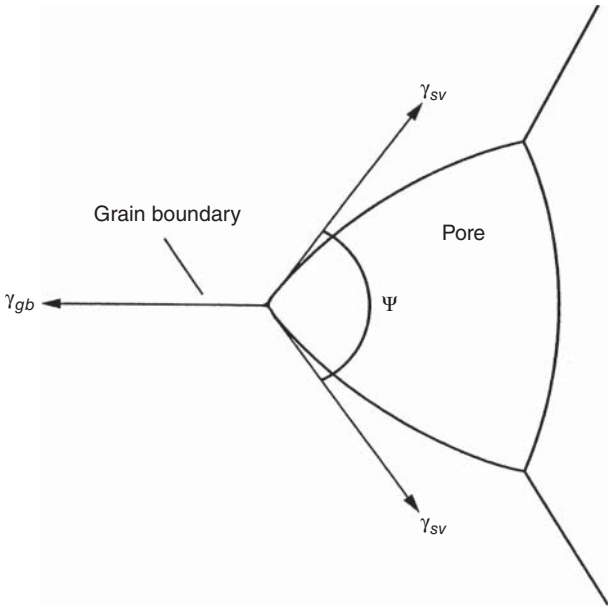

Figure 3.27 Equilibrium shape of a pore, during ceramics sintering, surrounded by three grains and schematic of the forces balance. Source: Rahaman 2003 [R5]. Reproduced with permission from CRC Press.

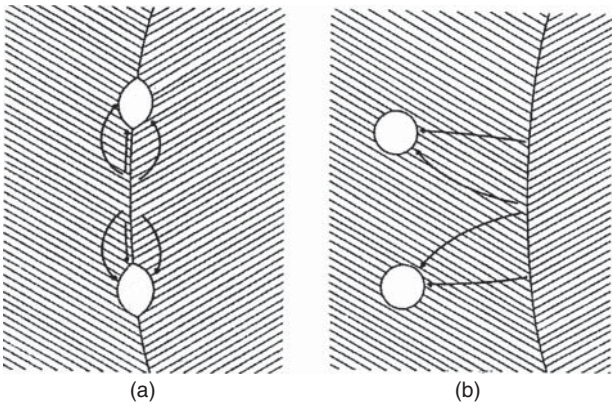

Figure 3.28 Matter transport paths (ionic diffusion mechanism) as a function of pore's location (dashed arrows indicate GB migration direction). Panel a (left): Diffusion paths – along the grain boundary and through bulk – for pores located on grain boundary. Panel b (right): Same paths, for occluded pores. Source: Rahaman 2003 [R5]. Reproduced with permission from CRC Press.

on the GS/r_p ratio. The conclusion is that for $N > N_c(\varphi)$, pores will grow. In all cases, the pore surface moves toward its center of curvature. Continuing the analysis, Lange [L4] has found that ensuring a large GS/r_p ratio reduces the coordination number N, thus helping in attaining the $N < N_c$ situation necessary for pore shrinkage. Observations showed [R5], however, that even pores of larger than N_c coordination numbers are not stable and shrink. Thus there is discrepancy between theory and practice. Further studies found the reasons for that. Thus it was shown that an aspect overlooked by Lange is that in practice the pores are rarely coordinated in a way leading to a **uniform curvature** over the entire pore surface. Pan has shown [P4] that if this is not fulfilled, pore stability driven by surface curvature is not maintained. Moreover, practice showed that a microstructure in which the GS/r_p ratio is small favors pores shrinkage more than the opposite case. Boulesteix et al. [B45] have also shown that while pores of a coordination number N, that is equal or larger than N_c, exist at a given moment (giving the impression that they are stable), they however all shrink during the firing cycle continuation. It has been further shown by Shlamovich and Lange [S38, S39] that in fact the pore surface curvature is not the only important factor controlling the pore shrinkage propensity. The number of grain boundaries intersecting a pore is also important. The larger this number, the more facile the matter transport, necessary for its closure, becomes; small grains size means many grain boundaries and thus is a feature favoring pores shrinkage. The distance between pores also influences shrinkage of each individual pore. This means that sintering behavior analysis that focuses on single pores overlooks important aspects.

Let us summarize this pore shrinkage discussion by reminding a fact more important to TCs than other ceramics undergoing sintering. Because the fact that availability of matter transport paths is critical as far as pore removal kinetics is concerned as long as pores are attached to grain boundaries (preferably more than one grain), their shrinkage is ensured (see Figure 3.28 [R5]).

Highest sinterability appears when the best trade of between pores coordination number N (low number favors thermodynamically closure) and matter transport paths availability (connection to as many as possible grain boundaries) is achieved.

In order to avoid misunderstanding, let us add that when pores are separated from grain boundaries, namely, occluded *inside* grains, some thermodynamic drive toward shrinkage still exists, but relative to other paths, shrinkage actually occurs only by slow lattice diffusion from the grain boundaries toward the pores. In some cases, especially when grain size rises quickly, the occluded fraction of porosity may become large. Occlusion does not necessarily mean full densification stoppage but pore shrinkage rates are, even in the best cases, dramatically reduced. In practice their elimination usually requires very long firing cycles. Sometimes it is even not achievable owing to the grains growth, and its consequences, associated with extensive firing cycles. Existing analytical equations – describing densification kinetics through various sintering stages – provide precious insights related to some factors of influence. They, however, fail to describe the behavior of occluded pores.

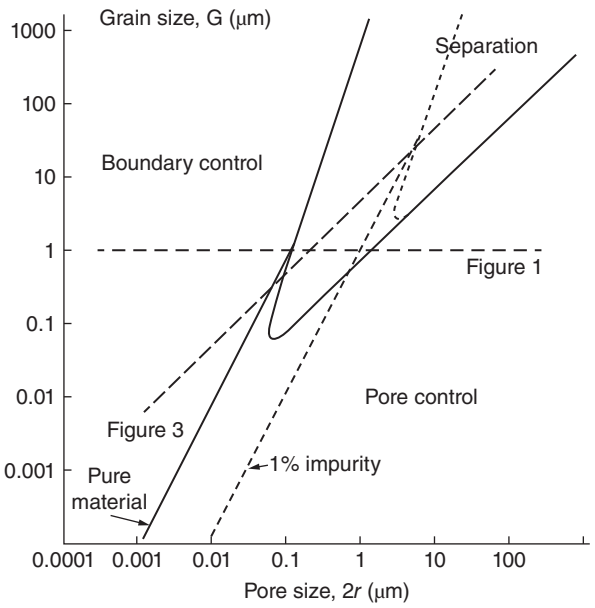

Figure 3.29 Dependence of pore-boundary interaction on microstructural features; the case of a pure system where pores move by surface diffusion. Source: Brook 1969 [B59]. Reproduced with permission from John Wiley & Sons.

These pores are important in the case of TCs because the existence of some occluded pores (the last ones present) while tolerable for most ceramics is not acceptable for them. The issue of occluded pores effect on densification has been theoretically treated by R. Brook. He worked under the assumption that occluded pores means densification end. As noted earlier in many cases this is what happens, when presureless sintering is effectuated; addition of pressure to temperature is one of the not too many options one has to encourage occluded pores closure. Brook examined the relationship between grain growth and pore/grain boundary interaction. One of the most useful results of the study is the microstructural maps he introduced [B59]. They can be helpful in the constructing a firing schedule, capable of retard or avoid the pores occlusion. An example is shown in Figure 3.29.

The map shows that for a given average grain size, which toward the end of sintering is likely to become of high pore occlusion, the occlusion can be avoided by keeping the pore size small. Boulesteix et al. [B45] also noted that features like the number of grain boundaries a pore is attached to, and the effect the dihedral φ angle has on inter-pore distances influences the occlusion process.

3.1.2.3.3 Grain Growth

During sintering, this second process occurs in parallel with densification. Grain growth has negative effect on mechanical properties and, as already seen, affects, usually in a negative way, densification. While a headache for most ceramists, the grain growth is an outstandingly difficult-to-handle case for transparent ceramics. One reason, for this, is the necessity to achieve complete densification before pores occlusion or alternatively provide means for occluded pores closing (not many options); this means that the level of tolerable grain growth is low. Another is the fact that some of the not so many levers available for grain boundaries velocity reduction are not usable in the case of TCs. For instance, addition of second phases is also not usable, because they cause scattering. Luckily at least the drag provided by certain (such as are not causing absorption of electromagnetic radiation (EMR)) impurities, solute in the grain boundaries (GB) region, remains an option for grain growth control. The grain boundary velocity v_b is the product of the boundary mobility μ_b and the driving force for boundary migration. Unfortunately, in certain cases, this drag-causing force may also decrease with grains growth. It is more effective in systems where impurities segregation toward boundaries is stronger.

To select a dopant capable of providing solute drag, one can look at the relationship among the real boundary mobility μ_b^r, the intrinsic mobility μ_b, and the solute affected mobility μ_s:

$$\mu_b^r \equiv \frac{v_b}{F} = \left(\frac{1}{\mu_b} + \frac{1}{\mu_s}\right)^{-1}, \tag{3.7}$$

where F is the total drag force on the grain boundary contributed by the intrinsically caused drag force F_b, and the solute-caused drag force F_s. The solute affected mobility depends, among other factors, on the diffusion coefficient across the boundaries, D_b, the width of the GB, the solute concentration in the lattice (C_0) and the level of segregation (Q) to the GB of the solute.

Solutes of low diffusion coefficient D_b and/or high solute segregation level-times-concentration product QC_0 are likely to be the most efficient. Extrinsic ions of large radiuses can satisfy such requirements. While this conclusion constitutes a useful guideline, dopants effective for a given material need to be selected by trial and error. For instance, one has to consider the fact that effective grain growth controllers may also slow down diffusion *along* the grain boundaries, thus hampering densification. A high solute segregation coefficient Q is a condition that seems to be satisfied by many dopants for the lattices relevant in the transparent ceramics domain. Among others, rare-earth type cations, fourfold ionized silicon Si^{4+}, or sulfur S tend to segregate significantly in the grain boundary zone [C33, W21].

3.1.2.3.4 Methods for Pores Closure Rate Increase

As we saw earlier, during sintering conditions causing full pore stability do not occur; their free surface is the

incentive for pores shrinkage. Thus in principle, the practically full densification, which is a must in transparent ceramics fabrication, is achievable. However, factors, like occlusion or pores coalescence may, in practice, dramatically reduce the rate of the pore closure process. Moreover, certain non-thermodynamic factors may practically prevent full densification; for example, counter-pressure exerted by gas trapped in pores. Let us remind that from a practical point of view, one has to achieve the full densification within a reasonable period of time and without involving too exotic help levers like, say, GPa level pressure.

The earlier suggests that it is important, when designing TC sintering procedures, to enroll factors able to assist the pores closure process. The number of such levers is not very large but their assistance can be, in many cases, substantial. We will review in the following text some of the most important ones.

3.1.2.3.4.1 Liquid Assisted Sintering

A method worth consideration in this context is the liquid assisted sintering (LAS). Ideally, after cooling, the used liquids would generate solid phases of optical refractive index, which is close to that of the main phase. Alternatively and better the liquids (for example, lithium fluoride LiF for spinel $MgAl_2O_4$ HP) are transient, i.e. able to exit the specimens before the end of the sintering process. In practice there are cases in which the constraint – on the difference $\mathbf{\Delta}n$ between refractive indices being small – may not be so severe. This is so when the microstructure can be brought to a configuration in which the residual liquid solidifies to form glassy films lying along grain boundaries. They are thus sufficiently thin to produce only insignificant scattering. Suitable liquids must have a proper set of characteristics. Specifically good wetting ability (of the specific ceramic processed), namely, small contact angle $\theta \ll 90°$, good penetration into the grain boundaries regions (namely, having a large grain boundary surface tension compared to that at the surface between grain and vapor) are requested. Some proper liquid-generator materials have been found, suitable for certain TCs, like spinel. More effort in this direction would be justified, considering the potential benefits.

3.1.2.3.4.2 Pressure Assisted Sintering

Often, transparent ceramics sintering includes a stage in which pressure assists the densification process. The application of an external pressure during firing is in many cases able to significantly raise the densification rates, especially in the final stage, as illustrated by [G10, G29, I3, I4, R35]. One of the popular kinetic equations describing the densification rate, in the presence of pressure, is [H22]

$$\frac{d\rho}{d\tau} = 31.5\frac{V_M}{kT\overline{GS^2}}(1-\rho)\left[D_L + \frac{\pi\delta_b D_b}{\overline{GS}}\right]P \qquad (3.8)$$

here ρ is the density, τ is time, GS^- the average grains size, V_M the molar volume of the diffusing species, λ_b is the grain boundary width, D_b is along the boundary diffusion coefficient, D_L is the lattice diffusion coefficient, and P is the effective pressure acting on the powder compact.

The applied external pressure P_A is amplified owing to the porous structure of the sintering part, and it supplements the normal sintering stress. A rough correlation between the sintering effective pressure P and the external P_A one is given by

$$P = \frac{P_A(1-V_G)}{{V_S}^2(V_S - V_G)}, \qquad (3.9)$$

where V_S is the fractional density (fraction of TD, at a given densification stage; meaning a given size of the inter-grain neck) and V_G is the fractional green density.

In a compact of particles, pressure is transmitted through their contact region where a concentrated stress appears. Thus, the number of inter-particle contacts and their size influences the effectiveness of an external pressure. Unidirectional pressure via a solid punch can be applied directly to the compact. Gas pressure, which is basically isotropic, requires the compact encapsulation in a gastight flexible container. Alternatively, the latter is applied directly, but only after open porosity is closed. The pressureless sintering stress, usually of the order of ~1 MPa, can be significantly augmented by application of the external pressure. In regular HP, the external pressure may become as high as 50 – 60 MPa even for large parts. In spark plasma sintering (SPS) type machines, it may reach up to 100 – 200 MPa. For part diameters larger than 80 – 100 mm, however, the energy consumption of such machines reaches levels often difficult to accept in industrial production. Thus, while the effective increase of the sintering stress decreases as the densification progresses (Figure 3.30 [G12]), the pressure assistance may raise markedly the sintering rates. Under unidirectional pressing, the stress left by contacts aligned with the direction of applied force are about twice larger than those set on perpendicular directions.

Rate equations such as Eq. (3.8) fail to illustrate an important aspect, namely, that pressure assisted sintering is especially helpful in closing occluded porosity. It is not clear why it is so but its effect on existing defects (vacancies, dislocations) or the ability to form new ones seem to facilitate matter transport, from the GBs to the trapped pores; an additional, related, aspect is discussed in the following text, in relation to Figure 3.31.

Let us also note that it is generally considered that pressure increases the grain growth rate [G12]. However,

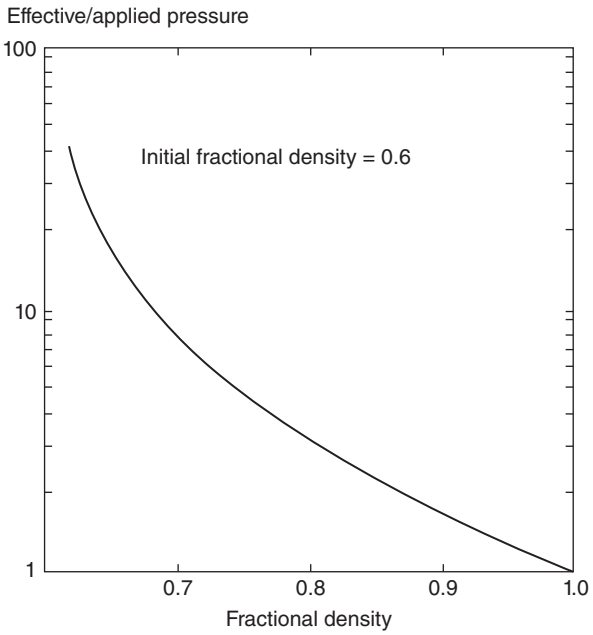

Figure 3.30 Plot of the effective pressure divided by the applied pressure vs. the fractional density for spherical particles with an initial packing density of 0.6. Source: German 1996 [G12]. Reproduced with permission from John Wiley & Sons.

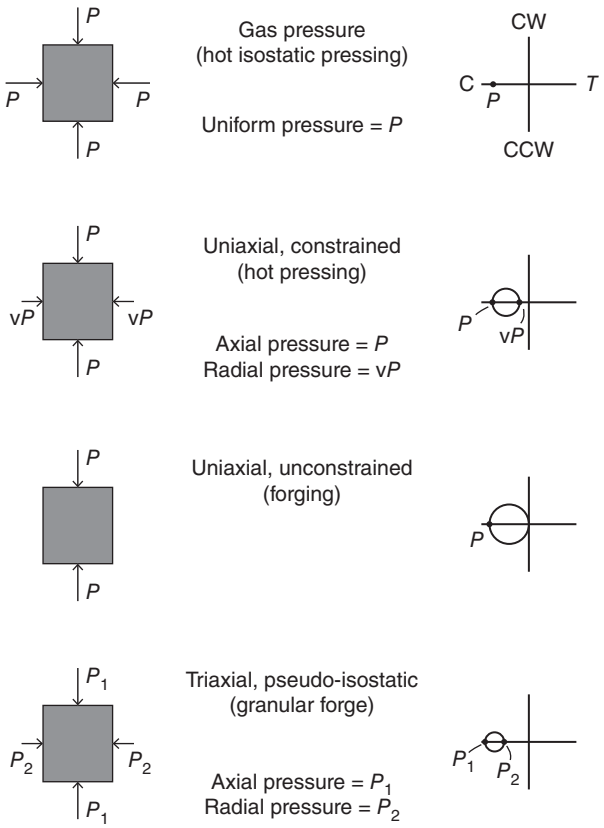

Figure 3.31 Pressure application configuration with indication of the type of mechanical stress induced in the specimen. Source: German 1996 [G12]. Reproduced with permission from John Wiley & Sons.

existing data on transparent ceramics is not that conclusive. Up to ~200 MPa, limited available practical data related to pressure assisted sintering of spinel $MgAl_2O_4$ and yttrium aluminum garnet $Y_3Al_5O_{12}$ (YAG) don't show marked grain growth rate rising with pressure.

Comparing the efficiency of various existing options for pressure application, it is necessary to consider the way they act upon pores. For instance, while hot isostatic pressing (HIP) allows uniform shrinkage and application of large forces, it produces only hydrostatic stress, much like pressureless heating. This reduces the effectiveness of action upon large pores. Where radial constraints exist during HP, a certain level of shear stress appears. As shown in Figure 3.31 [G12], shear stress is helpful in pore closure, when HIP is compared with forging, for which shear stress is even larger than in HP.

In certain cases, this state of affairs is observed when transparent ceramics are sintered. For instance, in the case of large and very large parts of spinel $MgAl_2O_4$, it is possible to obtain a more complete elimination of opaque spots by the use of HP rather than by combining pressure assisted sintering with hot isostatic pressing (AS + HIP). In unidirectional HP, a significant densification boost may be produced by the action of high temperature transient lubricants. Certain additives are able to generate liquids, in the presence of which marked densification takes place. That effect is so strong, that it suggests rearrangement of particles by viscous flow, possibly with the induction of some local grains plasticity. More details will be presented in the Section 4.2.1.1.2 dedicated to transparent spinel $MgAl_2O_4$ fabrication.

In HIP of transparent ceramics, gases exhibiting low solubility in the processed solid are selected. Despite that, some gas penetration inside the specimens is unavoidable. Gas penetration may have undesired consequences, especially during post HIP thermal annealing treatments (done for black color elimination). Examples of pressure assisted sintering will be given in Chapters 4 and 5. Most transparent ceramics HP is effectuated at pressures under 60 MPa; in administering SPS – which is basically also a sort of HP – the pressure may go up to 120 MPa, and, rarely, up to 300 – 400 MPa (the latter by using silicon carbide SiC dies). The more efficient SPS HP allows, for instance, to achieve full densification while keeping the grain size low. A very low grain size besides improving mechanical properties also reduces scattering loss in the case of non-cubic ceramics [A22]. Here we exemplify with the case of mullite ($3Al_2O_3 \cdot 2SiO_2$). This is a quite birefringent material but the 200 nm grains possessing parts fabricated by L. Ren

et al. [R16], achieved a high IR transmission ($T = 83\%$ for $T = 1$ mm at 2.5 μm and around 65% at 600 nm); sintering temperature was 1350°C and pressure 80 MPa. The use of special die/punch systems allows raising the pressure up to ~8 GPa, yet for only small specimens. It allows achieving advanced densification at temperatures lower than 1000° C. Pore size left by such operations is under 60 nm, thus provoking only weak optical scattering. Therefore, even when relatively large amounts of remnant porosity remain, it doesn't markedly reduce the parts transparency. For example, spinel $MgAl_2O_4$ discs exhibiting ~40% optical transmission at 1.5 μm were obtained at 620° C under 3.7 GPa [Z4]. Such specimens maintain an average grain of 70 – 80 nm, and nano-sized pores located mostly at triple junctions. The hot-pressed BD, however, is as low as 98.8% of the theoretical density. Cerium Ce-doped transparent yttrium aluminum garnet $Y_3Al_5O_{12}$ (YAG) was obtained at temperatures of less than 500° C under 8 GPa [G47].

3.1.2.3.4.3 Sintering Under Electromagnetic Radiation

A solid that includes electrical dipoles absorbs energy when exposed to electromagnetic radiation of frequency appropriate to flip the dipoles. Ultimately, most absorbed energy converts into heat. The absorbed power P_A is given by [S74]

$$P_A = \omega\varepsilon_0\varepsilon'' \, VE_i^{\,2}/2 + \omega\mu_0\mu'' \, VH_i^{\,2} \tag{3.10}$$

where P_A is the absorbed power, E and H the strength of the electric (V/m) and magnetic field (A/m), respectively, ω the angular velocity of the field (rad/s), and V the sample's volume (m^3), while $\varepsilon_0 = 8.85 \times 10^{-12}$ C/V m is the free-space permittivity, $\mu_0 = 4\pi \times 10^{-7}$ T/A m is the free-space magnetic permeability, ε'' is the imaginary part of the dielectric function, and μ'' is imaginary part of the material's ε^*. The penetration depth (D_p) of the EMR is defined as the depth inside the specimen at which the incident power P_0 is reduced to a level equal to a fraction of $1/e$ the initial value. The incident power is reduced with a progressing penetration path "d," owing to absorption, according to (3.11):

$$P(d) = P_0 e^{-2\alpha d} \tag{3.11}$$

where α is a constant (calculated by Von Hippel) dependent on $1/\lambda$ (wavelength of the MW radiation) and the real and imaginary parts of ε^*.

The two terms of (3.10) represent respectively the electric and magnetic fields contribution to the energy absorbed by the specimens from the EMR. The EMR used here has Gigahertz frequencies (MW region, between 1 mm and 1 m wavelength), and as a result the amounts of energy, brought to the specimens, are sufficiently high to allow fast heating to high temperatures. Of course this is true if the specimens are able to absorb the energy provided, viz the D_p is significant. If the electrical and/or magnetic components of the EMR are reflected (case of metals), then only a thin skin of the specimens is heated (too low D_p). Therefore, metals or ceramics possessing metallic conductivity can be effectively MW processed only when dispersed as small particles. Fortunately most ceramics are linear dielectrics (a notable exception is provided by the ferroelectrics like La containing PZT (PLZT) and similar). Those with a sufficiently high dielectric loss (e.g. Y stabilized zirconias), at low temperatures, are suitable for direct MW processing; as will be clarified later even for those that do not exhibit high loss at room temperature (RT) a method to make them amenable to such firing exists.

In practice, the 2.45 GHz frequency is the most popular, due to the low cost of the cyclotron type sources. In addition the existing MW machines – which were developed, initially to heat water containing materials – when the study of ceramics processing, by their aid, was started were working at this frequency readily absorbed by the water dipolar molecules. Higher frequencies, in the 28 – 80 GHz range, are, in fact, more effective for ceramics and allow more uniform heating, yet they require the use of very expensive gyrotrons as radiation sources. In the case of MW heating, the heat develops inside the specimen, reducing the energy losses existent in traditional heating where the specimens are heated by thermal radiation provided by heating elements external to the load.

It is believed that besides the ability to heat up the specimens, MW fields also induce ionic diffusion, and as a result may facilitate densification (a process addressed as non-thermal MW effects) [S74]. Thus, MW heating seems attractive for transparent ceramics sintering. A significant problem is, as noted previously, the low dielectric loss at low temperatures of most of the relevant ceramics. However, fortunately the coupling to MWs improves markedly at high temperatures, or at frequencies exceeding about 10 GHz. Therefore, an arrangement called susceptor-assisted MW processing can be used to circumvent the low room temperature material polarizability, at 2.45 GHz. In this approach, a material capable of coupling to the MW electromagnetic radiation at room temperature (for example, silicon carbide SiC or zirconia ZrO_2), is introduced in the applicator (the metal-walled container to which the electromagnetic waves are directed, and in which it is confined). Initially, the heated susceptor further heats the specimens by emitting far-infrared radiation (radiative thermal contact). Then, at the high temperatures, the specimens start to couple directly to the electromagnetic MW field. Suitable selection of susceptor material and its spatial distribution pattern allows the specimen/MW interaction to become the main source of heating at high temperatures.

Figure 3.32 Applicator of an MW (2.45 GHz) sintering system (large L/λ ratio, multimode operation, mode stirrer Al wall). Source: ICSI, Haifa.

Figure 3.32 presents an MW heating system that was used for ceramics sintering allowing among other things achievement of transparent silica and spinel [G26, G30].

By an alternative approach, an "internal" susceptor is used, namely, a material which is a part of the specimen. It may be either transient or stable. In the case of the transparent ceramics, the internal susceptor must be benign, namely, never affect the optical properties. This requirement obviously restricts the set of usable options.

A major practical problem is the maintenance of the electromagnetic radiation field uniformity during processing. A use of two high-frequency wavelengths system is able to alleviate the problem. When needs for large loads at reasonable cost are considered, the most practical setup is obtained by working at 2.45 GHz in large multimode applicators provided with mode stirrers. Another problem is thermal "runaway" prevention. Such a process may start in those temperature regions where the specimen radiation absorption increases too fast with temperature, causing an exponential increase in temperature. Thus, only materials with a suitable temperature profile of the loss tangent can be heated without causing thermal runaway. Even for such materials, the time profile of the inserted power has to be harmonized with the temperature profile of electrical loss tangent ($\tan\delta$ or its equivalent ε''), for example, by pulsed irradiation. Densification temperatures and treatment duration reductions have been achieved for certain ceramics by MW heating [G26, J6, S74].

3.1.2.3.4.4 Sintering Slip-Cast Specimens Under Magnetic Field

In the previous section dealing with green-body formation, it was shown that slip-casting under magnetic fields allows orientation of certain anisotropic materials like ytterbium Yb- or neodymium Nd-doped fluoroapatite $Ca_5(PO_4)_3F$ (FAP). This approach, when perfected, would allow a significant extension of the compositional range open for production of transparent ceramics, which is currently limited to cubic materials. It is interesting to note that under such processing, the grain growth, a deleterious phenomenon that is important to curb during sintering, has a positive effect. More specifically, the abnormal sort of grain growth is able to enhance the orientation effect achieved during slip-casting under magnetic field. The degree of crystallographic orientation is much enhanced in the sintering stage (orientation levels attained solely in the green body is insufficient for providing optical transparency [S11]). Laser-grade parts could be derived by such processing from ytterbium-fluoroapatite $Yb:Ca_5(PO_4)_3F$ (Yb:FAP).

3.1.2.3.4.5 Reaction-Preceded Sintering

Before treating the issue let us clarify the term. The expression reaction sintering is widely used sometimes covering situations, which we prefer to call reaction preceded sintering. For those who introduced the term "reaction sintering" describes a situation in which the two processes more or less superpose and where exothermal reactions provide energy used by the sintering. Situations of the type we describe here are different: reaction takes place earlier than sintering and possible energy produced is consumed before sintering starts.

This approach is rather deleterious for most poly-oxide materials; among the worst cases are those of magnesium Mg- or zinc Zn-spinels ($MgAl_2O_4$ or $ZnAl_2O_4$, respectively) [G33]. The reason is that during the inter-oxides reaction, the resulted particles arrangement in the compact green body is disrupted owing to a volume expansion brought about by the reaction. Thus the specimen arrives at sintering temperatures with a configuration less sinterable that it had after forming. The disadvantage of the method can be compensated [E6] by applying an external pressure that opposes particles rearrangement during reaction. If such a pressure assisted format is adopted, transparent spinel, for instance, can be derived from a mixture of oxides applying reaction precede sintering. In certain, very important cases like that of yttrium-aluminum-garnet $Y_3Al_5O_{12}$ (YAG), no expansion accompanies the reaction between yttria Y_2O_3 and alumina Al_2O_3 [I3]; on the contrary, shrinkage

occurs during the two oxides reaction. As a result in this case, use of reaction-preceded sintering allows the achievement of ceramic parts of high-transparency even when pressureless sintering is applied.

3.1.2.3.4.6 Use of Sintering Aids

Ceramic technologies use various additives to enhance densification rate. In some cases, the additives concentrations may be low, or even below about 1%, such that they may be addressed as dopants. This approach can be efficient also in the case of certain transparent ceramics; however, their selection must assure that the resultant part optical properties are not degraded. We hereby describe several examples of transparent ceramics densification assisted by additives.

In the case of ceramic alumina Al_2O_3, transparency was made possible by doping with magnesium oxide MgO. As noted in the Section 4.2.3 devoted to this material, the mechanism by which MgO exerts its beneficial influence is still a matter of some debate (which actually started already in the late 1950s) [C32, N7]. In the case of spinel $MgAl_2O_4$ or magnesium oxide MgO, addition of $0.7-4$ wt% lithium fluoride LiF allows the achievement of up to ~1 m large parts by low pressure ($P < 50$ MPa) HP [E6, G29, R35]. Fabrication of laser-level yttrium aluminum garnet $Y_3Al_5O_{12}$ (YAG) parts is facilitated by doping with silica, which introduces fourfold ionized silicon cations Si^{4+} into the lattice [I3, R2]; grain growth, however, is also accelerated by this dopant [B43]. It was shown [Z1] that the solubility limit of Si^{4+} in the YAG lattice (fired at 1700°C/6 hours) is around 980 ppm, on fast cooling, and it is reduced to some 650 ppm if cooling is slow. If the initial amount of SiO_2 added is higher (such an amount is carried by some 0.2% SiO_2) than the solubility limit liquid may form, in the grain-boundary regions and this may facilitate grain growth. On cooling the liquid solidifies to silica and a Y silicate, introducing second phases with a refraction index different from that of YAG. A significant amount of silica is lost during sintering in vacuum; as a function of temperature (1700–1800°C) and length of dwell the loss varies in the 30–90% range. As it will be discussed later, the Si^{4+} entering the YAG lattice facilitates also reduction of some Y^{3+} to Y^{2+}. YAG doped with low amounts of MgO (~0.03%) was also processed to high level of transparency ($T = 80\%$; $t = 3$ mm at 400 nm) [Z19]; it was proposed that improved densification is owed to the formation of oxygen vacancies upon substitution of Al^{3+} by Mg^{2+}. If the good transmission is a consequence of the Mg addition, it was not however clearly demonstrated; the spectrum of undoped YAG, fabricated in the same conditions – which is needed as a reference – was not provided by the authors.

Krell et al. [K53] discovered that in the case of spinel $MgAl_2O_4$, additions of ~0.1 wt% calcium oxide CaO or other earth-alkaline oxides allows reductions of sintering temperatures. The same dopant (0.04%) was used as sintering aid for YAG [Z7], giving results similar to Mg^{2+}, viz a transmission of 80% at 400 nm. Like in the case of the MgO effect examinations, the authors (the same team) did not provide the transmission of an undoped specimen so that claim about the effect of CaO is also not fully demonstrated.

New firing methods now under study, like flash-sintering, near room temperature sintering, or sintering by intense thermal radiation, are not yet used for transparent ceramics fabrication.

3.1.3 Bulk Chemical Vapor Deposition (CVD)

The CVD is a technology in which gaseous reactants generated by the vaporization of adequate solid or liquid sources react and/or decompose after coming in contact with a solid substrate, thus generating a solid deposit. A wide variety of CVD techniques exist, differing in the reactant gases generation means, the atmosphere in the reaction chamber (in most cases various levels of vacuum), and sometimes the presence of reaction enhancing fields, like plasma creating electrical fields and/or ultraviolet (UV) light. A schematic of an installation used to fabricate large zinc-selenide ZnS parts by a CVD method is depicted in Figure 3.33 [H15].

The CVD technique, while having many attractive features, is a slow method. It is therefore most useful for depositing of thin coatings on various substrates. However, under certain conditions and for specific materials, sufficiently *thick* deposits can be generated within a reasonable time to allow fabrication of bulky (three-dimensional) parts. An acceptable rate would be about 10 µm/h. In the field of transparent ceramics production, the technique is used especially for the production of zinc sulfide or selenide ZnS/Se, silicon carbide SiC, gallium phosphide GaP, silicon nitride Si_3N_4, and diamond C; in the case of polycrystalline diamond plates, ~1 mm thick plates of 100 cm^2 surface have been grown [H15].

Further details on the CVD method as used for specific materials are given in Chapter 4.

3.1.4 Glass-Ceramics Fabrication by Controlled Glass Crystallization

3.1.4.1 Introduction

The ceramics of interest in this book, the TCs, contain more than 99.5% crystalline phases. Beyond powder sintering (the major technical ceramics fabrication approach), the short list of methods usable to fabricate

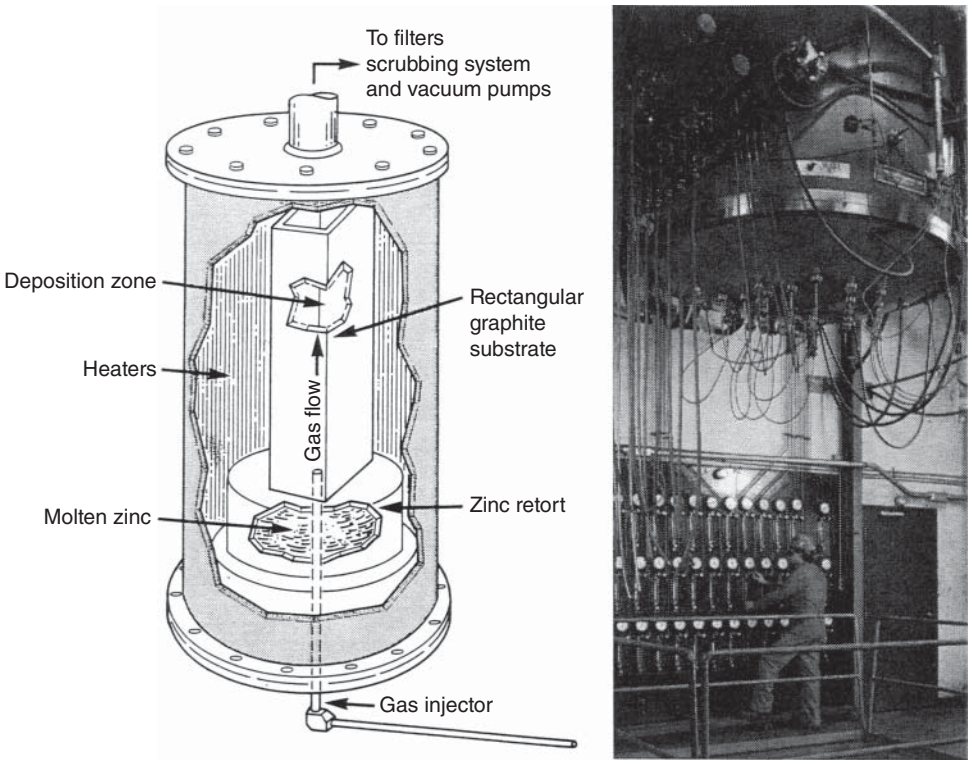

Figure 3.33 Schematic of CVD reactor. Source: Harris 1999 [H15]. Reproduced with permission from SPIE Publishing.

transparent ceramics also contains the controlled glass crystallization approach. In glass fabrication (still the main transparent solid), crystallization is an undesired occurrence [R8, R9]. It might occur locally, in an uncontrolled manner while the glass is maintained at temperatures located between the melting and the rigidizing limits (t_f°–t_g range). For instance, in the most ubiquitous silica-lime-soda (SLS) type glass fabrication, large, randomly dispersed crystallites sometimes precipitate (mostly sodium–calcium–silicate $Na_2Ca_3Si_6O_{10}$), which impair in-line transparency properties (especially during window glass drawing).

Let us recall, from the field of glass technology, that liquids failing to crystallize below freezing temperature ($t^0 < t_f$) are said to assume a supercooled (or undercooled) condition [T33, U4]. It is of course, thermodynamically speaking, a metastable state. This is the reason that crystals, like those previously mentioned, may appear during glass processing. It was observed that the process may be controlled. Controlled crystallization of glasses – which may occur in the same temperature range – as opposed to the deleterious random one can lead to generation of useful materials. For instance, precipitation, in silicate glasses, of very low amounts of colloidal metal crystalline particles like gold Au or copper Cu imparts beautiful ("ruby-like") colors to the glass. Precipitation of certain fluorides like calcium fluoride CaF_2 and sodium fluoride NaF (usually less than ~4 wt%) produces opal-like materials, exhibiting a milky appearance owing to a relatively mild scattering of light. The amount of crystallites in such systems, while able to influence optical properties, is too low to alter significantly the glassy structure. Such materials are basically glasses, a subject we refrain from addressing thoroughly in this book. However, a type of material that while also having a glass matrix includes higher amounts of crystalline phases than the materials discussed earlier – high enough to significantly influence also non optical properties – called glass–ceramic, will preoccupy us. Experiments toward development of glass–ceramics actually started more than 200 years by de Reaumur [R11]. During the 1950s, that new class of materials was successfully developed [S1, S56–S60]. Objects are considered glass–ceramic when the product of the initial fabrication stage appears as a bulk (compact) or a powdered glass. This state is then altered by controlled crystallization, which converts the part into a state in which crystalline phases constitute a considerably large fraction (20 – 75%) to significantly modify the mechanical, thermal, and chemical properties of the initial glass. Let us underline that, in best cases, the crystalline part may approach 100%. The final products in such best cases are similar, in appearance and properties, to those fabricated by powder sintering. These hybrid transparent

solids, the glass–ceramics, have to be considered, for obvious reasons, by both glass makers and ceramists; therefore, they are discussed also in this book.

Discovery of the practical usefulness of glass–ceramics was accidental, much like those of penicillin or the radioactivity. As always, it required an observer capable of understanding the implications of the accidentally observed facts. Thus, during experiments regarding metal colloids precipitation in glass, S.D. Stookey observed that a glass specimen, inadvertently heated to 850° C instead of the required 450° C, morphed into a white opaque object without being distorted (even though the softening temperature of the glass was exceeded). Also accidentally, Stookey dropped the part and observed its unusual strength. He realized that the observed symptoms were the result of a controlled crystallization process. The rest is history. An example of a glass–ceramic made part is shown in Figure 3.34 [S58].

Glass-ceramics quickly became a topic for research and manufacturing efforts at Corning Works, the base for many appreciated commercial products. The applications range from home appliances to telescope mirrors, dental restoration or radomes, the latter actually being the first practical application. Most glass–ceramics are opaque or translucent [P29]. Some, however, can be obtained in a transparent form despite including significant fractions of a crystalline phase. Like transparent ceramics, such systems combine transparency with other functional properties, in many cases high desirable for a variety of other applications. Also like TCs their non-optical properties are controlled mostly, by their crystalline phases content. To understand the preparation conditions required for glass–ceramics, transparent or not, a brief recap of the basic controlled crystallization (ceramming) process is hereby provided; its relationship to optical transparency is also discussed. This topic is discussed here in a more depth than the powders sintering related processes were (3.1) because it is too summarily treated in most of the ceramic text books.

Figure 3.34 Corning ware (opaque bowl) in both finished state (left) and initial (glass) state.

3.1.4.2 Glass Crystallization: Basic Theory

Crystallization is the process by which a regular crystal lattice is generated from a disordered lattice of a liquid. In fact a glass is actually a supercooled liquid [P14, R9]. Crystallization off a supersaturated aqueous solution and off a supercooled oxides liquid takes place in a quite similar manner. It basically occurs by two stages: nucleation and crystal growth. The process is presented in the following text mostly following McMillan [M27].

Crystallization proceeds from localized centers (nuclei). Such centers either pre-exist (external seed/nucleator, crucible surface) causing heterogeneous crystallization, or form spontaneously – when certain conditions regarding concentration temperature and pressure are fulfilled – causing a homogeneous nucleation. In the latter case, regions of long range order appear, at the centers mentioned above, when the conditions are such that for the dissolute material an ordered state becomes thermodynamically favored. Then re-arrangement can be kinetically quite fast. The homogeneous spontaneous nucleation is due to fluctuations in the mobile matrix structure, and it occurs at random locations under high degrees of solution supersaturation or at a marked level of supercooling. Glass-ceramics formation, based on homogeneous crystallization, is rarely feasible; heterogeneous crystallization is the approach most often used. In both homogeneous and heterogeneous cases, nucleation is followed by a crystal growth stage, in which matrix material flows toward the nuclei, depositing on their surfaces in an ordered fashion. The temperature profile of the two processes, in the case of a supercooled liquid, is shown in Figure 3.35 [M27] as determined by Tamman [T8] a long ago.

Nuclei growth does not occur in the marked metastable zone. Crystal growth, however, is possible if nuclei are provided. No solid exists in the $T_1 - T_2$ zone because the melting point of small nuclei is lower than that of bulk materials [M27]. The segments of decreasing rate are owed to increase of viscosity, which slows down the atomic rearrangements required for nucleation and growth. Below T_3 the viscosity is so high that even nuclei are unable to form. Below a brief presentation of the two processes involved in crystallization, from a thermodynamic perspective, is given.

3.1.4.2.1 Nucleation

Formation of nuclei implies formation of free surfaces, namely, an increase of the free energy [H27]. On the

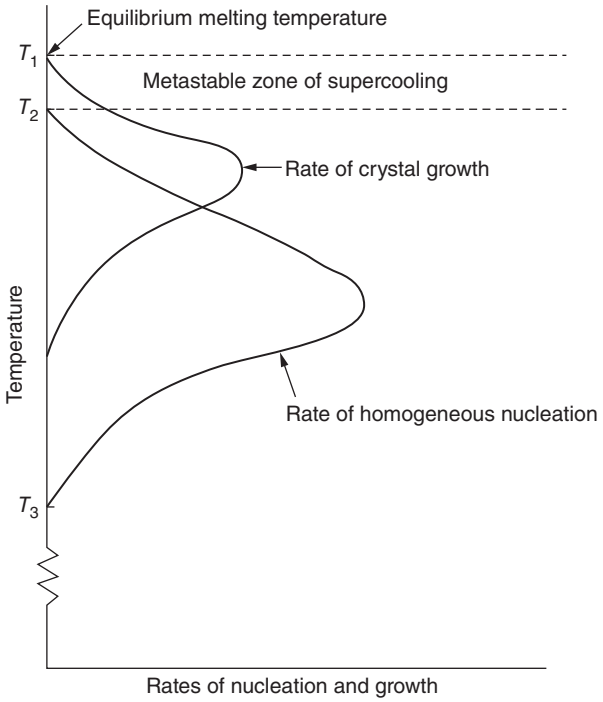

Figure 3.35 Rate, as a function of temperature (within the t_g–t_f range) level, of the two basic processes at work during controlled crystallization of glass (nucleation and crystal-growth); case of homogeneous crystallization. Source: McMillan 1971 [M27]. Reproduced with permission from Elsevier.

other hand, the more ordered compact arrangement of atoms compared with the viscous fluid leads to free energy reduction. According to Gibbs, the total free energy change $\mathbf{\Delta}F$ due to the formation of a spherical nucleus of radius r is given by

$$\mathbf{\Delta}F = -\frac{4}{3}\pi r^3 \cdot \mathbf{\Delta}F_{\mathrm{v}} + 4\pi r^2 \mathbf{\Delta}F_s \tag{3.12}$$

where $\mathbf{\Delta}F_{\mathrm{v}}$ is the free-energy change per unit volume upon solidification, and $\mathbf{\Delta}F_{\mathrm{s}}$ is the free-energy change per unit area of solid–fluid interface created upon solidification. At a critical value of the radius (r_c), the free energy change attains its maximum. The maximal value of the $\mathbf{\Delta}F$ function can be retrieved, of course, by differentiation of (3.12). For radii values larger than this critical value, $r_c = 2\mathbf{\Delta}F_s/\mathbf{\Delta}F_{\mathrm{v}}$, the first term in Eq. (3.12) becomes dominant, and further growth is eased. Based on statistical mechanics it can be shown that the homogeneous volume nucleation rate (volume nucleation per unit time) can be expressed as

$$I = \frac{nD'}{{a_0}^2} \exp\left(-\frac{16\pi(\mathbf{\Delta}F_s)^3 V^2 {T_m}^2}{3L^2(\mathbf{\Delta}T)^2 k_B T}\right) \tag{3.13}$$

where n is the atomic volume density (number of atoms per unit volume), a_0 is the inter-atomic distance, k_B is the Boltzmann constant, T_m (in other parts of the book this is spelled as t^0_f) is the melting temperature, T is the actual temperature (in K), $\mathbf{\Delta}T$ is the undercooling level (viz the difference between the actual T and T_m; T is of course lower than T_m), L is the volumetric latent heat of fusion, and V is the molar volume of the crystal phase. D' is the molecules transport diffusion coefficient, across the liquid/solid interface. According to the Stokes–Einstein equation, it is given by $D' = RT/N_A 6\pi\eta a_0$, where η is the melt viscosity, N_A is Avogadro's number, and R is the gas constant. The parameters in Eq. (3.13) are not fully independent since $\mathbf{\Delta}F_{\mathrm{v}}$ actually relates to the latent fusion heat L and other system parameters by $\mathbf{\Delta}F_{\mathrm{v}} = L\,\mathbf{\Delta}T/VT_m$. Notably, the diffusion coefficient D' is inversely proportional to the melt viscosity η, and to the squared inter-atomic distance, a_0.

As already noted the homogeneous nucleation, discussed earlier, is rarely relayed upon in glass–ceramics fabrication; the faster heterogeneous variant is preferred. The most important difference between heterogeneous and homogeneous nucleation is the pre-existing surfaces in the former, like inclusions, wall or liquid/air surfaces. This reduces drastically the value of the effective $\mathbf{\Delta}F_s$. There are two important factors that enhance the efficiency of an external nucleator. First, very effective, is similarity between the nucleator lattice and that of the phase which has to grow on it as a substrate (viz possibility of epitaxial growth). Second is a low interfacial tension between the involved phases. Considering the contact angle θ of the substrate-melt-precipitate junction, then $\mathbf{\Delta}F^*_h = \mathbf{\Delta}F^* f(\theta)$ where $\mathbf{\Delta}F^*_h$ is the free energy change in the case of the heterogeneous nucleation. Then the heterogeneous volume nucleation rate I_n is given by

$$I_n = A^1 \exp[-(\mathbf{\Delta}F^* f(\theta) + Q)/kT], \tag{3.14}$$

where A^1 is a constant, Q is the diffusion activation energy, and $f(\theta) = (2 + \mathbf{cos}\,\theta)(1 - \mathbf{cos}\,\theta)^2/4$ is a geometric factor related to the interfacial energy relations between the nucleator and the melt (supercooled fluid). It derives from the relation $\sigma_{HL} = \sigma_{SH} + \sigma_{SL}\,\mathbf{cos}\,\theta$, where σ_{HL} tension exists owing to the interfacial free energy of the surface between the nucleator and the melt (supercooled fluid) and σ_{SH} because of the interfacial free energy between the nucleator and the new crystallizing phase. σ_{SL} tension coefficient is due to the free energy at the interface between the new crystallized phase and the supercooled fluid. θ is the angle at the heterogeneity-melt-new crystal precipitate junction. For $\theta < 180°$, the free energy barrier for heterogeneous crystallization is lower than for homogeneous one. Therefore, heterogeneous crystallization occurs in preference. Its incubation time for crystallization τ_H is

$$\tau_H = \tau f(\theta) \tag{3.15}$$

The ratio of τ_H to τ has a value lower than 1; the lower this ratio the more efficient is the heterogeneous nucleator. τ is the incubation time for pure glass and $f(\theta)$ a function dependent on cos(θ) (differs from the function given earlier).

3.1.4.2.2 Crystal Growth

The grains size and morphology are determined during this stage of the crystallization. From the thermodynamic point of view, the work necessary for allowing the atoms to cross the fluid/solid interface has to be weighed against the loss of free energy due to the atoms, which change position from the fluid to the solids lattice. Denoting by $\mathbf{\Delta}G''$ the change in the Gibbs free energy related to the first process, and by $\mathbf{\Delta}G$ the change in the Gibbs free energy for the latter, an expression for the crystal growth rate U can be written as

$$U = a_0 \nu [1 - \exp(\Delta G/RT)] \exp(-\Delta G''/RT), \tag{3.16}$$

where ν is the dominant vibrational frequency at the interface between the fluid and the crystalline solid.

Considering aspects related to the mechanism of atoms attachment to a real crystal and the involved diffusion process, Eq. (3.16) can be re-written as

$$U = f\, RT[1 - \exp(\Delta G/RT)]/3\pi n a_0{}^2 \eta \tag{3.17}$$

where f here is the fraction of lattice sites available for atoms incoming from the fluid and the rest of the symbols have the same meaning as in the equations, related to nucleation, presented earlier. Equation (3.17) shows that as temperature T decreases below the melting point T_m, the thermodynamic drive for atoms transfer to the crystal lattice is strengthened, yet the viscosity rise reduces the rates at which the process may take place. At large undercooling, the viscosity influence turns dominant. In silicate glasses, the crystallites growth rates range between 1 µm/s and over 10 µm/s [M27].

3.1.4.2.3 Phase Separation in Glass

Such a process may occur in certain glasses; the system retains its overall amorphous character [C1]. Up to a certain limit, both over and under the fusion temperature, $t^0{}_f$: a liquid that dwells there too long may undergo separation of the initially single phase system into multiple phases. Above T_f, the process is addressed as "stable" separation, while below it the process is addressed as "metastable" separation. While not occurring in all glass-ceramic systems, the phase separation, when taking place, markedly influences the crystallization process (it is also used in fabrication of certain special glasses like the silica enriched Vycor glass [V9]). In Figure 3.36a, a free energy curve profile as a function of composition

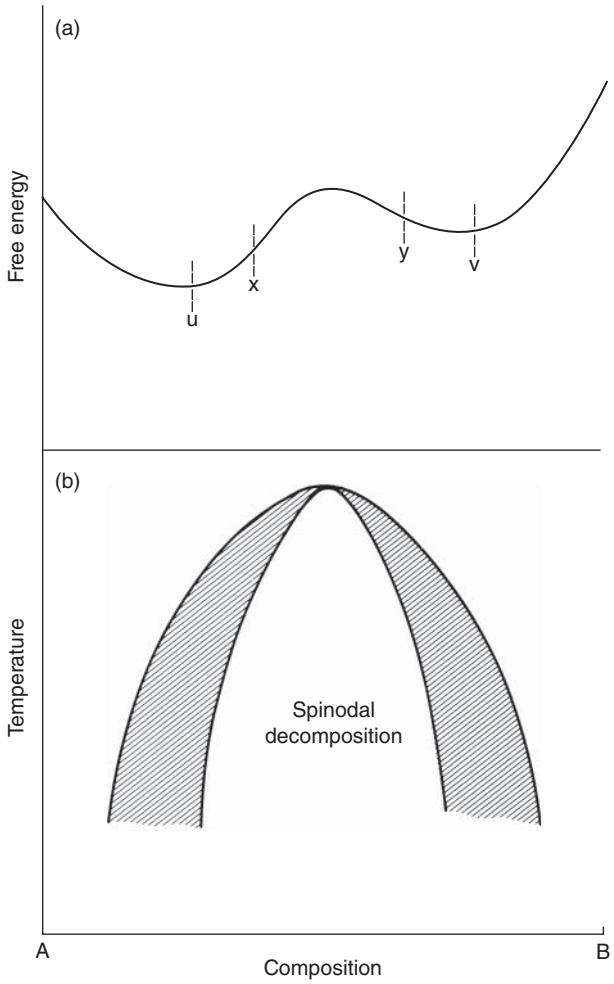

Figure 3.36 Free energy, as a function of composition and the ensuing phase composition at various temperatures. (a) Position of free energy minima. (b) Regions of phase separation by spinodal decomposition and by crystallization in a glass-melt during cooling (final result is glass–ceramic generation). Source: McMillan 1971 [M27]. Reproduced with permission from Elsevier.

is given for the case of a binary system comprising A and B components, which show phase separation [M27]. The presence of two minima in the phase free energy vs. composition curve profile prompts the phase separation. The resulting compositional changes as a function of temperature variation are shown in Figure 3.36b.

At low temperatures, the two minima are widely separated. One distinguishes two situations in such a system. Between x and y positions, located at the function inflection points, the second derivative d^2F/dC^2 is negative. Therefore, in that segment, small composition fluctuations lead to reductions in free energy, hence the results (viz two phase states) of such fluctuations have stability. Such phase separations can easily occur (they do not require nucleation), when the free-energy dependence on composition has the profile of Figure 3.36a,

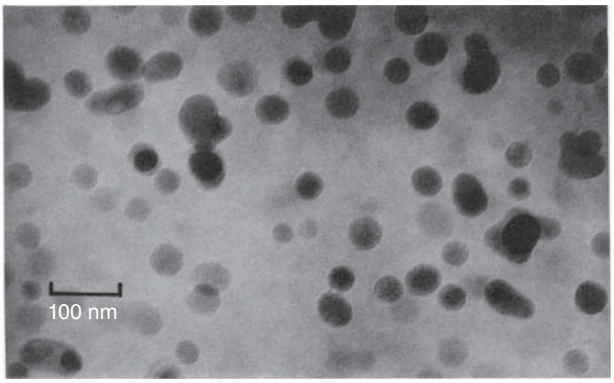

(a)

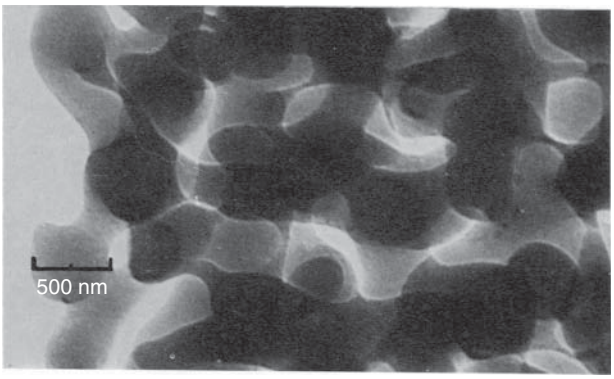

(b)

Figure 3.37 Examples of phase separated glasses that may lead to glass-ceramics if proper thermal treatments are applied; in the state depicted all phases are amorphous. (a) Phase separated glass ($70SiO_2 \cdot 30Li_2O$) with the black dots being potential nuclei of future crystals (bar = 100 nm). (b) Microstructure of phase separated sodium borosilicate glass (bar = 500 nm). Source: McMillan 1971 [M27]. Reproduced with permission from Elsevier.

and are called spinodal decomposition (spine-like shape of Figure 3.36b). In the segments between x, x, and U, v, the second derivative d^2F/dC^2 is positive; there, phase separation requires a succession of nucleation plus a growth type process. As the temperature raises the inflection points move closer together till they coincide.

Figure 3.37a shows the microstructure of a phase separated $30LiO_2 \cdot 70SiO_2$ glass. Figure 3.37b provides a magnified view of Figure 3.37a. It seems that phase separation enhances the crystals nucleation rates by hindering the coarsening process.

3.1.4.2.4 Crystal Morphologies

Besides size and concentration, the crystals morphology, resulting from the controlled glass crystallization, also influences the glass-ceramic properties. Uhlmann [U3] suggested that the growth front morphology depends on the entropy variation at fusion. Materials of low entropy change upon freezing $\mathbf{\Delta}S_f$ tend to grow isometric crystals, while those with high entropy change tend to facet, and generally exhibit anisotropic growth. If, in addition to large $\mathbf{\Delta}S_f$ values, the system is cerammed at large supercooling levels, spherulites (fibers radiating from a center) formation is favored. Spherulites presence is deleterious to mechanical properties. If spherulite-forming glasses are cerammed at lower supercooling levels, then lathe or needle shapes are favored.

3.1.4.3 Requirements for the Obtainment of Performant Glass-Ceramics

For achieving the purpose described by the section title, mother-glass compositions capable of generating valuable crystals need to be selected. The composition and nucleator package has to ensure high nucleation rates. Macroscopic surface nucleation need to be prevented by administering faster internal nucleation. Réaumur (the researcher who seems to be the first to produce a glass-ceramic, as mentioned above) used a procedure that caused macroscopic surface (undercooled liquid/solid interface) initiated crystallization. Except for very few systems, like silicates of very high lithium oxide Li_2O content, homogeneous nucleation, or nucleation caused by the macroscopic surface, cannot be relied upon for fabricating glass-ceramics. High density of nucleator particles and their uniform volumetric distribution are necessary. The nucleators may also act by facilitating sub-liquidus phase separation. This may subsequently favor crystal-growth nuclei formation by providing interface surfaces (preferred nucleation sites). In a phase separated system, the probability for homogeneous nucleation in one of the phases may be increased compared with the initial state, thus leading to formation of nuclei on which other phase(s) might deposit. Crystal growth rate has to be sufficiently high to allow ceramming over reasonable durations, but not so high as to lead to microstructure coarsening.

3.1.4.3.1 Nucleators

The first class of nucleators used for glass-ceramics production were colloidal metal particles (S.D. Stookey [S59]), which formed in situ as a result of redox reactions between noble metal oxides and reductor oxides like arsenic oxide As_2O_3, antimony oxide Sb_2O_3, or tin oxide SnO_2. For example, the reaction $2Au_2O_3 + 3Sb_2O_3 \rightarrow 4Au^0 + 3Sb_2O_5$ or $Sn^{2+} + 2Cu^+ \rightarrow Sn^{4+} + 2Cu^0$. Such metals have low solubility in glass so that they can easily survive as a second phase. When a melt containing gold oxide Au_2O_3 converts into glass, the reaction is prevented by fast cooling. In a subsequent stage, the glass is treated thermally at a temperature that is only slightly above the annealing point, thus creating favorable conditions for the reaction to proceed.

UV light or X-ray radiation, together with thermal treatment, is also able to generate metal precipitates within suitable glass hosts. In order to function as crystallization nuclei for oxide phases, the metal particles size need to be in the $5-100$ Å range. The work on copper containing photosensitive glasses [S60] suggested that the photon absorption cause electron "*e*" ejection from suitable cations, as, for example, from triply ionized cerium Ce^{3+} in the reaction $Ce^{3+} + h\nu \rightarrow Ce^{4+} + e$. The electrons can then reduce singly ionized copper Cu^{+} by the reaction $Cu^{+} + e \rightarrow Cu^{0}$. As already remarked by Weyl [W22], the research on colloidal metal coloration shows that individual metal atoms like copper Cu^{0} can be "dissolved" in the supercooled liquid (glass). In coloration works, used metal concentrations are in the $0.2-1.0$ wt% range. For nucleation applications, lower metal concentrations are used, in the $0.01-0.1$ wt% range. The solubility levels vary markedly with glass composition. For example, gold Au is much more soluble in lead Pb-containing glasses than in the usual soda-lime type hosts. Among the metals most used as nucleators one can cite silver Ag, copper Cu, and gold Au, but also ruthenium Ru, osmium Os, iridium Ir, and platinum Pt [M27]. Aggregation by atoms diffusion takes place when the glass viscosities range between η values (in) satisfying $\mathbf{log}\eta = 13.4$ at annealing point and satisfying $\mathbf{log}\eta = 7.6$ at fiber softening point. Tiny oxide crystals form on the metal colloids. For example, phases like $Li_2O_3 \cdot SiO_2$, $Li_2O \cdot Al_2O_3 \cdot 4SiO_2$, or of a beta spodumene quartz solid solution, form in a system like $Li_2O - SiO_2 - Al_2O_3$; they were among the first to be explored. Higher temperature treatment triggers crystals growth, and the formation of the primarily crystalline material. As already noted, the effectiveness of metallic nuclei is related to similarities between the metal lattice and the phase supposed to crystallize on the nuclei. For instance, Rindone and Ryder [D6, R26] has shown that the (111) lattice plane platinum Pt, which is able to assist the $Li_2O \cdot SiO_2$ crystallization, exhibits high similarity with the (002) plane of the disilicate with a disregistry of less than 5%. In fact, Turnbull and Vonnegut determined in 1952 that a disregistry of less than 15% between the nuclei and the phase(s) to grow on them is admissible [M27].

Further research showed that besides metals, other classes of nucleators exist. The most important class includes oxides like titanium dioxide TiO_2, zirconia Zr_2O_3, di-phosphorus oxide P_2O_5, vanadium oxide V_2O_5, chromium oxide Cr_2O_3, molybdenum oxide MoO_3, tungsten oxide WO_3, and iron oxide Fe_2O_3 [M27]. Certain mixed oxide packages proved to be more effective than a single oxide. In the case of titanium dioxide TiO_2 sub-liquidus, phase separation seems to be important. Nuclei in the form of titanium Ti compounds appear in many cases. Fluorides in concentrations less than 1 wt% can be accommodated in the glass lattice; however, when concentration in the $2-4$ wt% range is used, fine precipitates form during cooling. It is also possible to conduct the process so as to keep the cooled glass clear, and precipitate the fluorides on subsequent thermal treatments. The fluorine ion F^{-} radius of 1.36 Å is close to the oxygen ion O^{2-} radius of 1.4 Å. This seems to explain why fluorine F can replace oxygen O in the glass lattice. The replacement, however, generates weaker $Si - F'$ bonds replacing the basic $Si - O - Si$ bonds. This weakening of the average bond strength means that during reheating above the glass-forming temperature atomic rearrangement is facilitated. Then, owing to the thermodynamic drive, small fluoride crystals precipitate. This process in itself is sufficient to produce opal glasses, but may also generate nuclei like sodium fluoride NaF, sodium-aluminum fluoride Na_3AlF_6, and sodium-sulfur fluoride Na_2SF_6, for substantial crystallization of certain glass types like alumino-silicates including alkaline oxides.

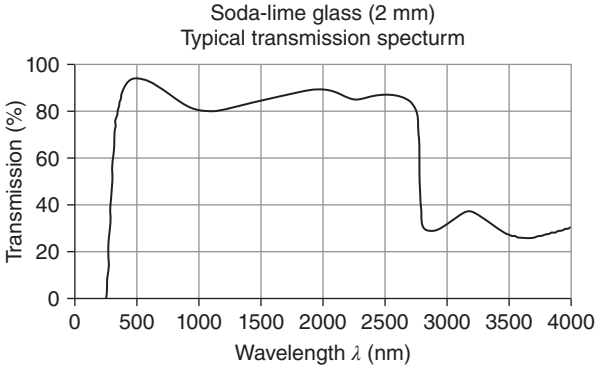

Figure 3.38 Transmission spectrum of typical soda-lime silicate glass. Band at ~1 μm due to Fe^{2+} impurities while further IR bands are vibrational (both OH^{-} and silica skeleton related).

3.1.4.4 Influence of Controlled Glass Crystallization on Optical Transmission

The bulk soda-lime commercial glass exhibits high optical transmission between the near ultraviolet and the near infrared (NUV–VIS–NIR range), as shown in Figure 3.38.

Besides having a low refractive index ($n = 1.52$), which makes reflective losses low, the high optical transmission of soda-lime is owed to its isotropic nature and absence of scattering centers. Glasses colored by metal particles also exhibit very low scattering loss, owing to their nanometric size; when larger crystals are present, like in opal or aventurine glasses, scattering in even low weight fraction ($<2-4$ wt%) becomes significant. Prevention of light ray deflection by scattering for obtaining transparent glass-ceramics requires avoidance of materials, which include crystals with refraction index

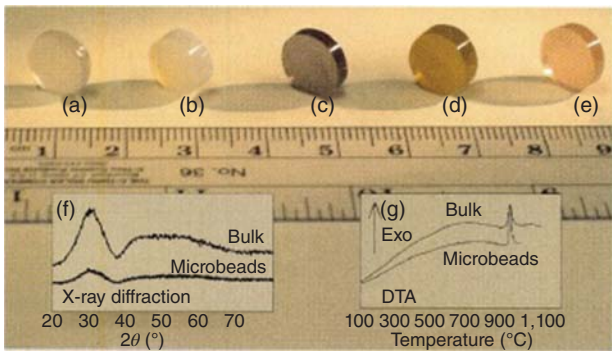

Figure 3.39 Transparent (moderately) ceramics fabricated by full glass crystallization (basic system La_2O_3: AlO_3–ZrO_2); mother-glass (cooling of melt beads prepared by flame-spraying) cerammed by hot pressing. (a, b) No rare-earth oxide additions. (a) 5% Nd_2O_3. (b) 5% Eu_2O_3. (c) 5% Er_2O_3. (d, g) XRD and derivatographic thermal analysis (DTA) curves demonstrating the amorphous nature of material shown in (a). Source: Rosenflanz et al. 2004 [R30]. Reproduced with permission from Springer.

significantly different from that of the host glass. Also, as the discussion of scattering (Section 2.1.3.4) suggests, it requires that crystals size be low (less than around 200 nm); larger crystals are acceptable if their refraction index matches that of the glass matrix phase fractions. Undesired absorption, which can be effectuated by transition metal (TM) and/or RE^+ cations, is also a potential problem. It is, however, quite easily solvable by using clean raw materials and clean processing.

Examples of useful transparent glass-ceramics that exploit either of the scattering reducing possibilities mentioned earlier are provided in Section 4.2.11.

3.1.4.4.1 Full Crystallization

As will be detailed in Section 4.2.11.6, the crystallization process under certain conditions may be conducted in a manner that converts more than 99 vol% of the mother-glass into a crystalline phase [B51, M29, R30]. This is labeled in this book as "full-crystallization"; it is obviously "full" in the practical, not theoretical sense. When those crystals comply with either or both the scattering avoidance requirements, the resulting specimens may show remarkable transmissive properties. The fabrication techniques used are those already presented earlier in this section, and applied to specific systems. Where the crystals need to be kept at micron size, highly refractory mother glass compositions are preferred, namely, melted by exotic procedures; those include high field-strength cations, the low self-diffusion of which reduces drastically the grain-growth rates during ceramming. Figure 3.39 [R30] provides an example of transparent ceramics, produced by full glass crystallization.

3.1.5 Bulk Sol–Gel

Sols are colloid suspensions with liquids as suspending media. They are made of dense particles (particulate sols) or of branched macromolecules, able to generate three-dimensional polymeric structures, called polymeric sols [B56]. Sol–gel processing is well known to ceramists, but mostly for thin films and powder fabrication. The technique was developed in the 1930s in Germany for optical coatings fabrication. It is however an approach that in principle is also usable for bulk green-body forming. For that purpose, the technique has several very attractive features, alas combined with the critical disadvantage of very difficult drying. In the sol–gel approach, forming is achieved by casting sols in containers, usually glass made coated with special layers aimed at allowing end-specimen release. Therefore, complex shapes and large size gels can be easily achieved at low cost. The widespread interest in sol–gel seen in the 1980s was initially fueled by the hope of easily forming highly sinterable, large, and/or complex shaped bulky glass and ceramic parts. The drying related issues drastically moderated the initial enthusiasm; currently, industrial scale applications of the method do exist, but mostly in the domain of submicron thickness, amorphous or crystalline coatings.

If suitably processed, the sols can be transformed into inorganic gels. Processing may involve physical or chemical operations. For particulate sols, this means reducing inter-particles repulsion, while for polymeric ones, it means facilitating condensation reactions. In both cases, the resulting gel is made of a rigid skeleton, which traps large amounts of the suspending liquid into its voids. In that respect, it may be viewed as a semi-solid. Sol–gel processing leading to obtainment of dense bulk ceramics is presented schematically in Figure 3.40 [B57]. The processing route leading to thin films coating or to fibers is also shown in the figure.

The most popular polymeric gel is produced by partial hydrolysis of the tetraethoxysilane, alkoxide, $Si(OC_2H_5)_4$, abbreviated as TEOS. The hydrolysis reaction reads

$$\equiv Si—OR + H_2O \leftrightarrow \equiv Si—OH + ROH \qquad (3.18)$$

where R is an organic radical and ≡ indicates three covalent bonds.

It is followed by the condensation reactions:

$$\equiv Si—OR + OH—Si \equiv \leftrightarrow \equiv Si—O—Si \equiv + ROH \qquad (3.19)$$

$$\equiv Si - OH + HO - Si \equiv \leftrightarrow \equiv Si - O - Si \equiv + H_2O \qquad (3.20)$$

During the condensation stage, the silanol groups (Si-OH), produced by the hydrolysis, generate the

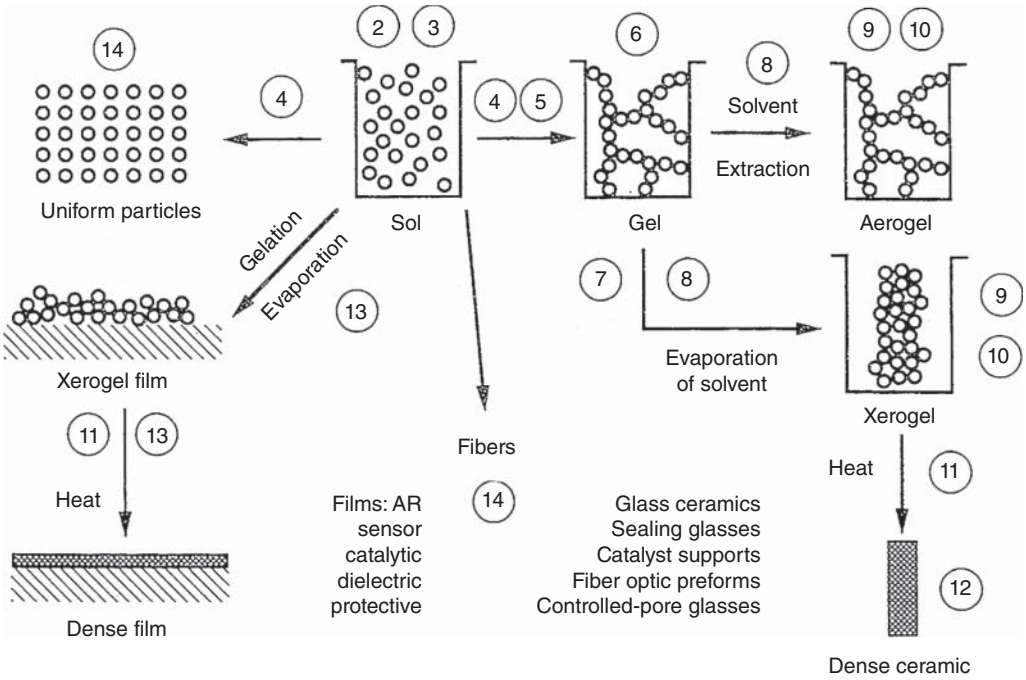

Figure 3.40 Processing routes one can base on a sol–gel approach and types of products can thus be generated (dense parts, particulates, films, and fibers). Source: Brinker and Scherer 1990 [B56]. Reproduced with permission from Elsevier.

Si-O-Si siloxane bonds. For gel obtainment, certain conditions have to be met. First is that the hydrolysis be only partial, since a fully hydrolyzed $Si(OH)_4$ unit behaves differently from a partially hydrolyzed TEOS. It is a situation realized for sufficiently low H_2O/TEOS concentration ratios and acidic conditions. Under such conditions, the condensation reactions start before all −OR groups are hydrolyzed. Alkoxides including inorganic atoms different from Si, and other precursors capable of behaving similarly to TEOS, also exist for elements like aluminum Al, yttrium Y, zirconium Zr, and magnesium Mg, including "double" ones, like the Al – Mg alkoxide. As a result, a variety of gels relevant for bulk transparent ceramic parts can be prepared. The family of materials obtainable in the form of bulk gels is further widened if those derived from particulate sols are included. Liquid elimination, from the gel, generates a stage called "xerogel." Xerogels are systems that include a huge volume of void space, namely, porosity may account for more than 90 vol%. This void is constituted from equally spaced very small (<10 nm) pores; see Figure 3.31a. The xerogel pores are so small, that visible (VIS) light scattering is very modest. As a result, the specimens are evaluated as translucent or even transparent. The pore size in transparent γ - Al_2O_3 (a cubic form of Al_2O_3) bulk part obtained by Yoldas [Y16] was less than 40 Å ($A = 200\,m^2/g$) as shown in

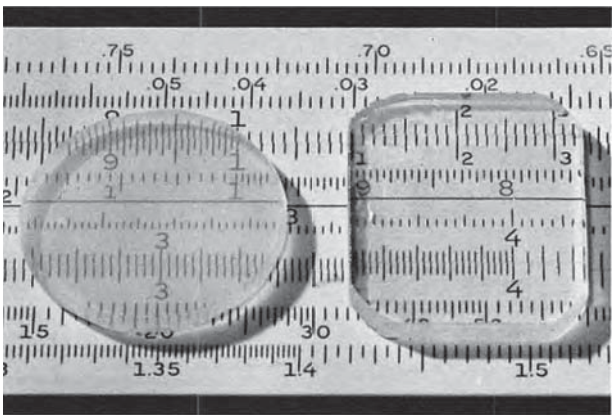

Figure 3.41 Bulk sol–gel transparent (nanometers pore containing gamma alumina) ceramic parts; sintering at 1000 °C. Source: Yoldas 1975 [Y16]. Reproduced with permission from John Wiley & Sons.

Figure 3.41 [Y16]. He was able to conduct the drying plus organics elimination so that the xerogel could be obtained as non-cracked parts of 5 – 6 cm size. Such a part is illustrated in Figure 3.41. Its pore size distribution is provided in Figure 3.42.

Despite a porosity exceeding 60 vol%, such parts are transparent; the parts cannot be densified due to their disruptive phase transformation to the trigonal form

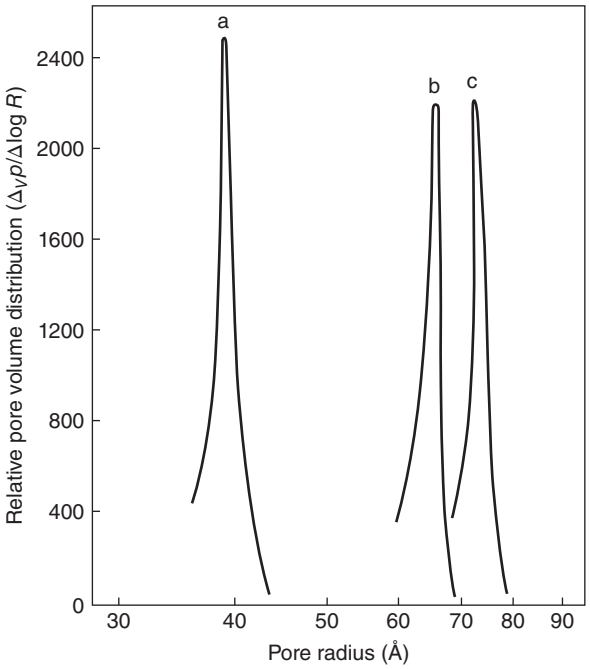

Figure 3.42 Pore size distribution curves of alumina xerogel fired, for 24 hours, at, respectively, 500, 900, and 1000 °C (nanometric pore size allows transparency despite high, 60%, volume fraction of void space). Source: Yoldas 1975 [Y16]. Reproduced with permission from John Wiley & Sons.

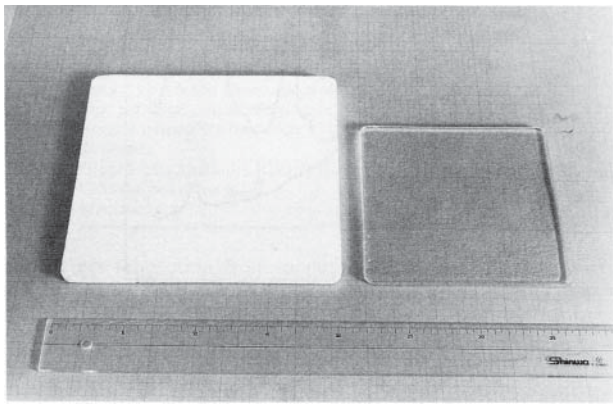

Figure 3.43 Massive shrinkage during sintering of xerogels (gel prepared from silica particulates); pores shrinkage leads to transparency). Source: Brinker and Scherer 1990 [B56]. Reproduced with permission from Elsevier.

α - Al_2O_3 at around 1000° C. However, xerogels that do not exhibit such phase transformations can be sintered at very low temperatures. For instance, a pure silica dense parts can be obtained below 1000° C; melt cooled similar specimens necessitate sintering temperatures exceeding about 2000° C. Such a part is shown in Figure 3.43 [B56].

During drying, warpage and cracking occur frequently. In the case of silicon dioxide SiO_2 gels derived from aqueous sols of sodium Na or potassium K silicates, which include larger pores of up to 300 nm, drying of relatively large parts is a much easier task than when alkoxide gels are processed. The former gels can be dried within several hours. To avoid cracking, the alkoxide-derived warped bulk silica xerogels need to be dried under a controlled humidity for weeks. The as-cast gel size is reduced by half at the end of the drying process (most cracking occurs while the last, ~5 vol% of liquid are eliminated). Various methods have been proposed to avoid fracturing during drying. Ageing the gels, producing large-pore ones, addition of surface-energy reducing chemicals, drying under supercritical conditions, and freeze drying are among those yielding best results. The potential of this processing approach in the domain of transparent ceramics production is significant. Only a very low fraction of it has yet been exploited.

3.1.6 Polycrystalline to Single Crystal Conversion via Solid-State Processes

Scott and Levinson [S18] pointed out that transformation into single crystals by solid-state processing of initial polycrystalline ceramics would be of high interest for many applications. Since no intermediate liquid phase is needed that way, fabrication temperatures can be significantly reduced, and certain properties enhanced.

In the 1980s S. Matsuzawa and S Mase [M18] already proposed an approach of allowing conversion of polycrystalline parts into single crystals. Such an operation eliminates grain boundaries and may also reduce the number of defects in the final ceramics. The initial experiments concerned ferrites for applications as magnetic heads of magnetophones, and also spinel and iron-yttrium Fe, Y garnet. In these efforts, optical transparency was not sought.

For transparent ceramics, at the translucent level, this method was first examined by Scott and Levinson [S18]. The work concerned large extended tubes of magnesium-oxide MgO-doped alumina Al_2O_3 with ~650 ppm MgO. It was not possible to convert a full tube length of 30 – 40 cm into a single crystal, but in certain specimens, crystalline section, 20 – 30 cm long developed, along with some smaller, 4 cm-long ones. Unconverted grained regions survived, of average 35 – 40 µm size. Cracking at interfaces between polygrained regions and single crystals was the main practical problem. The approach was also applied to $Y_3Al_5O_{12}$ (YAG) crystals by A. Ikesue in 2005 with

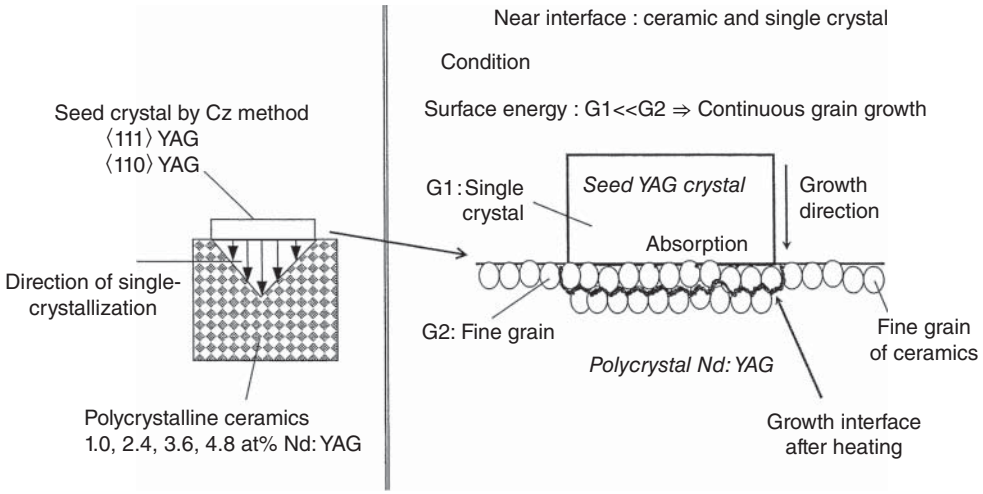

Figure 3.44 Transformation of polycrystalline ceramic to single crystal part by its thermal treatment when joined to a seed crystal (solid-state process). Source: Ikesue et al. 2013 [I3]. Reproduced with permission from Cambridge University Press.

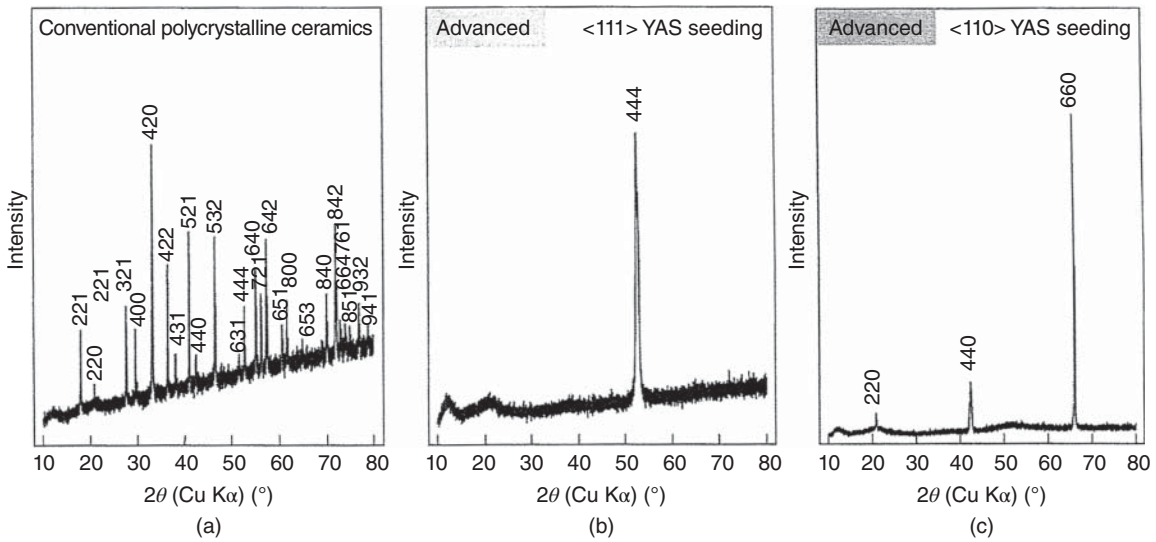

Figure 3.45 Demonstration of solid-state single-crystal formation I the case of a seeded YAG ceramic part, by the aid of XRD data ((a) shows the pattern for the case of a ceramic YAG; (b) show XRD diagrams the same part, (c) after thermal treatment with two single crystal seeds viz <111> and <110>). Source: Ikesue et al. 2013 [I3]. Reproduced with permission from Cambridge University Press.

excellent results [I3, I8]. In Figure 3.44 the procedure used by Ikesue is schematized. In Figure 3.45 [I3] the XRD patterns of a Nd : $Y_3Al_5O_{12}$ (Nd:YAG) ceramic and those of the specimen resulting after a polycrystalline to single-crystal treatment (PC → SC) are shown; the single-crystal nature of the processed specimen is shown by the data in Figure 3.45b,c. Growth rates of 5 mm/h were measured; lasing ability of the single crystals was demonstrated (see Figure 3.46).

In the said method, bulky polycrystalline transparent silicon dioxide SiO_2 doped YAG items exhibiting *BD* as high as 95% of the theoretical density *TD* are converted into single crystals at 4 mm/h growth rate by suitable thermal treatments after being bonded to a single-crystal seed [I3, I8]. Bonding was done after prior polishing and chemical etching of the relevant surfaces. The surface energy of a polycrystalline grain is larger than that of the seed, providing a thermodynamic reason for the single-crystal expansion by integration with the polycrystals.

The lack of grain boundaries may have a beneficial effect on useful properties. For example, the thermal conductivity can increase owing to less phonon reflections at the grain boundaries. Spherical single

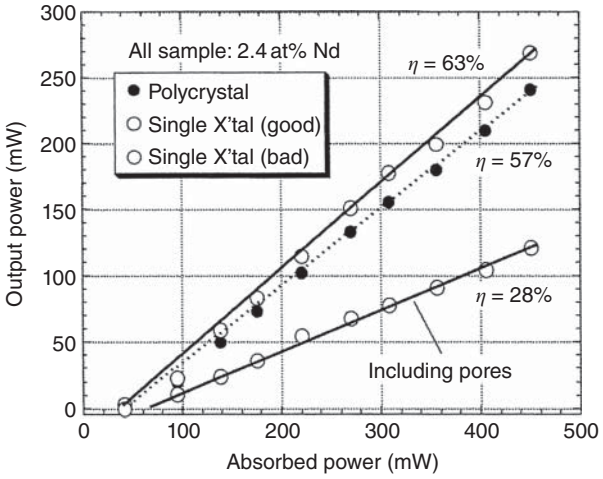

Figure 3.46 Lasing efficiency of Nd:YAG ceramic compared with that of solid-state produced single crystals. Source: Ikesue et al. 2013 [I3]. Reproduced with permission from Cambridge University Press.

crystals microspheres could also be obtained by applying this technique (Figure 3.47 [I3]).

3.1.7 Transparency Conferred to Non-cubic Materials by Limited Lattice Disordering

Introduction of some disorder into an ordered cubic lattice may help on some aspects, especially in the case short-pulse lasers fabrication, owing to the introduction of some variability in the geometry of a given site. When such sites serve as hosts for lasing dopant ions, a broadening of the absorption and fluorescence spectra ensues. Such added disorder has been realized, for instance, by introducing scandium Sc^{3+} ions into the $Y_3Al_5O_{12}$ (YAG) lattice. More importantly, a similar operation, when applied to certain non-cubic lattice materials, may provide the host with a measure of transparency. For instance, consider some perovskites like $BaMg_{1/3}Ta_{2/3}O_3$ (BMT) that owing to a 1 : 2 ordering of the B-site cations (the smaller sized cations of magnesium Mg and tantalum Ta) exhibit an hexagonal lattice along the [111] direction of the parent perovskite cell; the latter is parallel with the "*c*" direction of the so-called super lattice formed by the B-cations. This crystal can be modified by introduction of suitable amounts of tetravalent ions like titanium Ti^{4+}, tin Sn^{4+}, or zirconium Zr^{4+}. The distortions caused by such replacements to the B-cations super lattice modify the initial hexagonal symmetry toward an almost cubic one, thus reducing scattering at the ceramic grain boundaries. As a result, translucent parts can be produced [K22]. The absolute transmission levels of the A partial reason for the relatively modest transmission, of such specimens, is the occurrence of significant optical loss during the reflections from the front and back sample surfaces. The loss is large due to the large refractive index of those materials. Still, for thin small parts like camera lenses, such materials may be useful. Figure 3.48 [K22] presents the transmission spectra of a modified lattice BMT ceramic. By introducing lanthanum La ions into a PMN-PT host, its monoclinic lattice could be modified to a pseudocubic one, also causing increased transmittance.

3.1.8 Transparent Non-cubic Nanoceramics

We have seen earlier that alignment, of particles suspended in liquids, is a procedure allowing to coopt non-isometric crystals into the family of TCs. For the achievement of such an objective, another alternative exists, namely, densifying such materials, to a pore-free level, while maintaining a grain size small enough to make scattering harmless. Theory (see Section 2.3.4) showed that for such a result the grains size is to be reduced under 20 nm. However, practice shows that for many systems (especially if reflection losses, owed to a large "*n*," are not present) a grain size around 100 nm is good enough to allow achievement of significant transparence levels [C12, E4, L31, M42]. As the particles alignment, during forming, has its specific difficulties, nano-structured ceramics fabrication is not an easy task. A useful approach is the combination of high pressure (up to 8 GPa) with low temperatures. While pressure over 1 GPa requires specific installations, allowing fabrication only of cm size parts pressure in the 100–400 MPa may be realized in SPS machines that have a brighter perspective as becoming relevant in industrial operations, at least for high added-value parts.

3.1.9 Grinding and Polishing

These operations have as task to make certain surfaces, of the TC item, parallel and remove surface defects and asperities. Like in the case of other processing operations, what is specific to the TCs, compared with most other representatives of the advanced ceramics family, is the severity of the quality requirements; the techniques used are in most cases the conventional ones. This topic is not detailed here. We will limit us in mentioning two cases that require more exotic treatments. For instance, for the sub nanometer scale finishing, required by YAG gain media for high power laser devices, it is necessary to make use of special approaches like magnetic field assisted finishing [R31]. One of the most problematic parts, in this context, is the various shape (more or

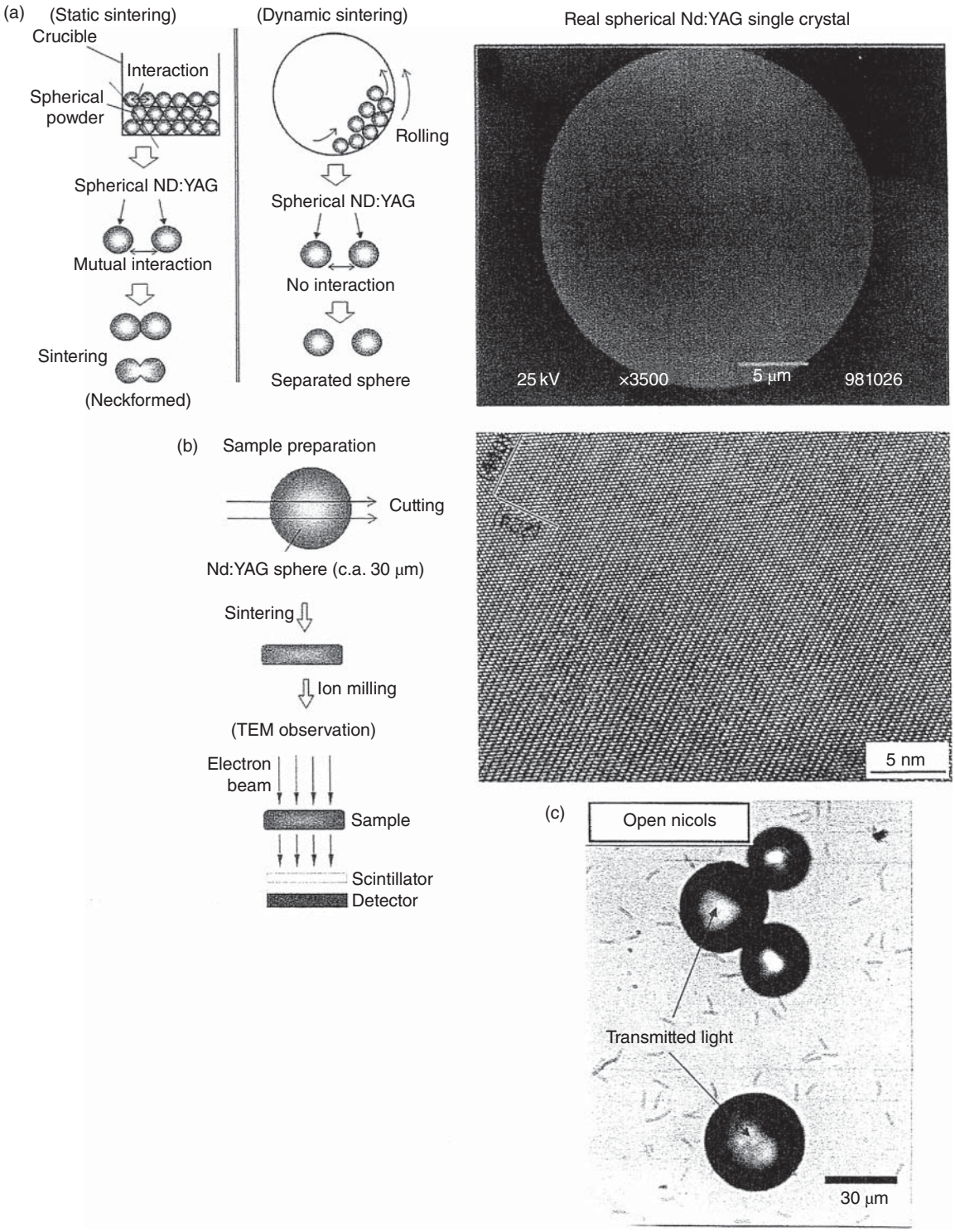

Figure 3.47 Spherical shape individual YAG single-crystals prepared by the solid-state processing of ceramic. (a) Schematic of two sintering approaches. (b) Preparation of a section (from a spherical shape crystal) and results of its SEM (top panel of column at the right) and HRTEM examination (below panel with SEM photo). (c) Imaging with optical microscope. Source: Ikesue et al. 2013 [I3]. Reproduced with permission from Cambridge University Press.

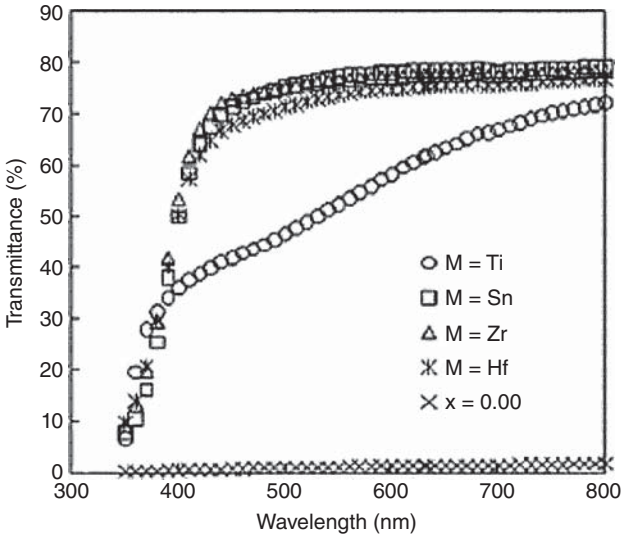

Figure 3.48 Transmission spectrum of thin (0.8 mm) plates of BMT and distorted lattice materials, derived from the basic one by introducing heterovalent, additional cations. Source: Kintake et al. 2010 [K22]. Reproduced with permission from John Wiley & Sons.

less aerodynamic) missile noses (made of sapphire, ceramic alumina, ceramic spinel or AlON). The surface processing requires, here, the use of techniques like magnetorheological fluid jet (for instance the systems developed by QED Technologies of Rochester NY) in which the grinding fluid stream is confined by the aid of a magnetic field; during the process the work piece geometry has to be measured by quite sophisticated equipment based on laser sensors or interferometry (e.g. systems developed by OptiPro and respectively applied science innovations, in the United Stated).

3.2 Characterization

Besides processing, ceramics engineering involves materials and parts characterization along the various fabrication stages, obviously including the stage of finished products. These measuring operations are conducted at different levels, from the nanoscale of the lattice, through the microscale of the grains and particles, till the macroscale of green or sintered part. Of course, most of the characterizations required by the general ceramic technologies are relevant in the case of the transparent ones as well. Their presentation is not within scope of this book segment. The section 3.2 will present only results, obtained with general ceramic characterization methodology, on materials relevant for TC fabrication technology. As opposed to the previous certain methods that are specific to the transparent materials characterization, are briefly described in the following text before results they produced are presented.

3.2.1 Characterization of Particles, Slurries, Granules, and Green Bodies Relevant in Some Transparent Ceramics Fabrication

As noted when discussing processing (reminded here because the importance of the issue), characteristics of powder particles, of the made thereof slurries and granules, and finally of the shaped green bodies, govern the sintering process, and thus the resulting microstructure hence the properties of the manufactured transparent ceramics. For understanding which characteristic data of the particles and intermediate products are most important, we have to consider some processing requirements specific to the TCs, namely:

A. While advanced high ceramics used for tools or medical applications are considered "dense" when sintered to 99.0% …99.7% relative density, for VIS transparency we have to eliminate the last 0.01% of residual porosity [I6, P19, R35]. The **consequences** are the following:
   (1) For transparent ceramics one needs powders with an extreme sintering activity, namely, with *small*, ≤200 nm primary particles, and *large*, $A \geq 10\ m^2/g$, specific surface values.
   (2) Unfortunately, because of their high surface curvature, such fine particles are subject to strong agglomeration.
   (3) The powder particles should exhibit
      (a) A narrow size distribution (close to "monosize")
      (b) A highly equiaxed multi-faceted shape, preferentially spherical
B. Since scattering losses are caused by second phases as well as by pores, a single-phase character of transparent microstructures is equally important as the high sintering density [K53]. Note that, among other things, a minimum content of second phases minimizes choice and amount of allowed sintering additives.
   However, without, or with an absolute minimum of such sintering aids, elimination of the last 0.01% porosity (requirement specific to TCs) is the most demanding objective of sintering. Therefore, other additional measures will be indispensable. The consequences are as follows:
   (1) Extreme sintering densification with a minimum of additives needs extremely homogeneous shrinkage enabled by a most homogeneous arrangement of particles in the green bodies [K53].

(2) Target 1. puts additional emphasis on the need for a de-agglomerated structure of the raw powder.

3.2.1.1 Powder Characterization

As known the specific surface is measured according to the Brunauer-Emett-Teller (BET) standard by commercially available equipment. Together with the density (measured by a pycnometer), the "BET" value A_{BET} (m^2/g) allows a first (and frequently quite informative) estimate of the average basic-particle size. Note however that in the case of agglomerated powders, the data on basic-particles size has to be supplemented with additional information. Assuming monosized spherical particles, the particle diameter derived from BET is given by

$$D_{BET} = 6/(d{\cdot}A_{BET}). \tag{3.21}$$

where "*d*" is the density of the particulate material.

Owing to the typically small size, less than 0.2 µm, of powders for transparent ceramics, an accurate check of particles size (as opposed to the approximations offered by BET) will need the high magnification of transmission electron microscopy (TEM); simple scanning electron microscopy (SEM) images are, usually, not sufficient. Figure 3.8 (see section 3.1.2.2.1) shows typical examples of three commercial powders of high-purity spinel $MgAl_2O_4$ powders that have been successfully used for sintering of transparent components. In Figure 3.8(a): $A_{BET} = 14\ m^2/g$ and $D_{BET} = 120$ nm; in Figure 3.8(b): $A_{BET} = 31\ m^2/g$ and $D_{BET} = 54$ nm; and in Figure 3.8(c): $A_{BET} = 29\ m^2/g$ and $D_{BET} = 58$ nm.

None of the powders of Figure 3.8 exhibits "monosize" particles. They do exhibit some aggregation, resulting from partial "sintering" during calcination of these powders, as seen in these micrographs. Nevertheless on a qualitative level, Figure 3.8 *confirms* the expected particles sizes level as derived from the BET data. For powder showing this agreement, there is generally no need for special quantitative particle *shape* analysis. On the other hand, if a larger deviation of the particle size is observed by TEM compared with D_{BET} estimation, this is a significant indication of a powder structure (agglomeration).

Measurement of particle size *distributions* is important not only for complete characterization of a given powder, but even more for understanding of processing performance. Comparing D_{BET} with the D_{50} (median value of *D*) of a measured particle size distribution is a valid tool to evaluate the dispersibility of powder subject to de-agglomeration processes, and to check the *reliability* of the measuring approach. For powders of grade (a) in Figure 3.8 (namely, having $A_{BET} < 20\ m^2/g$), such distribution records are readily obtained by preparation of dilute and de-agglomerated measuring slurries, subsequently examined with commercial equipment that analyzes laser light scattering caused by the particles in this slurry; for example, Mastersizer 2000, Malvern Instruments [Malvern, UK]. Here, the agreement with D_{BET} is quite close. However, as explained by Table 3.1, this approach becomes increasingly incorrect for powders of higher amount of particles sized less than 100 nm, a feature that applies to many powders in transparent ceramics technology! For nano-powders belonging to grades (B) and (C) of Figure 3.8 with $S_{BET} > 25\ m^2/g$, these measurements are highly challenging. Notably, the difficulties were demonstrated by the commercial manufacturers of these powders themselves:

(1) Spinel-b per Figure 3.8a was delivered with manufacturer's claimed particle size distribution $d_{90} = 112$ nm with "no particles > 112 nm"; it was in obvious conflict with the TEM micrographs that revealed numerous primary particles sized up to 300 nm (admittedly not with the high concentration of the selected photograph of Figure 3.8b).

(2) On the other hand, the manufacturer of spinel-c shown in Figure 3.8c provided a conservative particle size distribution of $d_{50} = 210$ nm, whereas closest

Table 3.1 Comments on particle size distribution records by different light scattering analyses.

	***Static* laser scattering (SLS)**	***Dynamic* laser scattering (DLS)**
Analyzed process	Mie scatter	Brown's movement
Commercial examples	Mastersizer 2000 (Malvern)	Zetasizer Nano ZS (Malvern)
Good for particle sizes	≥100 nm (theoretical lower bound: 20 nm)	>1 nm
Comments	Imprecise for powders with high amount of particles 20–100 nm, i.e. with $S_{BET} > 20\ m^2/g$!	Difficult influences from (i) viscosity of fluid medium: *high* viscosity immobilizes larger particles/ agglomerates = particles >150 nm are eliminated from record! (ii) signal processing ($I{\sim}D^6$!): signal of larger particles shadows weak signal of finer constituents at *lower* viscosity. ⇒DLS • ideal for *mono*sized nano-powder • may be "wrong" for real distributions!

inspection of TEM micrographs did not reveal any primary particles larger than 100 nm (Figure 3.8).

The reasons for such, sometimes too modest, in other cases too optimistic "measurements," are insufficient understanding of the complex physics of laser light scattering by transparent nanoparticles. For example, commercial equipment as Malvern's "Mastersizer 2000" and "Zetasizer Nano ZS" make use of fundamentally different processes with specific advantages and shortcomings (Table 3.1). It has been demonstrated that for flame spray pyrolysis (FSP) of spinel powders, A_{BET} takes values ranging between 15 and 31.5 m^2/g (depending on the calcination temperature). It is important to note that:

(1) The static laser scattering (SLS) approach (used, for example, by the Mastersizer 2000) has the ability to reveal the crash of *larger* agglomerates when milling decreases their median size from as-received 2.55 µm after 1000° C calcination, to less than 0.5 µm, but it cannot resolve 50 – 60 nm small basic particles [K54].
(2) The dynamic laser scattering (DLS) approach may deliver nearly all imaginable and irrational results with D_{50} from 75 up to 650 nm, for a 15 m^2/g specific surface area powder, depending on the fluid viscosity; thus, DLS delivers only selective (partial) records of the real size distribution [K54].

Regarding this "selective" characterization by the DLS method, it was attempted to recompose the complete distribution by *sequential* measurements, with graded viscosities ranging between 20 and 1000 mPa s, and record the effective solid loadings (namely, the amounts of particles contributing to these "partial" distributions) in the individual tests. The final superposition of these partial distributions reproduced a similar distribution to that obtained for the same powder also by SLS, namely, with median D_{50} values that are about twice as big as D_{BET}. Nevertheless, the described approach was able to show a clearly positive influence of lower temperature powder calcinations: FSP (spinel-b per Figure 3.8b) ended with almost the same $A_{BET} = 31\ m^2/g$ when the calcination temperature was reduced from 1000 to 700° C. That decrease, however, reduced the median agglomerate size from about 2.5 µm to ~123 nm, which was measured after simple ultrasonication, namely, without any milling [K54].

It thus appears that all currently available measuring approaches are unable to distinguish whether 120 – 150 nm medians represent really existing size limits of the investigated nano-powders (Figure 3.8b,c) or the measurement limits of size within the frame of the available measuring approaches. More progress in this field is urgently still needed.

3.2.1.2 Granules Measurement and Slurry Characterization

As noted in the processing part (Section 3.1.2.2.3), granules are prepared to increase the powder filling density in pressing dies. This requires, among other things, reduction of the pressing path on compaction for minimizing friction and elastic deformation. Therefore, considering the technological targets addressed at the beginning of this characterization chapter, a careful control of granule properties – an imperative for the manufacturing of any advanced high-purity, high density, and low-defect ceramics – is even more critical for transparent ceramics. Granule properties that are most important for matching the target of green bodies *homogeneity*, and thus need to be measured, are:

(1) Their average size (measured for example by sieving), which should be at about 35 – 65 µm (larger granules deteriorate the homogeneity of the pressed bodies, whereas too fine granules may eliminate the actual goal of granulation).
(2) Their crashing strength, and most importantly their inelastic fracture deformation (to be measured by special equipment). Obviously, the granules need some minimum strength to be stable on handling. However, hard and brittle granules with a specific fracture load of 1 – 2 MPa at 50 µm granule size and only 2 – 4% strain-to-fracture will hardly be destroyed completely on pressing, and their remnants will deteriorate the green-body homogeneity. Such agglomerate fractions will also introduce flaws in the pressed bodies. Preferred granules are *soft*, with a specific fracture load of, for example, 0.5 MPa, and a strain-to-fracture ratio of 7 – 8%. Under such conditions, even smaller granules may perform, in an excellent way. For example, after freeze-drying, typical granule sizes are less than 15 µm.

Another important issue for the achievement of an optimum homogeneity of the green bodies is dispersants distribution control in slurries (case of casting based forming), and of organic additives in granules. To a certain extent, the distribution of organic polymers in powder suspensions can be visualized by using adequate examination methods. For instance, cryogenic scanning electron microscopy (cryo-SEM) has allowed the taking of "snapshots" of frozen spinel aqueous suspensions containing 5 wt% NH_4-polyacrylate dispersant after intense ball-milling (Figure 3.9 - see section 3.1.2.2.1) [K1]. It is also important to note that the size and shape of the particles could be visualized as they are dispersed within the suspending liquid, rather than in dried specimens where re-agglomeration occurs.

For granules imaging, a careful sectioning procedure that avoids preparation damage of these soft "bodies" has

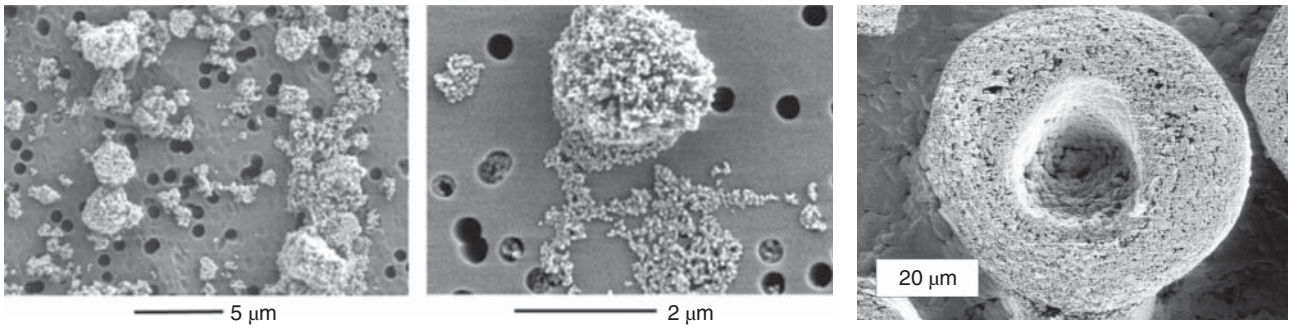

Figure 3.49 Ion beam preparation of ceramic granules (IKTS Dresden). (a) Full agglomerates: agglomerates on filter plate; lower magnification on left panel. (b) Cross section of agglomerate.

to be applied to the examined specimens. A preferred approach is ion-beam sectioning (see Figure 3.49). This technique is often referred to as "focused ion beam" (FIB) method [B18].

3.2.1.3 Green-Body Characterization

Green (pre-sintered) ceramic body characterization should be performed in view of the dramatic influence its configuration has on the parts prospects to achieve full densification on sintering. For the visual microscopic examination of high porosity, low strength green body's microstructure preparation strategies as addressed earlier in discussion of granule characterization, are preferred; obviously after elimination of humidity and organic additives. Seeking for the most homogeneous particle arrangement in green bodies of highest possible density (closest particles packaging) is required. Thus, we have to distinguish different degrees of "disorder" or "order" in green microstructures as illustrated by the schematics of Figure 3.50.

By experience, for records of the degree of "order/disorder" in green bodies, it is beneficial to increase the particles bond strength (after shaping) in the green bodies by annealing to the temperature of first-neck formation; commonly, this step is possible without shrinkage, and without significant porosity change (for example, in 150 nm sized alumina Al_2O_3 particles at 700 – 800° C). Alternatively, the porous structure can be stabilized by impregnation with an organic resin. Cutting preparations readily deliver micrographs not only of the original green body, but even allow some tracing of the densification process in Figure 3.51.

With all the doubtless illustrative value of visualization, a *quantitative* discrimination of different degrees of homogeneity or heterogeneity in particle coordination is impossible by such means. Quantitative discrimination needs a different, real *measuring* approach. After elimination of humidity and organic additives, quantitative experimental evidence for different green microstructures as schematically addressed in Figure 3.50 was obtained by measurement of pore-size distributions by mercury porosimetry using commercial equipment (for example, Autopore IV-9500, Micromeritics Instrument Corp., GA, USA). On this basis Figure 3.52 [K43] reveals significant and very important differences between pressed and gel-cast green alumina Al_2O_3

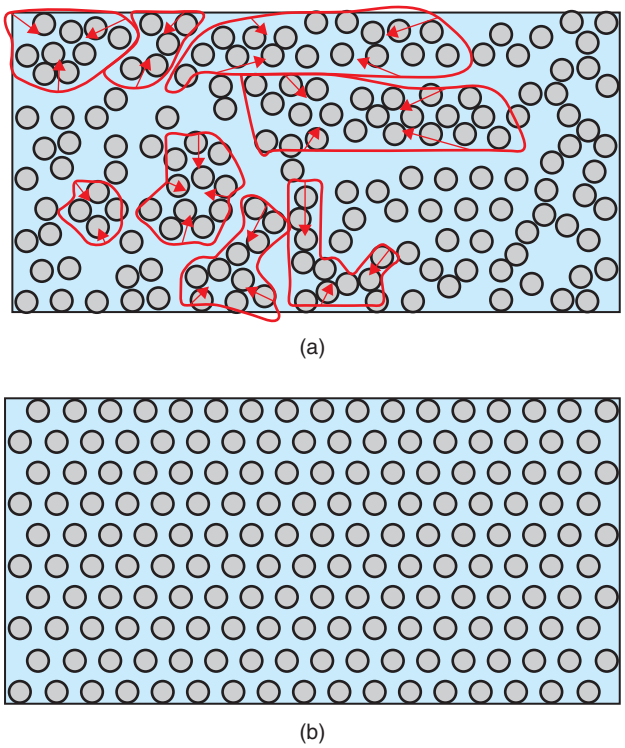

Figure 3.50 Schematics of green ceramic bodies of identical green density. (a) Heterogeneous, agglomerated powder (b) Homogeneous particle coordination. On sintering, (b) provides best promise for *homogeneous shrinkage* up to high density at low temperature whereas in (a) all agglomerates will shrink toward their individual centers with poor chances to improve the homogeneity during sintering.

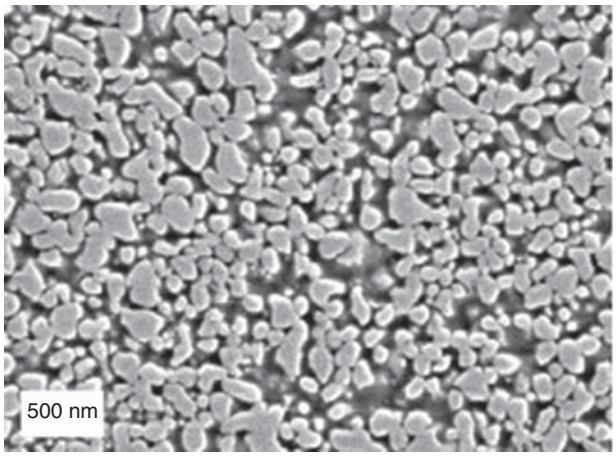

(a)

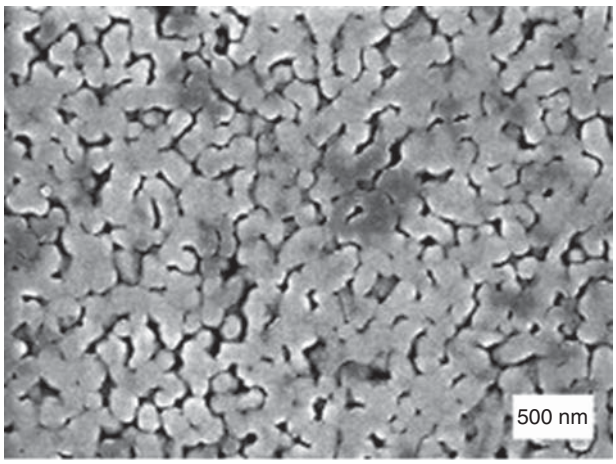

(b)

Figure 3.51 Preparation of sections through highly porous Al_2O_3 bodies prepared from an α-Al_2O_3 powder with particle size of 150–200 nm by cold-isostatic pressing. (a) Green body heated to 800°C: porosity 37%, average grain size 0.17 µm (identical to the original powder). (b) Sintered state after heating to 1150°C: porosity reduced to 24%, average grain size slightly increased to 0.19 µm. Source: Krell and Klimke 2006 [K43]. Reproduced with permission from John Wiley & Sons.

bodies; micrographs (Figure 3.53a,b [K43]) would rather suggest an opposite conclusion about the degrees of homogeneity. The improved homogeneity obtained by gel-casting is clearly documented by the most narrow pore size distribution of these green bodies and correlates perfectly with improved sintering densification. On starting from similar green densities, same intermediate densities of 99% are reached at 200 K lower sintering temperatures [K43].

In the very special case of an *hexagonal-close* coordination of *monosized* spherical particles of D diameter, the geometrical model predicts an average pore size of about $D/5$. It is not clear whether the different D_{50} values in

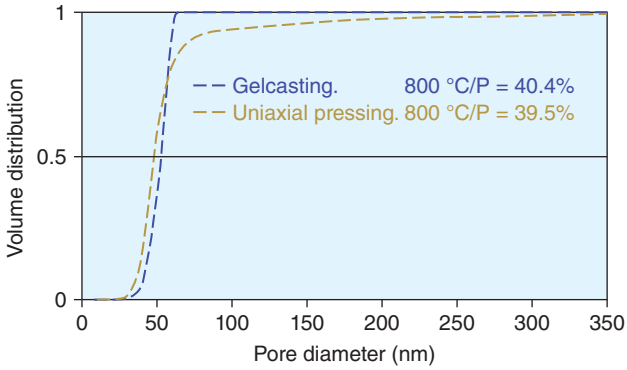

Figure 3.52 Pore size distribution of green bodies formed by, respectively, pressing and gel casting; micrographs are given by Figure 3.53 (same powder as in Figure 3.51 [K43]).

Figure 3.52 represent real differences of the two samples or are attributed to the measuring uncertainty of the mercury porosimetry. However, regarding the average 170 nm particle size of the powder, the median pore size of about 55 nm of the gel-cast body shown in Figure 3.53 is obviously *larger* than $D/5$. The question arises whether this difference is simply due to the idealized geometric model, hence has to be accepted, *or* should be diminished. The question has been answered by experiments, where gel-casting with large organic molecules was substituted by binderless slip-casting, and again mercury porosimetry provided a clear answer. This issue is of fundamental importance, namely, that the green slip-cast body does not only exhibit a higher green density (68%!) and a substantially narrower pore size distribution than gel-casting, but its median pore size of ~35 nm (see Figure 3.54) comes close to the $D/5$ limit predicted by the applied model! Once more, porosity measuring was confirmed as a *realistic* tool for homogeneity evaluations. Made of the same high-purity powder, the bodies prepared by slip-casting enabled a further decrease of the HIP temperature to 1130° C compared to 1200° C after gel-casting, which reduced their final grain size by 40% (!), namely, to 0.33 µm (compared with 0.53 µm after gel-casting). It also raised the real in-line transmission (RIT) of 0.8 mm thin discs to above 70%; notably, until now the latter is the international benchmark for birefringent ceramic alumina Al_2O_3 [K58].

3.2.2 Scatters Topology Illustration

We have seen in Section 2.1.3.4 that scattering of electromagnetic radiation by any microstructural features of different refractive index n from the matrix represents a major factor negatively affecting transparency. Scatterers elimination (especially porosity) are a most difficult task to fulfill in TC fabrication. The defects that

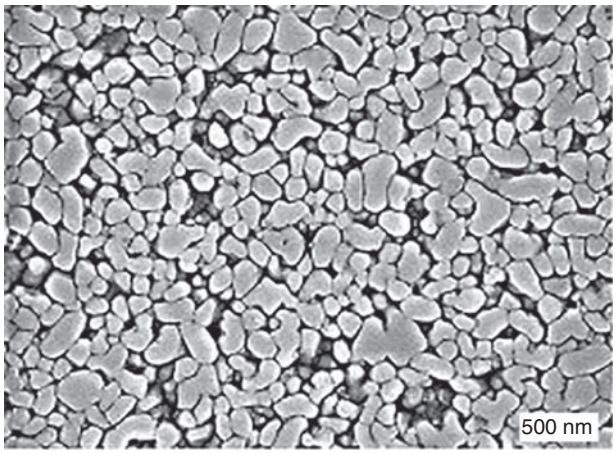

(a)

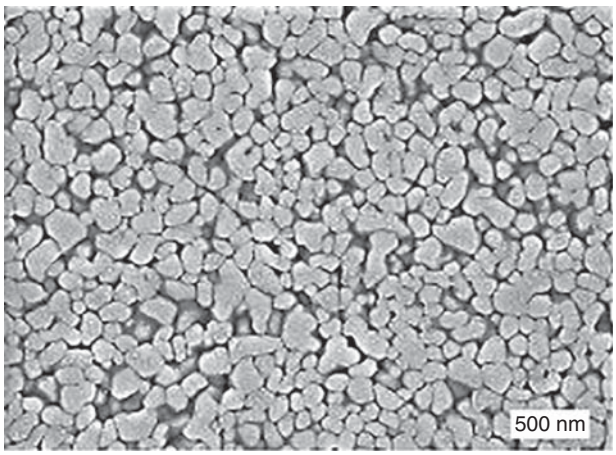

(b)

Figure 3.53 Green microstructures of bodies made (a) by gel-casting and (b) by uni-axial pressing (at 200 MPa), respectively, with about 60% green density (same powder as in Figure 3.51). Note that porosimetry records are also an alternative tool for the evaluation of the green density (which is commonly calculated by the ratio of weight to volume). Source: Krell and Klimke 2006 [K43]. Reproduced with permission from John Wiley & Sons.

cause scatter may also affect negatively the mechanical properties and thermal conductivity and reduce the damage threshold under high intensity irradiation. This means that thorough identification of the nature, size, morphology, and **topology** of the scatterers present in the transparent ceramic is very important. General methods like SEM, TEM, XRD, optical microscopy, and turbidity measurements are of significant help in this context. Lately, as additions to the list of classical tools, some more exotic techniques were made available to the transparent ceramics technologists. One of those is laser-scattering based tomography. The data discussed in Section 3.2.2.1 are drawn mostly from [G8].

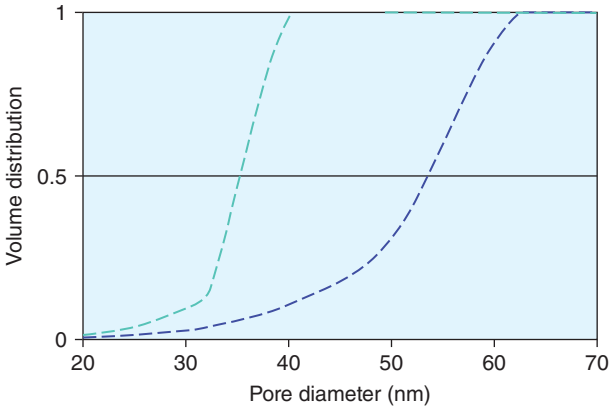

Figure 3.54 Pore size distributions of green bodies prepared by slip-casting and by gel-casting, respectively, of same powder as in Figures 3.51 and 3.53 (average particle size 150–200 nm). Green curve is for slip-casted specimen. Blue is for gel-casted specimen [K43].

3.2.2.1 Laser-Scattering Tomography (LST)

A setup for scattering defects localization is shown in Figure 3.55.

Measurement results on a single-crystal yttrium aluminum garnet $Y_3Al_5O_{12}$ (YAG) (of no scattering pores) and on two ceramic YAG parts sintered by different methods are shown in Figure 3.56.

It can be seen that the reactively sintered specimen has a larger population (10^5 cm^{-3}) of scatterers that also exhibit a wider size distribution than the normally densified one. The technique is also capable of providing a quantitative relationship between the volume of inclusions, and the amount of the inclusions deviation from the $Y_3Al_5O_{12}$ stoichiometry: toward excess Al_2O_3 or toward excess T_2O_3.

3.2.3 Discrimination Between Translucency and High Transmission Level

Certain languages (like German) may give rise to misunderstanding when, for example, a tracing paper is

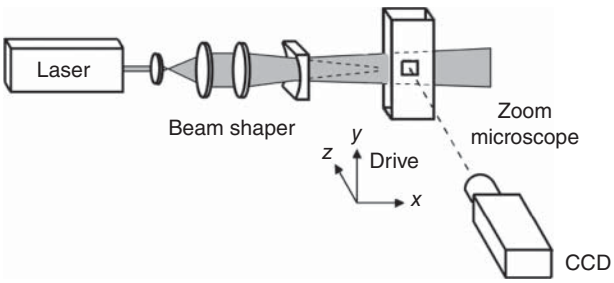

Figure 3.55 Setup of laser tomography system used for scattering defects localization. Source: Courtesy of R. Gaume [G8].

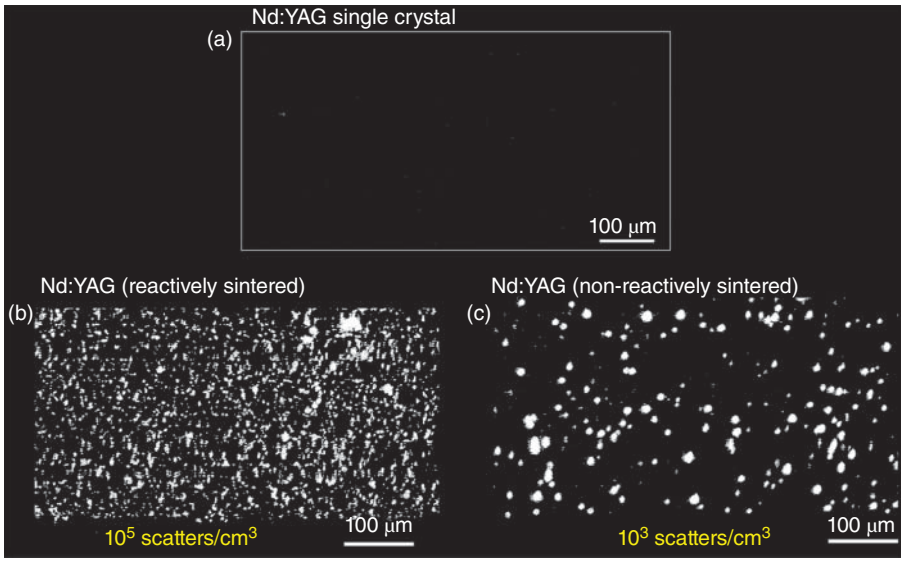

Figure 3.56 Image of scattering defects topography in a single-crystal YAG (top panel) and two sintered YAG ceramics. Source: Courtesy of R. Gaume [G8].

called "transparent paper," in disagreement with its only *translucent* appearance. Recall that in science and technology, window components are considered transparent only if they provide clear images even for a large distance between the object and the window. Obviously, "clear" images occur only when most light intensity remains in-line and is not scattered. Frequently, a first qualitative evidence of transparency can be obtained by simple visual observation of a target object trough the tested window. For a correct visual evaluation, one needs to do the examination in a setup that ensures a certain distance between object and window (Figure 3.57a [K56]). Placing of the windows directly on a printed matter is not a good set up for such an examination. It provides similarly "clear" images for both translucent and highly transparent windows (Figure 3.57b) [K56].

Only Figure 3.57a clearly reveals the characteristic transmission differences among these materials, whereas the inappropriate positioning in Figure 3.57b hides valuable information about the different degrees of transmittance.

Similar misleading conclusions on "transparency" (namely, a high proportion of "in-line" transmittance) may be derived from transmission measurements using optical devices with unspecified, large aperture (half of the opening angle). For correct RIT, measurements have to be limited to about 0.5° as leading manufacturers of ceramic discharge lamps, like Philips and NGK Spark Plug, recommend [A23, Y3]. The reason is that if, on transmission through a medium, some part of the aside-scattered beam remains relatively "in-line" with its original direction, it is obvious that with an opening angle of say 5° instead of 0.5°, significant amounts of scattered rays will contribute to the measured intensity. Note that a 10-fold angle increase means a 100-fold signal collection area raise; thus such a measurement is not of the pure RIT (the fraction of transmitted light responsible for transparency) but of the RIT augmented with forward scattered radiation. The issue of the actual aperture size is, of course, less important for the characterization of windows that are indeed close to being "fully transparent." It is, however, very important for components exhibiting significant scatter (haze). As an example of the latter, Figure 3.58a shows the scattering losses in a thick plate of material, as, for example, a window of birefringent sintered sub-micron alumina Al_2O_3 ceramic powder; on visual inspection it looks translucent. The degree of scattering losses decreases, for a thinner plate of the same material, as shown in Figure 3.58b, so that it looks quite transparent. If the spectral measurement is made with a wide angle aperture, the difference in the transmission curves recorded will not correctly reflect the transparency differences. Thus, the valid determination of a "real" in-line transmission needs a narrow measuring aperture (as shown in the Figure 3.58b) and a specification of the specimen thickness.

Yet another option of transparency measurement and quantitative specification is the determination of the image resolution of a black/white bar lattice as it is common in optics as record of the modulation transfer function (MTF) [M12, M37].

3.2.4 Bulk Density Determination from Optical Transmission Data

A ceramic exhibiting a relative $BD > 99.99\%$ TD is often addressed in engineering as "fully dense," without strictly being so. The reason is that for many properties such an approximation is quite reasonable. That because a residual porosity of, say, $P_0 = 200$ ppm has

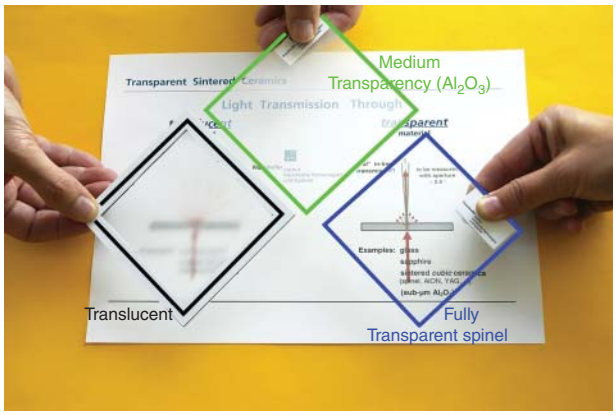

(a)

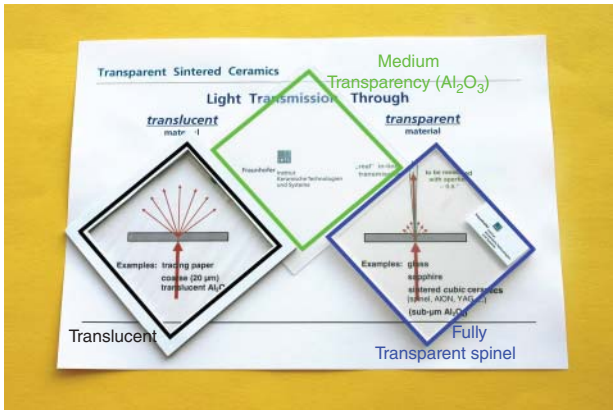

(b)

Figure 3.57 Different visual evaluation of 0.06 mm thin translucent organic film, sintered window of sub-micrometer Al_2O_3 ceramic (thickness 0.8 mm, real in-line transmission ~60%), and 6 mm thick transparent Mg–Al-spinel ($MgAl_2O_4$). Only panel (a) clearly reveals the characteristic differences in the transmission of these materials, whereas the inappropriate positioning in panel (b) hides valid information about the different degrees of transmittance: without a larger distance between object and window there is no apparent difference of (even extremely thin!) translucent and transparent materials. Source: Krell et al. 2009 [K56]. Reproduced with permission from Elsevier.

usually only negligible influence on those properties. The situation is different when transparency is considered. Recall that high transparency levels is achieved only for $P_0 \leq 200$ ppm; at even slightly higher porosity P_0 levels, specimens rapidly become translucent, and then opaque. The optical transmission T level varies, significantly also when the porosity P_0 varies within the $2-100$ ppm range. The residual porosity amount is, usually, derived from BD measurements based on the Archimedes technique. It is worth noting that, with this method, second digit accuracy of P_0 measurement already requires high quality measurements; the third digit after the decimal point cannot be satisfactorily measured by the Archimedes technique. Thus, Archimedes technique based estimation of P_0 is not reliable in the region relevant for distinguishing among high transparency degrees. On the other hand, a positive conclusion also becomes apparent: if the known pore size distribution is narrow, RIT values can be used for calculating P_0 [A23].

3.2.5 Lattice Irregularities: Grain Boundaries, Cations Segregation, Inversion

In reality, most cubic oxide lattices exhibit a structure different from the ideal model. The defects may have either adverse or beneficial effects on the processing ease and/or the properties of the transparent ceramics. Therefore, knowing the details of the real lattice structure at grain and atomic scales is quite important as it facilitates control of densification and grain-growth-influencing processes. It also helps in efforts to improve dopant distribution uniformity. This issue is, like some of the above-treated ones, relevant for all ceramic types; here, however, the various effects need to be controlled more accurately than in other cases. From the many types of possible lattice irregularities only a few are considered in this section.

A first such irregularity is the grain boundaries. Aspects of grain boundary structure in ceramics, relevant to the transparent ceramics domain, have been examined using various techniques, e.g. [B64, C28]. For instance, West et al. [W21] used high resolution transmission electron microscopy (HR-TEM) to study rare-earth cations (RE^+) like yttrium Y, lanthanum La, gadolinium Gd, europium Eu, and ytterbium Yb-doped alumina Al_2O_3 and spinel $MgAl_2O_4$; the most interesting results obtained were those related to dopant segregation at GBs. Before discussing those data, let us present the general configuration, of the GB zone that the study revealed. No second phase has been observed and the lattice structure of each grain remained un-perturbed as close as about 0.5 nm from the grain-boundary median plane. That means the width of the perturbed, more relaxed, lattice region was smaller than about 1 nm, as illustrated by the diffuse fringes in TEM images. Coming back to the impurities let us first underline that the authors put to work an impressive number of high resolution analytical tools like secondary ions mass spectroscopy (SIMS), Auger electron spectroscopy (AES), HR-TEM, scanning transmission electron microscopy (STEM), parallel electron energy-loss spectroscopy (PEELS), and high-angle annular dark field imaging (HAADF). In Figure 3.59a [W21], a TEM image (the use of the HAADF allows a very good Z contrast achievement) shows the accumulation of Eu at the GB. In

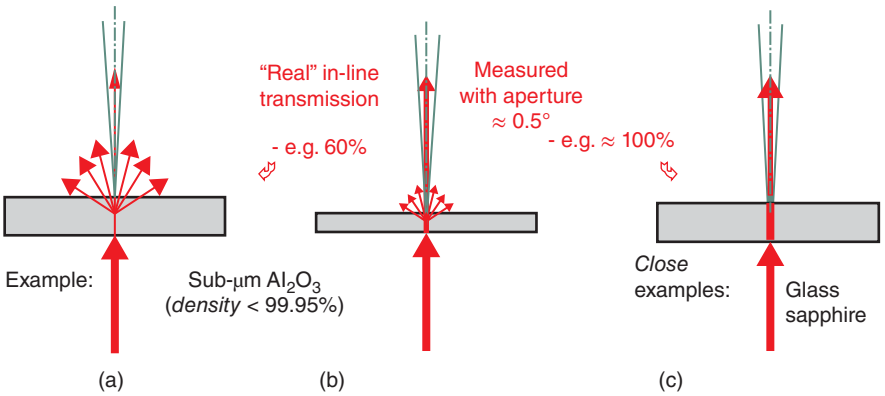

Figure 3.58 Effect of specimen thickness on the scattering loses. (a) Scattering losses in a thick component of a translucent material as, e.g. sub-micrometer birefringent α-Al_2O_3 ceramic. (b) Thinner slice of the plate of panel (a). (c) Thick plate lacking scattering centers (like glass or sapphire). Source: Krell et al. 2009 [K56]. Reproduced with permission from Elsevier.

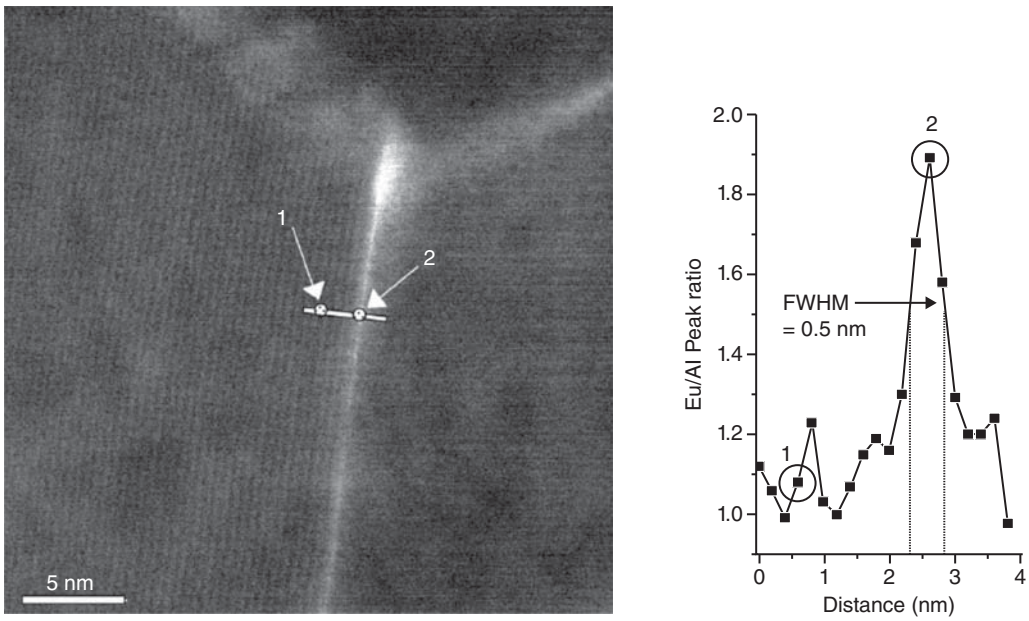

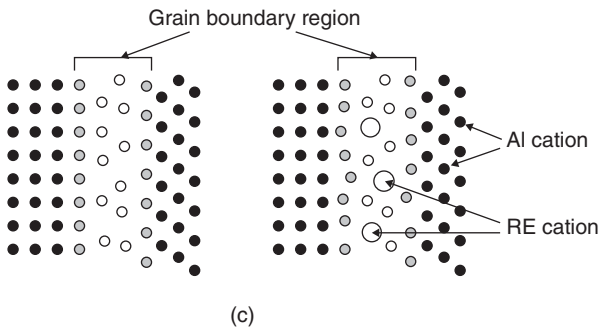

Figure 3.59 Chemical composition of grain-boundaries. (a) Map of Eu distribution in spinel ceramic grains (STEM; PEELS with HAADF detector); massive segregation toward the grain-boundary is seen. (b) Eu/Al peaks ratio (image shown in panel (a)) as a function of testing point position on the grain. (c) Schematic representation of the GB region of spinel and the pattern of Eu distribution along it. Source: Reproduced from [W21] with permission from Springer.

Figure 3.59b the europium Eu concentration line (line crosses the GB) profile, (PEELS signals), is given; it confirms the dopant distribution pattern suggested by Figure 3.59a. The schematics of a rare-earth cations containing grain boundary, and a clean one, are depicted in Figure 3.59c. The rare-earth cations seem to be distributed in an almost monolayer arrangement, continuous along the grain boundary, and apparently their presence leads to a broadening of the grain boundary. The GB width increase is confirmed by examination done so as to reveal the lattice fringes – as shown in Figure 3.60. The fringes become diffuse in the grain boundary region owing to lattice disorder. The diffuse region is widened, here, by the presence of a dopant, in this case triply ionized lanthanum La^{3+} (compare panels (c) and (d) in Figure 3.60). The situation depicted earlier characterizes the regular GBs. In special or very low angle boundaries, discontinuities appear in the rare-earth distribution pattern.

In another work, on spinel, sulfur was found to be located solely in the grain boundary region of spinel parts [C33].

A.M. Thomson et al. showed, mostly by SIMS imaging, that yttrium Y^{3+} and lanthanum La^{3+} cations tend to segregate at the grain boundaries of ceramic alumina Al_2O_3 [T18]. Figure 3.61 illustrates the location of Y^{3+} cations; observe also some small precipitates; examination of this type of doped aluminas was also described in [B63].

Ikesue et al. has shown [I3] that silicon Si^{4+} cations that substitute aluminum Al^{3+} cations causing lattice shrinkage also accumulates mostly in the grain boundaries regions. It seems to compensate the expansion caused by dopant neodymium Nd^{3+} cations thus facilitating the Nd^{3+} cations entrance into the YAG lattice. In YAG and other similar garnets, the cerium Ce^{3+} and neodymium Nd^{3+} cations having radii, which are significantly different from that of the lattice yttrium Y^{3+} cations, also tend to accumulate at grain boundaries

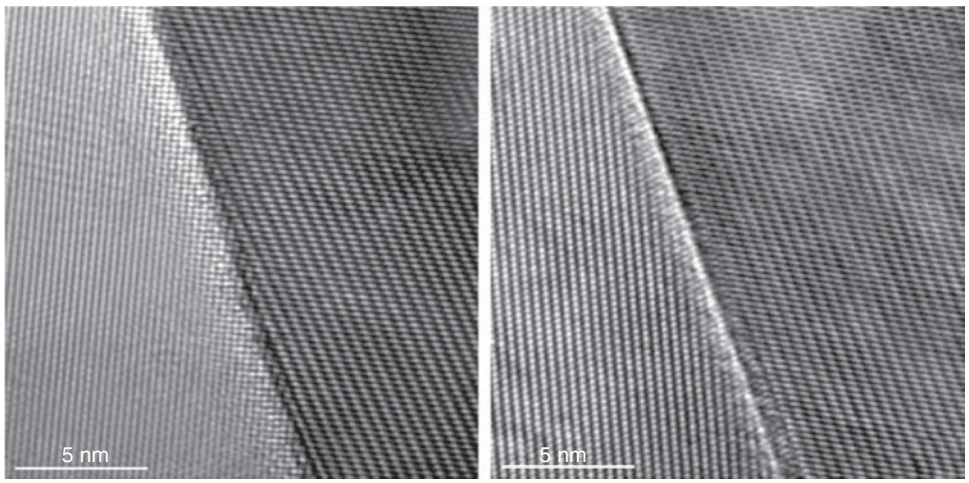

Figure 3.60 HRTEM image of a grain boundary in transparent spinel. (a) Undoped host. (b) Spinel doped with La^{3+} (widened diffuse region, around GB, caused by presence of dopant). Source: Reproduced from [W21] with permission from Springer.

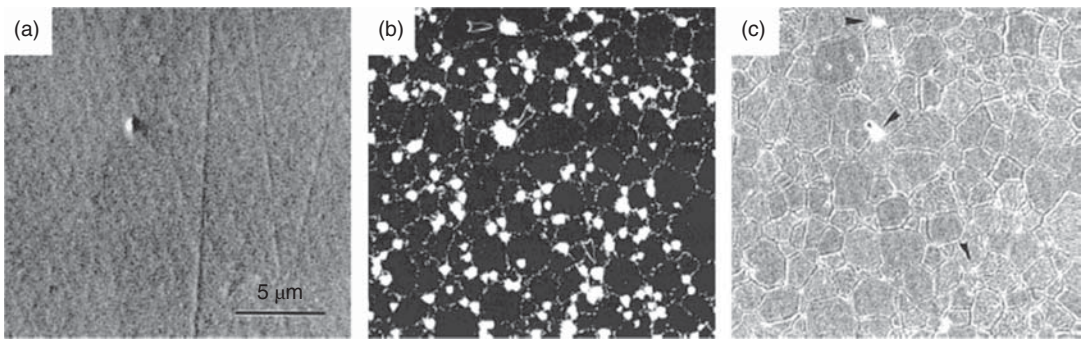

Figure 3.61 Segregation of Y^{3+} (1000 ppm of dopant) at the grain boundary of doped transparent alumina ceramic (SIMS data). (a) Total ion-induced secondary-ion signal topographic image of polished but unetched surface. (b) Y rich spots (white) by SIMS map of region shown in (a). (c) SEM image of same region. Source: Thomson et al. 1997 [T18]. Reproduced with permission from John Wiley & Sons.

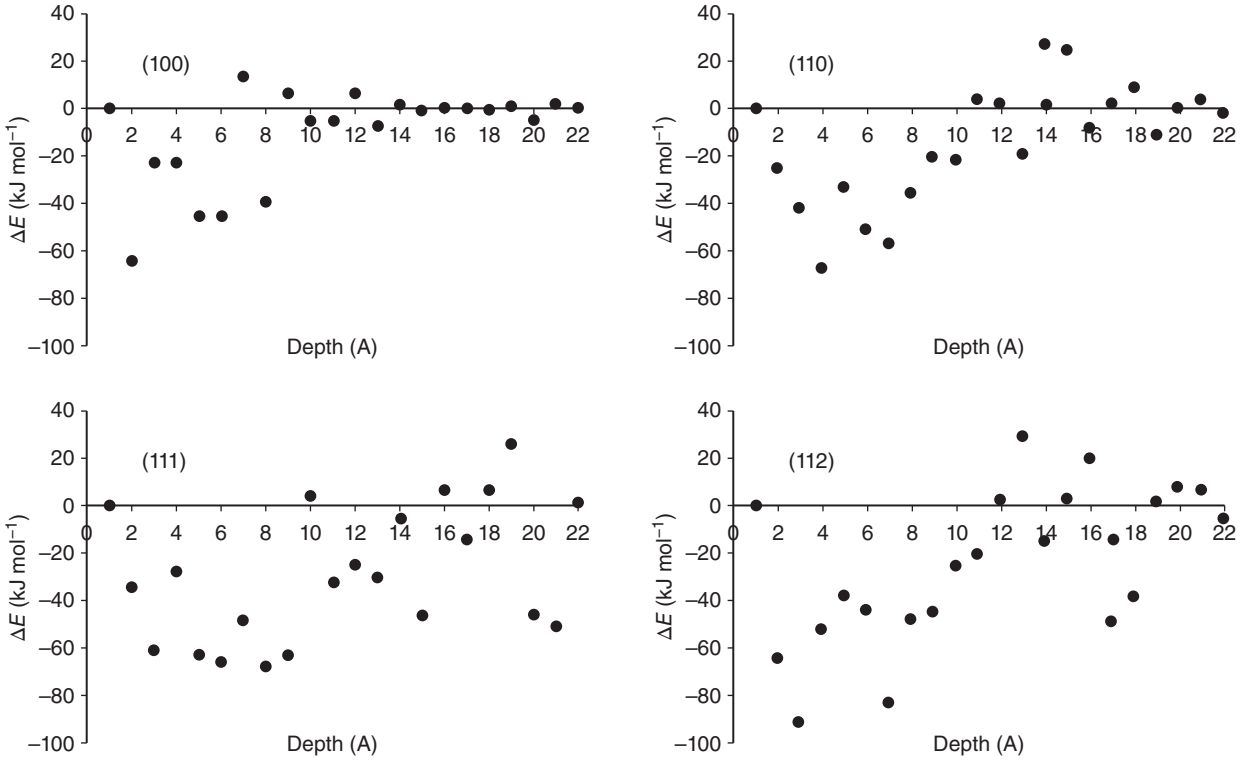

Figure 3.62 Nd penetration depth as a function of the plane type in alumina lattice. Depth of penetration for various planes are presented in the four panels of the figure; the (111) planes are able to incorporate more dopants than other plane types (modeling). Source: Aschauer et al. 2006 [A27]. Reproduced with permission from John Wiley & Sons.

[Z11, Z12]. Atomistic modeling suggests Nd^{3+} to concentrate within a 5 Å deep zone at the surface of a polyhedral body. The (111) surface can incorporate about twice the number of dopant ions than (100) planes (Figure 3.62) [A27].

Confocal microscopy imagery based on fluorescence and Raman signals confirms the occurrence of Nd^{3+} segregation. Demonstration of segregation is important owing to the multiple, mostly deleterious, consequences of the process. For instance, the clustering of dopants – occurring in all the grain but facilitated, in the GB region as a result of the agglomeration caused by segregation – introduces weak satellite fluorescence lines, and thus leads to deleterious inter-ionic energy transfer that reduces fluorescence yields. Variation of neodymium Nd^{3+} cation concentrations, within the grain, also leads to refractive index fluctuations, which may enhance scattering and wave front distortions. A combination of confocal microscopy with TEM (energy dispersive X-ray spectroscopy – EDS) revealed the correlation existing between the segregation coefficients in melt/crystal systems and the strength of the tendency of a given dopant to pileup at the grain boundaries. Thus, neodymium Nd^{3+} and cerium Ce^{3+}, both of low segregation coefficients $k = 0.22$, segregate strongly, while ytterbium Yb^{3+} of close to a unity segregation coefficient ($k \cong 1$) is more uniformly distributed through a grain [B47, B48, B46, E3, C17]. For instance, Figure 3.63a,b [Z11] depict the distribution of Ce^{3+} cations in $Y_3Al_5O_{12}$ (YAG) grains, based, respectively, on confocal fluorescence microscopy, and on SEM (electron-microscope-probe-elemental-analysis – EMPA) data. Discussion concerning the topology of ytterbium Yb^{3+} cations data is provided in Section 5.2.9.5.

The segregation of Mg^{2+} and Ca^{2+} to the GBs of alumina was examined, among others, by the authors of [S42, S43], while segregation in MgO and Cao was studied by [T15]. The effect of segregation on diffusion of ions is examined, by modeling, in [K9].

The last issue related to lattice irregularities, discussed here, is the inversion of cationic sites. The provided example relates to the transparent ceramic material where the strongest effects of this type were documented. It is the stoichiometric spinel ($MgO_nAl_2O_3$ with $n = 1$), where only one-eighth of the available tetrahedral sites are occupied by magnesium Mg^{2+} cations and one half of the octahedral sites occupied by aluminum Al^{3+} cations. This lattice exhibits a significant propensity for cation exchange and formation of interstitial defects. The degree of cation exchange (Al going to

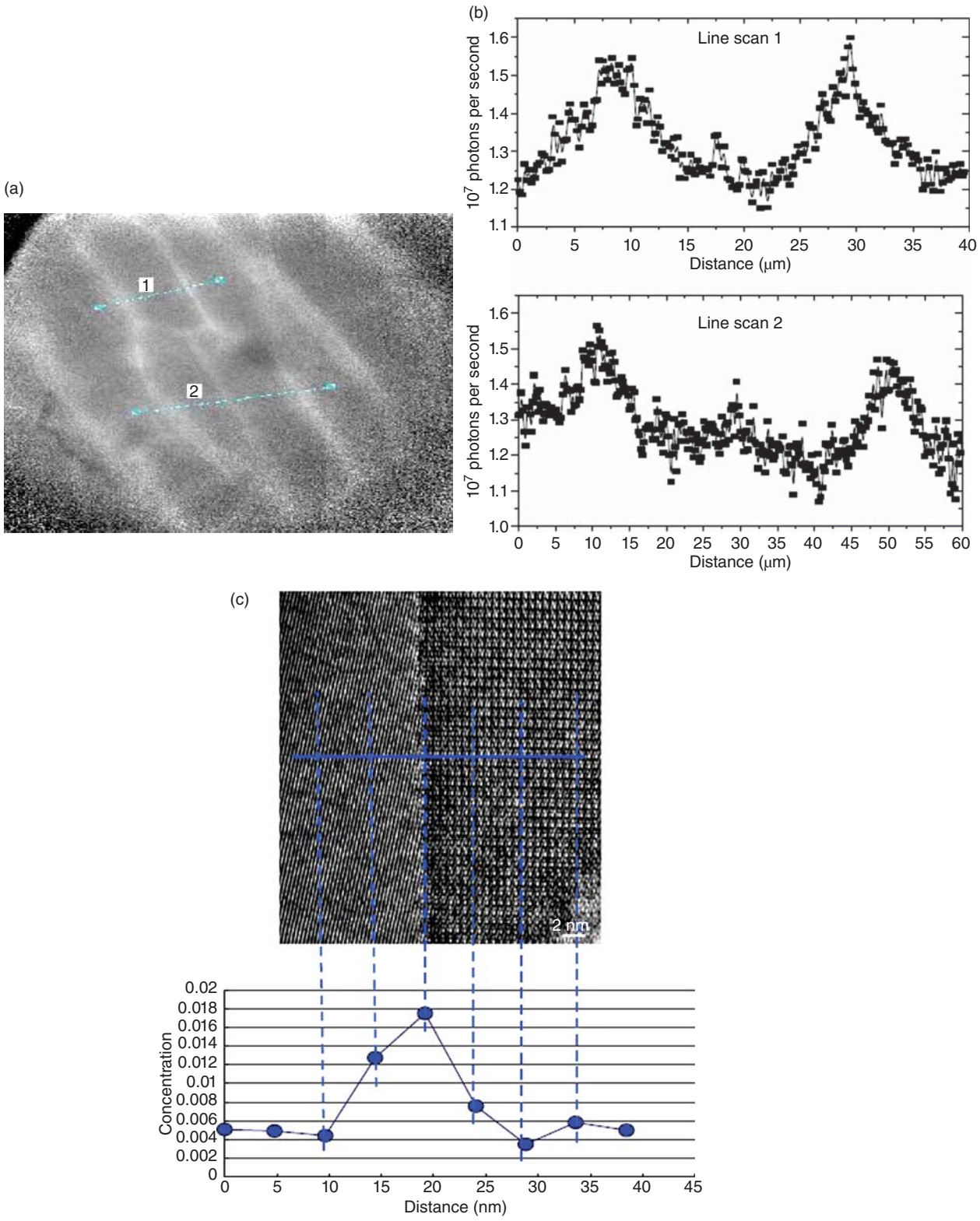

Figure 3.63 Distribution of Ce^{3+} over a YAG grain. (a) According to confocal microscopy data. (b) According to confocal data (fluorescence). (c) SEM (EDS) data. Source: Zhao et al. 2011 [Z11]. Reproduced with permission from Elsevier.

Mg sites and vice versa) is described by an "inversion parameter" *i*, defined as the fraction of tetrahedral sites occupied by Al^{3+} cations. This formation of antisite defects can be investigated by ^{27}Al nuclear magnetic resonance (NMR). An application of this technique to two laboratory-designed spinels (A) and (B), confirmed an expected and reasonable feature: spinel (A) built on a preexisting cubic template lattice of magnesium oxide MgO particles exhibited less disordered Al^{3+} cations than in spinel (B), which was ab initio chemically synthesized. This finding explained the lower sintering temperature of the disordered spinel (B), because increasing cation inversion in stoichiometric spinel is associated with Schottky defect clusters, which include oxygen vacancies. Such vacancies facilitate the diffusion of the oxygen anions, which are the biggest, and therefore slowest diffusing species; thus sintering is facilitated and it can be completed at lower temperatures. Similarly, an NMR comparison of commercial spinel powders obtained by different syntheses (for example, FSP vs. an alum processing), established a clear explanation for their different sintering activities (other factors are also at work): at similar particle sizes, the difference of cation disorder in the spinels synthesized respectively by FSP ($i = 0.36$), and alum calcination ($i = 0.29$), was as large as in the example reported above; so was also the difference between their sintering temperature [K42]. Thus, the difference of cation inversion levels in material prepared by FSP and alum-derived one is sufficiently strong to account for the different sintering temperatures of green bodies produced using these commercial powders.

3.2.6 Parasitic Radiation Absorbers' Identification and Spectral Characterization

For both passive and active TCs (see Section 5.1 for definition), it is important that at the end of the fabrication process they exhibit a transmission curve profile matching that defined by the developers of the part.

In practice, the transparent ceramic parts are never totally devoid of defects – in the various stages of their fabrication, including the finished product stage – intrinsic or extrinsic. Such defects are introduced by the raw materials and/or the processing. Some of these defects may be involved in absorption or emission of radiation. They are hereby addressed as parasitic absorbers (or emitters). Parasitic defects need to be practically eliminated before the product may be considered as finished. (Defects not spectrally active need also consideration in as much as they affect non-spectral properties; here, however, only the spectrally parasitic defects are considered.) Their spectral features may simply reduce the transparency of the passive TCs or, in the case of the active ones, modify the absorption/emission profile defined by the dopants. The list of parasitic defects includes items like native ions vacancies (especially of oxygen anions), and impurity transition metal and rare-earth cations. Some principal group element cations like Pb^{3+} [D21] may also introduce intense charge transfer bands, located in the near ultraviolet (NUV) which widen toward the VIS range. Also adsorbed molecules may possess vibrational overtone bands in the near infrared (NIR) (for example, OH^- is an ubiquitous one). In certain cases, significant spectral damage may be caused by very low (around 10 ppm) defect concentrations (for example, impurity Ce^{3+} cations in $Y_3Al_5O_{12}$ (YAG) laser rods; see the following). The EMR absorbing defects are of most concern, and the following discussion focuses on such; a more detailed treatment of this topic can be found in [G31].

3.2.6.1 Absorption by Native Defects of Transparent Hosts

A recent study (A. Goldstein, unpublished results) examined quite high purity (99.99% = 4 N) oxide-based transparent ceramics exposed to various sintering atmospheres. The study focused on oxygen lacking atmospheres (encountered in most transparent ceramics fabrication processes), at temperatures exceeding ~1500° C. The set of materials examined included $MgAl_2O_4$, $Y_3Al_5O_{12}$ (YAG), cubic zirconia c - ZrO_2, TiO_2, Al_2O_3, Y_2O_3, and MgO. A first important conclusion was that even in vacuum (where their formation is facilitated) the oxygen vacancies rarely influence the optical transmission curve profile in the VIS range (viz color) by themselves; their direct influence is limited to the NUV. This is so because such defects, when not integrated in defect associates, absorb in the NUV [S71]. Defect aggregates – which may be able to generate absorption bands also in the VIS – form only as result of irradiation not simple heating, no matter the atmosphere's nature; so such potential absorbers are not considered here. The oscillation strength of the single vacancy absorbers is not large. Let us also clarify, in passing, that an oxygen vacancy proper ($V^{\cdot\cdot}_O$) is not a light absorber. To become one it has to trap one or two electrons and form local absorbing units of the V_O or V'_O (lower probability) form; the necessary electrons may result from the breakup of the oxide anion the exit of which generates the vacancy. When a vacancy forms in order to electrostatically compensate, say, the formation of a reduced oxidation state cation (e.g. Ti^{4+} goes to Ti^{3+} state), a non-absorbing oxygen vacancy forms because the electrons are consumed in the cation reduction process. Practice showed us that when sintering is executed at around 10^{-3} Pa vacuum levels, at temperatures up to ~1700° C, and dwelling times no longer than five hours, the concentration of electron

trapping vacancies does not reach the limit needed to expand their NUV bands into the visible, so as to cause coloration. Another conclusion was that, during vacuum firing, the hosts behavior differs as a function of their chemical composition, namely, if they may or may not generate absorbing type transition metal, by reduction of their native un-absorbing ones. Hosts unable to generate such cations (magnesia, alumina, spinel) remain colorless even after vacuum firing. Some of the oxides, able to produce d^n cations, of the absorbing type, acquire color. Let us illustrate the statements earlier by an example. Titanium dioxide TiO_2, and with more difficulty zirconium dioxide ZrO_2, can generate – when exposed to reducing favoring atmospheres, like vacuum – respectively Ti^{3+} and Zr^{3+}. The incentive to do that comes from the loss of free-energy brought about the formation of complexes of the reduced ions with the O^{2-} anions of the host as ligands; the electric field of the ligands generates a stabilization, negative, energy when such complexes form. In our view the reduced species form polyheteronuclear complexes involving Ti^{3+} its neighboring oxide anions and the Ti^{4+}; a similar process happens in zirconias. Such complexes have excited electronic states of a nature making transition to them, from the ground state, orbitally allowed; as a consequence the corresponding absorption bands are very strong. As the concentration of Ti^{3+} (or Zr^{3+}) increases, the bands widen. From the absorption in NUV (where the bands are located), their effect extends to the VIS range and thus colors in the order: yellow, orange, brown, red, and finally black may appear. Such color effects are actually obtained when heating in vacuum titania or zirconia [S13] but not alumina or magnesia. Zirconia may be colored also by subjecting crystals to the action of electric potential [N1, P1, W32]; in our opinion the effect is also due to Zr^{3+} formation. TiO_2 is already partially reduced to include Ti^{3+} even by heating in air to, say, 1500°C (brown to black colors form); in vacuum the process is more intense. The titania is more easily reduced than zirconia because the Ti is located above Zr in the periodic table of elements. Therefore air is reductive enough to allow, at sintering temperatures, Ti^{3+} formation by simple heating in such atmosphere. In Figure 3.46a, the reflection spectrum of an air sintered (1500°C; brown and black regions) titania disc is presented; in zirconia the same processes occur with lower intensity and only under vacuum firing. The tendency of reduction, from higher to lower oxidation states, of TM^+ cations, as the result of increasing temperature, is observed easily in glasses [B10]. In our view the reason for that (both in glasses and ceramics) is the fact that the formation of oxygen vacancies – required to compensate the negative charge increase produced by the cation reduction – is made easier by high temperatures. In Figure 3.64b–d, the electron paramagnetic resonance (EPR) signals of Ti and Zr^{3+} (identified by the aid of [O6, Z14]) formed in sintered titania (air heating) and zirconia (vacuum heating) are shown.

The ease of formation of reduced species, from non-absorbing TM^+ higher oxidation state cations, depends on the features of the considered lattice; aspects like the oxidation potentials, electron donor ability of the oxide anions, and cation anion distance are among the most important. Therefore, the behavior of a specific oxide is not so easy to predict. For instance, yttria or YAG may also produce Y^{2+} (d^1 type cation) by reduction of Y^{3+}. However, practice shows that reduction of the Y^{3+} does not occur upon vacuum heating (only traces of a color, produced by Y^{2+}, can be occasionally detected, after long such heating) of pure YAG or yttria. However, if the lattice of YAG is stressed by introduction of low amounts of Si^{4+} or Zr^{4+} cations (in oxide terms concentrations are around the 0.1% level), Y^{2+} and the associated purple color appear. In Figure 3.65 the optical spectrum and the EPR signal of a YAG specimen, doped with 0.2% zirconia and vacuum sintered at 1700°, is shown (the EPR and the transmission spectrum of a silica doped transparent and colored YAG are given in Section 4.2.5); yttria specimens, doped with silica, do not produce Y^{2+} cations.

EMR absorption by other mechanisms also occurs. For example, that owed to carbon impurities, acquired during processing, or coming from the raw materials (like sulfur or RE^+ cations) will be exemplified for the cases of spinel and YAG (see Chapter 4).

3.2.7 Detection of ppm Impurity Concentration Levels

In some of applications of transparent ceramics, it is important to minimize, eliminate if possible, any light attenuating parasitic defects. For that goal, the defects producing the disturbance of the EMR incident on the TC need to be first identified and characterized. A methodology lately developed at Cornell University is able to detect variations in the light absorption coefficient α that are as low as several ppm/cm [A10]. It is called **photo-thermal common-path interferometry**, in short **PCI**; what the technique measures, actually, are very small variations of the refraction index introduced by the presence of the parasitic defects. Usually conventional electronic spectroscopy is used for identification and characterization of the attenuators. The PCI becomes useful when the variation of absorption

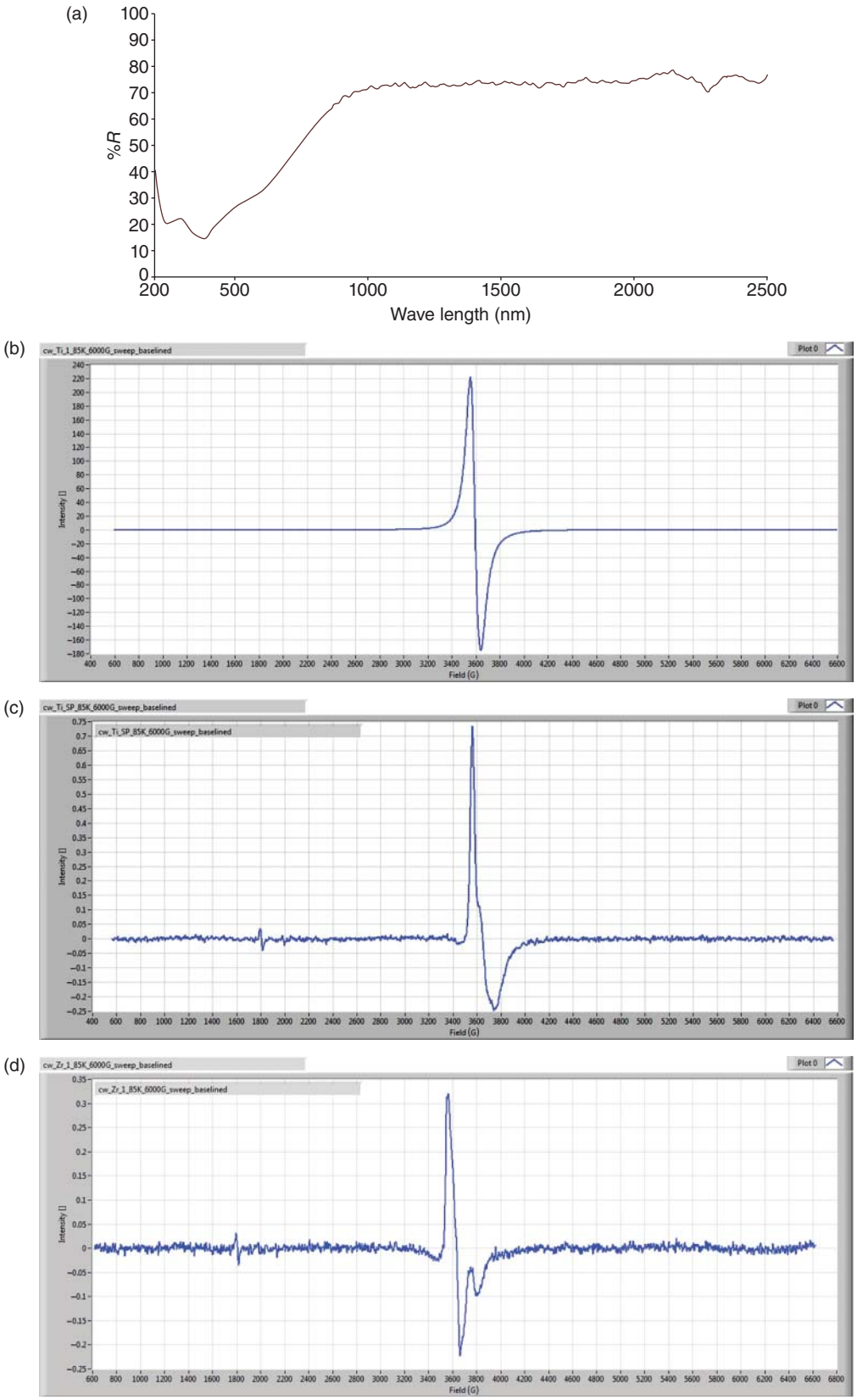

Figure 3.64 Reflection spectra of TiO_2 sintered in air (shows Ti^{3+} absorption band) and EPR signals of Ti^{3+} and Zr^{3+} in various hosts. (a) Reflection spectrum. (b) Ti^{3+} EPR signal in titania. (c) Ti^{3+} EPR signal in spinel. (d) Zr^{3+} EPR signal in zirconia. (Intensity in arbitrary units in b, c and panels).

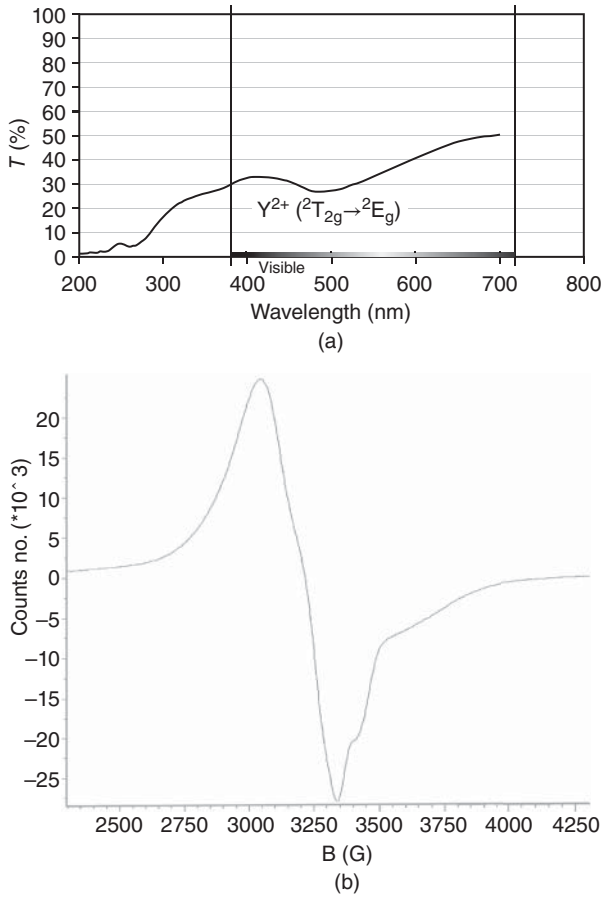

Figure 3.65 Optical transmission curve of a Zr doped YAG and its EPR signal. (a) Transmission curve with Y^{2+} generated absorption band (purple color of specimen). (b) EPR signal produced by Y^{2+} (resulting from YAG's Y^{3+} reduction).

coefficient α is so small, that it is undetectable by usual spectroscopy. Impurities able to produce such weak (but not negligible absorption) are OH^- anions, oxygen vacancies, iron Fe, and manganese Mn cations.

For example, using photo-thermal common-path interferometry, Gaumé et al. [G8] detected a very small absorption in Si doped Nd: $Y_3Al_5O_{12}$ at ~1 µm (the most sensitive gain wavelength of that material). They attributed the absorption to bound polarons, formed by oxygen vacancies which capture electrons. The vacancies formation is thought to be caused by silicon cations Si^{2+} derived from the Si^{4+} cations introduced by tetraethyl-orthosilicate $Si(OC_2H_5)_4$ (TEOS), used as a sintering aid. While the mechanism proposed to explain the action of the Si dopant is open to questions, the detection of such a small EMR absorption amount is quite impressive. Laser-induced breakdown spectroscopy, a very sensitive method, was shown, lately, to be also be able to monitor the evolution with processing of low Si amounts present in YAG.

3.2.8 Mechanical Issues for Windows and Optical Components

Mechanical properties are of obvious interest for users of security windows, transparent armor, or ceramic lenses and are subject to variation (occurring even between items of a given fabrication batch) – due to microstructure imperfections – existent even in highly transparent parts devoid of visible defects.

The strength of brittle materials, thus also the TCs, is governed by (i) their critical stress intensity K_{IC} (frequently called fracture "toughness," though none of these materials is really "tough") and (ii) the size of "fracture initiating" flaws. As to critical stress intensity K_{IC}, transparent ceramics must be strictly single phase, which unfortunately excludes common "toughening" concepts and fixes their critical stress intensity to the inherent value they exhibit; only moderate variations depending on grain sizes are possible. The optical specifications, of the TCs, impose drastic limitations on the flaws size: typically less than 100 µm in transparent windows, or less than 20 µm in optical components. Therefore, strength exhibits little variations in a given type of transparent ceramic. Measurement of the factors that determine strength poses no special adaptation problems for the standard methods previously developed for other high tech ceramics. Therefore, their correct measurement is not an issue of focus in TC development and fabrication. The same is valid for the Young modulus, which is not significantly influenced by grain size, and whose dependence on porosity is unimportant in ceramics that anyhow need to be sintered to over 99.99% of theoretical densities for becoming transparent.

A quite different situation prevails in the case of *hardness*, which changes markedly with both testing load and grain sizes, as demonstrated by Figure 3.66 for transparent spinel $MgAl_2O_4$-tested by Vickers (HV) and Knoop (HK) diamond indenters [K40].

It is important to understand that both grain size and testing load influences are exerted through the same processes, occurring in the specimen, during creation of the indent. Even in the less brittle ceramics, the high stress concentration beneath the testing diamond tip exceeds the yield stress (viz the level till which the specimen strains elastically) of the tested material. A permanent indent is thus shaped at room temperature by purely *plastic* deformation exhibiting twins and dislocations that follow the same laws as in metal physics [H29, K52]. Thus, ceramics hardness is in fact a measure of the localized *plastic* deformability of these brittle materials. The smaller the volume within which the primary elements of plasticity can grow and move, the more difficult local plastic deformation, beneath the tip of the

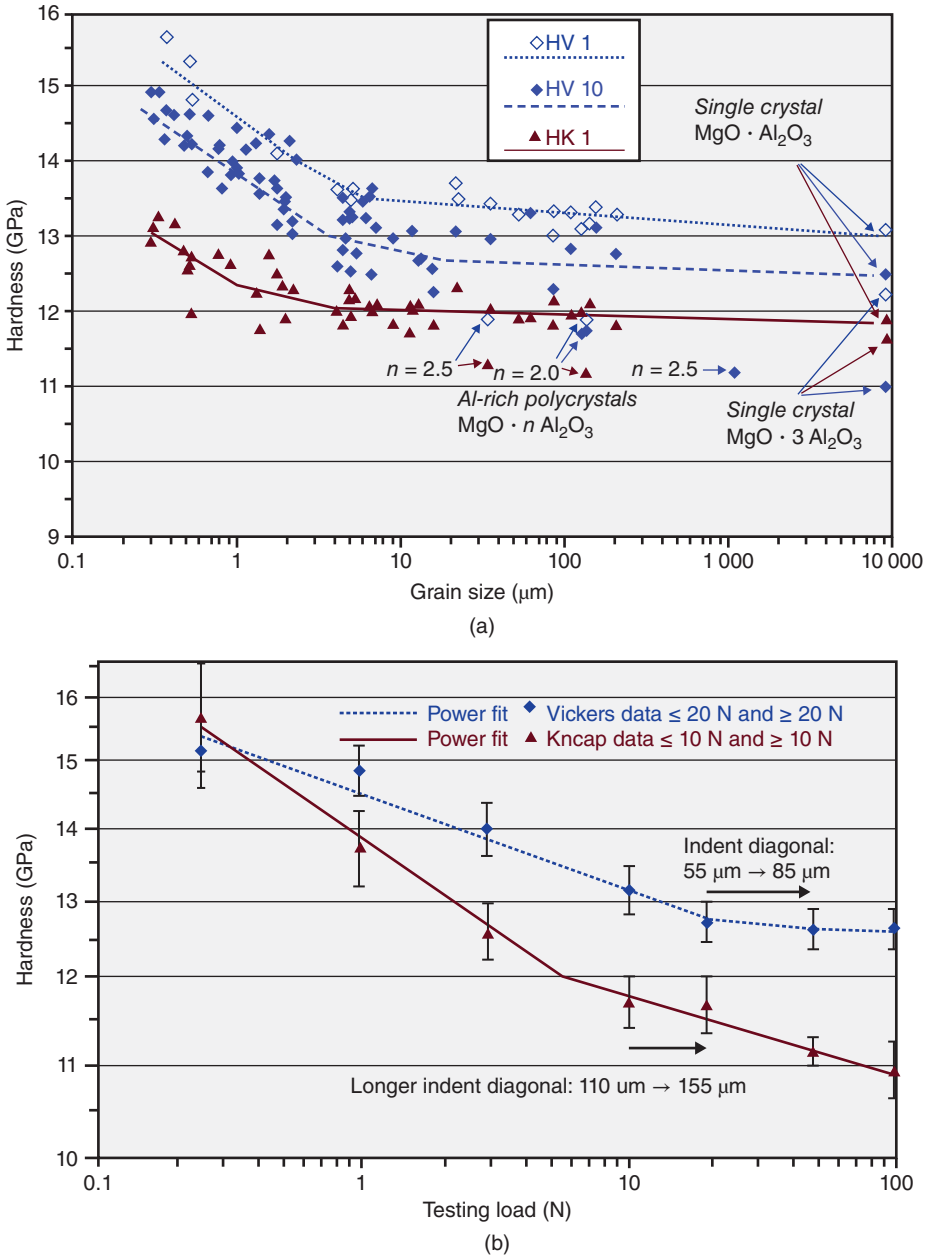

Figure 3.66 Influences of (a) grain sizes and (b) of testing load on the Vickers (HV) and Knoop (HK) hardness of transparent stoichiometric spinel ceramics and single crystals ($MgO{\cdot}nAl_2O_3$; $n = 1$); additional data are given for Al-rich species with $n > 1$ at some grain sizes and for the single crystals. Since for Vickers as for Knoop testing the indentation size effect decreases at larger loads, the set of experimental data in plot (b) could not be matched by one fit, different fits were applied for data <10 N (Knoop) and <20 N (Vickers), respectively, and for loads beyond this transition. Source: Krell and Bales 2011 [K40]. Reproduced with permission from John Wiley & Sons.

indenter, becomes. Thus a smaller size indent forms and an artificially enhanced value of hardness is measured by low testing loads [K49].

The reason – of the similarity between the profile of the curves showing hardness dependence on grain size and respectively testing load (Figure 3.66a/b) – is that on indentation, the available volume for dislocations growth and movement as elements of plastic deformation is limited by the extension of the *stress field* beneath the indenter tip (in the zone where shear stresses exceed the yield stress of the ceramic crystal lattice), and/or by the *grain size* of the microstructure. Important consequences of this analogy are illustrated by Figure 3.67 [K49]:

The influence of the testing load (also known as "indentation size effect" (ISE) is *strongest* for the hardness of the *single crystal*, whereas it *decreases* (because of the *additional* effect of grain *boundaries*) in sintered polycrystalline ceramics the *smaller* their *grain size* is. The influence of the *grain size* disappears (!) at very low testing load, namely, smaller than 1 kgf (<10 N) when the hardness is measured as "micro-hardness." At very low load, the stress zone for allowed plasticity is so narrow, that any further effect by wider or closer grains becomes unimportant.

In brittle materials as ceramics, however, measuring the *micro*-hardness is *easier* (because it is less

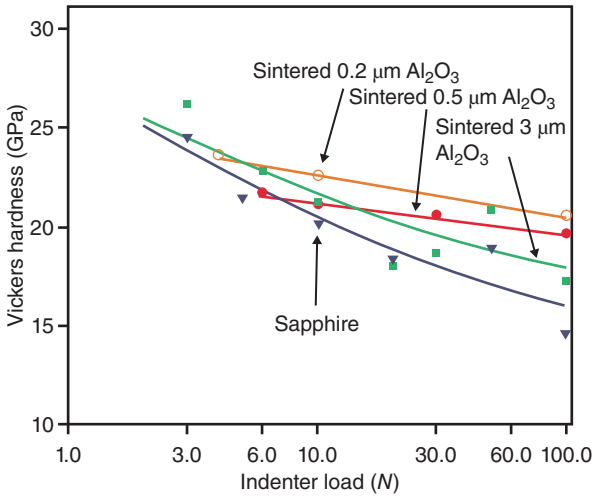

Figure 3.67 The influence of grain size on the indentation size effect (the load influence) of Al_2O_3 single crystal and polycrystalline sintered ceramics. Attached to the curves of the latter are the grain sizes of these sintered (dense) bodies. Source: Krell 1998 [K49]. Reproduced with permission from Elsevier.

complicated by microfracture) than testing at loads of 2 – 10 kgf (20 – 100 N). It is quite common to make 20 or more indents for getting 5 of them measurable. Also, Figures 3.66 and 3.67 demonstrate the "benefit" of getting "nice" (namely, high) hardness results for a given ceramic just by choice of a low testing load. Observation of Figure 3.67, however, makes it obvious that measuring of *micro*-hardness *eliminates* the *real* hardness differences between different grades; the measurement is then useless. Unfortunately, this imperative request of *macro*-hardness measurements is the more stringent for a *coarser* microstructure (because of its stronger ISE) despite the increasing difficulty of obtaining perfect indents just in such coarser ceramics and single crystals.

A correct hardness record of the different grades of transparent ceramic windows is an important, albeit not a single criterion for a successful design of transparent ceramic armor [K47, K60] or of transparent ceramic tools. Similarly, in *all* applications with *wear attack* on polished transparent surfaces (such as watch "glasses" and smartphones front windows), fine, preferentially submicron grain sizes with the associated high hardness are clearly preferred, since raising of grain size increases the risk for pull-out events of individual grains (Figure 3.68) [K52].

On first glance, people are tempted to regard hardness as unimportant for components like the ceramic lenses. However, definite benefit is obtained by smallest grain sizes, because the lenses need to be ground and polished. Regarding these operations the ceramics, which are

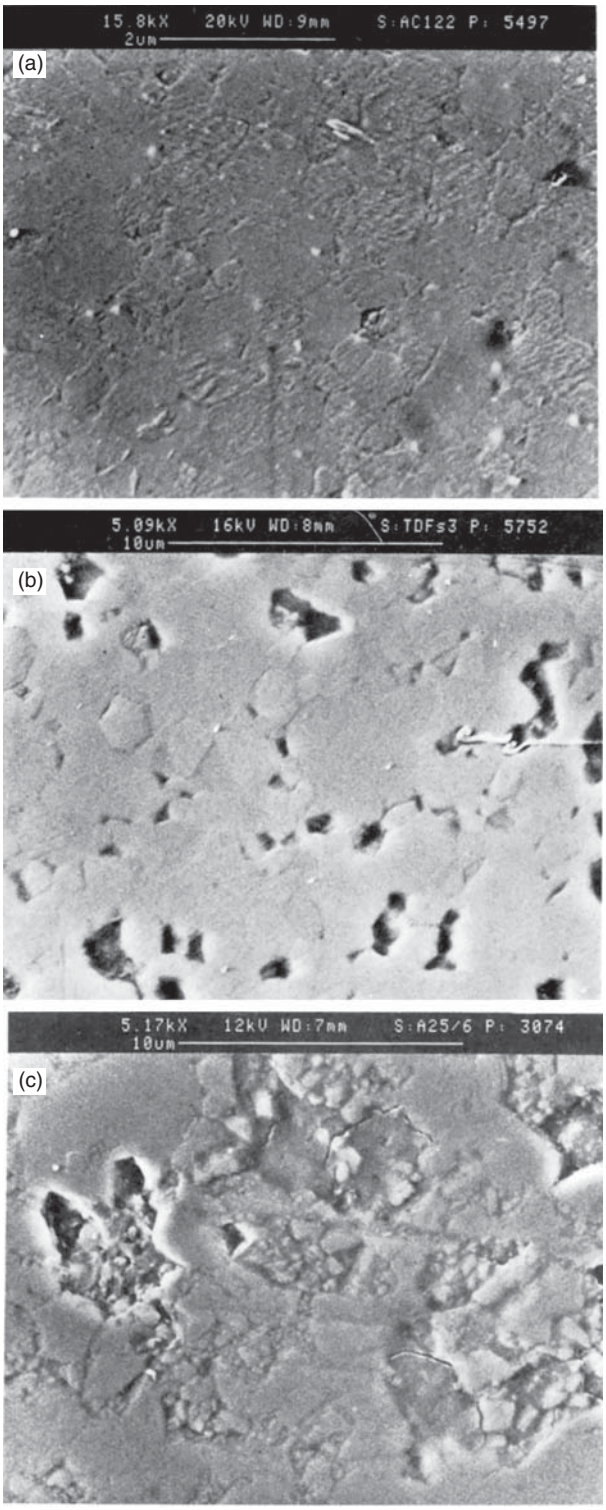

Figure 3.68 Increasing grain size of Al_2O_3 ceramics promotes pull-out of grains during sliding wear. Average grain sizes are (a) 0.6 μm, (b) 1.6 μm, (c) 3 μm. Source: Krell 1996 [K52]. Reproduced with permission from Elsevier.

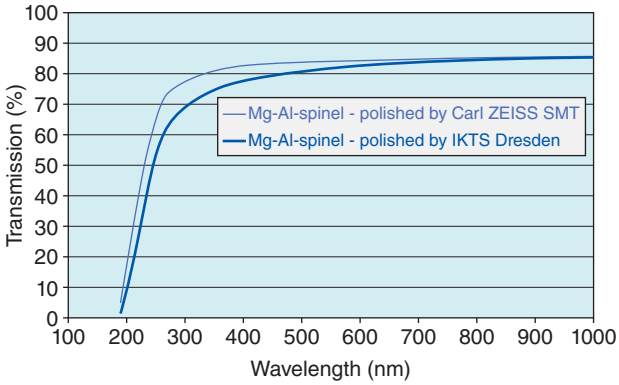

Figure 3.69 Improved performance of transparent spinel ceramic ($MgAl_2O_4$; by IKTS Dresden) by advanced optical polishing.

polycrystalline (their microstructure can vary regarding the grains size), differ from glasses or single crystals where no crystals or respectively one crystal exist. Figure 3.69 demonstrates the positive effect of grain size reduction on the polish level achieved on $MgAl_2O_4$ discs. The effect is illustrated by the aid of transmission curves: As it is known diffuse reflection (caused by roughness) is reduced by a better polish – increasing the transmission. And with the experience of Figure 3.68, the *extent* of the polishing related transmission improvement – expressed by the curves in Figure 3.69 – increases with smaller grain size of the polycrystalline ceramic. A readily measured *criterion* for small grain size is *hardness*.

It has to be remembered, however, that there is also a direct impact of *intrinsic* hardness on the polishing performance of polycrystalline transparent ceramics. Optical grade polishing is more difficult for lower hardness. While fine-grained Mg–Al-spinel $MgAl_2O_4$ ceramic is readily polished, the process is much more difficult for softer ceramics as for example for MgO.

4

Materials and Their Processing

4.1 Introduction

4.1.1 General

In this chapter the most important ceramic materials, which, up to now, could be brought to transparent condition, will be presented; transparent glass-ceramics are also included. For each material aspects regarding the structure, processing and properties of the sintered parts are discussed. Their applications form the object of Chapter 5.

These polycrystalline materials form, together with single crystals, glasses and some organic polymers, the larger class of transparent solids (that is, transparent in the 0.15–25 μm λ range).

In the next subsection of the chapter's introduction, a list of the relevant materials and a tabulated collection of their main functional properties, in addition to transmissivity, are given. For the most important materials, specific tables are given in the sections discussing them. These sections form the second part of the chapter.

4.1.2 List of Materials and Their Properties

As detailed in Section 1.5.2, the first relatively transparent ceramic was the LUCALOX alumina, developed toward the end of the 1950s [B66]. In the time period elapsed from then, the family of transparent ceramics (TCs) was substantially expanded, including now new materials like MgO, Al_2O_3, Al_2SiO_5–Al_2O_3, $MgAl_2O_4$, N–Mg-spinel, $ZnAl_2O_4$, γ-AlON, α-SiAlON, PLZTs, *c*,*t*-ZrO_2, YAG, LuAG, Y_2O_3, Y_2O_3–MgO composites, Sc_2O_3, Lu_2O_3, $Lu_2Ti_2O_7$, L. An et al. [A13], $Ca_5(PO_4)_3F$ and other fluoro-apatites, $PbTiO_3$–$Pb(Mg_{2/3}Nb_{5/3})O_3$ (PT-PMN) solid solutions and other relaxors, $Ba(Zn_{2/3}Ta_{5/3})O_3$ derivatives, $12CaO7Al_2O_3$ [H18,M28] $Sr_3Al_3O_6$, $Gd_3Ga_5O_{12}$, Gd_2O_2S, ZnO, $BaAl_4O_7$, $SrRE^+Ga_3O_7$, $La_2Zr_2O_7$, $Y_2Ti_2O_7$, $Tb_3Al_5O_{12}$, $Tb_3Ga_5O_{12}$, ZnS(Se) and similar, CaF_2, CaF_2–SrF_2, CaF_2–LaF_3, MgF_2, KBr, polycrystalline diamond, SiC, c-BN, Si_3N_4, FOX type, and other glass-ceramics; this list is expanding all the time.

Tables 4.1 and 4.2 provide data regarding the relevant (for TC apps) properties of the most popular TCs:

4.2 Principal Materials Description

4.2.1 Mg and Zn Spinels

In 1967 the US army still considered **single-crystal** Mg-spinel only, as a candidate for applications where transparent solids were needed. The first moderately transparent **ceramic** spinel parts appeared around 1970; spinel is thus one of the earliest (together with MgO) inorganic polycrystalline (cubic) materials brought to transparency [G21]. Efforts related to transparent polycrystalline spinel (TPS) development are motivated especially by military applications (see Chapter 5) like armor, imaging system windows, and missile noses protecting IR sensors; some civilian applications, like inspection windows for furnaces, sand blasting machines, chemical reactors, top market end watches, possibly cell phone displays and IR barcode reader systems, and high index optics for microlithographic machines operating in the near ultraviolet (NUV) [B68, P28] also exist. The applications development from potential to actual depends, mainly, on the progress in fabrication cost reduction.

4.2.1.1 Mg-Spinel

4.2.1.1.1 Structure

Magnesium spinel $MgAl_2O_4$ is the archetypal crystal representing a wide range of solid solutions of a similar crystallographic structure (Figure 4.2). $MgAl_2O_4$ is the stoichiometric composition, as the phase diagram in Figure 4.1 [L19] indicates, at elevated temperatures. Owing to kinetic reasons, the high temperature composition may be preserved down to room temperature (*RT*)

Transparent Ceramics: Materials, Engineering, and Applications, First Edition. Adrian Goldstein, Andreas Krell, and Zeev Burshtein.

Table 4.1 Nonoptical properties of selected transparent ceramics.

Material	Space group	*TD* (g/cm^3)	$t°_r$ (°C)	*E* (GPa)	*HV* or *HK* (GPa)	TRS (MPa)	RT-800 °C $\alpha_L \times 10^{-6}$
α-Al_2O_3 s.c.	$C_{3v}^6(R3C)$ No. 161	3.987	2040	~400	14–16	400–1000	(‖ to "c") 5.0
α-Al_2O_3 p.c.	$C_{3v}^6(R3C)$ No. 161	3.578	2040	~400	19–20.5	500–700	6.0
$MgAl_2O_4$	$O_h^7(F4_1/d\bar{3}2/m)$ No. 227	3.578	2140	290	16	220	5.6
AlON	$O_h^7(F4_1/d\bar{3}2/m)$ No. 227	3.64	2140	330	15–16	300	5.8
$ZnAl_2O_4$	$O_h^7(F4_1/d\bar{3}2/m)$ No. 227	4.61	1950	230	10.5	160	8.7
YAG	$O_h^{10}(I4_1/a\bar{3}2/d)$ No. 230	4.56	1940	280	17	200	4.2
Y_2O_3	$T_h^7(I2_1/a\bar{3})$ No. 206	5.03	2410	165	6.6	201	6.6
Y_2O_3 (La)	$T_h^7(I2_1/a\bar{3})$ No. 206	5.3	2420	165	7.3	150	7.0
c-ZrO_2(Y)	$T_d^1(P\bar{4}\bar{3}m)$ No. 215	5.97	2750	230	13.5	300	7.3
t-ZrO_2	$D_{4h}^{15}(P4_2/n2_1/m2/C)$ No. 137	6.06	2750	220	13.9	800–1100	10.5
65 : 35 PLZT	$O_h^1(P4/m\bar{3}2/m)$ No. 221	7.92	1450	105	5.0	80–120	4.2 (average)
$Ca_5(PO_4)_3F$	$C_{6h}^2(P6_3/m)$ No. 176	3.20	—	—	4.3 K	—	—
Diamond (CVD)	$O_h^7(F4_1/d\bar{3}2/m)$ No. 227	3.52	—	1050	90–57	H-P313 280–780	4.9
GaP (CVD)	$T_d^2(F\bar{4}3m)$ No. 216	4.14	1470	100	8.5	120	5.3
ZnS	$T_d^2(F\bar{4}3m)$ No. 216	4.08	1186 sub.	75	2.5 K	100	7.0
CaF_2		3.18	1500	76	1.6	55	18.9
MgF_2	$D_4^h(P4_2/m2_1/n2/m)$ No. 136	3.18	1265	140	4.4	120	10.4
KBr	$O_h^5(F4/m\bar{3}2/m)$ No. 225	2.75	734	27	0.06 K	3.3	38.5
a-SiO_2		2.20	1620	73	4.5 K	70	0.5

Table 4.2 Optical properties of selected transparent ceramics.

Material	*n*	ε_f	UV edge (μm)	T_{th} [a] at 0.60 μm (%)	$ILT_{75\%}$ at λ (μm)	IR edge (μm)
αAl_2O_3 s.c.	1.77	9.5 ⊥ on c	0.14	86	4.5	6.5
	1.76					
αAl_2O_3 p.c.	1.77	9.5	0.35	86	4.4	6.3
	1.76					
$MgAl_2O_4$	1.72	12 ‖ "c"	0.15	87	4.9	6.2
AlON	1.79	8.5	0.21	85	4.0	5.8
$ZnAl_2O_4$	1.79	10.5	0.35	85	4.8	7.0
YAG	1.82	12	0.30	84	5.0	6.3
Y_2O_3	1.94	16	0.21	82	7.2	8.0
Y_2O_3 (La)	1.97	16	0.25	82	7.3	8.0
c-ZrO_2 (Y)	2.17	22	0.35	76	0.58	7.5
t-ZrO_2	2.17	26	0.45	76	3.5	7.5
65 : 35 PLZT	2.79	2500–5000	0.35	64	—	11.0
$Ca_5(PO_4)_3F$	1.63	—	0.25	—	—	—
	1.64					
Diamond (CVD)	2.42	5.7	0.21	75	1.0	>50
GaP (CVD)	2.95 (IR)	11.1	0.54	—	—	11.0
ZnS	2.36	8.35	0.36	73	11.0	14.5
CaF_2	1.49	6.5	0.13	—	—	12
MgF_2	1.37	5.1	0.41	90	8.0	3.0
KBr	1.56	4.9	0.25	92	25.0	40
a-SiO_2	1.46	3.8	0.16	92	3.4	4.2

a) $T_{th} = \frac{2n}{n^2+1}$ = theoretical transmission.

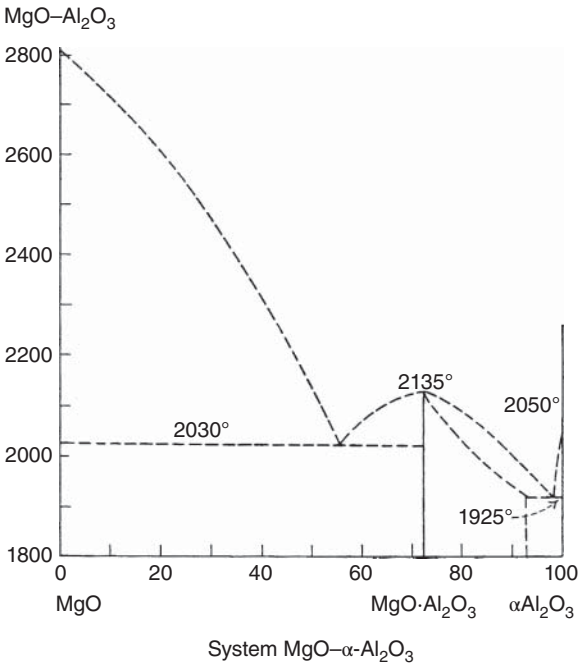

Figure 4.1 Phase diagram of the Al_2O_3–MgO system. Source: Levin et al. 1956 [L19]. Reproduced with permission from The American Ceramic Society.

by fast cooling; the natural cooling rate of the sintering furnaces (peak temperatures are in the 1300–1600 °C range) used for its fabrication is, in most cases, fast enough; very slow cooling leads to split of the high temperature phase in new phases.

4.2.1.1.1.1 Ideal Lattice Structure

Figure 4.2 presents the generic spinel crystallographic structure. It is a face-centered cubic crystal belonging to the #227 space group $O_h^7(F4_1/d\bar{3}2/m)$ and contains eight formula units in the unit cell. The lattice period is $a =$ 8.09 Å. The space group symbol is abbreviated as $Fd\bar{3}m$. The lattice name stems from one of the most important substances belonging to that lattice type: $MgAl_2O_4$ mineral. So "spinel" designates both a substance and a lattice type. Many other crystals exhibit a spinel-type lattice, specifically oxides including aluminum Al^{3+} cation, and a second metal cation different than magnesium; those materials are sometimes addressed as "spinelids." The unit cell contains a close-packed array of 32 oxygen $O^{\delta-}$ anions occupying sites of C_{3v} symmetry, 8 magnesium Mg^{2+} cations occupying tetrahedrally coordinated sites (four nearest-neighbor $O^{\delta-}$ anions) of T_d symmetry, and 16 Al^{3+} cations occupying octahedrally coordinated sites (six nearest-neighbor $O^{\delta-}$ anions) of D_{3v} symmetry. For a number of spectroscopic considerations, the Al^{3+} cation sites are approximated to have an octahedral O_h

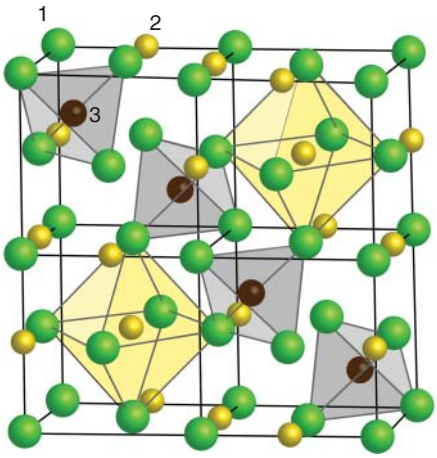

Figure 4.2 Spinel ($MgAl_2O_4$) lattice. (1) oxide anions. (2) Al^{3+} cation. (3) Mg^{2+} cation. Source: Reproduced from the archive of Shutterstock Images with purchased permission.

symmetry. The ionic radius of tetracoordinated Mg^{2+} is 0.57 Å, and that of hexacoordinated Al^{3+} is 0.54 Å [S28].

4.2.1.1.2 Inversion

Most synthetic spinels exhibit a measure of crystallographic disorder [B3, G48, J2, K42, S36]. It is caused by a change in the occupancy pattern in the ordered lattice: a fraction of the Mg^{2+} cations occupy Al^{3+} sites and vice versa. This occurrence is called "inversion," as it seems that for each Mg^{2+} entering an octahedral site, an Al^{3+} enters a tetrahedral site. Designating the letter "*i*" to describe the fraction of exchanged ions, it is also used to describe the disorder measure. The disordered material lattice formula is more accurately described as $[Mg_{1-i}Al_i]^{IV}[Mg_iAl_{1-i}]^{VI}O_4$, where the IV and VI superscripts represent the coordination number of respectively the T_d (tetragonal) and D_{3v} (octahedral) sites. Such a site exchange creates local imperfections ("antisite" defects) of unbalanced charge; the exchange may be formally described as a "reaction:"

$$[Al^{3+}_{oct}]^0[Mg^{2+}_{tet}]^0 \leftrightarrow [Al^{3+}_{tet}]^+[Mg^{2+}_{oct}]^- \quad (4.1)$$

Under changed thermodynamic conditions, the lattice rearranges itself and the "*i*" is modified. There are three degrees of freedom: the mentioned "*i*" disorder measure, the lattice unit cell parameter "*a*," and the unit of the $O^{\delta-}$ sub-lattice "*u*." The actual electrostatic compensation does not always follow the process described by Eq. (4.1). These defects enter as components of the general varied lattice defect population. As a result, in some cases, the conditions change, which requires defect formation is better responded to by formation of a multi-defect system, which may involve both native and extrinsic defects.

The actual compensation mechanisms (viz. those that require minimal free energy increase) put into motion depend on thermodynamic and kinetic factors and the entire composition of the defects system. The "*i*" value of a given material may change as a function of thermodynamic conditions, mostly temperature; "*i*" values of 0.2 or higher are common in the case of as-prepared $MgAl_2O_4$. Often during heating, the order degree increases. The opposite happens in natural (mineral) crystals [K62].

4.2.1.1.1.3 Native Point Defects and Their Effects

The densification process and properties – including optical and spectral ones – of transparent polycrystalline (viz. ceramic) spinel (TPS) are markedly influenced by the population of defects existent in the lattice. In real lattices various types of intrinsic defects, from quasi-zero (point) to 3D configuration, exist. From the line defects, the dislocations are the most important regarding spinel properties and sintering (especially when assistance of pressure is used). Planar defects, like inter-twin boundaries (created by shear stress), stacking faults, special inter-grain boundaries or cracks also influence properties. So do extrinsic defects like molecular solutes or GB-located layers. The most important, however, are the point defects on which attention will be focused here; their presence was already mentioned in relation to the inversion process.

We would like to recall first the fact that intrinsic and extrinsic point defects form an interactive population. While obvious, this fact is often overlooked when point defect-based equations are proposed for the explanation of various occurring processes. It is also useful not to forget that various point defect combinations may form, owing to fluctuations in concentration of each defect, in various regions. For instance, significant differences are often seen when moving from the core of a grain toward the grain boundaries.

For a given material, in our case $MgAl_2O_4$, the defect population composition varies massively with factors like powder synthesis method, thermal history, sintering atmosphere, irradiation, etc.

The main individual point defects list includes, in the case of spinel, $V_O^{\cdot}$, $V_O^{\cdot}$, V_{Al}''', V_{Mg}'', $Al_{Mg}^{\cdot}$, Mg_{Al}', and interstitials like O_i'' (defects are designated by the standard Kroger notation). One of the defects with the lowest formation energy is the $V_O^{\cdot\cdot}$; the concentration of this vacancy varies strongly as a function of the sintering atmosphere composition and the value of "*N*"; the phase diagram shows that besides stoichiometric spinel a quite wide solid solutions range exists: $MgO{\cdot}NAl_2O_3$ (see Figure 4.1). The $V_O^{\cdot\cdot}$ concentration controls $O^{\delta-}$ diffusion despite the fact that O_i'', also present, is faster [U1]. In spinel the O_i'' is of the split type, aligned with $V_O^{\cdot\cdot}$ along $\langle 1\bar{1}0\rangle$. The stronger effect of $V_O^{\cdot\cdot}$ stems from the fact that $[V_O^{\cdot\cdot}] \gg [O_i'']$. However, the interaction of the two defects modifies the migration speed of both. The densification process is therefore influenced also by the interaction of O_i'' point defect with $V_O^{\cdot\cdot}$. This is a good exemplification of the more general issue of interaction effects on the diffusion rates of the lattice's native ions. Point defects may, especially at high concentration, interact in various forms, including clusters formation or precipitation into large aggregates. In the case of the $V_O^{\cdot\cdot}/O_i''$ pair, the type of interaction depends on defect concentration and their relative position [U1]. These parameters vary with changing processing conditions. As far as sintering is concerned, it is important to note that the $O^{\delta-}$ seems to be the slowest ion. Measurement results vary, but a typical value is D_O (viz. at RT) $(O^{2-}) \approx 10^{-4}$ m^2/s, while for both cations it is $\approx 10^{-2}$ m^2/s [R12, T23]. While this view is widely accepted, it has to be said that simulation work suggests that in certain conditions Al^{3+} may exhibit the lowest diffusion rate [U1]. In this context it is worth noting also a few other interaction effects. For instance, anion + cation interstitials cluster formation drastically reduces the mobility of the participants. On the other hand, they act as nuclei for larger defects formation. The inversion – for which the spinel lattice offers a particularly attractive configuration – is, among other things, facilitating clustering. It can be shown that certain trimers are very convenient for charge compensation (that triggered by the inversion), with minimal lattice distortion. Certain dimers also show high binding energy, less than that of the trimers, owing to entropy loss.

An important structural aspect is the stoichiometry of spinel. It has been observed, as already noted above, that the molar ratio of the cations can depart significantly from the $MgO:Al_2O_3 = 1$ stoichiometry without severely disrupting the lattice. So, in fact, a range of $MgO{\cdot}NAl_2O_3$ solution-type materials can be prepared. For the case of alumina-rich compositions, "*N*" may vary from 1.0 to 7.0 [G48]. Stable compositions rich in MgO are also known, but *N* is rarely lower than ~0.8. According to the phase diagram of the $MgO–Al_2O_3$ system, the stability of materials with $N \neq 1$ is restricted to high temperatures. In practice, however, such materials can be kept stable (freeze of high temperature state) if cooling from the suitably high sintering temperature is done quickly enough (practical cooling rates satisfy this requirement).

It is quite obvious that departures from the $MgAl_2O_4$ composition requires point defect formation, for maintenance of electrostatic neutrality. Various point defect systems have been proposed. A quite elaborate one – tasking to explain also some of the observed processes associated with *N* variation – was proposed

by Chiang and Kingery [C33]. The major issue addressed was the enhanced GG rate for $N < 1$. The specific point defect systems put forward are not reproduced here because while they are supported by reasonable considerations, they remain speculative. Regarding this one has to remark that, in general, point defects are on a large scale and in quite liberal ways (present authors included) used to explain various lattice modifications. Seldom solid proofs (difficult to find), for the existence of the proposed schemes, as opposed to other possible variants, accompany the proposals; overall this approach does more harm than good. Returning to the important issue, of the way "N" influences sintering, it has to be noted that contradictory opinions exist. This is an issue yet needing a lot of further study. The only well-established conclusion is the marked increase of the grain growth rate in the $N < 1$ region [C33]. Certain consequences of spinel composition deviations from stoichiometry will be addressed in Section 4.2.1.3.

4.2.1.1.1.3.1 Extrinsic Atomic Size Defects (Cationic Point Defects and Molecular Impurities)

Any real lattice, including that of spinel, includes impurities introduced accidentally or by design. Even single crystals with less than 50–100 ppm of various impurities are hard to come by. They are mostly ionic species, but certain neutral atoms or oligo-clusters of atoms may also be present. The extrinsic point defects often play a significant role in the sintering process and they also influence properties, especially spectral behavior. Theory suggests that in order to minimize elastic energy, the impurities would concentrate at interfaces, especially brain boundaries. A neutralized space charge, resulting from non-stoichiometric cation/anion ratios at free surfaces [C33], is usually present at grain boundaries. In some cases the arrival of foreign species offers the possibility of constituting lower energy neutralization schemes, including the extrinsic components. This is a second mechanism, leading to crowding of extrinsic species at free surfaces. Experimental evidence has confirmed these assumptions. For instance, G.B. West et al. (see Section 3.2.5) showed that lanthanide cations strongly segregate to GBs in both spinel and alumina. Kingery showed, for spinel, that Si, Ca, and S behave in a similar way [C33]. Even for cubic lattices the segregation drive is a function of surface crystallographic characteristics [A27]. The impurities may affect characteristics like γ_{SV} (surface tension at the solid/vapor interface) and diffusion, thus influencing, in turn, both densification and grain growth. In this context we note that our sintering experiments, concerning doped spinel, showed (qualitative data only available yet) that TM^+-type additions tend to significantly slow down densification; Zr and Mo cations proved to be particularly "effective." Examples of the optical and magnetic spectra produced by extrinsic defects, produced by TM^+ and RE^+ cations when located in spinel hosts, are given in Sections 2.1.3.5.2 and 3.2.6.

Units made of single neutral atoms or of oligo-atomic clusters are also extrinsic "point defects" of a size similar to that of transition element cations. As far as their bonding and location are concerned, obvious differences, which lead to specific types of effect on properties, exist between neutral atom based and cationic defects. Among the neutral atoms or molecules that may accommodate themselves in void spots of the lattice and/or the less compact grain boundary zone, the most ubiquitous species are C, Ar, and S [G22, G29]. Oxygen, nitrogen, or Ar may also accumulate, during sintering, into the residual closed porosity. From there they can transit toward the furnace atmosphere, or become solutes [G12], in the lattice (mostly GB region). Molecule state change may occur not only during sintering but also on subsequent post-sintering thermal treatments. Thus the oxygen molecules, trapped in the pores of specimens subjected to sintering in air, may diffuse out quite easily; nitrogen is slower, but given enough time it will also exit the pores. Vacuum sintering prevents air accumulation in pores and therefore should be more effective in spinel sintering. Practice however shows that this effect is quite weak; it seems that air molecules' out diffusion is quite fast. Airborne graphite particles are present in most of the hot pressing (HP) and hot isostatic pressing (HIP) machines and some vacuum furnaces used in transparent spinel sintering. They easily enter the specimens, which are porous initially. In the case of (HIPing, closed porosity), carbon atoms diffusion through grain boundaries seems to be possible according to observations [B30, G31]. Practice shows that carbon tends to noticeably hamper densification when present inside oxide specimens, including spinel. Carbon may remain as such, once it entered the spinel part or react with the host (significantly at temperatures over 1200 °C) during HIPing or HPing stages, forming carbides with the cations, and carbon oxides with the anions [E6, S2]; experiment shows that, despite being thermodynamically favored, reactions are absent in the conditions offered by the hot pressing and HIPing machines even at quite high temperatures. Post-sintering treatments in oxygen-containing atmospheres, may lead to oxidation of the residual carbon, thus allowing its removal. The CO, CO_2 formed, as a result of carbon oxidation, may generate then gas bubbles, owing to the increase of their pressure on heating, which act as scattering centers. Therefore the annealing schedule has to avoid too high temperatures, viz. at which residual gas pressure in pores becomes excessive.

4.2.1.1.2 Fabrication

4.2.1.1.2.1 By Powder Compact Sintering

4.2.1.1.2.1.1 Powder Synthesis and Processing: Green-Body Forming/Powder Processing Correlation

Various spinel powder synthesis methods have been developed. The developers focused – with good results – especially on basic particles and purity. Because the requirements related to the low particle size, purity, and compositional uniformity, the preparation methods are based on either wet chemistry or gas phase reaction. Practically it is important to note that all these methods include stages that expose the materials to high (>600 °C) temperatures. During such a stage, at least one of the following processes takes place:

- Chemical reaction and/or polymorphic phase transformation.
- Elimination of raw material residues (organic or inorganic) and adsorbed species (OH^-, CO_3^{2-}, etc.).
- Basic particle growth.
- Contacts formation among basic particles (first stage of agglomeration).

Review of the literature shows that the main synthesis approaches that were investigated are

- Coprecipitation.
- Sol–gel.
- Flame spray pyrolysis.
- Combustion synthesis.
- Alkoxide decomposition under supercritical conditions.
- Mechanosynthesis.
- Sonochemistry.
- Hydrothermal synthesis.
- Self-propagating high temperature synthesis.

Only some of the many readily accessible papers describing spinel powder synthesis procedures are mentioned in the references list of this book [B25, B33, B53, L13, L18, M13, P15, R40].

A few general remarks, regarding the various types of powder – suggested by our own work and the literature data – may help one to determine the advantages and drawbacks of the different methods. For instance, the highest level of cationic mixing (atomic scale) is ensured by the use of Al–Mg double alkoxides. The alkoxides also allows one to keep very high purity levels as high as desired. A serious practical drawback is the high cost of alkoxides. The morphology of the particles resulting from hydrothermal synthesis suggest low sinterability, and testing confirms that. However, more suitable versions of this technique led to highly active powders in the case of Zn-spinels [G33] so that there is no reason for discarding the approach. Coprecipitation is simple and cheap, generating high purity fine powders; however agglomerates, forming during calcination may impair sinterability. For each powder type, pros and cons exist. Up to now the most successful trade-off between performance and cost was achieved by using sulfates as raw materials. The most widely sold spinel powder is such a material; a serious drawback is the residual SO_4^{2-} in the powder (leading to parasitic coloration).

If one recalls (see Section 3.1.2.1) the general requirements regarding green-body configuration, it is apparent that forming of green bodies, for windows (especially of a size larger than 15 cm), is a very challenging task indeed. Only by correlating – in an optimal fashion – the powder synthesis method with processing and the forming process, the task can be fulfilled. Regarding powder synthesis, it is worth noting that, as opposed to what many papers devoted to the issue claim, the easy part is to produce nanometric material, viz. ensure a basic particle size lower than 80 nm, of high purity. Most of the cited methods are able to provide these. The really difficult part is to synthesize spinel powders that, directly or after suitable processing, can be consolidated (despite their agglomerates and/or after breaking of the agglomerates) into green bodies exhibiting high sinterability. Powders having nanometric basic particles do not become sinterable only by virtue of this feature; nanometric basic particles represent a necessary but not sufficient condition for high sinterability. Let us recall that as far as the powders are concerned, both an adequate green-body configuration (see Section 3.1.2) and high rates of for the ions diffusion should be ensured; agglomeration may prevent the powders to ensure the former condition. Owing to the above, identification of the suitable powder(s) and adequate processing procedures is not so simple as it looks. In order to exemplify the complexities of such, a task spinel is a good example for the larger family of nanopowders and therefore we elaborate a bit below. Three different types of spinel powder are compared. One of the conclusions, suggested by the comparison, is that based on the data we usually measure, for such materials, their sinterability level cannot be predicted correctly. All the materials are made of nanosize basic particles. The size of those particles, their morphology, and also the clustering pattern (first level of agglomeration) are illustrated in Figure 4.3 [G22].

The powders are labeled SN-1,2,3.

All the three powders have a stoichiometry corresponding to $N = 1.0$. In Figure 4.4 the pores size distribution of green bodies derived from these powders by pressing is given; the basic particles average size (X, in nm), the specific surface area (A, in cm^2/g) and the green bulk density (BD_g, in g/cm^3) are indicated for each material. In Figure 4.5 the agglomerate (particle) size distribution of the as-received materials (already subjected to comminution by short jet millings) and after

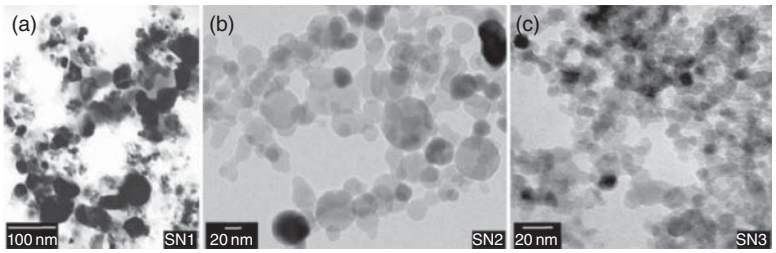

Figure 4.3 Morphology, size, and clustering pattern of three different spinel fine powders. (a) SN1 Alums derived powder having faceted basic particles. (b) SN2 powder synthesized by FSP with round shaped basic particles. (c) SN3 powder synthesized by a method similar to that used for SN2, round-shaped basic particles. Source: Goldstein 2012 [G22]. Reproduced with permission from Elsevier.

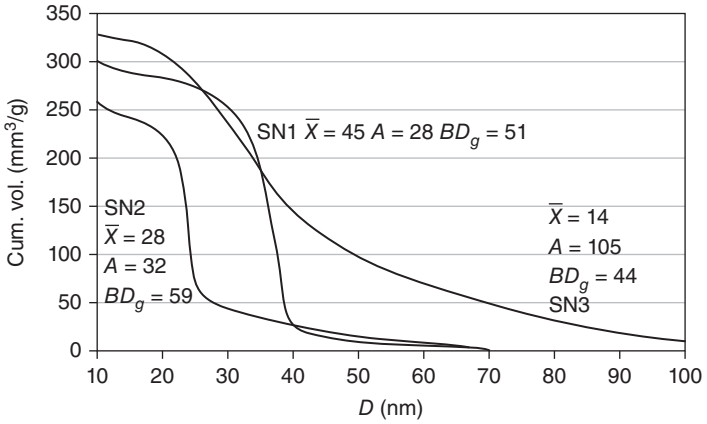

Figure 4.4 Pore size distribution of green bodies derived from SN1–SN3 powders by pressing of granulated material (the basic particle size, X in nm; the specific surface area, A in m^2/g; and the green bulk density BD_g in g/cm^3 is indicated for each material). Source: Goldstein 2012 [G22]. Reproduced with permission from Elsevier.

final milling is given, for SN1,2. The SN3 had a mode at ~6 μm, in as-received state, and kept a median of ~3 μm even after final milling. A few aspects are worth noting. The SN3 is the finest powder but generates a wide pore size distribution and a low BD_g. The SN1 is slightly coarser than SN2, but the latter generates a green body exhibiting the lowest average sizes (and a narrow distribution), of pores, coupled with the most compact particles arrangement ($BD_g = 59\%TD$). We think that in comparison with SN1 the main advantage of the SN2 – allowing the powder to be better compacted – is the rounded shape of its basic particles (as opposed to the more faceted SN1 basic particles); that is combined with a larger surface area than S1. The kinetic individual units, which travel within the die during pressing, are not basic particles, neither in the case of S2 nor that of S1, but various size and shape aggregates of those. Between these traveling units, the contact surface and contact strength are lower if the basic particles, which make them up, are spheroidal. The strength of the bonds that form between neighboring aggregates is lower if on the particles surface adsorbates, can create interparticle bonds by interaction, which are in short supply. It is probable that, owing to the specific synthesis conditions, the SN2 particles also possess a cleaner surface. Thus the basic particles shape and, to a certain extent, lack of adsorbates makes the inter-aggregate friction lower, because less bonding points appear and the granules (and fragments of those, resulting from granule breakup), have more travel freedom than it is the case in the SN1. In addition, the granules are soft enough to allow, under the action of the external force, substantial fragmentation of the initial agglomerates. Thus optimal conditions are created for a compact arrangement of the material in a configuration where enlargement, during sintering, of inter-aggregate porosity will not occur. The SN3 has also rounded basic particles, but its excessive surface area (too low basic particle size) allows the formation of too many interparticle contact points, despite the spherical shape of the basic particles. As a result sets of agglomerates are interlocked in low density large structures – in which the participants are strongly bonded; this prevents formation of a uniform, compact green body, viz. a sinterable green body configuration. According to the X-ray diffraction (XRD) peak profile, the degree of order in the three lattices was quite similar. In Figure 4.6 [G22], the densification curves of the three green bodies is given. The sintering temperature needed to obtain, say, 97%TD are 1300 for SN2 [G25] and 1500 °C for SN1, while SN3 did not attain this level.

The sintering temperatures correlate clearly with the configuration of the green body. Where a suitable one was achieved, impressively low sintering temperatures were made possible (SN2). As the example suggests the variation in sintering ability, caused by differences in the green-body structure, may be very large. The powder feature, which seems most useful, is the morphology of the basic particles, together with their optimal size (not excessively small, like in the case for SN3 where this led to too high aggregate strength). Particles surface

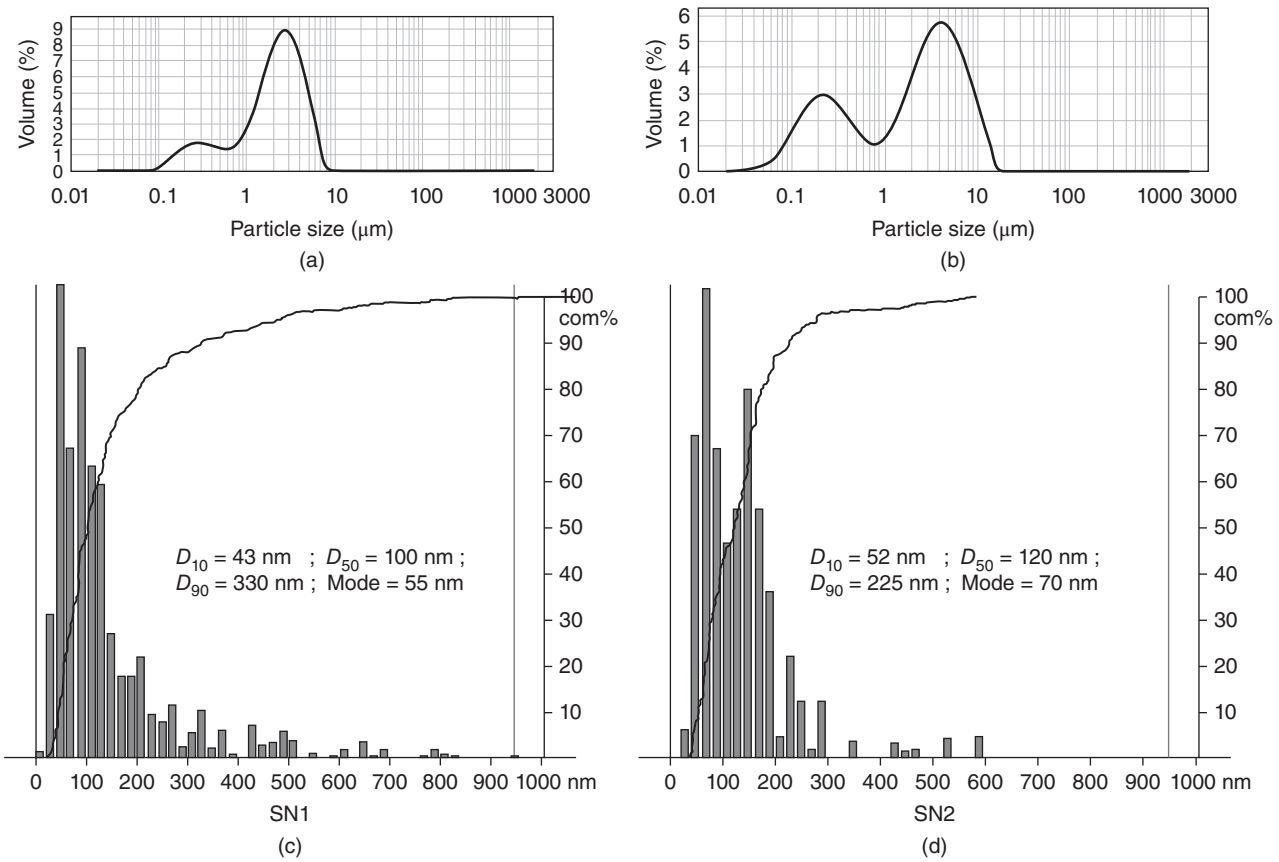

Figure 4.5 Particles (agglomerates) size distribution of SN1 and SN2 materials in as-received and after final comminution, respectively. (a,b) As-received condition. (c,d) After final milling. Source: Goldstein 2012 [G22]. Reproduced with permission from Elsevier.

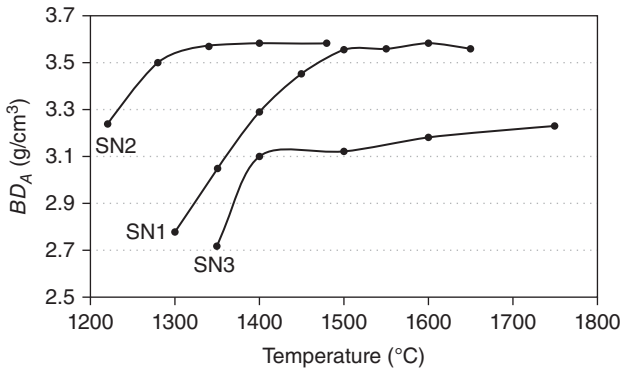

Figure 4.6 Sintering curves of SN1–3 powders. Source: Goldstein 2012 [G22]. Reproduced with permission of Elsevier.

chemistry and structure may have also played a role in the sintering results, shown in Figure 4.6, but we feel that the van der Waals bonding (influenced by surface area and particles morphology) represented the decisive factor. Monospherical powders were achieved also in the case of YAG (see Section 4.2.5) using a solvothermal synthesis method; if they behave, during sintering, like S2 or S3 here is not known [Z9, Z13]. In the case of Y_2O_3 the same result was reached by the aid of homogeneous precipitation [S44].

In the case of large spinel parts, the most difficult task is the achievement of green-body stage macroscale uniformity, viz. throughout the whole volume of the part. As a result it is difficult to produce parts exhibiting transmission levels in the 80–84% range (theoretical level is $T \approx 87\%$) when the size exceeds 10 cm. Even when such parts are highly transparent, on the average, they exhibit some randomly dispersed, white, opaque spots (50–2000 μm in size) of the type illustrated in Figure 4.7.

Full elimination of such spots is a very challenging task. It can be accomplished when the forming – both by pressing and pressure casting – is done in an optimal way. Most of the errors done during forming cannot be corrected by clever firing.

4.2.1.1.2.1.2 The Sintering of Spinel

In the early stage of transparent spinel fabrication technologies development, it was attempted to use one stage pressureless firing [H14]. Temperatures as high

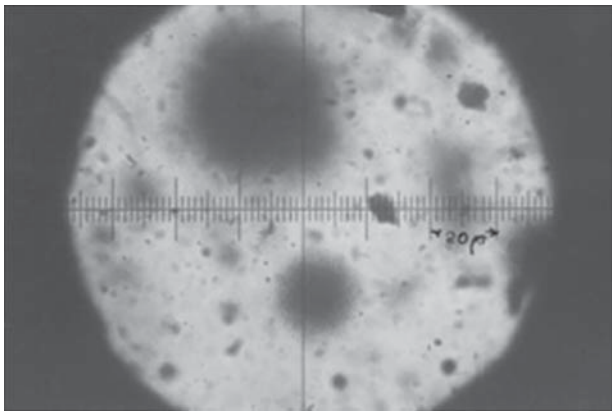

Figure 4.7 Opaque white spots (regions not fully densified) frequently seen in transparent spinel parts, especially of large size; a few may appear even in high quality parts. Source: Goldstein 2012 [G22]. Reproduced with permission from Elsevier.

as 1900 °C and H_2-based atmospheres were employed. Transmission in the VIS was lower than 40%, even for $t \sim 1$ mm. Let us note that in those experiments, while quite sinterable powders were available, the green parts forming methodology used was far from optimal [B53, B62, G6, P3]. It was quickly realized that pressure assisted methods may facilitate the achievement of real transparency [G15, R36, R37].

The early hot pressing procedures developed led to promising results. Thus, using micron-sized powder and an incremental pressure rise (up to 40 MPa), 3 mm thick, relatively transparent, small discs could be obtained (by G. Gazza and Dutta) by applying unidirectional hot pressing to undoped, cold-pressed powder compacts ($BD_g \sim 45\% TD$) at ~1500 °C [G10]. Significant improvement – regarding the level of transparency and size of the fabricated specimens – was achieved by adding LiF, a sintering aid that gave good results when used for MgO powder densification with a view of producing transparent parts [B11, H14, R20, R23]. LiF was proposed as a sintering aid for spinel hot pressing by W.H. Rhodes et al., D.W. Roy, and R.W. Rice, with inspiration from their earlier study of MgO sintering [R35]. Based on work done, with the aid of LiF, at the Avco Corporation and Coors, moderate size flat discs and even domes, exhibiting visible transmission in the 75–80% range, could be obtained [H14], around 1980. Most of the subsequent technological research, effectuated in the United States, employed HPing of LiF (Coors, Raytheon, AT&T, MER) containing powder as a sintering method. Hot pressing, by the aid of LiF, gave, at the end of the development, better results than for MgO; MgF_2 was also demonstrated as an attractive sintering aid lately, albeit somewhat less efficient than LiF [G29]. The main objectives included the obtainment of large size, complex shape, and better mechanical properties, at reasonable cost. In Figure 4.9 a few spinel discs, fabricated by hot pressing, are illustrated, while their spectra are given in Figure 4.8.

As of now plates exhibiting high transmission and a size varying from 10 to 75 cm have been manufactured (see Figure 4.10b) [S46] by the technique mentioned above; some fairly large size IR domes were also demonstrated,

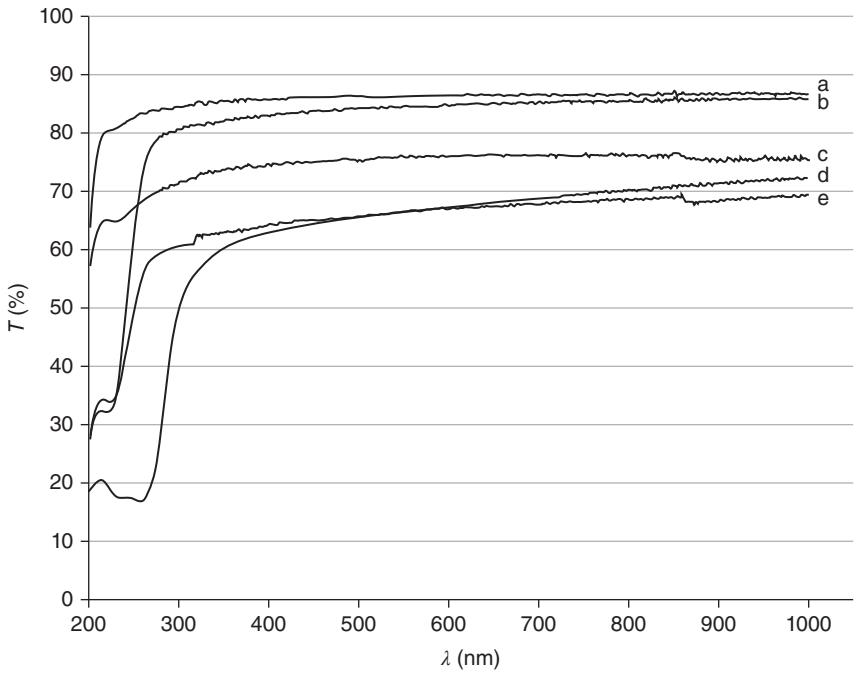

Figure 4.8 Transmission spectra of some spinel discs with different amounts of residual carbon. (a) Good quality commercial spinel plate ($t = 3$ mm) fabricated by sinter/HIP (benchmark). (b) Disc fabricated by LiF-assisted HPing ($t = 3$ mm); optimized schedule. (c) Same as (b), but less good schedule (slightly grayish). (d) HPed disc using LiF + MgF_2 as sintering aid package. (e) HPed disc using MgF_2 as sintering aid. Source: Goldstein et al. 2016 [G29]. Reproduced with permission from Elsevier.

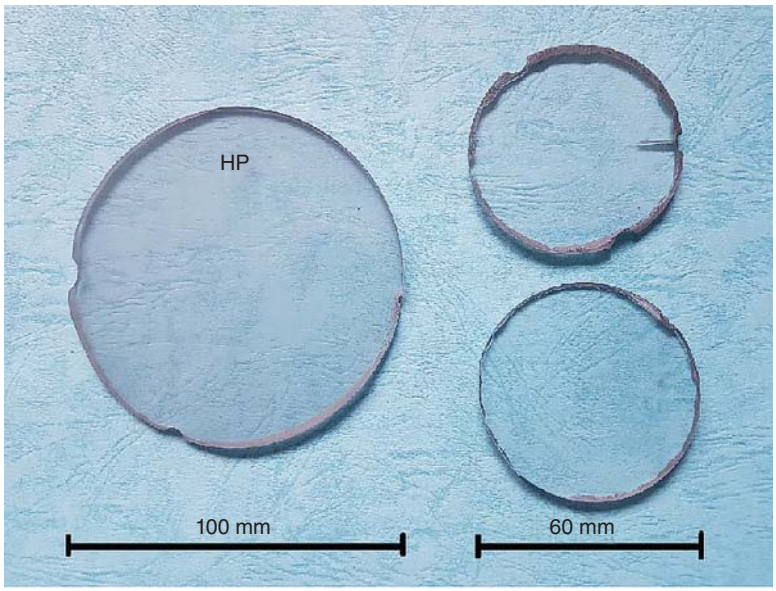

Figure 4.9 Imaging of some transparent, medium size, spinel discs fabricated, by HPing at ICSI. Source: Goldstein et al. 2016 [G29]. Reproduced with permission of Elsevier.

(a)

(b)

Figure 4.10 Large transparent spinel windows fabricated by AS + HIP and HPing. (a) $L = 25$ cm; produced at IKTS Dresden (A. Krell group). (b) $L = 75$ cm. Source: Spilman et al. 2013 [S46]. Reproduced with permission from of SPIE Publishing.

especially by the American Surmet Corporation, which continued developments started by Raytheon. By the AS + HIP approach fairly large plates (as shown in Figure 4.10a) can also be produced the latter also having the advantage of finer microstructure. The above notwithstanding, **commercially viable fabrication**, able to mass produce stable quality and large ($L > 30$ cm) TPS plates or domes is yet a thing of the (near?) future.

The mechanism(s) by which LiF operates were the subject of extensive studies [R14, R15]; the topic is still under discussion. Our views on the issue are collected in [G29], a paper that lists also the relevant bibliography. Related to this issue let us remark, first, that the spacers and the rest of the graphite (sublimation and/or wear) hot press furniture are sources of a large population of individual carbon atom and small clusters of them [B30]. Either as such or as CO (residual water molecules and oxide ions, able to oxidize carbon, are also present in the press's atmosphere and the spinel lattice, respectively), some carbon enters the specimens and remains in the sintered product, significantly affecting transmission (if CO is the penetrating species, it may generate carbon by a disproportionation reaction, which generates C and CO_2, or remain as such and effectuate reductive actions). Mitigation of the problem by post-HPing annealing in air is possible but it is a difficult operation. What is obvious, in this context, is the ability of LiF to prevent carbon penetration. LiF melts at ~850 °C and its vapor pressure is significant over 1000 °C. At low temperatures (under 1250 °C), its main effect is that of lubricant and liquid sintering aid, allowing consolidation of the specimens to bulk densities of around 95%*TD*, under 1300 °C. In Table 4.3 the way the densification state and LiF content

Table 4.3 Characteristics of spinel/LiF (0–3.5%) discs (diameter = 58 mm) after hot pressing (50 MPa; Ar) at various peak temperatures, lower than 1400 °C.

LiF concentration (initial) (%)	Peak $t°$ (°C)	Dwell time (min)	BD_{HP} (g/cm^3)	OP (%)	Residual LiF (%)	Visual aspect
1.0	*RT*	10[a)]	1.48	47	1.00	White, opaque
1.0	700	30	2.10	38.0	1.00	↓
1.0	860	30	2.70	18.0	0.89	
1.0	860	120	3.10	4.2	0.85	
1.0	1050	40	3.30	2.0	0.49	
1.5	1050	120	3.44	1.0	0.60	
3.5	1050	120	3.47	0.9	2.90	
3.5	1270	20	3.20	7.0	0.28	White, translucent
1.0	1350	40	3.00	4.0	0.05	↓
3.0	1350	40	2.90	8.0	0.20	
1.0[b)]	1300	40	3.50	0.4	0.08	
1.0[b)]	1350	40	3.52	0	0.08	
1.0	1400	60	3.55	0	0.05	
—	*RT*	10	1.70	—	—	White opaque
—	1100	120	2.05	28.0	—	↓
—	1270	30	2.25	22.0	—	
—	1350	30	3.25	3.5	—	
—	1400	60	3.30	2.5	—	Gray, opaque

a) Cold isostatic pressing.
b) Schedule different from that used for the rest of the specimens (see text in Section 3.2.2).

vary, as a function of increasing temperature – during hot pressing – is presented.

This early massive increase of compaction level achievable owing to the presence of liquid LiF facilitates the general densification process. It also makes carbon penetration more difficult. As opposed to early views, [G29] suggests that carbon becomes mobile, within the hot press only at temperatures higher than 1250 °C (somewhat lower in spark plasma sintering (SPS)-type presses) so that the early pores closure, facilitated by LiF, becomes a significant obstacle for carbon entrance in the specimens. In this context it is important to also add that experiments (A. Goldstein, unpublished results) we ran lately suggest that carbon reaction with LiF (under Ar) is absent below 1300 °C (low temperature reaction with sulfates, however, was observed). The above led us to think that LiF vapor, present in small amount but under high pressure, within the void space of the spinel part, which still undergoes densification at temperatures where carbon mobility is substantial, is the main factor preventing carbon penetration; the liquid fraction of it also constitutes a protective grain coating, further obstructing carbon penetration [E6]. The LiF in gas phase is, at all temperatures, in movement through the void system of the specimens, as it tries to exit the specimen. Exactly when its vaporization rate becomes large, the pore's closure obstructs the process; the result is internal gas pressure formation. Eventually LiF is expelled totally from spinel but only when temperatures reach the 1550–1600 °C; the last fraction of the sintering aid molecules need to move along the GBs of the specimen because the pores are closed (this is also the path that, at high temperature, atomic carbon may penetrate the spinel part, mostly entropic driving force for penetration) . The mechanism of LiF action is discussed in more detail in [G29]. Here we just note that luckily under the conditions prevalent during hot pressing, a set of reactions, which in other conditions can occur, do not take place. Thus no $LiAl_2O_4$ forms, LiF does not produce fluorocarbonates by reaction with carbon, and the carbothermal reduction of spinel is not observed [E6]. Also as long as temperatures are kept under 1650 °C, the vaporization of MgO is weak (especially if Ar is employed instead of vacuum).

It was determined that full spinel powder may be replaced by mixture of the oxides when HPing-based sintering was used (reaction preceded sintering approach) [E6]; despite the volume increase, caused by the reaction, disruption of the green microstructure is not severe, owing to the constraint imposed by the external pressure.

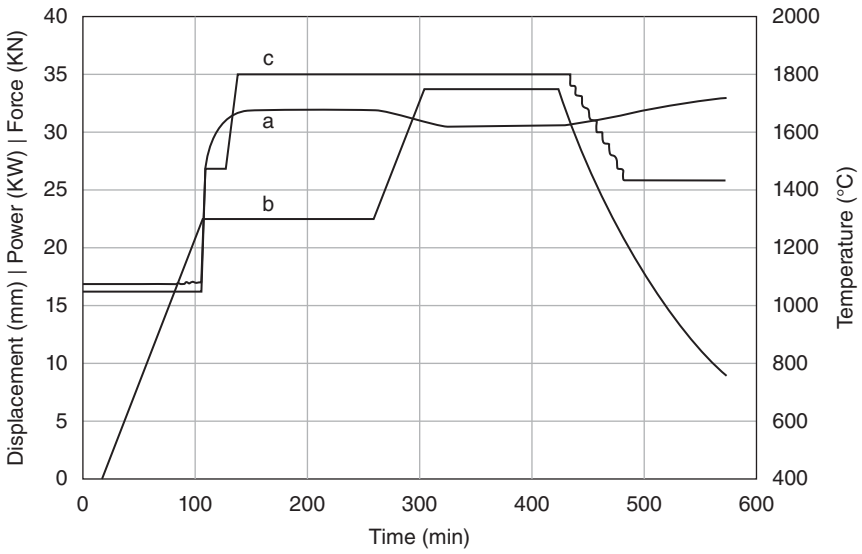

Figure 4.11 HPing schedule when MgF_2 is used as a sintering aid (see transmission level achieved in Figure 4.8 [curve e]). (a) Punch movement. (b) Temperature time profile. (c) Pressing force time profile. Source: Goldstein et al. 2016 [G29]. Reproduced with permission from Elsevier.

We determined that MgF_2 or mixtures of MgF_2 and LiF act in a manner similar to that of the latter when alone. An HPing schedule developed for MgF_2 is illustrated in Figure 4.11; NaF is not an efficient sintering aid.

In the last two decades, pressureless sintering was reintroduced in procedures for TPS fabrication, but in two-step sintering stages, with the final densification effectuated by HIP machines. A large disc thus fabricated is shown in Figure 4.12.

Let us have a closer look to this approach now. When the right size equipment is used, this approach may cost less than HPing, not to mention HP + HIP variations. This was one of the reasons that led to renewed interest in pressureless sintering (PS). Even more important was the hope of getting more robust products. Mechanical properties improvement was expected because it was realized that the PS + HIP approach can generate fully densified parts at temperatures markedly lower than in hot pressing. In such conditions lower size grains would predominate, a feature that according to the Hall–Petch rule would increase strength. Let us note that while applying the rule to ceramics is an accepted procedure, this is not necessarily a correct idea, at least in our view. This relationship was derived, based on experimental observations, for metals. The main reason it works well there is the fact that in the case of metals the grain boundaries are often the most influential type of defect existent; processing induced defects – like voids, microcracks, and foreign particles – are relatively rare. Such defects, when present, have a stronger influence than grain size (*GS*) on mechanical properties. A fine microstructure really makes a difference only when the other types of defect, mentioned above, are eliminated or at least their concentration is low. Only for such cases the Hall–Petch relationship is reasonably realistic. In the case of ceramics, such a situation rarely appears. It is true, however, that in the case of good quality TCs with their drastic requirements regarding defects, the conditions for the Hall–Petch relationship relevance are more or less met. For instance, experiments effectuated at IKTS, Dresden [K40] (also at Beersheva Univ. [S40]), on specimens free of processing defects, showed that hardness and, to some extent, transversal rupture strength (TRS) can be significantly improved by microstructure refinement, as the Hall–Petch relationship suggests. When *GS* drops under certain limits (around 50 nm), an inverse dependence of mechanical properties, on *GS*, seems to set in [S40].

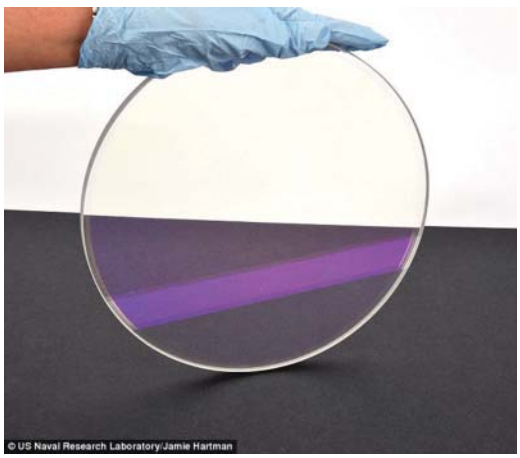

Figure 4.12 Large disc, produced by pressing followed by sinter/HIP at the Navy Research Lab in Washington DC. Source: Courtesy of Jas Sanghera.

Examination of microstructure evolution as a function of sintering temperature revealed certain important features. The average grain size increases at a quite

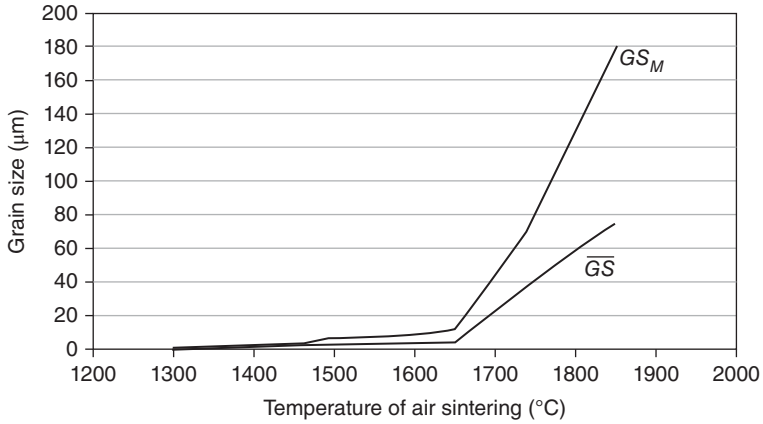

Figure 4.13 Average and maximal grain size, as a function of sintering temperature of spinel ceramics (three hours dwell at peak temperature). Source: Goldstein 2012 [G22]. Reproduced with permission from Elsevier.

moderate rate up to ~1650 °C. In Figure 4.13 [G22], the $\overline{GS} = f(t^{\circ}_{S})_{\text{curve}}$ is given for the case of air-sintered specimens (three hours dwell) derived from the commercial SCR-30 powder (Baikowski). The size distribution is quite narrow so that the grain population can be characterized as unimodal. Abnormal grain growth (curve $GS_{M,}$ in Figure 4.13, relates to the largest grains) starts to be significant about the temperature (1650 °C) where the average grain size rate also shows a marked and sudden increase. The average size, at that temperature, is $\overline{GS} \sim 20$ μm. As a result hot-pressed spinel microstructure is often (because peak sintering temperatures are higher than 1650 °C) are characterized by a bimodal (or multimodal) size distribution. In Figure 4.14 [G22], typical microstructural patterns for three different temperatures are given.

Another problem created by grain growth is pore occlusion. In the case of alumina, it is believed [B67] that occlusion occurs only when abnormal grain growth operates. Our observations (qualitative) suggest that in the case of spinel, occlusion may occur even in quite low size grains; the probability of its occurrence seems to be correlated (not linearly) with $\overline{GS}$.

As it is seen, there are good reasons (in addition to the requirements related to optical performance) to keep the TPS grains small. The most efficient way to do that – when industrial fabrication is envisaged – is the optimization of the green-body configuration so as to achieve sufficiently low values for t°_{S}. From the 1700–1900 °C domain ($\overline{GS} > 80$ μm) used by early PS-based methods and HPing schedules, the t°_{S} could be brought to the 1400–1550 °C range ($\overline{GS} \sim 10$ μm) currently [G24, K57]. For the best green bodies (derived, however, only from extremely expensive powders prepared by flame spray pyrolysis [G23]), temperatures in the 1270–1350 °C were high enough for full densification and, as a consequence, really fine grains ($\overline{GS} \sim 0.5$ μm) could be achieved. Efficient sintering aids are in scarce supply. For the case of VS + HIP, B_2O_3 was found useful (0.15%) [T30]. It allowed obtainment of transparent ($T = 80\%$ for $t = 1$ mm) small discs, at temperatures not higher than 1350 °C. The authors of the study consider that the positive affect is owed to the percentage of pores occlusion by slowing down GG. The same authors found that LiF, SiO_2, or CaO is not suitable as sintering aid. We examined LiF, SiO_2, B_2O_3, and PbO for the case of air sintering, also without getting good results. Recently it was shown that CaO can function as an efficient sintering aid [K53].

Densification rates are dependent also on matter transport rates. It is not known whether significant difference exists between the diffusion rates of the ions (especially the slowest $O^{\delta-}$) in the different raw materials – including the commercial ones – used in TPS-related research. Studies aiming to determine the effect of "N" (stoichiometry) variation on diffusion rates, while clarifying

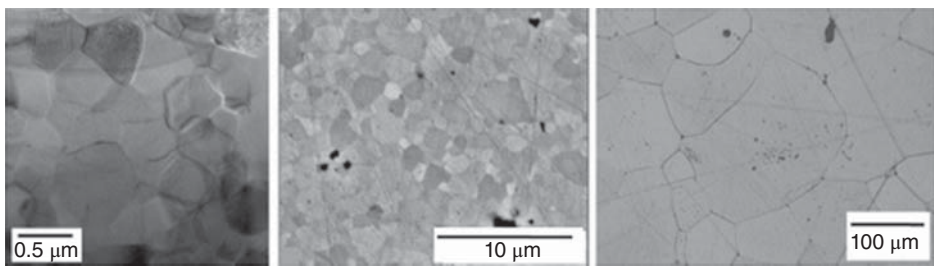

Figure 4.14 Microstructural patterns of transparent spinel ceramics fabricated by sintering at different temperatures. (a) Sintering (AS + HIP) at around 1320 °C. (b) Sintering (AS + HIP) at around 1500 °C. (c) Sintering (HP) at around 1750 °C. Source: Goldstein 2012 [G22]. Reproduced with permission from Elsevier.

certain points left many questions without satisfactory answers [C33, K62]. We tried to quicken mass transport by employing liquid-assisted sintering, a method proved to be highly efficient in some ceramic systems like SiC + alumina and yttria. Of course in the case of TPS, one is limited to the use of either transient liquids or others, which, on cooling, generate glasses with a refraction index similar to spinel. We could obtain, based on the SiO_2–Al_2O_3–Y_2O_3 system, glasses obeying the latter condition. The resulting liquids, however, did not exhibit the wetting and solution/re-precipitation characteristics needed for densification rates enhancement.

The use of vacuum, which has a low oxygen gas pressure, instead of air **may** also enhance $O^{\delta-}$ out-diffusion by creating $V_O^{\cdot\cdot}$ type vacancies according to

$$O_O \leftrightarrow V_O^{\cdot\cdot} + {}^1\!/_2\, O_2 + 2_e^{'} \tag{4.2}$$

$$[V_O^{\cdot\cdot}] = \frac{K_n}{n^2 \bullet P_{O_2}^{1/2}}\,[e'] = n \tag{4.3}$$

The lowering of O_2, in Eq. (4.3) raises the concentration of oxygen vacancies.

The lack of gas in pores is an additional benefit brought about by a vacuum type "atmosphere." The MgO vaporization, enhanced by vacuum, is not a problem at low temperatures (<1600 °C).

Practice shows, however, only a very slight reduction (~20 °C) in the sintering temperatures when air is replaced by vacuum. This suggest that the amount of oxygen vacancies generated by the vacuum is not large enough to significantly influence the anion's diffusion. It also indicates that the elimination of air, which might have accumulated in the closed pores, takes place also in air at a rate that does not disturb pore closure.

After the HIPing step, however, the frequency and size distribution of the residual opaque spots was similar for both air and vacuum specimens. Thus, from a practical point of view, substitution of AS by VS is not an option we can suggest as useful in the case of spinel.

The ultimate attainable densification level may be influenced also by the firing schedule, of course. In the case of spinel, most of the known approaches – rate-controlled sintering, fast firing, two-step firing – have been examined [C25, G6, P3]. Neither approach brought about significant improvements compared with the basic one (moderate constant rate heating to peak, followed by a single dwell [two to three hours] at peak $t°$). What has to be underlined, however, is the fact that by limiting the densification temperature, in the PS stage, even if it meant achievement of bulk densities not higher than 96–97%*TD*, better specimens were obtained after HIPing than if the first stage sintering was allowed to progress to higher densities (99%*TD*) by setting higher peak temperatures (A. Goldstein, unpublished results). It was ensured that the lower densities do not bring about residual porosity; that required the lengthening of the dwell times at peak temperature; the long dwells caused very little grain growth. We underline this because we think that this approach makes the task of the HIPing easier by maintain a lower grain size. This means less occluded pores. HIPing temperatures in the range used for the PS stage, or somewhat higher (50–80 °C), are usually needed to bring to transparency the spinel specimens. It means the 1500–1600 °C range, except the exceptionally sinterable powders like the SN2 discussed above. It has to be noted, however, that further increase of HIPing temperatures up to 1800 °C is instrumental in reducing the frequency of residual opaque spots. The price is, of course, a massive increase of the *GS*. In the case of HIP – as opposed to say HPing under vacuum – decomposition of spinel (MgO vaporization) does not occur at a level able to hamper densification. In theory, pressure may facilitate GG [G12]. In practice while the high HIPing pressures (150–200 MPa) we used were observed as contributing to GG the effect was quite weak, the *GS* is determined, in the first place, by temperature. Besides grain size, an important aspect is the impurities' penetration. Carbon particles and the gas used for pressure application (usually Ar) constitute the main threat in this context. In Figure 4.15a,b [G31], it is shown that carbon can penetrate relatively deep into spinel, despite the fact that when entering the HIP machine the parts lack open porosity [G31]. In Figure 4.15a, it can be seen that carbon accumulates at the difficult to cross interface between the fully dense matrix (transparent) and the less well-densified (white, opaque) spots. It seems that carbon atom diffusion, along grain boundaries, rather than that of CO small molecules represents the main impurity material transport mechanism. However formation of some small linear CO molecules – by interaction of part of the incoming carbon atoms with the oxide lattice – cannot be excluded; such molecules may operate reductive actions during their diffusion inside the spinel lattice. The most deleterious effect of carbon penetration is the electromagnetic radiation (EMR) absorption; these atoms are able to effectuate, which leads to grayish or black hue formation. The spectral effects of carbon penetration are shown in Figure 4.16 [G31]. Coloration intensity gradually fades toward the middle of a plate. Carbon atoms may also reduce, like CO molecules, TM^+ cations located in the GB zones of the spinel lattice. Carbon also slows down densification (intermediary stage of sintering) of oxides (this is mostly a problem for HPing; during HIPing the specimens are almost fully dense at the start).

When HIPed spinel is heated in air to temperatures of ~1200 °C, the gray to black hues introduced by carbon intakes can be weakened or eliminated. This is possible

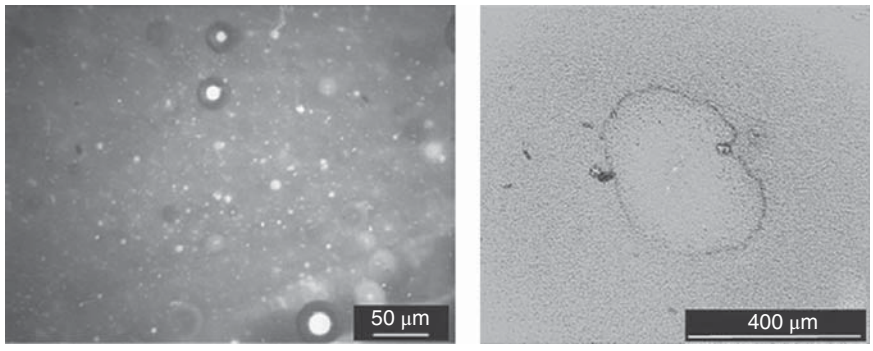

(a)

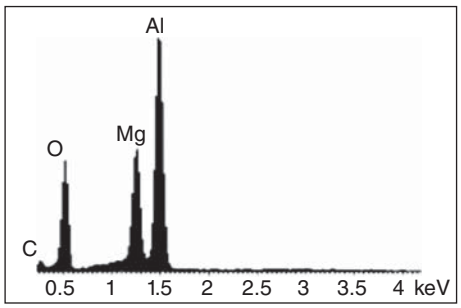

Element	Weight (%)	Atomic (%)
C K	12.92	19.64
O K	44.10	50.31
Mg K	13.26	9.95
Al K	29.72	20.10
Total	100.00	

(b)

Figure 4.15 Carbon penetration into dense spinel. (a) Poorly sintered (white) spots coated by carbon particles in transparent spinel part (after sintering by pressureless air firing + HIP). (b) Presence of carbon on the major (after slight polishing on a major surface of grayish, transparent spinel disc sintered by air firing followed by HIPing). Source: Goldstein et al. 2013 [G31]. Reproduced with permission from John Wiley & Sons.

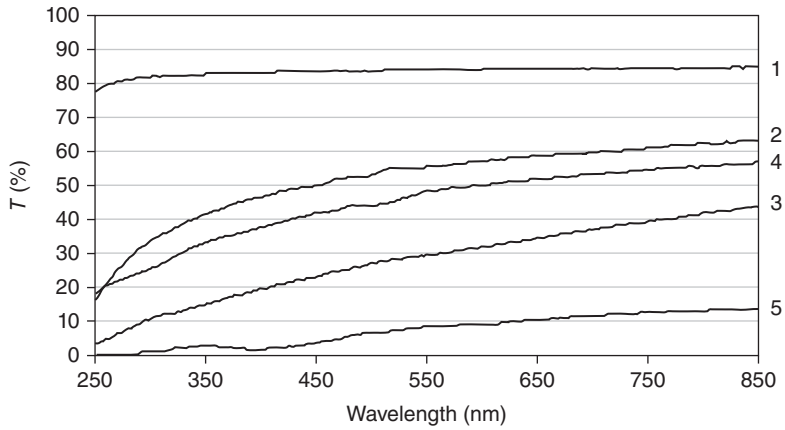

Figure 4.16 Spectral effects of carbon penetration in spinel during HIPing. (1) Clear, transparent part, free of carbon. (2) Slightly gray part. (3) Hot-pressed part, deeply gray. (4) A clear disc on the surface of which very thin carbon coating was deposited (observe spectral profile identical with those of specimens containing carbon taken up during HIPing). (5) Black part. Source: Goldstein et al. 2013 [G31]. Reproduced with permission from John Wiley & Sons.

because O_2 from air, diffusing along the GBs, reaches the carbon particles and oxidizes them to CO_2 and/or CO. A similar phenomenon was described by Harmer and Bennison for the case of HIPed alumina [H10]. If the annealing has to be done over 1250 °C, owing to larger amounts of residual carbon, the gray hues can be removed, but the parts become "milky"; at $t°_a > 1400$ °C, they acquire the look of porcelain (only translucent). One of the reasons for such a development is the increase of pressure exerted by the CO_2 molecules trapped inside the part; this leads to residual pore size increase and thus scattering. Post HIP heating was effectuated also on carbon-free specimens and yet some scattering was still present. The above implies that besides carbon oxidation, another gas bubble-forming mechanism may be active. It is known [G12] that under pressure gas is dissolved in solid hosts in higher concentration than at atmospheric pressure. We consider that the facts described above can be understood looking at what happens to Ar during these operations. Under the high pressure of HIP, some Ar – which penetrates into the dense part – is dissolved and remains so after the system is brought to *RT*. When the parts are reheated (no matter what kind of atmosphere prevails), at 1 atm, the gas dissolved previously separates from the lattice and forms pores. Thus bubbles, which lead to scattering, are formed.

The sinter/HIP process was brought, lately, to a level allowing a small-scale industrial production in

Germany. Thus plates, up to 10 cm in size, can be now produced in larger batches albeit at quite high price, as CeramTec (product name: Perlucor) demonstrated. At Rafael (Israel), relatively large batches of similar parts are fabricated; impressive reproducibility of optical and mechanical properties was achieved. The products of both manufacturers exhibited excellent behavior during ballistic tests. This is the good news; the bad ones refer to the still high prices and lack of large-scale fabrication facilities.

Transparent spinel could be obtained also from oxide mixture, by the reaction preceded sintering approach, without the assistance of pressure [W1]. However temperatures as high as 1750 °c were needed owing to the green-body microstructure's disruption during the reaction accompanied by significant volume increase.

Mg–Al–O–N As will be shown in Section 4.2.2, introduction of nitrogen in the oxide anions-based lattice of α-alumina (from Al–O, one goes over to the Al–O–N compositional system) modifies it markedly even regarding its symmetry, which becomes cubic. Thus certain Al–O–N compositions allow fabrication of valuable transparent ceramics (see Section 4.2.2). In a similar way introduction of nitrogen in certain magnesia + alumina mixtures generates what may be called N-spinel. Such materials retain a cubic lattice despite that their composition (e.g. $MgO_{0.27}$ $Al_{2.58}$ $N_{0.27}$) differs from that of the stoichiometric oxide spinel. N-spinel can be fabricated, starting from $AlN + Al_2O_3 + MgO$ mixtures, by various firing procedures including pressureless sintering. Sintering requires significantly higher temperatures (around 1850 °C) than the normal oxide Mg-spinel [L27, L34, M1]. Properties are similar to those of oxide spinel; the average TRS values around 270 MPa are slightly higher.

4.2.1.1.2.2 Fusion Casting

While powder sintering is the approach of choice for mass production of spinel ceramics, melt casting followed by cooling is a forming method also usable. R. Gentilman demonstrated this for parts up to 10 cm in size [G11]. In this approach, after melting, a slow cooling (heat extracted from the bottom) leads to the formation of a void-free ingot. The directional cooling is essential for crystallization orientation, without which inter-grain pores would form. Melting under He at $t° \geq 2100$ °C (Mo crucibles) is necessary, and cooling times are long. The optical quality of the parts, however, is very good, transmission of up to 84% ($\lambda = 0.8$ μm) being obtained for 3 mm thick discs. Hemispherical domes were also obtained. Such processing leads, of course, to very large (3–5 mm) columnar grains. With *HK* 0.2 values of 17.5 GPa and TRS of 175 MPa, the mechanical properties are acceptable for many optical applications. The shaping of initially flat discs into dome-like parts, by press-forging, was also demonstrated. At ~1750 °C, under loads of 50–100 MPa, plastic deformation was achieved, and thus the desired macroscopic shape changes [M5].

4.2.1.1.3 Properties of Spinel

4.2.1.1.3.1 Mechanical Properties

For most of the applications, the attractiveness of spinel stems from its ability to combine transparency with functional properties, especially mechanical, better than most its competitors. In Table 4.1 the main properties of spinel were inserted, in terms of best values. Here, in Table 4.4, the value range of the main properties is given; some additional properties are introduced.

One of the most important mechanical properties, considering the applications of spinel, is hardness, which characterizes the ceramics resistance to local plastic deformation displacement and also to fracture (measurements under high loads). The hardness of polycrystalline spinel is higher than that of stoichiometric single crystals (HV10 = 12.8 GPa) [K40] ranging from 13 to 15.5 GPa (see Figure 3.66 in section 3.2.8). Measurements with Vickers, Knoop, or spherical indenters each offer specific results; it is needed to corroborate these for better estimating parts behavior during service. For armor applications, Vickers results, under loads of 5–10 kg (HV5, 10), are the most used. Such macrohardness measurements are more sensitive to microstructure variation than results obtained at lower testing loads

Table 4.4 Main properties of transparent spinel ceramics.

Properties of spinel	Values
N (at 600 nm)	1.715
$HV5,10$	12.0–15.0 GPa
TRS	80–250 MPa
$t°_f$	2140 °C
TD	3.578 g/cm^3
$\alpha_{85-1000\,°C}$	60–80 × 10^{-7} K^{-1}
E	250–310 GPa
λ_{th}	10–15 W/mK
th. shock $_{(R')}$	1.1–1.9
K_{IC}	1.48–3.50 MPa m$^{0.5}$
$\rho_{e\,25\,°C}$	>10^{12} Ω m
$\varepsilon_{1\,KHz-9.3\,GHz}$	8.2
tan δ	2.5 × 10^{-4}
μ (Poisson coefficients)	0.26–0.28
σ_C	2.7–3.3 GPa
Shear modulus	120–140 GPa

(see Figure 3.67 in section 3.2.8) [K40, R24]. The values of hardness achieved are a function of the level of densification, concentration, and type of local defects (especially in the surface layer) left by processing (especially polishing), grain size distribution, structure, and composition of grain boundaries. Residual thermal stress also exerts a certain influence. In Figure 3.66 the dependence of *HV* and *HK* on *GS* is given.

The results in that Figure 3.66 are collected from specimens fabricated and tested so as to minimize the effect of factors other than *GS*. As it is seen, the *HV* is not very sensitive to $\overline{GS}$ after the grains get larger than ~2 μm. One of the reasons very fine microstructures raise hardness is the reduced mobility of dislocations in confined volumes; ergo, plastic deformation is impeded. Significant increase can be obtained by reducing the $\overline{GS}$ under 1 μm. For instance, using deformable punch SPS (750 °C), Muche et al. achieved transparent spinel parts having average grain size in the 7–190 nm. Hardness (micro-indenter) values in the 18–28 GPa were measured [M42]; Hall–Petch relationship was respected down to the lowest grain size. However, according to Sokol et al., who prepared similar materials, the relationship between hardness and grain size was inversed under 30 nm [S40]. Remarkably, alumina-rich spinel shows lower hardness than stoichiometric parts (see Figure 3.66). In earlier works results indicated that at very high $\overline{GS}$ values, the hardness may increase when compared to values obtained for, say, $\overline{GS} \sim 10$ μm; this is not confirmed by more recent works [K40, K41]. The effect of the indentation size on hardness measurement results was also examined [K40, P13]. The works showed, once again, how important is to measure complete hardness load curves. The transition load, where the major deformation mechanism switches from plastic deformation to fracture (lateral cracks, hidden subsurface cracks, those starting from the tips of the indent are all involved). The Vickers hardness at the transition load (~4 N) is $HV = 13.5$ GPa. Interesting insights regarding spinel damage mechanisms under indentation were provided using a hard sphere- type indenter [M45]. Such an approach models, to some extent, the early stage of certain types of projectile impact; this makes it useful especially when armor apps are envisioned. It was observed that increasing the $\overline{GS}$ from the submicron to that of a few microns domain makes the part more prone to cracking damage; ring (first to form), cone, and lateral cracks are produced by such an indentation. Grain boundary fine cracking was seen in the inelastic zone and anisotropic elastic recovery accompanied unloading. The measurements also indicate that TPS loaded by a spherical indenter develops a stress system, which leads to elastic plastic behavior, i.e. yielding prior to fracture. In the inelastic region adjacent to the indent (high contact stress), an intergranular fracture pattern predominates, revealing the tendency to GB micro-cracking.

A number of early studies examined the correlation between mechanical strength and microstructural pattern [G16, S53, W23]. Data regarding the behavior of single crystal spinel also exists. It seems that for coarse-grained specimens ($\overline{GS} \sim 150$ μm), a crack face bridging-based mechanism functions as a toughening mechanism; there is a tendency for nonlinear fracture behavior, at various temperatures. An interesting study, in which property dependence on microstructure and the slow crack growth process (important for service life estimation) were examined, also detected significant correlation between the microstructural pattern and mechanical behavior [S5]. Elastic constants are not sensitive to *GS* variation. The K_{IC} (1.8–1.9 MPa $m^{1/2}$) also does not vary significantly with $\overline{GS}$, as long as $\overline{GS}$ remains lower than 25 μm. For *GS* larger than 80 μm, however, it drops to 1.4–1.5 MPa $m^{1/2}$. The toughness decrease seems to be concomitant with a transition from trans-granular to intergranular fracture. This drastic change seems to be caused mostly by some residual submicron porosity localized at grain boundaries of the largest grains. The large grained spinel also included some alumina as second phase and variation of the Al_2O_3:MgO ratio; cleavage of the coarse grains also contributes to K_{IC} decrease. The strength is also decreased by coarser and/or bimodal microstructures [W24, G16]. The crack velocity is reduced to values close to alumina in fine-grained spinel and rises to values close to SiO_2 glass in the coarse ones. The rate of property improvement is highest when $\overline{GS}$ changes from 150 to 25 μm and less so below that limit. For the case of hot-pressed submicron spinel, it was found that the K_{IC} is also a function of the "N" ratio. The best K_{IC} values appear for "N" in the 1.01–1.04 range. Doping with Cr^{3+}, Mn^{2+}, and $Fe^{2+,3+}$ had a slight positive influence on K_{IC}. It seems that Cr^{3+} can enter with more ease, the lattice being able to penetrate deep inside the grains, while Mn^{2+} and $Fe^{2,3+}$ are mostly segregated at GBs. Fe is able to raise K_{IC} to 2.7 MPa $m^{1/2}$. Chinese researchers also found a dependence (parts produced by VF + HIP) of flexural strength on "*N*." The optimal value determined for obtaining the best trade-off for TRS, K_{IC}, and *HV* was $N = 1.5$. Flexural strength peaked at $N = 1.34$ [H38] at ~220 MPa. Separation of some α-Al_2O_3 in the GB regions is considered as the factor allowing mechanical property improvement when X moves from the 1.0 value. Apparently the size of the alumina precipitates is such that optical transmission is not impaired. A strong dependence of the TRS on $\overline{GS}$ was found also by the measurements of J.L. Sepulveda et al. on hot-pressed parts [S21]. The compressive strength of fine-grained spinel was measured to be of ~3.3 GPa.

4.2.1.1.3.2 Optical and Spectral Properties

Perfectly polished plates may exhibit, considering the inevitable specular reflection loss, a maximal transmission of ~87%. In practice, values close to this limit have been obtained, when plates a few mm thick were measured. For a perfect specimen, thickness increase is not supposed to reduce T%; in practice the imperfections, present in any specimen, lower more or less transmission when thickness increases. In Figure 4.17 the transmission curves of a few specimens, fabricated by the sinter/HIP approach, are shown (in addition to some fabricated by HPing; Figure 4.16). As it can be seen high transmission is exhibited by properly processed spinel specimens; however this is achieved only when the action of all (many) factors able to exert a negative influence is eliminated (in Figures 4.16 and 4.17, the effect of impurification with carbon is shown).

In Table 4.1 the average (VIS domain) refraction index value is listed. The acceptable level of transmission and the relevant frequency range differ for various apps, but in general it is desired to obtained as high as possible transmission levels. It may be worth noting here that such an approach is sometimes counterproductive. In practice it is advisable to determine the minimal level of transmittance acceptable for a given application so as to be able to correctly determine the optimal trade-off between price and optical quality. For instance, for armor applications, a T around 80%, for $t = 5$ mm or lower, is satisfactory. Such transmission levels can be achieved at reasonable cost. Insisting for higher levels will hardly improve windows functionality but markedly increase production cost to levels unaffordable even to rich customers. What is acceptable for armor may not be so for sensor protector windows. Transmission can be reduced by reflection, absorption, and scattering. Diffuse reflection is minimized by ensuring planar and clean macroscopic surfaces. Specular reflection can also be reduced by the aid of suitable antireflection coatings. From an engineering point of view the most difficult task is the elimination of scattering. Being based on a cubic lattice, spinel, as opposed to α-Al_2O_3, has no birefringence-related scatter. Post-sintering thermal annealing can take care of the birefringence that residual thermomechanical stress fields may introduce. Second phases – which have a refraction index different from that of the matrix – are also a potential scattering source. While, in this context, clean grain boundaries are preferred, minor amounts of second phase, located there, can be tolerated. The probability, in the case of thin ($t \leq 5$ mm) plates, that the light waves encounter GBs at an angle conferring to the second phase sufficient size to act as scatterer is low. Dispersions of second phase particles with a size larger than 60 nm are not acceptable; even smaller units may have some effect. In practice the most ubiquitous second phase are the residual pores (air, for instance, if present inside, confers an "n" value of 1.0) left by the sintering process. The amount of tolerable porosity is dependent on the application considered; it is also markedly dependent on the size distribution of the pores (Figure 2.14). A given pore size scatters strongest wavelengths similar to its diameter. At the "natural" high frequency edge of the window (~160 nm; matrix absorption at lower wavelengths), the loss of transmission imposed by the refraction index is only slightly higher than in VIS. Figure 2.18 shows, however, that 100 vol. ppm of porosity, even of a size as low 30 nm, still significantly scatters 200 nm waves. While such small pores do most of the damage in the UV, the effect of others (50–200 nm) is still significant in the VIS and felt up to the IR domain. The maximal scattering intensity increases in inverse proportion to the pore size. The relationship between the illuminating EMR and scattering

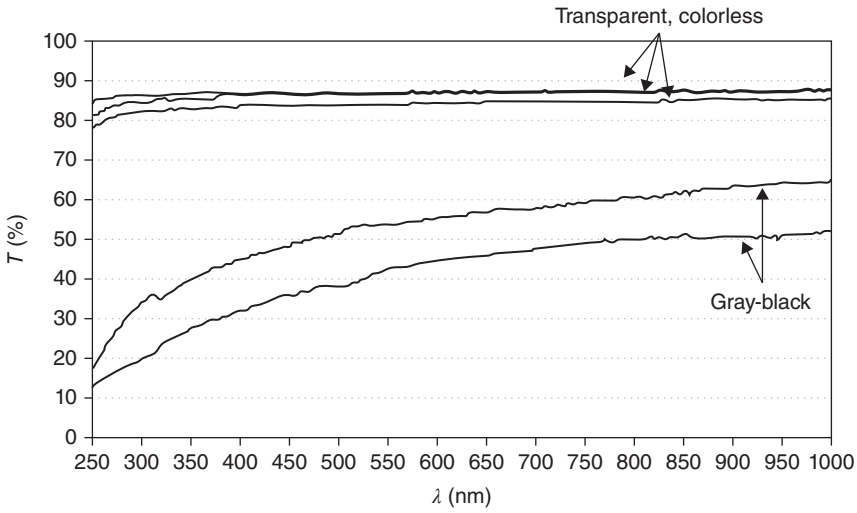

Figure 4.17 Transmission curves of spinel discs ($t = 3$ mm) fabricated by sinter/HIP. Source: Goldstein 2012 [G22]. Reproduced with permission from Elsevier.

pores has certain interesting practical consequences. For instance, let us consider the apps where the VIS range is of interest. If we consider a given number of pores per unit volume (pores number density), those having a size of, say, 2 μm cause less transmission loss than the same number if their size is located in the 0.4–0.6 μm domain despite the fact that the larger pore collection represents a larger volume of porosity. Practice suggest that the pores size distribution of most HIPed spinels is such that a given P_0 has a negative effect strongest in the VIS. The scattering angle specific to a given scatterer is also a useful information, because it influences, of course, the level of transmission given, by various measurement arrangements (e.g. detector acceptance angle). This affects the level of accuracy of real in-line transmission data reported. In Figure 4.18 [G15] the bi-dimensional scatter (forward scatter half) distribution function of two spinel plates is given.

The B0 represents that of an as HPed plate, while B5 is that of the plate after additional HIPing. The HIPing is able to reduce the scattering angle, either by reducing porosity level or moving pore size at values less close to λ (633 nm). The porosity, which produces scattering, is in most cases the residual one left by the sintering stage. If post-sintering thermal treatments for parasitic color elimination are also effectuated, the expansion of dissolved gas may also cause porosity formation. Scattering by pores is, in practice, the most important transmission reducing mechanism operating within the "window." The effect of the "*n*" dispersion is weak (somewhat more significant only for $\lambda < 350$ nm), leading to a reduction of the reflection loss with an increasing λ.

In principle some transmission loss, in the IR range, may result also from the lattice vibrations and in any case the low energy side window cutoff (~5 μm) is caused by the photon–phonon interactions. In Table 4.5 the frequency of the spinel lattice fundamental vibrational frequencies is given.

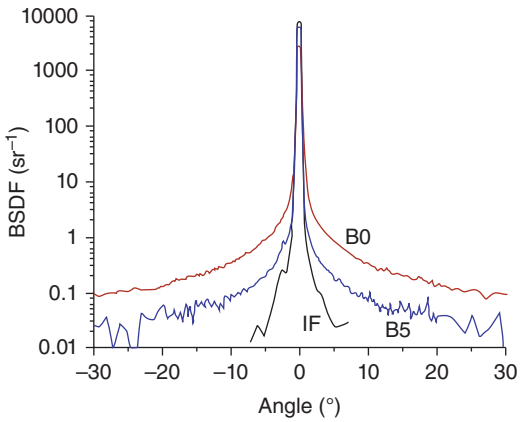

Figure 4.18 Bidimensional scatter function of spinel plates. IF – instrument's function. B0 – as-HPed plate. B5 – plate after HP + HIP. Source: Gilde et al. [G15]. Reproduced with permission from John Wiley & Sons.

Table 4.5 Frequency of spinel lattice fundamental vibrations.

ν (cm^{-1})	
307	0.40
488	2.48
510	1.07
589	0.07
671	0.70
808	0.022
ν	**Int. and width**
510	Wide 3
573	Shoulder
685	Width 3
765	sh

Recorded band positions are listed in Table 4.5. The low energy cutoff of the transmission window is not caused by the basic vibrations but lies on the 3-phonon region, at higher frequencies (~2000 cm^{-1}). It has to be noted that real specimen spectra often include also the bands produced by impurities like OH^- or H–OH (3300–3600 + 1600–1700 cm^{-1}). The OH^-, the most frequent impurity, has bands in the 2.7–4.2 μm domain (including the fundamental ν_3 stretches) and overtones at 1.4, 0.95, and 0.75 μm.

4.2.1.1.3.2.1 Thermal Variation and Radiation Effects on Transmittance

The transmission window existent at *RT* is modified, to a certain extent, if temperature is changed. Increase of temperature tends to narrow the window, the effect being most pronounced at the long wavelength edge. The cause is the enhancement of vibrations by a temperature increase. Anharmonic components of the vibration modes set are stronger, and this facilitates phonon interactions. The long wavelength cutoff is located in the 3-phonon domain. The extension of this domain toward higher frequencies, as a result of the phonon interaction strengthening, pushes the cutoff toward shorter wavelengths. The absorption coefficient at 5.0 μm increases from 0.4 to 1.3 cm^{-1} when temperature rises from 25 to 500 °C.

Exposure to radiation also induces, among other effects, parasitic absorption. The absorption is mainly a result of the point defects produced by irradiation. Some of them constitute local electronic systems, which

interact with the EMR in a manner similar to that of the TM^+ cations. For instance, under Co irradiation, an initially colorless spinel plate acquires a dark brown hue owing to the formation of a wide band in the 320–600 nm region (peak at ~470 nm). Under intense artificial UV radiation (1250 μW/cm^2; 0.25 μm, 2 cm distance of source), spinel transmission starts to degrade after ~120 hours (the same effect appears in optical glasses after 15 minutes) [G39]. Spinel is quite resistant to the effect of corrosive agents at *RT* and even at 100 °C for moderate exposure times (<50 hours). The UV–VIS transmission is degraded more than that in the IR range by chemical attack. Curiously NaOH has a milder effect than oxides. H_2SO_4 is more corrosive than HNO_3 of HF. Transmission is significantly degraded (~30% at 0.4 μm) by long exposure (1000 hours) [G39]. Sand blasting for 10 minutes, which makes a silica glass opaque (0.4 μm), reduces spinel transmission by ~8%.

4.2.1.1.3.2.2 Parasitic Absorption Owed to Electron Transitions

As discussed in Section 2.1.3.5.1.2, transition between the electronic states of various types of impurity may also cause absorption of various segments of a TC "window" frequency domain. The impurities introduce localized electronic states, the energy of which is located within the bandgap of the host. Below we will see what this means for the specific case of spinel.

The effect of carbon penetration was discussed above (see the spectral effects in Figure 4.16). Most of the spinel powders used for TPS fabrication are prepared in a way that precludes the presence of second phases including absorber ions. The lattice of spinel itself is quite rigid, accepting with difficulty foreign ions (those present are concentrated in the GB's region). Therefore the number and concentration of potential parasitic cation-type absorbers are quite low. Rarely does the total concentration of $TM^+ + RE^+$ ions exceed 150 ppm. One of the most ubiquitous TMs present in the oxide lattices is Fe. It may be accommodated either as Fe^{3+} and Fe^{2+}. The charge, radius, and octahedral site stabilization energy (ligand field related) of a d^5 configuration make the hexa-coordinated Fe^{3+} the most stable species in a spinel host. Analytical chemistry suggests that Fe concentration is in the 20–70 ppm in spinel powder. Even if all Fe appears as Fe^{3+} (O_h), it is not able to cause coloration. This is because, for coloration, absorption in the 380–780 nm range is necessary. In the case of Fe^{3+}, such bands do exist but they are of the spin-forbidden type [$^6A_1 \rightarrow {}^4T_2$ (D), $^6A_1 \rightarrow {}^4E_1$, $^4A_1$ (G) are the strongest] and, as such, too weak to cause coloration, which can be seen by naked eyes. Despite not manifesting itself as a pigment, some Fe^{3+} present in TPS are demonstrated by the EPR signal it generates (see Figure 4.19).

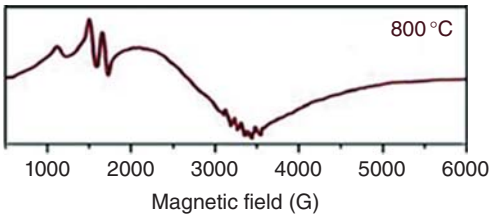

Figure 4.19 EPR signal of minute Fe^{3+} impurity present in spinel.

Outside the VIS range Fe^{3+} and Fe^{2+} bands (of the charge transfer type) are located at $\lambda \approx 260$ and 220–220 nm. At the low concentrations of Fe in spinel, these (in principle, strong bands) are not so intense as to enter the VIS domain; in practice they need consideration in the case of certain applications like optical components for lithographic machines. In the case of Fe^{2+} presence ($3d^6$) (it may appear as a result of HIPing), a strong d–d band, located in the near infrared (NIR, 1050–1250 nm), would be expected; in practice absorption in that zone is not seen.

We give here also an example of impurification owed to Ti^{3+} in order to show that problems, in this context, may be created by rather unexpected sources. Thus it was determined that the faint bluish-green hue observed in some specimens, produced by the sinter/HIP approach, appeared only in the case of specimens derived from powders processed with an ultrasonicator, which had a shaft made of a Ti alloy. This suggested the presence of Ti^{3+}. To verify this hypothesis, Ti-doped (introduced as TiO_2) spinel specimens were examined. The air-sintered $MgAl_2O_4$ (TiO_2) specimens had a white opaque look, similar to that of undoped spinel. After HIPing, however, the transparent discs exhibit a bluish-green color and an optical spectrum as shown in Figure 4.20a. The HIPed discs also presented a strong EPR signal (Figure 4.20b) [G31]. $MgAl_2O_4$ (0.1% TiO_2) specimens sintered in one step (1580 °C/3 h) under an oxygen-scarce atmosphere (Ar) are translucent and exhibit colors and EPR signals, like the sintered/HIPed ones.

It is immediately obvious that the optical spectrum has a profile similar to that of Ti^{3+} in single-crystal spinel [G31]. The weak band centered at 530 nm corresponds to an approximatively O_h site ($6O^{\delta-}$ anion ligands around the cation $|\delta| < 2$), whereas the wide band at ~785 nm is produced by Ti^{3+} cations coordinated by $4O^{\delta-}$ anions (T_d site). The EPR signal shows that, in fact, the octahedron of ligands is slightly distorted to a D_{3v} symmetry (Jahn–Teller effect). The above shows that an oxygen-scarce atmosphere causes a Ti^{4+} to Ti^{3+} reductive process to occur.

Air (relatively rich in oxygen)-sintered specimens are colorless (Ti^{4+} has no bands in the visible domain), while those fired under Ar (1 or 2000 atm) are blue-green

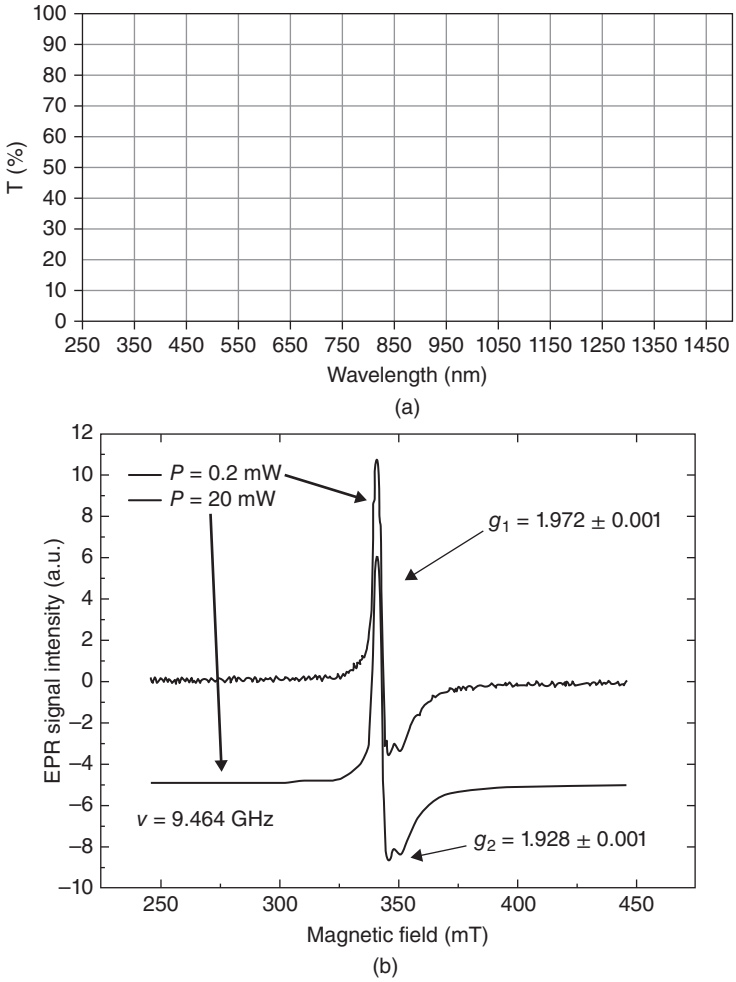

Figure 4.20 Electronic spectra of sintered/HIPed spinel doped with TiO_2. (a) Transmission spectrum (the characteristic absorption band of Ti^{3+} (a $3d^1$ cation) is seen at ~800 nm) of the greenish-blue disc. (b) EPR signal (shape characteristic to d1 ions) of the same specimen. Source: Goldstein et al. 2013 [G31]. Reproduced with permission from John Wiley & Sons.

(Ti^{3+}). This behavior suggests that the faint colorations mentioned at the start of this subsection are due to Ti from the ultrasonication shaft; the Ti^0 is oxidized to Ti^{4+} during air sintering and then reduced to Ti^{3+} during the HIPing in Ar.

4.2.1.1.3.2.3 Origin of Yellow Color in Spinel

The optical spectrum of a transparent spinel disc, exhibiting a yellowish hue, is presented in Figure 4.21 [G31] (curve 2).

The yellowish tints were observed only in the case of specimens fabricated from powders derived from sulfates. Edge-polished specimens (which allow one to view the cross section of discs) show that the coloration fades toward the specimen middle plane. Chemical analysis shows that the as-received spinel material contains S-including species (S content up to 600 ppm). That is a consequence of the fact that during the synthesis of the powder, a small fraction of the SO_4^{2-} anions substitute oxide ions in the forming spinel lattice. Such substituents can remain in the oxide lattice (air environment) at high temperatures, surviving the pressureless

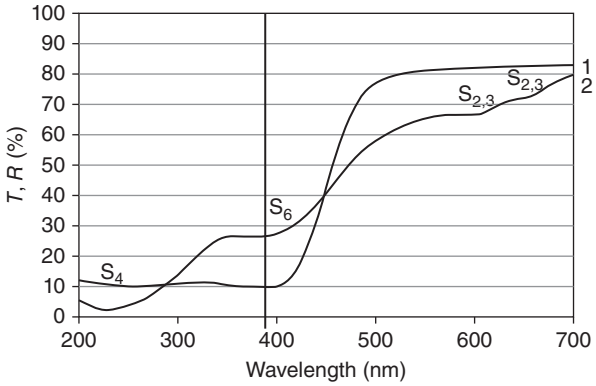

Figure 4.21 Optical spectra of sulfur-containing materials. (1) Reflection curve of sulfur powder compact. (2) Transparent spinel disc (sinter/HIP) derived from powder containing some 300 ppm of S (as $SO4^{2-}$ anions). Source: Goldstein et al. 2013 [G31]. Reproduced with permission from John Wiley & Sons.

(under air) sintering stage. The reductive atmosphere in the HIP machines can reduce the S^{6+} cations of these sulfate anions to S^0. The fact that practically no oxygen is present in the anti reflective (AR) atmosphere of the

HIP encourages oxide ions to exit from the spinel lattice (as oxygen molecules). The electrons thus produced are the ones effectuating the reduction of the S^{6+} present in the sulfate anions. The CO molecules and the atomic carbon, if they penetrate inside the spiel lattice, are also able to effectuate reductive actions. Sulfur was detected in spinel grain boundaries (hot pressed under reductive atmosphere) by Chiang and Kingery [C33]. The yellow-colored HIPed specimens we obtained retained some 60–90 ppm of S. Curve 1 in Figure 4.23 represents the reflectance curve of a yellow sulfur powder compact. Such orthorhombic sulfur powder is made of S_8 cycles corrugated by van der Waals bonds. The main spectral features of both the powder and the HIPed spinel plate are two absorption bands located at 225 and 410 nm, respectively. The latter is the cause of the yellow coloration. The strong similarity between curves 1 and 2 in Figure 4.21 suggests that the yellow color of the HIPed specimens can be assigned to S_8 molecules. The assignment of the bands – produced by yellowish HIPed plates – to S_8 is supported also by comparing the experimentally observed spectral profile (in the domain relevant for color) with that predicted by S_8 molecular electronic structure models. For instance, Krasovska et al. [K39] determined (ab initio-type method) the set of electronic states that make up the valence and conduction bands of a solid sulfur polymorphs. Owing to the structure of such solids (S_8 molecules kept together by van der Waals forces), these electronic states are, in fact, molecular orbitals of the S cycles, which make up the solid. The calculated absorption bands – generated by interband transitions – have peaks at energy values corresponding exactly to the wavelength of the band centers in Figure 4.21. Despite the p–p nature of the transitions, the oscillation strength is yet orders of magnitude larger than that of d–d transitions; this means that very low amounts of S_8 can generate intense bands and thus color. The source of the two weak bands, located at 600 and 630 nm (curve 2 in Figure 4.21), is not clear. They may be produced by a small fraction of the S_0 atoms assembled in smaller cycles (S_4, S_3, S_2); S_2 and S_3 molecules are known to produce absorption in that region. From a practical point of view, it may be worth noting that residual sulfate distribution varies markedly in the raw material, from batch to batch and even within the same batch. Owing to this, while many specimens derived from a given batch are colorless, some exhibit the coloration described above. The coloration introduced by S disappears if HIPed specimens are subjected to annealing in air, owing to the re-oxidizing of the sulfur. However the temperatures required are higher than those needed to eliminate moderate intensity gray tints (produced by carbon) and this may cause bubble reformation. Therefore in cases where both carbon and sulfur impurities coexist – with the sulfur concentration exceeding ~200 ppm – the thermal annealing in air, effectuated at the maximal temperatures not causing bubble reformation, is able to eliminate the gray hues but not the yellowish ones; in the specimens, as they appear before the thermal treatment, the yellow is masked by the gray hues. In practice the above means that coloration induced by sulfur cannot be eliminated without reducing transmission. Therefore one has to reduce drastically the residual sulfate content of the as-prepared powders.

4.2.1.2 Zn-Spinel

$ZnAl_2O_4$ (gahnite) is a spinelid, viz. a material having a lattice similar to $MgAl_2O_4$ ($a = 0.808\,48$ A), the model spinel; the difference is the presence of Zn^{2+} cations instead of Mg^{2+} in the tetrahedral sites. The properties are, overall, somewhat less attractive than those of Mg-spinel – as far as TC applications are considered. The density at $TD = 4.61$ g/cm^3 is larger, while the TRS and Young's modulus similar and the hardness a bit lower. The thermal conductivity, at lambda = 25–30 W/mK is higher and that is useful for thermal shock resistance.

In ceramic form the material was first produced in transparent state in 2012 [G33], from powder prepared by hydrothermal synthesis by a sinter/HIP approach. In further efforts various raw materials (prepared by sol–gel, coprecipitation, solid-state oxide reaction) and densification procedures (sinter/HIP, HP, or PECS) were used [K12]. The transmission curves of the first *T*-gahnite specimens produced are shown in Figure 4.22a [G34]. Better optical quality specimens were obtained as seen in Figure 4.22b [K12].

The *T*-gahnite is examined mostly as a host for Co^{2+}-based Q-switches [G27].

4.2.2 γ-Al-oxynitride

4.2.2.1 Composition and Structure

The hexagonal α-Al_2O_3 lattice precludes (owing to birefringence) obtainment of thick, highly transparent polycrystalline parts, except if perfect orientation of the grains is effectuated. Orientation is feasible but only for small specimens and in conditions not usable in industrial production (see Section 3.1.2.2.2). The γ-Al_2O_3 is cubic but can be obtained in bulk form [Y16], by sol–gel technology, only as small and highly porous (yet transparent, owing to the nanometric pore size) parts. Sintering, even of small parts, was not achieved. Al_2O_3-based transparent ceramics (large size, thick) would be of high practical interest owing to the excellent mechanical properties of the material. An elegant approach, available for the obtainment of transparent ceramics, derived

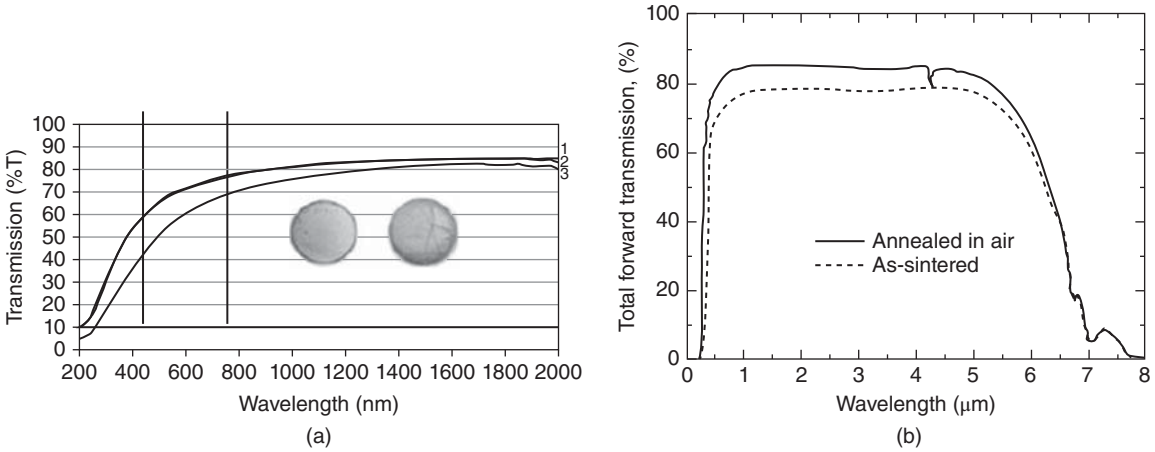

Figure 4.22 Transmission spectra of T-gahnite ceramics. (a) First transparent ceramic developed. Source: Goldstein et al. 2012 [G34]. Reproduced with permission from John Wiley & Sons. (b) High transparency specimen. Source: Kim et al. 2014 [K12]. Reproduced with permission from The Ceramic Society of Japan.

from alumina – exhibiting properties not far from those of α-Al_2O_3 – is the use of the cubic oxynitride lattice, which is proper to certain compositions of the Al–O–N system; this approach is the object of the current section.

Substitution of part of the O^{2-} anions with nitrogen is possible in a number of oxide lattices; a well-known example are the SiAlONs [D19, T5]. The resulting oxynitrides have properties different from both oxide and nitride, owing to the bonding scheme and lattice symmetry modifications. Such a substitution may take place, when the right conditions are created, also in the case of alumina. As a result the hexagonal corundum lattice is transformed into a spinel-type cubic one. A cubic lattice means birefringence elimination so that polycrystalline AlON may exhibit high transparency.

Yamaguchi and Yanagida observed that suitable AlN (wurtzite structure)–Al_2O_3 mixtures can be processed into cubic materials, which include both oxygen and nitrogen [Y2]. The diagram of the AlN–Al_2O_3 – as drawn by McCauley and Corbin [M21] – pseudobinary system is shown in Figure 4.23 (for 1 atm of N_2).

Within this system the compositions rich in AlN tend to exhibit complex layered structures, while in the Al_2O_3-rich part, there is a segment where defective spinel lattices dominate. For the case of γ-AlON the segment goes from 60 to 73 mol% Al_2O_3 (1700–2000 °C region). The 1AlN:1Al_2O_3 composition is not within that range. The γ-AlONs are able to form solid solutions with $MgAl_2O_4$ [R25]. AlON does not form under 1700 °C (from AlN + Al_2O_3 mixtures); it seems to melt congruently around 2160 °C. The exact configuration of the γ-AlON's lattice is yet a matter of debate. In Figure 4.24 a projection along the [100] axis is shown, for a lattice model built, by calculation, by C. Fang et al. [F1] for $Al_8(Al_{15}Vac.)O_{27}N_5$. This lattice is **similar** to that of the ideal γ-AlON but refers to a composition outside the proper γ-AlON range. In any case the basic space group considered for γ-AlONs is, of course, the $Fd\bar{3}m(O_h^7)$ #227 of the oxide spinel (based on XRD [W25]).

As it was said, $Al_{24}O_{24}N_8$ as single phase does not appear. The $Al_{23}O_{27}N_5$ (35.7 mol% AlN) would have a γ-AlON lattice. The number of atoms in a spinel unit cell is 56 (eight FCC anion subcells in a cubic array with the cations in the voids). For an ideal $Al_8(Al_{16})O_{24}N_8$, the 8a (Wyckoff notation [W35] of positions in the lattice) tetrahedral sites (T_d) and the 16d octahedrally coordinated D_{3d} sites are fully occupied with a total of 24 Al^{3+} cations. The 24O^{2-} and 8N^{3-} ions occupy the 32e trigonal (C_{3v}) sites of the cell. It seems (calculations [W25]) that Al^{3+} of the 8a position shifts somewhat along the [111] direction (the anion fraction parameter "*n*" ceases to be 0.375 and is 0.3826) so that a more accurate space group assignment would be a $D_{3d}^5(R32/m)$ #166 space group. Then, a tetrahedrally coordinated Al^{3+} has three O^{2-} nearest neighbors and one N^{3-}; the Al–N distance (1.79 Å) is shorter than the Al–O (1.82 Å). Four of the Al^{3+}s, at the octahedrally coordinated sites, have only O^{2-} neighbors (Al–O = 190 Å) and the remaining 12 have two N (in trans positions) and four O^{2-} nearest neighbors. Every anion is four coordinated (one Al in an a (T_d) site and three in D_{3d} sites). The experimental (XRD) cell volume is of 507.2 Å [W25]. In γ-AlONs electrical neutrality requires the existence of vacancies (if all Al=Al^{3+}) and/or interstitials (oxygen and/or nitrogen). The currently accepted model ("constant anion model"; anion sites are fully occupied) indicates that electrostatic is achieved by the formation of Al^{3+} (16d points) vacancies. About the nature of the bonding in AlONs little

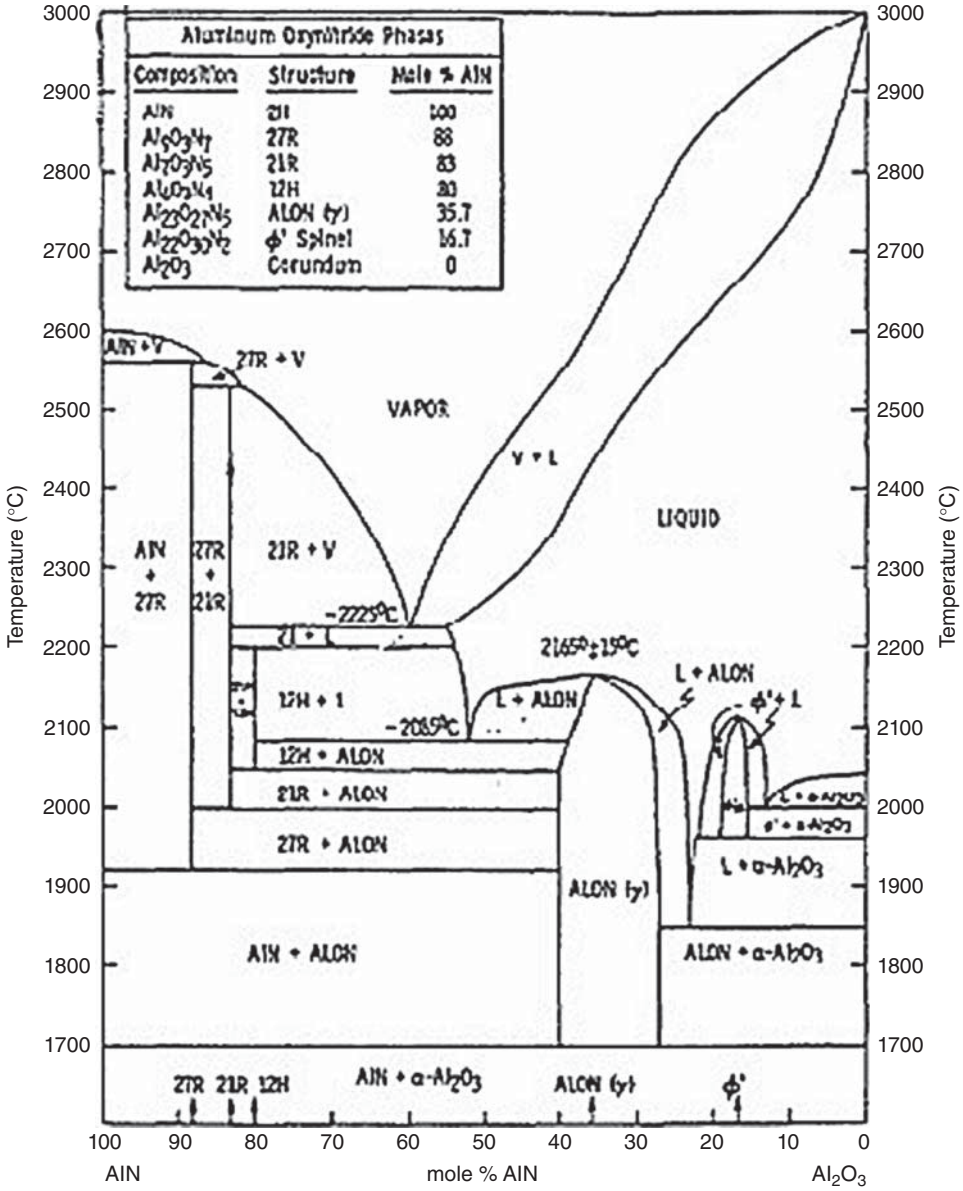

Figure 4.23 Phase diagram of the AlN–Al_2O_3 pseudo binary system. Source: McCauwley and Corbin 1979 [M21]. Reproduced with permission from John Wiley & Sons.

is known. Considering properties, its strength seems somewhat inferior to that of corundum of a similar grain size.

4.2.2.2 Processing

In a remarkable first effort – despite the fact that only coarse powders were available – McCauley and Corbin were able to sinter 1 cm discs, exhibiting noticeable transmission [M21, M23] with grain size in the 50–100 μm range and AlN content of 30 mol%.

4.2.2.2.1 Fabrication Approaches

Fabrication of AlON requires high firing temperatures, suitable composition, and fine and pure active powders. Up to now the most efficient procedure allowing achievement of high transmission, large size, and complex shape is that developed by Raytheon [G18, G19]. The outline of the Raytheon process is in the public domain but less so certain "details," which makes the products better than those of the few existing competitors, from France and China.

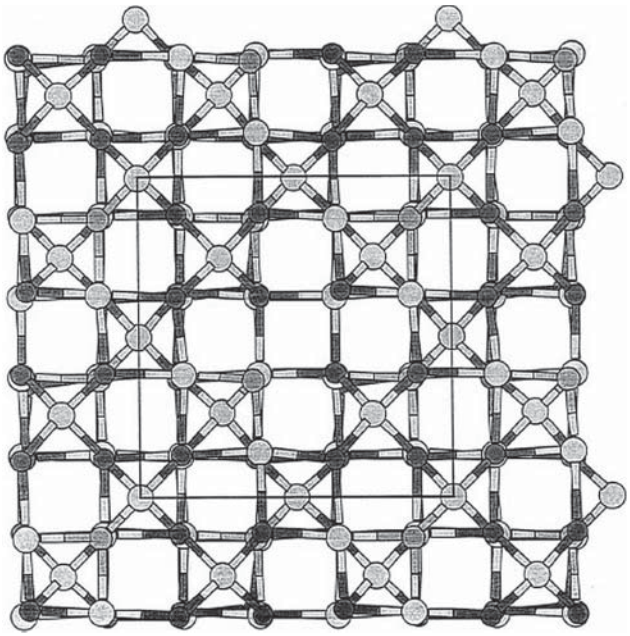

Figure 4.24 AlON ($Al_8(Al_{15}Vac.)O_{27}N_5$) lattice model; projection along the [100] axis. Source: Fang et al. 2001 [F1]. Reproduced with permission from John Wiley & Sons.

It was used in attempt to obtain T-AlON parts mostly by three approaches [A28]. In the first, densification precedes reaction, while in the second, the two processes run in parallel, with reaction ending first. In the third approach, AlON powder is sintered; the best results were obtained using the last two approaches.

4.2.2.2.2 Powder Synthesis

The AlON raw material can be synthesized using quite a lot of chemical reactions (including Al_l + air → AlON at ~1500 °C). The most used is a solid-state reaction of Al_2O_3 with AlN: $Al_2O_3 + 5AlN \rightarrow AlON$. This approach was used, for instance, in the early attempts to produce AlON by reaction sintering [M23]. The AlON fraction in the mixtures becomes dominant over 1700 °C but single phase AlON requires attainment of temperatures ≥1800 °C. First an oxygen-rich AlON forms, which slowly incorporates the residual AlN. The rate of nitrogen diffusion through the AlON lattice controls the kinetics. In practice powder beds of suitable composition, absence of carbon, and optimal levels of N_2 pressure (3–5 bars) are required.

Carbothermal nitridation of Al_2O_3 over 1700 °C is a second popular way to effectuate reaction sintering: $23Al_2O_3 + 15C + 5N_2$ (g) → AlON + 15CO (s). Alternatively the milled powder is used in sintering only firings. The powder is reacted in the first step at 1600 °C and then a final calcination at ~1800 °C is done. CO additions to the N_2 atmosphere helps in getting single phase AlON. Owing to the high preparation temperatures, the comminution of the synthesis product is very difficult, especially because impurification levels have to be limited. Al alkoxides or other fine Al containing sources, like $Al(OH)_3$ or γ-Al_2O_3, were also used in preparations. While reaction temperatures were reduced, formation of single phase γ-AlON was not always achieved [A28]. The best results were obtained with γ-Al_2O_3.

An interesting method [A28] reacts Al_2O_3 with BN at ~1850 °C/1 h (molar ratio between 82/18 and 77/23). The resulting powder is free of carbon, unlike what is obtained by carbo-nitridation. The low temperature (950 °C) synthesis path, which generates AlON, is a vapor phase reaction involving the nitridation of $AlCl_3$ [A28]. The procedure was reported only for thin film obtainment; aluminothermic reduction followed by nitridation was also examined [W14].

4.2.2.2.3 Green Parts Forming. Sintering

When normal sintering is used, the comminution of the synthesized AlON is a major challenge, owing to the high calcination temperatures (≥1700 °C). In the case of raw material obtained by the method described in [I14, S29], we had to use long (~2 hour) attrition milling and tetragonal zirconia polycrystals (TZP) balls to obtain powders with average particles size smaller than 5 μm; the milled materials retained 0.2–0.4% ZrO_2. The zirconia, while a relatively efficient GG inhibitor, further reduced the densification rate of an already low sinterability material; densification of the powder did not allow obtainment of transparent pieces. As of today milling with super dense Al_2O_3 balls is possible and this markedly reduces the amount and nature of deleterious impurities introduced. Sintering at ~2000 °C, under N_2, of pressed powder, gave specimens (0.5% MgO) exhibiting an alternation of translucent regions with ones exhibiting somewhat higher transparency. Besides pressing, liquid-state forming procedures could also be used, including specimens for reaction sintering (AlN hydrolysis can be prevented by coating [K66]). Good quality green discs have been obtained by slip casting, filter pressing, and even injection molding. The reaction sintering approach allows the use of submicron starting powder, which can be thoroughly mixed. It is customary to add sintering additives, most of them being previously examined in relation to the sintering of alumina. MgO, Y_2O_3, and La_2O_3 alone, or combined, are the most popular [G19]. Dilatometry

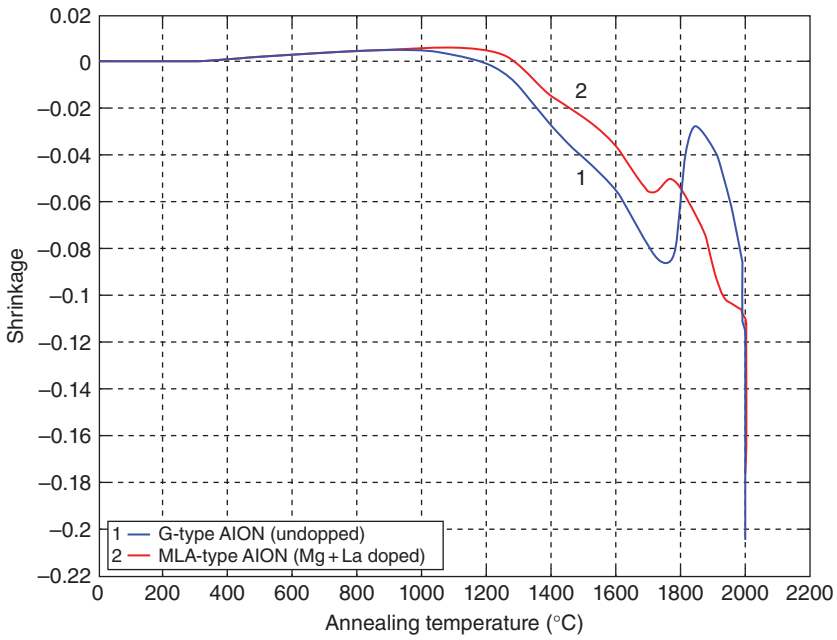

Figure 4.25 Shrinkage during dilatometric heating of two AlON powders. Source: Courtesy of H. Asucah, Israel [A28].

shows that in the temperature range where AlON forms, expansion ($\Delta V \sim 6\%$) occurs (see Figure 4.25).

This is a consequence of the difference between the reacting materials cell volume and that of AlON. When a standard 9 : 5 mixture is used, one has $9V_{Al_2O_3} + 5V_{AlN} = 486.6\,Å^3$, while V_{AlON} is $502.1\,Å^3$. The microstructure is disturbed by this marked volume increase, leading to pore size increase, stress formation, and, possibly, microcracking. The ΔV is much reduced (under 1%) when a mixture of La_2O_3 and MgO is added [A28]. The ΔV reduction is important because its consequences are deleterious for densification. A similar effect appears also when reaction sintering of $MgAl_2O_4$ or $ZnAl_2O_4$ is effectuated, but in the case of YAG processing – where the formation of YAM is accompanied by a negative ΔV – sintering is not hampered by the preceding reaction. The uptake of carbon is another process (relevant for both normal and reaction sintering) with negative influence of sinterability; it can be solved by using furnaces, which do not contain graphite parts. While not indicated by the phase diagrams, nitrogen loss starts to be noticeable over 1850 °C, especially when dwells of 15–20 hour are used for sintering. The addition of sintering aids seems important for transparency achievement not only in the case of reaction sintering (see above effect on ΔV) but in all densification approaches. Little is known about the mechanism(s) on which their influence is based. For the case of regular sintering, Hart et al. [H12] speculate that liquid forming is involved. They point out that BN specimen containers are required so that B-containing vapor can react with the additives to produce liquid. Whether this happens or not is difficult to say, but the team that proposes this explanation was able to produce large size, highly transparent AlON plates. In fact, to the best of our knowledge, the technology(ies) developed by Raytheon are the only ones able to generate commercial parts exhibiting the combination of properties requested by the main applications. It was attempted to reaction sinter AlON also by the aid of MW heating. Translucent discs ($T \sim 40\%$ at 650 nm) could be obtained after sintering (N_2) for one hour at ~1800 °C [C24]. Pressureless sintering of MgO-doped powder, at temperatures under 1800 °C, succeeded in generating quite transparent small thin plates [S73].

4.2.2.3 Characteristics of Densified Parts

In Figure 4.26a [A29], the XRD pattern of a translucent polished AlON disc is shown. In Figure 4.26b the electronic diffraction pattern is given.

A transparent AlON plate (produced by Surmet) has a chemical composition indicating 57% Al, 38% O, and 5% N. The microstructure, as revealed by SEM, is shown in Figures 4.27–4.29.

The $\overline{GS}$ is ~180 μm. The pore size and location in a translucent specimen ($T_{700\,nm} \sim 20\%$) is shown in Figure 4.28. The transmission of a 5 mm thick Surmet plate is shown in Figure 4.29.

Some of the AlON properties, important for applications, are given in Table 4.6; the data refer to

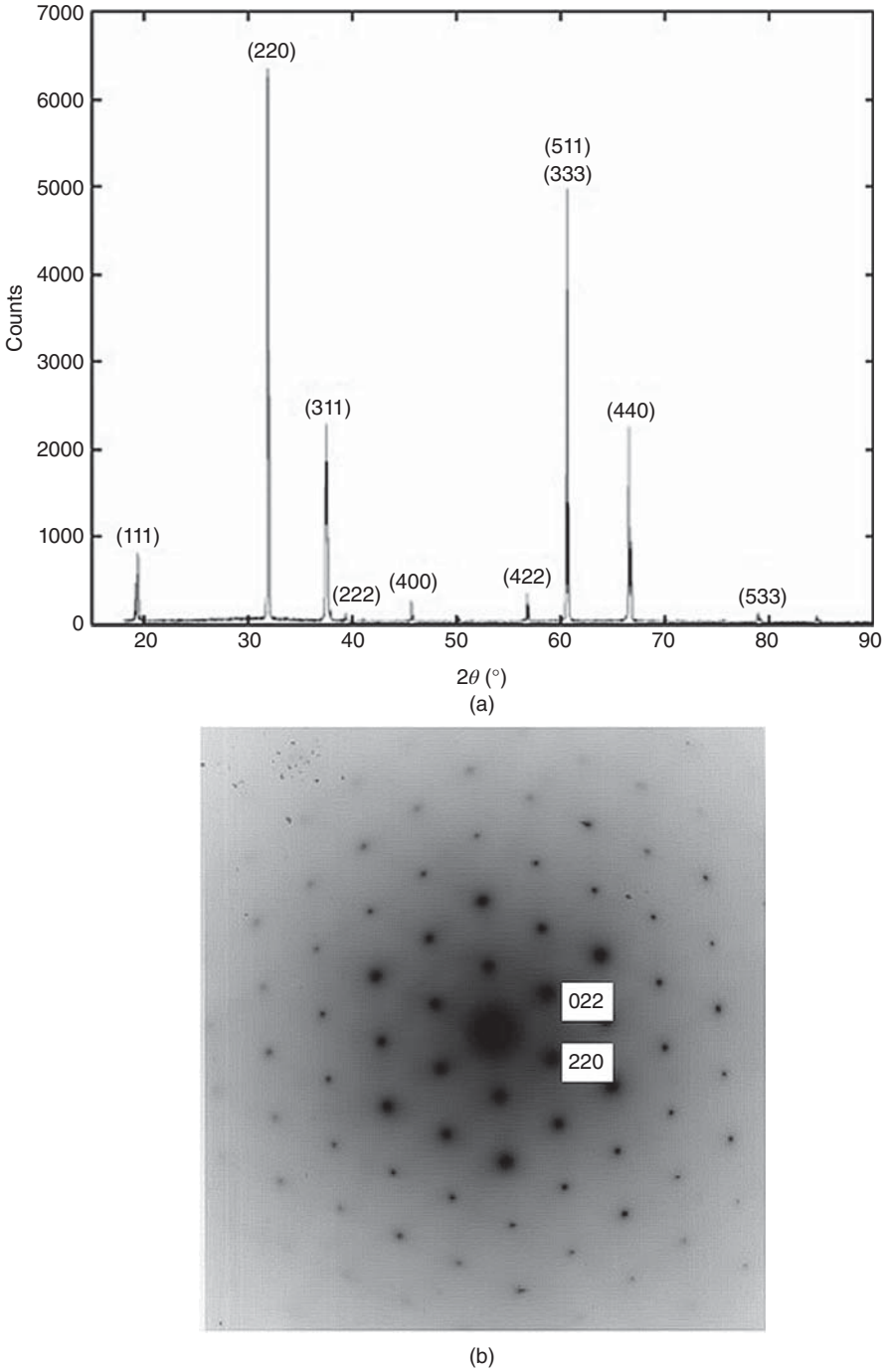

Figure 4.26 Diffraction patterns produced by translucent AlON specimens. (a) XRD. (b) Electron diffraction. Source: Courtesy of H. Asucah, Israel [A28].

highly transparent parts produced based on Raytheon technology.

The behavior of AlON, under high velocity impacts, was examined by *E*. Strassburger on specimens produced by a US army research team [M22, M23]. In Figure 4.30 [M23], the event of an edge-on impact of a steel ball on AlON plate is imaged by the aid of high speed photography; the images are compared with the prediction of an FEA simulation.

4.2.3 Transparent and Translucent Alumina

Polycrystalline α-Al_2O_3 (corundum; PCA) sintered parts constitute one of the oldest, most important,

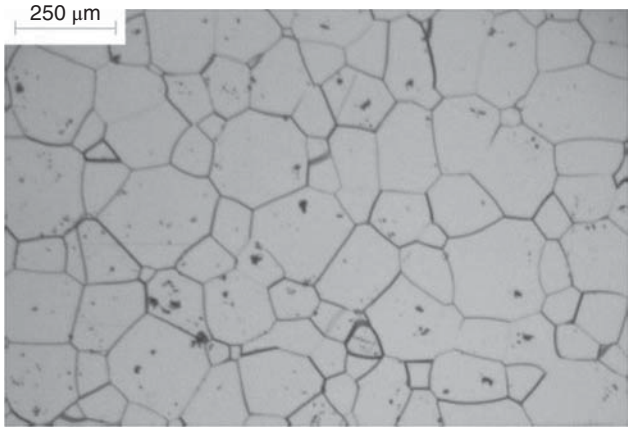

Figure 4.27 Microstructure of dense AlON (polished and etched surface). Source: Courtesy of H. Asucah, Israel [A28].

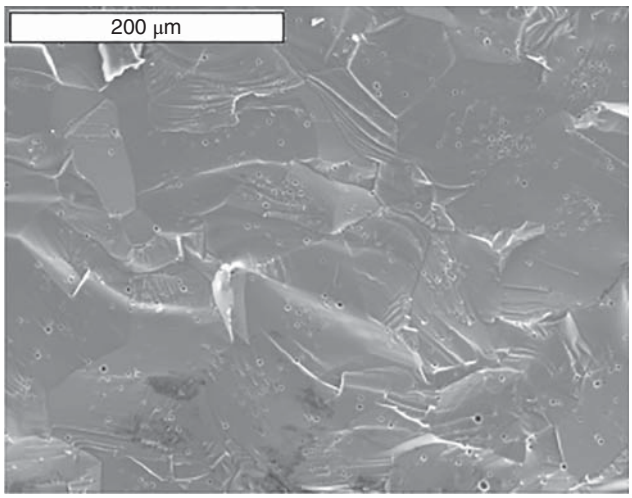

Figure 4.28 Microstructure of dense AlON (fracture surface). Source: Courtesy of H. Asucah, Israel [A28].

and ubiquitous family of technical ceramics, which, owing to its outstanding thermal, mechanical properties, and chemical inertness, finds many applications. By the end of the 1950s, it also was the first technical ceramic obtained in a sufficiently dense state to exhibit a significant level of visible range transmission (high translucency) [B67] with a thickness of about 1 mm.

4.2.3.1 Structure

Corundum is not a material suitable for production of highly transparent ceramics owing to its non-cubic lattice symmetry. Figure 4.31a displays the α-Al_2O_3 lattice shape. Figure 4.31b shows the ions packing in a basal plane.

In terms of spherical ion arrangements, this oxide lattice consists of large oxygen anion array, stacked in an A–B–A–B sequence so as to form a hexagonal close-packed structure. The Al^{3+} cations are located within a 2/3 fraction of the octahedral voids so as to achieve charge neutrality against the oxygen anions (formally O^{2-}). Considering the position of the vacant cation sites within a layer, a given cationic layer is repeated only after the sixth oxygen layer. The Al^{3+} cations and O^{2-} anions have first sphere coordination numbers of 6 and 4, respectively. For this coordination the ionic radii are $r_{Al^{3+}} = 0.54$ Å and $r_{O^{2-}} = 1.38$ Å. The crystal lattice is trigonal (rhombohedral) belonging to the #167 space group D^6_{3D} ($R\bar{3}2/c$). The lattice parameters are $a = 4.7591$ Å and $c = 12.9894$ Å, and the unit cell contains four formula units. The theoretical density is $TD = 3.9862\,g/cm^3$ [A23]. There are six cubic or quasi-cubic other polymorphs labeled gamma (γ), delta (δ), eta (η), theta (θ), kappa (κ), and chi (χ). Only the η polymorph is fully cubic, with a lattice constant $a = 7.94$ Å. The γ-Al_2O_3 easily forms solid solutions with magnesium spinel $MgAl_2O_4$. In Section 3.1.5 devoted to sol–gel processing, it has been shown how, despite higher porosity, the method can be used to fabricate transparent bulk parts from gamma alumina gels.

4.2.3.1.1 Utility of T-PCA

At first sight the section above means that PCA is of little practical interest within the field of transparent ceramics. In reality, however, highly translucent (or moderately transparent)ceramic aluminas (T-PCA) find a large volume use as envelopes for the popular high pressure Na lamps (16 million sold/year during the 1960s; decorative objects were also produced [C32]), owing to its excellent chemical and thermomechanical properties. For the lamp-related application diffuse forward transmission is an advantage, as long as the total transmission remains reasonable. Therefore considerable effort was invested in the development of procedures allowing the fabrication of pore-free, fine grain size (see Section 2.1.3.4 for effect of *GS* on the transmissivity of T-PCAs) alumina. As it will be detailed in Chapter 5, T-PCA-based parts were shown as competitive in IR dome and even armor application (owing to the fact that quite thin layers are good enough for strike–face production) [P9, S61]. Remarkably large RE^+-type cations (like Tb, Er, and Ce) or smaller TM^+ ones (Ti^{3+} or Cr^{3+}) could be pushed into T-PCA grains, in modest amounts (mostly segregated at the GBs), but in some cases big enough, to elicit fluorescence signals (e.g. [D20, L32, L33, P21]). Remarkable is the fact that the radius difference between the cations involved in such exchanges may be close to 100%, viz. much over the limit (15%) considered as allowing easy substitutions. It is very likely that RE^+ cation penetration leads to local lattice modification like host–site distortion, modification of the chemical bond characteristics, formation of vacancies, etc. The

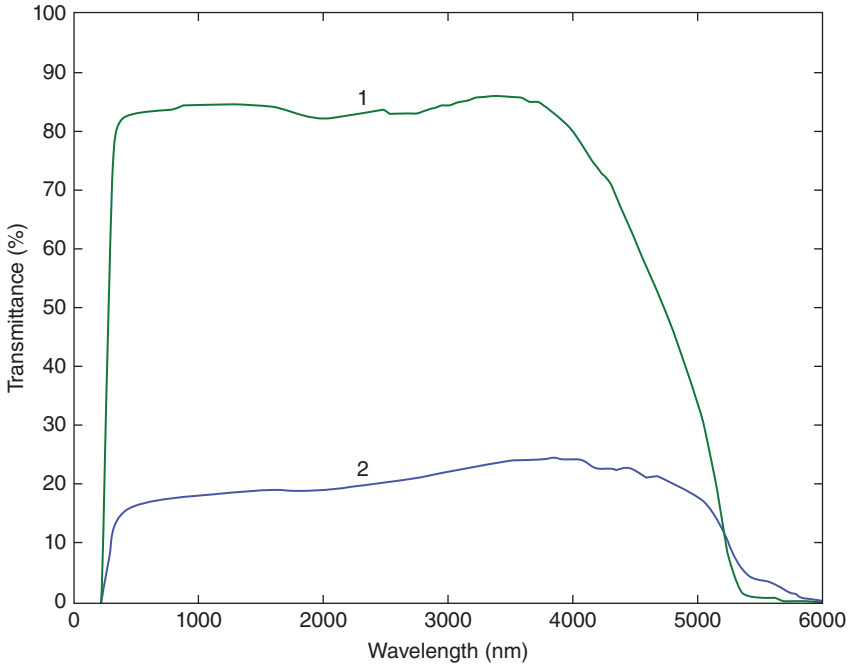

Figure 4.29 Transmission curves of commercial (Surmet) plate (2) and specimen produced by the author of A28 (1). Source: Courtesy of H. Asucah, Israel [A28].

Table 4.6 Properties of AlON ceramics.

Property (unit)	Value
Density (g/cm^3)	3.69
a_0 (Å)	7.946
E (GPa)	330
Shear modulus (GPa)	135
HK0.2 (GPa)	18
K_{IC} (MPa m$^{0.5}$)	2.0
TRS (MPa)	~350
λ_{th} (W/(m K))	9.62 (at 75 °C)
α_{30-200} (°C^{-1})	$5.65 \cdot 10^{-6}$
ε_r (1 GHz)	~9.2
tan δ	3×10^{-4}

insertion of such cations into corundum lattice affects also the way the sintering process plays out [M16]. Further progress in controlling this process may be of interest in applications like phosphors or scintillators or (more difficult but not impossible) gain media, owing to the robustness of the host. The considerations made right above may apply also to other (cubic) hosts like spinel.

4.2.3.2 Processing of Transparent Ceramic Alumina

4.2.3.2.1 Raw Materials

Some of the conventional powders, derived by the aid of the Bayer process from bauxite, could be comminuted enough ($\overline{GS} \sim 0.5$ µm) to generate materials usable in TC's processing. The impurities level was maintained under 500 ppm, a level acceptable only for some of the less demanding, in this respect, applications (e.g. armor windows). In most cases, however, more fine and pure powders, prepared from pure Al salts (ammonium alum, alkoxides, ammonium dawsonite) by wet chemistry, are used [B36]. Thus the current wet chemistry powders are of the 4N type (i.e. 99.99% purity), having as main impurities Na (K), Si, and Mg and exhibiting specific surface areas of 5–15 m^2/g. The basic crystallites of the wet chemistry materials are more isometric than those milled, which exhibit a more plate-like morphology. The former tend, however, to aggregate in two to three level spheroidal aggregates as opposed to the coarser powders, which exhibit a remarkably large faction of individual basic particles. Of course, the calcines of wet chemistry-prepared materials also require milling, but the deagglomeration process is more simple than in the case of spinel powders. The particles size of such raw materials is in the 0.15–0.3 µm range.

4.2.3.2.2 Processing

The alumina (which adopts, at temperatures over 1100 °C, the corundum, viz. α-Al_2O_3, polymorph state) melts at a quite high temperature (~2050 °C), owing to the strong bonding (which has ionic, predominant, and covalent character) between the lattice atoms. The high ionic strength of Al^{3+} makes cationic diffusion within the corundum lattice slow. Such features suggest that advanced densification is not easy to achieve and is

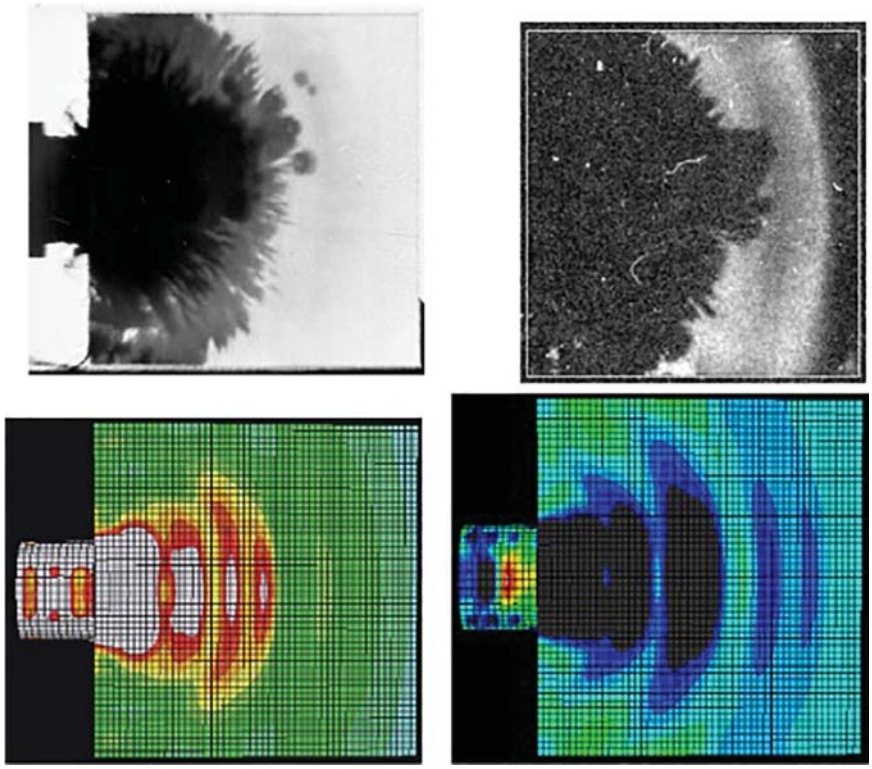

Figure 4.30 Imaging of an edge-on impact between a steel ball and an AlON plate; comparison with the results of FEA model; two penetration stages. Source: From McCauley and Patel 2013 [M22].

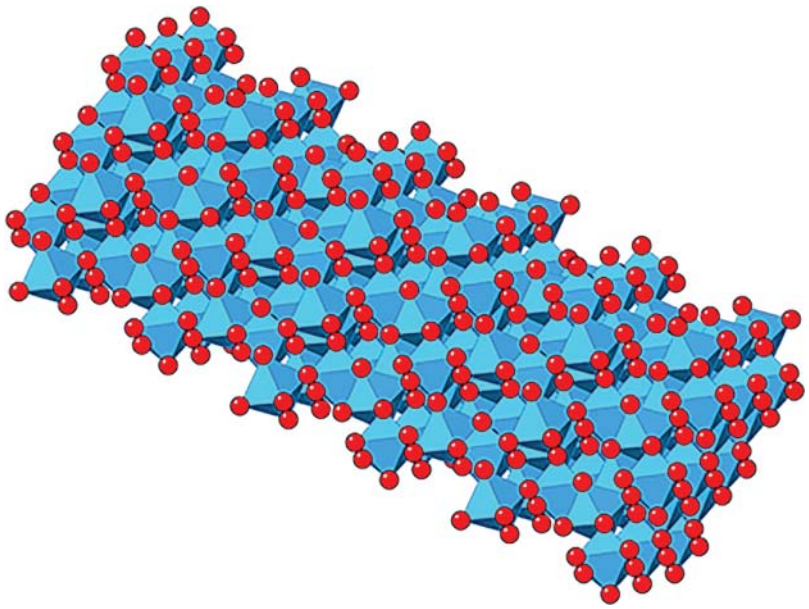

Figure 4.31 Lattice structure of corundum (α-Al_2O_3); oxide ions in red. Source: Reproduced from Shutterstock Images with purchased permission.

likely to require high temperature. Indeed, the first fully sintered alumina exhibiting significant transparency required long sintering under H_2 at temperatures of ~1900 °C [B67]. However processing improvements made significant reduction of sintering temperatures possible. Currently T-PCA is obtainable at temperatures as low as 1050 °C, under certain conditions [K41]. The sintering temperature exerts a significant influence on the characteristics of densified alumina [K69]. A specific problem posed by alumina densification is a tendency toward abnormal grain growth, which leads to early and massive pores occlusion. The occluded voids could not be fully eliminated by processing high purity alumina even when very fine powders were used. Cahoon and Christensen [C2] observed that accidental MgO impurities were effective in suppressing the formation of very

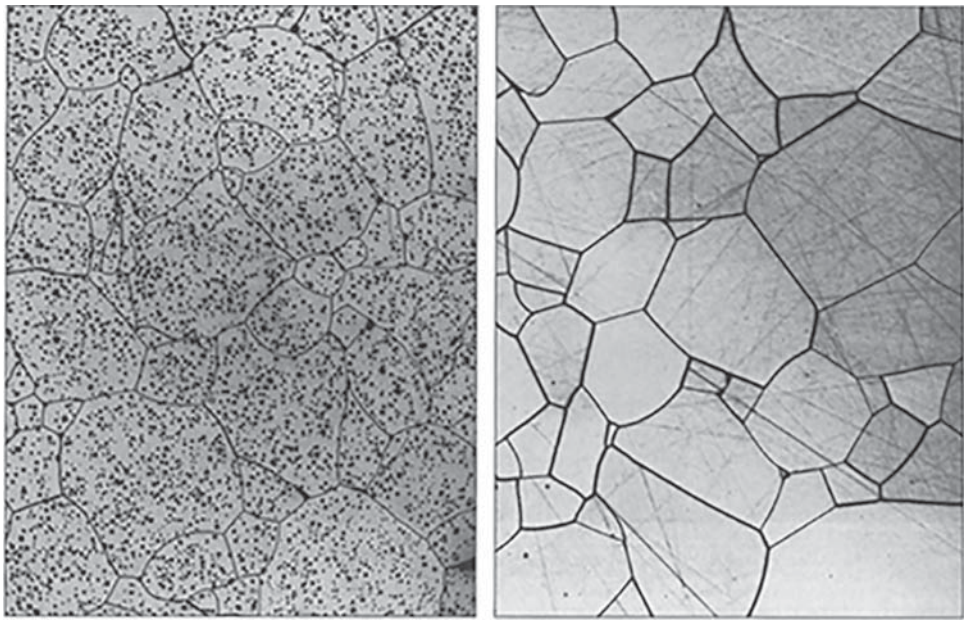

Figure 4.32 Microstructure of dense alumina ceramics (derived from highly sinterable and pure Linde grade A powder) fabricated by General Electric (1958). (a) Undoped powder; abnormal grain growth and ensuing trapped porosity are observable. (b) MgO-doped alumina ceramic with no trapped porosity; parts exhibit significant translucency. Source: Adapted from Burke 1996 [B67].

large grains during Al_2O_3 firing. Coble then purposely introduced ~0.3% MgO in an ultrapure, alum-derived, submicron alumina powder (Linde grade A) and was able to obtain practically pores free alumina, albeit made of grains of quite large average size [B67]. The microstructures of a MgO doped and a pure Al_2O_3 are compared in Figure 4.32 [B67], while their respective transparency level is shown in Figure 1.3.

The MgO effect was studied by many, following Coble, e.g. [P20]; it proved to be a useful sintering aid also when HPing was used. Many other additives, like CaO, SrO, ZnO, and ZrO_2, were examined without anyone being effective [R22]; $MgAl_2O_4$, as well as MgO, was also found useful and so was, to a lesser extent, NiO. It is widely accepted that the main effect of MgO is on grain boundary mobility. Its reduction leads to a general slowing down of grain growth, but, probably more important, makes it much more uniform, reducing the number of abnormal size grains, which form in a random way. Details of the way MgO accomplishes its effects are still a matter of debate. The difference in radius between Mg^{2+} ($r_6 = 0.72$ Å) and Al^{3+} ($r_6 = 0.54$ Å) is quite large, but in the case of Mg-spinel, it is known that significant fractions of the bivalent cations occupy octahedral Al^{3+} sites. Therefore theoretically one may expect some solubility of Mg^{2+} in the corundum lattice. Measurements have shown that indeed a small amount of Mg^{2+} ion enters the alumina lattice but strong segregation to the GBs occurs, starting from very low impurity cation concentrations [C32]; spinel particles (able to pin GBs) were identified at MgO concentrations able to ensure transparency achievement. Drag of the GB, performed by the Mg^{2+} located in the GB region and possibly assisted by that, owed to the spinel clusters located at the same grain boundaries, is almost surely one, if not the most, important factors, slowing down the grain growth. As a result, of the drag, pore/GB contact is maintained toward higher densification levels than in pure alumina. Coble suggested that Mg enhances pores drag by changing the equilibrium pore shape (by changing surface energy values). So Mg^{2+} may reduce the dihedral angle so that a larger area of GB intersects the pore. Magnesia also may increase surface diffusion rates, thus increasing pore mobility and retarding pore/GB separation. J. Peelen [P20] suggested a double pronged action pattern of the dopant. The fraction becoming a solute distorts the lattice, thus enhancing native ion's self-diffusion. He also considered that the insoluble fraction reacts with the grains and generates spinel fine particles, which pin down the alumina grains. In our view the Mg^{2+}'s ability to reduce surface energy differences (as a function of their crystallographic orientation) and possibly also those of the GBs may constitute an additional beneficial influence. It would reduce the tendency of certain planes to create higher mobility GBs, thus leading to discontinuous grain growth. It is probable that in the case of Mg^{2+} all these factors contribute to pore occlusion reduction, their interaction being optimized in comparison to what

other additives provide. Whatever the mechanism(s) of action MgO is even now a standard addition to the powders used for T-PCA production. Research that followed conducted by Coble and colleagues, at GE, showed that besides abnormal grain growth, another problem may be constituted by bloating, especially for large parts. Bloating is caused by gas trapped in the shrinking pores. Atmospheres based on gases soluble in alumina like H_2 or O_2, but much less Ar, or even the small molecule He, or vacuum, allowed achievement of higher density owing to their ability to diffuse out of the closed pores to the macroscopic surfaces of the part. For instance, Ar – which filled residual open porosity left by the PS stage (PS + HIP processing), subsequently closed by HIP – made full densification impossible. It did not leave the pores during HIP [C38]. It was [Y17] also shown – for the case of firing temperatures lower (1350–1550 °C) than those used by the GE team – that occlusion propensity is rising with *GS* also in the case of normal grain growth. Occluded pores, when not too large and/or numerous and located close to GBs, can be eliminated by HIPing. When $\overline{GS}$ becomes too large, however, even high pressure HIPing is not effective. Kang showed, in this context, that it is better – in the pressureless stage of a sinter/HIP approach – to sinter at a lower temperature if, by doing so, one can maintain a significantly lower $\overline{GS}$, during the last stage of sintering. Such a microstructure would reduce the number of occlusion events and maintain a shorter average grain boundary to pore distance; the size of all pores will be minimal. Thus the optimal sintering temperature is not the one that gives the highest *BD*, before HIP, but that produces the optimal microstructure (pore size and location). These results are similar with what we found later in the case of spinel (A. Goldstein, unpublished results). The use of vacuum firing allows a reduction of sintering temperatures (from 1850–1900 °C) to less than 1700 °C. For instance, after sintering at 1670 °C/5 minutes, a submicron powder, discs ($t \approx 0.5$ mm) exhibiting a residual porosity of ~20 ppm, and a $\overline{GS}$ of ~10 μm coupled with a transmission of 37% ($\lambda = 700$ nm) were obtained. At 1670 °C, for higher *GS*, the transmission increased to 50%. It has to be noted that regarding transmission values, comparison of values given by different authors is difficult. Many results labeled "in-line" are in fact measured in conditions that lead to collection also of light pertaining to the scattered fraction; this is also the case in the paper now discussed. A massive reduction of the t°_S and, in consequence, of the *GS*, could be obtained by combining green-body structure optimization with the use of pressure assistance during sintering [H17, K41, K50, K57]. The *GS* reduction, from >100 to less than 1 μm, allowed significant improvement of the mechanical properties, with *HV*10 raised to ~22 GPa and TRS to 7–950 MPa for $\overline{GS} \sim 0.5$ μm. The further reduction of $\overline{GS}$ to 0.4 μm allowed the simultaneous achievement of excellent mechanical properties and RIT values of ~60% at $\lambda = 640$ nm and $t = 0.8$ mm [K57, P9]. The improvements regarding green state processing (see Figures 3.50–3.54 in section 3.2.1.3 and 3.2.2) allowed the obtainment of low average size, narrow distribution pore populations, simultaneously with compact material arrangements (BD_g 54–60%*TD*; the green-body microstructure was **uniform** throughout the volume of the parts at both microscale and larger scale. The morphology and surface chemistry of corundum particles makes them, in relative terms, one of the most "friendly" as far as green-body forming is concerned. Suspensions of up to 50 vol% solid can be prepared with relative ease using peptization control by pH (and/or deflocculants). Not only by pressure filtration and gel casting but also by pressing could green densities $BD_g = 56$–62%*TD* be attained while maintaining uniform, narrow size distribution porosity, with $X_P = 30$–55 μm [K57, K58]. A key element was the selection of suitable powders and dopant addition methods allowing uniform distribution of the additive. Fine (basic particles <0.5 μm) of pure alumina powders and suitable means for agglomerates breaking were available as early as 1950s. Identification of the right powder requires usually tedious experimental work. Progress in green structure came mostly from more informed raw material selection, better pressing, and harmonization of powder characteristics with the forming methods. Significant advances were made also regarding the forming methods themselves. It may be noted that on the average the alumina powders are easier to deagglomerate than those of Mg-spinel. Currently powders with basic particles (~80 nm) are also available. Both spray drying and spray freeze drying-based granulation methods leading to performant RTP granules were developed [S68]. Gel and high pressure slip casting forming methods allowed forming of highly sinterable green-bodies; the high quality green bodies allowed significant sintering temperature reduction. In Figure 4.33 this is illustrated. The figure shows the progress achieved by forming techniques which lead to an optimal green-body configuration, allowing complete pores elimination during sintering. Thus, Figure 4.33a compares opaque (white) and transparent Al_2O_3 grades, both made from same, fine and well processed powder, enabling quite similar grain sizes of the sintered 100×100 mm^2 tiles (white: 0.7 μm, transparent 0.55 μm [Figure 4.33b]) with similar hardness HV10 = 20–21 GPa. The one structural difference that gives rise to transparency is a residual porosity of about 0.3% in the white but <0.03% in the transparent ceramic (better densified and which also exhibits a higher bending strength of 709 ± 49 MPa

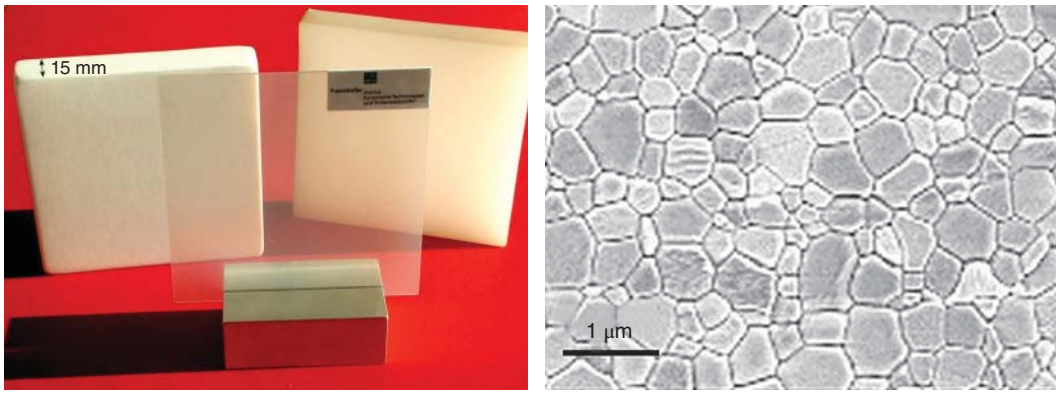

Figure 4.33 Effect of residual pores content (a function of green body sinterability) and plate thickness on transparency of alumina ceramics. Specimens produced at Fraunhofer IKTS, Dresden (grain size of ~0.5 µm and HV10 ~ 20 GPa). (a) Imaging: Transparent plate ($P_o < 0.03\%$; t = 0.8 mm; RIT at 640 nm = 60%) and thicker tiles behind: Left side ($P_o = 0.3\%$; opaque), right side ($P_o = 0.03\%$; translucent). (b) Microstructure of the transparent alumina plate imaged in (a). The white body was shaped by powder *pressing*, the light transmitting grade by *gelcasting* of the same powder. Source: Krell et al. [K57]. Reproduced with permission from Goeller Verlag.

vs 526 ± 55 MPa of the opaque grade) [K57]. The translucent plate on the right side of the figure is made in the same conditions as the transparent part; the two items differ only regarding the thickness of the plate. Comparison of these two items reveals the way an increasing thickness influences transmission; however for items lacking radiation attenuating constituents a thickness increase does not affect transmission. Observe that the low sintering temperature, at which the optimal green-body allows complete pores elimination, allows combination of transparency with high level mechanical properties (a consequence of the fine microstructure).

Other parts also derived from fine powders by the technology developed at CeraNova [P9] exhibit the high transmission shown in Figure 4.34a (the specimen microstructure is shown in Figure 4.34b).

Considerable effort was invested in the examination of the PECS as a firing procedure for T-PCA [G37, K11, L1, L7, R34, S30, Z5]. Transparent alumina could be obtained at temperatures in the 950–1300 °C range, but the pressures employed ranged in the 80–500 MPa interval. In conventional HPing, the range of pressures used extends from 20 to 50 MPa. As in the case of MW firing, it is debated whether "nonthermal" effects act during PECS.

Like Langer et al. [L7], currently we think that PECS is an efficient form of HPing (heating pattern, high pressure). It is difficult to see how in high breakdown resistance insulators, like Al_2O_3, the low PECS voltages may have effects. In any case practically useful results have been achieved, applying this method to various types of alumina powders. One example is shown in Figure 4.35. Another processing operation relevant for the green-body forming stage, which, in principle, may bring birefringent materials almost on a par with cubic ones, as far as TC fabrication is concerned, is the orientation of particles prior to sintering. In the case of α-Al_2O_3, the crystal habitus is quite favorable for such operations (certain orientations). The orientation method examined for the case of α-Al_2O was the magnetic interaction between a very strong external field and the weak magnetic momentum of the material particles [S75]. The principle of the method and results achieved were described earlier (see Section 3.1.2.2.3).

Mullite ($3Al_2O_3$ $2SiO_2$), a compound based mostly on alumina, and translucent ceramics were also developed [P33]; transparent glass-ceramics having this compound as its crystal phase will be described in Section 4.2.11.3, which deals with this kind of material.

4.2.3.3 Properties of Transparent Alumina

In Table 4.7 the properties that T-PCA parts can offer, together with optical transmission, are given.

4.2.4 Transparent Magnesia and Calcia

Chronologically MgO is the second polycrystalline system (1962), a ceramic that is obtained in a transparent state (after Al_2O_3) [B27, R20, R23]. Being cubic, the levels of transmission (VIS) attained, at thickness levels larger than 1 mm, were significantly higher than in the case of alumina. The material exhibits, as a specific feature, an exceptionally high thermal conductivity (for an oxide); at 50 W/(m K), it is double that of a good alumina and triple of that of spinel. Practical applications were found in the field of optical components for the IR range. The processing leading to transparent MgO and the properties of resulting parts are presented in this section. MgO is a relatively useful TC in its own right but not one of

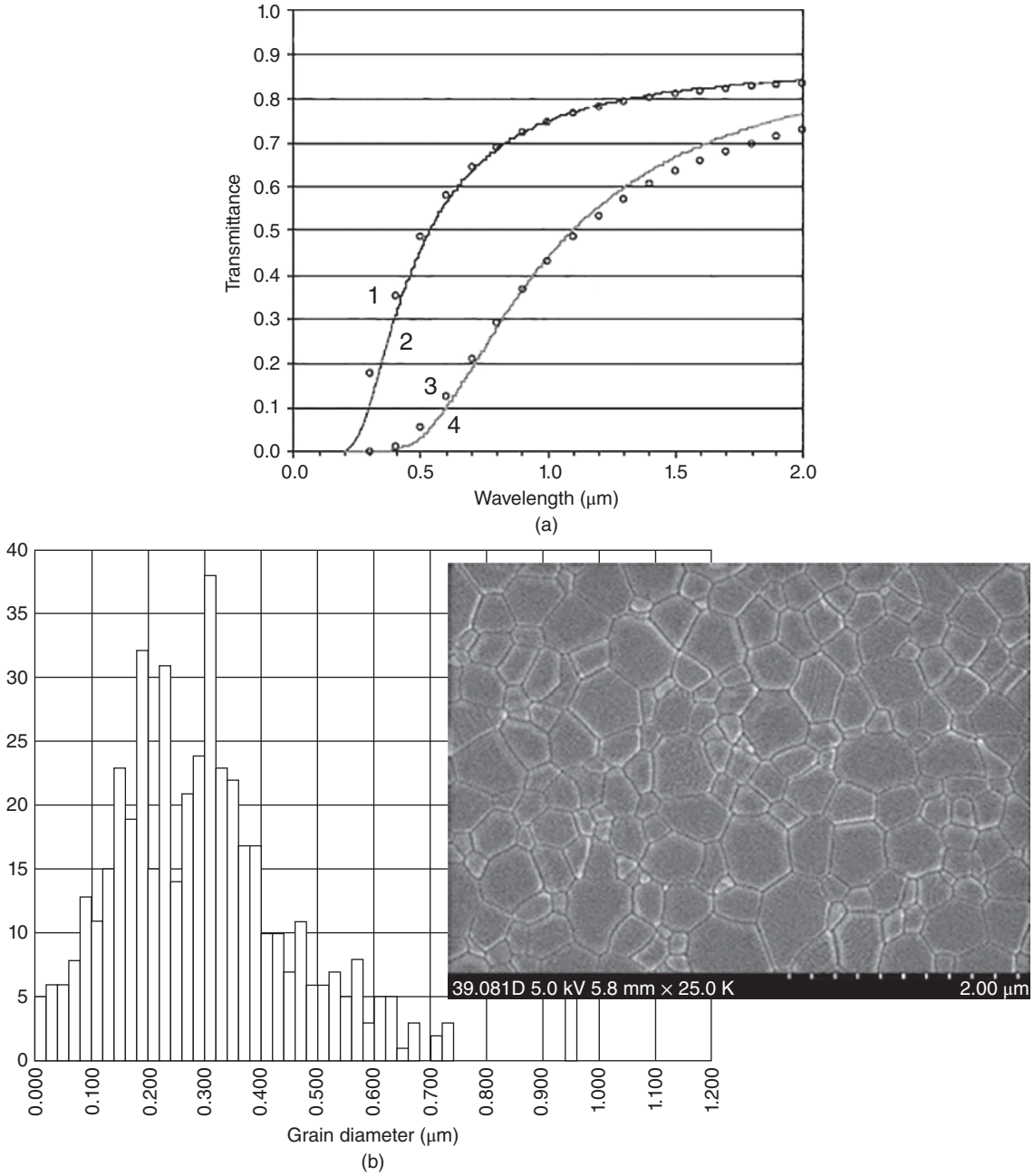

Figure 4.34 Characteristics of transparent alumina parts fabricated by the technology developed at CeraNova. (a) Transmission spectra of parts having an average grain size of 0.4 μm. 1, 2 – plate of 1 mm thickness 3, 4 – plate of 5 mm thickness (1, 3 – experimental data; 2, 4 – calculated curves). (b) Grain size distribution in the microstructure of the parts (SEM imaging and histogram). Source: Parish and Pascucci [P9]. Reprinted with permission from SPIE Publishing.

outmost importance. However regarding its processing, details will be given also for a method (hot pressing) that was not developed to a level permitting fabrication of very transparent parts. This is done because aspects of this method (especially certain sintering aids) were used later, by its developers, with great success in the fabrication of highly transparent spinel – one of the most important TCs. It is an example that teaches us that sometimes a discovery looking like a dead-end when it emerges may change its status in the future.

4.2.4.1 Structure

Magnesium oxide MgO is the basis of a mineral named periclase. Its crystal is rock salt cubic type with a lattice period $a = 4.212$ Å. The lattice is face centered cubic belonging to the #225 O_h^5 ($F4/m\bar{3}2/m$) space group, and

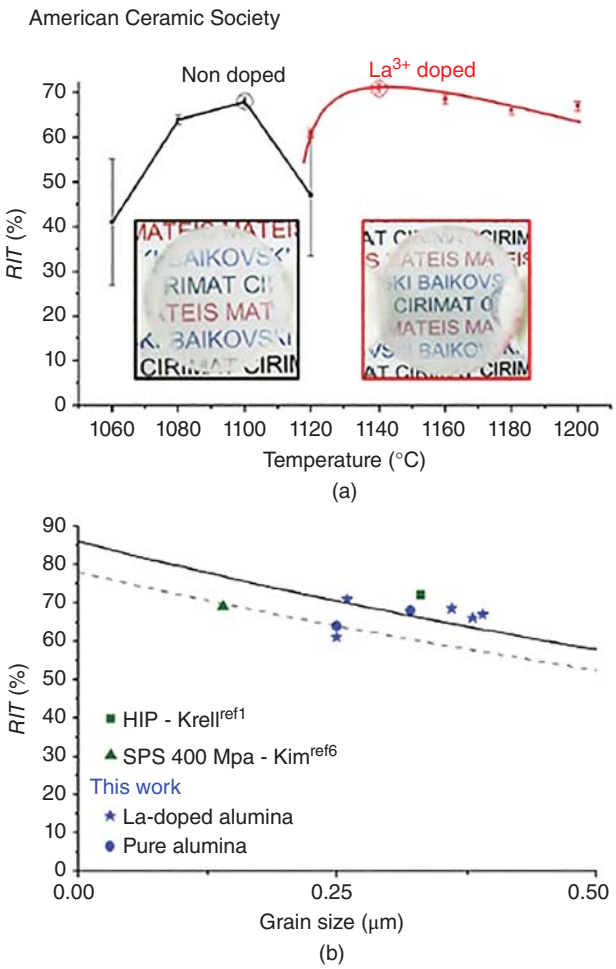

Figure 4.35 Characteristics of translucent alumina discs fabricated by PECS. (a) RIT as a function sintering temperature and doping status. (b) RIT as a function grain size. Source: Roussel et al. 2013 [R34]. Reproduced with permission from John Wiley & Sons.

the unit cell contains four formula units. The bonds are considered 80% ionic. Both ions are sixfold coordinated with the nearest neighbors located at the vertices of a regular octahedron. The hexa-coordinated Mg^{2+} cation radius is 0.72 Å and that of the O^{2-}anion is 1.35 Å. A semiconducting phase of Mg_3O_2 exists at very high pressures.

4.2.4.2 Raw Materials and Processing

Powders: Quite suitable powders were already available in the late 1950s when interest in transparent MgO started. The initial studies regarding T-MgO obtainment, used mostly carbonate-derived powders of sufficient fineness (30–200 m^2/g) and reasonable purity as far as cationic impurities are concerned (Si, 50–120 ppm; Ca, 100–150 ppm; Fe, <50 ppm). The most damaging impurities were the anionic adsorbates, like CO_3^{2-}, OH^-, H_2O, or SO_4^{2-} (for sulfate-type raw materials). Even higher purity (up to 99.999%) nanopowders (A up to 400 m^2/g) became available later. Most powders were synthesized by wet chemistry (from chlorides, oxalate; mostly precipitation) or other techniques, like laser ablation [J3, T28].

Table 4.7 Properties of alumina ceramics.

Property	Value range
n	1.78
TD	3.987 g/cm^3
TRS (3 point bending)	450–800 MPa ($GS \leq 1$ μm)
$HV10$	14–21.5 GPa (depending on GS)
E	~400 GPa
ε_r	8.5–9.5
T % (average); Δn, n(average)	~84%; 0.008; 1.76

The nonoptical properties of T-MgO suggest it can be useful for various applications and therefore considerable effort was spent for the development of suitable processing route(s). Thus, it was tried to obtain T-MgO by approaches like AS, VS, PS + HIP, MWS + HIP, HP + air annealing ($t°_a$), or, more recently, PECS. Initial AS tests (on high purity but low sinterability powders) were conducted on low density green compacts [A30], at temperatures of ~1400°C/2 h; they were not able to achieve high densification levels (BD_A~63%TD). Increase of $t°_S$ (up to 1700 °C) raised BD_f, but modestly. Interestingly these early attempts detected the beneficial effect of Li compounds, including LiF. An elegant hypothesis by S. Tacvorian was advanced to explain the effect of LiF [T1]. The lattice structure similarity between MgO and LiF leads to solid solution formation, in the external layers of the oxide particles. As a result of the more disordered system (vacancies), ion diffusion and thus densification rates are enhanced. In hindsight however it is clear that more important was the lubricating action of LiF and some other halides (0.25% LiCl raised the BD_g of pressed powder compacts, from 46%TD to 57%TD), which melted at low temperatures. At the end of these studies, BD_f levels around 95%TD were achieved at 1400 °C. Their main contribution to T-MgO obtainment was to attract attention to the sintering aid potential of certain alkaline metal halides, LiF among them. It was also tried to enhance the sinterability of MgO in a way similar to what was done in the case of Al_2O_3 by MgO addition, i.e. by introducing a grain growth inhibiter. Banerjee and Budworth [B11] considered that 0.25% NaF can fulfill such a function. Firing under O_2-enriched air, at 1600 °C for ~100 h, small discs (BD_f = 99.3%TD; $\overline{GS} \cong 30$ μm) exhibiting moderate translucency were obtained; a fine oxalate-derived powder was used in

those experiments. The study underlined the necessity of thorough particles surface "cleaning" (from CO_3^{2-}, OH^-, and other adsorbates) by long 12 h dwells at 600 °C. The results also indicated that grain growth inhibition alone, while helpful, cannot provide high transparency. CaO used for the same purpose, in PECS-type sintering, has a moderate influence, like NaF [T28].

Vacuum sintering: by vacuum sintering densities >99%*TD* could be obtained at 1450 °C and levels leading to significant transparency albeit not excessive were obtained [M36]. Simultaneous use of SiO_2 and B_2O_3 as sintering aids was necessary.

Hot pressing: The first, relatively efficient way, to produce T-MgO proved to be HPing of LiF containing powder. Hot pressing of pure MgO led initially to fine microstructure and high densification levels [V5] when performed at high (yet in the $^2/_3\, t_f^\circ$ range usually needed for advanced densification of oxides) temperature (1700 °C) at pressures in the 60–70 MPa range. The use of high pressure (~350 MPa) allowed reduction of sintering temperatures to as low as 850 °C, as shown by Carnall [C7, C8]. Parts thus fabricated exhibited noticeable levels of transparency, especially in the IR range (see Figure 4.36).

Under 6 GPa T-MgO was achieved, even at *RT*. Pressure needed, when firing around 1000 °C, could be substantially reduced (down to ~80 MPa) by adding one of the sintering aids suggested by the AS experiments: LiF [R23]. While LiF's efficiency, in the case of pressureless sintering, was moderate, it proved to be a much more valuable additive in the case of hot pressing. This approach was developed mostly owing to the works of Benecke et al., Carnall, Rhodes et al., and Rice [B27, C8, R20, R23]. G.D. Milles et al. [M33] contributed to making the process reproducible. The way LiF operates is yet a debated issue, but it is clear that the mechanism(s) involved are different from that suggested by its initial students [T1] who examined it for PS-based densification. Rice (1962), Milles (1967), and Benecke (1967) have determined that adding 0.3–5% LiF to a submicron relatively pure (problematic residual impurities were of the anionic type) dramatically raises the attainable densification level (99+ % of *TD*). The optimal addition amount was determined by Rice to be 2%; occasionally 0.5–0.8% LiF were also able to generate transparent parts. The pressure required when sintering at ~1000 °C was in the 20–25 MPa range. In this stage the product was highly translucent and retained 0.05–0.5% LiF. Good densification could be obtained under various types of atmosphere, but vacuum was the optimal one. A post-HPing annealing (preferably in air) at 1250–1350 °C was necessary to achieve transparency. Most annealed specimens were virtually LiF free. A hot-pressed specimen including initially 4% LiF had 0.1% LiF, which further dropped to 75 ppm [B27] after annealing. While helping densification, LiF additions also caused marked grain growth. Depending on the length of the annealing, $\overline{GS}$ varied between 5 μm and 3 mm. It was noted that for the annealing to be efficient the amount of residual LiF, after HP, had to be very low. When this requirement was not fulfilled, a milky ("cloudy") specimen resulted. It was observed that not only LiF vapor but also gaseous species resulting from the desorption of impurities (like CO_3^{2-}, OH^-, SO_4^{2-}), present on the surface of even the best powders available in the 1960s, constituted a major impediment in the reproducible constituted a major impediment in the reproducible obtainment of highly transparent specs [M33]. In the case of LiF, annealing led to its elimination, leading to bloating, only if the residual amount (after HP) was present as a film ($t < 60$ Å) along the grain boundaries. On one hand LiF creates vapor (which by proper processing can be eliminated), but on the other, it helps in the removal of OH^- and CO_3^{2-} [M33]. A dwell at ~750 °C is helpful in surface cleaning, even in

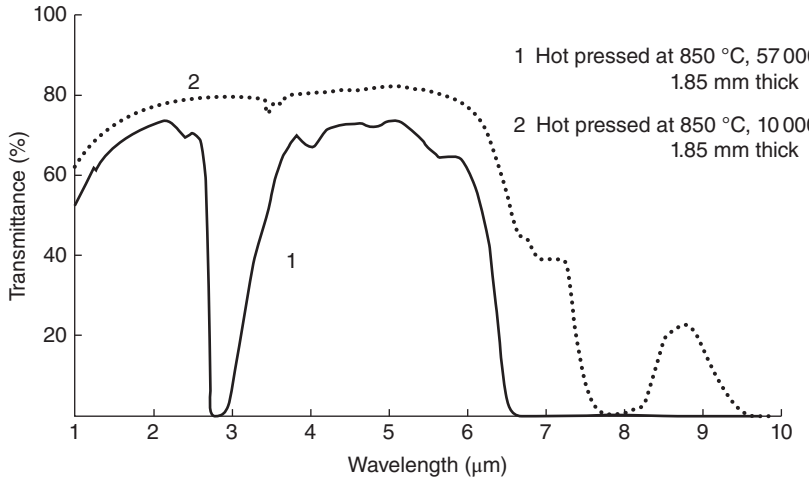

Figure 4.36 Transmission spectrum of hot pressed MgO ceramics as a function of LiF content. Source: Carnall 1967 [C8]. Reproduced with permission from Elsevier.

the absence of LiF. Outgassing continued also if T-MgO parts were put to service at high temperatures. Under such conditions reduction of transparency occurred. Various mechanisms were proposed to explain the dramatic influence of LiF additions on the densification of MgO subjected to hot pressing [B27, R23]. It is clear that a first effect concerns particle rearrangement. The liquid LiF ($t^\circ_f \sim 850\,^\circ$C) wets well MgO and has a low viscosity features that make it a good lubricant. It is also clear, considering the near-theoretical densities achieved, that besides facilitating particle rearrangement, LiF was able to influence other processes involved in densification. Plastic deformation of particles, even considering stress enhancement, at interparticle contacts, is not likely to be a major contributor to densification, considering the quite low pressures used during LiF-assisted hot pressing. The dislocation's motion, required for plastic deformation, on the relevant for MgO slip systems, cannot occur at such low stress levels. Probably, the most important mechanism active is liquid-assisted sintering enhancement (when relevant) by pressure. MgO has a low, but certain, solubility in LiF, as required by LAS no reaction takes place between MgO and LiF in the temperature domain used for hot pressing. Carnall [C8] calculated that for 1 μm grains LAS would require a solubility of 0.1% with 10^{-5}% being necessary for GS~0.1 μm. Auger electron spectroscopy confirmed the presence of Li and F in the GB zone [J14]. With an increase of % of LiF, temperature, and dwell time, the shape of the grains evolves toward that of a tetra-kai-decahedron. This shape allows good packing. Such an evolution is consistent with the occurrence of LAS rather than solid-state diffusion-based densification. The data on D_0 varies widely from author to author, but even the highest values proposed are low. Typical values are $D_0^{Mg^{2+}} = 2.20 \times 10^{-5}\ m^2/s$ and $D_0^{O^{2-}} = 1.24 \times 10^{-5}\ m^2/s$ [O4]. Thus it is very unlikely that at temperatures so much lower than $\leq t^\circ_f$ of MgO, solid-state processes can lead to the densification levels measured. Diffusion through GB liquid can be much faster, consistent with the observed densification pattern. The residual LiF, after HP, is able to diffuse out of the parts – as long as they are not too large – seemingly along the GBs. The process is not leading to bloating if the residual amount of LiF and other sources of vapor phases is low enough.

MgO was the first cubic oxide ceramic, brought to a certain measure of transparency (especially in the NIR). As it will be shown below, firing methods, other than HPing [H45, H46], lead to best results. The hot pressing of MgO was, however, discussed in detail above. The main reason is that essential aspects of this procedure (like the addition of LiF as a sintering aid) were subsequently used in the development of an HP-based firing approach for the fabrication of transparent spinel.

Sintering by PECS: The PECS is a more potent – compared to the variant discussed above – directional hot pressing. The more efficient heat distribution pattern (which also allows fast heating) and higher pressure levels facilitate densification. In a few early studies [C12, C14], the abilities of PECS were combined with the potentially high sinterability of nanopowders. Under pressures of 100–200 MPa/5 min and temperatures around 800 °C, translucent parts could be obtained. Compared to conventional hot pressing, the grains size could be kept at a narrow size ($\overline{GS} \sim 50$ nm). The effect of increasing pressure to 3–500 MPa was also examined [T28]. No LiF was added in these studies. Nanopowders prepared by laser ablation in an anhydrous atmosphere were used. This is practically important because it eliminates a bloating cause (OH^- desorption), which, as discussed above, may significantly impair transparency. Transmission levels of ~65%, at 750 nm, were attained in combination with a nanosize of the grains. The low GS was made possible by the low sintering temperatures (~800 °C) and short dwells, at 15–30 minutes. In the case of PECS, the densification mechanisms operating may be more complex than those acting in the processing of LiF/MgO materials by simple hot pressing. Plastic deformation may occur, more easily, especially when high pressures are used. GB diffusion-based creep may occur too. For the case of PECS, on LiF-free powders, high transmission of up to 70% in the VIS range (significantly better than those reported by the papers discussed above) was obtained by combining high temperatures (1600–1900 °C) with a pressure of 100 MPa (45 minutes dwell) [W3]. The transmission spectra of parts produced by Tran et al. are shown in Figure 4.37 [T28].

Sintering by the aid of high-frequency induction field, applied to nanopowders, was also examined [J19].

Sintering by AS + HIP: Interestingly the best combination of optical and functional properties was obtained by applying the AS + HIP approach; the necessity of adding HIP to the AS stage was made clear, among other things, by the data obtained theoretically on Mg^{2+} diffusion rates [V8]. A. Krell et al. at IKTS used quasi-nano ($A \sim 10\ m^2/g$) high purity (99.99%) powders when applying this approach. After densification specimens exhibiting an optical spectrum like in Figure 4.38 were obtained [H45]. Such parts exhibit a $\lambda_{th} \cong 54$ W/mK. Direct HIPing of encapsulated MgO powder compacts could not produce transparent specimens [L17].

Other sintering methods: Densification by fast MW heating was also examined [J6].

4.2.4.3 Properties

Because the bond strength between Mg and the oxide ions is weaker than, say, in alumina, the IR cutoff is at longer wavelength (~8.5 μm vs. 6 μm for corundum).

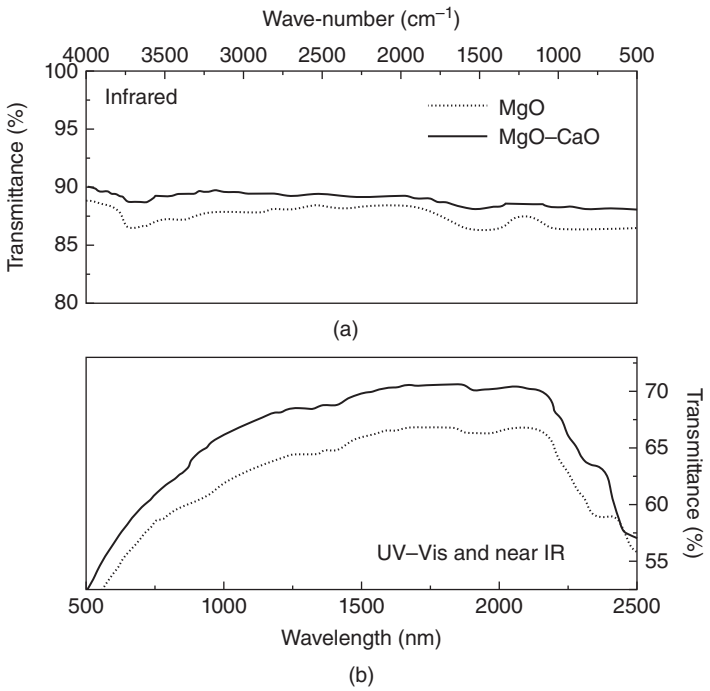

Figure 4.37 Transmittance of MgO ceramics densified at low temperature by PECS. (a) 2.5–10 μm. (b) 0.5–2.5 μm. Source: Tran et al. 2012 [T28]. Reproduced with permission from John Wiley & Sons.

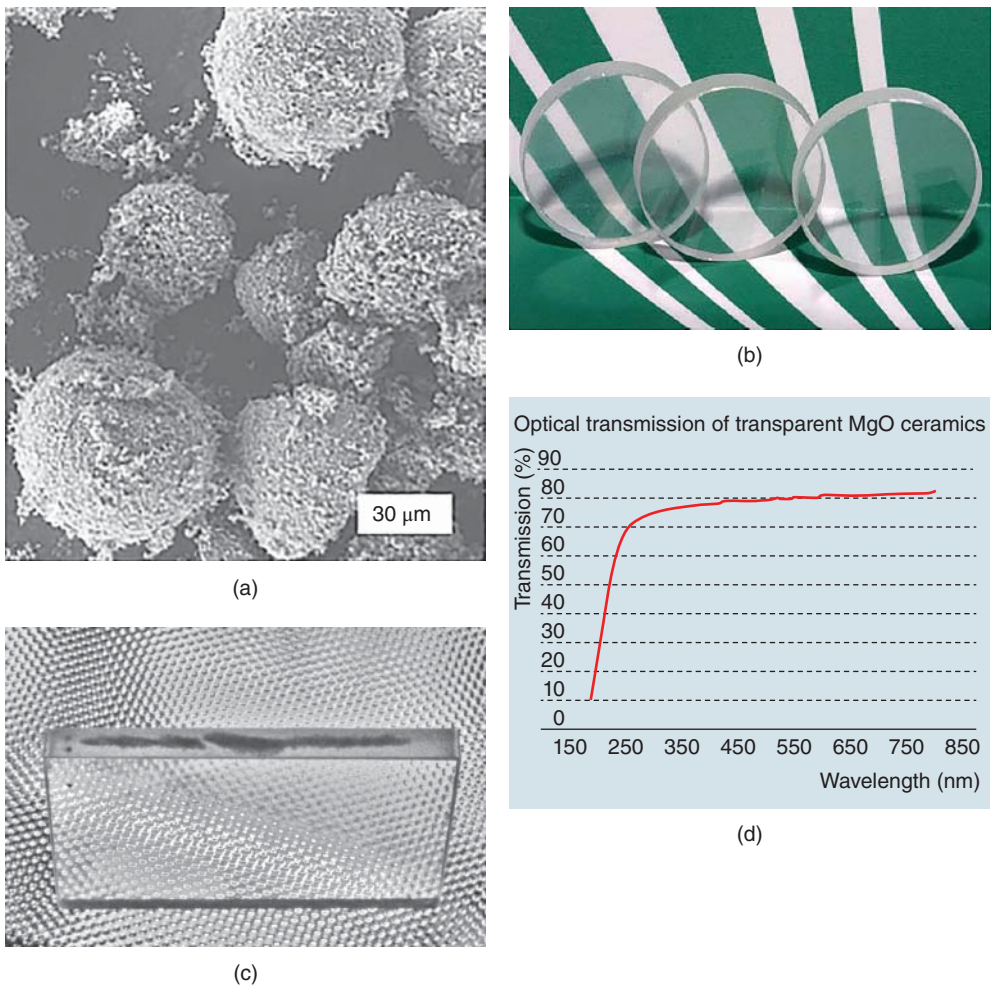

Figure 4.38 Characteristics of MgO powder and dense ceramics used in fabrication of the sinter/HIP approach at IKTS, Dresden. (a) Morphology of powder granules. (b) Imaging of sintered disc-shaped MgO ceramics. (c) Imaging of sintered plate-shaped MgO ceramic. (d) Transmission spectrum of discs shown in (b).

Table 4.8 Properties of MgO ceramics.

Properties	Unit	Value
t°_{f}	°C	2852
t°_{b}	°C	3600
α	$^{\circ}C^{-1}$	11×10^{-6}
E	MPa	250
μ	—	0.18
ρ_e	Ωm	9.65 (1 MHz)
ε_r	—	$>10^{12}$
TD	g/cm^3	3.58
TRS	MPa	180–230
λ_{th}	W/mK	54
n	—	1.736 (600 nm)
T_{theo} 600 nm	%	86.5
$HV10$	GPa	6–7 (single crystal)
$HV0.5$	GPa	8.5–9.0 (single crystal)

Besides transparency a TC's utility depends, of course, on the nonoptical properties it exhibits. Some of those, relevant for applications, are given in Table 4.8.

The most outstanding property is the very high thermal conductivity (for an oxide). Mechanical properties are modest compared to alumina or even spinel.

4.2.4.4 Transparent Calcium Oxide

This cubic lattice material has its transmission curve cutoff (the IR region) at a wavelength somewhat longer than MgO (A. Goldstein, unpublished results); this is the main practical reason for interest in the material. The main practical difficulty – when powder sintering is attempted – is the powder's hygroscopicity. In Figure 4.39 [G52], the transmission spectrum of parts obtained by hot pressing is shown. As it can be seen for thin discs, the transmission achieved is remarkable.

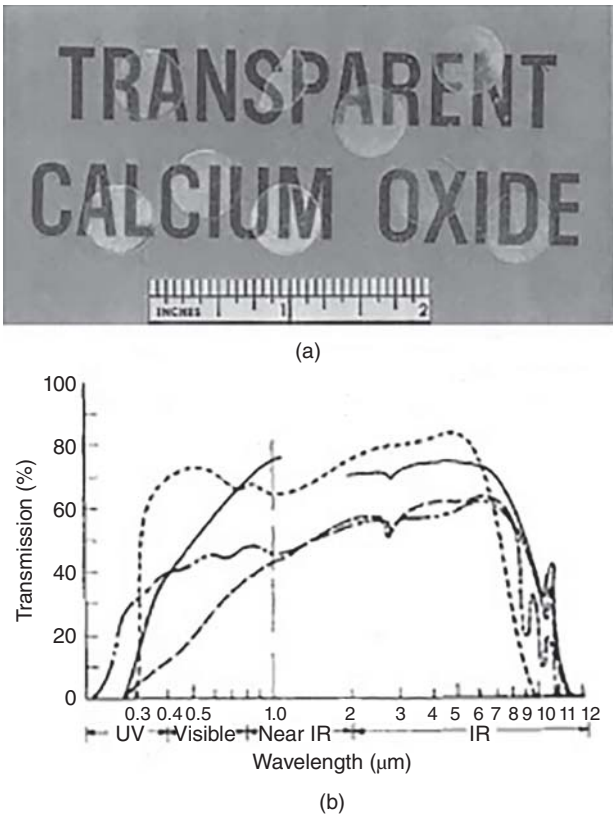

Figure 4.39 (a) Imaging and (b) transmission spectra of translucent CaO ceramics hot pressed by the aid of CaF_2. Full bodied line – CaO ceramic developed here (the rest of the curves – single crystals of different cut references). Source: Gupta et al. 1973 [G52]. Reproduced with permission from John Wiley & Sons.

4.2.5 Transparent YAG and Other Garnets

The yttrium aluminate with the $Y_3Al_5O_{12}$ ($3Y_2O_3{\cdot}5Al_2O_3$) chemical formula is one of the compounds that form within the Y_2O_3–Al_2O_3 binary (see Figure 4.40 [L19]). The polymorph, stable at high temperature, has a garnet-type lattice (the phase once achieved remains stable [like we have seen in the case of spinel] on cooling owing to kinetic causes, without reverting to the thermodynamically stable perovskite structure). Therefore at *RT* one has a cubic material suitable for TC fabrication.

In the field of transparent ceramics, it is used for a small number of applications, mostly gain media for laser devices and yellow-red light emitter in certain solid-state

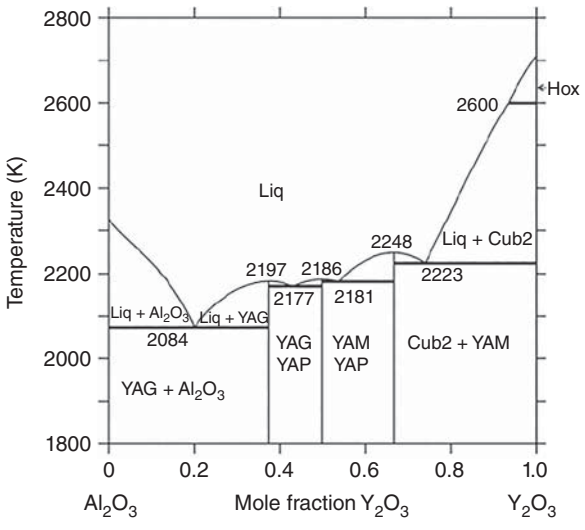

Figure 4.40 Phase diagram of the Y_2O_3–Al_2O_3 binary system. Source: Levin et al. 1956. Reproduced with permission from The American Ceramic Society.

light sources. For those applications, however, it is so dominant that overall it is considered one of the most relevant transparent ceramics. The cubic YAG as single crystal was selected early as a preferred RE^{+} host for gain media, and interest subsequently arose for its fabrication also as a transparent polycrystalline host. In practice reference is made to this ceramic as YAG where the last letter indicates the fact that its lattice is of the garnet type. The other two compounds of the system, richer in Y_2O_3, i.e. $Y_4Al_2O_9$ (YAM) and $Y_2Al_2O_6$ (YAP), are not used in this domain owing to a number of factors, the main being lattice non-cubic symmetry (monoclinic for YAM and orthorhombic for YAP).

4.2.5.1 Structure, Processing, and Properties of YAG

The YAG's lattice belongs to the cubic body-centered #230 space group O_h^{10} ($I4_1/a\bar{3}_2/d$). The unit cell contains eight formula units. The lattice period is $a = 12.004$ Å. Twenty-four Y^{3+} cations reside in Wyckoff c-sites of $D_2^{'}$ symmetry, $16Al^{3+}$ cations reside in Wyckoff a-sites [W35] of S_{36} symmetry, $24Al^{3+}$ reside in Wyckoff d-sites of S_4 symmetry, and $96O^{2-}$ anions reside in Wyckoff h-sites of C_1 symmetry. Each Y^{3+} is eightfold coordinated by O^{2-} located at the vertices of a distorted cube forming a dodecahedron. Each of the $16Al^{3+}$ is sixfold coordinated by O^{2-} located in the corners of an octahedron, and each of the $24Al^{3+}$ is fourfold coordinated by O^{2-} in the vertices of a tetrahedron. Note that the said octahedron exhibits a slight trigonal distortion, and the said tetrahedron exhibits a slightly stronger tetragonal distortion. Each oxygen anion is bonded to one tetrahedron/one octahedron and two dodecahedral sites. The large rare-earth doping cations best fit the (c) sites. Figure 4.41 displays the YAG lattice structure.

The correlation between microstructure and performance was examined theoretically in [A26].

Of interest, especially for short pulse lasers, are also YAG lattices in which a measure of disorder is introduced, by partially substituting the Al^{3+} with other trivalent cations like Sc^{3+} or Ga^{3+} (e.g. [C9, S8]).

4.2.5.1.1 Processing

The objectives of processing are the usual ones, in the case of any TC fabrication [B6, B43]. It has to be noted, though, that owing to the fact that the main application is in the domain of gain media, the requirements regarding low residual porosity are particularly drastic (<20 vol ppm). Let us first briefly describe the main raw materials available and then the processing approaches developed for T-YAG obtainment; a comparative analysis of the methods will try to identify remaining weak points, which require further improvement of the state-of-the-art tools.

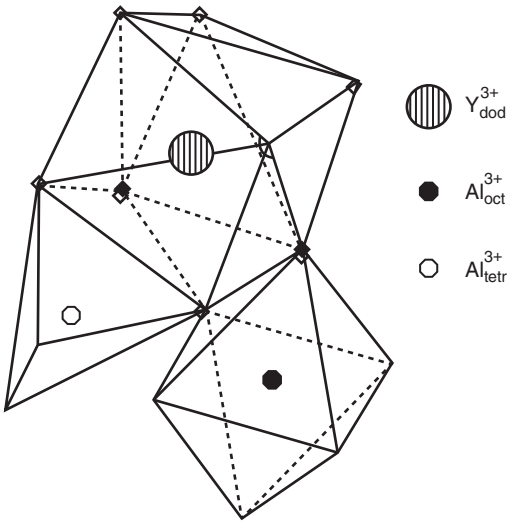

Figure 4.41 Fragment of garnet lattice and examples of T-YAG-based parts. (a) Lattice fragment. (b) YAG parts. Source: Reproduced with permission from Konoshima, Japan.

4.2.5.1.1.1 YAG Powders

Because of the widespread interest in T-YAG, a lot of effort was invested in the development of an optimized method for highly sinterable YAG powder synthesis and processing. The solid-state reaction-based route is more important here than for other TCs, owing to the possibility of using the reaction preceded sintering approach [I6]. For this approach, reactive Y_2O_3 and Al_2O_3 fine powders were synthesized. A wide variety of wet chemistry and gas-phase reaction-based YAG synthesis methods were also developed.

For full YAG preparation, various types of coprecipitation techniques have been examined. First the formation of hydroxide precursors (with NH_4OH or even NaOH-containing solutions) was examined, as for most TC-generating powders. One of the early conclusions drawn was that reverse strike ensures higher quality powders obtainment [A24, P2, V11]; the result is, in fact, not specific to YAG. It was determined that a pH of ~9 is optimal for a mixing of the hydroxides (initial sulfate solution) in a way that reduces the calcination temperature for YAG formation; washing with IPA or acetone reduces agglomerate strength and size. Palmero et al. (chlorides starting solution; pH ~9 with NH_4OH) [P2] observed the significant effect the synthesis temperature has on the crystallization temperature and phase composition. Precipitation at 5 °C allows YAG formation at ~900 °C.

S. Matsuda [M17] showed, for the case of Mg^{2+} and Al^{3+}, that a good precipitant is generated also by NH_4HCO_3. The method was applied to a mixture of Y^{3+} (nitrate) + Al^{3+} (sulfate) for YAG obtainment [L22]. A voluminous precipitate – with an approximate composition of $NH_4AlY_{0.6}(CO_3)_{1.9}(OH)_2{\cdot}0.9H_2O$ – results,

and after calcination (1100 °C), a fine ($\overline{GS} \sim 70$ nm) YAG powder with rounded basic particles is achieved. A sintering test (VS 1700 °C/1 h) of the powder (which was not subjected to special post-synthesis processing) showed an encouraging level of transparency. A similar powder (derived from chlorides) – sintered by PECS [S47] – showed even better transparency ($T \sim 70\%$ at $\lambda = 700$ nm, $t = 1.5$ mm). Excellent transmission showing parts ($\alpha = 0.002\ cm^{-1}$) were derived from such powder, after suitable processing and forming, by Yanagitani et al. [Y6]. The triethanol amine ($(HOCH_2CH_2)_3N$, TEA) generates a ligand able to produce stable complexes with cations like Al^{3+}, Mg^{2+}, and Y^{3+}. In the case of the Mg^{2+}, Al^{3+} couple even seems to generate heteropolynuclear complexes, which ensure intimate cations mixing. Therefore it was used also for generating active YAG precursors. Nano-YAG powder ($\overline{X} \sim 50$ nm) could be derived from the TEA-generated precursor at a quite low temperature (~950 °C). A quite large number of teams examined combustion-based methods for YAG synthesis. For instance, J. Kingsley et al. used NO_3^- species as oxidizer and urea/carbohydroxide mixtures as fuels, obtaining YAG after a short combustion ignited at 500 °C [K19]. The ignition temperature is not the peak temperature attained during the combustion process; the latter cannot be accurately measured usually. Using amino acids as fuel and NO_3^- as oxidizer, H.D. Lee et al. ignited combustion at lower temperature (200–240 °C) but had to calcine then at 1000 °C the product [L9]. Combustion (500 °C) of a gel derived from an Al-alkoxide and using TEA as both a chelating agent and fuel lead to, as reported by D. Chen et al. [C21], a powder having basic particles as small as 20 nm (500 °C post-combustion calcination). Further reduction to 800 °C of the YAG formation temperature (combustion synthesis) was reported by M.K. Cinibulk [C36], J. Li et al. [L23], D. Chen et al. [C21], and R.S. Azis et al. [A31]. The combustion-based approach, while relatively fast, has significant drawbacks. The temperature profiles tend to vary from batch to batch, with consequence on powder properties, and the resulting material is a carbon containing fluffy, strongly bonded mass, difficult to process into an RTP material. Classical sol–gel, microemulsion, sonochemistry, mechanochemical synthesis, and citrate- or oxalate-based precipitation were also examined [C5, L10, V6, W9, Z13]. For some of these methods, the assistance of MW fields was studied [P5, W9]. Positive effects on the kinetics of some of the physical and chemical processes involved in the synthesis were obtained, but no significant nonthermal effects were reported. Combination of initial coprecipitation, followed by hydrothermal treatment (over 350 °C; 8–30 atm) led to isometric, faceted (not spherical as claimed by the authors) nanopowders [Z9]. The application of the solvothermal approach (ethanol–water mixtures as suspending liquid) allows the obtainment of fine, really spheroidal, particle-based powder after autoclave treatment at 280 °C. Remarkably the pressure assistance leads to YAG formation at this low temperature. The morphology of the powder, prepared by the first of the two methods described, is illustrated in Figure 4.42. Here the starting material was a precipitate prepared with NH_4HCO_3.

Up to this point liquid phase precursors synthesis results were presented, because this is the most widespread approach studied for performant YAG powder preparation. This is so because the solid-state reaction-based approach – as long as it uses micron or even submicron oxide mixtures – requires temperatures higher than 1450 °C for YAG phase formation. However certain nanosized solid precursors may generate the desired phase at around 1300 °C, making such an approach more attractive. For instance, X. Li et al. [L37] mixed γ-Al_2O_3 and a nano-Y_2O_3 in ethanol by simple ball milling (12 hours). The mixture, after following the usual phase transformation sequence, ends as pure YAG at 1300 °C. The powder could be vacuum sintered (1700 °C/5 h) to high level of transparency ($T = 81\%$ for $\lambda = 700$ nm). Flame spray pyrolysis is an approach able to

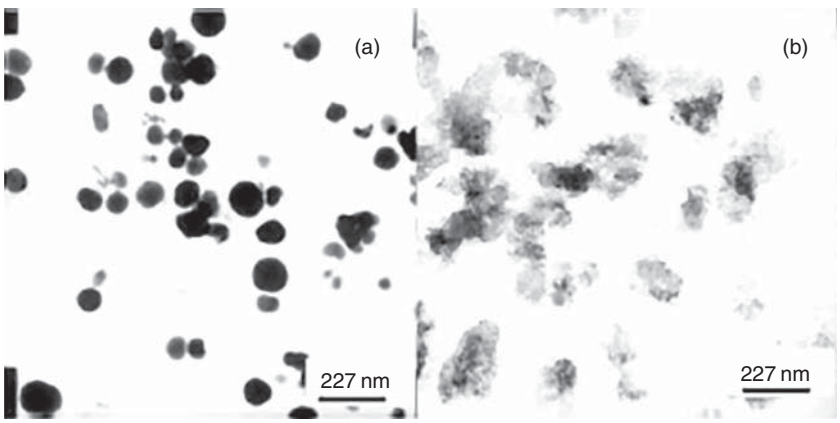

Figure 4.42 Morphology and basic particle size of YAG powder prepared by the solvothermal approach. (a) and (b) represent particles morphology in two different sets of preparation conditions. Source: Zhang et al. 2004 [Z9]. Reproduced with permission from Elsevier.

generate highly sinterable ceramic powders. Especially so the procedure was developed by R.M. Laine and collaborators [B33]. As noted in Section 4.2.1, also the most sinterable spinel powders were prepared by this method. In the case of YAG, the 800 °C calcine is, in fact, a mixture of YAM and YAP. Such mixtures sinter well, however, after transforming first in YAG. We were able to obtain transparent specimens (t = 2 mm, T ~78% at λ = 600 nm) by relatively short and low temperature vacuum sintering of CIPed compacts (1750 °C/5 h, 10^{-3} MPa); the powder was processed by a proprietary ICSI procedure prior to forming.

4.2.5.1.1.2 Processing Procedure Description

The idea that YAG has the potential to generate transparent ceramics was proposed already during the 1970s by people dealing with fabrication of translucent ceramics by hot pressing [G10]. Quite probably the first transparent YAG ceramic (moderately in the VIS, and up to 80% at λ = 5 μm) was reported by Pantelyeva et al. [P6]. Additives like ZrO_2 and MgO (~1%) or MgO (1%) + 2% of either Nd_2O_3 or Er_2O_3 were used by that team. G. de With and coworkers selected SiO_2 and MgO (already made famous by alumina) as sintering aids for vacuum firings [M44, W27]. They prepared (from Y and Al sulfates; calcination at 1300 °C/6 h) a relatively fine powder (A = 5 m^2/g) to which SiO_2 (as TEOS 0.15%) or MgO (0.05%) were added. The additives were considered as grain growth inhibitors. The vacuum sintering at 1850 °C/4 h produced moderately transparent (absorption coefficient of ~0.7 mm^{-1}) 1 mm thick discs, with $\overline{GS}$ of 5–10 μm; the cutoff was at 6.2 μm. Al-rich inclusions were present along the GBs and randomly distributed; rare, large grains were also detected. The parts thus developed, while showing some transparency, were not at a level usable for lasing.

The approach described above was significantly improved in the late 1980s and early 1990s in Japan and then the United States [L11]. The description we give here about the seminal work effectuated by the two main Japanese teams [I3, I6, S19, Y1] is based both on literature and an oral account of Ken-ichi Ueda, one of the main players. One group prepared a high purity powder by the coprecipitation method (vide supra) using urea as a reactive [S19]. While the disadvantage of the method is the formation of bulky, intermediary compounds (including OH^- and CO_3^{2-} anions), it allows an intimate mixture of the cations, reducing calcination temperatures (~1000 °C); thus agglomerate strength and size is kept low. As opposed to the earlier studies, in [S19] a lot of effort was invested in determining powder processing operations and matched forming techniques, so as to get small pore size of narrow size distribution in the green parts. The SiO_2 was introduced as a colloidal powder. The team was able to obtain YAG parts exhibiting an optical loss coefficient as low as α = 0.25 cm^{-1} (VS at 1700 °C/5 h/10^{-6} Torr). However in the late 1980s, the developers considered (wrongly in our opinion; formed with the advantage of hindsight) that no lasing is possible in such a host and limited themselves to fluorescence measurements, forgoing laser tests. While the α-values were indeed somewhat higher than those of conventional hosts existing at the time (glass, simple crystal), these early T-YAGs would have quite likely lase if tested under appropriate pumping conditions. An interesting, essential modification – within this framework – was introduced by A. Ikesue et al., the leader of the second team. Instead of using YAG powders, a mixture of Y_2O_3 + Al_2O_3 – having YAG stoichiometry – was sintered [I6]. Such an approach is usually called "reaction sintering." This is correct as long as the energy produced by reaction is used by for sintering; the two processes occur more or less simultaneously. For the case we discuss here a more appropriate definition would be "reaction-preceded sintering" because the latter process occurs after completion of the solid-state reaction. At this point one has to underline an important specific feature of the reaction leading to YAG formation. As opposed to binaries like MgO + Al_2O_3 (for $MgAl_2O_4$) or ZnO + Al_2O_3 ($ZnAl_2O_4$), the volume changes, brought about by the reactions leading to YAG formation, do not disturb the microstructure of the green compact, in a way hampering densification. No expansion, but only a dwell in shrinkage, occurs during the firing of a suitable Al_2O_3 + Y_2O_3 mixture, as shown in Figure 4.43.

This type of green structure evolution is not frequently encountered in the domain of transparent ceramics. It facilitates the use of pressureless sintering for full densification of yttria+alumina mixtures. The YAG state is reached only after a three-stage reaction

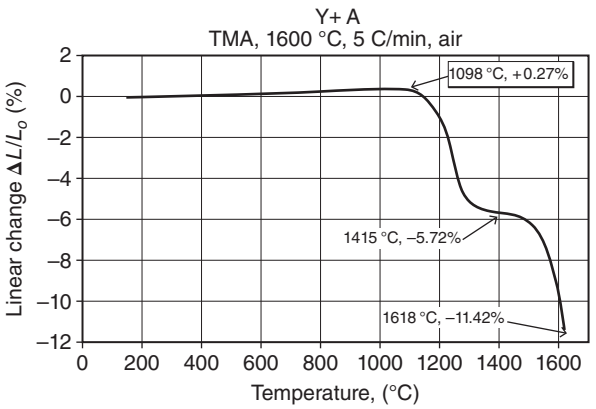

Figure 4.43 Shrinkage, during reaction-preceded sintering of YAG derived from an yttria and alumina mixture, in air; specimen fabricated at ICSI, Haifa.

sequence. Despite the YAG stoichiometry of the initial powder batch, the first compound formed, as a result of reaction between Y_2O_3 and Al_2O_3, is the $Y_4Al_2O_9$. $2Y_2O_3 + Al_2O_3 = Y_4Al_2O_9$ (YAM). The temperature range during which the reaction is completed depends also on the characteristics of the reactant powders, but starts around 1000–1050 °C. This Y_2O_3-rich compound continues to react with Al_2O_3, and around 1200 °C, YAP forms according to $Al_2O_3 + Y_4Al_2O_9 = 4YAlO_3$ (YAP). Finally, starting from 1300 °C, YAG appears from $3YAlO_3 + Al_2O_3 = Y_3Al_5O$. This reaction sequence, while always present, can be moved to significantly lower temperatures (7–900 °C range) by the use of wet chemistry-based synthesis of the initial powders. This approach allowed the fabrication of parts having a residual porosity amount of no more than 2 ppm. As a result, a transmission level equaling the theoretical value (~84%) was achieved [I3, I6]. The sintering was significantly aided by the use TEOS (as a silica source). In fact really high transparency was achieved only in the presence of around 0.5% TEOS (or directly fine SiO_2); the mechanism by which this dopant operates was examined by various authors, e.g. [B44, I3, K68, M7, S6, Z1] (see Section 3.1.2.3 on sintering aids). It was later observed that Si also causes grain growth; lately Ikesue managed to achieve the desired transparency levels also without the help of silica (personal communication). Returning to history we note that the excellent host transparency (achieved during the 1990s in Si-doped parts), and **selection of an efficient pumping method** allowed the author to obtain high efficiency lasing from Nd^{3+}-doped specimens, which become an efficient gain media. This was the first polycrystalline YAG shown to be able to lase and the first ceramic the lasing of which had good efficiency (poor efficiency lasing [bad pumping] was achieved in 1973 with Nd in an yttria host; see Section 4.2.6). The excellent densification achieved was the result of a patient optimization of all the stages of the processing, made possible by an in-depth understanding of the complex physical and chemical processes involved. For instance, a new Y_2O_3 reactive powder was prepared by pyrolysis of a basic Y carbonate (60 nm basic particles). This powder, combined with the use of an adequate mixing procedure, allowed the formation of uniform intimate mixtures in which Y_2O_3 particles coated the larger alumina powders. Matching the CIPing schedule to the strength of the ~50 μm granules (spray-drying) and obtainment of uniform strength spheroidal granules led to uniform die filling and full crushing of the granules. A pores size distribution with a narrow mode at ~40 nm (radius), and the quasi-absence of larger voids, created the conditions for full, uniform sintering. Ikesue et al. also examined a VS + HIP procedure for obtaining minimal possible residual porosity [I3]. The authors came to the conclusion that in order to prevent Ar penetration, encapsulation (Pt foil) is mandatory for achieving the desired results. Dwell times (peak temperature at ~1750 °C) have to be short, i.e. less than one hour. For a $7 \times 10 \times 70\,mm^3$ part, the measured pore concentration was as low as 3×10^{-12}. Other work showed, however, that the combination of VS with capsule-free HIPing is also able to generate specimens of high transparency [L12]. A transmission of ~80% in the VIS and $\overline{GS} \sim 0.5$ μm was obtained after HIPing under Ar (200 MPa) at 1750 °C specimens previously VSed in the 1650–1700 °C range. Grain size was low in the 2–5 μm range. The processing times were significantly reduced (2 h VS + 2 h HIP) compared to one stage VS. The team that worked for the first manufacturer, able to put out a commercially significant YAG (Konoshima Chemical), has used also a sinter/HIP approach. One of their standard powders (coprecipitation with NH_4HCO_3 of chlorides) was used, and forming was done by pressure (5 atm) slip-casting in gypsum molds a 15 m^2/g powder (calcined at 1200 °C/5 h). The BD_g of the de-bindered compact was 61.5%*TD*. The first firing (VS at 1500 °C/2 h $P \leq 10^{-3}$ Torr) gave a $BD_f = 99.4\%TD$ ($\overline{GS} \sim 0.5$ μm). The second stage was HIPing under Ar (1450–1800 °C); the $\overline{GS}$ moved from 1 to 9 μm with a rising temperature. In the second part of the HIPing, the atmosphere was changed from pure Ar to 80% Ar 20% O_2. The final annealing was carried out at ~50 °C below the HIPing temperature in an atmosphere (~4.5 MPa) rich in O_2. As a result any gray tints acquired during HIPing disappeared. The resulting parts shows very low loss coefficients with $\alpha \leq 0.02\,cm^{-1}$.

The sinter/HIP was quite successfully used also in a variant in which the first stage is effectuated under flowing O_2 [F21]. This procedure was developed for garnets of various composition, including YAG, by Greskovich et al. [G44]. Powders derived from either oxalate or hydroxide precursors were used, and sintering at ~1650 °C under oxygen for three hours was performed. Further HIPing (~1500 °C/200 MPa/Ar/1 h) brought the sintered specimens (98%*TD*) to a transparent state ($T \sim 80\%$ in the VIS). The experiments were made especially on Gd-containing garnets. Following this approach, for the case of YAG, H. Lee et al. effectuated later the first stage of the sintering at ~1600 °C/5 h, under O_2 [L9]; the HIPing (200 MPa of Ar) was done at low temperatures at 1500–1550 °C/5 h. $\overline{GS}$ of ~2 μm and a transmission of $T = 80\%$ at $\lambda = 700$ nm ($t \cong 1$ mm) are characteristics that make the parts attractive for various applications, including gain media. A specific feature of this work is the use of YAG powders derived from a suspension including α-Al_2O_3 and Y-nitrate, by the combustion (250 °C) approach. The basic particles ($X < 100$ nm) are not finer than those of powders

produced by other methods, neither do they show ability to generate unusual levels of green-body compactness ($BD_g = 45–50\%TD$). However the material clearly shows higher than usual sinterability considering the mild sintering conditions it requires for generating transparent parts.

A team at ICSI-Haifa (A. Goldstein et al.) studied recently a sinter/HIP approach in which vacuum sintering was replaced by firing in air, in an effort to reduce sintering stage costs. Good results were obtained with yttria + alumina mixtures but only when TEOS was added as a sintering aid [G28, S72]. While significant transparency was achieved, the parts were not of laser quality; further improvement is clearly possible. In Figure 4.44 the visual aspect and microstructure of such specimens are shown. The specimens are purple in color owing to formation of Y^{2+}, under the reductive atmosphere (Ar + carbon colloids); this issue is discussed toward the end of this section.

Sintering in vacuum was used in T-YAG fabrication because it is considered, especially for TCs, as more efficient than that done in air. This is because during VS, N_2 molecules, which accumulate in the closed porosity, during air sintering, are not present. Our results related to spinel sintering showed, however, little benefit, if at all, in the use of vacuum. It seems that N_2 is less deleterious, for densification, than its low diffusion rate might suggest.

While SiO_2 remains the most ubiquitous sintering aid the effect of others, like some divalent cations [Z17, Z18] was also studied.

The early attempts at firing by PECS [C13–C15] gave only translucent parts ($T \sim 30\%$ at $\lambda = 800$ nm), but further studies led to higher transparency. For instance, using a very high sinterability (astronomic price) powder, prepared by FSP, Frage et al. were able to raise T to ~78% in the VIS after sintering (0.25% LiF as sintering aid) at 1400 °C/20 min/65 MPa/vacuum [F11]. The $\overline{GS}$ was kept at ~3 μm. In fact, over $\lambda = 500$ nm the transmission of LiF-free discs is also at ~78% and is coupled with a $\overline{GS}$ of ~0.8 μm only. Using less costly (prepared by coprecipitation) powder, G. Spina et al. [S47] were able to further reduce densification temperature to ~1350 °C (15 minutes dwell, 75 MPa, vacuum), without using sintering aids. Submicron-grained ($\overline{GS} \sim 0.35$ μm) quite transparent ($T = 66\%$ at $\lambda = 600$ nm $t = 1$ mm) discs were obtained after post-sintering annealing in air (~800 °C).

4.2.5.1.2 Properties of YAG

In Table 4.9 the most relevant characteristics of YAG, for applications, are presented.

The YAG has a relatively high specific gravity and moderate mechanical properties. Some studies found the ceramic parts as exhibiting better mechanical properties than single crystals [K4], but this issue is yet open for discussion. It is a refractory material but with a moderate resistance to thermal shock. It exhibits a wide transparency window between ~0.3 and ~6.0 μm; some undoped discs transmission curves are shown in Figure 4.45.

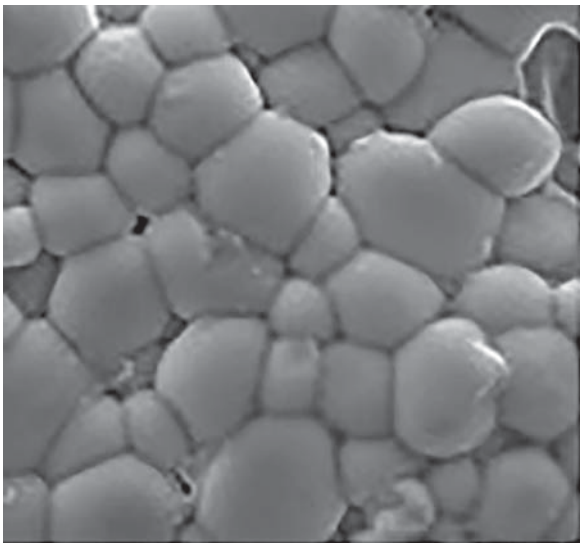

(a)

(b)

Figure 4.44 Imaging and microstructure of YAG disc fabricated by sinter(air)/HIP approach at ICSI, Haifa. (a) Microstructure. (b) Image.

4.2.5.1.2.1 Spectral Effects of Impurities

The main applications of YAG require insertion of different types of dopant. Their spectral effects are discussed

Table 4.9 Properties of YAG ceramics.

Property	Unit	Value
Density	g/cm^3	4.56
t°_f	°C	1940
λ_{th}	W/(m K)	14
α_{th}	$K^{-1} \times 10^{-6}$	7.5
n at 800 nm	—	1.8245
n at 1 μm	—	1.8192
HV	GPa	14
TRS	MPa	220
E	GPa	290
K_{IC}	$MPam^{0.5}$	1.7
T_{theo}	%	~84

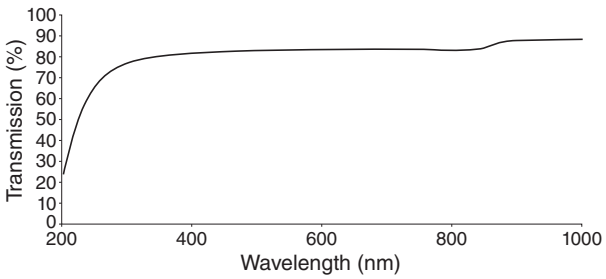

Figure 4.45 Transmission curves of undoped YAG discs fabricated at ICSI, Haifa, shows progress of transparence during development process; spectral quality is not good enough for lasing experiments.

in the Chapter 5, devoted to applications. Here only the spectral effect of two impurities, damaging when they occur, is addressed.

4.2.5.1.2.1.1 Ce^{3+} Is a Desired Dopant for Phosphor-Related Application

However it sometimes appears as an undesired impurity, in YAG (introduced mostly by yttria when the reaction-preceded sintering fabrication approach is used). In certain cases, the powder compact acquires a yellowish tint already during the air sintering stage, before experiencing reductive conditions. The hue of the yellow parts – as revealed by visual inspection – is similar but not identical to that of S-containing transparent spinel, but S may appear only after exposure to reductive atmosphere. Closer inspection reveals that the color, while similar, is not exactly the hue produced by sulfur. In addition the yellow color discussed here does not fade away on heating as opposed to the one produced by sulfur. In Figure 4.46a,b, the spectral curves of HIPed specimens (one transparent + one opaque [reflection]) are shown, together with that of a yellow (caused by sulfur presence) spinel plate.

The YAG curves differ from that of the sulfur-containing spinel as the color hue difference suggest they need to. Most of the cationic-type (TM $(RE)^+$), potential yellow tint producers, such as Fe^{3+}, Ti^{3+}, Cr^{6+}, Sm^{3+}, and Tb^{3+}, exhibit spectra dissimilar to the curves of Figure 4.46. However the spectral curves mentioned above do resemble spectra produced by Ce^{3+}, doped to oxide hosts. Therefore we analyzed the curves based on the electronic configuration of the Ce^{3+} ion. The most popular format of the electronic state set configuration – for the $4f^1$ ground state and the first excited ($4f^05d^1$) state of Ce^{3+} – is given in Figure 4.47 [R27].

The bands resolved in our spectra (Figure 4.46) fit well the electronic levels scheme so that it was concluded they are produced by Ce^{3+} impurity carried by the YAG specimens. The yellow color is caused by the orbitally allowed [$U'(4f^1)$ to $^2A_{1g}(5d^1)$] band located at $\lambda = 465$ nm. The low impurity content measured is yet enough to generate quite strong coloration because the responsible transition is an orbitally allowed one. Owing to this in single-crystal Ce^{3+}:YAG, a yellowish coloration was observed for Ce concentrations as low as 10 ppm (d ions such as Fe^{3+}, Ti^{3+}, or Cr^{6+} need to be present in concentrations of hundreds of ppm to cause color as they introduce Laporte forbidden bands). The lack of color in unsintered specimens suggests that, there, Ce is accommodated as Ce^{4+} in the YAG lattice; Ce^{4+} has been identified in single-crystal YAG when the crystal growth conditions were not sufficiently reductive.

While the existence of Ce^{3+}, under reductive atmospheres, is an intuitive occurrence, its formation, during air sintering (as the accompanying yellow color reveals), is less so. Things can be clarified, however, if one recalls that the reduction in metal cation oxidation state, by simple heating, is a common occurrence in glass processing [B10] at high temperatures. We think that both in glass and YAG the reduction is explained by the facilitation of oxygen vacancy formation; the latter process is a necessary companion to the oxidation state reduction of Ce. Checking by EDS (see Figure 4.46b), ICP-AES and TOF-SIMS confirmed the presence of a small (up to 60 ppm) amount of Ce in our air-sintered YAG specimens. In the specific case where a YAG powder raw material, prepared from sulfates, is used, both S and Ce^{3+} may contribute to coloration (sulfate-generated coloration we have seen also in the case of certain spinel powders; see Section 4.2.1.3).

4.2.5.1.2.1.2 Effect of Native Y^{3+} Cation Reduction

HIPed YAG specimens sometimes exhibit a purple hue, which can be fairly strong. The optical spectrum of a purple sample (the main feature of which is a wide asymmetric band at $\lambda = 490$ nm) together with that of a colorless disc are shown in Figure 4.48a.

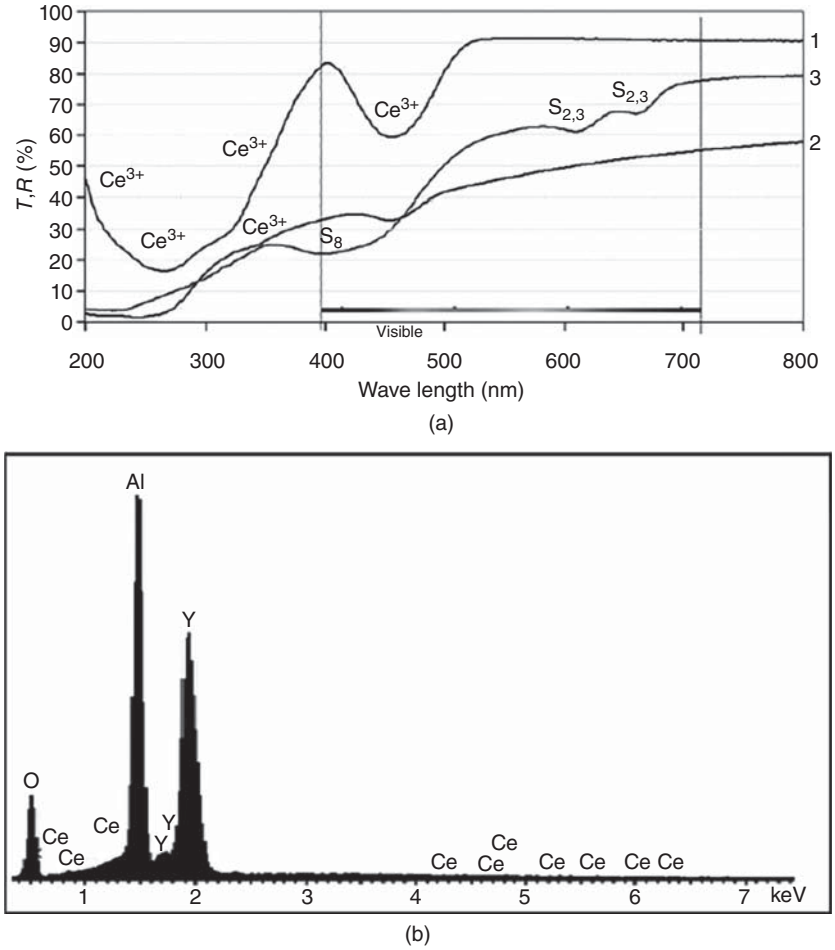

Figure 4.46 Transmission spectra of Ce^{3+} containing YAG and the impurity's EDS signal. (a) Optical spectra: 1. Transparent YAG (containing some 10 ppm of CE as impurity); transmission curve. 2. Sulfur-containing spinel part; transmission curve. 3. Yellow, opaque and highly dense but not transparent YAG disc; reflection curve. (b) EMPA scan on specimen used for curve A1; small Ce peak present. Source: Goldstein et al. 2013 [G31]. Reproduced with permission from John Wiley & Sons.

In Figure 4.48b, the EPR signal of the colored specimen is shown. A review of the spectra produced by lanthanide and transition element cations did not provide evidence for any potential source for the curve recorded. Y^{2+}:$SrCl_2$ and Y^{2+}:CaF_2, however, show optical spectra similar to that of the purple disc of Figure 4.48a. This suggests that the spectrum in the figure is produced by Y^{2+} (a $4d^1$ ion). The bathochromic shift of the band in the halides (compared with Y^{2+}:YAG) is normal considering the lower Lewis basicity of the Cl^- or F^- ligands, compared to that of the oxide anion, which therefore generate a weaker "crystal field." The EPR signal, produced here by the purple specimens, can be thus assigned to a Y^{2+} ion. To the best of our knowledge, Figure 4.48a is the first Y^{2+} optical spectrum, and Figure 4.48b, the first EPR signal, in a polycrystalline oxide host, published [G31]. Regarding its overall profile (not band position), the optical spectrum obtained here is quite similar to that of other d^1 ions, such as Ti^{3+}, V^{4+}, or Mo^{5+}. The asymmetric wide band clearly shows that the site is non-cubic. It was thought that the reduction of Y^{3+} to Y^{2+} was caused by reduction operated by carbon atoms, diffusing along the GBs, like in the case of Ti-doped spinel (see Section 4.2.1.3). Further work revealed, however, an initially overlooked aspect. The formation of purple color was specific to YAG parts including SiO_2; in its absence only very faint pink hues were observed – and only rarely on HIPed specimens. In specimens including the sintering aid, coloration always appeared and was intense. The presence of carbon, or an agent with similar abilities, is a necessary participant to the process of Y^{3+} reduction but not a sufficient one. In our view the role of SiO_2 is the introduction into the YAG lattice of Si^{4+} cations [S51]. Such cations cause distortion of the host lattice inducing stress. The silicon cations are accommodated in the GB region and affect the lattice there. The carbon atoms also travel in that region. **The Y^{3+} cations of a stressed lattice, as opposed to those of a normal one, can be reduced to Y^{2+}**. Also in the case of YAG sintered under vacuum in the presence of Si dopant, purple hues (indicative of Y^{2+} formation) were obtained, but not so (or only to a very low effect) in pure YAG. We observed that Zr^{4+} doping to YAG had an effect similar to that of Si^{4+}. However when Zr^{4+} was codoped with Mg^{2+} (which

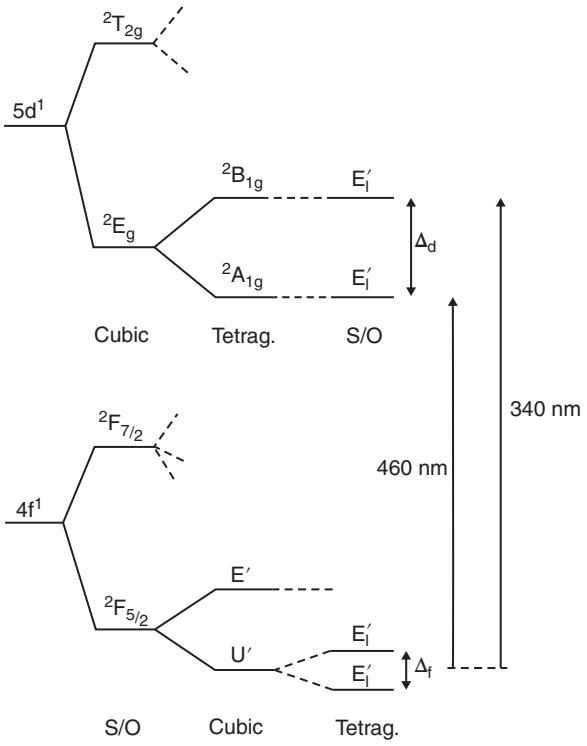

Figure 4.47 Energy level diagram of Ce^{3+} in YAG assuming that its cubic site (the cation enters Y^{3+} sites) experiences a strong tetragonal compression (on cation substitution) with a slight rhombic distortion; the ground state and the first excited state are shown considering the action of both crystal field and spin/orbital coupling. The lowest energy transitions, including the one responsible for coloration (460 nm), are indicated by arrows. Source: Robbins 1979 [R27]. Reproduced with permission from The Electrochemical Society.

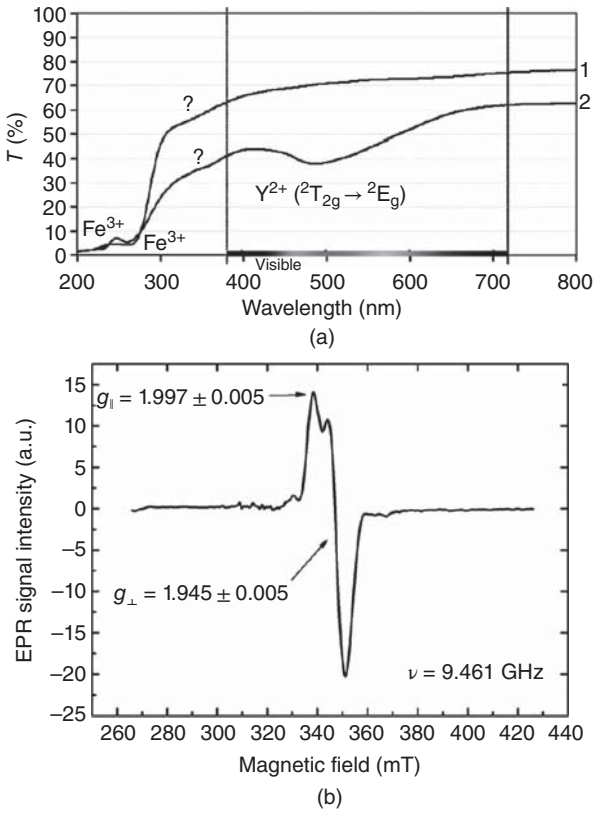

Figure 4.48 Electronic spectra generated by Y^{2+} (a d^1-type ion) formed in Si-doped YAG specimen processed in HIP furnace. (a) Transmission curves of undoped specimen (curve 1, of colorless disc = reference) and Si-doped one (curve 2, of purple color disc). (b) EPR signal of doped specimen; signal features characteristic of d1-type cations. Source: Goldstein et al. 2013 [G31]. Reproduced with permission from John Wiley & Sons.

tends to shrink the lattice while Zr^{4+} leads to expansion), no purple tint appeared (monodoping with Mg^{2+} does not lead to coloration). TEOS-doped YAG specimens, subjected to long (more than 15 hours) vacuum firings (around 1780 °C) and then HIPed, remained colorless, presumably owing to Si exit from the YAG lattice.

4.2.5.2 LuAG

LuAG may be viewed as a garnet in which the Y^{3+} cation is substituted by Lu^{3+}. This difference may confer to LuAG an advantage, over YAG, when laser hosts of chip geometry are compared for high power laser applications. A thin-chip shape, heavily doped Yb:LuAG single-crystal laser was able to produce a 5 kW output at optical to optical efficiency higher than 60% [B26]. The advantage can be understood looking at Figure 4.49 where the thermal conductivity of the two garnets, in single-crystal state, are compared.

The comparison is given as a function of the Yb dopant content variation. As it can be seen, the conductivity

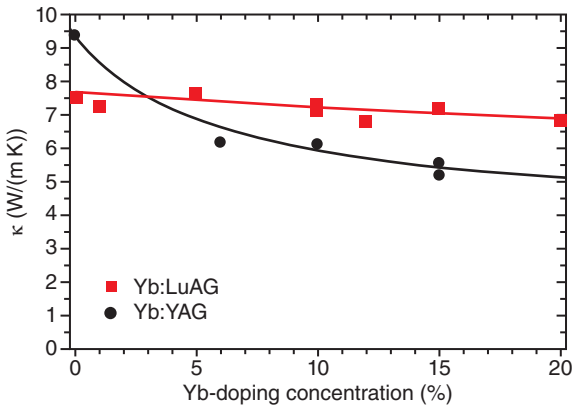

Figure 4.49 Thermal conductivity of two garnets (single crystal state): YAG and LuAG as a function of Yb^{3+} content. Source: Beil et al. 2010 [B26]. Reproduced with permission from OSA Publishing.

of the two hosts is quite equal, in undoped state, but remains some 20% higher (less decrease) in LuAG when the Yb concentration reaches 10% (the value found in most thin disc high power Yb lasers). The reason for this difference is the atomic weight of Lu, which is closer to that of Yb than is the case for Y. As a result the heavily Yb-doped LuAG lattice causes less phonon scattering than that of a similarly doped YAG [S10]. Now, one has to note that the difference discussed above may be less pronounced in ceramics than in single crystal. In the former the scattering of phonons produced by grain boundaries (similar in the two garnets compared) affects their propagation as significantly as the mass difference discussed above; in such conditions the thermal conductivity variation, due to the mass difference between Lu and Y, has a smaller relative effect. Yb^{3+} emission cross section is also larger in LuAG than in YAG [A11, D13]. For the case of Ho-based laser, this garnet has the advantage of a lower manifold separation and this leads to a lower thermal occupation factor of the terminal lasing level. For scintillators, LuAG also presents the advantage of a higher effective atomic number and density; for 193 nm lithography, the high refractive index is attractive [M12]. The potential benefits, outlined above, are the main drivers, which were determined by quite a lot of teams studying the fabrication and lasing host behavior of LuAG. Here only a brief account of the results is presented.

The processing of LuAG follows quite closely the pattern developed for YAG [F21]. Full LuAG powders – prepared by coprecipitation, combustion sol–gel, or flame spray pyrolysis – were used in most cases, but the reaction-preceded sintering approach (starting from Lu_2O_3 and Al_2O_3 mixtures) was examined. The first relatively transparent RE^+-doped LuAG was produced by Wagner et al. [W2]. Best results were achieved by long vacuum sintering (up to 30 hours), in the 1750–1850° range [X2], occasionally followed by HIPing. W.H. Rhodes et al. [R21] used a high sinterability nanopowder, prepared by FSP, to produce ceramic Pr:LuAG. Sintering was done under He5H_2 at 1650 °C/4 h ($BD_H \sim 95\% TD$) followed by HIPing (1675 °C/4 h, 200 MPa). The average grain size was low ($\overline{GS} \sim 2$ μm), but transparency levels attained were relatively low ($T_{400m} \approx 22\%$, $T_{800m} \approx 65\%$ for $t \approx 1.5$ mm). The transparency was significantly affected by the presence of parasitic absorber(s), which required annealing in air and repeated HIPing. Lu_2O_3 is also more expensive than Y_2O_3. The potential benefits of LuAG do not seem significant enough [P31, S37] to place the material in the position of a strong competitor for T-YAG (moreover, not all the data show an increased λ_{th} value of Yb:LuAG over Yb:YAG, for example). In any case the transmission values achieved are exemplified in Figure 4.50 where the spectra of Yb-doped YAG and

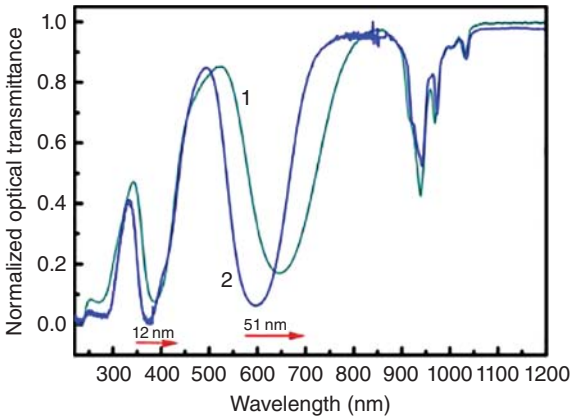

Figure 4.50 Optical spectrum of Yb-doped garnets: YAG (1) and LuAG (2) ceramics fabricated by vacuum sintering. Source: Ma et al. 2015 [M4]. Reproduced with permission from Elsevier.

LuAG are compared (single-crystal LuAG has in the VIS domain a transmission of around 82%). While relatively transparent specimens could be fabricated also by PECS, their transparency was lower than that achieved by vacuum sintering.

Doped transparent parts were tested in view of various applications. For instance, Ho^{3+}-doped ceramics showed lasing at the eye-safe wavelength of 2.1 μm [H11, Y5]. Doping with Yb^{3+} allowed achievement of short pulses (650 fs at 200 mW output), in a mode-locked cavity configuration [L58, N5]. Thin disc-type gain media showing slope efficiency of 64% (multimode operation) at an output of 101 W was also demonstrated. Scintillator abilities were also examined, for both single crystals and ceramic LuAg, and results were promising. A potential problem was the relative ease with which V'_o -type defects form under irradiation [B1].

4.2.5.3 Garnets Based on Tb

Another group of garnets of interest are those including terbium as the companion cation to aluminum (TAG). Tb^{3+} is paramagnetic and this is a condition for a transparent material to sense a significant Faraday effect; for reasons not discussed here, TAG is one of the paramagnetic materials most sensitive to the effect of a longitudinal external magnetic field. Such magneto-optical (if transparent) ceramics find important applications in devices, which are part of laser (especially high power) systems (see details in Section 5.2.8); they compete with certain single crystals and doped glasses. Therefore, as is the case with YAG (as RE^+ host for laser gain media), Tb-containing transparent ceramics are a desired product. Terbium–gadolinium–garnet (TGG) and gallium–gadolinium–garnet (GGG; see next section) are also relevant in this context – the latter being less performant than the Tb-containing materials.

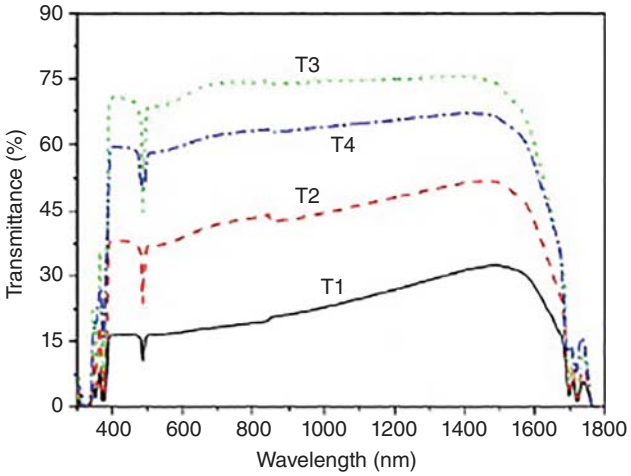

Figure 4.51 Transmission spectra of TAG ceramics, fabricated by vacuum sintering; T1 to T4 indicate different sintering temperatures (1550°–1700° range). Source: Lin et al. 2011 [L30]. Reproduced with permission from Elsevier.

The first attempts to produce ceramic TGG (around 2003) led to parts of relatively low transparency. Then Konoshima Chemical has produced highly transparent, albeit small size ($5 \times 1 \times 6\,mm^3$), TGG [Y5, Y11]. In parallel, quite transparent TAG ceramics were obtained, as shown in Figure 4.51 [L30].

It was also determined that doping TAG leads, in certain cases, to materials with improved Verdet constant. Doping with Ti, Ho, Si, and Ce was examined. Materials with the best properties (considering both optical aspects and thermal conductivity) were achieved by Ce^{3+} doping [S49]. In processing either commercial oxides (purity 4–5 nines) or coprecipitated powders were used [C20, L30]. Pressed compacts were sintered by firing, under high vacuum (1550–1650 °C); following practices used in YAG-sintering SiO_2 and MgO have been added as sintering aids. In Figure 4.52 the transmission spectra and specimen size is given, for the case of a few Ce-doped TAG ceramics [D1].

The TGG ceramics exhibit Verdet constants (see Section 5.2.8 for definition) of −37 rad/Tm (at a wavelength of 1064 nm) while that of,say, Ti-doped TAG obtains a level of −58 rad/Tm [F19].

4.2.5.4 Garnets Based on Ga

As far as we know such materials are yet used only in single-crystal form. We intend to say a few words here, about them, because fabrication of such compositions in ceramic form is feasible and probably useful, for microchip laser applications. Both ordered and disordered lattices, Ga including garnets, exist. In the first group, materials of the type $RE_3Ga_5O_{12}$, where RE is Gd, Y, or Lu, are included. Yb, when doped into the garnet

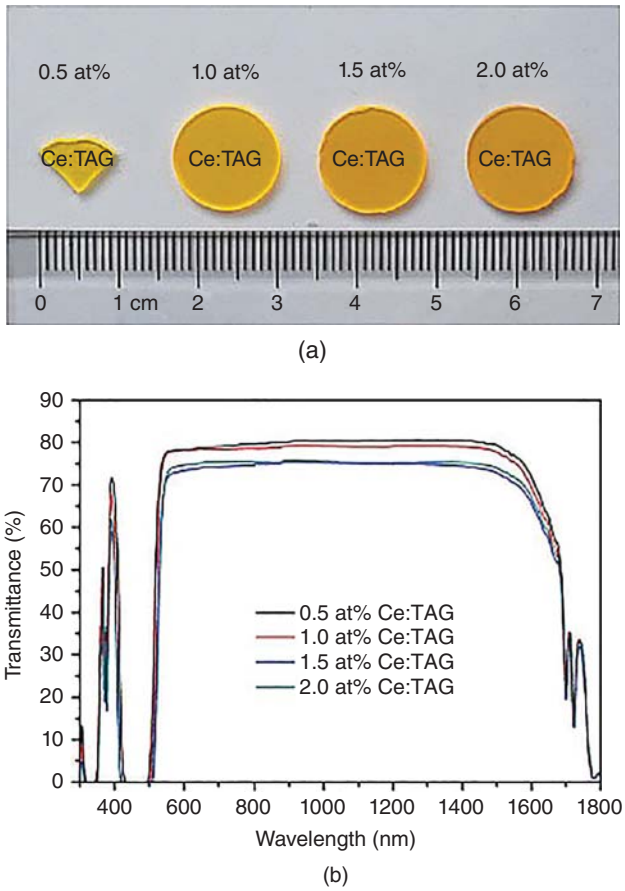

Figure 4.52 Imaging and transmission spectra of some TGG ceramics, as a function of Ce^{3+} dopant content; transmission decreases with increase of Ce^{3+} content. Source: Dai et al. 2018 [D1]. Reproduced with permission from Elsevier.

including Gd, shows a thermal conductivity similar (slightly lower) with that of YAG. However absorption at the zero phonon line is three times higher than for YAG as host, thus allowing efficient diode pumping [S24]. A disordered garnet, like the one achieved by introducing Ca and Nb, has poor thermo-optic properties but provides an emission line width, significantly wider than that offered by YAG, thus eliciting interest for the development of short pulse lasers.

4.2.5.5 Other Materials Usable for Magneto-Optical Components

In order to reduce, as much as possible, the number of sections, we will shortly describe here a few other TCs with magnetic properties albeit not having garnet lattice. But let us first recall that ceramics – having a suitable composition for exhibiting significant magnetic moments – are based on elements that make them very likely to absorb EMR, in the spectral region of interest in this book, even in single crystal form. Therefore the most

used magnetic ceramics, like the ferrites, are not transparent in the spectral region of interest in this book. On the other hand certain, less popular materials – which are magnetic in single crystals state ($FeBO_3$, FeF_3, or $GdFe_3(BO_3)_4$) – exhibit some, albeit moderate, transmittance in certain segments of VIS [G9]. It is possible to consider their fabrication as ceramic (polycrystalline) parts if these non-cubic particles are aligned, say, by subjecting suspensions to strong magnetic fields (like in the case of doped apatites) or if the sintered nanoparticle compacts retain their small size after firing. One of the rare magnetic ceramics brought to transparent condition is Lu-niobate (Lu_3NbO_7) [A13, A14], a cubic material (defect, fluorite-type lattice; $a = 0.5179$ nm). Its specific magnetic properties are not well studied but comparison with similar compounds suggest it may exhibit interesting magnetic properties (it is paramagnetic at RT [W4]). It was fabricated by spark plasma sintering, at around 1450 °C. It has a hardness of 13 GPa.

Owing to their large content of paramagnetic ions, some rare-earth oxides, like Ho_2O_3, Tb_2O_3, or Dy_2O_3 ceramics, may also be considered for the production of magneto-optical components relevant for the NIR range (for shorter wavelength lasers, hosts like CeF_3 or PrF_3 may be of interest). These materials that exhibit f–f transitions (owing to the native cation's electronic structure) in various domains of the VIS are, of course, not transparent over all the visible or NIR range. However they may be so in certain subdomains, relevant for lasing.

The Verdet constant of Ho_2O_3 ceramics may reach a value of −46 rad/Tm, larger than that of what is considered the commercial benchmark value, viz. that of TGG ceramics (−36.4 rad/Tm) [F19, F20]; it is hoped that doping of this host may further raise the value achieved in the un-doped material.

A family of quite exotic materials that may find application in the fields of magneto-optics and magnetic actuators is that of composites having an aerogel matrix and nanometric functional second phase dispersions. An example is that of magnetic silica aerogel-based composites in which hard magnetic $Nd_2Fe_{14}B$ particles confer the functionality [G14]. Such parts besides exhibiting transparency and significant magnetic susceptibility are also of ultralight weight. An interesting feature of the processing procedure is the fact that dispersed particle alignment is obtained by applying an external magnetic field on the sol-containing test tube, during the gelation process. The materials exhibit high coercivity ($Hc \sim 13$kOe), reasonable loop squareness, some transparency, and densities of around 0.2 g/cm^3. It is also possible to disperse crystalline nanoparticles exhibiting magnetic properties in a diamagnetic glass hosts or grow them in situ by adequate thermal treatments. Interesting glass-ceramics, acting as transparent magnets, were thus fabricated in borate hosts to which Fe_2O_3 and MnO were added [E1]. Another approach is based on infiltrating nanoporous Vycor-type glass hosts, with nitrate salts of components, which, on thermal treatment (ceramming stage), generate spinel structure ferrite nanocrystals [D7]. In such a way, samples exhibiting NIR transparency associated with saturation magnetizations of up to5.6 emu/g and a moderate Verdet constant value were prepared.

4.2.6 Transparent Yttria and Other Sesquioxides

4.2.6.1 Structure of Y_2O_3

A sesquioxide is a compound material containing three oxygen atoms like Y_2O_3. The latter is cubic at room temperature and has a relatively wide energy gap $E_g = 5.5$ eV [C35, M15, X3]. It is thus a potential candidate for functioning as a transparent ceramic between the NUV till the NIR. Light attenuation due to electronic transitions in native cations is also not a danger, since the Y^{3+} cation has the same electronic configuration as the krypton Kr noble gas. This situation may change if reduction of Y^{3+} to Y^{2+} occurs, forming a $5d^1$ configuration as also occurring for $Y_3Al_5O_{12}$ (YAG). Practice shows, however, that such reduction does not occur in Y_2O_3 during HIPing. The said native cation's oxidation state reduction requires an atmosphere more drastically reductive than in the case of YAG, owing to the smaller negative charge on the oxide anions.

Y_2O_3 is one of the earliest (c. 1965) ceramics for which technologies allowing their production in transparent form were simultaneously developed at General Electric, Sandia Labs, and Avco Corporation [A18, B58, L15]. Y_2O_3 exists in three different polymorphs with the cubic room temperature form transforming into a monoclinic variant at 1800 °C and then into a hexagonal one at 2200 °C [F10]. The body-centered cubic lattice belongs to the #206 space group $T_h^7(I2_1/a\bar{3})$ with a lattice period of $a = 10.604$ Å. (By the way, it exhibits the same structure as the bixbyite Mn_2O_3 mineral of $a = 9.411$ Å.) Figure 4.53a shows the Y and O atomic locations and coordination patterns. Notably, the lattice contains two inequivalent Yatoms (Y1 and Y2) hosting 8*a* and 24*d* Wyckoff sites of S_6 and C_2 symmetries, respectively; oxygens are located at 48*c* sites of C_1 symmetry. The unit cell contains 16 formula units (a total of 80 atoms).

Figure 4.53a also shows the coordination of the *Y*1and *Y*2 atoms. An approximate octahedral coordination exists for both Y1 and Y2. The Y1—O bonds are of equal 2.261 Å length within an octahedral ligand of oxygen anions. There are three different Y1—O bond lengths, 2.249, 2.278, and 2.336 Å within its octahedral ligand of oxygen anions. The (average) Y1—O bonds

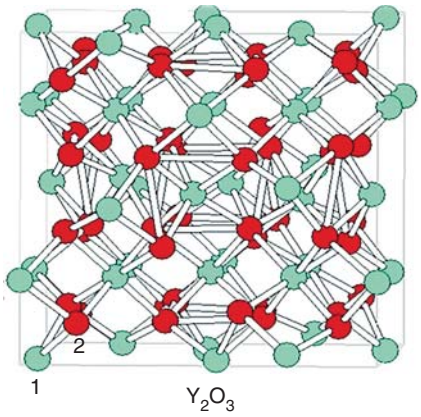

(a)

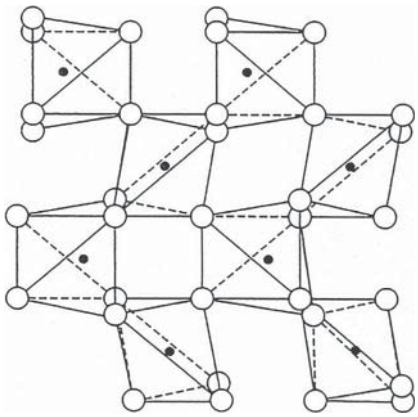

(b)

Figure 4.53 Images of Y_2O_3 lattice. (a) Structure (cubic) stable at *RT*. 1 Oxide anion, 2. Y^{3+} cation. Source: Reproduced from the Images Archive of Shutterstock with purchased permission. (b) The oxide may also assume, under certain conditions, this structure (C type of M_2O_3 ; derived from fluorite lattice) (hollow circles are Y^{3+} cations).

length is shorter than the Y2—O one. Each oxygen atom is linked to one Y1 and three Y2 atoms forming an approximate tetrahedral coordination. Calculations indicate formal electrical charges on the ions expressed as $Y_2^{2.16+}O_3^{1.44-}$, thus indicating the existence of a significant covalent fraction of the bonding. The Y^{3+} sites density is 2.681×10^{22} cm^{-3}.

4.2.6.2 Processing of Y_2O_3

In this context after presenting the available raw materials, the various approaches developed for T-Y_2O_3 fabrication are reviewed.

4.2.6.2.1 Y_2O_3 Powders

As it was noted in the Section 3.1.2.1 presenting general processing issues, the availability of performant powders is a prerequisite for transparency achievement in the case of most ceramics. The good results obtained already in the early experiments [A9, D25, R19] were possible also owing to the availability of quite good quality raw materials. For instance, the Lindsay YO code 1116 used in [A17] had a 99.99% purity and a micron size. Greshkovich et al. [G43, G40] developed a few synthesis methods including the conversion of Y, Nd, and Th nitrate solution to complexes based on oxalate as ligand. Low (800 °C) calcination was enough to generate a fine Th including Y-oxide powder (basic particles of 20–40 nm; milled state particles of ~0.1 μm). Pure fine powders have been also prepared by coprecipitation, with various anions. Using NH_4OH, as OH^- source, produced $Y_2(OH)_5(NO_3)\cdot H_2O$ precipitate, which was converted to an agglomerated nanomaterial (basic particles ~60 nm) at 1100 °C. Carbonate $[Y_2(CO_3)_3\cdot 2H_2O]$ precipitation with addition of $(NH_4)_2SO_4$ for agglomeration control also produced pure Y_2O_3 (calcination at ~1000 °C). Monodisperse particles were reported by Ikegami et al. [I1], who precipitated hydroxide and doped it with SO_4^{2-}. The FSP procedure (which gave the most sinterable Mg-spinel) was applied by its developer, R. Laine and collaborators, also for Y_2O_3 preparation. Single-crystal basic particles of a size <50 nm were obtained, but some non-cubic fraction exists in the as-synthesized powder. It was also shown that planetary milling (~3 hours) is able to convert micron size initial powders into submicron (~0.5 μm) quite sinterable material [W34]. As shown in Figure 3.4, even spherical, monosize (0.1–0.4 μm) Y_2O_3 precursor ($YOHCO_3$) powders were prepared [S44]. The spherical shape is conserved by the Y_2O_3 resulting from the carbonate precursor calcination (~600 °C).

4.2.6.2.2 Processing Approaches

A quite large number of approaches for the fabrication of T-Y_2O_3 were examined. For instance, a very interesting initial achievement was the inducing of transparency into the central zone of an opaque fine-grained highly dense (*BD* > 99%*TD*), hot-pressed Y_2O_3 ceramic (see Figure 4.54) [B58] by forging; it is one of the first Y_2O_3 ceramics exhibiting a significant level of transparency. The press forging (i.e. no die to exert lateral confinement) – effectuated at temperatures of 1400–1500 °C and stress levels of up to 5–600 MPa – was able to squeeze out the gas from the residual, low porosity, bringing about their collapse. The deformation rates (~8×10^{-3} in/min, in early stage) were, of course, much lower than those known from metals forging and increased with the decrease of the grain size.

Hot pressing at low temperature, by the aid of LiF (see also spinel and MgO), gave also good results [G2]; work was done at Sandia Labs [L15]. In fact this process also includes a late forging stage. At a temperature of only 950 °C (high pressure pressing of ~70 MPa and

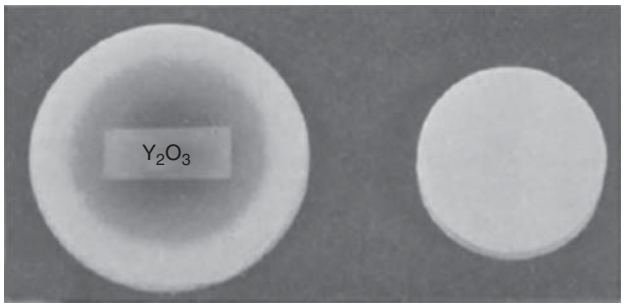

Figure 4.54 Sintered Y_2O_3 ceramic exhibiting some transparency (central region) after being subjected to forging; disc on the left side was subjected to forging, while that on right side is in as-sintered state. Source: Brissette et al. 1966 [B57]. Reproduced with permission from John Wiley & Sons.

long dwells of ~50 h), specimens 1–2 mm thick showing transparency similar to that of a single crystal, in the NIR–MIR zone, could be obtained in conjunction with a $\overline{GS}$ of only 3 μm. LiF was removed during the long dwell and (BD_f had a value of 5.030 g/cm^3, comparing well with the theoretical 5.031 g/cm^3). Hot pressing of pure Y_2O_3, under vacuum (10^{-5} Torr), was successfully tested also (US army lab), but it required temperatures of up to 1500 °C [D25]. After outgassing at 600 °C/1 h, the pressure (40–50 MPa) is applied, and a dwell on only two hours is held at ~1500 °C. Despite the relatively high t_s°, the $\overline{GS}$ was in the 0.5–1.0 μm range, with an IR transmission similar to that given in [L15], viz. it reached a T = 83% level, for a thickness of 2.5 mm. Residual carbon is eliminated by a post-HP annealing in air (~1000 °C/1 h). The process gives reproducible results. It is critical to apply the pressure around that used for outgassing and not too close to t_s°.

The technology, developed at GE, at about the same time with the forging approach, was based on high (>1700 °C) temperature sintering (which gave good results also in the case of both alumina and spinel). An important feature of that procedure is the use of H_2 atmospheres in order to facilitate gas evacuation from the pores. Another feature, specific for the T-Y_2O_3 development, was the importance attached to grain growth prevention as a densification facilitator; the approach used for that was growth control by additives. In this technology yttria was alloyed with other refractory oxides like ThO_2, HfO_2, or ZrO_2, viz. powders able to form solid solutions with the matrix [J18].

The solute tends to segregate at the GBs of yttria grains and, by that, turns on a drag mechanism able to reduce grain boundary migration rates. The importance of maintaining pore/GB contact was noted by Alexander and Balluffi [A6] for metals and then by Burke for ceramics [B67]. This seems to be achieved by slowing down diffusion in directions relevant for GB movement. It is not likely that diffusion along the GB – essential for densification – is not affected too, but this drawback is, probably, weaker than the gain brought about by the GG rate slowdown. In turn, this keeps, at high densification levels, the pores in contact with the GBs significantly, thus facilitating densification. In Figure 4.55 the microstructure of a thoria alloyed and a pure Y_2O_3 part microstructure are shown. Observing the massive amount of occluded porosity in the pure material, similar to the case of MgO-free alumina, the microstructure in Figure 4.55 (bottom) is that of a ceramic having the excellent transmission shown in Figure 4.56 [A9]. The transmission level obtained is close to that of Y_2O_3 single crystals.

The seminal work of R.C. Anderson was further pursued, leading to excellent hosts for lasing RE^+ cations

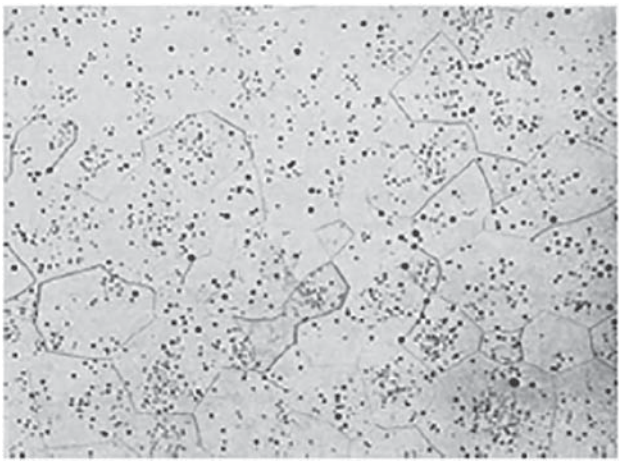

(a)

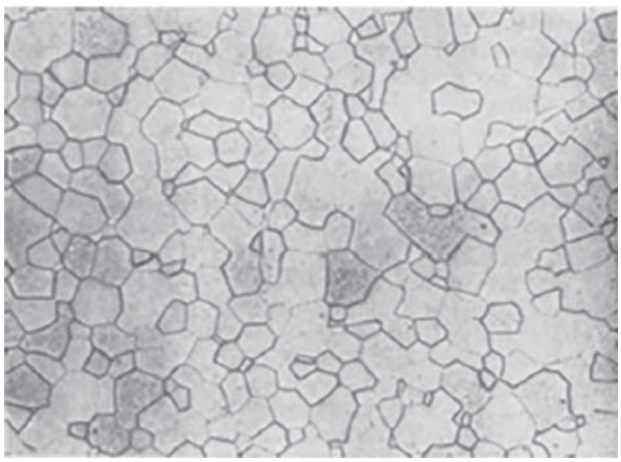

(b)

Figure 4.55 Microstructure of sintered Y_2O_3 ceramics. (a) Pure yttria showing abnormal grain growth and the ensuing trapped porosity. (b) Yttria including thoria showing relatively fine microstructure and lack of porosity; as a consequence specimen is highly transparent. Source: Jorgensen and Anderson 1967. Reproduced with permission from John Wiley & Sons.

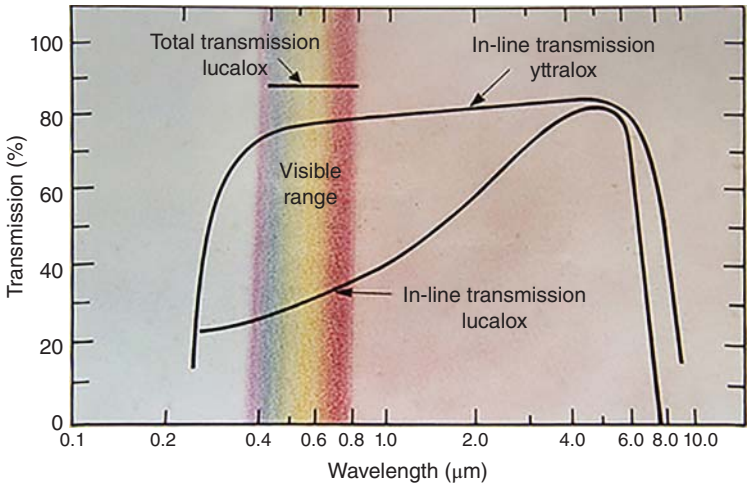

Figure 4.56 Transmission curve of transparent yttria ceramic (YTTRALOX) compared with that of translucent alumina (LUCALOX). Source: From Anderson 1970 [A9].

[G43, I4]. For instance, Greskovich et al. showed that the ThO_2 additions need to be in the form of particles <1 μm and dispersed at a high level of uniformity in order to accomplish its task [G40–G45]. Using oxalate route synthesized powder, he was able to reduce the level of residual porosity to a few ppm. In Figure 4.57 [G40] the microstructure of a high optical quality yttria part is shown (a) together with its transmission spectrum (b).

The homogeneity of composition is critical also because its absence leads to random variations of refraction index, which macroscopically translate in scattering (optical waviness called "orange peel"). Long sintering

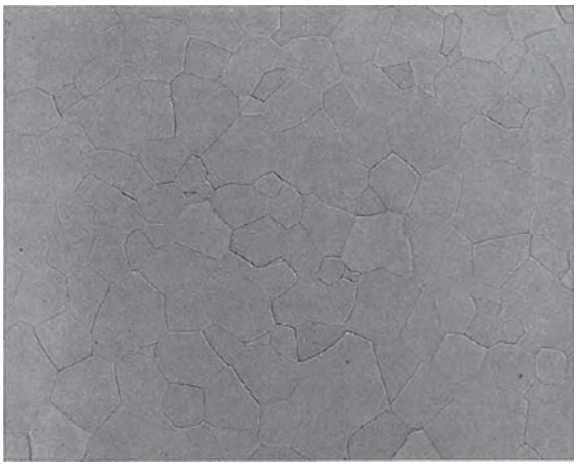

(a)

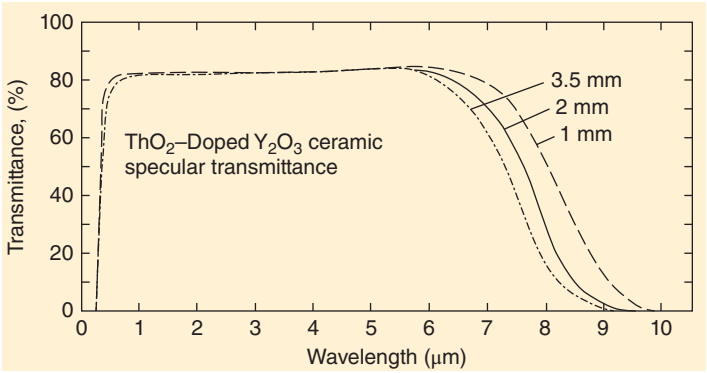

(b)

Figure 4.57 Microstructure and transmission spectra of thoria-doped yttria ceramic. (a) Microstructure (SEM image on polished and etched surface). (b) Transmission curves as a function of specimen thickness. Source: Greskovich and Chernoch 1973 [G40]. Reproduced with permission from AIP Publishing.

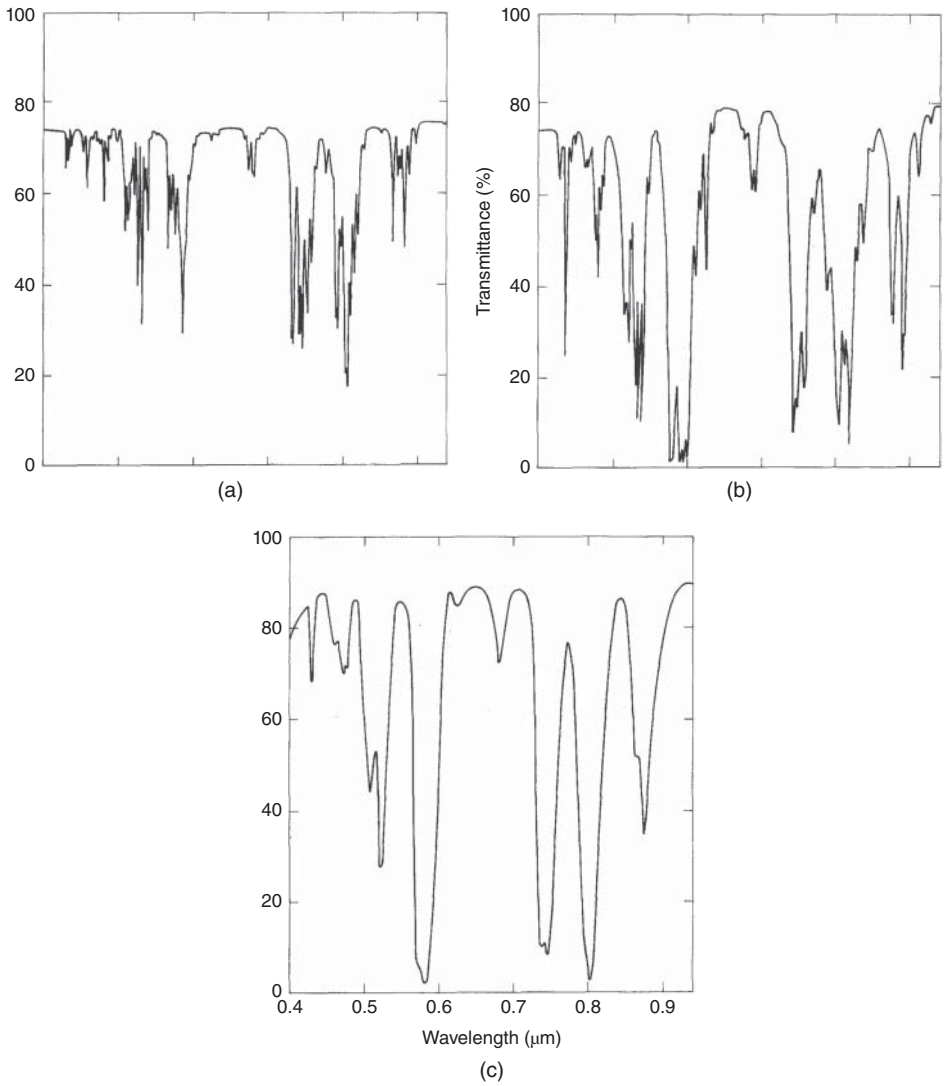

Figure 4.58 Transmission spectrum of Nd-doped yttria (thoria) transparent ceramic compared to that of two other hosts (Yttria, 89 mol%; ThO_2, 10 mol%; Nd_2O_3, 1 mol%). (a) Nd:YAG. (b) Nd:Y_2O_3. (c) Nd:glass. Source: Greskovich and Chernoch 1973 [G40]. Reproduced with permission from AIP Publishing.

times improve homogeneity (heating up to 2170 °C in 6 hours followed by dwells of 20–125 hours). In the case of sulfate-derived powders, the long dwells ensure vaporization of GB located sulfur-rich phases, which otherwise represent liquid able to facilitate GG. The spectrum of a Nd-doped yttria transparent part is shown in Figure 4.58 [G40]. Lasing was achieved in 1974 with such gain media; the efficiency was modest (mostly owed to poor pumping). The relevant curve is shown in Figure 4.59 [G39].

Ikesue et al. has followed the $Y_2O_3 + HfO_2$ variant proposed by R. Anderson [A10] and was able to significantly reduce sintering temperatures and time by combining VS (1650 °C/1 h; 1×10^{-3} Pa) with HIPing (1700 °C/3 h/Ar 1200 MPa) [I4]. The *GS* was also reduced to ~30 μm, while the transmission was quasi-theoretical. A variant of the Anderson concept of Y_2O_3 grain growth control by GB chemistry modifications was examined by Rhodes et al. [R17–R19]. In this case the alloying oxide was La_2O_3. This sintering strategy of has an important specific element. The solid solution compositions are selected in the range for which the lattice stable at *RT* is cubic, but at higher temperatures (>2000 °C) there is a range where a hexagonal and cubic state can coexist. Firing in the two phase field triggers a GG rate reduction mechanism, which facilitates densification. Then it is necessary to stop during cooling, in the temperature range where the cubic lattice is stable, and keep a dwell long enough to ensure the 20–50 vol% hexagonal phase (source of scattering) conversion to cubic. Typically sintering at 2170 °C (H_2) is followed by a five hours dwell at 1920 °C for alloys including 8.5–12.1 mol% of La_2O_3. The two phase field has to be at ~0.8 of the melting point in order to fast enough diffusion. A proper matching of composition and processing conditions allows that hexagonal phase elimination take place without causing

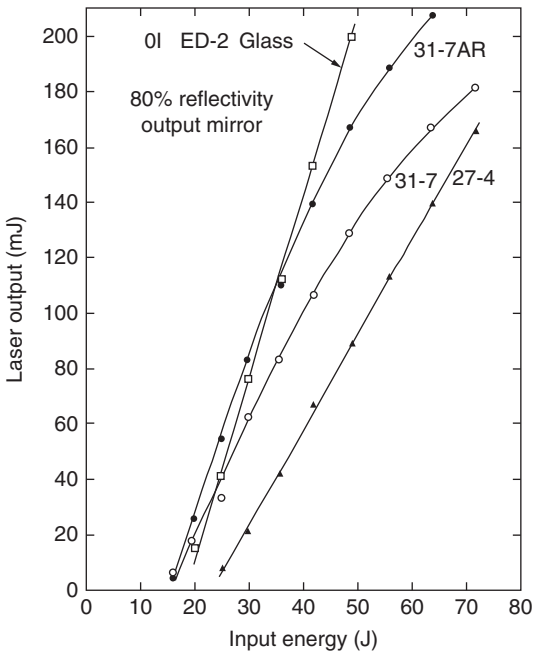

Figure 4.59 Lasing efficiency of specimen shown in Figure 4.58 (poor efficiency pumping procedure); 12-1 and 13-4 cooled slowly, while 12-1A, 13-4A, and 27-4 rapidly cooled; OI = Owens–Illinois-grade ED-2 laser glass. Source: Greskovich and Chernoch 1974 [G40]. Reproduced with permission from AIP Publishing.

pore formation. Total transmission of the best parts was of ~81%, with the $\overline{GS}$ of the equiaxed grains went up to ~90 μm. Other oxide additives like MgO, Al_2O_3, $MgAl_2O_4$, or TiO_2 were also found to help Y_2O_3 densification [G5]. As opposed to La_2O_3 or ThO_2, these oxides are effective in low amounts. This is practically important because it was observed that Y_2O_3 with low amounts of additive is more performant than highly alloyed materials [R17] in certain applications like envelopes for Na vapor-based lamps. It was shown, for instance, that Y_2O_3 containing low amounts of ZrO_2 (0.5%) or La_2O_3, can be sintered so as to exhibit high transmission (~76% at $\lambda = 500$ nm). Vacuum sintering was examined by a number of workers, e.g. [J12]. A low grain size (~2 μm) is ensured by the low sintering temperature (~1650 °C) made possible by using O_2 as firing atmosphere [H41]. O_2 can diffuse out of the pores (being ionized to O^{2-} at high $t°$), making, as far as this aspect is concerned, closure of final porosity easier than, say, air. Air contains also nitrogen. While lately it was determined that N_2 molecules out-diffuse at higher rates than previously thought, these rates are still significantly lower than those concerning oxygen. O_2 also seems to slow GG rate. Sintering in an O_2-containing atmosphere, like air (leaner mix than that used by Huang et al.), supplemented by HIPing, was also examined [H41]; low transparency ($T_{800\,nm} \approx 55\%$) was achieved. Generally, the transient liquid-assisted densification is a useful procedure because it leaves the matrix without a deleterious second phase; a downside is that it facilitates GG. In the case of Y_2O_3, it was tried to use BeO for such an approach [T24]. The sintering takes place at high temperatures of ~2200 °C for five hours under H_2. The amount of BeO has to be lower than 2%, optimally within the 0.3–0.7 range. The parts thus obtained exhibit transmission levels close to the theoretical, similar to those reported in [G40]. More recently efforts have been focused on achieving high transmission coupled with low grain size. In terms of processing this requires sintering temperature reduction and correlated GG rate decrease. For instance, Hinklin et al. [H28] prepared a highly sinterable powder by the FSP method. After sintering under mild vacuum, at 1400 °C for five hours, the final densification was achieved by HIPing at 1400 °C/3 h/Ar/120 MPa. Reoxidation was done by $t°_a = 1250$ °C/3 h. A $\overline{GS}$ of 0.4 μm coupled with reasonable, in the IR range (up to 70%), transmission (low in the VIS, however) was obtained. Saito et al. [S3] also maintained fine microstructure by sintering at ~1500 °C, but transmission was low (~20% at $\lambda = 500$ nm). It was also tried to simplify processing by replacing vacuum firing with air sintering. Eilers [E2] obtained starting from commercial nanopowder (no additives) – by combining AS (1600–1700 °C) with HIPing – specimens of low transparency ($T \sim 50\%$ at $\lambda = 800$ nm) coupled with $\overline{GS} \sim 2.5$ μm, as noted above. Using a two stage sintering process ($T_1 = 1500$ °C and $T_2 = 1400$ °C/20 h) – in order to minimize GG – Serivalsatit et al. [S23] obtained good transparency ($T = 75\%$ for $\lambda = 800$ nm) coupled with a $\overline{GS}$ as low as 0.3 μm while not at a par with [G40]. An interesting relatively short (two to four hours) one stage sintering at moderate (~1750 °C) temperature was effectuated by Balabanov et al. [B7] using high frequency (24 GHz) MW heating. The obtained specimens ($Y_{1.7}La_{0.2}Yb_{0.1}O_3$ material) exhibited a transparency good enough to allow lasing ($\lambda = 1030$ nm) with a reasonable slope efficiency. A number of teams (e.g. [Y18]) fabricated transparent yttria by the aid of SPS; combining HP with HIP was also tried with very good results [Z22].

The yttria has a high "*n*" (1.926, at 600 nm), and that with the aid of La_2O_3 an even higher one (1.937). While this is interesting – for certain applications like lenses – as a downside it contributes to transmission reduction.

4.2.6.2.3 *Discussion of Processing*

Looking at the data accumulated on the various aspects of T-Y_2O_3 processing, certain conclusions, some of them specific to Y_2O_3 or a small set of TCs, can be drawn. For instance, it can be seen that a wide variety of sintering approaches have been examined, and many types of fine powder (including optimal monosphere particles) were

made available quite early. On the other hand, relatively little was made regarding powder processing so as to bring it into optimal ready-to-form (mostly press) state. Most of the research effort was focused on aspects of the sintering stage. Quite early, information was available on issues like identification of controlling mass transfer processes, grain boundary mobility and drag factors, effect of cationic substitutions, effect of solid solutions forming and coexistence of variable symmetry polymorphs, and Y^{3+} diffusion rates. Ways to preserve nanograin size at near-theoretical bulk density levels were also examined [C14]. For instance, Chen and Chen [C28] suggest, based on a smartly chosen type of experimental data (effect of sintering atmosphere, nature, and amount of the Y^{3+} substitution with acceptor and donor dopants), that for Y^{3+} diffusion the interstitial track is the one preferred. The bixbyite type lattice of Y_2O_3 favors such a track owing, among other characteristics, to its resemblance – regarding certain features – to the fluorite lattice characteristic for c-ZrO_2 or CeO_2. As a result, the former is able to dissolve large amounts of extrinsic cations. The Y^{3+} diffusion is the rate limiting process in the case of GB migration and also densification. Oxygen vacancies tend, of course, to enhance Y^{3+} movement, while oxygen interstitials have the opposite effect. In pure Y_2O_3 the $[O_i^{''}]$ and $[V_o^{\bullet\bullet}]$ seem (based on electric conductivity data) rather low in air. This is in accord with the high formation energy of both Schottky and Frenkel defects in refractory oxides like Y_2O_3 [B72]. Let us note that one consequence of this is the enhancement of solute dopants influence on host's ion diffusion. Dopants markedly affect ionic diffusion processes in Y_2O_3 also, because the dopant ↔ intrinsic lattice defect interaction is strong. Severely undersized dopant cations also tend to distort the lattice, a fact that further facilitates diffusion. Atomistic simulation [B71] suggest that dopant cation size is a critical factor in determining the type of site it locates on, solution mechanism (type of point defects that compensate charge due to dopants), and clustering patterns. Modeling more specifically shows that for low radius M^{2+} cations, charge compensation by M_i'' formation is favorited energetically. For larger M^{2+}, compensation by V_o'' or M_i'' is equivalent. If clustering is possible, the $V_o^{\cdot\cdot}$ is chosen. For M^{4+} substituents, O_i'' is always preferred. Cosolubilization of M^{2+} and M^{4+} does not lower solution enthalpy, except in a few cases like $Ca^{2+} + Zr^{4+}$ [B71]. The GB migration rates are increased by divalent (introducing oxygen vacancies) or trivalent (less) substitutional cations, and reduced by tetravalent ones (introducing oxygen interstitials). A similar trend is observed also in the later work of Kodo et al. [K32]. The effect of acceptor cation dopants on M_b is illustrated in Figure 4.60 [K32], at various temperatures (air). Zn^{2+} (1 mol%), for instance, is able to raise the M_b (1550 °C)

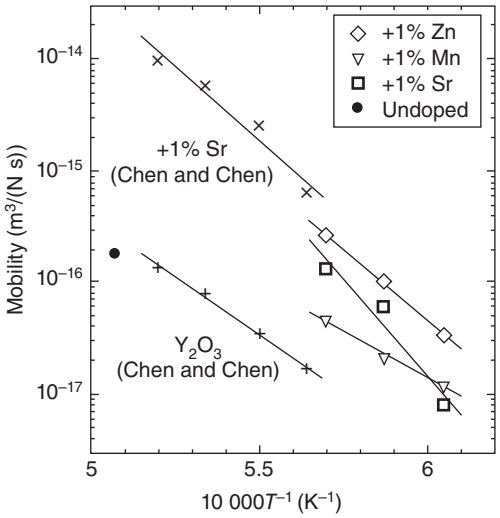

Figure 4.60 Effect of doping on the grain boundary mobility (Mb), at various temperatures, in the case of yttria specimens are subjected to sintering. Source: Kodo et al. 2010 [K32]. Reproduced with permission from Elsevier.

from 3×10^{-17} to $\sim 7 \times 10^{-15}$ $m^3/(N\,s)$. While M_b increase is not, of course, desirable, it is brought about by diffusivity increases, which also accelerates matter transport along the GBs. This effect is prevalent and, in practice, despite the increase in pore/GB separation probability, the densification rate is raised more, and this brings about advanced (close to *TD*) BD_f levels at temperatures as low as 1300 °C. The dopants, while segregating at the GBs, are producing neither amorphous layers nor second phases, as shown in Figure 4.61 [K32].

An important additional effect of $M^{2+} \rightarrow Y^{3+}$ substitution was also described. If this introduces a lower radius cation (in six coordination $r_{Y^{3+}} = 0.9$ and $r_{Zn^{2+}} = 0.8$ Å) – which also reduces surrounding $O^{\delta-}$ basicity – the $Y–O^{\delta-}$ bond length increases; the distorted lattice facilitates Y^{3+} movement, significantly raising the quite low speed of this movement (in the range 1400–1670 °C). In pure Y_2O_3, the self-diffusion coefficient D has values in the $1.4–2.67 \times 10^{-10}$ cm^2/s; $E_a \sim$ 69 200 cal/mol [B29]. Such effects supplement the influence of V_o'' formation ($M^{2+} \rightarrow Y^{3+}$) on diffusivity of Y^{3+}.

The structural information previously detailed was, in part, used to guide the technological developments by some of the teams. The correlation of the progress in scientific understanding with processing procedures should have been stronger; a significant part of the engineering development went in parallel with the scientific efforts. The above notwithstanding the data shows that more than one approach was developed enough to allow T-Y_2O_3 fabrication. In order to compare them, the figure of merit has to include transmission level, grain size, and processing cost and difficulty, at least.

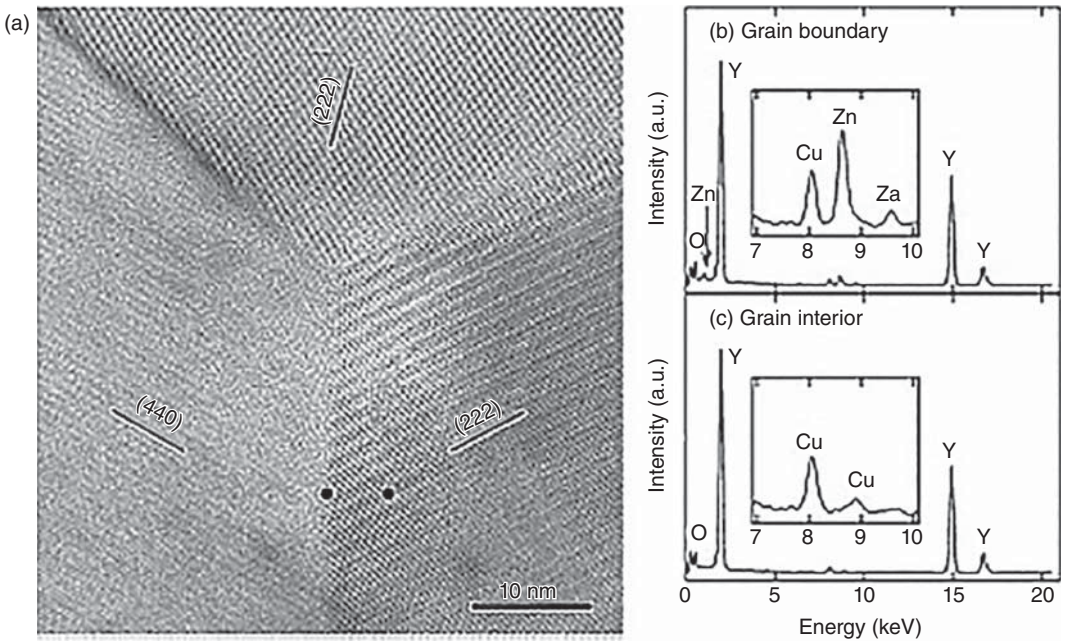

Figure 4.61 Dopants segregation at the GBs of yttria ceramics without amorphous layer formation. (a) HRTEM image of three grains junction indicating chemical analysis points. (b) Chemical analysis at point on the grain boundary. (c) Chemical analysis at point inside a grain. Source: Kodo et al. 2010 [K32]. Reproduced with permission from Elsevier.

4.2.6.3 Properties of Y_2O_3

The mechanical properties of Y_2O_3 are less good than those of α-alumina or YAG, but the thermal conductivity is competitive. A selection of properties relevant for applications is shown in Table 4.10.

4.2.6.4 Other Sesquioxides with Bixbyite Lattice

Some other sesquioxides like Sc_2O_3 and the rare-earth Lu_2O_3 have a cubic bixbyite lattice (C-type M_2O_3) like that of yttria and the heavy lanthanides. In fact La_2O_3 can also be obtained with a bixbyite structure at low temperature (kinetic effect), but a hexagonal (A-M_2O_3) form (seen in the lighter lanthanides too) is the thermodynamically stable state. So while La_2O_3 cannot be produced in transparent form by simple powder sintering, both Sc_2O_3 and Lu_2O_3, cubic materials, can be fabricated as transparent ceramic bulk objects. While the cubic lattices ensure absence of birefringence-related scattering – EMR attenuation the electronic configuration of the cations prevents absorption-related transmission reduction; the Sc^{3+} has an [Ar] electronic configuration, while Lu^{3+} has an f 14 external electron shell. In this context, however, one has to note that if reduction to Lu^{2+} occurs ($5d^1$ ion), absorption of light occurs.

Practically parts or thin films [X4], made of Sc_2O_3 or Lu_2O_3, are of most interest as hosts to RE^+-type dopant cations with applications in lasing, scintillator devices, etc. To what extent these hosts bring any benefit(s) compared to Y_2O_3 or garnet-type TCs, like YAG, must be analyzed for each application. In the case of Lu_2O_3, the thermal conductivity of the pure oxide is practically not reduced by doping heavily with Yb as opposed to what is seen in YAG and, to a lesser extent, in the other relevant bixbyites (the comparison is correct for *RT* and down to some 100 K; at lower temperatures things change). In relative terms the difference between doped Lu_2O_3 (say, with a 10 mol% of Yb^{3+}) and YAG is impressive as Figure 4.62 [S10] shows.

Table 4.10 Properties of Y_2O_3 ceramics.

Property	Unit	Value
t_f°	°C	2410
λ_{th} *RT*	W/(m K)	13
α	K^{-1}	4.1×10^{-6}
ρ	g/cm^3	5.04
E	GPa	175
Mohs	—	7
*HV*0.5	GPa	8
TRS	MPa	150
K_{IC}	$MPa \times m^{0.5}$	1.1
ε_r	11	—
n, at 600 nm	—	1.9263
n at 1 μm	—	1.8892

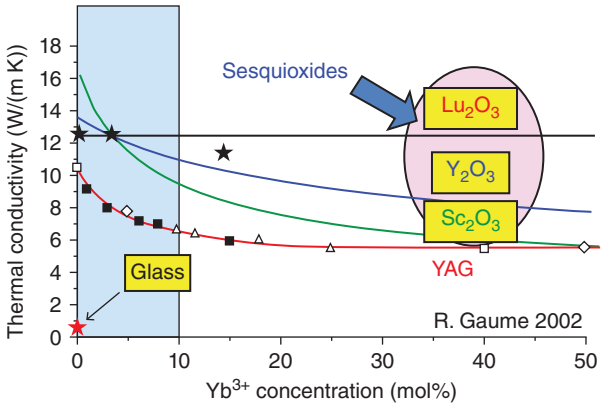

Figure 4.62 Thermal conductivity variation, as a function of their Yb^{3+} content, in the case of a few transparent ceramic sesquioxides (temperatures in excess of 100 K). Source: Sanghera et al. 2011 [S10]. Reproduced with permission from SPIE Publishing.

In absolute terms the gain is moderate so that the effect on thermal shock resistance is not that large, not even when YAG is compared to Lu_2O_3 (the largest difference). However even the moderate differences seen are of practical relevance. Bourdet et al. calculates [B49] that Yb, doped to bixbyite sesquioxides, may generate for 15 cm apertures (a size achievable with ceramics and not single crystals) as much as 1 kJ per beamline (cryogenic operation; diode pumping at 940 nm) without breaking; this is more than achievable using YAG ceramics.

4.2.6.4.1 Sc_2O_3

The specific feature of this bixbyite structure (sesquioxide of most interest for doped TC-type parts) seems to be the short dopant interaction distance its lattice provides [L62]. The "a" value is the smallest, within the set of bixbyites we compare (0.986 nm), and the density of cationic sites the highest (3.34×10^{22} per cm^3). This facilitates the use of sensitizing schemes exploiting energy transfer (on the other hand also facilitates self-quenching of the lasant cations). A ceramic-type host is attractive, when compared to a single crystal form, because the latter is produced at very high temperatures and the segregation coefficient of both Nd and Yb, especially the former, are low [L62, L67]. This oxide melts at 2430 °C and has a TD of 3.68 g/cm^3; the thermal conductivity, at 19.8 W/mK, is higher than that of other bixbyites, but it drops under that of Lu_2O_3 when heavily doped with Yb^{3+}.

Sc_2O_3 transparent ceramic bulk parts are fabricated mostly by the aid of the conventional TC production technology in which powder compacts are vacuum sintered. The high refraction index ($n = 2.0$ at 300 nm) means quite high reflection loss so that theoretical transmission is not very high at ~79%. The bandgap is good at 5.7 eV and so is chemical stability.

Powders are prepared mostly by coprecipitation techniques, used also for YAG synthesis – in which precipitants like NH_4OH, NH_4HCO_3, or $N_4(CH_2)_6$, are used on salts like chloride, nitrate, or hydrated basic sulfate carbonate; pyrolysis of hydroxyl sulfate was also used [B54, L21, L40, L43, L47, L56, W13, Y6]. Vacuum firing has to be effectuated at temperatures in the 1700–1850 °C for 5–30 hours; in some cases HIP was used for the final pore closure [L43].

T-Sc_2O_3 parts were characterized as to their thermal lensing propensity (comparison with other TCs [P31]), transmission, and emission spectra [L21, L43, L56, L62, T26, W13]. The highest transparency was achieved by the team of Ikesue and that working at Konoshima [I3]. Here, in Figure 4.63, the transmission spectrum of an Yb doped part is given [L56] as an example.

An interesting study regarding sensitization of Yb^{3+} emission with the better absorbing Nd^{3+} cation was effectuated by V. Lupei et al. In Figure 4.64 the emission spectra of diode-pumped (825 nm) codoped Sc_2O_3 specimens is shown [L63].

The study shows, inter alia, that energy transfer between Nd^{3+} and Yb^{3+} is taking place, with a high yield in this host; the crystal field influence is stronger than in other sesquioxide hosts, and the superposition of the bands, involved in RE^+ energy transition, is better. As a result the level of Yb doping (a bad absorber of pumping light), necessary for significant laser power achievement, may be reduced markedly.

A few lasing experiments are also reported [B49, L47, T26]. The tests of Bourdet et al. showed Sc_2O_3 as being the less attractive host, for Yb, among the bixbyites. Tokurakawa et al. showed that a multigain

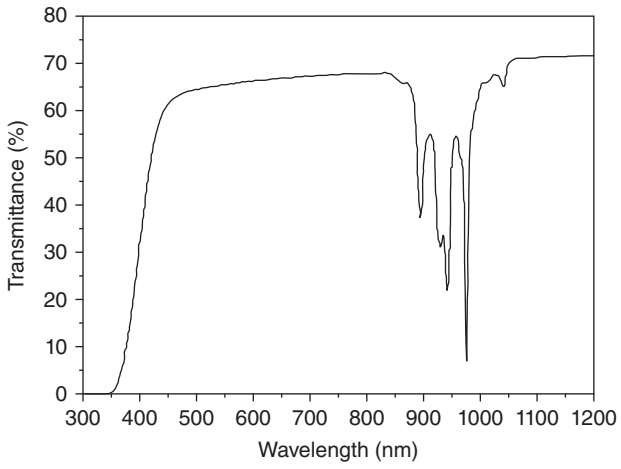

Figure 4.63 Transmission spectrum of Yb-doped Scandia transparent ceramic. Source: Lu et al. 2013 [L56]. Reproduced with permission from Elsevier.

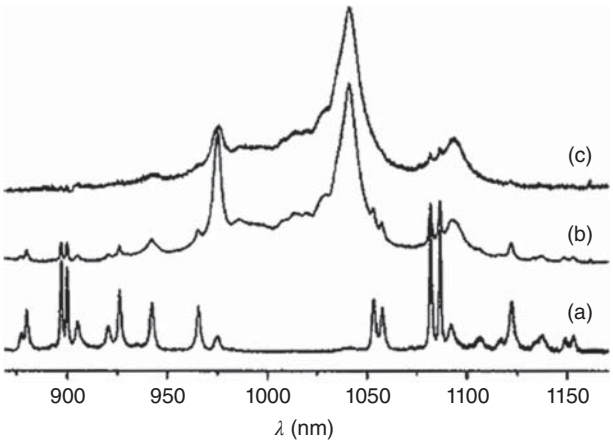

Figure 4.64 *RT*, emission spectra of Yb, and Nd co-doped scandia ceramic host pumped at 825 nm, in a Nd^{3+} absorption band. (a) 0.3 at% Nd and 0.1 at% Yb. (b) 0.3 at% Nd and 1 at% Yb. (c) 0.3 at% Nd and 3 at% Yb. Source: Lupei et al. 2009 [L63]. Reproduced with permission from Elsevier.

arrangement (allowing the exploitation of a wider emission line) offers the possibility to produce quite short pulse lasers (at 1042 nm, 66 fs pulses were obtained; average 1 W power); a 2.5 at%Yb-doped Sc_2O_3 plate was combined with a 1.8 at%Yb containing Y_2O_3. J. Lu et al. also achieved lasing with a 2.5 at%Yb, pumping at 940 nm. Laser oscillation of low efficiency (around 10%) was recorded at both 1041 and 1094 nm, on 1 mm thick plates. In any case lower pumping intensity than in YAG is needed when Sc_2O_3 is the host of Yb and because the FWHM of the relevant emission line is larger, in the latter host, it may ensure achievement of shorter pulses than those of Yb:YAG.

4.2.6.4.2 Lu_2O_3

Lu_2O_3 ($TD = 9.41\ g/cm^3$) is a bixbyite structure, refractory oxide ($t°_f = 2500\,°C$) in which the cation is an RE^+; the Lu^{3+} cation has an electronic structure in which both the d and f orbitals are full ($Lu^{3+} = (Xe)4f^{14}$), so that the host will not introduce parasite absorption or emission peaks in the NUV–MIR range (behavior similar to Y_2O_3 and Sc_2O_3, which do not include RE^+ cations). Like Y^{3+}, Lu^{3+} can be reduced to Lu^{2+} ($5d^1$), which does absorb EMR. The main reason it elicited attention seems to be its ability to maintain, as opposed to other sesquioxides, its thermal conductivity under heavy Yb doping [P22, P23]. Its reflection losses are somewhat higher than those of YAG, owing to a higher refraction index [$n_{900m} \approx 1.94$; n_{500m} (YAG) ≈ 1.87]. Y. Shi et al. [S33] prepared – using the coprecipitation of hydroxide by the aid of $NH_4OH + NH_4HCO_3$ – sinterable Lu_2O_3 powders, which were subjected to sintering under H_2 (six hours at 1850 °C). Small ($\phi = 10$ mm) transparent ($T_{600\,m} \sim 81\%$, $t = 1$ mm; $T_{theo} \sim 81\%$) discs ($GS \sim 10$ µm) could be obtained. Using vacuum sintering (~1800 °C) followed by HIPing, A. Ikesue [I7] obtained heavily (at 10%) Yb^{3+}-doped Lu_2O_3 by the aid of sintering additives. The optical transmittance of an Yb:Lu_2O_3 disc is shown in Figure 4.65.

Vacuum sintering at 1700 °C/5 h powders prepared by precipitation (urea) also led to transparent parts allowing lasing when doped with Nd as shown by J. Lu et al. [L52]. Yb-doped Lu_2O_3 highly transparent parts were obtained also by an HP + HIP firing at 1600 °C/2 h, as reported by J. Sanghera et al. [S10]. The quality of the specimens was good enough to allow lasing of Yb^{3+} at 1.08 µm under diode laser pumping.

More recently the PECS approach was also tested as a way of densifying Nd-doped Lu_2O_3 [B41]. As shown by R. Boulesteix et al. [B41], high transparency parts can be thus fabricated (1400 °C/130 MPa). The authors formed green bodies by slip-casting instead of pouring powder in the PECS machine's die. Discs with a 2 mm thickness exhibited a transmission $T \sim 81\%$ at $\lambda = 750$ nm ($T_{theo} \sim 82.5\%$). Similar results were reported also by L. An et al. [A14].

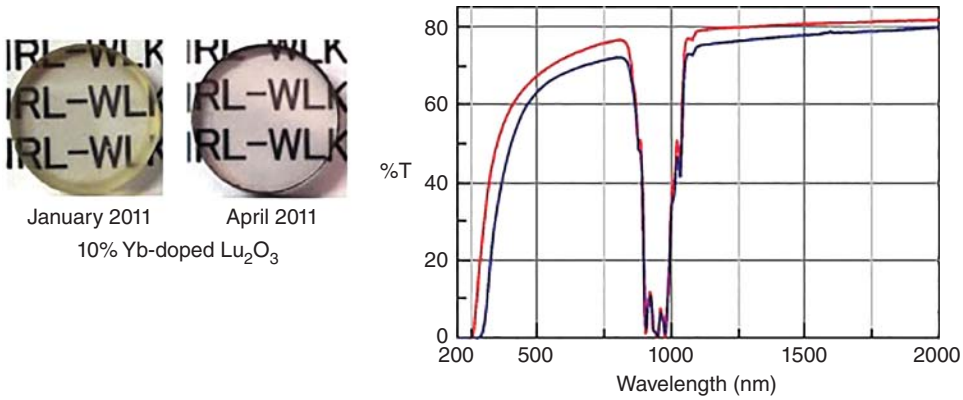

Figure 4.65 Imaging and transmission spectra of two 10 mol% Yb containing lutetia ceramic parts; curves at various stages of fabrication technology development. Source: Courtesy of A. Ikesue [I7].

4.2.7 Transparent Zirconia

Zirconia is one of the poster boys of the "advanced ceramics" domain. This oxide can be obtained in different forms that exhibit various useful combinations of properties [S69]; for instance, one modern application, fuel cells, can use it owing to its ability to function as an ionic conductor(O^{2-}) [B5]. Such a versatility makes zirconia relevant for many applications; this is one of the reasons for the wide industry interest in this material. The main reason for the attention this ceramic draws from the community of ceramics scientists stems, however, from the fact that smart engineering allowed a massive boasting of its normal mechanical properties. The main mechanism explaining the dramatic mechanical properties improvement – when pure zirconia is suitably alloyed (for stabilization of its tetragonal polymorph) – was quite quickly understood [G4]. The understanding was used for further improvement. Smart engineering means combination of fine powder with suitable chemical alloying (especially with Y_2O_3) and firing schedules. In short, when an adequate amount of Y_2O_3 is added to pure zirconia, which is monoclinic (m-ZrO_2), it converts to a tetragonal polymorph at high temperature, whose form is retained – due to a kinetical effect – also at *RT*, where it is not the thermodynamically preferred phase. As a result if a crack develops in a sintered part, its development is slowed down by the presence of the t-ZrO_2 according to a mechanism that will be described below. At the macroscopic level an increase of the K_{IC} values to ~10 MPa $m^{1/2}$ and of the TRS to 1.5 GPa (and in certain cases to 2.5 GPa) was measured. Owing to the above, such materials are among the best ceramics available, as far as mechanical properties are concerned. Cubic zirconias also exhibit high anionic electrical conductivity over 400 °C [G7]; this feature makes the material interesting for applications in the domain of energy conversion. The material is relevant also for us because, under certain conditions, ZrO_2 can retain a cubic lattice also at *RT*, thus becoming a potential transparent ceramic. In fact, as will be shown below, a measure of transparency may also be conferred to t-ZrO_2; even monoclinic zirconia made parts may achieve translucency.

4.2.7.1 Structure: Polymorphism, Effect of Alloying

At atmospheric pressure, zirconia (ZrO_2) exists in three crystallographic modifications [S69]: monoclinic $\overset{1170\,^\circ C}{\longleftrightarrow}$ tetragonal $\overset{2370\,^\circ C}{\longleftrightarrow}$ cubic $\overset{2680\,^\circ C}{\longleftrightarrow}$ liquid. Of special interest is the $m \leftrightarrow t$ transformation, which occurs according to a martensitic mechanism. In Figure 4.66 [S69], unit cells of the *m*, *t*, and *c* lattices are depicted.

In such transformations a habit plane (or two as some consider that is the case for ZrO_2 [W16]) of optimum fit, between the parent and the resulting lattice, exists. This leads to a precise orientation relationship between the phases; a shear-like shape change in the structure is involved. A transformation occurring according to such rules can be triggered with relative ease by mechanical straining. This feature is critical because it is the base of the toughening effect of a $t \rightarrow m$ transformation.

When certain alloying oxides like CaO, MgO, Al_2O_3, Sc_2O_3, Y_2O_3, or various Ln_2O_3 are added to pure ZrO_2, the t-ZrO_2 phase, formed during sintering ($t > 1000\,^\circ C$), remains stabilized down to *RT*. For instance, additions of 2.8–6 mol% of Y_2O_3 are quite effective. The Y^{3+} (0.96 Å) cation, larger than the Zr^{4+} (0.82 Å) – when present in a suitable amount within a zirconia host – generates a less stressed (i.e. more stable) tetragonal lattice [R39]. This effect is even more pronounced when larger concentrations of Y_2O_3 are introduced (>8 mol%) and the fluorite-type lattice [E8] of c-ZrO_2 is stabilized.

When within a stabilized, dense t-ZrO_2 a crack forms, its growth may be slowed down. This happens only if the grains are of an optimal size (0.5–0.8 μm). Ahead of the crack tip there exists a "process zone," like that in Figure 4.67a [C37] in which stress is induced by the presence of the crack. The stress causes a "*t*" to "*m*" conversion, which is accompanied by a positive ΔV of 3–5%. This expansion puts the crack under compression [R42], thus slowing down its progress. In Figure 4.67b, a crack

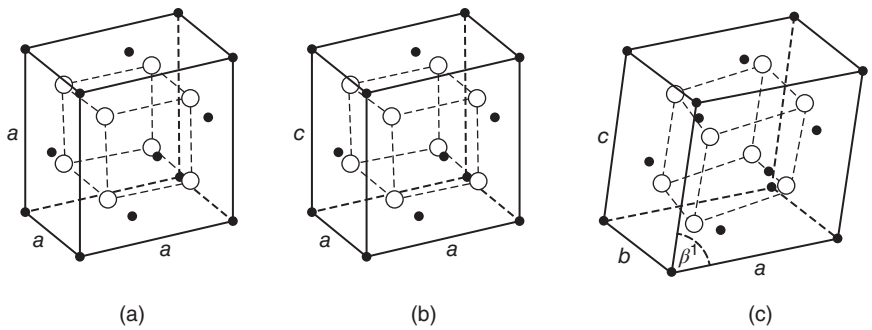

Figure 4.66 Unit cells of various zirconia polymorphs (states the oxide assumes varying with temperature and dopants nature and content). (a) Cubic. (b) Tetragonal. (c) Monolinic. Source: Subbarao 1981 [S69]. Reproduced with permission from John Wiley & Sons.

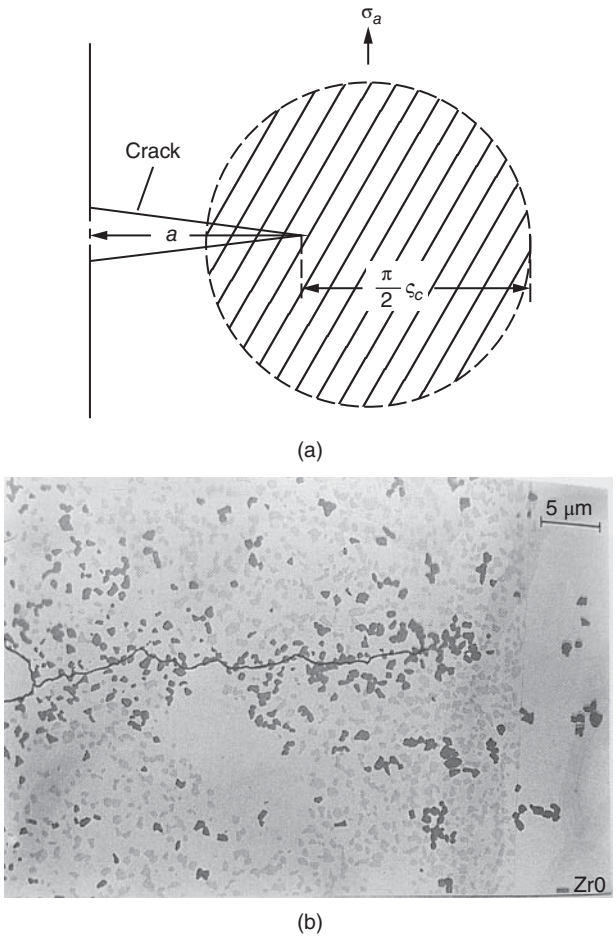

Figure 4.67 Mechanism of crack arresting, operating in TZP ceramics of fine microstructure. (a) Schematic representation of the "process zone," around the tip of a crack formed in TZP ceramic, under the influence of the stress field generated by the crack. (b) The visualization of grains (*GS* of 0.8 μm or less), brought to a monoclinic state (from their initial tetragonal one) by the propagation of the crack (transformed grains in black color). Source: Ruhle et al. 1984 [R41]. Reproduced with permission from John Wiley & Sons.

and its process zone are shown [R41]. The volumetric number density of "particles," present in the transformation zone, significantly affects the effectiveness of this mechanism. If this density is low, like in alumina (say, toughened with less than 15 vol% TZP) adverse stress concentrating side effects may occur. If this density is high, like in a partially stabilized zirconia (PSZ), then in the process zone a quasi-hydrostatic state of compression develops and the cracking arresting effect is very strong; hence the toughness of TZP may obtain the high values we know, say, K_{IC} of 11 MPa $m^{1/2}$.

Another possible mechanism of toughening is the formation of a system of microcracks, having a specific topographical distribution, as a result of the $t \rightarrow m$ process around the grains. The grains need a $GS > 1$ μm and be of angular morphology. Interaction of the main crack with such microcrack systems provides an energy dissipation mechanism, hence slowing down the main crack development. It has to be stressed that the microcracking process is helpful only when it is controlled so as to possess this specific configuration, characterized by a uniform spacing and a narrow size distribution; uncontrolled microcracks significantly weaken the part.

Two types of toughened stabilized, monolithic zirconias are in use. The first type, called TZP, includes an amount of yttria sufficient to keep all the material as t-ZrO_2, the phase generated during the calcination stage of the powder preparation. When the Y_2O_3 concentration is >2 mol%, t-ZrO_2 remains stable also during the cooling stage of sintering. The sintering is done so as to maintain the *GS* in 0.3–1.0 μm region. Another form is the PSZ, which is produced so as to allow the formation of small (~0.2 μm) ellipsoidal t-ZrO_2 coherent "precipitates" within the large grains of a c-ZrO_2 matrix. The "precipitates," oriented along the {100} direction of the cubic phase, are shown in Figure 4.68 [H26]. Such a microstructure is obtained using adequate alloying and processing.

For PSZ formation the amount of stabilizer oxide has to be lower than that which leads to full stabilization of the fluorite structure c-ZrO_2. An alternative is the post-sintering thermal treatment (two phases field) of a c-ZrO_2 (including a suitable alloying oxide amount) composition so as to cause a partial $c \rightarrow t$ transformation. For instance, Porter and Hewer, after sintering at ~1750 °C, have effectuated a solution anneal at 2000 °C/4 h of an 8.1 mol% Mg-PSZ. Further ageing at $t° \approx 1500$ °C enhanced the amount of tetragonal phase. Optimal ageing allows obtainment of 25–30 vol% of tetragonal

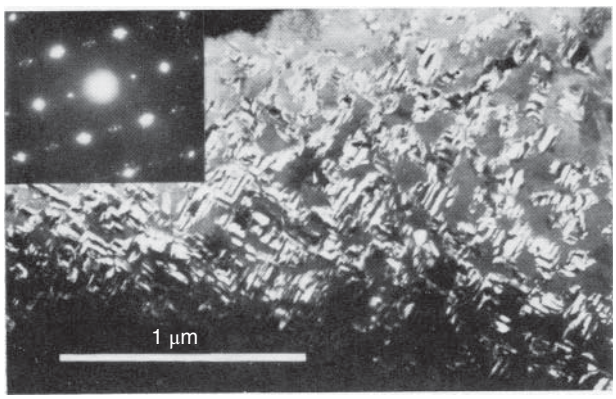

Figure 4.68 Dark field image of overaged PSZ-type zirconia ceramic showing twinned monoclinic grains. The inset shows the picture of the pattern of a selected area electron diffraction measurement (variants of monoclinic state and some twins are visible). Source: Heuer and Ruhle 1984 [H26]. Reproduced with permission from John Wiley & Sons.

phase. The toughening mechanism is the same as in TZP, i.e. crack compression by the $+\Delta V$ associated with the $t \rightarrow m$ transformation, triggered by the stress raise ahead the crack tip. PSZ materials have typical strengths of 1 GPa and K_{IC} of 8–10 MPa [H26]. While our interest here is in monolithic zirconias, let us note in passing that dispersion of TZPs within other ceramics is instrumental in the improvement of the host's toughness [C37]. In most cases the controlled microcrack process operates. Large amounts of alloying oxides (in the case of Y_2O_3 more than ~8 mol%) lead to the stabilization of the cubic polymorph if it was formed during sintering.

4.2.7.2 Processing–Transparency Correlation in Cubic Zirconia Fabrication

Of course the main objective of processing is to generate and maintain the cubic polymorph when transparency is the goal. The other objectives of processing can be described, like in the case of other TCs, by three negative requirements: no pores, no solid second phase(s), and no electronic absorbers. Achievement of these requirements would provide transparency. For optimal values of the parameters that describe mechanical or other properties, additional requirements stand, for instance, fine microstructure.

An aspect with influence, in this context, is the quality of the available powders and therefore this issue will be first discussed.

4.2.7.2.1 Zirconia Powders

In the case of ZrO_2, excellent powders, as far as purity and fineness are concerned, have been available starting with the late 1960s. Besides, of course, HfO_2 (3–5%), the powders used for transparent parts fabrication include as main impurities the oxides listed in Table 4.11.

For instance, Mazdiyasni et al. [M20] derived cubic material by sol–gel processing of alkoxide Zr and precursors. The intimate mixture allowed stabilization of a fully cubic state for 6 mol% of Y_2O_3, while in other cases at least 8 mol% are necessary. The cubic state was not modified by heating/cooling cycles $RT \leftrightarrow 2000\,^{\circ}C$. Basic particles of ~40 nm characterized the oxide in its calcined (850 °C) state. An interesting particles morphology and low size of the basic particles was realized by the sol–gel-based synthesis method, as shown in Figure 4.69 [M20]. The powder shows excellent sinterability; full densification is achievable by simple air sintering of pressed compacts, at temperatures as low as 1450 °C/16 h. Trunec and Maca [T29] have obtained 10 nm TZP powders (3 mol% Y_2O_3; 110 m^2/g) mixing a Zr alkoxide with Y-nitrate.

Table 4.11 Most frequent oxide impurities present in zirconia powders.

Impurity	Concentration (%)
SiO_2	0.02–0.2
Al_2O_3	0.2–0.4
Na_2O	0.002–0.04
Fe_2O_3	0.004–0.1
TiO_2	0.01–0.2

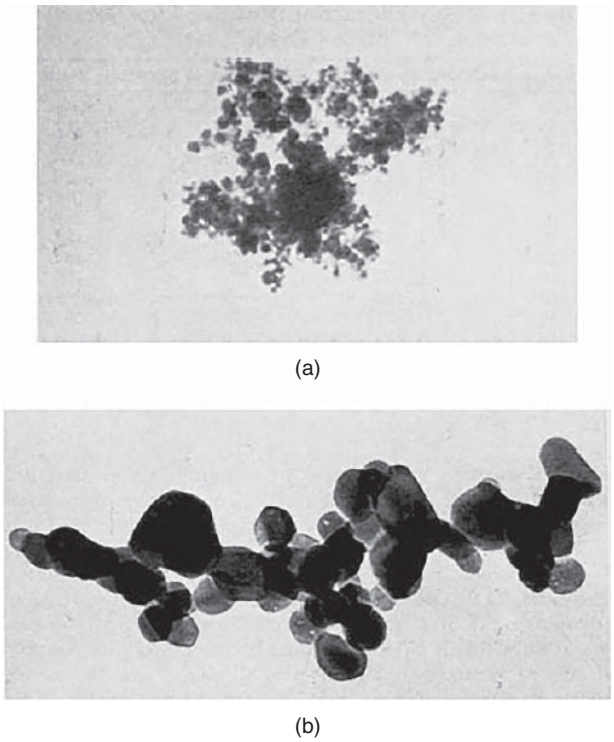

(a)

(b)

Figure 4.69 TEM images of yttria-stabilized, superfine powder synthesized by sol–gel processing. (a) A few low level aggregates; primary clusters of the basic particles are visible. (b) Primary clusters; basic particle size and morphology are clearly visible. Source: Mazdiyasni et al. 1967 [M20]. Reproduced with permission from John Wiley & Sons.

Microsphere basic particle-based powders could also be produced by sol–gel processing [G36] as illustrated in Figures 4.70 and 4.71. The spherical agglomerates (the smallest with $\phi = 1$ μm) are made of 8 nm crystallites separated by 4 nm pores. The authors report poor sinterability, but they applied CIP as a forming method to the as-synthesized powders (lacking proper processing) and worked with wide size distributions. Such an approach is not adequate to fully exploit the main advantage of such particles, i.e. the ability to generate compacts of **uniform** pore size (the size being also smaller than that of the particles).

Spherical powders could also be obtained by emulsion processing [aqueous solution of $Zr(SO_4)\cdot 4H_2O$] after

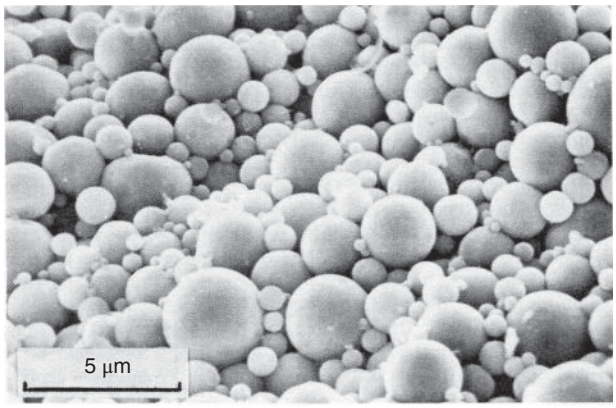

Figure 4.70 Stabilized zirconia powders, based on microspherical particles, prepared by sol–gel processing; relatively wide size distribution. Source: Graaf and Burggraaf 1984 [G37]. Reproduced with permission from John Wiley & Sons.

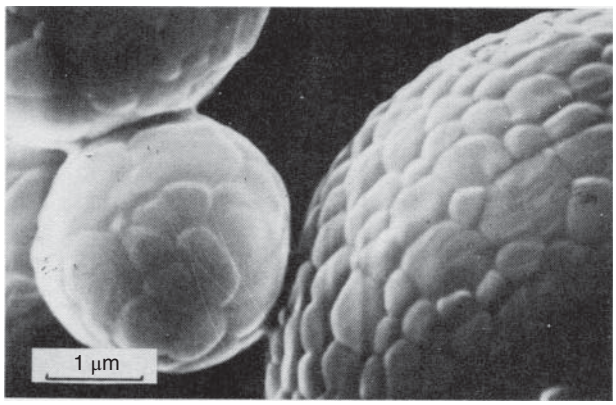

Figure 4.71 The basic grains of the particles of Figure 4.67 (SEM on thermally etched material at 1300 °C); a sintering neck visible. Source: Graaf and Burggraaf 1984 [G36]. Reproduced with permission from John Wiley & Sons.

low temperature 600 °C calcination. The citrate method (citrate complexes are combusted by nitrates oxidants) was also used for fine powders preparation; the loosely packed powders show an $A \sim 60\,m^2/g$. Coprecipitation of cations introduced as chlorides is feasible and relatively cheap. Haberko [H1], who introduced the method, showed on that occasion the useful effect of alcohol washing in reducing some of the intra-agglomerate bond strength. Such a treatment, as our own experience also shows, is able in many cases to improve noticeably nanometric powder's sinterability.

Starting with $ZrCl_4$ fine zirconia can be obtained also by CVD (vapor is oxidized in a H_2/O_2 flame) [H34]. Starting with $ZrOCl_2$ instead of $ZrCl_4$ allowed the obtainment of more sinterable powders, especially if freeze drying was used. Among the interesting gas phase-based synthesis methods, one has to list also the procedure used by Srdic et al. [S48] to prepare *m*-ZrO_2 of ~5 nm. The reactor used is quite complicated, but the molecular-scale reaction (Zr tetrabutoxide with O_2), in a reaction zone with strict control of the critical factors (mass flow, temperature, and pressure), generates **uniform** composition oxide clusters; on cooling highly pure nanozirconia results. Other methods, like hydrothermal decomposition of zirconia or the heating in air of cellulose soaked with $ZrOCl_2$ and a soluble yttrium salt, also generate interesting powders.

4.2.7.2.2 *Forming and Sintering*

Processing and then forming procedures adapted to the specific structure of the aggregates produced by the various preparation methods are necessary to convert the powders described above in transparent parts. A straightforward approach is the use of high compaction pressure for the green body forming. It is worth remembering, however, that spring back effects – caused by elastic deformation of the particles – and formation of nonuniform (spatial distribution) but strong stress fields occur when too high forming pressures are used. Only if the organic additives package, pressing schedule, and aggregate structure are suitably correlated, high pressure is beneficial related to the obtainment of green bodies, which have a configuration facilitating sintering. A successful use of this approach allowed Klimke et al. [K31] to form such green bodies (low pores size, $BD_g = 56\%TD$) and, as a result, be able to fabricate the transparent 3Y-TZP thin parts mentioned above. In this context it is probably also useful to note that powders including 3–5 mol% of Y_2O_3 are intrinsically more sinterable than other compositions within the ZrO_2–Y_2O_3 binary, or zirconias in general. Compared to other materials, like spinel, in the case of zirconia, a larger number of powder types form aggregates that can be efficiently broken by the aid of high pressure. For instance, the nanometric material prepared by Srdic et al. [S48] could be compacted under 800 MPa (without special processing; 20 mm discs) to a $BD_g = 3.0\,g/cm^3$ and very fine pores.

Sinterable green-body configurations can be realized also by other approaches. For instance, small parts could be formed (centrifugal casting) from suspensions of *c*-ZrO_2 in which only basic particles or small clusters of them were present. The compact cast – exhibiting low average size, narrow size, and uniform distribution of pores – could be sintered to full density at ~1150 °C, as is shown in Figure 4.72.

The figure also shows that another suitable green body configuration, derived from a sol–gel-produced microsphere and formed by pressing, also sinters at low temperature. The alkoxide derived powder – which when pressed under 400 MPa generates compact pores

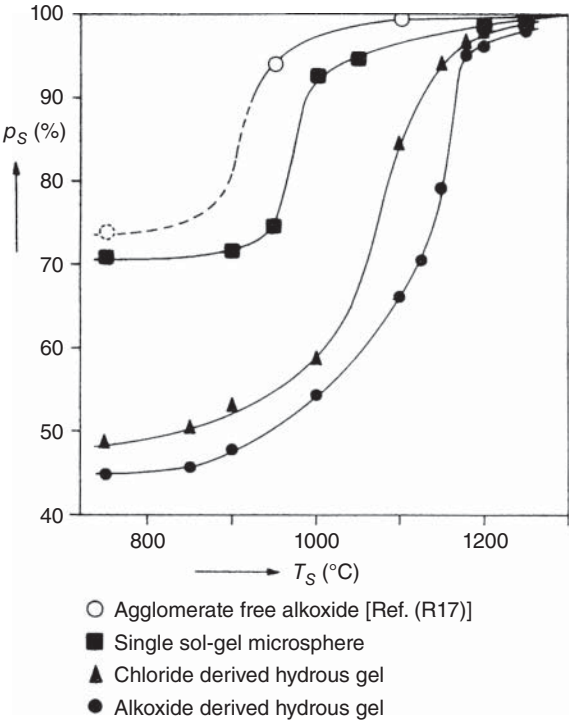

Figure 4.72 Sintering curves of zirconia green bodies formed by various procedures and from powders synthesized by different methods. Source: Graaf and Burggraaf 1984 [G37]. Reproduced with permission from John Wiley & Sons.

having a diameter between 3 and 10 nm – gives quite good results even when agglomerates are not eliminated prior to forming (as in the case of centrifugal cast). It was shown [W28] that by electrophoretic deposition (EPD), in membrane-separated cells, it is also possible to form a few millimeter thick parts having an as-deposited configuration suitable for good densification. In the case of EPD, a helpful feature is the possibility to use as-comminuted stabilized suspensions in which agglomerate reformation caused by drying is avoided. The deposits (when the process is well performed) are quite compact ($BD_g \geq 50\% TD$) and, more important, exhibiting a narrow pore size distribution. Relatively transparent parts were obtained after sintering around 1600 °C ($GS < 5$ μm). The use of a 30 GHz microwave furnace allowed some reduction of temperature and dwell time required for sintering.

The use of sintering aids is also an approach that was shown to be efficient for transparent cubic zirconia fabrication. The most effective one proved to be TiO_2 [P26, R4, T31]. Initially it was considered that TiO_2 (together with impurities) forms a liquid phase and that an LAS process occurs in its presence. Tsukuma [T31], however, pointed out that even 10 mol% TiO_2 dissolve in the c-ZrO_2 (Y) fluorite, as expected from the phase diagram. Solid solution formation was found also by Peuchert et al. [P26] who consider that entrance of TiO_2 distorts the fluorite lattice, which becomes very slightly tetragonal. An amount of 5 mol% TiO_2 seems to bring about maximal sinterability increase. The distortion can be prevented by increasing the Y_2O_3 content; the favorable effect on sinterability of TiO_2 seems not to be affected by the yttria additions. While the exact mechanism by which TiO_2 enhances sinterability is not yet determined, it is clear that it is based on influence upon the lattice characteristics. The insertion of TiO_2 also induces a slight yellowish coloration. The effect of TiO_2 was complemented by the use of vacuum sintering (1×10^{-3} Pa) and subsequent HIPing. While the sintering temperatures were significantly higher than in the case of PECS, here transparency was achieved for the case of thick (up to ~6 mm) parts.

Regular hot pressing was, up to now, only seldom used for zirconia's advanced densification, despite the promising results of the early attempts. For instance, Vahldiek [V2] was able to densify m-ZrO_2 (under 100 MPa; 1700 °C/1 h) to an uncracked cylinder; discs of $t \sim 2$ mm showed a RIT of ~14%.

4.2.7.3 Properties

In our context the interest in zirconias stems from their ability to provide, simultaneously with transparency, good (in the case of c-ZrO_2) and exceptional (in the case of t-ZrO_2) mechanical properties. In Table 4.12 the main properties of t,c-ZrO_2 are listed.

4.2.7.3.1 Density of Zirconias

In the case of the materials alloyed with Y_2O_3, the density shows an almost linear dependence on (Y_2O_3), decreasing as the amount of additive increases [I11]. Considerable evidence exists for the view that an alloying Y^{3+} enters Zr^{4+} sites; oxygen vacancies form in

Table 4.12 Properties of zirconia ceramics.

Properties	*c*	*t*
n at 600 nm	2.23	—
TRS (MPa)	250–350	800–1500
E (GPa)	200–220	—
$HV2$ (GPa)	12	12
K_{IC} (MPam$^{1/2}$)	1.8–2.3	6–11
α (°C^{-1})	11×10^{-6}	—
t_f (°C)	2700	2700
λ_{th} (W/km)	~3	—
ε	33	—
$\sigma_{e\,1200}$ (S/cm)	3×10^{-1}	—

Table 4.13 The density of a few types of zirconia ceramic.

Y_2O_3 (mol%)	Density[a] (g/cm^3)
12.0	5.89
8.0	5.99
3.1	6.08
0	5.67
(m)	(5.83 [JCPDS 37-1484])

a) Measured on single crystal.

order to preserve lattice electrical neutrality. At the compositional boundaries – separating "*t*" from "*m*" regions and "*t*" from "*c*" – two phase materials ("*m*"+"*t*" and, respectively, "*t*"+"*c*") exist. The tetragonal precipitates are coherent with the cubic matrix so that the slight lattice distortion has a low influence on density; the effect of the monoclinic phase, i.e. reduction of density, is more significant. The density reduction comes from both V_0 formation and the atomic mass difference between Zr (91.12 a.u.) and Y (88.91 a.u.); the fluorite lattice a_0 is also increasing with $[Y_2O_3]$.

In Table 4.13 density (*TD*) values are given for a few types of zirconia materials [I11].

4.2.7.4 Types of Transparent Zirconia

Owing to the impressive nonoptical properties of the zirconias, if they could be obtained in transparent forms, valuable materials from many applications would result. A first problem common to all types of ZrO_2 is the large value of the refraction index, which reduced the *T*% of a single *c*-ZrO_2 single crystal to ~77%, owing to reflection [A20]. A second problem, specific to TZP and monoclinic pure zirconia, is the non-cubic lattice, which leads to scattering, caused by birefringence. Below the various types of transparent zirconia are presented.

4.2.7.4.1 TZPs

These materials, as it was shown above, excel in the domain of mechanical properties. The problem is their non-cubic lattice symmetry, which leads to light scattering of an intensity proportional to the level of birefringency, higher for Y-TZPs than for α-Al_2O_3. It was shown in prior chapters that a smaller grain size is instrumental in reducing birefringence-related scattering of Al_2O_3 [A23]. It was calculated by Klimke et al. [K31] (based on Mie treatment of scattering) that a Y-TZP plate of 0.5 mm thickness, which has a $\Delta n = 0.03 - 0.04$, may (in fully dense state) provide a 50% transmission ($\lambda = 500$ nm) if $\overline{GS} < 40$ nm; for $T = 70\%$ grains smaller than 20 nm are required. The RIT of a 0.5 mm thick poreless plate of Y-TZP is shown in Figure 4.73.

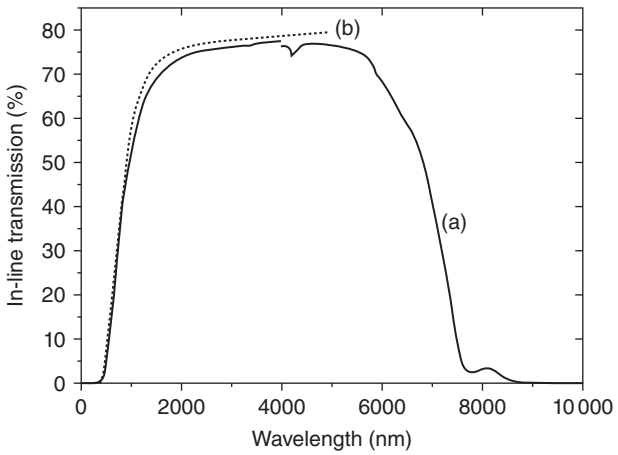

Figure 4.73 Transparent tiles of tetragonal ZrO_2 (+3 mol% Y_2O_3) ceramic made by IKTS Dresden. (a) Measured transmission of a 0.5 mm thin disc, (b) Calculation assuming scattering by birefringence of 0.035, zero porosity and 120 nm grain size. Source: Klimke et al. 2011 [K31]. Reproduced with permission from John Wiley & Sons.

The plates are made of special, 10 nm particles based (A = 110m^2/g) 3Y-TZP powder synthesized at a very low temperature (450 °C). The fine particles allowed full densification at 1100 °C/5 min followed by HIPing at 1100 °C/8 h (air annealing at 800 °C/10 h). With 0.5 mm thickness, the in-line transmission was 15% at 640 nm wavelength with an increase to about 35% at 800 nm [K31]. As the figure shows the transmission levels attainable are too low for apps requiring transmission in the VIS, but high enough to allow the consideration of such materials for MIR domain apps. Values close to this level were also obtained in dense 3Y-TZP, with a $\overline{GS}$ of ~50 nm; sintering was done by PECS [A19].

4.2.7.4.2 Cubic ZrO_2

The zirconias alloyed so as to assume a single phase fluorite type cubic lattice are expected, of course, to allow the fabrication of parts more transparent than those based on TZPs. The PSZs are an intermediary case, but they are not discussed here because specifics of their fabrication (vide supra) make them unsuitable candidates for TC obtainment. The cubic zirconias, if fully dense, may exhibit, in the VIS region, a maximal transmittance of ~76%. The low level is owed to the massive reflection triggered by $n = 2.18$ ($\lambda = 500$ nm). Using a material that could be stabilized to the cubic form, Mazdiyasni et al. [M20] produced 1 mm thick specimens – having a transmission in the VIS of 11% of that of glass – as early as 1966. Similar transmission was achieved also by hot pressing [V2]. Using an 8Y-CZ material, Tsukuma et al. [T31] obtained, for $t = 0.7$ mm plates, a transmission of 53% in the VIS. The specimens had a light yellow hue. In that study, in fact, a ZrO_2–TiO_2 (8 mol%) cubic solid

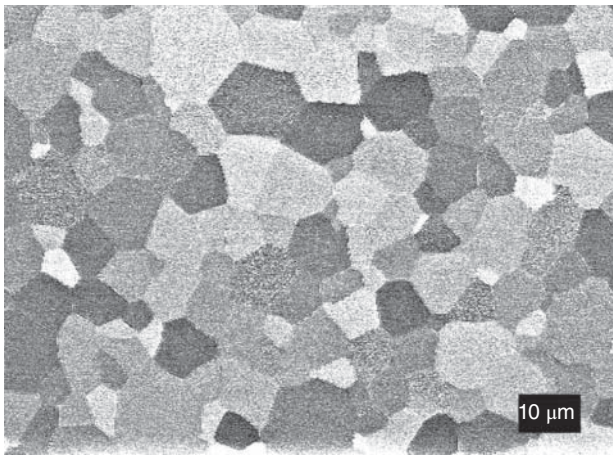

Figure 4.74 Microstructure of transparent cubic zirconia parts fabricated by sinter/HIP (1290°C/1470°C) at IKTS Dresden; without thermal etching, the individual grains of the single-phase ceramic are distinguished by orientational contrast. The associated transmission spectrum is shown in Figure 4.75, polished tiles in Figure 4.76.

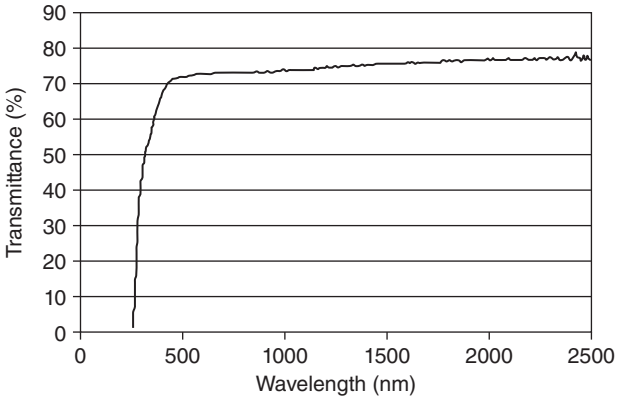

Figure 4.75 Optical spectrum of cubic (stabilized with 8 mol% yttria) zirconia part (t = 1 mm).

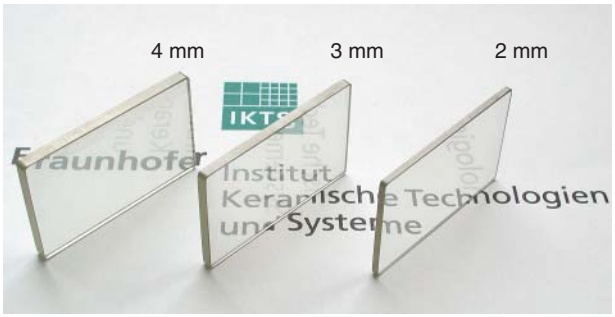

Figure 4.76 Imaging of transparent plates, made of cubic zirconia, having various thicknesses (RIT, for t = 2 mm is 65%; for t = 3 mm, 59%; and for t = 4 mm, 57%). Source: Krell et al. [K57]. Reproduced with permission from Goeller Verlag.

solution was used. The authors considered TiO_2 as a sintering aid. This idea was further examined by Peuchert et al. [P26], which were able to significantly improve transmission. Specimens with a thickness of ~8 mm exhibited a T of ~58% at $\lambda = 800$ nm and of almost theoretical level at $t = 5.8$ mm. The specimens also showed a slight yellow tint. These authors found out that TiO_2, while helping sintering, also has a deleterious effect on transmittance because it causes a slight distortion of the lattice. The resulting stress field generates birefringence. By raising the Y_2O_3:TiO_2 ratio the negative effect could be mitigated. One millimeter thick small pieces of cubic Y-ZrO_2, formed by EPD, could be brought to a $T = 60\%$ at 750 nm [W28]. Nanometric grain-based parts, sintered by PECS, also showed a respectable $T = 55\%$ ($\lambda = 750$ nm) for a 1 mm thickness; yellow to orange hues were observed [A19, C10] and the volume of residual porosity was of ~0.1%. A low grain size (see Figure 4.74) – finer than that of similar parts previously developed – ceramic of cubic ZrO_2 stabilized by 8 mol% Y_2O_3 was developed at IKTS, Dresden via a sinter/HIP approach [57]. In the visible spectrum at 640 nm wave length these specimens exhibit a transmission of 73% at 1 mm thickness (Figure 4.75) which compares, due to the high refractive index of ZrO_2, with a theoretical maximum of 76%; the hardness HV10 = 13 GPa is equivalent to the upper limit which is possible with zirconia. Transparent specimens of this grade are shown in Figure 4.76 with thicknesses up to 4 mm.

4.2.7.4.3 Monoclinic Zirconia

In few certain cases, a nanometric grain size does lead to a material behavior significantly different from what is seen in the case of coarser microstructures. Zirconia offers such an example. V.V. Srdic et al. [S48] have shown that 5 nm powders of undoped zirconia could be pressed into green pellets having the pores size in the 2–10 nm range ($BD_g \sim 50\%TD$) (see Section 4.2.7.2 for preparation). As a result, even in the green state, the specimens ($t = 0.4$ mm) exhibit considerable transparency. The green parts showed an interesting feature. The high symmetry fractions (as-synthesized material included in c, m, and t-ZrO_2) of the powder reverted to a monoclinic lattice. A similar process, as described above, is observed in sintered TZP subjected to mechanical strain (leads to toughening). The relevant XRD patterns are shown in Figure 4.77 of Srdic et al. [S48].

Sintering, under vacuum, leads to almost full densification at 950 °C ($TD = 5.82$ g/cm^3); air firing results in lower (~94%TD) levels of densification. The specimens are not pore free but still exhibit noticeable transmittance, owing to the nanometric size of the remnant porosity.

One of the specific features of such specimens is the monoclinic symmetry of its grains. Subjecting to heating/

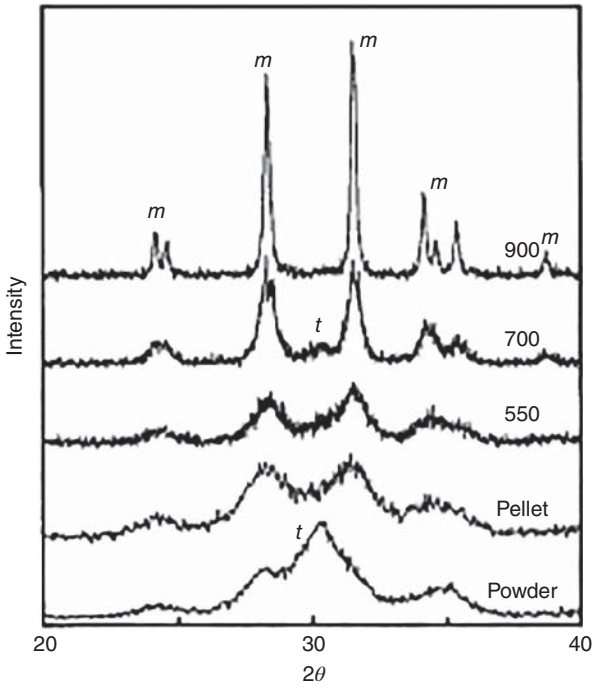

Figure 4.77 XRD patterns of monoclinic zirconia powder compacts as a function of thermal treatment temperature. Source: Srdic et al. 2000 [S48]. Reproduced with permission from John Wiley & Sons.

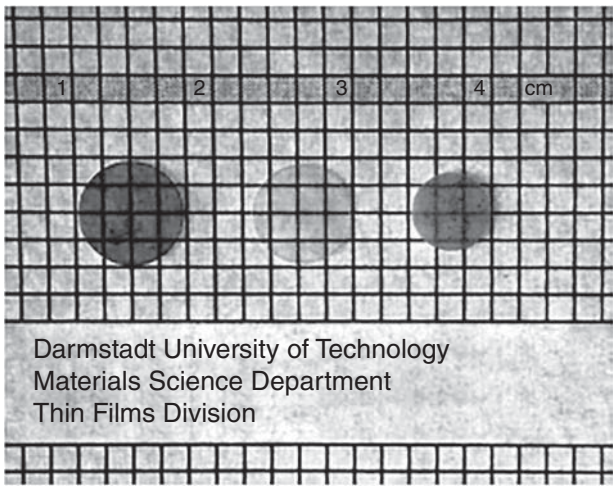

Figure 4.78 Imaging of monoclinic zirconia discs ($t = 0.35$ mm) as a function of the thermal treatment temperature they were subjected to. Disc on the left: as CIPed (500 MPa). Disc in the middle: after VS at 550 °C/1 h. Disc on the right: after VS at 950 °C/1 h. Source: Srdic et al. 2000 [S48]. Reproduced with permission from John Wiley & Sons.

cooling cycles, such parts is not leading to cracking because $m \leftrightarrow t$ transitions are not occurring. The sintered state grain size is ~70 nm, and a certain level of transparency is maintained ($t < 0.5$ mm; see Figure 4.78 [S48]).

4.2.7.4.4 *Electronic Absorption*

Single crystals of *c*-ZrO2 (Y) (as a function of growth conditions) either are colorless or exhibit pale yellow to yellowish brown hues. The UV absorption edge is located at 290 nm and it seems to represent the low energy edge of host's band-to-band transitions. In Figure 4.79 [N1], the NUV edge of such crystals is shown together with the profile of the absorption generated by their exposure to electrical field action.

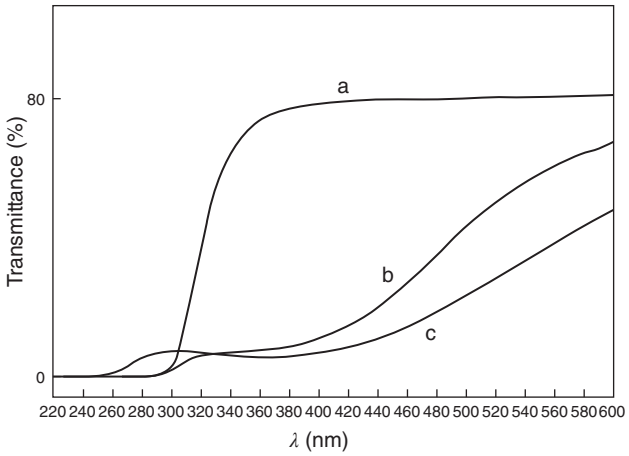

Figure 4.79 Transmission spectra of as-grown zirconia single crystal and the same after being subjected to the action of electric field (under Ar). (a) Pristine crystal (colorless). (b) After electroreduction at 600 °C and 10 V (yellow). (c) After electroreduction at 600 °C and 30 V (dark brown). Source: Nagle et al. 1989 [N1]. Reproduced with permission from Elsevier.

In most of the cases both "*t*" (much lower average transmission in VIS than cubic specimens) and "*c*" transparent ceramic zirconias exhibit some coloration (yellow to orange or brown) or at least their NUV absorption edge is pushed toward the VIS [A19]. In Figure 4.80a,b the spectra of such ceramics are illustrated.

In some cases, mostly when HIPing was used, additional gray to black tints appeared. Such effects need to be eliminated or at least minimized – as the scattering on pores, discussed in the previous section – if one aims to obtain high and controlled transparency. For this it is important to understand their origin. This is an issue yet under study and will not be discussed in detail here. What can be said with certainty is that impurities present in the zirconia powders (see "Powders" subsection) are not able to produce the colors observed. Scattering on pores can contribute a bit to the loss of transmission in the regions that can explain at least yellow hue formation, as shown by the calculated transmission curves presented in Figure 4.81 [A19].

However the amount and size of the pores measured by electron microscopy, in the case of top quality

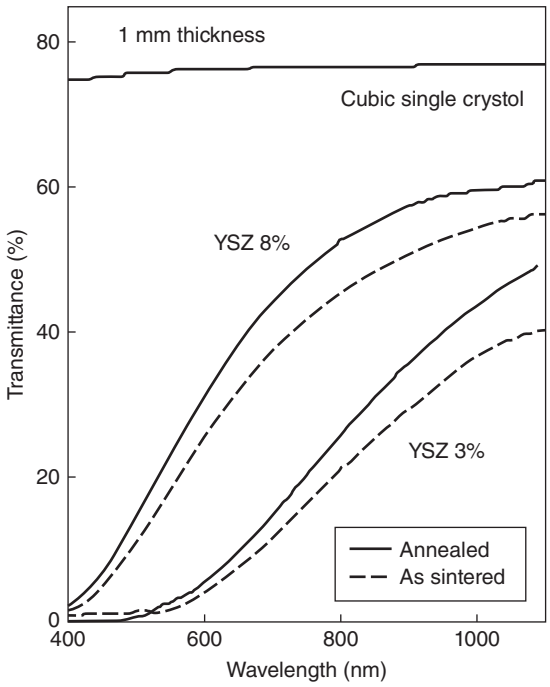

Figure 4.80 Transmission spectra of cubic and tetragonal zirconia ceramics discs ($t = 1$ mm) in as-sintered (PECS 800 MPa, 950 °C/5 min) and after annealing in air (750°C/24 h). Source: Anselmi-Tamburini et al. 2007 [A19]. Reproduced with permission from John Wiley & Sons.

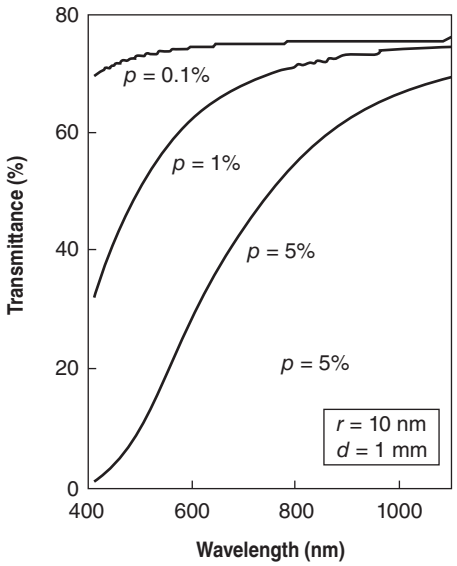

Figure 4.81 Calculated transmission curves of sintered cubic ceramics with the assumption that the only EMR attenuation mechanism active is scattering on porosity (thickness of disc "*d*" and pore radius "*r*" are indicated in the figure together with porosity amount "*p*"). Source: Anselmi-Tamburini et al. 2007 [A19]. Reproduced with permission from John Wiley & Sons.

cubic zirconia ceramics (like those in Figure 4.81), is not consistent with the large porosity volume values required for coloration exclusively by pore scattering. Moreover, the coloration is sensitive to the character of the atmosphere during thermal treatments. Therefore scattering on pores cannot be the major cause of coloration. It is also clear that carbon clusters – which are able to penetrate into the host during sintering in certain machines including graphite parts [G31] – may be a major contributor to coloration but only to the gray to black hue formation. Current studies try to determine whether coloration scenarios based on the action of factors like oxygen vacancies, partial reduction of Zr^{4+} to Zr^{3+}, and presence of carbon atoms clusters acting alone or in conjunction may explain the observed facts. We determined (A. Goldstein, unpublished results) that the main cause of coloration is the formation of Zr^{3+}, which forms hetero(Zr^{3+} and Zr^{4+}) polynuclear complexes exhibiting a high EMR absorption capability (see Section 3.2.6).

4.2.8 Transparent Metal Fluoride Ceramics

There are a number of metal fluorides relevant to the domain of transparent ceramics, owing to their attractive optical properties. Their low refraction index $n < 1.46$ ensures low reflection losses (compared with, say, ZrO_2 spinel or YAG), allowing a theoretical transmission of around 92.5% in the VIS domain. So certain cubic fluoride ceramics combine a higher transmission than the corresponding oxide, with lack of vibrations till quite far in the IR (three phonon bands start over 10 µm); as a result infrared cutoff of the transparency window is located at a wavelength in a more bathochrome position than of most of the oxide TCs (not dramatic difference though compared to, say, Y_2O_3). This happens owing to a weaker bonding, inside the fluoride lattice and a slight mass increase of the anion, compared to the oxides (compare CaO and CaF_2). The first ceramic laser (of low performance owed to both low optical quality of the host and low efficiency pumping) was of the CaF_2:Dy^{2+} type [H16]. Unfortunately their non-spectral properties, especially mechanical, are less good than those of the oxides, making them less suitable than the oxides for arduous applications. The above notwithstanding their properties still represent, for certain applications, a better combination than what oxides can offer and for those cases fluoride ceramics remain a serious competitor for the latter materials family. For instance, the low phonon energies reduce the probability of energy loss by non-radiative transitions (from the starting level of the lasing process); last but not least the refraction index shows a negative variation with an increasing

temperature. It is worth noting that fluorides can function either as monolithic parts or as a fine dispersion in transparent components. In the latter case the low size of the dispersion particles makes the use also of non-cubic fluorides possible. An example is constituted by the FOG-type glass-ceramics (presented in Section 4.2.11.5) in which features attractive when lasing ion hosts are sought are exploited.

Owing to the above a brief presentation of these materials is the subject matter of this section.

4.2.8.1 Crystallographic Structure

In Table 4.14 the crystallographic system and the melting point of some fluorides are given. Many fluorides have lattice symmetries similar to those of certain oxides [L45], for instance, $CaF_2 \leftrightarrow c\text{-}ZrO_2$.

The lattice of CaF_2, the most important fluoride ceramic related to TC applications, is depicted in Figure 4.82.

In the CaF_2 lattice, the Ca^{2+} cations are coordinated by 8 F^- anions located at the apexes of a cube, while the F^- is tetra-coordinated by cations within a tetragonal site. Every alternate F^- cube has no Ca^{2+} at its center; the (111) plane is the natural cleavage plane. Vacancies form much more easily in the anionic sub-lattice. Such vacancies can form color centers by electrons trapping. Introduction of energy into the lattice leads also to the creation of more exotic defects, like H^- centers (an interstitial fluorine covalently bonded [along the ⟨111⟩ direction] to an F^- present on a normal lattice site). The ionic radii are $r_{Ca^{2+}} = 1.12$ Å and $r_{F^-} = 1.31$ Å. Clustering of V_F is easy in CaF_2 and it also may lead to the formation of colloidal metal particles (of up to 10 μm in size) close to the cluster. Another interesting feature is the super-ionic electrical conductivity shown by CaF_2 (and other fluorite structure compounds). It is the result of the disorder possible in the anionic sub-lattice (see also $c\text{-}ZrO_2$). The degree of disorder increases, of course, with temperature; for CaF_2 a state leading to massive super-ionic conductivity is attained at $T_C \sim 1150$ °C.

Table 4.14 Space group (for cubic lattices, also the "a" values are given) melting points and refraction index of some fluorides.

Chemical formula	Space group	a	$t°_f$ (°C)	n_a
CaF_2	$FM\bar{3}mn$ no 225	5.46	1420	1.43
MgF_2	—	—	1260	—
SrF_2	—	5.81	1477	1.44
LiF	—	4.03	870	1.40

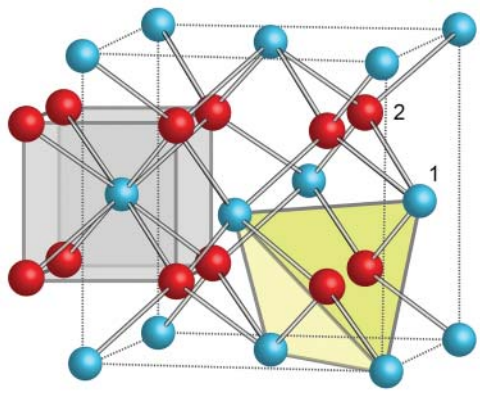

Figure 4.82 Imaging of CaF_2 lattice. (1) Ca, (2) F. Source: Reproduced from Shutterstock Images with purchased permission.

4.2.8.2 Processing of Transparent-Calcium Fluoride

While a number of fluorides were found to be useful for optical applications [S52], most of the work done for transparent fluoride fabrication was focused on CaF_2 and therefore the processing of this material is discussed here; processing and properties of SrF_2 are quite similar. The powders are synthesized by wet chemistry [A30, D17, S52], with the most popular raw materials being hydrated Ca nitrates and acetates, dissoluted in aqueous HF solutions. The washed precipitates are dried and in some cases annealed, under Ar (~400 °C) in order to reduce the level of residual absorbed water. A thorough powder surface cleaning is important to prevent closed pore formation during sintering and also oxidation (CaO or $Ca(OH)_2$ in the GB zone). The forming is usually done by CIPing at various pressures, up to 200 MPa.

The most popular sintering procedure, introduced by the Kodak company – which used as optical components, in its devices, both single and polycrystalline fluorides – is low temperature hot pressing [A1]. The temperature range was 800–1100 °C, with most of work around 900 °C, while that of pressure between 20 and 60 MPa [H15]. In some cases [B14] a preliminary vacuum sintering at 600 °C is used, in order to bring the BD_f to ~95%TD; this procedure was followed by most of the teams that worked on this issue. The sinter/HIP approach was also examined [B13–B16, D17]. A somewhat peculiar procedure, introduced by Basiev et al., is based on hot forging (1200 °C, 250 MPa), which transforms a large single crystal in a polycrystalline system made of a succession of layers having a nanometric ($t \sim 50$ nm) thickness. The advantage is an improved set of mechanical properties owed to cleavage rate reduction. Also raw

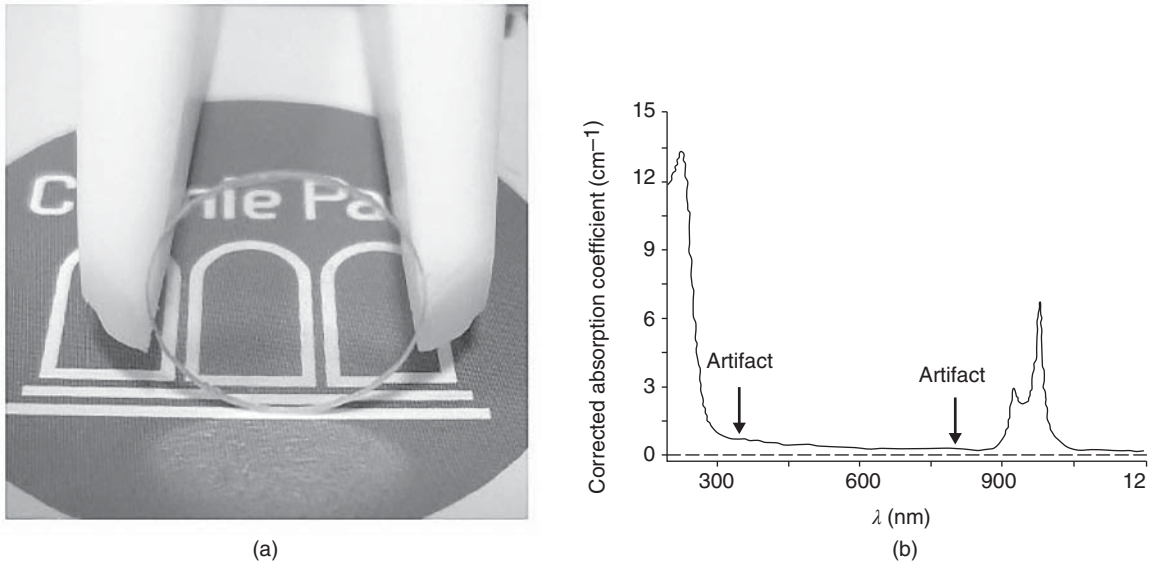

Figure 4.83 Imaging of transparent CaF_2 ceramic disc and its absorption spectrum. (a) Photo. (b) Absorption spectrum. Source: Lyberis et al. 2011 [L68]. Reproduced with permission from Elsevier.

material resulting fromccomminution of single crystals was sintered to a dense ceramic [J9]. In the case of SrF_2 parts polycrystalline parts were obtained by melt cooling; a polycrystalline natural transparent CaF_2 also exists.

The best developments led to parts exhibiting transmission spectra similar to those of single crystals [A2, A30, B14–B17, C30, J9, K24]. In Figure 4.83 [L68], a good optical quality CaF_2 disc is shown together with its absorption spectrum (in the IR range, alpha values are around 0.15–1 cm). For high power lasers, heavily Yb-doped CaF_2 seems one of the interesting candidates. Yb segregation, at grain boundaries (see Figure 4.84), and some thin layers of oxide (at some grain boundaries) are the main defects discovered in such parts [A31].

The use of lattices where both Ca and Sr^{2+} cations are present (Nd^{3+} doping) may lead to fluorescence enhancement [Z21]. Thus Zhu C. et al. prepared, by hot pressing at 900 °C (under 30 MPa), transparent ceramics from a mixture including besides CaF_2, also 10 at% of SrF_2 and a high concentration of Nd^{3+} (5 at%). The fluorescence band of Nd^{3+}, at 1058 nm, is definitely wider (good for short lasing pulses) and more intense than that generated by a CaF_2 host. The moderate disorder generated by a mixed native cations host is probably the main reason for the observed facts; the presence of Sr may have some effect also on the self-quenching propensity of Nd^{3+}.

4.2.8.3 Properties

Fluorides, like CaF_2 or MgF_2, are exhibiting maximal TRS values of no more than ~150 MPa [H15] and very

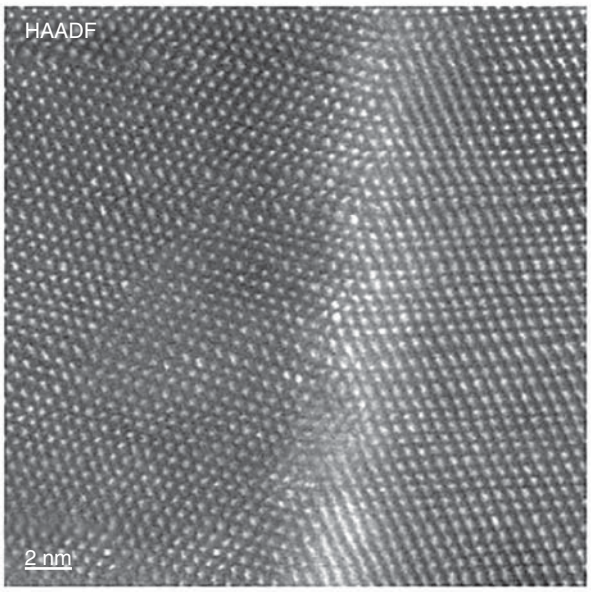

Figure 4.84 HAADF-STEM image of Yb segregation at the grain boundaries of a CaF_2 ceramic doped with 0.5 at% of Yb. Source: Lyberis et al. 2011 [L68]. Reproduced with permission from Elsevier.

low hardness (e.g. $HK0.5$ of $CaF_2 \cong 1.6$ GPa). The Young modulus is $E = 75–140$ GPa, $\alpha_{th} = 10–20 \times 10^{-6}$ K^{-1}, and $\lambda_{th} = 10–15$ W/mK; the ε_r of $CaF_2 \approx 7$; the refraction index of CaF_2 at 600 nm is $n = 1.4338$. As the values above suggest, the resistance of fluorides to rain erosion, thermal shock, ballistic impact, or even low rate mechanical stress is in the modest to low range.

The spectrum of a CaF_2 ceramic, in the MIR domain appears in Figure 4.85 [H15]. In Figure 4.86a,b the microstructure of Er^{3+}-doped CaF_2 parts and their visual aspect are shown. Besides monolithic CaF_2 an interesting set of materials is provided also by the solid solutions of this fluoride with LaF_3 [K24].

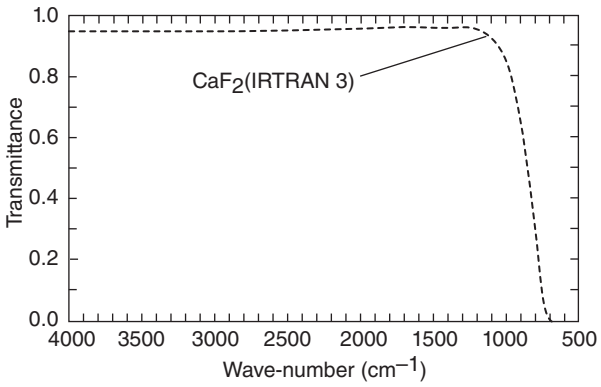

Figure 4.85 Transmission spectrum (MIR range) of transparent CaF_2 ceramics. Source: Harris 1999 [H15]. Reproduced with permission from SPIE Publishing.

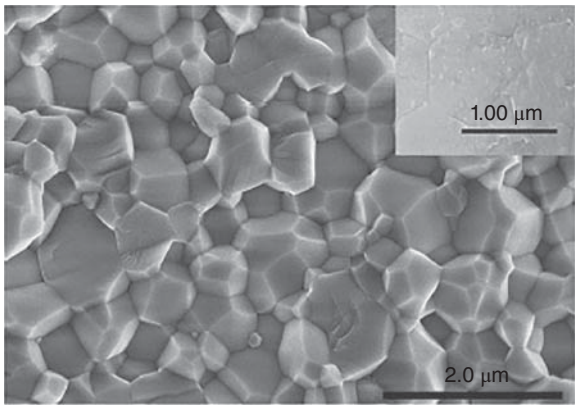

(a)

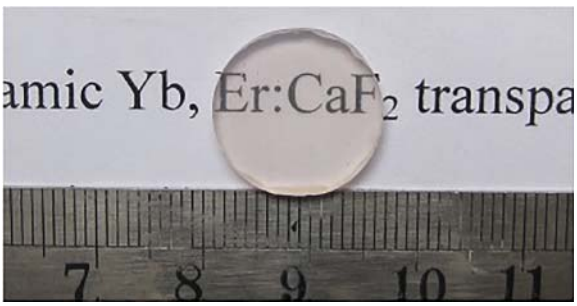

(b)

Figure 4.86 Microstructure and imaging of Er-doped CaF_2. (a) Microstructure (SEM). (b) Imaging. Source: Liu et al. 2014 [L35]. Reproduced with permission from Elsevier.

4.2.9 Transparent Chalcogenides

4.2.9.1 Composition and Structure

Besides the oxides, in which the common anion is the O^{2-}, materials based on other divalent anions are also relevant for the TC domain. It is the case of materials based on chalcogenide ions like S^{2-} or Se^{2-}. In this section chalcogenides formed by interaction with the Zn^{2+} cation are discussed. These materials, while not being the only chalcogenides of interest (for instance, CdSe or CdMnTe are also used), are, by far, the most important to date. As it will be detailed in Chapter 5, dealing with applications, ZnS(Se) are used for IR sensor protection domes or MIR range lasing cation (Fe^{2+}, Cr^{2+}) hosts.

At *RT* both ZnS and ZnSe are cubic, with a zinc blende structure ($SG = F\bar{4}3m$; Figure 4.87).

The a_0 is 5.67 Å for ZnSe and 5.41 for ZnS. Both ions are tetra-coordinated, sitting in the center of a tetrahedron of ligands. The bond length is 2.34 and 2.45 Å in ZnS and ZnSe, respectively. At temperatures higher than 1020 °C, the ZnS is converted to a hexagonal (SG = #186 $C_{6V}^4(P6_3mc)$) lattice (wurtzite type). This structure can be maintained also at lower temperatures if fast cooling is used (metastable state with tendency to morph to a sphalerite-type lattice). In qualitative terms, the bonding in these materials can be described as predominantly ionic, with a noticeable percentage of a covalent component, however. The strength of the bonds is low if comparison is made with the oxides relevant for TCs. This is, of course, reflected in the properties, especially mechanical, of parts derived from such materials.

4.2.9.2 Processing

For these materials the main processing approach is based on CVD, usually followed by HIPing. CVD is a basic technique in domains like semiconductor fabrication, thin films and coatings, etc. It may generate both single and polycrystalline materials. It is rarely used for bulk parts; one of such cases is the fabrication transparent chalcogenide ceramic parts. Here the deposits on graphite substrates are of the polycrystalline variety. From a chemical point of view, one of the most used reactions (600–750 °C) is

$$Zn\,(g) + H_2S\,(g) = ZnS\,(s) + H_2\,(g) \qquad (4.4)$$

High pressure gases, in mixture with Ar, are introduced in vacuum chambers. The reaction products are deposited on the substrates at rates of ~50 µm/h. The grain size varies in a wide range, from submicron to 0.8 mm. Color of the deposits varies from yellow to red. In many cases some hexagonal crystallites are present along the cubic majority. Post CVD HIP is then used to eliminate scattering centers and produce transparent

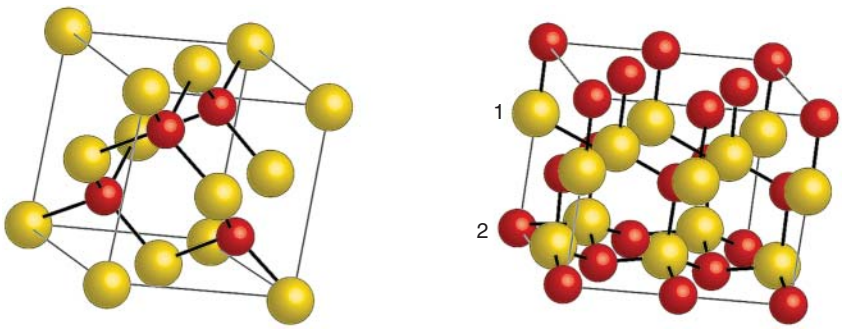

Figure 4.87 ZnS lattice. (1) Zn, (2) S. Source: Reproduced from Shutterstock Images with purchased permission.

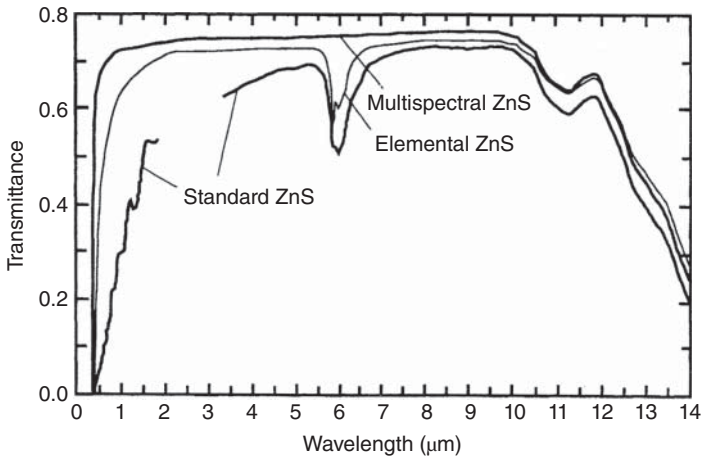

Figure 4.88 Transmission spectra of different grades of ZnS ceramics. Source: Harris 1999 [H15]. Reproduced with permission from SPIE Publishing.

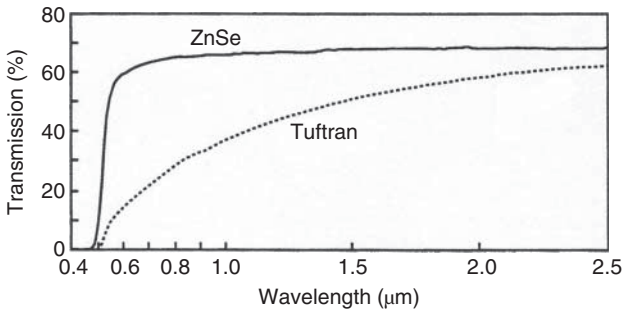

Figure 4.89 Transmission spectra of two grades of ZnSe ceramic. Source: Harris 1999 [H15]. Reproduced with permission from SPIE Publishing.

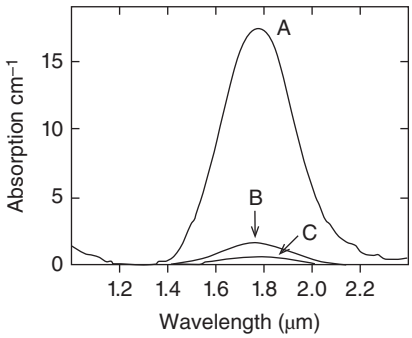

Figure 4.90 Absorption spectra of some Cr^{2+}-doped ZnSe ceramics. (A) Polycrystalline host grown by CVD and doped by thermodiffusion. (B) Ceramic fabricated by hot pressing at 1500 K. (C) Ceramic fabricated by hot pressing at 1400 K. Source: Mirov et al. 2011 [M34]. Reproduced with permission from OSA Publishing.

parts. Very large and thick parts can be thus manufactured. The spectra of ZnS and ZnSe thus produced is shown in Figures 4.88 and 4.89.

The more conventional (within the ceramics industry) HP approach is also used, especially for the production of low size parts. This method was developed by teams led by S.B. Mirov et al. [G1, M34, M35]. Quite coarse ZnSe powders (~10 μm) were compacted (60 MPa). The maximal temperature used during the hot pressing was in the 1220–1320 °C range; pressure of 30–35 MPa was applied; $BD_{HP} = 5.1 \pm 0.1$ g/cm^3 values were achieved. In Figure 4.90 the absorption spectrum of a Cr^{2+}-doped ZnSe discs (fabricated by HPing) is shown together with that of a sample fabricated by CVD. The quite high transparency achieved by HPing was demonstrated by the obtainment of lasing (MIR wavelength) in a Cr^{2+}-doped specimen. HP and SPS were used also by C. Chlique et al. [C34] for ZnS part fabrication, but transparency was obtained only for the 8–12 μm range. Because ZnS

is a semiconductor material with many applications, various methods for powder synthesis were developed, including nanosized ones [I12]. For instance, starting from $ZnCl_2$, solutions mixed with polyvinyl-alcohol PVA and Na_2S + trisodium citrate led to a white wurtzite powder based on ~5 nm crystallites. The methods developed make use of both water and organic solvents like methanol or dimethyl formamide. Coprecipitation, starting with aqueous solutions of $ZnSO_4{\cdot}5H_2O$ and $Na_2S{\cdot}7H_2O$, led to cubic ZnS nanoparticles; such powders were used also for HPing experiments.

4.2.9.3 Properties

The relatively weak bonds and high atomic weight of the constituting ions shifts the low energy edge of the window to quite high λ values ($\lambda = 14$ μm for ZnS, and 20 μm for ZnSe). Their bandgaps – at 3.5 or 3.9 eV (cubic and hexagonal) ZnS and 2.8 eV for ZnSe – place the high energy edge of the window at points that leave most of the VIS open: $\lambda \sim 0.4$ μm for ZnS and ~0.5 μm for ZnSe. In Figures 4.88 and 4.89 the transmittance of ZnS and ZnSe TCs is shown. In Table 4.15 the properties of ZnS and ZnSe ceramics are listed.

4.2.10 Ferroelectrics

Certain multioxide ceramics, many based on perovskite-type lattices, exhibit ferroelectric behavior [S50, Y12], being simultaneously more or less transparent [K63]. Let us recall here the fact that ferroelectric behavior is, in the case of ceramics (as opposed to single crystals), also a necessary condition to piezoelectric activity and implies the possibility of pyroelectric behavior too. The integration of transparency with such exotic properties opens new application fields. These materials are also of high scientific interest regarding domains like ferroelectric and electro-optic behavior, point defects/properties relationship, and oxide sintering.

A review of the relevant materials, their properties, and processing is given in this section. Ferroelectric glass-ceramics are discussed in Section 4.2.11.

Table 4.15 Properties of ZnS and ZnSe ceramics.

Property (units)	ZnS	ZnSe
TD (g/cm^3)	4.09	5.27
TRS (MPa)	100	50
K_{IC} (MPa m$^{0.5}$)	1.0	0.5
E (GPa)	75	70
HK (GPa)	1.6–2.5	1.0
$\alpha \times 10^{-6}$ (°C^{-1})	17–25	18
ε_r	~8.5	~9
$n_{6\mu m}$	2.19	2.40
$n_{0.6\mu m}$	2.36	2.61
$t°_f$ (°C)	1700	1520
Start of sublimation (under low pressure atmosphere) (°C)	Over 1200	Over 400
Oxidation	Significant over 800 °C	—
Safe use temperature (°C)	450	320

4.2.10.1 Ferroelectrics with Perovskite-Type Lattice

The lattice type called "perovskite" borrows its name from that of the $CaTiO_3$ mineral. A wide variety of ceramic materials – having an ABX_3 general formula with X^{2-} being, in most cases, the oxide anion – have a crystallographic structure conform to this type of lattice. They find application as capacitors, piezoactuators, superconductors, etc. For instance, certain superconducting ceramics, like YBCO, are based on such a lattice type, as are $BaTiO_3$ (the basic material in the ceramic capacitors industry) or the PZTs, the basic material in the piezoceramics industry. Most of the ferroelectric ceramics – which could be brought to a transparent state – possess lattices of this type. In its state, over the Curie temperature (T_C; temperature where transition from dielectric to ferroelectric state occurs), the unit cell of this cubic lattice looks like that depicted in Figure 4.91 [M39] for the case of $BaTiO_3$.

Below T_C slight distortions of the cubic lattice, with important effect on properties, occur; the most important consequence is the apparition of spontaneous polarization, along axes determined by the type of distortion. Some perovskites are already cubic at room temperature, while others have a Curie temperature lower or over 100 °C (like $BataTiO_3$) or even in the 300–380 °C region (the PZTs). $BaTiO_3$, for instance, has at RT a tetragonal lattice resulting from a slight distortion of the cubic one, stable over ~120 °C. The cations present in the perovskites of interest here are divided in

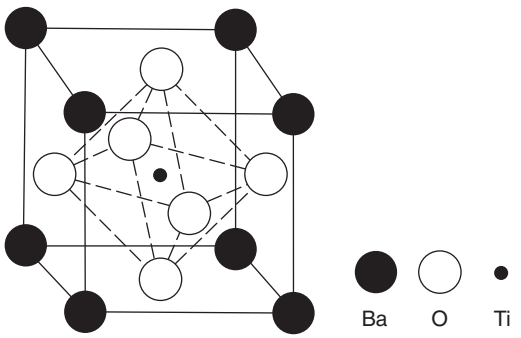

Figure 4.91 The unit cell of $BaTiO_3$. Source: Adapted from Moulson and Herbert 1990 [M39].

two groups. One group, labeled "A" type, includes low oxidation state (mostly 2+ and 3+) large radius cations like the Ba^{2+} of meta barium titanate. The second group, labeled "B" type, includes higher oxidation state (mostly 4+, 5+) small radius cations like Ti^{4+}. The large alkaline earth ions (e.g. Ba^{2+}) replace a fraction of the anions of the O^{2-} of the perovskite lattice, with the small cations (like Ti^{4+}) occupying all the octahedral interstices that are surrounded only by O^{2-}. In another perspective the lattice can be described as a cubic array of corner sharing MO_6 (M = B type cations) with the interstices filled with A type cations.

In certain perovskites, instead of one B cation type, one has two cations (B′, B″), in a ratio leading to electrostatic compensation; such materials are also addressed below.

Here the main interest is in perovskites with Pb on the A sites and Ti^{4+} on the B sites and derivatives of this model ($PbTiO_3$; PT). The most important derivative has part of Ti^{4+} substituted by Zr^{4+} and part of Pb^{2+} by La^{3+}. The family of compounds thus resulting is abbreviated as PLZTs.

4.2.10.2 PLZTs: Fabrication and Properties

Certain compositions located in the $PbO–ZrO_2–TiO_2$ system represent (when properly doped) the most performant family of piezoceramics [H3, J1, M39]; most of them cannot be brought to a transparent state. First of all these materials are ferroelectric – a condition required from a polycrystalline ceramic in order to become piezoelectric, after suitable poling [M39]. Based on potential applications, it is worth noting that it was clear from experience with single crystal ferroelectrics that if optical transparency can be conferred to such materials, conditions for electro-optic behavior will be realized [H3]; that knowledge stimulated efforts to bring, at least some PZTs, to a transparent (in the VIS range) condition. As it is detailed below, the efforts paid off. The PLZT family of transparent ceramics was, in fact, developed early in the history of TCs, viz. late 1960s.

Various methods and additives (e.g. Ba, Sn, La) were tried for transparency achievement. The successful one (1968–1969) combined the use of excess PbO (promotion of full densification), increase of the La^{3+} content from the usual 1–3 at% up to at least 6 at% and sintering by hot pressing [H3, L2, L3]; the best results were obtained with an 8/65/35 composition. The potential of HPing for full densification of ferroelectrics was observed in work on Bi-doped PZTs (1961–1965) [H3]. Very high transparency PLZT plates have been produced by 1972 [B61, H3]. The development of T-PLZTs was one of the first in which the importance of nanosize powders (coprecipitation) in TC obtainment was remarked.

First it was observed that substantial amounts of La_2O_3 can be homogeneously distributed within PZT lattices. The $Pb_{1-x}La_x(Zr_yTi_{1-y})_{1-x/4}O_3$ family includes a wide domain for "x"; the amount of La^{3+} one can introduce, as Pb^{2+} substituent, varies with the $PbZO_3/PbTiO_3$ ratio but may attain values as high as 32 at% of La. La^{3+} is unique, among dopants to PZT, in its ability to promote transparency. It is believed that one of its effects on structure important in this context is the causing of a PZT cell's distortion to a degree low enough to keep it quasi-cubic. This, of course, means a low anisotropy of the lattice and thus keeps at a low level the birefringence related scattering, at the ceramic's grain boundaries. La^{3+} also seems to promote uniform grain growth and reduce pore occlusion probability and thus remnant porosity level and the scattering associated with it. The *RT* phase diagrams of the PZT and PLZT systems are shown in Figure 4.92 [H2].

Like in the case of PZT, most of the practically useful PLZT compositions are located near the morphotropic phase boundary (MPB), which separates the ferroelectric materials based on rhombohedral and tetragonal phases, respectively; this location is known to maximize most of the nonoptical properties of interest and it was found also to facilitate achievement of transparency [H2]. The PLZT materials are specified as $x/y/1-y$, where x = La at% and $y/1-y$ is the Zr/Ti ratio. For transparency the La_2O_3 concentration has, as it was already noted, to provide at least 6 at% of La^{3+} but also not much more than that. For different reasons both too low and too high La^{3+} concentrations negatively affect transparency. Too low concentrations leave too high a level of anisotropy and the consecutive light scattering at the GB of misoriented grains. At too high La_2O_3 content, second phases precipitate in the grain boundary region. For the most popular 65/35, Zr/Ti ratio hosts, the optimal dopant concentration range, based on transparency, lies between 8 and 16 at% of La^{3+}.

In Figure 4.93 the optical spectrum and the photo of a specimen (t = 1.8 mm) fabricated at ICSI (1994) are shown.

Transmittance remains high, out to 6.5 μm, and then gradually decreases to the cutoff at 12 μm. Scattering owed to microstructure imperfections has been found as more intense when $\overline{GS} > 2°$μm; under 2 μm the birefringency level dictates the optical behavior.

In order to understand the transparency and good electro-optic characteristics of some of these materials, it is useful to give a closer look at Figure 4.92. It can be observed that for the 65/35 ratio ($PbZrO_3$:$PbTiO_3$), at ~9 at% of La, the ferrostate (rhombohedral) converts to the paraelectric one (cubic; which enhances transparency). However the slim area (hatched in the Figure 4.92) lying along the $FE_{RH} + FE_T$ vs. PE cubic delineates an area of compositions where a **metastable** ferrostate can be induced (despite the ~ cubic lattice) by

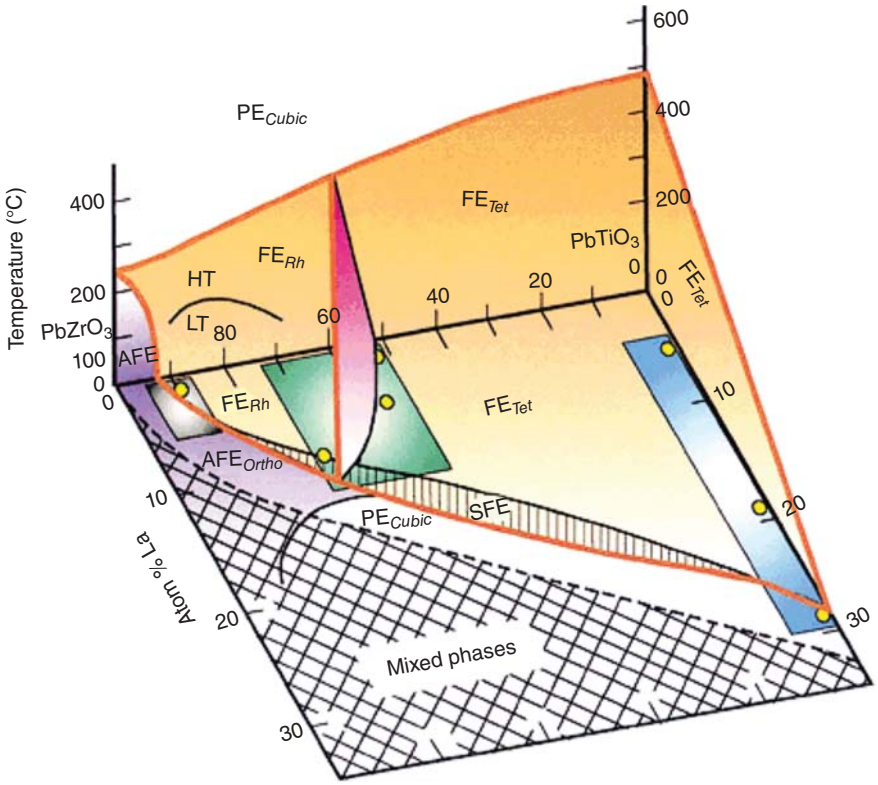

Figure 4.92 Phase diagram of the pseudo-ternary system $PbTiO_3$–$PbZrO_3$–La_2O_3. Source: Haertling and Land 1971 [H2]. Reproduced with permission from John Wiley & Sons.

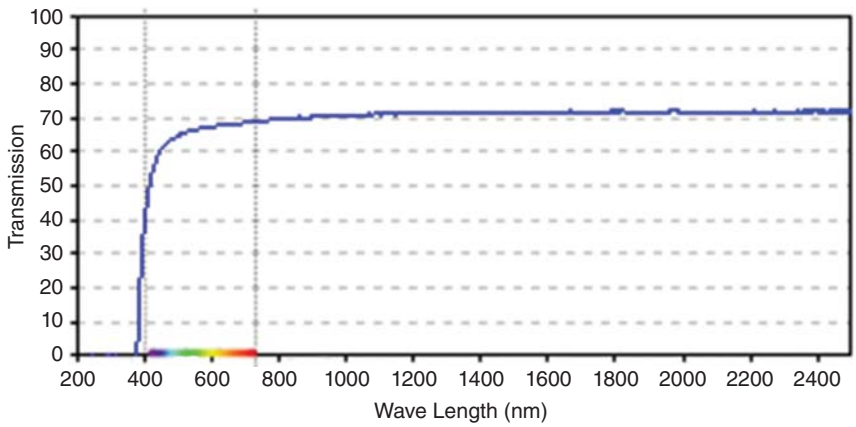

Figure 4.93 Imaging and transmission spectrum of PLZT thin plate fabricated by hot pressing (ICSI, Haifa, 1995).

application of a sufficiently strong electric field. As it is seen, simultaneously conditions for both transparency (the near-cubic lattice) and electro-optic behavior (metastable ferroelectricity) are fulfilled. Experiment shows that these materials exhibit, as expected, a quadratic (Kerr) electro-optic effect. Compositions in the "mixed phase" region of the diagram (double cross-hatched zone) are opaque, while the single phase cubic compositions are of significant transparency but not ferroelectric. The highest transparency of ferroelectric materials is exhibited by compositions situated within 1 at% of the phase boundary separating FE phases from the cubic. The addition of La, besides its positive effect on transparency, brings about, as known from the case of nontransparent PZTs (at% La < 6), benefits regarding a number of the basic properties of these materials: increased squareness of the hysteresis loop, lower coercive field (E_C), higher values of ε_r, maximized values of the electromechanical coefficients (as long as the matrix stay close to the MPB), and increased mechanical compliance (lower stiffness coefficients). A number of compositions throughout the diagram are suitable for pyroelectric devices [A23, M39]. Like in the case of the opaque PZT piezoceramics, the PLZT raw material batches need to be formulated in correlation with the temperature of sintering and the firing enclave

atmosphere composition, if transparency is sought. The main reason for this is the fact that the substitution of Pb^{2+} by La^{3+} is compensated by vacancies on both the B and A cationic sites, according to

$$Pb_{1-x}La_x(Zr_yTi_{1-y})_{1-0.25x}V_{0.25x}O_3 \quad (4.5)$$

$$Pb_{1-0.5x}La_xV_{0.5x}(Zr_yTi_{1-y})O_3 \quad (4.6)$$

where "V" symbolizes a vacancy, on the B and A sites, respectively.

The A site vacancies are predominant for compositions with high amounts of $PbZrO_3$ and the B site ones for materials including large fractions of $PbTiO_3$. In $PbZrO_3$ rich materials up to 85% of the total number of vacancies may exist on the A sites; the La_2O_3 amount has only a slight effect on the site distribution of vacancies. The most important 65/35 ratio materials include 74% A site vacancies; its measured bulk density (highly transparent parts) is of 7.82 g/cm^3, a bit higher than that calculated according to (4.6), which is $TD = 7.77$ g/cm^3. If a batch is formulated according to (4.5), the excess Pb^{2+} will exit as PbO, which accumulates at GBs, facilitating densification. If the formulation is according to (4.6), the lacking Pb^{2+} has to be provided by a sintering atmosphere rich in PbO (the necessary oxide is usually provided by the vaporization of a PbO containing "setter" powder). The powders are prepared using pure alkoxides (as Ti^{4+} and Zr^{4+} carriers) and fine PbO powder dispersed in IPA. After thorough blending of these components, a La-acetate/water solution is introduced. The hydroxides of Ti and Zr react with PbO and the La acetate to provide a complex mixture of oxides and hydroxides suspended in an alcohol–water liquid. After drying, calcination at 500 °C (~15 hours) is effectuated. In the case of PLZTs, this is high enough to convert the amorphous dry material to PZT crystalline powder. The comminution is effectuated in nonpolar liquids. Other synthesis methods – in which all cations are introduced as alkoxides or nitrates and alkoxide mixtures – have also been developed [T19]. Forming can be done both by unidirectional and isostatic pressing. The most delicate stage of the fabrication is the sintering. Various methods based on long pressureless firings, sinter/HIP, and hot pressing, were developed. Hot pressing can be done either under flowing atmosphere [H2, L3] or, best, in two stages (vacuum up to 700 °C) followed by 18 hours dwells at 1250 °C under ~15 MPa. A typical setup for the case of a vacuum + oxygen two stage HPing is shown in Figure 4.94. The typical microstructure of large and fine grain size PLZT is shown in Figure 4.95.

Scattering is less intense for large grain size. The optimal $\overline{GS}$ depends on the application, but a narrow distribution around $\overline{GS}$ is always desired. The PLZTs are, in air, stable to ~800 °C; at higher temperature PbO starts to significantly volatilize. Reductive gases like CO or H_2 lead to massive $V_O^{\cdot\cdot}$ formation as low as 550 °C and, as a result, darkening of the parts. Stability to basic reactant attack oxides is poor; resistance to moisture is reasonable. In Table 4.16 some of the important, for apps, properties of PLZTs are collected; typical values of compositions based on 65 : 35 Zi:Ti ratio and La = 7–9 at% were selected. Additional data on optical properties are given in [M24, M25], while the dielectric ones are discussed by Pytel et al. [P34].

The hysteresis loops for PLZTs having different types of electro-optic behavior will be shown in Figure 5.45. The switching speed and total switched polarization are

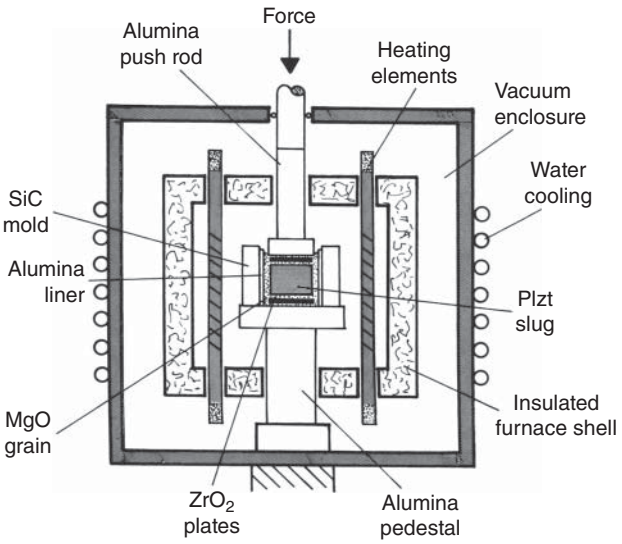

Figure 4.94 Schematic of hot pressing system used for fabrication of transparent PLZT ceramics. Source: Haertling 1988 [H3]. Reproduced with permission from Taylor & Francis.

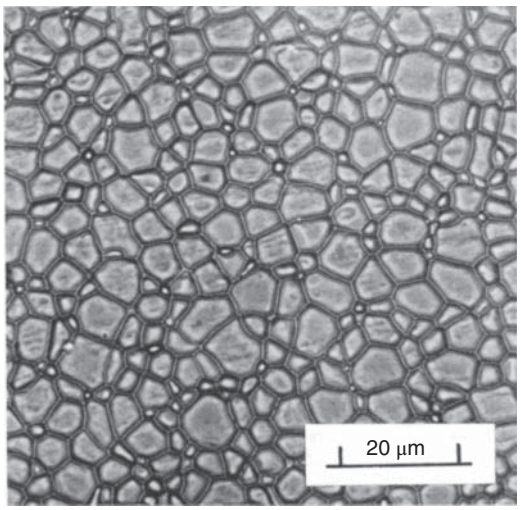

Figure 4.95 Microstructure of PLZT ceramic (SEM on plasma etched surface). Source: Haertling 1988 [H3]. Reproduced with permission from Taylor & Francis.

Table 4.16 PLZT general properties.

Property	Value
n at 630 nm	2.425
TRS	~100 MPa
$\alpha_{RT\text{-}300°C}$	$3–5 \times 10^{-6}$ °C^{-1}
ρ_e at RT	$>10^{11}$ Ωm
Breakdown strengths	100–120 kV/cm
ε_r	2–4000
Dielectric loss	0.1–6%
P_R	35–40 μC/cm
E_C	4–15 kv/cm
k_p	0.45–0.65

composition dependent and can be altered by residual stress; some materials show speeds as high as 10 ns.

4.2.10.2.1 *Electro-optic Properties of PLZTs*

There are several types of electro-optic behavior a PLZT may exhibit quadratic birefringence, quadratic depolarization, linear birefringence, memory birefringence, and memory scattering.

In Table 4.17 the value of the relevant EO coefficient, for each composition, is quadratic = R $[m^2/v^2 \times 10^{-16})$ and linear = r_C $[m/v \times 10^{-10})$. For comparison the values for the most used single crystal EO materials are also given. As it can be seen, most ceramics compare well with their single-crystal counterparts.

4.2.10.3 Other Perovskites Including Pb

While the PLZTs possess the optimal combination of characteristics based on commercially relevant applications, other perovskites have been also studied, some of them exhibiting better individual properties than the PLZTs.

Table 4.17 Electro-optic properties of PLZT; comparison with other ferroelectric ceramics.

Composition La/Zr/Ti	R (m^2/v^2)	r_c (m/v)
8.5/65/35	38.60×10^{-16}	—
9/65/35	3.80	—
9.5/65/35	1.50	—
10/65/35	0.80	—
12/65/35	0.16	—
8/40/60	—	1.02×10^{-10}
12/40/60	—	1.20
KTN (65/35)	0.17	—
KDP	—	0.52
SBN (50/50)	—	2.10
SBN (75/25)	—	14.00
$LiNbO_3$	—	0.17
$LiTaO_3$	—	0.22

A wide range of perovskites result by using on the B sites various cations, B_a to B_f, having a radius $r_6 \in$ (60–80) pm. They respond to the formula $Pb(B_a{}^{+1}B_b{}^{2+}B_c{}^{3+}B_d{}^{4+}B_e{}^{5+},B_f{}^{6+})O_3$ where

$$a + b + c + d + e + f = 1$$
$$a + 2b + 3c + 4d + 5e + 6f = 4$$

As opposed to PLZT, the cations are not both of the TM^{4+} type; they are combined so as to ensure electrostatic balance. The most usual B^{5+} is Nb^{5+}; popular materials of this type are $PbMg_{1/3}Nb_{2/3}O_3$ (PMN), $PbFe_{0.55}W_{0.1}Nb_{0.35}O_3$, and $Pb_{1.02}(Zr_{0.58}Fe_{0.20}Nb_{0.20}Ti_{0.02})_{0.006}O_3$ (pyroelectric TC used in videocams [M39]). Pb^{2+} can also be partially replaced by Bi^{3+} or La^{3+} [H3]. Besides stoichiometric materials, various solid solutions are also relevant here. For instance, $Pb(Mg_{1/3}Nb_{2/3})O_3$–$PbTiO_3$ (PMN-PT), $(Pb,La)(Sc_{0.5}Nb_{0.5})O_3$ (PLSN), and $Pb(Zn_{1/3}Nb_{2/3})O_3$–$PbTiO_3$ (PZN-PT) are materials of practical value. Also studies were made on a few more complicated compositions like $(Pb,La)(Hf,Ti)O_3$, $(Pb,Ba,Sr)(Zi,Ti)O_3$, $(Pb,Sn)(In,Zr,Ti)O_3$, $(Pb,Ba,La)Nb_2O_6$, $(Pb,La,Li)(Zr,Ti)O_3$, $(Pb,La)(Zn,Nb,Zr,Ti)O_3$, or $(Pb,La)(Mg,Nb,Zr,Ti)O_3$ [C18, H3]. The PMN-PT [L57] and PZN-PT sets of solid solutions are among the most relevant, from applications based on the electro-optic effects, because electrooptic coefficients are better than those of PLZTs; some of these materials also have a transparency range wider than that of PLZT. Suitable compositions from the PMN-PT series exhibit a $T_C > RT$ (as opposed to pure PMN) combined with good properties; the substitution, in PMN, of Ti^{4+} by Mg + Nb is the structural factor leading to the property enhancement. The system, like PZT, has around MPB a region of compositions, which maximizes properties [J10]. The processing of PMN-PT goes along the lines defined for PLZTs. Interesting thin films and coatings [T27] can also be derived, by specific processing, from such compositions (this issue is not further developed here). A problem plaguing compositions containing Pb and Zn coupled with Nb is the ease of formation of polymorphs based on a pyrochlore (RNb_2O_6; R = mixture of divalent cations) lattice. For instance, when pure PMN is fabricated, a second phase $Pb_{1.83}Nb_{1.71}Mg_{0.29}O_{6.39}$ (paraelectric) is difficult to completely avoid. The pyrochlore phases form preferentially in the 700–850 °C region. Besides their effect on the dielectric characteristics, they have a negative influence on sintering and mechanical strength. The addition of PT to PMN stabilizes the perovskite structure polymorphs [S35]. Further doping with La^{3+} promotes densification and, as a result, transparency achievement [B4, J10, L39]. Processing by HPing, like in the case of PLZTs, is

widely used for PMN-PT materials. Other approaches were also demonstrated as being able to generate quite transparent parts. For instance, W. Ruan et al. [R38] describe an approach in which first pellets (3/75/25) are sintered in O_2 atmosphere 1200–1250 °C and then HPed at $t° \sim 1050$ °C for eight hours at pressure in the 50–100 MPa range; at $t = 0.5$ mm plates exhibiting a $T \approx 60\%$ were obtained, about 95% of T_{theo}. In Figure 4.96 [R38], the birefringence induced by electric field application is shown.

The fingerprint shape of the ferro domains differs from that of La-free PMN-PT, the latter having strip shape domains. The domain morphology of the La containing PMN-PT is different from that of "normal" ferroelectrics (PMN-PT is a "relaxor"). The ferro domain's shape may be a factor influencing their mobility. That of the La-doped relaxor seems to favor high mobility, thus reducing the threshold of the E value leading to birefringence; a smaller domain size (specimen "A" sintered at 1150 °C) seems to also increase domain mobility compared to parts exhibiting larger domains (specimen "C" sintered at 1230 °C). It was shown that addition of RE^{+} cations, like Er^{3+} (0.5–2 at%) is also, like La^{3+}, positively influencing transparency, but at higher amounts (5.0 at%) it favors pyrochlore phase formation [W20]. The PZN-PT materials became lately also (like PMN-PT) a competitor for the PLZTs. Certain compositions of this solid solution series (La^{3+} doping also present) show certain advantages over the PLZTs. For instance, higher quadratic electro-optic coefficients and, more important, slimmer hysteresis curves, thus allowing faster switching and better optical modulation (this feature is not good for memory devices); somewhat lower sintering temperatures are possible (HPing procedure like that for PLZTs is the preferred fabrication approach also for PZN-PT materials). In Table 4.18 the electro-optic properties of PMN-PT and PZN-PT materials are exemplified.

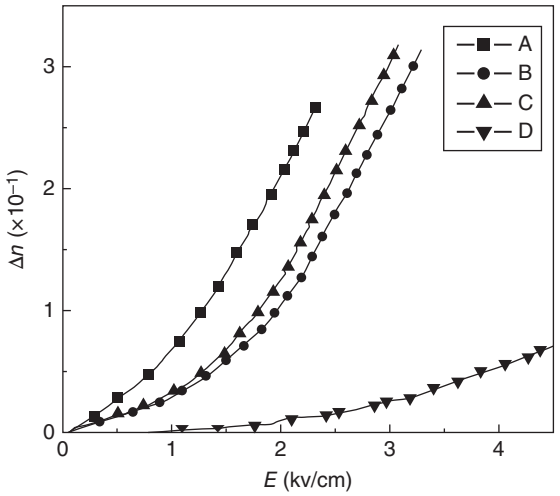

Figure 4.96 The Δn as a function of external electrical field strength (EO effect) existent in PMN-PT-type transparent ceramics ($n = 2.44$); A to C = various sintering temperatures in the 1150–1230 °C range; D = a 9/65/35 PLZT. Source: Ruan et al. 2010 [R38]. Reproduced with permission from John Wiley & Sons.

Table 4.18 Electro-optic properties of PMN and PZN-PT ceramics.

Material composition	Property	Value	Observations	Literature
PT-PMNs	R	14–65 (m^2/v)	—	—
	ε_r	20–30 000	—	—
	n_λ	2.45–3.00	—	—
PT-PZN	R	—	3.0×10^{-16} (m/v)	—
	ε_r	6–16 000	—	—

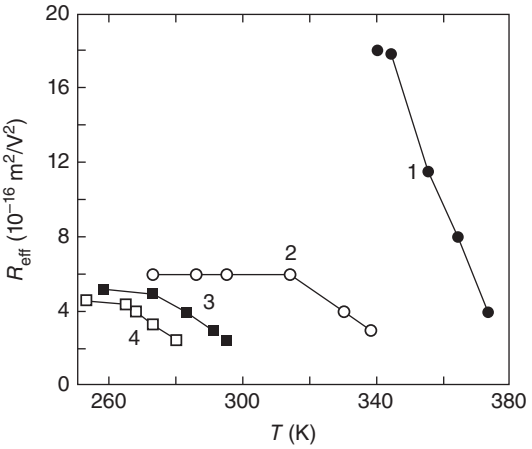

Figure 4.97 The value of the R_{eff} coefficient as a function of temperature for ceramics derived from PMN-PZT; the molar concentration of PZT = x. (1) $x = 33$ mol%. (2) $x = 23$ mol%. (3) $x = 16$ mol%. (4) $x = 10$ mol%. Source: Kamzina et al. 2012 [K8]. Reproduced with permission from AIP Publishing.

PMN-PZT mixtures have been studied too. Some of the compositions show promising electro-optical properties, as suggested by the values of the relevant coefficients present in Figure 4.97 [K8].

4.2.10.4 Perovskites Free of Pb

From the ecological point of view, it is preferable to use Pb-free materials. Therefore transparent ferro ceramic perovskites fulfilling this requirement were sought for.

4.2.10.4.1 Ba Metatitanate

J. Liu et al. [L31], using commercial nano meta barium titanate (BT) powders and SPS (950 °C/3 min/200 MPa), have been able to obtain nanograin size translucent thin pellets, as shown in Figure 4.98.

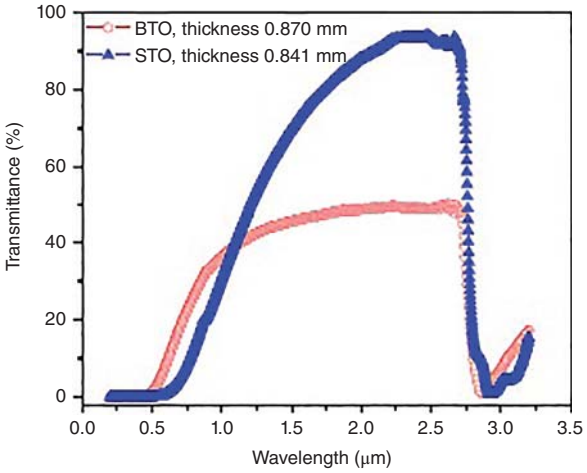

Figure 4.98 Transmission window, in the NIR range, of ferroelectric lead-free ceramics derived from nanopowders by SPS sintering. (1) $BaTiO_3$. (2) $SrTiO_3$. Source: Liu et al. 2010 [L31]. Reproduced with permission from IOP Publishing.

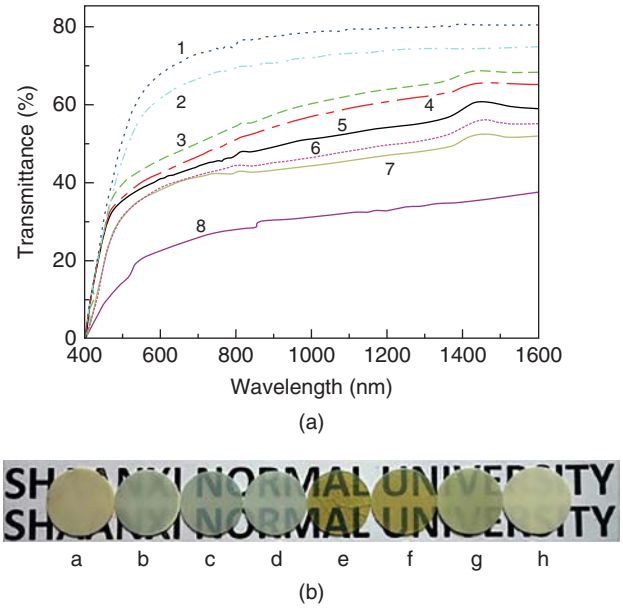

Figure 4.99 Imaging and optical spectra of lead-free translucent ceramics derived from a potassium/sodium niobate base by additions of $LaBiO_3$. (a) Optical spectra. (b) Imaging numbers and letters represent various $LaBiO_3$ additive concentrations. Source: Yang et al. 2016 [Y9]. Reproduced with permission from John Wiley & Sons.

The ε_r of the specimens is lower than that of the normal (micrograin) BT. This is a known phenomenon related to the effect of grain size on the way the ferro to paraelectric state transition occurs.

4.2.10.4.2 Materials Based on the Potassium Niobate-sodium Niobate System

The ferroelectricity and moderate piezoelectricity of $KNbO_3$ ceramics and more complex compositions, based on this leadless perovskite, were known already in the 1950s [J1]. Later it was also observed that the piezo coefficients can be significantly improved and brought closer to those of the PZTs (e.g. $d_{33} = 416$ pC/N) [Y9]. It was also found out that modification of a $(K_{0.5}Na_{0.5})NbO_3$ base material (KNN), using various strategies, can generate ceramics, which, owing to a low grain size and/or change of the lattice to a near-cubic symmetry, exhibit various levels of transparency [C16]. Addition like Bi_2O_3, $LaBiO_3$, $Sr(_{Mg0.33}Nb_{0.67})O_3$, $Sr(Al_{0.5}Nb_{0.5})O_3$, or $Sr(Zn_{0.33}Nb_{0.67})O_3$ were all instrumental in this endeavor. In Figure 4.99 the transmission spectrum of ceramics derived from an KNN base by addition of $LaBiO_3$ is illustrated [Y9].

The relaxor while quite transparent has modest ferroelectric properties. The addition of $Sr(Al_{0.5}\ Nb_{0.5})O_3$ while causing a reduction of transparency offered, simultaneously $d_{33} = 105$ pC/N and $P_r = 15.1$ mC/cm^2 (P_r here means remnant polarization).

In certain perovskites, instead of one B cation, one has two (B′, B″), in a ratio leading to electrostatic compensation. For instance, substituting Ca^{2+} with Ba^{2+} (A sites) and Ti^{4+} with Mg^{2+} and Ta^{5+}, perovskites of the $Ba(Mg_{0.33}Ta_{0.66})O_3$ form appear. It was also shown that the larger the radius and formal charge differences between the B′ and B″ cations, an "ordering" process is facilitated, leading to the stabilization of a superlattice. As a result the actual symmetry of the lattice is changed. The $Ba[Mg(Zn)_{0.33}Ta_{0.66}]O_3$ (useful as a dielectric resonator) satisfies the requirements for ordering.

4.2.10.4.2.1 Perovskites Including B^{2+} and B^{5+} Cations

Researchers of Murata who developed dielectric resonators based on various $A(B'_{0.33}{}^{2+}B''_{0.66}{}^{5+})O_3$ compounds have also produced cubic perovskites to which a measure of transparency can be conferred. The cubic materials were derived from $Ba(Mg_{0.33}Ta_{0.66})O_3$ by adding cations like Sn^{4+}, Zr^{4+}, etc. [K21, K22, W5]. These additions lead to disordering in the lattice and, as a result, formation of a cubic lattice. The D^3_{3d} $Ba(Mg_{0.33}Ta_{0.66})O_3$ lattice's unit cell transforms to a cubic one of the O^5_h symmetry the lattice proper to the "disordered" materials, which form upon Sn^{4+} and/or Zr^{4+} addition. Owing to the cubic nature of these materials, they can be fabricated as transparent polycrystalline parts. An incentive to examine these materials is their high (similar to c-ZrO_2) refraction index ($n = 2.128$ at $\lambda = 436$ nm [K7, K22]); this is useful for miniaturization of camera lenses. The fabrication follows the pattern of conventional ceramic technology, comprising the sintering (~1550 °C), under O_2-enriched atmosphere, of pressed compacts of mixed oxide powders. A high level of transparency was attained

(the T_{theo} at ~72% is low, owing to high reflection losses caused by the high refraction index). The mechanical properties are modest (e.g. $HK1 = 9.5$ GPa) and the density quite high ($TD \sim 7.5$ g/cm^3). This will be in more detail described in the part devoted to applications, the main use is in the domain of small (non-glass) optical lenses. Lasing of Nd^{3+} in such a host was also demonstrated together with nonlinear behavior based on which Raman vibrations influence the characteristics of an Nd^{3+}:YAG laser beam (stimulated Raman scattering) [K67].

4.2.11 Transparent Glass-Ceramics

As discussed in Section 3.1.4, there exists besides powder sintering another processing approach allowing the production of transparent specimens containing moderate to very large amounts (nearly fully crystalline parts) of crystalline phase(s): controlled crystallization of glass (ceramming). Only a limited number of the glass-ceramics are also transparent (abbreviated here as TGC); in this section a brief review of the most interesting is given. Properties of these systems, both spectral and nonoptical, are determined by the type of crystalline phase(s) precipitated, crystals size, the distribution pattern, and amount and structure of the residual glass. The structure of the interface between glass and crystal also has a significant influence. The discussion will consider not only those products in which the initial glassy phase amount is reduced below 0.5% in the ceramming stage – making in fact regular ceramics of the finished parts (see Section 4.2.11.6) – but also materials containing more substantial glassy fractions (30–80%). The latter form an intermediate class, between transparent ceramics and glass, which owes transparency to both its glass content and crystalline material. Therefore they constitute a topic both a book on glass and one on TCs has to consider; they exhibit practically useful properties and appear in many commercial products.

Before proceeding to the descriptive part of the discussion of TGCs, let us note that such material can be made transparent in two ways:

- By precipitating during ceramming, a crystalline phase having an "n" similar to that of the residual (not the initial) glass.
- By generating crystals, preferably (but not necessarily) cubic, which have a size lower than 100 nm (preferably lower than 50 nm) and thus produce little loss by scattering of the incident light.

Below the main TGCs are presented as a function of their crystalline constituent(s).

4.2.11.1 Transparent Glass Ceramics Based on Stuffed β-Quartz Solid Solutions

In Figure 4.100 [H31], the lattice of both α and β quartz is visualized.

These polymorphs of SiO_2 pertain to the group of tectosilicates, being framework structures in which all the O^{2-} anions of the basic $[SiO_4]^{4-}$ tetrahedron, are shared. As the Figure 4.100 shows the two α and β structures are quite similar and the β polymorph (the high temperature form) changes easily at 573 °C into the α-form stable at RT. For TGCs the β-quartz is of most interest because it has a specific thermal behavior relevant for a few high-tech applications. Its lattice includes eight member rings (i.e. SiO_4 units). In this structure, paired helical chains of tetrahedrons spiral in the same sense around a hexagonal screw symmetry axis, parallel to the "c" basic axis. The quite specific property of the β-quartz-type solid solution lattices (β-quartz$_{ss}$), alluded to above, is an expansion coefficient "α" close to zero (for % $SiO_2 \in 50$–80); it is 150×10^{-7} K^{-1} for αQ. This low level of "α" is maintained in some of the derivatives, especially those with composition on the SiO_2-β-eucryptite line. The quartz polymorphs precipitate with relative ease from a silicate glass matrix because they have a structure relatively similar to that of the glass; silicate glasses have lattices very similar to those achieved by introducing certain types of disorder into a β cristobalite (another SiO_2 polymorph). Another important similarity relevant in this context is that exhibited by the lattice of some of the SiO_2 polymorphs with the lattices of certain aluminosilicates containing R^+ and/or R^{2+} compensator cations [B65]. In those silicates, Si^{4+} is substituted (up to 50%) by Al^{3+} at the center of the O^{2-} tetrahedrons. The charge balance is obtained by entrance into interstitial locations of R^+ or R^{2+} cations, the size of which makes them able to fit in there. Such materials are called "stuffed derivatives" of the basic silica forms; they are, as far as structure is concerned, solid solutions, of course. In the case of the βQ (β-quartz) base, besides Al^{3+}, cations like Li^+, Mg^{2+}, and Zn^{2+} may enter the lattice generating many useful solid solutions (abbreviated below as βQ_{ss}). Most used are phases that can be described by a general formula like $Li_{(2-2x+y)}Mg_xZn_yO{\cdot}Al_2O_3{\cdot}SiO_2$ [H31, S67] where $x + y \leq 1$. These Bertholide type materials (as opposed to stoichiometric Daltonides) are, in principle, only metastable, except certain compositional zones like one around β-eucryptite ($Li_2O{\cdot}Al_2O_3{\cdot}2SiO_2$). In practice, however, many such systems remain stable even after 100 hours at 1200 °C. One of the most useful compositions approaches the stoichiometry $LiMgAl_3Si_9O_{24}$ [H31]. For the materials that include MgO, ZrO_2 alone seems to be a good nucleator (3–6%). The "α" is raised to 10–20×10^{-7} K^{-1}, but even heating for long time, close

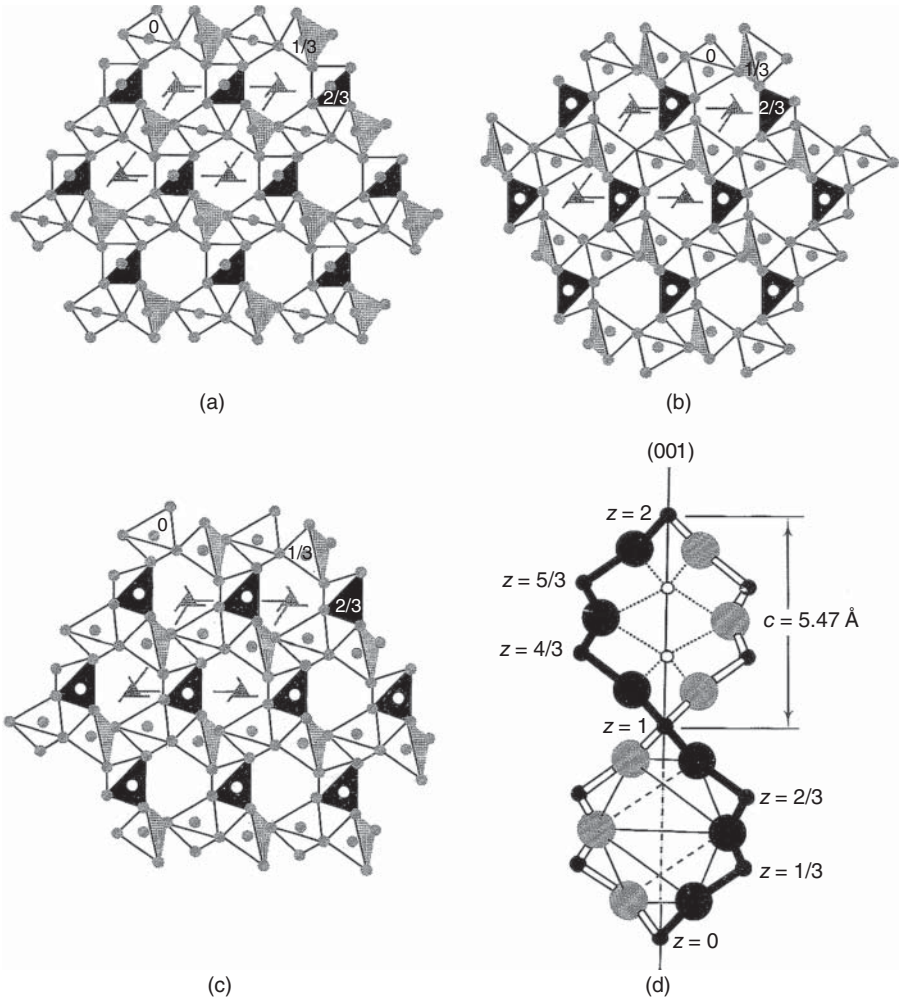

Figure 4.100 Projections along the *c*-axis of α- and β-quartz lattices. (a) α-Quartz. (b,c) β-Quartz. (d) Double helix structure of β-quartz. Source: Holland and Beall 2002 [H31]. Reproduced with permission from John Wiley & Sons.

to the softening point, does not lead to phase separation [B22]. In these glasses ZrO_2 forms quasi-cubic ZrO_2 nucleii, stabilized by the forming of solid solution with Al_2O_3 or MgO; on them crystals precipitated from the glass can develop. After crystallization these TGCs include >80% crystalline phase with a composition similar to the mother glass. Luckily glasses can be obtained in most of the compositional region where such crystalline phases can be produced. In practical terms the lattices of derivatives of the β-quartz–β-eucriptyte line are the most useful. Such phases not being cubic can generate transparent systems only when their crystal size is <80 nm. The birefringence of many of these hexagonal crystals is moderate [B22]. Pure β-Eu crystals grow too large to allow formation of TGC. A very interesting structural similarity between βQ and $AlPO_4$ was exploited to fine-tune the properties of important products like tiles for telescope mirrors. Into an βEu based up to ~50 mol% of $AlPO_4$ can be introduced so as to form solid solutions [H31]. By adding to SiO_2 Al_2O_3, P_2O_5, and small amounts of MgO and ZnO, TGC-type materials with a $\overline{GS} \leq 0.1$ μm (75–80% crystal) and very low thermal expansion could be produced [P25] by ceramming suitable composition mother glasses. Such materials can be described as $Li_{2-x}(v + w)Mg_vZn_wOAl_2O_3{\cdot}AlPO_4$ $(y - 2x)SiO_2$. In addition to the specific "α" values, the mixed silicate–phosphate-based materials (for instance, Schott's product Zerodur) exhibit high E values of up to 90 GPa and TRS of 110 MPa. The transmission of such a material is shown in Figure 4.101.

The β-quartz$_{ss}$ materials not including $AlPO_4$ units can be made to exhibit transparency levels quite close to that shown in Figure 4.101 [P10]; examples are materials derived from the compositional range shown in Figure 4.102.

Nucleation is optimal when certain ZrO_2:TiO_2 mixtures are used ($TiZrO_4$ nuclei), but with single ZrO_2 also good results (microstructure different from those of materials crystallized by the aid of Zr-titanate) were obtained. In order to obtain enough nuclei volumetric concentrations ($10^{20}/m^3$ is a good value), the nucleation stage has to be effectuated (~760 °C) not much above

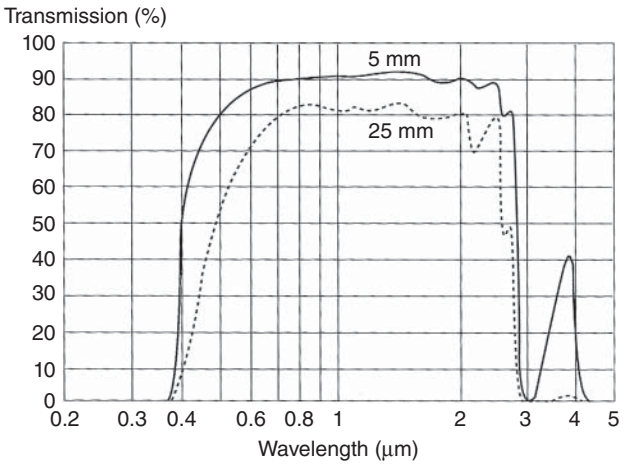

Figure 4.101 Transmission of grade Zerodur transparent glass-ceramic (Schott) plates at two thickness levels. Source: Holland and Beall 2002 [H31]. Reproduced with permission from John Wiley & Sons.

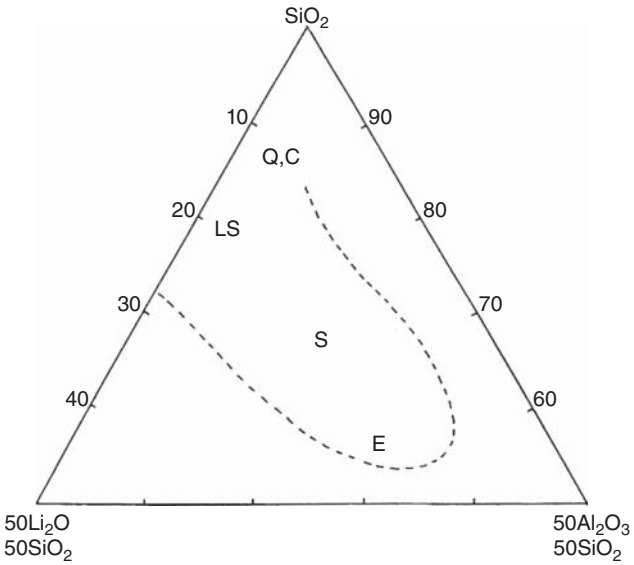

Figure 4.102 The glass-forming regions of the SiO_2–Li_2O_3–Al_2O_3 system. Q = quartz, C = cristobalite, S = β-spodumene, E = β-eucryptite, LS = lithium disilicate. Source: Partdrige and Phillips 1991 [P10]. Reproduced with permission from Society of Glass Technology.

t_g° and optimally for long time, up to 24 hours; after 10 minutes, however, thousands of nuclei/mm^3 are already formed. Thus transparent materials including up to 70% crystalline phase can be produced. As a problem (often present in various transparent ceramics and glass-ceramics), one has to mention the presence of absorbed into the lattice OH^- ions. Certain stretching and bending vibrations of the O—H bond introduce IR absorption bands like that centered at 2.8 μm; vacuum heating alleviates the problem. Annealing for a long time over 700 °C of most of such materials (a few can be heated up to 1100 °C) diminishes transparency both because crystal growth and transformation to β-spodumene ($Li_2O{\cdot}Al_2O_3{\cdot}4SiO_2$). Interesting materials resulted also when βQ_{ss} phases, lacking R^+ cations, were used [A15, B22]. Only R^{2+} cations like Mg^{2+} (MgO 3–10%) or Zn^{2+} (ZnO: 1–7%) enter the interstitial voids of the lattice. The "α" is in the $10–30 \times 10^{-7}$ K^{-1} region. Some of these systems exhibit transparency based on the second possibility offered by the Mie scattering intensity relationship, i.e. n_1 very similar to n_2. So β-quartz$_{ss}$ crystals (materials derived from glasses of the SiO_2–Al_2O_3–MgO–ZnO system) of 1–10 μm size that form during the ceramming stage do not prevent transparency. After a two stage ceramming (8–900 °C range), the β-quartz$_{ss}$ crystals precipitate on the *c*-ZrO_2 nuclei. Phase stability is restricted to ~980 °C [B22]. Glass-ceramics based on $Li_2O{\cdot}SiO_2$ + α-quartz (secondary phase) nucleated with ~3% ZrO_2 also show transparency despite a crystal size of ~0.7 μm; the index matching is, like above, the reason of the low intensity scattering. Such glasses can be nucleated also with colloidal metal [S56].

4.2.11.2 Transparent Glass Ceramics Based on Crystals Having a Spinel-Type Lattice

Spinel TCs have been discussed, at length, in other chapters. Crystals having a spinel-type lattice can be obtained also by ceramming of glasses having suitable composition, located within the SiO_2–Al_2O_3–MgO–ZnO basic system. $MgAl_2O_4$ alone could not be obtained, as the precipitated crystalline phase, for a long time; other phases like the $ZnAl_2O_4$ spinel or solid solutions, on the $ZnAl_2O_4$–$MgAl_2O_4$ line (Zn rich), were easily precipitated [B22]. Very fine crystals, 30–40 nm in size, making up 30–40% of the volume could be obtained. These glass-ceramics can be nucleated by both TiO_2 and ZrO_2 or their combination. In the case of TiO_2, the first stage is phase separation within the amorphous state. The first stage of spinel crystallization takes place within the globular smaller regions, rich in TiO_2 + Al_2O_3. Ti^{4+} compensated by $2Al^{3+}$ enters the lattice of the precipitating crystals. Because the modifier cations partition, in the crystalline phase, the residual glass is of higher strength than the mother glass. Addition of small amounts of R^+, especially Cs^+, prevents devitrification to cristoballite of the residual glass. These TGCs can be used at temperatures as high as 900 °C and have excellent chemical stability. Such glass-ceramics are among the strongest, exhibiting TRS of up to 165 MPa [H31]. Based on the mechanical properties, pure $MgAl_2O_4$ is the most desired spinel phase in such TGCs. As noted above, it was not obtained alone in the early work. During recent research regarding the improvement of nucleation in

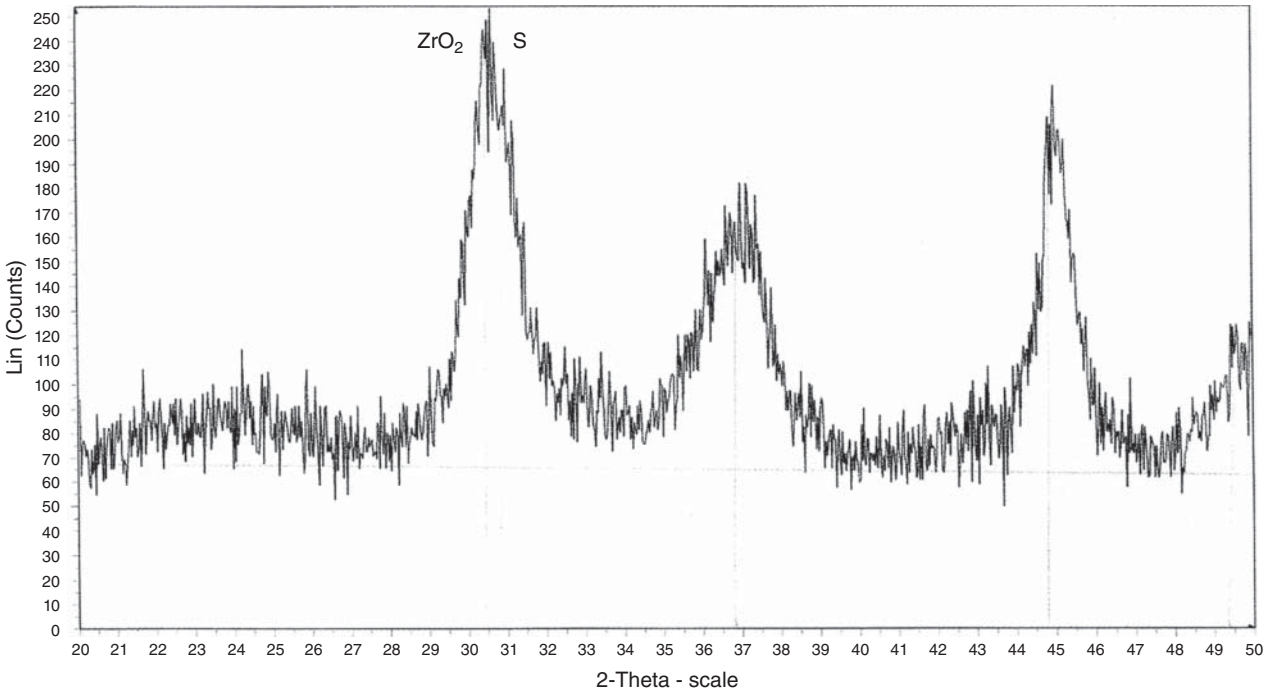

Figure 4.103 XRD pattern of transparent glass-ceramic derived from the SiO_2–Al_2O_3–MgO (K_2O) system, showing peaks of spinel (the one marked ZrO_2, S) includes a ZrO_2-related reflection; specimen fabricated at ICSI, Haifa.

the basic oxides system SiO_2–Al_2O_3–MgO, it was found out that if suitable R^+-type cations are added, especially K^+, the crystallization can be guided toward formation of $MgAl_2O_3$ (A. Goldstein, unpublished results). For certain ZrO_2:TiO_2 nucleator ratios (TiO_2:$ZrO_2 \geq 0.8$, $ZrO_2 + TiO_2 \geq 14\%$) transparent glass-ceramics containing up to 10 vol% of nanometric crystal and exhibiting only a pale yellowish hue could be obtained; coloration is caused by TiO_2 and melt viscosity increase by ZrO_2. The XRD pattern of such a TGC is shown in Figure 4.103.

One of the best compositions, the balance between coloration level, transparency, and hardness ($HV0.3 = 7.5$ GPa; $\rho = 2.5\,g/cm^3$), includes 41.8% SiO_2, 29.0% Al_2O_3, 11.5% MgO, 1.0% K_2O, 6.5% TiO_2, and 10.8% ZrO_2.

4.2.11.3 Mullite-Based Transparent Glass-Ceramics

A range of solid solutions in the Al_2O_3–SiO_2 system extending between the stoichiometries $3Al_2O_3{\cdot}2SiO_2$ to $2Al_2O_3{\cdot}SiO_2$ goes by the name of mullite. In the lattice, chains of AlO_6 octahedra are cross linked by $(Si,Al)O_4$ tetrahedra. The B^{3+} cation, present if some B_2O_3 is added, may enter the tetrahedral sites ($9Al_2O_3{\cdot}2B_2O_3$ has a mullite lattice). The boron cation is mentioned because, for reducing melting temperatures and melt viscosity (η), one has to add fluxes like B_2O_3, MgO, BaO, or Na_2O. These additives also prevent uncontrolled phase separation on melt cooling. During the thermal treatment, however, the first process happening is a controlled phase separation creating Al_2O_3-rich droplets within a highly siliceous matrix. The SEM produced a good image of the phase separated glass state as shown in Figure 4.104.

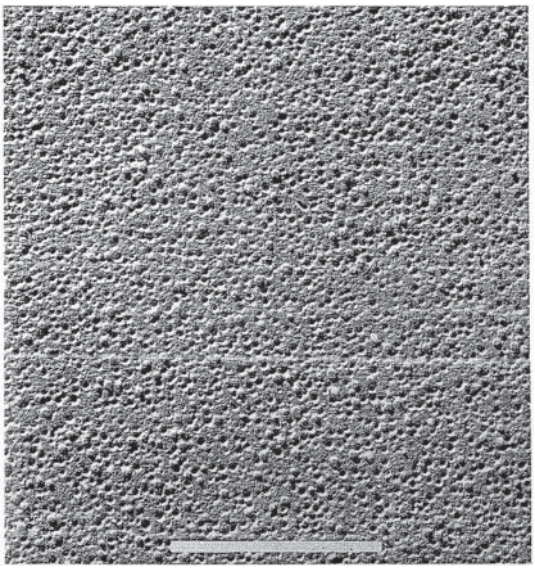

Figure 4.104 Microstructure of phase-separated binary aluminosilicate glass (white bar = 1 μm) via SEM. Source: Beall and Pinckney 1999 [B22]. Reproduced with permission from John Wiley & Sons.

The droplets crystallize to fine rods (~30 nm), a morphology not otherwise seen for mullite, which normally crystallizes in needlelike manner. The specific morphology induced by the phase separation allows the maintaining of a small $\overline{GS}$. Ceramming is done in the 800–900 °C range. A performant composition [B23] includes 48.0% SiO_2, 29.0% Al_2O_3, 11.0% B_2O_3, 10.0% ZnO, 2.0% K_2O, and 0.4% As_2O_5. Such systems keep a reasonable level of transparency up to a 0.25 μm size of the crystals; they can be used up to ~1100 °C [B22].

4.2.11.4 Other Transparent Glass-Ceramics Derived from Polinary Oxide Systems

Suitable compositions from the basic $CaO–Al_2O_3–SiO_2$ system – to which small amounts of MgO were added – precipitated during ceramming (~1000 °C) a sizable amount of a complex composition phase: $Ca_{20}Al_{32-2\alpha}Mg_\alpha Si_\alpha O_{68}$ ($\alpha \sim 4$), which exhibits a fibrous microstructure. Transmission ($t = 2$ mm) is still as high as 80% at $\lambda = 8$ μm; this makes the material interesting for MIR window fabrication. Using mother glasses from the $BaO–Al_2O_3–SiO_2$ system, relatively transparent TGCs, containing hexacelsian ($BaO{\cdot}Al_2O_3{\cdot}6SiO_2$) crystals, were obtained when using SnO_2 as nucleator. Sodium niobate and barium niobate containing TGCs were also derived from the $Na_2O–BaO–Nb_2O_5–SiO_2$ system. Owing to these crystals, the TGCs exhibit ε_r of up to 300. Some of these systems may be crammed so as to generate a crystalline fraction of up to 70% (crystallites ~10 nm in size) [P10]. Such materials exhibit useful electro-optic properties like large Kerr constant values. Introduction of Ni in certain hosts led to fluorescence [W33].

4.2.11.5 Oxyfluoride Matrix Transparent Glass-Ceramics

As noted above, fluoride's easy precipitation, from oxide glassy matrices, was exploited early for translucent (owing to large crystals size) opal-type glasses (glasses containing crystalline phase at a level that affects only its optical properties ≠ glass-ceramics). In the early 1990s, Wang and Ohwaki [W12] have introduced an interesting new type of TGC, in which the crystalline phase is constituted of fine (<50 nm) fluoride crystals, dispersed in an oxide glass matrix. It was initially thought that in fluorite lattice, $Pb_xCd_{1-x}F_2$ crystals form. Further study showed that in fact the dopant Er^{3+} enters the lattice of βPbF_2 forming $Pb_4Er\,F_2$ hexagonal, nanometric crystals. Such systems are transparent despite the fact that they include much larger amounts of fluoride than the opal glasses. Of course the transparency is a result of the low crystal size. This group of materials will be labeled below as FOG (fluoro-oxide glass-ceramics). As it will be detailed in the part dedicated to applications, the FOGs are of most interest in relation to lasing systems. The fluoride zones represent an advantageous matrix for RE^+ lasing cations compared to oxides. Monolithic fluoride hosts (both glasses and crystals), however, exhibit lower chemical stability than oxides, low melting points, low mechanical strength, and low resistance to thermal shock; resistance to laser damage is however surprisingly high [L69]. In a FOG-type composite, the fluoride zones are protected by an oxide matrix, which is more performant as to the aspects noted above. As a result, for certain applications, a FOG is a better choice than either fluoride or oxide monoliths. There is a strong tendency of RE^+-type dopants to partition in the fluorides in these composites. This was already illustrated by Wang and Ohawki who showed that Er^{3+}'s 972 nm emission was upconverted (viz. brought to higher frequency) to 545 and 660 nm, in a way like that observed in BaY_2O_8 single crystals. Various types of fluoride crystals have been precipitated out of FOG-type mother glasses. Among the most studied, one can list: LaF_3, βPbF_2, CaF_2, $CdF_2–GdF_3–PbF_2$, or BaF_2 [B2, C22, D9, G36, K23, M38, Q1, S7, T22]. In most used oxide matrices, compositions lie in systems like $SiO_2–Al_2O_3–Na_2O$, PbO, BaO, or $GeO_2–PbO$. At ICSI the focus of research in this domain was on the use of commercial, relatively cheap glasses like regular SCS (float type) or Pyrex type ($SiO_2–B_2O_3–Al_2O_3–Na_2O$ basic system) as a carrier of the fluoride crystals. That work (A. Goldstein, unpublished results) showed, among other things, that it is important to harmonize the peak glass melt temperature (that was needed for homogenization and fining) with the vapor pressure of the fluoride(s) present. Even in the case of lidded crucibles, loss of ~35% was measured for PbF_2, 25% for BaF_2, and ~15% for CaF_2 and LaF_3 after heating at 1600 °C/2 hours of a window glass + fluoride mixture. Addition of CaF_2 reduces the viscosity of float or Pyrex glass melts. For potential students of this domain, let us note that the fluorides are aggressive chemically attacking crucibles made of alumina, platinum, or nickel. Examination showed that annealing of glass by stopping the cooling around 560 °C is critical for thermal stress control. Addition of CaF_2 introduce an exothermal peak at 670 °C in the DTA curves of float glass + CaF_2 mother glasses. XRD showed that this peak results from CaF_2 crystallization. One step thermal treatment at 670 °C/0.5 h generates a transparent material after ceramming of a float glass + 20CaF_2.The IR spectra of a float glass and the TGC derived from a mother glass made of 80% float + 20% CaF_2 are shown in Figure 4.105 together with two glass-ceramics doped with Er^{3+}.

From a practical point of view, the LaF_3 merits a special mention, because, despite being hexagonal (bad for scattering), such a crystal can accommodate many of the RE^+ fluorides of interest for lasing and other applications

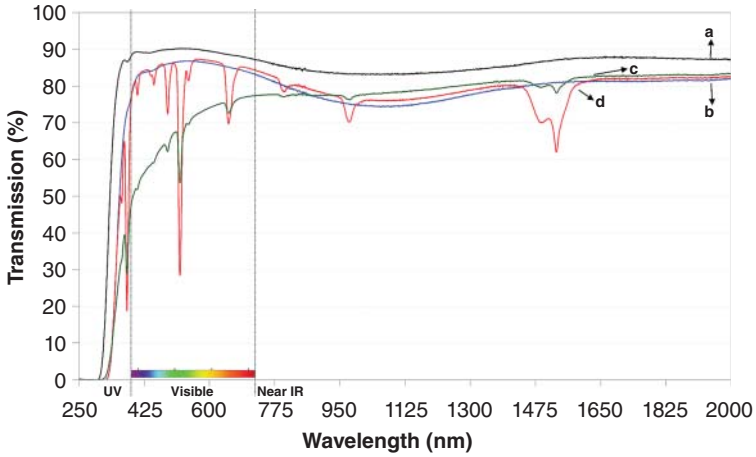

Figure 4.105 Transmission spectra of a float glass plate and that of doped and undoped glass-ceramics (CaF_2 is the precipitated nanocrystalline phase); specimen fabricated at ICSI, Haifa. (a) Transmission curve of undoped mother glass. (b) Spectrum of transparent glass-ceramic produced by ceramming at 680 °C/3 h. (c) Glass-ceramic doped with Er^{3+}. (d) Er^{3+} in the mother glass.

[D8, D9]. In Figure 4.106 the LaF_3 crystallites – obtained after 48 hours annealing at 650 °C – are illustrated. The ~20 nm crystallites are spaced at ~50 nm. Such a TGC has an $n_d = 1.672$.

An important finding was reported in a paper by F. Goutaland et al. [G35]. By the aid of RE^+ spectroscopy, they showed that even in the mother glass (in this case a composition of the SiO_2–Al_2O_3–Na_2O–LaF_3–AlF_3 system) phase separation of zones very rich in F^- occurs. RE^+ ions like Er^{3+} or Pr^{3+} tend to partition to the F^--rich regions. The level of partitioning depends on the radius of the dopant. Such glasses behave, in fluorescence tests, in a way similar to that of FOG glass-ceramics.

Practically, especially related to laser gain media fabrication, it is worth mentioning the fact that from FOG glass-ceramics, fiber-shaped parts can be also fabricated as exemplified by B. Samson et al. [S7]. The fluorescence spectrum and lasing frequencies of a Nd-doped FOG is shown in Figure 4.107a; the same information is given in the panel b., for the case of glass-ceramic.

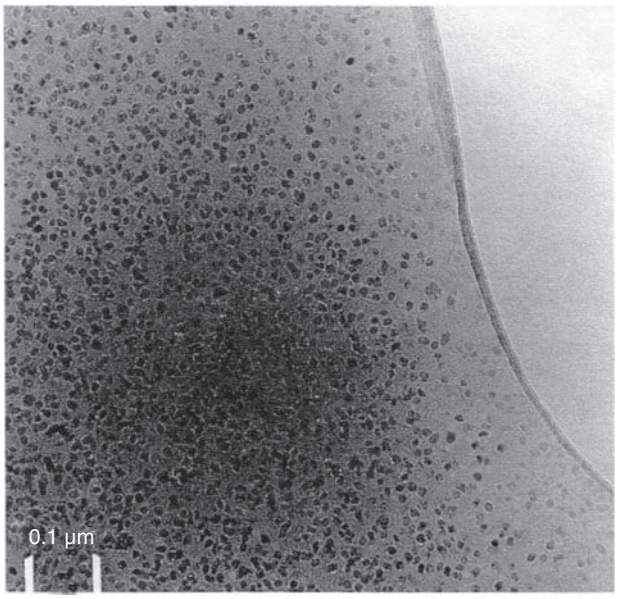

Figure 4.106 Imaging of the LaF_3 nanocrystallites developed in a FOG-type glass-ceramic after ceramming at 650 °C. Source: Dejneka 1998 [D8]. Reproduced with permission from Elsevier.

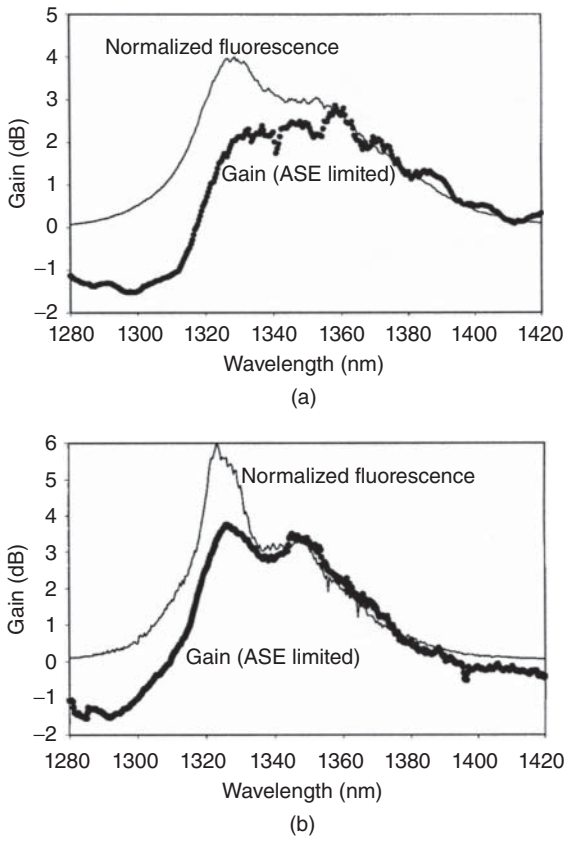

Figure 4.107 Fluorescence and lasing gain spectra of Nd^{3+}-doped FOG-type glass and glass-ceramic (ASE = amplified spontaneous emission). (a) Glass fiber. (b) Glass-ceramic fiber. Source: Samson et al. 2001 [S7]. Reproduced with permission from OSA.

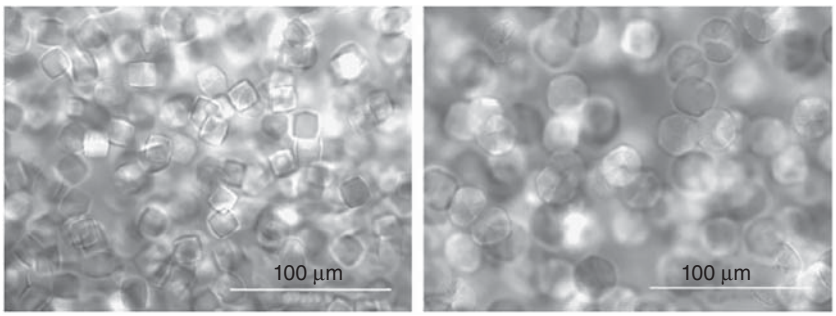

Figure 4.108 Effect of mother glass composition on the habitus of crystals precipitating, during ceramming, of glasses of the SiO_2–CaO–Na_2O system. Source: Berthier et al. 2008 [B31]. Reproduced with permission from Elsevier.

4.2.11.6 Transparent Glass-Ceramics Including Very High Crystalline Phase Concentration

4.2.11.6.1 Materials of Extreme Hardness (Al2O3–La2O3, ZrO2)

Using flame ($H_2 + O_2$) spray melting, glasses could be obtained from compositions lacking conventional glass former oxides. For instance, glassy beads (75–100 µm) were obtained from compositions of the Al_2O_3–La_2O_3 or Al_2O_3–La_2O_3–ZrO_2 in which Al_2O_3 amounts of 75–80% were present. Such beads can be densified, by viscous sintering, to dense transparent pieces. They also can be fully crystallized (1000 to ~1300 °C ceramming range). Owing to the high viscosity of these systems, in the temperature range between the $t_g{}^0$ and the melting point, the crystals resulting maintain a low size, despite the not so low ceramming temperatures. As a result the ceramics, thus fabricated, retain noticeable transparency levels (~40% in the VIS ($t = 2$ mm)). Phases like $LaAlO_3$, $LaAl_{11}O_{18}$, or $La_3Al_5O_{12}$ develop and produce hardness values of up to 18 GPa [R30]. A specific very interesting structural effect, seen in such systems, stems from the nanometric crystal size coupled with the full crystallization. The directly connected nanocrystals show hardness values larger than standard when present as larger units in conventional ceramic ($HV < 14$ GPa). The interface characteristics seem to dominate, at the nanoscale, over the bulk lattice features. This behavior was analyzed by S. Yip [Y14].

4.2.11.6.2 TGCs of High Crystallinity Including Na_3Ca Silicates

Transparency can be achieved in glass-ceramics also by keeping $n_g \approx n_C$ – as exemplified above for certain βQ_{ss}-based materials. Further developments of this type of TGC – where the processing and composition were selected so as to allow a convergent evolution of the refraction indexes of crystal and residual glass – allowed the obtainment of materials with a fraction of crystalline phases of up to 97% and 5 µm size crystals [B31]. Of course such a course of events is not ubiquitous and does not necessarily happen in the most useful compositional systems. As an illustration for the $n_C \approx n_g$ approach to TGC production, the examination of the SiO_2–CaO–Na_2O system is, however, instructive; the commercial soda lime (SCS)-type glasses are based on basic compositions located in this system. The compositions selected for the study were close to the join $Na_2Ca_2Si_3O_9$–$Na_2Ca_2Si_4O_{11}$. The crystals precipitated were solid solutions of the $Na_{4+2x}{\cdot}Ca_{4-x}[Si_6O_{18}]$ ($0 \le x \le 1$) type. They are based on hexagonal lattices similar to that of $Na_2Ca_2Si_3O_9$. The variation of "x" requires substitution of $1Ca^{2+}$ by $2Na^+$. Interestingly the crystals habitus is cubical or spheroidal, as a function of the mother glass composition, like shown in Figure 4.108 [B31].

The cubes favor higher transmission because the transmittance depends, among other factors, on the area of the interface between crystals and glass. In Figure 4.109 the dependence of this area, together with that of the transmittance, on the volume fraction of crystalline phase (α) is shown.

As it can be seen, the drastic reduction of the area, at α values >0.9, significantly enhances transmission. The refraction index of the various phases involved differs only slightly with $\Delta n = 0.015$. The birefringence of the

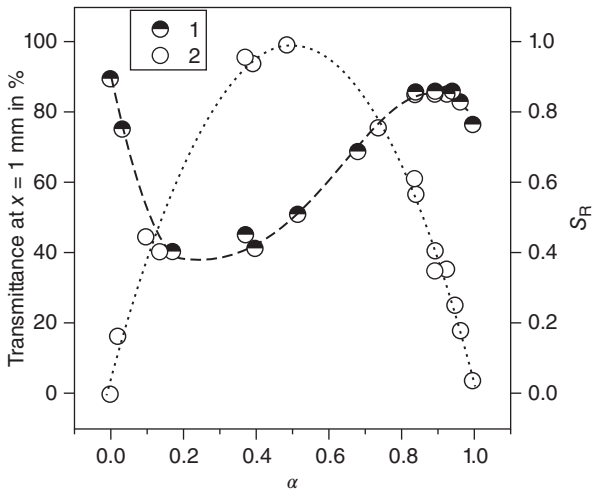

Figure 4.109 Dependence of transmittance of glass-ceramics and glass/crystal interface area on the volume fraction of crystalline phase (α). (a) Interface area. (b) Transmittance. Source: Berthier et al. 2008 [B31]. Reproduced with permission from Elsevier.

hexagonal crystals is also very low. The nucleation stage depletes the residual glass in Na^+. This effect contributes to the reduction of the Δn between glass and crystal, as the crystallization progresses, to values much smaller than if the composition of glass and crystal remains identical.

The spectroscopic quality factor of some of the Nd^{3+} containing TGCs – as described by the Ω_4/Ω_6 ratio (the Ωs are the Judd–Ofelt parameters) – is better than that calculated for Nd:YAG crystals. This indicates strong fluorescence of the emission relevant for laser apps.

4.2.11.6.3 Materials for Scintillators

Interesting results were obtained also by M. Allix et al. working with glasses of the refractory $BaO–Al_2O_3$ and $SrO–Al_2O_3$ systems [A9]. Of course besides the high melting points of most compositions in the system, such glasses are not easy to prepare also because alumina is only a conditional glass former, requiring very high cooling rates if the melting approach is used. These authors brought the melts to around 2000 °C by laser melting of an aero-levitated alumina and $BaCO_3$ powders spherical batch; cooling a small batch (a few grams), from such a high temperature, provides the needed fast cooling rate. In Figure 4.110a [A8], a glass disc and two cerammed (950 and 1100 °C) specimens (full crystallization to α- and β-Ba Al_4O_7, respectively) are shown. Their transmission spectra appear in Figure 4.110b.

The crystals are not nanometric and the lattices are not cubic. The remarkable transparency of the α-$BaAl_4O_7$ is ensured by the absence of pores coupled with a very slight birefringence (~0.01). Doping with Eu^{2+} makes such parts to scintillate under X-ray bombardment. An innovative improvement in this context, viz. further reduction of small birefringency by introduction of chemical disorder, was devised. For instance, working in the $SiO_2–SrO–Al_2O_3$ system (SiO_2 helps vitrification), new disordered phases were achieved, by appropriate chemical adjustment, within the $SrAl_2Si_2O_8–SrAl_2O_4$ segment. The transmission spectrum of such a specimen together with a STEM-HAADF image of a grain boundary (shows thinness of it) are given in Figure 4.111.

4.2.11.7 Pyroelectric and Ferroelectric Transparent Glass-Ceramics

A few years after the emerging of the glass-ceramics, efforts started to develop materials including crystalline phases able to confer pyro, ferro, and piezoelectric [D4] properties. An extensive review of the early work is given by A. Halliyal et al. [H4]. The focus was not

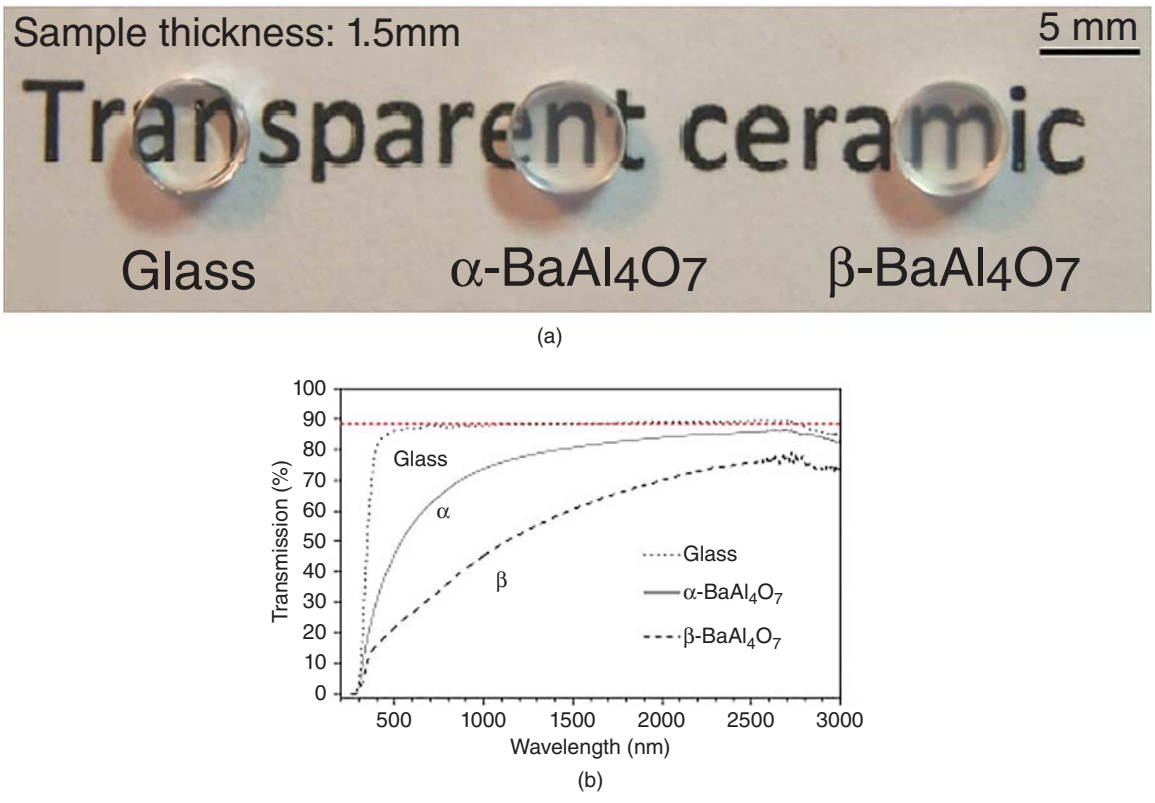

Figure 4.110 Imaging and transmission spectra of transparent ceramics fabricated by full crystallization of glasses of the system $BaO–Al_2O_3$. Source: Courtesy of Allix M.

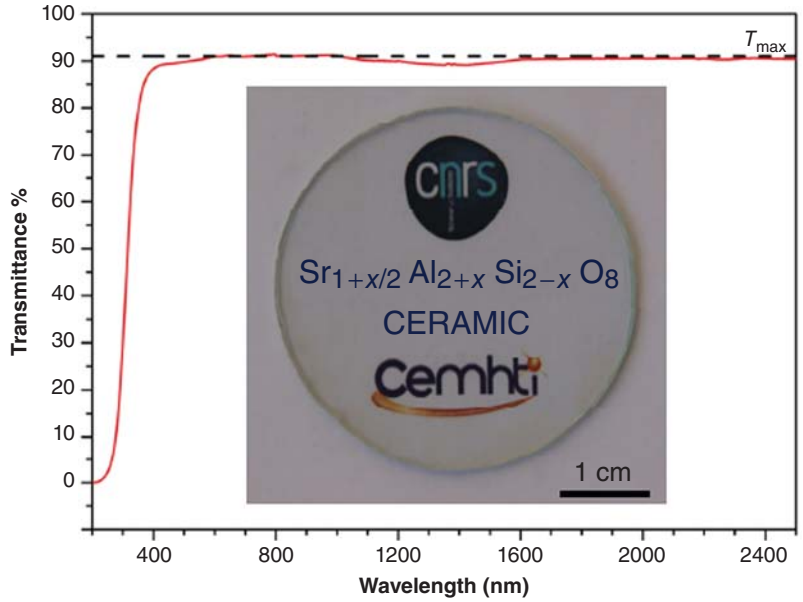

(a)

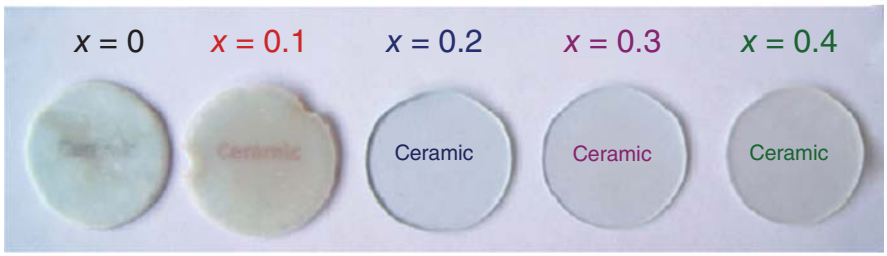

(b)

Figure 4.111 Imaging of ceramics, produced by full ceramming of glasses having compositions located in the $SrO–Al_2O_3–SiO_2$ system, as a function of the Si molar fraction "*x*." (a) Image and transmission spectrum of the most transparent part. (b) The visual aspect of the ceramics as a function of the value of "*x*." Source: Courtesy of Allix M.

on transparency. The early work devised a method based on the use of vertical thermal gradients for the production of textured materials with strong crystallization at the surface [G3]. Among the first transparent ferro-glass-ceramic S (T,F-GC) materials were those based on $BaTiO_3$ and $Na_{1-x}K_xNbO_3$ crystals, developed by N.F. Borelli and M.M. Layton [B38]. The pure ferroelectrics could not be obtained in amorphous state but addition of relatively low amounts of glass forming oxides allowed fabrication of well-fined mother glasses. Their ceramming produced glass-ceramics containing up to 70 vol% crystalline phases. It was measured that as long as the $\overline{GS}$ was lower than 0.2 µm, scattering (low refraction index value difference between residual glass and crystalline fraction) was low enough to permit the obtaining of reasonable levels of transparency; high transparency required crystals with $\overline{GS} < 0.1$ µm. In Figure 4.112 [B39], the optical density spectrum is given for materials with different of $BaTiO_3$ crystallite size.

Now, it is known that under a certain size, owing to stress relaxation, $BaTiO_3$ crystals (even in ceramic parts) lose their domains and thus cease to behave like ferroelectrics [M39]. This phenomenon was observed by Borelli and Layton, also in the case of glass-ceramics. They established that good ferroelectric behavior requires $GS > 0.2$ µm. It results that transparency and ferroelectric behavior coexist within a limited range of *GS*. In Figure 4.113 [B39], the $\varepsilon_r = f(t°)$ of T-GC based on $NaNbO_3$ is shown.

The profile of the curves suggests the presence of a Curie point (T_C), i.e. ferroelectric behavior. The first stage of crystallization leads to a dendritic habitus and size small enough to prevent ferro behavior. Further heat treatments cause spherulite formation and concomitant with this ferroelectric behavior is measured. These glass-ceramics also exhibit electro-optic properties in the form of Kerr effect. In Figure 4.114 optical hysteresis loops of a $Na_{0.4}K_{0.6}NbO_3$-based glass-ceramic are compared as a function of the *GS*.

In the case of $GS = 0.05$ µm, there is almost no hysteresis and the remnant polarization P_R is zero. In the case of 0.2 µm (where transparency is still reasonably high), the hysteresis curve (indicating indirectly ferroelectric properties) is less anemic and a P_R of up to

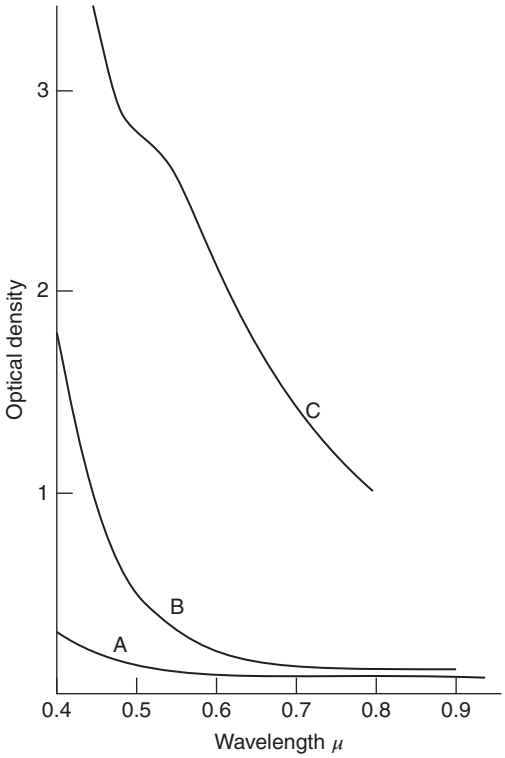

Figure 4.112 Transmission spectrum ($t = 0.9$ mm) of transparent ferroelectric glass-ceramic plates ($BaTiO_3$ crystalline phase); the curves correspond to various sizes of the crystallites. (A) Mother glass. (B) Crystals of 50 nm. (C) Crystals of 200 nm. Source: Borelli and Layton 1971 [B39]. Reproduced with permission from Elsevier.

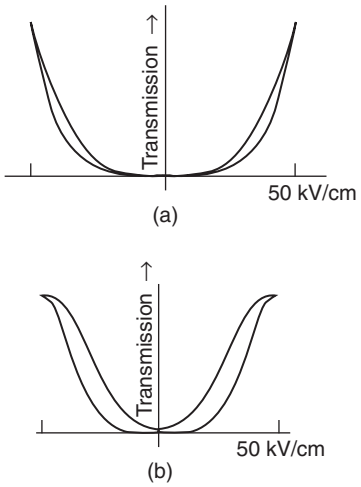

Figure 4.114 Hysteresis loops (the polarization vs. field strength curve) as a function of grain size in the case of glass-ceramics based on Na, K niobate crystals. (a) $GS = 0.05$ μm. (b) $GS = 0.2$ μm Source: Borelli and Layton 1971 [B39]. Reproduced with permission from Elsevier.

0.2 μC/cm^2 (quite low) could be measured. In most cases it was necessary to start with compositions including a glass former like SiO_2, B_2O_3, P_2O_5, TeO_2, or GeO_2 or a chalcogenide system. A relatively large number of crystals exhibiting nonlinear optical behavior could be grown in these mother glasses. Among them one may cite $BaTiO_3$, Li, Na, K, Sr, Ba, niobates, $LiTaO_3$, $Ba_2TiSi_2O_7$, $K_2Nb_3Si_2O_{13}$ [T10], $KTiOPO_4$, $Bi_4Ti_3O_{12}$,

Figure 4.113 Variation of the dielectric constant, as a function of temperature, for the case of glass-ceramics based on $NaNbO_3$ (Curie points are present on the curves representing well-crystalized materials = ferroelectric behavior). Source: Borelli and Layton 1971 [B38]. Reproduced with permission from Elsevier.

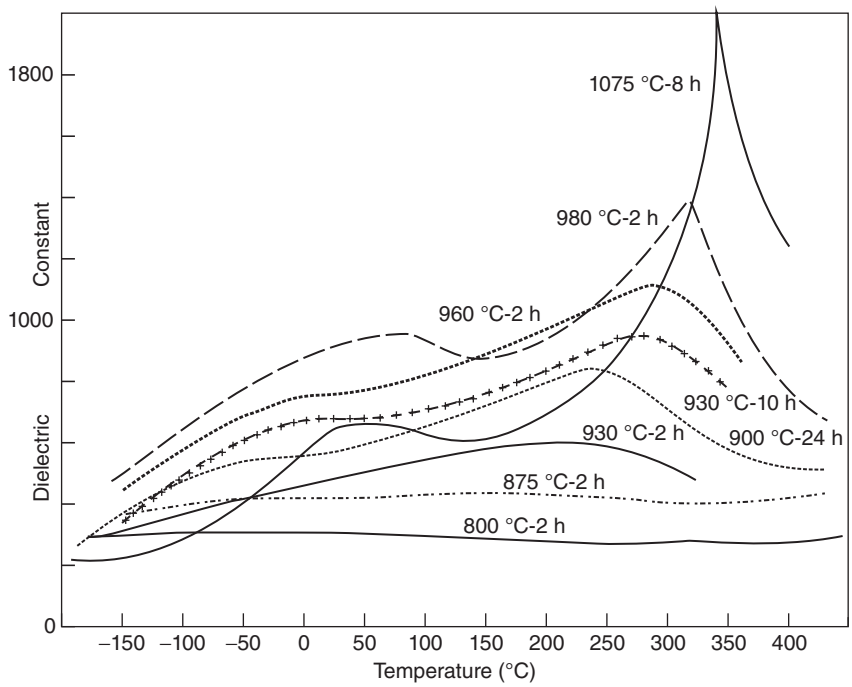

β-BaB_2O_3, $K[Nb_{1/3}Te_{2/3}]O_{4.8}$, Bi_2GeO_5, $K_{3.8}Nb_5Ge_3O_{20.4}$, β-GeS_2, or $Ge_{23}Sb_{11}S_{65}Cd$. The glasses involved vary as to their chemical stability and nonoptical properties. The nonlinear effects intensity also varies significantly with the nature, amount, and structure of the noncentrosymmetric phases produced by the ceramming stage; the behavior of some of the crystals, when embedded in the glassy matrix, is different from that in "free" state. Thus the practical value of these materials varies drastically. However, even those of less practical significance are contributing to the effort to better understand the rules that govern the behavior of these quite peculiar materials. For instance, it was observed that in many of the glassy hosts, the first stage of crystallization – which in all glasses occurs at the macro surface – forms a thin layer of highly oriented crystal, while in the deeper layers the orientation is quite random. Ultrasonic treatments seemed able to influence, to a certain extent, the degree of orientation in the surface layer. Below some of the most interesting results obtained are briefly presented. T,F-GCs based on $Sr_xBa_{1-x}Nb_2O_6$ (SBN) 40 nm crystallites (tetragonal tungsten bronze [TTB] lattice; $x \in [0.25–0.75]$) have also been prepared; such ferroelectric crystals exhibit large EO coefficients [Y4]. Mother glass compositions located in the $SiO–BaO–B_2O_3–Nb_2O_5$ system were used. Such glasses have a t_g at ~600 °C, high density (~4.25 g/cm^3), and refraction index ($n \approx 1.96$). In Figure 4.115b the rod-like crystallites formed, during ceramming at 628 °C/10 h of a 19.5SrO, 12.5BaO, $32Nb_2O_5$, and $36B_2O_3$ glass, are

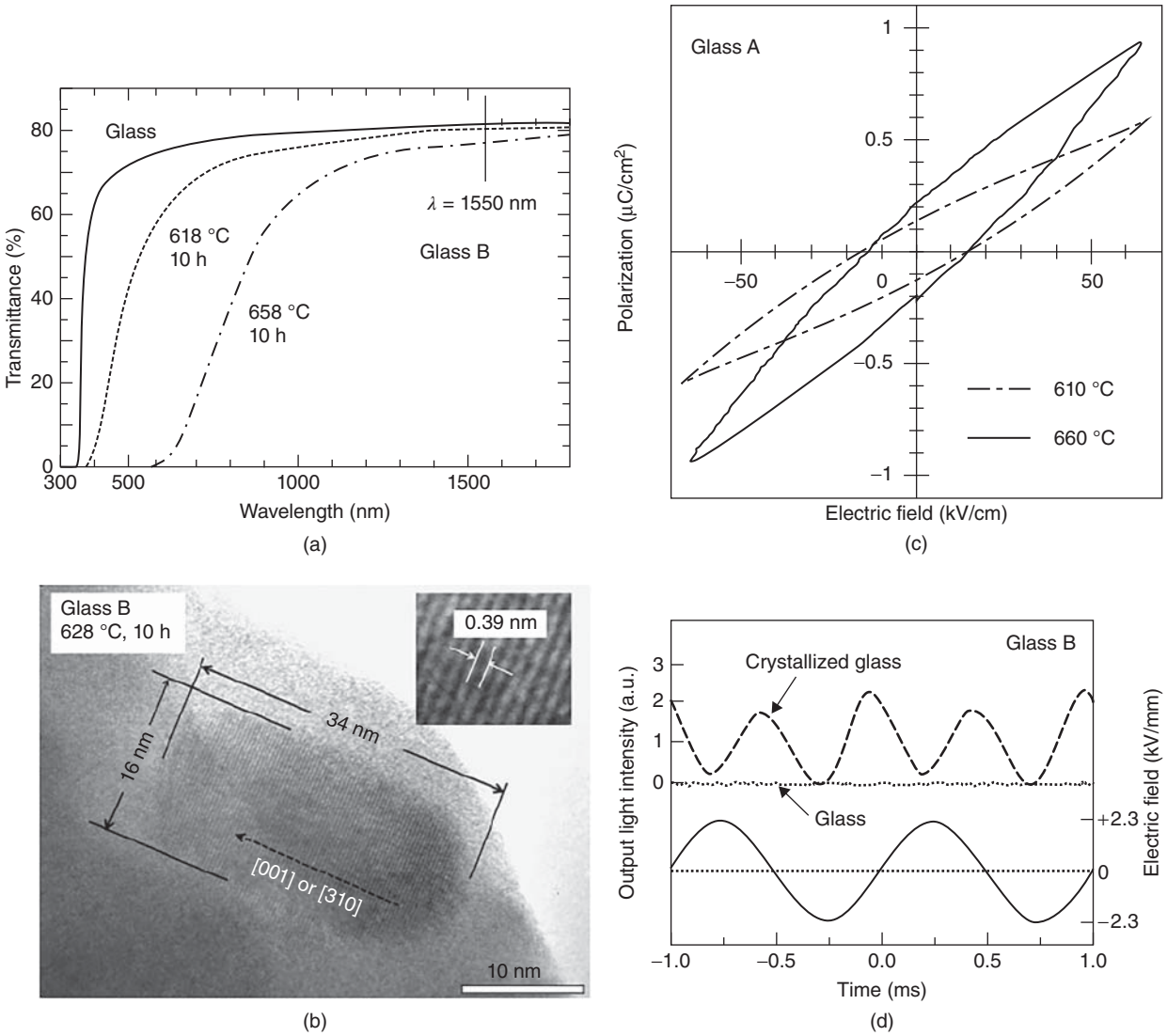

Figure 4.115 Characteristics of mother glass and transparent ferroelectric glass-ceramics (based on Sr,Ba niobate crystals). (a) Transmission spectra. (b) Ellipsoidal crystallite (HRSEM). (c) Hysteresis loops as a function of ceramming conditions. (d) Optical phase modulation curve (demonstrates EO abilities). Source: Yamazawa et al. 2009 [Y4]. Reproduced with permission from John Wiley & Sons.

shown; the long axis of the ellipsoidal crystallites is along the [001] or [310] directions.

The noticeable transparency in the VIS domain and that quite high in the NIR, kept after ceramming, are illustrated by Figure 4.115a. The ferroelectric nature of the crystalline phase ($\varepsilon_r = 66$) is demonstrated clearly by the profile of the P–E curve in Figure 4.115c. The electro-optic abilities are demonstrated in the form of an optical phase modulation curve in Figure 4.115d ($E = 2.3$ kV/mm). $LiNbO_3$ was precipitated from matrices including TeO_2 as a glass former (e.g. $50TeO_2{\cdot}50LiNbO_3$ [K33]). In such systems, oriented crystalline surface layers could be obtained. Testing with a Nd^{3+} laser (1064 nm) revealed ability for second harmonics generation. The TeO_2-based glasses exhibit refractive index values in the 2.20–2.30 range, which match well that of certain ferroelectric niobates. In such a way the scattering produced by the crystals is reduced and their size can be increased without reducing too much transparency; for instance, $K_3Li_2Nb_5O_{15}$ crystals of 10–20 μm ($n = 2.27$) do not prevent transparency of the T-GC [J7]. The TeO_2-based glasses have low melting points and good transmission in the IR domain, as shown in Figure 4.116 [A3].

An interesting matrix effect on the precipitated crystals was reported for mother glasses in the K_2O–Nb_2O_5–TeO_2 system. For instance, the $K[Nb_{1/3}Te_{2/3}]O_{4.8}$ phase results after ceramming from a $15K_2O15Nb_2O_570TeO_2$ host. Such crystals have a cubic (fluorite-type) lattice. The difference in thermal expansion between the matrix and crystals strains the crystals so that the lattice is slightly distorted. As a result the symmetry center disappears and electro-optic effects became possible. In

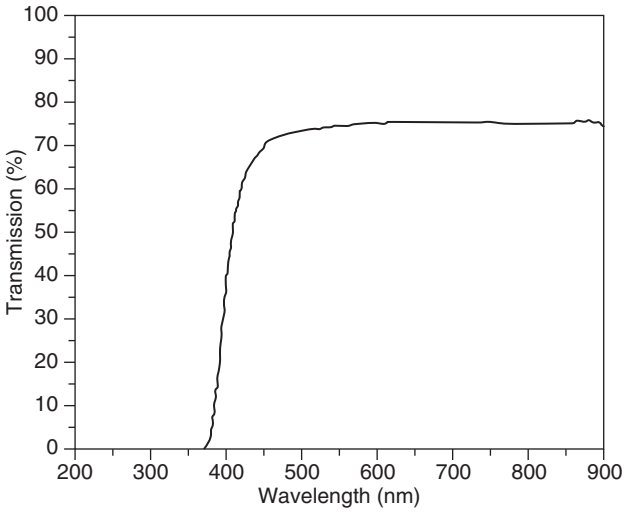

Figure 4.116 Transmission spectrum of TeO_2-based glass. Source: Ahamad et al. 2009 [A3]. Reproduced with permission from Elsevier.

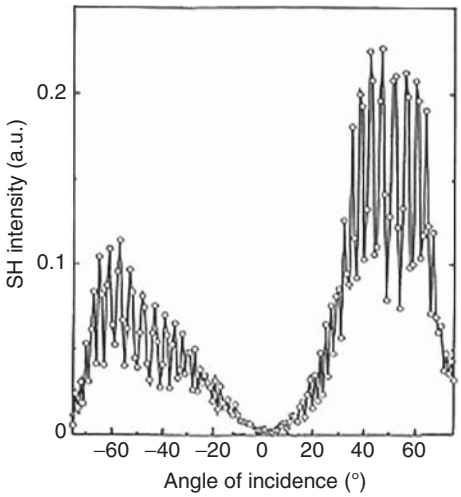

Figure 4.117 Second harmonic signal generated by stress, induced by expansion coefficient mismatch between residual glass and crystalline phase (stress distorts lattice and thus creates symmetry consistent with ferroelectric behavior), in the case of a transparent glass-ceramic derived from a tellurite base glass. Source: Jeong et al. 2007 [J7]. Reproduced with permission from Hanyang University Press.

Figure 4.117 [J7], the second harmonic generation (SHG) effect thus produced is shown.

A similar effect worked on the $K_3Li_2Nb_5O_{15}$ previously mentioned. The ability for SHG, based on the ferroelectric state of the crystals, while drastically reduced, did not disappear immediately over the T_C, as happens to the crystals not in glass [A3]. The TGCs discussed above comprised mother glasses based on the presence of at least one glass former oxide. As a result the electro-optic effects owed to the precipitated crystals were dampened. In the case of fresnoite ($Ba_2TiSi_2O_6$; a ferro and piezocrystal with strong electro-optic properties), it was possible to obtain glass having the oxide composition of the compound itself [T6]; because it is a silicate involved, such a glass is chemically stable. Ceramming in the 710–750 °C produced quite transparent glass-ceramics. Second harmonic generation was demonstrated with a Nd^{3+} laser's strongest emission (1.06 μm) at 532 nm; the intensity of the signal reached up 1% of that of the α-quartz single crystal. Shinozaki has studied the fresnoite crystallization and observed surface crystallization as a first stage of the ceramming process; the crystals formed in the bulk had an ellipsoidal morphology. It was found out also that specimens prepared under reductive conditions (7% H_2 for 93 hours) had a more intense surface crystallization and stronger SHG signals. Another case in which it was possible to prepare glass ($25La_2O_3{\cdot}25B_2O_3{\cdot}50GeO_2$) without a glass former was $LaBGeO_5$. As single crystal (stillwellite structure), it is ferroelectric and shows EO activity. Nd^{3+}:$LaBGeO_5$

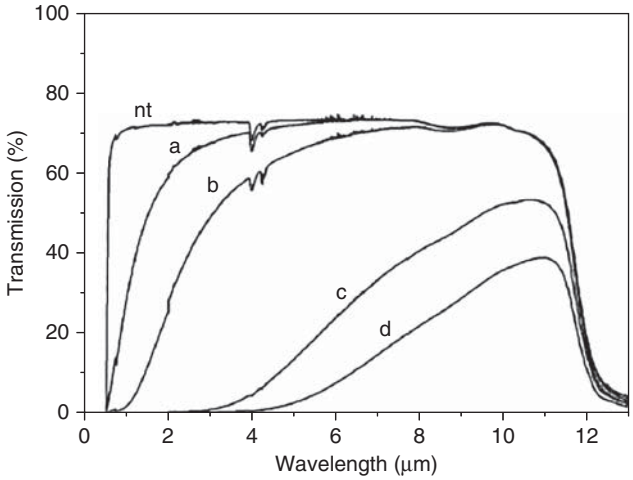

Figure 4.118 Transparent (IR range) glass-ceramic based on a chalcogenide mother glass (Ge-B-S–Cd system). Source: Guignard et al. 2007 [G49]. Reproduced with permission from Elsevier.

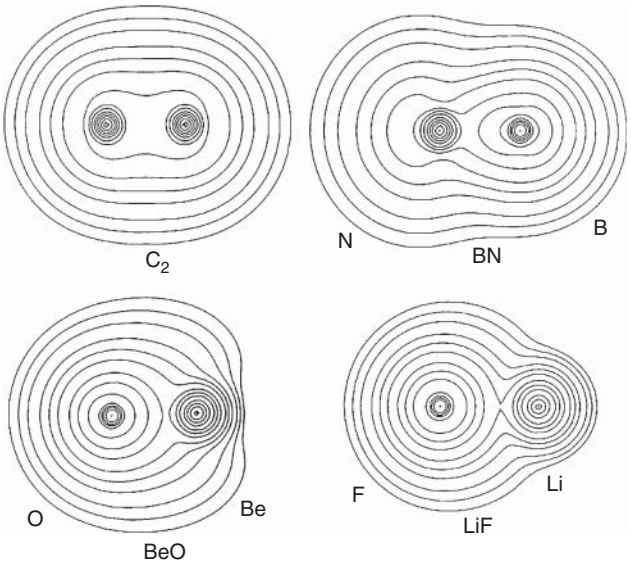

Figure 4.119 Electron density spatial distribution in chemical bonds connecting atoms in pairs with various levels of electronegativity difference. C2 = atoms of identical electronegativity (pure covalent bond). BN = slight difference of electronegativity (predominantly covalent bond). BeO = significant difference of electronegativity between atoms (partly ionic bond). LiF = significant difference of electronegativity (strongly ionic bond).

crystals could be pumped so as to emit in the green region (frequency doubling). Transparent glass-ceramics in which only surface crystallization (up to a thickness of 60 μm) or one involving also the bulk were obtained. The T_C (530 °C) is under the t_g (670 °C) and therefore the matrix strains the spherulitic crystals.

In the non-oxide chalcogenide glasses like those derived from the Ge–Sb–S system, crystals like β-GeS_2 could be precipitated [G49]. Introducing also Cd led to the formation of $Ge_{23}Sb_{11}S_{6.5}Cd$ crystals in glass-ceramics showing significant transparency in the IR (see Figure 4.118) despite the large size of the crystals (1–6 μm); the crystals are quite far away one from another.

4.2.12 Cubic Boron Nitride

The material has a structure similar to that of diamond and the covalency degree – while different from that of the C—C bond – is still high (charge displaced heavily toward N; see Figure 4.119).

As opposed to the hexagonal boron nitride (h-BN), which is structurally related to graphite (finds application as high temperature lubricant), the cubic (c-BN) variety exhibits (as the lattice pattern and nature of chemical bonding suggest) very high hardness, even in its polycrystalline form (~45 GPa); it finds application in the domain of abrasives.

Recently a production procedure was perfected [T20] by which small slabs of c-BN, exhibiting nanograins (~5 nm) and transparency, can be produced. In Figure 4.120 the photo of such a part ($t < 1$ mm) is shown.

The parts were derived from a special powder in which the particles have an onion-like nested structure (see Figure 4.120) where the BN layers are puckered and include many plane stacking faults. This raw material was hot pressed at 1600 °C under 15 GPa. The fine microstructure (Hall–Petch relationship) allowed increase of hardness to the ~100 GPa level (close to that of diamond) and of the K_{IC} to the impressive (for brittle ceramics) level of ~12 MPa $m^{0.5}$. The combination of translucency with such extreme mechanical properties makes the material likely to be useful in exotic applications if a viable technology, allowing fabrication of industrially relevant (not necessarily very large ones) parts can be derived from the method proposed by Tian.

4.2.13 Ultrahard Transparent Polycrystalline Diamond Parts

4.2.13.1 Structure

Diamond is a valuable optical material because it combines transparency in a wide range with exceptional mechanical and thermal properties and chemical stability. Optical windows for the IR range, lenses, and components of lasing systems are among the main potential applications. The applications are a result of its excellent properties; for instance, for IR domes, among other things, it offers very high resistance to rain erosion [S26]. Natural single-crystal gems, mostly used for their

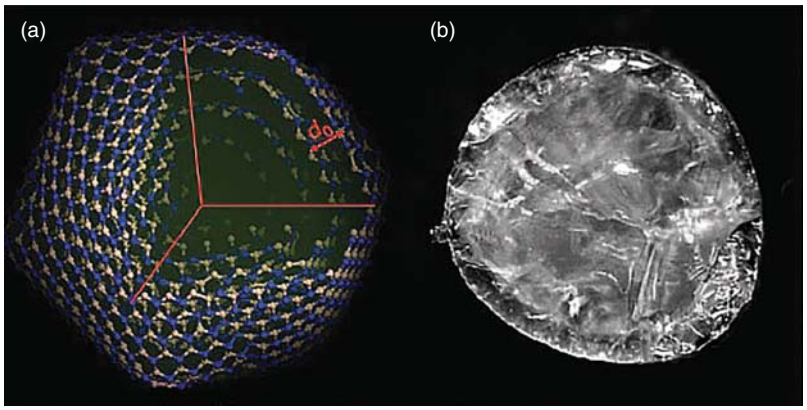

Figure 4.120 Imaging (b-panel) and lattice model of five shell basic particle (c-panel) of cubic polycrystalline (5 nm crystallites) transparent ($t = 1$ mm) BN piece. Source: Tian et al. 2013 [T20]. Reproduced with permission from Springer Nature.

esthetic value, are, on a very small scale, used also for the applications mentioned above. Here parts made of polycrystalline (viz. ceramic), man-made, diamond are presented.

Diamond is one of the polymorphs of solid carbon. Therefore before its presentation, it is necessary to say a few words about this element ($Z = 6$; C).The electronic configuration of carbon is $1s^2 2s^2 2p^2$, being able to engage in up to four bonds with neighboring atoms. In solid pure carbon, the lattices include, of course, only C atoms. In such a situation, the bonding is massively covalent owing to the identical electronegativity of the charge devoid atoms. Grosso modo, examination of the existing carbon polymorphs indicates – as far as the stereochemistry of these atoms is concerned – that two coordination patterns occur. In one, each carbon is bonded covalently (strong bonding) to other three atoms located at the vertices of a triangle; for such a pattern the atoms have to assume, of course, an sp^2 hybridization; the triangle (linked in hexagonal cycles) based layers (graphenes) are bonded by much weaker van der Waals forces. Such a lattice is encountered in graphite (space group #194 D^4_{6h} [$P6_3/m2/m2/c$]), the polymorph stable under standard conditions. A much compact atoms packing is possible (it occurs under adequate temperature and pressure conditions) if the carbon atom assumes an sp^3 hybridization and covalently bonds to four neighbors; a polymorph in which such a cubic lattice (space group $Fd\bar{3}m$) exists is diamond. A simplified phase diagram is given in Figure 4.121 [H15]; it allows one to see that diamond exists at high pressures and temperature. A fraction of diamond lattice is shown in Figure 4.122.

At *RT* it is metastable, of course, but the rate of its graphitization is practically negligible (like that of a window glass crystallization). At 2100 °C, however, 0.2 g of diamond revert to a graphite lattice each minute. The number spatial density of atoms, at $N = 1.76 \times 10^{23}$ atoms/cm^3, is the largest known for any material. At high pressure and temperature graphite may transform also in a "hexagonal diamond" (lonsdaleite), as it happens

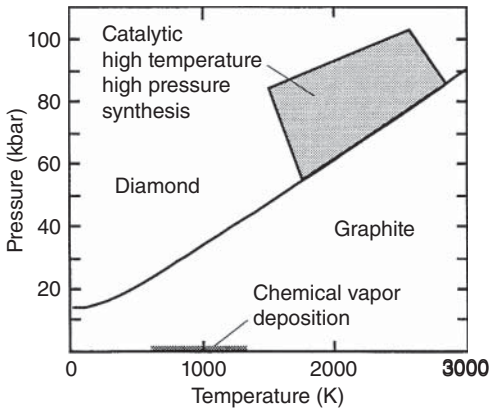

Figure 4.121 Phase diagram of carbon showing a region of stability of diamond; domain used for synthetic diamond fabrication is shaded. Source: Harris 1999 [H15]. Reproduced with permission from SPIE Publishing.

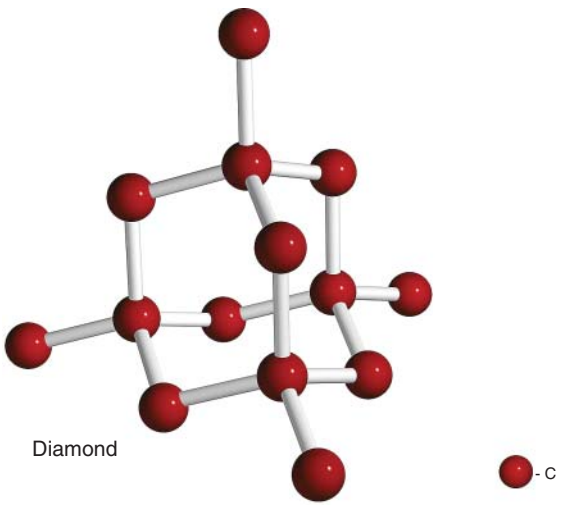

Figure 4.122 Bonding scheme and atom coordination pattern in diamond lattice. Source: Reproduced from Shutterstock Images with purchased permission.

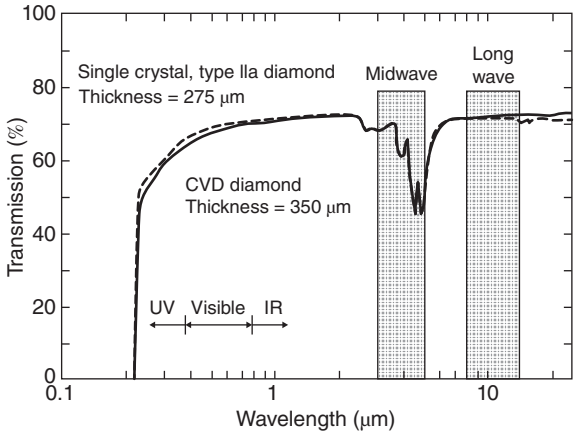

Figure 4.123 Transmission of diamond thin plates; CVD bulk diamond and type IIa natural diamond are compared (note the very wide spectral range of transparency). Source: Hartnett et al. 1984 [H13]. Reproduced with permission from SPIE Publishing.

when a graphite-carrying meteorite impacts the surface of the Earth. (In fact, it usually has a cubic lattice with a large number of defects leading to hexagonal stacking sequences present along cubic ones.) It is only translucent in the VIS, showing yellow-brownish hues. Diamond, on the other hand, shows quite high transmission (tempered by the high value of the refraction index; $n \cong 2.43$ in VIS), as Figure 4.123 [H15] suggests, in a wide portion of the EMR spectrum.

It is customary to classify natural diamond based on the amount of nitrogen it carries in four varieties:

Ia: (98% of natural diamond) has 0.1% N_2, strong UV absorption.
Ib: 0.2% N_2, yellowish.
IIa: Traces of N_2, colorless, highly transmissive over 225 nm.
IIb: Traces of N_2 but also traces of B; blue, showing p-type semiconduction ($\sigma = 10$–100 S/m).

Of course type IIa is the most useful for optical purposes, especially in the IR; nitrogen absorption bands strongly reduce transmission in the $\lambda = 7.5$–25 μm range, while B generates sharp bands at $\lambda = 3.58$ and 4.07 μm, supplemented by some weak absorption also in the 8–15 μm domain.

4.2.13.2 Fabrication

One of the coatings procedures, adopted in the eighties for bulk ($t \geq 1$ mm) diamond fabrication, is the CVD (see Section 3.1.3) [C6, M37]. Typical temperatures are ~950 °C and 0.2 bar. The process takes place in conditions where the thermodynamically stable phase is graphite (see Figure 4.124). The growth process is accomplished in a variety of reactor types, which may

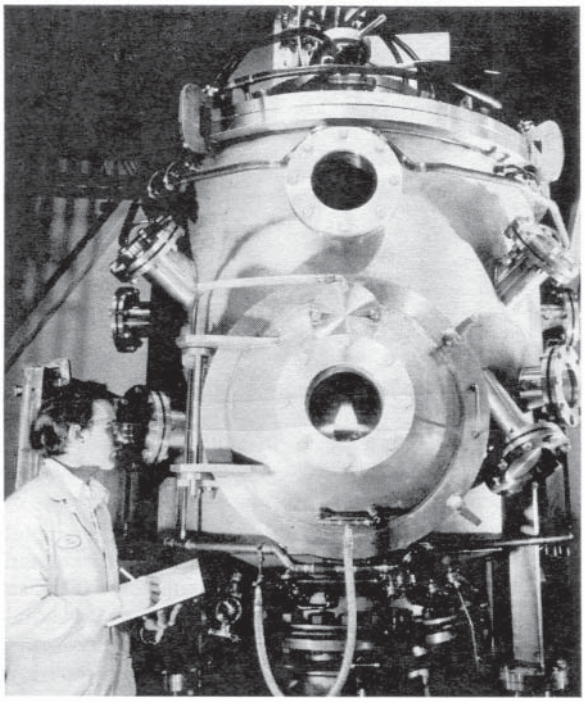

Figure 4.124 Industrial scale dc arc jet-type diamond deposition reactor in which plasma volume distribution pattern is controlled by the aid of a magnetic field (Norton Industries). Source: Hartnett et al. 1984 [H13]. Reproduced with permission from SPIE Publishing.

be based on MW, dc, or acetylene torch or hot filament (tungsten)-generated plasma; in Figure 4.124, a dc arc jet-based system is shown. Polycrystalline material, as illustrated in Figure 4.125, results.

The presence of hydrogen atoms in the reactor is essential to stabilize the diamond relative to graphite, because the reactors work in a pressure zone where, for pure materials, graphite is the stable phase. A typical gas mixture is 99 vol% H_2 and 1 CH_4 with some Ar, O_2 or N_2 (ppms). Silicon and Mo are the most common substrates, but fused silica or sapphire were also used. Diamond crystallites nucleate at the surface of the substrates and layers of 1 mm over a surface of 100 cm^2 can be grown at rates of 0.1–10 μm/h.

Another technique usable is the high-temperature high-pressure (HPHT) method in which graphite (without metal binder) is subjected to enormous pressure (15–25 GPa) at 2100–2500 °C. In such conditions multiple spontaneous nucleation is facilitated and nanocrystalline (10–30 nm granular crystals) transparent diamond is produced [I13]. The hardness of such plates may obtain 140 GPa and cylinders 10 mm in height and diameter can be obtained; the parts exhibit a specific yellowish tint. Polishing is done by laser surface melting.

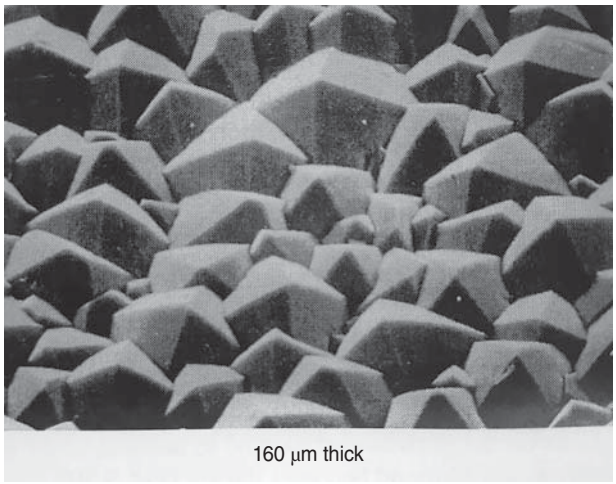

Figure 4.125 Imaging of the as-deposited surface of polycrystalline diamond layer ($t = 1$ mm) produced by the aid of the machine depicted in the previous figure. Source: Hartnett et al. 1984 [H13]. Reproduced with permission from SPIE Publishing.

4.2.13.3 Properties

As said above, the nonoptical properties of diamond are exceptional. Table 4.19 lists some with a significant influence on the applications potential range open to this transparent material.

4.2.14 Galium Phosphide (GaP)

Gallium phosphide is an interesting optical material [V1]. It has a cubic lattice (ZnS lattice; S.G. #216 $T_d^2(F\bar{4}3m)$ with semiconducting abilities ($E_g = 2.26$ eV) and a wide window of transparency (0.6–11 μm). Some of the important properties are given in Table 4.20.

The transmission spectrum of GaP is given in Figure 4.126 [V1] where it is compared with other IR transmitting materials.

Table 4.19 Diamond properties.

Property (unit)	Value
Long wave IR cutoff	None
HV (GPa)	90
TRS (MPa)	200
E (GPa)	1150
ν (Poisson coefficients)	0.07
α (ppm/K)	0.8
λ_{th} (W/(m K))	2000
R' (kW/m)	410
ε_r (1 GHz)	5.7
tan δ	$<4\times10^{-4}$
n	2.42 (at 600 nm)

Table 4.20 Properties of GaP.

Property (unit)	Value
Density (g/cm^3)	4.14
*HK*0.2 (GPa)	8.5
TRS (MPa)	100
K_{IC} (MPa m$^{0.5}$)	0.9
n (1.4 μm)	3.16
λ_{th} (W/(m K))	110
Verdet constant (rad/(m T)) at 633 nm	160

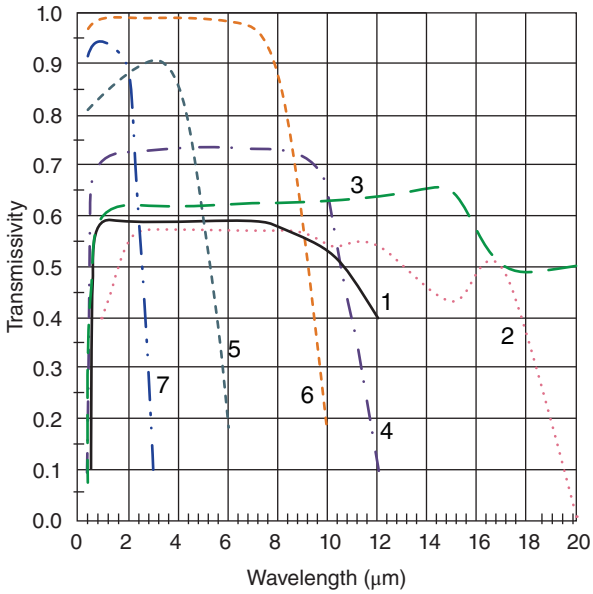

Figure 4.126 Comparison of GaP transmission spectrum with those of competitor IR transmitting materials. Source: Courtesy of Vaclavik J [V1].

GaP has applications both as coating and bulk parts. Bulk parts can be fabricated in the form of single crystals by the Czhoralski method (~900 °C) under 40 mm of Ar and a B_2O_3 layer to prevent phosphorous vaporization. The CVD method allows fabrication of both bulk plates and coatings. In Figure 4.127 [H15], a 1 mm thick piece of GaP, produced by CVD, is shown. The CVD produced parts are polycrystalline.

The coatings, for instance, on Ge, have various functionalities, like antireflections, electromagnetic shielding, or protection against erosion. Bulk parts in pure and doped (N, Zn) state are used for LEDS; white light is formed by using layers of different doping, which can emit green, yellow, and red light. The CVD materials can be used for IR windows and domes.

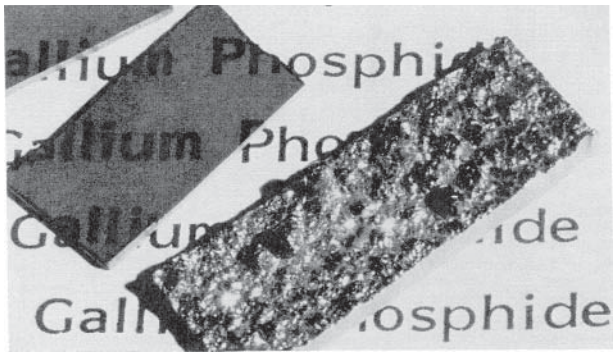

Figure 4.127 Bulk GaP plate produced by CVD; bottom piece is in as-deposited state, while the upper plate is shown after it underwent polishing. Source: Harris 1999 [H15]. Reproduced with permission from SPIE Publishing.

4.2.15 Transparent Silicon Carbide and Nitride and Aluminium Oxynitride

These materials are best known for their structural applications owing to their excellent mechanical, thermal properties, and high thermal shock resistance. In the case of SiC, the attractive structural properties are those of the nonisometric lattice-based impurities carrying, a set of polytypes. The β-polymorph of SiC, however, is cubic belonging to theSG#216 ($T_d^2 - F\bar{4}3m$) and $\mathbf{\Delta}E_g = 2.50$ eV, large enough to allow VIS transmission [G17, K16] around *RT* (at high temperatures over 500 °C, it is a semiconductor), thus eligible as a TC. When fabricated by CVD, from CH_3CCl_3 in the presence of excess H_2 and HCI (~1400 °C; [H15]), freestanding layers of high purity ($t \approx 0.3$ mm) can be produced; the spectral curve of such a part is illustrated in Figure 4.128; spectral data are also given in [L16]. As it may be seen such parts show remarkable transparency, making the material a good candidate for IR applications. In fact, artificial β-SiC has a limited use also as a gem when wafers of the quality shown in Figure 4.128 can be obtained.

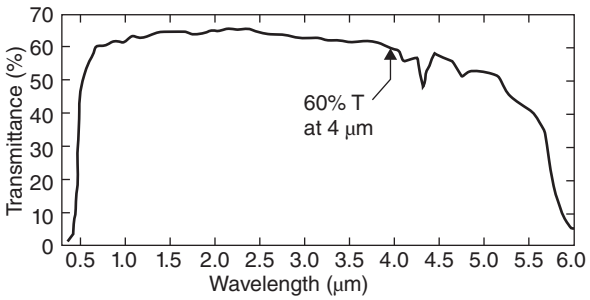

Figure 4.128 Transmission spectrum of thin cubic SiC freestanding, polycrystalline layer ($t = 0.3$ mm). Source: Harris 1999 [H15]. Reproduced with permission from SPIE Publishing.

Currently efforts are made to develop also a method based on powder sintering (PECS) for the production of transparent SiC [B20].

CVD freestanding thin layers of Si_3N_4 (from $SiCl_4$ and NH_3) have a significant transmission within the 3–5 μm IR window [T12]. As early as 1992, A. Pechenik et al. – using amorphous, nanoparticles (~15 nm) pressed at ~500 °C under 5 GPa – were able to produce discs ($t = 0.15$ mm) exhibiting some VIS transparency and very high hardness ($HV1 \sim 20$ GPa) [P18]. Lately it was shown that a cubic c-Si_3N_4 polymorph-based ceramic (which in principle can be made transparent) can be produced over 1700 °C and pressures larger than 15 GPa [Z2]. Later transparent small c-Si_3N_4 were fabricated in Japan [N11] (see Figure 4.129); the technique also allows fabrication of amorphous SiO_2 parts by sintering around 1200 °C of powders.

Freestanding, 100 μm thick plates of Y and Ca-α-SiAlONs exhibiting considerable transparency were produced recently [T5].

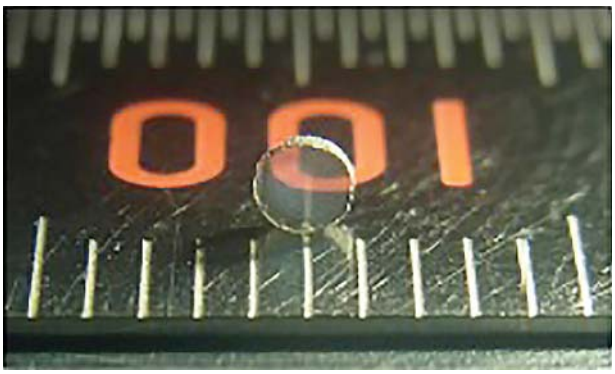

(a)

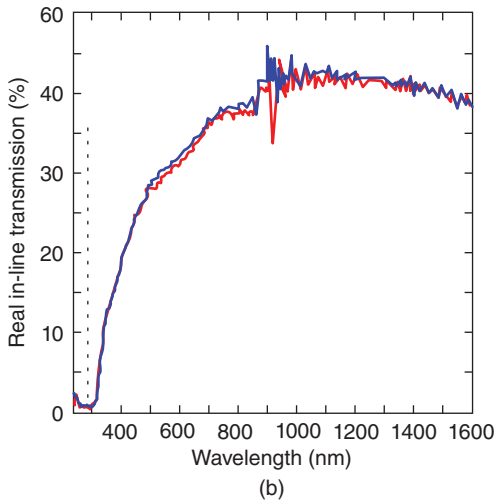

(b)

Figure 4.129 Small transparent Si_3N_4 ceramic disc and its transmission spectrum. Source: Nishiyama et al. 2017 [N11]. Reproduced with permission from Springer Nature.

5

TC Applications

5.1 General Aspects

As we have seen in Section 4.1, the family of transparent ceramics is a quite numerous one, by now. Many of them find application in various domains of human endeavor. The transparent ceramic (TC) parts are sometimes used alone but more frequently they constitute part of more or less complex devices, the latter functioning as such or being themselves elements of yet more complex systems.

Some of the TCs are destined to applications that imply medium or large scale production, like is the case of armored windows or envelopes for Na vapor-based high intensity incandescent lamps. Others are considered for highly sophisticated individual systems like laser-assisted plasma-wake field mechanism particles, accelerators, or fusion reaction ignitors (e.g. the American National Ignition Facility – NIF or the extreme light infrastructure [ELI] European power lasers program).

The applications are based on the fact that besides transparency – in various segments of the (0.15–25 μm range) – the TCs exhibit various functional properties (one or more) like high hardness and/or strength, refractoriness, ferroelectric (and its consequences) or magnetic behavior, fluorescence, high refraction index, or chemical inertness.

In some cases it is useful to classify the TC based products also by using as classification criterion the way they affect the spectral composition of the incident electromagnetic radiation (EMR). According to such a criterion, one has the as a first subclass spectrally passive TCs, viz those ceramics that are not modifying the spectral composition of the incident EMR (we would include here also the lenses). Others, the transmitted fraction of which has a spectral composition differing from that of the incident beam one may call spectrally active TCs. In the last class one can include mostly of the TM^{+} and/or rare-earth cation (RE^{+}) containing cations. In the following text, first the passive TCs are discussed with the active ones making the object of Sections 5.2.9.1–5.2.9.4). Of course, one may argue that also the modification of other aspects, of the EMR, like, say, its polarization state, makes a ceramic "active"; in such a case also lenses or magnetic ceramics will fall in this category.

It is important not to forget that for most applications the TCs compete with other transparent solids like glass, single crystals, or organic polymers. In order to prevail, besides high performance, the TCs have to show also a good cost per performance ratio; in some cases the possibility to offer large size and complex shapes is important. In Table 5.1 quantifying the requirements was tried, regarding optical quality, for different type of applications. While the numbers may not find universal acceptance, being a result of the practical experience of the authors, we feel they can constitute a useful guide for estimation of the worth of various results reported in the literature.

5.2 Brief Description of Main Applications

In this section the most interesting – from a technical and/or commercial point of view – applications of the TCs are reviewed.

5.2.1 Envelopes for Lighting Devices

In the lighting source industry, TCs find application related to two distinct tasks. In this section their role as transparent containers of the light-generating systems of certain types of high pressure metal-halide lamps is discussed. In Section 5.2.9.3 the TCs as phosphors (part of solid-state light sources, SSLSs) will be discussed. As it was detailed in Section 1.3, the first translucent ceramic found application as an envelope for high pressure Na^{0}

Transparent Ceramics: Materials, Engineering, and Applications, First Edition. Adrian Goldstein, Andreas Krell, and Zeev Burshtein.

Table 5.1 Guiding quality criteria for transparent ceramics in major fields of applications [K53].

Quality parameters	Important field of applications		
	Ceramic front for security window	Optical lenses	Laser ceramics
Optical loss factor (in-line) at 600 nm	$\alpha \leq 0.05\ cm^{-1}$	$\alpha \leq 0.01\ cm^{-1}$; best $\alpha \leq 0.001\ cm^{-1}$	$\alpha \leq 0.001\ cm^{-1}$
In-line transmission at 600 nm, 4 mm thick	$T \geq 0.95\ T_{th}$	$T \geq 0.99\ T_{th}$	$T \geq 0.999\ T_{th}$
Optical homogeneity Δn	—	<0.05 ppm	0.01–1 ppm[a)]
Tolerable frequency of visible defects > 20 µm	$f \leq 100\ cm^{-3}$ (critical size limit here: ≥ 50–100 µm)	$f \leq 10\ cm^{-3}$	$f = 0 - 10\ cm^{-3}$

a) For comparison: Sapphire Al_2O_3 single crystal used in lasers exhibits refractive index inhomogeneity $\Delta n = 0.5 - 0.9$ ppm.

vapor based discharge lamp [B67]. It allowed, compared with the silica glass conventional envelope, a raise in the work temperature and, as such, an increase of the Na^0 vapor pressure; more efficient lamps resulted. The advantage of Al_2O_3 was a better chemical to that of the a-SiO_2 envelopes. This application was relevant for a fairly large market, making the translucent polycrystalline ceramic alumina (PCA) a commercial success (in hindsight one even can tell that at a level not yet repeated in the TCs further history). The lamps were used for illumination of factories, sport arenas, parking lots, airport takeoff tracks, retail stores, etc. This application has a number of stringent, sometimes contradictory, requirements (in addition to transparency). For instance, a very good resistance to thermal shock is desired (on this point a-SiO_2 is a strong competitor) coupled with chemical inertness vis-à-vis high pressure vapor (1100–1300 °C) of highly corrosive chemicals like metal (Na, Hg), salts (mostly halides) of Na, Cs, Tl, In, Ho, Tm, Dy, etc. In addition, good bonding to feed-through metal parts and availability in complex envelope shapes (besides tube) like ellipsoidal, spherical, are requested.

These lamps cover a wide range of power, extending from 20 W to several kW [W18]. The image of such a lamp is given in Figure 1.5 in section 1.5.2. The PCA (released on the market in 1966 [B67]) was translucent, which was acceptable for wide area overhead lighting systems. Later the introduction of metal halide-containing lamps (with a much improved color rendering index, CRI) opened the door for other types of illuminators, like automotive head lights or projector lamps, where the envelope needed much higher levels of transparency, than the Na lamps envelopes, in order to allow undistorted passage of focused beams. For such requirements the "classical" PCA was not good enough as far as transparency was concerned. First, efforts were directed toward improvement of PCA transmission either by reducing grain size (to reduce, by this, scattering [H17, K43, R34]) or by converting the PCA into a single crystal (see details in Section 3.1.6). The former approach is based on the fact that in the case of the non-cubic PCA, a fine microstructure leads to increased transmissivity [A23]. In Figure 2.21 the in-line transmission of micron grained, translucent alumina was presented, as a function of sintering time (1280 °C) [H17]. For the application discussed here translucency levels attained were reasonably good.

As discussed in section 2.3.4 [A23] further reduction of the grain size is instrumental in efforts to increase transmission. Of course, even when submicron grained, alumina parts (owing to a moderate, but not zero, birefringence) remain reasonably transparent only at thickness levels <2 mm. For certain lamps envelopes of this thickness will suffice. At IKTS, Dresden, increased transparency (compared to what was possible using the Japanese aluminas) envelopes made of submicron alumina ceramic were developed, during the early 2000s. In Figure 5.1 the real image and the thermal mapping photos of a burning 400 W ceramic envelope-based, discharge metal-halide ("CDM"), lamp with a maximum temperature of about 1150 °C is shown [K50].

The sub-micrometer α-Al_2O_3 envelope (one-piece gel-casting of the complex shape with "lost" wax-core) lamp demonstrator was tested by Philips, Eindhoven. The lower photo shows the sintered envelope before its mounting on the lamp socket: at 0.8 mm wall thickness the transparency is visualized by a black wire, along the axis and the XXXX text, marked on the back [K57]. However, the commercial use of such a material remains limited mostly owing to problems raised by grain growth during service-life (which has to exceed 2000 hours). Owing to the distribution of grain size (GS) in such products, a grain-growth process starts quite early – at the ~1200 °C existent during service in high pressure Na^0 vapor lamps. Because the grain-growth inhibitor's, Mg^{2+}, solubility in the corundum lattice is GS dependent (the fine grains dissolving much more MgO), this starting of growth leads to exsolution of Mg^{2+} (with the spinel formation in the grain boundaries (GB) regions). As a result the rate, of a volumetrically non-uniform,

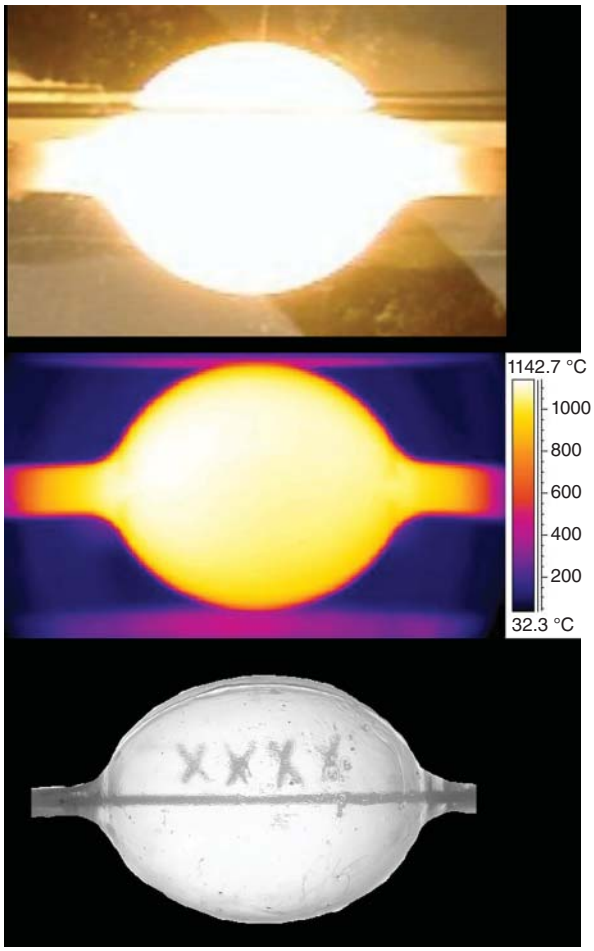

Figure 5.1 Imaging and thermal mapping of a 400 W metal-halide lamp with PCA envelope for 1150°C working temperature. Al_2O_3 body by IKTS Dresden, lamp fabrication and thermal mapping by Philips Research, Eindhoven.

grain growth is increased; pores coarsen too [W18]. Such microstructural changes reduce the transparency of the alumina tubes in time, degrading thus their quality, especially for metal halide containing lamp apps. Multiple doping (in which La_2O_3 or similar oxides supplement MgO) can alleviate, to a certain extent, the grain growth problems of submicron alumina. Infact, the Al_2O_3 ceramic of Figure 5.1 was therefore, doped with a fine dispersion of nanoscale ZrO_2 known for its low solubility in the alumina lattice.

For the lamp applications where high transparency is a must, the use of cubic TCs (spinel, γ-AlON, Y_2O_3, or YAG) was also considered. For γ-AlON a specific problem is the lack of phase stability outside a narrow N_2 concentration range in the service atmosphere; these concentrations differ from those existing in lamps. For the rest of the tested materials, the main problem is the absence of long time chemical stability vs. the very corrosive atmosphere prevailing in the lamps.

5.2.2 Transparent Armor Including Ceramic Layers

5.2.2.1 Armor: General Aspects

King Solomon considered that "wisdom" is better than weapons of war (Ecclesiasts 9, verse 18; cited in [H19]). Unfortunately this view was and is not shared by many so that one of the ways often used by mankind, from its dawn, to settle disputes, is the launching of various types of fast projectiles toward the opposition. Rocks, knives, arrows, content of improvised explosives devices, and ammunition fired by the aid of guns, are among the more common types of projectile soldiers and civilians are confronted with. People attacked by these projectile tried – from the dawn of interhuman warfare – to defend themselves with armor, made of various materials like leather, wood metal, or, more recently, glass and ceramics.

In this section first some general aspects – regarding projectiles, armor, and their interaction – are presented; this will reveal how armor works and which are its main functional characteristics. Then, based on this background the specifics of transparent armor are discussed.

5.2.2.1.1 The Threats Armor Has to Defeat (Projectiles)

Small arms ammunition ($\phi < 20$ mm) is the kind of projectile most people have to worry about; a schematic description, of this kind of threat, appears in Figure 5.2a,b.

Armor is also expected to protect against shock waves, from blasts, but this aspect is not treated later.

Regular army ordnance projectiles are made of a "core," the task of which is penetration into the target, and a jacket (usually led). The core may be made of various types of steel, WC/Co, and similar cermets. Penetrators made of high quality steel or cermet are called "armor piercing" (AP) bullets. Shard, propelled from fragmenting artillery shells, aviation bombs or roadside explosive devices are also an ubiquitous presence on battle fields. In addition to the aforementioned, lately, kinetic energy penetrators (higher caliber [>20 mm] long rod ammunition, armor piercing discarding sabots [APDS]) are among the fastest, more damaging projectiles. For all the threats mentioned earlier (with impact velocities < 3 km/s), the "ballistic strength" of the armor is relevant because the energy of the generated shock is of the same order of magnitude as the strength of armor solids. Various types of strength viz *tensile* and *compressive* strength are measurable together with other mechanical characteristics like *toughness, dynamic* strength, *Hugoniot Elastic Limit* (HEL), and armor *hardness*. The HEL is a parameter useful in understanding the way brittle materials yield, under the stresses resulting from loading under dynamic conditions. It is defined

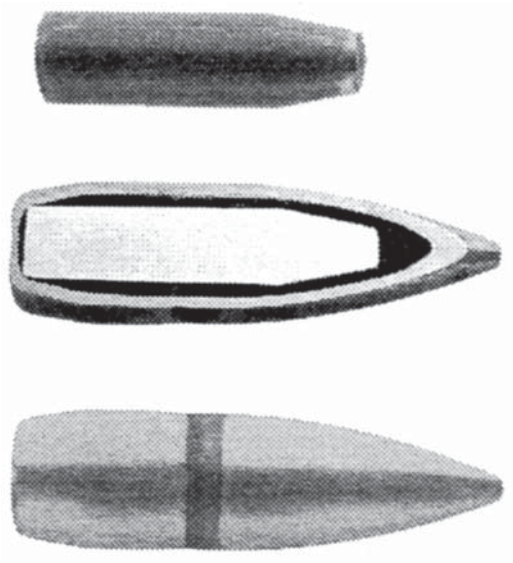

(a)

(b)

Figure 5.2 Various small, armor piercing, projectiles (medium-to-high threat level). (a) Schematic of the bullet structure. From top downward: steel core, longitudinal cross-section, and full bullet. (b) Projectiles imaging. From left to right: 14.5 mm armor piercing incendiary (API; steel core), 7.62 mm API, 7.62 mm FFV (tungsten carbide core). Source: Hazel 2006 [H19]. Reproduced with permission from Argos Press.

as the maximal stress level sustainable by the solid, subjected to one dimensional shock compression, without undergoing irreversible deformation at the elastic shock wave front. It is a complicated matter to determine the hierarchy of these mechanical parameters, viz which one has the strongest influence, on the destructive abilities of the projectile. This also varies with the type of impact; see, e.g. the discussion by Krell and Strassburger K45, K46]. Threats of higher speed, than the 3 km/s mentioned earlier, also exist, for some time now. In Figure 5.3 a high speed threat (shaped metal jet) is depicted.

At the speed of these jets 5–10 km/s, the mechanical strength of the armor is largely irrelevant. Penetration takes place in hydrodynamic mode, i.e. the solids behave like fluids (no resistance to shear); a projectile may create such conditions, even at low speed, when attacking a polymer made target. Projectiles of even higher speed, say, >10 km/s, also exist (satellite fragments, space weapons launched projectiles, etc.); for the moment they are quite rare.

Projectile velocity spans, as we saw previously, a wide range of values. This range is, usually, divided in a few domains like subordinance domain (25–500 m/s) followed by ordnance domain (500–1300 m/s) and ultraordinance (1300–3000 m/s); over 3000 m/s lies the domain of hypervelocity.

5.2.2.1.2 The Role of Armor

The existence of the scary objects, depicted earlier, requires a response; it is provided by armor. The role of armor is to defeat the projectiles and/or shock waves previously mentioned. This implies dissipation of their kinetic energy, deformation, and fragmentation (these processes are interrelated). Defeat means to bring the threat to a state in which it is not able to harm – over an acceptable limit – its target. In Figure 5.4a projectile before impact and the same, after being brought to a standstill by an SiC armor, are depicted. The ability of an armor kit to accomplish its task depends on certain mechanical characteristics of the materials it is made of, on its geometry (especially thickness) and the general design of the whole armor system. The performance of a given armor type is of course strongly dependent on the type of the attacking threat. Universal use armor is not available; one has to optimize the armor for specific threat types.

Especially under heavy threat, materials available for the opaque parts exhibit, on the average, better mechanical properties than those usable for the transparent sectors. Another important classification distinguishes *heavy* (e.g. steel) vs. *light* (e.g. ceramic, textile) armor. Ceramics are brittle but offer a unique combination of high hardness with relatively low specific weight. Most of the modern armor kits are multilayer, multi-material systems; this holds for both opaque and transparent armor. Such a structure allows the synergetic combination of the useful characteristics of different kinds of material so that the resulting macroscopic composite performs better than monolithic components taken alone. The reason ceramic layers are so useful will be better understood after the brief presentation of the

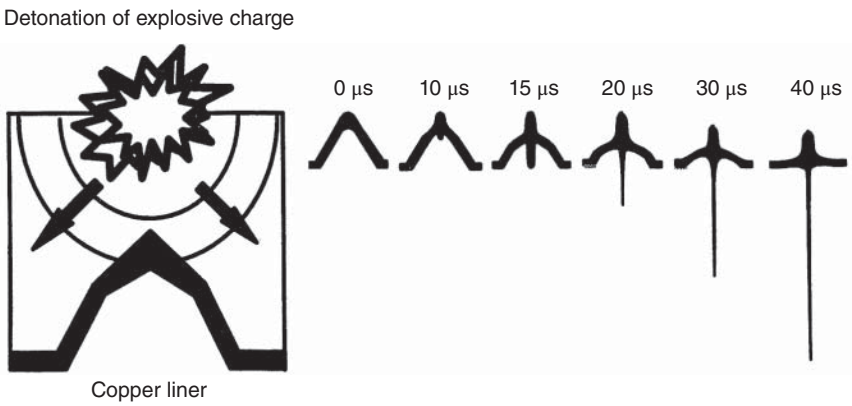

Figure 5.3 Schematic presentation of the way a copper shaped-charge forms. Source: Hazel 2006 [H19]. Reproduced with permission from Argos Press.

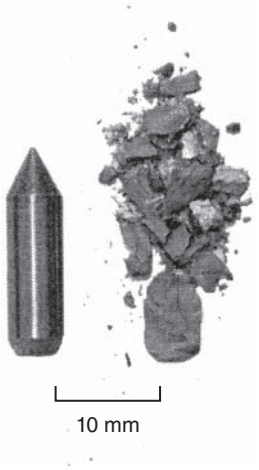

Figure 5.4 Imaging of the core of a 7.62 mm FFV AP round before impact (left) and after fully penetrating (920 m/s impact speed) a 6.5 mm thick SiC armor plate (right). Source: Hazel 2006 [H19]. Reproduced with permission from Argos Press.

threat/armor interaction given in the Section 5.2.2.1.3. Understanding of this interaction is also needed for an optimal selection of the materials, chosen for the fabrication of a transparent armor kit, and correct design of its geometrical features.

The discussion in the following concerns projectiles shot from small caliber arms, at speeds lower than 1.5 km/s, where hydrodynamic flow does not occur.

5.2.2.1.3 Processes Generated by the Impact of a Projectile on a Ceramic Strike-Face (Small Arm Launchers)

When an armor system includes ceramics, the material always forms the first, ballistically significant (not necessarily the outer one) layer to come in contact with the threat (strike face). As it will be seen, this is due to the specific mechanical properties of ceramics. Depending on the energy and other features of the projectile, the ceramic plate (called, sometimes, target below) may be impacted in different ways [B2]. In a fortunate situation, armor penetration does not occur. Provided a sufficient target thickness, this happens when the striker velocity is low enough to lead to only *elastic* deformation without target cracking.

Permanent damage with plastic deformation and/or fracture appears at higher impact velocities. A very special projectile/target interaction form is called "interface defeat" and is observed when a metallic kinetic energy projectile impacts a thick ceramic target: up to some critical ("transition"), velocity the impacting projectile crashes and flows radially outwards *without significantly penetrating* (i.e. without seriously damaging!) the ceramic. In a remarkable experiment Rosenberg et al. [R28, R29] have shown this surprising behavior even for an *unconfined* (!) and *low*-grade (85%) alumina ceramic with some residual porosity impacted by an AP projectile with steel core – when the ceramic target was 200 mm thick (see Figure 5.5). In the experiment schematized by Figure 5.5 metallic projectile (in the figure impacting from the left) impacts the surface of a 200 mm thick block of *low-grade* opaque sintered Al_2O_3 (AD85) *without penetrating* the ceramic. With its density of 3.42 g/cm^3, the weight of the tested Al_2O_3 block is 61.56 kg equivalent to an extreme areal density of 684 kg/m^2.

The ceramic plate – depending on the energy and other features of the projectile – may find itself in two situations. A first one, presented earlier, is that in which penetration does not occur. In the second, permanent, plastic deformation appears at higher striker velocities.

High speed flash X-ray photos, at the interface of tungsten projectiles and SiC ceramic tiles, have been published by Lundberg et al. [L54]. The main reason, for the success of such spectacular experiments, is, of course, that with its large dimensions the ceramic block produces its own confinement, while its large thickness prevents bending and associated tensile load. For real technical armor, the design of Figure 5.5 is, however, impractical: with the given thickness even the "light" ceramic of this example would be associated with an inacceptable specific areal weight of 684 kg/m^2.

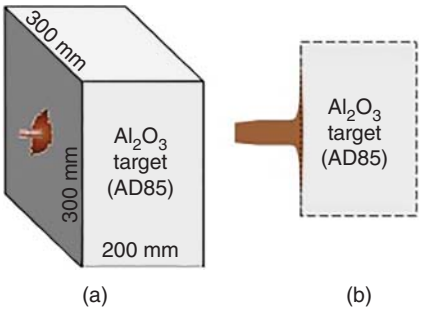

Figure 5.5 (a) Schematic of an impact in which the armor thickness is large enough at the projectile velocity low enough that the impactor crashes *without* target penetration (interface defeat). (b) Enlarged cross-section at the site of impact. The given size data and the commercial alumina grade are that of the study by Rosenberg et al. [R28].

An essential aspect of the projectile/armor tile interaction is the mechanical waves generated when contact between the two occurs. The main wave types and their relative amplitudes are depicted in Figure 5.6 [W7].

At any velocity various types of normal waves propagate within the target. Over a velocity v_{HA} higher than $K/\rho^{0.5}$ (ρ = density; K = bulk modulus; resistance to compression [GPa]), shock waves appear; above $\sim 3 \times v_{HA}$ processes like cracking, comminution, and phase change or even impact explosion may occur. This is the start of the second situation in which penetration does occur. Early studies already determined that hard, brittle targets (like ceramics or glass) suffer damage according to a sequence, which is the same for all the materials having the said mechanical behavior [F14]. In Figure 5.7a penetration event (not resulting in full perforation) is schematically depicted for the situation of a backed ceramic armor tile. With unified conditions, measurements of the "depth-of-penetration" in Figure 5.7 are valuable means for armor efficiency characterization (see Depth-of-Penetration [DoP] testing in Section 5.2.2.1.4).

Let us now consider a ceramic strike-face backed by a ductile metal plate of a thickness (low to medium) similar

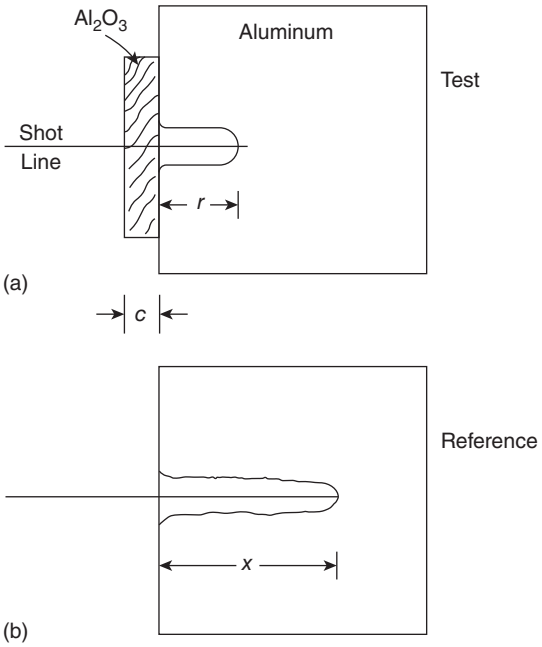

Figure 5.7 Schematic of the main stages of the penetration process; small arms launched bullet impacting a ceramic-faced two layer armor kit. *Note*: The figure represents a situation in which the armor is not very efficient (damage to projectile not high enough). Source: Hazel 2006 [H19]. Reproduced with permission from Argos Press.

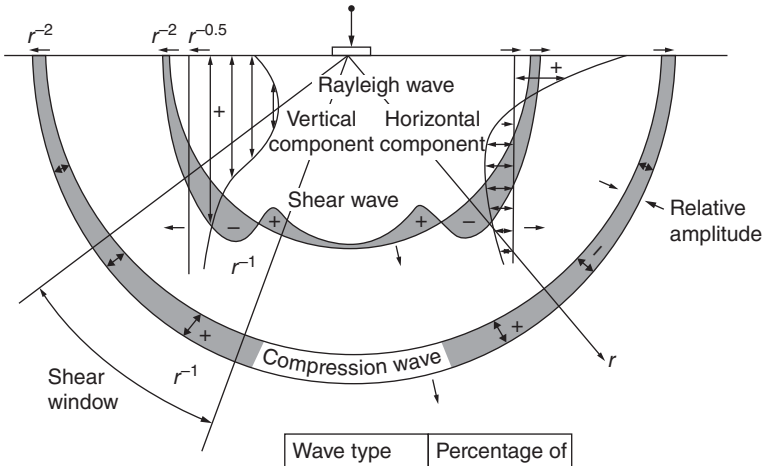

Wave type	Percentage of total energy
Rayleigh	67
Shear	26
Compression	7

Figure 5.6 The main wave types that form consecutive to the impacting of a ceramic tile by a high speed projectile, and their relative amplitudes. Source: Walley 2010 [W7]. Reproduced with permission from Taylor and Francis.

to that of the target, and describe the processes, at the macroscopic scale – after an impact leading to penetration. At the moment of impact (projectile incident normal to target major surface), a strong compressive, transient wave is launched into the region of the target located beneath the projectile. If the bullet has a conical nose (shape given mostly owing to aerodynamic considerations), it usually shatters and leaves a more or less blunt rod; the penetrator may be blunt from the start also. In the range of velocities considered here, the blunt front of the projectile also deforms (getting the shape of a nail cap), but it is not yet able to start penetration because the hardness of the target exceeds its own (usual, steel or WC/Co, projectiles). This stage, called "dwell," is over in 6–10 μs. During the initial stage of the impact, both target and projectile experience a measure of hydrodynamic flow. The failure of the ceramic starts, during this stage, with the formation of a set of longitudinal cracks (i.e. here in the direction of plate thickness), which start at the perimeter of the penetration and are located on a conical surface (large base of cone is closer to back surface of target). The cracks are a result of the energy transferred from the projectile to the target. This energy (introduced by the initial compressive wave and then distributed within a more complex system of waves) dissipates part, but only a very low one, of the bullets energy. Regarding the energy distribution, it is important to note that the brittle ceramics are strongly affected, among other factors, by their macroscopic boundaries, which cause reflection (along with partial transmission) of the highly energetic mechanical waves. Especially when lacking a back plate, the tile experiences the return, from the back surface, of a tensile wave. Ceramics exhibit much higher yield stress when loaded in compression than when tensile stress is generated (e.g. a typical alumina may exhibit a compressive strength of 2900 MPa associated with a flexural one of only 450 MPa). The microcracks, preexistent in the ceramic tile, will be amplified by the tensile stress leading to fracture crack bifurcation. The specific trajectory of the "conical" macro cracks is explained by the cracks tending to follow trajectories of maximal tensile stress. They are also called Hertzian cracks, after the physicist who analyzed them first.

Before turning to some basics of impact-induced crack formation in ceramic targets, we have to resume some historic achievements in terminal ballistics. Regarding relevant processes, Woodward summarized previous observations in 1990 by stating that only a negligible portion of the projectile's kinetic energy (~0.2%!) goes into fracture of the ceramic, whereas most (45–70%) of this energy is transferred to the debris of the fracturing ceramic [W29]. This highlights the importance of the abrasive interaction between the hard ceramic fragments and the core of the projectile: " … the interaction with the ceramic is dominated by penetrator erosion" [W30]. Because the magnitude of the maximal stress, induced by the impact, is much higher than the yield stress of the ceramic, in fact a two wave structure is excited; in it the elastic waves are accompanied by inelastic components. In this first stage, of the impact, other important processes also start [H19]. Toward its end, after the Hertzian fracture begins, an axial crack formation also starts, at the rear of the ceramic plate (the ceramic tends to follow the motion of the back plate – if the back plate is not fully rigid; this is the case of thin and intermediate thickness of back plates). In the wake of the initial waves, radial cracks also form (see Figure 5.8), leading to spall (scabbing) if the plug formed by the Hertzian fracture is held in place. The Hertzian cracks arrive, in time, to the rear surface of the ceramic. The conical slab thus created is ejected in front of the impactor, if no backup plate retains it (plugging). If a back plate is present, the cone will spread the impactor's energy on a larger surface than the projectile's and thus pressure is lowered; energy will be dissipated also by back plate deformation. In the top surface region, lateral cracks, related to tensile stress, also appear. These "late" cracks extend rapidly, markedly increasing the damage zone. The interaction of waves is quite complex and dynamic, leading to various types of stress, including shear. The penetration takes another 9–15 μs after the dwell. At the end of this period, another macroscopically visible process is completed, besides the cracking: comminution of a small oval region located immediately under the projectile's nose (see Figure 5.9) [L8].

In this region, even before the return of a tensile wave, in the ceramic materials, both mono- and bi-axial

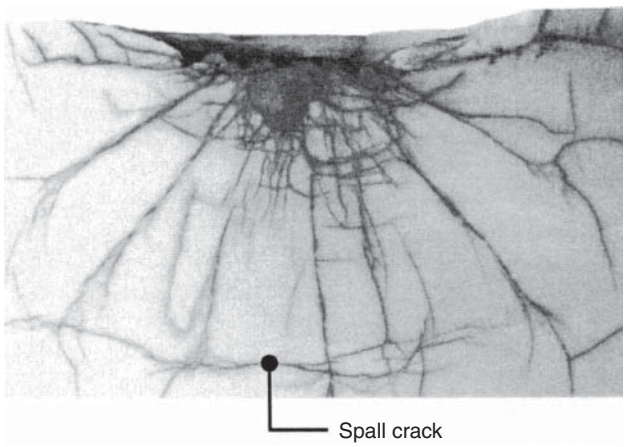

Figure 5.8 Cracks system generated in an alumina target by a 6.35 mm steel ball launched at 1.5 km/s; Hertzian and spall cracks are visible. Source: Hazel 2006 [H19]. Reproduced with permission from Argos Press.

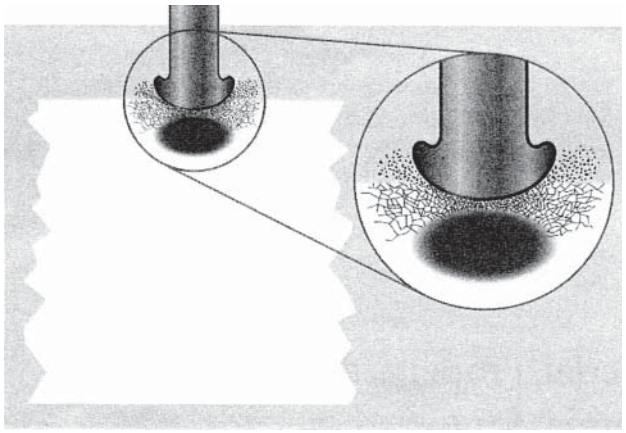

Figure 5.9 Comminution zone, developing in the armor tile, under the nose (flattened) of the impacting projectile. Source: Lankford 2004 [L8]. Reproduced with permission from John Wiley & Sons.

compressive stress develops. In such conditions the microcracks grow in a relatively uniform fashion throughout the region (as opposed to the effect of tensile stress which may catastrophically, and at high speed, extend a single crack). Eventually the cracks link up, generating a mass of comminuted material. The fracture toughness under high pressure and shear, and the frictional resistance to flow under high pressure, determine the level of opposition the ceramic rubble can raise against the penetrator. Owing to the high strain rate ($10^5\ s^{-1}$) proper to the ballistic loading, rate dependent local plasticity may appear. The loading is so fast that strain is quasi one-dimensional and, owing to inertial effects, a situation close to a transient confinement (no radial expansion) is formed; in fact these conditions mean that the system is in the vicinity of the HEL. According to Lankford the type of yielding, induced by reaching the HEL, is, owing to crack inertia, mostly plastic flow (instead of crack nucleation and/or growth) on multiple slip systems. While this is a mechanism able to consume some of the energy injected by the impactor, its presence represents bad news. The confinement is strong close to the penetrator's central line, but decreases laterally, owing (among other factors) to ceramic debris back jetting along the projectile axis. Dislocation pileups thus may form and serve as nucleators of microcracks, which then extend. Shear cracks also form and combine action with the axial ones. The result is comminution. Comminution is of course the worst form of damage the target may experience. The product of this damage, however, participates, significantly, to the destruction of the impactor. The rubble formed is pushed, for a while, by the penetrator, but at a certain point it will start to stream back around the progressing projectile, at high speed; the result is erosion of the projectile. The penetration resistance of rubblized material is dependent mainly on its residual shear stress strength. The process described earlier emphasizes the importance of friction. Up to 40% of the projectile's mass may be carried off as erosion product. Because the penetrator has to push comminuted material and, to a certain extent, even move through it, the properties of rubblized ceramic are very important. Crushed ceramic retains a certain mechanical resistance due to particles interlocking and friction. Owing to volume increase, the rubblized material also exerts considerable outward pressure on its surrounding (bulking). It is also noteworthy the fact that the various friction processes occurring (between rubblized particles and between projectile and ceramic) have noticeable consequences. For instance, the latter contributes to energy dissipation, while the former contributes to the strength of the ceramic in pulverized state.

The tensile strength of the pulverized material is close to 0, but the compressive strength $R_c = \alpha + \beta P$ (=tile strength in rubblized state) is still significant; it also depends on the pressure exerted by lateral confinement (if it is provided). In the formula defining R_c: P = external pressure applied to the ceramic plate by the confining system; α, β = empirical parameters not analyzed here. There is a limit of the influence P may exert, but practically it is beneficial to use some confinement scheme in the design of any armor system. While beneficial such a scheme is not always easy to come up with – especially in the case of transparent armor systems.

5.2.2.1.4 Final State of the Projectile/Armor Impact Event Participants

As we have seen the interaction after impact – between penetrator and the ceramic armor – can unfold according to various scenarios, depending on the interplay of factors like:

- Projectile speed
- Angle between projectile velocity vector and the normal to the target upper surface ("obliquity angle," θ)
- Target ceramic mechanical properties, geometry (especially thickness), microstructural pattern (including grains size, defects, impurity segregation at interface, etc.)
- Geometry and mechanical behavior of backup plates
- Presence, pattern, and pressure exerted by confinement and others

The final state of the participants, to the impact event, depends on the way the factors listed earlier interact. A few possible situations are described here. In a first one projectile obliquity increases to more than 90° after impact, so that it is deflected. Desired but rare situation occurs if armor is very efficient at stopping projectiles or the latter's speed is low. Projectile is stopped and

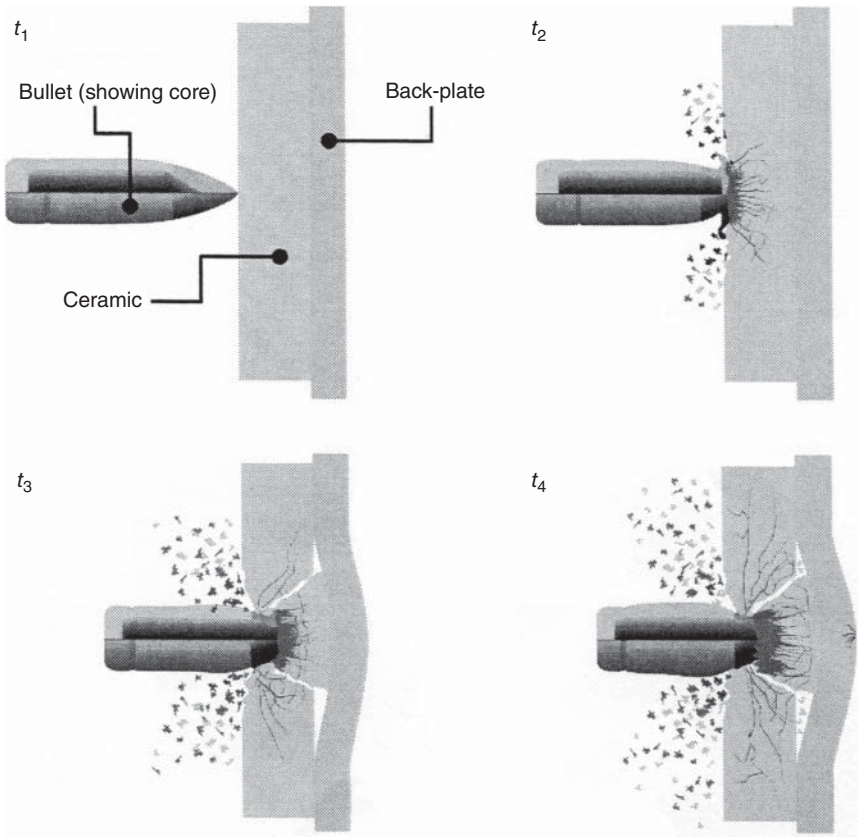

Figure 5.10 Schematic of the setup used in a depth of penetration (DoP) type armor efficiency test. Source: Walley 2010 [W7]. Reproduced with permission from Taylor and Francis.

deformed (mostly plastic deformations) or shattered before penetration. Bending and associated shattering occurs at high θ impacts. Projectile also may perforate the ceramic but after fractioning and erosion significant enough to allow full stopping in the backup layer or be able to effectuate only partial penetration. Another possibility is that the projectile be deformed, eroded, and fractured, but yet be able to perforate the armor backup system. It may unfortunately perforate while suffering only moderate damage itself.

5.2.2.1.4.1 Armor Performance Descriptors

Practically important descriptor, able to specify armor performance, is the "areal density" of the armor ceramic, A_D, defined as

$$A_D = \frac{\rho A t}{A} = \rho t \tag{5.1}$$

where ρ is the bulk density of the material, A is the area of the plate's major surface, and "t" is the thickness of the plate.

Another useful parameter is the "V-50," i.e. the velocity of a given type of projectile, at a given angle, which leads to defeat of 50% of the armor specimens tested. The "Ballistic limit" is also measured. It is usually defined as the average of two striking velocities:

- The highest velocity giving partial penetration
- The lowest leading to full perforation

The "depth of penetration" (DoP) is an important and relatively easy to measure performance indicator. It is defined as shown in Figure 5.10.

An approximate but still useful parameter – defined by Rosenberg et al. [R28], and which one may calculate, based on DoP measurements – is the "Ballistic efficiency" (*BE*) defined as

$$BE = \frac{\rho_{\mathrm{Al}(\mathrm{DoP}_{\mathrm{Al}} - \mathrm{DoP}_{cer})}}{\rho_{cer}\, t_{cer}} \tag{5.2}$$

where ρ's are the densities of the backing Al and respectively bulk density of the tested ceramic plate and "t" its thickness. A useful relationship, between projectile and armor tile characteristic, is expressed by (5.3):

$$0.5\rho_P V_2 + Y_P \leq R_t \tag{5.3}$$

where V is the projectile velocity; ρ_P is the projectile density; Y_P is a parameter selected to express the compressive strength of the rubelized ceramic; R_t is the tensile strength of the ceramic tile – before damage produced by projectile impact decreases it; another useful approximation is (5.4) [W7].

$$R_t \approx 3.5\mathrm{HEL} \tag{5.4}$$

Another interesting figure of merit can be defined using the parameters Y_S, the strength under uniaxial stress applied at low strain rate and Y_d, the strength under shock loading. It is expressed by the parameter $\overline{Y}$, which was defined as

$$\overline{Y} = \frac{Y_S + Y_d}{2} \tag{5.5}$$

and it was determined that

$$\overline{Y} \cdot \rho^{-1} \tag{5.6}$$

is a good figure of merit for ceramic armor (ρ is the density of ceramic tile), designed to withstand small arms ammunition. This parameter allows one to calculate a gross estimation of armor performance based on measurable ceramic tile characteristics.

5.2.2.1.5 Characteristics which Influence Armor Performance

Based on the sections earlier, let us summarize the characteristics that influence the ballistic performance of ceramics.

A high Young modulus, of the ceramic, is clearly desirable. First of all, a stiff ceramic is able to prolong dwell time and thus projectile damage, during this phase. It also raises the sonic impedance (Z) a characteristic that depends on E according to $Z = \sqrt{\rho E}$, where ρ is the bulk density of the ceramic. A high sonic impedance of the ceramic is important because that of the penetrators is high [V7]. It is desirable that the two match and thus ensure the smooth transfer of kinetic energy from the projectile to a large volume of the ceramic strike-face. It is worth noting, however, that increasing impedance via the density is rarely useful – when the overall performance of the armor kit is considered.

A high hardness is directly useful in the process of projectile erosion. It also implies good resistance to plastic deformation (which, ultimately, leads to formation of crack nucleation sites). In many cases hardness is proportional to HEL, a parameter with direct influence on the ability of a ceramic to withstand penetration [K44]. High friction coefficients contribute to a better destructive ability of the armor, in its rubblized state. In order to prolong erosive action of the ceramic fragments – which make up the rubble jets – a higher thickness (for a given areal density) is desired. In certain cases transgranular fracture (a feature that depends not only on the material but also on the way the tile is produced) is preferred to intergranular one, which usually means a grain boundary region weaker than the lattice. On the other hand grain boundary engineering – in a fashion allowing optimal ceramic fragmentation patterns – is sometimes feasible. Therefore, the strength and toughness measured under quasistatic loading conditions, or even dynamically, are not easy to connect with resistance during ballistic events. An interesting analysis of the way comminuted ceramic may affect the resistance of the ceramic tiles against projectiles is given in [G48, K44]. Based on measured dynamics of APM bullets (hard steel cores), it was estimated that ~2 mm of alumina debris particle impinge, on the projectile fragments, with a force of ~1 kN owing to their high acceleration ($\sim 10–50 \times 10^6$ m/s^2) [K44]. It is also shown there that the erosion ability of the rubblized material is strongly dependent on particles morphology and size. These parameters, in turn, also depend on plate microstructure. A fine grain size leads, somewhat unexpectedly, to a comminution pattern that creates a ceramic particles size distribution closer to the one optimal for strong erosion. The stiffness of the backing and the presence of backing affect the grains comminution pattern. One of the consequences of the volume expansion of the rubblized material, the "bulking," is a reduction of the hole diameter, i.e. a "pinching" action on the projectile; this can damage or totally disrupt the bullet. A large size of the tile and certain geometries (e.g. hexagon vs. square) ensure delays in wave reflection, but, on the other hand, create conditions for extension of the damage zone.

5.2.2.1.6 Ceramic Armor Study and Design

For both opaque and transparent armors, designers endeavor to devise systems of ever increasing performance and/or low cost. The mission of the armor is to defeat, i.e. prevent, the incoming projectiles from harming the protected item. To achieve this the armor has to survive the impact without perforation and no or a minimum of deformation or energy transmission of the kind able to harm the protected item. Better performance mostly means the ability to do so at lower areal density. The designer needs information regarding various topics for effective work. A first domain of interest is the material and design characteristics of the threats (projectiles or sonic waves) likely to attack the armor and their velocity. A second domain is represented by the engineering properties of the materials available for armor fabrication. Such data help one to obtain a good understanding of the interactive processes that affect the participants to an impact event. The aspects addressed by the armor designer are the kind of materials used, the thickness of the various layers, the pattern of the layers arrangement, the kit's shape, the confinement schemes, and the contact with the opaque region of the armor system.

A lot of the armor development process is represented by Edisonian trial and error work [M22, P12]. The shooting tests in which the examined armor kit functions as target are conducted so as to allow determination of one or more of the parameters used for performance

description. It is tried to reduce the volume of such work by improving the understanding of the projectile/armor interaction and its results. For this, one approach is to conduct tests, both with ordnance and ordnance simulating projectiles, in configuration allowing recovery of target and, possibly, impactor fragments in a state permitting determination of the effects of impact on the participants. For the impacted target examination, the usual ceramographic methodology is used with an accent on scanning electron microscope (SEM). The visualization of the projectile/armor interaction event stages is a tool able to give precious information to the armor developer. This was first was achieved by the aid of high speed photography [S61–S64]. The method was developed at the Ernst Mach Institute (EMI) for the observation of fracture propagation in glass. It was adopted, for armor ceramics, in the late eighties, also at EMI; most of the specimens were fabricated by one of us (A. Krell). Usually an edge-on impact test format is used (see Figure 5.11). Later, radiography, based on X-rays, was introduced.

For opaque ceramics light reflected from a perfectly polished specimen side major surface is used. In the case of transparent ceramics, a shadowgraph technique is employed.

In Figure 5.12 the results of the impact on a B_4C/Al armor of a steel cylinder (see Figure 5.11) are shown, as revealed by ballistic cinematography. Such examinations can visualize the sequence of damage features formation. For instance, the cone cracks could be shown to appear, as previously conjectured, first. Primary cracks (those that form in the region limited by the cone cracks) of various shape (branching is ubiquitous), exhibiting fuzzy tips and edges were then seen to form. Secondary crack zones appear later (wedge shaped). Significant differences in the cracking pattern are seen for different materials. This is illustrated by comparing (schematics drawn based on photographic data) in Figure 5.13 where the behavior of SiC-B (v_p = 150 m/s) and TiB_2 (v_p = 85 m/s) targets are shown. In fact, over a certain v_p all ceramics transit to a behavior as the one shown by TiB_2. For instance, aluminas effectuate the transition for v_p values in the 200–350 m/s, depending on the grade examined. SiC behaves in a similar way. High speed cinematography allows also the determination of damage velocity, i.e. the speed at which different types of crack advance. Usually focus is on the fastest crack type. Of course, this type of investigation offers experimental data useful for the validation of damage models.

Since about 2005 the flash X-ray cinematography [S61], allowing collection of images at really high speed, up to 100 000 f/s, is preferred to light based examinations. In fact today, compared with 2005 both conventional ballistic cinema and X-ray flash photography allow collection of data at rates over 1 Mframe/s.

Modeling is a complicated but powerful means used for the better understanding of projectile/armor interaction. Pioneering work regarding modeling was done at the Lawrence Livermore National Laboratory (LLNL) in the late sixties by M. L. Wilkins followed by others [S9].

In Figure 5.14 the simulation of an impact on a TiB_2 plate is shown together with the high speed photography of the event. Walley have examined the effect of defects on the behavior of armor kits having transparent spinel as strike-face, impacted by a 3 cm long steel projectile (975 m/s) [W7]. For modeling they used a commercial code ANSYS/AUTODYN. It was observed that increase of elliptical defects number significantly reduces armor

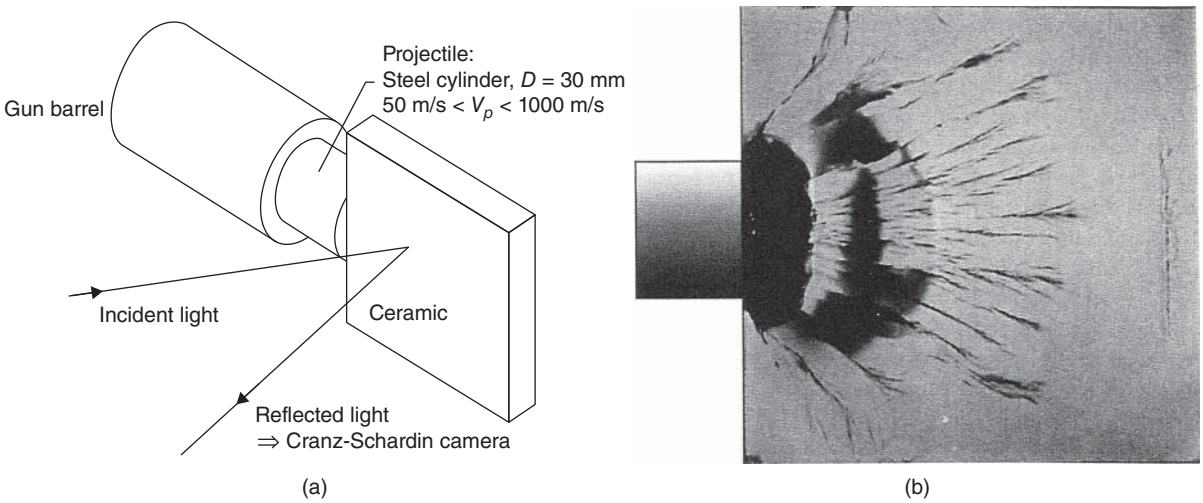

Figure 5.11 (a) Schematic and (b) imaging of an edge-on impact (EOI) test by high speed photography. Source: Strassburger 2004 [S64]. Reproduced with permission from John Wiley & Sons.

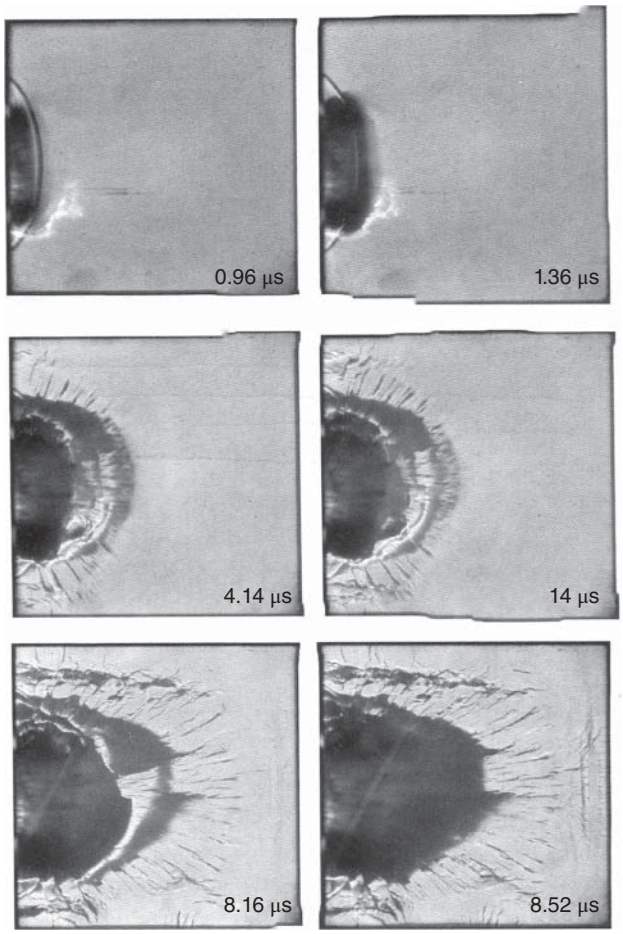

Figure 5.12 Ballistic cinematography of the impact, on B_4C/Al plate, of a steel cylinder (EOI test). Source: Strassburger 2004 [S64]. Reproduced with permission from John Wiley & Sons.

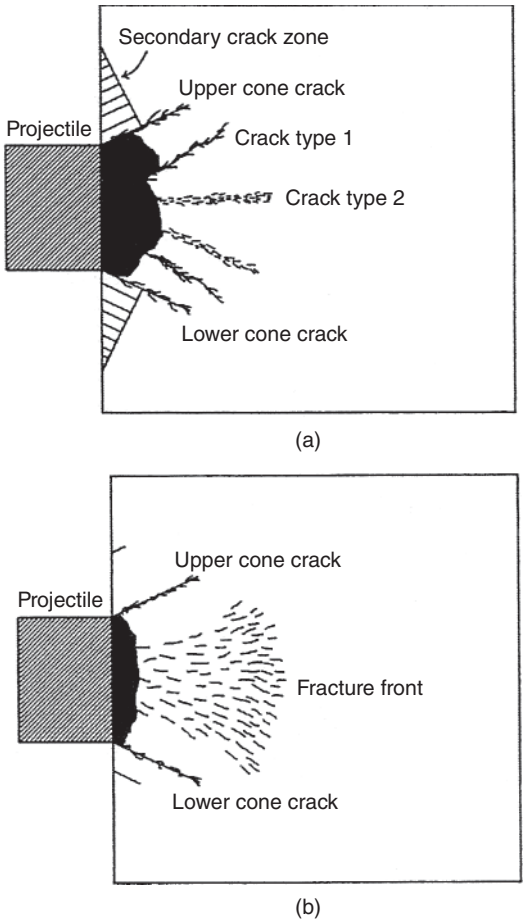

Figure 5.13 Dependence of the cracking pattern on the nature of the target. Schematic constructed based on results provided by ballistic cinematography. (a) SiC (projectile velocity = 150 m/s). (b) TiB_2 (projectile velocity = 85 m/s). Source: Strassburger 2004 [S64]. Reproduced with permission from John Wiley & Sons.

efficiency; the defects seem to reduce the local stiffness. For instance, increasing the number of defects from zero to five leads to an increase of projectile exit velocity from (zero; no perforation) to 50 m/s, while for nine defects the v_p reached 70 m/s. It was also determined that defects located in a layer close to the impact surface are much more damaging than others located deeper inside the ply. In this context an interesting aspect was revealed regarding the way damage progression pattern is influenced by defects morphology and spatial distribution [W7]. The simulation showed first that elliptical defects are more damaging than circular or rectangular ones and that those with the long axis aligned to that of impactor – the worst. It also showed that damage grows continuously till the midpoint between two defects, and then reappears with the same length at the next defect, where it continues to grow. A somewhat unexpected, but interesting, conclusion suggested by this study is that defects, while unwelcome, do not influence in a major way the armor behavior unless they are very large and located at impact surface. Investigations have also shown that *glass* backing (which does not reduce transparency significantly), with its high HEL and dynamic spall strength, increases the erosive power of a transparent ceramic front (on further fragmenting the impacting projectile) much more efficiently than the metallic aluminum backings used, sometimes, in opaque ceramic armor systems [K47, K48].

What has to be noted, in order not to entertain exaggerated hopes, is that the abilities of modeling to support armor design are limited. The processes occurring after impact interact in a complex way, and the data available regarding characteristics of the target, for use as input values of the calculations are not always complete and accurate. Therefore, while modeling was already shown to be able to provide guidelines, armor design still has to rely a lot on tedious and expensive trial and error based optimization work.

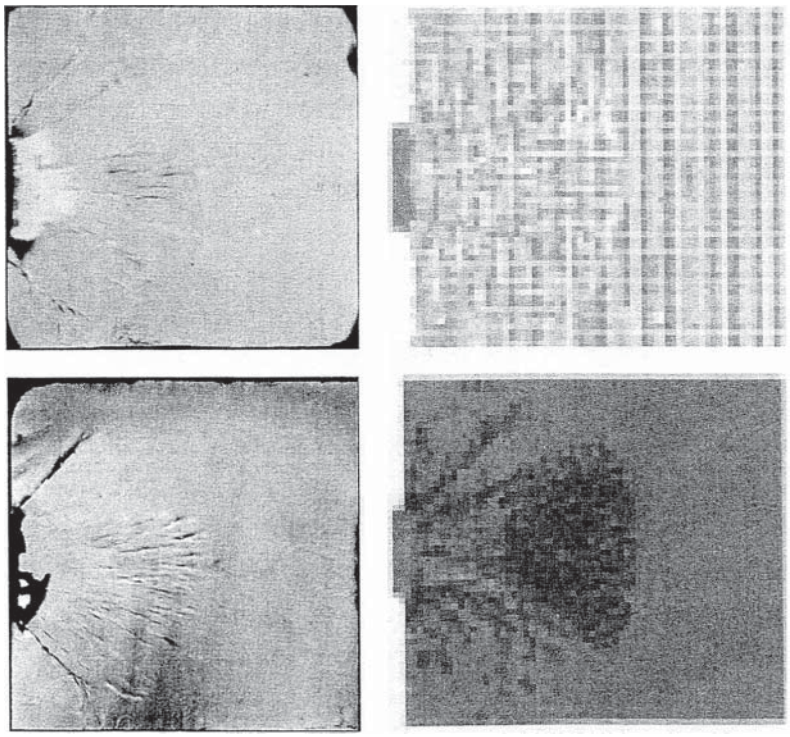

Figure 5.14 High speed photography of EOI event (a, TiB_2 plate) and simulation (b). Source: Strassburger 2004 [S64]. Reproduced with permission from John Wiley & Sons.

5.2.2.2 Specifics of the Transparent-Ceramic Based Armor

The aspects discussed earlier apply to both opaque and transparent armors. The latter are the sections of armor systems (e.g. of a vehicle), which need to function also as windows – for the visible (VIS) range of EMR; those windows for sensors – which need transparency outside the VIS domain are discussed in the section dedicated to infrared (IR) windows. The transparent armor has specific problems that are presented in this section.

Generally, the materials able to offer transparency (glass, ceramics, or single crystals) possess, in most cases, significantly less good mechanical properties than those usable for opaque armor. The work horse, in the domain of transparent armor, is still glass (the worse – as far as mechanical properties are considered – transparent material). Lately single-crystal corundum and a set of ceramics started to challenge the dominance of glass, as far as strike-faces are considered. The transparent backup materials (necessary for both all-glass kits and those based on non-glass striking-faces) are based on organic low stiffness polymers that are much less efficient than the rigid opaque polymers – one can use, for the same task in case of the non-transparent armor. The organic polymer layer's only task is to ensure, at the moment of partial window failure on impact, that the armor plate remains stable with respect to the people behind; their contribution to projectile fragments energy absorption is very modest.

The systems that use ceramic strike-faces need, besides the organic polymer backup layers, some inorganic glass layers – which are also part of the ceramic's "backing." The major component of standard transparent non-polymeric backings is laminated glass. Atop of it, various thickness, ceramic front layers are put. Recent work has shown that optimal strike-face thickness is located in the 2–4 mm domain [S61]. Fortunately for the request of *transparency*, investigations have also shown that *glass* backing, with its high HEL and dynamic spall strength, *increases* the erosive power of a transparent ceramic front (on further fragmenting the impacting projectile) much *more efficiently* than the *metallic* aluminum backings used, sometimes, in opaque ceramic armor systems [K47, K48]; this issue will be addressed below in more detail. Armor composed of only ceramic and a transparent polymer back up is, all in all, less attractive than TC/GLASS/POLYMER structures.

Glass alone remains an efficient option for transparent armor systems. However, for a certain level of performance, all-glass option has, compared with a system including a ceramic strike-face, the drawback of significantly higher weight and thickness; it has the advantage, critical in many cases, of substantially lower cost.

In order to give a quantitative feel of the above statements, let us note that for the threat levels, now of interest, laminated glass stops the projectiles (or the debris of an explosion) only at a thickness of about

10 cm or more. Together with the typical densities of borosilicate or soda-lime glasses, this thickness gives a total areal weight of 140–170 kg/m^2 – with only slightly lower values for advanced glass-ceramics (~130 kg/m^2). The thickness of such windows complicates the construction and the consequences of the high weight (e.g. for the mobility of armored vehicles) are such that the armies, relevant departments, are "fighting for each minus of 50 kg on the front axes of vehicles." Let us note that a reasonable transparency, after projectile(s) hit, is also a feature desired for a good "transparent" armor.

The general projectile/armor interaction process was discussed previously (Section 5.2.2.1.3). For the specific case of transparent ceramics, more details are put into evidence by the aid of a direct comparison of the interaction of an AP projectile (a) with laminated glass armor and (b) with a thin transparent (sub-micrometer) Al_2O_3 ceramic – illustrated in Figure 5.15. In this figure flash X-ray cinematography of the impact of a 7.62 mm AP projectile (steel core, 850 m/s) is shown.

The panels of the Figure 5.15 provide a direct comparison of the different mechanisms operating in an all-glass and respectively a kit including a ceramic strike-face: (a) In the glass laminate, the steel core of the projectile perforates the subsequent layers without significant change of its shape. Dynamic analysis shows that velocity is decreased by friction, but this effect is too small to stop the projectile within the laminate. Thus, the projectile leaves the window after complete perforation with a still deadly velocity of about 100 m/s. (b) 4 mm of completely dense (transparent) sub-micrometer Al_2O_3 ceramic (the strike-face) are locally crashed by the impacting projectile after a very short dwell, and these ceramic fragments work as alumina abrasives are known to work [K51]: they erode, fast, the tip of the projectile's steel core and the blunted projectile hardly penetrates the first and second of the three glass layers. The consequences of the interaction with the ceramic layer are twofold: (i) heavy stress, which develops *in the projectile,* fractures its steel core into several pieces; (ii) beginning at about 40–50 µs after impact an increasing amplitude elastic bending *of the backing glass laminate* initiates local cracks formation in the glass. By these processes, the energy of the projectile fragments is decreased in a way that enables this *lightweight* armor kit, with only 60 kg/m^2 areal weight, to stop the projectile [K44].

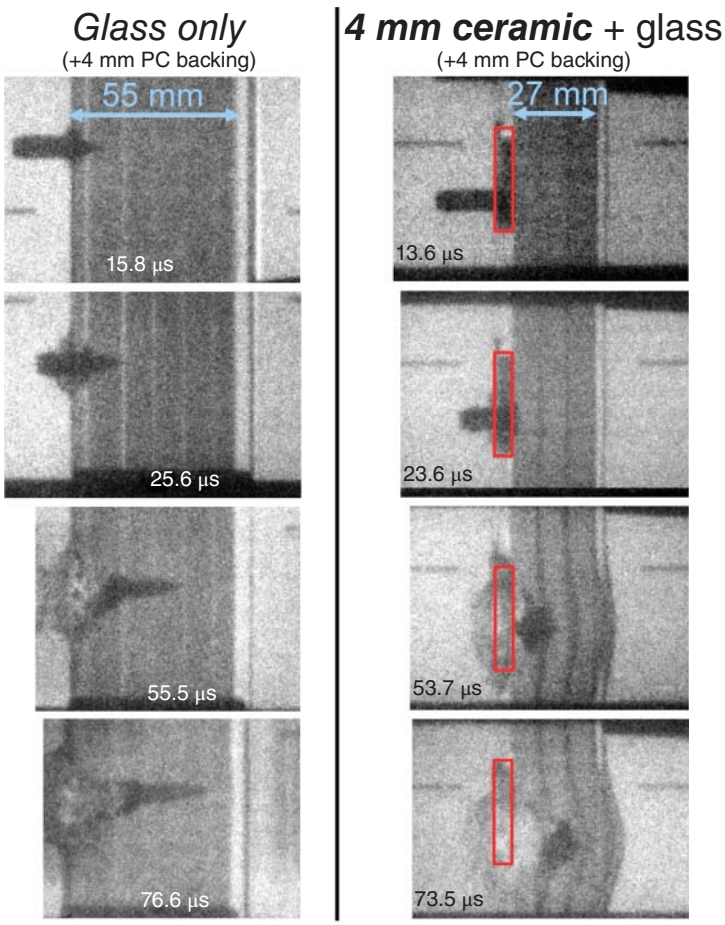

Figure 5.15 Flash X-ray cinematography of impact of 7.62 mm AP projectile (steel core, 850 m/s). Comparison of the way penetration progresses in a glass-only multilayer armor and in a much *thinner* (!) one with a ceramic strike-face (marked by frame). The final layer of both laminates is 4 mm thin polycarbonate. Source: Strassburger 2009 [S61]. Reproduced with permission from Elsevier.

As outlined earlier (Section 5.2.2.1.3), the idea of understanding – the mechanism of projectile defeat by ceramic armor – as the result of mainly an *abrasion process* has a long history: regarding relevant processes, Woodward summarized previous observations, in 1990, by stating that only a negligible portion of the projectile's kinetic energy (~0.2%!) goes into fracture of the ceramic, whereas most (45–70%) of this energy is transferred to the debris of the fracturing ceramic [W29]. This means an abrasive *wear* interaction between the hard ceramic fragments and the core of the projectile: " … the interaction with the ceramic is dominated by penetrator erosion" [W30].

Several important questions arise:

1. If the projectile is eroded by an abrasive action of *broken* ceramic fragments – which force keeps these fragments in interaction with the penetrator?
2. What recommendations can be given for an optimum microstructure of transparent armor ceramics, and which of their *mechanical* parameters are beneficial for the ballistic stability?

Other questions regard the role of appropriate backing. Hence:

3. Is there an influence of (which?) mechanical parameters of the transparent *backing*?
4. What about the transparent binders for joining the ceramic tiles to each other and to their backing?

Discussing influences of strength, Young's or compressive modulus of opaque ceramic armor and backing materials previous literature has often neglected the specific role of *dynamic* parameters and remained, sometimes, speculative. Mayseless et al. [M19] and Woodward [W29] presented and analyzed data of an *improving* ballistic limit velocity when aluminum backings were exchanged for (stronger, harder) steels, and Walley [W7] addressed, more specifically, the stiffness of such backings as most important for the success of the ceramic front tiles. In contrast, a recent review by Rosenberg et al. compared the ballistic efficiency of Al_2O_3 ceramics backed by differently "soft" aluminum alloys and different steels concluding that "a backing material with a *higher strength* (!) results in a *lower* ballistic efficiency for a given ceramic" [R29]. Such conflicting statements did not allow reliable conclusions for a right choice of (harder or softer, stronger or stiffer?) transparent backing materials. New tests compared, therefore, the performance of *same* ceramics (Al_2O_3, transparent Mg–Al spinel) impacted by 7.62 mm × 51 AP projectiles at 850 m/s in front of different backings (steel, aluminum, glass) and revealed an especially positive message for *transparent* grades: the steel core of the projectile was slightly damaged by Al_2O_3 or spinel ceramics in front of Al backing, whereas the same (!) ceramics exhibited coarser own fragmentation and eroded the AP projectiles *completely* when combined with a glass backing [K48]. This behavior was explained by the exceptionally high *dynamic* stiffness of glass, exemplified by a high HEL and a high dynamic spall strength (see [K46, K47] for the ballistic importance of dynamic vs. static strength, *dynamic* hardness and HEL of transparent ceramics and backing materials and for correlations with the static Vickers hardness).

As to the abrasive action of the ceramics, it is obvious that *inertia* is the one force, which can bring the broken ceramic fragments into close contact with the penetrating projectile [K45] – and this force depends primarily on *the size* of the ceramic fragments [K44, K47]. Ceramic fragmentation was, therefore, subject to several ballistic studies for the past 20 years (e.g. Woodward [W29], Krell and Strassburger, and Strassburger et al. [K45, S63]) and explains, in the field of *transparent* ceramic armor, important differences in the ballistic efficiency of polycrystalline sintered ceramics and their single-crystalline counterparts (e.g. comparing Al_2O_3 and cubic Mg–Al spinel *ceramics vs. single crystals* [K60]). Most important for a focused development of advanced transparent ceramic armor are the following conclusions [K47]:

- Laminated glass is a perfect backing material for ceramic front tiles.
- The ballistic impact stability of transparent armor ceramics and single crystals is governed by a strict hierarchy of a few major influences:
  - (1) Top priority is the mode of ceramic fragmentation governed by microstructural features and the dynamic stiffness of the target (ceramic + backing); these influences also affect the relative importance of first dwell and subsequent penetration.
  - (2a) On a lower rank of the hierarchic order, Young's modulus of the ceramic is responsible for projectile damage during dwell but the importance of this influence depends on the priority of ceramic fragmentation.
  - (2b) On penetration, the abrasive benefit of a high ceramic hardness depends on the size of the ceramic debris, i.e. on priority (1). In contrast, all average *strength* data (bending strength, static and dynamic compressive strength, critical stress intensity ["fracture toughness"] K_{IC}) are weakly correlated with the ballistic efficiency.

It is the priority role of fragmentation in this hierarchy, which *increases* the ballistic power of transparent Mg–Al spinel *ceramics* over that of trigonal sapphire in spite of *lower* (!) basic mechanical data of these ceramics [K44, K45], whereas cubic spinel *single crystals* outperform

their *ceramic* spinel counterparts and exhibit a similarly high stability as (rather translucent than transparent but harder) sub-µm Al_2O_3 ceramics [K60].

Different from the making of opaque ceramic armor, *windows* have to be designed not only with respect to a *mechanical* multi-hit stability but also regarding the residual *visibility* after impact: composite windows with substantially *different* transparencies *retained after impact* are exemplified later by Figure 5.19 compared to Figures 5.21 and 5.22b. Transparent glasses and ceramics are brittle materials where cracking seriously deteriorates the optical together with the mechanical performance; means for limiting crack extension are similar to those known from the design of traditional opaque ceramic armor. Instead of working with very large ceramic tiles, the backing is covered by a mosaic of smaller parts the size, arrangement, and shape of which have to be optimized according to the expected threat (see a few possible designs in Figure 5.16a). Other important influences, described by the relevant literature [J4, L38], come from the thickness of the organic glue and the inclination of tile edges (Figure 5.16b).

A large armor window, having its strike-face made of a mosaic of spinel tiles (submicron grains), is depicted in Figure 5.17. The large *glass* panes of such a multilayer have smooth surfaces, while the sintered *ceramic* tiles have to be ground and polished for becoming transparent. The interface with the glass backing is viewed, during service, mostly along a direction perpendicular on the major faces of the multilayer so that the deleterious influence of the difference in refractive index between ceramic and the transparent glue is reduced. However, *ceramic polishing* costs could be much lower if organic binders were available that (i) perfectly wet coarsely *ground* tiles *and* (ii) have their refractive index matched to that of the transparent ceramic (avoiding, thus, light-scattering at the rough lateral ceramic/glue interface). Note that in such a situation a higher roughness of the ceramic surface is admissible; thus a less advanced polishing becomes tolerable and the high cost of polishing is reduced.

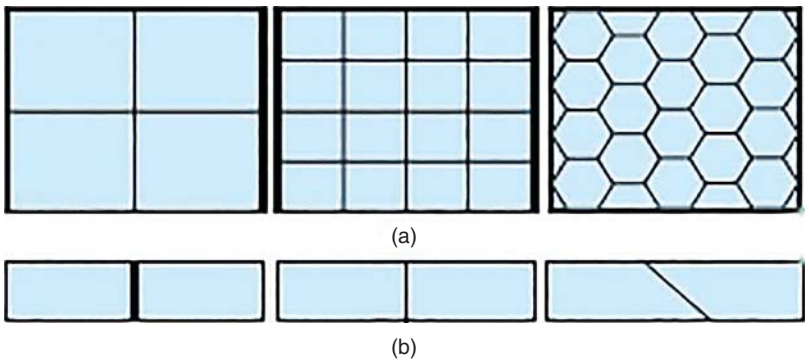

Figure 5.16 Options for structured ceramic top layers on glass backing. (a) Variations of size and shape of ceramic tiles. (b) Different thickness of glue and different edge orientation.

Figure 5.17 Mosaic of transparent Mg–Al spinel tiles with sub-micrometer microstructure on glass backing. Source: Courtesy of T. Hutzler, Fraunhofer Inst.-IKTS Dresden, Germany.

An even more difficult problem are, however, costs associated with the visibility of *the edges* of transparent ceramic tiles. (Figure 5.17). Again, transparent binders that match the refractive index of the ceramic and wet its rough (diamond-cut) edges would make these edges hardly visible. The joining binder has not only to match the high refractive index of the ceramic at some selected wave length – it should also match the ceramic's *dispersion*, from short blue wave lengths through the entire visible spectrum up to near infrared (NIR). Special developments are under way to tackle this issue but they are extremely complex. Unfortunately, even expensive perfect polishing of ceramic tile edges does not lead to full success because, for perpendicular edge-orientation, any local index-difference will make polished edges completely *opaque* by total reflection (see Figure 5.18a). The problem can be solved with optically good results and almost independent of the observation angle by a smart inclination of the polished edges (Figure 5.18b).

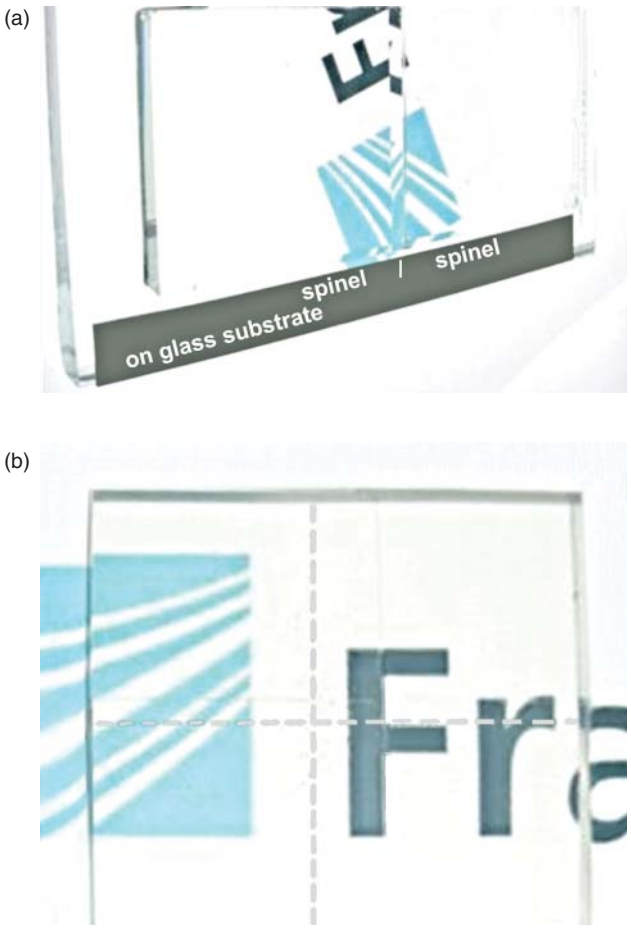

Figure 5.18 Ceramic Mg–Al spinel tiles (refractive index $n = 1.72$) with polished edges of different inclinations bonded by an organic glue with lower index $n = 1.53$. (a) *Perpendicular* edges are visible (opaque!) by total reflection. (b) Straight view on composite of four spinel tiles with almost invisible *inclined* edges (positions indicated by interrupted lines). Source: Courtesy of T. Hutzler, Fraunhofer Inst.-IKTS Dresden, Germany.

In many applications it is, thus, an important question for which type of windows some visibility of edges as e.g. in Figure 5.17 can be tolerated. Figure 5.19 illustrates the excellent residual transparency, after impact, of a spinel/glass composite window made by IKTS with a mosaic front of ceramic tiles that were diamond cut without any polishing of edges.

In finding an optimum assembling design for transparent ceramic-front/glass/polycarbonate (PC) windows, investigations with a high speed laser flash camera were performed by the Fraunhofer Ernst-Mach-Institut at Freiburg/Germany (ball round ammunition 7.62 mm × 51 DM41, $v_{hit} = 833$ m/s) with transparent sub-micrometer Al_2O_3 tiles manufactured by IKTS Dresden/Germany. Figure 5.20 presents a multilayer transparent laminate (2 mm thin sub-µm transparent Al_2O_3 strike-face/glass/PC glass) impacted by ball round projectile 7.62 mm × 51 DM41 ($V_{hit} = 833$ m/s). In (a) a design with 52 kg/m^2 areal weight is illustrated while in (b) the minimal laminate deformation under impact by slightly thicker glass backing (57 kg/m^2) is shown [K57]. Both parts of Figure 5.20 are obtained by superposition of photos taken with time-intervals of $\Delta t = 1$–1.5 ms. Figure 5.20a demonstrates the extreme dynamic load-bearing capacity of the multilayer laminates tested by Fraunhofer. Figure 5.20b describes a successful approach for minimizing the window deformation on impact – a feature of outstanding importance not only for the mechanical safety (including multi-hit stability) but also for the degree by which cracking reduces the residual transparency of the composite window (cp. the different examples of originally transparent laminate windows after impact in Figures 5.19, 5.21 and 5.22b).

5.2.2.3 Materials for Transparent Armor

In the following text, the ceramic materials suitable for transparent armor applications are presented. Glass and single crystals, the main competitors to TCs and organic transparent polymers (which are used together with the TCs in armor kits), are also discussed. In fact glass, as was already discussed earlier, is a competitor (all-glass armor) but also a part of TC including designs.

5.2.2.3.1 Ceramics

Despite the fact that the density of suitable ceramics (3.5–4.0 g/cm^3) is higher than that of glass (2.1–2.5 g/cm^3), the superior mechanical properties of the former allow fabrication of armor windows – especially of the TC-strike-face/glass/polymer configuration – more lightweight and thin than those made of glass. In Figure 5.21 the fact that a TC type window can stop a

(a) (b) (c)

Figure 5.19 Imaging of a transparent spinel (4 mm)/glass (46 mm)/polycarbonate (3 mm) composite window that has stopped an armor-piercing 7.62 mm × 51 AP8 projectile with about 850 m/s; window made by Fraunhofer IKTS Dresden. (a) Impact front. In the foreground of photo (a), the smaller square is an individual several millimeter thick piece of same spinel ($MgAl_2O_4$) ceramic as used for the window. (b) Illustrating the reduced specific weight achieved by the ceramic front, the side view compares the thickness of the tested composite panel (left) with that required for a pure glass laminate stopping the projectile (right). (c) Rear side of panel. See Figures 5.21 and 5.22b for comparing the impact-induced transparency loss here and in other originally transparent laminates.

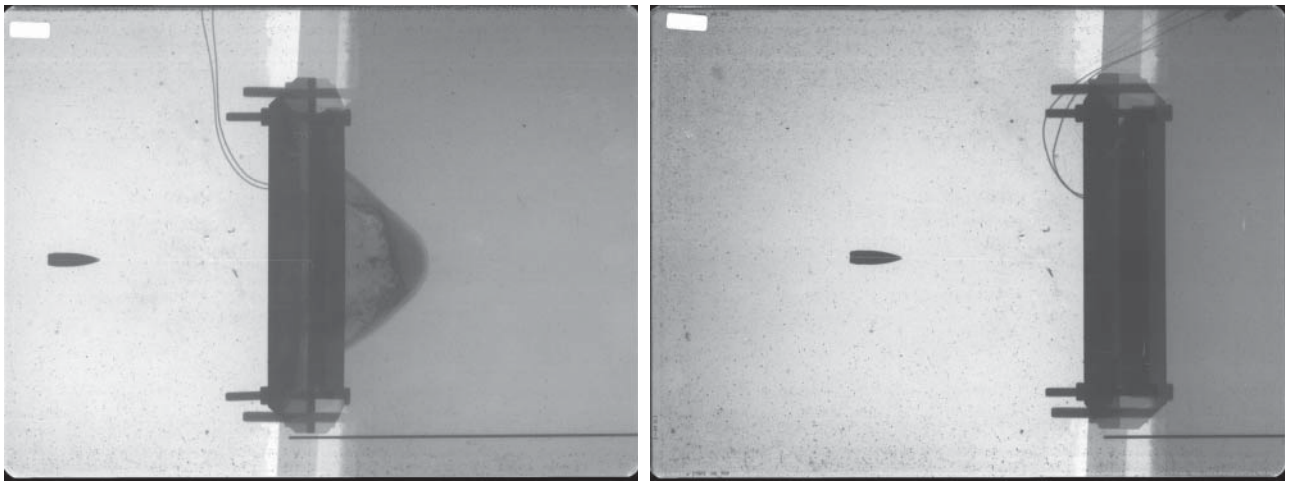

(a) (b)

Figure 5.20 Multilayer transparent laminate (2 mm thin sub-µm transparent Al_2O_3 strike-face /glass/ PC glass) impacted by ball round projectile 7.62 mm x 51 DM41 (V_{hit} = 833 m/s); superposition of laser-flash images with Δt = 1–1.5 ms. (a) Limiting design with 52 kg/m^2 areal weight demonstrating a high dynamic load bearing capacity. (b) Minimal laminate deformation under impact by slightly thicker glass backing (57 kg/m^2). Source: Krell et al. 2007 [K57]. Reproduced with permission from Goeller Verlag.

projectile that penetrates a glass panel twice as thick is illustrated.

If the mechanical properties of TCs are examined, it is easily seen that the TCs, most suitable for armor apps, are $MgAl_2O_4$, γ-AlON and α-Al_2O_3 (the latter at thickness levels <1.5 mm where it is sufficiently transparent [K55]). A number of glass-ceramics are also relevant in this context with, however, a ballistic performance much closer to laminated glasses than competitive with transparent ceramics [K44].

The technologies developed for the fabrication of T-Spinel, T-AlON, and T-Al_2O_3 have been described in Chapter 4. Let us only recall that, from a technical point of view, those technologies allow fabrication of armor

(a) (b)

Figure 5.21 Imaging of armor windows of the all-glass type (panel (a): bullet penetrated) and respectively with a transparent ceramic strike-face (half the thickness of the all-glass type; panel (b): no penetration). Source: Ramisetty et al. 2014 [R7]. Reproduced with permission from John Wiley & Sons.

windows with a size of up to 1 m (e.g. [S46]). Below the types of material used, for transparent armor fabrication, in addition to TCs are presented.

5.2.2.3.2 Single Crystals

Inorganic single crystals are used, for a long time now, by Nature to fabricate transparent segments of bio-armor. For instance, in the opaque, multilayered aragonite ($CaCO_3$ polymorph) made armor, of chitons – a small sea-dwelling mollusque – a large number of "ocelli" made of transparent aligned aragonite crystals exist [L28]. Artificial ones can, lately, also be considered for armor systems of interest to humans.

One of the prominent ones is corundum. Regarding denomination let us note, in passing, that technicians use to call colorless trigonal corundum (α-Al_2O_3) single crystals "sapphire" though in mineralogy sapphire is the Ti and/or Fe doped colored corundum. Corundum (sapphire) is a major competitor for transparent ceramics – because of its excellent mechanical properties and the fact that, lately, it became available at costs similar to that of ceramics and which further drop each year. Technical specifications of the raw powders, used for *crystal* growth, are less severe than in *ceramic* technology, and crystal growth *productivity* was significantly increased since edge-defined film-fed growth (EFG) technology turned able to generate large plates (up to $77 \times 31 \times 1\,cm^3$). In Figure 5.22 [J15] a "sapphire" plate, drawn by an EFG machine, is shown together with a few other plates. EFG is now a mature technology, able to produce quite large amounts of plate per year even though for large sizes the yield in defect-free items is not yet very high; improvements are expected in the near future. The Saint-Gobain owned (now) EFG facility, located in Milford (US), became a commercial supplier of armored windshields and door windows, to the US army, a few years ago. A first contract (valued at 20 million dollars) called for the fabrication of parts suited for an artillery rocket launcher; the number of vehicles concerned was 540. So, at least for now, single-crystal strike-face laminates (layers of glass and PC are included) have some advance – as far as commercialization is concerned – over TCs. Growing chemically more complex single crystals as cubic $MgAl_2O_4$ spinel is more difficult. Pretty large boules with up to 100 mm diameter were grown with Al-rich composition ($MgO{\cdot}3Al_2O_3$) by Saint-Gobain (Milford, NH) and exhibited excellent optical properties (high costs *of the* Mg-source make Al-rich compositions economically interesting). Unfortunately, the hardness of spinel *decreases* with rising Al contents [K40] – with, nevertheless, very promising ballistic results observed with this grade as discussed later. Ballistic tests comparing Al_2O_3 single crystals ("sapphire") with both their *polycrystalline ceramic* counterparts as also with armor *glass* have provided repeated evidence of substantial improvements compared with float glasses: sapphire windows may be addressed as working in the "same league" as the sintered ceramics. Surprisingly Al_2O_3 *single crystals* performed less well in ballistic tests than certain transparent ceramic, sub-micrometer Al_2O_3 grades. And even transparent $MgAl_2O_4$ *spinel* ceramics (*inferior* to sapphire *in all* their mechanical parameters!) exhibit a significantly higher ballistic performance than sapphire plates – cut perpendicular on certain crystallographic directions – in both depth-of-penetration tests (steel-core 7.62 mm × 51 AP projectiles, 850 m/s, table 3 in [K45]) and in tests that measured the residual velocity of bullets after perforation of (sufficiently thin) targets [K47].

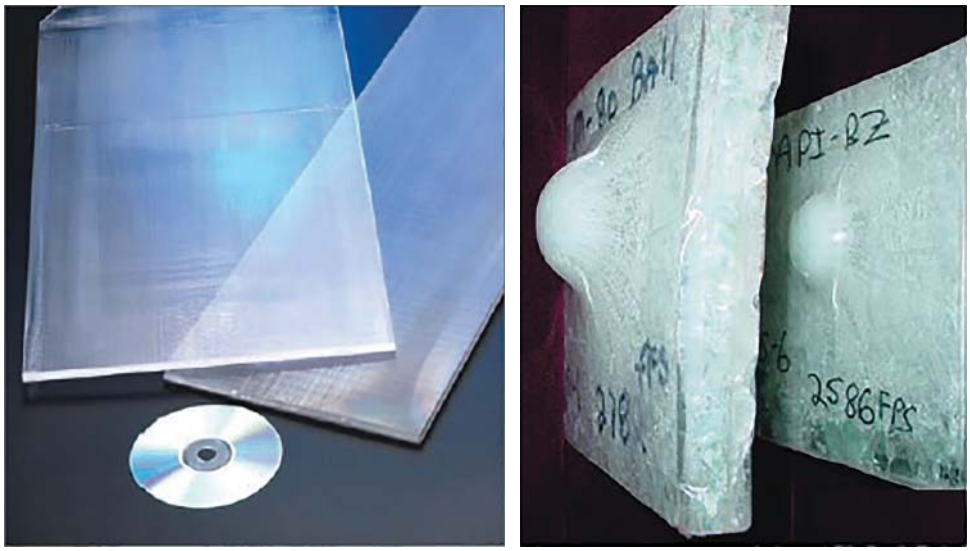

(a) (b)

Figure 5.22 Imaging and ballistic testing of transparent corundum single crystal large plates, fabricated by the EFG technique. (a) As-grown Class 225 (225 × 600 mm²) and Class 300 (305 × 510 mm²) plates. (b) Transparent laminates, after being impacted by an AP projectile (left projectile velocity of 835 m/s and right velocity of 770 m/s). Source: Jones et al. 2006 [J15]. Reproduced with permission from John Wiley & Sons.

In a recent ballistic DoP study (DoP with steel-core 7.62 mm × 51 AP projectiles, 845 m/s), in which corundum and spinel single crystals and ceramics were examined, the spinel single crystal turned out as a ballistic champion [K60] being equaled only by sub-micrometer Al_2O_3 ceramic that showed, however, a lower in-line transparency.

The somewhat less good ballistic performance of sapphire compared with spinel single crystals appears as a consequence of their different crystal structure, which leads among other things, to a different fragmentation pattern. A detailed evaluation of the static (on indentation) and of the dynamic (on projectile impact) fragmentation of *single* and *poly*crystalline (lab-made high-purity, high density) Al_2O_3 tiles provided clear experimental evidence of a significantly higher number of cracks (i.e. *closer* crack *spacing*) in statically or dynamically impacted *sapphire* with less cracking in sub-micrometer alumina ceramics [K45]. In agreement with this observation, at a same time after impact, the high speed record of an about 30% *smaller* average *fragment size* was correlated with visibly less projectile damage caused by *sapphire* – because its smaller fragments are subject to a lower force of inertia, thus decreasing the abrasive effect compared with the effect of (larger) fragments of polycrystalline Al_2O_3 ceramics. The *coarsest* fragments were always produced by the most efficient, ballistic material, viz single crystal spinel.

Looking for an explanation of the intense crack formation with small fragment sizes in impacted sapphire, it appears that the different modes of fragmentation of Al_2O_3 *single crystals* and *ceramics* might be associated with the homogeneity of their microstructure [K47]. Because homogeneity is not perfect, zones differing in strength (or K_{IC}) probably exist within the volume of the tiles. If this is true, the surprisingly weak ballistic resistance of sapphire has to be attributed to its fracture resistance anisotropy: a strong basal plane ($K_{IC}^{(0001)} \sim 7\,\mathrm{MPa}\sqrt{\mathrm{m}}$) exists accompanied by three others, almost orthogonal, exhibiting low toughness ($K_{IC}^{(1012)} \sim 2\,\mathrm{MPa}\sqrt{\mathrm{m}}$). The existence of the mechanic anisotropy described earlier was observed on static indentation as well as during dynamic impact. This anisotropy of sapphire has to be compared with the much more homogenous crack resistance of sintered polycrystalline Al_2O_3 or spinel ceramics with few local variation of their average K_{IC}. No measured data of K_{IC} depending on the orientation of spinel are known from the literature, but with its cubic structure the fracture anisotropy of spinel is probably much weaker compared with trigonal sapphire (mineralogists classify the cleavage of spinel as "indistinct") – with less ease of closely spaced crack formation ending in *coarser* spinel fragments which enhance the abrasive power of this "rubble" acting on the projectile [K47].

5.2.2.3.3 Glass-Ceramics

The glass-ceramics, as plain glasses, can be produced at relatively low cost (while significantly higher than that of simple glass), compared with TCs, in the

form of large, defect-free, straight, or more complex geometry plates [M27]. The amount of suitable (as far as mechanical properties are concerned) crystalline phase, compatible with sufficient transparency, varies with the composition considered and processing used, between 20 and 95 vol%. The fabrication of glass-ceramics, including those transparent, was presented in Sections 3.1.4 and 4.2.11. As the literature [J4] and our own experience [K44] suggest the glass-ceramics exhibit a ballistic resistance somewhat higher than one would expect looking to their properties. The reason(s) for this is not clear (possibly related to the simultaneous presence of phases with different stiffness and of many interfaces); perhaps their fragmentation pattern, different from that of simple glass, is also a factor. But because the demonstrated practical usefulness of the transparent glass-ceramic (TGCs) here, a short presentation of the transparent glass-ceramics suitable for armor applications is made. As it was described in Section 4.2.11, the number of crystalline phases that could be grown in the various mother-glasses, so as not to hinder transparency, is rather low. Some of these T-GCs performed better (not dramatically but yet interestingly so) than monolithic glass, in ballistic tests, as long as projectiles of low to moderate penetration abilities were used. There is no simple correlation between the mechanical properties of the crystalline component (or the glassy matrix) or even its content and the ballistic performance. This is so because the influence of additional factors – like grain size, morphology, nature of the glass/crystal interface, etc. – needs to be convoluted with that of those previously named, in order to estimate the ballistic worth of a TGC. For instance, it was established [B65] that T-GCs derived from the SiO_2–Al_2O_3–Li_2O basic system, based on $Li_2O{\cdot}2SiO_2$ (with, probably α-Quartz, as secondary crystalline phase) exhibit a relative (soda-lime glass taken as unity) ballistic index of 1.17–1.20. The transmission is good despite the large size ~0.7 μm of the crystals, probably due to "*n*" matching (glass/crystal). The same group at GEC Alstom determined that strengthening, by surface ionic exchange ($K^+ \leftrightarrow Na^+$), improved the performance of such armor. By raising the Al_2O_3 content from around 4.5% (hosts that generate Li di-silicate) to 25–29%, T-GCs exhibiting Knoop hardness (HK) 0.5 values of up to 11.5 GPa were obtained. Work done at Schott determined that materials (especially the ROBAX grades), which generate stuffed β-Quartz-like solid solutions [βQ_{ss} (Li^+, Zn^{2+}, Al^{3+})] are also usable as transparent armor. A useful feature, of the ROBAX, is the quite high transparency owed, in part, to the closeness of "*n*" of the residual glass and the crystal produced by ceramming. The more complex (includes also $AlPO_4$ units) ZERODUR (developed for telescopes) material is not less useful (it has very small, ~100 nm, crystallites); its transparency is excellent. The Japanese (Nippon Electric Glass) developed the transparent NEOCERAM (grade N-0), which is slightly superior, to the German products, as far as the hardness is concerned. Our own work in this domain (unpublished) showed that interesting materials can be derived from glasses with basic compositions located in the ZnO–Al_2O_3–SiO_2 system. Using suitable $TiO_2 + ZrO_2$ nucleator packages and one-stage, very long dwell, low (800–820 °C range) temperature ceramming schedules, glass-ceramics including 30–35% crystalline phases (one of them cubic) were developed. The low crystal size (10–15 nm) ensures reasonable transparency. The density of parts lays in the 2.5–2.8 g/cm^3 range (viz close to that of glasses and significantly under the that of the relevant TCs (3.58–4.0 g/cm^3 domain)). It was observed that hardness was higher when the crystalline fraction was comprised of a mixture of $ZnOAl_2O_3$ (Gahnite) and βQ_{ss} (Zn^{2+}, Al^{3+}). The best materials showed Vickers hardness (HV1) values in the 8.0–8.5 GPa range (most armor relevant TGCs exhibit HV1 values in the 5.8–7.5 GPa). The transversal rupture strength (TRS) values were quite modest (90–120 MPa). A light coloration (yellow to orange domain) was always present but transmission values around 85% ($t = 5$ mm), in the 600–800 nm domain, can be easily achieved.

As we see the glass-ceramics – while exhibiting certain advantages regarding absence of scattering, cost, and fabrication ease of large size (curved if necessary) parts, over ceramics – are, from the point of view of their ballistic efficiency, quite close to glasses (improvements of no more than 20% they may bring to the ballistic performance) and significantly below the TCs. Such levels of performance improvement, while not seeming impressive, are commercially relevant. Thus, for more than 20 years now, transparent armor, including glass-ceramics, is used by military and civilian vehicles on a quite large scale, bringing considerable revenue to the manufacturers. The TGC layers (may attain 15 mm each) are included in laminates, which contain also borosilicate and PC (spall collector) layers [W19]; a top supplier is Schott USA. Such laminates in order to stop AP projectiles (medium aggressivity; say, a 0.3 caliber AP-M2 projectile flying at 950 m/s out of the muzzle) exhibit thickness values in the 80–110 mm. Let us recall that TC strike-face (thickness around 5 mm) including similar laminates may reduce the thickness to 40–50 mm. However, for the moment, no manufacturer can offer such products at a price and volume enticing armies procurement departments to disburse the kind of money spent on solutions based on TGC containing laminates.

The properties of some popular transparent glass-ceramics usable in armor applications are collected in Table 5.2.

Table 5.2 Properties of some transparent glass-ceramics usable in armor applications.

Property	Density (g cm^{-3})	*E* (GPa)	HV03 (GPa)	TRS (MPa)	*T* at *t* = 3 mm (%)
Value	2.5–2.8	70–100	5.5–9.0	80–120	75–90

5.2.2.3.4 *Glasses*

The advantages of glass, over crystalline competitors, in the armor domain are as follows: a high transparency (to a large extent owed to low "*n*" values; $n < 1.5$ and lack of voids), low cost and the fact that large size, even non-planar components, can be made with relative ease; their low density (2.1–2.55 g/cm^3) compared with that of the relevant ceramics (3.55–4.00 g/cm^3) is also an advantage. The one but critical disadvantage is their less good mechanical properties. In Table 5.3 the properties of a few glasses used in transparent armor kits are presented.

The glass most widely used for armor is the common soda-lime glass, produced as glazing panes (for the building industry) by the float technique. More expensive, but exhibiting lower density (2.2 vs. 2.53 g/cm^3) and somewhat better mechanical properties are certain borosilicate type glasses like the Borofloat 33 manufactured by Schott. Perforation tests preformed by Strassburger at Fraunhofer EMI in Freiburg (Germany) revealed a difference: AP projectiles with 850 m/s impact velocity were stopped by about 137 kg/m^2 of borosilicate laminate whereas the soda-lime reference had to be as heavy as about 165 kg/m^2 for the same effect [K44].

Organic glasses – with specific properties, different from those of inorganic ones – can be fabricated based on organic polymer's processing [F9]. The so-called PC glass, used for backing, is produced by reacting a bisphenol's Na salt with phosgene. It is highly transparent and has significant tensile strength. Another organic material, sometimes used, is the poly(methyl-methacrylate) (PMMA), widely known as Plexiglass or Perspex. Polyurethane (PU) made transparent layers is the most popular material used for gluing the inorganic layers together.

In all-glass armor kits, a number of inorganic glass plates are bonded with PU [L38] (when plies differing in composition are used these organic interlayers also accommodates differences in the expansion coefficient), while the last layer is one made of PC; the latter acts both as a spall shield and, owing to its ductility, as (low efficiency) absorber of energy. The thickness of the PC layers used in such a role has to be optimized; too thick layers tend to undergo brittle failure.

Table 5.3 Properties of some armor glasses.

Property	Density (g cm^{-3})	*E* (GPa)	HV03 (GPa)	TRS (MPa)	*n*	*T* at *t* = 3 mm (%)
Value	2.20–2.45	45–72	4.0–8.8	40–55	1.47–1.52	90–93

The organic polymer-based glasses differ in behavior, owing to a different structure, from their inorganic counterparts; marked differences exist also within the organic materials family due to the structural differences between the base polymers. The PC glasses basic unit is the bisphenol-A molecule. The ductility of the material is associated to motions, under straining, of the main chains; these motions can occur even under the high-rate straining present at high velocity impacts, thus allowing a relatively efficient energy dissipation. In PMMA only the side chain (carbonyl + ester group) can easily move, when the system is strained. As a result the PMMA is brittle, as opposed to PC, and much more strain rate sensitive; the side groups are frozen into place when the strain rate exceeds a certain, quite low, limit [P12]. Thus, PMMA is not useful as spall-collecting energy absorbing back-layer. Its higher rigidity, however, makes it useful in layers close to the strike-face. Indeed, testing by Patel P. et al. showed the PMMA may replace part of the inorganic glass-layers – in all-glass kits – reducing the areal density and improving multi-hit abilities. The latter aspect is related to the viscoelasticity of the PMMA. Materials like PMMA exhibit a viscoelastic behavior much more pronounced than that of inorganic glasses. This also means that at high strain rates the brittle failure changes to a mode in which massive, but localized, cracking occurs [P12]. Geometrical constraint may enhance the drive toward localized failure by augmenting bending stiffness; thick mono-block plies of PMMA are more efficient than a set of thin layers of the same thickness.

5.2.2.4 Examples of Transparent Ceramics Armor Applications

Personnel armor includes only face shields as transparent sectors. Usually these are made of lightweight polymers because the threats considered are of low energy (stones, knives, and similar). However, in some cases, like improvised explosive devices neutralization or urban rioting in which firearms may be used, more efficient armor, like that provided by transparent glass-ceramic or ceramic items, is necessary.

Windows for civilian VIP cars, military armored cars, or tanks for fixed wing or helicopter types aircraft laser cannon igniters are the main market the for TC-based armor. Also, in the case of naval vessels protection of certain IR, operating sensors or emitters of laser based weapons require transparent ceramic-based windows.

5.2.3 Infrared Windows

The main inspiration source for Section 5.2.3 was the excellent book authored by D.C Harris [H15].

5.2.3.1 The Infrared Region

The IR region of the EMR spectrum starts at 0.70 μm and extends to $\lambda = 1000$ μm (30 GHz). It is divided in three sub-regions: NIR, mid infrared (MIR), and far infrared (FIR). The limits of the sub-regions are differently set by different communities of users. For instance, according to ISO 20473 NIR extends from 0.7 to 3.0 μm, MIR from 3.0 to 50 μm, and FIR from 50 to 1000 μm. For the applications where TCs are relevant, we will consider a segmentation in which NIR = 0.7–3.0 μm, MIR = 3.0–25.0 μm, and FIR = 25.0–1000 μm.

It is important to recall that loss of EMR intensity owed to scattering and (mostly molecular) absorption, occurring in air, limits good atmospheric transmission (within the NIR + MIR domain) to the 3–5 μm (called mid-wave) and 8–14 (called long wave) windows; (between 1.6 and 1.8 μm and between 1.9 and 2.85 μm some narrow windows of reasonable transmission also exist). Molecules like O_3, H_2O, and CO_2 are the principal absorbers, operating in NIR and MIR. Over 15 μm the main air constituents (N_2 and O_2) do not exhibit strong absorption but other molecules like CO_2 are still active. The distribution of windows in the 15 μm to 1 mm range is not well known. Luckily in the FIR domain the applications number is – compared with NIR + MIR – much lower (mostly spectroscopy, with relevance in astronomy); this is fortunate because the number of robust TCs on offer, for this spectral region, is also low.

Owing to the aforementioned, most IR emitters and sensors, used in devices, are developed to work in the 3–5 μm and respectively 8–14 μm domains. Depending on the nature of the devices, one or the other of the frequency ranges are more useful. The long wavelength range permits collection of more IR energy at room temperature (RT) and is more tolerant with window emission; the mid-wave one allows higher sensitivity at higher temperatures. As we shall see certain ceramics may work with both windows; they are called "two color" by most. There is interest also in so-called dual materials, transmissive in both an IR window and in the low-frequency microwaves (MW) region. In the MW and radio regions, EMR absorption is also caused by dipole–dipole or dipole multi-pole type interactions but the relevant dipoles are different from those operating in the near ultraviolet subdomain (NUV-IR) region. For many applications materials transparent in both IR and the MW regions are needed. Here the MW frequency range is not covered.

5.2.3.2 Background Regarding Heavy Duty Windows

Detection of the IR emission of various sources is useful for many practical purposes. It is relevant for night vision devices, furnace control and laser windows, spectrophotometers, and others. For instance, certain types of missiles carry sensors for the IR radiation emitted by the engines of enemy vehicles. Most of the sensors used for IR signals detection need to be protected from the environment. For instance, those mounted on missiles are carried at speeds varying from slightly subsonic to ~6 Mach; intercontinental ballistic missiles (ICBMs) may attain, though, 10+ Mach.

The sensor-protective parts have to allow passing of IR radiation, coming from the target, especially in the domains corresponding to the atmospheric windows. From the previous, it results that components we can call heavy duty (owing to the strong thermomechanical stresses they are subjected to) IR windows are required for most of such devices. The main tasks of the IR windows are to maintain integrity, during service, provide a good transmission of the radiation the sensors use in their work, and contribute only low amounts of their own emission at the relevant frequencies. TCs can provide such components.

5.2.3.2.1 Threats to Missile IR Domes: Material Characteristics Relevant for Their Protection

5.2.3.2.1.1 Impact of Particulates (Erosion)

One of the most important threats, an IR dome faces, is the impact of particulates like: rain drops (or ice particles), bugs, or sand; acids or other chemicals also present in the atmosphere may also etch the surface, reducing mechanical resistance. The high speed impact of particles, similar to a certain extent to that of bullets on armor plates, can easily produce significant local damage in the crack-prone brittle ceramics. Accumulation of large numbers of impact points may impair the optical properties and the physical integrity of the dome. Material is removed from the ceramic part and cracking may – in certain cases – be severe enough to cause breaking. In Figure 5.23 [H15] the damage produced by 2 mm raindrop (impact speed 540 m/s) is shown.

The effect of multiple particles impact on ceramic parts is called "erosion" [F7]. In the case of liquid drops, there is no penetration (as opposed to the attack of bullets on armor). The damage is produced by the intermediation of mechanical waves launched into the ceramic [T16]. Like in the case of ballistic events, the liquid drops introduce a compression wave followed by a slower shear wave. The tensile reflected wave interacts with the compressive wave and may catch even the Rayleigh lateral surface wave (dependent on thickness), enhancing damage. The Rayleigh wave is shallower, but its amplitude attenuates only after longer travels (attenuation $\sim\frac{1}{v_r}$)

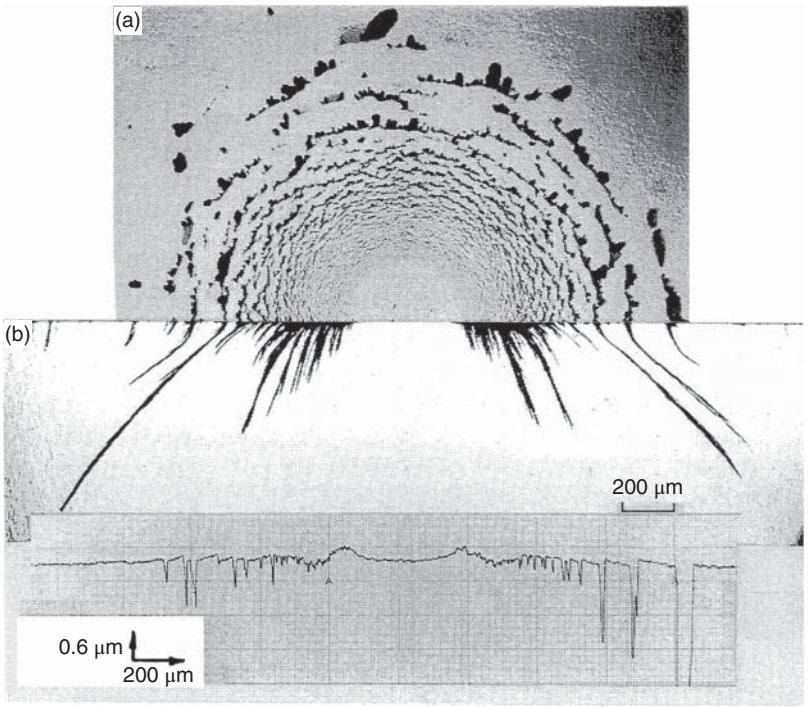

Figure 5.23 Crater and cracks produced by the impact (at 540 m/s) of a 2.3 mm rain drop on a ZnS plate; panel (a) shows a top view of the crater, the middle one is a cross-sectional view of the crater and panel (b) shows a profilometer trace showing the surface profile of the plate. Source: Harris 1999 [H15]. Reproduced with permission from SPIE Optical Eng. Press.

than the compressive and shear waves going out from the impact point. An important parameter regarding rain erosion is the threshold velocity for fracture, that is for loss of mechanical strength. Oxide ceramics based domes exhibit threshold velocities, for fracture, in the 400–530 m/s range, while non-oxides (like ZnS, ZnSe, or Si) have values <250 m/s.

A classification of materials based on their resistance to erosion shows the oxides as being by far superior to fluorides or chalcogenides. The optical transmission loss, owed to erosion effects, is another practically essential parameter. It is a function of factors like drop diameter, number of impacts (liquid water content of the rain field), pre-existing stress, drop velocity, or time of exposure. Mass loss is also dependent on impact velocity and exposure time. Erosion by solid particles, mostly quartz, causes more severe mass (and, as a consequence, optimal transmission) loss than liquid drops. The difference between oxides and other materials resistance to sand erosion is more marked than that to liquid drops attack; similar test conditions produce a rate of 20 g/kg in the case of ZnS and only 83 mg/kg in that sapphire. High hardness seems to be of considerable help in withstanding sand erosion. A ceramic having a sand eroded external surface may lose up to 70% of its strength; such erosion also makes the part susceptible to more severe damage by a subsequent raindrops attack than one opposing a pristine surface. The flaws such erosion produces are stress concentrators that act as fracture initiators [H25].

5.2.3.2.1.2 Thermal Shock

Friction with air – leading to heating – is significant at the high velocities attained by most missile types. The heating is both fast and non-uniform within the volume of the ceramic nose. As a consequence the thermal expansion in different regions of the nose varies. This creates mechanical stress that, if too large, leads the ceramic to its typical response in such conditions: catastrophic, rapid failure. The effect of fast and **non-uniform** heating is called "thermal shock." The fracture pattern in a spinel nose produced by thermal shock is given in Figure 5.24 [H15].

Guidance on the resistance to thermal shock can be attained calculating the figure of merit "R" introduced by Hasselman:

$$R = \frac{S(1-\nu)}{\alpha E} \tag{5.7}$$

where "S" is the transversal rupture strength (TRS in general abbreviations) of the material and "ν" is the Poisson coefficient.

The relationship between the coefficient "R" (an expression of resistance to thermal shock) and the factors influencing the process differs as a function of heat transfer conditions. The rate of thermal diffusion is described by the Biot number β (no units) with: $\beta = \frac{th}{k}$ t = thickness; h = heat transfer coefficient (W/m^2 K); k = thermal conductivity (W/m K).

A low β means fast thermal transfer and such conditions increase R. For fast heating (i.e. idle heat transfer) $\beta \gg 1$:

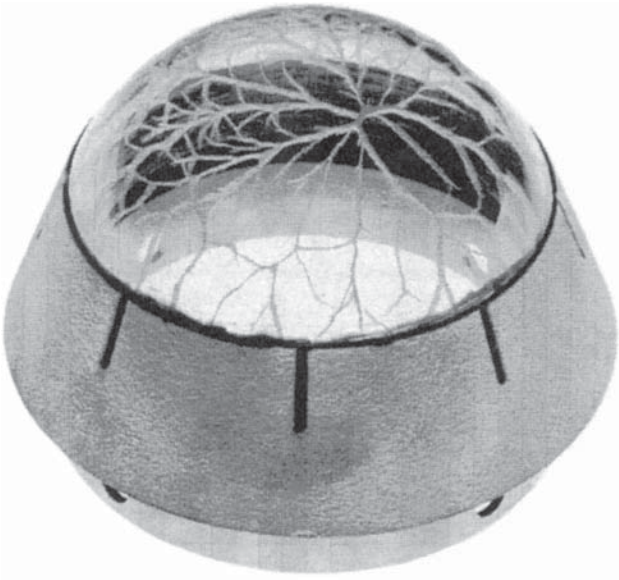

Figure 5.24 Pattern of the fracture system produced, on a spinel dome, by its exposure to a fast air stream (Mach 4.6), which applied a 6.2 MPa pressure at a temperature of 1390 K. Source: Harris 1999 [H15]. Reproduced with permission from SPIE Optical Eng. Press.

For $\beta \ll 1$ the parameter used, R', is a modified version of "R":

$$R' = \frac{S(1-\nu)k}{\alpha E} \tag{5.8}$$

An important value that can be calculated (with certain difficulties) [K26] is the maximal speed (in Mach units) an *IR* nose may reach, at a given altitude, without failure due to thermal shock.

5.2.3.3 Applications of infrared transparent ceramics

The main and most well-known app for IR–TCs is that of IR sensors protection domes [F13, H30]. Such domes (hemispheric, conic, or pyramidal) form the nose of missiles. The hemispherical domes have the advantage of being less sensitive to incident radiation's angle; the conic ones are preferable from an aerodynamic point of view. Windows for airborne laser ($\lambda = 1.55$ μm) based communication systems are another application likely to grow in importance in the near future. Similar components are used in reconnaissance systems, with imaging capabilities, which protect sensors working in IR and also VIS. Other items, the applications list includes, are windows for night vision devices, windows for cannon igniters, laser weapons, targeting devices for tanks, CO_2 lasers for cutting tools, and laser "radar" (in fact light detection and ranging [LIDAR]), mirrors for IR telescopes, optical parts (prisms, lenses, gradient-index [GRIN] systems), cook-stove tops, windows for cryo-vacuum chambers or filters for therapeutic lamps. Many hosts of lasing cations (RE^+ and/or TM^+) also need transparency in the IR (mostly NIR segment) because the dopants emit in this domain. Lasing systems related components are discussed in Section 5.2.9.1. Let us now shortly describe the some applications listed earlier.

Figure 5.25 IR sensors protective dome made from alumina. Source: Parish and Pascucci 2009 [P9]. Reproduced with permission from SPIE Optical Eng. Press.

5.2.3.3.1 Missile Domes and Windows for Aircraft-Sensor Protection

Such items need to ensure undistorted transmission of EMR (with frequencies located in the IR or IR + other domains) and protect various types of sensor. The damaging factors and their "work conditions" threatening the integrity and performance of the items discussed here, differ, to a significant extent, from those relevant for armor. Missiles (or aircraft) and armored vehicles have travel trajectories (also evaluate at different altitudes) and speed specific to each group; the former group travels at high altitude and much higher speed – which may approach 6 Mach – than the ground vehicles. As we shall see in the following, as a result the requirements as far as properties go, in the case of TCs mounted on flying objects, differ from those encountered when armor was discussed. In Figure 5.25 [P9] a missile nose made of alumina is shown while in Figure 5.26 one made of spinel is illustrated.

The IR (or IR + other EMR domains; e.g. $\lambda = 0.65$ and 3.1 μm) windows have to be, in some cases, very large. For instance, those needed to protect the electrooptic sensors mounted on naval vessels, like the American DDG 1000, require panes of 48×68 cm^2 area [P9].

5.2.3.3.2 Laser Windows: Igniters, Cutting Tools, LIDARs

5.2.3.3.2.1 Igniters

Ignition of cannon fire by the aid of Nd:YAG (or Er:YAG or glass) solid-state lasers operating at 1064 nm is under study. The window through which the laser beam is

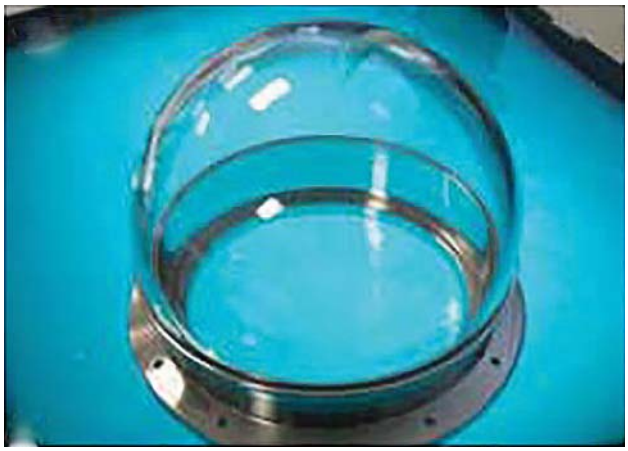

Figure 5.26 IR sensors protective dome made of spinel ceramic.

admitted into the combustion has to meet stringent optical and survival related specifications. For instance, the divergence of the laser beam must stay under 10 mrad. The window's integrity is a problem owing to the harsh environment in the combustion zone (temperature on the window surface has 0.1 second spikes of up to 800–1000 °C [2000 °C] flames) and combustion products may exert pressures of up to 400 MPa. Thus, resistance to thermal shock (for instance, an cannon mounted on Apache choppers fires up to 625 rounds/min) and chemical attack are required. Glasses and sapphire windows have been tested with mixed success. Laser igniters developed for car engines (see Section 5.2.9.1) also need admission windows transparent in the NIR, where the Nd^{3+}:YAG laser operates.

5.2.3.3.2.2 LIDAR-Windows

The LIDAR devices, also called "laser radar," work, usually, at λ around 10 µm (NIR). Suitable are especially CO_2 lasers – used, among other devices, also in cutting tools – which operate at $\lambda = 10.6$ µm. TCs, able to function as windows in such systems, exist but things are complicated by their, modest thermomechanical properties, not optimal for conferring resistance to illumination with these laser sources of quite high power.

5.2.3.3.3 Windows for Vacuum Systems

The main engineering challenge, here, is the large size required for some devices. In Figure 5.27 a large window of a cryo-vacuum chamber chemical vapor deposition (CVD-ZnSe) is shown.

The factors that need be considered in the definition of performance estimating figures of merit, for IR components, are discussed in detail in the basic text, regarding IR ceramics, authored by D.C. Harris [H15].

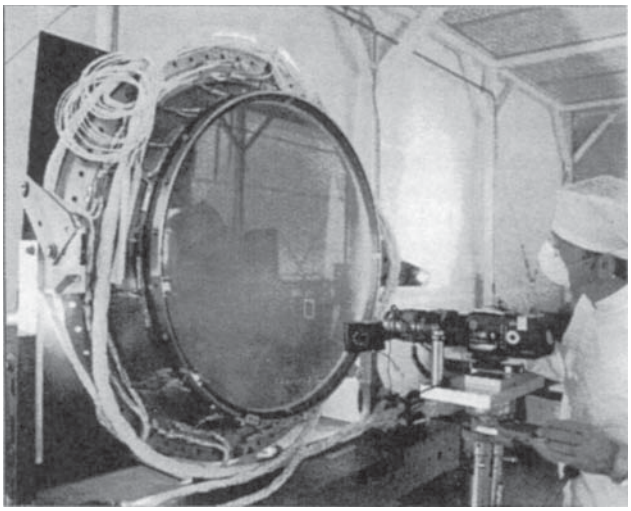

Figure 5.27 Very large cryo-vacuum chamber window, made of transparent ZnSe-fabricated by CVD. Source: Harris 1999 [H15]. Reproduced with permission from SPIE Optical Eng. Press.

5.2.3.4 Ceramic Materials Optimal for the Various IR Windows Applications

Examining the requirements, posed to the IR windows by different applications, together with the properties of available TCs (see Chapter 4, tables), one can select the types of TC most suitable. For instance, it is clear that the thermomechanical behavior, requested for windows installed on flying objects, makes Mg-spinel, the AlON spinel like material, and also thin ceramic Al_2O_3 the best suited. The fact that the latter can be used at all is remarkable considering its non-cubic (trigonal) lattice. In Figure 4.34a the transmission in IR of T-Al_2O_3 disks (CeraLumina products of CeraNova) is shown. Such parts attain a hardness $HV = 22.8$ GPa, high strength, and failure threshold velocity (under water drop impacts) comparable with that of sapphire; ogive geometry is allowed by the powder sintering based fab technology. The initial beneficiary considered by the developers was the AIM-9X Sidewinder, American, missile. In Figure 5.25 two domes, usable for the 3–5 µm range, were illustrated. For the 8–14 µm window the only robust (oxide) material usable is yttria. In practice less robust materials, but transparent within a larger segment of the window, like MgF_2 or ZnS (uncoated ZnSe is too weak for outdoor uses), are used. While currently not commercially available, CVD diamond domes can be produced (see Figure 5.28); the combination of properties the material offers is, of course, difficult to meet by any other competitor materials.

For LIDARs CVD diamond and ZnSe are used. The same materials are, lately, starting to replace cheap but short service time acrylic glasses as windows for the CO_2 lasers used in cutting tools. ZnSe was used also for large

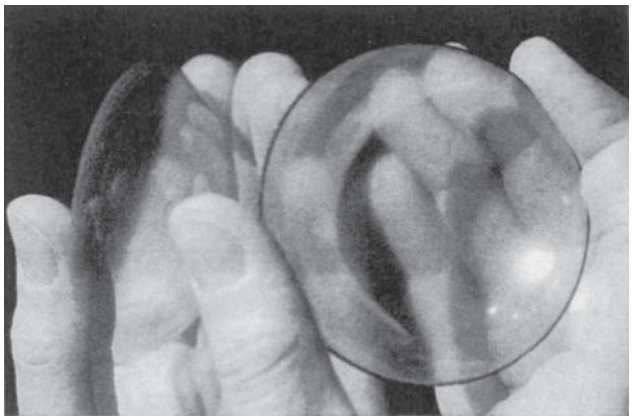

Figure 5.28 Polished polycrystalline diamond dome fabricated by CVD (t = 1 mm). Source: Harris 1999 [H15]. Reproduced with permission from SPIE Optical Eng. Press.

furnace windows. For laser ignitors, tests suggest AlON as a promising option, offering longer endurance than alternative non-ceramic materials. This material is also very useful for the fabrication of optical components, like prisms, lenses, and GRIN (optics) multilayers.

5.2.3.4.1 Competitor Materials: Glasses and Single Crystals

Examination of properties reveals that certain single-crystals and glasses [M32] are suitable, as far as transmission is concerned, for applications in the IR, constituting thus serious competition for the IR ceramics.

5.2.3.4.2 Glasses

The usual silicate glasses, which contain large amounts of SiO_2 (>70%), have an early IR cutoff edge because the first (and even the second) overtone of the Si–O–Si fundamental stretching vibration (9.1 μm) are intense enough to cause significant IR energy absorption down to ~4.5 μm. In conventional (Si–Ca–Na) glass the strong absorption of OH^- and Fe^{2+} impurities (band at 1.05 μm) further reduce the window's width (fundamental vibration, of the OH ions is located at 2.73 μm and a strong first overtone lies at 1.38 μm). The effect of the hydroxyl ions can be reduced in pure silica glass, so that such a material exhibits reasonable transparency up to ~3.5 μm; its thermomechanical properties are the best glass can offer. Silicate glasses including large amounts of cations with lower field strength (weaker bonds with the O^{2-}) exhibit IR cutoff edges shifted to higher wavelengths. Various glasses, not base on SiO_2 as the glass-former are useful in IR applications. For instance, it is possible to use the "conditional network former" abilities of Al^{3+}. Alumina is a conditional network former because while pure Al_2O_3 cannot be obtained as glass (at normal cooling rates), compositions in which very low amounts of SiO_2 or other oxides are added to alumina allow glass formation. In such glasses where the silicate lattice vibrations are massively reduced in intensity or eliminated (being substituted with that of AlO_6 groups; fundamental vibrations at ~12 μm), the cutoff is shifted by up to 1 μm in a bathochrome direction. One such glass family is that of calcium aluminates, which was used for the domes of the Redeye missile (Corning 975B) [D22]. However, such glasses have poor chemical stability and moderate thermomechanical properties, not being a strong competitor for IR ceramics. The expensive germanate glasses (GeO_2 glass former; hardness up to 5 GPa, softening point over 600 °C and $\alpha \sim 6 \times 10^{-6}$ °C^{-1}) have been used for the Stringer Port missile domes and have a cutoff at ~6 μm. Certain glass-ceramics derived from germanate glasses show an α reduced to 4.3×10^{-6} °C^{-1} and a HK 1 of ~6 GPa. As far as transmission range is concerned, glasses based on lead and bismuth oxides (conditional glass-formers) allow cutoff λ shifting to 8 or even 9 μm (Bi–Pb–Cd system). Mechanical properties are not good, with hardness lower than 2 GPa, expansion coefficients of $\sim 10 \times 10^{-6}$ °C^{-1}; chemical stability is low and avoidance of fabrication induced scattering centers – very difficult. Such materials are not suitable for applications where arduous conditions exist. Some oxynitride glasses (strong VIS absorption) exhibit better properties than silica glass (and cutoff at ~5.5 μm for compositions of the La–Si–O–N [18% N] system), but are very difficult to process in complex shape and/or large size parts. Fluoride glasses are also weak materials, so that they cannot compete with TCs in aerospace apps, but exhibit wide IR windows, which make them useful in less demanding conditions. The compositions most suitable for practical use are located in systems based on ZrF_4 or HfF_4 as formers; cutoffs in the 9–9.5 μm range. Softening temperatures are under 300 °C and thermal shock resistance minimal. Some compositions resisting reasonably well weather attack have been developed. The chalcogenide glasses are of interest for the 8–12 μm window, where most of the other candidates, including ceramics, tent to exhibit poor non-optical properties. Glasses including S (like As_2S_3) have windows in the 1–10 μm (the high energy windows edge, owing to the small band gaps, is located also in the IR), those based on Se – in the 1–20 μm range, while the Te containing materials extend their window to 30 μm. Avoiding oxide contamination is difficult; α is in the $13–25 \times 10^{-6}$ °C^{-1} range and hardness <1.5 GPa. The most interesting systems are S–As–Te, S–Ge–As–Te, and Ge–P–S.

5.2.3.4.3 Single Crystals

A number of single crystals also compete with the ceramics in IR applications – as we have seen in the case of armor. For the 3–5 μm range, the prominent one is the

corundum (α-Al_2O_3), while for the second window the most useful are Si, Ge, GaAs, GaP, and also CaF_2, NaCl, or KBr.

5.2.3.4.4 Sapphire

Owing to its excellent thermomechanical properties "sapphire" (in fact corundum as we detailed when talking about armor) is used for parts, which need to operate in demanding conditions. The "EFG" crystal growing technique was first used for IR domes fabrication; it was already mentioned in the section dealing with armor because, after suitable adaptation, it allows now also the drawing of large plates. Other methods are also used to grow large single crystals from which domes or windows are cut. For sapphire, while the Verneuil method was used a lot in the past, the currently most popular method (besides EFG) is the heat exchanger method (HEM) [H15]; it allows fab of large size and excellent optical quality boules. The entire charge solidifies over a few days and then annealing, close to the melting point, is applied to relieve residual stress. Boules having a diameter of 35 cm are routinely obtained and development of equipment for 50–75 cm parts are underway. The sapphire can be used for high power laser windows, domes, and windows for IR sensors mounted on aircraft. For zero birefringence (0001) oriented boules are needed, but growth in this orientation is difficult. From more easily grown $(11\bar{2}0)$ or $(10\bar{1}0)$ oriented boules, one can reduce birefringence by fabricating components that are perpendicular to the growth axis.

5.2.3.4.5 Crystals for the 8–12 µm Window

GaAs is mostly fabricated by a horizontal variant of the Stockbarger–Bridgman technique, while large GaP windows (ϕ = 25 cm) can be grown by the Czochralski method; Si is produced mostly by the float-zone technique.

5.2.3.5 Radomes

As mentioned earlier ceramics transparent in the MW region are not treated here. Let us, however, note in passing that such domes have the same tasks as the IR ones but they protect sensors or antennas operating in the microwave region. Large landlocked radomes also exist, but here we are interested only in smaller units mounted on flying vehicles. The most popular missile radomes are made by slip-casting and sintering amorphous silica powders, better erosion resistance is obtained by replacing silica with cordierite ($2MgO{\cdot}2Al_2O_3{\cdot}5SiO_2$) glass-ceramics (see Figure 5.29).

For the radomes, a low dielectric constant ($\varepsilon_r \approx 4.0$ for silica) and loss tangent are desired. Spinel and AlON, with ε_r values of 8–10, are among the IR dome materials, which may be considered for the production of dual IR-MW domes.

Figure 5.29 Radome (transparent to MW range radiation) made of cordierite crystals based glass-ceramic at ICSI, Haifa.

5.2.4 Transparent Ceramics for Design, Decorative Use, and Jewelry

Numerous "sky walk" constructions have attracted countless visitors for the past decade. These transparent walkways (e.g. Figure 5.30a) are made of laminated glass that has to be pretty thick because of the comparably low strength of glass. A key problem is the low scratch resistance, which deteriorates the optical performance of the glassy floor with time, and special measures as allowing access only with special textile shoes (Figure 5.30b) are not able to keep off the impact of sandy and rocky particles from the nature, transported by the winds. Obviously, front layers of a transparent ceramic with high hardness, fracture toughness, and (thus) scratch resistance, similar to the mosaic design of transparent armor windows would substantially extend the life-time of these exciting and expensive constructions. Regarding the different mechanical properties of fully-transparent ceramics – as well as the availability of the requested raw powders and their prices – transparent spinel appears as a promising candidate for future improvements in this area.

The high scratch resistance of ceramic surfaces compared with glass and the availability of *colored* ceramics may also be used for other decorative elements in the inner architecture of housing concepts. Figure 5.31 shows

(a) (b)

Figure 5.30 Grand Canyon Skywalk imaging. (a) Laminated glass floor. Source: Photo by Aerographics. Reproduced with permission from Grand Canyon Resort Corp. (b) Access with special shoes only. Source: Photo by Madison Kirkman. Photography reproduced with permission from Grand Canyon Resort Corp.

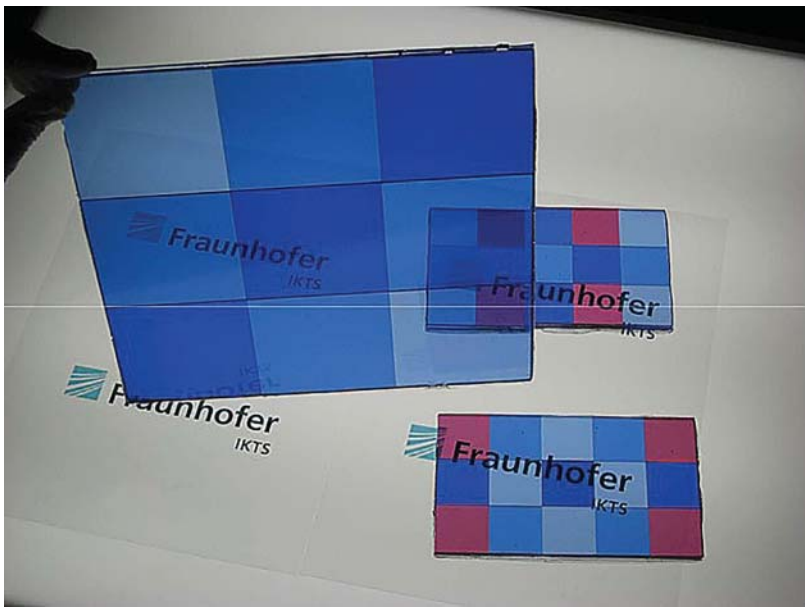

Figure 5.31 Composite windows made of fully-transparent colored tiles (each about $85 \times 85\ mm^2$) of sintered spinel ceramic. Source: Courtesy of T. Hutzler, Fraunhofer-IKTS Dresden.

an example of a composite window that consists of colored fully-transparent spinel tiles.

The feasibility of large dimensions and specific manufacturing costs *per kilogram* are less important for premium jewelry, watches, fashion, and home accessories: here, the main factor in the figure of merit is the optical appearance. A second desired feature is scratch resistance. TC or single-crystal based items, in this field, can improve both appearance and scratch resistance compared with the situation in which simple

Figure 5.32 Cubic zirconia single crystal, ground and polished as a brilliant (diamond) imitate. Source: https://en.wikipedia.org/wiki/Cubic_zirconia. Licenced under CC BY SA 3.0.

glasses are used. Regarding appearance this is less so when comparison is made with the lead containing "crystal" (a misnomer) glasses. However, even in such a comparison crystalline materials win because at similar level of aesthetic appeal they have better mechanical properties. In some cases, like artificial jewels, the high refraction index makes the crystalline items to look better than the best crystal glass gems. Figure 5.32 shows an artificial zirconia single crystal-based jewel.

The history of this product is quite curious: the melting temperature of zirconia is beyond those of all available crucible materials. Therefore, zirconia single crystals are grown from a melt of ZrO_2 powders (plus additives that stabilize the cubic structure) by a process that is known as "skull melting." First approaches originate from the 1960s in France (Y. Roulin and R. Collongues), but their "cold crucible" process (with some kind of microwave heating of a molten phase contained within a powder bed of solid-phase zirconia) did not yield larger crystals. Aiming for larger laser crystals that could substitute natural ruby, scientists at the Lebedev Physical Institute in Moscow published results of an improved approach in 1973. Commercial manufacture started in 1976, and within few years the global annual yield had come to a total of about 10 tons (50 million carats!) – not for lasers but stimulated preferentially by the use for synthetic gemstones, as diamond imitators.

The volume of the manufacture of raw artificial single crystals gives an idea of the commercial importance of this business – and of the amount of labor and costs for cutting, grinding, and polishing the raw pieces! There exists, therefore, an immediate and huge commercial interest in a substitution of skull-melting *single* crystals by making *polycrystalline* "near-to-end-shape" pieces, which can be sintered from similar ZrO_2 powders as used for growing the single crystals. In fact, it is "only" *one* major difficulty that complicates the use of sintered *polycrystalline* cubic ZrO_2 ceramics for making artificial gems which can compete with single crystals as those of Figure 5.32. Being intended as natural gems based brilliants, these transparent *ceramic* products have to be as completely free of visible defects as the grown single crystals. Making this "optical-grade" cubic ZrO_2 ceramic is, presently, still under work. The open structure of the ZrO_2 crystal lattice is a special feature of this compound with the consequence that numerous most different cationic species of the system of elements can be incorporated into this lattice up to high concentrations of about 10 or even more than 20 mol% as a solid solution (e.g. via sintering or melting). These doping options are used not only for stabilizing the cubic structure (e.g. by an yttria additive) but also for coloring effects. The industry offers a wide variety of different colors and color distributions (Figure 5.33), but the share of this sub-market is modest compared with the colorless species: *color* is caused

(a) (b) (c)

Figure 5.33 (a) Purple, (b) multi-color, and (c) tree-tone cubic zirconia single crystals. Source: Reproduced from https://en.wikipedia.org/wiki/Cubic_zirconia.

by *absorption* – and absorption reduces the effect of brilliance, which is important for the "diamond-like" appearance of cubic zirconia with its high refractive power.

As outlined earlier for colorless grades, the costs of making zirconia gems can be significantly reduced when the scull melting of *single* crystals is substituted by *sintering* powder compacts, which may be provided as intermediate products with shapes (as e.g. rods or discs) that in one or two dimensions come close to the final size of the cut and polished species. Additionally, however, this approach enables another important benefit, viz scratch resistance improvement. This is owed to the presence of grain boundaries in ceramics; they are absent in single crystals. Grain boundaries hinder the generation, growth, and movement of dislocations and twins (the defects that increase plasticity); as a result hardness of these ceramics is higher than that of the same composition single crystals. This, in turn, improves the scratch resistance and optical durability of the polished surfaces

With all its *optical* advantages cubic zirconia is, however, compared with other transparent ceramics or gemstones *the softest* compound: measured as HV10 (i.e. Vickers hardness at 10 kg testing load), the hardness of transparent cubic ZrO_2 ceramics is 12–13 GPa, whereas that of a fine grained polycrystalline spinel ceramic can be 14–15 GPa (similar to sapphire single crystals!), and that of transparent/translucent sub-micrometer Al_2O_3 ceramics is as high as 20–21 GPa. So imitating precious stones based on alumina ceramics is of interest although the alumina lattice is based on a very closely packed ions arrangement – a feature leading to *low* solubility of coloring dopants. As a result only Cr^{3+} (red) and small amounts of Ti^{3+} and Fe^{3+} (blue, yellow, or green) are taken up by the corundum lattice. In Figure 5.34 colored alumina *single crystals* are shown.

In contrast, Figure 5.35 displays some artificial gem stones based on *ceramic* spinel and also zirconia [K28–K30]. Blue and violet is doped $MgAl_2O_4$ spinel with a sub-µm microstructure, the other four pieces are sintered cubic zirconia (ZrO_2). The hardness HV10 of these sintered polycrystals manufactured by IKTS Dresden is 14–15 GPa for spinel and 12.5–13 GPa for sintered zirconia.

In such *polycrystalline ceramics*, grain boundaries – which have a more disordered structure than grain cores – accommodate more easily dopants [K56]. Thus, similarly as demonstrated for spinel and zirconia also light-transmitting Al_2O_3 ceramics can be prepared with a greater variety of colors around the circle of colors (see Figure 5.36). Because of the birefringence of this

Figure 5.34 Single-crystalline colored Al_2O_3 gemstones: (a) Red ruby by chromium (Cr) and (b) Blue sapphire by titanium (Ti) additives.

Figure 5.35 Sintered polycrystalline gemstones made of different ceramics. Blue and violet is doped $MgAl_2O_4$ spinel with a sub-micrometer microstructure, the other four pieces are sintered cubic zirconia (ZrO_2). The hardness HV10 of these sintered polycrystals manufactured by IKTS Dresden is 14–15 GPa for spinel and 12.5–13 GPa for sintered zirconia. Source: Courtesy of J. Klimke, Fraunhofer IKTS Dresden Germany.

(non-cubic!) lattice, a sufficient degree of light transmittance is achieved with very small grain sizes ≤ 0.5 µm only [A23], and this small grain size gives, then, rise to a second benefit: a high hardness HV10 = 20–21 GPa [K50] far above the much lower level of single crystalline Al_2O_3 gems [K49].

An especially challenging field is the use of transparent ceramics for premium watch housings: this application needs materials with a sufficient *strength* level, together with scratch resistance (hardness!) and an attractive optical appearance. All fully transparent ceramics exhibit quite low values of strength and fracture toughness. Therefore the less transparent (non-cubic)

(a) (b)

Figure 5.36 Polycrystalline sintered Al_2O_3 gemstone ceramics covering the circle of colors. The grain size is about 0.5 µm, the hardness HV10 is 21 GPa. (a) Light from above. (b) Through illumination.

Figure 5.37 "Mysterium" watch by Krieger, made in Switzerland, with translucent Al_2O_3 case. Source: Reproduced from http://www.kriegerwatch.com/ip.asp?op=Mysterium&m=x005000Collections.

but mechanically superior Al_2O_3 is more used for such items. In Figure 5.37 such a casing (2006; seems to be the first and only item of this kind advertised) is presented.

Tetragonal zirconia ceramics are much stronger than even hot-isostatically sintered alumina, but their high refractive index gives rise to even more scattering losses than Al_2O_3 ceramics of same sub-micrometer grain size [K31]. It is, therefore, the dominant present view that tetragonal ceramics may be a good choice for opaque (or *slightly* translucent) zirconia watch housings, whereas stronger cases with a higher degree of light transmittance can be made of sub-micrometer alumina ceramic only.

5.2.5 Components of Imaging Optic Devices (LENSES)

Lenses are used in a wide variety of optical devices having civil or military applications. The vast majority of the commercial lenses is made of various types of inorganic glass. Lately organic polymer-based glasses are also used in certain applications – some of them highly relevant commercially, like is the case of eyeglasses. At a first glance no room is left, in this domain, for transparent ceramics. More in-depth examination of the field reveals, however, that for certain current and under development devices, the glasses are not able to provide an optimal response (see Section 2.3.1; dispersion). As Figure 5.38 shows this is true especially for cases in which unusual combinations of the refraction index and the Abbe number are required.

A few TCs are known, which exhibit very high refraction index values. In Figure 5.38 the well-known $n = f$ (Abbe number) diagram shows the points for which glasses offer a good response but also indicates the regions not covered by the optical glass grades, developed till now. The points on the diagram occupied by recently developed TCs (Al_2O_3, YAG, and c-ZrO_2 (Y)) are also shown. Another target of the research, devoted to development of TCs for lenses applications, is finding materials that exhibit certain "anomalous" dispersion values; such values are requested by certain applications. Obviously, no single material can provide solutions for very special index-n vs. the Abbe-number combinations of practical interest (see e.g. Section 2.3.1 Refraction; chromatic aberration corrected by achromatic compound lenses). Figure 5.39 demonstrates how the partial dispersion of transparent ceramics can be tuned by

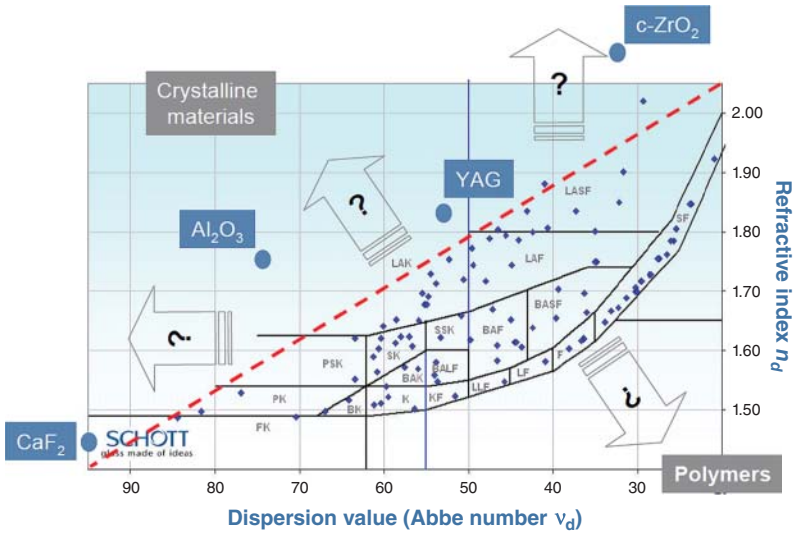

Figure 5.38 The Abbe diagram showing the relationship between the refraction index and dispersion (quantified by the Abbe number). Source: Courtesy of Y. Mencke, Schott-Mainz.

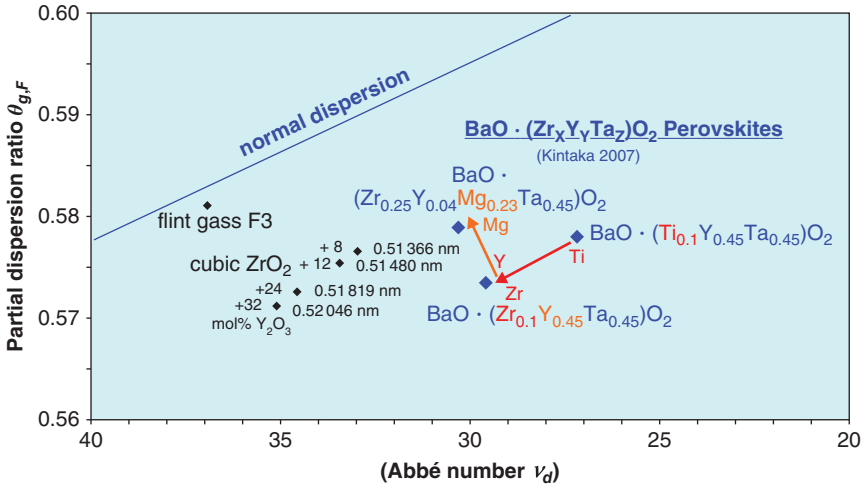

Figure 5.39 Tuning anomalous dispersion (partial dispersion ratio $\theta_{g,F}$ vs. Abbé number): Modifications are achieved by atomic substitutions, as in $BaO{\cdot}(Zr_xY_yTa_z)O_2$ perovskites [K20] or by changes of the lattice size. As it can be seen in cubic ZrO_2 with 8, 12, 24, or 32 mol% Y_2O_3 an increase in the lattice parameter from 0.51 366 to 0.52 046 nm raises the Abbé number, from the lowest to its highest value [K20].

compositional modifications of transparent zirconia and perovskite ceramics.

A number of highly transparent lens ceramics have been developed with a wide range of compositions and with tailored dispersive properties as an "anomalous" dispersion tuned by materials selection and/or continuous compositional variations. Information, on this issue, is, however, almost completely limited to published patent applications [K20], and a realization of such components with a sufficient optical quality at manufacturing costs that "pay" seems difficult yet. This special challenge in comparison with optical *glasses* is, of course, attributed to the difference between the natural *homogeneity* of a glass *melting* manufacture versus the much higher propensity for defect generation in ceramic *powder processing* followed by *solid state* sintering of single-phase transparent ceramics. Thus, the development of special defect-minimizing strategies has become imperative for new *optical* and *laser* grade ceramics [K53].

The TCs offer also a few additional benefits like better (than that of glass) resistance to fast temperature variation, environment attack, and higher mechanical strength; the shorter focal length they allow brings about reduction in weight and size.

The optical requirements, existing for lenses, can be seen in Table 5.1 in section 5.2.1.

As far as materials are concerned, the most promising TCs seem to be several perovskites and zirconia, especially its cubic polymorph. The general issue of transparent zirconia ceramics fabrication was discussed in Section 4.2.7. For lenses application one may consult, with profit, the paper of Peuchert et al. [P27]. Among other things the main problems confronting the zirconia ceramics based lens fabricator are addressed there. So it is shown that, processing induced, birefringence (owed to residual stress fields), discoloration due to sintering aids, refractory supports properties, etc. are, currently, impairing the optical quality of the fabricated lenses.

Figure 5.40 Small size ceramic zirconia lens fabricated at Fraunhofer, IKTS-Dresden.

Actual, small size lense samples were prepared at IKTS, Dresden, as shown in Figure 5.40. Once more this image highlights the imperative importance of matching "optical grade" quality criteria (which are self-understanding with glass lenses) [K53] for a commercial success of transparent *ceramics* in this field. Recently, also Ba (Zr, Mg, Ta) O_3-perovskite (disordered lattice variants), based ceramics – better known as materials for MW resonators – were brought to transparent state by the Murata company [K21, K22]; the trade mark is LUMICERA. The spectral range of the window of these ceramics has a low energy edge at around 6.5 µm and $n = 2.082$ at the wavelength of 587.6 nm (He d-line). Lumicera made small lenses are used by Casio – for some of their miniaturized cameras, like Exilim Card EX-100. The high refraction index, offered by the material, allows the necessary lens size reduction; its increased robustness (compared with glass) is an additional benefit. Competing developments are known at the Nippon Telegraph and Telephone Corp. [F18].

Other TCs can provide an optimized solution for the bottom lenses of immersion lithography systems (used in ICs fabrication) [B69, P28]. The EMR traveling, through those systems, has a wavelength of 193 nm; resolution of current systems is limited to 45 nm and the drive is to reduce it to 32 nm or less. Transparency, at this low wavelength, coupled with a high refraction index are the main factors relevant for the figure of merit, of this application; a low intrinsic birefringence (IBR) is also required. At short ultraviolet wave lengths even *cubic* single crystals exhibit increasing IBR values, e.g 50.6 nm/cm in stoichiometric $MgAl_2O_4$ spinel at 195 nm wave length. However, the problem can be eliminated if *polycrystalline* spinel is manufactured with sufficiently small grain size [K57, K59]. Such Mg spinel (no IBR problems) is the ceramic candidate that competes with single crystals (e.g. $BaLiF_3$ or LuAG) and La-doped silica glass for this important application.

5.2.6 Dental Ceramics

Transparent ceramics find applications also in the field of dentistry. Grosso modo TCs relevant here may be divided in two groups: items for restorative dentistry and orthodontic brackets. For the former group only a very moderate level of transparency is required while the latter are more transparent; the brackets will be treated first.

In the early 1970s metal brackets were substituted first by polycarbonate plastics (which, while transparent, suffered discoloration and slot distortion) and, later on in the mid 1980s, by monocrystalline sapphire and polycrystalline sintered alumina ceramics. The major problem to be solved was to find, at moderate costs, a material that exhibits a sufficient (not necessarily excellent) transmission through 1–2 mm thickness and stands the high multiaxial stress exerted by the metallic arc wire at the slot edges. Since the commercial success of first commercial products in the early 1990s sintered highly-pure and fine-grained Al_2O_3 ceramics turned out as the best fit to such demands. The alumina used had to be very fine grained, in order to exhibit transparency (see section 2.3.4). The first materials had a grain size around 1.5 µm. A later grade Clarity SL manufactured by Ceradyne was slightly more fine-grained with 1.096 µm grain size at a density of 3.95 g/cm^3 that is equivalent to 99.05% of the theoretical density of the corundum lattice; such a density corresponds to a significant residual porosity of about 0.9% – in fair agreement with scanned micrographs. The hardness was recorded at 0.5 kg testing load as HV0.5 = 21.5 GPa. Physical and manufacturing principles are taught by numerous patent applications. These ceramic bodies are attached directly to the tooth surface and make, thus, use of the effect of Figure 3.57b (see before section 3.2.5) where both transparent and translucent “windows” provide identically clear views when placed on the printed matter with zero distance. Therefore, in daily service these *translucent* Al_2O_3 products enable a perfectly *transparent* esthetic appliance (Figure 5.43a). Presently the ceramics enjoy a wide *public a*cceptance on all continents around the globe. They also constitute a significant commercial success reminding the halide lamp envelopes developed based on the first transparent ceramic (see 1.5.2).

Restorative dentistry is a quite large-scale business. Ceramics, glass-ceramics, and glasses are all used as materials from which dental crowns or inlays (onlays or overlays) are fabricated. Such products require a degree of controlled translucency, and therefore their mentioning in the context of this book is relevant. The level of translucency (and sometimes fluorescence) and shades of color sought is similar to that of natural teeth; neither higher levels nor lesser ones are acceptable. Besides

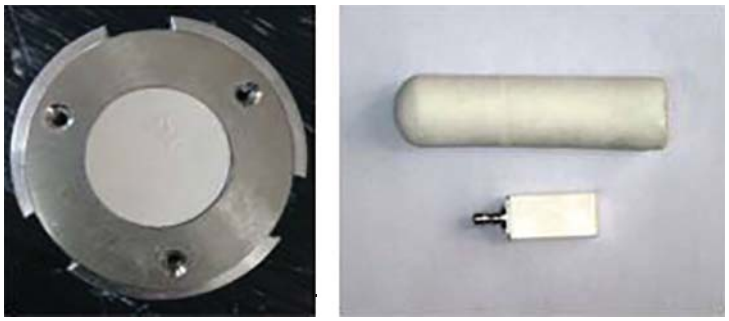

Figure 5.41 Porous near-green preforms (viz presintered at around 1000 °C), used for the fabrication of TZP based dental crowns; made at ICSI, Haifa. (a) Disc shaped preform. (b) Upper part: rod shaped initial preform; lower part: rectangular, second stage, preform cut from the rod (crown is machined out of this preform)

the optical requirements the artificial teeth need to be biocompatible with the oral environment and exhibit an abrasion resistance similar to that of natural teeth and higher chemical durability.

To the traditional dental crown materials like gold, stainless steel, acrylic polymers, or porcelain (the oldest crown material), new materials like glass-ceramics, zirconia, and alumina have been added lately. One variant are crowns made fully of zirconia. However, composite systems in which a zirconia core is covered with porcelain layers (veneer) seem to offer the best tradeoff between cosmetic and mechanical resistance requirements.

The fact that certain, especially oxide, ceramics are suitable for dental prosthetics, is not so surprising considering the fact that even in the natural teeth – both in dentine and enamel – large fractions of the volume (92% in enamel) are occupied by a natural ceramic: hydroxy-Ca-apatite; the need for a harder tissue, than in the rest of the human body, comes from the fact that during mastication mechanical stresses of 20–100 MPa may appear and fast temperature fluctuations may exceed 30 °C (thermal shock).

The dental porcelains are, in most cases, feldspathic ones reinforced with leucite ($KAlSi_2O_6$) and (much less frequent) ones with high alumina content. They exhibit a continuous internal pores system, impregnated with lanthanum–alumino–silicate glass.

The most recently added ceramic – to the list of commercially available dental restorative materials – is yttria stabilized tetragonal zirconia; this material, a TC, was presented in Section 4.2.7. The material found application also as transparent calvarium prosthesis [D3, D5]. We examined, for dental applications, also mixtures of cubic and tetragonal zirconia. The characteristics of the mixtures were not superior to those based exclusively on tetragonal zirconia polycrystalls (TZP).

Zirconia based crowns and implants do not yet represent more than 10%, of the total restorative dental parts (worth some US$300 million) market but their share grows at a fast rate.

The zirconia crowns are, in most cases machined out of presintered preforms, like those shown in Figure 5.41.

Such preforms are obtained by firing at low (~1000 °C) temperatures powder compacts consolidated by pressing; they retain a porosity of around 45%; the pores size has a narrow distribution around an average of 65 nm (see Figure 5.42). Let as call such preforms as near-green parts because they are only presintered to levels of porosity only slightly lower than that proper to the green parts, viz those in as-pressed state. In Figure 5.41a near-green disc shaped preform is shown. In Figure 5.41b cylindrical green preform and a near-green one, cut from the first are illustrated. In Figure 5.43b (left panel) machined crown (presintered state) and a sintered zirconia crown are shown; a sintered crown made of spinel is presented in Figure 5.43b (right panel).

The near-green parts are easily machined by computer assisted design/computer assisted machining (CAD/CAM) systems. The computer program guiding the machine is the result of conversion to digital files of the laser scanning of the buccal cavity of the patient.

The near-green zirconia parts are sintered to full density, around 1550 °C; such parts exhibit HV1 values of 12.8–13 GPa.

We developed also crowns made of spinel (see Figure 5.43b, right panel) and mixtures of tetragonal and cubic zirconia. The hardness of spinel based crowns is similar to those made of tetragonal zirconia but the forming of easy to machine preforms proved (surprisingly) to be more difficult than in the case of zirconia.

It is possible to form the dental crown also by machining them out of fully sintered preforms. The advantage is that no geometrical error, introduced by the sintering shrinkage (the crowns cut from near-green preforms undergo a second firing to obtain full pores closure), may affect the product; the disadvantage is the need to machine dense, quite hard parts instead of the partially sintered ones offered by the first fabrication approach described.

The desire of clients for similarity of restorations with the natural teeth, makes necessary that ceramic crown

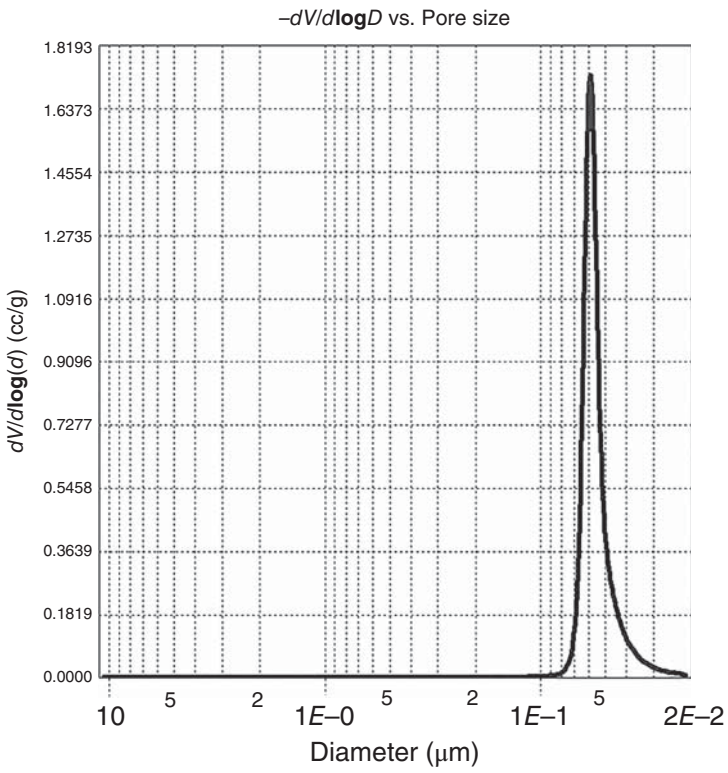

Figure 5.42 Pores size distribution in presintered zirconia preform.

(a) (b)

Figure 5.43 Dental products made of translucent ceramics. (a) Translucent alumina based orthodontic bracket. Courtesy of Dr. Ravi Kamisetti, Orthodontic Specialists of Melbourne (OSM), Melbourne, Australia. (b) Presintered stage and finished zirconia made crowns (left panel) and crown made of spinel (right).

preforms providers offer a quite wide game of transparency levels and color hues. The latter are produced by pigments added in the initial powders. The most popular are various shades of yellow; pure white while feasible is less popular. The desired transparency level is, in most cases moderate. Highly transparent crowns can be also produced; for such an endeavor mixing cubic and tetragonal zirconia or using spinel are useful solutions.

In the case of the castable or machinable glass-ceramics (another widely used material in dental prosthetics) the small crystals, embedded in the glass matrix (overall translucent systems), may be of mica, leucite, or ZrO_2 [H31]; a few glass-ceramic based dental products are illustrated in Figure 5.44.

5.2.7 Applications of Transparent Ferroelectric and Pyroelectric Ceramics

Some of the TC materials are also pyroelectric, ferroelectric, piezoelectric, electrooptic, or magnetic. Such properties open for them new application opportunities. As of now most of the applications of the ferroelectric transparent ceramics are based on their ability to combine transparency with electrooptic behavior [L26], which means showing sensitivity, to applied electrical fields, of characteristics like the refraction index or the state of polarization (of the light traveling through them); for the case of the materials relevant here, electrooptic abilities are a consequence of them being ferroelectric.

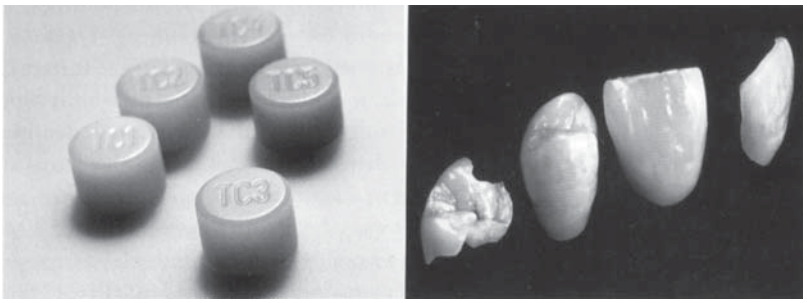

(a) (b)

Figure 5.44 Preforms and tooth parts made of translucent glass-ceramic. Source: Holland and Beall 2002 [H31]. Reproduced with permission from John Wiley & Sons.

The most widely used modes of electrooptic behavior, exploited in applications, are illustrated in Figure 5.45.

The figure presents the shape of the polarization as a function of the applied electric field ($P = f(E)$) hysteresis curve required for each type of application, the experimental arrangement needed to measure a certain effect and the profile of the light output intensity $= f(E)$ dependence. The compositional zones (in the La containing PZT (PLZT) system's phase diagram), which generate materials with the various types of electrooptic behavior shown in Figure 5.45 were indicated in the Section 4.2.10, which deals with the PLZTs [H3]. While not the only ferro, transparent ceramics, the PLZTs group is the main such material used in commercial devices, as of now (as discussed in the following, the PLZT's start to feel the heat of competition from other similar materials). As a general feature the electro-optic (EO) processes based applications require strong illumination when the device includes polarizers (which reduce transmission by their presence); antireflection coating on the polarizers can alleviate this problem. In the devices the active components are thin plates of transparent ferroelectric ceramic. Their use is not simple because they exhibit interactive properties (mechanical, electrical, electromechanical, pyro, and ferroelectric, EO); in many cases effectuating a certain action on a PLZT plate triggers a set of effects from which some are helpful, while other deleterious to the application. The light output's characteristics vary with the kind of electrooptic effect and for a given effect – with the variation of the electrical field intensity. One can transition from black to white running over a scale of gray, full color range, or limited ranges of color. This is exemplified in Figure 5.46.

Some of the main devices based on T,F-C materials are briefly described in the following text.

5.2.7.1 Flash Goggles

Goggles designed to protect the eyes of pilots from the effect of nuclear explosion generated flash are manufacturing using PLZT plates. In Figure 5.47 early variants (1980) of such goggles and a viewing port, presented in the cabin of B-1B American bombers aircraft, are illustrated [H2].

This device is a transverse mode shutter (see Figure 5.46); it comprises two 10 cm diameter frontal and two rectangular side lenses ($t = 0.4$ mm). A PLZT 9.2/6.5/35 material hot pressed (pale yellow, $GS \sim 2$ μm) is used for such components. The very slim loop of this quadratic material ($R \sim 4 \times 10^{-16}$ $m^2\,V^{-2}$) is the essential (quite specific to this material) feature for reproducible and quick reaction; starting from the 1990s, the reaction time of such PLZT parts is considered too long, by some device manufacturers. A 0.8 kV voltage acts, in normal state, on the PZT plate. The light is first polarized (by the first polarizer). The polarization plane is turned by 90° owing to the birefringence of the plate (induced by the E). The second polarizer (analyzer) is oriented so as to allow passing of the waves output by the plate. If there is a flash, a photodiode detects it and commands voltage switch off and thus closing of the interelectrodes circuit. As a result the plate ceases to rotate the incident light's polarization plane, so that it arrives of the analyzer in a polarization state that is not let to pass. The residual light intensity after the analyzer has nonzero but massively reduced intensity, compared with that of the incident light sent by the flash source. Transmission ratios are of 1 : 1000 and typical switching times are of ~100 μs; shortening of the latter is desirable. Welder helmets and inspection and safety googles function in a similar way.

5.2.7.2 Color Filter

An optical shutter, like that used for flash goggles, can be also used as a voltage controlled color filter. When voltage is off, incident white light is extinguished. As the voltage is raised the retardation (caused by the birefringence) is brought to a value for which the green segment of the spectrum is rotated with $\lambda/2$ and thus can fully pass the analyzer; the rest of the spectrum passes only partially. As the voltage is further raised, for the blue segment the retardation attains a value equal to λ so this segment is blocked by the analyzer. Because green and red are let over, the eye sees a resulting yellow.

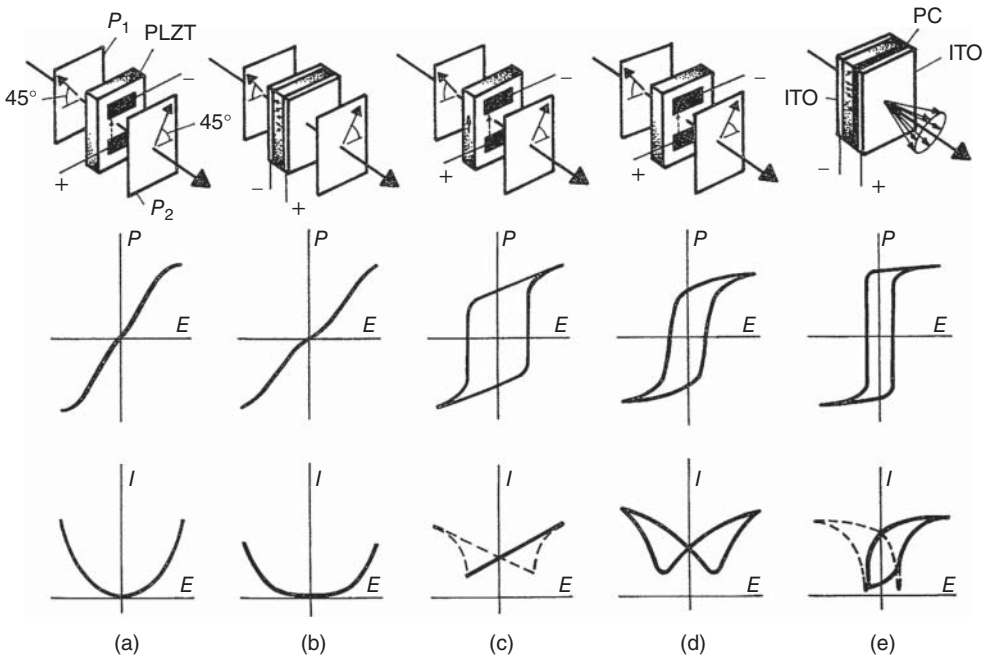

Figure 5.45 Operational configurations, hysteresis loops, and profiles of the light signal dependence on field strength of thin plates made of various types of PLZT. (a) Material having quadratic birefringence. (b) Quadratic depolarization. (c) Linear birefringence. (d) Memory birefringence. (e) Memory scattering. Source: Haertling 1988 [H3]. Reproduced with permission from Taylor & Francis.

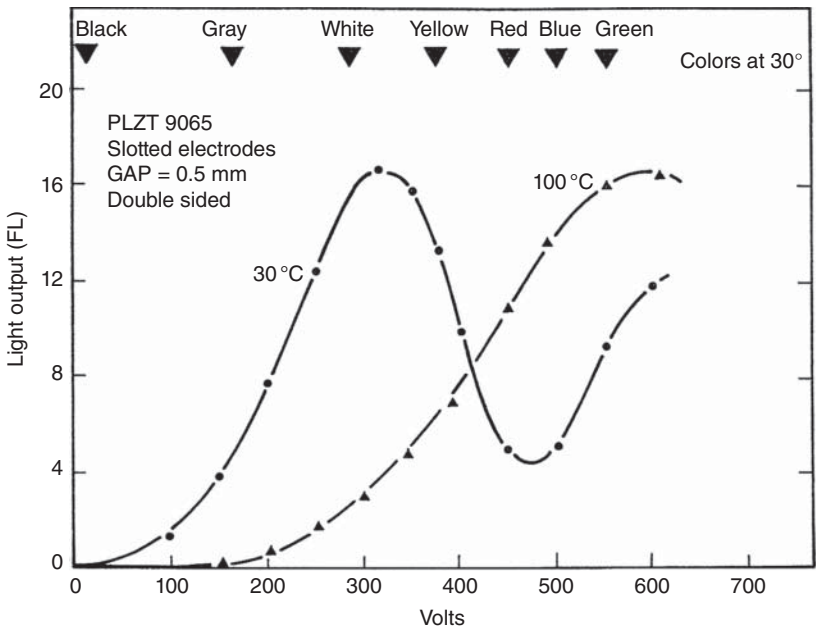

Figure 5.46 Electrooptic characteristics of PLZT slotted plate (6/95/3 composition) at RT and 100 °C. Source: Haertling 1988 [H3]. Reproduced with permission from M. Dekker Pub.

5.2.7.3 Stereo Viewing Device

In such a device the lenses of viewing system are separately controlled. An alternating pair of images is displayed on a cathode ray tube (CRT) display. The shutters are synchronized so that each eye sees one image. The alternation rate is 30 Hz. As a result the viewer sees only one image, thus getting a sense of object depth. Other devices are based on longitudinal mode operation. Examples are picture displays and storage, segmented, or matrix displays that, in certain cases, may still compete with the liquid crystal display (LCD) or light emitting diode (LED) technologies.

Figure 5.47 Anti-glare goggles based on PLZT plates kept under electric field. Source: Haertling and Land 1971 [H2]. Reproduced with permission from John Wiley & Sons.

5.2.7.4 Applications of Second-Generation (Non-PLZT) Ferroelectric Ceramics

As noted in Section 4.2.10, ferro-materials, developed in parallel with the PLZTs, may exhibit higher electrooptic coefficients than the latter. While the overall set of properties of such materials is not necessarily superior to that of the PLZTs, for some applications the higher sensitivity to the electric fields is, alone, an advantage significant enough to warrant their use. A case in point is the materials of the PMN-PT system. Such materials show R coefficients in the $13–28 \times 10^{-6}$ $m^2\,V^{-2}$, which compare well with $2–4 \times 10^{-16}$ $m^2\,V^{-2}$ for PLZTs [J10, L39, R38, X1]. The PMN-PT materials are also able to attain sub-microsecond response speed (10 ns for thin film and 100 ns for bulk; this is a feature which make them a good candidate to PLZT replacement in flash-goggle production). A useful device, based on PMN-PT plates, is the variable optical attenuator (VOA) [J10]; it is used to control signal strength in optical networks. The attenuation control is realized by adjusting the electric field within the ceramic; modification of the refraction index leads to changes in the level of light output through the second calibration. Typical dynamic range of such a VOA is 25–35 dB. Polarization controllers, variable gain tilt filter are other devices using PMN-PT ceramic as active components. Electrooptic Q-switches are also attractive owing to small size and agility. Compared with kalium di-phosphate (KDP) or $SiNbO_3$ single crystal based active switches, those based on PMN–PT require lower voltage for their operation (~50 V compared with >1 kV for KDP).

The electrooptic abilities of ferro transparent ceramics can be also exploited to enrich the set of wavelengths for which laser signals are available. This is done by using the second harmonic generation (SHG) ability of such materials. Solid-state lasers, which work mostly in the NIR, can be used to produce, by SHG, signals at double the initial λ, i.e. in the VIS or UV domain. For instance, transparent PLZT plates, doped by 1 at.% Nd [I3], pumped at 820 nm, lase at 1064 nm. A number of materials, which include various ferro phases (like meta barium titanate, fresnoite, etc.), have also been shown as being able to effectuate SHG operations.

A very useful application of transparent ceramics, which simultaneously exhibit pyroelectric properties, is in the domain of thermal imaging [M39]. Devices in this domain convert IR radiation emitted by a target into a visible image. Because the power density in the 8–14 μm band is larger (150 $W\,m^{-2}$) than that of the 3–5 μm window (~6 $W\,m^{-2}$), the former is preferred. A typical device called "vidicon" is shown in Figure 5.48.

In it the IR radiation, from the target scene, is chopped and focused onto an IR electrode, carried by a pyroelectric plate. The voltages (millivolts) developed across the plate are collected by a metal grid. The surface density of electrons passing between the elements of the grid depends on the **local** potential at the plate surface. The surface modulated current is used to produce a TV image. Pyroelectric devices can discriminate differences of 0.1 K and do not require cooling (as photoconductors like HgCdTe do). Certain transparent ceramics developed specifically for such applications have pyroelectric figures of merit good enough to compete with classic pyroelectric materials like triglycinesulfate (TGS), polyvinylidene fluoride (PVDF) or the $LiTaO_3$ or $(Sr,Ba)Nb_2O_6$ single crystals. The most used such ceramic is a modified PZT with the formula $Pb_{1.02}(Zr_{0.58}Fe_{0.20}Nb_{0.20}Ti_{0.02})_{0.094}V_{0.006}O_3$ (PZFNTV).

5.2.8 Applications of Ceramics with Magnetic Properties

In Section 4.2.5.3 a number of magnetic TCs (most of the having a garnet type lattice), many of them only moderately transparent, were described. All these materials

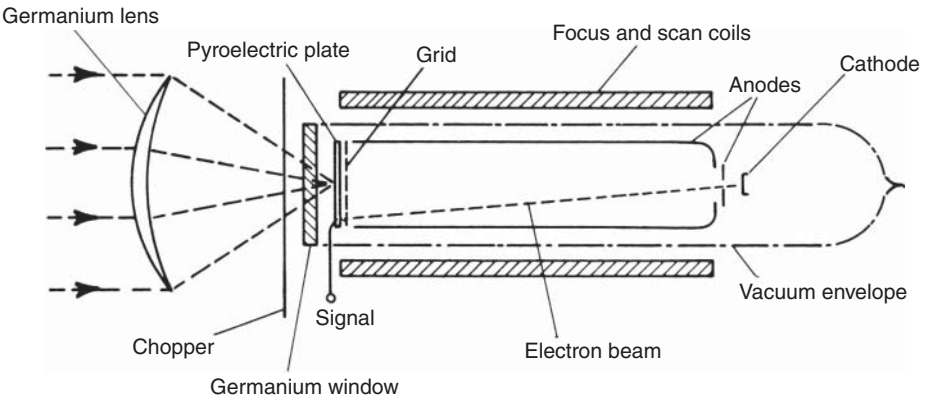

Figure 5.48 Vidicon type night-vision device the sensitive element of which is made of a transparent pyroelectric ceramic. Source: Moulson and Herbert 1990 [M39]. Reproduced with permission from Springer.

have at least one major component that may confer para or ferromagnetic properties to the host, viz a TM^+ and/or RE^+ type ion. Such materials have in common, with those, the applications of which are discussed in Section 5.2.9, the presence, in their lattice, of transition or REs. However, a major difference separates them: in the former materials the transition cations are a major constituent, while they appear as dopants in the latter. As a result the properties and finally applications of the two material types are significantly different. That's why they are discussed in separate sections. For many of them (those described in Section 4.2.5.3), one can envisage various applications – as components of opto-magnetical devices (actual use is still a thing mostly of the future, though). The main family described there (Tb-containing garnets), however, is already a strong candidate for the production of devices usable in laser systems for blocking reentry of undesired radiation, construction of multipass schemes (amplifiers) or thermal lensing compensation. These applications are all based on the sensitivity, of the said garnets, to the Faraday effect.

Before proceeding let us recall what is the Faraday effect. The most remarkable thing, regarding this process (discovered by the eponym physicist in 1845), is that it showed the link existent between light and magnetic fields. The rotation of the polarization plane, of a linearly polarized EMR wave, by the action of an external, longitudinal magnetic field that acts on a material of suitable composition is known as the Faraday effect. Solids including paramagnetic ions are one kind of such material. Some Tb containing ceramics, relevant in this context, have been described in Section 4.2.5.3. The parameter, most often used to quantify the magnitude of the Faraday effect, is the Verdet constant, V of the equation which links the "B" to the rotation angle "β":

$$\beta = V\,B\,d \tag{5.9}$$

where the B is the magnetic flux density, induced by an external magnetic field H, in the specimen; d is the length over which the specimen interacts with the field H; and "V" is an empirical constant having the units (Rad/Tm). The constant may have positive units, when a B parallel to the EMR direction of propagation causes an anticlockwise rotation and a clockwise one for an antiparallel B; the sign of the constant is negative in the opposite case. The constant "V" is markedly wavelength dependent. For instance, at 638.2 nm the TGG single crystal has a $V = 134$ Rad/Tm, while at 1064 nm it decreases to ~40 Rad/Tm.

The most popular device, constructed by the aid of the ceramics, sensitive to the magnetic effect described earlier, is the Faraday isolator (FI). This device is a type of optical isolator (viz isolates a device from unwanted optical signals coming from the environment) the essential part of which is a solid with Faraday rotating abilities. In laser systems, especially of high power, FIs – which let light passing in one direction while blocking it in the opposite one – are most used for blocking reentry of undesired reflections, mostly of pumping radiation, into the cavity. Faraday rotators are also used in laser amplifier schemes, for laser beam polarization control, and for mitigating thermal lensing effects; optomagnetic current transducers can also be produced. Currently TGG, terbium scandium aluminum garnet (TSAG), $NaF–TbF_3$ single crystals or certain rare-earth alumino silicate doped glass fibers are employed, in practice, to fabricate FIs [D7, L30, S49]. As compared with glasses, ceramics bring the critical benefit of higher thermal conductivity, for similar Verdet constant values. Compared with single crystals, the ceramics are advantageous because can be fabricated in larger size at lower cost. As of now it seems that Ce^{3+} doped TAG ceramics – which combine a $V = -190.4$ Rad/Tm with a transmission of 80% (630 nm; $t = 1.2$ mm) – are the best materials developed in this context [D1]. Tb^{3+}:Y_2O_3 ceramics (where Tb_2O_3 concentration exceeded 10%) of much higher Verdet constant (values over 400 Rad/Tm were measured at ~630 nm) were also produced lately; the transmission

and size of those specimens is not yet satisfactory, however.

5.2.9 Products Based on Ceramic Doped with Transition and/or Rare-Earth Cations

The TCs discussed in this section owe their functionality, besides their transparency, to the dopant cations they contain. This is based on the fact that TM^+ and RE^+ cations are able to actively modify characteristics of the incident EMR by selective absorption and emission processes. The applications discussed later (gain media, for solid-state lasers, Q-switches, phosphors, and scintillators) are among those that offer to the TCs the chance to access high volume and dollar value markets; most of the relevant devices are high-tech, high price, ones.

5.2.9.1 Gain Media for Solid-State Lasers

One of the applications – for which doped transparent ceramics are already providing, commercially relevant, products – is that of gain media for solid-state laser devices; this market has also a significant potential for further growth, owing to certain advantages vs. the competitor hosts (glass, glass-ceramics, and single crystals) they exhibit. Compared with glasses, ceramics provide better mechanical, thermal properties and higher resistance to chemical attack [L53]. Compared with single crystals the ceramics' main benefits are feasibility of fabricating large size and/or complex shape parts and lower fabrication costs. Some authors also attribute to ceramics the ability to accommodate larger concentration of active ions but this issue is still under discussion.

The first ceramic laser, of very low efficiency, was demonstrated soon after Maiman developed, in 1961, the first solid-state one (Cr^{3+} doped corundum single crystal [M6]) and Sorokin showed stimulated IR emission from uranium [S45]. It used CaF_2 as gain media doped with Dy^{2+} and it was announced in 1964 by S.E. Hatch et al. [H16]. Greskovich and Chernoch produced the first oxide based (Y_2O_3 gain media) ceramic laser, in 1973 [G40]. However, this type of product caught the attention of the scientific community only after A. Ikesue et al. presented the first YAG ceramic based reasonable efficiency laser [I6]. As of now the Japanese Konoshima company [Y1], manufactures and sells (for more than 20 years) significant amounts of high and reproducible performance ceramic gain media; they are based mostly on YAG but also a few sesquioxides are offered.

As in the case of armor, we felt that a brief general background on the way solid-state lasers operate may facilitate for many readers, the understanding of the discussed application. Therefore this topic, which forms the object of the introductory section in the following text, is presented before the gain media proper are addressed. Ceramic lasers are also presented – in more in depth and detailed fashion than here – in an excellent book, by A. Ikesue et al., focused on this domain only [I3]. Among other things the book underlines the fact that TCs for laser systems are among the most demanding products, quality wise. Parts need to be virtually defect free. For instance while for most of the TC based products remnant porosities of 50–100 vol ppm can be tolerated gain-media are limited to the 2–10 vol ppm level.

5.2.9.1.1 Lasers: Definition and Functioning Mechanisms

We are dealing with solid-state lasers, in this book, but the functioning principles are the same for all laser types.

Lasers are a family of light sources, capable of emitting monochromatic, coherent, and highly parallel light beams. Different **laser** sources may emit in different optical ranges, from the ultraviolet to the FIR. Some systems emit continuously (abbreviated as CW; acronym of "continuous wave"). Others emit pulses of various durations, in the microsecond (10^{-6} seconds) nanosecond (10^{-9} seconds), picosecond (10^{-12} seconds), or femtosecond (10^{-15} seconds) ranges. Efforts toward the attosecond (10^{-18} seconds) range are currently pursued. Ordinary CW power outputs may range from ~0.1 to ~100 mW. Pulse energies may range from ~0.01 to ~10 J/pulse. Single pulsing, and train pulsing up to ~10 kHz, and even ~100 MHz are achievable. Some systems are limited to a single wavelength; others may be tuned over a limited wavelength range. The **amplifying medium** component in a laser system may also vary; some media are gas-based, some are liquids, and some are solids.

The LASER naming stems from the acronym used to describe the physical core mechanism involved in the beam formation: **Light Amplification by Stimulated Emission of Radiation**.

A useful property of laser beams is their relative ease of being manipulated for achieving different polarization states, being concentrated to very small spots of exceptionally high peak powers, and undergoing frequency conversions like doubling, tripling, or dividing. There is a diverse use of laser beams; military, like range measuring and target marking; industrial, like printing and cutting; and medical, like tissue cutting and wound-stitching. The diversity in laser science and technology is huge. The following survey is aimed at acquainting the reader with basic physical phenomena and terms related to this area and indicate their relevance to transparent ceramics technology.

5.2.9.1.1.1 Lasing Mechanisms

Light crossing through a material bulk may cause transitions from occupied energy states to unoccupied ones when the photon energy $h\nu$ equals the energy gap

between the states. If the occupied state energy is lower than that of the unoccupied one, the process is called **absorption**, as energy taken from the electromagnetic radiation field has increased the material energy. If the occupied state energy is higher than that of the unoccupied one, the process is called **stimulated emission**. The "emission" term is obvious, because energy was "taken away" from the material to increase that of the radiation field. The adjective "stimulated" stems from the fact that this process occurs only in the presence of the radiation field; namely, it is "stimulated" by the presence of the radiation field.

Dynamic theory concerning the interaction between electronic states and electromagnetic fields show, that absorption, and stimulated emission processes are entirely symmetric: both occur only in the presence of the radiation field, and both are thus eligible to the "stimulated" adjective. It is, however, used only in conjunction with the emission process. The reason is to distinguish the latter from an additional emission process, the **spontaneous emission**, occurring in the absence of any radiation field; or in other words – even in total darkness.

In quantum mechanics, however, the spontaneous emission is also described as *stimulated* by the electromagnetic fluctuations of the vacuum (zero-point fluctuations). The quanta of this nature exhibit an energy of only $\frac{1}{2}h\nu$. Therefore, they lack sufficient energy to stimulate absorption transitions from lower to higher states; they are, however, still capable of stimulating transitions from higher to lower states, just like "real photons." The spontaneous emission is the source mechanism for material fluorescence emission. This process is so common that people tend to forget that it was theoretically difficult to be accounted for before the advent of quantum mechanics. In that respect it should be emphasized that the occurrence of spontaneous emission is consistent with the second law of thermodynamics. Recall that this law states that adiabatic thermal equilibrium occurs when a thermally isolated system reaches the largest possible **entropy**. Indeed, the combination of a lower state atom plus a photon propagating at a random direction in space is more disordered, hence of larger entropy than the excited atom, although the two configurations exhibit the same energy. One should further realize that the mechanisms by which all aspects of the second law of thermodynamics are realized, are the zero-point fluctuations of all physical fields. Insight of this relevance to thermodynamics allowed Einstein back in 1917 [K6] to achieve a quantitative theoretical expression relating the spontaneous emission to the stimulated emission and absorption.

A schematic illustration of the three-type transitions is provided in Figure 5.49.

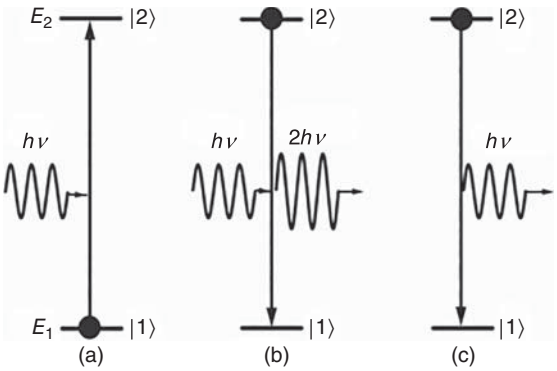

Figure 5.49 Schematic illustration of radiative transitions between energy states in matter. (a) Absorption; an electromagnetic radiation photon is being absorbed by an atom at the lower $|1\rangle$ state, and the radiation field energy correspondingly lowers. (b) Stimulated emission; the electromagnetic radiation field stimulates transition from the higher $|2\rangle$ state to the lower $|1\rangle$ one, and the radiation field strengthens by the addition of a single, in-phase photon. Note that the added energy expresses itself by increased amplitude, not by an increased frequency. (c) Spontaneous emission; an atom in complete darkness at the higher energy state $|2\rangle$ suddenly emits a photon by transition to the lower state $|1\rangle$, thereby enriching the electromagnetic field energy by a single photon.

A laser system exploits stimulated emission processes to form an optical gain medium, whereby a beam crossing this medium increases its intensity. Our interest is focused on systems where rare-earth or transition metal cations are the active players in the gain medium. These cations may be hosted in a solid glass, in a single-crystal, or in a polycrystalline (ceramic) solid. In technical laser-science terminology, lasers based on such gain media are termed **solid-state lasers**. Semiconductor diode lasers are also regarded as such, but won't be discussed in this book.

In contrast to the simplified two-state model of Figure 5.49, ionic states in a hosting medium broaden, either homogeneously by the medium vibrations, or heterogeneously due to the ions random residence in sites of slightly varying nature. The $|2\rangle \rightarrow |1\rangle$ fluorescence-transition spectrum (Figure 5.49) displays a broadened shape given by a $g(\nu)$ function of reciprocal frequency units (Hz^{-1}). This shape function is normalized to a unity integral ($\int g(\nu)d\nu = 1$) by dividing a measured fluorescence intensity at each frequency $F(\nu)$ by its integral $\int F(\nu)d\nu$. The medium gain spectrum $\Gamma(\nu)$ in reciprocal length units (cm^{-1} in the cgs system) is given by

$$\begin{cases} \Gamma(\nu) = \dfrac{(N_2 - N_1)c^2}{8\pi n^2 \nu_0{}^2 \tau_{rad}} \cdot g(\nu), & \text{for homogeneous broadening;} \\ \Gamma(\nu) = \dfrac{(N_2 - N_1)c^2}{8\pi n^2 \nu^2 \tau_{rad}} \cdot g(\nu), & \text{for heterogeneous broadening} \end{cases} \tag{5.10}$$

where N_1 and N_2 are the active cation volume densities at the lower and upper states, respectively, ν_0 is the center frequency of the fluorescence emission band, τ_{rad} is the radiative lifetime of the fluorescence emission, and n is the refractive index at ν_0. Obviously, $N_1 + N_1 = N$, the total cation volume density. For narrow fluorescence bands, the difference between the two expressions is minimal and may be disregarded. Note, that the appearance of both radiative transition lifetime τ_{rad}, and fluorescence spectral shape $g(\nu)$, provide a direct relation between the stimulated and spontaneous-type emissions. The difference between cations densities $(N_2 - N_1)$ is called **population inversion**, because under thermal equilibrium, the upper-states density (population) is always smaller than that of the lower states, as the Boltzmann thermal equilibrium population ratio indicates.

$$\frac{N_2}{N_1} = \mathbf{exp}\left(-\frac{E_2 - E_1}{k_B T}\right) \tag{5.11}$$

In (5.11) $k_B = 1.3806 \times 10^{-16}\,\mathrm{erg\,deg^{-1}}$ is the Boltzmann constant, and T is the absolute temperature. For example, in a typical case where $(E_2 - E_1) = 1.0\,\mathrm{eV}$ and $T = 300\,\mathrm{K}$ (room temperature), the ratio $(N_2/N_1) \cong 10^{-17}$. Positive gain thus requires a gross violation of thermal equilibrium, achieved by exciting the active cations to their upper state. Such excitation processes are called **pumping**.

Often, the gain relation dependence on the wavelength λ is more convenient to work with than the same equation expressed in frequency terms. Invoking the $g(\nu)d\nu = -g(\lambda)d\lambda$ relations yields:

$$\begin{cases} \Gamma(\lambda) = \dfrac{(N_2 - N_1)\lambda_0{}^2\lambda^2}{8\pi n^2 c\tau_{rad}} \cdot g(\lambda), & \text{for homogeneous broadening;} \\ \Gamma(\lambda) = \dfrac{(N_2 - N_1)\lambda^4}{8\pi n^2 c\tau_{rad}} \cdot g(\lambda), & \text{for heterogeneous broadening} \end{cases} \tag{5.12}$$

where the wavelength fluorescence shape function $g(\lambda)$, which exhibits the corresponding normalization $\int g(\lambda)d\lambda = 1$ property, is given in reciprocal length units ($\mathrm{cm^{-1}}$ in the cgs system).

The gain functions in Eqs. (5.10, 5.12) are obviously each a difference between two addends. For example, the homogeneous case of Eq. (5.12) may be written as

$$\Gamma(\lambda) = N_2\sigma_{em}(\lambda) - N_1\sigma_{abs}(\lambda) \tag{5.13}$$

where the equal **emission and absorption cross sections** $\sigma = \sigma_{em} = \sigma_{abs}$ are given by:

$$\sigma(\lambda) \equiv (\lambda_0{}^2\lambda^2/8\pi n^2 c\tau_{rad})g(\lambda) \tag{5.14}$$

These quantities are of area units ($\mathrm{cm^2}$ in cgs). In a simple broadened two-state system, where the lower one is actually the ground state, the absorption cross section may be conveniently obtained from the measured absorption coefficient spectrum $\alpha(\lambda)$ as

$$\sigma(\lambda) = \alpha(\lambda)/N \tag{5.15}$$

The previous equality statement between absorption and emission cross-sections (sometimes addressed as **reciprocity principle**) is not always simplistically applicable and should be administered very carefully. The simple two-state system situation is quite rare. In many cases, both "lower" and "upper" states are actually multiplets. Under thermal equilibrium, optical transitions take place from the *lowest* (thermally occupied) component of each multiplet, to the *entire* list of states comprising the counter multiplet. Absorption and emission spectra may thus appear quite different.

Often, optical transitions chosen for lasing involve states residing above the ground state [T32]. Then, measurement of σ_{abs} for the laser transition is not practical. Also, a number of additional states are involved in the pumping and lasing dynamics. Energy schemes used classify as **three-state**, and **four-state** systems, as shown in Figure 5.50. In the three-state system shown in Figure 5.50a, pumping is performed from the ground state $|1\rangle$ to the excited state $|2\rangle$. Within a very short time, state $|2\rangle$ decays non-radiatively to a somewhat lower state $|3\rangle$, which serves as the upper laser state. The radiative transition from that state to the ground state $|1\rangle$ forms the lasing transition. In the four-state system shown in Figure 5.50b, the lower laser state $|4\rangle$ resides above the ground state. Within a short time after the photon emission, state $|4\rangle$ decays (**drains**) non-radiatively to the ground state $|1\rangle$ and is again available for energy pumping. In the four-state system, Figure 5.50b has a great advantage over the three-state one when state $|4\rangle$ resides sufficiently above the ground state to be practically vacant at near-room-temperature

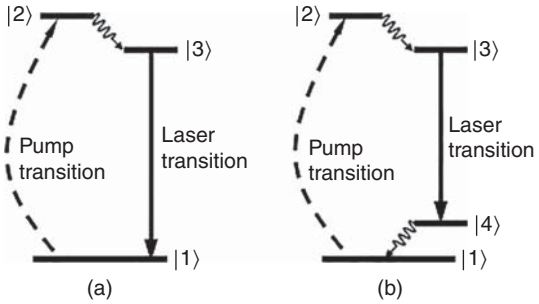

Figure 5.50 Energy schemes of amplifying media termed "Three-state system" (a), and "Four-state system" (b). Radiative transitions are indicated by solid arrows; non-radiative transitions by wiggled arrows.

thermal equilibrium. Population inversion is then achieved immediately after the pumping start. With efficient draining, the population inversion is maintained throughout the entire pumping duration.

As an example of a four-level system, in Figure 5.51 – we show a simplified energy scheme of the very popular solid-state laser gain medium, a Nd^{3+}:$Y_3Al_5O_{12}$ crystal (abbreviated as Nd:YAG). Optical pumping excites the Nd^{3+} ions from the lowest $^4I_{9/2}$ multiplet state to the $^4F_{5/2}$ multiplet. An immediate non-radiative transition follows to the $^4F_{3/2}$ multiplet. Laser transition occurs from the upper $^4F_{3/2}$ state to the lower $^4I_{11/2}$. A combined radiative and multi-phonon non-radiative transition drains the latter to the ground $^4I_{9/2}$ state. The laser emission wavelength is 1064 nm. Its fundamental radiative transition has a radiative lifetime $\tau_{rad} = 550\,\mu s$, and a room-temperature effective lifetime $\tau_{eff} = 230\,\mu s$.

After establishment of a population inversion, spontaneous emissions are amplified in all emission directions. The **amplification** is given by $e^{\Gamma(\nu)x}$, where x is the distance an emitted photon traverses through the gain medium. This emission is termed "**amplified spontaneous emission**," abbreviated as "ASE." The amplification is largest on the longest gain medium L_g, termed "**laser axis**." Due to the exponential nature of amplification, this beam is also spectrally much narrower than the regular fluorescence emission. Its spectrum peaks at the gain function $\Gamma(\nu)$ peak frequency, located very near, yet slightly smaller frequency than $g(\nu)$'s peak frequency (accordingly also at slightly longer wavelength than $g(\lambda)$'s peak wavelength; see Eqs. (5.10, 5.12)). These effects accentuate when the gain medium is placed inside an optical resonance cavity comprising two parallel mirrors. The mirrors cause the ASE to oscillate back and forth many times between the mirrors, rendering the effective **gain length** many times longer than L_g. One of the mirrors, termed **front mirror** or **output coupler**, is made partially transmitting. The light "leaking" through the front mirror establishes the laser beam output. The output is highly unidirectional perpendicularly to the front mirror plane and is highly monochromatic.

A schematic layout of a basic laser system is provided in Figure 5.52. The amplifying medium shape is assumed as a thick cylindrical rod of flat-polished, parallel bases, which is a common configuration. The pump source image is symbolized as a gas-discharge tube (arc tube), an arrangement that was popular at the most early days of laser science and technology and is still used in various laser systems. A disadvantage of gas-discharge tubes is the very broad spectral emission, rendering most its output useless for pumping. The current techniques evolve toward use of semiconductor **diode lasers** tuned to the pump transitions. Other solid-state, liquid-, or gas-based lasers are also used.

A typical spectral relation between fluorescence and laser emission is provided in Figure 5.53, exhibiting the previously described spectral features. A residual ASE of a broader spectrum may also accompany the very narrow spectrum of the high intensity laser output.

The stimulated emission occurring while lasing consumes strongly the upper states population, namely, reduces the $(N_2 - N_1)$ population inversion, hence the gain (Eqs. (5.10) and (5.12)). Lasing continues as long as the gain exceeds losses due to light re-absorption, scattering, and output. Mathematically, the net gain function

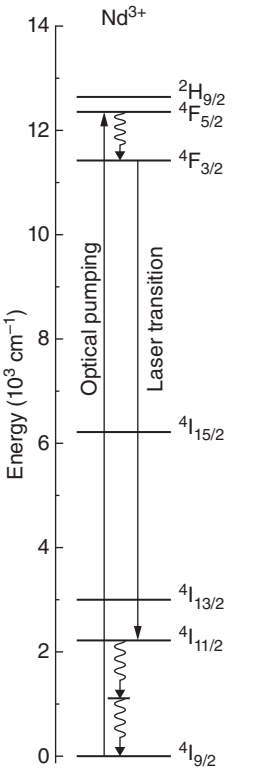

Figure 5.51 Energy levels scheme of Nd^{3+} cations hosted by c-type site of the YAG lattice; radiative transitions are represented by solid arrows while those non-radiative by wiggled ones.

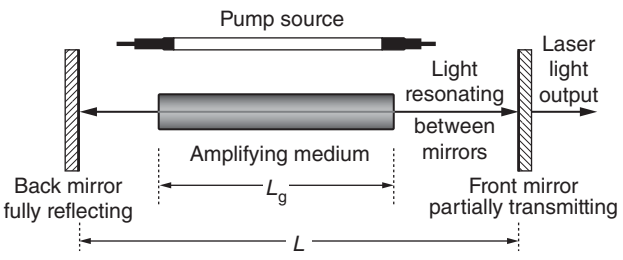

Figure 5.52 Schematic representation of a basic laser system layout.

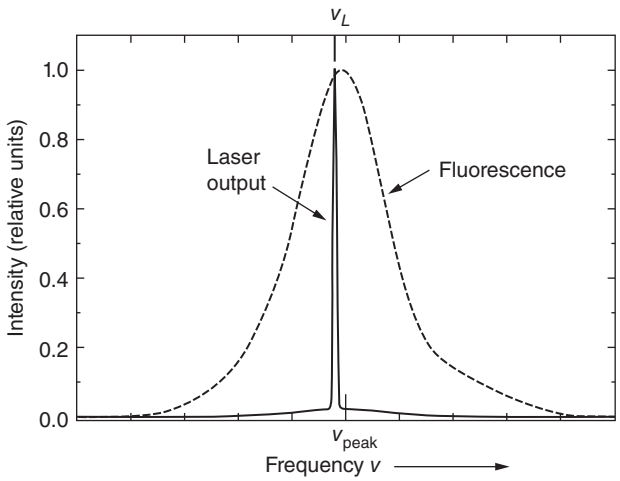

Figure 5.53 Comparison between the frequency profile of a fluorescence and laser emission bands.

$\Gamma_{net}(\nu)$ is actually the difference $\Gamma_{net}(\nu) = \Gamma(\nu) - \alpha_{loss}(\nu)$, where $\alpha_{loss}(\nu)$ is the frequency (wavelength) dependent summed losses. Lasing occurs as long as $\Gamma(\nu_L) > \alpha_{loss}(\nu_L)$. Polycrystalline ceramic hosts usually exhibit stronger scattering, namely, larger optical losses compared with glasses or single crystals. Their use for amplifying laser media should therefore be confronted against the virtues and/or disadvantages of other host material properties, such as mechanical strength, thermal conductivity, thermo-optic coefficient (refractive index temperature dependence dn/dT), as well as production cost. Bulk scattering turns small with increased wavelength. *Therefore, transparent ceramic hosts as gain media may compete successfully with other materials especially in the MIR and FIR.*

An important aspect in comparing gain vs. cavity losses relates to the presence of lumped loss factors in the cavity, particularly at faces and interfaces. For example, for R_B and R_F being the back and front mirror reflectance, respectively, the beam intensity after a single back-and-forth travel between the mirrors is reduced by a R_BR_F factor. An analogous distributed loss is expressed as $\alpha_M = -(1/2L_g)\,\mathbf{ln}(R_BR_F)$. Summed losses of an amplifying medium at the laser emission frequency may be assessed experimentally during the laser operation, from the measured **lasing threshold** occurring at the population inversion $\mathbf{\Delta}N_{th}$, hence the pumping power, which brings about equality between $\Gamma(\nu_L)$ and $\alpha_{loss}(\nu_L)$.

Sophistication in the laser resonance cavity construction, and addition of various inside components, allows exploitation of the resulted effects for different purposes, like tuning the output wavelength, selection of polarization state, control of the beam transverse spatial quality, production of short laser pulses of high peak power, and conversion continuous outputs into pulsed ones. In the following we discuss some of the said means.

{1} *Resonance cavity*: Consider a simple optical cavity consisting of two plane-parallel mirrors of distance L (Figure 5.52). Under steady-state conditions, the cavity may support waves exhibiting either an electrical field junction or a mound on any mirror surface (for metallic or dielectric mirrors, respectively). Allowed resonating frequencies thus satisfy $\nu_j = j\cdot(c/2L)$ for $j = 1, 2, 3, \ldots, \infty$, where c is the vacuum speed of light constant. These frequencies are called **longitudinal modes**. The frequency difference between modes, $\mathbf{\Delta}\nu_j \equiv \nu_{j+1} - \nu_j = c/2L$, is constant. In the optical range, where the distance L between mirrors is macroscopic, the density of allowed frequencies is very high, namely, $\mathbf{\Delta}\nu = c/2L$ is very small compared to the laser beam frequency. For example, we take $L = 15$ cm; then $\mathbf{\Delta}\nu_j \equiv 10^9$ Hz, very small compared with a typical optical light frequency, which is of the order of $\sim 5\times 10^{14}$ Hz near $\lambda \cong 600$ nm. A typical basic laser system exhibits a width of approximately 0.1 nm, equivalent to a $\sim 10^{11}$ Hz. This spectral output thus includes about a hundred longitudinal modes, contained in the "envelope" of the output spectral shape.

{2} *Output frequency tuning*: The output frequency (wavelength) may be tuned over most of the fluorescence spectral range by properly adding a dispersive medium inside the laser resonance cavity. Figure 5.54 shows a case where the dispersive medium is a triangular prism that separates angularly the frequency components of an amplified spontaneously emitted

Figure 5.54 Output frequency tuning by the aid of a triangular prism.

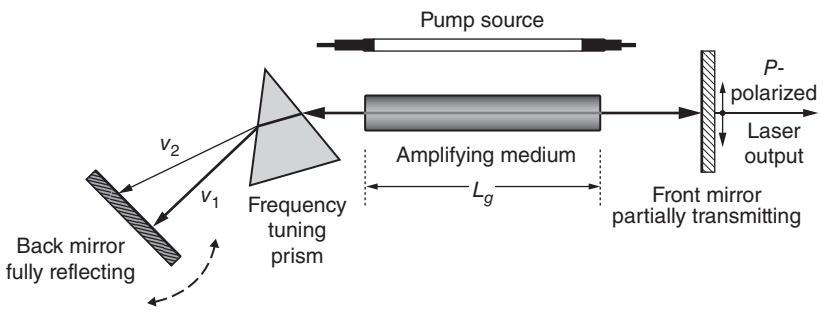

beam propagating in the axis direction. The back mirror is positioned perpendicularly to the beam component desired to be further amplified. Obviously, the other frequency components reflect sideways, undergoing only small amplification. The back-and-forth resonating beam, hence the output beam, thus tune to the frequency selected by the back mirror. The selected frequency may be varied (tuned) by rotating the back mirror about an axis perpendicular to the page plane. Often, an additional beam-broadening telescope is added between the amplifying medium and the prism, to exploit the prism's full frequency resolution capacity. A further advantage of the prism presence is the possibility of an automatic linear polarization selection: the intracavity beam incident on the prism occurs at an angle close to the Brewster angle. Therefore, the *P* polarization component (the page-plane in the figure) exhibits only minimal reflection, while the *S* polarization component (orientation perpendicular to the page) exhibits a relatively large reflection, directed entirely off the amplifying medium. In other words, the *S* polarization suffers an effectively large loss. Thus, only the *P* polarization component survives in the laser light output. The prism material and apex angle are usually selected to exhibit maximal refractive index dispersion, and minimal *P* polarization reflection on the required tuning range. Several intracavity means may allow narrowing of the shape, even ultimately to a single longitudinal mode. One means is replacing the back mirror by a **reflecting optical grating**. For the same beam width, gratings usually exhibit about an order of magnitude higher spectral resolution compared with a prism. The drawback to this arrangement is that a grating reflectance is only about 30–40%, namely, it adds considerable loss in the laser cavity. Another means is insertion of an optical Fabry–Pérot **etalon** inside the cavity. This component is in fact a thin transparent plate (~10 mm) with surfaces dielectrically coated to high reflectivity. It thus performs as a resonance cavity that allows transmission of only a single longitudinal mode of the longer laser cavity. Tilting the etalon to different angles about the laser axis allows transmission of different frequency modes, thus tuning among the longitudinal modes within the gain envelope, which forms the otherwise optically broader beam. This component also causes additional loss in the laser cavity. In this book we won't elaborate further on the previous two matters.

{3} *Passive Q-switching*: The *Q*-quantity of a laser system is a term borrowed from the first letter of the **quality-factor** concept used to describe electrical resonance circuits. The latter is 2π times the ratio between the electrical energy stored in the circuit to that lost (to heating or radiation) during a single period at resonance frequency. In the optical resonance cavity, the "*Q*" is defined analogically as 2π times the ratio between the electromagnetic energy stored in the cavity to that lost during a photon back-and-forth journey between the end mirrors. In principle, Q-switching is obtained by adding loss that stops lasing, during which, however, pumping still continues. Removal of the loss after sufficient time results in a "giant" output pulse.

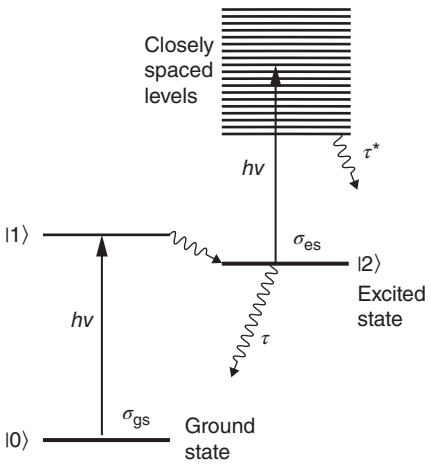

Figure 5.55 Typical energy levels scheme of a material able to act as passive Q-switch.

The mechanisms bringing about Q-switching are classified as "passive" and "active." In the passive mechanism, a light absorbing component is inserted into the cavity, such that the losses exceed gain. However, it gradually becomes transparent due to dynamic changes in its different states occupancy resulting from absorption. In the active mechanism, the loss-causing component ceases to do so by outside triggering. *Transparent ceramics containing proper saturable absorbing cation impurities could serve as passive Q-switching components.* The fabrication of ceramic Q-switches is presented in 5.2.9.2.

In Figure 5.55 we show a characteristic energy scheme of a substance described as a **saturable absorber**. The ground-state $|0\rangle$ of N_{tot} "dark" density population absorbs photons of $h\nu$ energy to the excited state $|1\rangle$. The latter decays immediately, by a non-radiative process, to populate the $|2\rangle$ excited state. The $|2\rangle$ state is **metastable**, namely, its effective lifetime τ is very long. Thus, for a sufficiently high light intensity, the $|0\rangle$ state population depletes, while that of the $|2\rangle$ state simultaneously increases. If the excited state absorption (ESA) cross-section σ_{es} is smaller than that of the

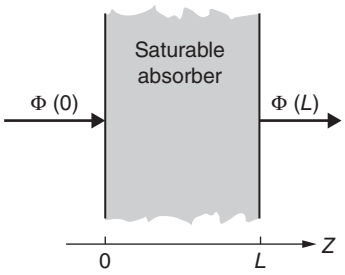

Figure 5.56 Reduction of pulse fluence by its travel through a passive switch of thickness "z."

ground-state σ_{gs}, the effective substance absorption coefficient decreases (an effect sometimes addressed as **bleaching**). Increase in light intensity results then in decrease of absorption coefficient. Saturation of the said decrease obtains after the first absorbed photons manage to transfer the entire absorbing ions population from the ground state to the excited state. The action on the beam of the passive-absorber is illustrated in Figure 5.56.

At an extreme condition, where the pulse duration is very short compared with the excited-state decay time τ, the absorber is addressed as "**slow saturable absorber**." The rate equation describing the distance z variation of photon fluence $\Phi(z)$ is given by [B70]

$$\frac{d}{dz}\Phi(z) = N_{tot}\frac{\mathbf{\Delta}\sigma}{\sigma_{gs}}[e^{-\sigma_{gs}\Phi(z)} - 1] - N_{tot}\sigma_{es}\Phi_{(z)} \tag{5.16}$$

where $\mathbf{\Delta}\sigma \equiv \sigma_{gs} - \sigma_{es}$. An absorber for which $\sigma_{es} = 0$ is termed **ideal saturable absorber**. For such absorber, the optical transmission $T_{FN} \equiv \Phi(L)/\Phi(0)$ of a plate of thickness L is then given as

$$T_{FN} = \frac{1}{\sigma_{gs}\Phi(0)}\mathbf{ln}[1 + T_0(e^{\sigma_{gs}\Phi(0)} - 1)] \tag{5.17}$$

where $T_0 \equiv e^{-N_{tot}\sigma_{gs}L}$ expresses the optical transmission in the limit of extremely low pulse fluence satisfying $\sigma_{gs}\Phi(0) \ll 1$. Equation (5.17) for the ideal saturable absorber is known as Frantz–Nodvik equation [F12]. On growing fluence, the transmission grows. For moderately low photon fluences satisfying $\sigma_{gs}\Phi(0) \tilde{<} 0.3$, the transmission growth is linear, given by

$$T_{FN} \cong T_0\left[1 + \frac{1}{2}(1 - T_0)\sigma_{gs}\Phi(0)\right] \tag{5.18}$$

On the other fluence limits, where $\sigma_{gs}\phi(0) \gg 1$, the optical transmission grows asymptotically toward a unity (namely, toward $T_{\max} \equiv e^{-N_{tot}\sigma_{es}L} = 100\%$).

As an example, Figure 5.57 displays a specific such case, where $T_0 = 50\%$. Excited-state absorption cross sections σ_{es} are usually non-zero, therefore $T_{\max} \equiv e^{-N_{tot}\sigma_{es}L} <$ 100%. Only an approximate solution exists then for Eq. (5.16), which is based on Eq. (5.17). The optical transmission is given by $T \cong T_0 + (T_{FN} - T_0)\frac{T_{\max} - T_0}{1 - T_0}$. which provides an excellent approximation when $T_{\mathbf{max}} > T_0$, and $(T_{\max} - T_0) \tilde{>} 0.3(1 - T_0)$. Here as well, on growing fluence, the transmission grows. In the high fluence limit, the transmission saturates at $T_{\mathbf{max}}$. At moderately low fluences satisfying $\sigma_{gs}\phi(0) < 1$, the transmission grows linearly as

$$T \cong T_0\left[1 + \frac{1}{2}(1 - T_0)(\sigma_{gs} - \sigma_{es})\Phi(0)\right] \tag{5.19}$$

Figure 5.57 provides theoretically calculated curves of the transmission as function of fluence for two cases where $T_0 = 50\%$: one for $T_{\mathbf{max}} = 100\%$ (ideal saturable absorber), second for $T_{\mathbf{max}} = 90\%$.

In an opposite extreme condition, where the pulse duration is very long compared with the excited-state decay time τ, the absorber is addressed as "**fast saturable absorber**." The relevant dynamic parameter is the incident light intensity $I(z) \equiv \Phi(z)/t_p$ (photons per unit area per unit time), where t_p is the incident pulse duration. The rate equation describing the photon intensity variation with distance $I(z)$ is given by [B70]

$$\frac{dI(z)}{dz} = -I(z)\left\{\frac{N_{tot}}{1 + \sigma_{gs}\tau I(z)}\mathbf{\Delta}\sigma + N_{tot}\sigma_{es}\right\} \tag{5.20}$$

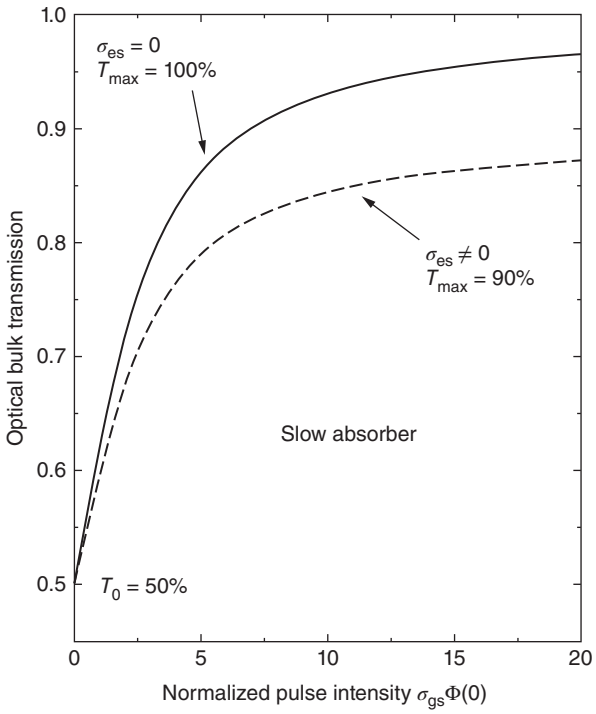

Figure 5.57 Theoretical bulk optical transmission of a saturable absorber as a function of the normalized pulse intensity.

The optical transmission obtained by solution of Eq. (5.20) for sufficiently low incident light intensities $I(0) \ll 1/\sigma_{gs}\ \tau$ is given by $T_0 = e^{-N_{tot}\sigma_{gs}L}$. On growing intensity, the transmission grows. For moderately low intensities $I(0) < 1/\sigma_{gs}\tau$, the transmission growth is linear, satisfying the equation

$$T \cong T_0[1 + (1 - T_0)(\sigma_{gs} - \sigma_{es})\tau I(0)] \tag{5.21}$$

For high incident light intensities $I(0) \gg 1/\sigma_{gs}\tau$, the optical transmission saturates at $T_{\max} = e^{-N_{tot}\sigma_{es}L}$.

We now denote $S \equiv 1/\sigma_{gs}T$ and $D \equiv \Delta\sigma/\sigma_{gs}$. A general solution of Eq. (5.20) yields the relation

$$\frac{I(0)}{S} = \frac{1 - (T_0/T)^{1/D}}{(T_0/T)^{1/D} - T} \tag{5.22}$$

Although Eq. (5.22) constitutes a closed equation only for expressing $I(0)$ as function of T, this expression is still useful for theoretical calculations and curve fitting of measured data, as one may readily swap between the $I(0)$ and T axes. An example is provided in Figure 5.58. The said swapping was administered to show the theoretical bulk optical transmission of a fast saturable absorber as function of the normalized pulse intensity $\sigma_{gs}\tau I(0)$. Two cases belonging to different relations between ground- and excited-state cross sections are presented: $\sigma_{es} = 0.05\sigma_{gs}$ and $\sigma_{es} = 0.15\sigma_{gs}$, both belonging to $T_0 = 50\%$. Both curves exhibit a linear growth as function of light intensity in the low intensity region, and saturation at high intensities.

All above calculations refer to bulk transmission, namely, after the actual transmission T_{act} has been corrected for the Fresnel combined reflectance of the two plate surfaces (each given by R). Denoting for a moment T as T_{bulk}, its relation to T_{act} and R.

$$T_{bulk} = \frac{1}{2R^2T_{act}}[\sqrt{(1-R)^4 + 4R^2T_{act}^2} - (1-R)^2] \tag{5.23}$$

A typical case of a saturable absorber is provided in Figure 5.59 [G27]. It shows the bulk optical transmission of a 1.43 mm thick polycrystalline Co^{2+}:$MgAl_2O_4$ ceramic plate by using 10 ns long pulse fluences at 1.573 μm wavelength. The Co^{2+} excited state lifetime of these materials is known to be longer than ~100 ns [G1]. Therefore, the material satisfies the conditions of a slow saturable absorber. Curve fitting by using Eqs. (5.17) and (5.19) is shown for the low and medium fluence range (0–0.8 J/cm^2). A departure from the basic theory occurs by a further increase in transmission in the higher fluence range. The figure thus demonstrates the occurrence of saturable absorption, but also a departure from the model assumptions, indicating that the process is more complex. Note that Figure 2.26 above provides a Co^{2+}:$MgAl_2O_4$ plate basic absorption spectrum and

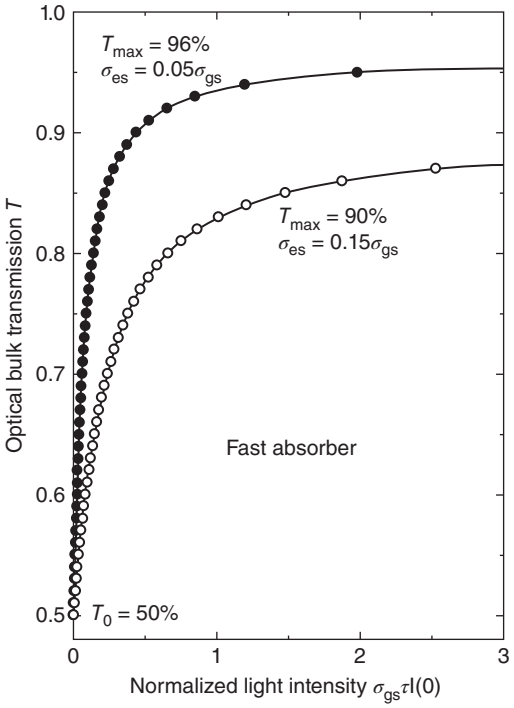

Figure 5.58 Theoretical bulk optical transmission of a fast saturable absorber as a function of the normalized pulse intensity incident perpendicularly to the front surface. Two cases belonging to a different form of the relation between ground and excited states cross-sections are depicted.

its energy state scheme. The ground-state absorption in Figure 2.26 is consistent with the $^4A_1(^4F) \rightarrow {}^4T_2(^4F)$ transition of Figure 5.59. The unexpected increased transmission in the high fluence range could, for example, relate to depletion of the excited state population by transition to a higher state. The identity of that end state, however, is unclear, as the $^4T_2(^4F) \rightarrow {}^4T_2(^4P)$ transition, while allowed, is too large for a single $h\nu = 1.263 \times 10^{-19}$ J photon. It may perhaps be related to two-photon transitions, or to charge-transfer transitions to some ligand matrix states. This issue is obviously open for further investigation.

{4} *Transverse beam modes*: Throughout previous consideration, the laser output beams were addressed as parallel, unidirectional, or in other words plane waves. Limited-size beam cross-sections, however, result in a sum of **transverse intensity modes**. Beams of cylindrical symmetry are most favorable in laser technology. Their modes are symbolized as $TEM_{p,\,m\pm}(r, \varphi, z)$, where z is the beam wave-front position along the propagation direction, r is the distance from the beam center, ϕ is the azimuth angle, and p; m; 0, 1, 2, 3, ... The function name transmission mode electron microscope (*TEM*) reflects the acronym of "transverse electromagnetic

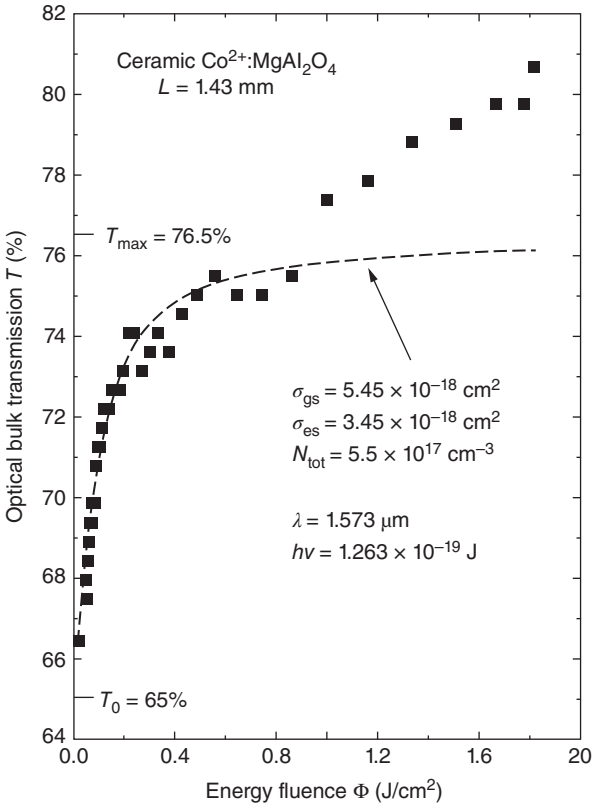

Figure 5.59 Fresnel reflection corrected optical transmission of a 1.43 mm thick transparent ceramic Co^{2+} plate (passive Q-switch) as a function of a 10 ns long pulse of 1.573 μm radiation; full squares are experimental results, while the dashed line represent a theoretical fit calculated according to equations 5.17 and 5.19.

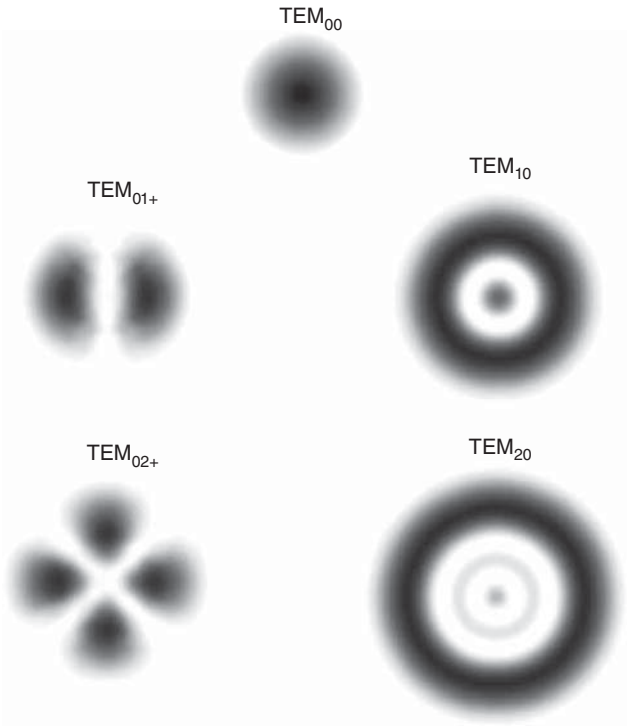

Figure 5.60 Examples of TEM profiles in the case of beams of cylindrical radial symmetry; computer generated models.

mode." The actual transverse intensity is a sum of those modes, several of which are demonstrated in Figure 5.60. The fundamental property of any mode is that it maintains its shape throughout the beam propagation, albeit radial dimension changes as discussed in the following.

Being of most compact effective cross section, the TEM_{00} mode is the most desired as a laser output. It is often addressed as the **fundamental mode** or **diffraction-limited mode**. The cross section, however, changes along the beam propagation Z-axis [Y10]. In the vacuum paraxial (near-axis) approximation, the entire scope of the single mode TEM_{00} beam characteristics is given by the following set of three equations:

$$I(z,r) = I_0 \frac{{w_0}^2}{w^2(z)} \mathbf{exp}\left(-\frac{2r^2}{w^2(z)}\right) \tag{5.24}$$

where $I(z,r)$ is the beam intensity at z position along the Z axis; r is the radial transverse distance from the axis; I_0 is the beam intensity on the axis for the specific $z = 0$ position. This position is termed **waist position**; w_0 is the beam "radius" at the waist, termed **waist radius**, and $w(z)$ is the beam transverse radius at z along the propagation axis. It is given by

$$w(z) = w_0 \left[1 + \left(\frac{\lambda z}{\pi {w_0}^2}\right)^2\right]^{1/2} \tag{5.25}$$

where λ is the wavelength (in a homogeneous material medium, λ/n replaces λ, where n is the material refractive index). Except in the waist position, the beam wave front is spherical, rather than planar; the radius of curvature $\mathbf{R}(z)$ is given by

$$\mathbf{R}\,(z) = z\left[1 + \left(\frac{\pi {w_0}^2}{\lambda\, z}\right)^2\right] \tag{5.26}$$

(Note that $\mathbf{R}(0) = \infty$, namely, the beam wave front is planar at the waist position). In the TEM_{00} mode, the beam intensity exhibits a Gaussian dependence on r (note the independence on the azimuth angle φ). The beam flux, namely, the total power crossing any $z = const$ plane, is independent of z. It is given by $P = I_0\, 2\pi(w_0/2)^2$. A transverse, axial circle of $r = w(z)$ radius delivers 86.5% of the power; a transverse axial circle of radius $r = 2w(z)$ delivers 99.9% of the power.

Figure 5.61 shows a longitudinal contour of the $w(z)$ function per Eq. (5.25). The beam shown is made to converge to a w_0 radius at $z = 0$ in a left-to-right propagation

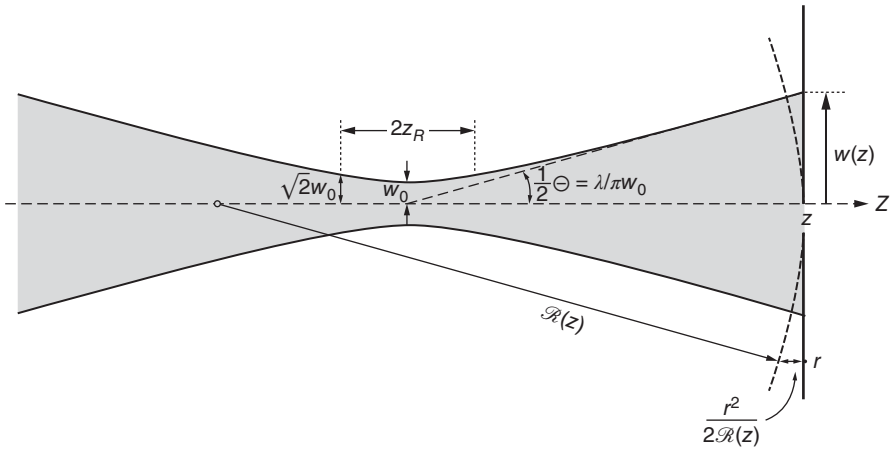

Figure 5.61 Fundamental parameters describing the propagation contour of a single-mode Gaussian beam.

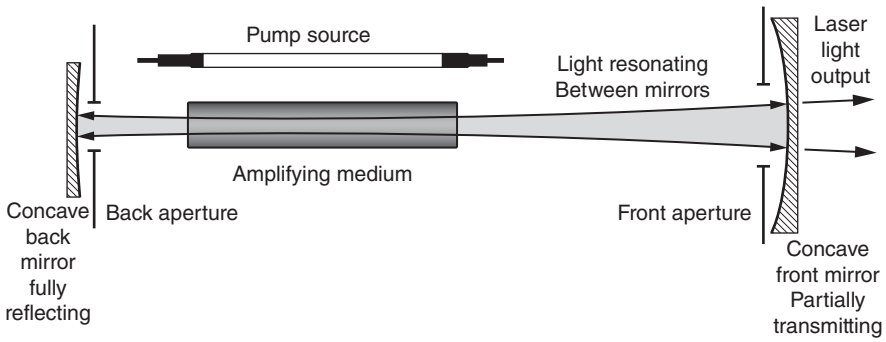

Figure 5.62 Schematic representation of a laser system designed so as to select and support the TEM_{00} transverse mode output.

direction, and then diverge. Such situation is obtained, for example, by installing a converging lens at some point on a beam propagation path. In the limit of very large z values ($z \gg \pi {w_0}^2/\lambda$), the line describing the $w(z)$ function (divergence function) is straight, intercepting the axis at $z = 0$, with a $\frac{1}{2}\Theta \cong \lambda/\pi w_0$ slope. The full beam divergence angle Θ at very large z distances is given by

$$\Theta \equiv \lim_{z\to\infty} \frac{2w(z)}{z} = \frac{2\lambda}{\pi w_0} = 1.27\frac{\lambda}{(2w_0)} \qquad (5.27)$$

Notably, the beam divergence turns greater for narrower w_0 waists. For example, a typical helium-neon (*HeNe*) laser beam whose output waist is 1.0 mm diverges by about 0.4 mrad. At a very long distance, the beam behaves as if emitted from a mathematical point source at the waist. The wave-front radius of curvature in that limit equals the distance z (Eq. (5.26)). A further important parameter of the Gaussian beam is the Rayleigh range $z_R \equiv \pi {w_0}^2/\lambda$; it is the distance from each side of the beam waist, where the beam radius becomes greater by a factor of $\sqrt{2}$; namely, $w(\pm z_R) \equiv \sqrt{2}w_0$.

Efforts to achieve a TEM_{00} output beam quality of a laser output basically involve two means. One is shaping of the pumped volume transverse population distribution to exhibit a Gaussian shape. Another is to provide a special shaping of the cavity, as in the example provided in Figure 5.62.

The cavity construction contains two fundamental changes compared with the basic construction of Figure 5.52. The two mirrors are curved by radiuses that coincide with the desired amplified wave fronts at the mirrors position, thus achieving perfect back and forth beam resonance. In addition, apertures are placed near the back and front mirrors of radiuses corresponding to $r = 2w(z)$ at the mirrors. Thus, 99.9% of the desired TEM_{00} mode are never interrupted, but other transverse modes are grossly filtered out (Figure 5.60).

The pure TEM_{00} mode is the least diverging beam and is sometimes addressed as the **diffraction limited mode**. Even minor irregularities in the laser resonance cavity components, such as in the refractive indices of the amplifying medium, may result in increased beam divergence. *Thus, transparent ceramics intended for functioning as amplifying laser media need to exhibit highly regular refractive indices*. A measure of a beam quality is obtained by measurement of its spatial divergence. The actual divergence angle Θ_{real} is compared against the theoretical diffraction-limited divergence $\Theta_{DL} \equiv 2\lambda/\pi w_0$. The ratio $M^2 \equiv \Theta_{real}/\Theta_{DL}$ is considered a figure of merit describing a laser output beam quality.

5.2.9.1.2 Laser Systems Efficiency: Characterizing Parameters

Since a wide variety of laser system types exists, most of the characterizing parameters are specific to the type under consideration. In CW lasers, the chosen parameters are wavelength, output power, and beam quality. In pulsed lasers, further parameters of interest are the pulse duration (usually the full width at half maximum – FWHM), pulse energy, pulse peak power, and repetition rate. In case of ultra-short pulsing, such as in the picoseconds (10^{-12} seconds) or femtosecond (10^{-15} seconds) ranges, the spectral width is also of prime importance. Two operational parameters, however, are of interest *in all cases*: the lasing pump energy/power threshold and the output slope efficiency. We have already mentioned that laser operation starts only when the gain exceeds losses. The unique input power where *gain equals losses* is called **lasing threshold**. Aforementioned threshold, the output usually increases linearly with input energy/power. The coefficient of that increase (slope) is called **slope efficiency**.

For demonstration of that issue and some other laser fundamental issues, in Figure 5.63 we show experimental results obtained for a pulse-pumped Nd : YAG laser [S31] of a basic laser construction (Figure 5.52). The pump source was a Xe gas-discharge flash tube driven by a current pulse, about 70 μs long. The latter was achieved by discharging a charged capacitor. The discharge energy, defined as "input energy," was varied by varying the initial charging voltage across the capacitor. The amplifying medium was a $Nd^{3+} : Y_3Al_5O_{12}$ rod, 5 mm in diameter and 75 mm long. "Free-running" output, namely, output obtained when the beam is not processed by any device (say, a Q-switch), provided about 50 μs-long non-polarized 1064 nm light pulses. The output laser energy vs. the system input energy exhibited a threshold of $E_{th1} = 2.5$ J, for the energy input to the flash tube, and a slope efficiency of 2.93%. The reason for the low efficiency is the very broad spectral emission of the Xe flash tube, most of it not being absorbed by the Nd^{3+} ions. Modern systems employ semiconductor diode lasers accurately tuned to the proper ions absorption. This renders the thresholds much smaller and the slope efficiency much closer to a unity.

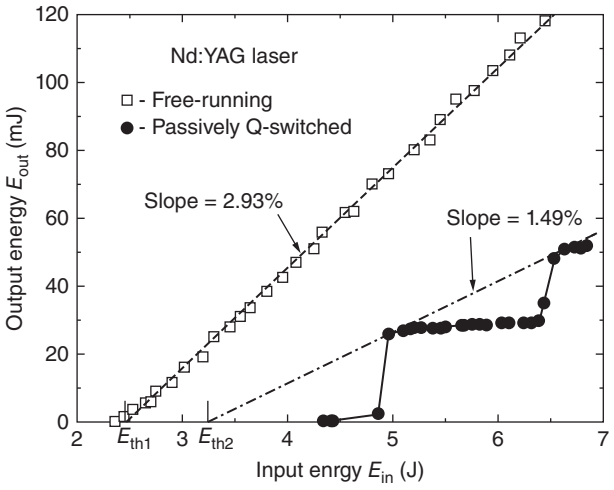

Figure 5.63 Output vs. input pump energy of an Nd : YAG laser under free-running and passively Q-switched conditions. The Cr^{4+} : YAG plate used for Q-switching was 2.65 mm thick, tilted to Brewster angle relative to the laser axis.

Insertion of a Cr^{4+} : YAG saturable absorbing plate tilted to Brewster's angle inside the laser cavity changed the output nature. When lasing, it provided several, linearly polarized separate 1064 nm light pulses, each ~70 ns long. At low input energies, only a single pulse appeared. Considerable added input is required to achieve a second consecutive pulse and so on. The time separation between consecutive pulses shortened as function of input energy. In the output vs. input curve, this behavior appears as a step-like function: when added input is sufficient to induce a consecutive pulse, the output steeply increases, forming a step-like contour: each step raiser belongs to the appearance of an additional short pulse within the pump pulse duration. The inserted saturable absorber, however, introduces additional cavity loss. The added loss expresses itself by a higher threshold and lower slope efficiency; particularly in Figure 5.63: $E_{th2} = 3.45$ J and the slope efficiency was1.49%.

In many cases, the energy absorbed by the amplifying medium is used on the abscissa instead of the input energy; in such cases one talks about "optical efficiency." This practice is useful for quantifying the amplifying medium gain and cavity loss parameters. It is usually done when the absorbed energy may be satisfactorily measured, for example, when pumping with a monochromatic light beam, such as the output of another laser.

5.2.9.1.3 Laser Oscillators and Amplifiers

For quite a number of applications, laser systems are required to provide high quality output beams of very high power. An obvious approach to increase output is to increase the input power/energy. In solid-state lasers, such an approach is often detrimental to the beam quality by inducing non-axial refractive-index variations ("lensing"), strain buildup and overheating, which sometimes causes fracturing of the solid gain medium.

A solution toward satisfying the high power needs is the using a chain of gain media, where each gain medium is only moderately pumped. Such a chain functions as a power amplifier. The first component is actually an individual laser oscillator providing a low power, yet a high-quality beam. That beam is directed so as to traverse successively the other chain components, each

only moderately pumped. The beam quality is thus preserved, yet its power increases toward the desired need. Such construction is called "**master oscillator power amplifiers**," abbreviated by its MOPA acronym.

5.2.9.1.4 Device Operation Related Improvements Allowing Increase of Ceramic Lasers Performance

The modest performances of the first solid-state laser devices, like those developed by Hatch et al., Maiman, or Snitzer and Woodcok [H16, M6, S41], have been constantly, and at high pace, improved. This has been accomplished by both device related improvements introduction and development of more efficient and powerful gain media. The latter are discussed in Section 5.2.9.1.5, while the former in this section. Introduction of diode laser based pumping, power scaling, pulse length reduction, beam optical characteristics control, device miniaturization, and versatility of gain-media geometry increase (bulk, chip, fiber) are among the achievements in the area of device related improvements one can highlight. Let us give some detail about these.

5.2.9.1.4.1 Diode Lasers as Pumping Sources

One of the essential steps forward, for all solid-state lasers, was the advent of the diode (semiconductor type) laser as a pumping source. The semiconductor based lasers (InGaAs/GaAs [900–1100 nm], AlInGaAs/GaAs [840–900 nm], AlGaInP/GaAs [630–670 nm], InGaAsP/GaS [1000–1650 nm], etc.), emitting in narrow bands (0.5–4 nm), as opposed to the wide spectra of flash lamps, can pump at energies well matched to the peaks of the absorption bands of the lasing ions or their sensitizers. Such pumps are also quite efficiently using the initial electrical energy (η = 50–70%) and operate in both CW and pulsed regimes. A major drawback is their low output power. Multiple unit diode batteries, of various geometrical arrangement in relation to the gain media, are needed for operation of high power lasers. For instance, J. Lu et al., for obtaining a 31 W output from a Nd^{3+}:YAG rod, had to use 32 sets of 10 W diodes (emitting at 807 nm) in order to gather the 215 W necessary to pump into the gain medium [L51]. The beam emitted by the diodes is not of very high quality, but it can be delivered via a fiber coupler at considerable distance. The initial cost of diode lasers was high, but they are much cheaper nowadays. Owing to this, diode pumped lasers are considered for fusion based future power plants. Yb:YAG laser was shown, by modeling, as requiring a smaller number of diodes per unit than the conventional Nd:glass solid-state laser [I3].

Solid-state, especially tunable lasers (e.g. Ti:shappire), can also be used, of course, for targeted frequency pumping. A significant advantage of such schemes is the reduction of quantum defect.

5.2.9.1.4.2 Cryogenic Operation

Certain perovskite-structure ceramics, when brought to temperatures lower than 100 K, exhibit a massive increase of their electrical conductivity (superconductivity). In a somewhat similar manner, albeit less dramatic in scale, the solid-state lasers, including those based on a ceramic host, show significant performance increases, related to various aspects of their functioning, on cooling. Thus both the beam quality and the lasing process efficiency can be improved at low ≤77 K temperatures. Cryogenic operation was used from the beginning of solid-state lases [F2]. For a given host, λ_{th} is increasing with a decreasing temperature. At suitable temperatures, which are significantly lower than RT, the higher λ_{th} of certain useful hosts compared with that of YAG, and the benefits this brings, can be maintained also after loading them with high levels of lasant cations' oxide.

The mass difference between Yb^{3+} (the optimal RE^{+} for higher power lasers) and host cations like Y^{3+} or Sc^{3+} leads to noticeable scattering of phonon waves and, as a result, to a marked thermal conductivity decrease. We have seen that because, in case of a host cation like Lu^{3+}, the mass difference is lower, the λ_{th} of heavily Yb-doped Lu_2O_3 decreases only mildly compared with pure Lu_2O_3; that even if measurement is done at "high" (in Kelvin) temperatures like RT. At liquid N_2 temperatures (77 K), because the reduction of phonons scattering intensity, the difference in λ_{th} of hosts like Y_2O_3 and Sc_2O_3 in, respectively, pure and doped (with Yb^{3+}), are reduced, bringing them closer to the performance of Lu_2O_3 as a host (as far as λ_{th} is concerned) for Yb^{3+}; thus cooling widens the list of suitable hosts for Yb; Yb^{3+} is an essential lasant for high power devices.

The lowering in phonons scattering intensity is mostly owed to increase of their mean free path when temperature decreases. This affects the thermal diffusivity, which is determined by "Λ" and the phonons velocity, according to the relationship:

$$\beta(T) = \Lambda(T)u(T) \tag{5.28}$$

u = phonon velocity, Λ = free mean path, $T = t°$ in Kelvin, β = theoretical diffusivity

$$\beta(T) = \frac{\beta_0 e^{\frac{aT_0}{T}} - 1}{e^a - 1} \tag{5.29}$$

$\beta_0 = \beta$ at a reference temperature T_0, $a = \frac{\theta_D}{bT_0}$ where $b \sim 2$ and θ_D is the Debye temperature.

The thermal diffusivity, in turn, is the major factor dictating the temperature profile of $\lambda_{th}(T)$ and the thermal conductivity, as shown in Eq. (5.30)

$$\lambda_{th}(T) = \rho(T)\beta(T)C_p(T) \tag{5.30}$$

where ρ is the density. ρ increases slightly when the temperature decreases, while C_p decreases at a rate which massively rises under the Debye temperature.

Considering (5.29) it is seen that β rises significantly on lowering of $t°$, so that overall $\lambda_{th}(T)$ increases noticeably on cooling.

Besides λ_{th} the thermal expansion coefficient α also decreases with $t°$.

A first positive macroscopic effect of the temperature variation profile, of the properties discussed above, is an increase, at low $t°$, of the gain-media resistance to thermal shock (a critical requirement in high power devices), according to

$$R_{tsh} = (1-\nu)\lambda_{th}\mathrm{K_{IC}}/\alpha E\,(10^{-20}\ \mathrm{m^2/W}) \tag{5.31}$$

ν is the Poisson coefficient, α is the thermal expansion coefficient, and $\mathrm{K_{IC}}$ is the fracture toughness.

On balance the temperature dependence of the factors present in (5.31), of which the strongest variation (positive) is that of λ_{th}, is such that R_{tsh} increases with a decreasing temperature (especially under θ_D). The R_{tsh} parameter (following Hasselman) given by (5.31) is used to compare the merits of different gain media.

Based on R_{tsh} values it results that Nd:YAG at 300 K is ~30× less resistant than Yb:YAG at 100 K.

A second useful effect of temperature decrease is the reduction of $\left|\frac{dn}{dT}\right|$. In the frequency domain of the transparency window, the sign of $\frac{dn}{dT}$ is positive.

Temperature gradients in the gain media, related to their functioning, raise the temperature over that of the surrounding medium. The temperature gradients are dependent on position on the radius of the point considered, calculated from the longitudinal axis. Mechanical straining, resulting in the formation of stress fields also result from temperature variation, within the gain-media piece's volume. Via the photoelastic effect (its variation from point to point), along the transverse axis, the stress field leads to formation of birefringence, despite the isotropic nature of the ceramic. These optical distortions (thermal lensing) contribute to radiation scattering, affecting both laser beam quality and lasing process efficiency. Considering the parabolic variation of the temperature along the radius of a cylindrical rod-shaped gain media, the optical path, of a laser beam parallel with the rod's axis, will vary as a function of its radial position. The result is a wave-front distortion similar to the action of a lens with a dioptric power, D_{th}:

$$D_{th} = 1/f_{th} \tag{5.32}$$

where f_{th} is the ratio between the power P of the beam at a given moment and the threshold power P_{th}.

For short laser rods, their end bulging, caused by the thermal gradients, also contributes to optical distortions.

Last but certainly not least, the effects of temperature variation on the absorption and emission of radiation need to be considered. The major process in this context, sensitive to temperature variation, is the electron–phonon interaction. Shift of position (e.g. by an increased crystal-field intensity) of absorption and emission lines, reduction of the homogeneous part of lines broadening (i.e. better resolution) are produced when substantial temperature changes occur. The population of the upper crystal-field state of the base manifold (the terminal state of the lasing) can be reduced, and thus three level lasers may work in a quasi-four level manner. For instance, the Cr^{3+} based ruby laser does not need, at low temperature, the strong pumping its operation at RT demands. Low temperature work is also beneficial for lasers based on Er^{3+} (1.54 µm), Tm^{3+} or Ho^{3+}.

In cases like Co^{2+}, the benefit of cryogenic conditions is related to metastable level's lifetime increase (certain non-radiative relaxation tracks reduce their rate).

Many of the diode-laser pumps function with higher efficiency at low temperatures.

For ions like Yb^{3+} flash lamp pumping is good enough only at low temperature. For RT work one is restricted to diode pumping. At RT the par between highest crystal field (CF) state of the base manifold and the ground state (~600 cm^{-1}) is approximately three hours at RT, while at 100 K it equals ~9 kT. Thus the occupancy of the terminal level, due to thermalization, is much lower at 100 K (quasi four levels scheme) for the 1030 nm lasing. Cooling also limits the laser re-absorption process [L60]. Regarding the beam quality, the most important deleterious effect of the thermal gradients is related to depolarization.

Cryogenic lasers (with moderate cooling), while more complex systems than RT devices, are though, not that difficult to build and operate. Liquid N_2 is readily available and not expensive [B61]. The benefits of cryogenic operation outweigh the disadvantages for some of the important types of laser devices. Examples are machining systems based on laser, weapons, or fusion triggers. For instance, a team at Snake Creek, US, demonstrated cryogenic operation of a Yb:YAG laser at an optical–optical efficiency of 86% [B61]. Work close to zero kelvin is another story.

5.2.9.1.4.3 Cavity-Loss Control

Such an operation can be effectuated by a number of techniques and may have various objectives – as it will be shown in the following text.

5.2.9.1.4.3.1 Q-Switching (see Section 5.2.9.1.1 for Mechanism Description)

The "normal" state of a lasing system cavity is one in which the optical loss is minimal, i.e. it exhibits a high quality factor "*Q*." Both the intrinsic to the cavity and

the out-coupling losses are small enough to keep the lasing threshold low. When such conditions are met, the laser works in a "free generation" mode. The device designers introduced other modes of operation which, for certain applications, lead to massive performance improvements. For instance, a controlled Q variation may help in the formation of short pulses of very high intensity. One technique, called "Q-switching," causes temporary reductions of the Q, which prevent laser emission. As a result, under suitable pumping conditions, the inverted population can be raised much above the lasing threshold, i.e. energy is accumulated inside the resonator. When a high Q is restored, the sudden de-excitation to the terminal level of this highly inverted population (unstable system configuration) means that a high energy pulse comes out of the cavity via the out-coupler mirror. Single pulse or trains of pulses can be obtained. Active and passive Q-switches can be used. The passive Q-switches can be based also on doped transparent ceramics, and their fabrication and properties are detailed in Section 5.2.9.2.

The length of the pulse produced by Q-switching is

$$\tau = \frac{t}{(1-R)} \tag{5.33}$$

t is the time it takes the laser light to made a round trip around the cavity and R the reflectivity of the output mirror.

Q-switching may be used only for lasing ions able to store energy in the excited state for a time longer than the pulse. This issue and the ceramics employed in their fabrication will be presented in more detail in Section 5.2.9.2.

5.2.9.1.4.3.2 Mode Locking

In the cavity the light, at the lasing wavelength, can establish a standing wave, because the resonance condition $N\lambda = 2L$ is satisfied (L is a cavity length, N is an integer). The standing wave's intensity variation profile, along the longitudinal axis, is called a mode. In practice a number of modes, slightly differing in wave length, can achieve resonance in a given cavity. Thus there exist a range of wavelengths (or frequencies) that can contribute to gain (gain band width), like shown in Figure 5.64 [H21].

Not all these modes are in phase and therefore their interference is not always constructive, as needed for intensity amplification. It is possible, however, to "lock" together many of the longitudinal modes (existing within the gain range), so that the laser simultaneously oscillates in phase on all of them. This is accomplished by inserting into the cavity special optical elements. In such conditions very short pulses can be formed. The length of the pulse depends on the range of frequencies involved, according to $\tau_{minimum} = 0.44/\Delta\nu$. Pulses of a few femtosecond duration can thus be obtained.

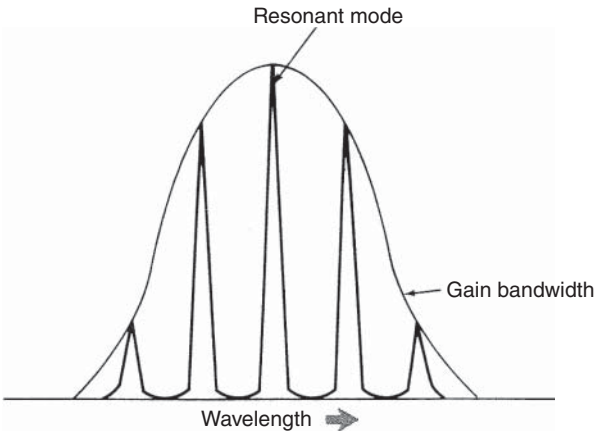

Figure 5.64 Resonances fitting within the gain band-width of a laser. Source: Hecht 1994 [H21]. Reproduced with permission from John Wiley & Sons.

5.2.9.1.4.4 Laser Output Signal Manipulation

The aspects discussed earlier were related to actions occurring inside the cavity. The laser devices performance can be significantly improved also by actions effectuated on the laser beam which leaves the cavity. Some of them are presented in the following text.

5.2.9.1.4.4.1 Chirped Pulse Amplification (CPA)

The "chirp" of an optical pulsed signal indicates the extent to which its instantaneous frequency is time dependent. Up-chirp means that the frequency rises with time. Chirps may appear owing to undesired external factors influence or be the result of voluntary signal processing. Chirped pulses may be used for laser signal amplification in a form that avoids deleterious effects of the amplification. The method was first used in the 1960s for radar systems. It was adapted to lasers by G. Mourou et al. and D. Strickland and G. Mourou (won a Nobel prize for this) [M41, S66]. The ultrashort laser pulses (for instance, produced by mode-locking) used in high power systems, when they exceed fluence levels of a few GW/cm^2, are subjected to some nonlinear effects like self-focusing, and also may damage the gain-media. In the chirped pulse amplification (CPA) operation an initial weak, short, pulse is stretched out (time and frequency), before entering the amplifier gain media. The stretching is done with a pair of suitable optical gratings. In a positively chirped signal the lowest frequency component lags after the highest frequency component and has a longer ($\times 10^3$–10^5) duration. Such a signal is not damaging to the gain media, which amplify it (up to $\times 10^6$ times). The signal is then recompressed, before exiting the system. Instead of gratings also prisms may be used. The CPA is widely used in the most powerful laser systems (power [watt] [PW] peak powers) in operation (installed in particles accelerators or fusion test systems).

5.2.9.1.4.4.2 Processing by the Aid of Nonlinear Optics

Certain optical and spectral parameters depend on various factors of influence in more complicated way than the linear form taken as a first approximation [H21]. For instance, the refractive index "n" depends on a bias electric field according to

$$n = n^0 + aE_0 + bE_0{}^2 + \ldots \tag{5.34}$$

where n^0 is the value of n in the absence of a bias field.

Besides the use in non-laser EO devices (like the flash-goggles described in Section 5.2.7), this dependence may be used also in laser systems with much benefit. In many practically encountered cases (especially for low levels of E_0), the coefficients of the terms of the series are so small that $n \approx n_0$. For certain conditions and type of optical material, however, this is not the case. The nonlinear relationship between the characteristics of the output and input waves of a laser system can be exploited in various forms, like, for instance, the multiplication of laser wavelength solid-state gain media can provide. This is crucial because the ceramic laser, and in general the solid-state lasers, can offer, at least currently, only a quite limited set of wavelengths. Using nonlinear effects in adequate materials (larger values of the higher power terms coefficients) and work conditions, a process called "harmonic generation" can be put to use. This means the formation of laser waves the frequency of which equals integral multiples of the basic one. The second harmonic has a $\nu_1 = 2\nu_0$ or $\lambda_1 = {}^1\!/_2\lambda_0$. This is so because an output wave of such frequency will appear if the coefficient (amplitude) K, of the quadratic term of the series, which describes the output waves $= f$(input waves), is high enough. The dependence is correctly written as Output $= Ke^{-i\omega t} + K^2e^{-12\omega t} + \ldots$, where ω is the frequency. The amplitude of the second harmonic wave (that of frequency $= 2\omega$) is K^2. For instance, one can double, in such a way, the basic 1064 nm Nd emission lines frequency (2.83×10^{14} Hz) to the equivalent of a $\lambda_1 = 532$ nm (5.66×10^{14} Hz). Another effect of nonlinearity is the possibility to produce sum or difference frequencies. For instance, starting with frequencies ω and φ, laser light of $(\omega + \varphi)$ frequency can be generated. The inverse operation is also feasible, i.e. to split an input $\omega + \varphi$ signal in two signals of respectively ω and φ frequencies. In terms of λ the resulting λ_1 and λ_2 lines are longer than the basic signal. This is usually done with a device called "optical parametric oscillator" (OPO). In an OPO pump, light of frequency $= \omega + \varphi$ enters a resonant cavity (like that of a laser), which includes a nonlinear medium (bonded by mirrors reflective of ω and φ). The output are signals at ω, φ, or both ω and φ frequency. The potassium titanyl phosphate (KTP) is currently the most popular nonlinear crystal used for such devices. Tuning of λ is possible by adjusting the cavity or changing the nonlinear crystal. An OPO can be a good source for molecular spectroscopy, providing output tunable in the 1.5–5 µm range. Combining CPA with the use of OPOs is another highly efficient amplification scheme.

5.2.9.1.4.4.3 Intensity Modulation

The intensity of a laser signal can also be modulated mechanically (shutters and choppers) by modulating the input power or with external electrooptical modulators (Kerr or Pockels effect based cells). An interesting additional option is that of electro-acoustic modulators.

5.2.9.1.4.4.4 Coherent Beam Combination

Owing to difficulties during fabrication and thermal management, the size of the gain media is limited. For very high power apps (e.g. laser peening, 2D laser machining, fusion drivers, or particles oscillators), the power delivered by single lasing units, even of large size, is not enough. One method to increase power is coherent combination of single-unit beams by a method that uses stimulated Brillouin scattering phase conjugation mirrors (SBS-PCMs). A method introduced by H.J. Kong et al. [K34] made possible the use of such mirrors despite the random phase of SBS processed waves. The system allows the correction of the wave front components (piston errors) when their integration is sought.

Current efforts are dedicated to enlarge the number of beams (up to 200). Such systems allow also self-navigation of the beam onto a target. This is critical for apps like fusion-driving, where the beams illuminating the small, spherical, target need to arrive at the calculated impact point with a 20 µm accuracy. The signal sources considered for such systems are Nd:YAG ceramic lasers.

5.2.9.1.4.5 Lasing Device Configuration Optimization

The performance of the available gain media units is limited regarding aspects like size, dopant concentration, or thermal conductivity. Various lasing system designs, in which the number of gain media units, their arrangement and other device features are optimized are instrumental in raising system performance, especially power, were developed. A few examples are listed in the following text.

5.2.9.1.4.6 ThinZag Configuration

A system design allowing an improved thermal management, and thus output power increase, was developed by the Textron company [K26, M11]. Such devices are called ThinZag and are based on the use of a specific oscillator design in which beam has a zigzagged path, like shown in Figure 5.65 [K27].

A very thin, long, slab of Nd:YAG (10–30 mm of width) is sandwiched between silica glass plates. The system is cooled by an adequate liquid. The system is pumped from both sides with flash lamps or (preferred now)

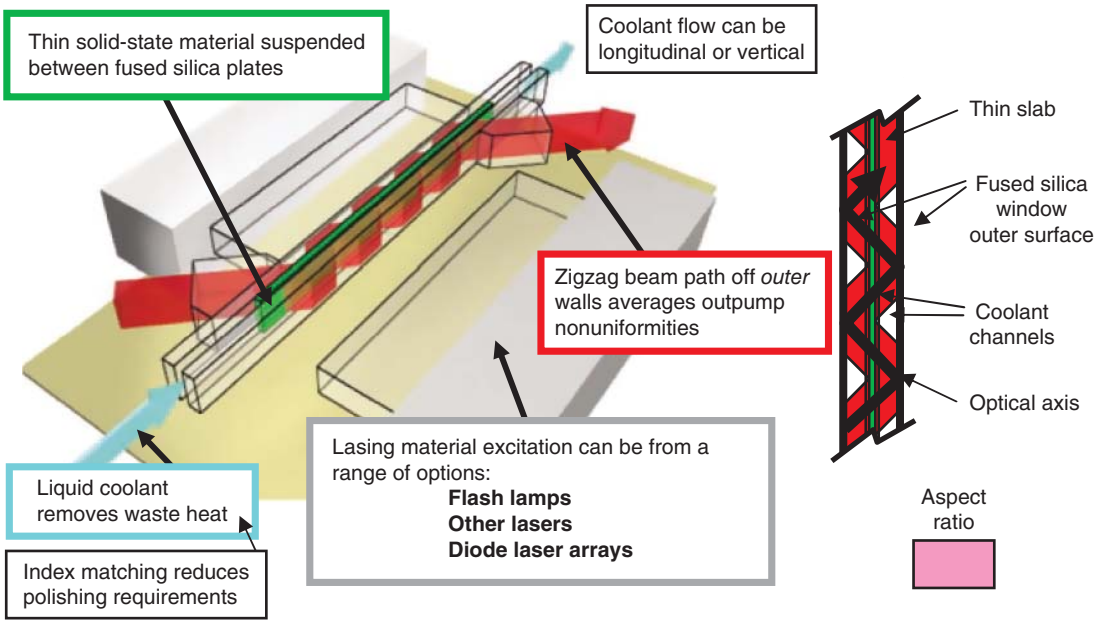

Figure 5.65 A laser system configuration (ThinZag design of Textron) allowing good thermal management which allows significant power scaling. Source: Klimek and Mandl 2011 [K27]. Reproduced with permission from McGraw-Hill.

diode laser arrays (currently diode bars, working at an optical efficiency of ~60% and costing less than US$10, are available). The silica plates act as waveguides and the beam reflects off the plates' outer surfaces, following a zigzag trajectory. The silica plates also act as scramblers for the pumping light (λ = 808 nm), making it more uniform. The aspect ratio of the beam cross-section is near unity. The thinness of the gain medium allows effective thermal management. Experiments made at Textron showed that ceramic Nd:YAG slabs exhibit a higher optical quality than their single-crystal counterparts. Designs in which each module (TZ-3) has more than one YAG slab were shown as working. Modules provide outputs of up to ~17 kW. By coupling six TZ-3 modules, output powers of ~100 kW could be obtained.

A problem is that at high power the beam quality starts to deteriorate.

5.2.9.1.4.7 Virtual Point Source Pumping

The virtual point source (VPS) configuration developed in the 1990s [L50] allows the use of diode-laser pumping multiple units batteries while maintaining pumping uniformity. The diodes are arranged so as to form a ring and their output beam is focused onto a point or line, as shown in Figure 5.66, by the aid of optical components made of cylindrical lenses and high-reflectivity spherical mirrors. The YAG:Nd rod is located inside a reflective, coaxial, transparent tube. The arrangement re-images the focus point along the tube length, so that uniform and

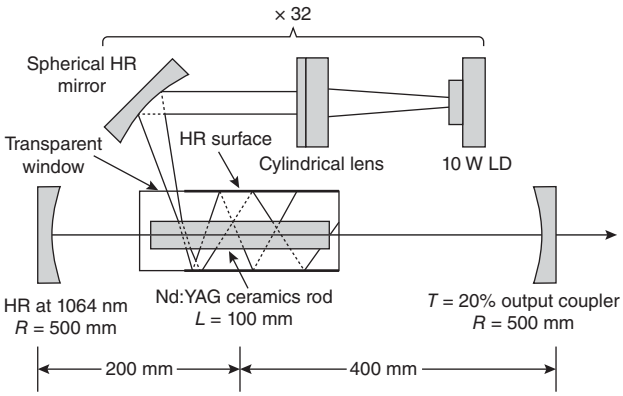

Figure 5.66 Schematic of laser system design that includes a virtual point source; allows significant power scaling. Source: Lu et al. 2000 [L50]. Reproduced with permission from Springer.

high power pumping is achieved. Using such a design and a Nd:YAG rod of 10 cm length (ϕ = 3 mm) located within a 60 cm cavity, an output of 31 W (18.8% slope efficiency) was generated at λ = 1064 nm (input = 214.5 W of λ = 808 nm).

Output beam corrections can be effectuated also by the action of optical components external, to cavity. A detailed presentation of this issue is not justified here – where the gain media proper are the objects of interest. Further details can be found in the literature of interest to people involved in laser devices development.

5.2.9.1.5 Ceramic Gain Media (Host + Lasant Ion) Improvements

5.2.9.1.5.1 The Hosts

We saw, in the sections earlier, how a laser device functions and how – effectuating specific actions on the laser beam inside the cavity and outside it – it is possible to improve the performance of such items. The improvements made – to the part of a laser device, which is of most interest to us, the gain medium – will be described in this section.

In order to be able to asses correctly the importance of the various contributions, let us start with the requirements, a ceramic host must satisfy.

5.2.9.1.5.1.1 Requirements Concerning Ceramic Lasing Ion Hosts

A requirement common to the solids that host the active dopants is high transparency in both in the pumping and emission spectral zones. As indicated in Table 5.1, the severity of requirements – regarding the optical characteristics – is higher, in the case of laser ceramics, than for other TC types. The general rules for transparency apply, however, also in the case of the gain media, viz a cubic lattice (except if anisotropic materials particles are orientated; see Section 3.1.2.2.2) a wide enough bandgap and absence of second phases or residual stress fields able to scatter EMR. The absence of porosity is, here too, the most difficult technology related requirement; the pores volume fraction has to be, in general, lower than 50 vol ppm but for top quality ≤2 vol ppm is necessary. The gain-medium lattice has to be made up of cations having a radius matched to that of the intended dopants (lasing ions). For instance, if a Ti^{3+} based tunable laser is considered a host like single crystal corundum or ceramic spinel may be adequate. Most of the solid-state lasers are based, however, on RE^{+} type ions. For such ions larger native cation containing hosts, like YAG sesquioxides of Sc, Y, and Lu are needed; in principle, size-wise, cubic zirconia may also accommodate some RE^{+} ions. In Table 5.4 the radius of RE^{+} and TM^{+} ions, relevant as emitters (some for non-laser apps), are given, together with those of potential host cations. The data is taken from the standard source for it: the paper of R. Shannon [S28] (it may be worth recalling, at this point, that the issue of ionic radii is yet an open question).

The lattice of the host has also to allow the accommodation of a sufficient amount, of the active dopants (without leading to deleterious dopant interactions). This requirement limits the number of TCs able to function in gain-media applications because the tolerance to extrinsic cations depends on may factors like the already mentioned native sites size and symmetry but also on the nature of the chemical bond, prevalent in the host or the stabilization energy, brought about by certain coordination patterns owing to ligand field (LF) effects.

Table 5.4 Radii of TM^{+} and RE^{+} cations.

Doping cations	Radius (Å)		
	r_8	r_6	r_4
RE^{+}			
Nd^{3+}	1.249	1.123	—
Yb^{3+}	1.125	1.008	—
Er^{3+}	1.144	1.003	—
Ho^{3+}	1.155	1.041	—
Tm^{3+}	1.134	1.020	—
Ce^{3+}	1.238	1.150	—
Sm^{3+}	1.219	1.098	—
TM^{+}			
Ti^{3+}			
Cr^{3+}	—	0.755	—
Cr^{2+}	—	0.870	—
Cr^{4+}	—	0.690	0.550
Co^{2+}			
Host cations			
Y^{3+}	1.159	1.040	—
La^{3+}	1.300	1.172	—
Lu^{3+}	1.117	1.001	—
Al^{3+}		0.675	0.430
Sc^{3+}	1.010	0.885	—
Sr^{2+}	1.400		—
Ca^{2+}	1.260		
Mg^{2+}			

The charge compensation schemes available – in cases where ions with oxidation states, differing from those of the native ions, are involved – also affect the way the ions substitution are undergoing; entropic effects also need consideration. The lasing dopants accommodation ability of a host is a critical feature. While the main structural characteristic influencing this ability are known, much remains to be understood regarding the interaction between the factors of influence, especially in quantitative terms. Progress regarding this issue would allow reduction in the amount of trial and error investigation currently needed when increase of dopant concentration is attempted. By selecting an optimal host, the pattern of the lasant ions set of electronic levels and their energy can be manipulated to a certain extent.

A specific feature of the polycrystalline (the case of ceramics) hosts is the existence of the grain boundary region, the structure and composition of which differ – to a certain extent – from that of the grain's core. As a result, the dopants located in such regions may exhibit spectral properties somewhat different from

those of the active ions located far from the GB [L66]. Many dopants tend to segregate toward the GB region, and the fraction such regions represent – from the total volume of a grain – becomes significant in the case of submicron or nano-microstructures. Therefore, the percentage of distorted sites can get high enough to be felt in the absorption and emission of radiation. So it is necessary to limit, in some cases, the intensity of segregation, by special measures. On the other hand the existence of GBs may bring about also positive consequences. For instance, in such disordered regions large RE^+ type cations may accommodate themselves in lattices possessing only small cationic sites [K29].

The hosts also need to exhibit a low variation of the refractive index with temperature, chemical stability, refractoriness, and reasonable thermal shock resistance. While the optical characteristics are essential, functional properties – like certain thermal, mechanical, and chemical characteristics – are also important. The optical properties stability, the length of service life, processability, and cost markedly depend on the latter.

Processing wise optimal host materials should allow fabrication, at commercially viable costs, of adequate (sometimes large) size, suitable shape, parts.

Most attractive are the hosts that exhibit optimal tradeoffs between the many, often contradictory, requirements existing vis-à-vis these materials (vide supra). Quantitative figures of merit, in which each factor of influence is allotted a coefficient, describing its relative importance, are difficult to define. As of now only qualitative treatments of the problem are possible; a comprehensive knowledge of performance (for the specific application(s) considered), non-spectral properties, processing, and cost issues, are required as a base for determination of the optimal host(s).

5.2.9.1.5.1.2 Improvements Achieved, Regarding Host Types Available, Their Processing, and Characterization, in the Last 60 Years

Hosts Diversity Enlargement A first important contribution, in this context – of the research and production of TCs – was to make available an ever growing portfolio of hosts. To the initial CaF_2 many other ceramics were added. Currently cubic oxides – like YAG, LuAG, Y_2O_3, Sc_2O_3, Lu_2O_3, ZrO_2, Mg_2AlO_4, PLZT, and other perovskites, together with CaF_2 and other fluorides or ZnS and ZnSe – are the most used materials. To them, lately, hosts – in which some disorder is introduced (say, scandium containing (YSAG) or $Bi(Mg_{0.5}Ti_{0.5})O_3$ (BMT) derivatives) thus facilitating pulse length reduction [K5, K7, K67, I3, S12] – were also added. Most of the materials, mentioned earlier, are presented in Chapter 4. In principle non cubic materials – the particles of which can be oriented, when suspended in liquids – also became, recently, candidates to lasing ion hosting [S11]. Non-cubic materials can also be brought to TC status by the aid of other approaches, like full glass crystallization or ultra-high pressure powder compacts densification, both effectuated so as to preserve a nanosize ($GS < 100$ nm) of the finished part grains (this strongly reduces scattering at grain boundaries). Certain partially crystalized glass-ceramics were also examined as lasant ion hosts. As early as 1968, lasing was demonstrated in a quite exotic and complex composition material (SiO_2–Al_2O_3–MgO–ZnO–La_2O_3–$AlPO_4$) exhibiting 25 nm crystals; Nd^{3+} was the lasing dopant (1.7% Nd_2O_3) [M46] (see Figure 5.67). The transmission of 4 mm thick discs exceeded 80% in the VIS range. The lasing efficiency was modest (see Figure 5.67; Xe flash light low efficiency pumping) but the damage threshold, at 70 J/cm^2 was much better than that of phosphate glass hosts. The fluoro-oxide glass (FOG) type glass-ceramics (see Section 4.2.11) developed in the 1990s are also useful, because they represent a type of soft phonon host for the lasant. Soft phonons lead to quantum efficiency and fluorescence decay time increase, emission line widening (pulse shortening), reduction of thermal lensing, and facilitate frequency upconversion operations (lasant ions are crowded in the fluoride nanocrystals). The emission intensity of some upconversion of Er^{3+} fluorescence lines, excited by a LED working at 972 nm, is shown in Figure 5.68 [W12], for the mother glass, the FOG glass-ceramic, and a fully fluoride reference glass. It can be seen that emission intensities at 550 and 660 nm of the FOG are much more intense than those of the mother and reference glasses [W12].

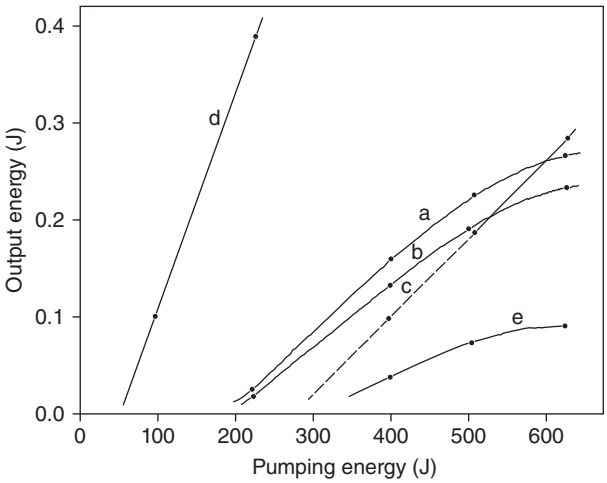

Figure 5.67 Lasing efficiency curves of some lasers based on rod shaped gain medium. (a, b) Glass-ceramic rods (diameter = 4 mm), doped with 1.7 at.% of Nd. (c) As above but 6 mm rod. (d). LG 630 glass host doped with 3 at.% Nd; 4 mm diameter rod. (e) LG 57 glass doped with 0.8 at.% Nd; 8 mm rod. Source: Muller and Neuroth 1973 [M46]. Reproduced with permission from AIP, USA.

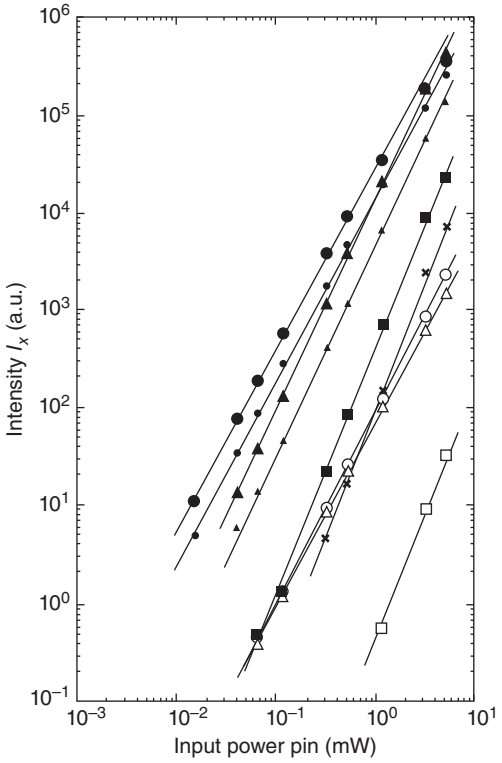

Figure 5.68 Upconversion intensity at 410 nm (squares), 550 nm (circles), and 660 nm (triangles) plotted against the excitation power (0.972 μm LD). Open symbols hold for mother oxyfluoride glass while full ones depict material after thermal treatment; small full symbols represent aluminofluoride glass. Source: Wang and Ohwaki [W12]. Reproduced with permission from AIP, USA.

Host Fabrication and Characterization Significant advances were achieved related to the processing and characterization of the materials mentioned earlier. A variety of methods for the synthesis and processing of extra purity nano-sized powders were developed (see Chapter 4). Most of the general advances, relevant for TCs processing – described in Chapter 3 – are relevant for gain media too. So are the advances concerning the characterization methods; the data given there is not repeated here.

An important point is the possibility to fabricate gain media in the shape of bulk units (say, discs, rectangles, or rods) but also as near two dimensional (chips [D10, O5]) and one dimensional (fibers) parts. The classical configurations are 3D gain media but as the thermal management problems became more difficult – when power scaling was attempted – the chips and fibers became more popular.

Fiber geometry of gain media: Glass fiber (mostly silica and some fluoride based) lasers – of various length – are highly popular, lately, especially for high power applications and other situations where thermal lensing reduction is critical [H8]. For such lasers fabrication the mature technologies, developed for optical communication systems, can be used. The reasons for wanting to produce similar items from ceramics, especially YAG, are evident: the higher thermal conductivity of the latter, small temperature change of "*n*," higher laser damage resistance including to photo darkening; less obvious but important the intensity of the stimulated Brillouin scattering (SBS) is much lower than in case of silica. In fact owing to the better thermomechanic properties also usable pumping powers is higher and the fiber length needed, for delivering a certain amount of energy, reduced. For crystalline (mostly single crystal) materials based fiber, fabrication attempts were made to adapt technologies from the glass field, like drawing (in drawing towers) from core/cladding collapsed preforms. While interesting kilometer length, fibers resulted the initial single phase YAG composition, of the core, could not be maintained [D18, H40] in the drawn fiber. For single crystalline short and relatively thin fibers, new specific methods like micro-pull down (μ-PD) and laser heated pedestal growth (LHPG) were developed [Y19]. The fibers obtained are relatively of large diameter (about 1 mm) and exhibit defects. While lasing could be demonstrated in them, such fibers are not yet showing the features need for high performance. The diameters sought for single-mode operation are around 30 μm. For ceramic fibers, methods starting from powders can be used. A. Ikesue has fabricated (undisclosed processing approach) YAG fibers of down to 100 μm in diameter and up to 15 cm of length. For Nd doped variants, output power of up to 10 W could be obtained at a 23.5 slope efficiency [I3]. H.J. Kim et al. reported a method of YAG fiber fabrication based on extrusion at 30 MPa, through 50 μm nozzle [K13, K14]. After further consolidation by CIPing, the fibers were sintered (air or vacuum) at 1600 °C. Such a fiber is shown in Figure 5.69. Ho doped fibers (31 μm diameter, 62 mm length, glass cladding), strengthened by polishing, were made to lase at a modest, initial, 7% slope efficiency [K14]. Considering the paper of G. Brasse et al., it seems that sol-gel processing may also be a possible approach to ceramic fiber laser fabrication [B51].

Planar waveguides: Such structures are very useful in amplification schemes, like MOPA. Here a seed laser's signal is processed and then injected into the amplifier. The pumping is done by the aid of diode laser arrays, according to the schematic of Figure 5.70a [W8]. The amplifier is constituted from a thin, 100 μm thick, layer (fabricated by tape-casting) of doped (1.5 at.% Nd) YAG sandwiched between two undoped YAG chips. The slab has a width of 10 mm and a length of 50 mm, in the case of the example presented in the

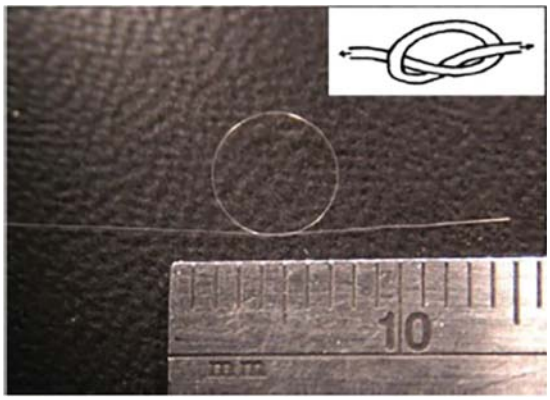

Figure 5.69 Ceramic YAG transparent fiber. Source: Kim et al. 2015 [K13]. Reproduced with permission from Elsevier.

figure. The major surfaces of the slab are coated with 4 μm thick silica and the end faces are cut and coated so as to minimize losses. The device allows the scaling of an initial 323 W signal to 1544 W at a single pass; O–O efficiency of up to 49% could be obtained.

Mitigation of Adverse Thermal Effects As discussed earlier, heat release occurs as a consequence of non-radiative processes taking place within the gain media. Temperature fluctuations have a number of not welcome effects on lasing. Considerable progress was made in the modeling of temperature distribution within gain media, under different work conditions [I3]. Thermal field distributions have been calculated taking into consideration the relevant material parameters (density, C_p, λ_{th}), shape and size of the gain media, and time and spatial profiles of the pumping energy. Developers of the ceramic gain media found engineering solutions mitigating the adverse effects of various thermal effects. For instance, the thermal bulging – caused by the radially dependent thermal expansion – was reduced by bonding, to the rod edges, discs of undoped material. Methods for increasing the resistance to thermal shock generated deformation and cracking were developed based on fracture mechanics concepts and using toughness increasing techniques previously developed for structural ceramics and glasses [F5]. In Figure 5.71 the temperature gradient in the radial direction of a Nd^{3+} based YAG rod, in service, is shown.

Such gradients and temporal temperature variations induce, among other effects, the kind of cracking illustrated in Figure 5.72.

As it is well known from the work of Griffith (early twentieth century), the stress concentrators – which facilitate the creation of conditions for cracks propagation (an occurrence the consequences of which are seen, at the macroscopic level, as rod breaking) – are mostly defects (voids, lattice dislocations, microcracks, striae, facets, contaminant particles, with an α_{th} differing from that of the matrix) located on the surface or a

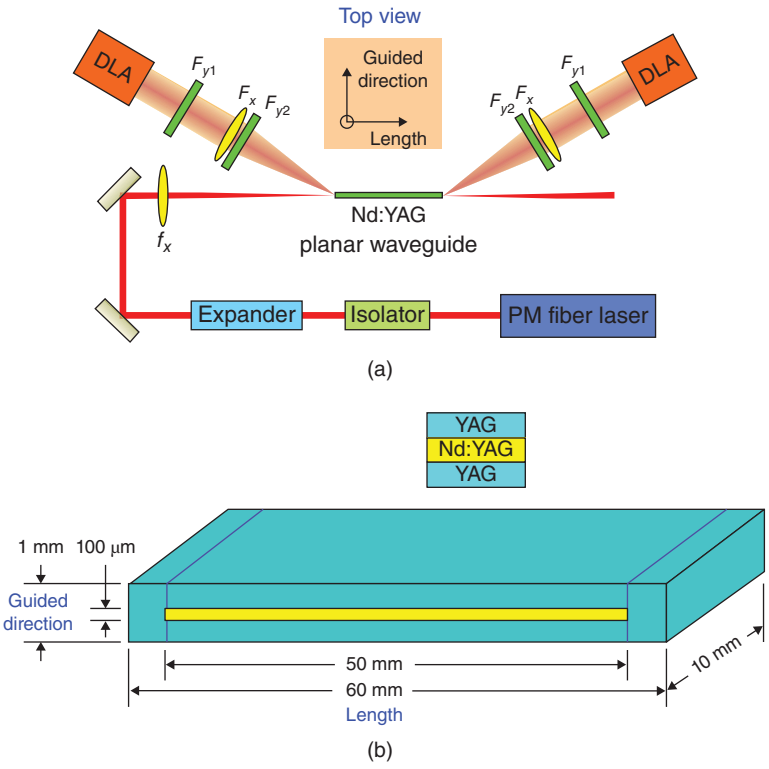

Figure 5.70 Nd:YAG planar wave guide based laser-amplifier. (a) Schematic of MOPA type amplifier: the seed-laser of the polarization maintaining type (PM) the pumping diode laser arrays (DLAs) and the lenses and Faraday isolator, used for signal optical processing is shown. Source: Wang et al. 2017 [W8]. Reproduced with permission from OSA, USA. (b) Doped YAG based planar waveguide sandwiched between undoped YAG chips. Source: Courtesy of Feldman [F5].

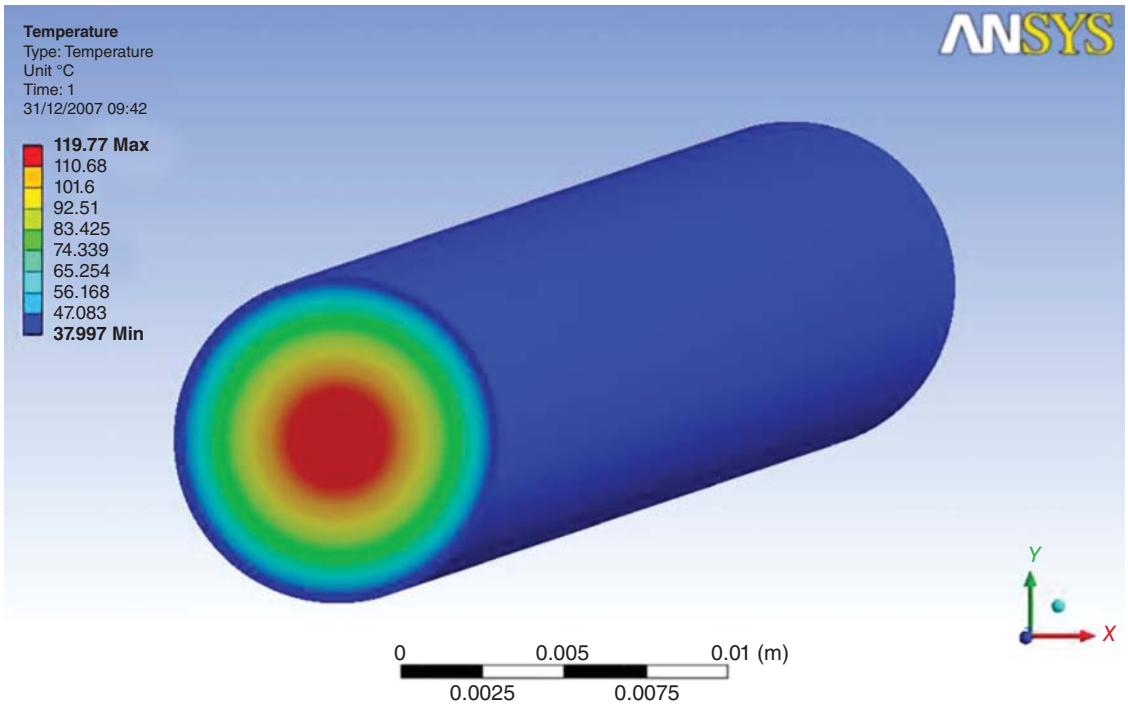

Figure 5.71 Radial distribution of temperature values in an Nd^{3+} doped YAG rod in service. Source: Courtesy of Feldman [F5].

Figure 5.72 Cracking and breaking of Nd:YAG gain media as a result of thermal shock. Source: Courtesy of Feldman [F5].

relatively thin layer subsequent to it. In the case of YAG rods, the theoretical tensile strength of 31 GPa (calculated based on bonds strength) is in practice reduced to 150–350 MPa, by the surface defects deleterious action. The increase of stress in a YAG rod, from center to surface, is illustrated in Figure 5.73.

Therefore, elimination of such layers may significantly raise the resistance to mechanical stress build ups, including that resulting from thermal shock. A method generally used (ceramics and glasses) is to eliminate the defective layers is the polishing of surface (combining mechanical, chemical, and thermal operations). Another approach is the covering, with thin "α" matched glazes, of the surface; thus compression stress is applied on the microcracks, making their expansion more difficult. Thermal annealing for reduction of stress induced during cooling is also used. Such methods succeeded in improving the resistance to mechanical failure of YAG rods – both ceramic and single crystal. R. Feldman and Y. Shimony [F5] have treated rods of YAG – with solutions including mixtures of H_3PO_4 and H_2SO_4 – in order to "clean" the surface layers from defects.

In Figure 5.74 the Weibull analysis of the strength (TRS; four points bending) results – of etched and as-received rods – are compared while in Figure 5.75 that related to thermal shock resistance is presented.

As it can be seen, significant strength was achieved, by etching. In another set of experiments, the authors polished and coated (transparent thin glaze) YAG rods before exposing them to thermal loading programs of variable severity. It was determined that untreated rods failed frequently for loads $P = 45$ W/cm, while processed rods were able to withstand levels of $P > 110$ W/cm. The strengthening processes seem to have better results in the case of single crystals than in the case of ceramics. Thermal shock resistance can be improved also by better thermal management. For instance, joining the active gain media to components exhibiting a higher λ_{th} is one option. For certain applications, complex shape gain media (which required assemblage of two or more basic components) is needed. In other cases the gain medium is joined to a TC performing another function. For

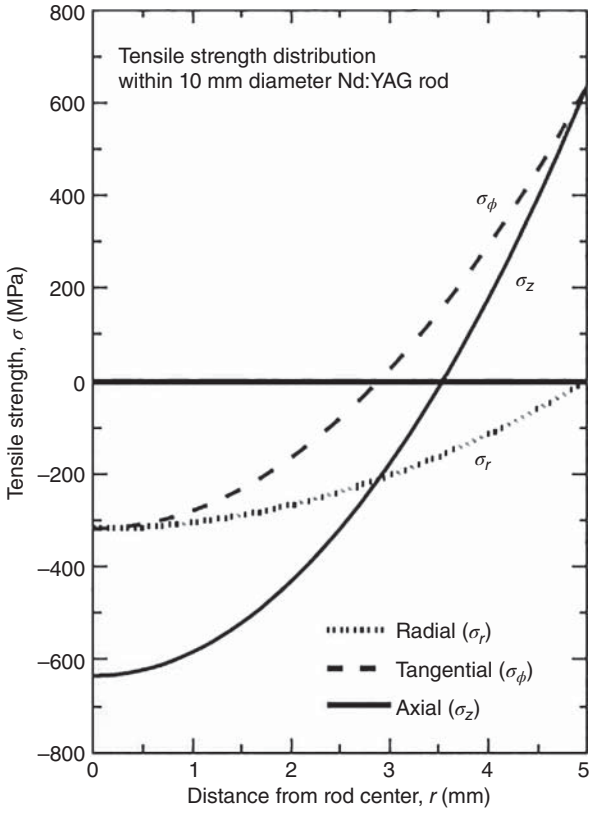

Figure 5.73 Radial variation of tensile stress level in YAG rod. Source: Courtesy of Feldman [F5].

instance, a gain-media/Q-switch bimorph is needed in chip type lasers. Thermal management can be improved by attaching, to the gain media, layers of higher thermal conductivity. The components may be all-ceramic or mixtures of single crystals and ceramics. Various designs like rod core/clad or waveguides can be used [I2]. Multilayers – in which each layer has a specific Nd content, in the green state – can be converted, by proper sintering, into a block exhibiting a graded Nd concentration variation along the long axis. In such a way the excessive heat – generated at rod ends when diode-laser pump is coupled there – is compensated by the lower lasant concentration. As a result temperature gradient profiles are smoothed out and resistance to thermal shock is increased. An elegant solution for a waveguide is to sandwich an Nd doped YAG layer between undoped layers (so as to get total internal reflection).

For certain lasant ions, like Yb^{3+} (leading dopant for high power lasers) selecting the optimal host may allow one to achieve parts with higher thermal conductivity, an improvement that also reduces thermal sock generated rod cracking risks; thus replacing YAG with Lu_2O_3, as a host, will prevent decrease of the thermal conductivity at heavy doping (see Section 4.2.4.6).

In the Section 5.2.9.1.5.2 the available lasing cations are presented, especially from a spectroscopically point of view. The TCs able to function as hosts for lasing ions were presented in Chapter 4. The most important are recapitulated here: YAG, LuAG, Y_2O_3, Lu_2O_3, Sc_2O_3,

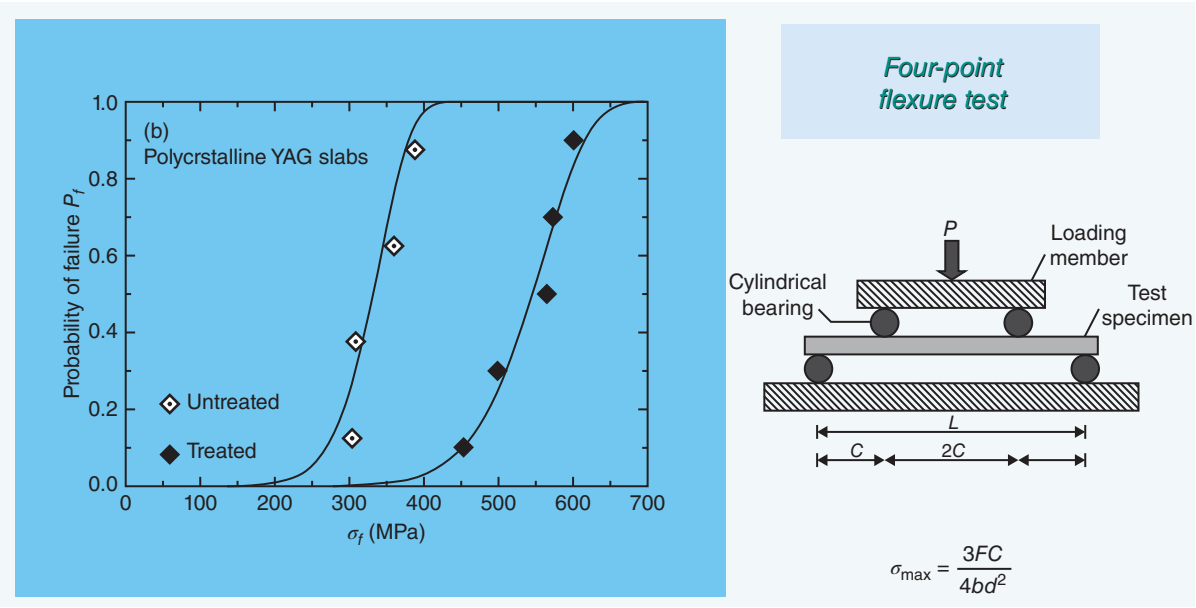

Figure 5.74 Results of TRS related Weibull analysis for the case of as-received and etched Nd:YAG rod shaped gain media. Source: Courtesy of Feldman [F5].

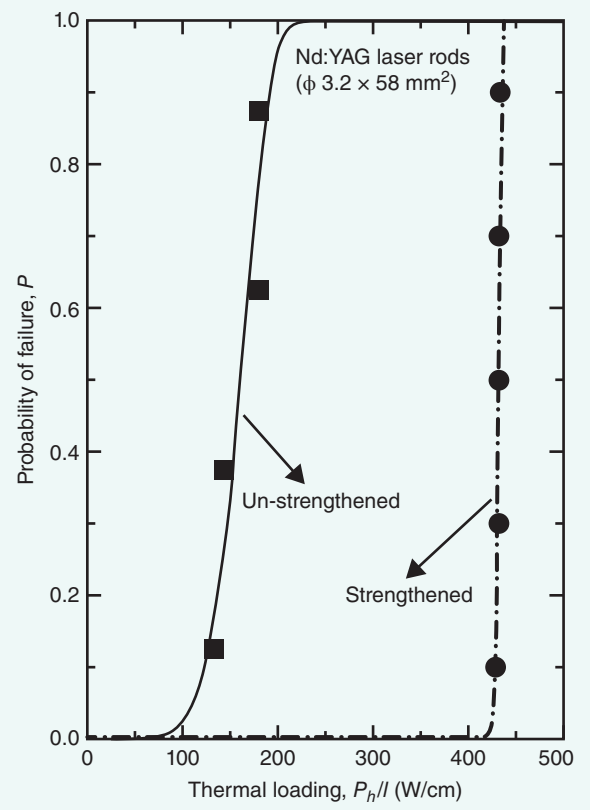

Figure 5.75 Results of thermal shock resistance data Weibull analysis. Source: Courtesy of Feldman [F5].

$MgAl_2O_4$, and Al_2O_3 (for Ti^{3+}); maybe also PLZT, ZrO_2, or some Ga containing garnets.

5.2.9.1.5.2 Principal Lasing Cations Operating in Ceramic Hosts

A ceramic gain medium is made up from a transparent host and a dopant (active lasing unit); the lasing ion may be aided by secondary dopants, acting as sensitizers, Q switchers, etc. In this section the main RE^+ and TM^+ type lasing ions are discussed; point defects lasing units are not addressed owing to lack of sufficient reliable information on this issue available. While for the data and discussion of the spectral properties and lasing behavior of these cations, many sources were used the main one was the presentation of V. Lupei and coworkers [I3]; this author had contributed many other important studies like [L59–L67].

5.2.9.1.5.2.1 General Aspects

The rare-earth (lanthanide) elements (sometimes called internal transition elements) occupy the $Z = 58$ (Ce) to $Z = 72$ (Lu) positions in the periodic table. Their distinctive electron goes from $4f^2$ to $4f^{14}$. The diffuse "f" orbitals are strongly bonded to the nucleus, and this bonding increases in strength with the number of protons in the nuclei, i.e. with a raising "*Z*." Therefore, along the series an almost linear contraction of the ionic radius is observed (from $r = 103$ pm for La^{3+} to $r = 86.1$ pm for Lu^{3+}). As it will be seen in the following text, this has a significant influence on the electronic states of the RE^+ ions located in solid hosts. The radius of the RE^+s is large, so that such ions may fit in only in host sites sufficiently large. Even in such hosts the RE^+ dopants may distort somewhat the sites they enter, with consequences on the spectral properties and the lasing process. On the other hand, the 4f orbitals are shielded toward potential ligands by the $5p^6$ outer orbitals. This reduces the ability of the 4f electrons to implicate themselves in covalent bonding, and as a result considerable ionic character is present in many of their compounds (only in complexes with a coordination number $(NC) > 9$ are the 4f orbitals more involved in bonding). The shielding also significantly reduces the effect of the electrostatic field of ligands like $O^{\delta-}$ or $F^{\delta-}$ anions; the shorter the radius, the stronger the CF effect. Therefore, the electronic states for the "free" RE^+ ion are, to a great extent, preserved when they enter a host site. The crystal field, as opposed to the case of d^n cations, is a second-order perturbation, acting on the states dictated by the l,s interaction. While less stronger, in relative terms, than in the case of TM^+ ions, the CF has, nonetheless, important effects on the levels of the free 4f ions and thus on the number, shape, position, and intensity of the spectral bands.

For reasons not detailed here, the most stable oxidation state is RE^{3+}, and most of the lasant ions of interest have this configuration. Many of the RE^{3+} cations can lase when doped to suitable ceramic hosts. The characteristics of the lasing process differ from cation to cation. The most attractive lasants are Nd, Yb, and Er^{3+}. There are also situations in which RE^+ pairs can be used; most useful combinations are seen in the case of Nd^{3+}, Yb^{3+}, and Er^{3+}. For certain applications cations like Pr^{3+}, Tm^{3+}, or Ho^{3+} are also of interest.

5.2.9.1.5.2.2 Nd^{3+}

This cation is the most popular lasing ion present in ceramic gain media. In a single crystal host (Y_2O_3), it was present in some of the earliest solid-state lasers (e.g. [H36]). It was also the lasing cation of both the first ceramic oxide host laser and in the first one exhibiting reasonable efficiency [G40, I6].

Located in the first part of the rare-earth row (third after Ce and Pr), Nd ([Xe] $4f^4\ 6s^2$), like most lanthanides, has as its most stable cation the Nd^{3+} ([Xe] $4f^3$). The Nd^{3+} "free" ion exhibits a complex set of electronic states, as depicted in Figure 2.32. It is worth noting that, as opposed to Yb^{3+}, which facilitates grain growth and hampers densification, the rare earth besides its optical emission abilities is also facilitating some of its hosts (like YAG) densification.

For lasing applications it is important to have a uniform Nd^{3+} concentration (or a controlled non uniformity profile, in some cases) at all scales of the gain-media volume. Non-uniformity at the grains scale is, however, always present at various degrees. It is dictated by various factors, like elastic energy minimization. The differences in radius vis-à-vis the substituted host cation lead to preferential segregation to grain boundaries of impurities like Nd^{3+} [K9]. Nd^{3+} cations, like Ce^{3+}, are somewhat too large replacements for Y^{3+} (for Nd^{3+} radius difference is of ~10%) in YAG, for instance. Atomistic modeling studies [A26] showed that the dopant tends to concentrate into a zone, 5 Å large, at the surface of a polyhedral body. There a differences, regarding the amount of dopant they can accommodate between the various types of crystallographic plane. Thus the (111) surfaces of YAG can incorporate approximately two times the amount located in (110) planes.

Experimental studies on the Nd^{3+} concentration pattern in ceramic YAG grains have been effectuated by the aid of confocal geometry microscopic imaging, collecting fluorescence, and Raman spectral signals [R6] (the YAG lattice generates a number of Raman active vibrational modes). The Raman results suggest an increase of the Nd^{3+} concentration in the GB zones; the profile of the segregation seems to change as a function of Nd's concentration (0–8 at.% range). The fluorescence spectra spatial scans indicate that satellite emission lines (caused by cations pairing) intensity increases across grain boundaries. This also suggests Nd concentration increase in that zone. The agglomeration of Nd^{3+} in the GB region leads to intensification of deleterious energy transfer processes, which reduce fluorescence quantum efficiency. It was also observed that Nd concentration non-uniformities exist also inside the grains; their level tends to increase with [Nd] increase. The $[Nd^{3+}]$ variation also affects the refraction index, the fluctuations of which enhance scattering related loss, wave front, and transverse modes distortion. Such adverse effects are mitigated by grains size reduction under 2 µm.

More complex examinations, especially of teams led by G. Boulon et al., combined confocal optical microscopy with TEM (energy dispersive X-ray spectroscopy [EDX]) [B46, B48]. One of the interesting points made by Chani et al. [C17] refers to the correlation existing between the segregation coefficients (melt/crystal) of single-crystal growing processes and that of the tendency to pile at GBs of sintered ceramics. Both techniques show that Nd^{3+} as Ce^{3+} – which have low K segregation coefficient – exhibit GB agglomeration tendencies (as opposed to say Yb^{3+}; $K \approx 1$).

An important issue is that of Nd^{3+} amounts one can insert into ceramic lattices, and of the effects on properties an increased concentration has [I3, N9, L65]. As it was seen earlier, the distribution pattern within the grains feels the influence of concentration. It was suggested that substantial, up to 10 at.% of Nd, can enter a YAG host lattice. The additives generate lattice modifications without leading to significant altering of the overall host's symmetry. Over 3 at.% the crystal cell parameter "*a*" increases, but segregation, leading to superlattice formation, does not occur, considering the X-ray diffraction (XRD) results [Z8]. Over 8 at.% the "*a*" increase is more significant. Interestingly the raise in Nd_2O_3 concentration in the raw materials batch causes a reduction of the temperature of YAG formation (from YAP + Al_2O_3). This evolution is related to the formation of small, disordered domains. The Nd^{3+} ions also tend, over 3 at.%, to segregate on the calcined powder particles and at grain boundaries. Between 3 and 8 at.%, the basic particles size decreases. Over 3 at.% more pronounced distortion of the lattice also occurs. The distortions generate planar lattice defects in the form of stacking faults; twining is intensified and interstitial Nd^{3+} ions concentration grows. The distortions are more intense at particles surfaces and grains boundaries within a layer, the thickness of which increases with $[Nd^{3+}]$. The structural changes affect various properties, including the characteristics of fluorescence. Closer Nd^{3+} cations interact, leading, for instance, to intensity reduction of the 1064 nm emission. The structural changes related to $[Nd^{3+}]$ increase are such that while up to 3 at.% the enrichment in dopant proportionally intensifies, as expected, fluorescence at higher concentrations emission is deleteriously affected (quenching). In single-crystal YAG the maximal Nd^{3+} amount that can be homogeneously inserted is limited to some 1.5 at.%, owing to the low K (~0.2). At such levels interaction probability is yet low. At higher concentration there is a tendency to phase separation (YAP forms) with the secondary phase rich in Nd [I3]. As seen previously, quite large amounts of Nd^{3+} can be accommodated by ceramic YAG. It is not yet fully clear, however, where the limit for uniform, at grain level, distribution is. The concentration range within which self-quenching is avoided depends also on the distribution uniformity.

A. Ikesue et al. has shown that doping with silica (resulting from 0.5% tetra-ethyl-ortho-silicate [TEOS]) improves the ability of the YAG lattice to accommodate Nd^{3+}. It is proposed that Si^{4+}, which substitutes Al^{3+} (and causes lattice shrinkage), compensates the expansion generated by $Nd^{3+} \leftrightarrow Y^{3+}$. As a result the lattice can tolerate more Nd^{3+} without being strained. Up to 4.8 at.% Nd^{3+} seems less prone than in undoped YAG to segregate at interfaces, or produce point defects. The fluorescence intensity (1064 nm line) showed an increase up to 2.4 at.% (roughly similar to the data in [Z8]), and then a decrease (self-quenching). The fluorescence

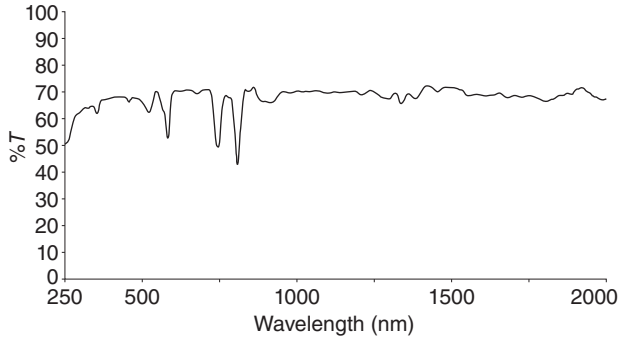

Figure 5.76 Transmission spectrum profile of ceramic Nd:YAG disc fabricated at ICSI.

lifetimes of single crystal and ceramic YAG are very similar (~250 μs before quenching sets in at ~1 at.%), being drastically reduced, by quenching, over 1.0 at.% of Nd^{3+}. According to [I3], despite fluorescence quenching, at high concentrations, certain lasing characteristics (σ_{abs}) can be improved by raising the [Nd^{3+}] in ceramic YAG up to ~6 at.%.

In Figure 5.76 the transmission spectrum of Nd^{3+} located in a YAG matrix are given.

As Figure 2.32 shows the Nd^{3+} has a number of convenient electronic levels (the manifolds are more or less split under crystal field influence), located in the VIS or NIR, able to receive electrons excited by the pumping, out of the ground state. Only the $^4F_{3/2}$ level is metastable and lasing can be obtained by relaxation of the electrons in a set of levels all originating from the ^4I term of the "free" ion. The relevant levels are $^4I_{9/2}$ (~900 nm emission), $^4I_{11/2}$ (~1000 nm; highest σ_e of ~10^{-19} cm^2), and $^4I_{13/2}$; the $^4I_{15/2}$ line is weak.

While lasing in the 0.9 and 1.3 μm range was demonstrated in practice, most of the work is focused on the ~1064 nm emission. An important feature of Nd^{3+}'s electronic structure is the ability of many of the excited levels to relax, toward the $^4F_{3/2}$, electrons by fast processes. Therefore, one can use various pumping sources (some of them are able to target specific, selected, excited levels, while others, of larger emission spectrum populate a set of excited levels). Higher brilliance flash lamps (X_e, Kr) or the sun are able to offer high pumping power but distributed at various frequencies so that large (50–60%) quantum defects characterize the transfer to the lasing level. Such sources also convert the electrical energy into optical power with quite low efficiency (≤20%). Despite such disadvantages, lamp pumping is a popular scheme, especially for CW work. Diode lasers are able to pump, targeted levels, chosen so as to minimize Stokes shift [L66]. Thus pumping with laser diodes into the $^4F_{5/2}$, with powerful Al GaAs diode lasers or directly in the $^4F_{3/2}$ (for this frequency only low power sources are available, but the scheme is optimal from the point of view of quantum defects), was examined. While quantum defects were reduced, the overall efficiency (wall plug to terminal state) was not very high, owing to the low efficiency of the pumping sources themselves. It is also worth noting that diode lasers, while good for CW format, are not usable for short pulse operation mode. While useful for pumping scheme flexibility, the complex levels structure of Nd^{3+} is also leading to easier self-quenching based on ion/ion interactions (both down- and upconversion may occur). The energy loss consequent to such processes raises the lasing threshold and heats the gain media. This limits the concentration of Nd^{3+} cations one can insert for increasing laser power to low levels (maximum ~3–5 at.% but in practice problems appear over 1.5 at.%).

The host most examined for Nd^{3+} as lasing ion is the YAG [I3, I5, Z3, Z15, Z18]. The largest gain media of optical quality suitable for lasing have been, as of now, produced using Nd^{3+}:YAG as the base material. First rods as long as 20 cm ($\phi \sim 3$ mm) and then plates of $4 \times 4 \times 0.5$ cm^3 (year 2000) and even $10 \times 10 \times 1$ cm^3 were produced and used in lasing experiments [L49].

The lasing efficiency is strongly influenced, among other features, by the porosity (size distribution and amount) [I3]. Most of the effort and the best results regarding porosity elimination are related to Nd:YAG ceramic [I6, L48, L49, S19]. The level of demands, concerning densification of the host, may be illustrated noting that in quite transparent YAGs, with the scattering loss $\alpha = 2$–7 cm^{-1}, lasing was not obtained; only reducing it to 0.9 cm^{-1} (some 150 ppm of porosity) allowed obtaining of quite good optical efficiency levels (lasing at $\lambda = 1064$ nm) of $\eta \sim 28\%$ (threshold power = 309 mW; 7.1 at.% Nd, $P_{max} \sim 70$ mW). Reduction of residual porosity to ~1 vol ppm allowed a raise of η to ~48% ($P_{max} = 31$ mW) [L48]. Even higher optical efficiency of $\eta = 65\%$, close to that of single crystal, YAG (67%) was achieved in 2005 [I8].

As far as output power up-scaling is concerned, Nd doped YAG is also an important player, as will be discussed later. In 2001, using thin rods ($L = 20$ cm) power output could be raised to ~1.5 kW [L52] and even 100 kW (16 kW/module) [S10]. Most of the progress, regarding this aspect, was a result, however, of laser device improvements. The gain media producers' main contributions were the elimination of porosity, a significant size increase (up to $10 \times 10 \times 2$ cm^3) and reduction of Nd^{3+} volumetric distribution non-uniformity.

Nd:YAG gain media are an important component also of the devices working with ultrashort (down to femtoseconds) intense pulses. Such devices are based on Q-switching (active or passive) [I3] or mode locking. Sensitized Nd^{3+} lased gain media were also developed [L59, L61] especially in order to improve excitation

energy collection, using, for instance, the strong VIS absorption bands of Cr^{3+}. Efficient energy transfer toward Nd^{3+} is a problem, though, due to the modest superposition of the Cr^{3+} emission with relevant Nd^{3+} absorption bands; the emission is also weak because it involves spine forbidden transitions. Increased [Cr^{3+}] helps, to a certain extent, triggering energy migration based transfer. Ce^{3+} shows a better tradeoff between absorption + transferred abilities (to Nd^{3+}) than Cr^{3+}. Intrinsic de-excitation problems, however, limit the use of this sensitizer.

Besides YAG, other garnets like LuAG, bixbytes, and perovskites have been examined as hosts with a view of exploiting certain specific features not offered by YAG: non-oxides like the fluorides were studied too. One of the aims of those studies was to determine whether the advantages are significant enough to make them realistic competitors of YAG, at least in some of the used lasing operation approaches.

By introducing disorder (aid of Sc^{3+}) in the lattice of YAG, the emission band width was increased, allowing the reduction of pulse length to 10 ps (optical efficiency = 40%).The emission of such a host is compared with that of regular YAG in Figure 5.77 [I3].

A compact short-pulse (300 ps; Q-switching), high peak power (>15 MW) Nd:YAG based laser was able to provide pulses carrying enough energy to ignite gasoline in a combustion engine [T3].

In sesquioxides, the bixbite type lattice, different from that of YAG, modifies the environment of a Nd^{3+} cation and thus, to some extent, its spectral behavior and the lasing characteristics. The volume density of cationic sites is higher, putting the dopant cations closer to one another, the crystal-field effects are stronger felt, and the manifolds stemming from the ^4F term are depressed (for instance, $^4F_{3/2}$ is split into levels separated by ~250 cm^{-1} in Sc_2O_3). As a result the position of the spectral lines is shifted.

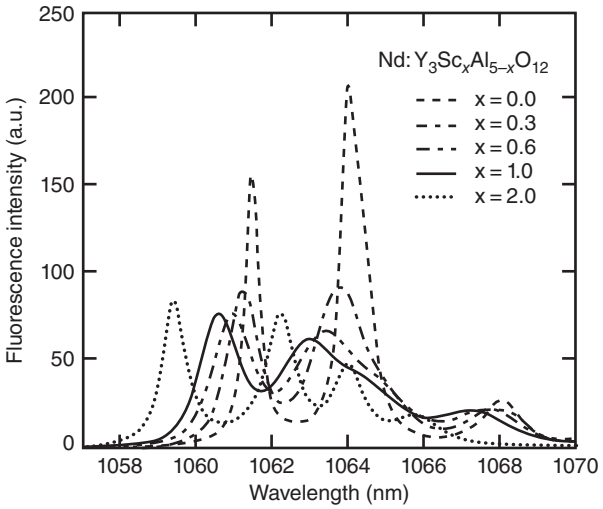

Figure 5.77 Fluorescence intensity of Nd:YSAG ceramic (x = 0.3–2.0) and Nd:YAG single crystal (x = 0) at RT. Source: Ikesue et al. 2013 [I3]. Reproduced with permission from CUP, Cambridge, UK.

The first tests regarding lasing of Nd^{3+} in an oxide ceramic host (Y_2O_3 – 10 mol% ThO_2) showed very low optical efficiency (<0.2%), mostly because poor pumping; the host is also less suitable than YAG for high concentration doping (vide infra). The optical quality of that first TC type host, while somewhat less high than that of the YAG used by A. Ikesue et al. [I6], would have warranted, nonetheless, better results were a better pumping format available. In time the improvement of processing (allowing one to dispense with ThO_2) permitted fabrication of Nd:Y_2O_3 ceramics exhibiting an optical quality and lasing abilities similar to that of single crystals. Thus the synergy between a higher optical quality yttria hosts and diode laser pumping led to a jump in (while not comparable to YAG, of course) efficiency [T11]. For instance, D. Tang et al. achieved, in a 0.6 at.% doped ceramic, a slope efficiency of 49.6% (lasing at 1074 nm). In bixbites the Nd^{3+} ions interact at lower Nd^{3+} concentration levels, so that self-quenching sets in earlier (<1 at.% Nd). This is felt in Y_2O_3 and even more in Sc_2O_3 or Lu_2O_3. In Lu_2O_3, while reasonable absorption could be obtained ($\sigma_{abs} = 1.29 \times 10^{-20}$ cm^2; 806 nm diode laser pumping), the lasing involved simultaneously two lines (1077 and 1081 nm) owing to their closeness. The optical efficiency was of only 14% and outpower was lower than 0.5 W [A14].

In perovskites and non-oxides like CaF_2 and SrF_2, Nd lasing was also obtained, but at lower efficiency and output power levels [B14, B16, L46, Z10]. In CaF_2 Nd ions clustering tendency could be reduced by introducing of Y^{3+} as buffering ions. The reduction of self-quenching, thus achieved, led to an intensified broad, fluorescence signal, centered on 1060 nm. Associated with the quite high transmission in the NIR (~87%; T = 2 mm) the lasing chances of the specimens were good; however, no testing, in this sense, was done by the authors. Of special interest is the PLZT type host, because its electrooptical functionalities. Pumping with 100 ms pulses (diode laser; 805 nm) a broad (36 nm) emission (1 at.% of Nd^{3+}) results, and it could be used for lasing [C3, Z10]. Output of 10 mW required 3 W of pumping power (λ = 1064 nm).

In non-cubic hosts, like apatites, the initial tests also indicate low efficiency of the lasing process [S11, T2].

Competitor Solid-state Hosts Comparison is made here regarding the lasing behavior between ceramic, single-crystal, and glassy hosts doped with Nd^{3+}. It

seems that the first demonstration of lasing in a Nd doped single crystal (the device was yet called "optical maser") was effectuated already in 1961 [J13] in hosts like $CaWO_4$ (0.5 at.%, $\lambda = 1058$ nm, output 10 mW, Hg lamp), $ScMoO_4$, and CaF_2. In 1964, J. Geusic et al. [G13] have realized that single-crystal garnets like YAG (or with Ga instead of Al and even the $Gd_3Ga_5O_{12}$) possess a package of properties highly suitable for high performance gain media fabrication. Such crystals, besides being cubic (not critical for single crystals but advantageous processing-wise), could accommodate RE^+ and TM^+ type dopants and exhibit thermomechanical properties and chemical stability good enough to make them robust hosts. At Bell, crystals (Verneuil procedure) of excellent optical quality were produced. Pumping with a W lamp (360 W), they achieved CW operation of YAG:Nd^{3+} ($\phi = 2.5$ mm, $L = 3$ cm) using the $^4F_{3/2} \rightarrow {}^4I_{11/2}$ emission line (6.5 cm^{-1} width at RT), at 1064 nm. Further work on Nd^{3+} spectroscopy and lasing behavior in single crystals and ceramics (of increasing optical quality) provided data that allows now comparison of these host types [K65, L60, L64]. Most of the data indicate – when hosts of similar optical quality are compared – close similarity, especially in the case of YAG, between ceramics and single crystals. In general uniform doping with Nd of YAG single crystals can be done up to ~1.5 at.% (vide supra), but certain growth techniques allow widening of this range, up to 3–4 at.%. In the case of YAG, their relevant thermochemical properties are also similar [K64]. In the case of nanoceramics (at least in powder form), the quantum yields can be reduced by surface features (surface layer to total volume is very high for such materials) like absorbed OH^- ions (induce vibrational losses). Lasing from Nd^{3+} placed in glass hosts was also obtained, as early as 1961 [S41] in a BaO containing crown type optical glass. It was found out that the best tradeoff between the various conflicting requirements of a performant gain media is offered by certain phosphate glasses. One of the advantages brought by the types of atoms and bonding patterns involved in such glasses is the low energy of the phonons traveling in the disordered lattice [C4]. Another is the relative ease with which large plates (meter size) of excellent optical quality can be fabricated. The low thermal conductivity, strength, and high expansion coefficient are the main drawbacks. Such glasses were selected for the ultra-high energy short pulses needed to ignite a controlled thermonuclear fusion reaction of the American National Fusion Ignition Facility located at the Lawrence Livermore Laboratory [C4]. The system operating there constitutes the largest laser and the largest optical system in the world. The Nd doped (1–2 at.%) glass works as an amplifier with the seed signal received from Nd:YAG lasers. In that laser each glass plate stores ~3 kJ of optical energy. During a typical 3 ns pulse, the full system liberates 3–4 MJ. Overall extraction efficiency is of 30–40%.

5.2.9.1.5.2.3 Yb^{3+}

General Ceramic hosts: Yb^{3+} [Xe] $4f^{13}$ has a structure of its electronic levels which significantly differs from that of Nd^{3+}, showing as a result specific spectral and lasing characteristics not seen in the case of the latter. The position of the element Yb, at the end of the RE's row, also means a smaller ionic radius, but an increased atomic mass. Therefore, the concentration of Yb^{3+} that can be accommodated by the important lasing ion hosts is much higher than in the case of Nd^{3+} the radius of which differs from that of the host cations, more than is the case for the ion discussed here. The higher radius compatibility with a host like YAG, for instance ($Yb^{3+} \leftrightarrow Y^{3+}$), leads to a segregation coefficient K around 1 (melt/crystal in crystals growth operations) for Yb^{3+}, while $K \sim 0.22$ for Nd^{3+} [C17]. It is possible to fabricate transparent specimens exhibiting a uniform – at atomic scale – mixing in the case of compositions like 20 at.% Yb:YAG [D12]. The radius compatibility suggests that also the segregation tendency, toward grain boundaries in ceramics, would be lower in the case of Yb^{3+} compared with ions of elements located at the beginning of the RE row, like Nd^{3+} or Ce^{3+}. Experimental examinations, like those led by G. Boulon and coworkers [E3] – in which high spatial resolution elemental analysis was effectuated (TEM-EDX) – confirmed this expectation. High resolution still means data collection from spots of minimum 4–5 nm in diameter including – when the grain boundary is analyzed – also material from the grains. That notwithstanding the profile of concentration of a dopant from grain center toward the GB can be quite accurately visualized in such an examination setup. In Figure 5.78 the variation of [Yb^{3+}] over a grains boundary is shown in the case of an 15 at.% Yb:YAG specimen [E3].

Higher resolution inspection of Yb:YAG ceramics (by STEM-HAAD) confirmed the absence of strong Yb segregation at GBs of YAG or also bixbite type like that of Y_2O_3. The Yb^{3+} distribution profile was examined also for the case of nano T-YAG ($gS \sim 20$ nm; made by hot pressing (HP) under 8 GPa at 450 °C). Lack of Yb segregation at GBs was determined also for this ultrafine microstructure configuration. The electronic configuration $4f^{13}$ generates a set of states for less rich than that of Nd^{3+}. In fact, it contains only two manifolds $^2F_{7/2}$ (ground) and $^2F_{5/2}$. The influence of the crystal field reduces the multiplicity of the "free" ion states, creating a set of four levels spaced on a range of ~1200 cm^{-1} out of $^2F_{7/2}$, and a set of three levels spanning some 600 cm^{-1} in the case of $^2F_{5/2}$. In Figure 2.49 the electronic structure of the "free" Yb^{3+} ion is shown. The electronic structure

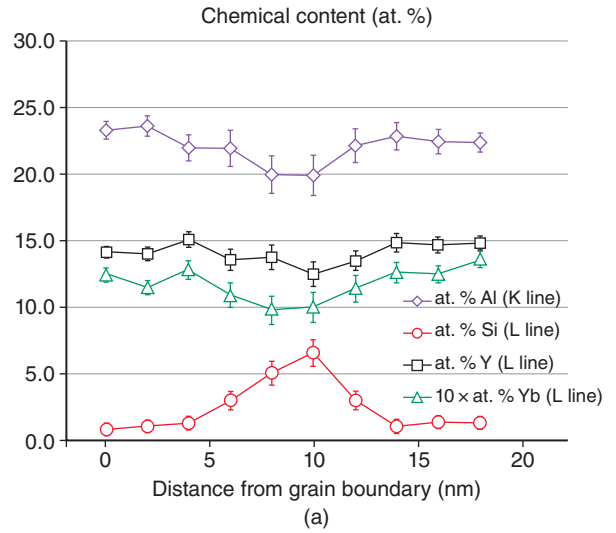

Figure 5.78 Concentration profile, along a line passing over a GB, in the case of a heavily Yb^{3+} doped ceramic YAG specimen; TEM (EDS). (a) Graphical representation of elements (including Si and Yb dopants) concentration. (b) HRTEM imaging of two grains and the GB separating them. Source: Epicier et al. 2012 [E3]. Reproduced with permission from RSC Pub., UK.

described earlier leads to a specific set of spectral characteristics, certain of which are advantageous for lasing, while for others the opposite is true. For instance, the absence of excited levels, lying in the VIS or NUV, means that flash lamps cannot be used for pumping. The pumping has to be into one of the states of the $^2F_{5/2}$ manifold and requires very narrow band sources, i.e. in practice diode lasers. Practically it is most convenient to populate the (2) Stokes level of $^2F_{5/2}$ from the ground (1) of $^2F_{7/2}$ state. One positive aspect is the fact that a Stokes shift, significantly lower than that occurring as a result of Nd^{3+} pumping, occurs. A negative aspect relevant at RT and higher temperatures is also the competition between two close lasing transitions: $^2F_{5/2}$ (1) → $^2F_{7/2}$ (4) and $^2F_{5/2}$ (1) → $^2F_{7/2}$ (3). The stronger electron–phonon interaction (compared with Nd^{3+}) causes a more marked spectral bands homogeneous broadening. The effect of the slight coordination polyhedral geometry differences is also stronger felt, owing to the more marked influence of the CF, and therefore the temperature independent band widening thus produced is also more significant. Fluorescence decay times are much longer (up to four times [P17]) than those of Nd^{3+}, thus allowing a higher level of energy storage. The benefits of cryogenic operation are more substantial than in the case of Nd^{3+}. This because the reduction of the thermal population of the excited levels of $^2F_{7/12}$, on cooling, can make the four levels laser format $^2F_{5/2}$ (1) → $^2F_{7/2}$ (3) dominant (1030 nm). Combination of this feature with the high slope efficiency, specific to the electronic configuration, and the high dopant concentration feasible, facilitates high power lasing. High [Yb^{3+}] can be introduced in the usual transparent hosts with relative ease, and the main excitation energy consuming mechanisms are not active (vide supra). However, interaction between excited states is possible, and it affects lasing efficiency.

Single Crystals In single crystals, lasing of Yb^{3+} was obtained a long time ago [B36]. Quite high optical quality Yb^{3+}:YAG single crystals could be obtained, especially by the temperature gradient technique (TGT). Such crystals – when pumped with suitable (InGaAs) diode lasers – exhibit efficient lasing (slope efficiency of 68%) even at RT, at both 1030 and 1049 nm (emission λ controlled by output coupler transmission level). At low temperature, around 100 K, the slope efficiency (pumping with a Ti:sapphire tunable laser at 969 nm) of a laser based on a 0.7 mm thick chip type gain media (19 at.% Yb^{3+}) could be raised to 85% for the 1030 nm lasing wavelength. Modeling has shown that performant – in the sense of high power – chip lasers can be developed based on such crystals [D13]. Yb^{3+}:apatite type crystals [$Ca_5(PO_4)_4F$, $Sr_5(PO_4)_3F$, $Sr_5(VO_4)_3F$, etc.], grown by the Czochralski method, were also shown as useful lasants (λ = 1044 nm), competing with Nd^{3+} based devices for low and medium power applications. An attractive feature of this host is the fact that the crystal field causes a splitting of the $^2F_{7/2}$ such as the raise one of the states enough above the ground state to prevent thermal population at RT. A comparison of the crystal hosts – which took into consideration most of the relevant performance determining parameters – suggested that crystals like $KY(WO_4)$, $YAl_3(BO_3)_4$, and Sc_2O_3 are the best

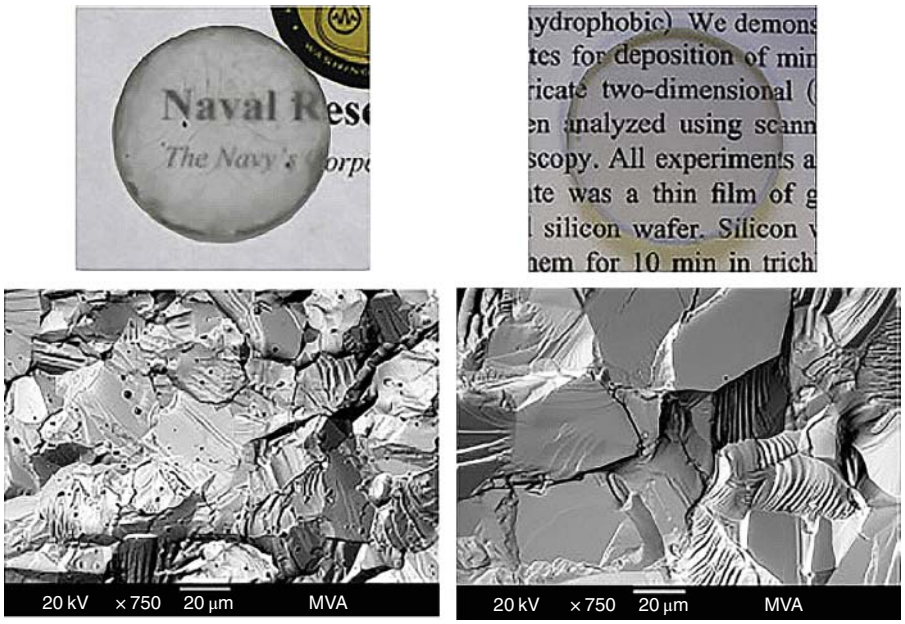

Figure 5.79 Lu_2O_3 doped with 10% Yb_2O_3 specimens fabricated by HP + HIP: imaging and microstructure. (a) Derived from commercial powder. (b) Derived from in-house prepared powder. HIP, hot isostatic pressing. Source: Sanghera et al. 2011 [S10]. Reprinted with permission from SPIE Optical Eng. Press.

option with YAG or fluro-apatites (FAPs) quite modestly placed in this list [B56]. For Lu_2O_3 crystals growing, the HEM was found to be optimal [P23]. Crystal boules of up to 30 cm^3 were obtained; no self-quenching was detected up to 10 at.% of Yb^{3+}. Slope efficiencies of up to 86% ($\lambda_e = 1034$ nm; $\tau_e = 970$ µs) could be obtained. The Lu_2O_3 has, as already been noted earlier, a certain advantage over other bixbites or YAG regarding the λ_{th}. Its lowering of the conductivity, on Yb_2O_3 insertion, is less pronounced (less phonons scattering). With 0.45 mm thickness disc (3 at.% Yb^{3+}), 32.6 W of output power was achieved ($\eta = 80\%$) [P22].

Ceramics Lasing of Yb^{3+} was demonstrated also in various oxide ceramic hosts, both garnet types like YAG and LuAg [M4, X2, N3] or bixbites like Y_2O_3, Sc_2O_3, and Lu_2O_3, and for a wide range of Yb^{3+} concentrations going in some cases up to 20 at.% [B7, B49, N4, N5, T7]. As an example the photo of a 10 at.% Yb doped Lu_2O_3 ceramic is presented in Figure 5.79 [S10] together with the fracture surface microstructure; the transmission spectrum is also given together with the slope efficiency in Figure 5.80 [S10].

Slope efficiencies of ~80% could be obtained in Y_2O_3 [$^2F_{5/2}$ (1) → $^2F_{7/2}$ (4)]. This represents a massive improvement on the first ceramic Yb^{3+} based lasers efficiency of ~26% [T7]. Comparing various transparent ceramic hosts – as to their resistance to thermal shock and thermal conductivity – G.L. Bourdet et al. [B49] concluded that for high power Yb^{3+} based lasers, the cubic sesquioxides are the most promising candidates; in cryogenic conditions Yb:Y_2O_3 proved the best.

Sc_2O_3 is a useful host – as far as pumping is concerned – because in it the lasant ion has a broad absorption band (932–955 nm) [L47]. Strict temperature control of the diode laser is thus not required. The position of the two lasing transitions in Sc_2O_3 is different from those present in YAG (Stark splitting of both manifolds is stronger in Sc_2O_3). The broader (FWHM = 15 nm) fluorescence line associated with the $^2F_{5/2}$ (1) → $^2F_{7/2}$ (3) transition suggests that shorter pulses may be achievable (at 1041 nm) in Sc_2O_3, as is the case in YAG (thermal population of the $^2F_{7/2}$ (3) requires work with thin chips, of ~1 µm, to limit re-absorption). The emission spectrum of Yb doped Scandia is given in Figure 5.81 [L47].

Tunable lasing in the 992–1111 nm range was also obtained in Yb:YAG ceramic [N2].

The fluoride hosts could be, in principle, an interesting host for Yb^{3+}. The phonons of such hosts are of lower energy (cutoff at ~500 cm^{-1} in CaF_2 vs. 830 cm^{-1} in YAG) than that of oxides and the gain media can be produced at temperatures under 1000 °C. The emission lifetime is also much longer in fluoride environment. The crystallographic environment, for the lasing ion, is different from that of oxides in such fluoride lattices, where the Yb^{3+} cation enters as a substituent of Me^{2+}, not Me^{3+} native ions. In single crystals (and it seems also in ceramics) of CaF_2, high [Yb^{3+}] leads to the occurrence of dopant ions clustering (a process occurring also in the case of Nd^{3+}). Such clusters, while on one hand facilitate autoquenching, generate broad emission lines, of interest for short pulse lasing [P24]; pulses as short as 150 fs could be generated by Yb:CaF_2 gain media [L44].

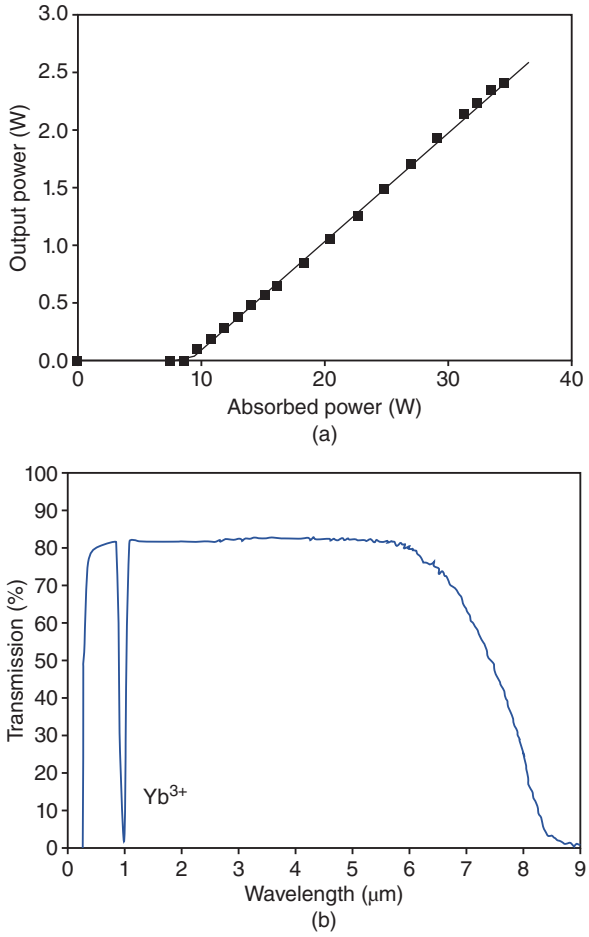

Figure 5.80 Slope efficiency and transmission spectrum of heavily Yb doped transparent Lu_2O_3 ceramic. (a) Transmission spectrum. (b) Slope efficiency plot. Source: Sanghera et al. 2011 [S10]. Reprinted with permission from SPIE Optical Eng. Press.

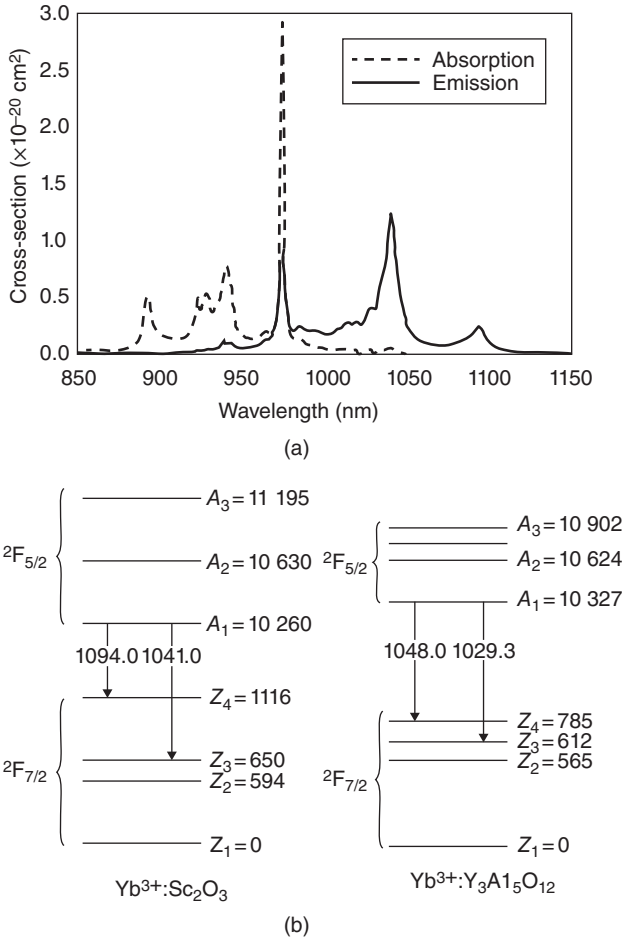

Figure 5.81 Absorption and emission spectra of Yb^{3+} located in a transparent Sc_2O_3 ceramic host together with comparison, of energy separation of levels involved in lasing, between a Sc_2O_3 and YAG hosts. (a) Optical spectra. (b) Electronic levels of Yb^{3+} in two hosts. Source: Lu et al. 2003 [L47]. Reprinted with permission from AIP, USA.

Interestingly, in some experiments, CaF_2 showed larger damage threshold than YAG [L68, L69]. T.T. Basiev et al. produced $0.65CaF_2–0.30SrF_2–0.05YbF_3$ by hot pressing single crystals grog [B14] (a procedure hardly fitted for industrial use). Lasing was obtained, but at efficiency levels are lower than in oxides. Introducing 4 at.% of Yb^{3+}, in CaF_2, Aballea P. et al. were able to demonstrate lasing with a slope efficiency of 43% after LED pumping at 977 nm; maximal output power of 1.6 W [A1]. As opposed to its behavior in oxide hosts, Yb^{3+} seems to segregate at GBs in CaF_2. Oxygen is also present there [L68]. The lines broadening were exploited for short pulses obtainment. For instance, 240 ps pulses with 0.72 MW peak power were obtained in a passively switched system. By mode locking, shorter pulses (68 and even 48 fs) could be demonstrated (at 1042 nm) when an extra wide emission band [K23] was achieved. Despite the aforementioned, all in all not many fluoride host gain media showing highly efficient lasing ability were described either for Yb, as active dopant, or for other RE^+s; these, in spite of the fact high quality hosts, especially in the case of CaF_2 (see 4.2.8) were fabricated by a number of teams and lasing was obtained already in 2004 [L44]. One of the exceptions is the material developed by Kitajima et al., in which CaF_2 was alloyed with LaF_3 [K24]; the authors considered that the presence of La^{3+} reduces the fraction of Yb reduced to a 2^+ oxidation state and also hampers the Yb cations clustering process (clustering affects both thermal conductivity and fluorescence pattern). In a highly transparent host, including 3 at.% of La^{3+}, doped with 1 at.% Yb^{3+} laser output of 4.3 W was achieved at a slope efficiency of 69.5%.

Another negative consequence of the specific electronic configuration of Yb^{3+}, with its lack of levels in the VIS, is the difficulty of finding suitable sensitizers.

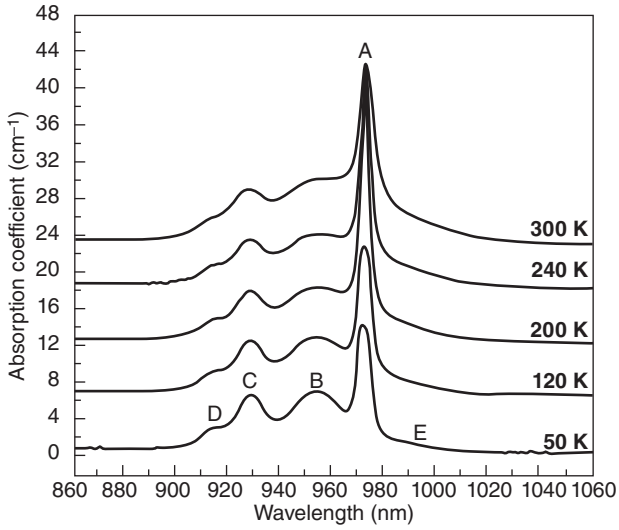

Figure 5.82 Variation with temperature of the broad Yb^{3+} emission spectrum when located in a glass host. Source: Dai et al. 2002 [D2]. Reprinted with permission from Elsevier.

In YAG Nd^{3+} can be useful, for such a purpose – with a resonance energy transfer made possible by a reasonably good bands superposition. Better superposition can be obtained in hosts like Sc_2O_3. In hosts where the crystal field is weak enough to bring its emission of in the region required by Yb^{3+}, the Cr^{3+} cation can be used as sensitizer [I3].

Yb^{3+} lasing was obtained also in glassy (silicate or phosphate) hosts, in fact as early as 1962 [P11]. Such gain media are available commercially, from the late nineties. Early devices pumped with Xe flashtubes (77 K) had of course very low efficiency. This was improved, later, by using more adequate pump sources like InGaAs diodes or even Nd:YAG lasers. Results obtained however remained – as far as efficiency was concerned – much under the levels achieved in ordered hosts. Values of η = 4%, 24%, or 49% Nd:YAG pumping were reported [D2, G45, H33]. The absorption and emission bands are excessively broad, especially at "high" temperatures like RT. The variation of the emission spectrum profile with temperature is shown in Figure 5.82 [D2].

Both the relatively low level of splitting of the $^2F_{7/2}$ ground level, by the host's electrostatic field, and the variable dopant sites geometry, contribute to bands widening. In glasses also the problem posed by the OH^- units (present in the lattice) – an important quenching factor – is also more acute than in crystals [D2]. In fact the glassy hosts seem useful mostly for short pulses obtainment pulses of 58 fs were demonstrated (mode locking) and also tangible in the 1025–1065 nm range. Considering the aforementioned and the bi-modal low thermal conductivity and strength of glasses, practical use of Yb:glass gain media, for higher power generation, does not seem likely as of now, even under cryogenic conditions [H33].

5.2.9.1.5.2.4 Er^{3+}

Er [Xe] $4f^{12}5d^06s^2$ is an element placed, like Yb, toward the end of the RE row. Its radius is thus closer to that of Y^{3+} (somewhat less than in the case of Yb) than it is the case for Nd^{3+}. As a result insertion of Er^{3+} ($4f^{12}$) into hosts like YAG or Y_2O_3 is easier than that of dopants from the start of the RE row. Transparent YAG including up to 50 at.% of Er^{3+} was obtained [H32]. The segregation tendency toward GBs was also found to be weak [H37].

As in the case of all RE^+ dopants, the specifics of its electronic states configuration has certain useful characteristics, as far as lasing is concerned, combined with others, which can be considered as drawbacks [W17].

The arrangement of the electronic states along the energy axis is illustrated in Figure 2.48.

The transmission spectrum of Er^{3+} in YAG is shown in Figure 5.83.

The absorption cross-sections of the states relevant for pumping are quite low, so that population inversion achievement is not an easy task. Thus, the most useful lasing process, occurring that at a wavelength of 1.54 µm, requires, at RT, very strong pumping and high dopant concentrations (without self-quenching); in practice it can be used in devices only if the ceramic gain-media is co-doped with a suitable sensitizer.

Lasing can be produced at various wavelength but of practical interest are especially the 1.50–1.60 µm ($^4I_{13/2}$–$^4I_{15/2}$) and 2.70–2.95 nm ($^4I_{11/2}$–$^4I_{13/2}$) ranges; the first one is very useful for all apps where eyes-safe operation is a must. The second is convenient for biological tissue "machining" (e.g. surgery) because absorption of such wavelength by OH^- groups is strong. In that

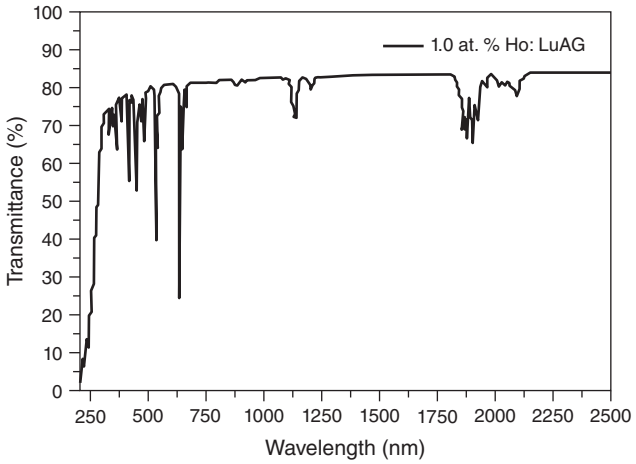

Figure 5.83 Transmission spectrum of YAG doped with Er^{3+}.

context we note the gain media are developed, for work at RT, by L. Wang et al. [W10] in which 7 at.% of Er^{3+} is introduced in a transparent ceramic Y_2O_3 host ($T = 80\%$ at 500 nm; $t = 1.5$ mm; LED pumping at 976 nm); the slope efficiency (around 10%) is small in absolute terms but for this kind of laser reasonable. Interesting results also for RT work have been reported by H. Uehara et al. [U2].

Cooperative interactions, of various forms, have a marked influence on all lasing capable emitting transitions of Er^{3+} YAG – helpful sometimes, but usually deleterious. Owing to the difficulties mentioned earlier, which reduce lasing efficiency, it is necessary to either make use of sensitizers and/or operate in cryogenic conditions. For instance, RT lasing could be obtained, with broad frequency emission pumps like the flash lamps, by the aid of Cr^{3+} (best results in glassy hosts). The broad and strong absorption, via the VIS located d–d bonds of the sensitizer, coupled with a reasonably good overlap between the Cr^{3+} and Er^{3+} relevant bands, ensure relatively efficient energy transfer. A more popular, albeit requiring large sensitizer concentrations, sensitizing scheme makes use of the closeness between the $^2F_{5/2}$ manifold of Yb^{3+} and the $^4I_{11/2}$ of Er^{3+} [Z16]. Co-doping with Ce^{3+} further improves efficiency by suppressing an inconvenient upconversion related to the sensitizer. The sensitizer based schemes introduce, of course, significant quantum defects.

For Er^{3+} the existence of laser-diode pumps, for the region around 970 nm, is very useful, allowing for much more efficient pumping than the lamps. Direct pumping into $^4I_{13/2}$ was also shown as attractive, especially for the case of sesquioxide hosts [T17]; interesting results were obtained also by doping the cation to very fine grained sesquioxide hosts [S22, S32]; in some cases lasing at wavelength like 2.8 μm (not easy to achieve with oxide hosts) was also demonstrated [U2].

5.2.9.1.5.2.5 Cr^{2+} and Fe^{2+} Based MIR Lasers

In many applications – including medical or cosmetic operations, sensing, polymers or glass parts surface treatment, optical signals transmission even X-ray generation, and elementary particles acceleration – laser beams (sometimes of high power), located at wavelengths further in the IR than the rays provided by the mainstream gain media and dopants, are needed [M34, T32]. For such cases certain Er^{3+} (vide supra) and, as will be shortly described later, certain emissions of Ho and Tm may be used. Another option is offered by 3d cation type lasants, like Co^{2+}, Fe^{2+}, or Cr^{2+}, inserted in transparent ceramic chalcogenides (Cr^{3+} has interesting spectral behavior even when doped to garnets [K64]). Such gain media were demonstrated, lately, especially as a result of the research work effectuated by various teams led by S.B. Mirov et al. [M34, M35]. Thus recently CW lasers ($\lambda = 1.8$–3.4 μm), based on Cr^{2+} lasant, inserted in ZnS or ZnSe (60% efficiency), were achieved together with pulsed systems of 30 W average power and pulses shorter than 60 fs. Based on Fe^{2+} lasing in the 3.4–5.2 region (CW mode systems of up to 10 W) were demonstrated.

5.2.9.1.5.2.6 Other Lasing Cations

Many of the RE^{3+} cations, like, say, Pr^{3+} or Ce^{3+} [T21], have spectral properties (when doped to transparent hosts; some of them quite exotic [H39, N6]), enabling them to lase at wavelength not provided by the main lasant cations; even some vacancy based emitters [B14] can lase in ceramics hosts. Some of them, like Pr^{3+}, Tm^{3+}, or Ho^{3+} [K15] do it with reasonable efficiency. Some of them operate at frequencies safe to the eye like is the case of Ho^{3+} [Y8] for which the lasing efficiency (at 2.1 μm) is illustrated in Figure 5.84 [Y7] together with the emission line. A Pr^{3+} doped ceramic CaF_2 gain media was developed, by the team of T.T. Basiev et al. [B17]. While the power (7.5 mW) and lasing efficiency (9%) are modest (pumping at 444 nm, with a GaInN LED), this material was able to provide, for the first time, in the case of a ceramic gain medium, a laser beam at a wavelength situated in the VIS domain (639 nm) as opposed to the IR position of all previous ceramic lasers.

Owing to various factors, like complicated pumping arrangements, weak absorption, requiring sensitization, etc., such dopants are of more limited practical used and will not be analyzed in detail here.

5.2.9.1.5.2.7 Advances in the Spectroscopy of RE^+ Cations

As we have seen in previous chapters, the most important lasants, doped to ceramic hosts, are members of the lanthanide series. Of course detailed knowledge – regarding the electronic structure of the REs, their bonding to the host's lattice, and the characteristics of the various types of transition (between the quantic states of the host/dopant) – is essential for laser development and use. Understanding the correlation between electronic structure and the features of the electronic spectra enables one to design optimized composition and structure gain media. Data collected by studies on this domain is the base required for meaningful modeling of lasing and related processing taking place in pumped gain media. A compact comprehensive review of the most relevant data regarding the absorption and emission spectroscopy is given by V. Lupei and coworkers [I3]. Besides the position and intensity of the spectral bands, data on aspects like the time profile of emission decay, emission quantum efficiency, and energy transfer, including sensitization, is given. From the vast literature of this domain, we highlight [L66, L67] and the references given therein.

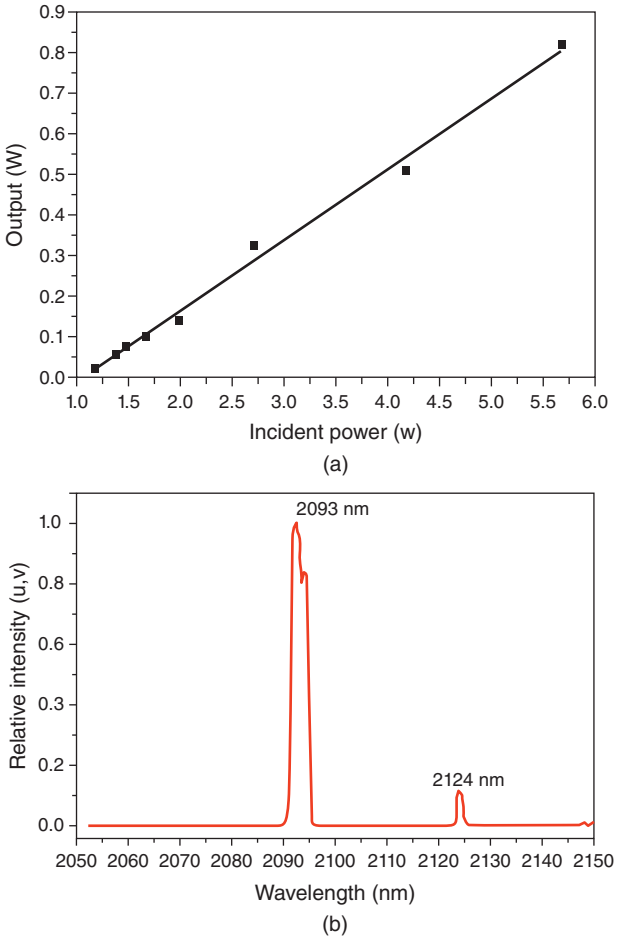

Figure 5.84 (a) Lasing efficiency and (b) emission peak position of Ho^{3+} in ceramic YAG host. Source: Yang and Kim [Y7]. Reprinted with permission from Elsevier.

Let us now present the main applications of the ceramic lasers.

5.2.9.1.6 Applications of Ceramic Lasers

When Hecht developed the Cr:Al_2O_3 first solid-state laser, such devices were considered as "a solution looking for a problem" [H21]. Quite rapidly laser systems found, however, a plethora of important applications in a wide variety of domains. The most interesting ones require high power [M41]. The global value of materials working laser based installations is approaching US10^9; the solid-state lasers represent some 15–20% of the total [H20]. In many of the applications the lasers compete with other options. There is competition also among the various types of laser, including those based on ceramic gain media now developed. In this section applications for which the ceramic lasers are potential candidates are briefly reviewed.

Among the specific features which make lasers useful one can enumerate: coherence, tightly defined wavelength, straight beam format, high power, possibility to focus on small spots one, or multiple beams in coordinated (timewise) short intense pulses, absorption by different materials depends on λ. There are also drawbacks like low penetration depth, possibility to reflect (and thus protect) with suitable materials, high power beams distance by interaction with the atmosphere (limits distance for accurate targeting), etc.

In the development of a ceramic laser one has to start from the targeted application's requirements. Usually the active ion has to be selected first. For instance, if eye safe operation is important one would look for cations like Er^{3+}, Ho^{3+}, or Tm^{3+}. For high power features like high efficiency are important and a good candidate is then Yb^{3+}. In fact a detailed comparative examination of the spectroscopic features of the potential active ions is necessary. It has to be done considering the potential hosts too. Hosts even, broadly similar, may differ regarding the size of the host sites one can fabricate the strength of the LF, the cation density, and the interaction distances. Such differences may lead to differences in the way energy transfer (if sensitization schemes are used) occurs, the emission line width (and thus pulse length), auotoquenching severity, and parasitic transitions intensity (like upconversion, ESA, etc.). The non-spectral properties of the host may influence thermal lensing and thermal sock resistance (critical in high power systems that heat up massively). When comparing hosts of different structures, also aspects like the number of sites – able to accommodate a RE^+ dopant – have to be considered. For instance, in garnets only one such site type exists while two are available in bixbytes. The ease of processing and its general cost need to be matched to the product type (cheap device, intended for mass production, or complex one for special apps). Only a detailed analysis of these factors (the list is not complete) may enable one to determine the dopant/host combination optimal for the application considered.

The following are a few popular applications for which ceramic lasers are the best or at least one possible candidates are described. The main source for the data given in the following was the book by Hecht [H21].

5.2.9.1.6.1 Materials Working

This operation is based on the energy transferred from the laser to the material when the beam impacts the target; the material at the surface impacted melts and vaporizes. Therefore one has to create conditions of significant laser absorption by the target. Because the dependence of reflecting on λ (reflection reduces absorption), one has to select optimal wavelength(s) for each type of material. For instance, metals reflect stronger at larger λ while skin absorbs better there. This makes Nd:YAG a good option for metals working because they

absorb much more at 1.06 μm than at $\lambda = 10.6$ μm where the popular high power CO_2 laser emits; human skin also absorbs fairly well at the basic Nd^{3+}:YAG wavelength. Deep cuts or holes are difficult to produce owing to material vapor evacuation problems.

Material working includes cutting, drilling holes, welding, marking, and heat treatments. Power levels are in the 5–10 kW range, with maximal levels up to 45–50 kW.

Various types of medical treatment imply the "working" of human tissue. Various forms of surgery, dermatologic, and even dental treatments or artery clearing can be effectuated. Laser acupuncture and "cold" laser treatments (milliwatts of power illuminate tissue without destroying it) are also examined.

Among the industries that widely use laser based materials working, the following are worth noting: cars, airplanes, agricultural equipment, electricity generating land based turbines, glass displayers, and fabricated metal products manufacturing.

The medical laser systems will attain a market value of ~US\$$2 \times 10^9$ in 2018; Ho^{3+} and Nd^{3+}:YAG systems are the main candidates coming from the domain of ceramic lasers.

A domain subject to a quite sudden, massive expansion (consecutive to demonstration of interesting abilities) is that of "additive manufacturing" (or free form manufacturing or rapid prototyping). In this method a 3D object is built, layer by layer, according to a digitally stored model, which guides the curing of a sequence of thin layers of liquid monomers. The curing is effectuated by low power laser beams, the movements of which are according to the model. The method was used initially only for monolithic polymers, especially for generation of complex configuration parts prototypes. Lately, however, the speed of the operation and size of the parts produced progressed in a way that suggests the possibility of using the approach for mass production. This seems a promising market for upconverted, low power ceramic lasers. Lasers are also a suitable light source for the more traditional 2D photolithography. Such a process is used, for instance, in the laying of the circuits pattern on semiconductor substrates. While pulsed excimer lasers are the current "workhorse," upconverted ceramic lasers are likely to enter into competition soon for this market.

5.2.9.1.6.2 Laser Weapons

The Star Wars dubbed American effort (Strategic Defense Initiative), funded by the Regan administration, which intended to develop laser based weapons able to destroy ICBMs or satellites, did not succeed. And, yet, the concept of laser weapons operating at a more modest scale than the initial fantasies, is discussed here instead of the Exotic Applications section (vide infra). This is because recently lasers with the ability to power usable weapons have been presented by some manufacturers. For instance, the Textron company came up with the ThinZag configuration (see Figure 5.65) [L27, M11]. In this design a Nd:YAG ceramic slab (amplifier), thin enough to arrest deleterious thermal effects, is pumped at high power levels by diodes. The laser flux zigzags bouncing off reflector walls (silica glass). All the system is cooled by liquid, which efficiently removes the heat created during service. Several such modules can be connected in series so that overall outputs in the 100 kW range can be achieved. High beam quality was also achieved. Designs by Boeing, LLL, and Northrop Grumman [A19, S20] based on Yb:YAG gain media also allow obtainment of similar level power outputs. The weapons based on such lasers can be used against various types of objects flying at distances not longer than a few kilometers, at relatively low speed. For instance, the United States has installed on the "Ponce," a 30 kW laser gun, which showed the ability to destroy targets like a unmanned aerial vehicles (UAV) in the Persian Gulf. In most cases these weapons target the sensor or driving electronics of the targets. One of the problems in such applications is the heating of the atmosphere by the laser itself. This creates turbulences that cause scattering of the beam. A low power laser based application is that of range finders (main uses are military). After aiming the laser at a target, one fires a short pulse and the reflected beams arrival time back (t) is measured. The distance results from $d = ct/2$. The uncertainty in measurement decreases with pulse time's reduction. Solid-state lasers are the most popular for this kind of application. Er based lasers are used in target designator devices because they can operate at $\lambda \approx 1.5$ μm. For such applications work within the λ ranges that do not strongly damage retina is important to prevent operators accidental blinding.

5.2.9.1.6.3 Combustion Ignitors: Cars and Guns

Currently the fuel ignition is fulfilled, in car engines based on internal combustion, by spark plugs. The combustion efficiency is not satisfactory mostly owing to the off center position of the spark within the cylinder. A laser beam can overcome this limitation. In Figure 5.85 the schematic of a laser based ignitor is presented. It is a Q-switched Nd:YAG ceramic rod that has to deliver short pulses (300 ps) of very high peak power (10–15 MW) at repetition rates ≥100 Hz [H5, H9, T2].

In Figure 5.86a ceramic laser ignitor, for a breech mounted howitzer, is depicted [H9]:

5.2.9.1.6.4 Other Applications

Here a partial list of applications for which the use of ceramic lasers is, as of now, not envisaged but for which

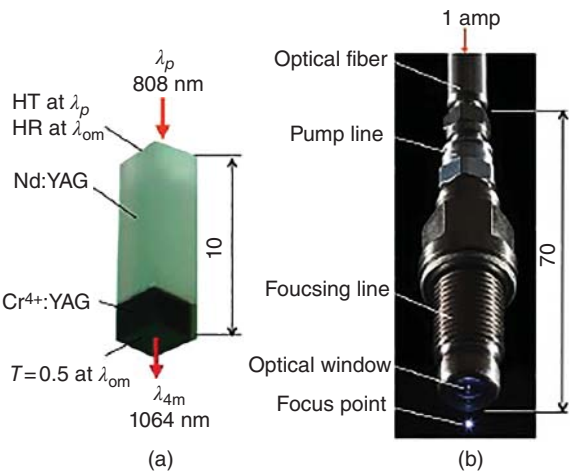

Figure 5.85 Nd:YAG ceramic laser based car engine igniter; (a) the gain medium joined to the passive Cr^{4+} based Q-switch and (b) the components of the igniter. Source: Courtesy of Taira [T2].

they may be as suitable or better solutions than the current ones is given. Best chances for market penetration seem to exist in the domains of optical computing, biomedical diagnostics, photochemistry, and isotope separation and holography.

5.2.9.1.6.4.1 Exotic (Current and Future) Applications

Ignition of Atomic Fusion Reactions Electrical power resulting from nuclear fusion is expected to cover a large fraction of the world's energy needs. One of the methods to ignite controlled fusion reactions is based on internal plasma confinement (as opposed to magnetic confinement). In this approach a hollow, millimeter sized, ball of deuterium tritiate (DT) is placed in a gold container. The ignitor system is an array of laser beams, which are targeted on the container. Very short, perfectly synchronized, massive laser pulses deposit energy in the container wall that as a result emits soft X-rays, which uniformly "coat" the capsule. A highly symmetric layer of the DT material is ejected at very high speed. For momentum conservation, the rest of the capsule implodes. In such a way the temperature rises to $>10^8$ K and the pressure brings the capsule to a density 20 times that of Pb; the material is brought to a hot plasma state. As a result the inter-particles repulsion forces are overcome and the nuclei are able to engage in a fusion process. Enormous amounts of energy are released as long as the fusion process proceeds. Perfect spatial uniformity of the energy flux impacting the target is critical. The laser driver is able to satisfy such a requirement.

Currently a number of fusion research installations, prominently among them, the American NIF (see Figure 5.87), are in operation or under construction [C4, D23, K35].

Among the most important high power laser facilities dedicated to fusion one may cite the Vulcan (UK), Omega (Rochester University, US), Nike (US Naval Research Labs), and GEKKO (Japan). Besides the use for power generation, other studies, in the domain of ultrahigh energy physics, are conducted there. Regarding power generation it is envisaged to construct smaller size replicas of the NIF or similar, dedicated to electricity production. A fusion based power plant concept called Laser Inertial Fusion Energy (LIFE) was developed at Lawrence Livermore Labs [E5]. Each plant is to generate 1 GW. Both the NIF and the future power plants are designed to use harmonically converted (to achieve suitable frequency) laser beams amplified in Nd:glass large ($81 \times 46 \times 4$ cm^3 at NIF) plates. The 200–400 beams combinations deliver pulses of ~2 MJ to ignite the cooled target. The progress of the ceramic lasers and the dramatic cost reduction of the diode lasers for pumping Nd^{3+}, it is considered now to replace glass based gain media with Yb:YAG or Yb:S-FAP. The ceramic, owing to longer storage times, requires smaller number of diodes like the glass. The ceramic has better resistance to thermal shock and laser damage. Modeling [E5] suggests ceramics are strong competitors for the phosphate glass based gain media.

Solar Power Harvesting NASA commissioned studied regarding applications of Nd^{3+} based lasers pumped with solar light. Weapons, RADARs, LIDARs, and transmission of power to users space based users were considered. The Japanese Aerospace Exploration Agency

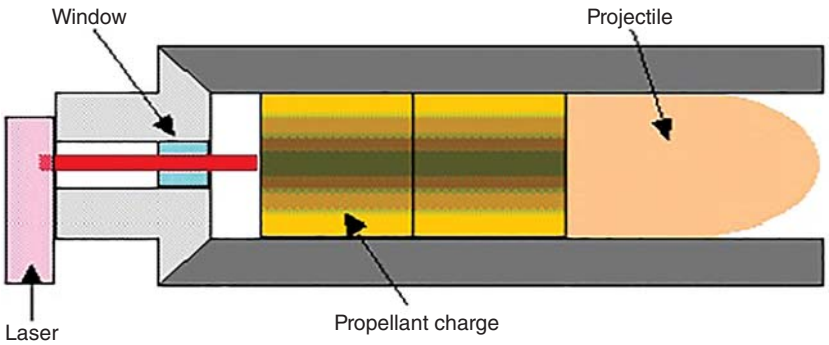

Figure 5.86 Nd:YAG ceramic based laser ignitor for breech mounted howitzer. Source: Hardy et al. 2007 [H9]. Reprinted with permission from SPIE Optical Eng. Press.

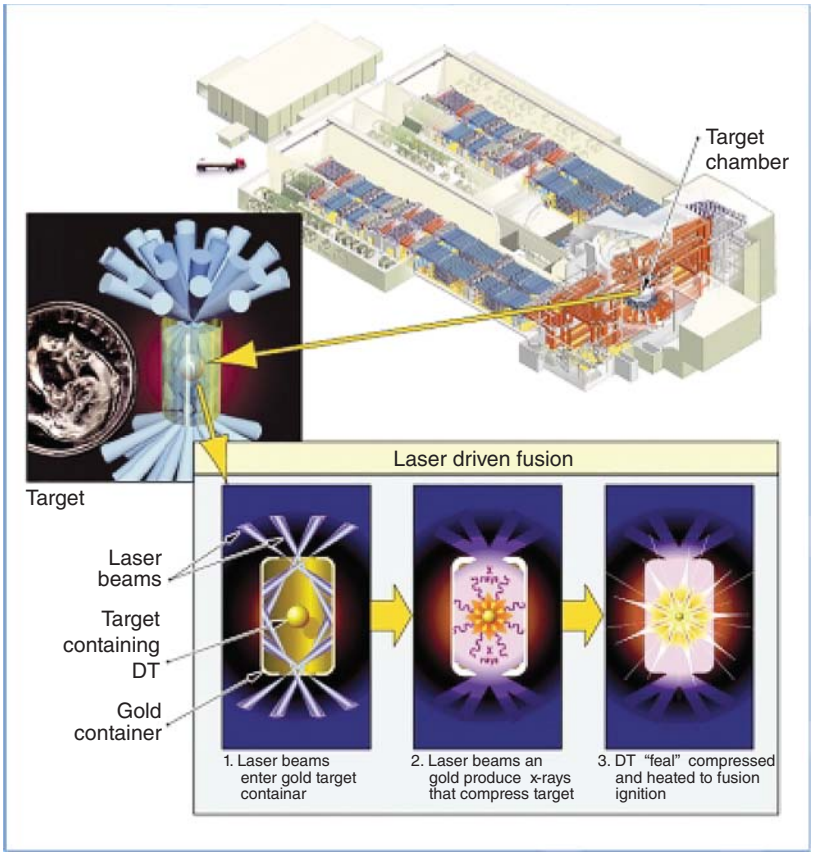

Figure 5.87 Schematic of the system (includes 192 Nd:glass plates generated laser beams) used for fusion experiments (DT fuel) at the National Ignition Facility (NIF) of the US located at LLNL, Livermore, CA; the overall system is shown together with enlarged images of the gold canister that contains a millimeter sized, hollow DT sphere the implosion of which generates conditions for ignition of fusion reaction. Source: Campbell 2004 [C4]. Reprinted with permission from John Wiley & Sons.

(JAXA) is currently actively involved in the design stage (actual deployment expected around 2025) of solar pumped laser systems located on space stations. The leading concept makes use of Nd-Cr:YAG ceramics lasers. Most of the Cr is stabilized as Cr^{3+}, a species with two intensive absorption bands in the visible. The Cr^{3+} can absorb a significant fraction of the broad spectrum solar light, much more than Nd^{3+} alone can do (it can directly absorb at 808 and 885 nm); the sensitizer transfers then energy to the lasant. A. Ikesue et al. currently examines a technology, based on components bonding, for the fabrication of gain media usable in the research phase of this project [I3]. A high efficiency solar power use approach is examined by C. Rotschild's Technion team [R32]. In it the energy, of the solar spectrum, suitable for a photovoltaic cell activation is collected by a doped YAG absorber which fluoresces at the wavelengths relevant for Si or GaAs semiconductors. Simultaneously the heat generated by impacting solar rays, not usable for emission, by the luminescent ceramic collectors, is employed for heating a liquid, which transfers energy to a turbine which generates electric power [R32].

Defensive Weapons Using Ultrahigh Power Lasers As noted earlier the early ambitious programs, like the Strategic Defense Initiative, where destruction of fast flying targets located at hundreds of kilometers was desired, failed to deliver usable systems. However, development of such systems may become possible in the future, albeit a distant one. A worthy target would be to deflect or destroy incoming asteroids (or similar), which pose a threat on humanity as a whole.

Laser Driven, Plasma Based Accelerator Colliders Particles accelerator colliders, like CERN, are the "lab" in which most of the current frontier research is effectuated. Particles are first accelerated to high speed, thus acquiring high energy and then collided to trigger physical processes otherwise not taking place on Earth.

An accelerator design, different from the classic one proposed a long time ago but for which the means were not yet available then [T4], makes use of extreme intensity laser beams as drivers. The main benefit of this approach is compactness: performance one can obtain from a classical design circular collider, which circumvents the Earth can be achieved by a 1 km long plasma accelerator. In a plasma accelerator first a neutral plasma is stabilized (e.g. by heating). Then this plasma is impacted either by a charged particles beam or (and this variant is of interest here) by a high intensity laser beam focused on a micrometers diameter spot. Owing to the

high laser intensity the nonlinear ponderomotive force is significant (the effect is a radiation [laser] "pressure"), which separates the lighter electrons from the more inert positive ions. The relatively strong separation of charges generates huge level fields (several MeV/μm). If external particles are now injected at the proper location, they will be accelerated to impressive speed levels. In fact this is also what happens in a normal accelerator but the mechanism here discussed is the most efficient in converting transversal oscillation into longitudinal impulse. Of course the laser wave pulse is very short (picoseconds or less) and so is the plasma's state fluctuation. It is important to note that if the driver laser beam is focused on spots small enough and the target material is thin enough (<0.1 μm), electrons are moved in tandem as bunches. The accelerated particles will also move as bunches (phase locking). Such accelerators are also called laser wake field accelerators (LWFAs) because the accelerating fields appear in the wake of a laser pulse passing. It is expected to create, with the aid of such accelerators, highly energetic particles (PeV range) and radiation.

In such "labs," issues like the origin of dark matter and energy, the way cosmic accelerators work, vacuum "boiling," can be studied.

For the laser part of the systems, the task is to create extreme laser intensity (up to 10^{28} W/cm^2) and this means very short (down to yocto seconds) energetic pulses. The existent methods of Q-switching mode locking, CPA, optical parameter amplifier (OPA)-CPA, or backward Raman amplification (BRA) are not efficient enough, not even for near future targets of further compressing 100 kJ, 5 ns starting signals down to ~20 fs, with good efficiency. It is hoped that combination of such methods (cascaded compression conversion) may provide an approach equal to the task.

A number of large-scale international projects have as a task the construction of ever stronger laser driven acceleration and their scientific exploration (high fields physics), and underway. Among the most important is the ELI, EU funded project. ELI, is a project that will have facilities in four distinct countries; each facility is focused on different tasks. The ELI is a structure constituted by IZEST = International Center for Zetta Exawatt Science and Technology. One of its components (located at Măgurele, Romania) will coherently combine two 10 PW peak power lasers to produce energy fluence of $10^{23–24}$ W/cm^2 and use them, among other things, in a LWFA to generate fields of 10^{15} V/m. Overall the Măgurele laser is conceived mostly for high energy physics basic studies. The laser works according to an OP-CPA format [S66]. The front end seems to generate a seed by the help of Ti:sapphire oscillator, while the two stage amplifier rows also use single-crystal Ti^{3+}:Al_2O_3 large (around 13 cm diameter) discs as gain media; as it was indicated earlier, this gain medium allows emission tuning in a quite wide range of wave lengths (NIR). The pulses are down to the 5–10 fs range and the energy per pulse of around staggering 300 J; repetition rates of round one minute seem possible. It is evident that for this application high power ceramic lasers like, say, Yb:YAG (Lu_2O_3) may be compete with the current gain media. Plasma accelerator issues are studied also by the aid of the UK based Vulcan laser facility (IR emission, eight beams produced by Nd-glass focusable on 5 μm spots, with irradiance of ~10^{21} W cm^{-2}; OP-CPA [see Section 5.2.9.1.4 for definition] based amplification) or the Texas Petawatt Laser, which works in fusion related research (electrons acceleration to 5–7 GeV is envisaged; 170 fs pulses of 190 J, with amplification based on OP-CPA).

5.2.9.2 Q-switches

5.2.9.2.1 General

One of solid-state laser systems components that can be based on doped TCs (besides the gain-media) are the Q-switches; alternative usable materials for such a component are single crystals and glass-ceramics. The *Q* (quality) factor – as noted in Section 5.2.9.1.2 – is a dimensionless parameter expressing the level of energy loss within a resonator; a high *Q* means low loss (low damping of oscillations). In a lasing resonator, Q-switching, proposed by G. Gould (1968) [G35, S76], is used for the formation of short, high energy pulses, as opposed to the CW operation mode. This action is realized by creating, inside the cavity, a shutter (attenuator) effect, i.e. a reduction, for a determined period of time, of the value of *Q*. When *Q* is reduced under a certain (quite high) level, lasing can occur no longer, of course, because not enough gain occurs in the resonator during a pass. In a CW laser, the population inversion is only slightly higher than the threshold level for lasing. When the shutter is on, in a Q-switched system, the amount of inversion can rise markedly and thus cause energy accumulation in the cavity. Depending on the characteristics of the system and those of the switch, saturation of the switches achieved when the beam incident on it attains a certain limit and at that moment *Q* is suddenly restored to a high value. At this moment lasing restarts and all the accumulated energy is released in a short pulse. Pulses with gigawatt peak powers and length in the nanoseconds range (in extreme cases, even less) can be obtained (for shorter, pico- and femtosecond pulses, however other techniques are more suitable). The physics of Q-switching was presented earlier – in the section devoted to lasers (see Section 5.2.9.1.2). The solid materials most useful for satisfying conditions for efficient switching are certain single crystals or ceramics (including also some suitable glass-ceramics) doped

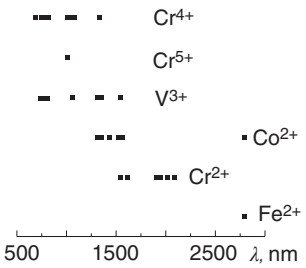

Figure 5.88 Lasing frequencies for which the specified TM^+ cations may function as Q-switches. Source: Malyarevich and Yumashev 2009 [M9]. Reprinted with permission from Springer.

with TM^+ cations. Spectral characteristics examination shows that such solids, by accommodating certain TM^+ cations in tetrahedral sites, become able to act as switches. Among the TM^+s able to assume a tetrahedral ligands coordination pattern one may cite: Co^{2+}, $Cr^{4+,2+,5+}$, V^{3+}, and Fe^{2+}. They have such a coordination in lattices similar to those of YAG, LuAG, GdAG, Mg, or Zn spinels, $ZnGa_2O_4$ spinelid ZnS(Se), YVO_4, Y_2SiO_5, Mg_2SiO_4, etc. Spectral curves also show that for many of the TM^+ noted earlier the expected bathochrome shift of the absorption bands, at an O_h to T_d site change, moves them in the NIR–MIR regions, where most of the important lasers operate. A much wider choice of hosts is available in the case of the single crystals. In the case of ceramics, currently Mg spinel and YAG and some sulfides (selenides) are the most accessible materials, these being accompanied also by a few transparent glass-ceramics. The structural, thermomechanical, and optical characteristics of the most popular hosts for tetracoordinated TM^+s are given in table 1 of [M9].

By the aid of TM^+ based saturable absorbers, lasers working in a quite large spectral range can be Q-switched, as shown in Figure 5.88 [M9].

This means that laser types like the ruby (Cr^{3+}:Al_2O_3), tunable ones like Ti^{3+}:Al_2O_3, alexandrite Cr^{3+}:$BeAl_2O_4$, Cr^{3+}:$LiSrAlF_6$, Pr^{3+}:$YAlO_3$, Nd^{3+}:YAG (emitting at 1.06 or 1, 3, 14 μm), Yb^{3+}:YAG(LuAG, $Gd_3Ga_5O_{12}$, YVO_4), Er^{3+}:glass, Er^{3+}:YAG (emission at 1.54 or ~3 μm), Tm^{3+} or Ho^{3+}:YAG, etc. Optimal performance for each type of laser is obtained with specific switch hosts (for a given TM^+). A rich listing of the switches optimal for a given laser can be found in the review paper by A.M. Malyarevich et al. [M10]. Let us now (briefly) review the most important TM^+s used for passive Q-switching, starting with those already introduced in ceramic hosts too.

5.2.9.2.2 Transition Metal Cations Usable for Switching

5.2.9.2.2.1 Co^{2+}

In crystals and glasses, Co is stabilized, in most cases, as Co^{2+}, the formation of Co^{3+} requiring special hosts and/or fabrication conditions [G20]. The oxidation potential of Co^{2+} to Co^{3+} is quite high. The d^7 Co^{2+} ion exhibits a considerable LF stabilization in the case of octahedral (as compared with tetrahedral) symmetry. Therefore in many hosts an equilibrium between O_h and T_d sites of Co^{2+} occurs, with the former symmetry representing the largest fraction. However the vibronically acquired increase of the oscillator strength, specific to T_d sites, confers significant intensity to the absorption bands, so that even low concentrations of tetrahedrally coordinated Co^{2+} are able to provide Q-switching work. Co^{2+} has been doped, for Q-switches fabrication, to various crystal types like: garnet, spinel, $LaMgAl_{11}O_{19}$, or chalcogenides like CdS and CdSe. The crystal field strength and its precise symmetry varies significantly from lattice to lattice, so that the absorption bands position, shape, and intensity, and also the $\frac{\sigma_a}{\sigma_{esa}}$ rate, vary accordingly; recovery times also differ. In Figure 5.89 the transmission spectrum of a spinel ceramic doped with Co^{2+} is shown, together with the profile of the α (λ) dependence [G27].

The absorption spectrum of Co^{2+} in a spinel host fabricated by authors, other than relevant for Figure 5.82, is given in Figure 5.90.

In Figure 5.91a few such ceramic, and one glass-ceramic, hosts doped discs are shown, together with the microstructure of the ceramic.

The electronic levels of a Co^{2+} in T_d are shown in Figure 5.92.

The saturation curve appears in Figure 5.93 (specimen different from that shown in Figure 5.59).

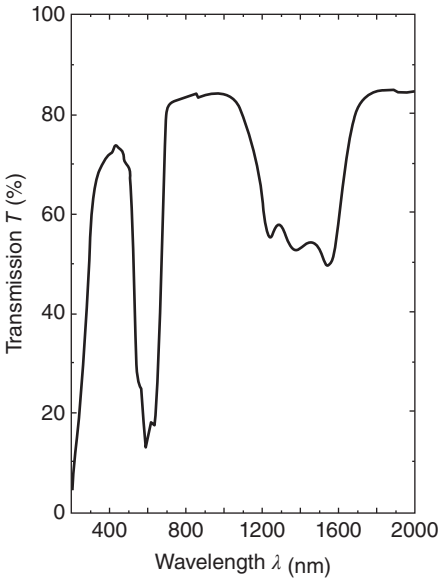

Figure 5.89 Co^{2+}: spinel ceramic's transmission spectrum. Source: Goldstein et al. 2016 [G27]. Reprinted with permission from John Wiley & Sons.

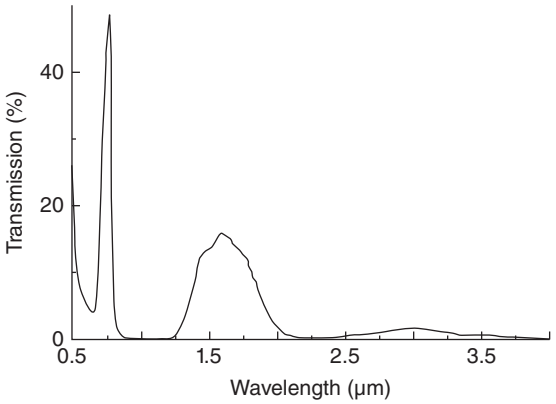

Figure 5.90 Absorption spectrum of Co^{2+}: spinel ceramic with highlighting of the absorption band relevant for Q switching. Source: Malyarevich and Yumashev 2009 [M9]. Reprinted with permission from Springer.

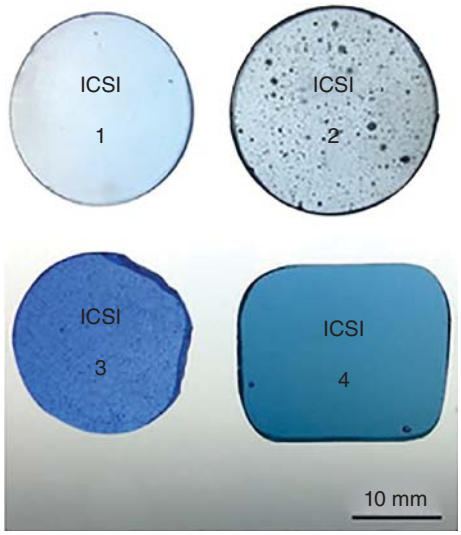

Figure 5.91 Imaging of different optical quality Co^{2+}: spinel ceramic specimens. Source: Goldstein et al. 2016 [G27]. Reprinted with permission from John Wiley & Sons.

Co^{2+} ZnSe ceramics have also been produced, but their Q-switch behavior is not yet well examined.

In a T_d site the allowed dipole–dipole transitions involving the ground state are $^4A_2(^4F) \rightarrow {}^4T_1(^4F), {}^4T_1(^4P)$ (increasing energy order), and these bands are therefore seen in the spectra of the oxides. In ZnSe also the low energy ($\lambda \approx 3.0\,\mu m$) $^4T_2(^4F)$ is also seen, because of a stronger vibronic coupling lends additional intensity to it. In such crystals the LF is also weaker redshifting all the bands of Co^{2+} (T_d) compared with those produced in a Mg-spinel host. A weaker $^4T_2(^4F)$ band seems to be present also in YAG, possibly owing to a slight distortion of the ligands polyhedra from T_d to S_4

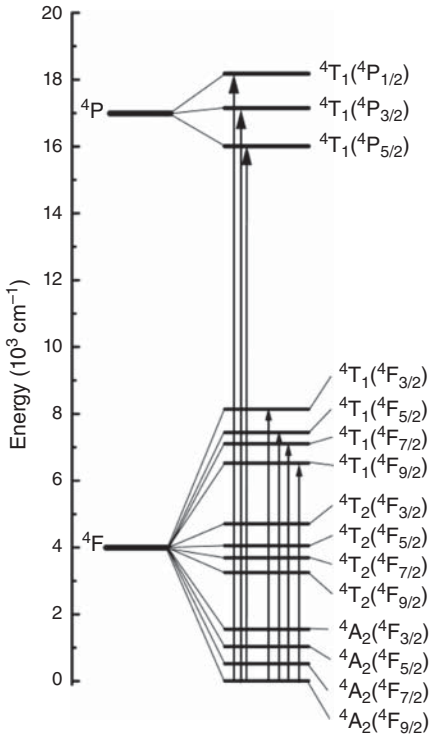

Figure 5.92 Detailed calculated electronic level scheme of Co^{2+} located in a T_d symmetry site. Source: Goldstein et al. 2016 [G27]. Reprinted with permission from John Wiley & Sons.

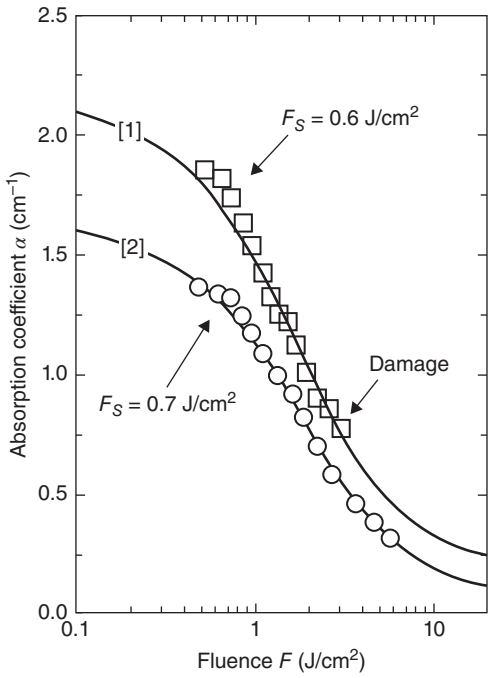

Figure 5.93 Plot of the absorption vs. incoming laser beam fluence ($\lambda = 1.54\,\mu m$) in the case of a Q-switching disc made of Co doped spinel. Source: Goldstein et al. 2016 [G27]. Reprinted with permission from John Wiley & Sons.

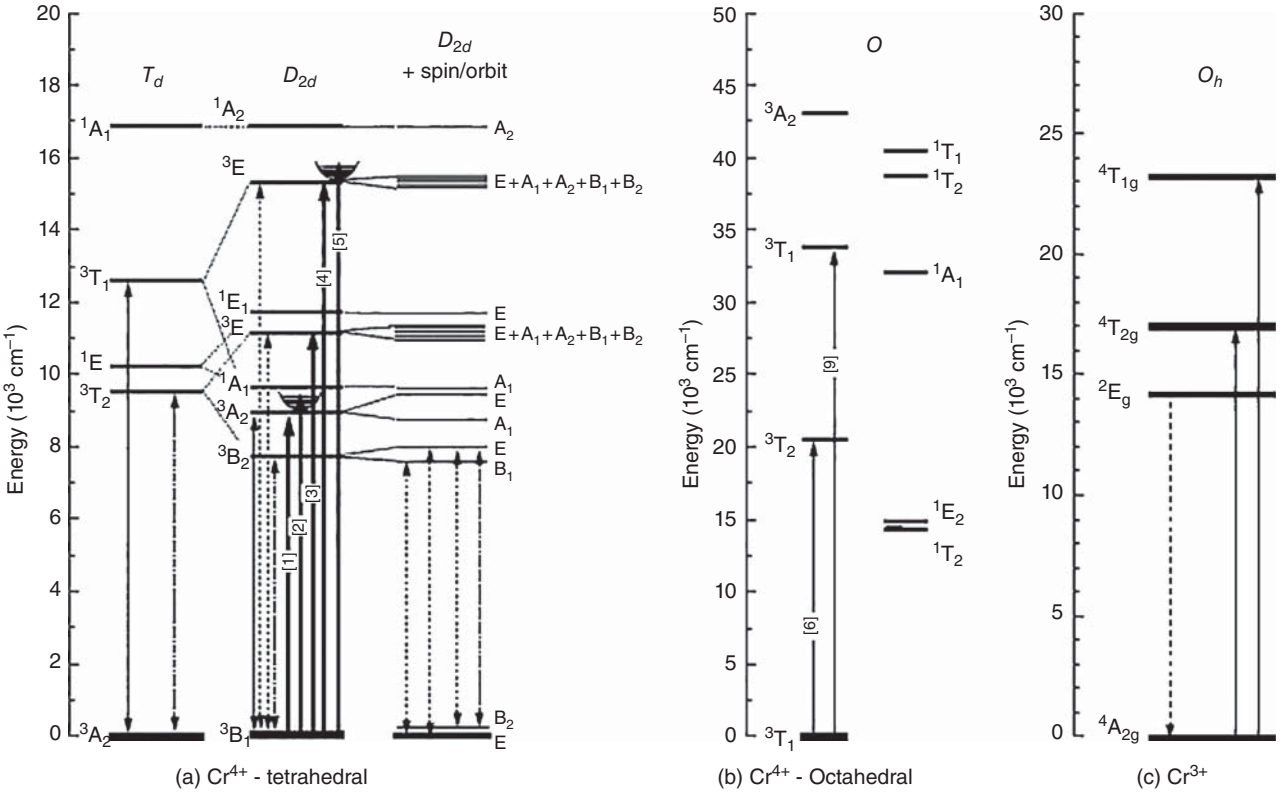

Figure 5.94 Schematic of the electronic energy levels of Cr^{4+} and Cr^{3+}. (a) Cr^{4+} in coordination complex with tetrahedral arrangement of ligands. (b) Cr^{4+} in coordination complex with octahedral arrangement of ligands. (c) Cr^{3+} in coordination complex with octahedral arrangement of ligands. Source: Feldman et al. 2003 [F3]. Reprinted with permission from Elsevier.

symmetry. In oxides, the strongest redshifting of $^4T_1(^4F)$ occurs in $Y_3Sc_2Ga_2O_{12}$ ($\lambda = 1.8\,\mu m$). The Co^{2+} bands are (especially those in the IR) quite broad and show a fine splitting. Both some Jahn–Teller distortion and the action of spin-orbital coupling (for Co^{2+} this interaction is larger than that characterizing other TM^+ ions of the 3d series) are responsible for these spectral features.

In spinel the $\sigma_{esa}/\sigma_a < 0.1$ because no convenient excited state for ESA from $^4T_2(^4F)$ exists.

The recovery time is controlled by the lifetime of the $^4T_2(^4F)$, being <1 ns in garnet and long, at 200–350 ns, in spinels. In glass-ceramics, which precipitate spinels, the behavior of Co^{2+} is similar, but not identical, to that of the doped crystals. The difference comes from the fact that a fraction of Co^{2+} is located in the glassy matrix. The recovery times are especially influenced, attaining values over 300 ns, up to 700 ns. In chalcogenide the relatively long lifetimes of $^4T_2(F^4)$ are due to the weak phonons that are not very effective in assisting decay. The low-frequency vibrations are the result of the presence of quite heavy anions; this also shifts the low energy edge of their transparency window to long wavelengths. The chalcogenides are good ceramic hosts also for bi-functional (lasing/switching) ions like Cr^{2+}, Ee^{2+}.

In glass-ceramics, the amount of uniformly distributed Co^{2+} can be significantly larger than in crystal [S27]. Sensitivity of τ_r to Co^{2+} concentration was observed [M10]; at higher concentration the lifetime of $^4T_2(^4F)$ is markedly reduced, down to 150 ns or lower.

5.2.9.2.2.2 $Cr^{4+,5+}$

This $3d^2$ cation is the most used in a Q-switching function because it works in a zone where Nd^{3+} lases. It was inserted in both single crystals and TCs [F6, I9, K3, L24, L25, M10, S4]. In the tested hosts it replaces, mostly, Al^{3+}. While not small, the differences in radius size between Al^{3+} (O_h, T_d) and Cr^{4+} (O_h, T_d) are not so large as totally prevent substitution.

It has to be noted that Cr doped to oxide hosts assumes a Cr^{3+} (O_h) configuration ($r_6 \sim 75$ Å) much more easily (strong LF stabilization) than any other option [S14]. Only a low fraction of the nominal amount of Cr introduced assumes a Cr^{4+} oxidation state in most hosts (oxidizing conditions during high temperature stages of the processing are helpful). The use of divalent charge compensators like Ca^{2+} or Mg^{2+}, able to enter the in the dodecahedral "c" sites of YAG, seems also to facilitate the stabilization of the Cr^{4+},

at least in YAG as host [F3, F4]. From the total Cr^{4+} amount, only 40% enter T_d sites. For single crystals it was shown that annealing under an O_2 rich atmosphere raises the concentration in Cr^{4+} (it also may generate some Cr^{6+} [G20]). In Figure 5.94 the energy levels of Cr^{4+} in T_d, D_{2d}, and O_h (sites present in YAG) are given. In oxide hosts, a slight distortion of the perfect T_d toward a D_{2d} actual ligands polyhedron is often seen.

Parts including both Cr^{4+} and Cr^{3+} exhibit a dark brown tint, different from the green or red Cr^{3+} induces in oxide hosts.

In Figure 5.95 the optical spectra of Cr, Ca:YAG, subjected to reducing and oxidation atmosphere, after growth, are shown [F3, F4].

The curve of Figure 5.95b (oxidized crystal) is almost entirely attributable to Cr^{4+} (the Cr^{3+} contribution was subtracted). Bands 1–5 belong to Cr^{4+} (T_d; $r_4 = 0.55$ Å), the desired state, but 6–9 show part of the Cr^{4+} is in O_h sites ($r_6 = 0.69$ Å).

In Figure 5.96 the effect of oxidation temperature on the spectral profile of Cr^{4+} is shown.

An interesting effect seems to occur. The spectra suggest that at 1000 °C the amount of Cr^{4+} in T_d is much larger than that seen in specimens oxidized at 850 °C. According to R. Feldman et al., the concentration of sites available for Cr^{4+} formation increases by oxidation. It seems that initially the Cr^{4+} formed occupy O_h sites, and only during oxidation a fraction (up to ~0.40) takes T_d sites. The tetracoordinated Cr^{4+} cations generate the broad band (750–1150 nm), which is a vibronic band including the transitions from $^3B_1$ to $^3A_2$, $^3B_2$ and ^3E (all from ^3F). In the 1.1–1.2 μm region, there is contribution from the weak (spin forbidden) ^1E band.

The Q-switching effect of Cr^{4+} can be obtained either by introducing it directly in the Nd^{3+} containing gain

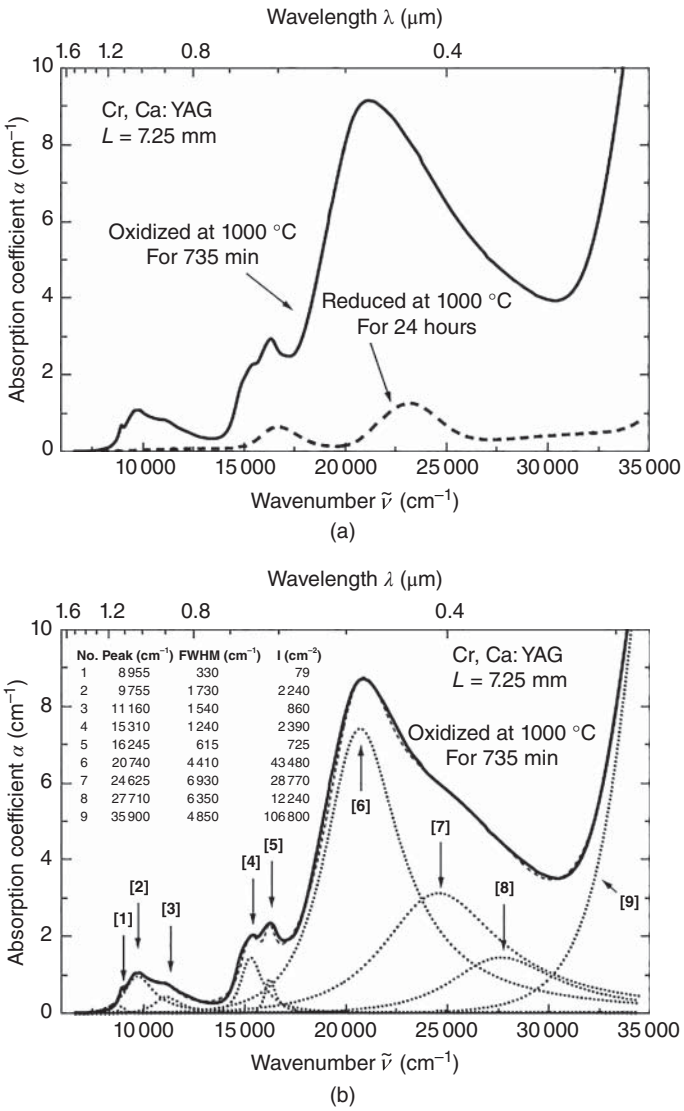

Figure 5.95 Absorption spectra of Cr,Ca:YAG crystal subjected to oxidizing and, respectively, reducing atmospheres. (a) Spectra in both atmospheres. (b) Deconvolution, into basic bands, of the spectral envelope obtained under oxidizing atmosphere. Source: Reproduced from [F3, F4] with permission from Elsevier.

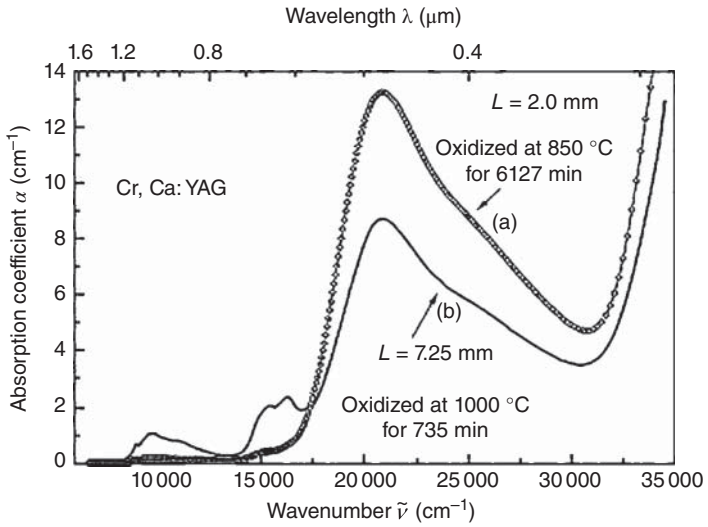

Figure 5.96 Effect of temperature on the spectrum of Cr^{4+} in the case thermal treatment was effectuated under oxidizing atmosphere. Source: Reproduced from [F3, F4] with permission from Elsevier.

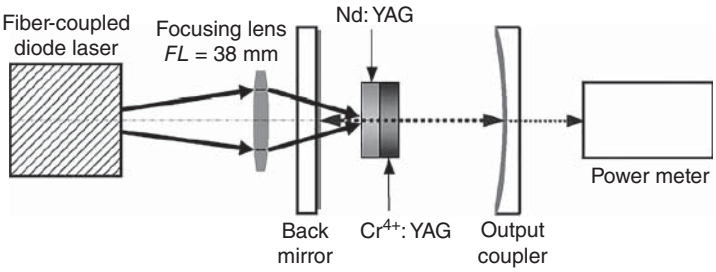

Figure 5.97 Set up of system used for Q-switched (Cr^{4+} based passive absorber) operation of a Nd^{3+}:YAG laser. Source: Feng et al. 2004 [F6]. Reproduced with permission from OSA, USA.

media or by producing an independent Cr^{4+}:YAG part. In the latter case the two parts can be joined so as to form a microchip Q-switched laser [F4]. T-YAG containing only Cr^{4+} or Nd^{3+}+Cr^{4+} was fabricated by a number of teams [D14, L24]. The ability of Cr^{4+}:YAG part to Q-switch a Nd^{3+}:YAG laser was demonstrated [F6]. The authors used the arrangement shown in Figure 5.97 to produce pulses like those in Figure 5.98.

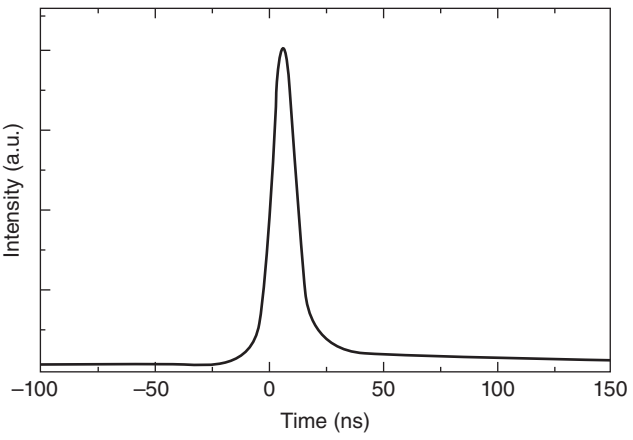

Figure 5.98 Lasing short pulse produced by the system depicted in Figure 5.97. Source: Feldman et al. 2003 [F3]. Reproduced with permission from OSA, USA.

Tests have been effectuated also on Yb^{3+} lasers Q-switched with Cr^{4+} (both in ceramic YAG hosts) [D14]. In microchip format 380 ps pulses, carrying 30 μJ, were obtained (peak power 82 kW). Improvement of the system raised the peak power to 150 kW. Further work produced pulses carrying up to 200 mJ and peak powers up to 100 kW [I3] or 237 ps pulses (172 μJ) and P_{peak} = 0.72 MW [P16]. While high peak power could be obtained, it was observed that the absorption of Cr^{4+} at the pumping (λ = 940 diode) and the strong fluorescence at high Cr^{4+} concentration limit performance. Using a special diodes pumping arrangement at 807 nm, a 1.1 at.% Nd^{3+}:YAG ceramic laser was made to emit 2.5 mJ pulses (peak of 2.8 MW; 10 Hz) usable for an engine fuel ignition. The idea of producing Cr^{4+}:YAG fiber to be used as a switch for Nd^{3+}:YAG fiber is under examination.

Cr^{5+} was examined only in YVO_4 single-crystalline hosts. The actual site is a tetrahedron stretched along the "*c*" axis, i.e. has a D_{2d} symmetry. The $^2A_1$–$^2B_2$ band at 1.1 μm is allowed for dipole–dipole transitions.

5.2.9.2.2.3 V^{3+}

Another useful d^2 ion is the V^{3+} [M31], and single-crystal YAG doped with it has been produced, and its Q-switch abilities tested. In the spectrum the high-energy bands

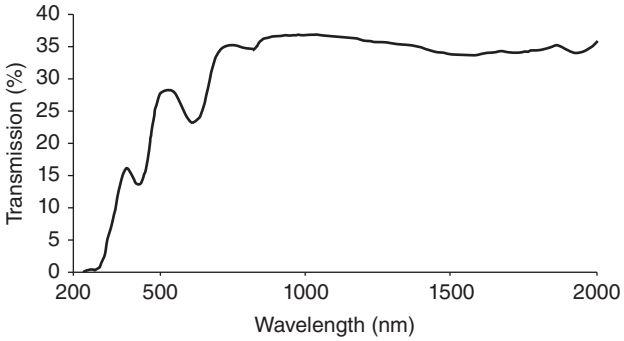

Figure 5.99 Transmission spectrum of V^{3+} doped YAG fabricated at ICSI-Haifa.

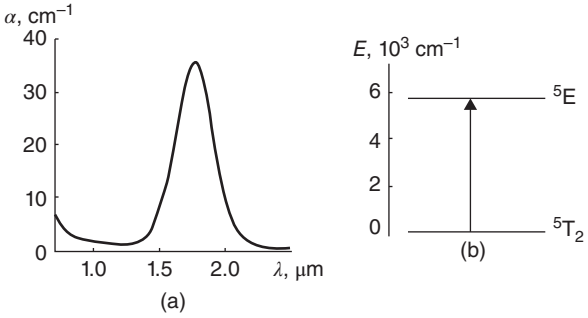

Figure 5.100 IR absorption band of Cr^{2+} located in a ZnSe single crystal. Source: Malyarevich and Yumashev 2009 [M9]. Reproduced with permission from Springer.

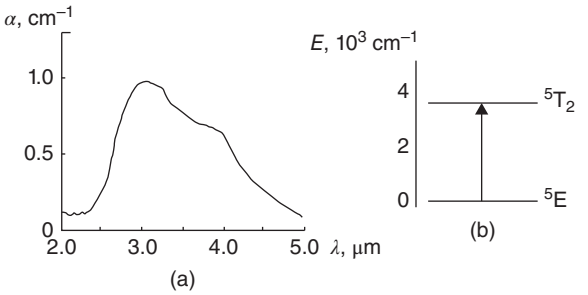

Figure 5.101 IR absorption spectral envelope of Fe^{2+} located in ZnSe single crystal. Source: Malyarevich and Yumashev 2009 [M9]. Reproduced with permission from Springer.

(till ~0.7 μm) are produced by V^{3+} in O_h, which are the dominant species. The minor (but critical for Q-switching) fraction of V^{3+} in T_d generates the $^3A_2(^3F) \rightarrow {}^3T_2(^3F)$ band at 1.32 μm, and that to $^3T_1(^3F)$ at 0.82 μm. The first (the most important here) is forbidden as a dipole/dipole transition in T_d but exists at relatively high intensity (and as a broad signal), owing to the slight D_{2d} distortion. So, in fact, the envelope includes the $^3B_1(^3A_2) \rightarrow {}^3E(^3T_2)$, with a weak contribution at 1.13 μm from $^3A_2(^3F) \rightarrow {}^1E(^1D)$. The $^3A_2(^3F) \rightarrow {}^3T_2(^3P)$ overlaps with the lowest energy band of the V^{3+} (O_h) species $[^3T_1(^3F) \rightarrow {}^3T_2(^3F)]$.

The recovery time is controlled by the non-radiative relaxation stage [from $^3T_1(^3F) \rightarrow {}^3T_2(^3F)$] being in the 5–37 ns range [M9]; ($\alpha_{ns}/\alpha_0 < 0.1$) in the 1.0–1.3 μm range.

V^{3+}:YAG crystals have been used for switching of Nd:YAG ceramic lasers (1.3 μm emission), but little data exists for use as Q-switches [M10] of the for ceramic passive absorber type. V^{3+}:YAG transparent ceramics have been produced in our lab; quality is not yet good enough for switching action. The transmission spectra is shown in Figure 5.99.

5.2.9.2.2.4 Cr^{2+} (d^4), Fe^{2+} (d^6)

The spectrum of Cr^{2+}, in a ZnSe single crystal, and electronic levels structure are shown in Figure 5.100 [M9]. In Figure 5.101 [M9] the spectrum of Fe^{2+} in sucha crystal is shown.

The spectra produced by Cr^{2+} and Fe^{2+} when inserted in a transparent chalcogenide ceramics [M34, M35] are given in Figure 5.102 [M34].

5.2.9.3 Ceramic Phosphors for Solid State Lighting Systems

One type of SSLS, which has become commercially relevant lately, is comprised of a semiconductor based LED layer on top of which a phosphor layer is located [S15, S16, C26, M26]. The LED emits blue light. Part of this light transits the top layer while another fraction excites luminescence in it. The phosphor, as a result, emits at one or more wavelengths, located in the VIS, selected so as to produce, together with the blue emission, white light. The principle of the device is shown in Figure 5.103, together with other possible approaches to the design of a SSLS [M26].

The phosphor layer may be constituted from various materials (monolithic or composite) like, for instance, a polymer matrix filled with a ceramic phosphor powder. One of the attractive options is a monolithic transparent ceramic suitably doped (TM^+ and/or RE^+ cations) so as to emit suitable light.

This kind of TC forms the object of the current section. Before presenting them, a sort general background on artificial light sources is given.

5.2.9.3.1 Artificial Light Sources: General Considerations

Lighting indoor and outdoor spaces and providing light sources for vehicles and devices are among the important tasks our civilization has to fulfill. Lighting devices represent a large size market. Transparent ceramics have been first involved in this domain when transparent thin-wall alumina tubes, for high pressure Na lamps, were developed at General Electric (end of the 1950s and

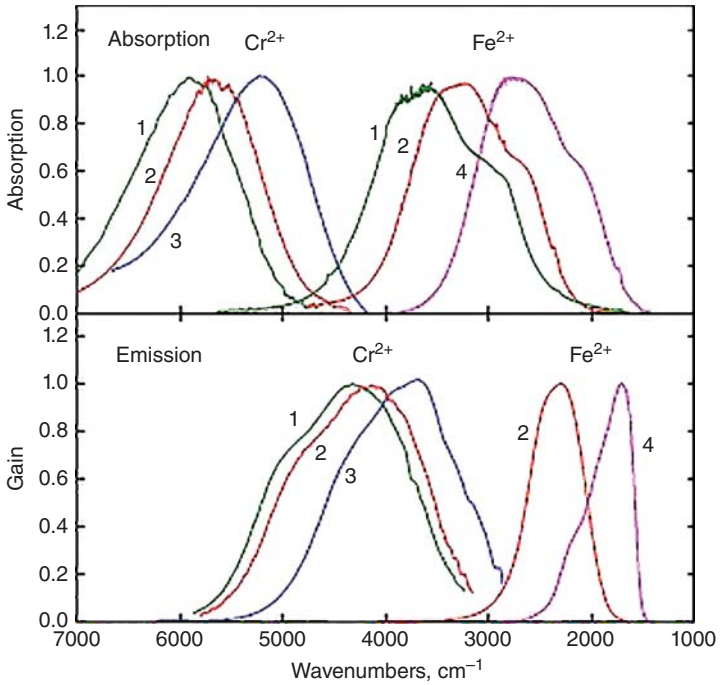

Figure 5.102 Optical spectra of Cr^{2+} and Fe^{2+} hosted by chalcogenide transparent ceramics. Source: Mirov et al. 2011 [M34]. Reproduced with permission from OSA, USA.

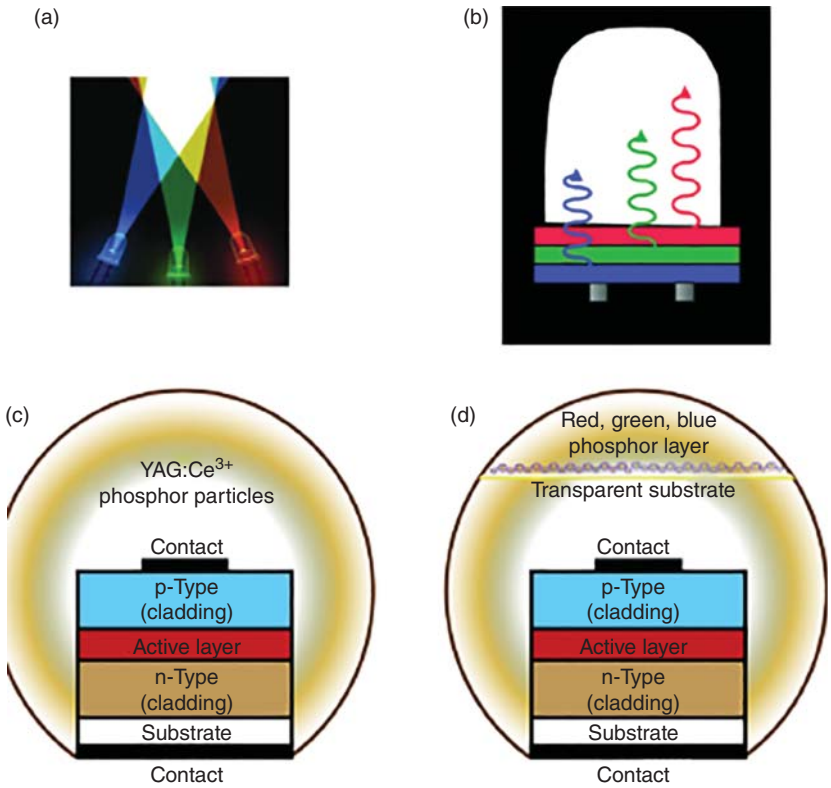

Figure 5.103 Schematic of SSLSs of various structure. (a) White light is produced by mixing of three colored LEDs. (b) Multilayer device constituted of a LED (bottom layer) emitting blue light on top of which layers, of phosphor doped so as to emit green respectively red light, are stacked. (c) Commercial SSLS design: over a LED emitting in blue, a polymer spherical layer – containing YAG ceramic particles doped so as to emit in the yellow domain – is mounted. (d) Commercial design: a remote polymer/YAG particles (doped so as to emit in red, green, and blue) phosphor layer covers an LED which emits in NUV. Source: McKittrick and Shea-Rohwer 2014 [M26]. Reproduced with permission from John Wiley & Sons.

early 1960s). Lately transparent ceramic parts become active components of certain SSLSs. The envelope application was discussed in Section 5.2.1. The subject of this section are the doped transparent ceramics, which partake in the active part of SSLSs.

5.2.9.3.1.1 Conventional Light Sources Powered by Electricity

In order to allow comparison of the SSLSs with the lighting devices, which constitute the competition (only devices powered by electricity are relevant currently),

a brief presentation of the latter is given here. Only the general traits of the operating mechanisms and some data regarding performance-controlling parameters and cost are addressed. These systems posed a number of engineering problems for which ingenious engineering solutions had been found; such aspects, while interesting, are beyond the scope of this book.

From the early days of the twentieth century, lighting sources (except those used in fancy candle-light dinners and similar occasions) are powered by electrical energy. They consume a sizable fraction of the produced electricity. In the United States, for example, ~22% of it (8% if the total energy used) is used for illuminating purposes. The first electricity based lamps used an arc discharge, struck between charcoal electrodes (in air). Based on the discoveries of V. Petrow and H. Dany (early 1800), engineers were able to develop commercial lamps around 1875; the lifetimes were in the 90–180 hours (electrodes were consumed during service) range and efficiency 2–7 lm/W (lumens).

The list of the main types of current lighting sources includes discharge (fluorescent lamps are a subclass here), incandescence (includes halogen lamps), and SSLSs.

5.2.9.3.1.2 Incandescent Lamps

The inventive genius of Edison provided an elegant, compact type of lamp at the beginning of the twentieth century. A thin W wire introduced in an electric circuit radiates, owing to the resistance it provides to electrons flow (Joule–Lenz effect). The W is a refractory metal that can be brought to high temperatures where its sublimation rate is quite modest even in vacuum. So it possible to use a vacuumized enclave made of glass to provide thermal insulation. While the λ of maximum emission intensity varies with the wire's temperature (Wien's law), the spectral range of the emission is wide, covering well the VIS (the UV fraction is, luckily, well absorbed by the conventional silicate glass used in low wattage bulbs; somewhat less well by the more refractory ones used in high wattage bulbs). As a result the CRI is high ~100. The correlated color temperature (CCT) is under 3000 K so that it is a warm light (a high CCT, around 6000 K, gives the feel of a cold light). Fabrication and exploitation costs are moderate and the technology relatively simple. Units adapted to the public power sources were developed and this type of lamp became fast ubiquitous all around the world. One of its disadvantages is a low efficiency ~15 lm/W and short lifetimes of around 1000 hours. A very smart solution to one major problem of this kind of lamp – W particles loss, during service at high temperatures – was found. The introduction of some halogen (Br or I) starts a cycle in which the W lost by the wire, and deposited on the glass envelope, is collected (reaction) by the halogen and redeposited on the filament (halogen is liberated). This allows one to raise work temperature and as a result the lifetime is increased five times and the efficiency by ~70% [M26].

5.2.9.3.1.3 Discharge Lamps

Most of them operate in conditions where arc type discharge is sustained, but glow-discharge based ones also exist. The physical processes occurring during discharge in gases are complex. Here a significantly simplified presentation suffices. In order to "strike" an arc, the voltage between an anode and cathode system has to be increased till a level able to cause the breakdown of a neutral gas (or mixture of gases) located within the electrodes. At breakdown the neutral gas molecules are ionized and, as a result, the inter-electrode insulating gap becomes conductive. The ionization creates a plasma (viz quasi-free electrons, separated from their source molecules which acquire charge, exist) in which the charged components move under the influence of the existent electric field and also collide. In the gap various species like cations, electrons and neutral molecules exist. The collisions of the fast electrons with the neutral molecules excite those, by energy transfer, to higher energy levels. Such states are unstable and the excited gas molecules relax to the ground state. There are certain relaxation paths available, the most important being photons emission. The energy of these photons is dictated by the electronic structure of the molecules. The interstate transitions being between quantic states have discrete and well-defined energies. The wavelengths of the emissions are gas specific, of course; for certain molecules they fall within the VIS domain. For instance, Na emits at a wavelength corresponding to yellow light, Ar is blue, He has a few lines (but their intensity ratios lead to perception of a resultant yellowish hue), Ne gives red, while the most intense visible line of Hg is blue (stronger lines are located in UV). In "cold" cathode lamps electron emission is caused by strong fields, while in "hot" ones the emission is thermally activated, so that such systems work under relatively low voltage; a popular "thermionic" cathode is made of Ba, Sr oxide deposited on a W substrate. Voltages of 1 to several kV are used in discharge lamps and the gas pressure varies in the 5–15 torr range (atmospheric pressure is not optimal for arc initiation).

Na lamps: One of the most important types of discharge lamp is those based on Na vapor. They are used mostly for outdoor illumination including airport runways. Low and high pressure varieties exist. This class is comprised of two groups, i.e. low pressure and high pressure lamps. In the former group (available from 1932; Philips) – also called solid oxides (SOX)

(from sodium) – the main ingredients are solid Na or sometimes Na–Hg amalgam and Ne–Ar gas mixture (starter mixture). In such items the starter gas pressure is much lower (~0.3 atm) than the atmospheric pressure in order to allow its breakdown under reasonable voltage levels. The materials are housed within a refractory (usually pure silica) glass tube. In the more simple variants quite long (usually U shaped) tubes are required to ensure enough light output. First the applied voltage is raised till an arc discharge is struck through the gas. Without getting into engineering details, we only note that the lamp can be connected to public AC current. It includes elements like the "ballast" solids, which are multifunctional ensuring both a starting voltage pulse and control of the current stability during operation. Without the ballast the negative resistivity gas arc would produce a runaway current. The plasma emission during this stage imparts a reddish hue to the light output. After heating of the enclave (as a result of the arc's striking), Hg^0, if present, vaporizes first and the fraction of its molecules that got excited by collisions with the complex plasma's components emits EMR, during relaxation. Strong emission lines at 185 and 254 nm are followed by one less intense located in the blue domain and a few faint longer λ lines. Appropriate design ensures that UV emissions are retained inside the envelope by the glass and are able to excite Na^0 atoms (this solid is also vaporized by the heat). Na has a very strong emission (D-line) at ~580 nm. This emission, in yellow, is the output of the lamps. The contribution, in the blue, from Hg makes the light more whitish. The Na D-line is located close to the $\lambda \sim 560$ nm to which the human eye is most sensitive. This kind of lamp is, in relative terms, very efficient providing ≥190 lm/W. The CRI is, of course, low at around 45; bulb lives of 15 000–18 000 hours are usual. The lamps are not expensive and the electrical control gear needed is not sophisticated. As opposed to the high pressure group, the presence of Hg is not strictly necessary. The low work temperature makes the use of glass envelopes (lately inside coated with In–Sn reflector layers) possible. The lamps are able to re-strike in case of a momentary power supply interruption. The burning position has to be within ±20° of the horizontal (except very low voltage units) to prevent Na accumulation at the lower end.

High pressure Na lamps: Such lamps, in order to increase light output, are loaded with more Na that, as vapor (over 240 °C), creates pressures of 2–3 atm. The operating voltage needed is higher, of course, than in the case of the low pressure lamp. The discharge gas is mostly Xe and Hg is always present. Luminous output of a typical lamp may exceed 38 000 lm (>300 W units) but efficiency is of only ~110 lm/W. Lifetimes that may reach 30 000 hours and a cost of US$0.003 lm^{-1} are among the attractive features of this kind of lamp. Owing, partly to the Hg emission contribution the CRI is high at ~90 and the light is warm (low CCT = 3100 K). The Na vapor in these lamps being more concentrated and at higher temperature than in the low pressure SOX is very aggressive chemically, so that, in time, the silica glass containers deteriorate. A more resistant container was provided by transparent ceramic alumina as detailed in Section 5.2.1; toward lamp life end Na is lost by reactions like $Na + Al_2O_3 \rightarrow Na_2O\uparrow + Al\uparrow$.

High pressure Hg and metal halide lamps: The Hg vapor based were developed before the Na lamps, around 1901; low and high pressure varieties are known. They work in a way similar to the Na lamps with the initial arc struck through Ar (warm period is thus characterized by a reddish glow). They are powered by AC (50–60 Hz) and either include an inductive ballast or are self-ballasted with a suitable resistor. Electrons are supplied with the thermionic approach. In conventional variants a bluish light is emitted by the Hg vapor (humans look green under such an illuminant), but Zn and Cd additions introduce additional emissions leading to a better CRI. The simple Hg lamps have a CRI around 20 but those with additives are able to surpass Na based high intensity discharges (HIDs). In HID form Hg lamps are available from 1936. The efficiency is moderate at 30–60 lm/W and the CCT is of 6800 K. Lamps of 40–1000 W are available. They are used outdoors or in high ceiling buildings. They do have outstanding service life of up to 25 000 hours (units in operation 40 years are known). Modern variants (developed during the 1960s) include various metal halides, for CRI improvement. The cations provided introduce emission lines that add to the blue of the Hg^0. Sc and other iodides or bromides are part of the fill of (up to 90) such lamps. The pumping electron source is a Xe based arc discharge (therefore such devices are sometimes called Xe lamp) and among the cations used one may cite Ta, In, Na, Dy, Ho, and Tm. These HIDs work at pressures in the 4–20 atm range. The discharge-arc tube is either silica glass or transparent alumina. The CCT may vary widely between 3 and 20 000 K – as a function of the gas mixture composition – and the efficiency is good 75–100 lm/W. These lamps are used for illumination of public spaces but also for auto headlamps; the most bright hand lamps are also using such light sources. Despite their high price this kind of lamp sells well currently having attractive service time 6–1500 hours.

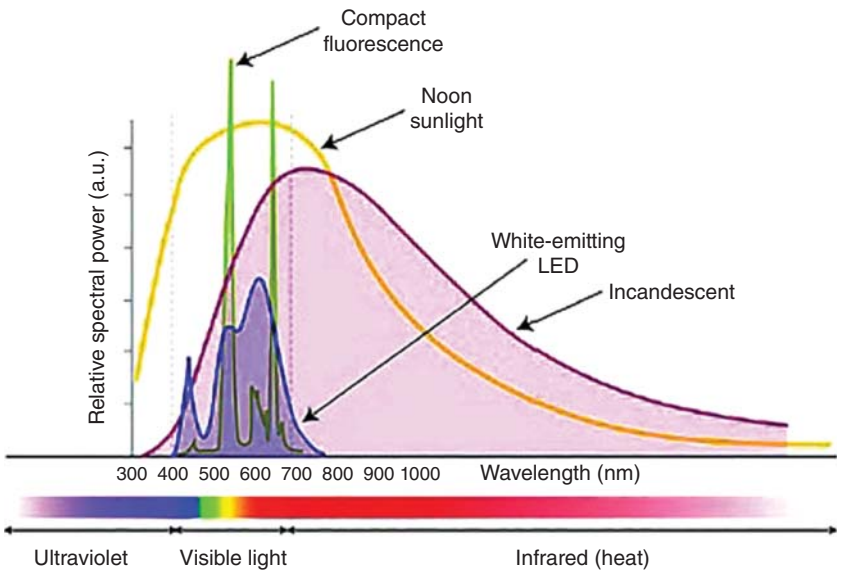

Figure 5.104 Spectral composition of light emitted by various illumination sources. Source: McKittrick and Shea-Rohwer 2014 [M26]. Reproduced with permission from John Wiley & Sons.

5.2.9.3.1.4 Fluorescent Lamps

Such lamps also use discharge but their final emission is not a result of excited molecules relaxation but the slower fluorescence of suitable solid salts. "Fluorescence," a term introduced by G. Stokes [S54], was derived from the name of the cubic mineral fluorite (CaF_2), which contains a variety of impurities like Ce, Sm, or Eu imparting to the host the ability to emit in the violet–blue or yellow. Becquerel observed that if one evacuates – by the aid of a Hg containing pump – a glass tube coated with fluorescent material the system glows. Interestingly Edison (1907) invented a lamp that used Ca_3WO_2 as fluorescent material and X-rays for excitation; it worked but was too complex (especially the excitation segment) for commercial use. Toward the end of the twentieth century, the components needed for a fluorescent lamp were in place. In fact the commercial fluorescent lamps are derivatives of Hg based discharge systems. In most cases Ne or Ne–Ar is the gas (~0.3 atm) through which the arc gas discharge is struck. The electrons are thermionically emitted by oxide coated W electrodes. The initial pulse voltage and arc-current limitation are ensured by the usual type of "ballast." The heating caused by the arc vaporizes Hg, which mixes in the plasma. The excited Hg^0 atoms emit in the UV most strongly; these emissions excite the fluorescence of adequate materials (Re^+ salts) deposited inside the glass tubes. In practice the fluorescent lamps were available as long straight tubes suitable for indoor illumination of small to quite large spaces (50 W lamps offer ~6000 lm). Later more compact, less strong (15 W → 950 lm) units – which can use sockets of the ubiquitous Edison lamp – also became available. The CRI of these sources is reasonable (can be optimized by using suitable RE^+ mixtures) being >80. The lifetime varies between 12 and 2.512 hours and the dollar efficiency is 0.6 and 3.5 klm^{-1} for the long and compact varieties respectively; the efficiency is around 110 lm/W for the linear and 65 lm/W for the compact units. In Figure 5.104 [B40, M26] the spectral distributions of some of the main types of lamp are compared, allowing one to form an idea of the CRI levels proper to each type.

5.2.9.3.1.5 Solid-State Lighting Sources

While the lighting systems discussed earlier possess many attractive features – as the commercial success of some demonstrates – certain disadvantages also exist, so that there is room in this market for the entrance of new types of light sources. Among the disadvantages of the various types of classic light sources, one may list the presence of noble gases, toxic substances like Hg, flammables like Na, high electricity consumption, bulkiness, low resistance to vibrations, and even short lifetimes and efficiency (the incandescent ones).

As indicated at the beginning of the section on SSLS, a new lighting mechanism – leading to entirely new format lamps – became available with the development of LEDs. This kind of device is a solid-state one requiring neither gas containing or vacuumized glass tubes or bulbs. LEDs based on both organic (organic light emitting diodes [OLEDs] or power LED [PLED] in case of polymers) and inorganic materials have been developed; the latter are of interest here. The inorganic material based p–n junctions most often used currently for lighting applications are based on InGaN alloy for UV, violet, blue, and green emission and an AlInGaP for red and amber; the efficiency at wavelengths in green or next segments, toward IR, is lower [S25].

The LEDs are narrow-band emitters of course. While LEDs, emitting in yellow or amber hues, were developed already in the late 1950s, varieties able to emit in the NUV and blue came about only during the 1990s [A17]. Technically the problems were in the field of high-quality GaN crystals growth and the control of p-doping in the case of high band gap semiconductors. Using the metalorganic vapor phase epitaxy (MOVPE), I. Akasaki was able to grow GaN on sapphire on which a polycrystalline 30 nm thick AlN coating could orient GaN growth. The AlGaN and InGaN needed to form heterojunctions were obtained in the early 1990s. For the development of the blue emitting diodes, a Nobel prize was awarded to Akasaki, Amano, and Nakamura in 2014.The advent of the blue emitting diodes permitted the development of performant, new SSLSs. As it was already mentioned and illustrated earlier (see Figure 5.94), two main approaches (with variants for each) are used. In the first one the emission of red, blue, and green LEDs is combined so that white light is obtained. These devices require complex optical parts for color mixing and are sensitive to temperature; their cost is high. In addition for physical reasons which cannot be corrected by improved engineering the longer λ LEDs exhibit lower efficiency than those working in blue or higher frequencies [S25]. Therefore another approach was considered. In it the blue LED excites the emission of phosphors – suitably located (see Figure 5.103) and able to emit in the green to red regions.

Combination of the signals generates white light. This approach is also among the best LED designs as far as electricity consumption is concerned. The LED-including phosphors (pc-LED), are among the most performant. For such systems lifetimes of 100 000 hours are predicted and their cost decreases quite rapidly. The fluorescent component of pc-LEDs can be obtained in two ways. A first option is to prepare fine fluorescent powders (submicron to nanometric particles) and to disperse them uniformly into a transparent polymeric host. The main disadvantages of this method are the low resistance to heat and moisture and the structural modifications that lead, in time, to the development of a yellow hue. The submicron particles (which are, as of now, present in most commercial pc-LEDs) also cause scattering and a fraction of this pumping radiation is wasted [M26]. A second option is to produce transparent ceramics, glass [L14], and glass-ceramic plates exhibiting the desired fluorescing properties. Such parts exhibit higher thermal conductivity, do not scatter, are refractory and do not change color in time as fast as the polymers. Such plates are a type of transparent ceramic and represent the topic of most interest for us here. Therefore, the science and engineering aspects of their development is addressed in the next Section 5.2.9.3.2.

5.2.9.3.2 Transparent Bulk Ceramics Based Phosphors for Light Sources Based on LEDs

Like in the polymer host/ceramic particulate phosphors, here the semiconductor layer's emission in the NUV-blue region is used also for the excitation of the bulk, transparent ceramic component's fluorescence in VIS regions (yellow to red) not covered by the semiconductor diode layer. The active (fluorescent) species are, as in the case of the gain media for solid-state layers, RE^+ or TM^+ type cations. Dopant packages including one or a few such dopants are used when the objective is to obtain white light. The most important spectral characteristics are the position, width, and intensity of the emission bands. Their convolution with the spectral characteristics of the blue LED determines the CRI, CCT, and efficiency of the lamp. The traditional fluorescent ions – used for the gas discharge fluorescent lamps – like Eu^{3+} ($4f^6$), Tb^{3+} ($4f^8$), or Mn^{2+} (d^5) are not optimal, certainly as unique dopants, for the pc-LED. The Mn^{2+} transitions are spin-forbidden and for Eu^{3+} the emission responsible transitions (most intense at 613 nm) are not very intense. A problem – causing phosphor quenching – is also the long decay time (>1 ms) of the relevant transitions. Such drawbacks may be circumvented by the use of ions like Ce^{3+} or Eu^{2+}. The former (f^7; half full configuration), as opposed to other RE^{3+} cations, has a $5d^1 \rightarrow 4f^1$ emission that is well placed (in the yellow region when the Ce^{3+} is hosted by suitable garnets [D15, D16]) and is also intense owing to its d → f character; the S,L splitting of the terminal level also contributes some breadth to the signals. In the case of Eu^{2+} also a convenient $4f^65d^1 \rightarrow 4f^7$ emission is available. Among other things these emissions are also characterized by short decay times (<100 ms for Ce^{3+} and <3 μs for Eu^{2+}) so that saturation based quenching is prevented [S25]. In many applications the phosphors for pc-LEDs need to operate at temperatures of 150–180 °C. As second dopants (for reinforcing emission in the red domain) cations like Eu^{2+} (590, 610 nm) Pr^{3+} (611 nm), Sm^{3+} (616 nm), Cr^{3+} (695 nm), and Mn^{2+} (593 nm) are used. As far as hosts are concerned, the most popular is the YAG. The host needs to be a transparent part but for some applications a translucent material causing a uniform controlled light diffusion is preferred. Transparent ceramic plate, Ce:YAG phosphors – as substitutes for polymer plates including dispersed ceramic phosphor powders – were introduced by Phillips [B23].

5.2.9.3.2.1 Ce^{3+}:YAG and Ce^{3+}, RE^{3+}:YAG Phosphors

Commercial white pc-LEDs using Ce^{3+}:YAG phosphors were among the first developed [P7, S16]. The emission profile of the whole LED is exemplified in Figure 5.105.

The semiconductor layer emission in the blue also excites (the phosphor adsorbs in the 440–460 nm) and then is convoluted with the broad fluorescence

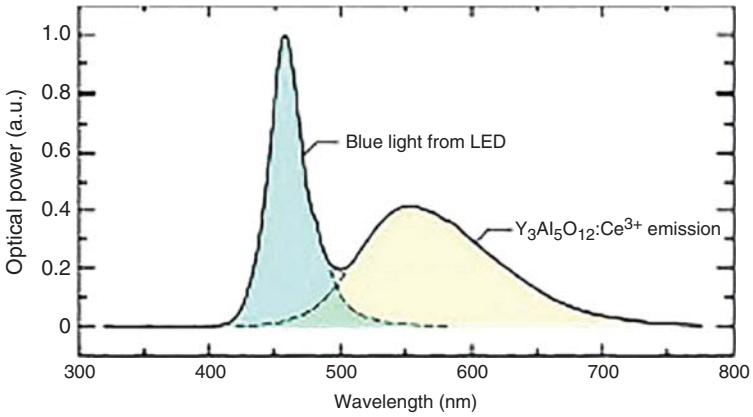

Figure 5.105 Emission spectrum of white light (cool = high CCT) providing SSLS in which the blue component is introduced by a LED and the yellow one by a Ce^{3+} YAG doped powder. Source: McKittrick and Shea-Rohwer 2014 [M26]. Reproduced with permission from John Wiley & Sons.

of Ce^{3+} (500–700 m; peak at ~560 nm). The profile in Figure 5.105 corresponds to a cool white (CCT = 5400 K) and the CRI is pretty low ~7.0. Such features are useful for illumination of outdoor spaces but not good enough for applications like illumination of offices, homes, schools, or hospitals; a positive characteristic is a quite high luminous efficiency of low power units (~1 W) at ~80 lm/W.

As it can be seen from Figure 5.105, the Ce^{3+} emission while broad becomes of low intensity over $\lambda = 600$ nm. The excitation spectrum for the yellow emission shows a weak band at 340 nm and a strong one at 460 nm; the Ce^{3+} is usually pumped at the strong band. The straightforward solution – to the wanting emission of Ce^{3+} in the orange, red – is to dope with additional activators emitting in that λ range. The activators need to be selected so as not to have too strong interference with the absorption and/or emission of Ce^{3+}. A popular option, despite some disadvantages, is Pr^{3+} [M8, M14, W11, Y7, Z6]. As opposed to Eu^{3+} (also a red emitter), the Pr^{3+} is not easily reduced to a lower oxidation state in oxygen lacking atmosphere. In Figure 5.106 the emission spectra of Ce,Pr doped YAG (excited at $\lambda = 450$ nm) is shown [J5] for different Pr^{3+} concentrations.

An optimum in Pr^{3+} concentration is suggested by the figure at 0.006 mol. In this case the sharp red emission of Pr^{3+} is seen while the emission of Ce^{3+} is not significantly reduced. The emission of Ce^{3+} is affected by the presence of Pr^{3+}, because the latter emits ($^3P_0$ $^1D_2 \rightarrow {}^3H_4$) after getting energy, by non-radiative transfer, from Ce^{3+} as shown in Figure 5.99; the strongest emission, from $^1D_2$, is located in YAG at $\lambda = 609$ nm. Another additional (to Ce^{3+}) activator usable is Mn^{2+}. Its excitation curve in YAG (Si^{4+} to compensate low charge of Mn^{2+} is included) shows three weak bands at 422 ($^6A_1 \rightarrow {}^4E(^4G)$), 466 (to $^4T_2(^4G)$) and 508 nm (to $^4T_1(^4G)$). According to Y. Shi et al. [S34] the signals are produced by the $^4T_1(^4G) \rightarrow {}^6A_1(^6G)$ transition of Mn^{2+} (weak, being spin forbidden). The different positions are attributed to the presence of Mn^{2+} in different lattice

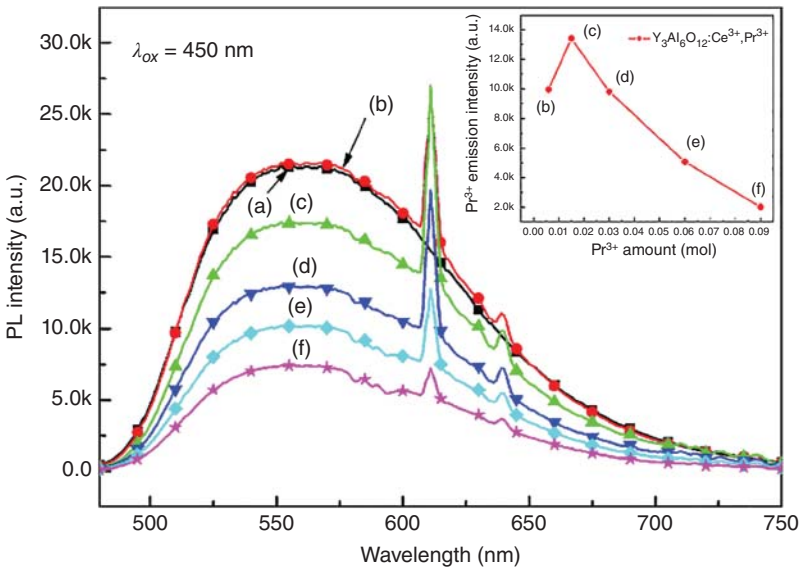

Figure 5.106 Emission spectrum of TC (YAG) type phosphor in which the Ce^{3+} doping is supplemented with Pr^{3+} for enhancing emission in the red domain. Source: Jang et al. 2007 [J5]. Reproduced with permission from Elsevier.

sites, namely, those occupied if replacing, respectively, Y^{3+} and Al^{3+} in both its octahedral and tetrahedral sites; the most intense ($\lambda = 466$ nm) signal is that related to Mn^{2+} in octahedral Al^{3+} sites. Doping with Mn^{2+} (in the presence of Si^{4+} compensators) YAG:Ce^{3+} leads to an overall emission color including more red allowing, thus, CCT reduction, i.e. facilitating the fab of pc-LEDs of warmer white. Mn^{4+} ($3d^3$) ions also have narrow emission in the red ($^2E \rightarrow {}^4A_2$), which can be excited through the $^4A_2 \rightarrow {}^4T_1$ and $^4A_2 \rightarrow {}^4T_2$ absorption bands [M26]. The hosts examined are mostly fluorides like K_2SiF_6 and K_2TiF_6. Another TM^+ ion usable for red zone emission strengthening is Cr^{3+} (d^5) [W11, Y15]. The Cr^{3+} located in YAG (by substituting Al^{3+} in octahedral sites) emits at 685, 695, and 705 nm. The excitation curve for the 685 nm emission includes strong bands at 230 (strongest, narrow), 450 (broad), and 630 nm (broad) and a very weak one at 275 nm. The transitions responsible for emission start from ^2E_g and arrive on the slightly split $^4A_{2g}$ ground state. In a Ce^{3+},Cr^{3+}:YAG plate, however, the excitation of Cr^{3+} is not direct, it implies energy transfer from Ce^{3+}. The authors, who studied Ce–Cr doping packages, showed that tuning of the emission color coordinates position can be achieved by using a system of two plates with one a Ce^{3+}:YAG material and the second a Ce^{3+}, Cr^{3+}:YAG. The color coordinates can be moved also by varying the thickness of the plates. The drawback is the reduction (not drastic) of the luminous efficiency (~75 lm/W) due to some reflection loss at the interface between the plates. In any case the CCT of such a multilayer system could be reduced to 4330 K (from 7080 K of a Ce^{3+}:YAG monolayer phosphor) while on $x = 0.33$, $y = 0.34$ excellent white color appeared. An interesting option – for compensation of Ce^{3+} emission weakness in the red – is to use triply doped materials like Ce^{3+},Pr^{3+},Cr^{3+}:YAG [W11]. According to [W11] Cr^{3+} alone cannot provide a satisfactory enhancement of the emission in the red and the triple doping is a must for high performance. While not true in a general sense – as the results of X. Yi show – this may be so for designs, which include one layer phosphors. The raising of Cr^{3+} concentration leads to an increase of emission in the deep red. The emission of the triply doped phosphors is stronger than that of one including only Ce and Cr – at a given Cr concentration; this is owed to the competition between the $Ce^{3+} \rightarrow Pr^{3+}$ and $Ce^{3+} \rightarrow Cr^{3+}$ energy transfer processes. The spectrum of a triply doped host is shown in Figure 5.107 [W11].

In practice however the triple doping has only a minor effect on the CRI. From a value of 80.4 – proper to an optimized doubly doped $(Y_{0.98}Ce_{0.02})_3(Al_{0.999}Cr_{0.001})_5O_{12}$ – the CRI raises to 81.4 for a $(Y_{0.978}Ce_{0.02}Pr_{0.002})_3(Al_{0.999}Cr_{0.001})_5O_{12}$ material. Eu^{3+} ($4f^6$) is also a cation emitting (not strongly) in the red (most intense peak at 613 nm); it may also be added in principle to Ce^{3+} (optimal excitation however is a problem). The structure and energy spacing of the set of electronic states produced by the Eu^{3+} ion – when accommodated in a ceramic host – depend of course on the host to a certain extent. Mostly the details are because this ion is, like any RE^+, not strongly influenced by the CF of its ligands. Considering the ground state $^7F_{0,1,2,3,4}$ the S,L produced levels are further split in 49 CF levels. The par between the ^7F_J and the next ^5D_J level is large approximately per 2000 cm^{-1}. For luminescence excitation, besides the bands corresponding to transitions between intraionic transitions, at least one charge transfer (from the 2p orbitals of the $O^{\delta-}$ toward the central ion) can be used. In YAG the excitation spectroscopy [T14] shows that the charge transfer band peaks at ~280 nm. A good f–f band is the $^7F_0$–$^5L_6$ located at ~395 nm. As it can be seen the most intense emission band is located at 613 nm ($^5D_0 \rightarrow {}^7F_2$). The decay times are of ~1.25 ms. The excitation spectrum shows that the excitation optimal for Ce^{3+} is not very efficient for Eu^{3+} but the use of NUV diodes optimizes fluorescence. In YAG the Eu^{3+} substitutes an Y^{3+} (C_S point symmetry). In Figure 5.108 [A20] the luminescence spectrum of Eu^{3+} is shown.

The other oxidation state of europium – which can be stabilized – in hosts relevant for the TC domain is Eu^{2+} ($4f^7$). This ion has on its external "f" orbitals half the number corresponding to total filling of the 4f sublevel, i.e. 14. As a result it is a high stability configuration, in principle. However, in hosts including ligands of low basicity, like YAG or Y_2O_3, the higher oxidation state $4f^6$ (Eu^{3+}) is more stable. So in practice only under highly reducing sintering conditions Eu^{2+} appears. The electronic levels scheme – of Eu^{2+} located in hosts relevant for the domain of TCs – is not very well determined [D16]. In any case it is clear that the ground state – resulting from the set of states generated by the $4f^7$ configuration – is of the $^8S_{7/2}$ format [B59]. It is also considered that the absorptions measured in the NUV VIS domain result from transitions to states derived (CF splitting) from a ^2D level generated by the excited $4f^65d^1$ configuration; the states resulting from ^2D seem to span a quite wide energy range. The excitations result from $f \rightarrow d$ transitions while the emissions start from states related to the $4f^65d^1$ configuration. The interest in Eu^{2+}, in the context of SSLs, comes from the mobility of its emission bands position, as a function of the characteristics of its ligands environment. It is possible thus to obtain, by varying the ceramic host, emission from blue to red [W15]. Because LEDs emitting in the NUV (where Eu^{2+} can be well excited; 380–420 nm) are available white (even warm white), light sources can be obtained by combining them with Eu^{2+} based phosphors [C27, G50, W15, Z23]. Two designs are possible. In that

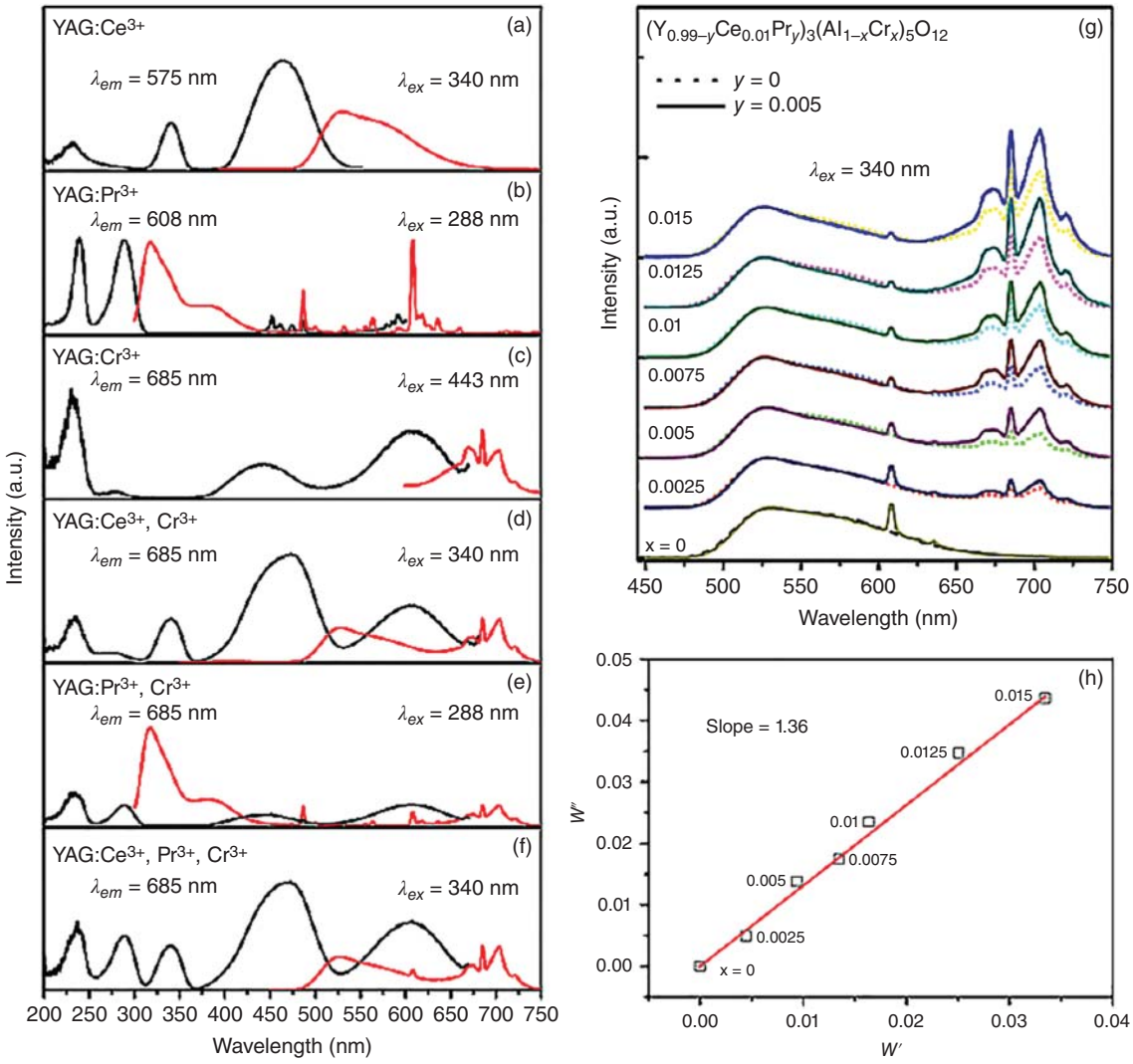

Figure 5.107 Emission (red line) and excitation (black line) spectra of transparent YAG plates triply doped with Ce^{3+}, Pr^{3+}, Cr^{3+}. a. to g. = emission spectra, h = lasing efficiency. g. comparison of emission spectra of Ce, Cr doped phosphor (y = 0; dashed lines) with Ce,Cr, Pr doped ones (y = 0.005; solid lines). Source: Wang et al. 2010 [W11]. Reproduced with permission from OSA, USA.

requiring a multilayer structure two different Eu^{2+} based phosphors (one emitting in blue and one in the yellow) are placed atop a NUV-LED. In another design a blend of Eu^{2+} in two suitable hosts is used or, alternatively, a host in which Eu^{2+} emits both on the blue and the yellow range is employed. It was shown for instance that in a host like $Sr_8(Mg,Zn)La(PO_4)_7$ both emissions are obtainable; their ratio can be varied so as to tune the CRI of the final light (white) output phosphors in which Eu^{2+} is combined with Mn^{2+} (red emission) have also been developed [G51, G52]. An elegant method for the obtainment of Eu^{2+}:YAG phosphors is that developed by Q. Zhu et al. [Z23]. In this method a sol-gel approach is used for powder synthesis. The specific approach used for Eu^{2+} stabilization is based on the effect of HI additions in the synthesis stage. The first reaction is

$$Eu_2O_3\ (\text{Eu source}) + 6HI = 2EuI_3 + 3H_2O$$

then

$$2EuI_3 = 2EuI_2 + I_2 \uparrow \tag{5.35}$$

A phosphor prepared in the absence of HI produces the photo luminescent emission (PLE) and photo luminescence (PL) curves specific to Eu^{3+}. In the case of that prepared in the presence of HI a wide emission (400–600 nm) generated by Eu^{2+} appears (NUV excitation). An interesting application is served by Eu^{2+} when inserted in certain nitridosilicates. Such materials can be used as down converters (b-LED base), in pc-LED, structures for the obtainment of amber hue SSLs [M43]. Amber light is used for vehicle turn lights

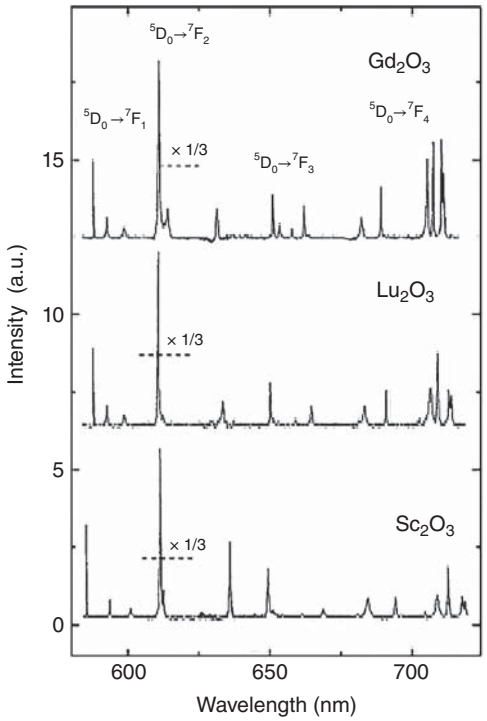

Figure 5.108 Emission spectra of Eu^{3+} in various transparent oxide ceramic hosts. Source: Antic-Fidancev 2003 [A20]. Reproduced with permission from IOP, UK.

and traffic signaling [S15]. The hosts relevant have either a $MSi_2O_2N_2$:Eu^{2+} (M = alkaline earth; 1-2-2-2 phosphors) or an $M_2Si_5N_8$:Eu^{2+} (2-5-8 phosphors) format. The latter emit quite strongly in red–orange, while the former in the green–yellow. The 2-5-8 phosphors, suitable for amber output, can be obtained as powder, which is then sintered (under N_2) to generate thin (~150 µm) translucent parts. Such phosphors exhibit high thermal and chemical (as opposed to sulfides) stability, 95% quantum efficiency, and low thermal quenching. These SSLs are more performant than their direct competitor AlGaInP based r-LEDs; these LEDs work efficiently at $\lambda > 620$ nm but not so in the 590–600 nm range of the amber tint ((Ga,I)M stops around $\lambda = 510$ nm). In the N containing hosts, both the excitation and emission bands are redshifted compared with oxide matrices. This is owed to the more covalent bonding in the former materials. This reduces the basicity of the ligands around Eu^{2+} and thus the strength of the CF; such a situation is known to cause bathochrome movements of the electronic transitions. The Eu^{2+} bands, in the 2-5-8 hosts, are also broader than those of Ce^{3+}:YAG.

5.2.9.3.2.2 Bathochrome Moving (Redshifting) of Ce^{3+} Emission by YAG Lattice Straining

Besides adding second fluorescing ions, to the Ce^{3+} doped host, it is possible to get improvements, of both CRI and CCT, also by suitably modifying the lattice of the host. Garnets and especially YAG are optimal for such exercises. Slight modifications, of the host lattice, can be achieved by replacing a fraction of the native cations by others which have a moderately different radius. Such a replacement leads to distortion of the lattice and, as a result, modification of the strength and symmetry of the CF acting upon the Ce^{3+} ions and other factors with influence on the emission characteristics like the Stokes effect. Ce^{3+} fluorescence is sensitive to the CF (unlike most other RE^+s) – owing to the fact that excitation, by irradiation at 460 nm, brings the ion from its $4f^1$ ground state to a $4f^0\ 5d^1$ state. Thus the starting level of the fluorescence is the that of a TM^+ cation – which, as opposed to RE^+ cations, have their external electrons exposed to interaction with those of the anions surrounding the central ion. Thus suitable host lattice distortions may cause redshift of the Ce^{3+} emission wavelength [J5, S25]. In this context one may cite the work of H.S. Jang et al. [J5] who examined the replacement of Y^{3+} with the larger cations Dy^{3+} and Tb^{3+}. The former dopant while able to move the λ_{em} of Ce^{3+} also significantly reduced its emission intensity. Better results were obtained with Tb^{3+}. A complete series of solid solutions (YAG-TAG) could be obtained. The value of "*a*" increases with [Tb^{3+}], from 12.012 Å (for $Y_{2.94}Al_5O_{12}$:$Ce^{3+}_{0.06}$) to 12.089 Å (for $Tb_{2.94}Al_5O_{12}$:$Ce^{3+}_{0.06}$). The spectra showed that the distance between $^2F_{5/2}$ and $^2F_{7/2}$ of Ce^{3+} is lowered from 0.19 eV in YAG to 0.07 eV in TAG; the emission band redshifted some 20 nm. This redshift is the result of changes in the characteristics of the coordination polyhedron of Y^{3+} – on substitution with Tb^{3+}. The color coordinates of a white pc-LED – in which the phosphor was of the $(Y_{0.2}Tb_{0.8})Al_5O_{12}$:$Ce^{3+}$ form – are $x = 0.322$ and $y = 0.326$; the efficiency is of 25 lm/W. While these results need further improvement, the study showed that the approach considered can affect the position of λ_{em} of Ce^{3+}. Y. Pan et al. showed that Y^{3+} substitution with Gd^{3+} also leads to a redshifting of the Ce^{3+} emissions [P7]. Substitution of Al^{3+} with Ga^{3+} or In^{3+} led to blue shifting.

The way the lattice modifications – induced by substitution of the native cations of garnet hosts – lead to the Ce^{3+} emission redshift are not always easy to explain. We will present here an example which succeeded in explaining the mechanism by which Y and Al substitution, in YAG (by Mg^{2+} and Si^{4+}) leads to the modification of luminescence. The analysis was presented, recently, by Z. Pan et al. [P8]. Before describing the matter, let us recall that Ce^{3+} in YAG is located in sites of D_2 symmetry (the polyhedron of the oxide ions ligands is a bis bisphenoid, with eight vertices, which may be imagined as resulting from a strong tetragonal compression of a cube, along one axis, followed by an additional slight rhombic distortion). So

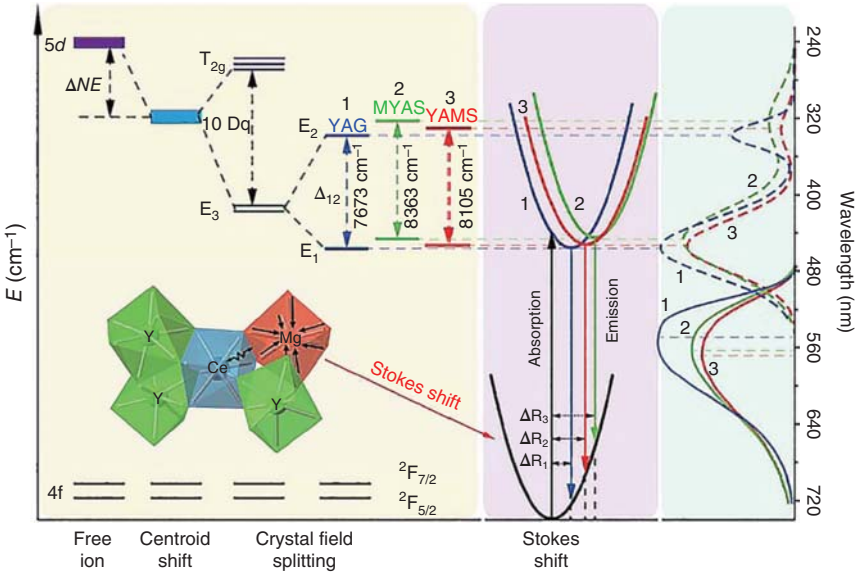

Figure 5.109 Schematic of the Ce^{3+} cation electronic levels energy as a function of the external fields considered (the corresponding spectra are also shown in the right part of the figure). Extreme left = free ion, next = considering the effect of covalency in the bond to ligands, next = considering the effect of ligands field of various symmetry (cubic, after tetragonal distortion for different doping situations), extreme right = Stokes shift effect included. Source: Pan et al. 2016 [P8]. Reproduced with permission from Royal Society of Chemistry (RSC), UK.

considering the LF, around Ce^{3+}, as of tetragonal symmetry [R27] is an approximation good enough for many spectral calculations. A schematic representation of the levels of a Ce^{3+}–$O^{\delta-}$ site, in YAG – and their relative positions on the energy axis – is given in Figure 5.109 [P8]. The Figure 5.109 also shows the effects of doping with Si and Mg the host. The aspect questionable in this scheme is the lack of representation of the substitutions effect on the covalency of the Ce–oxide bond. As it is seen a nephelauxetic effect is, in fact, considered and it moves the centroid, of the 5d derived levels set (**Δ***NE*). The covalency degree of the YAG and the substituted derivatives, however, is approximated as being the same. In case this is to gross an approximation, it means that the effects, of covalency variation, on 10 Dq were lost. However, the scheme, in Figure 5.109 allows, as it will be seen in the following, a satisfactory explanation of the observed emission redshift so that, it seems, the approximation used is reasonable.

Measurement shows that the two absorption (and fluorescence excitation) bands appearing as a result of transitions, from the ground state of Ce^{3+} complex, to the two E_g states, are located at 460 and 340 nm, respectively. In Figure 5.100 [P8] the ground state is represented by the two levels generated by a very slight split, caused by the tetragonal component of the LF, to the lowest level generated by the cubic component which splits the $^2F_{5/2}$ J level, produced by the spin-orbital interaction applied to the $4f^1$ ground state of Ce^{3+}. The two levels shown are very close (some 300 cm^{-1}) so that not four but only two resolved absorption bands need to be expected; so no contradiction between the scheme and the spectral measurements. Pan et al. prepared two phosphors by doping YAG with Si^{4+} and Mg^{2+}. A the first one, labeled MYAS is described by the formula $MgY_{2-x}Al_4SiO_{12}$:*x*Ce and the second labeled YAMS is described by $Y_{3-x}Al_3MgSiO_{12}$:*x*Ce. In both, Si^{4+} substitutes on Al tetrahedral sites. In the first Mg^{2+} is on Y^{3+} sites, while in the second it goes to Al octahedral sites. The structure of the MYAS lattice, as viewed along the [001] direction, is given in Figure 5.110.

Both types of substitution lead to a serious redshift of the fluorescence produced by exciting in the 460 nm band (λ_e moves from 542 nm in YAG to 570 in MYAS and 566 nm in YAMS). Now if one considers only the effect of the substitutions on the way the $^5d_1$ derived levels are split rather a slight blue shift of the emission is expected. To make the long story, short we note that by considering the integrated effect of substitution – on covalency, crystal field features and the Stokes effect when Y and Al, of YAG, are replaced with Mg and Si – the authors explained the Ce^{3+} emission redshift. Other authors examined the effect of gradually increasing the "*x*" of doped YAG where "*x*" is the atomic fraction of both Mg^{2+} and Si^{4+} doped to into the host (x = 0, 0.5, 1, and 2). Such YAG lattice substitutional modifications were shown as quite useful, for CCT and CRI simultaneous improvement while decent luminous efficiency. For instance, for x = 0.5 atm.% (Ce content = 0.5 atm.%) transparent ceramic layers (T% = 78 for $t \sim 1$ mm), luminous efficiency (LE) = 95 lm/W, CCT = 3760 K, and R14 = 90% were achieved. In Figure 5.111 the position, on the commission int. de l'èclairage (CIE) diagram, of the MYAS and YAMS phosphors, developed in [P7], is shown.

The CCT of such phosphors is around 4000 K.

As noted in the introductory part, to the section dealing with SSLSs, the phosphors can be also produced

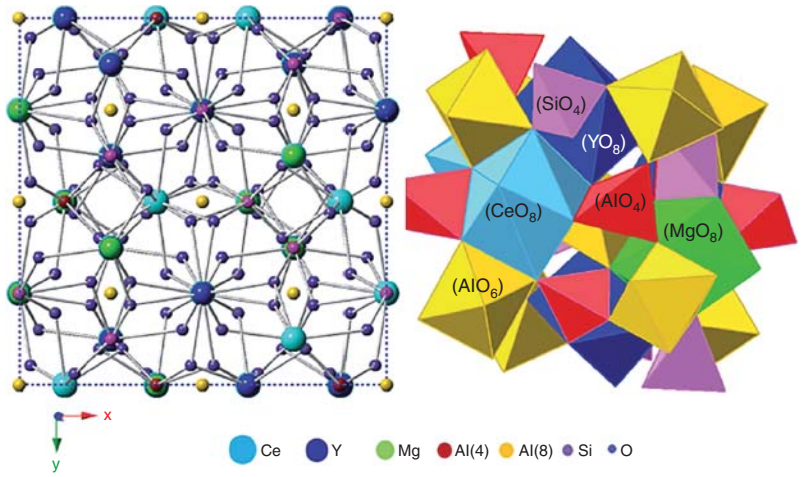

Figure 5.110 The view, along [001] direction, of a Si and Mg doped YAG lattice (Ce^{3+} doping). Source: Pan et al. 2016 [P8]. Reproduced with permission from Royal Society of Chemistry (RSC), UK.

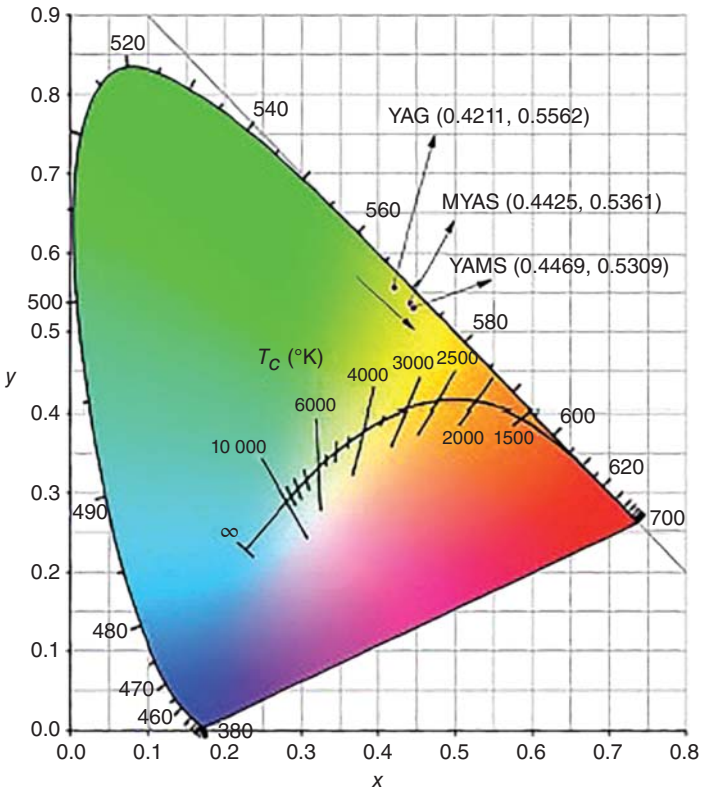

Figure 5.111 The position, on the CIE diagram, of Ce doped MYAS and YAMS type phosphors; the case of a YAG host is also given. Source: Pan et al. 2016 [P8]. Reproduced with permission from Royal Society of Chemistry (RSC), UK.

as powders that are dispersed in a transparent polymer. The transparent or translucent plates are polymer host based composites of a kind, which is not within the scope of this book. However, with the advent of well dispersed nano-phosphor powders interest – from the part of people dealing with TCs – may arise. Such powders can be dispersed within hosts like YAG or other more suitable hosts, without causing strong scattering. Of course issues like chemical inertness and effect on host sinterability need to be addressed. Such concerns may drastically reduce the length of a list with relevant powder phosphors, but in principle this is a track worth examination. Regarding powder phosphors a comprehensive review was published by J. McKittrick and L.E. Shea-Rohwer [M26]; also worth reading are papers produced by C.C. Lin and R.S. Liu and A. Setlur[L29, S25].

Transparent or translucent glass-ceramics are also a type of carrier usable for fluorescing activators; their combination can generate useful phosphors for pc-white light emitting LEDs (WLEDs). Like in the case of gain media, for lasers, the preference, for the crystalline phase,

in the glass-ceramic – of the RE^{+} or TM^{+} dopants – can be exploited here [T13, T14]. The available data is not sufficient to determine if this partition pattern occurs in all glass-ceramics, but it has been well documented for a number of fluoro-oxide glass (FOG) systems and also more simple oxide systems.

For phosphor applications the relevant dopants are those discussed for the case of all-ceramic hosts earlier. Among the first works in this context – which produced results with a perspective of practical use – one can mention that of S. Fujita et al. (2005 on) [F16, F17]. Translucent, yellow color, Ce^{3+} containing glass-ceramics were developed by those authors.

An interesting development was also reported by S. Nishiura and S. Tanabe [C23, C24, N10]. Ceramming a glass ($30SiO_2{\cdot}30Al_2O_3{\cdot}40CaO/0.1Eu_2O_3{\cdot}0.1Sm_2O_3$) melted under reducing conditions a glass-ceramic ($CoAl_2SiO_6$ and $Ca_2Al_2SiO_7$ crystals) including Eu^{3+} (in the glass phase) and Sm^{3+} in the crystalline phase resulted. The interesting aspect is that exciting at $\lambda = 378$ nm, the convolution of a high-frequency emission of Eu^{2+} and Sm^{3+} generates a reasonably white overall output despite the lack of Ce^{3+}. An alternative to ceramming way to produce glass-ceramics was proposed lately [Z20]. It is discussed here because the materials developed have application as phosphors. The authors describe the procedure as "co-sintering." Such a label is not suitable as the procedure description shows. A low melting temperature glass in powder form is mixed with a fine phosphor powder. The mixture is melted, the melt cooled to a suitable temperature annealing, and the specimen is further cooled to RT. An example of such a composition is $30TeO_2{\cdot}10ZnO{\cdot}30Sb_2O_5{\cdot}(5-x)Al_2O_3{\cdot}10B_2O_3{\cdot}15Na_2O{\cdot}xEu_2O_3$ ($x = 0$–1 mol%); the phosphor used was Ce:YAG (0–5%). The glass considered had also the advantage of a refraction index ($n = 1.79$) close to that of YAG ($n = 1.84$). The procedure is better described as melt immiscible powder multiphase system vitrification. The Eu^{2+} remains in the glass matrix and Ce^{3+} in the crystalline phase. By adjusting the Eu^{3+}/Ce^{3+} ratio, the color coordinates can be fine-tuned. The lack of interaction between the dopants and the low Δn difference ensures a high quantum efficiency (QE > 90%). The best light emission parameters combination obtained had been efficiency, LE of 139 lm/W, CCT = 4750 °C, and CRI = 66. While the CRI and CCT obtained require further (feasible) improvement, the QE and LE are quite good already. Borate and silicate glasses coupled with SiAlON or Ce:YAG were also examined [C23]. By dispersing more than one phosphor (e.g. Ce^{3+}:YAG + Ce^{3+}LuAG (green) + $Eu^{2+}CaAlSiN_3$ (red)) – into low melting silicate glass – phosphors leading to high quality pc-WLEDs (blue LED based) could be obtained (CRI = 85, CCT = 3923 K). A common problem to the materials prepared by melt vitrification is the relatively low chemical stability and softening temperature.

A robust transparent host (doping with Ce^{3+} or Eu^{3+}), namely, α-SiAlON, usable for WLED applications was developed lately [T5]; for the moment the free standing plates fabricated are thin, with a thickness of around 100 μm.

5.2.9.3.2.3 Summary of SSLSs

As it could be seen, a number of SSLS types in which ceramics participate have been or are in the development. It is hoped that SSLS – which have a high luminous efficiency – will be able to reduce by ~30 the amount of electricity used for lighting purposes. Currently the incandescent lamps (including halogen lamp) dominate the market of residential spaces, followed by fluorescent systems. The latter are dominant in illumination of commercial spaces, followed by HID units. The HIDs are more and more used also for outdoor applications. The SSLSs are expected to penetrate all this market segments in the not so distant future. For this to happen it is necessary to improve the CRI from the current 70–80 to the 80–85 domain, increase the luminous efficiency (current 65–75 lm/W) toward 150 lm/W and reduce the cost toward US$5–10 klm^{-1}; ability to provide a warm "light" is already good. These improvements are achievable and will occur in the next 5–10 years.

5.2.9.4 Scintillators

Scintillators are the main component of devices for medical diagnostics (e.g. positron emission based or X-ray CT scanning tomographs), radio dosimetry sensors, industrial parts and travelers' luggage inspection, gamma ray based systems (unfortunately highly relevant currently), high energy physics equipment (e.g. particle accelerators), etc.

A schematic presentation of an luggage inspection system is shown in Figure 5.112.

In a scintillator the high energy photons, emitted by the sources are converted into lower energy photons (3–6 eV), which produce electron positron pairs (electrons from the valence band are promoted into that of conduction). Instead of recombination, involving only the host's electronic levels, the decaying electrons are captured by suitable activator dopant's local electronic

Figure 5.112 Schematic of the setup of a luggage inspection device based on a scintillator type sensor. Source: Adapted from Barta 2012 [B13].

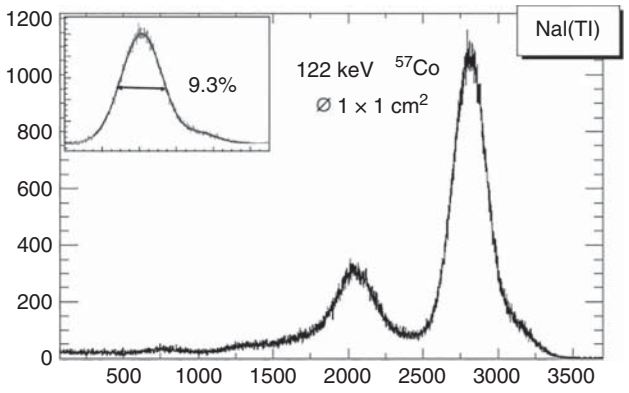

Figure 5.113 Schematic of the scintillation process. Source: Adapted from Barta 2012 [B13].

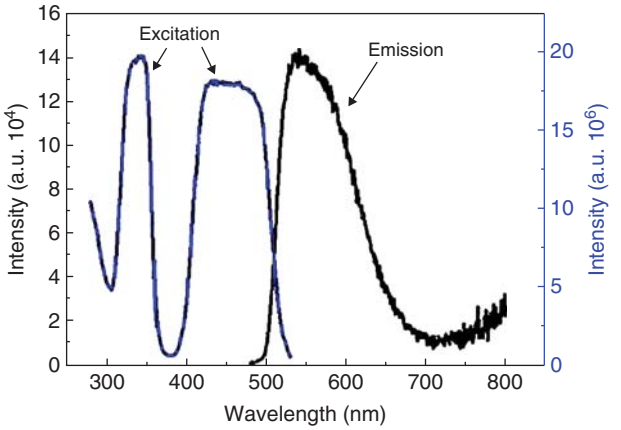

Figure 5.115 Excitation and emission spectra of Li, Ce doped YAG ceramic. Source: Chen et al. 2013 [C31]. Reprinted with permission from John Wiley & Sons.

levels, situated in the band gap. Therefore the final energy, emitted by the scintillator – usually having a convenient RE^+ as active dopant – falls somewhere in the VIS domain, as shown in Figure 5.113.

The luminescent output of the scintillator is converted into electric signal by a photomultiplier (PMT) or other type of sensors; the signals amplitude is proportional to the number of photons, emitted by the scintillator.

Efficient scintillators need to be ordered lattice based and to feature: energetic radiation stopping power (thus host has to include high Z elements, like, say, Gd), resistance to radiation damage and environmental attack, intense and fast fluorescence (low afterglow), and a sufficient EMR transmittance.

It was shown by Greskovich et al. [G44] and then by others that TCs can successfully compete with traditional single crystals (NaI:Tl, SrI_2:Eu, LaB_3:Ce^{3+}, $CdWO_4$:Tb^{3+}, etc.); regarding performance these are still the benchmark materials, in this application.

The first ceramic (TC based) scintillator ($Y_{1.34}Gd_{0.60}Eu_{0.06}O_3$:$Eu^{3+}$) had an X-ray absorption coefficient of 26 cm for 70 keV radiation and weak afterglow. Other TCs examined such as $Gd_3Ga_5O_{12}$:Cr,Ce; Li,Ce:YAG; Ce:LuAG (self-radiation problem); $Gd_2Hf_2O_7$:Ce^{3+}; Eu^{3+}:Lu_2O_3;Lu_3NbO_7 and even hexagonal ZnO (Li^+ or Ga^{3+}) have also been tested, with promising results [A14, C31, G41, P27]. For instance, an Li containing YAG ceramic (T, of 2 mm thick disc = 80%) could be vacuum sintered, at a temperature as low as 1700 °C, a poreless, clean grain boundaries condition; it seems that Li acts a sintering aid. The transmission, excitation, and emission spectra are shown in Figures 5.114 and 5.115

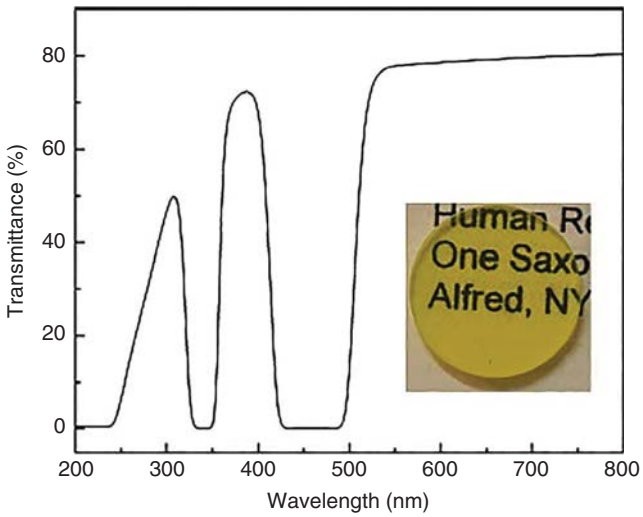

Figure 5.114 Imaging and transmission spectrum of Li doped Ce:YAG ceramic usable as scintillator. Source: Chen et al. 2013 [C31]. Reprinted with permission from John Wiley & Sons.

[C31]; the excitation and emission spectra are somewhat different from those exhibited by the same host when no Li is present in the lattice. It seems that the distortion, caused by Li^+ entrance into the lattice, distorts also the symmetry of the Stark field around the Ce^{3+} cations. Despite hygroscopicity and non-cubic lattice symmetry, Eu doped SrI_2 (one of the main materials used in single-crystal form) was shown to be promising also as hot-pressed ceramic [P32].

6

Future Developments

Whereas light transmitting orthodontic brackets (braces) are in millions of mouthes around the globe already, the establishment of large-scale production facilities and further reduction of production costs is for some other transparent ceramic (TC) components – in order to make such items more attractive commercially – the most urgent task at hand. The spinel-based armor window is the most prominent member of this group; the development of practically usable edge to edge joining procedures at reasonable costs would actively help in this context.

For the high-power laser gain media, the processing format for the fabrication of large size (30–80 cm) plates has to be perfected for challenging glass in nuclear fusion systems. Efficient sensitization schemes for Yb^{3+} may also contribute to the development of high-power lasers. Multilayer gain media with controlled dopant concentration gradients could mitigate problems posed by thermal lensing while transparent, low thermal expansion host materials such as $Al_{2-x}Sc_x(WO_4)$ can increase the thermal shock resistance. A significant leap forward in ceramic laser engineering would be provided by completion of the development of technologies allowing the use of non-cubic powders for TC fabrication, both by particle orientation and achievement of nanograins in the sintered parts.

In the domain of IR windows, introduction of more robust TCs for the 8–13 lm is desired. An issue relevant for the domain of doped TCs (with RE^+, TM^+ cations) is the insertion of large concentrations of dopant into the relevant – mostly oxide – hosts. According to Ikesue, straining of the YAG lattice by introduction of Si^{4+} cations makes insertion of large amounts up to 10 at% Nd^{3+} possible; the Si^{4+} tends to distort the lattice in a way opposite to that of Nd^{3+} thus compensating the effect of the latter. Yb^{3+}, which has a cationic radius similar to Y^{3+}, can also be introduced in substantial amounts in YAG. However, in most of the relevant hosts (be they based on spinel, garnet, bixbite , or fluorite type lattices) it is difficult to insert significant amounts of most of the TM^+ and RE^+ cations uniformly whereas high concentrations are needed for certain applications. Therefore, a better understanding and control of the factors that influence dopant dissolution into the TC hosts is required. Related to this issue is also the more general one of point defect formation and behavior.

Speculative point defect formation and interaction schemes are liberally used in the literature (including by the authors) to "explain" various processes occurring during fabrication, and many physical properties (including spectra profiles, dopant interaction, and photon beam attenuation) of the TCs. In fact, the correct identification of the type(s) of point defects present in a host under certain conditions is very difficult to achieve in most cases. Therefore, many of the explanatory conclusions derived by the aid of such schemes may have a heuristic value but must be treated with caution. Progress in the methodology usable for point defect identification would significantly raise the efficiency of attempts to establish the mechanism of various processes involved in TC engineering and functioning.

Transparent Ceramics: Materials, Engineering, and Applications, First Edition. Adrian Goldstein, Andreas Krell, and Zeev Burshtein.

7

Conclusions

This book, in most of its length, reviewed the experiments and results of the first 60 years of work on transparent ceramics related issues. The data accumulated shows that by the integrated work of engineers, physicists, experts in materials science and other enthusiasts, the initial one-member family of light-transmitting ceramics (represented by LUCALOX translucent alumina) has grown to a large, complex and dynamic one.

The potential and actual applications list spans the gamut from gemstones artificial replicas, to solid-state light sources, long-range laser weapons, scintillators, or non-spark internal combustion engines igniters.

We learned a lot on how to fully densify ceramics, the mechanisms of EMR attenuation in ceramics, and about ways to minimize it. Exotic techniques – like polycrystalline to single-crystal conversion, full ceramming of glass, gigapascal hot-pressing, magnetical orientation of particles in suspension, bulk CVD and sol-gel – were implemented or are under study for transparent ceramic (TC) fabrication. Non-cubic ceramic materials, like the apatites, were processed to a high transparency state, and transparent ceramics were shown as being able to lase, when properly doped. Transparent ceramic spinel windows of meter size have been demonstrated and even ferroelectric (piezoelectric) TCs were developed.

Total glass crystallization to nano-grained ceramics, usable as scintillators ($SrREGa_3O_7$), was achieved.

In certain applications TC based components became serious competitors for the other transparent solids, viz. single crystals, inorganic glasses, or transparent organic polymers (ordered, disordered, or hybrid lattice). Regarding this point, however, a lot remains yet to be done. Development of new, more cost-effective fabrication technologies – able to ensure the size, shape and parts amount users demand – is, arguably, the most important near-future challenge confronting the TC community.

Further tasks of the future are the development of more robust materials for the 8–13 μm IR window, higher power gain media, a more comprehensive understanding of the factor controlling $TM^+(RE^+)$ cations accommodation by the TC lattices, and of the formation and interactions among point defects.

The past of the TCs is impressive; the future looks bright.

Transparent Ceramics: Materials, Engineering, and Applications, First Edition. Adrian Goldstein, Andreas Krell, and Zeev Burshtein.

References

A

A1 Abalea, P. (2013). Yb doped CaF_2 ceramics: synthesis and sintering process optimization. *Comm. to ECerS XIII Conference*, Limoges, France (June 2013) (Transparent materials section).

A2 Akchurin, M.S., Basiev, T.T., Demidenko, A.A. et al. (2013). CaF_2:Yb ceramics. *Opt. Mater.* **35**: 444–450.

A3 Ahamad, M.N., Vasudevarao, A., Gopalan, V. et al. (2009). Temperature dependent blue second harmonic generation in $Ba_5Li_2Ti_2Nb_8O_{30}$ microcrystals embedded in TeO_2 glass-matrix. *J. Non-Cryst. Solids* **355**: 1517–1520.

A4 Akyama, J., Sato, Y., and Taira, T. (2011). Laser demonstration of diode-pumped Nd^{3+}-doped FAP anisotropic ceramics. *Appl. Phys. Express* **4**: 022703/1–3.

A5 Aldinger, B.S. (2016). Predicting the light transmittance of multilayer transparent armor. In: *Advances in Ceramic Armor XI* (eds. J.C. LaSalvia, J. Wang and S. Kirihara), 29–39. Hoboken, NJ: Wiley.

A6 Aleksandrov, V.I., Osiko, V.V., Prokhorov, A.M., and Tatarinzev, V.M. (1973). New manufacturing method of refractory single crystals and molten ceramic materials. *Vest. AN SSSR* **12**: 29–36.

A7 Alexander, B.H. and Balluffi, R.W. (1957). The mechanism of sintering of copper. *Acta Metall.* **5**: 666–677.

A8 Alexandrovski, A., Fejer, M., Markosyan, A., and Route, R. (2010). Photo thermal common-path interferometry: new developments. *Proceedings of SPIE 7193*, D 1–13.

A9 Allix, M., Fayou, F., Veron, E. et al. (2015). New transparent polycrystalline ceramics elaborated by full crystallization from glass. *Comm. at Journee technique ceramiques transparente*, Paris (20 Janvier 2015).

A10 Anderson, R.C. (1970). Transparent yttria ceramics and patent for producing the same. US Patent 3, 545, 987 A, December 1970.

A11 Andreev, N.S. (1978). Scattering of visible light by glasses undergoing phase separation and homogenization. *J. Non-Cryst. Solids* **30**: 99–126.

A12 An, L., Ito, A., and Goto, T. (2012). Effect of sintering temperature on transparency and mechanical properties of LuAG fabricated by spark plasma sintering. *J. Eur. Ceram. Soc.* **32**: 3097–3102.

A13 An, L., Ito, A., and Goto, T. (2011). Effects of sintering and annealing temperature on fabrication of transparent $Lu_2Ti_2O_7$ by SPS. *J. Am. Ceram. Soc.* **94**: 3851–3855.

A14 An, L., Ito, A., and Goto, T. (2013). Transparent Lu_3NbO_7 bodies prepared by reactive SPS and their optical and mechanical properties. *Ceram. Int.* **39**: 383–387.

A15 An, L., Ito, A., Zhang, J. et al. (2014). Highly transparent Nd^{3+}:Lu_2O_3 produced by spark-plasma sintering and its laser oscillation. *Opt. Mater. Express* **4**: 1420–1426.

A16 Anonymus (Corning Glass Works) (1961). Faabrication of glass-ceramics. Brit. Patent GB869,328, 1961.

A17 Anonymus (2014). Efficient blue light-emitting diodes leading to bright and energy saving white light sources. https://www.nobelprize.org/nobel_prizes/physics/laureates/2014/advanced-physicsprize2014.pdf (accessed November 13 2018).

A18 Anonymus (1966). GE has transparent ceramics. *Chem. Eng. News* **44**: 38.

A19 Anonymus (2009). Joint high power solid-state laser (JHPSSL) program. http://www.as.northropgrunmman.com/products/join/thi/power/index.html (accessed November 13 2018).

A20 Anselmi-Tamburini, U., Woolman, J.N., and Munir, Z.A. (2007). Transparent nanometric cubic and tetragonal zirconia obtained by high-pressure pulsed electric current sintering. *Adv. Funct. Mater.* **17**: 3267–3273.

A21 Antic-Fidancev, E., Holsa, J., and Lastussari, M. (2003). Crystal field energy levels of Eu^{3+} and Yb^{3+} in C_2 and S_6 sites of the cubic C-type R_2O_3. *J. Phys. Condens. Matter* **15**: 863–876.

A22 Antipov, O.L., Novikov, A.A., Zakharov, N.G., and Zinoviev, A.P. (2012). Optical properties and efficient laser oscillation at 2066nm of novel Tm:Lu_2O_3 ceramics. *Opt. Mater. Express* **2**: 183–189.

Transparent Ceramics: Materials, Engineering, and Applications, First Edition. Adrian Goldstein, Andreas Krell, and Zeev Burshtein.

A23 Apetz, R. and van Bruggen, M.P.B. (2003). Transparent alumina: a light-scattering model. *J. Am. Ceram. Soc.* **86**: 480–486.

A24 Appleby, D., Porter, S.G., and Ainger, F.W. (1976). The pyroelectric properties of FE/FE phase transitions in lead zirconate ferric niobate and related compounds. *Ferroelectrics* **14**: 715–717.

A25 Apte, P., Burke, H., and Pickup, H. (1992). Synthesis of yttrium aluminum garnet by reverse strike precipitation. *J. Mater. Res.* **7**: 706–711.

A26 Aschauer, U. and Bowen, P. (2010). Theoretical assessment of Nd:YAG ceramic laser performance by microstructural and optical modeling. *J. Am. Ceram. Soc.* **93**: 814–820.

A27 Aschauer, U., Bowen, P., and Parker, S.C. (2006). Atomistic modeling study of surface segregation in Nd:YAG. *J. Am. Ceram. Soc.* **89**: 3812–3816.

A28 Ashikaga, T., Kim, B.-N., Kiyono, H., and Suzuki, T.S. (2018). Effect of crystallographic orientation on transparency of alumina prepared using magnetic alignement and SPS. *J. Eur. Ceram. Soc.* **38**: 2735–2741.

A29 Asuach, H. (2003). The influence of sintering additives on the microstructure and properties of AlON. MSc thesis. Technion, Haifa.

A30 Atlas, L.M. (1957). Effect of some lithium compounds on sintering of MgO. *J. Am. Ceram. Soc.* **40**: 196–199.

A31 Aubry, P., Bensalah, A., Gredin, P. et al. (2009). Synthesis and optical characterization of Yb-doped CaF_2 ceramics. *Opt. Mater.* **31**: 750–753.

A32 Azis, R.S., Hollande, D., Smith, M.E., and Howes, A. (2013). DTA/TG, XRD and ^{27}Al MAS NMR of YAG by sol–gel synthesis. *J. Aus. Ceram. Soc.* **49**: 74–80.

B

B1 Babin, V., Laguta, V.V., Maaroos, A. et al. (2011). Luminiscence of F^+-type centers in undoped LuAG. *Phys. Status Solidi B* **248**: 239–242.

B2 Backman, M.E. and Goldsmith, W. (1978). The mechanics of penetration of projectiles into targets. *Int. J. Eng. Sci.* **16**: 1–99.

B3 Bacorisen, B.P., Smith, R., Uberuaga, B.P. et al. (2006). Atomistic simulations of radiation induced defect formation in spinels. *Phys. Rev. B* **74**: https://doi.org/10.1103/physrevb.74.214105.

B4 Badillo, F., Eiras, J.A., Milton, F.P., and Garcia, D. (2012). Preparation and microstructural, Structural, Optical and electro-optical properties of La doped PMN-PT transparent ceramics. *Opt. Photon. J.* **2**: 157–162.

B5 Badwal, S.P.S. and Ciacchi, F.T. (2000). Oxygen-ion conducting electrolyte materials for SOFCs. *Ionics* **6**: 1–21.

B6 Bagayev, S.N., Osipov, V.V., Solomonv, V.I. et al. (2012). Fabrication of Nd^{3+}:YAG laser ceramics with various approaches. *Opt. Mater.* **34**: 1482–1487.

B7 Balabanov, S.S., Bykov, Y.V., Egorov, S.V. et al. (2013). Transparent Yb:$(YLa)_2O_3$ ceramics produced by self-propagating high-temperature synthesis and MW sintering. *Opt. Mater.* **35**: 727–730.

B8 Ballhausen, C.J. (1962). *Introduction to Ligand-Field Theory*. New York: McGraw-Hill.

B9 Ballhausen, C.J. and Gray, H.S. (1965). *Molecular Orbital Theory*. New York: W.A. Benjamin Inc.

B10 Bamford, C.R. (1977). *Colour Generation and Control in Glass*. Amsterdam: Elsevier.

B11 Banerjee, M. and Budworth, D.W. (1972). Preparation of transparent magnesia bodies II: sintering. *Br. Ceram. Trans. J.* **71**: 51–53.

B12 Barizon, K.T.L. (2011). Relative translucency of ceramic systems for porcelain veneers. MS thesis. University of Iowa.

B13 Barta, M.B. (2012). Nanocomposite glass-ceramic scintillators for radiation spectroscopy. MSc dissertation. Georgia Inst. Tech.

B14 Basiev, T.T., Doroshenko, M.E., Fedorov, P.P. et al. (2008). Efficient laser based on CaF_2-SrF_2-YbF_3 nanoceramics. *Opt. Lett.* **33**: 521–523.

B15 Basiev, T.T., Doroshenko, M.E., Konyuskhin, V.A. et al. (2007). Lasing in diode-pumped fluoride $F2^-$:LiF_2 colour center ceramics. *Quantum Electron.* **37**: 989–990.

B16 Basiev, T.T., Doroshenko, M.E., Konyushkin, V.A. et al. (2010). SrF_2:Nd^{3+} laser fluoride ceramics. *Opt. Lett.* **35**: 4009–4011.

B17 Basiev, T.T., Konyushkin, V.A., Konyushkin, D.V. et al. (2011). First ceramic laser in the visible range. *Opt. Mater. Epress* **1**: 1511–1514.

B18 Bassim, N.D., De Gregorio, B.T., Kilcoyne, A.L.D. et al. (2012). Minimizing damage during FIB sample preparation of soft materials. *J. Microsc.* **245**: 288–301.

B19 Bates, T. (1962). Ligand field theory and absorption spectra of transition-metal ions in glasses. In: *Modern Aspects of the Vitreous State*, vol. 2 (ed. J.D. Mackenzie), 195. London: Butterworths.

B20 Bayya, S., Villalobos, G.R., Sanghera, J.S. et al. (2013). Development of transparent polycrystalline beta-silicon carbide. *Proceedings of SPIE 8837*, 3-1-7.

B21 Beall, G.H. and Duke, D.A. (1969). Transparent glass ceramics. *J. Mater. Sci.* **4**: 340–352.

B22 Beall, G.H., Karstetter, B.R., and Rittler, H.L. (1967). Crystallization and chemical strengthening of stuffed beta-quartz glass-ceramics. *J. Am. Ceram. Soc.* **50**: 181–190.

B23 Beall, G.H. and Pinckney, L.R. (1999). Nanophase glass-ceramics. *J. Am. Ceram. Soc.* **82**: 5–16.

B24 Bechtel, H., Schmidt, P., Busselt, W., and Schreinemacher, B.S. (2008). Lumiramic: a new phosphor technology for high performance solid state light sources. *Proceedings of SPIE 7058*, pp. 45–59.

B25 Beggiora, M., Reaney, I.M., and Islam, M.S. (2004). Structure of nanocrystals in oxyfluoride glass ceramics. *Phys. Chem. Glasses* **45**: 83–84.

B26 Behera, S.K., Barapanda, P., Pratihar, S.K., and Bhattacharyya, S. (2004). Synthesis of magnesium–aluminium spinel from autoignition of citrate–nitrate gel. *Mater. Lett.* **58**: 1451–1455.

B27 Beil, K., Fredrich-Thornton, S.T., Tellkamp, F. et al. (2010). Thermal and laser properties of Yb:LuAG for kW thin disc lasers. *Opt. Express* **18**: 20712–20722.

B28 Benecke, M.W., Olson, N.E., and Pask, J.A. (1967). Effect of LiF on hot-pressing of MgO. *J. Am. Ceram. Soc.* **50**: 365–368.

B29 Berard, M.F. and Wilder, D.R. (1969). Cation self-diffusion in polycrystalline Y_2O_3 and Er_2O_3. *J. Am. Ceram. Soc.* **52**: 85–88.

B30 Bernard-Granger, G., Benameur, N., Guizard, C., and Nygren, M. (2009). Influence of graphite contamination on the optical properties of transparent spinel obtained by spark-plasma sintering. *Scr. Mater.* **60**: 164–167.

B31 Bernard-Granger, G., Guizard, C., and Monchalin, N. (2011). Sintering of an ultrapure alpha- alumina powder: II. Mechanical, thermomechanical, optical properties, and missile dome design. *Int. J. Appl. Ceram. Technol.* **8**: 366–382.

B32 Berthier, T., Fokin, V.M., and Zanoto, E.D. (2008). New large-grain, highly crystalline, transparent glass-ceramics. *J. Non-Cryst. Solids* **354**: 1721–1730.

B33 Bethe, H. (1929). Termaufspaltung in Kristallen. *Ann. Phys.* **395**: 133–208.

B34 Bickmore, C.R., Waldner, K.F., Treadwell, D.R., and Laine, R.M. (1996). Ultrafine spinel powders by flame spray pyrolysis of a double magnesium aluminium alkoxide. *J. Am. Ceram. Soc.* **79**: 1419–1423.

B35 Bingham, R. (2006). Basic concepts in plasma accelerators. *Philos. Trans. R. Soc. A* **364**: 559–575.

B36 Bogomolova, G.A., Vylezhanin, D.N., and Kaminskii, A.A. (1975). Spectral and lasing investigations of garnets with Yb^{3+} ions. *Sov. Phys. JETP* **42**: 440–446.

B37 Bohren, C.F. and Huffman, D.R. (1983). *Absorption and Scattering of Light by Small Particles*. New York: Wiley.

B38 Borelli, N.F. (1967). Electro-optic effect in transparent niobate glass-ceramic systems. *J. Appl. Phys.* **38**: 4243–4247.

B39 Borelli, N.F. and Layton, M.M. (1971). Dielectric and optical properties of transparent ferroelectric glass-ceramic systems. *J. Non-Cryst. Solids* **6**: 197–212.

B40 Bosschaert, T. (2011). How to choose the best lamp for your purpose. In: *LED and Artificial Light Guide*. http://www.except.nl/en/articles/92-led-artificial-light-guide.

B41 Boulesteix, R., Epherre, R., Noyau, S. et al. (2014). Highly transparent Nd:Lu_2O_3 ceramics obtained by coupling slip-casting and spark plasma sintering. *Scr. Mater.* **75**: 54–57.

B42 Boulesteix, R., Maitre, A., Baumard, J.-F. et al. (2010). Light scattering by pores in transparent Nd:YAG ceramics for lasers: correlations between microstructure and optical properties. *Opt. Express* **18**: 14992–15002.

B43 Boulesteix, R., Maitre, A., Baumard, J.-F. et al. (2009). Mechanism of the liquid-phase sintering for Nd:YAG ceramics. *Opt. Mater.* **31**: 711–715.

B44 Boulesteix, R., Maitre, A., Baumard, J.-F. et al. (2009). The effect of silica doping on neodymium diffusion in YAG ceramics: implications for sintering mechanisms. *J. Eur. Ceram. Soc.* **29**: 2517–2526.

B45 Boulesteix, R., Maitre, A., Chretien, L. et al. (2013). Microstructural evolution during vacuum sintering of YAG transparent ceramics: toward the origin of residual porosity affecting the transparency. *J. Am. Ceram. Soc.* **96**: 1724–1731.

B46 Boulesteix, R., Matre, A., and Lemanski, K. (2017). Structural and spectroscopic properties of Nd^{3+} transparent ceramics fabricated by using two-step SPS. *J. Alloys Compd.* **722**: 358–364.

B47 Boulon, G., Alombert-Goget, G., Guyot, Y. et al. (2014). Conjugation of TEM-EDX and optical spectroscopy tools for the localization of Yb^{3+}, Er^{3+} and Co^{2+} dopants in laser glass-ceramics composed of $MgAl_2O_4$ spinel nanocrystals embedded in SiO_2 glass. *J. Mater. Chem. C* **2**: 9385–9387.

B48 Boulon, G., Guyot, Y., Guzik, M. et al. (2014). Yb^{3+} ions distribution in YAG nanoceramics analyzed by both optical and TEM-EDX techniques. *J. Phys. Chem. C* **118**: 15474–15486.

B49 Boulon, G., Zhao, W., Anghel, S. et al. (2010). Segregation phenomenon of rare-earth dopants in ceramics. *Proceedings ILCS-6*, Munster, Germany Comm. no. 4, pp. 1–48.

B50 Bourdet, G.L., Casagrande, O., Robin, N.D., and Garrec, B.L. (2008). Performances of cryogenic cooled laser based on Yb doped sesquioxide ceramics. *J. Phys. Conf. Ser.* **112**: 032054/1–4.

B51 Boyer, M., Carrio, J.F., Ory, S. et al. (2016). Transparent polycrystalline $SrREGa_3O_7$ melilite ceramics: potential phosphors for tunable solid state lighting. *J. Mater. Chem. C* **4**: 3238–3246.

B52 Brasse, G., Restoin, C., Auguste, J.-L. et al. (2009). Nanoscaled optical fiber obtained by the sol–gel processin the SiO_2-ZrO_2 system doped with rare-earth cations. *Opt. Mater.* **31**: 765–768.

B53 Bratton, R.J. (1969). Coprecipitation yielding spinel powders. *Am. Ceram. Soc. Bull.* **48**: 759–762.

B54 Bratton, R.J. (1974). Translucent sintered $MgAl_2O_4$. *J. Am. Ceram. Soc.* **57**: 283–286.

B55 Bravo, A.C., Longuet, L., Autissier, D. et al. (2009). Influence of the powder preparation on the sintering of Yb-doped Sc_2O_3 transparent ceramics. *Opt. Mater.* **31**: 734–739.

B56 Brenier, A. and Boulon, G. (2001). Overview of the best Yb^{3+}-doped laser crystals. *J. Alloys Compd.* **323–324**: 210–213.

B57 Brinker, C.J. and Scherer, G.W. (1990). *Sol–Gel Science. The Physics and Chemistry of Sol–Gel Processing*. Boston, MA: Academic Press.

B58 Brissette, L.A., Burnett, P.L., Spriggs, R.M., and Vasilos, T. (1966). Thermomechanically deformed Y_2O_3. *J. Am. Ceram. Soc.* **49**: 165–166.

B59 Brito, H.F., Felinto, M.C., Holsa, J. et al. (2012). DFT and synchrotron radiation study of Eu^{2+} doped $BaAl_2O_4$. *Opt. Mater. Express* **2**: 420–431.

B60 Brook, R.J. (1969). Pore-grain boundary interactions and grain growth. *J. Am. Ceram. Soc.* **52**: 56–57.

B61 Brown, D.C., Bruno, T.M., and Singley, J.M. (2010). Heat-fraction-limited CW Yb:YAG cryogenic solid-state laser with 100% photon slope efficiency. *Opt. Express* **18**: 16573–16579.

B62 Brown, L.M. and Mazdiyasni, K.S. (1972). Cold-pressing and low-temperature sintering of alkoxy-derived PLZT. *J. Am. Ceram. Soc.* **55**: 541–544.

B63 Bruch, C.A. (1970). Transparent magnesia-alumina spinel and method. US Patent 3, 516, 839, 23 June 1970.

B64 Bruley, J., Cho, J., Chan, H.M. et al. (1999). STEM analysis of grain-boundaries in creep-resistant Y and La doped alumina microstructures. *J. Am. Ceram. Soc.* **82**: 2865–2870.

B65 Budd, M.I. and Darrant, J.G. (1995). Glass-ceramic armour. GB Patent 2 284 655 A, 14 Jun 1995.

B66 Buerger, M.J. (1954). The stuffed derivatives of the silica structures. *Am. Mineral.* **39**: 600–614.

B67 Burke, J.E. (1996). Lucalox alumina: the ceramic that revolutionized outdoor lighting. *MRS Bull.* **21**: 61–68.

B68 Burke, J.E. (1957). Role of grain boundaries in sintering. *J. Am. Ceram. Soc.* **40**: 80–85.

B69 Burnett, J.H., Kaplan, S.G., Shirley, E.L. et al. (2005). High-index materials for 193 micron immersion lithography. *Proceedings of SPIE 5754*, pp. 611–621.

B70 Burshtein, Z., Blau, P., Kalisky, Y. et al. (1998). Excited-state absorption of Cr^{4+} ions in several garnet host crystals. *IEEE J. Quantum Electron.* **34**: 292–299.

B71 Burshtein, Z. (2010). Radiative, nonradiative, and mixed-decay transitions of rare-earth ions in dielectric media. *Opt. Eng.* **49**: 091005, 1–19.

B72 Busker, G., Chroneos, A., Grimes, R.W., and Chen, I.-W. (1999). Solution mechanisms for dopant oxides in yttria. *J. Am. Ceram. Soc.* **82**: 1553–1559.

C

C1 Cahn, J.W. (1965). Phase separation by spinodal decomposition in isotropic systems. *J. Chem. Phys.* **42**: 93–98.

C2 Cahoon, H.P. and Christensen, C.J. (1956). Sintering and grain-growth of alpha-alumina. *J. Am. Ceram. Soc.* **39**: 337–344.

C3 de Camargo, A.S.S., de O'Nunes, L.A., Santos, I.A. et al. (2004). Structural and spectroscopic properties of rare-earth (Nd^{3+}, Er^{3+}, and Yb^{3+}) doped transparent PLZT ceramics. *J. Appl. Phys.* **95**: 2135–2137.

C4 Campbell, J. (2004). Glasses for high-power/high-energy lasers. *Am. Ceram. Soc. Bull.* **83**: 9101–9109.

C5 Caponetti, E., Martino, D.C., Saladino, M.L., and Leonelli, C. (2007). Preparation of Nd:YAG nanopowder in a confined environment. *Langmuir* **23**: 3947–3952.

C6 Cardinale, G.F. and Robinson, C.J. (1992). Fracture strength measurement of filament assisted CVD polycrystalline diamond films. *J. Mater. Res.* **7**: 1432–1437.

C7 Carnall, E. Jr. and Hatch S.E. (1966). MgO infrared transmitting optical elements. US Patent 3, 236, 595, 22 February 1966.

C8 Carnall, E. Jr. (1967). The densification of MgO in the presence of a liquid phase. *Mater. Res. Bull.* **2**: 1075–1086.

C9 Carreaud, J., Labruyere, A., Boulesteix, R. et al. (2012). Wavelength switching in Nd:YSAG geramic laser induced by thermal effect. *Laser Phys. Lett.* **9**: 344–349.

C10 Casolco, S.R., Xu, J., and Garay, J.E. (2008). Transparent/translucent polycrystalline nanostructured yttria stabilized zirconia with varying colors. *Scr. Mater.* **58**: 516–519.

C11 Catalan, M.A., Frohlich, F., and Shenstone, A.G. (1954). Relations between the low atomic

configurations in the long periods. *Proc. R. Soc. London, Ser. A* **221**: 421–437.

C12 Chaim, R. and Margulis, M. (2005). Densification maps for spark plasma sintering of nanocrystalline MgO ceramics. *Mater. Sci. Eng., A* **407**: 180–187.

C13 Chaim, R., Kalina, M., and Shen, J.Z. (2007). Transparent YAG ceramics by spark plasma sintering. *J. Eur. Ceram. Soc.* **27**: 3331–3337.

C14 Chaim, R., Levin, M., Shlayer, A., and Estournes, C. (2008). Sintering and densification of nanocrystalline ceramic oxide powders: a review. *Adv. Appl. Ceram.* **107**: 159–169.

C15 Chaim, R., Marder-Jaeckel, R., and Shen, J.Z. (2006). Transparent YAG ceramics by surface softening of nanoparticles in spark plasma sintering. *Mater. Sci. Eng., A* **429**: 74–78.

C16 Chai, Q., Yang, D., Zhao, X. et al. (2018). Lead free (K,Na)NbO_3 – based ceramics with high optical transparency and large energy storage ability. *J. Am. Ceram. Soc.* **101**: 2331–2339.

C17 Chani, V.I., Boulon, G., Zhao, W. et al. (2010). Correlation between segregation of rare-earth dopants in melt crystal growth and ceramic processing for optical applications. *Jpn. J. Appl. Phys.* **49**: 075601/1–6.

C18 Chan, K.Y., Tsang, W.S., Mak, C.L., and Wong, K.H. (2005). Optical studies of PMN-PT thin films. *J. Eur. Ceram. Soc.* **25**: 2313–2317.

C19 Chawla, S., Parvaz, M., Kumar, V., and Buch, Z. (2013). Fabrication of dual excitation dual emission phosphor with plasmonic enhancement of fluorescence for simultaneous conversion of solar UV and IR to visible radiation. *New J. Chem.* **37**: 3991–3997.

C20 Chen, C., Yi, X., Zhang, S. et al. (2015). Vacuum sintering of TAG transparent ceramics with combined TEOS+MgO sintering aids. *Ceram. Int.* **41**: 12823–12827.

C21 Chen, D., Jordan, E.H., and Gell, M. (2008). Sol–gel combustion synthesis of nanocrystalline YAG powder from metal-organic precursors. *J. Am. Ceram. Soc.* **91**: 2759–2762.

C22 Chen, D.Q., Wang, Y.S., and Yu, Y.L. (2007). Upconversion emission of infrared excited Er^{3+}-doped transparent glass ceramics containing CaF_2 nano-crystals. *Key Eng. Mater.* **336–338**: 1846–1848.

C23 Chen, D., Xiang, W., Liang, X. et al. (2015). Advances in in transparent glass-ceramic phosphors for white light-emitting diodes - a review. *J. Eur. Ceram. Soc.* **35**: 859–869.

C24 Cheng, J.P., Agrawal, D., Zhang, Y.J. et al. (2000). Fabricating transparent ceramics by microwave sintering. *Am. Ceram. Soc. Bull.* **79**: 71–74.

C25 Chen, I.W. and Wang, X.H. (2000). Sintering dense nanocrystalline ceramics without final-stage grain-growth. *Nature* **404**: 168–171.

C26 Chen, J., Deng, Z., Liu, Z. et al. (2015). Optical enhancement brought by doping $Gd^{(3+)}$ ions into Ce:YAG ceramics for indoor white light-emitting diodes. *Opt. Express* **23**: A292–A298.

C27 Chen, L.Y., Cheng, W.C., Tsai, C.C. et al. (2014). Novel broadband glass phosphors for high CRI WLEDs. *Opt. Express* **22**: A671–A678.

C28 Chen, P.L. and Chen, I.W. (1996). Grain boundary mobility in Y_2O_3: defect mechanism and dopant effects. *J. Am. Ceram. Soc.* **79**: 1801–1809.

C29 Chen, Q.Y., Meng, C.M., Lu, T.C. et al. (2010). Enhancement of sintering ability of spinel ceramic nanopowders by shock compression. *Powder Technol.* **200**: 91–95.

C30 Chen, S. and Wu, Y. (2014). Influence of temperature on the spark plasma sintering of calcium fluoride ceramics. *J. Mater. Res.* **29**: 2297–2302.

C31 Chen, S., Zhang, L., Kisslinger, K., and Wu, Y. (2013). Transparent YAG:Li, Ce ceramics for thermal neutron detection. *J. Am. Ceram. Soc.* **96**: 1067–1069.

C32 Chiang, Y.M., Birnie, D.P. III, and Kingery, D.W. (1997). *Physical Ceramics*. New York: Wiley.

C33 Chiang, Y.M. and Kingery, W.D. (1990). Grain-boundary migration in nanostoichiometric solid solutions of magnesium aluminate spinel: II. Effects of grain-boundary nanostoichiometry. *J. Am. Ceram. Soc.* **73**: 1153–1158.

C34 Chlique, C., Delaizir, G., Merdrignac-Conanec, O. et al. (2011). A comparative study of ZnS powders sintering by hot uniaxial pressing (HUP) and spark plasma sintering (SPS). *Opt. Mater.* **33**: 706–712.

C35 Choi, H., Cho, S.H., Khan, S. et al. (2014). Roles of an oxygen Frenkel pair in the photoluminescence of Bi^{3+} doped Y_2O_3: computational predictions and experimental verifications. *J. Mater. Chem. C* **2**: 6017–6024.

C36 Cinibulk, M.K. (2000). Synthesis of YAG from a mixed-metal citrate precursor. *J. Am. Ceram. Soc.* **83**: 1276–1278.

C37 Claussen, N. and Ruhle, M. (1981). Design of transformation-toughened ceramics. In: *Advances in Ceramics*, vol. 3 (eds. N. Claussen, M. Ruhle and A.H. Heuer), 137–163. American Ceramic Society.

C38 Coble, R.L. (1962). Sintering of alumina: effect of atmospheres. *J. Am. Ceram. Soc.* **54**: 123–127.

C39 Coble, R.L. (1962). Transparent alumina and method of preparation. US Patent 3, 026, 210, 20 March 1962.

C40 Cotton, F.A. (1971). *Chemical Applications of Group Theory*, 2e. New York: Wiley.

D

D1 Dai, J., Pan, Y., Li, X. et al. (2018). Fabrication and properties of $(Tb_{1-x}Ce_x)_3Al_5O_{12}$ magneto-optical ceramics with different doping concentrations. *Scr. Mater.* **155**: 46–49.

D2 Dai, S., Sugiyama, A., Hu, L. et al. (2002). The spectrum and laser properties of ytterbium doped phosphate glass at low temperature. *J. Non-Cryst. Solids* **311**: 138–144.

D3 Damestani, Y., Reynolds, C.L., Szu, J. et al. (2013). Transparent yttria-stabilized-zirconia calvarium prosthesis. *Nanomedicine* **9**: 1135–1138.

D4 Davis, M.J., Vullo, P., Mitra, I. et al. (2008). Ferroelectric and nonferroelectric (polar) piezoelectric glass-ceramics. *J. Am. Ceram. Soc.* **91**: 2878–2885.

D5 Davoodzadeh, N., Cano-Velazquez, M.S., Halaney, D. et al. (2018). Evaluation of a transparent cranial implant as a permaent window for cerebral flow imaging. *Biomed. Opt. Express* **9**: 4879–4892.

D6 Day, D.E. and Rindone, G.E. (1962). Properties of soda aluminosilicate glasses: I, Refractive index, density, molar refractivity, and infrared absorption spectra. *J. Am. Ceram. Soc.* **45**: 489–496.

D7 Dejneka, M.J., Powell, C., and Borelli, N. (2005). Transparent magnetic glass-ceramics. *J. Am. Ceram. Soc.* **88**: 2435–2441.

D8 Dejneka, M.J. (1998). The luminescence and structure of novel transparent oxyfluoride glass-ceramics. *J. Non-Cryst. Solids* **239**: 149–155.

D9 Dejneka, M.J. (1998). Transparent oxyfluoride glass ceramics. *MRS Bull.* **23**: 57–62.

D10 Dong, J. and Ueda, K. (2005). Temperature-tuning Yb:YAG microchip lasers. *Laser Phys. Lett.* **29**: 429–436.

D11 Dong, J., Shirakawa, A., Ueda, K. et al. (2006). Efficient Yb^{3+}:YAG microchip lasers. *Appl. Phys. Lett.* **89**: 091114/1–3.

D12 Dong, J., Shirakawa, A., Ueda, K. et al. (2007). Laser-diode pumped heavy-doped Yb:YAG ceramic lasers. *Opt. Lett.* **32**: 1890–1892.

D13 Dong, J., Ueda, K., Yagi, H. et al. (2009). Comparative study of the effect of Yb concentrations on laser characteristics of Yb:YAG ceramics and crystals. *Laser Phys. Lett.* **6**: 282–289.

D14 Dong, J., Ueda, K., Yagi, H., and Kaminskii, A.A. (2008). Laser-diode-pumped self-Q-switched microchip lasers. *Opt. Rev.* **15**: 57–74.

D15 Dorenbos, P. (2002). 5-d level energies of Ce^{3+} and the crystalline environment. IV. Aluminates and simple oxides. *J. Lumin.* **99**: 283–292.

D16 Dorenbos, P. (2003). f→d transition energies of divalent lanthanides in inorganic compounds. *J. Phys. Condens. Matter* **15**: 575–594.

D17 Doroshenko, M.E., Demidenko, A.A., Fedorov, P.P. et al. (2013). Progress in fluoride laser ceramics. *Phys. Status Solidi C* **10**: 952–957.

D18 Dragic, P., Law, P.C., Ballato, J. et al. (2010). Brillouin spectroscopy of YAG derived optical fibers. *Opt. Express* **18**: 10055–10067.

D19 Drew, R.A.L., Hampshire, S., and Jack, K.H. (1981). Nitrogen glasses. In: *Special Ceramics 7* (eds. D. Taylor and P. Popper), 28–47. London: British Ceramic Society.

D20 Drdlikova, K., Klement, R., Drdlik, D. et al. (2017). Luminiscent Er^{3+} doped transparent alumina ceramics. *J. Eur. Ceram. Soc.* **37**: 2695–2703.

D21 Duffy, J.A. and Ingram, M.D. (1971). Establishment of an optical scale for Lewis basicity in inorganic oxyacids, molten salts and glasses. *J. Am. Chem. Soc.* **93**: 6448–6454.

D22 Dumbaugh, W.H. (1986). Infrared-transmitting oxide glasses. *Proceedings of SPIE 618*, pp. 87–91.

D23 Dunne, M., Moses, E.I., Amendt, P. et al. (2011). Timely delivery of laser inertial fusion energy (LIFE). *Fusion Sci. Technol.* **60**: 19–27.

D24 Duran, P., Recia, P., Jurado, J.R. et al. (1989). Preparation, sintering and properties of translucent Er_2O_3-doped tetragonal zirconia. *J. Am. Ceram. Soc.* **72**: 2088–2093.

D25 Dutta, S.K. and Gazza, G.E. (1969). Transparent Y_2O_3 by hot-pressing. *Mater. Res. Bull.* **4**: 791–796.

E

E1 Edelman, I., Ivanova, O., Ivantsov, R. et al. (2012). Magnetic nano-particles formed in glasses co-doped with iron and larger radius elements. *J. Appl. Phys.* **112**: 084331-1–084331-14.

E2 Eilers, H. (2007). Fabrication, optical transmittance, and hardness of IR-transparent ceramics made from nanophase yttria. *J. Eur. Ceram. Soc.* **27**: 4711–4717.

E3 Epicier, T., Boulon, G., Zhao, W. et al. (2012). Spatial distribution of the Yb^{3+} rare-earth ions in YAG and Y_2O_3 optical ceramics as analyzed by TEM. *J. Mater. Chem.* **22**: 18221–18229.

E4 Eriksson, M., Liu, Y., Hu, J. et al. (2011). Transparent hydxyapatite ceramics with nanograin structure prepared by high pressure SPS at a minimized temperature. *J. Eur. Ceram. Soc.* **31**: 1533–1540.

E5 Erlandson, A.C., Aceves, S.M., Bayramian, A.J. et al. (2011). Comparison of Nd:phosphate glass, Yb:YAG and Yb: S-FAP laser beamlines for laser inertial fusion energy (LIFE). *Opt. Mater. Express* **1**: 1341–1352.

E6 Esposito, L., Piancastelli, A., Miceli, P., and Martelli, S. (2015). A thermodynamic approach to obtaining transparent spinel by hot pressing. *J. Eur. Ceram. Soc.* **35**: 651–661.

E7 Ewsuk, K.G., Arguello, J.G., Bencoe, D.N. et al. (2003). Characterizing powders for dry pressing. *Bull. Am. Ceram. Soc.* **82**: 41–45.
E8 Eyring, L.R. (1966). Fluorite Related Oxide Phases of Rare-Earth and Actinide Elements. US Atomic Energy Commission, COO-1109-26.

F
F1 Fang, C.M., Metselaar, R., Hintzen, T.H., and de With, G. (2001). Structure models for γ-aluminium oxynitride from ab initio calculations. *J. Am. Ceram. Soc.* **84**: 2633–2637.
F2 Fan, T.Y., Ripin, D.J., Aggarwal, R.L. et al. (2007). Cryogenic Yb^{3+}-doped solid-state lasers. *IEEE J. Sel. Top. Quantum Electron.* **13**: 448–459.
F3 Feldman, R., Shimony, Y., and Burshtein, Z. (2003). Dynamics of Chromium ion valence transformations in Cr,Ca:YAG crystals used as laser gain and passive Q-switching media. *Opt. Mater.* **24**: 333–344.
F4 Feldman, R., Shimony, Y., and Burshtein, Z. (2003). Passive Q-switching in Nd:YAG/Cr^{4+}:YAG monolithic microchip laser. *Opt. Mater.* **24**: 393–399.
F5 Feldman, R. and Shimony, Y. (2010). Strength and strengthening of ceramic laser components. *Proceedings ILCS-6*, Munster, Germany, Comm. no. 20, pp. 1–28.
F6 Feng, Y., Lu, J., Takaichi, K. et al. (2004). Passively Q-switched ceramic Nd^{3+}:YAG/Cr^{4+}:YAG lasers. *Appl. Opt.* **43**: 2944–2947.
F7 Field, J.E., Hand, R.J., and Pickels, C.J. (1989). Strength and rain erosion studies of IR materials. *Proceedings of SPIE 1112*, pp. 306–315.
F8 Figgis, B.N. (1966). *Introduction to Ligand Fields*. New York: Wiley-Interscience.
F9 Flory, P.J. (1953). *Principles of Polymer Chemistry*. Ithaca, NY: Cornell University Press.
F10 Foex, M. and Traverse, J.P. (1966). Polymorphism of rare-earth sesquioxides at high temperatures. *Bull. Soc. Fr. Mineral. Cristallogr.* **89**: 184–205.
F11 Frage, N., Kalabukhov, S., Sverdlov, N. et al. (2010). Densification of transparent YAG by SPS processing. *J. Eur. Ceram. Soc.* **30**: 3331–3337.
F12 Frantz, L.M. and Nodvik, J.S. (1963). Theory of pulse propagation in a laser amplifier. *J. Appl. Phys.* **34**: 2346–2349.
F13 Fraser, B.S. and Hemingway, A. (1994). High-performance faceted domes for tactical and strategic missiles. *Proceedings of SPIE 2286*, pp. 485–492.
F14 Frechette, V.D. and Cline, C.F. (1970). Fractography of ballistically tested ceramics. *Am. Ceram. Soc. Bull.* **49**: 994–997.
F15 Fuji, A., Stolts, H., and von der Osten, F. (1983). Excitons and phonons in mixed silver halides studied by resonant Raman scattering. *J. Phys. C: Solid State Phys.* **16**: 1713–1728.
F16 Fujita, S., Sakamoto, A., and Tanabe, S. (2008). Luminescence characteristics of YAG glass-ceramic phosphor for white LED. *IEEE J. Sel. Top. Quantum Electron.* **14**: 1387–1391.
F17 Fujita, S., Umayahara, Y., and Tanabe, S. (2010). Influence of light scattering on luminous efficacy in Ce:YAG glass-ceramic phosphor. *J. Ceram. Soc. Jpn.* **118**: 128–131.
F18 Fujiura, K., Imai, T., Sasaura, M. and Nakamura, K. (2010). Optical medium, an optical lens and prism. US Patent 7, 647, 737 B2, 9 March 2010.
F19 Furuse, H., Yasahura, R., Hiraga, K., and Zhou, S. (2016). High Verdet constant of Ti-dped TAG ceramics. *Opt. Mater. Express* **6**: 191–196.
F20 Furuse, H. and Yasuhara, R. (2017). Magneto-optical characteristics of holmium oxide ceramics. *Opt. Mater. Express* **7**: 827–833.
F21 Fu, Y., Li, J., Liu, Y. et al. (2014). Effect of air annealing on the optical properties and laser performance of Nd:YAG transparent ceramics. *Opt. Mater. Express* **4**: 2108–2115.
F22 Fu, Y., Li, J., Liu, Y. et al. (2016). Fabrication, microstructure and laser performance of Nd^{3+}-doped LuAG transparent ceramics. *J. Eur. Ceram. Soc.* **36**: 655–661.

G
G1 Gallian, A., Fedorov, V.V., Mirov, S.B. et al. (2006). Hot-pressed ceramic Cr^{2+}:ZnSe gain-switched laser. *Opt. Express* **214**: 11694–11701.
G2 Gan, L., Park, Y.J., Kim, H. et al. (2017). The effect of temperature and pressure on ZrO_2-doped transparent yttria ceramics fabricated by a hot-pressing method. *Opt. Mater.* **71**: 109–116.
G3 Gardopee, G.J., Newnham, R.E., and Bhalla, A.S. (1981). Pyroelectric $Li_2Si_2O_5$ glass-ceramics. *Ferroelectrics* **33**: 155–163.
G4 Garvie, R.C., Hannink, R.H.J., and Pascoe, R.T. (1975). Cearmic steel ? *Nature* **258**: 703–704.
G5 Gasgnier, G., Baumard, J.F., Boncoeur, M., and Bougoin, M. (1994). Enhanced densification of yttria by addition of titanium oxide. *J. Eur. Ceram. Soc.* **13**: 67–72.
G6 Gatti, A. (1969). Development of a Process for Producing Transparent Spinel Bodies. Final Report of contract N00019-69-C-0133 of GE-space div.
G7 Gauckler, L.J. (1989). Processing and properties of advanced structural ceramics. In: *High-Tech-Ceramics* (ed. G. Kostorz), 83–102. London: Academic Press.
G8 Gaume, R., He, Y., Markosyan, A. et al. (2010). Characterization of Optical Losses in YAG

transparent ceramics. *Proceedings LCS-6*, Muenster, Germany, C-7.

G9 Gavriliuk, A.G., Kharlamova, S.A., Lyubutin, I.S. et al. (2005). Optical transitions in $GdFe_3(BO_3)_4$ and FeB_3 under high pressure. *J. Phys. Condens. Matter* **17**: 7599–7604.

G10 Gazza, G.E. and Dutta, S.K. (1977). Transparent ultrafine grained ceramics. US Patent 4, 029, 75, 14 June 1977.

G11 Gentilman, R.L. (1981). Fusion-casting of transparent spinel. *Am. Ceram. Soc. Bull.* **60**: 906–909.

G12 German, R.M. (1996). *Sintering Theory and Practice*. New York: Wiley-Interscience.

G13 Geusic, J.E., Marcos, H.M., and Van Uitert, L.G. (1964). Laser oscillations in Nd- doped yttrium aluminum, yttrium gallium and gadolinium garnets. *Appl. Phys. Lett.* **4**: 182–184.

G14 Gich, M., Casas, L.I., Roig, A. et al. (2003). High-coercivity ultralight transparent magnets. *Appl. Phys. Lett.* **82**: 4307–4309.

G15 Gilde, G., Patel, P., and Patterson, P. (2005). Evaluation of hot pressing and hot isostatic pressing parameters influence on the optical properties of spinel. *J. Am. Ceram. Soc.* **88**: 2747–2751.

G16 Ghosh, A., White, K.A., Jenkins, M.G. et al. (1991). Fracture resistance of transparent $MgAl_2O_4$. *J. Am. Ceram. Soc.* **74**: 1624–1630.

G17 Goela, J.S. and Taylor, R.L. (1994). Transparent SiC for mid-IR windows and domes. *Proceedings of SPIE 2286*, pp. 46–59.

G18 Goldman, L.M., Balasubramanian, S., Kashalikar, U. et al. (2013). Scale up of large AlON windows. *Proceedings of SPIE 8708*, pp. 1–15.

G19 Goldman, L.M., Twedt, R., Foti, R. et al. (2009). Large-area AlON windows for reconnaissance and armor applications. *Proceedings of SPIE 7302*, pp. 6–11.

G20 Goldstein, A. and Chiriac, V. (1988). *Electronic Spectra of Transition Ions Located in Vitreous Hosts*. Timisoara: University Timisoara (Romania) Press.

G21 Goldstein, A. and Krell, A. (2016). Transparent ceramics at 50: progress made and further prospects. *J. Am. Ceram. Soc.* **99**: 3173–3197.

G22 Goldstein, A. (2012). Correlation between $MgAl_2O_4$-spinel structure, processing factors and functional properties of transparent parts (progress review). *J. Eur. Ceram. Soc.* **32**: 2869–2886.

G23 Goldstein, A., Goldenberg, A., and Hefetz, M. (2009). Transparent polycrystalline spinel, with submicron grains, by low temperature sintering. *J. Ceram. Soc. Jpn.* **117**: 1281–1283.

G24 Goldstein, A., Goldenberg, A., and Vulfson, M. (2011). Technology for the obtainment of transparent $MgAl_2O_4$ spinel parts. *J. Ceram. Sci. Technol.* **2**: 1–8.

G25 Goldstein, A., Goldenberg, A., Yeshurun, Y., and Hefetz, M. (2008). Transparent $MgAl_2O_4$ spinel from a powder prepared by flame spray pyrolysis. *J. Am. Ceram. Soc.* **91**: 4141–4144.

G26 Goldstein, A., Kaplan, W.D., and Singurindi, A. (2002). Liquid assisted sintering of SiC powders by MW (2.45 GHz) heating. *J. Eur. Ceram. Soc.* **22**: 1891–1896.

G27 Goldstein, A., Loiko, P., Burshtein, Z. et al. (2016). Development of saturable absorbers for laser passive Q-switching near 1.5 μm based on transparent ceramic Co^{2+}:$MgAl_2O_4$. *J. Am. Ceram. Soc.* **99**: 1324–1331.

G28 Goldstein, A., Räthel, J., Cohen, Z. et al. (2016). Fabrication of transparent YAG ceramic by air-sintering followed by HIPing. *Comm. at LCS-12*, Saint-Louis, France (November 2016).

G29 Goldstein, A., Raethel, J., Katz, M. et al. (2016). Transparent spinel/LiF ceramics by hot-pressing: host additive interaction mechanisms issue revisted. *J. Eur. Ceram. Soc.* **36**: 1731–1742.

G30 Goldstein, A., Ruginets, R., and Geffen, Y. (1997). Microwave sintering of amorphous silica powders. *J. Mater. Sci. Lett.* **16**: 310–312.

G31 Goldstein, A., Shames, A.I., Stevenson, A.J. et al. (2013). Parasitic light absorption processes in transparent polycrystalline $MgAl_2O_4$ and YAG. *J. Am. Ceram. Soc.* **96**: 3523–3529.

G32 Goldstein, A., Vulfson, M., and Sirota, M. (2007). Optical spectra of copper-doped Zn-phosphate glasses. *J. Am. Ceram. Soc.* **90**: 3680–3682.

G33 Goldstein, A., Yeshurun, Y., Vulfson, M., and Kravits, H. (2012). Fabrication of transparent polycrystalline $ZnAl_2O_4$ – a new optical bulk ceramic. *J. Am. Ceram. Soc.* **95**: 879–882.

G34 Gould, G. (1971). Pulsed laser output control. US Patent 3, 586, 998A, 22 June 1971.

G35 Goutaland, F., Jander, P., Brocklesby, W.S., and Dai, G. (2003). Crystallization effects on rare earth dopants in oxyfluoride glass ceramics. *Opt. Mater.* **22**: 383–390.

G36 van der Graaf, M.A.C.G. and Burggraaf, A.J. (1984). Wet-chemical preparation of zirconia powders: their microstructure and behavior. In: *Advances in Ceramics*, vol. 12 (eds. N. Clausen, M. Riihle and A.H. Heuer), 744–765. American Ceramic Society.

G37 Grasso, S., Kim, B.N., Hu, C. et al. (2010). Highly transparent pure alumina fabricated by high-pressure spark plasma sintering. *J. Am. Ceram. Soc.* **93**: 2460–2462.

G38 Green, K.E., Hastert, J.L., and Roy, D.W. (1989). Polycrystalline $MgAl_2O_4$ spinel a broad band optical

material for offensive environments. *Proceedings of SPIE 1112*, pp. 1–8.

G39 Greskovich, C. and Chernoch, J.P. (1974). Improved polycrystalline ceramic lasers. *J. Appl. Phys.* **45**: 4495–4499.

G40 Greskovich, C. and Chernoch, J.P. (1973). Polycrystalline ceramic lasers. *J. Appl. Phys.* **44**: 4599–4606.

G41 Gresckovich, C. and Duclos, S. (1997). Ceramic scintillators. *Annu. Rev. Mater. Sci.* **27**: 69–88.

G42 Greskovich, C. and Roth, W.L. (1975). Polycrystalline ceramic lasers. US Patent 3, 897, 358 A, 29 July 1975.

G43 Greskovich, C. and Woods, K.N. (1973). Fabrication of ThO_2 doped yttria transparent ceramic. *Bull. Am. Ceram. Soc.* **52**: 473–475.

G44 Greskovich, C., Minnear, W.P., O'clair, C.R. et al. (1992). Transparent polycrystalline garnets. European Patent 0, 463, 369A1, 2 January 1992.

G45 Griebner, U., Koch, R., Schonnagel, H. et al. (1996). Laser performance of a new ytterbium doped phosphate laser glass. In: *Advanced Solid State Lasers*, OSA Trends in Optics and Photonics Series, vol. 1 (eds. S. Payne and C. Pollack). Optical Society of America, paper YL7.

G46 Grigorjeva, L., Millers, D., Smits, K. et al. (2012). The time-resolved luminescence characteristics of Ce and Ce/Pr doped YAG ceramics obtained by high pressure technique. *Opt. Mater.* **34**: 986–989.

G47 Gritsyna, V.T., Afanasiev-Charkin, I.V., Kobyakov, V.A., and Sickafuss, K.E. (1999). Structure and electronic states of defects in spinels of different composition $MgO{\cdot}nAl_2O_3$:Me. *J. Am. Ceram. Soc.* **82**: 3365–3373.

G48 Grove, D.J. and Rajendran, A.M. (1996). Effects of pulverized material strength on penetration resistance of ceramic targets. *AIP Conference Proceedings*, Volume 370, pp. 1143–1146.

G49 Guignard, M., Nazabal, V., Zang, X.H. et al. (2007). Crystalline phase responsible for the permanent second-harmonic generation in chalcogenide glass-ceramics. *Opt. Mater.* **30**: 338–345.

G50 Guo, N., Huang, Y., You, H. et al. (2010). $Ca_9Lu(PO_4)_7$:Eu^{2+}, Mn^{2+}: a potential single-phase white-light-emitting phosphor suitable for white light emitting diodes. *Inorg. Chem.* **49**: 10907–10913.

G51 Guo, N., Jia, C., Li, J. et al. (2015). Color tuning and energy transfer in Eu^{2+}/Mn^{2+}-doped $Ba_3Y(PO_4)_3$ eulytite-type orthophosphate phosphors. *RSC Adv.* **5**: 46517–46524.

G52 Gupta, T.K., Rossing, B.R., and Straub, W.D. (1973). Fabrication of transparent polycrystalline CaO. *J. Am. Ceram. Soc.* **56**: 339–340.

H

H1 Haberko, K. (1979). Characteristics and sintering behavior of zirconia ultrafine powders. *Ceram. Int.* **5**: 148–154.

H2 Haertling, G.H. and Land, C.E. (1971). Hot-pressed $(Pb,La)(Zr,Ti)O_3$ ferroelectric ceramics for electrooptic applications. *J. Am. Ceram. Soc.* **54**: 1–11.

H3 Haertling, G.H. (1988). Electro-optic ceramics and devices. In: *Electronic Devices: Properties, Devices and Applications* (ed. L.M. Levinson), 371–492. New York: Marcel Dekker.

H4 Halliyal, A., Bhalla, A.S., Newnham, R.E., and Cross, L.E. (1989). Glass-ceramics for piezoelectric and pyroelectric devices. In: *Glasses and Glass-Ceramics* (ed. M.H. Lewis), 272–314. London: Chapman and Hall.

H5 Hamlin, S.J., Beyer, R.A., and Forch, B. (1996). A Breech Mounted Laser Igniter for the Crusader XM297 155mm Howitzer. Army Research Laboratory Contract No. DAAL01-96-C-0064.

H6 Hanhn, T. (ed.) (2011). *International Tables for Crystallography, Space-Group Symmetry*, vol. A, 715–717. Wiley.

H7 Harari, Y.N. (2015). *Sapiens: A Brief History of Humankind*. New York: Harper and Collins.

H8 Harrington, J. (2003). *Infrared Fibers and their Applications*. Bellingham, WA: SPIE Press.

H9 Hardy, C.R., Guo, B., Myers, M.J., and Myers, J.D. (2007). High-efficiency side diode pumped breech mount laser ignition. *Proceedings of SPIE 6662*, p. 8.

H10 Harmer, M.P. and Bennison, S.J. (1985). Swelling of hot-pressed Al_2O_3. *J. Am. Ceram. Soc.* **68**: 591–597.

H11 Hart, D.W., Jani, M., and Barnes, N.P. (1996). Room-temperature lasing of end-pumped Ho:LuAG. *Opt. Lett.* **21**: 728–730.

H12 Hart, P.E., Atkin, R.B., and Pask, J.A. (1970). Densification mechanisms in hot-pressing of magnesia with a fugitive liquid. *J. Am. Ceram. Soc.* **53**: 83–86.

H13 Hartnett, T.M., Gentilman, R.L., and Maguire, E.A. (1984). Aluminum oxynitride having improved optical characteristics and method of manufacture. US Patent 4, 481, 300, 6 November 1984.

H14 Harris, D.C. (2005). History of development of polycrystalline spinel in the US. *Proceedings of SPIE 5786*, pp. 1–22.

H15 Harris, D.C. (1999). *Materials for Infrared Windows and Domes: Properties and Performance*. Bellingham, WA: SPIE Optical Engineering Press.

H16 Hatch, S.E., Parsons, W.F., and Weagley, R.J. (1964). Hot-pressed polycrystalline CaF_2:Dy^{2+} laser. *Appl. Phys. Lett.* **5**: 153–154.

H17 Hayashi, K., Kobayashi, O., Toyoda, S., and Morinaga, K. (1991). Transmission optical properties of polycrystalline alumina

with submicron grains. *Mater. Trans.* **32**: 1024–1029.

H18 Hayashy, K., Matsuishi, S., Kamyia, T. et al. (2002). Light-induced conversion of an insulating refractory oxide into a persistent electronic conductor. *Nature* **419**: 462–464.

H19 Hazel, P.J. (2006). *Ceramic Armour: Design and Defeat Mechanisms*. Canberra: Argos Press.

H20 Hecht, H.G. (1976). The interpretation of diffuse reflectance spectra. *J. Res. Nat. Bur. Stand. Phys. Chem.* **80A**: 567–583.

H21 Hecht, J. (1994). *Understanding Lasers: An Entry-Level Guide*. New York: Wiley-Interscience, IEEE Press.

H22 Helle, A.S., Easterling, K.E., and Ashby, M.F. (1985). Hot-isostatic pressing diagrams: new developments. *Acta Metall.* **533**: 2163–2174.

H23 von Helmholtz, H. (1925). *Physiological Optics* (ed. J.P.C. Southall) and and translation, 34–71. Washington, DC: Optical Society of America.

H24 Henderson, B. and Bartram, R. (2000). *Crystal-Field Engineering of Solid-State Laser Materials*. Cambridge: CUP.

H25 Herr, M.D. and Compton, W.R. (1980). Evaluation of statistical fracture criteria for MgF_2 seeker domes. *NWC Rep. TP 6226*.

H26 Heuer, A.H. and Ruhle, M. (1984). Phase transformations in ZrO_2-containing ceramics: I, The instability of c-ZrO_2 and the resulting diffusion controlled reactions. In: *Advances in Ceramics*, vol. 12, 1–13. American Ceramic Society.

H27 Hillig, W.B. (1951). Nucleation Catalysis in Glass Systems. *GE Res. Lab. Rep. 61*.

H28 Hinklin, T.R., Rand, S.C., and Laine, R.M. (2008). Transparent, polycrystalline upconverting nanoceramics: towards 3-D displays. *Adv. Mater.* **20**: 1270–1273.

H29 Hockey, B.J. (1971). Plastic deformation of aluminum oxide by indentation and abrasion. *J. Am. Ceram. Soc.* **54**: 223–231.

H30 Hogan, P., Stefanik, T., Willingham, C., and Gentilman, R. (2004). Transparent yttria for IR windows and domes – past and present. *Proceedings of 10th DoD Electromagnetic Windows Symposium*, Norfolk, Virginia (19 May 2004).

H31 Holland, W. and Beall, G. (2002). *Glass-Ceramic Technology*. Westerville, OH: American Ceramic Society.

H32 Hommerich, U., Hanley, C., Brown, E. et al. (2009). Spectroscopic studies of the 1.5 micron ($^4I_{15/2} \rightarrow {}^4I_{13/2}$) emission from polycrystalline ceramic Er:YAG and Er:KPb_2Cl_5. *J. Alloys Compd.* **488**: 624–627.

H33 Honninger, C., Morier-Genoud, F., Moser, M. et al. (1998). Efficient and tunable diode-pumped femtosecond Yb:glass lasers. *Opt. Lett.* **23**: 126–128.

H34 Hori, S., Yoshimura, M., Somyia, S. et al. (1984). Al_2O_3-ZrO_2 ceramics prepared from CVD powders. In: *Advances in Ceramics*, vol. 12 (eds. N. Claussen, M. Ruhle and A.H. Heuer), 794–805. Westerville, OH: American Ceramic Society.

H35 Horn, R.G. (1990). Surface forces and their action in ceramic materials. *J. Am. Ceram. Soc.* **73**: 1117–1135.

H36 Hoskins, R.S. and Soffer, B.H. (1964). Stimulated emission from Nd:Y_2O_3. *Appl. Phys. Lett.* **4**: 22–23.

H37 Hostasa, J., Esposito, L., Malchere, A. et al. (2014). Polycrystalline Yb^{3+}-Er^{3+}-co-doped YAG: fabrication, TEM-EDX characterization, spectroscopic properties and comparison with the single crystals. *J. Mater. Res.* **29**: 2288–2296.

H38 Huang, C.B., Lu, T.C., Lin, L.B. et al. (2007). A study on toughening and strengthening of Mg-Al spinel transparent ceramics. *Key Eng. Mater.* **336–338**: 1207–1210.

H39 Huang, J., Zhang, S., Chen, Y. et al. (2013). Spectral properties of Pr^{3+}-doped transparent-glass-ceramic containing $Ca_5(PO_4)_3F$ nanocrystals. *J. Am. Ceram. Soc.* **96**: 3569–3575.

H40 Huang, Y.C., Wang, J.S., Lu, Y.K. et al. (2007). Preform fabrication and fiber drawing of 300 nm broadband Cr-doped fibers. *Opt. Express* **15**: 14382–14388.

H41 Huang, Y., Jiang, D., Zhang, J. et al. (2010). Sintering of transparent yttria ceramics in oxygen atmosphere. *J. Am. Ceram. Soc.* **93**: 2964–2967.

H42 Huisman, W., Graule, T., and Gauckler, L.J. (1995). Alumina of high reliability by centrifugal casting. *J. Eur. Ceram. Soc.* **15**: 811–821.

H43 van der Hulst, H.C. (1981). *Light Scattering by Small Particles*. New York: Dover Publications Inc.

H44 Hu, S., Qin, X., Zhou, G. et al. (2015). Luminescence characteristics of the Ce^{3+}-doped garnets: the case of Gd-admixed $Y_3Al_5O_{12}$ transparent ceramics. *Opt. Mater. Express* **5** (12): 2902–2910.

H45 Hutzler, T. and Krell, A. (2014) MgO-Transparent Ceramics with High Thermal Conductivity. *Fraunhofer IKTS Annual report 2012/13*.

H46 Hutzler, T., Klimke, J., and Krell, A. (2013). *Internal Report 500747*. Fraunhofer IKTS Dresden, 26.11.2012.

I

I1 Ikegami, T., Li, J.-G., Mori, T., and Moriyoshi, Y. (2002). Fabrication of transparent yttria ceramics by the low-temperature synthesis of yttrium hydroxide. *J. Am. Ceram. Soc.* **85**: 1725–1729.

I2 Ikesue, A. and Aung, Y.L. (2008). Ceramic laser materials. *Nat. Photonics* **2**: 721–727.

I3 Ikesue, A., Aung, Y.L., and Lupei, V. (2013). *Ceramic Lasers*. New York: Cambridge University Press.

I4 Ikesue, A., Kamata, K., and Yoshida, K. (1996). Synthesis of transparent Nd-doped HfO_2-Y_2O_3 ceramics using HIP. *J. Am. Ceram. Soc.* **79**: 359–364.

I5 Ikesue, A., Kamata, K., and Yoshida, K. (1995). Synthesis of Nd^{3+}, Cr^{3+}-codoped YAG ceramics for high-efficiency solid-state lasers. *J. Am. Ceram. Soc.* **78**: 2545–2547.

I6 Ikesue, A., Kinoshita, T., Kamata, K., and Yoshida, K. (1995). Fabrication and optical properties of high-performance polycrystalline Nd:YAG ceramics for solid-state lasers. *J. Am. Ceram. Soc.* **78**: 1033–1040.

I7 Ikesue, A. (2011). Transparent Ceramic Yb^{3+}:Lu_2O_3 Materials. *AOARD Rep.-104113*. Tokyo.

I8 Ikesue, A., Aung, Y.L., Yoda, T. et al. (2007). Fabrication and laser performance of polycrystal and single crystal Nd:YAG by advanced ceramic processing. *Opt. Mater.* **29**: 1289–1294.

I9 Ikesue, A., Yoshida, K., and Kamata, K. (1996). Transparent Cr^{4+} doped YAG ceramics for tunable lasers. *J. Am. Ceram. Soc.* **79**: 507–509.

I10 Ilse, F.E. and Hartman, H. (1951). Termsysteme elektrostatischer Komplexionen der Ubergangsmetalle mit einem d-Elektron. *Z. Phys. Chem.* **179**: 239–246.

I11 Ingel, R.P. and Lewis, D. III (1986). Lattice parameters and density of Y_2O_3-stabilized ZrO_2. *J. Am. Ceram. Soc.* **69**: 325–332.

I12 Iranmanesh, P., Saeednia, S., and Nourzpoor, M. (2015). Characterization of ZnS nanoparticles synthesized by co-precipitation method. *Chin. Phys. B* **24**: 046104/1–4.

I13 Irifune, T., Kurio, A., Sakamoto, S. et al. (2003). Materials: ultrahard polycrystalline diamond from graphite. *Nature* **421**: 599–600.

I14 Ish-Shalom, M. (1982). Formation of aluminium oxynitride by carbothermal reduction of aluminium oxide in nitrogen. *J. Mater. Sci. Lett.* **1**: 147–149.

J

J1 Jaffe, B., Cook, W.R. Jr., and Jaffe, H. (1971). *Piezoelectric Ceramics*. London: Academic Press.

J2 Jagodinski, H. and Saalfeld, H. (1958). Cation distribution and structural relations in Mg–Al spinel. *Z. Kristallogr.* **110**: 197–218.

J3 Jain, M., Skandan, G., Singhal, A. et al (2003). Processing of nanopowders into transparent ceramics for infrared windows. *Proceedings of SPIE 5078*, pp. 193–198.

J4 James, B. (2002). Practical issues in ceramic armor design. *Ceram. Trans.* **134**: 33–44.

J5 Jang, H.S., Im, W.B., Lee, D.C. et al. (2007). Enhancement of red spectral emission intensity of $Y_3Al_5O_{12}$:Ce^{3+} phosphor via Pr co-doping and Tb substitution for the application to white LEDs. *J. Lumin.* **126**: 371–377.

J6 Janney, M.A., Calhoun, C.L., and Kimrey, H.D. (1992). Microwave sintering of solid oxide fuel cell materials: I, zirconia- 8 mol% yttria. *J. Am. Ceram. Soc.* **75**: 341–346.

J7 Jeong, E.D., Bae, J.S., Hong, T.E. et al. (2007). Thermal properties and crystallization properties of TeO_2 glasses. *J. Ceram. Process. Res.* **8**: 417–420.

J8 Jiang, B., Lu, X., Zeng, Y. et al. (2013). Synthesis and properties of Yb:LuAG transparent ceramics. *Phys. Status Solidi C* **10**: 958–961.

J9 Jiang, B., Jiang, Y., Su, L. et al. (2017). Nd doped $Ca_{1-x}Y_xF_{2+x}$ ceramics prepared by the ceramization of single crystals. *Mater. Des.* **113**: 326–330.

J10 Jiang, H., Zou, Y.K., Chen, Q. et al. (2005). Transparent electro-optic ceramics and devices. *Proceedings of SPIE 5644*, pp. 380–394.

J11 Jing, W., Li, F., Yu, S. et al. (2018). High efficiency synthesis of Nd:YAG powder by a spray co-precipitation method for transparent ceramics. *J. Eur. Ceram. Soc.* **38**: 2454–2461.

J12 Jin, L., Zhou, G., Shimani, S. et al. (2010). ZrO_2-doped Y_2O_3 transparent ceramics via slip casting and vacuum sintering. *J. Eur. Ceram. Soc.* **30**: 2139–2143.

J13 Johnson, L.F., Boyd, G.D., Nassau, K., and Soden, R.R. (1962). Continuous operation of a solid-state optical maser. *Phys. Rev.* **126**: 1406–1409.

J14 Johnson, W.C. and Coble, R.L. (1978). A test of the second-phase and impurity segregation models for MgO enhanced densification of sintered alumina. *J. Am. Ceram. Soc.* **61**: 110–114.

J15 Jones, C.D., Rioux, J.B., Locher, J.W. et al. (2006). Large area sapphire for transparent armor. *Bull. Am. Ceram. Soc.* **85**: 24–27.

J16 Jorgensen, C.K. (1971). *Modern Aspects of Ligand Field Theory*. Amsterdam: North-Holland.

J17 Jorgensen, C.K. (1962). *Orbitals in Atoms and Molecules*. London: Academic Press.

J18 Jorgensen, P.J. and Anderson, R.C. (1967). Grain-boundary segregation and final-stage sintering of Y_2O_3. *J. Am. Ceram. Soc.* **50**: 553–558.

J19 Jun, H.S., Ko, I.Y., Yoon, J.K. et al. (2011). Properties and rapid consolidation of nanostructured MgO by high frequency induction heating sintering. *J. Ceram. Proc. Res.* **12**: 165–168.

K

K1 Kadosh, T., Cohen, Y., Talmon, Y., and Kaplan, W.D. (2012). In situ characterization of spinel nanoceramic suspension. *J. Am. Ceram. Soc.* **95**: 3103–3108.

K2 Kagan, M.A. and Khazanov, E.A. (2003). Compensation of thermally induced birefringence in active medium made of polycrystalline ceramics. *Proceedings of SPIE 4968*, pp. 115–126.

K3 Kalisky, Y. (2004). Cr^{4+} doped crystals: their use as lasers and passive Q-switches. *Prog. Quantum Electron.* **26**: 249–303.

K4 Kaminskii, A.A., Akchurin, M.S., Gainutdinov, R.V. et al. (2005). Microhardness and fracture toughness of Y_2O_3 and $Y_3Al_5O_{12}$ based nanocrystalline laser ceramics. *Crystallogr. Rep.* **50**: 869–873.

K5 Kaminskii, A.A., Kurakawa, H., Shirakawa, A. et al. (2009). Ba(Mg,Zr,Ta)O_3:Nd^{3+} fine grained ceramics: a novel laser-gain material with disordered structure for high-power laser systems. *Laser Phys. Lett.* **6**: 304–310.

K6 Kaminskii, A.A. (1981). *Laser Crystals*. Berlin: Springer-Verlag.

K7 Kaminskii, A.A., Tanaka, N., Eichler, H.J. et al. (2007). Picosecond Raman induced Stokes and anti-Stokes lasing in fine-grained Ba(Sn,Zr,Mg,Ta)O_3 crystalline ceramics with the cubic perovskite structure. *Laser Phys. Lett.* **4**: 819–823.

K8 Kamzina, L.S., Ruan, W., Li, G., and Zeng, J. (2012). Transparent ferroelectric ceramics PMN-PZT: dielectric and electro-optical properties. *Phys. Solid State* **54**: 2024–2029 (translation from Russian).

K9 Kansuwan, P. and Rickman, J.M. (2007). Role of segregating impurities in grain-boundary diffusion. *J. Chem. Phys.* **126**: 094707/1–7.

K10 Kaygorodov, A.S., Ivanov, V.V., Khrustov, V.R. et al. (2007). Fabrication of Nd:Y_2O_3 transparent ceramics by pulsed compaction and sintering of weakly agglomerated nanaopowders. *J. Eur. Ceram. Soc.* **27**: 1165–1169.

K11 Kim, B.N., Hiraga, K., Grasso, S. et al. (2012). High-pressure spark plasma sintering of MgO-doped transparent alumina. *J. Ceram. Soc. Jpn.* **120**: 116–118.

K12 Kim, B.N., Hiraga, K., Jeong, A. et al. (2014). Transparent $ZnAl_2O_4$ ceramics fabricated by SPS. *J. Ceram. Soc. Jpn.* **122**: 784–787.

K13 Kim, H.J., Fair, G.E., Hart, A.M. et al. (2015). Development of polycrystalline YAG fibers. *J. Eur. Ceram. Soc.* **35**: 4251–4258.

K14 Kim, H.J., Hay, R.S., and Corns, R.G. (2018). Polycrystalline ceramic fibers for laser applications. *Proceedings LCS-14*, Okazaki, Japan (26–30 November 2018).

K15 Kim, W., Baker, C., Bowman, S. et al. (2013). Laser oscillation from Ho^{3+} doped Lu_2O_3 ceramics. *Opt. Mater. Express* **3**: 913–919.

K16 Kim, Y., Zangvil, A., Goela, J.S., and Taylor, R.L. (1995). Microstructure comparison of transparent and opaque CVD-SiC. *J. Am. Ceram. Soc.* **78**: 1571–1579.

K17 Kingery, W.D. and Francois, B. (1967). The sintering of crystalline oxides. I. Interactions between grain boundaries and pores. In: *Sintering Related Phenomena* (eds. G.C. Kuczynski, N. Hooten and C. Gibson). New York: Gordon and Breach Science Publishers.

K18 Kingery, W.D., Bowen, H.K., and Uhlmann, D.R. (1976). *Introduction to Ceramics*, 2e. New York: Wiley-Interscience.

K19 Kingsley, J.J., Suresh, K., and Patil, K.C. (1990). Combustion synthesis of fine particle rare-earth orthoaluminates and YAG. *J. Solid State Chem.* **88**: 435–442.

K20 Kintaka, Y., Translucent ceramic, process for producing the same, optical part and optical apparatus, European Patent Application EP-1 810 955 A1, Int. Class. 7 C04B35/00, 25.7.2007.

K21 Kintaka, Y., Kuretake, S., and Tanaka, N. (2008). Hybrid lens using translucent ceramic. US Patent 7, 431, 984 B2, October 2008.

K22 Kintaka, Y., Kuretake, S., Tanaka, N. et al. (2010). Crystal structure and optical properties of complex perovskites. *J. Am. Ceram. Soc.* **93**: 1114–1119.

K23 Kishi, Y. and Tanabe, S. (2006). Infrared-to-visible upconversion of rare-earth doped glass ceramics containing CaF_2 crystals. *J. Alloys Compd.* **408–412**: 842–844.

K24 Kitajima, S., Yamakado, K., Shirakawa, A. et al. (2017). $Yb3^+$-doped CaF_2-LaF_3 ceramics laser. *Opt. Lett.* **42**: 1724–1727.

K25 Kittel, C. (1963). *Introduction to Solid State Physics*. London: Wiley.

K26 Klein, C.A. (1980). Compendium of property data for Raytran zinc selenide and sulfide. *Report RAY/RDT/T-1154*. Lexington, MA: Raytheon.

K27 Klimek, D.E. and Mandl, A. (2011). Nd:YAG ceramic ThinZag high power laser development. In: *High Power Laser Handbook* (eds. H. Injeyan and G.D. Goodno), 207–223. New York: McGraw-Hill.

K28 Klimke, J. and Krell, A. (2004). Colored Transparent Sintered Corundum. *Fraunhofer IKTS 2004 Annual Report*, p. 39.

K29 Klimke, J. and Krell, A. (2016). Optical Ceramics with Specifically Adjusted Spectral Transmission. *Fraunhofer IKTS 2014/2015 Annual Report*, pp. 90–91.

K30 Klimke, J., Hutzler, T., and Krell, A. (2012). *Report E91/01-2011*. Fraunhofer IKTS Dresden, 16.02.2012.

K31 Klimke, J., Trunec, M., and Krell, A. (2011). Transparent tetragonal yttria-stabilized zirconia ceramics: influence of scattering caused by birefringence. *J. Am. Ceram. Soc.* **94**: 1850–1858.

K32 Kodo, M., Soga, K., Yoshida, H., and Yamamoto, T. (2010). Doping effect of divalent cations on sintering of polycrystalline yttria. *J. Eur. Ceram. Soc.* **30**: 2741–2747.

K33 Komatsu, T., Tawarayama, H., Mohri, H., and Matusita, K. (1991). Properties and crystallization behaviors of TeO_2-$LiNbO_3$ glasses. *J. Non-Cryst. Solids* **135**: 105–113.

K34 Kong, H.J., Park, S., and Cha, S. (2011). Coherent beam combination for high repetition rate/high energy lasers using SBS-PCM and its application to accurate target injection in LIFE. *Comm. at 7th Laser Ceramics Symposium*, Singapore (November 2011).

K35 Kong, H.J., Park, S., Cha, S. et al. (2014). Current status of the development of the Kumgang laser. *Opt. Mater. Express* **4**: 2551–2558.

K36 Kong, L.B., Huang, Y.Z., Que, W.X. et al. (2015). *Transparent Ceramics*. Berlin: Springer-Verlag.

K37 Kopylov, Y.L., Kravchenco, V.B., Bagayev, S.N. et al. (2009). Development of Nd^{3+}:YAG laser ceramics by high-pressure colloidal slip-casting. *Opt. Mater.* **31**: 707–710.

K38 Koster, G.F. (1957). Space groups and their representations. In: *Solid State Physics*, vol. 5 (eds. F. Seitz and D. Turnbull), 173–256. Academic Press.

K39 Krasovska, V., Vinkler, B., and Yanowsky, B. (1998). The color of Sulphur. *J. Phys. Condens. Matter* **10**: 4093–4100.

K40 Krell, A. and Bales, A. (2011). Grain size-dependent hardness of transparent magnesium aluminate spinel. *Int. J. Appl. Ceram. Technol.* **8**: 1108–1114.

K41 Krell, A. and Blank, P. (1996). The influence of shaping method on the grain size dependence of strength in dense submicrometer alumina. *J. Eur. Ceram. Soc.* **16**: 1189–1200.

K42 Krell, A. and Brendler, E. (2013). Influence of cation disorder in commercial spinel powders studied by ^{27}Al MAS NMR on the sintering of transparent $MgAl_2O_4$ spinel ceramics. *J. Ceram. Sci. Technol.* **4**: 51–58.

K43 Krell, A. and Klimke, J. (2006). Effects of the homogeneity of particle coordination on solid-state sintering of transparent alumina. *J. Am. Ceram. Soc.* **89**: 1985–1992.

K44 Krell, A. and Strassburger, E. (2007). Ballistic strength of opaque and transparent armor. *Am. Ceram. Soc. Bull.* **86**: 9201–9207.

K45 Krell, A. and Strassburger, E. (2012). Discrimination of basic influences on the ballistic strength of opaque and transparent ceramics. *Ceram. Eng. Sci. Proc.* **33**: 161–176.

K46 Krell, A. and Strassburger, E. (2007). Hierarchy of key influences on the ballistic strength of opaque and transparent armor. *Ceram. Eng. Sci. Proc.* **28**: 45–55.

K47 Krell, A. and Strassburger, E. (2014). Order of influences on the ballistic resistance of armor ceramics and single crystals. *Mater. Sci. Eng., A* **597**: 422–430.

K48 Krell, A. and Strassburger, E. (2013). Separation and hierarchic order of key influences on the ballistic strength of opaque and transparent ceramic armor. In: *Proceedings of 27th International Symposium on Ballistics* (Freiburg, Germany) (eds. M. Wickert and M. Salk), 1053–1064. Lancaster, PA: DEStech Publications.

K49 Krell, A. (1998). A new look at the influences of load, grain size, and grain boundaries on the room temperature hardness of ceramics. *Int. J. Refract. Met. Hard Mater* **16**: 331–335.

K50 Krell, A., Blank, P., Ma, H. et al. (2003). Transparent sintered corundum with high hardness and strength. *J. Am. Ceram. Soc.* **86**: 12–18.

K51 Krell, A., Blank, P., Wagner, E., and Bartels, G. (1996). Advances in the grinding efficiency of sintered alumina abrasives. *J. Am. Ceram. Soc.* **79**: 763–767.

K52 Krell, A. (1996). Improved hardness and hierarchic influences on wear in submicron sintered alumina. *Mater. Sci. Eng., A* **209**: 156–163.

K53 Krell, A., Hutzler, T., and Klimke, J. (2014). Defect strategies for an improved optical quality of transparent ceramics. *Opt. Mater.* **38**: 61–74.

K54 Krell, A., Hutzler, T., Klimke, J., and Potthoff, A. (2010). Fine-grained transparent spinel windows by the processing of different nanopowders. *J. Am. Ceram. Soc.* **93**: 2656–2666.

K55 Krell, A., Hutzler, T., and Klimke, J. (2005). Physics and technology of transparent ceramic armor: sintered alumina vs cubic materials. In: *Nanomaterials Technology for Military Vehicle Structural Applications*. http://www.rto.nato.int/abstracts.asp.

K56 Krell, A., Hutzler, T., and Klimke, J. (2009). Transmission physics and consequences for materials selection, manufacturing, and applications. *J. Eur. Ceram. Soc.* **29**: 207–221.

K57 Krell, A., Hutzler, T., and Klimke, J. (2007). Transparent ceramics for structural applications: Part 1 Physics of light transmission and technological consequences, and Part 2 Fields of applications. *Ber. DKG* **84**: (4) E41–E50, and (6) E50–E56.

K58 Krell, A., Klimke, J., and Hutzler, T. (2009). Advanced spinel and submicron alumina for transparent armor. *J. Eur. Ceram. Soc.* **29**: 275–281.

K59 Krell, A., Klimke, J., and Hutzler, T. (2009). Transparent compact ceramics: inherent physical issues. *Opt. Mater.* **31**: 1144–1150.

K60 Krell, A., Strassburger, E., Hutzler, T., and Klimke, J. (2013). Single and polycrystalline transparent ceramic armor with different crystal structure. *J. Am. Ceram. Soc.* **96**: 2718–2721.

K61 Krell, A., Waetzig, K., and Klimke, J. (2011). Effects and elimination of nanoporosity in transparent sintered spinel ($MgAl_2O_4$). *Proceedings of SPIE 8016*, 801602.

K62 Krell, A., Waetzig, K., and Klimke, J. (2012). Influence of the structure of $MgO{\cdot}nAl_2O_3$ lattices on transparent ceramics processing and properties. *J. Eur. Ceram. Soc.* **32**: 2887–2898.

K63 Krumins, A. and Sternberg, A. (1987). Transparent ferroelectric ceramics I. Composition, structure and requirements for production. In: *Electro-Optic and Photorefractive Materials* (ed. P. Gunter), 50–60. Berlin: Springer-Verlag.

K64 Krutova, L.I., Lukin, A.V., and Sandulenko, V.A. (1987). Phototropic centers in chromium-doped garnets. *Opt. Spectrosc.* **63**: 693–695 (translated from Russian by AIP).

K65 Kumar, G.A., Lu, J., Kaminskii, A.A. et al. (2004). Spectroscopic and stimulated emission characteristics of Nd^{3+} in transparent YAG ceramics. *IEEE J. Quantum Electron.* **40**: 747–758.

K66 Kumar, R.S., Rajeswari, K., Praveen, B. et al. (2010). Processing of aluminum oxynitride though aqueous colloidal forming techniques. *J. Am. Ceram. Soc.* **93**: 429–435.

K67 Kuretake, S., Tanaka, N., Kintaka, Y. et al. (2014). Nd-doped Ba(Zr,Mg,Ta)O_3 ceramics as laser materials. *Opt. Mater.* **36**: 645–649.

K68 Kuru, Y., Savasir, E.O., Nergiz, S.Z. et al. (2008). Enhanced co-solubilities of Ca and Si in YAG. *Phys. Status Solidi C* **5**: 3383–3386.

K69 Kwon, S.T., Kim, D.Y., Kang, T.K., and Yoon, D.N. (1987). Effect of sintering temperature on the densification of Al_2O_3. *J. Am. Ceram. Soc.* **70**: C69–C70.

L

L1 Lallemant, L., Fantozzi, G., Garnier, V., and Bonnefont, G. (2012). Transparent polycrystalline alumina obtained by SPS: green bodies processing effect. *J. Eur. Ceram. Soc.* **32**: 2909–2915.

L2 Land, C.E. and Thacher, P.D. (1969). Ferroelectric ceramic electrooptic materials and devices. *IEEE Proc.* **57**: 751–768.

L3 Land, C.E. (1968). Ferroelectric ceramic electrooptic storage and display devices. *IEEE Trans. Electron Devices* **15**: 425.

L4 Lange, F.F. and Davis, B.I. (1984). Sinterability of ZrO_2 and Al_2O_3 powders: the role of pore coordination number distribution. *Adv. Ceram.* **12**: 699–713.

L5 Lange, F.F. (1989). Powder processing science and technology for increased reliability. *J. Am. Ceram. Soc.* **72**: 3–15.

L6 Lange, F.F. (1984). Sinterability of agglomerated powders. *J. Am. Ceram. Soc.* **67**: 83–89.

L7 Langer, J., Hoffman, M.J., and Guillon, O. (2009). Direct comparison between hot pressing and electric field-assisted sintering of submicron alumina. *Acta Mater.* **57**: 5454–5465.

L8 Lankford, J. (2004). The role of dynamic material properties in the performance of ceramic armor. *Int. J. Appl. Ceram. Technol.* **1**: 205–210.

L9 Lee, H.D., Mah, T.I., and Parthasarathy, T.A. (2008). Low-cost processing of fine grained transparent YAG. In: *Ceramic Engineering and Science Proceedings*, vol. 25 (eds. E. Lara-Curzio and M.J. Ready), 147–152. Westerville, OH: American Ceramic Society.

L10 Lee, H.D., Mah, T.I., Parthasarathy, T.A., and Keller, K.A. (2006). Yttrium aluminum garnet powders and processing. US Patent 7, 022, 262, 4 April 2006.

L11 Lee, H.S., Kochawattana, S., and Messing, G.L. (2006). Solid-state reactive sintering of transparent polycrystalline Nd:YAG ceramics. *J. Am. Ceram. Soc.* **89**: 1945–1950.

L12 Lee, H.S., Kupp, E.R., Stevenson, A.J. et al. (2009). Hot isostatic pressing of transparent Nd:YAG ceramics. *J. Am. Ceram. Soc.* **92**: 1456–1463.

L13 Lee, P.Y., Suematsu, H., Yano, T., and Yatsui, K. (2006). Synthesis and characterization of nanocrystalline spinel by polymerized complex method. *J. Nanopart. Res.* **8**: 911–917.

L14 Lee, Y.K., Lee, J.S., Heo, J. et al. (2012). Phosphor in glasses with Pb-free silicate powders as robust color-converting materials for white LED applications. *Opt. Lett.* **37**: 3276–3278.

L15 Lefever, R.A. and Matsko, J. (1967). Transparent yttrium oxide ceramics. *Mater. Res. Bull.* **2**: 865–869.

L16 Lehovec, K., Accardo, C.A., and Jamgochian, E. (1951). Injected light emission of silicon carbide crystals. *Phys. Rev.* **83**: 603–607.

L17 Leipold, M.H. and Nielsen, T.H. (1968). Fabrication and characterization of isostatically hot-pressed MgO. *J. Am. Ceram. Soc.* **51**: 94–97.

L18 Lepovka, D., Batarjav, A., Samuneva, B. et al. (1991). Preparation and properties of spinel by sol–gel technology. *J. Mater. Sci.* **26**: 4861–4864.

L19 Levin, E.M., McMurdie, H.F., and Hall, F.P. (1956). *Phase Diagrams for Ceramists*. Columbus, OH: American Ceramic Society.

L20 Li, F. and Pan, J. (2013). Modelling "nano-effects" in sintering. In: *Sintering: Mechanisms of Convention Nano Densification and Field Assisted Processes* (eds. R.H.R. Castro and K. van Benthem). Berlin Heidelberg: Springer-Verlag.

L21 Li, J.-G., Ikegami, T., and Mori, T. (2005). Fabrication of transparent, sintered Sc_2O_3 ceramics. *J. Am. Ceram. Soc.* **88**: 817–821.

L22 Li, J.-G., Ikegami, T., Lee, J.H. et al. (2000). Fabrication of YAG powders by coprecipitation using NH_4HCO_3 as a precipitant. *J. Eur. Ceram. Soc.* **20**: 2395–2399.

L23 Li, J., Pan, Y., Qiu, F. et al. (2008). Nanostructured Nd:YAG powders via gel combustion: the influence of citrate-to-nitrate ration. *Ceram. Int.* **34**: 141–149.

L24 Li, J., Wu, Y., Pan, Y., and Guo, J. (2006). Fabrication of Cr^{4+},Nd^{3+}:YAG transparent ceramics for self-Q-switched laser. *J. Non-Cryst. Solids* **352**: 2404–2407.

L25 Li, J., Wu, Y., Pan, Y. et al. (2008). Solid-state-reactive fabrication of Cr,Nd:YAG transparent ceramics: the influence of raw material. *J. Ceram. Soc. Jpn.* **116**: 572–577.

L26 Li, K.K. and Wang, Q. (2004). Electro-optic ceramic material and device. US Patent 6, 746, 618, 8 June 2004.

L27 Li, K., Wang, H., Wang, W. et al. (2017). Mn^{2+} activated MgAlON transparent ceramic: a new green-emitting transparent ceramic phosphor for high-power LEDs. *J. Eur. Ceram. Soc.* **37**: 4229–4233.

L28 Li, L., Connors, J.M., Kolle, M. et al. (2015). Multifunctionality of chiton biomineralized armor with an integrated visual system. *Science* **350**: 952–956.

L29 Lin, C.C. and Liu, R.S. (2011). Advances in phosphors for light-emitting diodes. *J. Phys. Chem. Lett.* **2**: 1268–1277.

L30 Lin, H., Zhou, S., and Teng, H. (2011). Synthesis of $Tb_3Al_5O_{12}$ (TAG) transparent ceramics for potential magneto-optical applications. *Opt. Mater.* **33**: 1833–1836.

L31 Liu, J., Shen, Z., Yao, W. et al. (2010). Visible and infrared transparency in lead-free bulk $BaTiO_3$ and $SrTiO_3$ nanoceramics. *Nanotechnology* **21**: 075706/1–5.

L32 Liu, Q., Yang, H.Q., Zhao, G., and Lu, S. (2014). Titanium effect on the thermoluminiscence and optically stimulated luminescence of Ti,Mg:alpha-Al_2O_3 transparent ceramics. *J. Alloys Compd.* **582**: 754–758.

L33 Liu, Q., Yang, H.Q., Zhao, G.G. et al. (2013). The thermoluminiscence and optically stimulated luminescence of Cr-doped alpha alumina transparent ceramics. *J. Alloys Compd.* **579**: 259–262.

L34 Liu, X., Wang, H., Tu, B. et al. (2014). Highly transparent $Mg_{0.27}Al_{2.58}O_{3.73}N_{0.27}$ ceramic prepared by pressureless sintering. *J. Am. Ceram. Soc.* **97**: 63–66.

L35 Liu, Z., Mei, B., Song, J., and Li, W. (2014). Fabrication and optical characterization of Yb,Er codoped CaF_2 transparent ceramic. *J. Eur. Ceram. Soc.* **34–43**: 4389–4394.

L36 Li, W., Huang, H., Mei, B., and Song, J. (2018). Synthesis of highly sinterable Yb: SrF_2 nanopowders for transparent ceramics. *Opt. Mater.* **75**: 7–12.

L37 Li, X., Liu, H., Wang, J. et al. (2004). Production of nanosized YAG powders with spherical morphology and nonaggregation via a solvothermal method. *J. Am. Ceram. Soc.* **87**: 2288–2290.

L38 López-Puente, J., Arias, A., Zaera, R., and Navarro, C. (2005). The effect of the thickness of the adhesive layer on the ballistic limit of ceramic/metal armours - an experimental and numerical study. *Int. J. Impact Eng.* **32**: 321–336.

L39 Londono, F.A., Eiras, J.A., and Garcia, D. (2011). New transparent ferroelectric ceramics with high electro-optical coefficients: PLMN-PT. *Ceramica* **57**: 404–408.

L40 Longuet, L., Bravo, A.C., Autissier, D. et al. (2009). Preparation of Yb-doped Sc_2O_3 transparent ceramics for laser applications. *Mater. Res. Soc. Symp. Proc.* **1111**: https://doi.org/10.1557/proc-1111-d01-06.

L41 Lotgering, F.K. (1959). Topotactical reactions with ferromagnetic oxides having hexagonal crystal structure-I. *J. Inorg. Nucl. Chem.* **9**: 113–123.

L42 Low, W. (1960). Paramagnetic resonance in solids. In: *Solid-State Physics 2: Supplement* (eds. F. Seitz and D. Turnbull). New York and London: Academic Press.

L43 Lu, B., Wang, Y., Sun, X.D., and Sun, T. (2012). Synthesis of Sc_2O_3 nanopowders and fabrication of transparent, two-stepnsintere scandia ceramics. *Adv. Appl. Ceram.* **111**: 389–392.

L44 Lucca, A., Debourg, G., Jacquemet, M. et al. (2004). High-power diode-pumped Yb^{3+}:CaF_2 femtosecond laser. *Opt. Lett.* **29**: 2767–2769.

L45 Ludekens, W.L. and Welch, A.J. (1952). Reactions between metal oxides and fluorides: some new double-fluoride structures of type ABF_3. *Acta Crystallogr.* **5**: 841.

L46 Lu, G., Mei, B., Song, J. et al. (2014). Fabrication and properties of highly transparent Nd-doped CaF_2 ceramics. *Mater. Lett.* **115**: 162–164.

L47 Lu, J., Bisson, J.F., Takaichi, K. et al. (2003). Yb^{3+}:Sc_2O_3 ceramic laser. *Appl. Phys. Lett.* **83**: 1101–1103.

L48 Lu, J., Murai, T., Takaichi, T. et al. (2001). Nd^{3+}:Y_2O_3 ceramic laser. *Jpn. J. Appl. Phys.* **40**: L1277–L1279.

L49 Lu, J., Murai, T., Takaichi, K. et al. (2001). 72 W Nd:YAG ceramic laser. *Appl. Phys. Lett.* **78**: 3586–3588.

L50 Lu, J., Prabhu, M., Song, J. et al. (2000). Optical properties and highly efficient laser oscillation of Nd:YAG ceramics. *Appl. Phys. B* **71**: 469–473.

L51 Lu, J., Song, J., Prabhu, M. et al. (2000). High-power Nd:YAG ceramic laser. *Jpn. J. Appl. Phys.* **39**: L1048–L1050.

L52 Lu, J., Takaichi, K., Uematsu, T. et al. (2002). Promising ceramic laser material: highly transparent Nd^{3+}:Lu_2O_3 ceramic. *Appl. Phys. Lett.* **81**: 4324–4326.

L53 Lu, J., Ueda, K., Yagi, H. et al. (2002). Neodymium doped YAG nanocrystalline ceramics – a new generation of solid state laser and optical materials. *J. Alloys Compd.* **341**: 220–225.

L54 Lundberg, P., Renström, R., and Andersson, O. (2013). Influence of length scale on the transition from interface defeat to penetration in unconfined ceramic targets. *J. Appl. Mech.* **80**: 031804, 1–9.

L55 Lungu, S. and Popescu, H. (1954). Ceramics produced by controlled crystallization of silicate melts. *Light. Ind. (Romania)* **4**: 26–27.

L56 Lu, X., Jiang, B., Li, J. et al. (2013). Synthesis of highly sinterable Yb:Sc_2O_3 nanopowders for transparent ceramic. *Ceram. Int.* **39**: 4695–4700.

L57 Lu, Y.H., Zheng, J.J., Golomb, M.C. et al. (1999). In-plane electro-optic anisotropy of PMN-PT thin films grown on (100)-cut $LaAlO_3$. *Appl. Phys. Lett.* **74**: 3764–3766.

L58 Luo, D., Zhang, J., Xu, C. et al. (2013). Mode-locked Yb:LuAG ceramics laser. *Phys. Status Solidi C* **10**: 967–968.

L59 Lupei, A., Lupei, V., Petraru, A., and Petrache, M. (1998). Energy transfer processes in Cr^{3+}, Nd^{3+}:YAG. *Proceedings of SPIE 3405*, pp. 587–595.

L60 Lupei, V. (2009). Ceramic laser materials and the prospect for high power lasers. *Opt. Mater.* **31**: 701–706.

L61 Lupei, V. (2003). Efficiency enhancement and power scaling of Nd lasers. *Opt. Mater.* **24**: 353–368.

L62 Lupei, V., Lupei, A., and Ikesue, A. (2005). Transparent Nd and (Nd, Yb)-doped Sc_2O_3 ceramics as potential new laser materials. *Appl. Phys. Lett.* **86**: 111118/1–3.

L63 Lupei, V., Lupei, A., Ikesue, A. et al. (2009). Energy transfer–driven infrared emission processes in rare earth-doped Sc_2O_3 ceramics. *J. Lumin.* **129**: 1862–1865.

L64 Lupei, V., Lupei, A., and Ikesue, A. (2004). Single crystal and transparent ceramic Nd-doped oxide laser materials: a comparative spectroscopic investigation. *J. Alloys Compd.* **380**: 61–70.

L65 Lupei, V., Lupei, A., Ionita-Manzatu, V. et al. (1983). Combined mechanical-color center passive Q-switching of neodymium laser. *Opt. Commun.* **48**: 203–206.

L66 Lupei, V., Lupei, A., and Ikesue, A. (2007). High resolution spectroscopic properties and emission decay of rare-earth doped transparent laser ceramics. *Phys. Status Solidi C* **4**: 1376–1379.

L67 Lupei, V., Lupei, A., and Ikesue, A. (2008). Transparent ceramic laser materials. *Opt. Mater.* **130**: 1781–1786.

L68 Lyberis, A., Patriarche, G., Gredin, P. et al. (2011). Origin of light scattering in ytterbium doped calcium fluoride transparent ceramic for high power lasers. *J. Eur. Ceram. Soc.* **31**: 1619–1630.

L69 Lyberis, A., Stevenson, A.J., Suganuma, A. et al. (2012). Effect of Yb^{3+} concentration on optical properties of Yb:CaF_2 transparent ceramics. *Opt. Mater.* **34**: 965–968.

M

M1 Ma, B., Zhang, W., Wang, Y. et al. (2018). Hot isostatic pressing of MgAlON transparent ceramic from carbothermal powder. *Ceram. Int.* **44**: 4512–4515.

M2 Macfarlane, A. and Martin, G. (2002). *Glass, A World History*. University of Chicago Press.

M3 Ma, C., Li, X., Liu, S. et al. (2015). Fabrication of Lu_2O_3: Eu transparent ceramics using powder consisting of mono-disperse spheres. *Ceram. Int.* **41**: 9577–9584.

M4 Ma, C., Tang, F., Wen, Z. et al. (2015). Comparative investigation on Yb:YAG and Yb:LuAG transparent laser ceramics. *Ceram. Int.* **41**: 14635–14640.

M5 Maguire, E.A. and Gentilman, R.L. (1981). Press forging small domes of spinel. *Bull. Am. Ceram. Soc.* **60**: 255–256.

M6 Maiman, T.H. (1960). Stimulated optical radiation in ruby. *Nature* **187**: 493–494.

M7 Maitre, A., Salle, C., Boulesteix, R. et al. (2008). Effect of silica on the reactive sintering of polycrystalline Nd:YAG ceramics. *J. Am. Ceram. Soc.* **91**: 406–413.

M8 Malinowski, M., Szczepanski, P., Wolinski, R. et al. (1993). Inhomogeneity studies of Pr^{3+}-doped YAG using time-resolved spectroscopy. *J. Phys. Condens. Matter* **5**: 6469–6482.

M9 Malyarevich, A.M. and Yumashev, K.V. (2009). Saturable absorbers based on tetrahedrally coordinated transition-metal ions in crystals (Review). *J. Appl. Spectrosc.* **76**: 1–43.

M10 Malyarevich, A.M., Denisov, I.A., Yumashev, K.V. et al. (1998). V:YAG – a new passive Q-switch for diode-pumped solid-state lasers. *Appl. Phys. B* **67**: 555–558.

M11 Mandl, A. and Klimek, D.E. (2010). Textron's J-HPSSL 100 kW ThinZag® laser program. *Comm. at Conference on Lasers and Electro-Optics*, OSA Technical digest, paper JThH2.

M12 Mao, W., Qi, G., Hong, Q., and Xu, D. (2002). Objective lens used in multi-wavelength, multi-layer and multi-level optical storage. *Proceedings of SPIE 4930*, pp. 489–492.

M13 Marcilly, C., Courty, P., and Delmon, B. (1970). Preparation of highly dispersed mixed oxides and oxide solid solutions by pyrolysis of amorphous organic precursors. *J. Am. Ceram. Soc.* **53**: 56–57.

M14 Marin, R., Sponchia, G., Riello, P. et al. (2012). Photoluminescence properties of YAG:Ce^{3+}, Pr^{3+} phosphors synthesized via the Pechini method for white LEDs. *J. Nanopart. Res.* **14**: 886–899.

M15 Marsella, L. and Fiorentini, V. (2004). Structure and stability of rare-earth and transition metal oxides. *Phys. Rev.* **69**: 172103/1–4.

M16 Mata-Osoro, G., Moya, J.S., and Pecharroman, C. (2012). Transparent alumina by vacuum sintering. *J. Eur. Ceram. Soc.* **32**: 2925–2933.

M17 Matsuda, S. (1987). Production of ultrahigh purity magnesia powder. Jpn. Patent 1, 405, 552, March 1987.

M18 Matsuzawa, S. and Mase, S. (1982). Method for producing a single crystal of ferrite. US Patent 4, 339, 301, 13 July 1982.

M19 Mayseless, M., Goldsmith, W., Virostek, S.P., and Finnegan, S.A. (1987). Impact on ceramic targets. *J. Appl. Mech.* **54**: 373–378.

M20 Mazdiyasni, K.S., Lynch, C.T., and Smith, J.S. (1967). Cubic phase stabilization of translucent yttria-zirconia at very low temperatures. *J. Am. Ceram. Soc.* **50**: 532–537.

M21 McCauley, J.W. and Corbin, N.D. (1979). Phase relations and reaction sintering of transparent cubic aluminum oxynitride spinel (AlON). *J. Am. Ceram. Soc.* **62**: 476–479.

M22 McCauley, J.W. and Patel, P. (2013). Evaluation of IKTS Transparent Polycrystalline Spinel for Armor and IR Dome/Window Applications. *Rep. Army Res. Lab. (Aberdeen) ARL-SR-262*, pp. 1–162.

M23 McCauwley, J.W., Patel, P., Chen, M. et al. (2009). AlON: a brief history of its emergence and evolution. *J. Eur. Ceram. Soc.* **29**: 223–226.

M24 McHenry, D.A., Giniewicz, J.R., Jang, S.J. et al. (1989). Optical properties of hot-pressed relaxor ferroelectrics. *Ferroelectrics* **93**: 351–359.

M25 McHenry, D.A., Giniewicz, J.R., Shrout, T.R. et al. (1990). Electrical and optical properties of relaxor ferroelectrics. *Ferroelectrics* **102**: 161–171.

M26 McKittrick, J. and Shea-Rohwer, L.E. (2014). Review: down conversion materials for solid-state lighting. *J. Am. Ceram. Soc.* **97**: 1327–1352.

M27 (a) McMillan, P.W. (1974). *Glass Ceramics*. London: Academic Press. (b) Uhlman, D.R. (1971). *Advances and in Nucleation and Crystalization*, 91. Westerville, OH: ACerS.

M28 Medvedeva, J.E. and Freeman, A.J. (2004). Hopping versus bulk conductivity in transparent oxides: 12 CaO7Al_2O_3. *Appl. Phys. Lett.* **85**: 955–957.

M29 Mei, L., He, G., Wang, L.-L. et al. (2011). Fabrication of transparent $LaAlO_3$/t-ZrO_2 nanoceramics through controlled crystallization. *J. Eur. Ceram. Soc.* **31**: 1603–1609.

M30 Mie, G. (1908). Beitrage zur Optik Truber Medien, speziell kolloidaler Metallosungen. *Ann. Phys.* **330**: 377–445.

M31 Mikhailov, V.P., Kuleshov, N.V., Zhavoronkov, N.I. et al. (1993). Optical absorption and nonlinear transmission of tetrahedral V^{3+} (d^2) in yttrium aluminum garnet. *Opt. Mater.* **2**: 267–272.

M32 Miles, P. (1976). High transparency infrared materials - a technology update. *Opt. Eng.* **15**: 451–459.

M33 Milles, G.D., Sambell, R.A.J., Rutherford, J., and Stephenson, G. (1967). Fabrication of fully dense transparent polycrystalline magnesia. *Proc. Br. Ceram. Soc.* **66**: 319–335.

M34 Mirov, S.B., Fedorov, V.V., Martyshkin, D.V. et al. (2011). Progress in mid-IR Cr^{2+} and Fe^{2+} doped II-VI materials and lasers. *Opt. Mater. Express* **1**: 898–910.

M35 Mirov, S.B., Moskalev, L.S., Mirov, M.S. et al. (2018). Mid-infrared transition metal doped chalcogenide ceramic gain materials end lasers. *Proceedings of LCS14*, Okazaki, Japan (26–30 November 2018).

M36 Misawa, T., Moriyoshi, Y., Yajima, Y. et al. (1999). Effect of silica and boron oxide on transparency of Magnesia ceramics. *J. Ceram. Soc. Jpn.* **107**: 343–348.

M37 Mollart, T.P., Wort, C.J.H., Pickles, C.S.J. et al. (2001). CVD diamond optical components, multispectral properties, and performance at elevated temperatures. In: *Proceedings of SPIE 4375* (ed. R.W. Tustison), 180–198. Bellingham, WA: SPIE Publications.

M38 Mortier, M., Monteville, A., and Auzel, F. (2001). Progress in transparent rare-earth doped glass-ceramics. *Opt. Mater.* **16**: 255–267.
M39 Moulson, T. and Herbert, J. (1990). *Electroceramics: Materials, Properties, Applications*, 1e. Springer.
M40 Moulton, P.F. (1986). Spectroscopic and laser characteristics of Ti:Al_2O_3. *J. Opt. Soc. Am. B* **3**: 125–133.
M41 Mourou, G.A., Fisch, N.J., Malkin, V.M. et al. (2012). Exawatt-Zettawatt pulse generation and applications. *Opt. Commun.* **285**: 720–724.
M42 Muche, D., Drazin, J.W., and Castro, R.H. (2017). Colossal grain-boundary strengthening in ultra-fine nano crystalline oxides. *Mater. Lett.* **186**: 298–300.
M43 Mueller-Mach, R., Mueller, G.O., Krames, M.R. et al. (2009). All-nitride monochromatic amber-emitting phosphor-converted light-emitting diodes. *Phys. Status Solidi RRL* **3**: 215–217.
M44 Mulder, C.A.M. and de With, G. (1985). Translucent $Y_3Al_5O_{12}$ ceramics: electron microscopy characterization. *Solid State Ionics* **16**: 81–86.
M45 Muller, A.M. and Green, D.J. (2011). Elastic–plastic indentation response of two transparent fine-grained polycrystalline spinels. *J. Am. Ceram. Soc.* **94**: 3967–3975.
M46 Muller, G. and Neuroth, N. (1973). Glassceramic-a new laser host material. *J. Appl. Phys.* **44**: 2315–2318.

N

N1 Nagle, D., PaiVerneker, V.R., Petelin, A.N., and Groff, G. (1989). Optical absorption of electrolytically colored single crystals of yttria-stabilized zirconia. *Mater. Res. Bull.* **24**: 619–623.
N2 Nakamura, S. (2010). High-power and high efficiency Yb:YAG ceramic laser at room temperature. In: *Frontiers in Guided Wave Optics and Optoelectronics* (ed. B. Pal), 514–528. Zagreb: INTECH-OPEN Publishers.
N3 Nakamura, S., Matsubara, Y., Ogawa, T., and Wada, S. (2008). High-power high-efficiency Yb^{3+}-doped YAG ceramic laser at room temperature. *Jpn. J. Appl. Phys.* **47**: 2149–2151.
N4 Nakao, H., Inagaki, T., Shirakawa, A. et al. (2014). Yb^{3+}-doped ceramic thin-disk lasers of Lu-based oxides. *Opt. Mater. Express* **4**: 2116–2121.
N5 Nakao, H., Shirakawa, A., Ueda, K.-I. et al. (2012). CW and mode-locked operation of Yb^{3+} doped LuAG ceramic laser. *Opt. Express* **20**: 15385–15391.
N6 Nakielska, M., Kosko, J., Sarnecki, J. et al. (2008). Fluorescence properties in the visible of highly Pr^{3+} doped YAG planar waveguides. *Opt. Mater.* **30**: 759–762.
N7 Nam, J.C., Bae, I.-J., and Baik, S. (1998). Origin and control of abnormal grain growth in alumina. In: *Ceramic Microstructures Control at the Atomic Level* (eds. A.P. Tomsia and A.M. Glaeser), 323–329. New York: Plenum Press.
N8 Moore, C.E. and National Bureau of Standards (eds.) (1952). *Atomic Energy Levels*. NBS, reissued December 1971.
N9 Nedilko, S.G., Rybak, Y.O., Voznyy, V.L. et al. (2015). Development, spectral properties and lasing of the 1-4 at.% Nd^{3+} doped YAG ceramics. *Physics Procedia* **76**: 138–144.
N10 Nishiura, S. and Tanabe, S. (2008). Preparation and optical properties of Eu^{2+} and Sm^{3+} co-doped glass ceramic phosphors emitting white color by violet laser excitation. *J. Ceram. Soc. Jpn.* **116**: 1096–1099.
N11 Nishiyama, N., Ishikawa, R., Ohfuji, H. et al. (2017). Transparent polycrystalline cubic silicon nitride. *Sci. Rep.* **7**: 1–6, Article no. 44755.

O

O1 Oldfather, W.A. (1920). A note on the etymology of the word "ceramic". *J. Am. Ceram. Soc.* **3**: 537–542.
O2 Omatete, O.O., Janney, M., and Strehlow, R.A. (1991). Gelcasting: a new ceramic forming process. *Am. Ceram. Soc. Bull.* **70**: 33–41.
O3 Orgel, L.E. (1955). Electronic structures of transition-metal complexes. *J. Chem. Phys.* **23**: 1819–1823.
O4 van Orman, J.A. and Crispin, K.L. (2010). Diffusion in oxides. *Rev. Mineral. Geochem.* **72**: 757–825.
O5 Osipov, V.V., Shitov, V.A., Solomonov, V.I. et al. (2015). Composite Nd:YAG/Cr^{4+}:YAG transparent ceramics for thin disk lasers. *Ceram. Int.* **41**: 13277–13280.
O6 Osipov, V.V., Solomonov, V.I., and Konev, S.F. (2013). Trivalent zirconium and hafnium ions in yttria-based transparent ceramics. *Tech. Phys. Lett.* **39**: 377–9 (translation from Russian).

P

P1 Pai-Verneker, V.R., Petelin, A.N., Crowne, F.J., and Nagle, D.C. (1989). Color-center-induced band-gap shift in yttria-stabilized zirconia. *Phys. Rev. B* **40**: 8555–8557.
P2 Palmero, P., Simone, A., Esnouf, C. et al. (2006). Comparison among different sintering routes for preparing alumina-YAG nanocomposites. *J. Eur. Ceram. Soc.* **26**: 941–947.
P3 Palmour, H. III (1972). Development of Spinel for Transparent Armor Applications. *AMMRC-CTR 72-4, Final report of contract DAAG 46-69-C-0097*, from NCU, Raleigh, NC, October 1970, March 1972.

P4 Pan, J. (2013). Modelling sintering at different length scales. *Int. Mater. Rev.* **48**: 69–85.

P5 Panneerselvam, M., Subanna, G.N., and Rao, K.J. (2001). Translucent YAG: MW assisted route to synthesis and processing. *J. Mater. Res.* **16**: 2773–2776.

P6 Pantelyeva, I.F., Sakharov, V.V., Smolya, A.V. et al. (1977). USSR Patent 5642910.

P7 Pan, Y., Wu, M., and Su, Q. (2004). Tailored luminescence of YAG:Ce phosphor through various methods. *J. Phys. Chem. Solids* **65**: 845–850.

P8 Pan, Z., Li, W., Xu, Y. et al. (2016). Structure and red shift of Ce^{3+} emission in anisotropically expanded garnet phosphor $MgY_2Al_4SiO_{12}:Ce^{3+}$. *RSC Adv.* **6**: 20458–20466.

P9 Parish, M.V. and Pascucci, M.R. (2009). Polycrystalline alumina for aerodynamic IR domes and windows. *Proceedings of SPIE 7302*, pp. 32–40.

P10 Partdrige, G. and Phillips, S.V. (1991). A review of transparency in glass-ceramics. *Glass Technol.* **32**: 82–90.

P11 Patek, K. (1970). *Glass Lasers*. London: Butterworth.

P12 Patel, P.J., Hsieh, A.J., and Gilde, G.A. (2005). Improved Low-Cost Multi-Hit Transparent Armor. *Rep. Army Res. Lab(Aberdeen) ARL-TR-3155*, pp. 1–29.

P13 Patel, P.J., Swab, J.J., Staley, M. et al. (2006). Indentation Size Effect (ISE) of Transparent AlON and $MgAl_2O_4$. ARL-TR-3852, Aberdeen, MD.

P14 Paul, A. (1982). *Chemistry of Glasses*. Berlin: Springer-Verlag.

P15 Paulick, L., Yu, Y.F., and Tai, I.M. (1987). Ceramic powders derived from metal alkoxides precursors. In: *Advances in Ceramics (Conf. Proc. Series)*, vol. 21 (eds. G.L. Messing, J.W. McCauley, K.S. Mazdiasny and R.A. Haber), 121–129. Westerville, OH: American Ceramic Society.

P16 Pavel, N., Tsunekane, M., and Taira, T. (2011). Composite, all-ceramics, high-peak power Nd:YAG/YAG monolithic micro-laser with multiple-beam output for engine ignition. *Opt. Express* **19**: 9378–9384.

P17 Payne, S.A., DeLoach, L.D., Smith, L.K. et al. (1994). Ytterbium-doped apatite-structure crystals: a new class of laser materials. *J. Appl. Phys.* **76**: 497–503.

P18 Pechenik, A., Piermarini, G.J., and Danforth, S.C. (1992). Fabrication of transparent silicon nitride from nanosize particles. *J. Am. Ceram. Soc.* **75**: 3283–3288.

P19 Peelen, J.G.J. and Metselaar, R. (1974). Light scattering by pores in polycrystalline materials: transmission properties of alumina. *J. Appl. Phys.* **45**: 216–220.

P20 Peelen, J.G.J. (1975). Influence of MgO on the evolution of the microstructure of alumina. In: *Sintering and Catalysis*, Materials Science Research, vol. 10 (ed. G.C. Kuczynski), 443–453. Boston, MA: Springer.

P21 Penilla, E., Kodera, Y., and Garay, J.E. (2013). Blue-green emission in Tb doped alumina transparent ceramics. *Adv. Funct. Mater.* **23**: 6036–6043.

P22 Peters, R., Krankel, C., Petermann, K., and Huber, G. (2007). Broadly tunable high-power $Yb:Lu_2O_3$ thin disk laser with 80% slope efficiency. *Opt. Express* **15**: 7075–7082.

P23 Peters, R., Krankel, C., Petermann, K., and Huber, G. (2008). Crystal growth by the heat exchanger method spectroscopic characterization and laser operation of high-purity $Yb:Lu_2O_3$. *J. Cryst. Growth* **310**: 1934–1938.

P24 Petit, V., Camy, P., Doualan, J.-L. et al. Spectroscopy of $Yb^{3+}:CaF_2$: from isolated centers to clusters. *Phys. Rev. B* **78**: 085131/1–7.

P25 Petzoldt, J. (1967). Metastabile Mischkristalle mit Quartzstruktur im Oxidsystem Li_2O-MgO-ZnO-Al_2O_3-SiO_2. *Glastechn. Ber.* **40**: 385–396.

P26 Peuchert, U., Okano, Y., Menke, Y. et al. (2009). Transparent cubic-ZrO_2 ceramics for application as optical lenses. *J. Eur. Ceram. Soc.* **29**: 283–291.

P27 Peuchert, U. and Mencke, Y. (2012). Active optoceramics with cubic crystal structure. US Patent 8, 197, 711, June 2012.

P28 Pham-Gia, K., Rossner, W., Wessler, B. et al. (2006). Rapid prototyping of high-density alumina ceramics using stereolithography. *CFI/Ber. DKG* **83**: 36–40.

P29 Pinckney, L.R. and Beall, G.H. (2008). Microstructural evolution in some silicate glass-ceramics: a review. *J. Am. Ceram. Soc.* **91**: 773–779.

P30 Pinckney, L.R. Zhang, J.Z.J., and Cline, C.F. (2011). Transparent glass-ceramic armor. US Patent 7, 875, 565 B1, 25 January 2011.

P31 Pirri, A., Toci, G., Ciofini, M. et al. (2014). Thermal lens measurements in Yb-doped YAG, LuAG, Lu_2O_3, Sc_2O_3 ceramic lasers. *J. Phys. Conf. Ser.* **497**: 012013/1-5.

P32 Podowitz, S.R., Gaume, R.M., Hong, W.T. et al. (2010). Fabrication and properties of translucent SrI_2 scintillator ceramics. *IEEE Trans. Nucl. Sci.* **57**: 3827–3835.

P33 Prochazka, S. and Klug, F.J. (1983). Infrared-transparent mullite ceramic. *J. Am. Ceram. Soc.* **66**: 874–888.

P34 Pytel, K., Suchanicz, J., Livinsh, M., and Sternberg, A. (2013). Dielectric properties of PLZT-x/65/35 ($2 \leq x \leq 13$) under mechanical stress, electric field and temperature loading. *Condens. Matter Phys.* **16**: 31706/1–10.

Q

Q1 Quimby, R.S., Tick, P.A., Borelli, N.F., and Cornelius, L.K. (1998). Quantum efficiency of Pr^{3+} doped transparent glass ceramics. *J. Appl. Phys.* **83**: 1649–1653.

R

R1 Rabinovich, E.M. (1988). Particulate silica gels and glasses from the sol–gel process. In: *Sol–Gel Technology for Thin Films, Fibers, Preforms, Electronics and Specialty Shapes* (ed. L.C. Klein), 258–276. Elsevier.

R2 Rabinovitch, Y., Tetard, D., Faucher, M.D., and Pham-Thi, M. (2003). Transparent polycrystalline neodymium doped YAG: synthesis parameters, laser efficiency. *Opt. Mater.* **24**: 345–351.

R3 Racah, G. (1942). Theory of complex spectra. I. *Phys. Rev.* **61**: 186–197; (1942). II. *Phys. Rev*. 62: 438–462; (1943). III. *Phys. Rev*. 63: 367–382.

R4 Radford, K.C. and Bratton, R.J. (1979). Zirconia electrolyte cells. *J. Mater. Sci.* **14**: 59–65.

R5 Rahaman, M.N. (2003). *Ceramic Processing and Sintering*, 2e. San Diego, CA: CRC Press.

R6 Ramirez, M.O., Wisdom, J., Li, H. et al. (2008). Three-dimensional grain boundary spectroscopy in transparent high power ceramic laser materials. *Opt. Express* **16**: 5965–5973.

R7 Ramisetty, M., Sastry, S., Goldman, L.M. et al. (2014). Transparent polycrystalline cubic spinels protect and defend. *Am. Ceram. Soc. Bull.* **92**: 20–25.

R8 Rasmussen, S.C. (2012). How glass changed the world. In: *The History and Chemistry of Glass from Antiquity to the 13th Century*. Berlin: Springer-Verlag.

R9 Rawson, H. (1967). *Inorganic Glass-Forming Systems*. London: Academic Press.

R10 Rayleigh, L. (1899). On the transmission of light through an atmosphere containing small particles in suspension, and on the origin of the blue of the sky. *Philos. Mag.* **47**: 375–384.

R11 de Reaumur, M. (1740). Memoires sur làrt de faire une nouvella especе de porcelain, Par des moyens extremement simples et faciles, ou de transformer le Verre en Porcelaine. *Mem. Acad. R. Sci.* **1739**: 370–388.

R12 Reddy, K.P.R. and Cooper, A.R. (1981). Oxygen diffusion in spinel. *J. Am. Ceram. Soc.* **64**: 368–371.

R13 Reed, J.S. (1988). *Introduction to the Principles of Ceramic Processing*. New York: Wiley.

R14 Reimanis, I. and Kleebe, H.J. (2009). A review on the sintering and microstructure development of transparent spinel. *J. Am. Ceram. Soc.* **92**: 1472–1480.

R15 Reimanis, I. and Kleebe, H.J. (2007). Reactions in the sintering of spinel doped by LiF. *Int. J. Mater. Res.* **98**: 1273–1278.

R16 Ren, L., Fu, Z., Wang, Y. et al. (2015). Fabrication of transparent mullite ceramic from powders synthesized via sol–gel process combined with pulse current heating. *Mater. Des.* **83**: 753–759.

R17 Rhodes, W.H. (1981). Agglomerate and particle size effects on sintering yttria-stabilized zirconia. *J. Am. Ceram. Soc.* **64**: 19–22.

R18 Rhodes, W.H. and Reid, J.F. (1979). Transparent yttria ceramics and method for producing same. US Patent 4, 166, 831, 4 September 1979.

R19 Rhodes, W.H. (1981). Controlled transient solid second-phase sintering of yttria. *J. Am. Ceram. Soc.* **64**: 13–19.

R20 Rhodes, W.H., Sellers, D., and Vasilos, T. (1967). Development and Evaluation of Transparent MgO. AMRA CR 67-01.

R21 Rhodes, W.H., Wang, Y., Brecher, C., and Baldoni, J.G. (2011). Loss and recovery of transparency in pressure-consolidated LuAG. *J. Am. Ceram. Soc.* **94**: 3655–3658.

R22 Rice, R.W. (2003). *Ceramic Fabrication Technology*. New York: Marcel Dekker Inc., CNC Press, 2002.

R23 Rice, R.W. (1963). Production of transparent MgO at moderate temperatures and pressures. *Am. Ceram. Soc. Bull.* **41**: 271 (Abstract of Communication, 1962).

R24 Rice, R.W., Wu, C.C., and Boichelt, F. (1994). Hardness-grain-size relations in ceramics. *J. Am. Ceram. Soc.* **77**: 2539–2553.

R25 Rigopoulos, N., O'Donnell, R.G., Oh, A., and Trigg, M.B. (2009). Investigation of the solid state solubility between aluminum oxynitride and magnesium aluminate spinels. *J. Aust. Ceram. Soc.* **45**: 35–38.

R26 Rindone, G.E. and Ryder, R.J. (1957). Phase separation induced by platinum in sodium phosphate melts. *Glass Ind.* **38**: 29–31.

R27 Robbins, D.J. (1979). The effects of crystal field and temperature on the photoluminescence excitation efficiency of Ce^{3+} in YAG. *J. Electrochem. Soc.* **126**: 1550–1555.

R28 Rosenberg, Z., Ashuach, Y., Yeshurun, Y., and Dekel, E. (2009). On the main mechanisms for defeating AP projectiles, long rods and shaped charge jets. *Int. J. Impact Eng.* **36**: 588–596.

R29 Rosenberg, Z. and Dekel, E. (2012). *Terminal Ballistics*, 226–229. Berlin & Heidelberg: Springer-Verlag.

R30 Rosenflanz, A., Frey, M., Endres, B. et al. (2004). Bulk glasses and ultrahard nanoceramics based on alumina and rare-earth oxides. *Nature* **430**: 761–764.

R31 Ross, D. and Yamaguchi, H. (2018). Nanometer scale characteristics of YAG ceramic polishing. *CIRP Ann.* **67**: 349–352.

R32 Rotschild, C. (2018). Luminiscent solar power for a low-cost base-load solar energy solution. *Proceedings LCS-14*, Okazaki, Japan (26–30 November 2018).

R33 Rousseau, D.L., Bauman, R.P., and Porto, S.P.S. (1981). Normal mode determination in crystals. *J. Raman Spectrosc.* **10**: 253–290.

R34 Roussel, N., Lallemant, L., Chane-Ching, J.Y. et al. (2013). Highly dense, transparent alpha-Al_2O_3 ceramics from ultrafine nanoparticles via a standard SPS sintering. *J. Am. Ceram. Soc.* **96**: 1039–1042.

R35 Roy, D.W., Hastert, J.L., Coubrough, L.E. et al. (1988). Transparent polycrystalline body with high ultraviolet transmittance, process for making, and application thereof. Int. Patent WO1988008829, 17 November 1988.

R36 Roy, D.W. and Hastert, J.L. (1983). Polycrystalline spinel for high temperature windows. *Ceram. Eng. Sci. Proc.* **4**: 502–509.

R37 Roy, D.W. and Stermole, F.J. (1976). Method for manufacturing a transparent ceramic body. US Patent, 3, 974, 249, August 1976.

R38 Ruan, W., Li, G., Zeng, J. et al. (2010). Large electro-optic effect in La-doped 0.75Pb($Mg_{1/3}Nb_{2/3}$)O_3-0.25$PbTiO_3$ transparent ceramic by two-stage sintering. *J. Am. Ceram. Soc.* **93**: 2128–2131.

R39 Ruff, O. and Ebert, F. (1929). Beitrage zur Keramik hochfeuerfester Stoffe I. Die Formen des Zirkondioxyds. *Z. Anorg. Allg. Chem.* **180**: 19–41.

R40 Rufner, R., Anderson, D., van Benthem, K., and Castro, R.H.R. (2013). Synthesis and sintering behavior of ultrafine magnesium aluminate spinel. *J. Am. Ceram. Soc.* **96**: 2077–2085.

R41 Ruhle, M., Claussen, N., and Heuer, A.H. (1984). Microstructural studies of Y_2O_3 containing tetragonal ZrO_2 polycrystals (Y-TZP). In: *Advances in Ceramics*, vol. 12 (eds. N. Claussen, M. Ruhle and A.H. Heuer), 352–370. American Ceramic Society.

R42 Ruhle, M., Strecker, A., Waidelich, D., and Krauss, B. (1983). In-situ observations of stress-induced phase transformations in ZrO_2-containing ceramics. In: *Advances in Ceramics*, vol. 12 (eds. N. Claussen, M. Ruhle and A.H. Heuer), 256–274.

S

S1 Sack, W. (1959). Manufacturing of crystalline bodies by sintering and devitrification of glass powder by the aid of mineralizers. In: *Beitrage Angewandte Forschung* (ed. H.F. Muller), 111–120. Stuttgart: Schott–Herausg.

S2 Sainz, M.A., Mazzoni, A.D., Aglietti, E.F., and Caballero, A. (2004). Thermochemical stability of spinel ($MgO{\cdot}Al_2O_3$) under strong reducing conditions. *Mater. Chem. Phys.* **86**: 399–408.

S3 Saito, N., Matsuda, S., and Ikegami, T. (1998). Fabrication of transparent yttria ceramics at low temperature using carbonate derived powder. *J. Am. Ceram. Soc.* **81**: 2023–2028.

S4 Sakai, H., Kan, H., and Taira, T. (2008). > 1MW peak power single-mode high-brightness passively Q-switched $Nd3^+$ YAG microchip laser. *Opt. Express* **16**: 19891–19899.

S5 Salem, J.A. (2013). Transparent armor ceramics as spacecraft windows. *J. Am. Ceram. Soc.* **95**: 281–289.

S6 Salle, C., Maiter, A., Baumard, J.F., and Rabinovitch, Y. (2007). A first approach on silica effect on the sintering of Nd:YAG. *Opt. Rev.* **14**: 169–172.

S7 Samson, B.N., Tick, P.A., and Borrelli, N.F. (2001). Efficient Nd-doped glass-ceramic fiber laser and amplifier. *Opt. Lett.* **26**: 145–147.

S8 Samuel, P.D., Jambunathan, V., Yue, F. et al. (2018). Effects of Gd^{3+}/Ga^{3+} on Yb^{3+} emission in mixed YAG at cryogenic temperatures. *Ceram. Int.* https://doi.org/10.1016/j.ceramint.2018.08.241.

S9 Sands, J.M., Fountzoulas, C.G., Gilde, G.A., and Patel, P.J. (2009). Modelling transparent ceramics to improve military armour. *J. Eur. Ceram. Soc.* **29**: 261–266.

S10 Sanghera, J., Shaw, B., Kim, W. et al. (2011). Ceramic laser materials. *Proceedings of SPIE 7912*, Q 1–14.

S11 Sato, Y., Arzakantsyan, M., Akiyamaand, J., and Taira, T. (2014). Anisotropic Yb:FAP laser ceramics by micro-domain control. *Opt. Mater. Express* **4**: 2006–2015.

S12 Sato, Y., Saikawa, J., Shoji, I. et al. (2004). Spectroscopic properties and laser operation of Nd:$Y_3ScAl_4O_{12}$ polycrystalline gain media, solid-solution of Nd:$Y_3Al_5O_{12}$ and Nd:$Y_3Sc_2Al_3O_{12}$ ceamics. *J. Ceram. Soc. Jpn.* **112**: S313–S316.

S13 Savoini, B., Ballesteros, C., Munoz-Santiuste, J.E. et al. (1988). Thermochemical reduction of yttria-stabilized-zirconia crystals: optical and electron microscopy. *Phys. Rev. B* **57**: 13439–13447.

S14 Sazonov, V.N. (1978). *Chromium in Hydrothermal Processes*. Moscow: Nauka (in Russian).

S15 Schinck, W. (2009). Shine a light with nitrides. *Phys. Status Solidi RRL* **3**: A113–A114.

S16 Schlotter, P., Schmidt, R., and Schneider, J. (1997). Luminescence conversion of blue light emitting diode. *Appl. Phys. A* **64**: 417–418.

S17 Schuster, C., Klimke, J., and Schwingenschloegl, U. (2016). High energy transmission of Al_2O_3 doped

with light transition metals. *J. Chem. Phys.* **136**: 044522, 1–4.

S18 Scott, C.E. and Levinson, L. (1996). Solid state thermal conversion of polycrystalline alumina to sapphire using a seed crystal. US Patent 5, 549, 746, August 1996.

S19 Sekita, M., Haneda, H., and Shirasaki, S. (1991). Optical spectra of undoped and rare-earth doped transparent ceramic $Y_3Al_5O_{12}$. *J. Appl. Phys.* **69**: 3709–3718.

S20 Selinger, M. (2008). Boeing fires new thin-disk laser, achieving solid-state laser milestone. http://www.boeing.com/news/releases/2008q2/080603a (accessed November 2018).

S21 Sepuleveda, J.L., Loufty, R.O., Ibrahim, S., and Bilodeau, S. (2003). Large size spinel windows and domes. *Proceedings of SPIE 8708*, 6/1–6/15.

S22 Serivalsatit, K. and Ballato, J. (2010). Submicrometer grain-sized transparent erbium-doped Scandia ceramics. *J. Am. Ceram. Soc.* **93**: 3657–3662.

S23 Serivalsatit, K., Kokuoz, B., Yazgan-Kokuoz, B. et al. (2010). Synthesis, processing and properties of submicrometer-grained highly transparent yttria ceramics. *J. Am. Ceram. Soc.* **93**: 1320–1325.

S24 Serres, J.M., Loiko, P., Mateos, X. et al. (2015). Microchip laser operationof Yb-doped gallium garnets. *Opt. Mater. Express* **6**: 46–57.

S25 Setlur, A.A. (2009). Phosphors for LED-based solid-state lighting. *Electrochem. Soc. Interface* **18**: 32–36.

S26 Seward, C.R., Coad, E.J., Pickles, C.S.J., and Field, J.E. (1994). The rain erosion resistance of diamond and other window materials. *Proceedings of SPIE 2286*, pp. 285–300.

S27 Sirota, M., Galun, E., Goldstein, A. et al. (2008). Glass ceramics for laser systems. US Patent 7, 316, 986B2, January 2008.

S28 Shannon, R.D. (1976). Revised effective ionic radii and systematic studies of interatomic distances in halides and chalcogenides. *Acta Crystallogr.* **A32**: 751–767.

S29 Shan, Y., Zhang, Z., Sun, X. et al. (2016). Fast densification mechanism of bimodal powder during pressureless sintering of transparent AlON ceramics. *J. Eur. Ceram. Soc.* **36**: 671–678.

S30 Shen, Z., Johnsson, M., Zhao, Z., and Nygren, M. (2002). Spark plasma sintering of alumina. *J. Am. Ceram. Soc.* **85**: 1921–1927.

S31 Shimony, Y., Burshtein, Z., and Kalisky, Y. (1995). Cr^{4+}:YAG as passive Q-switch and brewster plate in a pulsed Nd:YAG laser. *IEEE J. Quantum Electron.* **31**: 1738–1741.

S32 Shirakov, A., Burshtein, Z., and Ishaaya, A.A. (2017). Private communication.

S33 Shi, Y., Chen, Q.W., and Shi, J.L. (2009). Processing and scintillation properties of Eu^{3+} doped Lu_2O_3 transparent ceramics. *Opt. Mater.* **31**: 729–733.

S34 Shi, Y., Wang, Y., Wen, Y. et al. (2012). Tunable luminescence YAG:0.06Ce^{3+}, xMn^{2+} phosphors with different charge compensators for warm white light emitting diodes. *Opt. Express* **20**: 21656–21664.

S35 Shrout, T.R. and Halliyal, A. (1987). Preparation of lead-based ferroelectric relaxors for capacitors. *Bull. Am. Ceram. Soc.* **66**: 704–711.

S36 Sickafuss, K.E., Wills, J.M., and Grimes, N.W. (1999). Spinel compounds: structure and property relations. *J. Am. Ceram. Soc.* **82**: 5279–5292.

S37 Siebold, M., Loeser, M., Roeser, F. et al. (2012). High energy, ceramic disk Yb: LuAG laser amplifier. *Opt. Express* **2**: 21992–22000.

S38 Slamovich, E.B. and Lange, F.F. (1992). Densification of large pores: I, Experiments. *J. Am. Ceram. Soc.* **75**: 2498–2508.

S39 Slamovich, E.B. and Lange, F.F. (1993). Densification of large pores: II, Driving potentials and kinetics. *J. Am. Ceram. Soc.* **76**: 1584–1590.

S40 Sokol, M., Halabi, M., Mordekowitz, Y. et al. (2017). An inverse Hall-Petch relation in nannocrystalline spinel consolidated by high pressure SPS. *Scr. Mater.* **139**: 159–161.

S41 Snitzer, E. and Woodcok, R. (1965). Yb^{3+}-Er^{3+} glass laser. *Appl. Phys. Lett.* **6**: 45–46.

S42 Soni, K.K. (1995). Solute segregation to grain boundaries in MgO-doped alumina. *Appl. Phys. Lett.* **66**: 2795–2797.

S43 Soni, K.K., Thompson, A.M., and Harmer, M.P. (1995). SIMS studies of Ca and Mg distribution in sintered Al_2O_3. *Appl. Phys. Lett.* **66**: 2795–3004.

S44 Sordelet, D.J. and Akinc, M. (1988). Sintering of monosized, spherical yttria powders. *J. Am. Ceram. Soc.* **71**: 1148–1153.

S45 Sorokin, P.P. and Stevenson, M.J. (1960). Stimulated IR emission from trivalent uranium. *Phys. Rev. Lett.* **5**: 557–558.

S46 Spilman, J., Voyles, J., Nick, J., and Shaffer, L. (2013). Manufacturing process scale-up of optical grade transparent spinel ceramic at ArmorLine corporation. *Proceedings of SPIE 8708-7/1-6*, 10pp.

S47 Spina, G., Bonnefont, G., Palmero, P. et al. (2012). Transparent YAG obtained by spark plasma sintering of co-precipitated powder. Influence of dispersion route and sintering parameters on optical and microstructural characteristics. *J. Eur. Ceram. Soc.* **32**: 2957–2964.

S48 Srdic, V.V., Winterer, M., and Hahn, H. (2000). Sintering behavior of nanocrystalline zirconia prepared by chemical vapor synthesis. *J. Am. Ceram. Soc.* **83**: 729–736.

S49 Starobor, A., Zeleznov, D., Palashov, O. et al. (2014). Study of the properties of Ce:TAG and TGG magnetooptical ceramics for optical isolators for lasers with high average power. *Opt. Mater. Express* **4**: 2127–2132.

S50 Sternberg, A. and Krumins, A. (1990). Applications and properties of transparent ferroelectric ceramics: trends and progress. *Proceedings of 7th IEEE International Symposium on Applications of Ferroelectric*, Urbana-Champaign, pp. 631–633.

S51 Stevenson, A.J., Li, X., Martinez, M.A. et al. (2011). Effect of SiO_2 on densification and microstructure development in Nd:YAG transparent ceramics. *J. Am. Ceram. Soc.* **94**: 1380–1387.

S52 Stevenson, A.J., Serier-Brault, H., Gredin, P., and Mortier, M. (2011). Fluoride materials for optical applications: single crystals, ceramics, glasses, and glass-ceramics. *J. Fluorine Chem.* **132**: 1165–1173.

S53 Stewart, R.L. and Bradt, R.C. (1980). Fracture of single crystal $MgAl_2O_4$. *J. Mater. Sci.* **15**: 67–72.

S54 Stokes, G.G. (1852). On the change of refrangibility of light. *Philos. Trans. R. Soc. London* **142**: 463–562.

S55 Stokowski, S.S. (1986). Glass lasers (section 2.3). In: *Handbook of Laser Science and Technology, vol. I. Lasers and Masers, section 2 Solid State Lasers* (ed. M.J. Weber), 215–264. Boca Raton, FL: CRC Press.

S56 Stookey, S.D. and Maurer, R.D. (1962). Catalyzed crystallization of glass - theory and practice. In: *Progress in Ceramic Science*, vol. 2 (ed. E. Burke), 77–102. Pergamon Press.

S57 Stookey, S.D. (1959). Catalyzed crystallization of glass. *Glastechn. Ber.* **32K**: 1–8.

S58 Stookey, S.D. (1959). Catalyzed crystallization of glass in theory and practice. *Ind. Eng. Chem.* **51**: 805–808.

S59 Stookey, S.D. (1958). Nucleation. In: *Ceramic Fabrication Processes* (ed. W.D. Kingery), 189–195. New York: Wiley.

S60 Stookey, S.D. (1950). Photosensitive copper glass and method of making it. US Patent 2, 515, 938, 18 July 1950.

S61 Strassburger, E. (2009). Ballistic testing of transparent armour ceramics. *J. Eur. Ceram. Soc.* **29**: 267–273.

S62 Strassburger, E., Bauer, S., and Popko, G. (2014). Damage visualization and deformation measurement in glass laminates during projectile penetration. *Defence Technol.* **10**: 226–238.

S63 Strassburger, E., Hunzinger, M., and Krell, A. (2010). Fragmentation of ceramics under ballistic impact. In: *Proceedings of the 25th International Symposium on Ballistics* (eds. Z. Wang, X. Zhang and Y. An), 1172–1179. Beijing: China Science and Technology Press. http://jewelryinfoplace.com/swarovski-crystals/.

S64 Strassburger, E. (2004). Visualization of impact damage in ceramics using the edge-on impact technique. *Int. J. Appl. Ceram. Technol.* **1**: 235–242.

S65 Strauch, D. and Dorner, B. (1990). Phonon dispersion in GaAs. *J. Phys. Condens. Matter* **2**: 1457–1474.

S66 Strickland, D. and Mourou, G. (1985). Compression of amplified chirped optical pulses. *Opt. Commun.* **56**: 219–221.

S67 Strnad, Z. (1986). *Glass-Ceramic Materials: Liquid Phase Separation, Nucleation and Crystallization in Glasses*, Glass Science and Technology. Amsterdam: Elsevier Science.

S68 Stuer, M., Zhao, Z., and Bowen, P. (2012). Freeze granulation: powder processing for transparent alumina applications. *J. Eur. Ceram. Soc.* **32**: 2899–2908.

S69 Subbarao, E.C. (1981). Zirconia - an overview. In: *Advances in Ceramics*, vol. 3, 1–24. Westerville, OH: ACerS.

S70 Sugano, S., Tanabe, Y., and Kamimura, H. (1970). *Multiplets of Transition-Metal Ions in Crystals*. Academic Press.

S71 Summers, G.P. (1980). Radiation damage in $MgAl_2O_4$. *Phys. Rev. B* **21**: 2578–2583.

S72 Sun, W.Y., Li, X.T., Ma, L.T., and Yen, T.S. (1984). Solubility of Si in YAG. *J. Solid State Chem.* **51**: 315–320.

S73 Sun, Z., Shi, Y., Zhang, J. et al. (2018). Fabrication of transparent AlON ceramics by pressureless sintering under 1800°C. *Proceedings LCS-14*, Okazaki, Japan (26–30 November 2018).

S74 Sutton, W.H. and Johnson, W.E. (1979). Method for MW heating. US Patent 4, 140, 887, 20 February 1979.

S75 Suzuki, T.S., Sakka, Y., and Kitazawa, K. (2001). Orientation amplification of alumina by colloidal filtration in a strong magnetic field and sintering. *Adv. Eng. Mater.* **3**: 490–492.

S76 Svelto, O. and Hanna, D.C. (1997). *Principles of Lasers*. London: Plenum Press.

T

T1 Tacvorian, S. (1952). Acceleration of sintering in a single phase: consideration of mechanism of action of minor additions. *Compt. Rendue* **234**: 2363–2365.

T2 Taira, T. (2010). Anisotropic ceramics as a next generation laser. *Proceedings ILCS-6*, Munster, Germany Comm. 22, pp. 1–39.

T3 Taira, T., Tsunekane, M., Fujikawa, F. et al. (2009). Engine ignition by high brightness pulse lasers. *J. Combust. Soc. Jpn.* **51**: 288–294.

T4 Tajima, T. and Mourou, G.A. (2012). Zettawatt-exawatt lasers and their applications in ultrastrong-field physics. *Phys. Rev. Spec. Top. Accel. Beams* **5**: 031301/1–18.

T5 Takahasi, T., Tatami, J., Ijima, M. et al. (2018). Fabrication of transparent and fluorescent α-SiAlON bulk ceramics. *Proceedings LCS-14*, Okazaki, Japan (26–30 November 2018).

T6 Takahasi, Y., Benino, Y., Fujiwara, T., and Komatsu, T. (2004). Large second-order optical nonlinearities of fresnoite-type crystals in transparent surface crystallized glasses. *J. Appl. Phys.* **95**: 3503–3509.

T7 Takaichi, K., Yagi, H., Lu, J. et al. (2003). Yb^{3+}-doped YAG ceramics - a new solid-state laser material. *Phys. Status Solidi A* **200**: R5–R7.

T8 Tamman, G. (1925). *States of Aggregation*. New York: Van Nostrand and Co.

T9 Tanabe, Y. and Sugano, S. (1954). On the absorption spectra of complex ions, I. *J. Phys. Soc. Jpn.* **9**: 753–766; (1954). II. *J. Phys. Soc. Jpn.* 9: 766–779.

T10 Tanaka, H., Yamamoto, M., Takahashi, Y. et al. (2003). Crystalline phases and second harmonic intensities in potassium niobium silicate crystallized glass. *Opt. Mater.* **22**: 71–79.

T11 Tang, D.Y., Wang, J., Yin, D.L. et al. (2018). Fabrication of rare-earth doped yttria laser ceramics and their high efficiency laser operations. *Proceedings LCS-14*, Okazaki, Japan, No. 26–30 2018.

T12 Tanzilli, R.A. and Gebhardt, J.J. (1982). Optical properties of CVD silicon nitride. *Proceedings of SPIE 0297*, pp. 59–64,

T13 Tarafder, A., Annapurna, K., Chaliha, R.S. et al. (2009). Processing and properties of Eu^{3+}:$LiTaO_3$ transparent glass-ceramic nanocomposites. *J. Am. Ceram. Soc.* **92**: 1934–1939.

T14 Tarafder, A., Molla, A.R., and Karmakar, B. (2010). Processing and properties of Eu^{3+}-doped transparent YAG nano glass-ceramics. *J. Am. Ceram. Soc.* **93**: 3244–3251.

T15 Tasker, P.W., Colbourn, E.A., and Mackrodt, W.C. (1985). Segregation of isovalent impurity cations at the surfaces of MgO and CaO. *J. Am. Ceram. Soc.* **68**: 74–80.

T16 Telling, R.H., Jilbert, G.H., and Field, J.E. (1997). Erosion of aerospace materials by solid-particle impact. *Proceedings of SPIE 3060*, pp. 56–67.

T17 Ter-Gabrielyan, N., Merkle, L.D., Ikesue, A., and Dubinskii, M. (2008). Ultralow quantum-defect eye-safe Er:Sc_2O_3 laser. *Opt. Lett.* **33**: 1524–1526.

T18 Thomson, A.M., Soni, K.K., Chen, H.M. et al. (1997). Dopant distributions in rare-earth doped alumina. *J. Am. Ceram. Soc.* **80**: 373–376.

T19 Thomson, J. (1974). Chemical preparation of PLZT powders from aqueous nitrate solutions. *Bull. Am. Ceram. Soc.* **53**: 421–425.

T20 Tian, Y., Xu, B., Yu, D. et al. (2013). Ultrahard nanotwinned cubic boron nitride. *Nature* **493**: 385–388.

T21 Tien, T.Y., Gibbons, E.F., DeLoach, R.G. et al. (1973). Ce^{3+} activated $Y_3Al_5O_{12}$ and some of its solid solutions. *J. Electrochem. Soc.* **120**: 278–281.

T22 Tikhomirov, V.K., Furniss, D., Seddon, A.B. et al. (2002). Er^{3+} doped ultra-transparent oxy-fluoride glass-ceramics for application in the 1.54 micron telecommunication window. *J. Mater. Sci. Lett.* **21**: 293–295.

T23 Ting, C.J. and Lu, H.Y. (1999). Defect reactions and the controlling mechanism in the sintering of spinel. *J. Am. Ceram. Soc.* **82**: 841–848.

T24 Toda, G., Matsuyama, I., and Tsukuda, Y. (1975). Method for producing highly pure sintered polycrystalline yttrium oxide body having high transparency. US Patent 3, 873, 657, 25 March 1975.

T25 To, D., Rajesh, D., Yin, X., and Sundaresan, S. (2009). Deagglomeration of nanoparticle aggregates via rapid expansion of supercritical or high-pressure suspensions. *AlChE J.* **55**: 2807–2826.

T26 Tokurakawa, M., Shirakawa, A., Ueda, K. et al. (2009). Diode pumped ultrashort-pulse generation based on Yb^{3+}:Sc_2O_3 and Yb^{3+}:Y_2O_3 ceramic multi-gain-media oscillator. *Opt. Express* **17**: 3353–3361.

T27 Tong, X.L., Lin, K., Lv, D.J. et al. (2009). Optical properties of PMN-PT thin films prepared using pulsed laser deposition. *Appl. Surf. Sci.* **255**: 7995–7998.

T28 Tran, T., Hayu, S., Navrotsky, A., and Castro, R.H.R. (2012). Transparent nanocrystalline pure and Ca-doped MgO by SPS sintering of anhydrous nanoparticles. *J. Am. Ceram. Soc.* **95**: 1185–1188.

T29 Trunec, M. and Maca, K. (2007). Compaction and pressureless sintering of zirconia nanoparticles. *J. Am. Ceram. Soc.* **90**: 2735–2740.

T30 Tsukuma, K. (2006). Transparent spinel ceramics produced by sintering and HIP. *J. Ceram. Soc. Jpn.* **114**: 802–806.

T31 Tsukuma, K. (1986). Transparent titania-yttria-zirconia ceramics. *J. Mater. Sci. Lett.* **5**: 1143–1144.

T32 Tsur, Y., Goldring, S., Galun, E., and Katzir, A. (2016). Ground state depletion - a step towards mid-IR lasing of doped silver halides. *J. Lumin.* **175**: 113–116.

T33 Turnbull, D. (1952). Kinetics of solidification of supercooled liquid mercury droplets. *J. Chem. Phys.* **20**: 411–424.

U

U1 Uberuaga, B.P., Bacorisen, D., Smith, R. et al. (2007). Defect kinetics in spinels: long time simulations. *Phys. Rev. B* **75**: 104116-1–13.

U2 Uehara, H., Tokita, S., Kawanaka, J. et al. (2018). Optimization of laser emission at 2.8 micron by Er:Lu_2O_3 ceramics. *Opt. Express* **26**: 3497–3507.

U3 Uhlman, D.R. (1971). Effect of entropy on the growth-morphology of crystallizing glasses. In: *Advances in Nucleation and Crystallization in Glasses* (eds. L.L. Hench and S. Freiman). Westerville, OH: American Ceramic Society.

U4 Uhlman, D.R. (1970). Coallescence of second phase particles in phase separation. *Discuss. Faraday Soc.* **50**: 108–121.

U5 Upadhyay, G.K. (2008). *Solid State Physics: Lattice Dynamics of Ionic Solids*. New Delhi: Laxmi Publications Pvt. Ltd.

V

V1 Vaclavik, J. and Vapenka, D. (2013). Gallium phosphide as a material for visible and infrared optics. *EPJ Web Conf.* **48**: 00028/1–4.

V2 Vahldiek, F.W. (1967). Translucent ZrO_2 prepared at high pressures. *J. Less Common Met.* **13**: 530–540.

V3 Vandiver, P.B., Soffer, O., Klima, B., and Svoboda, J. (1989). The origins of ceramic technology at Dolni Vestonice, Czechoslovakia. *Science, New Ser.* **246**: 1002–1008.

V4 Van Vleck, J.H. (1935). The group relation between the Mulliken and Slater-Pauling theories of valence. *J. Chem. Phys.* **3**: 803–806.

V5 Vasilos, T. and Spriggs, R.M. (1963). Pressure sintering: mechanisms and microstructures for alumina and magnesia. *J. Am. Ceram. Soc.* **46**: 493–496.

V6 Veith, V., Mathur, S., Kareiva, A. et al. (1999). Low temperature synthesis of nanocrystalline YAG and Ce-doped YAG via different sol–gel methods. *J. Mater. Chem.* **9**: 3069–3079.

V7 Viechnicki, D.J., Slavin, M.J., and Kliman, M.I. (1991). Development and current status of armor ceramics. *Am. Ceram. Soc. Bull.* **70**: 1035–1039.

V8 Vocadlo, L., Wall, A., Parker, S.C., and Price, G.D. (1995). Absolute ionic diffusion in MgO-computer calculations via lattice dynamics. *Phys. Earth Planet. Inter.* **88**: 193–210.

V9 Volf, M.B. (1961). *Technical Glasses*. London: Sir Isaac Pitman and Sons.

V10 Volpato, C.A.M., Fredel, M.C., Philippi, A.G., and Petter, C.O. (2010). Ceramic materials and color in dentistry. In: *Ceramic Materials* (ed. W. Wunderlich), 155–173. InTech-Sciyo, Rijeka and Shanghai.

V11 Vrolijk, J.W.G.A., Willems, J.W.M.M., and Metselaar, R. (1990). Coprecipitation of yttrium and aluminium hydroxides for preparation of YAG. *J. Eur. Ceram. Soc.* **6**: 47–51.

W

W1 Waetzig, K., Hutzler, T., and Krell, A. (2009). Transparent spinel by reactive sintering of different alumina modifications, with MgO. *Ber. DKG* **86**: e47–e49.

W2 Wagner, N., Herden, B., Dierkes, T. et al. (2012). Towards the preparation of transparent LuAG:Nd^{3+} ceramics. *J. Eur. Ceram. Soc.* **32**: 3085–3089.

W3 Wakahara, S., Yanagida, T., Yokota, Y. et al. (2013). Phosphorescent luminescence of pure magnesium oxide transparent ceramics produced by SPS. *Opt. Mater.* **35**: 558–562.

W4 Wakeshima, M. and Hinatsu, Y. (2010). Magnetic properties and structural transitions of orthorhombic fluorite related compounds Ln_3MO_7. *J. Solid State Chem.* **183**: 2681–2688.

W5 Wakino, K., Murata, M., and Tamura, H. (1986). Far IR reflection spectra of $Ba(Zn,Ta)O_3$-$BaZrO_3$ dielectric resonator material. *J. Am. Ceram. Soc.* **69**: 34–37.

W6 Walker, E.H., Owens, J.W., Etienne, M., and Walker, D. (2002). The novel low temperature synthesis of nanocrystalline $MgAl_2O_4$ spinel using "gel" precursors. *Mater. Res. Bull.* **37**: 1041–1050.

W7 Walley, S.M. (2010). Historical review of high strain rate and shock properties of ceramics relevant to their application in armour. *Adv. Appl. Ceram.* **109**: 446–466.

W8 Wang, J., Wu, Z., Su, H. et al. (2017). 1.5 kW efficient CW Nd:YAG planar waveguide MOPA laser. *Opt. Lett.* **42**: 3149–3152.

W9 Wang, J., Zheng, S., Zeng, R. et al. (2009). MW synthesis of homogenous YAG nanopowder leading to a transparent ceramic. *J. Am. Ceram. Soc.* **92**: 1217–1223.

W10 Wang, L., Huang, H., Shen, D. et al. (2017). Diode-pumped 2.7 micron Er:Y_2O_3 ceramic laser at room temperature. *Opt. Mater.* **71**: 70–73.

W11 Wang, L., Zhang, X., Hao, Z. et al. (2010). Enriching red emission of YAG:Ce^{3+} by codoping Pr^{3+} and Cr^{3+} for improving color rendering of white LEDS. *Opt. Express* **18**: 25177–25182.

W12 Wang, Y. and Ohwaki, J. (1993). New transparent vitroceramics codoped with Er^{3+} and Yb^{3+} for efficient frequency upconversion. *Appl. Phys. Lett.* **63**: 3268–3270.

W13 Wang, Y., Lu, B., Sun, X. et al. (2011). Synthesis of nanocrystalline Sc_2O_3 powder and fabrication of

transparent Sc_2O_3 ceramics. *Adv. Appl. Ceram.* **110**: 95–98.

W14 Wang, Y., Xie, X., Qi, J. et al. (2014). Two-step preparation of AlON transparent ceramics with powder synthesized by aluminothermic reduction and nitridation method. *J. Mater. Res.* **29**: 2325–2331.

W15 Wanjun, T., Fen, Z., and Shanshan, H. (2014). Structure-composition relationships and tunable luminescence properties in Eu^{2+}-activated $Sr_8(Mg,Zn)La(PO_4)_7$ phosphors. *ECS J. Solid State Sci. Technol.* **3**: R65–R69.

W16 Wayman, C.M. (1972). Crystallographic theories of martensitic transformations. *J. Less Common Mat.* **28**: 97–105.

W17 Weber, M.J. (1967). Probabilities for radiative and nonradiative decay of Er^{3+} in LaF_3. *Phys. Rev.* **157**: 262–272.

W18 Wei, G.C. (2005). Transparent ceramic lamp envelope materials. *J. Phys. D: Appl. Phys.* **38**: 3057–3065.

W19 Weinhold, C. (2013). Lightweight transparent armor window. US Patent 8, 603, 616 B1, December 2013.

W20 Wei, Z., Huang, Y., Tsuboi, T. et al. (2012). Optical characteristics of Er^{3+}- doped PMN-PT transparent ceramics. *Ceram. Int.* **38**: 3397–3402.

W21 West, G.D., Perkins, J.M., and Lewis, M.H. (2004). Characterization of fine grained oxide ceramics. *J. Mater. Sci.* **39**: 6687–6704.

W22 Weyl, W.A. (1959). *Coloured Glasses*. London: Dawson's of Pall-Mall.

W23 White, K.W. and Kelkar, G.P. (1991). Evaluation of crack face bridging mechanism in a $MgAl_2O_4$ spinel. *J. Am. Ceram. Soc.* **74**: 1732–1734.

W24 White, K.W. and Kelkar, G.P. (1992). Fracture mechanisms of coarse-grained transparent $MgAl_2O_4$ at elevated temperatures. *J. Am. Ceram. Soc.* **75**: 3440–3444.

W25 Willems, H.X., de With, G., Meteselaar, R. et al. (1993). Neutron diffraction of γ-aluminium oxynitride. *J. Mater. Sci. Lett.* **12**: 1470–1472.

W26 Wilson, E.B., Decius, J.C., and Cross, P.C. (1955). *Molecular Vibrations: The Theory of Infrared and Raman Vibrational Spectra*. New York: McGraw-Hill.

W27 de With, C. and Dijk, H.J. (1984). Translucent YAG ceramics. *Mater. Res. Bull.* **19**: 1669–1674.

W28 Wolff, M., Classen, R. et al. (2005). Investigation on the transparent polycrystalline zirconia. *CFI/Ber. DKG* **82**: 166–169.

W29 Woodward, R.L. (1990). A simple one-dimensional approach to modelling ceramic composite armor defeat. *Int. J. Impact Eng.* **9**: 455–474.

W30 Woodward, R.L. and Baxter, B.J. (1994). Ballistic evaluation of ceramics: influence of test conditions. *Int. J. Impact Eng.* **15**: 119–124.

W31 Woodward, R.L., Gooch, W.A. Jr., O'Donnell, R.G. et al. (1994). A study of fragmentation in the ballistic impact of ceramics. *Int. J. Impact Eng.* **15**: 605–618.

W32 Wright, D.A., Thorp, J.S., Aypar, A., and Buckley, H.P. (1973). Optical absorption in current-blackened yttria-stabilized zirconia. *J. Mater. Sci.* **8**: 876–882.

W33 Wu, B., Ruan, J., Qiu, J., and Zeng, H. (2009). Enhanced broadband near-infrared luminescence from Ni in Bi/Ni-doped transparent glass ceramics. *J. Phys. D: Appl. Phys.* **42**: 135110/1–135110/5.

W34 Wu, Y., Li, J., Pan, Y. et al. (2007). Refined yttria powder and fabrication of transparent Yb,Cr:YAG ceramics. *Adv. Mater. Res.* **15–17**: 246–250.

W35 Wyckoff, R.W.G. (1963). *Crystal Structures: Miscellaneous Inorganic Compounds, Silicates, and Basic Structural Information*, vol. 4. New York: Wiley.

W36 Wyckoff, R.W.G. (1930). *The Analytical Expression of the Results of the Theory of Space Groups*. Washington, DC: Carnegie Institution Press.

X

X1 Xiao, P., Wang, X., Sun, J. et al. (2012). Simultaneous measurement of electro-optical and converse piezo-electric coefficents, of PMN-PT ceramics. *Opt. Express* **20**: 13833–13840.

X2 Xu, C.W., Luo, D.W., Zhang, J. et al. (2012). Diode pumped highly efficient Yb:LuAG ceramic laser. *Laser Phys. Lett.* **9**: 30–34.

X3 Xu, Y.-N., Gu, Z.-G., and Ching, W.Y. (1997). Electronic, structural, and optical properties of crystalline yttria. *Phys. Rev. B* **56**: 14993–15000.

X4 Xu, Z., Daga, A., and Chen, H. (2001). Microstructure and optical properties of scandium oxide thin films prepared by metalorganic chemical-vapor deposition. *Appl. Phys. Lett.* **79**: 3782–3784.

Y

Y1 Yagi, H., Takagimi, Y., and Kazumori, T. (2005). Highly transparent YAG ceramics. *Comm. at E-MRS Fall Meting, Laser Ceramic Symposium*, Boston, MA.

Y2 Yamaguchi, G. and Yanagida, H. (1959). Study on the reductive spinel - a new spinel formula $AlN\text{-}Al_2O_3$ instead of the previous one Al_3O_4. *Bull. Chem. Soc. Jpn.* **32**: 1264–1265.

Y3 Yamamoto, H., Mitsuoko, T., and Iio, S. (2007). Translucent polycrystalline ceramic and method for making same. Eur. Patent EP1053983, 12 September 2007.

Y4 Yamazawa, T., Honma, T., Suematsu, H., and Komatsu, T. (2009). Synthesis, ferroelectric and electrooptic properties of transparent crystallized glasses with $Sr_xBa_{1-x}Nb_2O_5$ nanocrystals. *J. Am. Ceram. Soc.* **92**: 2924–2930.

Y5 Yanagitani, T. and Yagi, H. (2007) Production of Tb-Gd garnets. Jap. Pat. 10101333-2007Y 4.

Y6 Yanagitani, T., Yagi, H., and Yamazaki, H. (1998). Production of fine powder of yttrium aluminum garnet. JP-10-101411, 21 April 1998.

Y7 Yang, H. and Kim, Y.S. (2008). Energy transfer-based spectral properties of Tb-, Pr-, or Sm-codoped YAG:Ce nanocrystalline phosphors. *J. Lumin.* **128**: 1570–1576.

Y8 Yang, H., Zhang, L., Luo, D. et al. (2015). Optical properties of Ho:YAG and Ho:LuAG polycrystalline transparent ceramics. *Opt. Mater. Express* **5**: 142–148.

Y9 Yang, Z., Zhang, X., Yang, D. et al. (2016). Excellent transmittance induced phase transition and grain size modulation in lead free $(91\text{-}x)(K_{0.5}Na_{0.5})NbO_3\text{-}x LaBiO_3$ ceramics. *J. Am. Ceram. Soc.* **99**: 2055–2062.

Y10 Yariv, A. (1971). *Introduction to Optical Electronics*. Holt, Rinehart and Winston.

Y11 Yasuhara, R., Tokita, S., Kawanaka, J. et al. (2007). Cryogenic temperature characteristics of Verdet constant on terbium gallium garnet ceramics. *Opt. Express* **15**: 11255–11261.

Y12 Ye, Z.G. and Dong, M. (2000). Morphotropic domain structures and phase transitions in relaxor-based piezo-/ferroelectric (1-x)Pb$(Mg_{1/3}Nb_{2/3})O_3$-x$PbTiO_3$ single crystals. *J. Appl. Phys.* **87**: 2312–2319.

Y13 Yi, H., Mao, X., Zhou, G. et al. (2012). Crystal plane evolution of grain oriented alumina ceramics with high transparency. *Ceram. Int.* **38**: 5557–5561.

Y14 Yip, S. (1998). Nanocrystals: the strongest size. *Nature* **391**: 532–533.

Y15 Yi, X., Zhou, S., Chen, C. et al. (2014). Fabrication of Ce:YAG, Ce,Cr:YAG and Ce:YAG/Ce,Cr:YAG dual-layered composite phosphor ceramics for the application of the white LEDs. *Ceram. Int.* **40**: 7043–7047.

Y16 Yoldas, B.E. (1975). A transparent porous alumina. *Am. Ceram. Soc. Bull.* **54**: 286–288.

Y17 Yoon, K.J. and Kang, S.T. (1987). Densification of alumina ceramics containing MgO. *J. Am. Ceram. Soc.* **70**: C69–C70.

Y18 Yoshida, H., Morita, K., Kim, B.N. et al. (2011). Low temperature SPS sintering of yttria ceramics with ultrafine grain size. *J. Am. Ceram. Soc.* **94**: 3301–3307.

Y19 Yoshikawa, A., Boulon, G., Laversenne, L. et al. (2003). Growth and spectroscopic analysis of $Yb3^+$-doped YAG fiber single crystals. *J. Appl. Phys.* **94**: 5479–5483.

Z

Z1 Zamir, S. (2017). Solubility limit of Si in YAG at 1700 °C in vacuum. *J. Eur. Ceram. Soc.* **37**: 243–248.

Z2 Zerr, A., Miehe, G., Serghiou, G. et al. (1999). Synthesis of cubic silicon nitride. *Nature* **400**: 340–342.

Z3 Zhang, C., Zhang, X.Y., Wang, Q.P. et al. (2009). Diode-pumped Q-switched 946 nm Nd:YAG laser. *Laser Phys. Lett.* **6**: 521–525.

Z4 Zhang, J., Lu, T., Chang, X. et al. (2009). Related mechanism of transparency in $MgAl_2O_4$ nanoceramics prepared by sintering under high pressure and low temperature. *J. Phys. D: Appl. Phys.* **42**: 052002, 1–5.

Z5 Zhang, J., Meng, F., Todd, R.I., and Fu, Z. (2010). The nature of grain boundaries in alumina fabricated by fast sintering. *Scr. Mater.* **62**: 658–661.

Z6 Zhang, J., Wang, L., Jin, Y. et al. (2011). Energy transfer in YAG:Ce^{3+},Pr^{3+} and $CaMoO_4$:Sm^{3+}, Eu^{3+} phosphors. *J. Lumin.* **131**: 429–432.

Z7 Zhang, L., Zhou, T., Selim, F.A., and Chen, H. (2018). Single CaO accelerated densification and microstructure control of highly transparent YAG ceramic. *J. Am. Ceram. Soc.* **101**: 703–712.

Z8 Zhang, X., He, W., Yue, Y., and Zhang, Y. (2013). Influence of neodymium-doping on structure and properties of YAG. *CrystEngComm* **15**: 8029–8035.

Z9 Zhang, X., Liu, H., He, W. et al. (2004). Synthesis of monodisperse and spherical YAG powders by a mixed solvothermal method. *J. Alloys Compd.* **372**: 300–303.

Z10 Zhao, H., Sun, X., Zhang, J.M. et al. (2011). Lasing action and optical amplification in Nd^{3+} doped PLZT ceramics. *Opt. Express* **19**: 2965–2971.

Z11 Zhao, W., Anghel, S., Mancini, C. et al. (2011). Ce^{3+} dopant segregation in YAG optical ceramics. *Opt. Mater.* **33**: 684–687.

Z12 Zhao, W., Mancini, C., Amans, D. et al. (2010). Evidence of the inhomogeneous Ce^{3+} distribution across grain boundaries in Ce doped $(Gd,Y)_3Al_5O_{12}$ garnet optical ceramics. *Jap J. Appl. Phys.* **49**: 022602/1–6.

Z13 Zheng, Q.X., Li, B., Zhang, H.D. et al. (2009). Fabrication of YAG mono-dispersed particles with a novel combination method employing supercritical water process. *J. Supercrit. Fluids* **50**: 77–81.

Z14 Zheng, W.C., Fang, W., and Mei, Y. (2007). Optical spectra and spin Hamiltonian parameters for rhombic Zr^{3+} in YAG. *J. Appl. Phys.* **101**: 053911/1–3.

Z15 Zhou, D., Shi, Y., Xie, J. et al. (2009). Fabrication and luminescent properties of Nd^{3+}-doped Lu_2O_3 transparent ceramics by pressureless sintering. *J. Am. Ceram. Soc.* **92**: 2182–2187.

Z16 Zhou, J., Zhang, W., Huang, T. et al. (2011). Optical properties of Er,Yb co-doped YAG transparent ceramics. *Ceram. Int.* **37**: 513–519.

Z17 Zhou, T., Zhang, L., Li, Z. et al. (2017). Toward vacuum sintering of YAG transparent ceramic using divalent dopant as sintering aids: investigation of microstructural evolution and optical properties. *Ceram. Int.* **43**: 3140–3146.

Z18 Zhou, T., Zhang, L., Yang, H. et al. (2015). Effects of sintering aids on the transparency and conversion efficiency of Cr^{4+} ions in Cr: YAG transparent ceramics. *J. Am. Ceram. Soc.* **98**: 2459–2464.

Z19 Zhou, T., Zhang, L., Wei, S. et al. (2018). MgO assisted densification of highly transparent YAG ceramics and their microstructural evolution. *J. Eur. Ceram. Soc.* **38**: 687–693.

Z20 Zhou, Y., Chen, D., Tian, W., and Ji, Z. (2015). Impact of Eu^{3+} dopants on optical spectroscopy of Ce^{3+}:YAG-embedded transparent glass-ceramics. *J. Am. Ceram. Soc.* **98**: 2445–2450.

Z21 Zhu, C., Song, J., and Mei, B. (2016). Fabrication and optical characterization of CaF_2-SrF_2-NdF_3 transparent ceramic. *Mater. Lett.* **167**: 115–117.

Z22 Zhu, L.L., Park, Y.J., Gan, L. et al. (2017). Fabrication and characterization of highly transparent Y_2O_3 ceramics by hybrid sintering: a combination of hot-pressing and HIP treatment. *J. Eur. Ceram. Soc.* **38**: 3255–3260.

Z23 Zhu, Q.Q., Hu, W.W., Ju, L.C. et al. (2013). Synthesis of YAG:Eu^{2+} phosphor by a facile hydrogen iodide-assisted sol–gel method. *J. Am. Ceram. Soc.* **96**: 701–703.

Index

Transparent Ceramics: Materials, Engineering, and Applications, First Edition. Adrian Goldstein, Andreas Krell, and Zeev Burshtein.

d

e

f